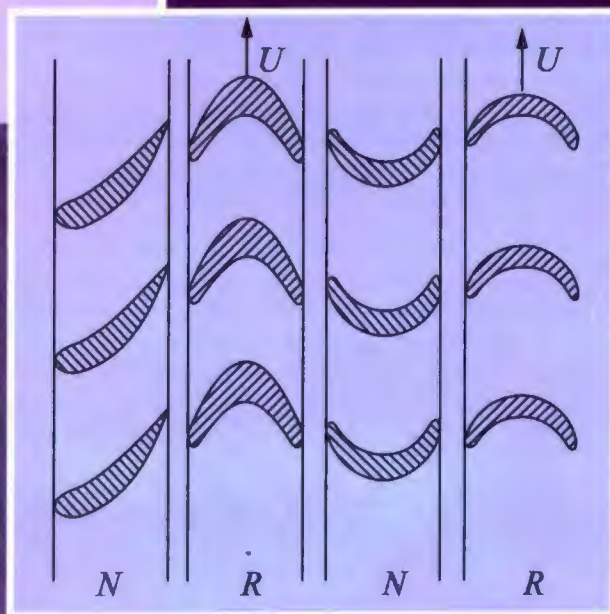


Circulation of this
edition outside
Indian subcontinent is
UNAUTHORIZED

Mechanics and Thermodynamics of Propulsion



Second Edition

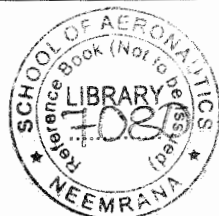
**Philip Hill
Carl Peterson**

ALWAYS LEARNING

PEARSON

SECOND EDITION

MECHANICS AND THERMODYNAMICS OF PROPULSION



PHILIP G. HILL
University of British Columbia

CARL R. PETERSON
Massachusetts Institute of Technology

PEARSON

Original Edition entitled *Mechanics And Thermodynamics Of Propulsion, Second Edition*, by Hill, Philip; Peterson, Carl, published by Pearson Education, Inc, publishing as Prentice Hall, Copyright © 1992.

Indian edition published by Dorling Kindersley India Pvt. Ltd. Copyright © 2010

All rights reserved. This book is sold subject to the condition that it shall not, by way of trade or otherwise, be lent, resold, hired out, or otherwise circulated without the publisher's prior written consent in any form of binding or cover other than that in which it is published and without a similar condition including this condition being imposed on the subsequent purchaser and without limiting the rights under copyright reserved above, no part of this publication may be reproduced, stored in or introduced into a retrieval system, or transmitted in any form or by any means (electronic, mechanical, photocopying, recording or otherwise), without the prior written permission of both the copyright owner and the above-mentioned publisher of this book.

ISBN 978-81-317-2951-9

First Impression, 2010

Nineteenth Impression, 2013

Twentieth Impression, 2014

This edition is manufactured in India and is authorized for sale only in India, Bangladesh, Bhutan, Pakistan, Nepal, Sri Lanka and the Maldives. Circulation of this edition outside of these territories is UNAUTHORIZED.

Published by Dorling Kindersley (India) Pvt. Ltd., licensees of Pearson Education in South Asia.

Head Office: 7th Floor, knowledge Boulevard, A-8(A) Sector-62, Noida (U.P) 201309, India

Registered Office: 11 Community Centre, Panchsheel Park, New Delhi 110 017, India.

Printed in India at Shree Maitrey Printech Pvt. Ltd., Noida

PREFACE

The basic premise of this book is that a few fundamental physical principles, rightly applied, can provide students of mechanical and aeronautical engineering with a deep understanding of all modes of aircraft and spacecraft propulsion. More—that they can lead directly to usefully quantitative assessments of performance; and still more—that they can illuminate possibilities for improvement. Doubtless, it is only at a fundamental level that one can properly address not only the questions of how and why things work but also the more challenging questions of why and how they can be improved.

It would not do, of course, to stress fundamental principles exclusively; only in application do the basic ideas really come alive to stimulate both analysis and invention. It is sometimes astonishing to see how a few basic ideas can reduce what would otherwise be an overwhelming mass of information into easily understood and manageable categories. Application of basic principles to specific engineering objectives can reward the student not only with a valuable appreciation of their practical significance but also with a much deeper understanding of the principles themselves.

The first edition of this book has been used by thousands of engineering students over the last twenty-five years, but it is now high time for a new edition. Not that the basic principles of propulsion have changed, but over this period the practical development of aircraft and spacecraft propulsion has been truly spectacular. The subject is now more richly interesting than it ever was before. It therefore seems appropriate to offer a new edition that can not only reflect on the great achievements of the recent past but also assess the reasons why we may yet expect great developments.

In preparing the second edition, one objective has been to provide a wide range of new illustrative material on modern aircraft and rocket engines. A second has been to present clearer explanations of pertinent physical phenomena. A third, to provide a much greater range of problem statements at the end of each chapter and a fourth, to introduce preliminary design procedures.

Today students have marvelous computers and graphics with which to calculate and display the implications of ideas that should control new designs. Realistic treatment of physical properties and mechanisms is quite easily possible within an appropriate time allotment. Hence this new edition encourages students, through design examples and problem statements, to consider the possibilities of preliminary design so as to identify physical possibilities and limitations as clearly as possible and to determine the consequences of uncertainty. This is not to say that in an introductory propulsion course one can use the complete Navier-Stokes equations to design turbomachinery, for example. But it does mean that the fluid mechanics of turbomachinery can be treated in realistic, albeit more approximate, simple ways that provide insight into how turbomachines work and how they can be designed.

Among the resources now available to students of propulsion are computer codes that they can use knowledgeably and critically to display the characteristics of specific important phenomena. One of these is the STANJAN code developed by W. C. Reynolds of Stanford University, for fast, versatile determination of the high-temperature equilibrium composition of combustion products. Treatment of boundary layer separation (which places such an important limitation on turbomachine behavior) is now quite easy, in the two-dimensional approximation, with the aid of a personal computer and the equations presented in the text. One can also readily use elementary computer procedures to take into account the effects of high-temperature variations on the specific heat of gases. Thus the power of the student to explore physical phenomena and design possibilities has in recent years been greatly enhanced.

The essentially difficult problem is that within a given course there is only so much time to take up new ideas. The book contains more than any one course can contain, so a choice must be made.

Part 1 of this text consists mainly of a review of those topics in thermodynamics, combustion, and fluid mechanics that are of vital importance to propulsion engines. One chapter reviews the thermodynamics of flow through control volumes with or without chemical reaction. Because of the prime significance of high-speed flows, a brief chapter is devoted entirely to review of compressible flows, Mach number, and shock waves. Because of the extremely important design limitation due to boundary layers, one chapter is concerned with boundary layer growth, separation, and heat transfer.

Part 2 of the text focuses on air-breathing turbine engines exclusively. First come analyses of propulsion efficiency, cycle performance, and the rationale for various types of turbine engines. This is followed by description and analysis of the ways in which successful flow behavior can be obtained in inlets, burners, and nozzles, then by detailed examination of the aerodynamics and performance of compressors and turbines. The development of high-flow-rate, high-efficiency compressors has for long been one of the most important challenges in turbine engine development, so these chapters present the topics of axial and centrifugal compressor (as well as turbine) aerodynamics in some depth. In each case the first section of the chapter deals mainly with the questions of why and how this

turbomachine works; the second, with the physical factors that limit its performance and with how these may be quantified; and the third, with a compact preliminary design procedure. The first section of each chapter would make a reasonably complete unit if there is no time to take up the second and third sections. (If one wishes to include both rockets and air-breathing engines in a one-term course, this kind of selection might be essential.)

Part 3 of the text is devoted to rocket propulsion. Chapter 10 presents an elementary treatment of rocket vehicle dynamics to demonstrate the significance of specific impulse and other variables and also to show how to decide on propulsion requirements for space missions. The latter requires some attention to the trajectories of space vehicles and the conditions under which the propulsion system may be optimized. Chemical rockets are the subject of Chapters 11, 12, and 13. Chapter 11 takes up those fundamental matters that govern the design and optimization of rocket nozzles; aerodynamics and heat transfer are two of the most important concerns. The next chapter analyzes the important features of liquid- and solid-propellant combustion. Key topics here include product mixture dissociation and equilibrium or nonequilibrium (or even two-phase) expansion processes. Chapter 13 focuses on the turbomachinery for a rocket vehicle and shows how one can make preliminary design decisions about system configuration, size, and speed for specified propellant flow rates and pressure rises.

Chapter 14 is devoted to the special feature of electrical propulsion, taking up fundamental considerations of why and how electrostatic, electrothermal, and electromagnetic propulsion can be used to best advantage.

A one-term course on rockets might consist of appropriate review of material in Chapters 2, 3, and 4 and a treatment of selected topics from Chapters 10 through 14.

A substantial effort has been made to improve the number and quality of problem statements at the end of each chapter. Objectives have been that each problem statement should refer to a substantial exercise that will illuminate an important question; that each problem should be doable (and that the average student should not be left baffled on how to start); that certain problem statements should, with guidance, take the student beyond what is clearly spelled out in the text; and that certain of them should be directed to preliminary design calculations feasible on a personal computer. However, no student should feel obliged to solve all the problems in a given chapter.

The mathematical portions of the text assume a knowledge of calculus, but mathematical complication has been minimized so that the reader can clearly discern physical principles. So much can be learned from steady-flow control volume analyses that these have been used again and again in the study of one- and two-dimensional compressible and incompressible viscous and inviscid flows.

To make the text as readable as possible, the equation sets derived for preliminary design have been relegated to the appendixes. The equations provided should be sufficient to allow exploration of many more design options than are specifically discussed in the text.

Referring back to the preparation of the first edition, the authors again would like to record our indebtedness to the late Edward S. Taylor, who was our teacher, critic, and friend during our years of association in the M.I.T. Gas Turbine Laboratory. We originally wrote the text largely as a result of his encouragement, and his influence will still be recognizable in some of the sections.

Throughout the text are several references to the work of J. H. Keenan and A. H. Shapiro. Their expositions of thermodynamics and fluid mechanics were so enlightening to us as students that they have heavily influenced our whole approach.

In the preparation of this second edition, the following people gave very helpful advice and encouragement: Alexander Bryans, Nicolas Cumpsty, John Denton, Edward Greitzer, Sir William Hawthorne, William Horne, Herbert Saravanamuttoo, George Serovy, and David Wilson, as well as the anonymous reviewers who pointed strongly and helpfully in the direction of needed improvements. I thank them all very much.

Claire Eatock, Bernie Gregoire, David Kenny, Joyce Lincoln, David Long, J. A. J. Rees, and Joe Stangeland helped greatly with provision of engine illustrations and data. They too deserve special thanks.

Marguerite, my wife, did the word processing and text assembly in such a skillful way that she transformed the whole task from difficulty to pleasure. But no acknowledgment could possibly state all that I owe to her.

Churchill College, Cambridge,

P. G. H.

CONTENTS

PART 1	Introduction and Review of Fundamental Sciences	1
Chapter 1	The Jet Propulsion Principle	3
1.1	Introduction	3
1.2	Fluid Momentum and Reaction Force	4
1.3	Rockets	8
1.4	Propellers	13
1.5	Turbojets, Turbofans, and Ramjets	16
	References	22
Chapter 2	Mechanics and Thermodynamics of Fluid Flow	23
2.1	Introduction	23
2.2	Fundamental Equations	24
2.3	Thermodynamics of Gases	32
2.4	Equilibrium Combustion Thermodynamics; Chemical Reactions	40
	Problems	56
	References	62
Chapter 3	Steady One-Dimensional Flow of a Perfect Gas	65
3.1	Introduction	65
3.2	General One-Dimensional Flow of a Perfect Gas	66
3.3	ISENTROPIC Flow	69
3.4	NONISENTROPIC Flow	72
3.5	Frictionless Constant-Area Flow with Stagnation Temperature Change	74
3.6	Constant-Area Flow with Friction	77
3.7	Shocks	83
	Problems	88
	References	92

Chapter 4	Boundary Layer Mechanics and Heat Transfer	93
4.1	Introduction	93
4.2	The Boundary Layer Equations	101
4.3	Laminar Boundary Layer Calculations	107
4.4	The Turbulent Boundary Layer	111
4.5	Boundary Layer Heat Transfer	124
	Problems	130
	References	137
PART 2	Air-Breathing Engines	139
Chapter 5	Thermodynamics of Aircraft Jet Engines	141
5.1	Introduction	141
5.2	Thrust and Efficiency	146
5.3	The Ramjet	155
5.4	Turbojet Engines	164
5.5	Turbofan Engines	177
5.6	Turboprop and Turboshaft Engines	189
5.7	Typical Engine Performance	196
5.8	Engine-Aircraft Matching	202
	Problems	208
	References	216
Chapter 6	Aerothermodynamics of Inlets, Combustors, and Nozzles	217
6.1	Introduction	217
6.2	Subsonic Inlets	218
6.3	Supersonic Inlets	226
6.4	Gas Turbine Combustors	242
6.5	Afterburners and Ramjet Combustors	257
6.6	Supersonic Combustion	262
6.7	Exhaust Nozzles	264
	Problems	269
	References	273
Chapter 7	Axial Compressors	275
7.1	Introduction	275
7.2	Angular Momentum	277
7.3	Work and Compression	282
7.4	Characteristic Performance of a Single Compressor Stage	288
7.5	Characteristic Performance of a Multistage Axial Compressor	294
7.6	Boundary Layer Limitations	303
7.7	Compressor Efficiency	319
7.8	Degree of Reaction	330
7.9	Radial Equilibrium	332

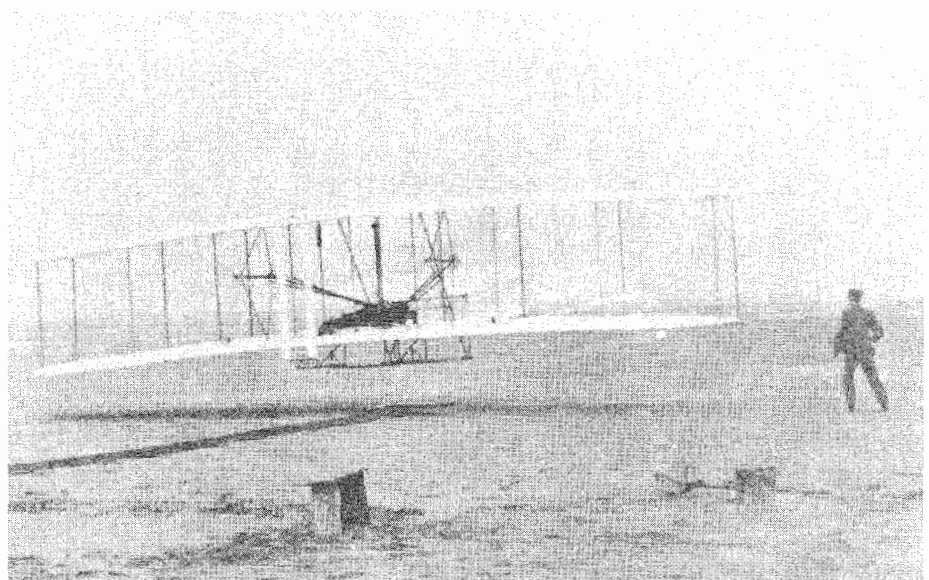
7.10	Design of a Subsonic Axial Compressor	336
7.11	Transonic Fan Stage	345
	Problems	355
	References	364
Chapter 8	Axial Turbines	367
8.1	Introduction	367
8.2	The Axial Turbine Stage	370
8.3	Stage Efficiency	377
8.4	Rotor Blade and Disc Stresses	384
8.5	Blade Cooling	393
8.6	Turbine Performance	400
8.7	Turbine and Compressor Matching	402
8.8	Turbine Stage Design	406
	Problems	414
	References	423
Chapter 9	The Centrifugal Compressor	425
9.1	Introduction	425
9.2	Centrifugal Compressor Stage Dynamics	427
9.3	The Inducer and Impeller	435
9.4	The Diffuser	445
9.5	Performance Characteristics	451
9.6	Centrifugal Compressor Stage Design	453
	Problems	460
	References	465
PART 3	Rocket Engines	467
Chapter 10	Performance of Rocket Vehicles	469
10.1	Introduction	469
10.2	Static Performance	470
10.3	Vehicle Acceleration	472
10.4	Chemical Rockets	478
10.5	Electrical Rocket Vehicles	490
10.6	Space Missions	495
	Problems	508
	References	512
Chapter 11	Chemical Rocket Thrust Chambers	513
11.1	Introduction	513
11.2	Performance Characteristics	515
11.3	Nozzles	520
11.4	Rocket Heat Transfer	541

11.5	Liquid-Propellant Rocket Performance Data Problems	559
	References	567
Chapter 12	Chemical Rocket Propellants: Combustion and Expansion	569
12.1	Introduction	569
12.2	Liquid Propellants	570
12.3	Equilibrium Composition	572
12.4	Nonequilibrium Expansion	578
12.5	Liquid-Propellant Combustion Chambers	581
12.6	Solid Propellants	589
12.7	Solid-Propellant Combustion Chambers	598
12.8	Combustion Instabilities Problems	606
	References	608
Chapter 13	Turbomachinery for Liquid-Propellant Rockets	615
13.1	Introduction	615
13.2	Centrifugal Pumps	621
13.3	Inducers and Axial Pumps	630
13.4	Axial Turbines Problems	640
	References	644
Chapter 14	Electrical Rocket Propulsion	651
14.1	Introduction	651
14.2	Electrostatic Propellant Acceleration	654
14.3	Bombardment Ionization	660
14.4	The Plane Diode	666
14.5	Electrostatic Thruster Performance	671
14.6	The Arcjet	674
14.7	The Pulsed-Magnetoplasma Accelerators Problems	679
	References	684
Appendix I	Conversion Factors and Physical Constants	689
Appendix II	Gases at Low Pressures	693
Appendix III	ICAO Standard Atmosphere	699
Appendix IV	Preliminary Design of a Subsonic Axial Compressor Stage	705
Appendix V	Preliminary Design of a Transonic Axial Compressor Stage	713

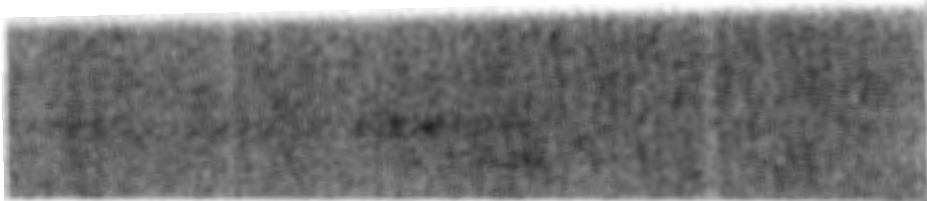
Appendix VI	Preliminary Design of an Axial Turbine Stage	717
Appendix VII	Preliminary Design of a Centrifugal Compressor Stage with Prewhirl	723
Appendix VIII	Optimization of Multistage Rockets	729
Appendix IX	Electrostatic and Electromagnetic Forces	733
Appendix X	List of Symbols	739
Answers to Selected Problems		743
Index		747

P A R T
1

INTRODUCTION AND REVIEW OF FUNDAMENTAL SCIENCES



Kitty Hawk, North Carolina, 1903: the world's first plane flight. The Wright brothers' famous flying machine was the first plane to lift a person into the air. Orville Wright took the first airplane ride, lying face downward on the lower wing of the biplane. His ride, which was only a few feet above the ground, lasted 12 seconds and covered 120 feet before running into the ground. (Photo courtesy Library of Congress and United Airlines.)



CHAPTER

1

THE JET PROPULSION PRINCIPLE

1.1 INTRODUCTION

The purpose of this chapter is to introduce the principle of jet propulsion and how it came to be understood and applied historically. Until jet and rocket propulsion became quite common, the jet propulsion principle had seemed mysterious. There had been much confusion on such questions as:

- Could a jet or rocket engine exert thrust while discharging into a vacuum (with no atmosphere to “push against”)?
- Could a rocket vehicle be propelled to a speed much higher than the speed at which the jet leaves the rocket nozzle?
- Could a rocket vehicle lift a payload far out into space?

Such questions have now been decisively answered by experiment, and the theory of jet propulsion (which may be said to have taken centuries to develop) is now so well established that today it seems accepted without question. Nevertheless, even today the theory deserves careful critical scrutiny because it is the foundation for understanding the behavior of real engines and their potential for improvement. The implications of the theory for various kinds of engines are given in some detail in successive chapters (though here we begin with an elementary explanation of how jet thrust is quantitatively related to fluid flow).

Within the framework of Newtonian mechanical and classical thermodynamics, the book aims to provide a unified explanation not only of how jet propulsion

devices work but also of why they have developed in certain ways and what the keys are to future development. An adequate understanding of both mechanics and thermodynamics is indispensable for the design and development of all kinds of jet propulsion engines.

Both rocket and aircraft engine design offer many examples in which it is economical to develop the best possible technology. This not only provides great incentive to the designer to use every possible means of making engines more powerful, efficient, durable, and safe; it also motivates the development of new technology and explains why in recent decades there have been huge improvements in design techniques as well as in materials and manufacturing. The computer has opened up wonderful possibilities for translating basic knowledge, and the results of test experience, into better designs. A study of what has happened and consideration of the reasons behind these developments can help us to see where future development is likely to be successful.

Before beginning a serious examination of any one type of propulsion device, it is logical to consider the characteristic features of the various kinds of rockets and turbine engines and why they have their own peculiar applications and limitations. For example: Chemical rockets being so powerful, why are they not used to propel large passenger aircraft? Why are other kinds of rockets more suitable than chemical ones for long journeys into space? Why is the conventional propeller limited but still the best choice in its characteristic application? Why is the turbojet engine decisively superior to the conventional propeller for high-speed flight? What about fan jets and ramjets? It seems in order in this chapter to respond to such questions with preliminary answers that will indicate the importance of the fluid dynamic and thermodynamic analyses to be presented later.

The chapter includes mention of future possibilities, not to prophesy, but to draw attention to topics on which work is already under way to develop the field of propulsion well into the twenty-first century. Because the chapter is introductory and rather approximate in its quantitative considerations, it bypasses some of the detailed logic that is examined with the help of problems attached to subsequent chapters.

1.2 FLUID MOMENTUM AND REACTIVE FORCE

An easy way to appreciate the idea of jet propulsion is to consider the tube shown in Fig. 1.1. Part (a) shows a closed tube of cross-sectional area A_i ; the internal pressure is p_0 and the external (ambient) pressure is p_a . The internal and external pressure forces in the x direction are clearly balanced, and no net thrust is exerted by the internal fluid or the external atmosphere on the tube. We suppose now that the right half of the tube is instantaneously removed at some time t_0 . Figure 1.1(b) shows the thrust \mathcal{T} that would be required at time $t_0 + dt$ to hold the left half of the tube stationary. At this instant of time fluid has not yet left the tube and the internal pressure on the left end is still p_0 . Balancing forces applied to the tube, the instantaneous thrust is

$$\mathcal{T} = A_i(p_0 - p_a)$$

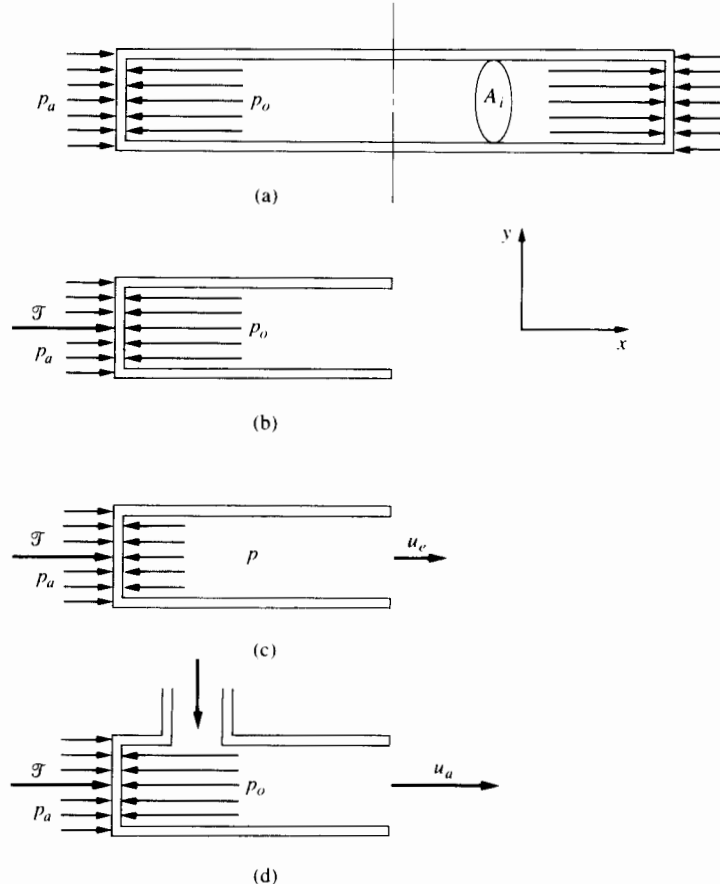


FIGURE 1.1 Jet propulsion. (a) Closed tube; no thrust. (b) Instantaneous thrust \mathcal{T} at the instant of sudden removal of right half of tube. (c) Transient thrust with jet exhaust but p still greater than p_a . (d) Steady-state thrust with sufficient air supply to maintain $p_0 > p_a$.

before a finite velocity has developed at the tube exit. After a small finite time increment, fluid instantaneously leaves the tube at exit velocity u_e , as shown in part (c), while the internal pressure on the left end drops to p . The thrust is now

$$\mathcal{T} = A_i(p - p_a)$$

and drops very rapidly to zero as $p \rightarrow p_a$.

Steady-state thrust could be generated, as shown in part (d), by supplying fluid (at the same rate as it leaves the tube) so that the internal pressure stays at p_0 and the thrust continues at

$$\mathcal{T} = A_i(p_0 - p_a).$$

These estimates ignore the effect of shearing forces the fluid exerts on the pipe wall (tending to reduce the thrust), but they illustrate the general idea that if we

know the internal and external distribution of pressure (and shear stress on the walls) of a thruster, we can calculate the thrust by summing the components of all forces exerted on all surfaces.

The difficulty with general application of this procedure is that the internal geometry of a thruster such as a turbojet is so complex that the estimation of thrust in this way would become unacceptably tedious. Fortunately, as we will see in Chapter 2, one can estimate the steady-state thrust in a much simpler way. Newton's laws (Chapter 2) can be used to show that, for the steady-flow thruster illustrated in Fig. 1.1(d), one can estimate the thrust by

$$\mathcal{T} = \dot{m} u_e,$$

in which \dot{m} is the rate at which mass flows out of the chamber and u_e is the mass-averaged exhaust velocity.

The existence of such an equation is plausible enough since we realize that a momentum flux can be created only by the application of a force. This equation, however, is true only if the pressure in the exhaust plane equals p_a , and if external shear forces are unimportant. (The more general case is discussed in Chapters 2 and 5.) Under such simplified conditions, one can see that, for a given exit momentum flux, the thrust is independent of the distribution of internal pressure and the details of internal geometry. It is also independent of the ambient pressure, p_a . Such an equation is directly applicable to a chemical rocket; here production of exit momentum flux in a nozzle follows combustion of a propellant stored in solid or liquid form on the vehicle and having no momentum, initially, with respect to the rocket nozzle.

If the rocket propellant burning is "nearly steady," the thrust can be roughly estimated by $\dot{m} u_e$ as before; if it is highly unsteady, then a more complicated expression is required, arising from the application of Newton's laws to a rapidly accelerating stream.

So far, we have discussed the application of thrust by a stationary "rocket." What if the rocket is moving rapidly? If it is traveling in a nearly straight line at nearly constant speed, then an observer traveling with the rocket (and measuring the exhaust velocity u_e relative to the rocket) would come up with the same thrust we have discussed already, namely, $\dot{m} u_e$. If the rocket itself were accelerating extremely rapidly, then dynamic corrections of this expression would be needed.

It is worth noting here that, for a given exit momentum flux relative to the rocket, the thrust is independent of the flight speed of the vehicle. Thus the vehicle can be propelled to a velocity much higher than u_e .

About two thousand years ago Hero of Alexandria demonstrated the idea of reactive thrust with his steam "turbine," imaginatively represented in Fig. 1.2. Steam generated by heating (possibly at a nearly steady rate), and at pressures appreciably greater than ambient, flowed tangentially through the nozzles and generated tangential thrust in each. A fundamentally sound explanation of how that thrust could be generated had to wait for the seventeenth century—for Newton and his formulation of the laws of dynamics. Alexander Pope, the com-



FIGURE 1.2 Artist's conception of the *aeolipile* of Hero of Alexandria.

poser of Newton's epitaph in Westminster Abbey, put it this way: "Nature and nature's laws lay hid in night. God said 'Let Newton be, and all was light.'"

It is notable, though, that Hero and many others—for example, the Chinese with their black-powder rockets dating back to the twelfth century—had demonstrated the reaction thrust principle long before Newton explained it. Thus the art of rocketry became established well before the underlying science. Such a situation has not been uncommon in the history of engineering. It has been said that the development of thermodynamics, for example, owed more to the steam engine than the steam engine to thermodynamics.

We should not, of course, discount the development of the basic science; it was only when the scientific principles were clearly expounded that rational design and development became possible. Sadly, this conclusion has not been appreciated by many a modern would-be inventor who, without the benefit of an adequate scientific understanding, has been willing to waste resources in a futile trial-and-error treatment of a fundamentally erroneous concept. The premise of this book is that science is absolutely needed for an adequate explanation of the field of propulsion—the ways things are and what might come to be.

The scientific soundness of a new development does not guarantee its success; the new invention has to be both needed and decisively advantageous. Furthermore, adequate materials have to be available to build it. The science may thus be said to be necessary, though not in itself sufficient. Many brilliant inventions have had to wait a long time for successful demonstration. The first patent for a gas turbine, for example, was granted in 1791 to John Barber in England [1]. At that time the materials, the design and manufacturing techniques, and the control methods needed to put the idea into a working machine were simply unavailable. It was only long after the steam turbine became a great commercial success that the necessary knowledge and materials could be exploited in solving the much more difficult practical problems of the gas turbine. Even in the 1930s these engineering problems were so difficult that many doubted they could be solved.

1.3 ROCKETS

The solid-propellant chemical rocket may be considered the oldest technical development in jet propulsion. In such a rocket the exit plane momentum is due to the flow of hot gas generated by rapid burning of a solid material that contains both the fuel and the oxidant necessary for combustion. The pressure of the gas inside the combustion chamber may or may not be steady during the combustion period.

Gunpowder appears to have emerged in China around A.D. 850 as an accidental result of the work of alchemists on its constituents—salmeter (potassium nitrate), sulfur, and charcoal. A formula for gunpowder was printed as early as A.D. 1044. Needham [2] reports that Chinese engineers “first made rockets fly... probably about 1150 A.D. or soon afterwards.” The first examples of rockets, called by their inventors “running rats,” probably each consisted of a bamboo tube filled with gunpowder; on ignition the products of combustion escaped at high speed through a small hole in one end of the tube. This caused the tube to shoot all over the floor, giving much pleasure at fireworks displays. It was not long before someone discovered that, fastened to a stick for flight stability, such a rocket could actually fly. The flying models were dubbed “meteoric running rats,” the new adjective brilliantly anticipating the age of true space flight.

Over a period of seven centuries or so, the Chinese, the Mongols, the Indians, and the Arabs did much trial-and-error development work on solid-propellant rockets for military use. In England, William Congreve developed solid-propellant rockets with a range of 3000 yards, which were used with dubious accuracy in the 1812 war between Britain and the United States and in other conflicts. By the end of the nineteenth century nonmilitary uses of solid-propellant rockets included whaling, signaling, and the transfer of lifelines between ships.

Apparently the desire to conquer space led to the most fruitful analytical thinking and subsequent experimental work on the potential for rocket vehicle propulsion. Though many were involved in one way or another, three pioneers—Ziolkovsky, Goddard, and Oberth—are credited with the main leadership in this new way of thinking [3].

Konstantin Ziolkovsky (1857–1935) was a quiet Russian schoolteacher who worked on the problem of how to send a vehicle into space. It was in his 1903 paper “Exploration of Space with Reactive Devices” (translated from Russian) that he showed how man could escape from the earth’s gravity field with a rocket. Ziolkovsky’s calculation led him to develop the idea of the multistage rocket (though Needham informs us that the Chinese had also developed multistaging). As early as 1903 he discussed the use of liquid oxygen and liquid hydrogen as propellants. Though his work was recognized to some extent in Russia, it was unknown elsewhere until after republication of his 1903 paper (with a German subtitle) in 1924, the year after the appearance of Oberth’s work, discussed below.

Robert Goddard (1882–1945) was a professor of physics at Clark University in Worcester, Massachusetts. In 1914 he was granted patents for the design of a rocket combustion-chamber nozzle and a propellant feed system and also for multistaging. His early experimental work began with black and smokeless powder

fuel, but he had seen the advantages of liquid propellant and realized that liquid hydrogen and liquid oxygen were an ideal combination for developing high jet velocity. In 1919 his most famous scholarly work, "A Method of Reaching Extreme Altitudes," was published by the Smithsonian Institute in Washington, D.C. It provided the mathematical analysis of methods not only of reaching high altitudes but also of traveling to the moon. His experimental work between 1920 and 1940 focused mainly on rockets using liquid-oxygen and gasoline propellants. He devoted much effort to thrust chamber development and to the turbomachinery needed for pumping the liquid propellants. He was granted some two hundred patents.

Herman Oberth was renowned for his work "The Rocket into Planetary Space" (translated from German), published in 1923. Oberth had been aware of Goddard's earlier publication but asserted that his own studies were quite independent of Goddard's work. Oberth's book also established the possibility of rocket journeys into space and included a proposed design as well as an assessment of the use of hydrogen and alcohol fuels. The book was very influential in Germany and was followed by a much longer edition, "The Road to Space Travel" (1929). The German Society for Space Travel was founded in 1927 and was associated with various demonstrations in which rockets were used to propel cars, a sled, and airplanes and also with experiments on liquid-oxygen and gasoline or alcohol rocket motors. This work was discontinued in 1934. Thereafter the German army began work at Peenemünde (under Walter Dornberger and Werner von Braun) on the liquid-oxygen and alcohol rocket motor that propelled the V-2 missile. At the same time France, Britain, Japan, the United States, and the Soviet Union were also heavily involved in both liquid and solid rocket development for military use.

For two decades rocket development was dominated by the race to build ever bigger and more destructive missiles. Then on October 4, 1957, a new era seemed about to begin, with the Soviet success in orbiting the first artificial satellite around the earth. Following this came the announcement by President John F. Kennedy in 1961 of a program to place a man on the moon within ten years. This effort was crowned with success only eight years later, when astronauts Neil Armstrong and Edwin Aldrin were able to visit the moon physically and return safely to earth.

Both liquid- and solid-propellant rockets have now reached high levels of performance (though not perfection). Their successes have been brilliantly demonstrated in many Apollo and space shuttle missions, for example. Occasional tragic failures have highlighted the design challenges necessary to guarantee safety as well as performance. The rapid exploitation of space for satellite communication systems has now introduced great incentive for the economic development of future rocket systems. (Putting a single satellite in space can cost 100 million dollars.) On the whole, chemical rocket systems have performed well. Since they can develop very large thrust per unit mass of rocket and have been of proven effectiveness in many applications, one may wonder why so much work continues to be devoted to alternatives.

The main reason for seeking alternatives to chemical rockets for vehicle propulsion is that with chemical rockets the thrust that can be developed per unit

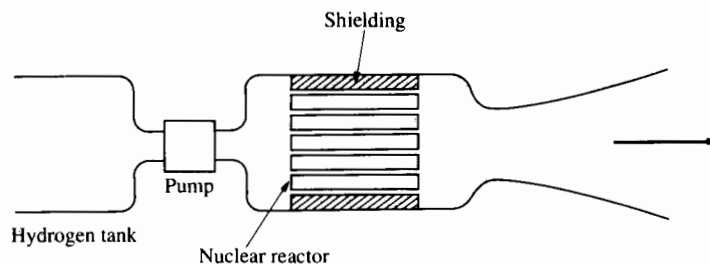


FIGURE 1.3 Rocket with nuclear heating of hydrogen propellant.

flow rate of propellant is strictly limited by the chemical energy of the propellant. This means that the mass of propellant that must be carried with the vehicle per unit impulse (thrust multiplied by time) is undesirably large for many missions. The higher the energy of the propellant, the higher its exhaust velocity and the lower its mass consumption rate for a given thrust. For various rocket vehicle missions, it would be desirable to have propellant energy very much greater than can be obtained with chemical rockets.

In principle, a nuclear propellant could provide orders-of-magnitude-higher fuel energy density. Discharge of radioactive material as propellant is of course unthinkable, but a relatively small amount of nuclear fuel could be used to supply energy to a hydrogen propellant. (Hydrogen would be a good choice of propellant in this case because, having the lowest molecular weight, it has the highest exhaust velocity for a given maximum temperature.) This concept (Fig. 1.3) has been seriously studied, but it too is subject to a physical limitation—this one associated with transfer of energy to the hydrogen from the nuclear fuel. If the heat has to pass through a solid wall, the maximum temperature of the hydrogen must be less than the maximum allowable temperature of the solid wall. One can expect this maximum to be much less than the temperatures typical of chemical propellant combustion. Hence, besides the difficulty of nuclear reactor control and recovery and of environmental protection, the nuclear heated-hydrogen rocket concept has not seemed to offer a strong performance advantage. Experiments have been conducted, but nuclear rockets have not yet been used for vehicle propulsion.

In contrast, much work has been done on electrical thrusters, and several types have been demonstrated in space vehicles, mainly at very low thrust levels and principally for the small impulses needed to reorient a satellite or to compensate for minuscule drag effects while in orbit. The most efficient use of electrical energy demonstrated to date has been in the electrostatic ion thruster (Fig. 1.4), in which atoms of mercury, xenon, or argon are ionized by electron bombardment. The ions so produced are accelerated to high velocity in a high-intensity electrostatic field. The energy added electrically (per unit mass) is typically 13 to 30 times as high as for chemical propellants. This means very much higher exhaust velocity and much less mass consumption per unit impulse imparted by the rocket to the vehicle.

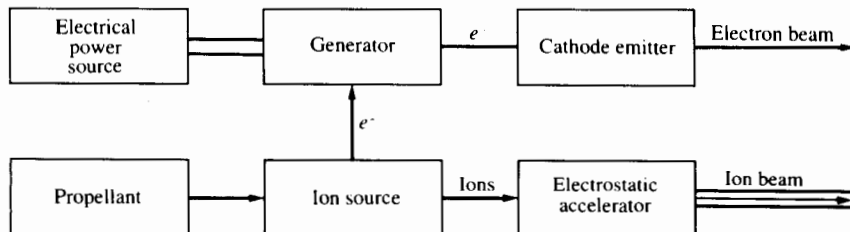


FIGURE 1.4 Electrostatic ion acceleration. Electrons and ions are accelerated to high velocity, but the more massive ions account for most of the thrust.

Other electrical rocket concepts include resistance heating and arc discharge heating, possibly with electromagnetic as well as pressure forces being used to accelerate the propellant. These concepts have now been demonstrated (again at very small thrust levels) with space vehicles. In early experiments, heating of rocket propellants by intense arc discharge has been associated with inefficient use of electrical energy and rapid erosion of the wall material. Nonetheless, on the assumption that such problems are solvable, arc discharge rockets are being considered for the range of propellant energies lying between the maximum for chemical rockets and the range at which ion accelerators perform most efficiently.

The great problem with electrical rockets, especially if large ones are to be used, is how to provide large amounts of electrical power to a space vehicle. Batteries with the capacity to supply large amounts of energy without recharging would be unacceptably massive. If the power plant must be located on the vehicle, there will be a serious mass penalty due to the power plant itself. If the power plant could be located on earth and its output beamed to the space vehicle with microwaves, most of this mass penalty could be avoided. The concept appears physically possible, but its practical feasibility remains to be proved, and most of the thinking on this subject to date has been concerned with on-board power generation.

Solar energy has been used with photovoltaic cells to generate electrical power for small electrical thrusters. Simple scale-up of such systems to very large size leads to an excessive mass penalty. With the best currently available solar cell technology, about 85% of the incident solar energy is not converted to electricity and must be radiated as waste heat. Adding to the problem, the radiator must be cooler than the maximum allowable photovoltaic cell temperature, perhaps 100 to 200° C. Since the radiation heat flux per unit area of radiation is proportional to the fourth power of the surface temperature, low radiator surface temperature means large surface area and massive structure per unit electrical power level. Figure 1.5 shows a schematic of a solar-thermal power system. Given the low power density of the incident solar energy (about 1.4 kW/m²), the mass of the solar cells and supporting structure will also be significant. Unfortunately, as the size of the system grows, the collector and radiator masses tend to increase with the cube of the typical linear dimension, whereas power level (proportional to surface area) will grow only with the square of that dimension. Thus the mass-

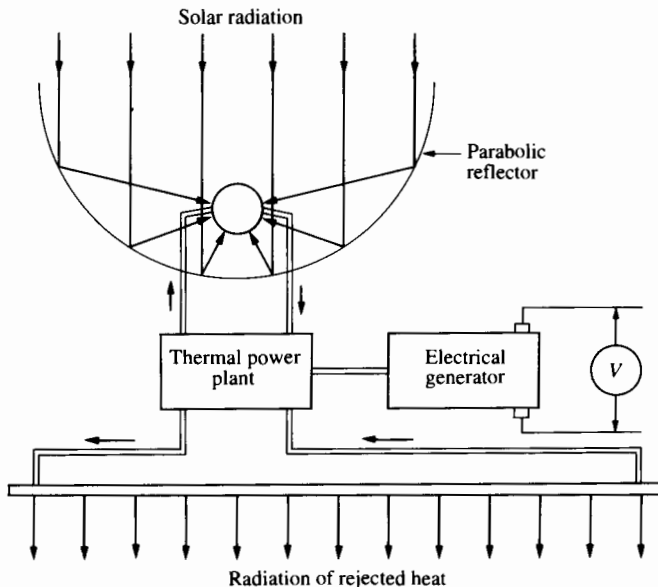


FIGURE 1.5 Solar-thermal power generation.

to-power ratio for solar systems will tend to increase with $\mathcal{P}^{1/2}$, in which \mathcal{P} is the electrical power level. The ratio would thus be 100 times higher for 10 MW of power than for 1 kW.

For any thermal-electric power system that must operate steadily in space, at large power levels the mass of the required radiator (per unit electrical power level) will tend to grow with $\mathcal{P}^{1/2}$. The penalty is especially severe with photovoltaics because of the low-radiator surface temperature (and because radiation heat flux per unit area will be proportional to T^4), and also because of low electrical conversion efficiency. In addition, solar systems have the same kind of penalty for the solar collector structure. Thus the outlook for use of solar energy for very large electrical power generation on space vehicles is rather bleak.

The use of chemical fuels for space power generation does not appear sensible for cases in which the mass of fuel to be lifted into space is much larger than the mass of the electrical power plant, that is, for relatively long-duration missions at large power level. The use of chemical fuel in this case would cancel the inherent advantage of electrical rocket propulsion.

It is for these reasons that nuclear fuel is viewed as the most promising energy source for large-scale long-duration electrical power generation in space. Figure 1.6 shows in schematic form a nuclear-thermal power plant for space. Nuclear reactor mass is certainly a problem at small power levels (given a minimum required mass for nuclear radiation shielding material). However, the reactor mass per unit power level can decline sharply with power level (in the 100-kW-to-10-MW range), and the fuel mass per unit energy can be considered negligible. For nuclear-electric power cycles, possibly using a liquid metal such as potassium

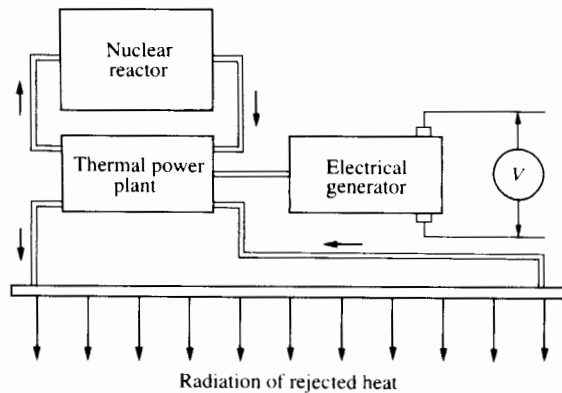


FIGURE 1.6 Nuclear-thermal power generation.

as working fluid, both cycle efficiency and radiator temperature could be much higher than with solar-electric power systems.

Suitable reactors for space nuclear-electric generation of large-scale power have not yet been built, but it is clear that system specific mass (kg/kW) will depend strongly on size and will reach a minimum total for reactor plus radiator at some high power level. The specific power will be a controlling factor in determining whether electrical propulsion is the best choice for a given mission for a given size of vehicle. Possible missions include transfer from low earth orbit to geosynchronous orbit (at which the satellite position relative to earth is fixed) or to missions deep into space.

If one takes the view that the development of space transportation systems is still in its infancy, one may expect that rocket propulsion has a long way to develop and that nuclear-electric propulsion for large-scale missions may have an important future. Whether or not this is so, one can certainly expect the search to continue for more economical systems for lifting massive loads from earth to near-earth or geosynchronous orbits.

1.4 PROPELLERS

For aircraft propulsion the big advantage of using a propeller rather than a rocket is that most of the propellant need not be carried on the vehicle. The rate of airflow through the propeller can be two to three orders of magnitude larger than the rate at which fuel is fed to its driving motor. Not having to carry so much propellant means that the aircraft can travel much greater distances before refueling. A second advantage is that much better propulsion efficiency is possible with a propeller than with a rocket. To show the importance of these advantages, we can resort to some simplified and approximate estimates (which will be considerably improved upon in succeeding chapters).

As Fig. 1.7 indicates, the task of the propeller is to accelerate an airstream passing through it from approach velocity u to exhaust velocity u_e . The propeller

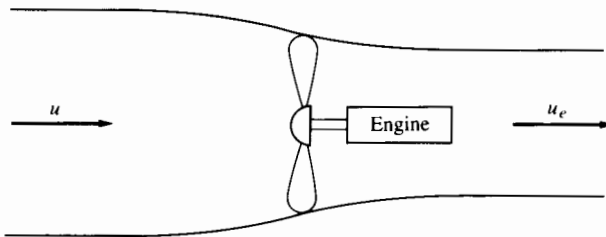


FIGURE 1.7 Acceleration of a stream tube of air through a propeller.

is operating in steady flow at moderate velocity so that the stream tube cross-sectional area drops as the stream accelerates during its passage through the propeller. Without worrying here about how the pressure forces are distributed on the propeller blades, we could show by a careful application of the general momentum equation (Chapter 2) that the thrust developed by the propeller is approximately

$$\mathcal{T} = \dot{m}_a(u_e - u),$$

where \dot{m}_a is the airflow rate through the propeller. The minimum possible energy added to the airstream in passing through the propeller is the change in kinetic energy. If the engine thermal efficiency is η_e (the ratio of shaft power to input chemical-energy consumption rate), the minimum possible fuel-energy consumption rate will be

$$\dot{E} = \frac{\dot{m}_a}{\eta_e} \left(\frac{u_e^2}{2} - \frac{u_a^2}{2} \right),$$

and thus the ratio of thrust to minimum possible fuel-energy consumption rate will be

$$\frac{\mathcal{T}}{\dot{E}} = \frac{2\eta_e}{u_e + u}.$$

A best value of η_e might be $2/5$. For positive thrust u_e must be greater than u , so that the maximum possible value of the thrust ratio for the propeller would be

$$\left(\frac{\mathcal{T}}{\dot{E}} \right)_{\text{propeller max}} \approx \frac{\eta_e}{u} \approx \frac{2}{5u},$$

in which u is the flight speed. For the chemical rocket we may write the thrust as

$$\mathcal{T} \approx \dot{m}_p u_{er}$$

and the minimum possible energy consumption as

$$\dot{E} \approx \dot{m}_p \frac{u_{er}^2}{2},$$

in which \dot{m}_p is the rate of propellant consumption and u_{er} is the rocket nozzle exhaust velocity. Most chemical rockets have appreciable unused thermal energy

in the exhaust, so the above estimate of \dot{E} is again a quite approximate value. Combining the equations, we may write

$$\left(\frac{\mathcal{T}}{\dot{E}}\right)_{\text{rocket}} \approx \frac{2}{u_{\text{cr}}}.$$

For the same (minimum) rate of chemical energy consumption, we can roughly estimate the ratio of propeller and rocket thrusts from the above as

$$\frac{\mathcal{T}_{\text{propeller}}}{\mathcal{T}_{\text{rocket}}} \approx \frac{u_{\text{cr}}}{5u}.$$

For maximum propulsion effect, chemical rockets have high exhaust velocity; 5000 m/s is not out of reach for a hydrogen-oxygen rocket, as we will see in Chapter 11. Taking this value, we have

$$\frac{\mathcal{T}_{\text{propeller}}}{\mathcal{T}_{\text{rocket}}} \approx \frac{1000}{u},$$

in which u is the aircraft flight speed. Thus for a low-speed aircraft (say, 100 m/s or 360 km/h), the propeller would develop perhaps 10 times the thrust (per unit energy consumption rate) of the rocket. Using ambient air as most of its "propellant," the propeller has the advantage that it can adjust to minimize the wastage of kinetic energy while propelling a vehicle at a given speed. With exhaust velocity fixed at a high value (to minimize wastage of thermal energy), the rocket would inevitably waste a great deal of kinetic energy in propelling a low-speed vehicle.

Figure 1.8 shows typical velocities at the tip of an aircraft propeller blade. Here again, the velocity of the air approaching the propeller is u , parallel to the

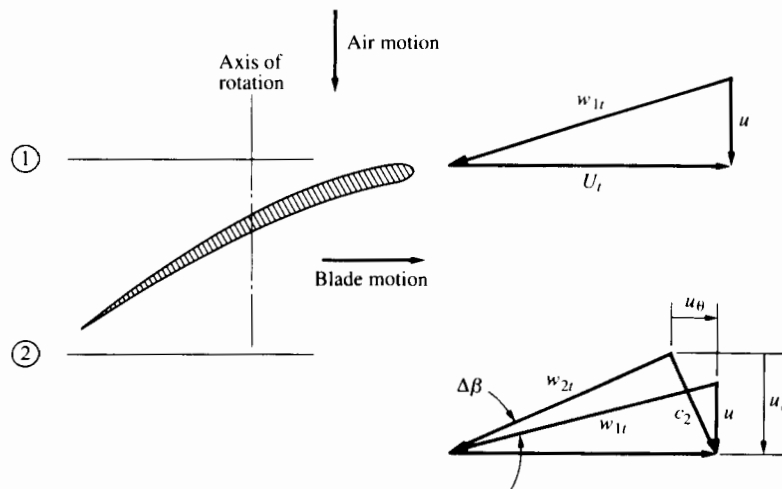


FIGURE 1.8 Velocities at the tip radius of a propeller blade. U_t is the blade speed, u is the air approach velocity, and u_e is the axial component of the leaving velocity (see Fig. 1-7). The swirling velocity component of the air leaving the propeller is u_θ ; w_{1t} and w_{2t} are the velocities relative to the blade—approaching and leaving, respectively.

axis of rotation and as seen by an observer on board the aircraft. Leaving the propeller, the component of velocity parallel to the axis of rotation is u_e , somewhat larger than u and accompanied by a swirling velocity component u_θ , which, as we will see, is a necessary result of the torque applied by the propeller to the airstream. The propeller tip speed is U_t , so that the approach velocity of the air relative to the blade is w_{1t} , the vector difference between u and U_t .

To maintain good flow over the blade, two conditions must generally be fulfilled:

1. The turning angle $\Delta\beta$ must be kept quite small; otherwise the flow will "separate" from the blade.
2. The relative approach velocity must not be too close to the speed of sound (to prevent shock waves from forming on the blade surface).

If these conditions are not satisfied, the fluid near the blade surface will not flow smoothly around the blade; instead, the flow pattern may become grossly disrupted with consequent loss of efficiency and with possibly intolerable generation of noise due to an unsteady disrupted flow field. Typically U_t is considerably larger than u for an aircraft propeller, and w_{1t} is maintained well below the speed of sound (which will be not much above 300 m/s). Thus conventional propellers have been used only for aircraft whose flight speeds are well below the speed of sound—commonly lower than 135 m/s or 300 mph.

The inherent efficiency of the propeller, relative not only to rockets but also to turbojets, has motivated much work in recent years to develop new propeller designs suitable for much higher flight speeds. A new generation of propellers has been developed, typically with many (8–12) blades specially adapted at the tip radius to accommodate transonic or supersonic relative velocities w_{1t} . Such blades are typically thin and flat (very little turning) and have highly rounded leading edges. These new designs have not entered commercial service but indicate that there is still potential for substantial development of aircraft propellers. Such developments will no doubt require deep understanding of the three-dimensional, viscous, transonic flow especially near the blade tip to determine the conditions under which the high-speed air will remain attached to the blade and excessive noise generation will be avoided. We will see, however, that this kind of knowledge is by no means needed uniquely for propeller design. It is needed for the best development of other kinds of turbomachinery for air-breathing engines.

1.5 TURBOJETS, TURBOFANS, AND RAMJETS

At 19 years of age in the year 1926, Frank Whittle was a Royal Air Force cadet at Cranwell, England, reflecting on the future of flight as he prepared a term paper. At that time the maximum speed of aircraft was around 150 mph, and 10,000 feet was the maximum flying altitude. Whittle reasoned that to improve efficiency, future aircraft would have to fly much faster and higher. At the same time he recognized the limitation of the propeller discussed earlier. He saw

that the rocket was not the answer and concluded that a new prime mover was needed—namely, a high-speed jet stream produced by a ducted fan. For some time he labored with the idea that the fan would have to be driven by a piston engine. But still thinking about the problem three years later, as a flying instructor, it occurred to him that the “fan” could be driven by a turbine if a combustor was placed in between, and the exhaust from the turbine could accelerate in a nozzle to form a high-speed jet. His idea met with a discouraging response from the experts. They knew that with the low levels of efficiency then typical of compressors, and the low temperature at which the turbine would have to be operated, the proposed engine would be unable to run. Nevertheless, on January 16, 1930, Whittle filed for patent protection, which was granted in 1933. In 1934 the RAF sent him to study mechanical engineering at Cambridge University, but there he found himself so short of cash and so discouraged that he decided he could not afford the five pounds sterling needed to keep the patent for his invention from lapsing. He persevered with his studies, however, and learned to his surprise that there were people who could raise the money for commercial development. As a result, a company called Power Jets was formed in March 1936 that set to work on the development of a new engine while Whittle was still finishing his degree program. After enormous technical, financial, and bureaucratic difficulties, Whittle was able to run the engine for 20 minutes at 16,000 rpm on June 30, 1939, in a demonstration that at last convinced the authorities that his concept was valid and worthy of substantial support. On May, 15, 1941, the first British jet aircraft, the Gloster Meteor, powered by the Whittle engine, flew from Cranwell in Lincolnshire.

While this was going on in England, there was action also in Germany. In 1933 Hans von Ohain was a 23-year-old Ph.D. student working on his thesis in aerodynamics at Göttingen University. He disliked the noise and vibration of the heavily loaded aircraft engines of those days and concluded that a better engine was needed. With some basic reasoning and without any knowledge of Whittle’s work, he came to the concept of a compressor and turbine spinning on the same shaft. By 1934, with the help and ingenuity of Max Hahn, the mechanic who looked after his car, von Ohain had begun, at personal expense, to translate his preliminary design to hardware. Early tests showed that the combustor was severely deficient, but by April 1936 the planemaker Ernst Heinkel took von Ohain and Hahn into his company and gave them excellent resources. To make the combustion problem easier, they fueled the first engine prototype with hydrogen, and it started successfully for the first time in September 1937. Then development was pressed strongly forward until the first successful flight test on August 27, 1938 in a Heinkel He 178 test aircraft. Thus in both Germany and England the jet aircraft age began.

Introducing the turbine engine and the turbojet principle into aircraft propulsion led to a revolution in transportation:

- It made supersonic flight possible.
- It greatly reduced the costs of air travel.
- It contributed to a radical improvement in aircraft safety.

The reductions in cost were due partly to increasing flight speed and partly to the ability to build much larger airplanes. The turbine engine was able to develop much greater thrust per unit weight and per unit cross-sectional area than its piston engine counterpart. Also it proved to have a much lower maintenance cost. The increase in thrust per unit engine mass directly led to improved payload and range, while increased thrust per unit cross-sectional area reduced engine nacelle drag and made possible the huge thrusts per engine developed by the modern long-range "wide-body" passenger aircraft. (See Figs. 5.1 and 5.2 for the configuration of typical turbine engines. Turbojet, turbofan, and turboprop versions are shown, each with a compressor-turbine gas generator.)

Though the mass and size advantages of turbine engines were first demonstrated on turbojets, it was not long before they were also used to drive propellers—the turboprop combination—for medium-speed, moderate-size aircraft. The turboprop is characterized by high efficiency, but its limitation on flight speed is a serious disadvantage; so is the necessity for geared transmission between the propeller and engine shafts. The gearbox typically is massive and requires heavy development effort to ensure reliability and durability. The reason the gearbox is a necessity is that whereas the tip speeds of propeller and turbine must be comparable for stress reasons, the tip diameter of the propeller must be much larger than that of the turbine because the volumetric rate of flow must be much greater through the propeller than through the turbine. Also the flow passing through the propeller must travel smoothly around the turbine engine housing whose outer diameter is necessarily much smaller than the propeller tip diameter. For these reasons substantial speed reduction is necessary. The massiveness of the required gearbox becomes especially serious for large turboprop engines, and the largest turboprop engines built to date have much smaller thrust than the largest turbojet engines.

If, as mentioned earlier, new kinds of propeller blading could be developed (possibly with contrarotating rotors) that could provide efficient, quiet operation at flight Mach numbers approaching those of conventional jet aircraft, large reductions in fuel consumption would be possible. The reason for this lies in a fundamentally important feature of aircraft propulsion, which we will discuss below with the aid of some approximate equations. First, though, it is in order to mention why high-speed, even supersonic, flight is feasible for jet engines but not for propeller-driven aircraft.

In Chapter 7, we will see that the flow at the tip diameter of the first-stage compressor rotor inside a turbine engine is limited in allowable Mach number (and allowable turning angle) in somewhat the same way as the flow near the tip of the propeller blade shown in Fig. 1.8. But the great difference is that the flow velocity approaching the blade can be greatly reduced by the design of the duct at the entrance to the compressor. Thus a supersonic flight speed can be transformed, as shown in Chapter 7, to a speed (approaching the first compressor rotor) that will be low enough to avoid serious flow disruption due to shock waves near the rotor tip diameter (where the relative Mach number is highest). One of the great advances in turbine engine design in recent years has

been the development of compressor blading that will tolerate transonic Mach number relative to the blade tip. For both propeller and compressor tip diameter the problem is the same: how to control the flow pattern with a transonic or even supersonic flow. More progress has been made in recent years in this respect with compressor than with propeller blading, but the last chapter in this story has certainly not been written. One of the lessons that will emerge from Chapter 7 is that the limitations associated with these tip diameter flows directly affect the minimum size and mass of an engine required to produce a given thrust.

We turn now to a fundamental propulsion consideration for air-breathing engines. As indicated earlier (and in Chapter 5), the thrust of an air-breathing jet engine is approximately

$$\mathcal{T} \approx \dot{m}_a(u_e - u),$$

in which \dot{m}_a is the engine flow rate. This implies that the rate of fuel flow into the engine is much smaller than the airflow rate (typically it is on the order of 2%).

We could define the thermal efficiency η_t of the turbine engine as the ratio of the rate of creation of kinetic energy in the working fluid divided by the rate of consumption of chemical energy of the fuel, \dot{E} , so that

$$\dot{E} \approx \frac{\dot{m}_a}{\eta_t} \left(\frac{u_e^2}{2} - \frac{u^2}{2} \right).$$

Subsequently we will mention the dependence of thermal efficiency on engine design parameters (maximum pressure ratio and maximum temperature), but for now we take η_t as a given quantity and focus on the required chemical energy consumption. Eliminating the term u_e by using the thrust equation, we can transform the above energy equation to

$$\dot{E} \approx \frac{\mathcal{T}u}{2\eta_t} \left[\frac{\mathcal{T}}{\dot{m}_a u} + 2 \right].$$

From this we can see that for a given thrust \mathcal{T} , flight speed u , and engine thermal efficiency η_t , minimum energy consumption is associated with largest possible airflow through the propulsion unit. Going to the extreme, a propeller of infinite diameter could be associated with $\dot{m}_a \rightarrow \infty$ and require the least possible chemical energy consumption, namely $\dot{E} = \mathcal{T}u/\eta_t$. Such a case is unrealistic; however, it helps us understand why, in low-speed flight, the propeller engine can have much lower fuel consumption than the turbojet.

For the turbojet all the airflow passes through the core engine and is strictly limited by the fuel-air ratio required to make the turbine inlet temperature as high as possible (so that the thermal efficiency and the thrust per unit engine mass are not compromised). In contrast, the airflow through the propeller of a turboprop engine can be 25 to 50 times as high as the rate of airflow through the core engine. Thus for a given thrust and flight speed, the turboprop engine can have significantly lower fuel consumption than a turbojet.

The disadvantages, as mentioned earlier, of the turboprop are its flight speed limitation and (less serious) the typical gearbox problem. In this discussion the turbofan engine (which is shown schematically in Figs. 5.1 and 5.2) can be considered a very important compromise between turboprop and turbojet designs. The turbofan engine has a large internal “propeller” (fan) rotor that actuates an airflow bypassing the core engine flow and that is typically five to six times the airflow rate through the core engine. This design has several important features:

1. Because the fan (propeller) is enclosed in a duct, its aerodynamics can be satisfactorily controlled even with flight Mach numbers as high as 0.85.
2. It can have substantially lower fuel consumption than a turbojet (for a given thrust and flight speed) for two reasons:
 - a. The total airflow \dot{m}_a is much larger than for a turbojet engine of the same thrust.
 - b. The engine efficiency η_e (as defined above) can be appreciably higher for the turbofan than for the turbojet engine. The reason is that the work required to drive the fan must come from the turbine so that, with the fan installed, the nozzle exhaust temperature tends to be significantly lower than for the turbojet engine. This in turn means that energy losses due to unused thermal energy in the exhaust are significantly lower—hence higher η_e .
3. With turbofan engines having ratios of bypass airflow to core engine flow of 5 or 6:1, it has been possible to avoid using the gearbox described earlier as essential for typical turboprop engines. This subject is not, however, closed. Designers are currently weighing the advantages of still higher bypass ratio against the disadvantages of the gearbox that would probably be needed to ensure satisfactory matching of fan and core engine aerodynamics.

While the above could be considered a preliminary explanation of why the turbofan has become the engine of choice for high-speed (subsonic) commercial aircraft, we need to say something here about engine thermal efficiency and engine mass per unit thrust.

In Chapter 5, which treats engine thermodynamics in some detail, we will see that turbine inlet temperature has a very strong effect on both thermal efficiency and thrust per unit rate of airflow through the core engine. The latter essentially controls the size and mass of engine required for a given thrust. Generally, full optimization analyses show that turbine inlet temperatures should be as high as the turbine blades can tolerate. In recent years researchers have devoted huge efforts, with remarkably successful results, to the development of hollow blades continuously cooled by air taken from the compressor and emitted through small holes to form a sheath of cooling air on the blade surface. One measure of the success of efforts to date is that engines can now be designed to operate with turbine inlet temperatures as high as 1700 K even though the melting temperature of the alloy material of the blade may be as low as 1600 K.

Along with blade-cooling techniques, much successful effort has been concentrated on the metallurgy and fabrication of blades. One notable achievement has been the fabrication of single-crystal turbine blades, which, free of grain boundaries, show superior resistance to creep under high centrifugal stress at high temperatures. Work continues on the development of ceramic coating and even ceramic blading (possibly ceramic composites) in efforts to develop still-higher-temperature blading.

Another design parameter having a strong effect on both thermal efficiency and engine mass per unit thrust is the compressor pressure ratio. In Chapter 5 we examine the way in which pressure ratio affects engine performance for various engine configurations in the context of a general thermodynamic analysis. Not surprisingly (because of the ram compression due to flight speed) the optimum pressure ratio depends strongly on flight speed. Whereas a "best" value for a subsonic-speed aircraft engine might be as high as 30:1, the best value for a flight Mach number of 2 might be only 10:1 or 12:1. At a flight Mach number of 3.5–4, thermodynamic analysis indicates that the compressor is no longer needed; the most efficient engine is the ramjet.

The ramjet has the virtue of maximum simplicity, with no need for turbomachinery, and maximum tolerance to high-temperature operation and minimum-mass-per-unit thrust at suitable flight Mach numbers. The ramjet also has its limitations. As well as being generally incapable of steady operation at subsonic Mach numbers, it has an upper Mach number limit. For the conventional ramjet (in which the supersonic inlet air is slowed to subsonic speeds to provide stable subsonic combustion prior to the nozzle expansion), there is a limiting Mach number of about 6, above which the temperature of the air entering the combustor is so high that combustion cannot be completed. Most of the chemical energy of combustion is nonusefully transformed into dissociation reactions that on expansion do not provide the exhaust velocity needed for satisfactory ramjet performance. To avoid this problem, substantial research has been, and is still being, focused on the supersonic combustion ramjet (SCRAMJET). The difference between this and the conventional ramjet is that combustion is to take place in a supersonic stream. Fuel must be injected into the supersonic airstream (without causing disruptive shock waves) and must mix and burn in a millisecond or so. Conventional fuels do not ignite quickly enough, and gaseous hydrogen seems the most likely candidate. Design of the fuel injector is a formidable challenge; so is the problem of cooling a vehicle designed to operate at Mach numbers of 4 or higher. Hydrogen could conceivably serve for structural cooling as well as for engine fuel.

It will be clear from this discussion that future designs for supersonic (or even hypersonic) aircraft must cope with the design challenges of a whole range of flight Mach numbers. If air-breathing engines are to be used along with rockets to put payloads in orbit or to propel hypersonic aircraft, engine configuration will have to vary with flight Mach number. Many "hybrid" combinations of turbojets, turboramjets, ramjets, and rockets are in the research and conceptual-design stage.

All of this is in addition to providing ever more efficient, safe, and durable aircraft and space vehicle transportation for an entire range of existing missions. In the field of propulsion, there is no shortage of future challenges!

REFERENCES

1. Constant, Edward W., II. *The Origins of the Turbojet Revolution*. Baltimore: Johns Hopkins University Press, 1980.
2. Needham, Joseph. *Gunpowder as the Fourth Power, East and West*. Hong Kong: Hong Kong University Press, 1985.
3. von Braun, Werner, and Frederick Ordway II. *History of Rocketry and Space Travel*. London: Nelson, 1967.
4. Jones, Glyn. *The Jet Pioneers*. London: Methuen, 1989.

CHAPTER

2

MECHANICS AND THERMODYNAMICS OF FLUID FLOW

2.1 INTRODUCTION

An understanding of fluid mechanics and thermodynamics is perhaps the most important prerequisite for the study of propulsion. In nearly all the propulsion methods discussed in this volume, thrust is developed by imparting momentum to fluid streams. Most of the methods involve thermal effects in one way or another. The purpose of this chapter is to set forth a concise statement of the principles of mass, momentum, energy, and entropy in a form suited to the treatment of fluid streams.

We assume that the student is familiar with the first and second laws of thermodynamics and their corollaries as applied to ordinary nonreacting continuum substances in equilibrium. This chapter states these laws in the forms presented by Keenan [1,2] and followed by Van Wylen and Sonntag [3] as well as by many other authors. The control-volume method and the widely useful analyses of one-dimensional flow by Shapiro [4] provide an excellent framework for understanding the fluid mechanics of propulsion devices. Much of Chapter 3 concerns this framework; we review the control-volume concept here so that we can express the laws of thermodynamics and fluid mechanics in their most generally useful forms.

The concepts of *system* and *control volume*, as applied in this text, have specific meanings. The purpose of these concepts is the specification either of a definite collection of material or of a region in space that is to be analyzed.

System. A system is a collection of matter of fixed identity. It may be considered enclosed by an invisible, massless, flexible surface through which *no matter*

can pass. The boundary of the system may change position, size, and shape. The terms *system* and *control mass* have identical meaning.

Control volume. A control volume is a region of constant shape and size that is fixed in space relative to the observer. One can imagine an invisible, massless, rigid envelope (the control surface) enclosing the control volume. The control surface offers no resistance to the passage of mass and is arbitrarily located. Analyses we develop later will show that the most suitable location of a control surface in any particular problem is a matter of convenience.

Most problems may be treated by either system or control-volume analyses. However, the proper choice often leads to substantial simplification. For example, most fluid-flow problems, and especially steady flows, are much more conveniently handled in terms of an appropriately specified control volume.

The following discussions treat the fluids under consideration as *continua*. That is, we will ignore their atomic structure and will consider them as capable of being subdivided into infinitesimal pieces of identical structure. In this way it is legitimate to speak of the properties of a continuum—for example, density, pressure, velocity—as point properties.

2.2 FUNDAMENTAL EQUATIONS

Mass Conservation and the Continuity Equation

The law of mass conservation applied to a system simply requires that the mass of the system remain constant regardless of its size or shape, the number of pieces into which it is divided, and the length of the time interval during which it is observed (for “nonrelativistic” system velocities).

Here as in most cases, the physical law is stated as it applies to a system. This is inconvenient for the stationary observer of fluid flow. Such an observer is unable to measure continuously the behavior of a moving fluid particle (a small system) and must therefore be content with measurements taken at specific points in the space through which the fluid moves. The basic law must then be expressed in terms of the required relationships between fluid properties at various stationary points, that is, at points within a control volume.

Consider a general control volume defined within a region of fluid flow as shown in Fig. 2.1. The conservation of mass simply requires that the rate of change of mass stored within the control volume be equal to the net rate of inflow of mass:

$$\frac{d}{dt}m_{cv} = \dot{m}_{in} - \dot{m}_{out}, \quad (2.1)$$

where m_{cv} is the mass within the control volume and \dot{m} is the indicated mass flow rate. We can express these terms in more convenient analytical forms. Consider the mass flow through a small surface element dA on the control surface. If the

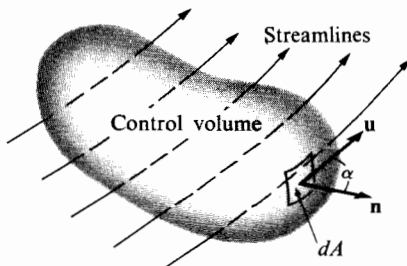


FIGURE 2.1 Fluid flow through a control volume.

local velocity is \mathbf{u} and a unit vector normal to dA is \mathbf{n} (outward pointing) as in Fig. 2.1, the elemental mass flow rate is

$$d\dot{m} = \rho |\mathbf{u}| \cos \alpha dA,$$

where ρ is the local density and α is the angle between \mathbf{u} and \mathbf{n} , the product $|\mathbf{u}| \cos \alpha$ being positive for outflow and negative for inflow. The mass within the control volume m_{cv} can be found by the integration

$$m_{cv} = \int_{cv} \rho dV,$$

where dV is a volume element and the integral extends throughout the control volume. Finally, writing the product $|\mathbf{u}| \cos \alpha$ as the usual *dot product* $\mathbf{u} \cdot \mathbf{n}$, we may express the *continuity equation* as

$$\frac{d}{dt} \int_{cv} \rho dV + \int_{cs} \rho \mathbf{u} \cdot \mathbf{n} dA = 0, \quad (2.2)$$

where the second integral extends over the entire control surface.

Newton's Second Law and the Momentum Equation

For a system of mass m acted on by a force \mathbf{F} , Newton's law requires that

$$\mathbf{F} = K \frac{d}{dt} (m \mathbf{u}),$$

where K is simply a proportionality constant whose numerical value depends entirely on the units selected for the three variables in the equation. It is possible to choose units of force, mass, length, and time such that K is unity, and we do so in all the following equations. In this text we use the S.I. (Système International d'Unités) international system of units, in which $K = 1$. Table 1 in Appendix I provides the conversion factors between SI and English units.

Since m by definition does not change with time for a system (or control mass), we might think at first of bringing m outside the derivative to write

$$\mathbf{F} = m \frac{d\mathbf{u}}{dt}.$$

This would be acceptable as long as we were concerned only with the velocity of the center of mass of the system. But if the velocity \mathbf{u} is quite nonuniform, it may be better to define the total momentum of the system as

$$\int_{\text{cm}} \rho \mathbf{u} dV,$$

where ρ and \mathbf{u} are the density and velocity of each system volume increment dV . The subscript cm with the integral sign denotes an instantaneous integration over the control mass. In this case the system (or control-mass) statement of Newton's law is

$$\mathbf{F} = \frac{d}{dt} \int_{\text{cm}} \rho \mathbf{u} dV. \quad (2.3)$$

In many propulsion problems—for example, ones in which we wish to relate the engine thrust to flow through an engine—a control-volume analysis is much more convenient to use than a control-mass one. In a derivation very similar to the preceding (see, for example, Chap. 1 of Ref. 4), the consequences of this system equation can be written for a control volume in the following vector equation form, where the notation is that of Fig. 2.1:

$$\sum \mathbf{F} = \frac{d}{dt} \int_{\text{cv}} \rho \mathbf{u} dV + \int_{\text{cs}} \rho \mathbf{u} (\mathbf{u} \cdot \mathbf{n}) dA. \quad (2.4)$$

The term $\sum \mathbf{F}$ is the vector sum of *all* forces acting on the material within the control volume. Forces may be one of two kinds: surface forces (stresses) and body forces. The two types of stress are pressure, which is a stress normal to the surface, and shear, which is a stress tangential to the surface. Body forces are those which are proportional to the mass or volume of the fluid and include gravitational, electrostatic, and electromagnetic forces.

In using Eq. (2.4), it is important to remember that $\sum \mathbf{F}$ is the sum of the forces applied to the control volume by its environment and that \mathbf{n} is the outward-facing normal vector at any point on its surface. The first integral on the right-hand side of (2.4) is simply the total (vector sum) of the momenta of all parts of the control volume at any one instant of time. The second integral can be shown to be the net rate of flow of momentum out of the control surface (outflow minus inflow). Thus we can say that the application of a set of forces to a control volume has two possible consequences: (a) changing the total momentum instantaneously contained within the control volume and (b) changing the net flow rate of momentum leaving the control volume.

Steady flow means that velocity, density, and so on, at any point in space do not change with time (though they may well vary from point to point in space). Thus for steady flow it follows that $\int_{\text{cv}} \rho \mathbf{u} dV$ cannot change with time, and the first term on the right-hand side of Eq. (2.4) disappears. This generally makes analysis much easier, since only a surface integral is required; it means that one can do a complete thermodynamic analysis by considering only the inputs and outputs of a control volume, not its contents. If one can convert an unsteady flow

problem to a steady one by moving the coordinate system of the observer, it is usually a good idea to do so.

The First Law of Thermodynamics and the Energy Equation

The first law of thermodynamics relates *heat* and *work* interactions between a system and its environment to changes in the state of the system. To avoid difficulty in applying this law, it is necessary to define each of these terms carefully. The following definitions are not the only acceptable ones, but they are the basis of the well-established method of expressing the principle of the first law that we use in this volume.

Heat. When two systems at different temperatures are brought together, an *interaction* occurs. This interaction is called *heat*. The mathematical sign of the heat is conveniently taken as positive for the lower-temperature (cold) system and negative for the higher-temperature (hot) system. It is common to speak of heat *transfer*, saying that heat transfers from the hotter system to the colder one. Thus heat transfer *to* a system is positive and *from* a system is negative. If we use this terminology, we must carefully avoid the implication that heat is a storable quantity. Heat exists only as a transfer process or interaction and *cannot be stored*. A process that does not involve a heat transfer is said to be *adiabatic*.

Work. A system is said to do work on its surroundings when the sole effect external to the system could be the rise of a weight in a gravitational field. Work done *by* a system on its surroundings is, by convention, positive; work done *on* a system by its surroundings is negative. Work, like heat, is an interaction between systems and is not a storable quantity. In general, the magnitude of the work depends on the motion of the observer.

We may state the first law of thermodynamics for a system in the form

$$Q = \Delta E_0 + W, \quad (2.5)$$

in which ΔE_0 denotes the change in internal energy of a system subjected to heat and work interactions Q and W , respectively.[†]

The internal energy, as its name suggests, is a property of the system. The first law in a sense defines this property except for an arbitrary datum value. Internal energy is a storable quantity, in contrast to heat and work, which may be considered energy transfers. The first law itself does not distinguish between heat and work; both contribute to changes in the internal energy. The second law, however, shows that they are fundamentally different.

[†] The notation throughout this text differs slightly from the more common fundamental texts in that it attempts to present a unified system for the several disciplines covered. E_0 (seldom used) refers to internal energy *including* kinetic and potential energies, whereas E refers to internal energy without these terms.

It is customary to treat separately those portions of E_0 due to motion (kinetic energy $mu^2/2$), to position in a gravitational field (potential energy mgz), to charge in an electrical field (electrical potential energy qV), and to other effects. For most ordinary fluid-mechanics problems, it is sufficient to consider kinetic and potential energies only and write, for a system of mass m ,

$$E_0 = E + m \frac{u^2}{2} + mgz, \quad (2.6)$$

where z is the height above some arbitrary datum and g is the (magnitude of the) local acceleration due to gravity. Further, for continua it is convenient to denote the values of E_0 and E per unit mass as e_0 and e , respectively. Using this and Eq. (2.6), we can write Eq. (2.3) as

$$Q = \Delta \int_{cm} \left(e + \frac{u^2}{2} + gz \right) \rho dV + W, \quad (2.7)$$

where \int_{cm} denotes integration throughout the entire control mass. To express the first law of thermodynamics for a control volume, it is often convenient to introduce heat and work transfer rates. We can transform Eq. (2.7) (see again Chap. 1 of Ref. 4) in the same way as Eqs. (2.2) and (2.4), with the result that

$$\int_{cs} \dot{\mathcal{Q}} dA = \frac{d}{dt} \int_{cv} (e_0 \rho) dV + \int_{cs} \left(h + \frac{u^2}{2} + gz \right) \rho (\mathbf{u} \cdot \mathbf{n}) dA + \mathcal{P}_s - \int_{cv} \mathbf{X} \cdot \mathbf{u} dV, \quad (2.8)$$

where $\dot{\mathcal{Q}}$ = local heat transfer rate (per unit time per unit area), positive *to* control volume,

$h = e + p/\rho$ = enthalpy of fluid,

\mathcal{P}_s = net "shear power" (work transfer rate), positive *from* control volume,

\mathbf{X} = body force per unit volume on fluid within control volume.

The shear power \mathcal{P}_s is that work done by the material within the control volume on the surroundings at control-surface points where both shear stress and material motion (parallel to the control surface) occur. Usually this term reduces to *shaft power* transmitted by shear stresses in rotating shafts. However, there are situations where the fluid may move along a control surface accompanied by a shear stress (at points within a boundary layer, for example). The last integral, which we will not often have to consider, represents work transfer via body forces. The dot product $\mathbf{X} \cdot \mathbf{u}$ is the rate (per unit volume) at which work is done *on* the fluid *by* the environment through body force \mathbf{X} (hence the negative sign preceding it).

It is instructive at this point to dwell on certain essential similarities of the continuity, momentum, and energy equations for a control volume. The common form of these equations may be seen by arranging them as follows:

Mass:
$$\frac{d}{dt} \int_{cv} \rho dV + \int_{cs} \rho (\mathbf{u} \cdot \mathbf{n}) dA = 0.$$

$$\text{Momentum: } \frac{d}{dt} \int_{cv} \rho \mathbf{u} dV + \int_{cs} \mathbf{u} \rho (\mathbf{u} \cdot \mathbf{n}) dA = \sum \mathbf{F}.$$

$$\begin{aligned} \text{Energy: } & \frac{d}{dt} \int_{cv} e_0 \rho dV + \int_{cs} e_0 \rho (\mathbf{u} \cdot \mathbf{n}) dA = \int_{cs} \dot{\mathcal{Q}} dA \\ & - \mathcal{P}_s + \int_{cv} \mathbf{X} \cdot \mathbf{u} dV - \int_{cs} p(\mathbf{u} \cdot \mathbf{n}) dA. \end{aligned}$$

In each equation the first term represents the rate of change of a certain quantity contained within the control volume. The second term is its rate of convection out of the control volume. The right-hand side of each equation may be called a production or source term. The zero on the right-hand side of the first equation means, of course, that mass can be neither produced nor destroyed. On the other hand, momentum can be brought into being by the application of force. Correspondingly, energy can be changed by heat transfer or work.

We will simplify these equations for application in the following chapters, usually by assuming steady flow and single inlet and outlet states, in which case the integrations become trivially easy.

To illustrate the use of these equations in a control-volume analysis, let us consider the generation of thrust by a stationary turbojet. Figure 2.2 shows the engine running steadily on a test stand. Air enters the inlet at a total mass flow rate \dot{m}_a and fuel at a rate \dot{m}_f . Since the flow is steady, there cannot be a continuous accumulation of fluid within the engine, and the rate at which the fluid exhausts from the engine must be $(\dot{m}_a + \dot{m}_f)$. The exhaust velocity is u_e , and the force necessary to balance engine thrust is T , as in Fig. 2.2.

To show how thrust depends on the properties of the jet, it is convenient to choose the control volume indicated in Fig. 2.2. Its surface intersects the exhaust jet in the plane of the nozzle, where the flow is nearly one-dimensional and the momentum flux can be measured more easily than at planes further downstream. The control surface extends far upstream of the engine and far from the floor on which it rests. Later we will select another control volume, simply to illustrate the

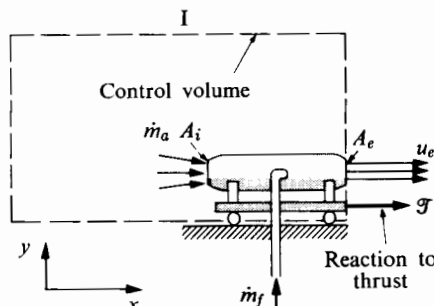


FIGURE 2.2 Stationary jet engine.

convenience of a suitable choice; but for now we proceed with the control volume of Fig. 2.2.

In applying Eq. (2.4) to this control volume, we confine our attention to those components of force and momentum parallel to the axis of the jet, so that we may write the momentum equation as

$$\sum F_x = \int_{cs} \rho u_x (\mathbf{u} \cdot \mathbf{n}) dA,$$

in which the subscript x denotes the direction indicated in Fig. 2.2. We have omitted the time-derivative term in Eq. (2.4) because the flow is steady.

No body forces act in the x -direction, so that the total x -force on the control volume is due to pressure distributed over its surface and the reaction to the thrust \mathcal{T} . We assume the fuel hose to be flexible, so that it does not transmit force to the control volume. We may consider the force \mathcal{T} to be a normal force on the plane where the control surface intersects the structural member that holds the engine stationary. The pressure forces always act normal to the control surface, so that only the pressure forces on the two ends of the rectangular surface of Fig. 2.2 contribute to the x -summation of forces. Further, we may consider the pressure on these surfaces to have the constant value p_a , except possibly in the exhaust plane of the jet. There it may have a different value p_e , if the jet is sonic or supersonic. Thus we can write the sum of the forces acting on the control volume in the x -direction as

$$\sum F_x = \mathcal{T} + A_e p_a - A_e p_e,$$

in which A_e is the nozzle exhaust area. We can evaluate the momentum flux integral simply by recognizing that the momentum flux is infinitesimal except in the exhaust plane of the jet. There the velocity is normal to the surface, so that

$$|\mathbf{u} \cdot \mathbf{n}| = u_x = u_e,$$

and the momentum flux integral is therefore

$$\int_{cs} \rho u_x (\mathbf{u} \cdot \mathbf{n}) dA = \int_{A_e} \rho_e u_e^2 dA,$$

in which ρ_e is the fluid density at the exhaust plane. Considering the flow in this plane to be uniform (i.e., one-dimensional), we may simplify the integral to $\rho_e u_e^2 A_e$. The mass flow rate at this plane is $\rho_e u_e A_e$, and this has already been shown to equal $(\dot{m}_a + \dot{m}_f)$. Thus the momentum flux from the engine is $(\dot{m}_a + \dot{m}_f)u_e$, and we may obtain the thrust from Eq. (2.4) as

$$\mathcal{T} = (\dot{m}_a + \dot{m}_f)u_e + A_e(p_e - p_a).$$

Consider now the alternative control volume III indicated in Fig. 2.3. If we assume the flow in the engine inlet plane to be approximately one-dimensional, with pressure p_i and velocity u_i , then by reasoning very similar to the foregoing we can establish from control volume III that

$$\mathcal{T} = (\dot{m}_a + \dot{m}_f)u_e - \dot{m}_a u_i + A_e(p_e - p_a) - A_i(p_i - p_a).$$

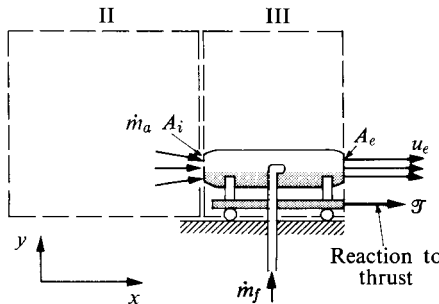


FIGURE 2.3 Stationary jet engine.

This thrust equation is of course not so convenient as the previous one, because it contains three additional terms: A_i , u_i , and p_i . Other choices of control volume could lead to even more inconvenient results.

We can easily show that the two thrust equations are equivalent, however. Using control volume II and Eq. (2.4) again, we can show in a similar way that

$$0 = \dot{m}_a u_i - A_i (p_a - p_i).$$

Using this equation, we can readily transform the second thrust equation to the first one.

The Second Law of Thermodynamics and the Entropy Equation

The second law of thermodynamics states that it is impossible for a system to describe a cyclic process (i.e., to go through a process and return to its original state) that produces work and exchanges heat with a single reservoir of uniform temperature. Although we will not use this statement directly, we will use several of its important corollaries. The absolute temperature scale that we will use is in fact based on this law [1]. Further, the second law permits the definition of the property entropy. For a system,

$$dS \equiv \left(\frac{dQ}{T} \right)_{rev}, \quad (2.9)$$

where dS is the change of entropy during a reversible heat exchange dQ at the temperature T . Keenan [1] and other thermodynamicists show how the second law itself may be used to specify the conditions which must be fulfilled if a process is to be reversible. For our purposes it is adequate to note that processes which involve any of the following are *not* reversible:

1. Friction,
2. Heat transfer with finite temperature gradient,
3. Mass transfer with finite concentration gradient,
4. Unrestrained expansion.

In general, irreversibility lessens the engineering usefulness of any given process. Though it may be impossible absolutely to eliminate irreversibility from any real process, its effects may often be substantially reduced in practical devices, so that a reversible process is the limit of possible performance. For any process one can show that

$$dS \geq \frac{dQ}{T}, \quad (2.10)$$

where the equality holds only for reversible processes. Thus if a process is reversible and adiabatic ($dQ = 0$), it must be *isentropic* ($dS = 0$), though the converse is not necessarily true. Finally, defining s as the entropy per unit mass of a continuum substance, we can write the control-volume form of Eq. (2.10) as

$$\int_{cs} \frac{\dot{Q} dA}{T} \leq \frac{d}{dt} \int_{cv} \rho s dV + \int_{cs} s \rho (\mathbf{u} \cdot \mathbf{n}) dA, \quad (2.11)$$

where again the equality holds only for reversible processes.

Equation (2.11) can be said to be the general and total requirement of the second law of thermodynamics for any control volume. To use it, we need to know how the entropy s is related to the directly measurable properties, such as pressure and temperature. We will discuss this in the next section.

The importance of Eq. (2.11) is that without it we could not specify the best possible performance of any propulsion engine or component thereof. Every time we use the term *efficiency* we are implying a comparison of actual and ideal performance. The efficiency of a turbine, for example, is the ratio of the actual work output to the maximum physically possible work output. We need Eq. (2.11) in order to calculate the ideal work. As a second example, suppose a new kind of propulsion engine is operating on an unusual fuel and producing actual thrust. The development engineer, in assessing possibilities for future improvement, will want to have some idea of how large the gap is between the actual and the best possible performance; if the gap is too narrow, further development effort may be wasteful. This means that the engineer will want to be able to evaluate the maximum thrust which that type of engine could possibly develop with this new fuel. Equation (2.11) or some form of it will be indispensable in making such a calculation. Calculating the ideal performance does not tell us how to redesign the engine. But if the gap between actual and ideal performance for the entire engine is very large, we may wish to compare ideal and actual performance for the engine components to see where there may be substantial possibilities for improvement. It is the second law of thermodynamics that provides a fundamentally sound method of comparing “actual” and “best possible.”

2.3 THERMODYNAMICS OF GASES

A pure substance may be defined, in the thermodynamic sense, as a substance that has only two independent static properties (in the absence of electricity, mag-

netism, and capillarity). Most engineering fluids, including gases such as oxygen, nitrogen, and vapors in equilibrium with their liquid phase, are pure substances.

Consider a small system composed of a pure substance in the absence of gravity and motion (of system relative to observer). If the properties are uniform throughout the system, the first law for an incremental change of state is

$$dq = de + dw,$$

where q and w are the heat and work per unit mass, respectively. Suppose the system experiences a reversible process for which $dw = p dv$, in which v is the specific volume. Then, using Eq. (2.9), we write

$$Tds = de + p dv. \quad (2.12)$$

Although we derived this equation for a reversible process, it must also be true for irreversible ones, since there are only two independent static properties for a pure substance, and all the terms in this equation are properties. The entropy change ds depends only on the change in state of the system, which is fixed by the values of de and dv . The increment ds is therefore independent of the process required to produce the increments de and dv . Thus, with the specified restrictions, Eq. (2.12) must hold true for any process whose end states could possibly be connected by a process for which the work is $\int p dv$.

The solution of a thermodynamic problem involving pure substances must include sufficient information on the relationships between the properties of the substance. The existence of only two independent static properties greatly simplifies the presentation of this information. If it is given algebraically, the equations are known as the *equations of state* of the substance. Equations of state are merely statements of experimentally observed relationships. Often the empirical relationships cannot be conveniently reduced to equation form, and the equations of state must be represented by graphs or tables. Equations, graphs, or tables are available for the properties of fluids of common interest. One of the simplest of these is the perfect gas.

Perfect gas. Here we define a perfect gas by the following equation of state:

$$pv = RT, \quad (2.13)$$

in which p is the absolute pressure, v the volume per unit mass, T the absolute temperature, and R a constant called the gas constant. The gas constant depends only on the identity of the gas. More generally, we observe that

$$pv = \frac{\bar{R}}{\bar{M}} T, \quad (2.14)$$

in which \bar{M} is the molecular weight and \bar{R} is the universal gas constant that has the value

$$\begin{aligned} \bar{R} &= 8.3143 \text{ kJ/kmol} \cdot \text{K} \\ &= 1545.43 \text{ ft} \cdot \text{lb}_f/\text{°R} \cdot \text{lb-mole.} \end{aligned}$$

Most real gases have a large range of temperatures and pressures over which they obey Eq. (2.14) very closely. One can use the Maxwell equations to show [1] that the internal energy of any gas whose state can be so described depends only on temperature:

$$e = e(T).$$

Since the enthalpy h is defined by

$$h = e + pv,$$

Eq. (2.13) indicates that the enthalpy also depends only on temperature

$$h = h(T).$$

In this case we may describe the relationship between internal energy, enthalpy, and temperature by defining the “specific heats” at constant volume and temperature as follows (for a perfect gas):

$$c_v = \frac{de}{dT}, \quad c_p = \frac{dh}{dT}. \quad (2.15)$$

These terms are actually misnomers, since heat is not a storable quantity. Also, the internal energy and the enthalpy can change in the complete absence of heat.

Using the definition of enthalpy and Eq. (2.13), we have

$$dh = de + RdT.$$

The relations (2.15) show that for a perfect gas the specific heats must be related by

$$c_p = c_v + R. \quad (2.16)$$

Figure 2.4 shows typical variations with temperature of the specific heat of gases at constant pressure. Figure 2.5 illustrates the corresponding enthalpy–temperature

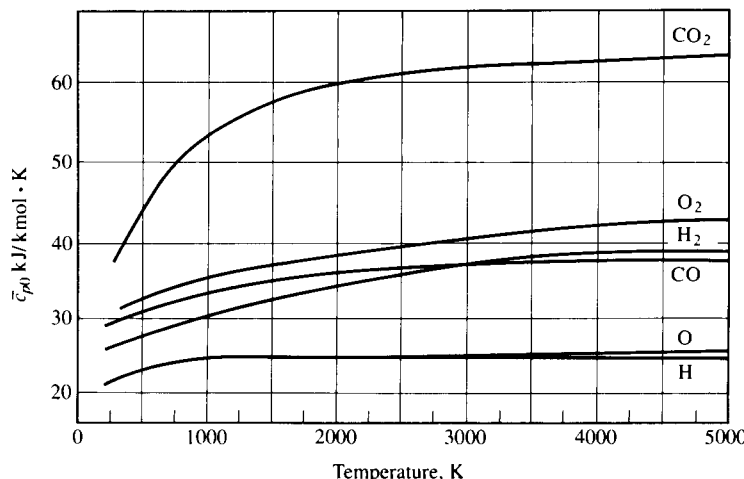


FIGURE 2.4 Specific heats of gases [5].

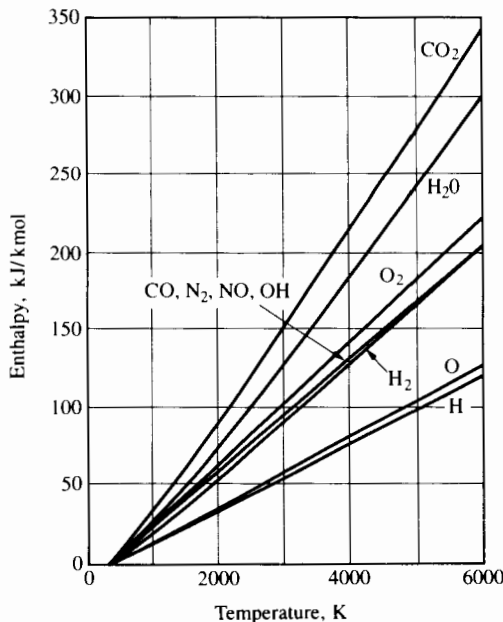


FIGURE 2.5 Enthalpy–temperature relationships for common gases [5].

dependence for a number of common gases where the zero has been arbitrarily set at 300 K.

Here we demonstrate two types of perfect-gas calculation.

Constant specific heats. Figure 2.4 shows that for a sufficiently small range in temperature it may be acceptable to approximate the specific heats by constants. Using the perfect-gas law, we may write Eq. (2.12) as follows:

$$ds = \frac{dh}{T} - \frac{dp}{\rho T}$$

or

$$ds = c_p \frac{dT}{T} - R \frac{dp}{p}. \quad (2.17)$$

For the particular case of constant specific heat and for an *isentropic* process, we can integrate Eq. (2.17), with the result that

$$\frac{p}{p_1} = \left(\frac{T}{T_1} \right)^{c_p/R}. \quad (2.18)$$

Defining the specific heat ratio γ ,

$$\gamma = \frac{c_p}{c_v},$$

and using Eq. (2.16), we may express Eq. (2.18) in the form

$$\frac{p}{p_1} = \left(\frac{T}{T_1} \right)^{\gamma(\gamma-1)}. \quad (2.19)$$

Using the perfect-gas law, we can transform this to

$$\frac{\rho}{\rho_1} = \left(\frac{T}{T_1} \right)^{1/(\gamma-1)} \quad (2.20)$$

or

$$\frac{p}{p_1} = \left(\frac{\rho}{\rho_1} \right)^\gamma, \quad (2.21)$$

in which $\rho = 1/v$ is the fluid density.

Variable specific heats. By defining a function ϕ according to

$$\phi = \int \frac{c_p dT}{T},$$

we can integrate Eq. (2.17) in the form

$$s - s_1 = \phi - \phi_1 - R \ln \frac{p}{p_1}, \quad (2.22)$$

in which the subscript 1 again denotes a reference value. The function ϕ depends only on temperature for a perfect gas and hence may be tabulated with the enthalpy against the temperature argument for each gas. If the process is isentropic, we can write Eq. (2.22) as

$$\frac{p}{p_1} = e^{(\phi-\phi_1)/R}.$$

For any given datum state 1, we can express this *isentropic* pressure ratio p_r by

$$p_r = \frac{p}{p_1} = e^{(\phi-\phi_1)/R} = \frac{e^{\phi/R}}{e^{\phi_1/R}},$$

which we can also tabulate as a function of temperature. Then if the temperature changes from any value T_A to another value T_B , we can find the isentropic pressure change from

$$\frac{p_B}{p_A} = \frac{p_r(T_B)}{p_r(T_A)},$$

for which we obtain $p_r(T_B)$ and $p_r(T_A)$ from tabulated functions.

We can designate the state of a gas having only two independent properties by a single point on a graph whose x - and y -axes correspond to any two properties. We can indicate a process between states by a line. The temperature–entropy diagram shown in Fig. 2.6 is an example of such a graph. The series of lines marked

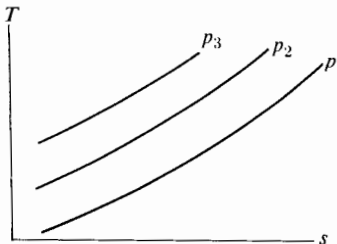


FIGURE 2.6 Constant-pressure lines on a T - s diagram.

with various pressures correspond to possible constant-pressure processes. We can obtain the shape of each line from Eq. (2.17),

$$\left(\frac{\partial T}{\partial s} \right)_p = \frac{T}{c_p}.$$

From this it is clear that the lines have positive slopes, increasing with temperature. Further, if c_p is a function of T only, the slope of the curve is a function of T only. Hence the curves are of the same shape displaced horizontally.

From Eq. (2.17) it is also clear that

$$\left(\frac{\partial p}{\partial T} \right)_s = \frac{c_p}{R} \frac{p}{T}.$$

Since this derivative is always positive, the upper curves represent higher values of pressure.

These relationships show how changes in entropy are related to changes in pressure and temperature for ideal gases. Even though the specific heat varies with temperature, it may be satisfactory for some purposes to use an average value for the specific heat c_p (and thus the specific heat ratio γ in Eqs. (2.20) and (2.21) for isentropic processes). For nonisentropic processes and constant specific heat, Eq. (2.17) becomes

$$s + s_1 = c_p \ln \frac{T}{T_1} + R \ln \frac{p}{p_1}.$$

To estimate entropy changes accurately over a wide temperature interval, one must use a relationship of the form of Eq. (2.22). The ideal-gas specific-heat variation with temperature is tabulated for many gases in the JANAF tables [5]. The gas tables [6] tabulate $h(T)$, $e(T)$, $p_r(T)$, and $\phi(T)$ for the following gases: air, products of combustion of hydrocarbon fuels with air (various fuel-air ratios), N_2 , O_2 , H_2O , CO_2 , H_2 , CO , and monatomic gases.

Table 1 in Appendix II provides $c_p(T)$ equations for N_2 , O_2 , H_2 , CO , OH , NO , H_2O , CO_2 , NO_2 , CH_4 , C_2H_4 , C_2H_6 , C_3H_8 , and C_4H_{10} . With these equations we can easily obtain the corresponding equations for $\phi(T)$ by integration. For other gases we can use the $c_p(T)$ data in the JANAF tables or other sources to fit equations of the typical forms of Table 1 of Appendix II and thence obtain corresponding ϕ functions.

In making calculations of isentropic or nonisentropic behavior of combustion gases, for example, one must determine the specific heat, enthalpy, and ϕ values for the appropriate mixture of gases. Next we review the thermodynamics of mixtures of gases.

Mixtures of Gases

The reactants and products of a chemical process each generally exist as a gaseous mixture of chemical compounds. One can determine the properties of the mixture from the properties of the constituents by using the *Gibbs-Dalton law*, which is expressed by Keenan [1] as follows:

1. The pressure of a mixture of gases is equal to the sum of the pressures of each constituent when each occupies alone the volume of the mixture at the temperature of the mixture.
2. The internal energy and the entropy of a mixture are equal, respectively, to the sums of the internal energies and the entropies of its constituents when each occupies alone the volume of the mixture at the temperature of the mixture.

Thus for a mixture of n constituents:

$$\text{Temperature} \quad T_m = T_1 = T_2 = \cdots = T_n, \quad (2.23a)$$

$$\text{Pressure} \quad p_m = p_1 + p_2 + p_3 + \cdots + p_n, \quad (2.23b)$$

$$\text{Volume} \quad \mathfrak{M}_m v_m = \mathfrak{M}_1 v_1 = \mathfrak{M}_2 v_2 = \cdots = \mathfrak{M}_n v_n, \quad (2.23c)$$

$$\text{Energy} \quad E_m = \mathfrak{M}_m e_m = \mathfrak{M}_1 e_1 + \mathfrak{M}_2 e_2 + \cdots + \mathfrak{M}_n e_n, \quad (2.23d)$$

$$\text{Entropy} \quad S_m = \mathfrak{M}_m s_m = \mathfrak{M}_1 s_1 + \mathfrak{M}_2 s_2 + \cdots + \mathfrak{M}_n s_n, \quad (2.23e)$$

$$\text{Enthalpy} \quad H_m = \mathfrak{M}_m h_m = \mathfrak{M}_1 h_1 + \mathfrak{M}_2 h_2 + \cdots + \mathfrak{M}_n h_n, \quad (2.23f)$$

in which \mathfrak{M} signifies mass, subscript m refers to the mixture, and subscripts 1, 2, ..., n refer to a series of constituents.

Since $de = c_v dT$, then

$$c_{vm} = \frac{\mathfrak{M}_1 c_{v1} + \mathfrak{M}_2 c_{v2} + \cdots + \mathfrak{M}_n c_{vn}}{\mathfrak{M}_m}. \quad (2.24)$$

Similarly,

$$c_{pm} = \frac{\mathfrak{M}_1 c_{p1} + \mathfrak{M}_2 c_{p2} + \cdots + \mathfrak{M}_n c_{pn}}{\mathfrak{M}_m}.$$

The pressures p_1, p_2, p_3 , and p_n that each constituent alone would exert in the volume of the mixture at the temperature of the mixture are called the *partial pressures* of each constituent. The partial pressure is related to the number of moles of a constituent present. For any constituent i ,

$$p_i v_i = R_i T_m$$

or, in terms of the universal gas constant \bar{R} ,

$$p_i v_i = \frac{\bar{R}}{\bar{M}_i} T_m,$$

where \bar{M}_i is the molecular weight of constituent i . Since

$$v_i = \frac{V_m}{\bar{M}_i},$$

$$p_i = \frac{\bar{M}_i \bar{R} T_m}{\bar{M}_i V_m} = n_i \frac{\bar{R} T_m}{V_m},$$

in which n_i is the *number of moles* of constituent i present in the mixture. Since, according to the Gibbs-Dalton law, the mixture pressure is the sum of the partial pressures,

$$\frac{p_i}{p_m} = \frac{n_i}{n_1 + n_2 + \cdots + n_n}. \quad (2.25)$$

Thus the ratio of the partial pressure to the mixture pressure is just the ratio of the number of moles of the constituent to the total number of moles. This ratio is called the *mole fraction*, X :

$$X_i = \frac{n_i}{n_1 + n_2 + \cdots + n_n}. \quad (2.26)$$

The entropy change of the mixture is the sum of the entropy changes of all the constituents, each behaving as though the other constituents were not there. Interestingly, during a process that is isentropic for the mixture, the constituents do not necessarily undergo isentropic changes. There is generally a redistribution of entropy among the constituents.

In determining partial pressures, it is convenient to use moles rather than unit masses. For this purpose one can define molar-specific heats by the equations

$$\bar{c}_p = \bar{M} c_p, \quad \bar{c}_v = \bar{M} c_v.$$

To avoid confusion the values per mole of a property are usually denoted with a bar, as

$$d\bar{h} = \bar{M} dh = \bar{c}_p dT.$$

We obtain the molar function $\bar{\phi}$ for a mixture of gases from

$$\bar{\phi} = \int \bar{c}_p \frac{dT}{T},$$

in which \bar{c}_p is the molar specific heat of the mixture. As for single-component gases, we can obtain the $p_r(T)$ function from

$$p_r = \frac{p}{p_1} = e^{(\bar{\phi} - \bar{\phi}_1)/\bar{R}}$$

with, as before, an arbitrarily chosen temperature for the evaluation of $\bar{\phi}_1$.

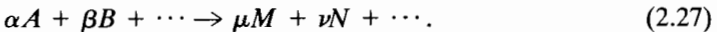
2.4 EQUILIBRIUM COMBUSTION THERMODYNAMICS; CHEMICAL REACTIONS

Up to this point we have not discussed thermodynamic processes in which system components change their chemical identity. Since combustion is of vital importance to many propulsion methods, it is necessary to show how thermodynamic laws govern chemical reactions. Fortunately we can simplify the discussion a great deal by adopting certain restrictions. First, chemical reactions of interest in propulsion systems nearly always occur between gases that can be closely approximated in behavior by a perfect gas. Second, with the exception of a few very rapid expansion processes, the important chemical processes usually take place between states that are approximately in equilibrium.

We may state the basic problem as follows: Given a mixture of gases capable of a chemical reaction and a set of conditions under which the reaction will occur, what will be the result of that chemical reaction? For example, one might be asked to determine the composition and temperature of the exhaust products of a constant-pressure adiabatic combustion process. To formulate methods for answering this kind of question, it is convenient to consider two separate topics: (a) chemical transformation and (b) composition of products.

Chemical Transformation

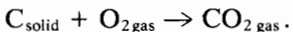
A general chemical reaction, in which α moles of reactant A and β moles of reactant B , and so on, combine to form μ moles of product M plus ν moles of product N , and so on, may be represented by



The coefficients α , β , and so on, are known from the mixture ratio of the reactants, and we may assume for the present that the product composition—that is, μ , ν , and so on—is also known.

Generally an exchange of energy with the surroundings accompanies a chemical reaction. Those reactions which tend to give off heat are called *exothermic*, and once started they will, under the proper conditions, proceed unaided. The other kind, called *endothermic*, require an energy input to proceed. Combustion processes, for instance, are exothermic.

One can determine the magnitude of these energy interactions from the composition and the heats of formation of the reactants and products. The constant-pressure heat of formation of a substance is the heat interaction that occurs when one mole of the substance is formed at constant pressure and temperature from its elements as they occur in nature. For example, the heat of formation of carbon dioxide (-393.522 kJ/gmol) is the heat interaction accompanying the following reaction from reactants to products at 298 K:



In this example, as in all exothermic reactions, the heat of formation is negative, since the system must give off heat to maintain (or return to) the reference temperature.

As another example, the formation of monatomic oxygen from naturally occurring oxygen is $\frac{1}{2}\text{O}_2 \rightarrow 0$. In this endothermic reaction the heat of formation (249.17 kJ/gmol at 298 K) is positive, since the heat transfer to the system must be positive.

One can determine these heat quantities experimentally with a simple constant-pressure container. Practically, it may be difficult to produce a reaction at constant temperature and pressure. It is not necessary, in any event, since from the standpoint of thermodynamics only the end states of the reaction are of interest. The intermediate conditions do not matter (although they may be important to the preservation of laboratory equipment).

A *steady-flow process* is another experimental method for determining the heat of reaction Q_f . Equation (2.8) states that, for a steady-flow process with no shaft work, the heat transfer of the fluid flowing through a control volume is equal to the change in enthalpy (neglecting changes in velocity and elevation). Thus

$$Q = \Delta H$$

or, per *mole* of product formed,

$$Q = Q_f = H_{\text{product}} - H_{\text{reactants}}. \quad (2.28)$$

For example, the formation of carbon dioxide in steady flow is represented by Fig. 2.7.

Table 2.1 gives the heats of formation for some common products of combustion, T_f being the reference temperature at which Q_f is measured. The heats of formation of naturally occurring elements are, by definition, zero.

In contrast, most common reactions are complex in the sense that the reactants are not naturally occurring elements and the products include more than one substance. Also, they do not generally occur at constant temperature. One can treat complex reactions as a combination of simpler reactions by the following method. Consider the steady-flow reaction indicated in Fig. 2.8, where Q is the heat interaction necessary to maintain constant temperature. It is convenient to consider this reaction to be the sum of distinct decomposition and formation reactions.

The decomposition reaction is just the reverse of the formation reaction; hence it is a simple one. However hypothetical the reverse process may be, the first law tells us that the decomposition heat interaction will be equal and oppo-

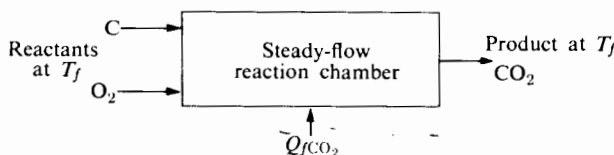


FIGURE 2.7 Schematic of steady-flow process for formation of CO_2 , with T_f being the reference temperature.

site to the formation heat interaction. Thus, summing over all the decomposition reactions, we obtain

$$Q_1 = - \sum_i (n_i Q_{fi})_{\text{reactants}}, \quad (2.29)$$

where n_i is the number of moles of reactant i and Q_{fi} is its heat of formation per mole.

Once the reactants are in elemental form, we may treat the remainder of the reaction as the sum of separate formations, so that

$$Q_2 = \sum_j (n_j Q_{fj})_{\text{products}}, \quad (2.30)$$

TABLE 2.1 Heats of formation (298.15 K)

Compound	Formula	Q_f , kJ/gmol	Reference number
Aluminum oxide	Al_2O_3	-1620.567 (l)	7
Ammonium nitrate	NH_4NO_3	-365.1	7
Ammonium perchlorate	NH_4ClO_4	-295.77 (s)	7
Aniline	$\text{C}_6\text{H}_5\text{NH}_2$	25.6	12
Boron	B_2	+ 829.7 (g)	5
Boron atom	B	+ 560 (g)	5
Bromine atom	Br	+ 111.86 (g)	5
Butane	C_4H_{10}	- 126.148 (g)	5
Carbon	C	+ 716.67 (g)	5
Carbon (graphite)	C	0 (s)	5
Carbon dioxide	CO_2	- 393.522 (g)	5
Carbon monoxide	CO	- 110.53 (g)	5
Dimethylhydrazine (unsymmetrical) (UDMH)	$(\text{CH}_3)_2\text{NNH}_2$	+ 53.28 (l)	8
Fluorine	F_2	0 (g)	5
Fluorine atom	F	+ 79.39 (g)	5
Hydrazine	N_2H_4	+ 50.2 (l)	8
Hydrazine hydrate	$\text{N}_2\text{H}_4\text{H}_2\text{O}$	- 43.1 (l)	
Hydrogen	H_2	0 (g)	5
Hydrogen atom	H	+ 217.999 (g)	5
Hydrogen bromide	HBr	- 36.44 (g)	5
Hydrogen fluoride	HF	- 272.546 (g)	5
Hydrogen peroxide	H_2O_2	- 136.106 (g)	5
Hydroxyl	OH	+ 39.463 (g)	5
JP-3	H/C 1.553	- 1.11 [†] (g)	10

(Continued)

[†]kJ/g in these cases.

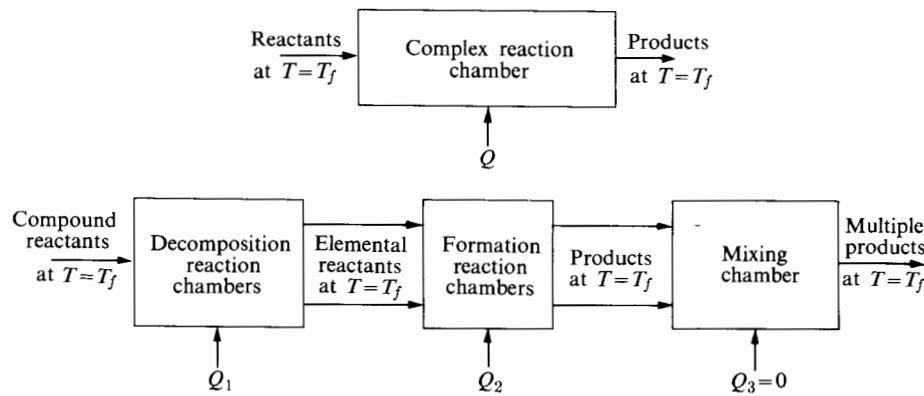


FIGURE 2.8 Schematic of complex reaction at constant temperature, showing equivalent elementary reactions.

TABLE 2.1 (Continued)

Compound	Formula	Q_f kJ/gmol	Reference number
JP-4	H/C 1.93	- 1.77 [†] (l)	11
Methane	CH ₄	- 74.873 (g)	5
Methyl alcohol	CH ₃ OH	- 201.07 (g) - 238.66 (l)	13 13
Monomethylhydrazine	CH ₃ NHNH ₂	+ 54.85 (l)	10
Nitric acid	HNO ₃	- 134.306 (g)	5
Nitric acid, red fuming	14% NO ₂ 1% H ₂ O	- 189.5 (l)	11
Nitric oxide	NO	90.291 (g)	5
Nitrogen	N ₂	0 (g)	5
Nitrogen atom	N	+ 472.68 (g)	5
Nitrogen dioxide	NO ₂	+ 33.10 (g)	5
Nitrogen pentoxide	N ₂ O ₅	+ 11.297 (g)	5
Nitrogen tetroxide	N ₂ O ₄	+ 9.08 (g)	5
Nitrogen trioxide	N ₂ O ₃	+ 82.843 (g)	5
Nitrous oxide	N ₂ O	+ 82.05 (g)	5
N-octane	C ₈ H ₁₈	- 208.447 (g) - 249.93 (l)	5 5
Oxygen	O ₂	0 (g) + 12.89 (l)	5
Oxygen atom	O	+ 249.17 (g)	5
Ozone	O ₃	+ 142.674 (g) + 126.8 (l)	5
Sulfur dioxide	SO ₂	- 296.9 (g)	7
Water	H ₂ O	- 241.827 (g)	5

where n_j is the number of moles of product j . Since the mixing process in the third chamber is adiabatic, the net heat interaction for the complex reaction at constant temperature T_f is

$$Q_R = Q_1 + Q_2 = \sum_j (n_j Q_{fj})_{\text{products}} - \sum_i (n_i Q_{fi})_{\text{reactants}}. \quad (2.31)$$

Also, using Eq. (2.28) we have

$$Q_R = H_{\text{products}} - H_{\text{reactants}} = \sum_j (n_j Q_{fj})_{\text{products}} - \sum_i (n_i Q_{fi})_{\text{reactants}}.$$

This difference in enthalpy is given the symbol H_{RPf} and may be interpreted as the change in enthalpy from products to reactants at the constant reference temperature T_f . Hence

$$H_{RPf} = H_{Pf} - H_{Rf} = \sum_j (n_j Q_{fj})_{\text{products}} - \sum_i (n_i Q_{fi})_{\text{reactants}}. \quad (2.32)$$

The value of H_{RPf} is tabulated for many common reactions, but if such a tabulation is not available for a particular reaction, one can calculate it from Eq. (2.32) and a table such as Table 2.1. Note that this calculation requires knowledge of the composition of the products.

If the products or reactants are not at the reference temperature T_f , we must somewhat modify the foregoing procedure. Hypothetically it is possible to bring the reactants to the reference temperature by heat transfer, allow the reaction to occur at constant temperature, and then bring the products to the final temperature by another heat transfer. Figure 2.9 indicates the required heat interactions.

We can express the net heat interaction from reactants at T_1 to products at T_2 as the sum of the three heat-transfer rates indicated in Fig. 2.9. Thus

$$Q = (H_{P2} - H_{Pf}) - (H_{R1} - H_{Rf}) + H_{RPf}. \quad (2.33)$$

Each of the parenthesized terms is a change in enthalpy from the actual state to the reference state (T_f) and may be calculated from tables of the mixture properties or by the methods of Section 2.3. The reference temperature T_f is simply that temperature for which the heat of reaction, H_{RPf} , is available.

Let us take a typical problem: We wish to determine the adiabatic flame temperature for a given reactant mixture. Once we know the product composition and determine the reference temperature, we can calculate H_{R1} , H_{Rf} , and

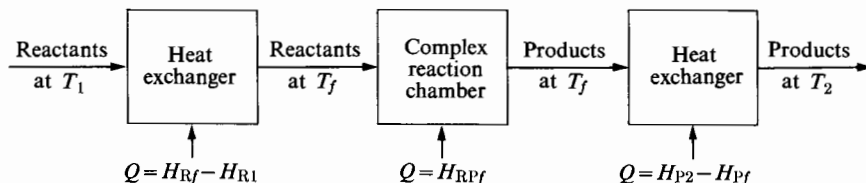


FIGURE 2.9 Reaction at variable temperatures.

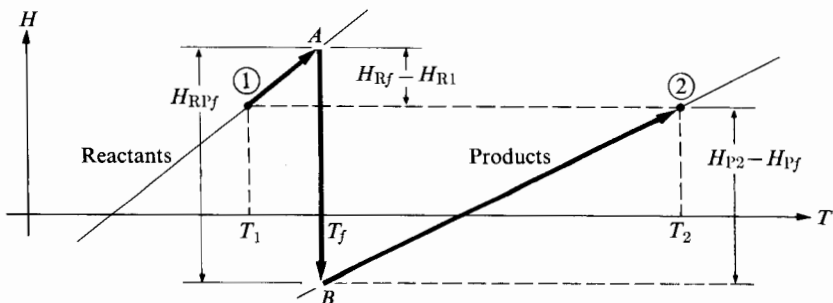


FIGURE 2.10 Enthalpy–temperature diagram for adiabatic combustion.

H_{RPf} . Then, since $Q = 0$, we can determine the product enthalpy H_{P2} , and from this the product temperature.

This can all be presented graphically on an enthalpy–temperature diagram that shows the relationship between enthalpy and temperature for both product and reactant mixtures. Figure 2.10 describes a hypothetical path of the process. The reactants at state ① are brought to T_f at state A, after which conversion to products occurs at constant temperature along line AB. Then the products are heated to the outlet state at ②, and T_2 is the outlet temperature. Since there is no net heat transfer in this particular example, H_{R1} must therefore equal H_{P2} , as may be seen by inserting the definition of H_{RPf} in Eq. (2.33) and setting Q equal to zero. From this diagram we can see that if the specific heats[†] of reactant and product mixtures are unequal, then the heat of reaction H_{RPf} must be a function of temperature.

Composition of Products

In all the aforementioned relationships, our calculations have depended on knowledge of the composition of the products of reaction. Once we know this composition, calculating the state of the product is a rather simple matter. However, determining the product composition is not always easy. The product composition depends on the temperature, which in turn has just been shown to depend on the composition. This suggests that we may need to use a trial-and-error procedure for the solution.

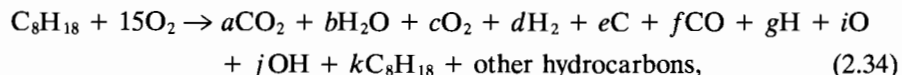
For certain reactions, it is relatively simple to determine product composition. For example, at sufficiently low temperature the combustion of a particular nonstoichiometric mixture of octane and oxygen yields the following products:



In this case we can easily determine the composition by requiring that the number of atoms of each element taking part in the reaction be constant.

[†] The specific heat of the mixture is given by the slope of its enthalpy–temperature curve in Fig. 2.10.

At high temperatures this expression may be a considerable oversimplification, because the compounds CO_2 , H_2O , and O_2 dissociate to some extent into free atoms and radicals. A more general statement is



where a , b , c , d , and so on, are the unknown numbers of moles of each substance. A reasonable first approximation may be made by recognizing that for all practical purposes C_8H_{18} and the “other hydrocarbon” molecules are present in negligible quantities. However, there are still nine unknowns— $a, b, c, d, e, f, g, i, j$ —for which we can obtain only three equations in terms of numbers of atoms. Atom balances yield:

$$\text{For carbon, } a + e + f = 8;$$

$$\text{For hydrogen, } 2b + 2d + g + j = 18;$$

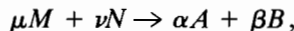
$$\text{For oxygen, } 2a + b + 2c + f + i + j = 30.$$

We need six more independent equations in order to determine the product composition. We can obtain them from the requirements for chemical equilibrium.

Chemical equilibrium. Consider a reaction in which a stoichiometric combination of A and B reacts to form products M and N with no A and B left:



At the same time this reaction is taking place, there is generally some tendency for the reverse reaction,



to occur, especially at high temperatures. Equilibrium is that state at which both forward and reverse reactions are occurring at equal rates. When equilibrium obtains, the concentrations of A , B , M , and N are constant. Using the second law of thermodynamics, we can express the conditions for equilibrium in algebraic form.

Suppose that an equilibrium mixture resulting from the combination of A and B is contained in a chamber that communicates through semipermeable membranes with each individual constituent substance in a pure form, as in Fig. 2.11. The entire apparatus is surrounded by a constant-temperature bath.

A semipermeable membrane is a hypothetical surface through which one substance may pass freely, though all others are prevented from passing. Such membranes are only approximated by certain real substances, but they are nevertheless useful analytical concepts. For example, in Fig. 2.11 substance A may pass freely into or out of the mixture at cylinder A , and the pressure of the pure A will be equal to the partial pressure of A in the mixture, whereas B , M , and N cannot pass through this membrane. Similarly, the membranes of cylinders B , M , and N admit only substances B , M , and N , respectively.

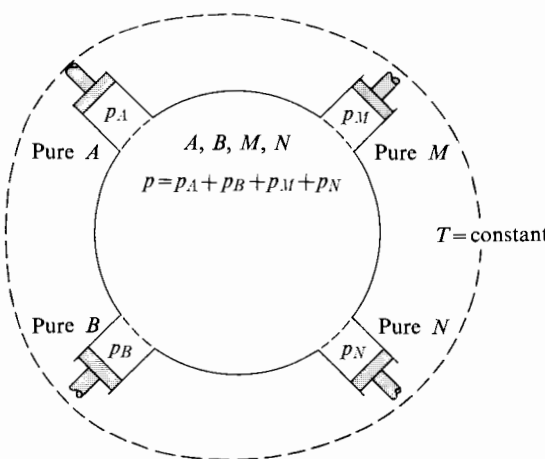
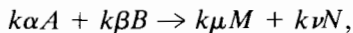


FIGURE 2.11 Reaction chamber for derivation of equilibrium constants.

The amount of any particular substance within the mixture chamber can be controlled by simply pushing or pulling on the piston in the cylinder containing the pure substance. This control process is reversible if done slowly.

Starting with an equilibrium mixture resulting from the combination of *A* and *B* in any proportion, consider the introduction of additional small amounts of *A* and *B* through the semipermeable membranes into the mixture chamber, in the stoichiometric ratio $k\alpha A + k\beta B$, where *k* is some small number. Once in contact within the main chamber, the *A* and *B* tend to react, forming *M* and *N*. There are two ways to restore the contents of the main chamber to their original condition. One is to withdraw from the chamber $k\alpha A + k\beta B$. The other is to withdraw $k\mu M + k\nu N$. In both cases the total number of atoms of each element in the chamber will have returned to its original value. After the mixture has again reached equilibrium, its composition will be restored to its former value. As a result of the reaction



there will be a heat interaction of magnitude kH_{RP} with the constant-temperature bath surrounding the apparatus, since the reaction occurs at the constant temperature *T* of the bath. In the limit this heat interaction will be reversible. Then, for a system composed of all the gases in the mixture and in the cylinders,

$$dS = \left(\frac{dQ}{T} \right)_{rev} = \frac{kH_{RP}}{T}.$$

For perfect gases it may be shown that H_{RP} is a function of temperature only. Thus for a given value of *k* the change in entropy of the system is a function of temperature only: $dS = kf(T)$.

Since the temperature, volume, mass, and composition of the mixture do not change, there will be no change of state of the system in the mixture chamber. Thus

$$dS_{\text{mixture}} = 0.$$

In addition, the partial pressure of each constituent does not change, and hence the pressure in each cylinder does not change. Since the temperature is also constant in each cylinder, the entropy *per mole* of each pure substance must be constant, and we may write the change in entropy within the cylinders as follows:

$$\begin{aligned} dS_A &= -k\alpha\bar{S}_A, & dS_M &= +k\mu\bar{S}_M, \\ dS_B &= -k\beta\bar{S}_B, & dS_N &= +k\nu\bar{S}_N, \end{aligned}$$

where \bar{S} is the entropy per mole of pure substance.

The total entropy change is equal to the sum of the changes in the mixture chamber and in the cylinders:

$$dS = -k\alpha\bar{S}_A - k\beta\bar{S}_B + k\mu\bar{S}_M + k\nu\bar{S}_N = k \frac{H_{\text{RP}}}{T}$$

or

$$\alpha\bar{S}_A + \beta\bar{S}_B - \mu\bar{S}_M - \nu\bar{S}_N = -\frac{H_{\text{RP}}}{T} = f(T). \quad (2.36)$$

We can obtain the entropy of a perfect gas *per mole* by integrating Eq. (2.17) with the result:

$$\bar{S} = -\bar{R} \ln p + \int_{T_1}^T \bar{c}_p \frac{dT}{T} + \bar{R} \ln p_1,$$

where the subscript 1 refers to an arbitrary datum state. Thus, for a given datum state, we can write Eq. (2.36) as

$$-\alpha\bar{R} \ln p_A - \beta\bar{R} \ln p_B + \mu\bar{R} \ln p_M + \nu\bar{R} \ln p_N = g(T),$$

where $g(T)$ is another function of temperature only. Adding the logarithmic terms and writing $g(T) = \bar{R} \ln K_p(T)$ leads to the following relationship between the partial pressures:

$$\frac{p_M^\mu p_N^\nu}{p_A^\alpha p_B^\beta} = K_p(T). \quad (2.37)$$

The term K_p is called the *equilibrium constant* for this mixture in terms of partial pressures.

Figure 2.12 gives typical values of the equilibrium constant K_p . We will make several general statements regarding equilibrium constants before demonstrating their use in a detailed example.

First, note that the partial pressures of the products appear in the numerator and those of the reactants in the denominator, each with an exponent taken from

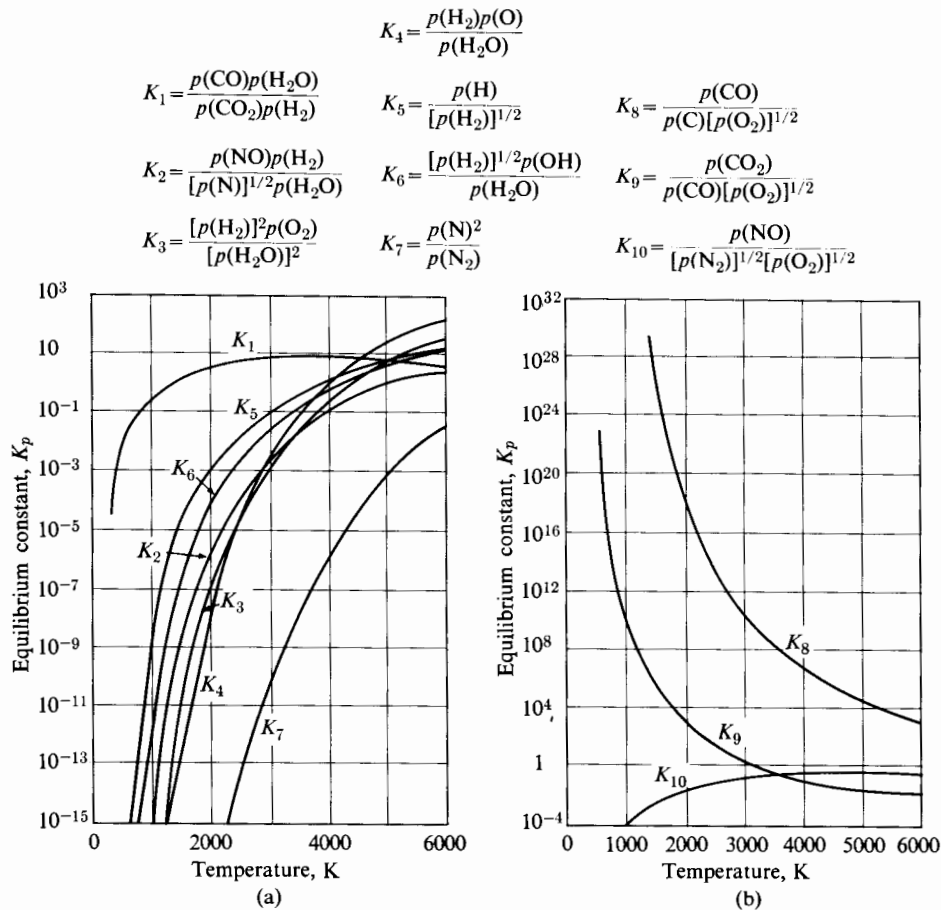


FIGURE 2.12 Equilibrium constants [9] in terms of partial pressures. Pressure in atmospheres.

Eq. (2.35). Qualitatively, then, one can expect a large K_p for subreactions that approach completion and a small K_p for those that do not. The number of constituents considered in this derivation is four, but the result can easily be extended to include any number of reactants and products.

Second, the exponents are the *stoichiometric* coefficients. For example, consider the relationship between carbon dioxide, carbon monoxide, and oxygen that would be of interest in our octane-combustion example:



In this case the equilibrium equation is

$$\frac{p(\text{CO}) [p(\text{O}_2)]^{1/2}}{p(\text{CO}_2)} = K_p.$$

Note that these exponents are not directly related to a , c , or f of Eq. (2.34) for the overall reaction. This equilibrium equation provides one of the six relationships necessary to the determination of product composition after the reaction (2.34). In a similar way we can state five other equilibrium requirements to govern the relative partial pressures of the products.

Third, since the object of this calculation is to determine composition, it is convenient to define an equilibrium constant K_n , based on *mole fractions* rather than partial pressures:

$$K_n = \frac{\chi_M^\mu \chi_N^\nu}{\chi_A^\alpha \chi_B^\beta}. \quad (2.38)$$

Since, according to the Gibbs-Dalton law, $\chi_i = p_i/p_m$, one can show that

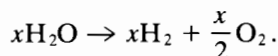
$$K_n = p_m^{\alpha+\beta-\mu-\nu} K_p, \quad (2.39)$$

where K_p is the equilibrium constant based on partial pressures. Note that K_n , though more convenient in calculating mole fractions, is a function of two variables, pressure and temperature, and is thus inconvenient to tabulate. In Eq. (2.39) p_m must be in the units for which K_p is tabulated.

We can best demonstrate the actual use of these concepts by an example that contains a considerably simplified description of an actual chemical reaction.

Example 1

One mole of H_2O is raised in temperature to 3600 K, and we may assume that it dissociates to an equilibrium mixture of H_2O , H_2 , and O_2 at a total pressure of 1 atm, according to $H_2O \rightarrow H_2 + \frac{1}{2}O_2$. The equilibrium constant for this reaction at 3600 K is $K_p = 0.25 \text{ atm}^{1/2}$. The concentration of the mixture may be determined as follows: During the dissociation, x moles of H_2O break down to form x moles of H and $x/2$ moles of O_2 , according to the reaction



The relative concentrations of the constituents of the mixture may be tabulated as shown below.

Constituents	Moles present at equilibrium	Mole fraction χ_i
H_2O	$1 - x$	$\frac{1 - x}{1 + x/2}$
H_2	x	$\frac{x}{1 + x/2}$
O_2	$\frac{x}{2}$	$\frac{x}{2(1 + x/2)}$
Total	$1 + x/2$	

We can determine the relative concentrations as follows:

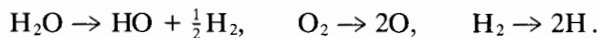
$$K_n = \frac{\chi_{H_2}(\chi_{O_2})^{1/2}}{\chi_{H_2O}} = K_p p_m^{-1/2}.$$

Substituting the equilibrium concentrations, we obtain

$$\frac{\left(\frac{x}{1+x/2}\right)\left(\frac{x/2}{1+x/2}\right)^{1/2}}{\frac{1-x}{1+x/2}} = 0.25.$$

We can then determine the quantity x by trial and error and obtain the mole fractions of H_2O , O_2 , and H_2 at equilibrium from the above tabulation.

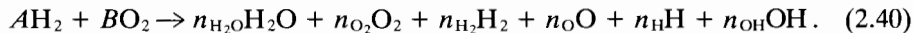
The foregoing calculation oversimplifies the dissociation. Strictly speaking, the following three dissociation reactions are also of importance at 3600 K:



Determination of the equilibrium concentrations of H_2O , H_2 , O_2 , O , and H then requires the simultaneous solution of three equilibrium conditions with known values of the three equilibrium constants for the above reactions.

Example 2

Consider a complete set of six products for a hydrogen-oxygen reaction:



We begin the analysis that leads to the determination of equilibrium composition by stating that the numbers of hydrogen and oxygen atoms are conserved, that is, are the same in products as in reactants:

$$\text{For hydrogen, } N_H = 2n_{H_2O} + 2n_{H_2} + n_H + n_{OH} = 2A, \quad (2.41)$$

$$\text{For oxygen, } N_O = n_{H_2O} + 2n_{O_2} + n_O + n_{OH} = 2B, \quad (2.42)$$

where N_H and N_O are the *known* numbers of hydrogen and oxygen atoms, respectively.

The equilibrium information available (e.g., in Ref. 3) is in the following form:

$$2H_2O \rightleftharpoons 2H_2 + O_2, \quad K_{p1} = \frac{p_{H_2}^2 p_{O_2}}{p_{H_2O}^2};$$

$$2H_2O \rightleftharpoons H_2 + 2OH, \quad K_{p2} = \frac{p_{H_2} p_{OH}^2}{p_{H_2O}^2};$$

$$O_2 \rightleftharpoons 2O, \quad K_{p3} = \frac{p_O^2}{p_{O_2}};$$

$$H \rightleftharpoons 2H, \quad K_{p4} = \frac{p_H^2}{p_{H_2}}.$$

If the temperature T of the product mixture is specified, then we can determine the values of K_p . Using Eq. (2.25), we can transform these equations to:

$$K_{p1}p^{-1} = \frac{n_{\text{H}_2}^2 n_{\text{O}_2}}{n_{\text{H}_2\text{O}}^2(n_{\text{H}_2\text{O}} + n_{\text{O}_2} + n_{\text{H}_2} + n_{\text{OH}} + n_{\text{O}} + n_{\text{H}})}, \quad (2.43)$$

$$K_{p2}p^{-1} = \frac{n_{\text{H}_2} n_{\text{OH}}^2}{n_{\text{H}_2\text{O}}^2(n_{\text{H}_2\text{O}} + n_{\text{O}_2} + n_{\text{H}_2} + n_{\text{OH}} + n_{\text{O}} + n_{\text{H}})}, \quad (2.44)$$

$$K_{p3}p^{-1} = \frac{n_{\text{O}}^2}{n_{\text{O}_2}(n_{\text{H}_2\text{O}} + n_{\text{O}_2} + n_{\text{H}_2} + n_{\text{OH}} + n_{\text{O}} + n_{\text{H}})}, \quad (2.45)$$

$$K_{p4}p^{-1} = \frac{n_{\text{H}}^2}{n_{\text{H}_2}(n_{\text{H}_2\text{O}} + n_{\text{O}_2} + n_{\text{H}_2} + n_{\text{OH}} + n_{\text{O}} + n_{\text{H}})}. \quad (2.46)$$

With the mixture pressure p known (as well as the mixture temperature T), Eqs. (2.41) to (2.46) determine the values of the six unknowns $n_{\text{H}_2\text{O}}$, n_{H_2} , n_{O_2} , n_{OH} , n_{O} , n_{H} . Because the equations are nonlinear, and because certain quantities may be vanishingly small in certain circumstances, iterative solutions can be difficult as well as time-consuming.

Reynolds [13] has, however, developed a robust computer program called STANJAN, which may conveniently be used for any such problem. In Figs. 2.13 and 2.14 we demonstrate the results of using STANJAN on the present problem,

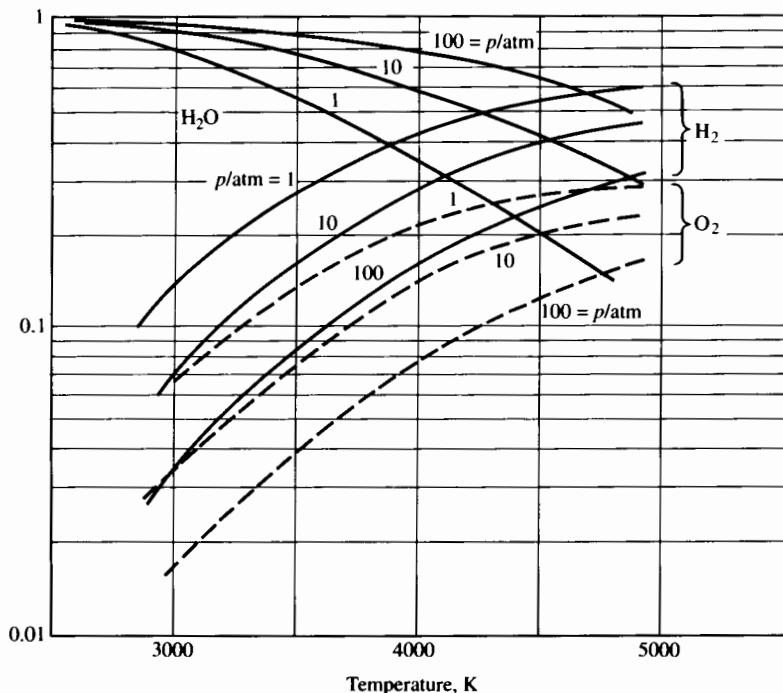
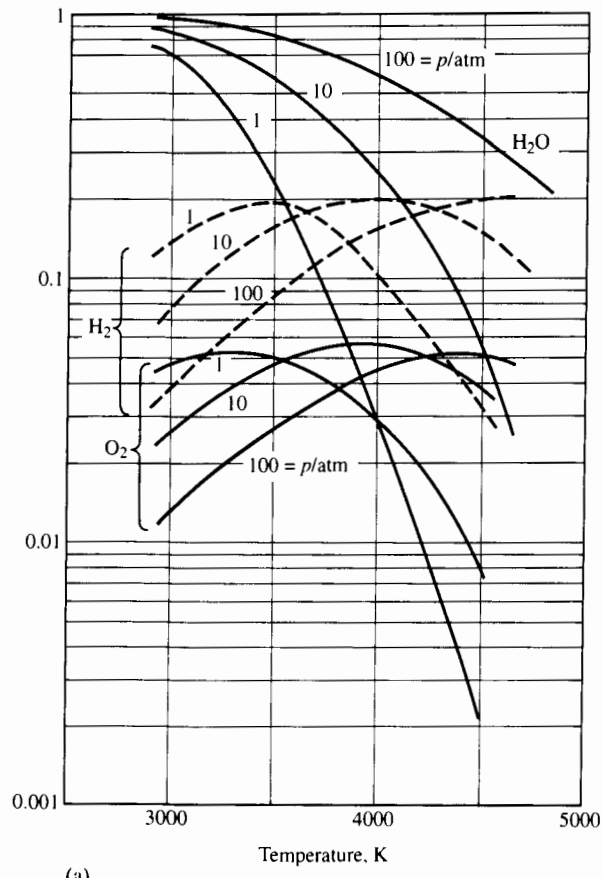
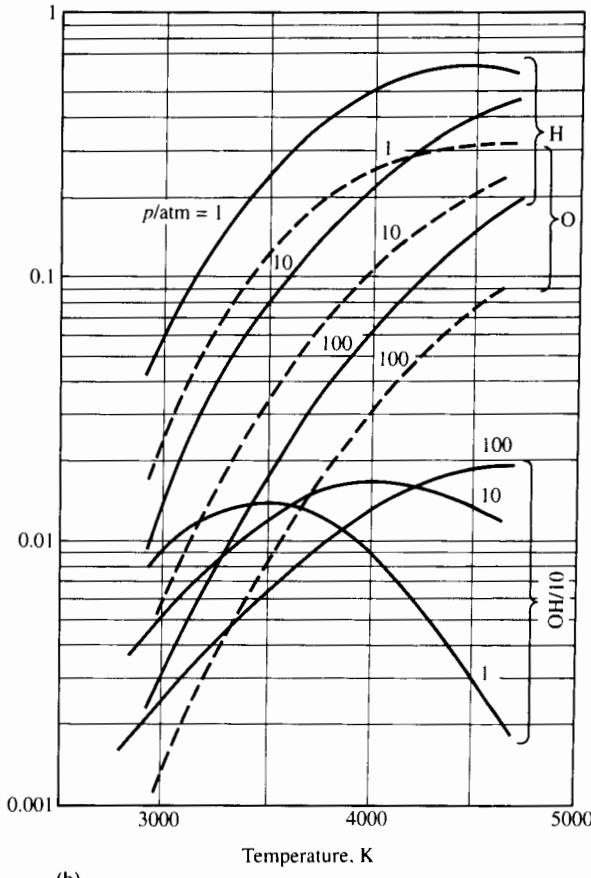


FIGURE 2.13 Equilibrium mole fractions. $\text{H}/\text{O} = 2$; products: $\text{H}_2\text{O}, \text{H}_2, \text{O}_2$.



(a)



(b)

FIGURE 2.14 (a) Equilibrium mole fractions of H_2O , H_2 , and O_2 with $\text{H}/\text{O} = 2$; (b) equilibrium mole fractions of OH , O , and H with $\text{H}/\text{O} = 2$.

taking the special case $A = 2, B = 1$, that is, the stoichiometric combustion of H₂ and O₂. Figure 2.13 shows the result if we assume only H₂O, H₂, and O₂ are present in the product mixture. Figure 2.14 is the result of the assumption that OH, H, and O are also present.

Before looking at these figures, we would like some verification that the computer program is doing what we hope it is doing. In Table 2.2 we see the output of STANJAN for one case (H/O = 2, $T = 4000$ K, $p = 10$ atm).

The mole fractions add very closely to unity, and we can calculate the equilibrium constants as follows:

$$K_{n1} = \frac{\chi_{\text{H}_2}^2 \chi_{\text{O}_2} p}{\chi_{\text{H}_2\text{O}}^2} = \frac{0.1944^2(0.05521)10}{0.2498^2} = 0.334 = e^{-1.095},$$

$$K_{n2} = \frac{\chi_{\text{H}_2} \chi_{\text{OH}}^2 p}{\chi_{\text{H}_2\text{O}}^2} = \frac{0.1944^2(0.1695)10}{0.2498^2} = 0.895 = e^{-0.110},$$

$$K_{n3} = \frac{\chi_{\text{O}}^2 p}{\chi_{\text{O}_2}} = \frac{0.1099^2(10)}{0.05521} = 2.189 = e^{0.782},$$

$$K_{n4} = \frac{\chi_{\text{H}}^2 p}{\chi_{\text{H}_2}} = \frac{0.2213^2(10)}{0.1944} = 2.519 = e^{0.924}.$$

These computed equilibrium constants are not precisely identical to those provided in Ref. 3, but the differences are unimportant for practical purposes.

With this typical result verified, we turn now to Fig. 2.13, which shows the results of the STANJAN calculations over a range of product mixture temperature and pressure if we assume that only H₂, O₂, and H₂O are present. At low temperatures (say, less than 2000 K) essentially no H₂ and O₂ are left, and so the mole fraction of H₂O tends toward unity at low temperature. At high temperature the dissociation of H₂O is large and strongly dependent on pressure. Raising the pressure tends to suppress dissociation, in accordance with Eq. (2.39). For a given temperature (and hence a fixed value of K_{p1}), the higher the value of p , the higher the value of $n_{\text{H}_2\text{O}}$, since as $n_{\text{H}_2\text{O}}$ rises, n_{H_2} and n_{O_2} must decrease.

TABLE 2.2 Sample STANJAN result
(H/O = 2, $T = 4000$ K, $p = 10$ atm)

Species	Mole fraction
H ₂	0.1944
O ₂	0.05521
H ₂ O	0.2498
OH	0.1695
O	0.1099
H	0.2213
Total	1.0001

Figure 2.14 shows the results of assuming that H₂, O₂, H₂O, OH, O, and H are all present in the product mixture. At a given pair of values of p and T , the fraction of H₂O is less when allowance is made for the presence of OH, O, and H.

Taking two moles of H₂ and one mole of O₂ from 298 K and transforming them to an equilibrium product composition at any given pressure and temperature would require heat transfer. If negligible work is done during the process and negligible change occurs in kinetic energy, we can use Eq. (2.33) to compute this heat transfer. Since the initial temperature is 298 K, the term ($H_{R1} - H_{Rf}$) is zero. We can write the other terms in Eq. (2.33) as

$$H_{RPf} = \sum_{i=1}^4 n_i Q_{fi},$$

where the subscripts $i = 1, 2, 3, 4$ denote H₂O, OH, O, and H, respectively, in the product mixture. Since the heats of formation of the H₂ and the O₂ are zero, they do not contribute to H_{RPf} by their presence in either reactant or product mixtures. The sensible enthalpy term $H_{R1} - H_{Rf}$ in Eq. (2.33) is zero since the reactants were at 298 K. The corresponding term for the products may be evaluated as follows:

$$H_{P2} - H_{Pf} = \sum_{j=1}^6 n_j (\bar{h} - \bar{h}_0)_j,$$

in which the subscripts $j = 1, 2, 3, 4, 5, 6$ denote H₂O, H₂, O₂, OH, O, and H in the product mixture, respectively. The enthalpy differences per mole ($\bar{h} - \bar{h}_0$)_j, in which \bar{h}_0 _j signifies the enthalpy of species j at 298 K, can be evaluated from tables [5] or from $c_p(T)$ equations.

Figure 2.15 shows the heat transfer required (per kg of reactant mixture) as a function of pressure and temperature. At lowest pressure the heat transfer is

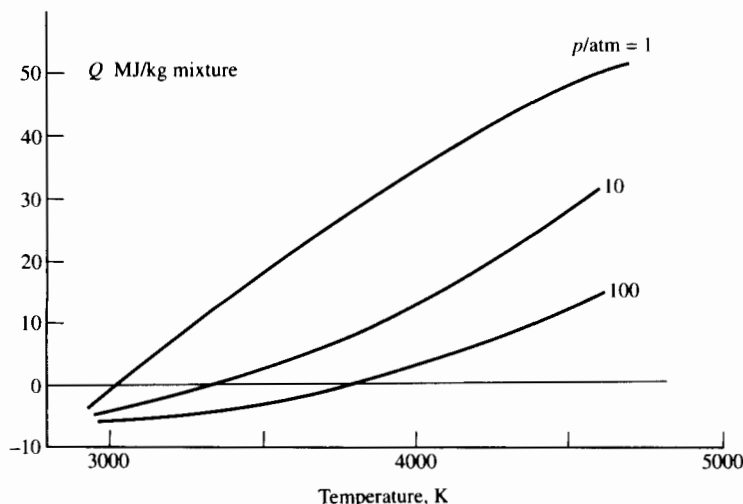


FIGURE 2.15 Heat transfer to reacting mixture reactants. H/O = 2; initially H₂(g) and O₂(g) at 298 K.

the greatest because the dissociation is greatest, and the enthalpy of formation of the dissociation products OH, O, and H is strongly positive. In each case the $Q = 0$ intercept shows the adiabatic flame temperature, which is a strong function of pressure in this case.

At high temperatures in rocket combustion chambers, or in the reaction zone of gas turbine combustors, there may be appreciable dissociation of combustion products, and the residence time may be long enough that the gas composition approaches equilibrium. In very rapid expansions—for example, in rocket nozzles—the degree of dissociation may not be well estimated by equilibrium procedures. We will discuss this further in Chapter 13.

PROBLEMS

1. A perfect gas of molecular weight $\bar{M} = 20$ and specific heat ratio $\gamma = 1.2$ expands adiabatically in steady flow from a pressure of 6 MPa, a temperature of 3000 K, and a velocity of 200 m/s to a final pressure of 0.101 MPa.
 - a. If the final temperature is 1800 K and the final velocity is negligible, how much work per unit mass of gas has been done during the expansion?
 - b. For any adiabatic expansion from the same initial conditions to the same final pressure, is it possible for the final temperature to be as low as 450 K? Consider the implication of Eq. (2.10) for an adiabatic process and use the link between entropy, temperature, and pressure indicated by Eq. (2.17), remembering that (purely for ease of calculation) γ is taken to be constant in this problem.
 - c. If no work is done on or by the gas during the process of expansion to the final pressure of 0.101 MPa, what is the maximum possible final velocity? In this case, how high would the final temperature be?
2. In certain components of propulsion engines, such as nozzles, compressors, and turbines, the residence time of the fluid within the component is so short that the heat transfer per unit mass of fluid is negligible compared to the specific work or the change in kinetic energy. For such adiabatic flows the $T-s$ diagram immediately indicates the range of possible states ($ds \geq 0$) that can be reached from any initial point.

Show that on a temperature–entropy plane constant-pressure lines for ideal gases must be concave upward, given that C_p must be positive. Show also that if any constant-pressure line p_1 is given on a temperature–entropy plane, a line corresponding to any other constant pressure p can be obtained by horizontal shift of magnitude:

$$\Delta s = -R \ln \frac{p}{p_1}.$$

Show that lines of constant volume must also be concave upward and have slopes that, at any given pair of T and S values, are steeper than those

for constant-pressure lines. Indicate also the layout of constant-enthalpy lines.

3. For adiabatic steady-flow compression processes, show from the laws of thermodynamics that the minimum possible specific work for given initial temperature T and pressure p and given final pressure p requires an isentropic compression process. Hence show that, based on second-law considerations, a reasonable way to define the “adiabatic compression efficiency” η_c is to write

$$\eta_c = \frac{w_{\text{isentropic}}}{w_{\text{actual}}} = \frac{\left(\frac{p_2}{p_1}\right)^{(y-1)/y} - 1}{\frac{T_2}{T_1} - 1}.$$

(For compression the actual work will be greater than the isentropic, and the term $w_{\text{isentropic}}$ is placed in the numerator of the η_c definition so that this “figure of merit” will have values ranging between zero and one.)

How should the adiabatic expansion efficiency for a turbine be defined for flow of a perfect gas with constant specific heat?

4. In an aircraft jet engine at takeoff, the combustion products expand adiabatically in the exhaust nozzle. At entrance to the nozzle, the pressure is 0.180 MPa and the temperature is 1200 K. The kinetic energy of the gas entering the nozzle is very much smaller than the kinetic energy of the gas leaving the nozzle.

The specific heat of the exhaust gas varies with temperature approximately as follows:

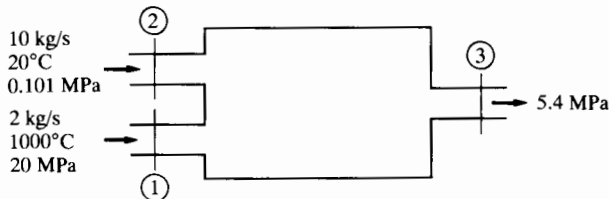
$$c_p = 0.959 + 1.16 \times 10^{-4}T + 3.65 \times 10^{-8}T^2,$$

in which the units of c_p are kJ/kg · K and T is the temperature in K. The molecular weight of the exhaust gas is 30.

Supposing the expansion to be frictionless (reversible) as well as adiabatic, show how the exhaust velocity and pressure will depend on the exhaust temperature for a series of values: 1100, 1000, and 900 K. At each temperature determine also the speed of sound $\sqrt{\gamma RT}$.

5. An inventor claims that a secret device, shown figuratively below, can take airstreams ① and ② and produce in steady flow a single high-pressure exhaust stream. Inside the device are mechanisms for mass, momentum, and energy exchange between the streams. Is it possible that such a device can be made to operate in steady state? Assume that kinetic energies at all stations are insignificant.

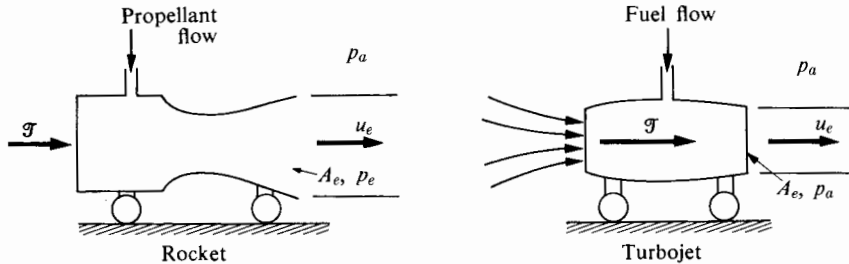
One approach to this problem is to examine whether the data given imply a contradiction of the conservation laws. Another would be to take the data specified at stations ① and ② and determine the maximum possible pressure at station ③.

**PROBLEM 5**

6. A new energy-conversion machine has been proposed that has two inflows of air. At one inlet port 10 kg/s enters at 10 MPa and 75°C. At the other, 2 kg/s enters at 2 MPa and 1000°C. There is a single air-outlet stream discharging to the atmosphere at 0.1 MPa. No fuel enters the machine, nor are there any other inflows or outflows of material. The casing around the machine is well insulated, so that heat transfer between the machine and the surrounding air is negligible. Inlet and exit kinetic energy fluxes are insignificant.

What is the maximum power that the machine could produce in steady flow if the exhaust pressure were 0.1 MPa? For air $\gamma = 1.4$ and $c_p = 1.0035 \text{ kJ/kg} \cdot \text{K}$.

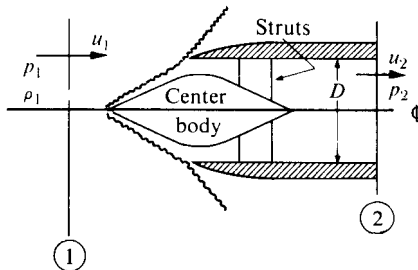
7. Calculate the static thrusts of the rocket and turbojet engines described in the figure. The thrust \mathcal{T} is the force necessary to prevent horizontal movement of the engine. Both engines exhaust a mass flow of 40 kg/s. The ratio of air and fuel mass flowing into the turbojet is 50:1, and in its exhaust plane the velocity is 500 m/s and the pressure is the same as the ambient pressure. The rocket propellant exhausts at a velocity of 3000 m/s through an area of 0.2 m^2 . The pressure in the exhaust plane of the rocket is 0.15 MPa and ambient pressure is 0.101 MPa.

**PROBLEM 7**

8. An idealized supersonic ramjet diffuser consists of an axisymmetric center body located in a cylindrical duct as shown in the figure. The flow at stations (1) and (2) may be assumed uniform at the values indicated, and the stream tube that enters the inlet has a diameter D far upstream.

Show that the aerodynamic drag on the center body and struts is

$$\mathcal{D} = -\frac{\pi}{4} D^2 [\rho_1 u_1 (u_2 - u_1) + p_2 - p_1].$$

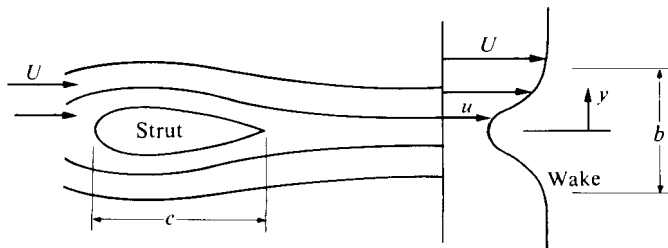


PROBLEM 8

9. A strut of chord c is placed in an incompressible flow that is everywhere uniform except for the illustrated effect of the strut. Velocity measurements at a certain plane far downstream of the strut indicate the presence of a wake, as shown. The velocity distribution across the wake is approximately a cosine function; that is,

$$\frac{u}{U} = 1 - a \left(1 + \cos \frac{2\pi y}{b} \right) \quad \text{for } -\frac{b}{2} < y < \frac{b}{2},$$

where U is the velocity of the uniform flow field far from the strut and its wake. If the measured values of a and b/c are 0.10 and 2.0, respectively, determine the drag coefficient C_d of the strut. The drag coefficient is defined by $C_d = \mathcal{D}/(\frac{1}{2}\rho U^2 c)$, where \mathcal{D} is the total drag per unit length on the strut due to pressure and viscous forces, and ρ is the fluid density.

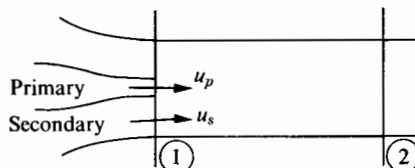


PROBLEM 9

10. Two streams of air mix in a constant-area mixing tube. The primary stream enters the mixing tube at station ① with a velocity of 300 m/s and a temperature of 900 K. The secondary stream enters with velocity 30 m/s and temperature 300 K. The flow at stations ① and ② may be assumed one-

dimensional. The pressure at station (1) is 0.1 MPa, and the ratio of primary to secondary flow areas at station (1) is 1:3.

- Using continuity, momentum, and energy equations, along with the perfect-gas law, show how the flow at (2) may be determined from conditions at (1).
- Determine the velocity, temperature, and pressure at station (2). State all assumptions.



PROBLEM 10

11. A mixture of gases containing 10 kg of nitrogen, 10 kg of hydrogen, and 15 kg of helium is contained at a pressure of 6.7 MPa and a temperature of 300 K. If the constituents are taken to be perfect gases and the Gibbs-Dalton law holds, what are the molecular weight and specific heat ratio of the mixture?

Gas	Mole wt, \bar{M}	Specific heat ratio, γ
Nitrogen	28	1.4
Hydrogen	2	1.4
Helium	4	1.67

12. Calculate the combustion temperature of a gaseous oxygen-hydrogen mixture whose mass ratio is 3:1 ($O_2:H_2$). Since this means a considerable excess of hydrogen over the stoichiometric proportion, assume that the product temperature will be low enough to prevent dissociation. The temperature of the reactants entering the chamber is 298 K, and the heat transfer to the coolant from the chamber walls is 8.4 kJ per mole of product. As a first approximation, the mean specific heats may be taken as in the table below.

Average specific heat, kJ/kmol · K			
	H_2	O_2	H_2O
Reactants	29.6	32.3	
Products	32.9		46.8

13. A mixture of air and a hydrocarbon fuel whose average composition is indicated by $CH_{1.9}$ undergoes complete combustion. Twice as much air is present

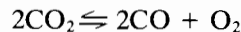
as needed to burn all the fuel. How high is the final temperature? The heats of formation are given in the table below. Assume that air is 79% nitrogen and 21% oxygen by volume. The reactants have a temperature of 25°C before combustion. The adiabatic flame temperature may be found either by using average values of the specific heats for each constituent.

Constituent	Q_f kJ/kmol · K @ 298 K	\bar{c}_p kJ/kmol · K
CH _{1.9}	9,358	
CO ₂ (g)	-393,522	51.9
O ₂ (g)	0	34.0
N ₂ (g)	0	31.6
H ₂ O (g)	-241,827	40.6

14. Find the flame temperature of the products of combustion of hydrogen and oxygen whose composition and average specific heats are given in the table below. The reactants enter the adiabatic combustion chamber at 250 K. In this table, \bar{C}_{pp} is the average molar specific heat of the component between 298 K and the flame temperature, \bar{C}_{pr} is the average molar specific heat of the component between 250 K and 298 K, and \bar{h}_f^0 is the heat of formation at 298 K in kJ/kmol.

Component	Moles	\bar{C}_{pp}	\bar{C}_{pr}	Q_f
O ₂	0.1008	36.3	32.3	0
H ₂	0.3170	32.9	29.6	0
O	0.054	20.9		+245,143
H	0.109	20.9		+216,093
OH	0.233	33.5		+ 41,870
H ₂ O	1.512	48.27		-241,827

15. One kmol of CO₂ is heated at atmospheric pressure to 3000 K. What is the equilibrium mixture composition if only CO, O₂, and CO₂ are present? If the pressure were raised to 10 atm, how would the composition change at that temperature? At 3000 K the equilibrium constant for the reaction



is

$$K_p = e^{-2.222}.$$

16. A hydrocarbon fuel whose composition may be represented by CH₂ burns with 30% excess air to reach a product temperature of 2200 K. At this temperature the mole fractions of the dissociation products OH, O, H, NO, and N are all very small; however, even at 10–100 parts per million NO is a seri-

ous environmental concern. Estimate the equilibrium concentration of NO present at the above temperature, assuming that the concentrations of N₂, O₂, H₂O, and CO₂ are the same as if no dissociation had taken place. The equilibrium constant for



at 2200 K is $K_p = e^{-6.866}$ (at 1000 K it is $K_p = e^{-18.776}$).

The equilibrium concentration of NO at 1000 K can be shown to be quite small. The problem is that during rapid cooling of the combustion products—for example, in the turbine of a gas turbine—the NO formed at high temperatures does not have time to revert to N₂ and O₂; it tends to be “locked in” to the mixture and discharged from the engine in undesirably large concentrations at low temperature. The equilibrium calculation at high temperature serves therefore to estimate the worst possible case.

17. It has been proposed that liquid nitrogen (LN₂) be considered the “fuel” for a new kind of nonpolluting engine that operates in steady flow and produces shaft power. Unlike conventional engines, this one can undergo heat interaction with the atmosphere. The engine is being tested at sea level on a stationary test bed.

The ambient air is at 100 kPa and 300 K. The LN₂ is supplied to the engine in the saturated liquid state at 77.3 K (1 atm). The enthalpy of evaporation at that temperature is $h_{fg} = 198.6 \text{ kJ/kg}$. For simplicity the specific heat of nitrogen vapor (in the temperature range 77–1000 K) may be taken as $c_p = 1.0 \text{ kJ/kg} \cdot \text{K} = \text{constant}$.

The nitrogen leaves the engine at ambient pressure (1 atm). The ambient temperature is 15°C.

- a. To maximize work output, what should be the exit temperature of the nitrogen stream?
- b. What is the maximum specific work (kJ/kg of LN₂) that could possibly be produced by such an engine?

REFERENCES

1. Keenan, J. H. *Thermodynamics*. New York: Wiley, 1941.
2. Hatsopoulos, G. N., and J. H. Keenan. *Principles of General Thermodynamics*. New York: Wiley, 1965.
3. Van Wylen, G. J., and R. E. Sonntag. *Fundamentals of Classical Thermodynamics*, 3rd ed. New York: Wiley, 1985.
4. Shapiro, A. H. *Dynamics and Thermodynamics of Compressible Fluid Flow*, vol. 1. New York: Ronald Press, 1953, Chaps. 1–8, 16. Reprint ed., Wiley.
5. Chase, Jr., M. W., et al. *JANAF Thermochemical Tables*, 3rd ed., pt. 1, Al–Oo;pt. 2, Or–Zr. *Journal of Physical and Chemical Reference Data* 14(1985), Supplement no. 1.

6. Keenan, J. H., J. Chao, and J. Kaye. *Gas Tables*, 2nd ed. New York: Wiley, 1983.
7. Rossini, F. D., et al. "Selected Values of Properties of Hydrocarbons," Circular no. 500, Washington, D.C.: National Bureau of Standards, Feb. 1, 1952.
8. "Heat of Formation of Hydrazine, Unsymmetrical Dimethylhydrazine and Monomethylhydrazine." Inorganic Research and Development Department, FMC Corp., Princeton, N.J., May 14, 1959.
9. Martinez, J. S., and G.W. Elverum, Jr. "A Method of Calculating the Performance of Liquid-Propellant Systems Containing the Species C, H, O, N, F, and One Other Halogen, with Tables Required; Thermochemical Properties to 6000°K," Memorandum no. 20-121. Jet Propulsion Laboratory, California Institute of Technology, Pasadena, Calif., Dec. 6, 1955.
10. Carter, J. M., and M. Protteau. "Thermochemical Calculations on the White Fuming Nitric Acid and JP-3 Propellant Combination," Research Technical Memorandum no. 58. Aerojet-General Engineering Corp., Azusa, Calif., April 5, 1950.
11. Perry, J. H. *Chemical Engineer's Handbook*, 6th ed. New York: McGraw-Hill, 1984.
12. Rice, H. E. "Performance Calculations of RFNA-Aniline and Three-Component Systems Using Hydrogen," Memorandum no. 9-2. Jet Propulsion Laboratory, Pasadena, Calif., June 30, 1947.
13. Reynolds, W. C. "STANJAN: The Element Potential Method for Chemical Equilibrium Analysis." Thermosciences Division, Department of Mechanical Engineering, Stanford University, Palo Alto, Calif., Jan. 1986.

C H A P T E R

3

STEADY ONE-DIMENSIONAL FLOW OF A PERFECT GAS

3.1 INTRODUCTION

In most of the propulsion methods discussed in this volume, the working fluid can be quite satisfactorily approximated by a perfect gas. In this chapter we apply the basic laws stated in the first chapter to perfect gases flowing in channels. For algebraic convenience we usually assume that the specific heat of the gas is constant.

Useful analyses of actual channel flows are relatively easy if one assumes that the fluid conditions vary in the streamline direction only. In this case the flow is said to be one-dimensional. The flow in the immediate vicinity of a wall can never be one-dimensional, since the velocity at the wall surface is zero and there are significant property variations across the streamlines. However, with the exception of a thin layer of fluid next to the wall, fluid conditions are often fairly uniform over a large part of a flow. Even if the bulk of the flow is not uniform on any surface normal to the streamlines, the one-dimensional approximation may still lead to useful solutions for the streamwise variation of average fluid properties. One-dimensional solutions exhibit the major characteristics of many important flows, including those in nozzles, diffusers, and combustors.

Using the one-dimensional assumption does not mean that we cannot consider the effects of wall shear stress and heat transfer. It does mean that we ignore the fact that the effects of wall stress and convective heat transfer can, strictly speaking, be transmitted to the bulk of the flow only if there are within it transverse gradients in velocity and temperature. We take up this matter in detail

in Chapter 4, which shows how, in real flows, viscous and thermal effects diffuse at finite rates in the transverse direction. In this chapter, by ignoring such diffusive effects, we effectively assume not only that transverse gradients are absent, but that rates of transverse diffusion are infinite. We assume that the entire cross section of the flow is immediately affected by a local application of wall shear stress or heat transfer. This assumption stands in contrast to the more realistic boundary layer concept, which is reviewed in Chapter 4, but it is useful for estimating the influence of the boundary wall on the cross-sectional average flow.

3.2 GENERAL ONE-DIMENSIONAL FLOW OF A PERFECT GAS

Fluid flows are governed by the equations of continuity, momentum, and energy, along with an appropriate equation of state. In this section we apply these equations to a one-dimensional differential control volume within a duct, as indicated in Fig. 3.1. The rates of heat and work transfer are $d\dot{Q}$ and $d\dot{\mathcal{P}}_s$, respectively. A body force of magnitude X per unit volume of fluid may act in the stream direction.

For steady flow the continuity requirement (from Eq. 2.2) is

$$\int_{cs} \rho \mathbf{u} \cdot \mathbf{n} dA = 0.$$

Since the flow of Fig. 3.1 is assumed one-dimensional, we may reduce this expression to $(d/dx)(\rho u A) = 0$, or

$$\frac{d\rho}{\rho} + \frac{dA}{A} + \frac{du}{u} = 0, \quad (3.1)$$

for the control volume of infinitesimal length indicated in Fig. 3.1.

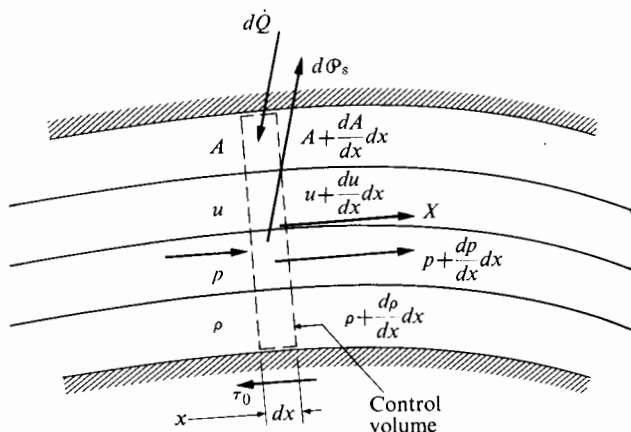


FIGURE 3.1 One-dimensional flow through a control volume.

The momentum equation for steady flow (from Eq. 2.4) is

$$\sum \mathbf{F} = \int_{cs} \rho \mathbf{u} (\mathbf{u} \cdot \mathbf{n}) dA.$$

Writing $\Sigma \mathbf{F}$ as the sum of pressure, wall shear, and body forces, and again considering the flow of Fig. 3.1, we can write this equation as

$$-(A dp + \tau_0 c dx) + X A dx = \rho u A du$$

or

$$-\left(\frac{dp}{dx} + \frac{\tau_0 c}{A}\right) + X = \rho u \frac{du}{dx}, \quad (3.2)$$

where τ_0 is the wall shear stress and c is the duct circumference.

For steady flow the energy requirement (from Eq. 2.8) is

$$d\dot{Q} = \int_{cs} \dot{Q} dA_{cs} = \int_{cs} \left(h + \frac{u^2}{2} \right) \rho \mathbf{u} \cdot \mathbf{n} dA - \int_{cv} \mathbf{X} \cdot \mathbf{u} dV + d\mathcal{P}_s,$$

where A_{cs} indicates the entire control-surface area (as opposed to the area A of the duct cross section). The gravitational potential energy term has been neglected, as is usually permissible. Further, except for special cases to be considered in Chapters 5 and 16, the body force \mathbf{X} will be zero. In this case the energy equation reduces to

$$\dot{m}(dh + u du) = d\dot{Q} - d\mathcal{P}_s \quad (3.3a)$$

or

$$dh + u du = dq - dw, \quad (3.3b)$$

where \dot{m} is the mass flow rate $\rho u A$ (a constant) and q and w are the heat and work transfer per unit mass.

If we can assume that the fluid is a perfect gas (as we do in this chapter), the equation of state is

$$p = \rho RT. \quad (3.4)$$

If we know the flow area, heat transfer, work, shear stress, and body force, we can obtain changes in the state of the fluid stream from these four equations. In general, one cannot express solutions in simple algebraic form. There are a number of important special cases, however, that can be integrated in closed form. Before we proceed to these special cases, let us introduce two concepts useful for all cases: the stagnation state and the Mach number.

Stagnation State

We define the *stagnation state* as the state that would be reached by a fluid if it were brought to rest reversibly, adiabatically, and without work. We obtain the energy equation for such a deceleration from Eq. (3.3b),

$$dh + u du = 0,$$

which may be integrated to

$$h_0 = h + \frac{u^2}{2}. \quad (3.5)$$

The constant of integration, h_0 , is called the stagnation enthalpy.

For any adiabatic flow viewed from a reference frame in which no work occurs, the stagnation enthalpy is constant. Note particularly that this conclusion holds for both reversible and irreversible flows. Unlike enthalpy, the pressure reached when there is adiabatic zero-work deceleration of a fluid is decreased by irreversible processes. This is illustrated in Fig. 3.2, an enthalpy–entropy diagram for a typical gas. The stagnation state corresponding to state ① is ①, and the stagnation pressure is p_{01} , which is the pressure attained by the fluid after it has been stopped isentropically. If the flow is brought to rest irreversibly, as at ③ (the increased entropy is a measure of the irreversibility), the stagnation enthalpy is the same as before, but the pressure attained is less than p_{01} . For any process, such as ① to ②, the stagnation state generally undergoes a change like the one from ① to ②. The decrease in pressure from p_{01} to p_{02} is, in the absence of work, an indication of the irreversibility of the process. If the fluid is a perfect gas, the stagnation temperature is related to the stagnation enthalpy through the relation

$$h_0 - h = \int_T^{T_0} c_p dT.$$

The stagnation temperature T_0 of the fluid is the temperature that would be reached upon adiabatic, zero-work deceleration. For a perfect gas with constant specific heats, we relate the stagnation temperature and pressure (using Eq. 2.19) by

$$\frac{p_0}{p} = \left(\frac{T_0}{T} \right)^{\gamma(\gamma-1)}, \quad (3.6)$$

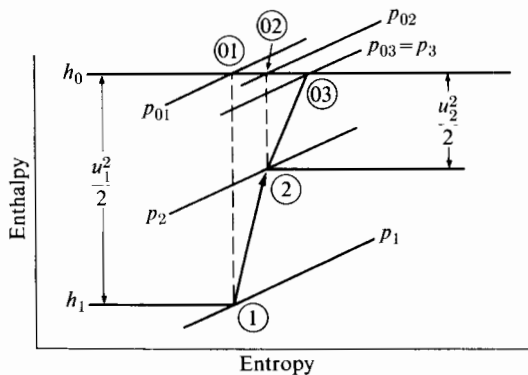


FIGURE 3.2 Definition of stagnation state.

since the deceleration process is, by definition, isentropic. We can determine other properties of the fluid at the stagnation state from p_0 , T_0 , and the equation of state. We may regard the stagnation conditions as local fluid properties. Aside from analytical convenience, the definition of the stagnation state is useful experimentally, since T_0 and p_0 are relatively easily measured. It is usually much more convenient to measure the stagnation temperature T_0 than the temperature T .

Mach Number

A very convenient variable in compressible-flow problems is the Mach number M , defined as

$$M = \frac{u}{a}, \quad (3.7)$$

where a is the local speed of sound in the fluid. The speed of sound is the speed of propagation of very small pressure disturbances. For a perfect gas it is given by

$$a = \sqrt{\gamma RT}. \quad (3.8)$$

The derivation of this result follows from thought about a sound wave standing in the control volume of Fig. 3.1. The wave can be seen as stationary only if its propagation speed a is equal to the local upstream flow speed u . The wave is taken to be infinitesimally thin, so that we can ignore wall effects and area change dA . We assume that it has infinitesimal strength, so the total pressure rise is dp , the total density change is $d\rho$, and the velocity change is from $u = a$ to $a + du$, the change du being negative. Applying Eq. (3.1) to this case, we have

$$\frac{d\rho}{\rho} + \frac{du}{a} = 0.$$

Since the wave is unaffected by τ_0 and χ , Eq. (3.2) reduces to

$$-dp = \rho a du.$$

Eliminating du from these two statements yields $a^2 = dp/d\rho$. At this point we introduce the assumption that the wave is isentropic, so that (as we could deduce from Eq. 2.21)

$$\frac{dp}{p} = \gamma \frac{d\rho}{\rho}.$$

This gives $a^2 = \gamma p/\rho = \gamma RT$, which is the same as Eq. (3.8).

3.3 ISENTROPIC FLOW

Many actual processes, such as flows in nozzles and diffusers, are ideally isentropic. It is therefore worthwhile to study the isentropic flow of a perfect gas in the absence of work and body forces. The simple results obtained with the con-

stant specific heat approximation are useful even for large temperature changes, so long as we use appropriate average values of c_p and γ .

For constant specific heat we may write Eq. (3.5) as

$$\frac{T_0}{T} = 1 + \frac{u^2}{2c_p T}, \quad (3.9)$$

which, with the definition of Mach number, becomes

$$\frac{T_0}{T} = 1 + \frac{\gamma - 1}{2} M^2, \quad (3.10)$$

since $c_p = \gamma/(\gamma - 1)R$. We may then write Eq. (3.6) as

$$\frac{p_0}{p} = \left(1 + \frac{\gamma - 1}{2} M^2\right)^{\gamma/(\gamma-1)}. \quad (3.11)$$

From the perfect gas law and Eqs. (3.10) and (3.11),

$$\frac{\rho_0}{\rho} = \left(1 + \frac{\gamma - 1}{2} M^2\right)^{1/(\gamma-1)}. \quad (3.12)$$

It is interesting at this point to consider the case of low-speed flow. If $M^2 \ll 1$, we can see from Eq. (3.12) that $\rho \approx \rho_0$; the flow, though not strictly "incompressible," is of essentially constant density. Also, for $M^2 \ll 1$ we can represent Eq. (3.11) quite accurately as

$$\frac{p_0}{p} = 1 + \frac{\gamma}{2} M^2 = 1 + \frac{u^2}{2RT} = 1 + \frac{\rho u^2}{2p}$$

or

$$p_0 = p + \frac{\rho u^2}{2}.$$

Thus for low-speed flow Eq. (3.11) reduces to the Bernoulli equation applicable to isentropic constant-density flow. The mass flow per unit area is

$$\frac{\dot{m}}{A} = \rho u.$$

Using Eqs. (3.7), (3.8), and (3.10), we may express the velocity as

$$u = M \sqrt{\frac{\gamma RT_0}{1 + \frac{\gamma - 1}{2} M^2}}.$$

Then, using this expression with Eq. (3.12), we may write the mass flow rate as

$$\frac{\dot{m}}{A} = \frac{p_0 \sqrt{\gamma}}{\sqrt{RT_0}} M \left(\frac{1}{1 + \frac{\gamma - 1}{2} M^2} \right)^{(\gamma+1)/2(\gamma-1)}. \quad (3.13)$$

For a given fluid (γ, R) and inlet state (p_0, T_0), we can readily show that the mass flow per unit area is maximum at $M = 1$. If we indicate those properties of the flow at $M = 1$ with an asterisk, the maximum flow per unit area is, from Eq. (3.13),

$$\frac{\dot{m}}{A^*} = \frac{p_0}{\sqrt{RT_0}} \sqrt{\gamma} \left(\frac{2}{\gamma + 1} \right)^{(\gamma+1)/2(\gamma-1)}. \quad (3.14)$$

Combining Eqs. (3.13) and (3.14), we have

$$\frac{A}{A^*} = \frac{1}{M} \left[\frac{2}{\gamma + 1} \left(1 + \frac{\gamma - 1}{2} M^2 \right) \right]^{(\gamma+1)/2(\gamma-1)}. \quad (3.15)$$

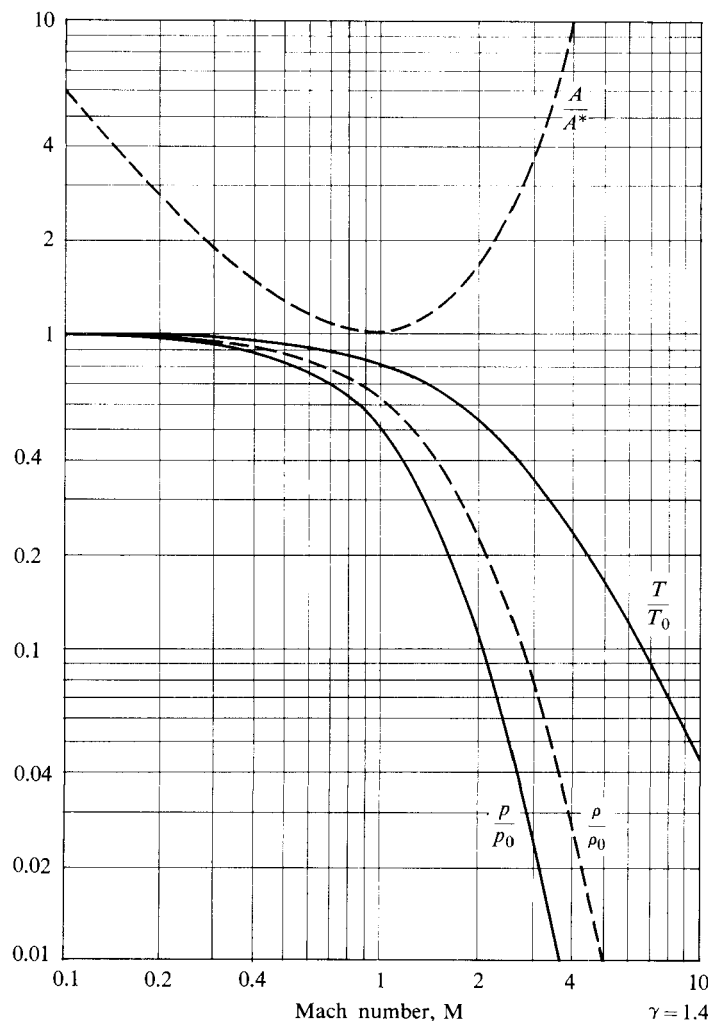


FIGURE 3.3 One-dimensional isentropic flow of a perfect gas. (From Shapiro [1].)

For a given isentropic flow (given $\gamma, R, p_0, T_0, \dot{m}$), it is clear that A^* is a constant, so that we may use it as in Eq. (3.15) to normalize the actual flow area A . Equations (3.10), (3.11), and (3.12) relate the fluid properties to the Mach number M , and Eq. (3.15) shows how the Mach number depends on the flow area. Expressing flow variables in terms of Mach number is a matter of great convenience, since the various flow functions can be plotted or tabulated as a function of M for the appropriate γ . Figure 3.3 gives the one-dimensional isentropic functions for a perfect gas of $\gamma = 1.4$. Tabulations for other γ are given by Shapiro [1], Keenan, Chao, and Kay [2], and others.

3.4 NONISENTROPIC FLOW

Equation (3.13), derived with isentropic flow in mind, shows that the local Mach number of the flow depends only on the dimensionless mass ratio $\dot{m}\sqrt{RT_0}/(p_0A)$ and the value of γ . Even if the flow is nonisentropic, the derivation leading to Eq. (3.13) is valid provided the stagnation values p_0 , T_0 , and ρ_0 are understood to be local values rather than initial—that is, far upstream—values. In a nonisentropic flow these stagnation values may change in the streamwise direction. To examine how they may vary, we return to Eq. (2.12):

$$Tds = de + p dv. \quad (2.12)$$

Since the enthalpy h is defined as $h = e + pv$, we can equally well write this equation as

$$Tds = dh - vdp. \quad (3.16)$$

For a perfect gas $h = h(T)$, $dh = c_p dT$, and $pv = RT$, so Eq. (3.16) can be written

$$\frac{ds}{R} = \frac{\gamma}{\gamma - 1} \frac{dT}{T} - \frac{dp}{p}.$$

At any point in the flow (whether or not the flow as a whole is being affected by friction), we can think of a local stagnation state that the fluid would reach if it were isentropically decelerated to zero velocity at that location. If its local temperature and Mach number were T and M , the local stagnation temperature would be T_0 and obtained from

$$\frac{T_0}{T} = 1 + \frac{\gamma - 1}{2} M^2. \quad (3.10)$$

Likewise, if its local pressure were p , the local stagnation pressure p_0 would be obtained from

$$\frac{p_0}{p} = \left[1 + \frac{\gamma - 1}{2} M^2 \right]^{\gamma/(\gamma-1)}, \quad (3.11)$$

where again M is the local Mach number. Letting $m = 1 + (\gamma - 1)/2M^2$, we now look at changes in T_0 and p_0 in the streamwise direction. From Eqs. (3.10) and (3.11) we can write

$$\frac{dT}{T} = \frac{dT_0}{T_0} - \frac{dm}{m}$$

and

$$\frac{dp}{p} = \frac{dp_0}{p_0} - \frac{\gamma}{\gamma - 1} \frac{dm}{m}.$$

Now substituting these expressions in Eq. (3.16), we find that dm/m disappears, and the result is

$$\frac{ds}{R} = \frac{\gamma}{\gamma - 1} \frac{dT_0}{T_0} - \frac{dp_0}{p_0}. \quad (3.17)$$

Several cases are of interest:

Isentropic flow ($ds = 0$). If the heat transfer and the work are also both zero, then $dT_0 = 0$, and it follows that, however much the flow accelerates or decelerates, the stagnation pressure cannot change.

If the work is nonzero, then $dT_0 \neq 0$, but from Eq. (3.17)

$$\frac{dp_0}{p_0} = \frac{\gamma}{\gamma - 1} \frac{dT_0}{T_0},$$

so that if γ is constant,

$$\frac{p_0}{p_{01}} = \left(\frac{T_0}{T_{01}} \right)^{\gamma(\gamma-1)}.$$

Nonisentropic flow. The second law of thermodynamics for a control mass tells us that

$$ds \geq \frac{\delta q}{T}.$$

Thus for adiabatic flows $ds \geq 0$. If there is zero work as well as zero heat transfer (but an increase in entropy due to friction), we have $dT_0 = 0$ and $ds > 0$. In this case Eq. (3.17) shows that

$$\frac{dp_0}{p_0} = - \frac{ds}{R},$$

and the stagnation pressure must decrease in the streamwise direction.

In general,

$$\frac{dp_0}{p_0} = \frac{\gamma}{\gamma - 1} \frac{dT_0}{T_0} - \frac{ds}{R},$$

so that the stagnation pressure may increase, even in the presence of friction, if work is being done on the fluid such that

$$\frac{\gamma}{\gamma - 1} \frac{dT_0}{T_0} > \frac{ds}{R}.$$

We now consider two special cases of nonisentropic flow that shed much light on the influence of friction and heat transfer on compressible flows.

3.5 FRICTIONLESS CONSTANT-AREA FLOW WITH STAGNATION TEMPERATURE CHANGE

Another special case for which we can solve the basic equations in closed form is frictionless flow in a constant-area duct in which a stagnation enthalpy change occurs. Four processes of interest in which the stagnation temperature of a moving stream changes include:

- Combustion,
- Evaporation or condensation of liquid drops traveling with the stream,
- Flux of electric current through a fluid or finite conductivity (Joule heating),
- Wall heat transfer.

In any real flow, frictional effects are always present, especially near solid boundaries. As we will discuss Chapter 4, wall heat transfer and wall friction are in fact so closely related that it is not realistic to discuss the former without at the same time talking about the latter. Nevertheless, the study of frictionless flow in a constant-area duct in which a T_0 change occurs illustrates some important features of the real flows in which the first three effects listed above are present. Combustion and evaporation or condensation processes may result in variations of molecular weight and gas constants, but for the sake of simplicity we may consider these negligible. The stagnation enthalpy change in these processes can be determined from

$$\Delta h_0 = q - w,$$

where q and w are net heat and work transfers per unit mass of fluid. For this case the continuity, momentum, and energy equations are from Eqs. (3.1), (3.2), and (3.3), respectively:

$$\text{Continuity: } \frac{dp}{\rho} + \frac{du}{u} = 0,$$

$$\text{Momentum: } dp = -\rho u du,$$

$$\text{Energy: } dh_0 = dh + u du.$$

We can readily integrate the first two of these to

$$\rho u = \rho_1 u_1,$$

$$p - p_1 = -(\rho u)(u - u_1) = -(\rho_1 u_1)(u - u_1),$$

in which the subscript 1 signifies an initial condition. The second of these we may also express as

$$p - p_1 = \rho_1 u_1^2 - \rho u^2.$$

By introducing the Mach number, we can transform this to

$$\frac{p}{p_1} = \frac{1 + \gamma M_1^2}{1 + \gamma M^2}.$$

Further, by using Eq. (3.11) we can derive the stagnation pressure ratio from this equation, with the result that

$$\frac{p_0}{p_{01}} = \left(\frac{1 + \gamma M_1^2}{1 + \gamma M^2} \right) \left(\frac{1 + \frac{\gamma - 1}{2} M^2}{1 + \frac{\gamma - 1}{2} M_1^2} \right)^{\gamma/(\gamma-1)}. \quad (3.18)$$

Thus the change in stagnation pressure is directly related to the change in Mach number.

We can in turn obtain the dependence of Mach number on stagnation enthalpy (or stagnation temperature) as follows: Using the perfect-gas law,

$$\frac{T}{T_1} = \frac{p}{p_1} \frac{\rho_1}{\rho}.$$

Invoking the continuity condition, $\rho u = \rho_1 u_1$, we can see that

$$\frac{T}{T_1} = \frac{p}{p_1} \frac{u}{u_1}.$$

Now if we introduce the Mach number relation $M = u/\sqrt{\gamma RT}$, we can easily show that

$$\frac{T}{T_1} = \left(\frac{p}{p_1} \frac{M}{M_1} \right)^2,$$

and, using the above relation between static pressure ratio and Mach number,

$$\frac{T}{T_1} = \left[\frac{1 + \gamma M_1^2}{1 + \gamma M^2} \left(\frac{M}{M_1} \right) \right]^2.$$

From Eq. (3.10) and this expression, we can show that the stagnation temperature ratio is governed by

$$\frac{T_0}{T_{01}} = \left[\frac{1 + \gamma M_1^2}{1 + \gamma M^2} \left(\frac{M}{M_1} \right) \right]^2 \left(\frac{1 + \frac{\gamma - 1}{2} M^2}{1 + \frac{\gamma - 1}{2} M_1^2} \right). \quad (3.19)$$

Thus the Mach number depends uniquely on the ratio of stagnation temperatures and the initial Mach number.

It is desirable in this case, as in the isentropic case, to simplify these relationships by the choice of a convenient reference state. Since stagnation conditions are *not* constant, the stagnation state is not suitable for this purpose. However, the state corresponding to unity Mach number is suitable since, as Eqs. (3.18) and (3.19) show, conditions there *are* constant for a given flow (i.e., for a given p_{01}, T_{01}, M_1). Again using an asterisk to signify properties at $M = 1$, we can show from the equations above that

$$\frac{T}{T^*} = \left(\frac{1 + \gamma}{1 + \gamma M^2} \right)^2 M^2, \quad (3.20)$$

$$\frac{T_0}{T_0^*} = \frac{2(\gamma + 1)M^2 \left(1 + \frac{\gamma - 1}{2} M^2 \right)}{(1 + \gamma M^2)^2}, \quad (3.21)$$

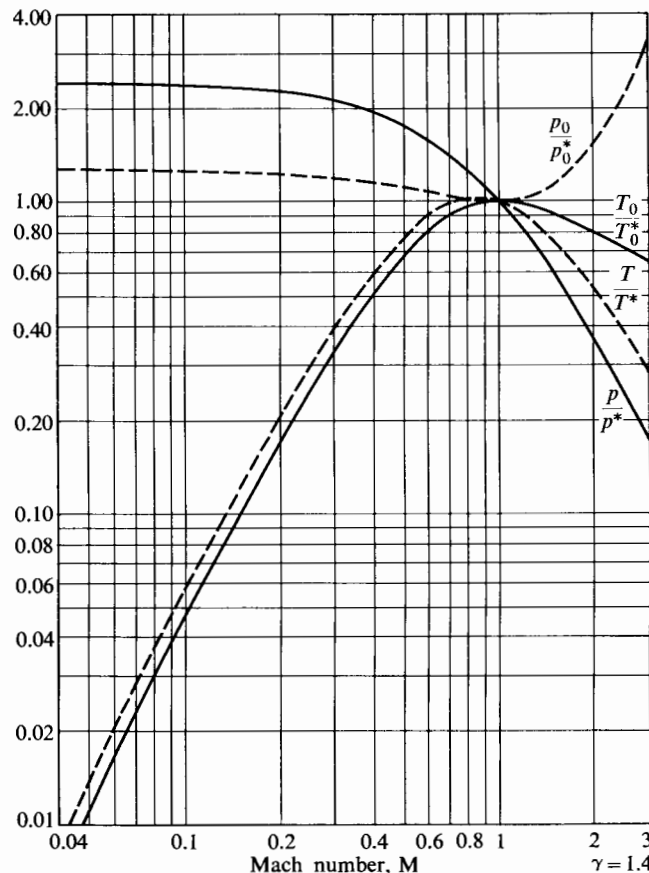


FIGURE 3.4 Frictionless flow of a perfect gas in a constant-area duct with stagnation temperature change. (From Shapiro [1].)

$$\frac{p}{p^*} = \frac{1 + \gamma}{1 + \gamma M^2}, \quad (3.22)$$

$$\frac{p_0}{p_0^*} = \left(\frac{2}{\gamma + 1} \right)^{\gamma(\gamma-1)} \left(\frac{1 + \gamma}{1 + \gamma M^2} \right) \left(1 + \frac{\gamma - 1}{2} M^2 \right)^{\gamma(\gamma-1)}. \quad (3.23)$$

In this way we can present the fluid properties as a function of a single argument, the local Mach number. Equations (3.20) through (3.23) are shown graphically in Fig. 3.4 for the case $\gamma = 1.4$. Given particular entrance conditions, T_{01}, p_{01}, M_1 , we can obtain the exit conditions after a given change in stagnation temperature as follows: The value M_1 fixes the value of T_{01}/T_0^* and thus the value T_0^* , since we know T_{01} . The exit state is then fixed by T_{02}/T_0^* , determined by

$$\frac{T_{02}}{T_0^*} = \frac{T_{01}}{T_0^*} + \frac{\Delta T_0}{T_0^*} \quad \text{or} \quad \frac{T_{02}}{T_0^*} = \frac{T_{01}}{T_0^*} + \frac{q - w}{c_p T_0^*}.$$

Then $M_2, p_2/p^*$, and p_{02}/p_0^* are all fixed by the value of T_{02}/T_0^* (for a given value of γ).

As Fig. 3.4 shows, increasing the stagnation temperature drives the Mach number toward unity whether the flow is supersonic or subsonic. After the Mach number has approached unity in a given duct, further increase in stagnation enthalpy is possible only if the initial conditions change. The flow may be said to be thermally choked.

It is interesting to note the variations in stagnation pressure as the stream is subjected to energy transfer. The stagnation pressure always drops when energy is added to the stream and rises when energy is transferred from the stream. Thus, whether the flow is subsonic or supersonic, there may be significant loss of stagnation pressure due to combustion in a moving stream. Conversely, cooling tends to increase the stagnation pressure.

3.6 CONSTANT-AREA FLOW WITH FRICTION

We can obtain another solution to Eqs. (3.1) through (3.4) for constant-area adiabatic flow with friction but no body force or work. In this case, from Eqs. (3.1), (3.2), and (3.3) the continuity, momentum, and energy relations are, respectively,

$$\text{Continuity: } \frac{dp}{\rho} + \frac{du}{u} = 0,$$

$$\text{Momentum: } \frac{dp}{p} = -\frac{\tau_0 c dx}{pA} - \frac{\rho u du}{p},$$

$$\text{Energy: } 0 = dh + u du.$$

For flow in long pipes (see Fig. 4.14), the wall shear stresses τ_0 can be correlated as follows:

$$\frac{\tau_0}{\rho u^2/2} = f\left(\frac{\rho u D}{\mu}, \frac{S}{D}\right)$$

or

$$C_f = f\left(\text{Re}, \frac{\mathfrak{H}}{D}\right),$$

in which C_f is the skin friction coefficient $\tau_0/(\rho u^2/2)$, Re is the Reynolds number $\rho u D/\mu$, \mathfrak{H} is the average height of surface roughness elements and D is the duct diameter. For Mach numbers greater than unity, the Mach number is also a significant variable. The effects of roughness (or at least of variations in roughness) are usually fairly unimportant for surfaces that have a reasonably smooth finish. We discuss this point in more detail in Chapter 4.

We can show how friction affects the Mach number as follows: First, we transform the conservation equations (by introducing the perfect-gas law and the definition of Mach number) to read:

$$\begin{aligned} \text{Continuity: } & \frac{dp}{p} - \frac{dT}{T} + \frac{1}{2} \frac{du^2}{u^2} = 0, \\ \text{Momentum: } & \frac{dp}{p} = -\frac{\gamma M^2}{2} \left(4 \frac{C_f dx}{D} \right) - \frac{u du}{RT}, \\ \text{Energy: } & 0 = \frac{dT}{T} + \frac{\gamma - 1}{\gamma} \frac{u du}{RT}. \end{aligned}$$

Since

$$M = \frac{u}{\sqrt{\gamma RT}},$$

then

$$\frac{dM^2}{M^2} = \frac{du^2}{u^2} - \frac{dT}{T}.$$

And now, if we use the continuity equation to eliminate du^2/u^2 , it follows that

$$\frac{dM^2}{M^2} = -2 \frac{dp}{p} + \frac{dT}{T}.$$

Also, combining the momentum and energy equations, we can easily show that

$$\frac{dp}{p} = -\frac{\gamma M^2}{2} \left(4 \frac{C_f dx}{D} \right) + \frac{\gamma}{\gamma - 1} \frac{dT}{T}.$$

Combining these last two expressions yields

$$\frac{dM^2}{M^2} = \gamma M^2 \left(4 C_f \frac{dx}{D} \right) - \frac{\gamma + 1}{\gamma - 1} \frac{dT}{T},$$

which, for constant stagnation temperature (using Eq. 3.10) becomes[†]

$$\frac{dM^2}{M^2} = \frac{\gamma M^2 \left(1 + \frac{\gamma - 1}{2} M^2\right)}{1 - M^2} \left(\frac{4C_f dx}{D}\right). \quad (3.24)$$

Equation (3.24) shows that $dM^2 > 0$ for $M < 1$ and $dM^2 < 0$ for $M > 1$. That is, friction *always* changes the Mach number toward unity. For constant C_f , we can integrate Eq. (3.24) between the limits $M = M_1$ and $M = 1$ to yield

$$\frac{4C_f L^*}{D} = \frac{1 - M^2}{\gamma M^2} + \frac{\gamma + 1}{2\gamma} \ln \frac{(\gamma + 1)M^2}{2 \left(1 + \frac{\gamma - 1}{2} M^2\right)}, \quad (3.25)$$

in which L^* is the length of duct necessary to change the Mach number of the flow from M_1 to unity.

Consider a duct of given cross-sectional area and variable length. If the inlet state, mass flow rate, and average skin friction coefficient are fixed, there is a maximum length of duct that can transmit the flow. Since the Mach number is unity at the exhaust plane in that case, the length is designated L^* and the flow may be said to be friction-choked. From Eq. (3.25) we can see that at any point 1 in the duct, the variable $C_f L^*/D$ depends only on M_1 and γ . Since D is constant and C_f is assumed constant, then at some other point a distance x ($x < L^*$) downstream from point 1,

$$\left(\frac{4C_f L^*}{D}\right)_x = \left(\frac{4C_f L^*}{D}\right)_1 - \frac{4C_f x}{D}.$$

From this we can determine M_x . Other relationships that one can derive [1] by using the definition of Mach number and the continuity and energy relations are:

$$\frac{T}{T^*} = \frac{\gamma + 1}{2 \left(1 + \frac{\gamma - 1}{2} M^2\right)}, \quad (3.26)$$

$$\frac{p}{p^*} = \frac{1}{M} \left[\frac{\gamma + 1}{2 \left(1 + \frac{\gamma - 1}{2} M^2\right)} \right]^{1/2}, \quad (3.27)$$

$$\frac{p_0}{p_0^*} = \frac{1}{M} \left[\frac{2}{\gamma + 1} \left(1 + \frac{\gamma - 1}{2} M^2\right) \right]^{(\gamma+1)/2(\gamma-1)}. \quad (3.28)$$

Equations (3.26), (3.27), and (3.28) are plotted in Fig. 3.5 for $\gamma = 1.4$. Again the asterisk denotes properties at that point where $M = 1$.

[†] For noncircular ducts, one can use the hydraulic diameter $D_H = 4A/c$ as an approximation in place of the diameter D .

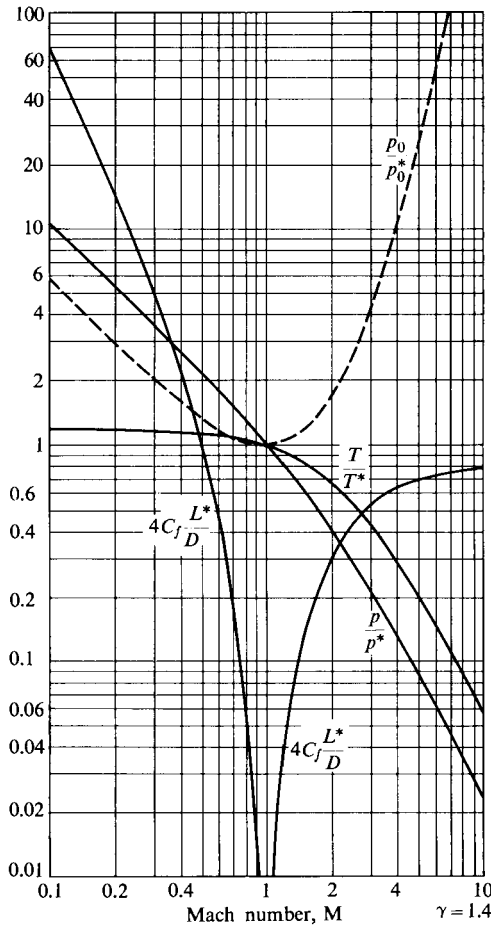


FIGURE 3.5 Adiabatic flow of a perfect gas in a constant-area duct with friction. (From Shapiro [1].)

In Sections 3.3, 3.5, and 3.6 we have treated three special problems to show the separate effects of area change, energy transfer, and friction. In each case we referred to a state where $M = 1$ and properties at that point were distinguished by an asterisk. Note that properties at that point are used as convenient normalizing quantities only, and the state need not actually exist in the real flow studied.

For a given inlet condition, the $M = 1$ conditions represent *three distinctly different states*. This is clearly indicated in Figs. 3.6 and 3.7. For two initial states, one subsonic and the other supersonic, three processes to reach a Mach number of one are shown on a typical $T-s$ diagram. The energy-transfer path is called a Rayleigh line, and the friction path is called a Fanno line. On both these lines the * condition occurs on the nose of the curve. The notations $*s, *f, *h$ indicate the $M = 1$ states reached by isentropic, friction, and heating processes, respectively.

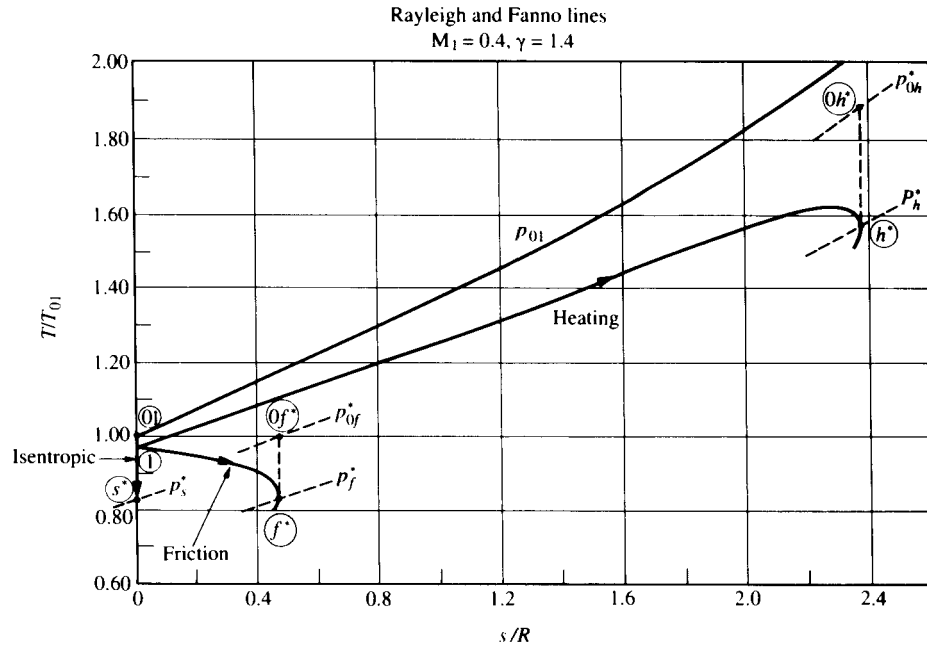


FIGURE 3.6 Typical temperature–entropy diagram for the choking process (subsonic).

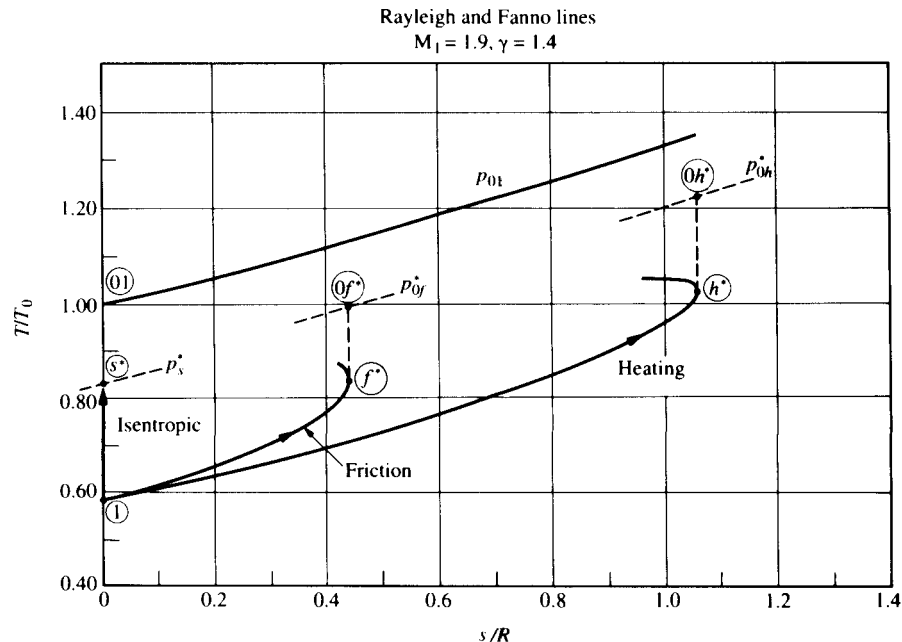


FIGURE 3.7 Typical temperature–entropy diagram for the choking process (supersonic).

Subsonic states are above the nose of the appropriate curve, and supersonic states are below it. Note also that travel in either direction is possible along the isentropic and energy-transfer curves, whereas only one direction is possible on the friction curve.

If it is important to study combined effects of these processes, then simple solutions are not available. However, the complete equations may be integrated numerically according to procedures described by Shapiro [1]. In particular, if area change, stagnation temperature change, and friction are simultaneously important, we can write the Mach number change as

$$\frac{dM^2}{M^2} = \frac{1 + \frac{\gamma - 1}{2} M^2}{1 - M^2} \left[-2 \frac{dA}{A} + (1 + \gamma M^2) \frac{dT_0}{T_0} + \gamma M^2 4C_f \frac{dx}{D} \right] \quad (3.29)$$

and the stagnation pressure change as

$$\frac{dp_0}{p_0} = -\frac{\gamma M^2}{2} \frac{dT_0}{T_0} - \frac{\gamma M^2}{2} \frac{4C_f dx}{D}. \quad (3.30)$$

Thus if we know the variation of area, stagnation temperature, and friction along the duct, we can determine the streamwise variation of M and p by numerical integration. With A , M , p , and T specified at a given point, we can determine all other flow properties, such as p_0 , T_0 , u , ρ , ρ_0 , and \dot{m} . With friction, heat transfer, and area change occurring simultaneously, the location of the sonic point $M = 1$ no longer coincides with the geometric throat defined by $dA/dx = 0$, and we must carefully arrange the terms to integrate the above equations successfully through the $M = 1$ point. To deal with the essence of this problem, we might suppose that in the vicinity of the throat $4C_f/D$ and dT_0/dx as well as A were known as functions of x . Writing Eq. (3.29) as

$$\frac{dM^2}{dx} = M^2 \left[1 + \frac{\gamma - 1}{2} M^2 \right] \frac{\left[-\frac{2}{A} \frac{dA}{dx} + (1 + \gamma M^2) \frac{1}{T_0} \left(\frac{dT_0}{dx} \right) + 4\gamma M^2 C_f / D \right]}{1 - M^2}, \quad (3.31)$$

we see that a solution can exist only if the numerator disappears as $M \rightarrow 1$, that is, if

$$\frac{dA}{dx} \rightarrow \left(\frac{1 + \gamma}{2} \right) \frac{1}{T_0} \left(\frac{dT_0}{dx} \right) + \frac{2\gamma C_f}{D}.$$

Depending on the sign and relative magnitude of dT_0/dx , the $M = 1$ point could be upstream or downstream of the geometric throat. Using l'Hopital's rule for the $M \rightarrow 1$ situation, we can show that Eq. (3.31) reduces to

$$\frac{dM^2}{dx} = \frac{\gamma(\gamma + 1)}{4} \left[\frac{1}{T_0} \left(\frac{dT_0}{dx} \right) + \frac{4C_f}{D} \right] (\sqrt{1 + \frac{8C_f}{D}} - 1), \quad (3.32)$$

in which

$$\mathcal{C} = \frac{8 \left[\frac{2}{A} \left(\frac{d^2 A}{dx^2} \right) - \frac{2}{A^2} \left(\frac{dA}{dx} \right)^2 - (1 + \gamma) \left[\frac{1}{T_0} \left(\frac{d^2 T_0}{dx^2} \right) - \frac{1}{T_0^2} \left(\frac{dT_0}{dx} \right)^2 \right] - 4\gamma \frac{d}{dx} \left(\frac{C_f}{D} \right) \right]}{\gamma^2(\gamma + 1) \left[\frac{1}{T_0} \left(\frac{dT_0}{dx} \right) + \frac{4C_f}{D} \right]^2}.$$

We can use this equation for numerical integration of dM^2/dx when M is very close to 1, provided we can specify the dependences of A , T_0 , and C_f/D on x .

3.7 SHOCKS

A shock is a discontinuity in a (partly) supersonic flow fluid. Fluid crossing a stationary shock front rises suddenly and irreversibly in pressure and decreases in velocity. It also changes its direction except when passing through a shock that is perpendicular (normal) to the approaching flow direction. Such plane normal shocks are the easiest to analyze.

Normal Shocks

For flow through a normal shock, with no direction change, area change, or work done, the continuity, momentum, and energy equations are:

$$\text{Continuity: } \rho_1 u_1 = \rho_2 u_2, \quad (3.33)$$

$$\text{Momentum: } p_1 - p_2 = \rho_1 u_1 (u_2 - u_1), \quad (3.34)$$

$$\text{Energy: } T_{01} = T_{02}, \quad (3.35)$$

where the subscripts 1 and 2 indicate initial and final states, respectively. Two solutions to these equations are possible, one of which states simply that no change occurs. By introducing Mach number $M = u/\sqrt{\gamma RT}$ and $p = \rho RT$, we can transform Eqs. (3.33) through (3.35) to

$$\frac{p_2}{p_1} = \frac{M_2}{M_1} \sqrt{\frac{T_2}{T_1}},$$

$$\frac{p_2}{p_1} = \frac{1 + \gamma M_1^2}{1 + \gamma M_2^2},$$

$$\sqrt{\frac{T_2}{T_1}} = \frac{\sqrt{1 + \frac{\gamma - 1}{2} M_1^2}}{\sqrt{1 + \frac{\gamma - 1}{2} M_2^2}},$$

respectively. Then, eliminating p_2/p_1 and T_2/T_1 , we arrive at

$$\frac{M_2 \sqrt{1 + \frac{\gamma - 1}{2} M_2^2}}{1 + \gamma M_2^2} = \frac{M_1 \sqrt{1 + \frac{\gamma - 1}{2} M_1^2}}{1 + \gamma M_1^2},$$

which, with considerable effort, we can transform to

$$M_2^2 = \frac{M_1^2 + \frac{2}{\gamma - 1}}{\frac{2\gamma}{\gamma - 1} M_1^2 - 1}. \quad (3.36)$$

With this result we can obtain

$$\frac{p_2}{p_1} = \frac{2\gamma}{\gamma + 1} M_1^2 - \frac{\gamma - 1}{\gamma + 1}, \quad (3.37)$$

$$\frac{p_{02}}{p_{01}} = \frac{\left[\left(\frac{\gamma + 1}{2} M_1^2 \right) / \left(1 + \frac{\gamma - 1}{2} M_1^2 \right) \right]^{\gamma(\gamma-1)}}{\left(\frac{2\gamma}{\gamma + 1} M_1^2 - \frac{\gamma - 1}{\gamma + 1} \right)^{1/(\gamma-1)}}, \quad (3.38)$$

and

$$\frac{T_2}{T_1} = \frac{\left(1 + \frac{\gamma - 1}{2} M_1^2 \right) \left(\frac{2\gamma}{\gamma - 1} M_1^2 - 1 \right)}{\frac{(\gamma + 1)^2}{2(\gamma - 1)} M_1^2}. \quad (3.39)$$

In Figure 3.8, M_2 and p_{02}/p_{01} are plotted for case $\gamma = 1.4$. We can see that rather large losses of stagnation pressure occur across Mach numbers greater than about 1.5. Tables of all the functions for various γ are provided by Keenan, Chao, and Kaye [2].

It is interesting to consider that Eqs. (3.33) and (3.34) are requirements for Rayleigh flow (which is one-dimensional, constant area, and frictionless), and that Eqs. (3.33) and (3.35) are requirements for Fanno flow (which is one-dimensional, constant area, and adiabatic). Thus a normal shock process can be interpreted as the simultaneous satisfaction of Fanno and Rayleigh conditions. Problem 3.10 explores the implication of this situation.

Even if a normal shock is curved (e.g., spherical) rather than planar, it will be described by Eqs. (3.38) through (3.39) because its thickness (of the order of a few mean free paths of the molecules) will generally be very much less than its radius of curvature. Hence one could generally draw a control volume enclosing a small part of the shock surface in which the shock surface would appear to be very nearly planar.

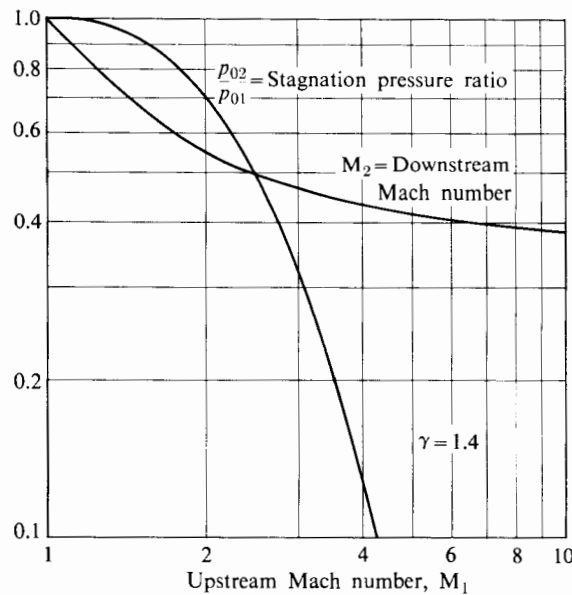


FIGURE 3.8 Normal shock functions. (From Shapiro [1].)

Oblique Shocks

If a plane shock is inclined at an angle to the flow, the fluid passing through suffers not only a sudden rise in pressure and decrease in speed but also a sudden change of direction. The situation is illustrated in Fig. 3.9 for an oblique shock $s-s'$ in one-dimensional flow. In passing through the shock, the fluid is deflected

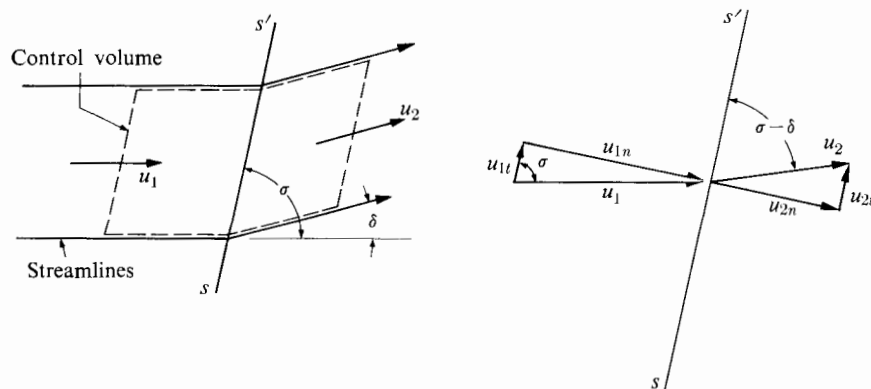


FIGURE 3.9 Oblique shock geometry.

through an angle δ . The basic equations applied to the indicated control volume are:

$$\text{Continuity: } \rho_1 u_{1n} = \rho_2 u_{2n},$$

$$\text{Energy: } T_{01} = T_{02}.$$

We can write two momentum equations for this flow, one for changes in momentum perpendicular to the shock, the other for changes parallel to it:

- a. Momentum normal to the shock, $p_1 - p_2 = \rho_2 u_{2n}^2 - \rho_1 u_{1n}^2$,
- b. Momentum parallel to the shock, $0 = \rho_1 u_{1n}(u_{2t} - u_{1t})$,

in which the subscripts n and t indicate directions normal to and parallel to the shock, respectively. From the second equation,

$$u_{2t} = u_{1t}.$$

Since the velocity component parallel to the shock is the same on both sides of it, we can see that an oblique shock becomes a normal shock relative to a coordinate system moving with velocity $u_{1t} = u_{2t}$. This fact permits us to use the normal shock equations to calculate oblique shocks. For example, given the up-

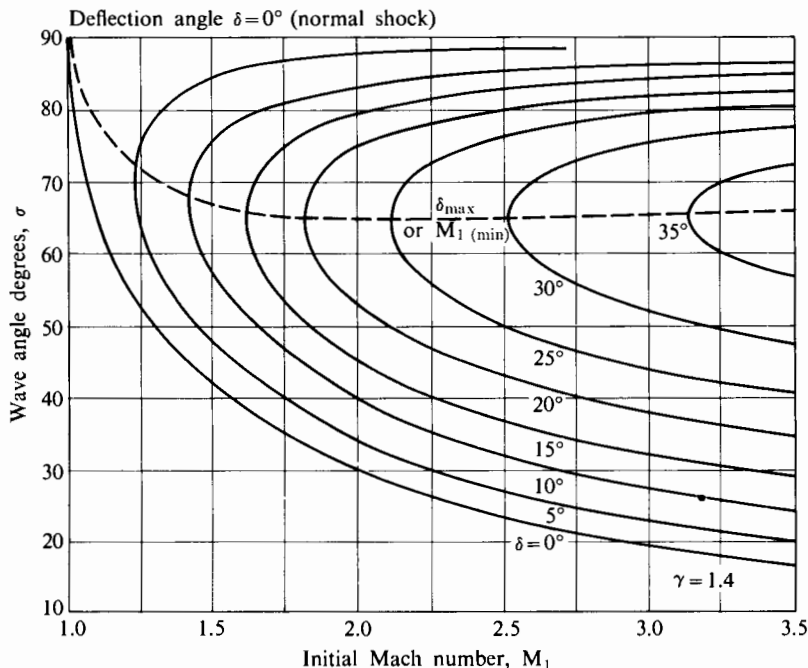


FIGURE 3.10 Shock angle versus inlet Mach number and turning angle [1]. Curves above dashed line hold for $M_2 < 1$, and curves below hold for $M_2 > 1$. (From Shapiro [1].)

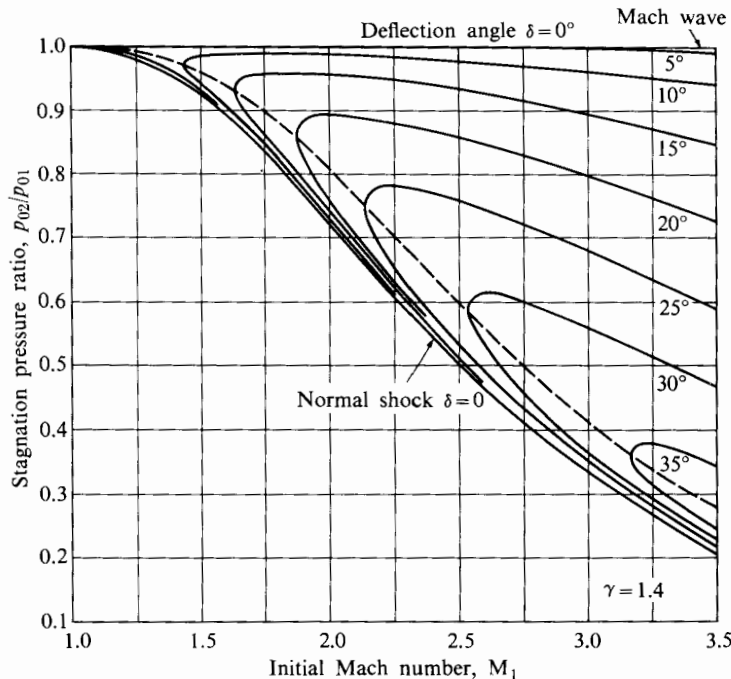


FIGURE 3.11 Stagnation pressure ratio versus inlet Mach number, with turning angle as parameter [1]. Curves above dashed line hold for $M_2 > 1$, and curves below hold for $M_2 < 1$. (From Shapiro [1].)

stream (or initial) Mach number M_1 and the wave angle σ , we could calculate $M_{1n} = M_1 \sin \sigma$ and subsequently M_{2n} by substituting M_{1n} for M_1 in Eq. (3.36). The condition $u_{2i} = u_{1i}$ can be expressed as $M_{2i} = M_{1i} \sqrt{T_1/T_2}$, and T_1/T_2 can be calculated from Eq. (3.39) by substituting M_{1n} for M_1 . In this way, the downstream Mach number M_2 and the deflection angle δ can be determined. We can show that

$$\tan(\sigma - \delta) = \frac{2\left(1 + \frac{\gamma - 1}{2} M_1^2 \sin^2 \sigma\right)}{(\gamma + 1) M_1^2 \sin \sigma \cos \sigma}. \quad (3.40)$$

Alternatively, the four equations given above, along with the equation of state, can be reduced to a set of four independent equations relating the variables $M_1, M_2, p_2/p_1, \rho_2/\rho_1, \sigma$, and δ [1]. If any two variables are given—for example, M_1 and the turning angle δ —then all others are determined, and the downstream (or final) conditions can be found in terms of the upstream conditions.

The solution of these equations from Shapiro [1] is given in Figs. 3.10, 3.11, and 3.12 for the case $\gamma = 1.4$ and for various values of δ . In particular, Fig. 3.10 represents, for $\gamma = 1.4$, Eq. (3.40).

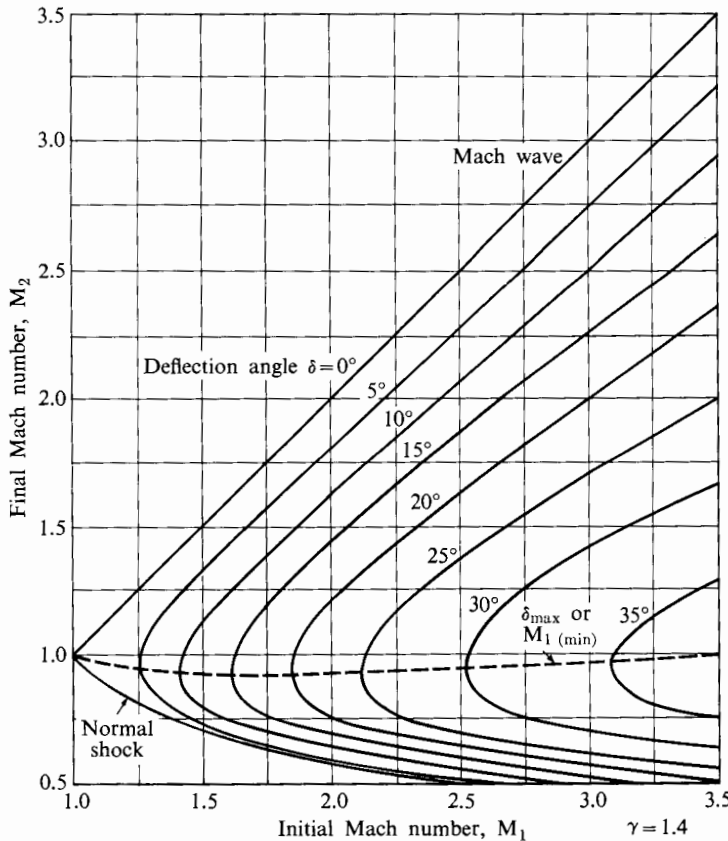


FIGURE 3.12 Exit Mach number versus inlet Mach number, with turning angle as parameter [1]. Curves above dashed line correspond to small σ , and curves below correspond to large σ . (From Shapiro [1].)

Axisymmetric oblique shocks are discussed by Shapiro [3], who represents a complete solution for the case of the conical shock as well as methods of treatment of the general axisymmetric shock problem. The axisymmetric oblique shock is not related to the plane normal shock in a simple way, and its solution is considerably more complicated than that of the plane oblique shock.

PROBLEMS

1. A perfect gas expands in a frictionless nozzle from stagnation conditions $p_0 = 4 \text{ MPa}$, $T_0 = 2500 \text{ K}$ to ambient pressure 0.1 MPa . Given that the expansion is isentropic, determine the following conditions at the final pressure: (1) velocity, (2) Mach number, (3) temperature, and (4) area per unit mass flow. How does the final flow area compare with the throat area for a

given mass flow? The specific heat ratio γ is 1.4, and the molecular weight \bar{M} is 30.

2. Air flows through a cylindrical combustion chamber of diameter 0.3 m and length 3 m. Stations (1) and (2) are the inlet and outlet, respectively. The inlet stagnation temperature is 1000 K and the inlet stagnation pressure is 1.5 MPa.

- If the skin friction coefficient is $C_f = 0.0040$ (approximately uniform) and no combustion takes place, what will the inlet Mach number be if it is subsonic and the exit Mach number is unity? What are the values of static and stagnation pressures at the exit?
- If combustion takes place and the heat of reaction is 600 kJ/kg of mixture, neglecting frictional effects, and if the inlet Mach number is 0.25, what is the exit Mach number?

The combustion process may be simulated by simple heating with constant specific heat ratio.

- If, in a similar problem, the effects of combustion and skin friction on the flow are of the same order of magnitude, how might their simultaneous effects be estimated?

The fluid may be considered a perfect gas with $\gamma = 1.4$ and $\bar{M} = 29$.



PROBLEM 2

3. A given steady flow of a perfect gas in a constant-area duct is affected by friction. For subsonic flows the wall friction coefficient is not very sensitive to Mach number and may be represented approximately (for smooth-walled ducts) as

$$C_f = 0.045 \left(\frac{\dot{m}}{\sqrt{A} \mu} \right)^{-0.2},$$

the same as for incompressible flow.

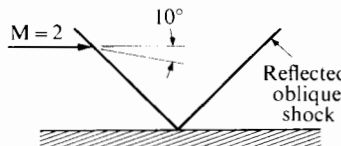
Consider two ducts operating with an inlet Mach number of 0.2 and $\gamma = 1.4$. With a Reynolds number in both ducts of 10^5 , the exit Mach numbers are 0.25 for one and 0.95 for the other. Determine the relative pressure drop $(p_1 - p_2)/p_1$ for both.

Now let the Reynolds number be changed to 10^7 with the same inlet conditions and the same duct lengths as before. Determine the new relative pressure drops.

4. Show that for a perfect gas the Mach number at the nose of the Fanno line (friction and no heating) and at the nose of the Rayleigh line (heating and no friction) is unity. The nose of these lines, examples of which are given in Figs. 3.6 and 3.7, is defined by $ds/dT = 0$. If a duct is sufficiently long that frictional effects (with no heating) have driven the Mach number at exit to unity, what would happen to the flow rate if, without changing the upstream values of p_0 and T_0 , the length of pipe suddenly increased?

If, in another duct, friction is negligible but heating has caused the exit Mach number to approach unity, what must happen if the heating rate is suddenly increased?

5. A Mach 2 flow passes through an oblique shock as shown and deflects 10° . A second oblique shock reflects from the solid wall. What is the pressure ratio across the two-shock system? Assume that there is no boundary layer near the wall; that is, the flow is uniform in each of the regions bounded by the shocks.



PROBLEM 5

6. Air enters a constant-area duct at Mach 3 and stagnation conditions 750 K and 1.3 MPa. In the duct it undergoes a frictionless energy-transfer process such that the exit Mach number is unity. Consider two cases: (a) normal shock at inlet to the duct and (b) shock-free supersonic heating. Determine the stagnation temperature and pressure at the exit in each case. Is there any reason why the total energy transfer should differ (or be equal) in the two cases?
7. A uniform mixture of very small solid particles and a perfect gas expands adiabatically from a given chamber temperature through a given pressure ratio in a nozzle. The particles are so small that they may be considered to travel with the local gas speed. Since the density of the solid material is much higher than that of the gas phase, the total volume of the particles is negligible. The ratio of solid to gas flow rates is μ , where $0 < \mu < 1$.

Consider two cases:

- No heat is transferred between solid and gaseous phases, and
- the solid particles have the local gas temperature at all points in the flow.

Qualitatively, how does the presence of the solid particles affect the velocity at the end of the expansion? Show that for both cases the mixture is equiva-

lent to the adiabatic expansion of a homogeneous gas of different molecular weight \bar{M} and specific heat ratio γ .

8. A 1 m^3 rocket-propellant chamber is filled with combustion gases at 3000 K and 7 MPa at the instant combustion ceases. The throat area of the nozzle is 0.1 m^2 . Estimate the time it takes for the chamber pressure to drop to 0.7 MPa . Assume that at the instant combustion ceases, the chamber propellant supply stops completely, and also that $\gamma = 1.2$ and $\bar{M} = 20$.
9.
 - a. Compare the work of compression per unit mass of air for both reversible adiabatic and reversible isothermal compression through a pressure ratio of 10 with initial conditions 300 K and 0.1 MPa . Why should cooling during compression reduce the work?
 - b. In an effort to provide a continuous cooling process during compression, water is sprayed into an airstream entering the axial compressor of a gas turbine engine. The compression may be taken to be reversible, and the evaporation rate is approximately $dw/dT = k$, where w is the water-air mass ratio, T is the mixture temperature, and k is a constant. If $w \ll 1$, the process may be simplified by considering the sole effect of the evaporation to be energy transferred from the gas phase. Show how the final temperature and the work of compression depend on k .
10. Air at 300 K and 1.5 MPa travels with a Mach number of 2.5 just before it is decelerated by a normal shock wave. Setting the entropy of the air equal to zero at this initial condition, draw the Rayleigh and Fanno lines that pass through this initial state point in a state diagram whose x - and y -coordinates are S/R and T/T_1 , respectively. Look for a second intersection of these Rayleigh and Fanno lines and show that this point must represent the state of the air immediately downstream of the shock wave. Show from the second law of thermodynamics why it is possible to have a sudden jump from supersonic to subsonic flow, but not vice versa. Take $\gamma = 1.4$.

In constructing these lines, it may be helpful to select a series of supersonic and subsonic Mach numbers and calculate for each the entropy from the state relationship

$$\frac{S}{R} = \frac{\gamma}{\gamma - 1} \ln \frac{T}{T_1} - \ln \frac{p}{p_1}.$$

Show that for the Fanno line (friction but constant T_0)

$$\frac{T}{T_1} = \frac{2 + (\gamma - 1)M_1^2}{2 + (\gamma - 1)M^2} \quad \text{and} \quad \frac{p}{p_1} = \sqrt{\frac{T}{T_1} \frac{M_1}{M}},$$

whereas for the Rayleigh line (heating but no friction)

$$\frac{p}{p_1} = \frac{1 + \gamma M_1^2}{1 + \gamma M^2} \quad \text{and} \quad \frac{T}{T_1} = \left(\frac{p}{p_1} \frac{M}{M_1} \right)^2.$$

11. A stream of air whose Mach number is 2 is suddenly deflected and decelerated by a plane oblique shock wave originating from the tip of a stationary wedge. A schlieren photo shows that the wave angle is at 45° to the original forward direction of the air. Using the normal shock equations for the component of Mach number perpendicular to the wave, and recognizing that the velocity component parallel to the wave will pass through the wave unchanged, estimate the wedge—that is, the air-deflection—angle. Compare your result with Fig. 3.10.
12. A perfect gas with $\gamma = 1.4$ expands in a cylindrical nozzle whose area distribution (with axial distance x) is given by

$$\frac{A}{A^*} = 1 + \left(\frac{x}{D^*} \right)^2 \quad -0.1 \leq \frac{x}{D^*} \leq +0.1,$$

in which $A^* = 0.01 \text{ m}^2$ is the throat area and D^* is the throat diameter. In the vicinity of the throat the wall friction coefficient is known, from test data, to be given by

$$C_f = C_{f\max}(D^*/D)^{0.8},$$

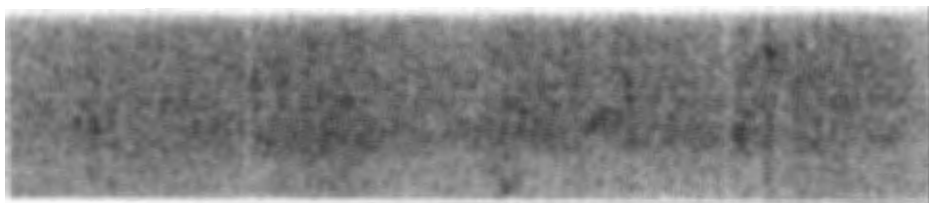
in which $C_{f\max} = 0.008$ and D^* is the throat diameter. Up to the point $x = -0.1D^*$, the flow may be considered isentropic and one-dimensional.

Determine the location of the Mach 1 point and show how to calculate the variation of Mach number in the range $-0.1 \leq x/D^* \leq 0.1$.

13. Show how oblique shock graphs similar to those of Figs. 3.10 to 3.12 could be generated for the case $\gamma = 1.35$. After deriving Eq. (3.40) from consideration of a normal shock with a moving coordinate system, show how one may use Eq. (3.40) with the normal shock equations to present a complete solution.

REFERENCES

- Shapiro, A. H. *The Dynamics and Thermodynamics of Compressible Fluid Flow*, vol. I. New York: Ronald Press, 1953, chaps. 1–8, 16. Reprint ed., Wiley. (Reprinted by permission.)
- Keenan, J. H., J. Chao, and J. Kaye. *Gas Tables*. New York: Wiley, 1988.
- Shapiro, A. H. *The Dynamics and Thermodynamics of Compressible Fluid Flow*, vol. II. New York: Ronald Press, 1954. Reprint ed., Krieger. (Reprinted by permission.)



C H A P T E R

4

BOUNDARY LAYER MECHANICS AND HEAT TRANSFER

4.1 INTRODUCTION

Historically the development of boundary layer theory followed the development of mathematical solutions for flows assumed to be nonviscous. In the latter half of the nineteenth century—after Euler had formulated the basic equations of motion—Helmholtz, Kelvin, Lamb, Rayleigh, and others applied them to a number of physical situations. By neglecting the effects of viscosity, they obtained elegant mathematical descriptions of various flow fields. It was argued that a fluid like air, for example, which is so rarefied as to be invisible, must have negligible viscosity. With some exceptions, however, the so-called perfect-fluid theory disagreed strongly with the results of experiment.

One particular example, which came to be known as *d'Alembert's paradox*, attracted a great deal of attention. As an illustration, the flow of a fluid over a cylinder as predicted by nonviscous theory is shown in Fig. 4.1(a). The theory predicts that the velocity and pressure fields are both symmetrical about a plane normal to the upstream velocity vectors. Thus the fluid can exert no net forces (lift or drag) on the cylinder. Moreover, this conclusion is independent of the shape of the body; if the fluid is truly inviscid, it can be shown mathematically that for any body shape the net integrated pressure force on the body will be zero. Of course, this conclusion directly contradicts experience. Everyone knows that it takes a finite force to hold a body immersed in a moving stream or to propel it through a stationary mass of fluid; hence the paradox.

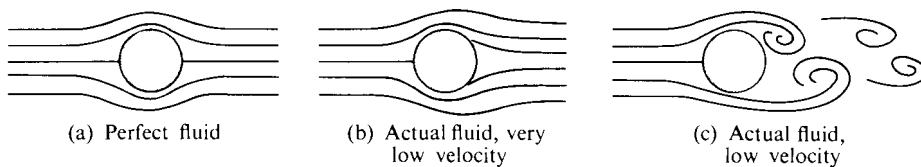


FIGURE 4.1 Flow patterns about a cylinder.

Observations of the actual streamline pattern around the cylinder reveal something like Fig. 4.1(b), which suggests that the streamline symmetry is grossly disturbed. On the rear side of the cylinder the fluid seems almost stagnant when the stream velocity is quite low. For higher speeds, fairly violent oscillations take place, which affect the entire streamline pattern near the cylinder. Under certain conditions it is possible to observe a periodic shedding of vortices alternately from the top and bottom sides, as suggested by Fig. 4.1(c). This downstream flow pattern has been called a *vortex street*.

The drag of the actual fluid on the cylinder is largely due to the asymmetry of the pressure distribution on its surface. Figure 4.2 shows measured pressure distributions on a cylinder and, for comparison, the prediction of perfect-fluid theory. The symbol ρ stands for fluid density, and the pressure and velocity far upstream are denoted by p_∞ and u_∞ . One can see that two experimental pressure distributions may be measured (we will discuss the difference between the two later) and that both differ greatly from the theoretical result. The fact that the average pressure on the cylinder is much higher on the upstream hemisurface explains most of the drag. In addition to this, the viscous force of the fluid on the cylinder imposes a drag force that, in this particular case, is considerably smaller than the pressure drag. For "streamlined" bodies, which have much less pressure drag, the viscous force is relatively more important.

For quite a period the discrepancy between existing theory and physical results was unexplained, and a marked rift developed between the theoreticians,

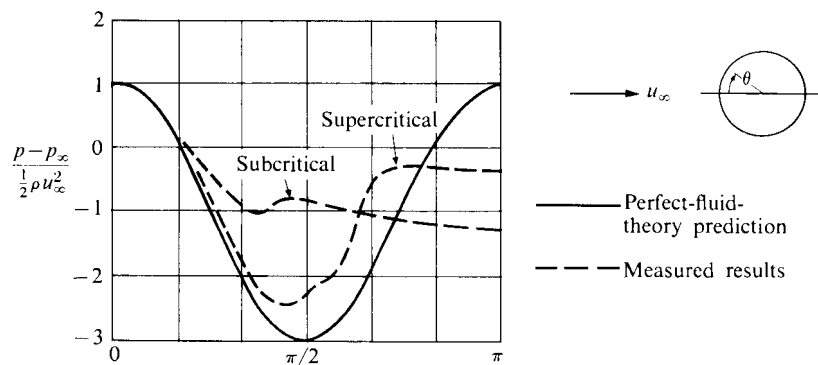


FIGURE 4.2 Pressure distribution on a cylinder.

who continued to expound the perfect-fluid theory, and the engineering-oriented workers like Bernoulli and Hagen, who actively developed the empirical body of knowledge generally called hydraulics. The equations of motion that do take viscosity into account—the Navier-Stokes equations—were formulated but were so complicated that they could not, in general, be solved. It appeared exceedingly difficult to improve mathematically on the perfect-fluid theory except in a few very special cases.

Then Prandtl (in 1904) made a major contribution to the solution of the problem by introducing the concept of the viscous boundary layer. He showed that even for fluids of vanishingly small viscosity there is a thin region near the wall in which viscous effects cannot be neglected. Since the velocity of the fluid particles on the wall is zero, there may be, under certain conditions, a region of large velocity gradient next to it. Then, even though the viscosity μ may be small, the shear stress on a fluid layer, $\tau = \mu(\partial u / \partial y)$, may be large in that region since $\partial u / \partial y$ is large. This region is called the viscous boundary layer. A boundary layer of thickness δ is indicated in Fig. 4.3. Outside the layer, the velocity gradient $\partial u / \partial y$ will be so small that viscous shear may be quite unimportant, so that the fluid behaves as though it actually had zero viscosity.

Thus Prandtl showed that the flow field may be broken into two parts: a thin viscous zone near the wall, and an outer zone where the nonviscous theory is adequate. This suggested the major simplification of the Navier-Stokes equations that is the basis of boundary layer theory. For fairly high-speed flow, in which the boundary layer is so thin that the pressure gradient normal to the wall is negligible, Prandtl and others showed how to treat the boundary layer mathematically for special cases, many of which have been solved.

Given that a boundary layer exists on a body, we can easily see qualitatively why the case of vanishing viscosity is fundamentally different from the case of zero viscosity. Figure 4.2 shows that for zero viscosity a particle on the surface streamline of the cylinder rises in pressure to the stagnation value when it impinges on the cylinder ($\theta = 0$). Then the pressure falls to a minimum (and the velocity rises to a maximum) at the position $\theta = \pi/2$. From that point it travels to the rearward stagnation point ($\theta = \pi$), having just enough momentum to climb the “pressure hill” and arrive at the stagnation point.

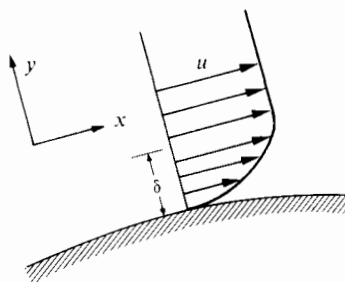


FIGURE 4.3 Boundary layer velocity distribution.

However small the viscosity, the viscous case is fundamentally different. Viscous action has slowed the fluid near the wall. When a particle in the boundary layer reaches $\theta = \pi/2$, it will have reduced momentum so that only a small pressure rise will stop its forward motion, or actually send it moving backward. For this reason the particle can no longer follow the contour of the wall. The accumulation of stagnant fluid on the back part of the cylinder deflects the outer streamlines, as suggested in Fig. 4.1(b). This in turn greatly modifies the wall pressure distribution, as shown in Fig. 4.2. When the streamlines in the vicinity of the wall cease to follow it, they are said to *separate*.

This accumulation of stagnant or near-stagnant fluid and the resultant gross distortion of the streamlines means that the boundary layer behavior can have an important influence on overall flow behavior even though the quantity of fluid directly affected by viscosity is a small fraction of the total flow. Figure 4.4 shows three separated flows of practical significance. Both the compressor cascade and the subsonic diffuser are designed so that the mainstream velocity decreases in the flow direction; hence the flow is against an adverse pressure gradient. If the pressure rise is too great, the boundary layer will separate, creating regions of near-stagnant fluid as shown. Within rocket nozzles the pressure gradient is usually favorable, so that separation need not be a problem. Under certain off-design conditions, however, shocks can occur within rocket nozzles, and the sudden pressure rise across the shock can cause separation.

Separation and its consequences in these devices will be discussed in the following chapters where appropriate. Our purpose in this chapter is to establish the nature and cause of separation and to indicate how one might predict its occurrence. Separation is, of course, only one phase of boundary layer behavior. We will be interested also in the behavior of nonseparated boundary layers, since they are of importance to heat transfer and other phenomena.

The classic picture of separation is illustrated in Fig. 4.5, which shows a series of velocity profiles in a boundary layer as it approaches and passes the separation

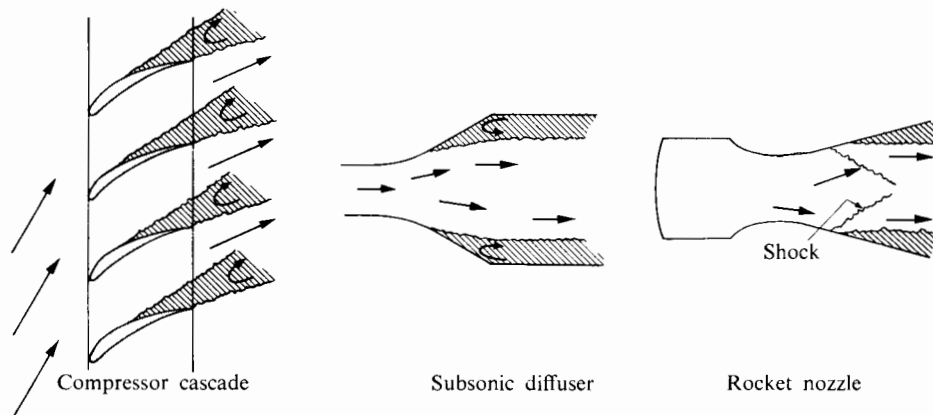


FIGURE 4.4 Some practical devices in which separation may occur.

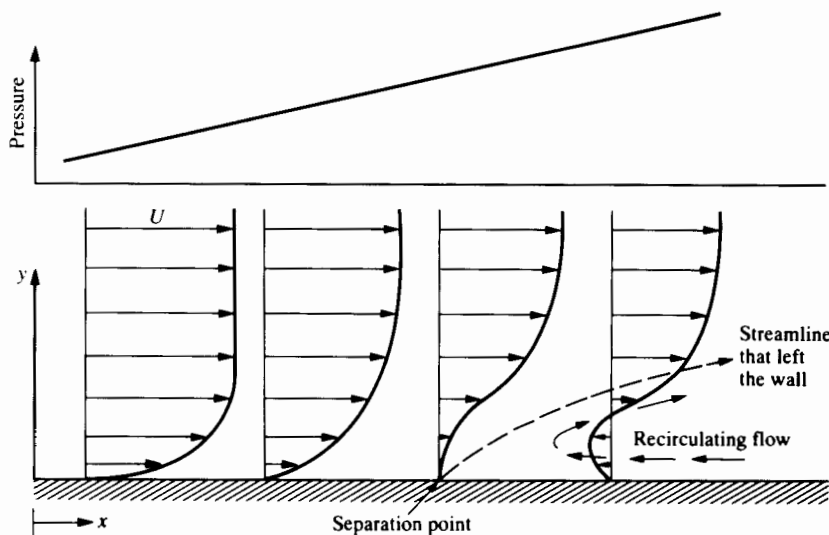


FIGURE 4.5 A simplified picture of the development of separation.

point. As the pressure rises, the free-stream velocity U falls, as the Bernoulli equation would predict. However, the effect of a given change in pressure is greater on the slow-moving fluid near the wall than on the free-stream fluid. The fluid near the wall can be slowed to a stagnant state and then be made to flow backward if the adverse pressure gradient continues.

The separation point is generally defined as that point where a streamline very near the wall leaves the wall. In two-dimensional flow this corresponds to the point at which the velocity profile has zero slope at the wall. That is,

$$\left(\frac{\partial u}{\partial y}\right)_{y=0} = 0 \quad (\text{two-dimensional separation}).$$

Figure 4.5 suggests that, past the separation point, there is a region of recirculating flow. In practice this region is highly unstable. It may be quite difficult to determine analytically, since once separation occurs, there is a strong interaction between the body of stagnant fluid and the free stream. Often an adjustment of the free-stream geometry results such that the adverse pressure gradient is reduced to practically zero, in which case there is no force to drive the recirculating fluid.

The effects of *pressure gradient* on the shape of the boundary layer, which are shown in Fig. 4.5, may be explained in a simplified manner as follows: Let the boundary layer be replaced by a hypothetical discontinuous flow shown in Fig. 4.6, in which the continuous variation in velocity normal to the wall is replaced by two step changes. Further, in order to focus on the effect of pressure gradient, let us for the moment neglect shear stresses. (We will discuss the effects

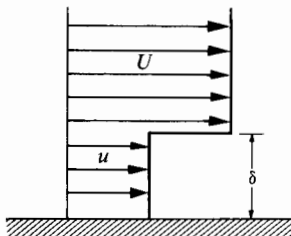


FIGURE 4.6 Discontinuous boundary layer.

of shear stresses subsequently.) With these assumptions, the momentum equation requires that

$$\frac{dp}{\rho} = -U dU \quad (\text{free stream}), \quad \frac{dp}{\rho} = -u du \quad (\text{boundary layer}),$$

where, in keeping with boundary layer assumptions, the free stream and the boundary layer experience the *same* pressure change. Equating the two expressions for dp and defining the ratio $\alpha = u/U$ results in

$$d\alpha = -\frac{dp}{\rho U^2} \left(\frac{1 - \alpha^2}{\alpha} \right).$$

Hence if the pressure rises ($dp > 0$), α decreases, and the boundary layer fluid is decelerated more than the free stream. Noting that $-dp/\rho U^2$ is simply dU/U , we can integrate this expression (for constant density):

$$\frac{1 - \alpha^2}{\alpha - \alpha_1^2} = \frac{U_1^2}{U^2},$$

where the subscript 1 refers to an initial condition. We can find the thickness δ of the boundary layer from the equation for continuity, which requires that

$$\rho u \delta = \rho u_1 \delta_1$$

or, again for constant density,

$$\frac{\delta}{\delta_1} = \frac{u_1}{u} = \frac{\alpha_1 U_1}{\alpha U}.$$

The two quantities α and δ are plotted against U/U_1 in Fig. 4.7 for the particular case $\alpha_1 = \frac{1}{2}$. We can see that this boundary layer separates ($\alpha \rightarrow 0, \delta \rightarrow \infty$) when the free-stream velocity has decreased by less than 14%.

With this picture of the relatively large effect of a given pressure rise on the more slowly moving fluid, it would appear that *any* pressure rise applied to a real boundary layer would cause separation since, if the velocity goes continuously to zero at the wall, there will always be *some* fluid with insufficient momentum to negotiate the pressure rise. However, this tendency toward separation is resisted, up to a point, by viscous stress. That is, the slowly moving fluid can be “dragged”

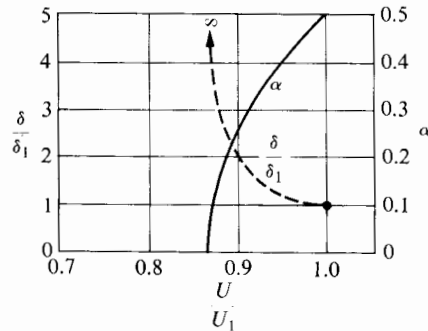


FIGURE 4.7 "Growth" of step boundary layer near separation for $\alpha_1 = \frac{1}{2}$.

through a pressure rise by the faster fluid farther from the wall. An important method of reducing the separation tendency is to enhance this "drag" force by increasing the effective shear stress through turbulent motion.

The mention of turbulent motion introduces another important aspect of boundary layer behavior. In 1883 Reynolds showed that under certain conditions dye particles injected into a pipe flow moved smoothly along streamlines without lateral fluctuations. In the same pipe at higher velocities, this smooth laminar motion broke down into turbulent motion consisting of rapid random fluctuations superposed on the mean motion. After the flow had become turbulent, the dye lines rapidly mixed with the surrounding fluid, the macroscopic turbulent mixing process being at least an order of magnitude faster than molecular diffusion (the only agency for mixing in laminar flow).

The same transition behavior takes place in the boundary layer, resulting in a significant reduction in its tendency to separate. The reason for this is that the turbulent fluctuations constitute a mechanism for transporting high momentum from the outer part of the layer to the region near the wall. The effect is as if there were an increased shear stress or, as we will see, an increased coefficient of viscosity. This tends to raise the wall shear stress, but it also means that the turbulent boundary fluid can climb higher up the "pressure hill" than the fluid in the laminar layer. Figure 4.8 compares typical turbulent and laminar boundary layer velocity profiles.

The fact that the turbulent layer tends to have much higher momentum (and shear stress) near the wall gives it an increased resistance to separation. As a method of specifying the resistance of a boundary layer to separation, it is useful to define a pressure coefficient C_p as

$$C_p = \frac{\Delta p}{\frac{1}{2} \rho U^2},$$

where U is the free-stream velocity at the point where the pressure begins to rise and Δp is the total increase in pressure up to the point in question.

For an approximate comparison of cases in which the adverse pressure gradient is not abrupt (i.e., where the shear stress has time to act), it may be said that

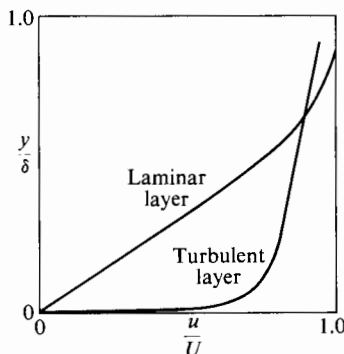


FIGURE 4.8 Comparison of laminar and turbulent velocity profiles.

the laminar boundary layer will support a pressure rise given by $0.15 < C_p < 0.2$, whereas the turbulent boundary layer can tolerate without separation a pressure rise corresponding to $0.4 < C_p < 0.8$, depending on the Reynolds number and the upstream pressure distribution of the flow.

The onset of turbulence, or transition as it is called, is dependent in a given device on fluid properties and velocity, the general or upstream turbulence level, and the geometry of the particular device. In the case of pipe flow, for example, geometry is completely specified (far from the entrance) by pipe diameter D and wall roughness. The pertinent fluid properties are density ρ , viscosity μ , and the average velocity \bar{U} . One can arrange these variables in a dimensionless form known as the Reynolds number, Re , that is defined by

$$Re = \frac{\rho \bar{U} D}{\mu}.$$

Reynolds found that for "smooth" pipes (commercial pipes and tubing are usually "smooth") and very quiet inlet conditions, the transition process could in fact be correlated with a critical Reynolds number below which the flow was laminar and above which it was turbulent.

More generally, we find that transition in any series of *geometrically similar* devices can be correlated with the Reynolds number, where D is replaced by some characteristic length L and \bar{U} by some characteristic velocity U . Thus

$$Re = \frac{\rho U L}{\mu}.$$

Obviously, a critical value for Re can have meaning only within the geometry for which it was defined. With these facts in mind, the explanation of the two pressure distributions observed on the cylinder of Fig. 4.2 becomes straightforward. For reasonably low velocities (below a "critical" Reynolds number), the boundary layer remains laminar and separates readily on the back of the cylinder before much pressure rise has taken place. At the critical Reynolds number, the bound-

ary layer becomes turbulent and is able to flow considerably farther around the back of the cylinder before separation. As it does so, it rises in pressure, thus reducing the discrepancy between inviscid and actual pressure distributions. Since the drag on a blunt body such as a cylinder is primarily a pressure force (as opposed to skin friction), the onset of turbulent flow in this case is actually accompanied by decreased drag.

In most practical fluid machines that we discuss in this book, the boundary layers are turbulent, and so long as this is true, the influence of Reynolds-number variations on overall performance is usually minor. But under extreme conditions, as, for example, at very high altitudes, the Reynolds number can become low enough that portions of the flow revert to laminar flow. There usually follows a rather substantial reduction in efficiency and other measures of performance, due to the increased tendency toward separation.

4.2 THE BOUNDARY LAYER EQUATIONS

The general equations for the flow of Newtonian viscous fluids are called the Navier-Stokes equations [1]. Because of their mathematical complexity, it is possible to obtain their exact solutions for only a few physical situations. In many cases, however, it is legitimate to make simplifying approximations and thereby obtain solutions that have a useful range of validity. The boundary layer equations are much more tractable than the Navier-Stokes equations. One can derive them by neglecting certain terms in the Navier-Stokes equations that can be shown to be quite unimportant in boundary layer flows. Schlichting [1] develops the method in careful detail.

In the following discussion we develop equations less rigorously, but more directly, for the special case of the steady, two-dimensional, incompressible boundary layer. Shapiro [2] uses this approach to develop equations for compressible flow and includes a good discussion of the range of validity of the simplifications. The object in view is to lay a foundation for a quantitative description of both laminar and turbulent boundary layers, with particular emphasis on skin friction, separation, and heat transfer. Although the solutions of the boundary layer equations that are available are seldom exactly applicable to the complex flows in real machines, they at least illustrate the forces at work and the behavior typical of the boundary layer.

Consider a very small control volume within a boundary layer, as shown in Fig. 4.9. Velocities in the x - and y -directions are u and v , respectively, and the shear stresses in these directions are τ_x and τ_y . To apply the continuity and momentum equations to this control volume, we need to know the mass and momentum flux across each surface and the force (shear and pressure) acting on each surface.

The outward fluxes of mass and x -momentum are shown in Table 4.1. Since the flow is taken to be two-dimensional, no fluid crosses the surfaces parallel to the xy -plane.

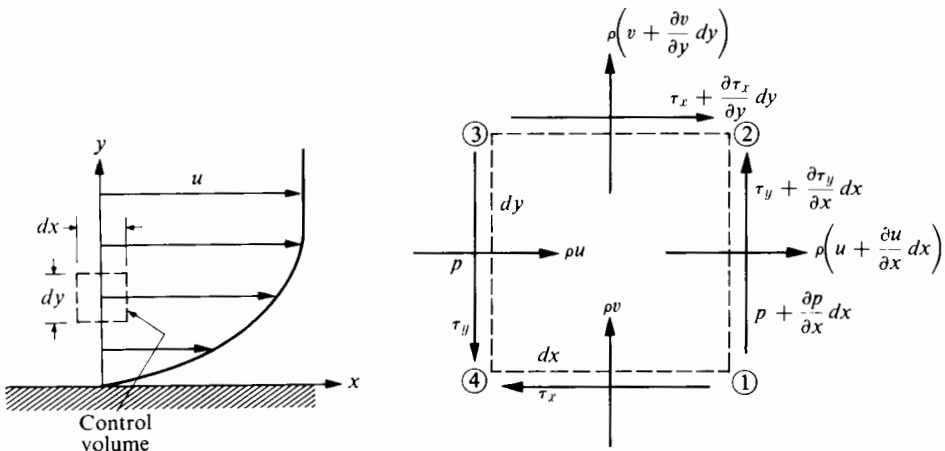


FIGURE 4.9 Small control volume for development of boundary layer equations.

The continuity equation for steady, two-dimensional, incompressible flow requires that

$$\rho \left(u + \frac{\partial u}{\partial x} dx \right) dy - \rho u dy + \rho \left(v + \frac{\partial v}{\partial y} dy \right) dx - \rho v dx = 0$$

or

$$\frac{\partial u}{\partial x} + \frac{\partial v}{\partial y} = 0. \quad (4.1)$$

Using Table 4.1 to obtain the net outward momentum flux and applying Eq. (2.4), we derive the momentum equation in the x -direction:

$$\sum F_x = \rho \left(u + \frac{\partial u}{\partial x} dx \right)^2 dy - \rho u^2 dy + \rho \left(v + \frac{\partial v}{\partial y} dy \right) \left(u + \frac{\partial u}{\partial y} dy \right) dx - \rho uv dx.$$

TABLE 4.1 Fluxes of mass and x -momentum

Surface	Mass flux	Flux of x -momentum
①–②	$\rho \left(u + \frac{\partial u}{\partial x} dx \right) dy$	$\rho \left(u + \frac{\partial u}{\partial x} dx \right)^2 dy$
③–④	$-\rho u dy$	$-\rho u^2 dy$
②–③	$\rho \left(v + \frac{\partial v}{\partial y} dy \right) dx$	$\rho \left(v + \frac{\partial v}{\partial y} dy \right) \left(u + \frac{\partial u}{\partial y} dy \right) dx$
④–①	$-\rho v dx$	$-\rho vu dx$

Expanding and disregarding second-order terms, we have

$$\sum F_x = \rho \left(2u \frac{\partial u}{\partial x} + u \frac{\partial v}{\partial y} + v \frac{\partial u}{\partial y} \right) dx dy.$$

Using the continuity equation, we may simplify this to

$$\sum F_x = \rho \left(u \frac{\partial u}{\partial x} + v \frac{\partial u}{\partial y} \right) dx dy.$$

Since only pressure and shear forces act on the control surface, we may write the force summation, in accordance with Fig. 4.9, as

$$\begin{aligned} \sum F_x &= p dy - \left(p + \frac{\partial p}{\partial x} dx \right) dy + \left(\tau_x + \frac{\partial \tau_x}{\partial y} dy \right) dx - \tau_x dx \\ &= \left(-\frac{\partial p}{\partial x} + \frac{\partial \tau_x}{\partial y} \right) dx dy. \end{aligned}$$

Thus we may write the momentum equation as

$$\rho \left(u \frac{\partial u}{\partial x} + v \frac{\partial u}{\partial y} \right) = -\frac{\partial p}{\partial x} + \frac{\partial \tau_x}{\partial y}.$$

The shear stress τ developed in a Newtonian fluid is proportional to the rate of shearing strain. For the particular case of the boundary layer, in which there is a large velocity gradient close to the wall, the shear stress is very nearly equal to

$$\tau_x = \mu \frac{\partial u}{\partial y},$$

where μ is the coefficient of viscosity.

Using this definition, we may write the momentum equation for the x -direction as

$$\rho \left(u \frac{\partial u}{\partial x} + v \frac{\partial u}{\partial y} \right) = -\frac{\partial p}{\partial x} + \mu \frac{\partial^2 u}{\partial y^2}.$$

Because of the thinness of the boundary layer, we can neglect pressure changes normal to the wall inside the layer, so we can assume that p is a function of x only. Then we may write the momentum equation as

$$u \frac{\partial u}{\partial x} + v \frac{\partial u}{\partial y} = -\frac{1}{\rho} \frac{dp}{dx} + \nu \frac{\partial^2 u}{\partial y^2}, \quad (4.2)$$

where $\nu \equiv \mu/\rho$ is the kinematic viscosity.

The momentum equation as derived here assumes a fluid of constant viscosity and constant density. Although these conditions may be satisfied within many low-speed laminar boundary layers, we will see that the “effective” viscosity in turbulent flow may vary strongly through the boundary layer. Further, ρ and μ could vary as the result of temperature variation within the boundary layer, due either to high heat-transfer rates or, in compressible flow, to the variation of

static temperature in response to velocity variation. In such cases a complete set of equations must include at least an energy equation and an equation of state. However, even in cases not requiring the simultaneous solution of an energy equation, Eqs. (4.1) and (4.2) can present considerable difficulties in the solution for u and v (where p is assumed a known function of x). It is desirable, indeed necessary in most cases, to utilize approximate methods for solving the boundary layer equations.

A useful approximation, the *momentum integral method*, has been developed and widely applied. The object of the method is to find a solution that will satisfy the integral of the momentum equation across the boundary layer even though it may fail to satisfy the equation at particular points. The integration of the momentum equation (4.2) may proceed as follows:

$$\int_0^h \left(u \frac{\partial u}{\partial x} + v \frac{\partial u}{\partial y} \right) dy = \int_0^h -\frac{1}{\rho} \frac{dp}{dx} dy + \int_0^h v \frac{\partial^2 u}{\partial y^2} dy,$$

where h is an undefined distance from the wall outside the boundary layer. In the free stream,

$$-\frac{1}{\rho} \frac{dp}{dx} = U \frac{dU}{dx}.$$

Thus we may write this equation as

$$\int_0^h \left(u \frac{\partial u}{\partial x} + v \frac{\partial u}{\partial y} - U \frac{dU}{dx} \right) dy = \int_0^h v \frac{\partial^2 u}{\partial y^2} dy.$$

Integrating the right-hand term and noting that the wall shear stress is given by

$$\tau_0 = \mu \left(\frac{\partial u}{\partial y} \right)_{y=0},$$

while $\partial u / \partial y$ is zero outside the boundary layer, we may write (for constant ν)

$$\int_0^h \left(u \frac{\partial u}{\partial x} + v \frac{\partial u}{\partial y} - U \frac{dU}{dx} \right) dy = -\frac{\tau_0}{\rho}.$$

Integrating the second term in the integral by parts, we have

$$\int_0^h v \frac{\partial u}{\partial y} dy = vu \Big|_0^h - \int_0^h u \frac{\partial v}{\partial y} dy.$$

From the continuity equation, v at $y = h$ is given by

$$v = \int_0^h \frac{\partial v}{\partial y} dy = - \int_0^h \frac{\partial u}{\partial x} dy.$$

Thus

$$\int_0^h v \frac{\partial u}{\partial y} dy = -U \int_0^h \frac{\partial u}{\partial x} dy + \int_0^h u \frac{\partial u}{\partial x} dy.$$

We may then write the momentum equation as

$$\int_0^h \left(2u \frac{\partial u}{\partial x} - U \frac{\partial u}{\partial x} - U \frac{dU}{dx} \right) dy = - \frac{\tau_0}{\rho}$$

or, rearranging, as

$$\int_0^h \frac{\partial}{\partial x} [u(U - u)] dy + \frac{dU}{dx} \int_0^h (U - u) dy = + \frac{\tau_0}{\rho}. \quad (4.3)$$

Both the integrands are zero outside the boundary layer, so h can be indefinitely large.

Equation (4.3) is arranged in this particular form because of the physical significance (and the common usage) of the individual integrals. In the second integral, $(U - u)$ is the mass flux *defect* (actually $1/\rho$ times the defect) that occurs as the result of the deceleration of the boundary layer fluid. In the case of flow within a duct, for example, if there is a mass flux defect near the walls, there must be an *increased* mass flux within the free stream. This effect on the free stream would be the same if there were no boundary layer but the duct walls were displaced inward by an amount δ^* so that

$$U\delta^* = \int_0^\infty (U - u) dy.$$

With respect to mass flux then, the boundary layer has the effect of making the thickness δ^* unavailable for free-stream flow; δ^* is called the *displacement thickness* of the boundary layer.

We can treat the first integral in a similar manner. Note first that since the limits of integration are not functions of x , the partial differentiation $\partial/\partial x$ can be carried outside the integral, where it becomes d/dx . In this case we interpret u as $1/\rho$ times the actual mass flux, while $(U - u)$ is the *momentum defect* per unit mass of the boundary layer fluid. Hence the integral is the momentum defect in the boundary layer that, as above, could be accounted for by the loss of free-stream thickness θ such that

$$U^2\theta = \int_0^\infty u(U - u) dy.$$

Here θ is called the *momentum thickness* of the boundary layer. We then define the two terms as follows (for incompressible flow):

$$\delta^* = \int_0^\infty \left(1 - \frac{u}{U} \right) dy, \quad (4.4a)$$

$$\theta = \int_0^\infty \frac{u}{U} \left(1 - \frac{u}{U} \right) dy. \quad (4.4b)$$

With these definitions we may write the momentum integral equation, Eq. (4.3), as

$$\frac{d}{dx}(U^2\theta) + \frac{dU}{dx}(U\delta^*) = \frac{\tau_0}{\rho}$$

or

$$\frac{d\theta}{dx} + \left(2 + \frac{\delta^*}{\theta}\right) \frac{\theta}{U} \frac{dU}{dx} = \frac{\tau_0}{\rho U^2}. \quad (4.5)$$

As it stands, this equation applies to both laminar and turbulent boundary layers. The solution, say for a given $U(x)$, requires knowledge of the relationship between δ^* and θ , which may be found if an approximate velocity profile shape is assumed (δ^*/θ is often called the *shape factor* H) and the skin friction τ_0 is known. Note that shear stress is evaluated only at the wall where, even in turbulent flow, it is given by $\mu(\partial u / \partial y)$, since turbulent fluctuations must go to zero at the wall.

In Section 4.3 we discuss the use of this momentum integral method in a procedure for calculating the growth of two-dimensional laminar boundary layers in pressure gradients. In Section 4.4 we present a momentum integral method useful for estimating the growth of turbulent boundary layers. Both methods can be coded for calculation on a small computer. The chief preoccupation of both is with the momentum thickness and the displacement thickness. These quantities are independent, so that in addition to the momentum integral equation, both methods require one other relationship for the calculation.

For both methods the applied pressure gradient must be specified, and neither can be expected to be valid past the point of flow separation; indeed, both become progressively more uncertain as the point of separation is approached. Both methods are restricted to nearly two-dimensional flow.

Once calculated, the displacement thickness of a boundary layer shows how the walls of the duct or body would need to be displaced for an ideal-flow calculation to produce the same surface pressure gradients as those that would be found in a real flow. In principle one could proceed iteratively: First use an ideal potential flow solution (see Refs. 3, 4, and 5 for appropriate methods) to determine the ideal pressure gradients on the internal surface of a duct or the external surface of a body immersed in a fluid stream. Then apply a boundary layer calculation method with these ideal-flow pressure gradients to determine the displacement thickness. Next add the computed displacement thickness to the actual geometry and generate a new “displacement surface” to be used in the next ideal-flow calculation (for recomputing the surface pressure gradients). The process could be repeated a number of times, though it will not always converge; convergence is especially unlikely if the boundary layer is close to separation.

If the streamlines just outside the boundary layer are not straight, but instead have curvature in a plane parallel to the wall, the boundary layer is said to be three-dimensional. It is subject to a lateral pressure gradient that will affect the slow-moving fluid near the wall differently from the relatively fast-moving fluid just outside the boundary layer. Slow-moving boundary layer fluid will tend to be laterally transported and perhaps to accumulate—for example, at an “inside” corner of a curved flow passage. Application of a two-dimensional boundary layer calculation method in such a location would no doubt underpredict the likelihood of boundary layer separation. We mention methods that deal with three-

dimensional boundary layers and general viscous flow calculations for ducts and submerged bodies at the end of Section 4.4.

In the foregoing paragraphs several cautions and reservations have been expressed. It remains true, however, that we can learn much by studying the behavior of boundary layers in pressure gradients.

4.3 LAMINAR BOUNDARY LAYER CALCULATIONS

Before describing the approximate but easily applied momentum integral method for treating laminar boundary layers, we review two of the few cases in which exact solutions[†] of Eqs. (4.1) and (4.2) have been found (see Ref. 1 for other exact solutions). These solutions provide insight into boundary layer behavior and serve also to check general approximate methods incorporated into computer codes.

The simplest flow is that over a flat plate where dp/dx is zero. In this case Eqs. (4.1) and (4.2) reduce to

$$u \frac{\partial u}{\partial x} + v \frac{\partial u}{\partial y} = \nu \frac{\partial^2 u}{\partial y^2}, \quad \frac{\partial u}{\partial x} + \frac{\partial v}{\partial y} = 0,$$

with the boundary conditions

$$\begin{aligned} y = 0: \quad u &= v = 0, \\ y = \infty: \quad u &= U = \text{constant}. \end{aligned}$$

A stream function ψ may be defined such that

$$u = \frac{\partial \psi}{\partial y}, \quad v = -\frac{\partial \psi}{\partial x}.$$

The convenience of this form is that it automatically satisfies the continuity equation so that the two equations given above reduce to

$$\frac{\partial \psi}{\partial y} \frac{\partial^2 \psi}{\partial x \partial y} - \frac{\partial \psi}{\partial x} \frac{\partial^2 \psi}{\partial y^2} = \nu \frac{\partial^3 \psi}{\partial y^3}. \quad (4.6)$$

We can simplify this equation considerably by substituting

$$\eta = y \sqrt{U/\nu x} \quad \text{and} \quad \psi = \sqrt{\nu x U} f(\eta),$$

with the result that

$$ff'' + 2f''' = 0,$$

where the primes signify differentiation of the function f with respect to η . The transformed boundary conditions are

$$\begin{aligned} \eta = 0: \quad f &= f' = 0, \\ \eta = \infty: \quad f' &= 1. \end{aligned}$$

[†] Exact in the sense that they do not neglect any of the terms in the boundary layer equations. Most solutions are, however, expressed in terms of series expansions.

This equation is an ordinary differential equation, but the fact that it is nonlinear makes it hard to solve. The method of solution employed by Blasius, a series expansion, is described by Schlichting [1]. We present here only the results of his calculation.

The velocity profile u/U obtained from the Blasius solution is shown in Fig. 4.10. Very careful experiments have verified this result almost exactly. As the figure shows, a single curve can be used to represent in dimensionless form the velocity profiles corresponding to all locations on the flat plate. The velocity profiles are said to be similar.

The solution gives the growth of the boundary layer with distance x from the leading edge as

$$\delta \approx 5.0\sqrt{\nu x/U}, \quad (4.7a)$$

$$\delta^* = 1.72\sqrt{\nu x/U}, \quad (4.7b)$$

$$\theta = 0.664\sqrt{\nu x/U}, \quad (4.7c)$$

where δ is defined as that point where $u = 0.99 U$. The skin friction is

$$\frac{\tau_0}{\rho U^2} = 0.332\sqrt{\nu/Ux}. \quad (4.7d)$$

The drag on a flat plate may be computed by integrating the skin friction over the entire area. One can see that the local wall shear stress decreases with distance

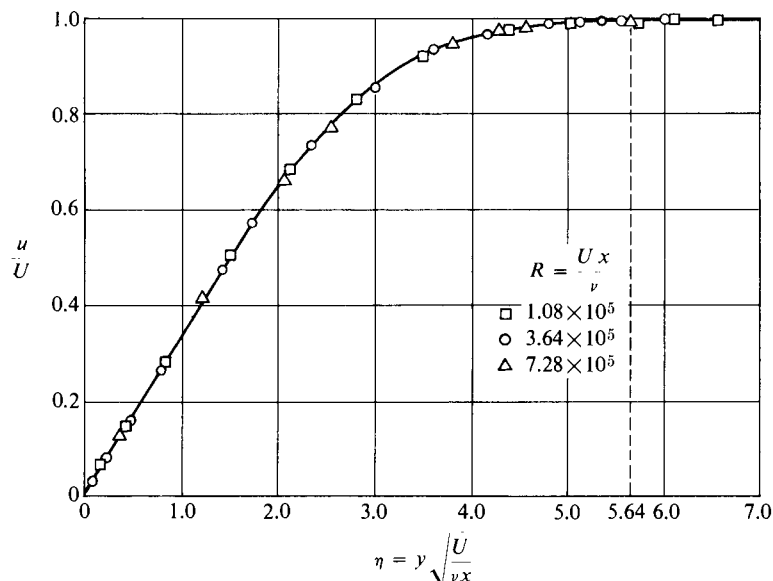


FIGURE 4.10 Velocity distribution in the laminar boundary layer on a flat plate at zero incidence, as measured by Nikuradse [1].

downstream but approaches zero only at infinity. Thus separation cannot occur in flow over a flat plate of finite length unless there is an adverse pressure gradient.

A flow in which separation can occur was examined by Howarth [1], who assumed a free-stream velocity variation

$$U = U_1 - \alpha x.$$

Such a velocity would occur in a two-dimensional duct of diverging ($\alpha > 0$) straight walls in which the initial free-stream velocity is U_1 at $x = 0$. Defining the parameters

$$\eta = \frac{y}{2} \sqrt{\frac{U_1}{\nu x}}, \quad \xi = \frac{\alpha x}{U_1} = -\frac{x}{U_1} \frac{dU}{dx} = \frac{U_1 - U}{U},$$

Howarth calculated a series expansion solution from which the velocity profiles shown in Fig. 4.11 are derived. Separation occurs when ξ reaches the value 0.125. (More accurate solutions give 0.1198 [1].)

In contrast to the foregoing cases, the velocity profiles at various locations on the wall for a given pressure distribution cannot be made to lie on one nondimensional curve, so they are not similar in this sense. Again the Blasius solution appears, this time for the case $\xi = 0$. Separation of the flow occurs with $\xi = 0.12$, that is, a 12% reduction of the initial free-stream velocity. (This result is not very different from the result shown in Fig. 4.7 for the “single-step” boundary layer approximation with $\alpha_1 = 0.5$, but it is, of course, much more significant because it is the consequence of taking seriously the effect of viscosity on a continuously varying profile—for a special case of $U[x]$.)

The Thwaites integral momentum method [7] has been widely used over the past forty years for estimating the growth of laminar boundary layers subjected to general pressure gradients. The method utilizes Eq. (4.5) multiplied by $2\theta/\nu$ to read

$$\frac{d}{dx} \left(\frac{\theta^2}{\nu} \right) + \frac{2}{U} \left[(2 + H) \frac{dU}{dx} \left(\frac{\theta^2}{\nu} \right) - T \right] = 0, \quad (4.8)$$

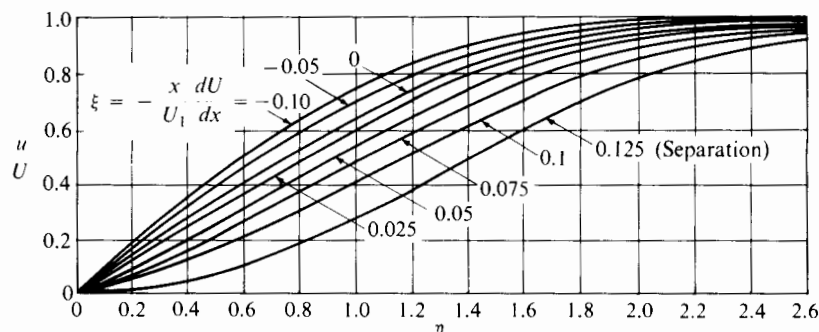


FIGURE 4.11 Velocity distribution in the laminar boundary layer for the potential flow given by $U = U_1 - \alpha x$. (After Howarth [1, 6].)

in which

$$T = \tau_0 \theta / \mu U.$$

In studying all available exact solutions of the boundary layer equations, Thwaites observed that the quantities H and T depend almost entirely on the dimensionless parameter

$$\lambda = \frac{\theta^2}{\nu} \frac{dU}{dx}.$$

This had been known before, but Thwaites was able to show that to a good approximation T , H , and λ could be related by a simple equation

$$T = (H - 1)\lambda + 0.225. \quad (4.9)$$

Use of this empirical relation happily allows us to write Eq. (4.5) in the form

$$\frac{d}{dx} \left(\frac{\theta^2}{\nu} \right) + \frac{6}{U} \frac{dU}{dx} \left(\frac{\theta^2}{\nu} \right) = \frac{0.45}{U}.$$

With the aid of an integrating factor $(U/U_1)^6$, this becomes

$$\frac{d}{dx} \left[\frac{\theta^2}{\nu} \left(\frac{U}{U_1} \right)^6 \right] = \frac{0.45}{U} \left(\frac{U}{U_1} \right)^6$$

(in which U_1 can be considered the free-stream velocity at a position x_1 where the momentum thickness is θ_1), so that we can obtain a very simple general solution,

$$\frac{\theta^2}{\nu} = \frac{\theta_1^2}{\nu} \left(\frac{U_1}{U} \right)^6 + \frac{0.45}{U_1} \left(\frac{U_1}{U} \right)^6 \int_{x_1}^x \left[\frac{U(\xi)}{U_1} \right]^5 d\xi, \quad (4.10)$$

in which ξ runs from x_1 to any position x at which the momentum thickness is to be calculated.

Trying this solution out on the flat-plate case for which $U/U_1 = 1$, we obtain (for $\theta_1 = 0$)

$$\frac{\theta^2}{\nu} = \frac{0.45x}{U} \quad \text{or} \quad \theta = 0.67 \sqrt{\frac{\nu x}{U}},$$

which is very close to the value of the exact solution (Eq. 4.7c). Checking the Thwaites solution for the special case calculated by Howarth (Fig. 4.11) is an exercise suggested in the Problems section of this chapter.

Sherman [8] points out an important lesson, apparent in the form of Eq. (4.12), concerning the effect of pressure gradient on laminar boundary layer growth. If the flow accelerates, $(U_1/U)^6$ decreases very rapidly, and the term involving θ_1 almost disappears: An accelerating flow therefore tends to forget its initial condition. On the other hand, if the flow decelerates, $(U_1/U)^6$ increases very quickly, and the effect of θ_1 on the downstream value of θ can be very strong indeed.

As we pointed out earlier, a key feature of Thwaites's method is the recognition that, for most laminar boundary layers, the quantities $H = \delta^*/\theta$ and $T =$

$\tau_0/\mu U$) are dependent almost entirely on λ . White [9] has shown that (taking into account the information available from various exact solutions) the $T(\lambda)$ relationship can be approximately expressed as

$$T = (\lambda + 0.09)^{0.62}. \quad (4.11)$$

Combining Eqs. (4.9) and (4.11), one could write that

$$\delta^* = \frac{\theta}{\lambda} [\lambda + (\lambda + 0.09)^{0.62} - 0.225]. \quad (4.12)$$

Thus, once we know θ and $\lambda = (\theta^2/\nu)(dU/dx)$, we can easily determine the displacement thickness δ^* .

Equation (4.12) implies that the shape of the boundary layer depends only on the local free-stream velocity gradient (multiplied by θ^2/ν) and not on the previous distribution $U(x)$. This will tend to be true as long as the pressure gradient is applied sufficiently gradually that the boundary is not far from an “equilibrium” state.

4.4 THE TURBULENT BOUNDARY LAYER

In most engineering applications where boundary layers are important, the Reynolds numbers are high enough that most of the flow is turbulent. A very advantageous consequence of this fact is the superior pressure recovery that one can obtain with a turbulent boundary layer as compared with a laminar one. This means that airfoils, compressor blades, and diffusers will perform very much better than they would if the flow remained laminar. On the other hand, the skin friction of a turbulent layer is generally much greater.

Analytically the onset of turbulence renders important features of the flow, such as skin friction and separation, essentially indeterminate except by semiempirical methods. At present a satisfactory purely theoretical treatment of turbulence does not exist; nor is there a very bright prospect of one coming into being. This means that the understanding of turbulent flows relies heavily on experimental observation. Researchers have developed numerous semiempirical methods in which the effects of turbulence are represented by more or less simple approximations.

Fully developed turbulent pipe flow can be said to be well known because quite general correlations of experimental data are available. Other special cases—for example, turbulent jets and wakes—have been investigated in fine detail and may be said to be well understood. Only approximate semiempirical methods, though, are available for turbulent boundary layers in general adverse pressure gradients, particularly if the flow is three-dimensional. Prediction of separation with existing methods is especially uncertain.

As flows in real machines are seldom, if ever, exactly two-dimensional, the predictions of two-dimensional boundary layer theory have always to be regarded with a little scepticism. Nevertheless, they often help us to understand how the flow develops, and may be useful in establishing performance limits. For these

reasons we here outline the essential features of turbulent shear and then present a practical method for fairly rapid calculation of the two-dimensional turbulent boundary layer.

For flows in which the geometry and free-stream velocity can each be described by a single parameter—within geometrically similar devices—the technique of dimensional analysis has been of inestimable usefulness in correlating measurements of friction, drag, and heat transfer. Examples of general correlations of this kind will follow shortly. For more complex situations in which the wall pressure or free-stream velocity varies in an arbitrary manner, existing analytical methods usually employ the momentum integral equation (4.5), along with some suitable assumption about the turbulent diffusion of momentum. This involves the concept of the turbulent shear stress that can be understood by considering the fluctuations of which turbulence is composed.

Discussion of turbulent flow is greatly facilitated by the assumption that all velocity components at each point may be considered the sum of two parts, one steady and one fluctuating, according to

$$u(x, y, t) = \bar{u}(x, y) + u'(x, y, t),$$

$$v(x, y, t) = \bar{v}(x, y) + v'(x, y, t),$$

$$w(x, y, t) = \bar{w}(x, y) + w'(x, y, t).$$

In each case the first term on the right-hand side is the time-mean value defined, for the u velocity component, by

$$\bar{u} = \frac{1}{t_m} \int_0^{t_m} u dt,$$

where t_m is a time period that is very long compared with the period of the fluctuation. The second term is the instantaneous fluctuating component (which can be measured by a velocity probe with a very rapid response, such as a hot-wire anemometer). Even in a flow that is two-dimensional on the average (that is, having $\bar{w} = 0$), it is necessary to recognize that three-dimensional disturbances do, in general, exist.

Generally speaking, the turbulent fluctuations are greater in the boundary layer than in the free stream, as we will see. Measurements have shown that the outer third or half of the boundary layer may be only intermittently turbulent. Spasms of turbulence may be separated by periods of negligible fluctuation intensity.

The effect of turbulence in changing the shape of the velocity profile can be ascribed to the operation of the so-called turbulent shear stress. Consider an element of fluid dm indicated in Fig. 4.12, which through turbulent motion is about to enter a control volume situated within a boundary layer and bounded by sides L_1 and L_2 . As the element dm crosses the control surface, it adds x momentum to

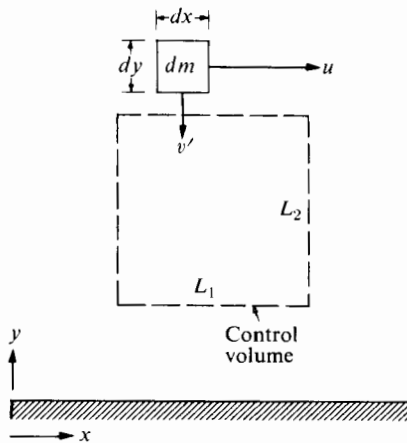


FIGURE 4.12 The turbulent transfer of momentum.

the control volume in the amount $dm u$. This momentum is added in a time $dt \approx dy/-v'$, so that the momentum addition rate is

$$\frac{dm u}{dt} = \frac{\rho(dx dy dz)}{dy/-v'} u = -\rho u v' dx dz,$$

which is equivalent to a shear force acting on the area $dx dz$. The equivalent or turbulent shear stress τ_t is then, if one averages over a time that is long compared with the period of the individual fluctuations,

$$\tau_t = -\rho \bar{u}' \bar{v}' .$$

Writing u as $\bar{u} + u'$ and noting that $\bar{u}\bar{v}'$ is zero (since \bar{u} is a constant and $\bar{v}' = 0$), we obtain

$$\tau_t = -\rho \bar{u}' \bar{v}' ,$$

where $\bar{u}' \bar{v}'$ is called the *correlation* of the velocity fluctuations u' and v' . Assuming that the turbulent motion does not seriously alter the molecular (laminar) transport of momentum, one may treat a turbulent boundary layer in much the same manner mathematically as a laminar layer, if the shear stress is written as

$$\tau = \mu \frac{\partial u}{\partial y} - \rho \bar{u}' \bar{v}' .$$

The second term may be two orders of magnitude larger than the first in the outer part of the boundary layer, though it must be negligible in an exceedingly thin region near the wall where the fluctuations approach zero. The great difficulty with the term $\rho \bar{u}' \bar{v}'$ is that no general method has been found for predicting its magnitude. Measurements with two hot wires set up to measure fluctuation components v' and u' simultaneously can provide accurate knowledge of the correlation in a particular flow. A typical variation of the average and fluctuating

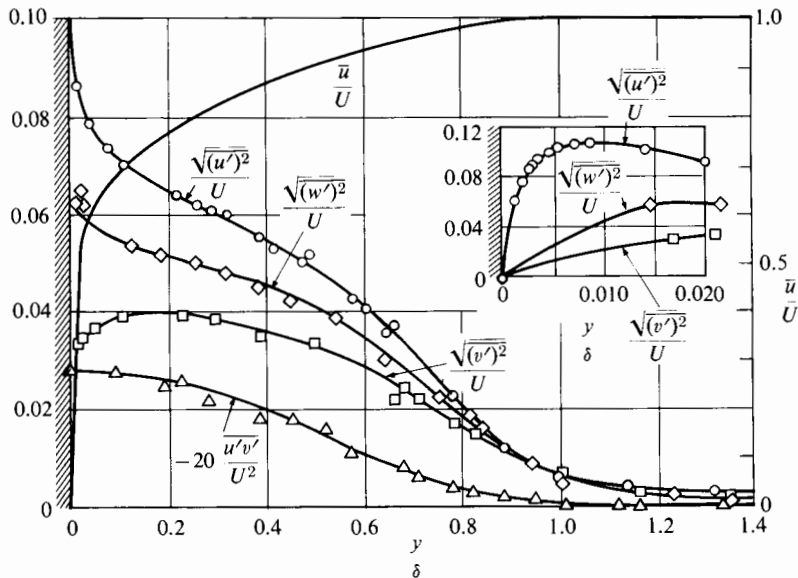


FIGURE 4.13 The correlation between average and fluctuating velocities in the boundary layer on a flat plate at zero incidence [1].

velocities and their correlation is shown in Fig. 4.13; the fluctuations are much smaller in the free stream than in the boundary layer.

The existence of this turbulent-shear-stress concept has led to several simplifying hypotheses, all of which have been shown to lack universal validity, though they can be of considerable usefulness in certain situations. In each, the effect of the turbulence on the boundary layer is expressed by a single variable, or at most by two variables.

For example, Boussinesq postulated that, by analogy with the viscous shear stress, the turbulent shear stress τ_t could be written

$$\tau_t = -\rho \bar{u}' v' = \rho \epsilon \frac{d\bar{u}}{dy},$$

in which ϵ is the so-called eddy viscosity. If ϵ can be assumed constant, then any boundary layer problem that has a solution for laminar flow can be solved for turbulent flow, if the appropriate value of ϵ is used. Provided great accuracy is not required, the constant-eddy-viscosity solution may be quite useful at some distance from the wall. Very near the wall, the fluctuations and the eddy viscosity must approach zero. The utility of this concept is greatly restricted by virtue of the fact that the eddy viscosity is not a property of the fluid.

Prandtl proposed, in what is called the mixing length theory, that the eddy viscosity ϵ should be proportional to the mean velocity gradient $d\bar{u}/dy$. His reasoning was based on the idea that as a small “package” of fluid moves suddenly from one point in a velocity gradient to another, it moves a finite distance l before

mixing out with adjacent fluid. The idea is analogous to some extent with the kinetic-theory explanation of viscosity, in which the “mixing length” is the mean free path. Prandtl proposed that

$$\tau_t = -\rho \bar{u}' \bar{v}' = \rho l^2 \left| \frac{d\bar{u}}{dy} \right| \left| \frac{d\bar{u}}{dy} \right|.$$

The mixing length, which must be experimentally deduced, is not itself constant. In fully developed pipe flow it is found to be proportional to distance from the wall in the region near the wall.

These hypotheses and other similar ones do not reveal any fundamental information on the general problem of turbulence. They are, however, useful in certain instances in correlating experimental results for application to engineering problems.

Fully developed flow in a long pipe has provided much valuable experimental information on wall shear stress in turbulent flow. This information happens to be useful in a surprisingly wide variety of boundary layer flows. Pipe flow is said to be fully developed when, far from the pipe entrance, the velocity profile does not change with axial position. Under these conditions wall shear stress, which is ordinarily difficult to measure, is easily determined.

Consider a control volume of length L that fills a pipe of radius R . For fully developed flow there is no net momentum flux out of the control volume, so that the momentum equation gives the wall shear stress as

$$\sum F_x = \pi R^2 \Delta p - 2\pi R L \tau_0 = 0$$

or

$$\tau_0 = \frac{\Delta p R}{2L},$$

where Δp is the pressure drop in length L . Similarly, for a smaller control volume of radius $r < R$ within the pipe, the local shear stress τ is given by

$$\tau = \frac{\Delta p r}{2L},$$

so that the variation of τ across the pipe is

$$\frac{\tau}{\tau_0} = \frac{r}{R} = 1 - \frac{y}{R},$$

where $y = R - r$ is the distance from the wall. Hence with a simple pressure measurement one can determine shear stress, and from a determination of the velocity profile one can deduce the variations in eddy viscosity, mixing length, and so on.

The velocity profile within the pipe can be broken into two or three regions. Very near the wall the flow must be laminar, since the presence of the wall pro-

hibits turbulent velocities. Here we can write (and from now on we omit the bar for the temporal mean velocity u),

$$\tau \approx \tau_0 = \mu \frac{du}{dy} \approx \mu \frac{u}{y}$$

or, for convenient comparison with subsequent results,

$$\frac{u}{\sqrt{\tau_0/\rho}} = \frac{y\sqrt{\tau_0/\rho}}{\nu}. \quad (4.13)$$

This is the so-called *laminar sublayer*. The group $\sqrt{\tau_0/\rho}$, which has the dimensions of velocity, is often called the *friction velocity*.

Farther from the wall, where turbulent shear is dominant, the velocity is given by the empirical relation [1]

$$\frac{u}{\sqrt{\tau_0/\rho}} = 2.5 \ln \frac{y\sqrt{\tau_0/\rho}}{\nu} + 5.5. \quad (4.14)$$

This expression has been called the *law of the wall*, since it shows the velocity u to depend only on conditions near the wall.

Near the center of the pipe the velocity is given by

$$\frac{U_c - u}{\sqrt{\tau_0/\rho}} = -2.5 \ln \frac{y}{R}, \quad (4.15)$$

where U_c is the center-line velocity. The form of these equations may be derived by various semitheoretical methods, as described by Schlichting [1], but the numerical constants are obtained experimentally.

The velocity profiles of Eqs. (4.14) and (4.15) do not depend explicitly on Reynolds-number and surface-roughness variations. However, both these affect the wall shear stress in general and thus do have an effect on the velocity profiles.

Over limited Reynolds-number ranges the velocity profile may be approximated (except close to the wall) by the very much simpler form

$$\frac{u}{U_c} = \left(\frac{y}{R} \right)^{1/n}, \quad (4.16)$$

where n is a constant within a reasonable range of Reynolds number. For a pipe Reynolds number of about 1×10^5 , n should be about 7 [1], and this value is often used to represent turbulent boundary layers.

It can be shown (see Problem 4.9) that the requirement that Eqs. (4.14) and (4.15) both apply in an intermediate range of y is sufficient to specify τ_0 (actually the skin friction coefficient $\tau_0/(\frac{1}{2}\rho U_c^2)$) as a function of the Reynolds number $U_c R / \nu$. For other profile assumptions, such as the power law given above, it is necessary to have additional information on τ_0 to solve the momentum integral equation. Physically, τ_0 must depend on the following variables for fully developed pipe flow:

$$\tau_0 = f(\rho, \mu, \bar{U}, D, \text{roughness}),$$

where \bar{U} is the bulk mean velocity ($\dot{m}/\pi R^2 \rho$). Defining the *skin friction* coefficient C_f , dimensional analysis yields

$$C_f = \frac{2\tau_0}{\rho \bar{U}^2} = f\left(\frac{\rho \bar{U} D}{\mu}, \text{roughness}\right) \quad \text{or} \quad C_f = f\left(\text{Re}, \frac{\delta}{D}\right),$$

where δ/D is the ratio of average wall roughness height to pipe diameter. This function is shown in Fig. 4.14, which includes both laminar and turbulent flows. The laminar flows have Reynolds numbers less than about 2000 and a friction factor that may be obtained theoretically as

$$C_f = 16 \left(\frac{\bar{U} D}{\nu} \right)^{-1} \quad (\text{laminar}). \quad (4.17)$$

The pipe roughness is characterized by a ratio of average roughness height δ to diameter D . It has been shown that roughness elements have no effect on the flow if they are smaller in size than the laminar sublayer thickness, which is approximately

$$y = \frac{5\nu}{\sqrt{\tau_0/\rho}}.$$

For smooth pipes the friction factor for turbulent flow can be approximated over a fairly wide range of Reynolds numbers [11] ($3 \times 10^4 < \text{Re} < 10^6$) by

$$C_f = \frac{2\tau_0}{\rho \bar{U}^2} = 0.046 \left(\frac{\bar{U} D}{\nu} \right)^{-1/5} \quad (\text{turbulent}). \quad (4.18)$$

With these equations one could, for any Reynolds number, determine C_f and hence τ_0/ρ so that pipe velocity profiles could be constructed from Eqs. (4.13) through (4.15).

Far fewer experimental data are available for turbulent flow over plates than for flow in pipes. However, Prandtl and Von Karman have suggested a method

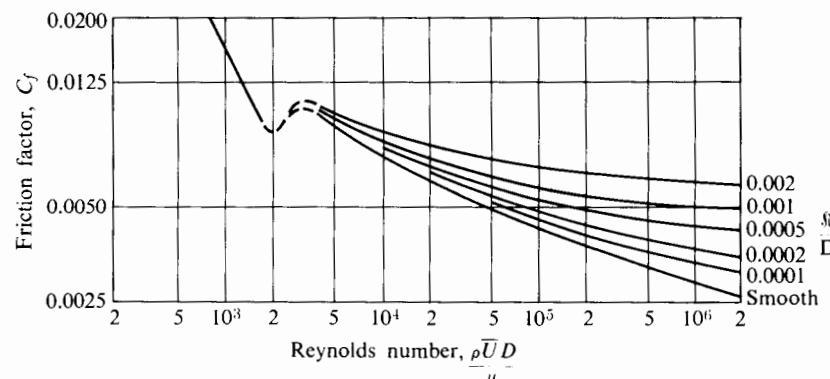


FIGURE 4.14 Curves showing relation between friction factor and Reynolds number for pipes having various values of relative roughness. (Adapted from Moody [10].)

for utilizing pipe measurements to predict the behavior of the two-dimensional turbulent flow on plates. The boundary layer of thickness δ over a plate is taken to be identical to the flow in a pipe of radius R equal to δ when the free-stream velocity of the former is the same as the center-line velocity of the latter. The two cases are not exactly equivalent because the pipe will always have some pressure gradient. However, the difference can be negligible if the Reynolds number is reasonably large.

The equation for the skin friction coefficient for fully developed pipe flow, Eq. (4.18), can be written

$$C_f = \frac{2\tau_0}{\rho \bar{U}^2} = 0.040 \left(\frac{\bar{U}R}{\nu} \right)^{-1/5},$$

where R is the pipe radius. The ratio of bulk mean velocity to center-line velocity, \bar{U}/U_c , depends on the exact shape of the velocity profile. For our present purposes, however, it is legitimate to use the approximation $\bar{U}/U_c = 0.8$ for all Reynolds numbers. In this way we may write the pipe friction as

$$C_f = \frac{2\tau_0}{\rho U_c^2} = 0.027 \left(\frac{U_c R}{\nu} \right)^{-1/5},$$

and in accordance with the Prandtl-Karman hypothesis the local friction coefficient for the flat plate (identifying U_c with U_∞ and R with δ) is then

$$C_f = \frac{2\tau_0}{\rho U_\infty^2} = 0.027 \left(\frac{U_\infty \delta}{\nu} \right)^{-1/5}, \quad (4.19)$$

where U_∞ is the free-stream velocity and δ is the boundary layer thickness. With the approximation

$$\frac{u}{U_\infty} = \left(\frac{y}{R} \right)^{1/7},$$

this can be expressed in terms of momentum thickness. Using Eq. (4.4b), we have $\theta/\delta = 7/72$. Substituting in Eq. (4.19), we get

$$C_f = 0.017 \left(\frac{U_\infty \theta}{\nu} \right)^{-1/5}. \quad (4.20)$$

The momentum integral equation becomes, in the absence of pressure gradient,

$$\frac{d\theta}{dx} = \frac{\tau_0}{\rho U_\infty^2}. \quad (4.21)$$

Solving Eqs. (4.20) and (4.21) for the growth of the two-dimensional boundary layer of zero pressure gradient yields

$$\theta = 0.022 \left(\frac{Ux}{\nu} \right)^{-1/6} x, \quad (4.22)$$

$$\delta = 0.23 \left(\frac{U_x}{\nu} \right)^{-1/6} x, \quad (4.23)$$

if the turbulent boundary layer begins to grow at $x = 0$.

As a first approximation, we can assume that the velocity profile for turbulent flow over a flat plate is the same as that within a pipe. That is, we can use Eqs. (4.13) through (4.15) or (4.16) if we simply replace R by δ and U_c by U_∞ .

Moses [12] has provided a momentum integral method for estimating the growth of turbulent boundary layers in nearly-two-dimensional flow in pressure gradients. His method uses a modification of Eq. (4.3), namely,

$$\int_0^{y_1} \frac{\partial}{\partial x} [u(U - u)] dy + \frac{dU}{dx} \int_0^{y_1} (U - u) dy = \frac{\tau_0}{\rho} - \frac{\tau_1}{\rho}, \quad (4.24)$$

in which y_1 is any location within the boundary layer and τ_1 is the local (turbulent plus laminar) shear stress at $y = y_1$. If $y \geq \delta$, the local shear stress $\tau_1 = 0$. As with the Thwaites momentum integral method for laminar boundary layers, two equations are needed to obtain the unknowns θ and δ^* at any streamwise location. The first of these relations is equivalent to Eq. (4.5), which is obtained by setting $y_1 = \delta$.

For the second relationship it is not feasible in turbulent flow to relate local wall shear stress and local shape factor H to local pressure gradient (as was done for laminar flow). Instead, Moses obtained a second equation by integrating Eq. (4.24) from the wall, $y = 0$, to $y = 0.3\delta$. To perform this integration, he made use of a velocity profile suited to turbulent boundary layers and expressible in two parts for each of the regions:

- 1. Inner layer (the nearly-laminar region).** The laminar sublayer thickness y_s was estimated [10] as

$$y_s = 52.7\delta/(\alpha R_\delta),$$

in which

$$\alpha = \frac{1}{0.41} \sqrt{\frac{C_f}{2}},$$

$$C_f = \frac{\tau_0}{\frac{1}{2}\rho U^2},$$

and

$$R_\delta = \frac{U\delta}{\nu}.$$

For this inner region the velocity profile is expressed as

$$\frac{u}{U} = \alpha \left[8.86 \left(\frac{\eta}{\eta_s} \right) - 3.73 \left(\frac{\eta}{\eta_s} \right)^2 \right] - \beta [3\eta^2 - 2\eta^3], \quad (4.25)$$

in which

$$\eta = \frac{y}{\delta}$$

and

$$\beta = \alpha[\ln(\alpha R_\delta) + 1.1584] - 1.$$

This satisfies the conditions

$$u = 0 \quad \text{at} \quad y = 0$$

and

$$\frac{u}{U} = 5.13\alpha - \beta[3\eta_s^2 - 2\eta_s^3] \quad \text{at} \quad y = y_s.$$

- 2. Outer layer.** For the region $\eta_s < \eta < 1$, which contains most of the boundary layer, the velocity profile that Moses used is expressed as

$$\frac{u}{U} = 1 + \alpha \ln \eta + \beta[1 - 3\eta^2 + 2\eta^3], \quad (4.26)$$

which satisfies the conditions

$$u = U \quad \text{at} \quad y = \delta$$

and, at $y = y_s$,

$$\frac{u}{U} = 1 + \alpha \ln \eta_s + \beta[1 - 3\eta_s^2 + 2\eta_s^3]$$

(which can be shown to be equivalent to

$$\frac{u}{U} = 5.13\alpha - \beta[3\eta_s^2 - 2\eta_s^3],$$

so the inner and outer layers are matched at $y = y_s$).

In past decades researchers have tried assiduously to specify velocity profiles that explicitly incorporate the well-known logarithmic region and that satisfy the important boundary conditions at the wall and at the outer edge of the boundary layer. Equations (4.25) and (4.26) provide a description that appears to be as simple as can be hoped for, though they seem complex at first sight. Note that the pressure gradient does not explicitly appear in either equation, though it does affect R_δ and α .

By using the velocity distribution given above and the integrating limits $y = \delta$ and $y = 0.3\delta$, Moses obtained two momentum integral equations that can be expressed in the form

$$F_{11}d\alpha + F_{12}dR_\delta = G_1 \frac{dU}{U} + H_1 \frac{Udx}{\nu}, \quad (4.27)$$

$$F_{21} d\alpha + F_{22} dR_\delta = G_2 \frac{dU}{U} + H_2 \frac{U dx}{\nu}. \quad (4.28)$$

We can calculate the functions F_{ij} , G_i , and H_i from

$$F_{11} = (-.0792 - .58253\alpha - .02005\beta)R_\delta + 300$$

$$+ (-.5 + 1.58333\alpha - .74286\beta)R_\delta \log_e(\alpha R_\delta),$$

$$F_{12} = (.5\alpha - .5\beta - .41667\alpha^2 + .84048\alpha\beta - .37143\beta^2),$$

$$F_{21} = (.06321 - .73792\alpha + .091566\beta)R_\delta + 300$$

$$+ (-.27705 + .91759\alpha - .29708\beta)R_\delta \log_e(\alpha R_\delta),$$

$$F_{22} = (.02295\alpha - .04185\beta - .043606\alpha^2 + .10214\alpha\beta - .039934\beta^2),$$

$$G_1 = (-2\alpha + \beta + 2\alpha^2 - 1.58333\alpha\beta + .37143\beta^2)R_\delta - 300\alpha,$$

$$G_2 = (-1.32238\alpha + .5541\beta + 1.75725\alpha^2 - 1.25115\alpha\beta + .25714\beta^2)R_\delta - 300\alpha,$$

$$H_1 = (0.41\alpha)^2,$$

$$H_2 = (0.41\alpha)^2 - \left(\frac{\alpha}{0.3} - 1.26\beta \right) (0.0225 + 125/R_\delta) \frac{\theta}{\delta}.$$

For axially symmetric flow the terms

$$+(-\alpha + .5\beta + 2\alpha^2 - 1.58333\alpha\beta + .37143\beta^2 + 49.5/R_\delta - 300\alpha/R_\delta)R_\delta dr/r$$

and

$$+(-.3\alpha + .04185\beta + .96118\alpha^2 - .3992\alpha\beta + .0399\beta^2 + 49.5/R_\delta$$

$$- 300\alpha/R_\delta)R_\delta dr/r$$

should be added to the right-hand sides of Eqs. (4.27) and (4.28), respectively.

Though the coefficients are quite numerous, we can code this boundary layer calculation procedure quite easily and establish a marching solution for the development of α and R_δ in the streamwise direction.

For a given boundary layer thickness we obtain the momentum and displacement thicknesses from

$$\frac{\theta}{\delta} = \alpha - 0.5\beta - 2\alpha^2 + 1.58333\alpha\beta - 0.37143\beta^2 + (-49.5 + 300\alpha)/R_\delta. \quad (4.29)$$

and

$$\frac{\delta^*}{\delta} = \alpha - 0.5\beta + 49.5/R_\delta. \quad (4.30)$$

To begin the marching calculation we must know two parameters. If, for example, we knew or assumed the initial velocity profile, we could obtain θ and δ^* (perhaps by numerical integration). We would know the value of δ as well as U

and ν , so we could determine $R_\delta = U\delta/\nu$ from Eqs. (4.29) and (4.30) by iteration or by rearranging them to form a quadratic in α or β .

With R_δ , α , and β established at the initial point, we can evaluate the coefficients F_{ij} , G_i , and H_i and take a step dx in the streamwise direction. Since we know $U(x)$, we can evaluate dU/U as well as Udx/ν ; then we can obtain the changes $d\alpha$ and dR_δ from Eqs. (4.27) and (4.28) by inversion of a 2×2 matrix.

High precision should not be expected of this boundary layer calculation very close to separation; nor should it be expected if the Reynolds number R_δ is less than about 3000 or if the flow is not "nearly two-dimensional." Apart from these conditions, however, the method can supply useful guidance on turbulent boundary layer development in ducts or on bodies submerged in fluid streams.

Figure 4.15 shows typical results of computations performed with the Moses integral momentum method (for three cases of adverse pressure gradient, each with the same initial conditions).

For case I, the free-stream velocity decreases linearly with distance, and the wall friction coefficient decreases but remains above zero at $x = 0.1$ m, so the boundary layer does not appear to be separated.

For case II, the free-stream velocity gradient is twice as large as in case I, and separation ($C_f \rightarrow 0$) is apparent with $U/U_1 = 0.62$, which is equivalent to a pressure coefficient of $C_p = 1 - (U/U_1)^2 = 0.62$.

For case III, the boundary layer is first allowed to grow in zero pressure gradient ($dU/dx = 0$) before the free-stream velocity decreases with the same gradient as in case II. Here separation occurs with $U/U_1 = 0.69$, that is, $C_p = 0.52$.

Figure 4.15(b) shows for each of the three cases the growth of momentum-thickness Reynolds number and the shape factor $H = \delta^*/\theta$. Separation is associated with large values of H (approaching 3 or more) and with very rapid growth in H .

High-speed computers have now enabled researchers to simulate numerically many complex viscous and turbulent flows for which boundary layer theory is inadequate. In such cases the full Navier-Stokes equations can be used in the solution by means of either finite-difference or finite-volume techniques. In such computations the flow field is considered to contain a large number of volume elements, for each of which the conservation equations are expressed in linearized form. The solution consists of an iterative procedure in which these linearized equations are simultaneously satisfied by an appropriate computer algorithm. Much effort has been devoted to developing faster algorithms for solution of these equations. Great increases in computational speed have been realized, both with better algorithms and with faster computers [13]. Though, in principle, mathematical uncertainties can be eliminated by using smaller and smaller volume elements to represent the flow field, such testing is in practice expensive because computational time increases rapidly with the number of grid points used. Further, it may not be appropriate to use the same representation of turbulent stresses as grid-point spacing—for example, very near walls—is reduced. Thus such grid-space testing may not be fully conclusive.

The largest uncertainty, however, in full numerical modeling of viscous flows in ducts and over bodies immersed in fluid streams is associated with representa-

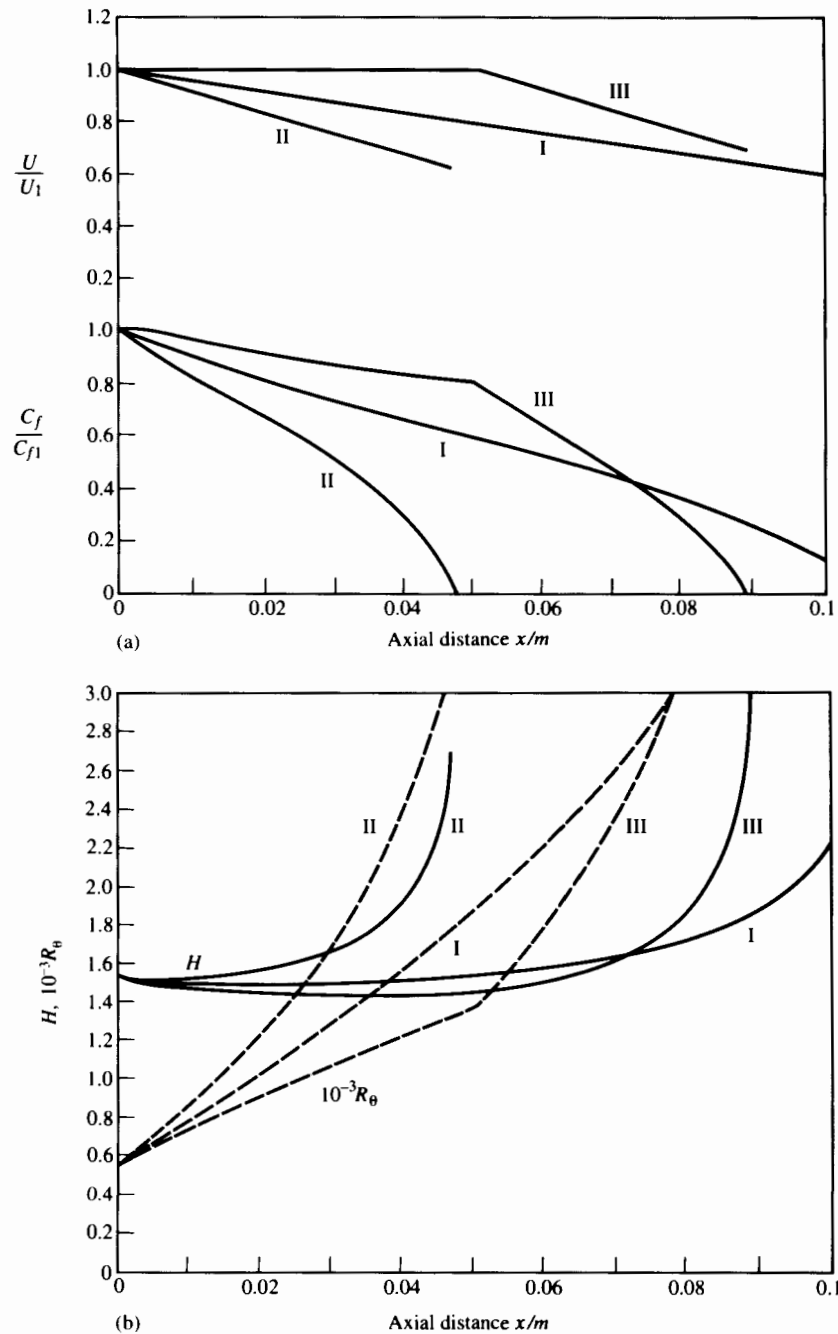


FIGURE 4.15 (a) Free-stream velocity U and wall friction coefficient C_f . Initial values $U_1 = 100$ m/s, $C_{f1} = 0.005$, $R_{\delta 1} = 5000$, $R_{\theta 1} = 555$, and $\nu = 1.4 \times 10^{-5}$ m²/s. (b) Shape factor H and momentum-thickness Reynolds number R_θ . Same initial conditions and free-stream velocity distributions as in (a).

tion of the important turbulent stress components. Pletcher [14] has reviewed the principal methods of characterizing these stresses through the use of the turbulence kinetic energy and other transport equations. Despite the numerical and physical difficulties that have made the development of general methods difficult, great progress has been made. Even somewhat uncertain prediction methods for fully viscous and turbulent flow fields have proved their worth in design and development, when used in conjunction with experimental data. The great value of high-speed numerical computations of propulsion engine flow fields appears not to have been in eliminating the need for experimental tests but in contributing a rational framework for understanding and exploring the implications of experimental knowledge. Wise use of numerical results has sometimes greatly reduced the number of expensive experimental tests required to optimize an engine component design.

4.5 BOUNDARY LAYER HEAT TRANSFER

When a temperature difference exists between a wall and the fluid flowing past it, heat transfer occurs between the two by conduction and radiation. Conduction accelerated by motion of the fluid is called *convection*, the process that concerns us here. We limit the discussion to so-called forced convection, in which the fluid motion is generated by an external device such as a fan, a pump, or a propulsion engine. (For more detailed discussions of the material reviewed here and for treatment of radiative heat transfer, see complete texts on the subject, such as Refs. 15, 16, and 17.)

Whenever there is heat transfer between a fluid and a wall, there is generally a smooth variation in fluid temperature in the region near the wall, as suggested by Fig. 4.16. We will see that in many interesting cases the thickness of the layer in which the temperature variation is large, the so-called thermal boundary layer thickness, δ_T , has the same order of magnitude as the velocity boundary layer of thickness δ .

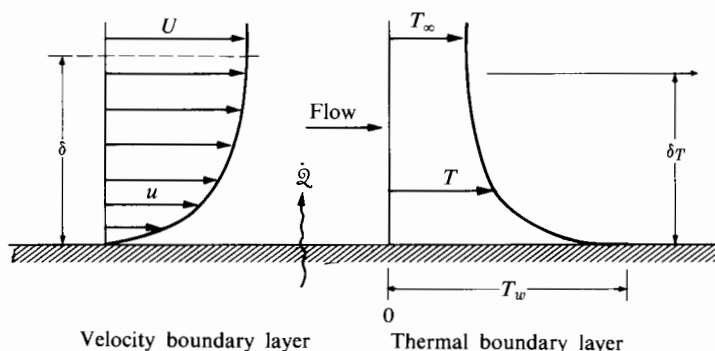


FIGURE 4.16 Velocity and thermal boundary layers.

Assuming the wall heat transfer rate per unit area \dot{Q}_0 to be proportional to the overall temperature difference $T_w - T_\infty$, we may define a *heat transfer film coefficient* h_f by

$$\dot{Q}_0 = h_f(T_w - T_\infty), \quad (4.31)$$

where h_f is the coefficient of heat transfer across the liquid or gas film (i.e., boundary layer) near the wall, and T_w and T_∞ are the wall and free-stream temperatures, respectively. The shape of the temperature profile and the determination of h_f require the use of the energy equation within the boundary layer.

In general, viscosity and density depend on temperature, so that temperature variations in the fluid affect the flow field to some extent. If these properties are essentially constant, we can determine the velocity distribution from Eqs. (4.1) and (4.2), which are then independent of temperature.

The appropriate energy equation for two-dimensional steady flow may be derived by considering a control volume within the boundary layer, as shown in Fig. 4.17, where enthalpy flux, heat transfer, and shear work are shown separately. In Fig. 4.17 the velocity components parallel and normal to the wall are u and v , respectively. The symbol h designates the local enthalpy per unit mass, and k is the thermal conductivity. As before, τ is the local shear stress. If the fluid is a gas (the case of principal interest in the following chapters), the heat transfer is almost entirely normal to the wall. Therefore heat transfer parallel to the wall has been neglected in Fig. 4.17. Cases where this is not permissible (for instance, heat

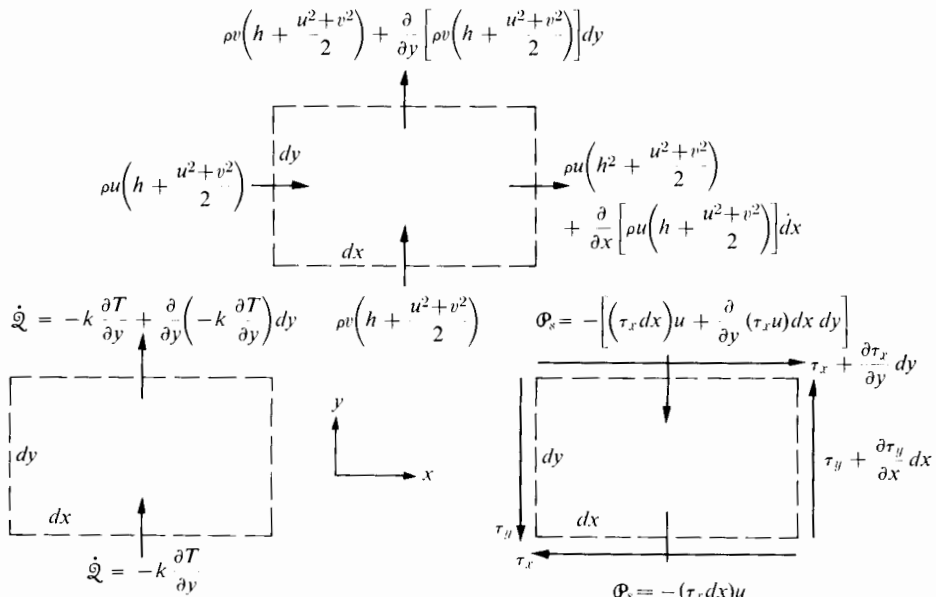


FIGURE 4.17 Approximate enthalpy flux, heat transfer, and shear work transfer for elemental control volume.

transfer to liquid metals of high conductivity) are treated in heat-transfer texts. (See, for example, Ref. 17). Also the shear work is neglected on the surfaces normal to the wall since, as we have seen, both v and τ_y are much less than u and τ_x .

The net enthalpy flux from the system is

$$\frac{\partial}{\partial y} \left[\rho v \left(h + \frac{u^2 + v^2}{2} \right) \right] dy dx + \frac{\partial}{\partial x} \left[\rho u \left(h + \frac{u^2 + v^2}{2} \right) \right] dx dy,$$

which may be expanded to

$$\begin{aligned} & \left(h + \frac{u^2 + v^2}{2} \right) \left[\frac{\partial}{\partial x} (\rho u) + \frac{\partial}{\partial y} (\rho v) \right] dx dy + \rho u \frac{\partial}{\partial x} \left(h + \frac{u^2 + v^2}{2} \right) dx dy \\ & + \rho v \frac{\partial}{\partial y} \left(h + \frac{u^2 + v^2}{2} \right) dx dy. \end{aligned}$$

From the continuity equation, the term in square brackets is zero.

The net heat transfer to the control volume is simply $+(\partial/\partial y)[k(\partial T/\partial y)]dy dx$, where k is the thermal conductivity of the fluid.

Shear work is done on or by the fluid in the control volume through the shear stresses

$$\tau_x \quad \text{and} \quad \tau_x + \frac{\partial \tau_x}{\partial y} dy,$$

since the fluid along these boundaries is moving in the shear direction. The net work transfer rate from the control volume is $-(\partial/\partial y)(\tau_x u)dx dy$.

The energy equation for steady flow requires that the net enthalpy flux from the control volume be equal to the net heat flux minus the net shear work. Thus, combining these expressions, we have

$$\begin{aligned} & \rho u \frac{\partial}{\partial x} \left(h + \frac{u^2 + v^2}{2} \right) dx dy + \rho v \frac{\partial}{\partial y} \left(h + \frac{u^2 + v^2}{2} \right) dx dy \\ & = \frac{\partial}{\partial y} \left(k \frac{\partial T}{\partial y} \right) dy dx + \frac{\partial}{\partial y} (\tau_x u) dx dy. \end{aligned}$$

This equation can be expressed in neater form by using the momentum equation to eliminate the velocity derivatives. Multiplying Eq. (4.2) by ρu , we obtain

$$\rho u \left(u \frac{\partial u}{\partial x} + v \frac{\partial u}{\partial y} \right) = \rho u \frac{\partial}{\partial x} \frac{u^2}{2} + \rho v \frac{\partial}{\partial x} \frac{u^2}{2} = -u \frac{dp}{dx} + \frac{\partial}{\partial y} \left(\mu u \frac{\partial u}{\partial y} \right) - \mu \left(\frac{\partial u}{\partial y} \right)^2.$$

Then, if we assume laminar flow so that $\tau_x = \mu(\partial u/\partial y)$ in the energy equation, neglect the small terms

$$\rho u \frac{\partial}{\partial x} \frac{v^2}{2} \quad \text{and} \quad \rho v \frac{\partial}{\partial y} \frac{v^2}{2},$$

and assume a perfect gas, the energy equation becomes

$$\rho u c_p \frac{\partial T}{\partial x} + \rho v c_p \frac{\partial T}{\partial y} = u \frac{dp}{dx} + \frac{\partial}{\partial y} \left(k \frac{\partial T}{\partial y} \right) + \mu \left(\frac{\partial u}{\partial y} \right)^2. \quad (4.32)$$

If we choose to consider an incompressible fluid rather than a perfect gas, then

$$dh \approx c dT + (1/\rho) dp,$$

in which c is the specific heat of the fluid. Using this expression in Eq. (4.32) yields

$$\rho u c \frac{\partial T}{\partial x} + \rho v c \frac{\partial T}{\partial y} = \frac{\partial}{\partial y} \left(k \frac{\partial T}{\partial y} \right) + \mu \left(\frac{\partial u}{\partial y} \right)^2. \quad (4.33)$$

In either case the last term, $\mu(\partial u / \partial y)^2$, represents viscous dissipation, or work done on the fluid within the control volume. In many cases it is negligible compared with the other terms.

We can see an interesting and useful analogy between wall heat transfer \dot{Q}_0 and wall shear stress τ_0 if we compare the momentum and energy equations for the special case of no axial pressure gradient, negligible viscous dissipation, and constant fluid properties. The equations are then

$$\begin{aligned} \text{Momentum: } & u \frac{\partial u}{\partial x} + v \frac{\partial u}{\partial y} = \nu \frac{\partial^2 u}{\partial y^2}, \\ \text{Energy: } & u \frac{\partial T}{\partial x} + v \frac{\partial T}{\partial y} = \frac{k}{\rho c_p} \frac{\partial^2 T}{\partial y^2}. \end{aligned}$$

It is evident that the equations are quite similar if

$$\nu = \frac{k}{\rho c_p} \quad \text{or} \quad \frac{\mu c_p}{k} = 1.$$

Since $\mu c_p/k$, the Prandtl number, is in fact of the order of unity for most gases, this similarity is worth examining. It means that a solution for u from the momentum equation will be a solution for T from the energy equation if velocity and temperature are expressed in terms of variables that have the *same* boundary conditions. Suitable variables are u/U and $(T_w - T)/(T_w - T_\infty)$, since both go from zero at the wall to unity in the free stream.[†] In this case the variations of u/U and $(T_w - T)/(T_w - T_\infty)$ are the same, and the thermal and velocity boundary layers are of the same thickness. Thus, to relate \dot{Q}_0 to τ_0 for the case of constant wall temperature T_w ,

$$\frac{\tau_0}{\dot{Q}_0} = \frac{\mu (\partial u / \partial y)_{y=0}}{-k (\partial T / \partial y)_{y=0}} = \frac{U \mu}{(T_w - T_\infty) k} \left[\frac{[(\partial / \partial y)(u/U)]_{y=0}}{\frac{\partial}{\partial y} \left(\frac{T_w - T}{T_w - T_\infty} \right)} \right]_{y=0} = \frac{\mu}{k} \frac{U}{(T_w - T_\infty)}.$$

Rearranging, we can write this as

$$\frac{\tau_0}{\rho U^2} = \left(\frac{\mu}{\rho U x} \right) \left[\frac{\dot{Q}_0 x}{(T_w - T_\infty) k} \right],$$

[†] Since both U and T_∞ are constant, then the case examined is for T_w constant.

where x , the distance from where the boundary layer began to grow, is introduced because of its known importance in the development of the velocity boundary layer. With Eq. (4.31),

$$\frac{\tau_0}{\rho U^2} = \left(\frac{\mu}{\rho U x} \right) \left(\frac{h_f x}{k} \right).$$

Defining the Nusselt number Nu_x (based on length x) as $h_f x / k$, and with the Reynolds number Re_x (also based on x) and skin friction coefficient C_f , we can write this as

$$\text{Nu}_x = \frac{1}{2} \text{Re}_x C_f.$$

Thus, for laminar flow of a fluid of Prandtl number unity, one can determine heat-transfer characteristics from skin friction and Reynolds number. In fact, with Eq. (4.7d),

$$\text{Nu}_x = 0.332 \sqrt{\text{Re}_x}. \quad (4.34)$$

For laminar flow over a flat plate with constant fluid properties, "exact" solutions are available for any Prandtl number, as discussed in heat transfer texts. For the case of constant wall temperature the Pohlhausen solution, together with the Blasius solution for the velocity boundary layer, gives [14]

$$\text{Nu}_x = 0.332 \sqrt{\text{Re}_x} \sqrt[3]{\text{Pr}}, \quad (4.35)$$

where Pr is the Prandtl number. This result is valid for $\text{Pr} > 0.5$; that is, for most gases. We can see that Eqs. (4.34) and (4.35) are in agreement for $\text{Pr} = 1$. For the case of uniform \dot{Q}_0 rather than constant T_w , the constant changes from 0.332 to 0.458.

Turbulence affects the thermal boundary layer much as it does the velocity boundary layer. This would seem reasonable since one can expect that turbulent motion would enhance the transverse transfer of enthalpy very much as it affects the transfer of momentum. By analogy then, one can define an energy transfer diffusivity ϵ_h to account for the turbulent conductivity in the form

$$\frac{\dot{Q}}{\rho c_p} = - \left(\frac{k}{\rho c_p} + \epsilon_h \right) \frac{dT}{dy} = -(\alpha + \epsilon_h) \frac{dT}{dy}, \quad (4.36)$$

where $\alpha = k/\rho c_p$ is called the thermal diffusivity of the fluid. Lacking functional relationships for ϵ_h (just as for ϵ), we must use empirical knowledge in the treatment of turbulent heat transfer.

Since momentum and enthalpy transfer are affected similarly by turbulence, one might expect a heat transfer-skin friction analogy as in laminar flow. The analogy can in fact be demonstrated in fully developed turbulent flow in pipes. For such flow we have seen that $\tau/\tau_0 = 1 - y/R$. Similarly, for a fully developed temperature profile, the variation of heat transfer with radius can be approximated by $\dot{Q}/\dot{Q}_0 = 1 - y/R$, while the velocity and temperature profiles are also similar, so that

$$\frac{\tau}{\dot{Q}} \approx \frac{\tau_0}{\dot{Q}_0} \quad (4.37)$$

and

$$\frac{d}{dy} \left(\frac{u}{\bar{U}} \right) = \frac{d}{dy} \left(\frac{T_w - T}{T_w - \bar{T}} \right), \quad (4.38)$$

where \bar{U} and \bar{T} are the bulk mean velocity and temperature, respectively. The ratio of shear stress to heat transfer rate is

$$\begin{aligned} \frac{\tau}{\dot{Q}} &= \frac{\rho(\nu + \epsilon)(du/dy)}{-\rho c_p(\alpha + \epsilon_h)(dT/dy)} \\ &= \frac{\rho(\nu + \epsilon)\bar{U}(d/dy)(u/\bar{U})}{\rho c_p(\alpha + \epsilon_h)(T_w - \bar{T})(d/dy)[(T_w - T)/(T_w - \bar{T})]}. \end{aligned}$$

Assuming turbulent flow where $\epsilon \gg \nu$ and $\epsilon_h \gg \alpha$, and using Eqs. (4.37) and (4.38), we have

$$\frac{\tau_0}{\dot{Q}_0} = \frac{\epsilon \bar{U}}{c_p \epsilon_h (T_w - \bar{T})}$$

which can be written

$$\frac{\dot{Q}_0}{T_w - \bar{T}} \frac{1}{\rho \bar{U} c_p} = \frac{\epsilon}{\epsilon_h} \frac{\tau_0}{\rho \bar{U}^2}$$

or

$$\frac{h}{\rho c_p \bar{U}} = \frac{(\epsilon/\epsilon_h) C_f}{2}. \quad (4.39)$$

It has been common in the past to assume that $\epsilon/\epsilon_h \approx 1$, but measurements have revealed values in the range [14] of $0.9 < \epsilon/\epsilon_h < 1.7$.

Equation (4.39) relates measured friction losses and heat transfer quite well. If the variation in the ratio of $(\nu + \epsilon)/[(k/\rho c_p) + \epsilon_h]$ through the zones of laminar and turbulent flow is taken into account, an improved relationship can be obtained. This has been done in different ways by Taylor, Von Karman, and Martinelli, as discussed in Rohsenow and Choi [17].

Experimentally it has been found that heat transfer data for long smooth tubes correlate very well, with

$$\frac{h_f D}{k_b} = 0.023 \left(\frac{\rho \bar{U} D}{\mu} \right)_b^{0.8} \left(\frac{\mu c_p}{k} \right)_b^{0.33}, \quad (4.40)$$

where the subscript b denotes evaluation at the bulk mean fluid temperature. This may also be written

$$\frac{h_f D}{k} = 0.023 \left(\frac{\rho \bar{U} D}{\mu} \right)^{0.8} \left(\frac{\mu c_p}{k} \right)^{0.33}$$

or

$$\frac{h_f}{\rho c_p \bar{U}} = 0.023 \left(\frac{\bar{U} D}{\nu} \right)^{-0.2} \left(\frac{\mu c_p}{k} \right)^{-0.67}. \quad (4.41)$$

Comparing Eq. (4.41) with Eq. (4.18), we may see that

$$\left(\frac{h_f}{\rho c_p \bar{U}} \right) \text{Pr}^{0.67} = \frac{C_f}{2}. \quad (4.42)$$

Written in this way, the turbulent heat transfer–skin friction analogy takes the form due to Colburn,

$$\text{St } \text{Pr}^{0.67} = \frac{C_f}{2},$$

where $\text{St} = h_f/\rho c_p \bar{U}$ is the Stanton number.

Colburn's form of the analogy is used to calculate the heat transfer to the turbulent boundary layer of a flat plate as follows [17]:

$$\frac{h_f}{\rho c_p U_\infty} \text{Pr}^{2/3} = \frac{C_f}{2}.$$

To evaluate the skin friction coefficient C_f in this case, we may use Eq. (4.20). Experimental data have shown that this analogy is useful in a fairly wide range of pressure gradient, so that convective heat transfer across turbulent boundary layers can be estimated by quite simple, though rather approximate, methods.

Given the huge progress that has been made in numerical simulations of viscous and turbulent flow fields for which boundary layer methods are not well suited, it is not surprising that large advances have been made in heat transfer simulation of such flow fields also. Patankar [15] has reviewed the progress that has been made with numerical simulation of convection and diffusion in complex flow fields. Both finite-difference and finite-element methods are widely used. As for the fluid-mechanics problem, the essential elements in such simulations are the methods of application of the conservation equations to small-volume elements, the algorithms needed for simultaneous solution of the large number of linear equations that result, and the estimation of turbulent transport terms. Patankar briefly reviews the methods of treating convection and diffusion in complex flow fields, the development of faster algorithms, and the kinds of flows to which these new methods are being applied.

PROBLEMS

1. Show that for fully developed laminar flow in a round tube, the velocity profile is given by

$$\frac{u}{U} = 2 \left[1 - \left(\frac{r}{R} \right)^2 \right]$$

and the pressure gradient is given by

$$\frac{dp}{dx} = - \frac{8\mu U}{R^2},$$

in which U is the mean velocity, $\dot{m}/A\rho$, R is the tube radius, and u is the velocity at any radius r .

Notes: (a) For axisymmetric laminar flow, the momentum equation that replaces Eq. (4.2), which was derived for two-dimensional flow, is

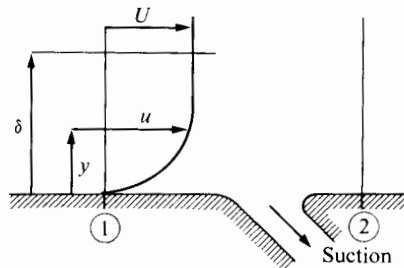
$$u \frac{\partial u}{\partial x} + v \frac{\partial u}{\partial r} = - \frac{1}{\rho} \frac{\partial p}{\partial x} + \frac{\nu}{r} \frac{\partial}{\partial r} \left(r \frac{\partial u}{\partial r} \right),$$

and the continuity equation that replaces Eq. (4.1) is

$$\frac{\partial u}{\partial x} + \frac{1}{r} \frac{\partial (rv)}{\partial r} = 0.$$

(b) If the flow is fully developed, the axial velocity component u will (by definition) be a function of r only.

2. Fuel flows in a 3.5-m pipe from a fuel tank to the pump of a jet engine. The flow rate is 200 l/min. At high altitudes the fuel-tank pressure is low, and there may be considerable danger of the fuel “boiling” or cavitating as it enters the pump. In such a case the pump would be vapor locked and would cease to deliver fuel to the engine. Show qualitatively how the pressure drop in the line varies with its diameter (over a wide range). What would the minimum pipe diameter be if a pipe pressure loss of only 3 kPa were tolerable? The pipe has no sharp bends or elbows. The kinematic viscosity of the fluid is 2.6×10^{-6} m²/s, and its specific gravity is 0.8.
3. An incompressible boundary layer is subjected to a pressure rise Δp between stations ① and ②, which are very close together. The shape of the boundary layer at station ① is satisfactorily described by $u/U = (y/\delta)^{1/7}$, in which U and δ are known quantities. Neglecting the action of viscous forces between stations ① and ②, determine how much boundary layer fluid would need to be removed by suction to prevent separation at station ②. How would viscosity tend to affect this result?



PROBLEM 3

4. Show that the definitions of displacement thickness δ^* and momentum thickness θ that will have the same physical significance for compressible flow as Eqs. (4.4) do for incompressible flow are

$$\delta^* = \int_0^\delta \left(1 - \frac{\rho u}{\rho' U}\right) dy,$$

$$\theta = \int_0^\delta \frac{\rho u}{\rho' U} \left(1 - \frac{u}{U}\right) dy,$$

where ρ' is the free-stream density and U is the free-stream velocity. Calculations of the boundary layer on the wall of a regeneratively cooled rocket motor may indicate a negative δ^* . Is this physically reasonable? Would a negative value of θ be physically reasonable?

5. For certain of the velocity profiles shown in Fig. 4.11, Howarth provides the momentum and displacement thicknesses in dimensionless form as follows:

ξ	$\frac{\alpha^{1/2} \theta}{\nu^{1/2}}$	$\frac{\alpha^{1/2} \delta^*}{\nu^{1/2}}$
0	0.000	0.000
0.0125	0.076	0.199
0.0250	0.110	0.292
0.0375	0.137	0.371
0.0500	0.162	0.447
0.0625	0.186	0.523
0.0750	0.209	0.603
0.0875	0.231	0.691
0.1000	0.254	0.794
0.1125	0.276	0.931
0.120	0.290	1.110

For $\xi = 0.100$ the velocity profile shown in Fig. 4.11 is given by:

η	$\frac{u}{U}$	η	$\frac{u}{U}$	η	$\frac{u}{U}$
0	0	1.2	0.498	2.4	0.936
0.2	0.052	1.4	0.598	2.6	0.962
0.4	0.120	1.6	0.692	2.8	0.978
0.6	0.202	1.8	0.776	3.0	0.989
0.8	0.294	2.0	0.844	3.2	0.994
1.0	0.394	2.2	0.897	3.4	0.998
				3.6	0.999
				3.8	1.000

With this profile and numerical integration, make an approximate check of the above θ and δ^* values for $\xi = 0.100$. Use the Thwaites method to predict the change in θ and δ^* from the initial values for $x = x_1$ and $U = U_1$, and compare these values with the values provided by the Howarth solution for the whole range of ξ .

6. The boundary layer of an axisymmetric nozzle is sufficiently thin that it can be expected to be both two-dimensional and laminar. The free-stream velocity adjacent to the wall surface accelerates linearly with distance from an initial value $U_1 = 100$ m/s to $10U_1$, over a distance of 0.3 m to the nozzle outlet. The kinematic viscosity of the air is about 1×10^{-5} m²/s. At the entrance of the nozzle, the boundary layer momentum thickness is 0.23 mm.
- a. Using the Thwaites method, estimate the growth in boundary layer thicknesses δ^* and θ along the length of the nozzle.
 - b. Schlichting [1] mentions that on a flat plate (with zero pressure gradient), transition from laminarity to turbulence occurs at a Reynolds number of $R_{\delta^*} = U\delta/\nu = 950$. Calculate the displacement thickness Reynolds number for the nozzle and consider whether transition is likely as the boundary layer develops.
 - c. Suppose the initial boundary layer thickness is 10 times as large as cited above. By how much would this change the momentum thickness at the end of the nozzle?
7. Laminar airflow enters a 10° (total included angle) conical nozzle whose outlet area is 0.65 times the inlet area. The inlet air velocity is 10 m/s and the initial boundary layer momentum thickness is 0.001 m. The entrance duct diameter is 14 cm. The kinematic viscosity of the air is 2×10^{-5} m²/s. Assume the core of the flow is incompressible and one-dimensional and that the flow remains entirely laminar. Use the Thwaites method to estimate the growth of θ and δ^* with distance along the nozzle. For the first attempt, assume that the free-stream velocity can be estimated sufficiently well by ignoring the presence of the boundary layer. For the second attempt, calculate the free-stream velocity from the flow area remaining after the “displacement area” from the previous attempt is subtracted from the geometric area. If this process is continued, is it likely to converge?
8. Show that, if the two expressions for velocity of Eqs. (4.14) and (4.15) are to match in some intermediate y -region, then the skin-friction coefficient is in fact determined by this velocity profile, and that (taking $\bar{U}/U_c \approx 0.8$) it can be expressed as a function of the Reynolds number as follows:

$$\frac{1}{\sqrt{C_f}} = 3.3 \log_{10}[\text{Re}\sqrt{C_f}] + 1.7,$$

in which

$$\text{Re} = \frac{\bar{U}D}{\nu} \quad \text{and} \quad C_f = \frac{2\tau_0}{\rho\bar{U}^2}.$$

For comparison, the experimental result given by Nikuradze is

$$\frac{1}{\sqrt{C_f}} = 4.0 \log_{10}(\text{Re}\sqrt{C_f}) - 0.4.$$

How close are these expressions in the Reynolds number range 10^4 – 10^7 ?

9. A long duct of fairly complex geometry is to transmit a given mass flow of hot gas at a constant average velocity. The pressure drop for the duct is to be determined experimentally by passing cold gas at an equal mass flow rate through it and measuring the pressure drop, the mean pressure level being the same in the two cases. The temperatures of the hot and cold gas streams are 300 K and 1200 K, respectively. How should the pressure drop in the two cases compare? The Mach number is small in both cases, and the Reynolds number is high enough so that changing it by a factor of three or less would have an insignificant effect on the flow pattern in the duct.
10. Estimate the pressure drop due to friction in a tube 20 diameters long in which air flows at 200 m/s. The inlet air temperature and pressure are 550 K and 0.65 MPa, respectively, and the tube diameter is 0.3 m. If the wall temperature were maintained at 1200 K, how much increase in fluid temperature could be expected during flow through the tube? As an approximation assume that the velocity profile at entrance is fully developed.
11. An airstream of speed 160 m/s and temperature 3000 K travels on the inside of a 30 cm I.D. steel tube whose wall thickness is 2.5 mm. On the outside of the tube, water coolant flows coaxially in an annular space 6.1 mm thick. The coolant velocity is 10 m/s, and it has a local temperature of 15°C. Both flows are approximately fully developed. The pressure of the airstream is around 140 kPa. Estimate the maximum wall temperature of the tube.
12. A sudden expansion with an area ratio of 2 decelerates a flow between station ① and station ②. At ① the static pressure may be assumed uniform on a perpendicular plane just downstream of the sudden expansion. At ② and just upstream of the enlargement, the flow may be taken to be one-dimensional. The fluid density may be considered uniform between ① and ②.

If the effects of wall friction between 1 and 2 are negligible, estimate

- a. the static pressure recovery ratio,

$$(p_2 - p_1)/\frac{1}{2}\rho u_1^2$$

- b. the stagnation pressure loss ratio.

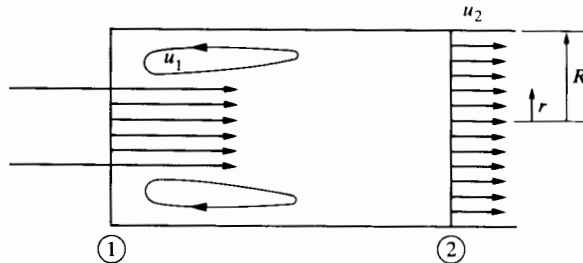
$$(p_{01} - p_{02})/\frac{1}{2}\rho u_1^2$$

If the effects of wall friction between ① and ② were equivalent to a wall friction coefficient $C_f = 0.005$ acting on the downstream flow over an L/D of 3, how would this revise your estimates of static pressure recovery ratio and stagnation pressure loss ratio? Here assume that the downstream velocity is still uniformly U_2 .

If, instead of uniform velocity at station ②, the velocity profile there could be described by

$$U_2 = U_{\max} \left[1 - \left(\frac{r}{R} \right)^4 \right],$$

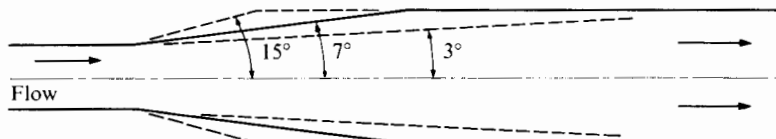
how would this revise your estimates of the static pressure recovery? Here u_{\max} and R are the maximum velocity and duct radius at station (2). In this case neglect the effect of wall friction.



PROBLEM 12

13. A conical diffuser can potentially increase the static pressure recovery and reduce the stagnation pressure losses below the values estimated in Problem 4.12. Tests have been made of the 3 conical diffusers shown in the sketch with the same inlet flow and each with area ratio of 2:1. The measurements indicate least stagnation pressure loss for the 7° divergence angle. We observed that the flow in the 15° cone is separated. The flow in the 3° cone is not separated.

Why would the flow in the 15° cone be more likely to separate than in the 3° cone? How might the relatively large loss in the 3° cone be explained? Might it be possible to design an optimum expansion shape to minimize stagnation pressure loss? If so, what kind of a calculation method would be required?



PROBLEM 13

14. Examine the velocity profiles used in the Moses turbulent boundary layer calculation method by plotting the normalized velocity u/U vs y/δ for a Reynolds number R_δ of 5000 and for friction coefficient values C_f of 0.005, 0.004, 0.003, 0.002, 0.001, and 0.000. For the last case that is the boundary layer at the point of separation, show that as y_s approaches infinity, it becomes irrelevant and that the dimensionless velocity profile is given by

$$\frac{u}{U} = 3\eta^2 - 2\eta^3.$$

For these plots use linear length and velocity scales. Show that for the unseparated turbulent boundary layer the boundary between the inner and outer layers is quite close to the wall. For the cases $C_f = 0.005$ and $C_f = 0.001$ plot the normalized velocity on a linear scale on the y axis against $y\sqrt{(\tau_0/\rho)/\nu}$, on a logarithmic scale on the y axis. The term τ_0 signifies the wall shear stress that may be evaluated from

$$\tau_0 = \mu \left(\frac{\partial u}{\partial y} \right)_{y=0}$$

What happens to the “logarithmic region” as the point of separation is approached?

15. Prepare a computer code for calculating the growth of two-dimensional turbulent boundary layers using the Moses method. Check your code against the following test case for the stated choice of integration step size dx . When you are sure the code is producing correct results, determine the effect of varying the step size on the computed results, taking the step size to be some fraction of the boundary layer thickness δ . How small does that fraction need to be to obtain accuracy to three significant figures with both constant pressure and separating boundary layers?

Standard Case (step size 0.001 m; initial velocity, $U_1 = 100$ m/s; kinematic viscosity $\nu = 1.4 \times 10^{-5}$ m²/s)

x/m	U/U_1	R_δ	C_f	R_θ	H	θ/mm
0	1	5000	0.00500	555	1.534	77.68
0.01	0.96	7068	0.00452	791	1.491	115.3
0.02	0.92	8843	0.00407	1031	1.487	156.9
0.03	0.88	10,560	0.00369	1284	1.494	204.4
0.04	0.84	12,280	0.00334	1559	1.510	259.8
0.05	0.80	14,050	0.00300	1863	1.536	326.1
0.06	0.76	15,930	0.00265	2211	1.575	407.3
0.07	0.72	17,990	0.00227	2619	1.632	509.3
0.08	0.68	20,370	0.00184	3114	1.721	641.3
0.09	0.64	23,420	0.00132	3744	1.877	819.0
0.10	0.6	28,385	0.00065	4607	2.243	1074

16. Explore the behavior of turbulent boundary layers in constant pressure flow by calculating their growth from a starting Reynolds number R_δ of 5000 and for three initial friction coefficients $C_f = 0.001, 0.003, 0.005$. Plot the variation of skin friction coefficient C_f , Reynolds number R_δ , and the shape factor $H = \delta/\theta$ against the Reynolds number based on the distance from the starting point. Take the initial free-stream velocity as 100 m/s and the kinematic viscosity as 1.4×10^{-5} m²/s.

What trends do you observe in the behavior of these constant pressure boundary layers?

17. Consider a family of diffusers designed to have free-stream velocity varying linearly with distance from the diffuser inlet plane

$$U = U_1 - bx$$

All are axisymmetric and have inlet diameter of 10 cm. At the inlet of each the free-stream velocity is 100 m/s and the inlet boundary layer is characterized by $R_\delta = 5000$ and $C_f = 0.005$. The kinematic viscosity is $\nu = 1.5 \times 10^{-5} \text{ m}^2/\text{s}$. Calculate the boundary layer growth for a series of values of b ; for each determine the distance x at which separation occurs, and the pressure coefficient $C_p = 1 - (U/U_1)^2$ at that point. One criterion of separation is $C_f = 0$, but in using this in the calculation avoid negative numbers. The Moses method is not valid past the point of separation, and the user is sharply reminded of this if negative values of C_f begin to appear. (Moses observed that separation is generally imminent if the value of αR_δ falls below 150.) Show from your results for this family of diffusers the tradeoff between maximum pressure coefficient and diffuser length.

18. Stratford has suggested that an optimum diffuser geometry might be determined by adjusting the free-stream velocity gradient so that everywhere in the diffuser the wall friction coefficient has a value of nearly zero. Assuming that the diffuser is axisymmetric and that the pressure is uniform on all planes perpendicular to the axis, and that the wall friction coefficient is everywhere held to a value of say $C_f = 0.00001$, show how the Moses method may be used to determine the required axial variation of free-stream velocity and diffuser diameter, taking displacement thickness into account. Assume the same starting conditions (except for C_f) as in Problem 4.17 and proceed, time permitting, to determine the diffuser wall geometry.

REFERENCES

1. Schlichting, H. *Boundary Layer Theory*, 7th ed. New York: McGraw-Hill, 1979.
2. Shapiro, A. H. *The Dynamics and Thermodynamics of Compressible Fluid Flow*, vol. 2. New York: Ronald Press, 1954, chap. 26. Reprint ed., Krieger.
3. Massey, B. S. *Mechanics of Fluids*, 2nd ed. London: Van Nostrand Reinhold, 1970.
4. Sabersky, R. H., A. J. Acosta, and E. G. Hauptmann. *Fluid Flow*, 2nd ed. New York: Macmillan, 1988.
5. Milne-Thomson, L. M. *Theoretical Hydrodynamics*, 5th ed. London: Macmillan, 1968.
6. Howarth, L. "On the Solution of the Laminar Boundary Layer Equations," *Proc. Royal Soc., London A*164 (1938): 547.
7. Thwaites, B. "Approximation of the Laminar Boundary Layer," *Aero Quarterly* 1 (1949): 245–280.
8. Sherman, F. S. *Viscous Flow*. New York: McGraw-Hill, 1990.
9. White, F. M. *Fluid Mechanics*, 2nd ed. New York: McGraw-Hill, 1986.

10. Moody, L. F. "Friction Factors for Pipe Flow," *Trans. ASME* 66 (1944): 671-784.
11. Rohsenow, W. M. and J. P. Hartnett (eds). *Handbook of Heat Transfer*. New York: McGraw-Hill, 1973.
12. Moses, H. L. "A Strip-Integral Method for Predicting the Behavior of Turbulent Boundary Layers," *Proc. AFOSR-IFP-Stanford Conference on Computation of Turbulent Boundary Layers*, Stanford University, Palo Alto, Calif., 1968.
13. Patankar, S.V. "Recent Developments in Computational Heat Transfer," *J. Ht. Transf. Amer. Soc. of Mech. Eng.* 110 (1988): 1037-45.
14. Pletcher, R. H. "Progress in Turbulent Forced Convection," *J. Ht. Transf. Amer. Soc. of Mech. Eng.* 110 (1988): 1129-44.
15. Holman, J. P. *Heat Transfer*, 6th ed. New York: McGraw-Hill, 1986.
16. White, F. M. *Heat and Mass Transfer*. Reading, Mass.: Addison-Wesley, 1988.
17. Rohsenow, W. M., and H.Y. Choi. *Heat, Mass, and Momentum Transfer*. Englewood Cliffs, N.J.: Prentice Hall, 1961.

P A R T

2

AIR-BREATHING ENGINES



Boeing 747-400 on its first flight with Pratt & Whitney 4056 engines.
(Photo courtesy Boeing Company.)



C H A P T E R

5

THERMODYNAMICS OF AIRCRAFT JET ENGINES

5.1 INTRODUCTION

Modern aircraft engines have the ability to actuate massive airstreams. The total airflow ingested by the engines of a large passenger aircraft during takeoff is of the order of a ton per second. The engine airflow rate is perhaps 50 times the fuel flow rate, so that the term *air-breathing engine* is quite appropriate. It is with air-breathing jet and propeller engines that this and the following four chapters are concerned.

Given that thrust is proportional to airflow rate and that large thrust per unit engine size must be a design objective, it follows that the jet engine designer will generally attempt to maximize the airflow rate per unit size of engine. This means maximizing the speed at which the air can enter and the fraction of the inlet area that can be devoted to airflow. Turbine engines generally are far superior to piston engines in these respects, so one never hears of a piston-type jet engine.

For low flight speeds, propellers (ingesting 20 to 30 times the airflow rate of the engine) are well able to handle the massive airflow rate required for propulsion. Though piston engines may have superior efficiency at low power levels, gas turbines are favored for driving large propellers because they can generally be designed to do so with much less engine mass per unit power output. This too is related to their ability to accommodate greater airflow for a given size of engine.

At low flight speeds, propeller propulsion is considerably more efficient than jet propulsion. Conventional propellers, however, become inefficient and noisy at flight speeds higher than 0.5 or 0.6 times the speed of sound. In contrast, turbo-

jet and turbofan engines can function efficiently and quietly at flight speeds as high as 0.85 times the speed of sound. Turbojets can also operate at supersonic flight speeds. It is high-speed flight that is the chief advantage of using jet, rather than propeller, engines.

In very small sizes piston engines can be made to operate more efficiently than turbine engines so, at low flight speed with very small aircraft, piston engines will have a continuing role in driving propellers. In these chapters we will not discuss piston engines (see Refs. 1, 2, and 3), but we will return to a discussion of propellers. Much work has been done in recent years to develop new designs of propellers that may be able to operate efficiently (and with tolerable noise) at flight speeds as high as 0.6 or 0.7 times the speed of sound.

These chapters are based on air-breathing engines that operate in the gas turbine cycle. As the schematic of Fig. 5.1 indicates, they may take a number of forms depending on what is added to the basic gas generator of Fig. 5.1(a). The output of the gas generator can be used entirely in a single propulsion nozzle

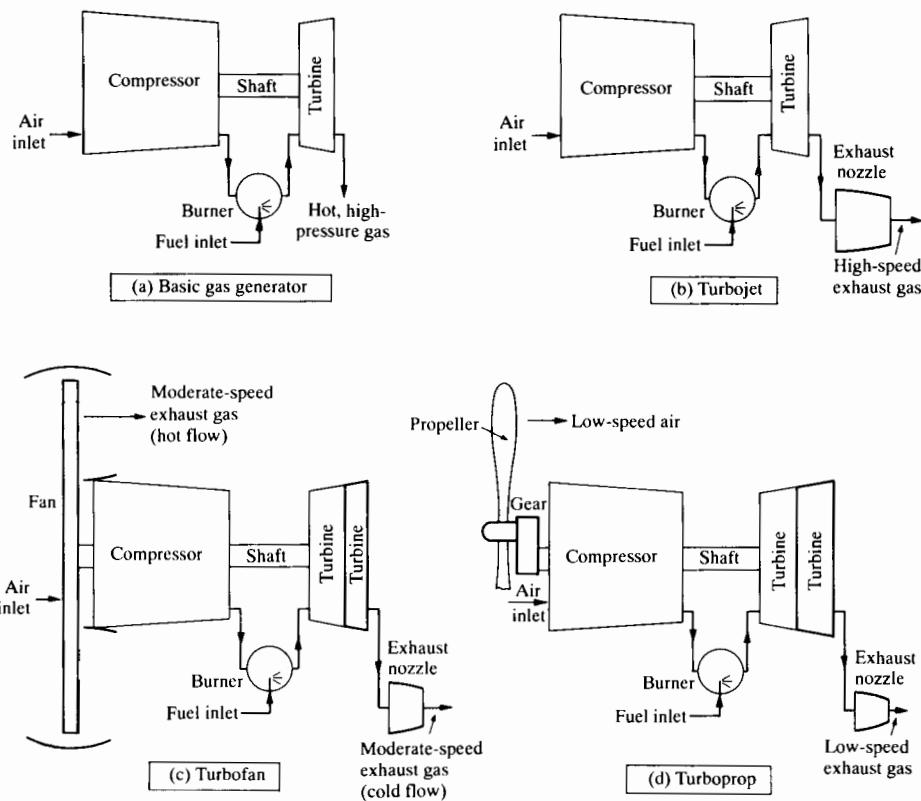


FIGURE 5.1 Development of turbine engines from the basic gas generator.

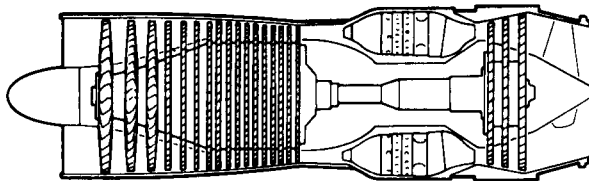
(Fig. 5.1b) or, before expansion in the core engine nozzle, to activate additional turbine stages needed to drive a fan (Fig. 5.1c) that accelerates a large stream of air passing around the engine core. The flow through the outer part of the fan may be five or six times the flow through the engine core. The engine produces thrust both from the hot jet leaving the main nozzle and from acceleration of the cold bypass flow outside the engine core.

The turboprop concept of Fig. 5.1(d), whose development preceded that of the turbofan, could be considered an extension of this concept; the rate of airflow through the propeller may be 25 to 30 times the airflow rate through the core engine. The gearbox is necessary so that both propeller and core engine can operate at optimum rotational speed. For subsonic flight there are substantial improvements in efficiency to be gained in moving from turbojet to turbofan. The turboprop can be still more efficient, but the use of a propeller with no surrounding duct limits the application of the turboprop to relatively low flight speeds.

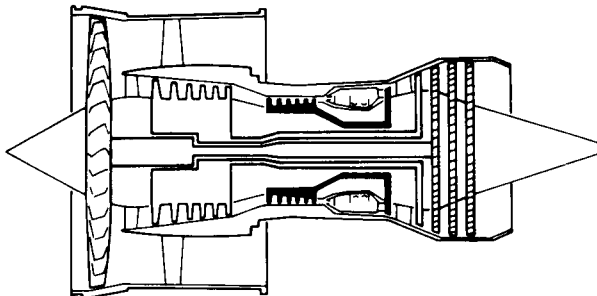
Figure 5.2 shows scale drawings of typical axial flow turbojet, turbofan, and turboprop engines as well as the propfan concept. In the turbojet sketch (Fig. 5.2a) one can see the individual compressor and turbine rotors mounted, in this case, on a single shaft. Figure 5.3 shows, for this engine, the typical pressure distribution through the engine. Later we will see why the compressor has many more rotors than the turbine, though the pressure change across the compressor is only about 20% greater than across the turbine. The burner chambers are shown between the compressor and the turbine. The exhaust nozzle is short, supplied with an internal cone, and simply converging, that is, designed for subsonic (or sonic) exit flow.

Figure 5.2(b) shows a typical sketch of a turbofan engine. This one has three concentric shafts. The outer one takes power from the single high-pressure turbine rotor to the high-pressure compressor rotor, which has six sets of rotor blades. The intermediate shaft takes power from the single-stage intermediate-pressure turbine to drive the six-stage low-pressure compressor. Three turbine stages drive the fan through the innermost shaft. In this drawing one sees relatively small area convergence in the hot-gas nozzle and even less in the fan nozzle. Figure 5.2(c) shows a two-shaft axial flow turboshaft engine. Concealed in the front housing is the planetary speed reduction unit connecting the innermost engine shaft to the propeller (not shown). Figure 5.2(d) shows a drawing of a "propfan" engine, indicating two counterrotating propellers (or "unducted" fans, as they are sometimes called) driven by separate turbines. The propellers differ from conventional ones in that they are multibladed and specially shaped for aerodynamic efficiency at high flight speed.

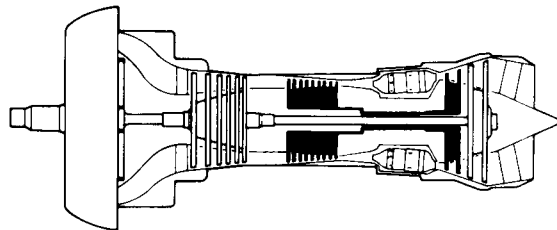
Any jet engine develops thrust by imparting momentum to the fluid passing through it. With Newton's laws in mind, it is easy to say that the thrust exerted by the jet engine is the reaction to the net force that the engine exerts on the fluid passing through it. However, the internal distribution of the components of this net force is complex. Figure 5.3 shows calculated internal forces on a turbojet engine whose net thrust is 11,158 lb_f. As shown, the internal forces on the turbine



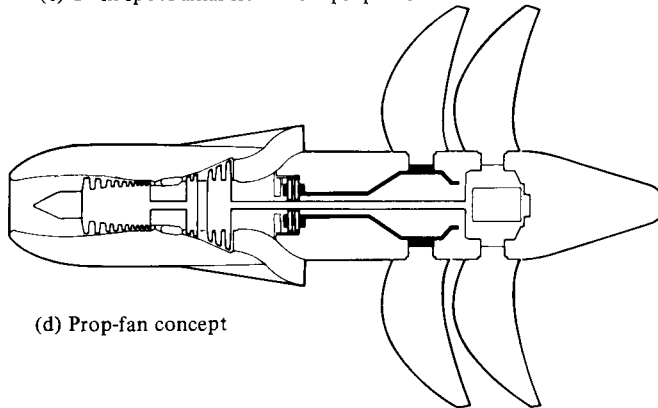
(a) Single-spool axial flow turbojet



(b) Triple-spool front fan turbojet (High bypass ratio)



(c) Twin-spool axial flow turbopropeller



(d) Prop-fan concept

FIGURE 5.2 Gas turbine engines. (Courtesy Rolls-Royce, plc.)

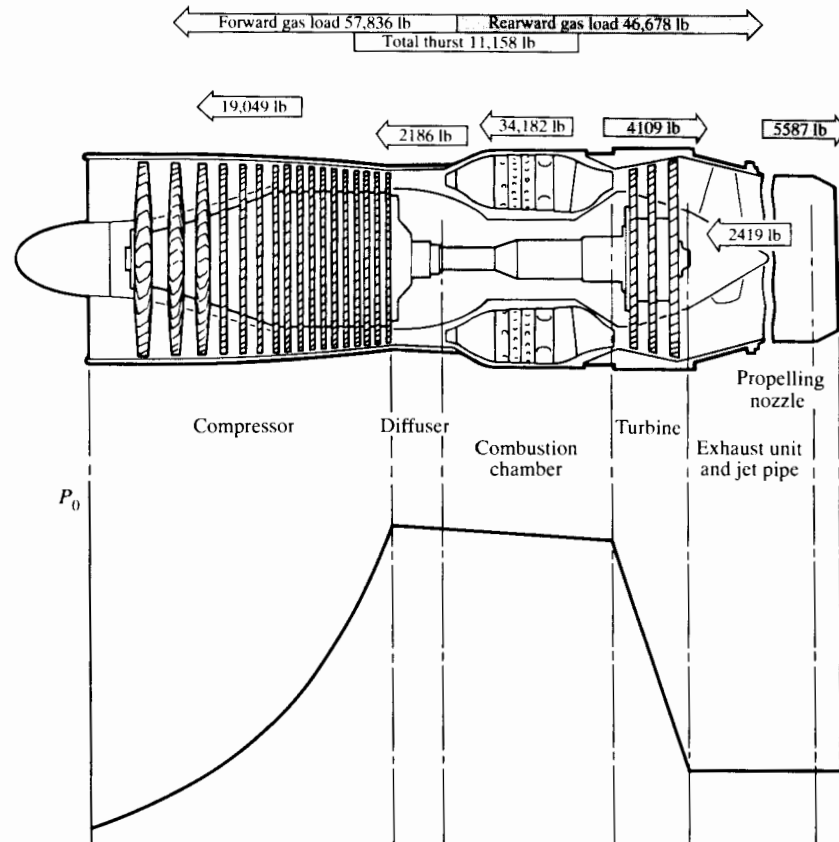


FIGURE 5.3 Internal total pressure and thrust distribution; single-shaft turbojet engine.
(Adapted from Rolls-Royce, plc [4].)

and nozzle total $46,678 \text{ lb}_f$ and act in the wrong direction! The thrusts on the turbine exhaust cone, burner, and compressor are positive, however, and total $57,836 \text{ lb}_f$; the net force acting on the metal surfaces of the engine is therefore positive after all.

Evaluating an integral of the pressure and shear forces acting over every surface element inside the engine to determine the net thrust at all flows and speeds would be an unacceptably tedious and uncertain procedure. Calculations such as those whose results are shown in Fig. 5.3, and that are used in a wide variety of design evaluations, are best performed with the control volume method introduced in Chapter 2 and further demonstrated in the next section.

The general purpose of this chapter is to apply the laws of thermodynamics and mechanics to air-breathing jet propulsion engines in such a way that one can:

1. Estimate the best possible engine performance as a function of principal design parameters—for example, maximum allowable engine temperature, pressure ratio, flight speed, and ambient conditions;
2. Evaluate the effects of departure from ideality (“losses”) in engine components—for example, compressor, turbine, and nozzle;
3. Appreciate the rationale for the development of specific engine configurations—for example, turbofan and afterburning turbojets;
4. Establish a method for evaluating the effects of future increases in turbine inlet temperature, component efficiency, and so on;
5. See how principal engine components—for example, compressors and turbines—can be designed to match each other under design conditions;
6. See how, in principle, the essential performance characteristics of engine and aircraft can be considered together in estimating the performance of the flight vehicle.

5.2 THRUST AND EFFICIENCY

Fairly general equations for thrust and efficiency of air-breathing jet engines can be derived from the momentum and energy laws without the need for detailed consideration of the internal mechanisms of particular engines. Consider, for example, the generalized thrust-producing device illustrated in Fig. 5.4, as observed from a position stationary with respect to the device. While this device looks like a pod-mounted ramjet or turbojet, the results obtained will be applicable to the calculation of thrust produced by any air-breathing engine with a single exhaust

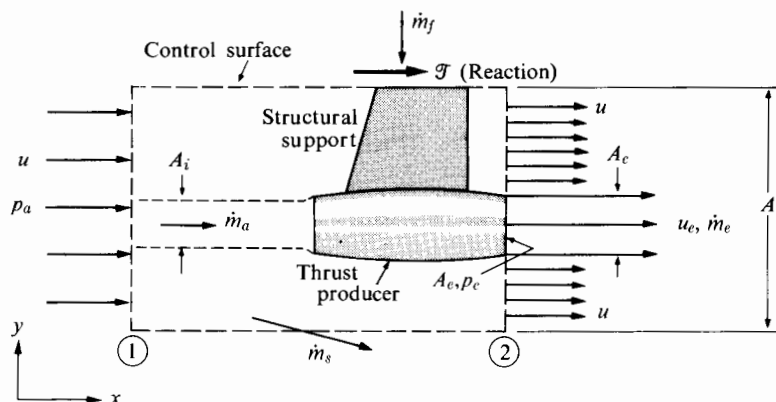


FIGURE 5.4 Generalized thrust-producing device.

jet. In Chapter 2 we derived the thrust of a stationary jet engine; we now generalize this result to show the effect of aircraft flight speed on thrust. An additional effect of flight speed—the drag on the external surface of the engine nacelle or pod—is of secondary importance in this discussion, so for simplicity we will assume that the flow external to the engine is reversible.

In Fig. 5.4 a control surface is specified that passes through the propellant outlet plane at ② and extends far upstream at ①. The side surfaces of the control volume are parallel to the upstream (flight) velocity \mathbf{u} and far removed from the thrust device. We assume that the thrust and conditions at all points within the control volume do not change with time.

The Thrust Equation

The reaction to the thrust \mathcal{T} transmitted through the structural support is indicated in Fig. 5.4. In this sense we may define the engine thrust as the vector summation of all forces on the internal *and* external surfaces of the engine and nacelle.

The thrust of the generalized thrust producer may be derived from Eq. (2.4) as it applies to steady flow:

$$\sum \mathbf{F} = \int_{cs} \mathbf{u} \rho (\mathbf{u} \cdot \mathbf{n}) dA .$$

Considering the components of force and momentum flux in the x -direction only, we have

$$\sum F_x = \int_{cs} u_x \rho (\mathbf{u} \cdot \mathbf{n}) dA . \quad (5.1)$$

With the assumption of reversible external flow, both the pressure and the velocity may be assumed constant over the entire control surface, except over the exhaust area A_e of the engine. If the exhaust velocity u_e is supersonic, the exhaust pressure p_e may differ from the ambient pressure p_a . The net pressure force on the control surface is therefore $+(p_a - p_e)A_e$. The only other force acting on this control volume is the reaction of the thrust \mathcal{T} . Adding up the forces on the control surface that act in the x -direction, we obtain

$$\sum F_x = (p_a - p_e)A_e + \mathcal{T} . \quad (5.2)$$

Far upstream at station ①, the air that is drawn into the engine crosses the control surface through capture area A_i at a rate \dot{m}_a given by $\dot{m}_a = \rho u A_i$, in which ρ is the ambient density and u is the flight velocity. The mass flux crossing the exhaust area A_e is $\dot{m}_e = \rho_e u_e A_e$. Taking account of the fuel flow rate \dot{m}_f , we have $\dot{m}_e = \dot{m}_a + \dot{m}_f$, or

$$\dot{m}_f = \rho_e u_e A_e - \rho u A_i . \quad (5.3)$$

Now, if we consider the requirement of continuity for the control volume as a whole and assume that the fuel flow originates from outside the control volume, Eq. (2.2) for steady flow is

$$\int_{cs} \rho \mathbf{u} \cdot \mathbf{n} dA = 0,$$

which for the present case we may write as

$$\rho_e u_e A_e + \rho u (A - A_e) + \dot{m}_s - \dot{m}_f - \rho u A = 0,$$

in which A is the cross-sectional area of the control volume normal to the velocity u , and \dot{m}_s is the mass flow of air through the side surfaces of the control volume (Fig. 5.4). Rearranging, we get

$$\dot{m}_s = \dot{m}_f + \rho u A_e - \rho_e u_e A_e.$$

When we use Eq. (5.3), this equation becomes

$$\dot{m}_s = \rho u (A_e - A_i). \quad (5.4)$$

If the sides of the control volume are sufficiently distant from the thrust producer, we may assume that this flow crosses the control surface with a very small velocity in the y -direction and an essentially undisturbed velocity component in the x -direction. Thus the momentum carried out by the control volume with this flow is simply $\dot{m}_s u$, and when we take components only in the x -direction, the right-hand side of Eq. (5.1) may be written

$$\int_{cs} u_x \rho (\mathbf{u} \cdot \mathbf{n}) dA = \dot{m}_e u_e + \dot{m}_s u + \rho u (A - A_e) u - \dot{m}_a u - \rho u (A - A_i) u,$$

which is the net outward flux of x -momentum from the control volume. Using Eq. (5.4), we may reduce this to

$$\int_{cs} u_x \rho (\mathbf{u} \cdot \mathbf{n}) dA = \dot{m}_e u_e - \dot{m}_a u. \quad (5.5)$$

When we use Eqs. (5.2) and (5.5), the momentum equation (5.1) becomes

$$\mathcal{T} = \dot{m}_e u_e - \dot{m}_a u + (p_e - p_a) A_e$$

or, defining the fuel-air ratio $f = \dot{m}_f / \dot{m}_a$, we have

$$\mathcal{T} = \dot{m}_a [(1 + f) u_e - u] + (p_e - p_a) A_e. \quad (5.6)$$

The term $(p_e - p_a) A_e$ is not zero only if the exhaust jet is supersonic and the nozzle does not expand the exhaust jet to ambient pressure. It can however be a substantial contribution to the thrust if $p_a \ll p_e$.

Bear in mind that in the derivation of Eq. (5.6) the flow external to the engine has been assumed reversible. If this is not so, because of significant boundary layer effects such as separation, the actual force transmitted by the structural support of Fig. 5.4 could be appreciably less than Eq. (5.6) would predict. Alter-

natively, one could regard the effect of aerodynamic friction on the strut and the external surface of the engine nacelle to be a part of the total drag of the aircraft.

For engines that have two distinct exhaust streams, one must apply Eq. (5.1) separately to each stream. As shown in Section 5.1, the additional propellant streams of turbofan and turboprop engines may be distinguished according to whether they pass through or around the combustion chamber and turbine of the engine. The propellant streams may be labeled “hot flow” and “cold flow,” respectively. The thrust equation for such an engine, if we neglect pressure terms, becomes

$$\mathcal{T} = (\dot{m}_{aH} + \dot{m}_f)u_{eH} - \dot{m}_{aH}u + \dot{m}_{aC}(u_{eC} - u),$$

where the subscripts *H* and *C* refer to the hot and cold flows, respectively. Basing the definition of the fuel–air ratio on the air that is actually mixed with the fuel, $f \equiv \dot{m}_f/\dot{m}_{aH}$, we obtain the thrust equation

$$\mathcal{T} = \dot{m}_{aH}[(1 + f)u_{eH} - u] + \dot{m}_{aC}(u_{eC} - u). \quad (5.7)$$

Engine Performance

In describing the performance of aircraft engines, it is helpful if we first define several efficiencies and performance parameters. We will now give various definitions and, for simplicity, present representative expressions as they would apply to an engine with a single propellant stream (i.e., a turbojet or ramjet). Turbofan and turboprop engines would require slightly more complex expressions, but the qualitative conclusions regarding comparative engine performance would be similar.

Propulsion efficiency. The product of thrust and flight velocity, $\mathcal{T}u$, is sometimes called thrust power. One measure of the performance of a propulsion system is the ratio of this thrust power to the rate of production of propellant kinetic energy. This ratio is commonly known as the *propulsion efficiency*, η_p . For a single propellant stream,

$$\eta_p = \frac{\mathcal{T}u}{\dot{m}_a[(1 + f)(u_e^2/2) - u^2/2]}. \quad (5.8)$$

With two reasonable approximations we may considerably simplify this relationship. First, for air-breathing engines in general, $f \ll 1$ and may therefore be ignored in Eqs. (5.6) and (5.8) without leading to serious error. Second, the pressure term in Eq. (5.6) is usually much smaller than the other two terms, so that $\mathcal{T} \approx \dot{m}_a(u_e - u)$. Thus

$$\eta_p \approx \frac{(u_e - u)u}{(u_e^2/2) - u^2/2} = \frac{2u/u_e}{1 + u/u_e}. \quad (5.9)$$

The thrust equation shows that u_e must exceed u so that the right-hand side of Eq. (5.9) has a maximum value of unity for $u/u_e = 1$. However, for $u/u_e \rightarrow 1$, the

thrust per unit mass flow is practically zero; and of course for a finite thrust the engine required would be infinitely large. Thus it is not realistic to try to maximize the propulsion efficiency of a jet engine, and other parameters are required to evaluate its overall performance.

It is interesting to note that if the "propellant" of a traction vehicle on the earth's surface is considered to be the earth itself, then according to this expression the propulsion efficiency of such a vehicle is unity.

Thermal efficiency. Another important performance ratio is the *thermal efficiency*, η_{th} , of the engine. For ramjets, turbojets, and turbofans it is defined as the ratio of the rate of addition of kinetic energy to the propellant to the total energy consumption rate $\dot{m}_f Q_R$, where Q_R is the heat of reaction of the fuel as defined by Eq. (2.31). Thus we may write the thermal efficiency, again for a single propellant stream, as

$$\eta_{th} = \frac{\dot{m}_a[(1+f)(u_e^2/2) - u^2/2]}{\dot{m}_f Q_R}$$

or

$$\eta_{th} = \frac{[(1+f)(u_e^2/2) - u^2/2]}{f Q_R}. \quad (5.10)$$

The output of a turboprop or turboshaft engine is largely shaft power. In this case thermal efficiency is defined as for other shaft-power devices by

$$\eta_{th} = \frac{\mathcal{P}_s}{\dot{m}_f Q_R}, \quad (5.11)$$

where \mathcal{P}_s is shaft power.

Propeller efficiency. Shaft power is converted to thrust power of a moving aircraft by a propeller. *Propeller efficiency*, η_{pr} , is customarily defined as the ratio of thrust power to shaft power, or

$$\eta_{pr} = \frac{\mathcal{T}_{pr}u}{\mathcal{P}_s}, \quad (5.12a)$$

where, in this case, \mathcal{T}_{pr} is that portion of the thrust due to the propeller. However, since many turboprop engines derive appreciable thrust from the hot exhaust of their turbines, an *equivalent shaft power*, \mathcal{P}_{es} , may be defined such that the product of η_{pr} and \mathcal{P}_{es} is equal to the total thrust power (at some arbitrarily selected flight speed). Then

$$\eta_{pr} = \frac{\mathcal{T}u}{\mathcal{P}_{es}}. \quad (5.12b)$$

Overall efficiency. The product of $\eta_p \eta_{th}$, or $\eta_{pr} \eta_{th}$ as applicable, is called the *overall efficiency*, η_o , and is defined by

$$\eta_o = \eta_p \eta_{th} = \frac{\mathcal{T}u}{\dot{m}_f Q_R}. \quad (5.13)$$

Using Eq. (5.9), we find that (for $f \ll 1$)

$$\eta_o = 2\eta_{th} \left(\frac{u/u_e}{1 + u/u_e} \right).$$

Thus the overall efficiency depends only on the velocity ratio u/u_e and on the thermal efficiency η_{th} , which depends somewhat on the velocity ratio. The importance of overall efficiency will be demonstrated by a simple aircraft range analysis, but first we consider takeoff thrust.

Takeoff Thrust

One of the most important characteristics of a turbine engine installed in an aircraft is its ability to provide static and low-speed thrust so that the aircraft may take off under its own power (ramjets cannot provide static thrust and so are excluded from this discussion). We may derive the static thrust from Eq. (5.6), ignoring the pressure term and neglecting f relative to unity:

$$\frac{\mathcal{T}}{\dot{m}_a} = u_e \quad (\text{static}). \quad (5.14)$$

Thus the static thrust per unit mass flow of air is directly proportional to the exhaust jet velocity. But another important question arises: For a given fuel flow rate, how does thrust depend on exhaust velocity? The answer to this question illuminates one of the major differences between turbojets, turbofans, and turboprops, and it plays a significant role in the choice of propulsion system for many applications. Using Eqs. (5.10) and (5.14) for the static case, we have (for $f \ll 1$)

$$\mathcal{T} = \frac{2\eta_{th} Q_R \dot{m}_f}{u_e} \quad (\text{static}). \quad (5.15)$$

This equation shows that for a given fuel flow \dot{m}_f and thermal efficiency η_{th} , the takeoff thrust is inversely proportional to exhaust velocity. In other words, for a given rate of energy consumption, the takeoff thrust can be increased by accelerating a larger mass flow of air to a smaller exhaust velocity.

The importance of thrust per unit fuel consumption rate, other than fuel economy (which is relatively unimportant during takeoff), is that it roughly determines engine size for a given thrust requirement. Turbine engines that have been developed for high performance have approximately the same peak temperature limit and therefore about the same fuel-air ratio. Thus equal fuel flow rates imply approximately equal “hot”-air flow rates, and it is the hot-air flow that, to a large extent, determines the size of the basic gas generator and engine.

Aircraft Range

In many cases the distance or range that an aircraft can travel with a given mass of fuel is an important criterion of the excellence of performance of that aircraft-engine combination. Ignoring the climb to and descent from cruise altitude, and assuming that all aircraft and engine characteristics except total mass are constant throughout cruise, one can easily obtain an estimate of range.

In level flight at constant speed, engine thrust and vehicle drag are equal, as are lift and vehicle weight. Therefore

$$\mathcal{T} = \mathcal{D} = L \left(\frac{\mathcal{D}}{L} \right) = \frac{mg}{L/\mathcal{D}}, \quad (5.16)$$

where m is the instantaneous vehicle mass, g is the acceleration due to gravity, \mathcal{D} is drag force, and L/\mathcal{D} is the lift-drag ratio. The thrust power is then

$$\mathcal{T}u = \frac{mgu}{L/\mathcal{D}}.$$

By using Eq. (5.13) with this expression, we obtain

$$\dot{m}_f = \frac{mgu}{\eta_o Q_R(L/\mathcal{D})}. \quad (5.17)$$

However, since the fuel is part of the total aircraft mass m ,

$$\dot{m}_f = -\frac{dm}{dt} \quad \text{or} \quad \dot{m}_f = -u \frac{dm}{ds},$$

where s denotes distance along the flight path. Substituting this expression in Eq. (5.17), we have

$$\frac{dm}{ds} = -\frac{mgu}{\eta_o Q_R(L/\mathcal{D})}. \quad (5.18)$$

If, as an approximation, the denominator $\eta_o Q_R(L/\mathcal{D})$ is assumed constant, the range s of the vehicle can be obtained by integrating Eq. (5.18) to obtain Breguet's range formula,

$$s = \eta_o \left(\frac{L}{\mathcal{D}} \right) \ln \frac{m_1}{m_2} \frac{Q_R}{g}, \quad (5.19)$$

where m_1 and m_2 are the initial and final masses of the vehicle, the difference being the mass of fuel consumed. Thus the range is directly proportional to the overall efficiency η_o .

The importance of this term prompts an interest in its variation with flight speed and engine variables. If $f << 1$ and the pressure term in the thrust equation is neglected, and if we again consider a single propellant stream for simplicity, it follows that

$$\eta_o = \frac{(u_e - u)u}{fQ_R},$$

and that for given u_e , η_o is maximum for $u = u_e/2$.

We can show that this may be modified to express the overall efficiency of an engine of double propellant streams. It is only necessary to replace the exhaust velocity u_e by the “thrust-averaged” exhaust velocity \bar{u}_e , which is defined by

$$\bar{u}_e = \frac{\dot{m}_{aH}(1+f)u_{eH} + \dot{m}_{aC}u_{eC}}{\dot{m}_{aH}(1+f) + \dot{m}_{aC}}, \quad (5.20)$$

and to replace the fuel-air ratio f by the term $f/[1 + (\dot{m}_{aC}/\dot{m}_{aH})]$; the fuel-air ratio is defined by $f = \dot{m}_f/\dot{m}_{aH}$. Thus

$$\eta_o = \left(1 + \frac{\dot{m}_{aC}}{\dot{m}_{aH}}\right) \frac{(\bar{u}_e - u)u}{fQ_R}. \quad (5.21)$$

For a given ratio $\dot{m}_{aC}/\dot{m}_{aH}$ and a given exhaust velocity \bar{u}_e , the overall efficiency is approximately maximized for $u = \bar{u}_e/2$, a generalization of the previous result.

In Section 5.4 we show the reasons why and the ways in which the exhaust velocity u_e and the fuel-air ratio f vary with flight speed (or flight Mach number M). Figure 5.5 shows that with existing engine materials and the best design configurations, η_o typically increases continuously with flight Mach number.

This does not mean, however, that for maximum range the aircraft should fly at maximum Mach number; the aircraft lift-drag ratio L/D is also dependent on flight Mach number, as shown in Fig. 5.5. The ratio is typically much lower for supersonic than for subsonic flight, and the product $\eta_o L/D$ reaches a peak at a high subsonic flight Mach number. In long-range commercial passenger aviation, 30% to 50% of the total direct aircraft operating expense may consist of fueling cost, so there is great incentive for maximizing the range s for a given fuel consumption $m_1 - m_2$ (i.e., minimizing fuel consumption per unit distance traveled). This is why most long-range commercial passenger turbojet aircraft are designed to fly at subsonic Mach number.

For supersonic flight in which fuel economy is important, Fig. 5.5 suggests that the higher the flight Mach number, the better. But maximizing $\eta_o L/D$ is not the whole story; the higher the flight Mach number, the higher the surface temperature of the aircraft and thus the heavier the structure may need to be to keep stresses at safe levels. Therefore the ratio m_1/m_2 has also to be considered in determining the most economical supersonic flight Mach number.

If we use Eq. (5.13), we may transform the range formula Eq. (5.19) to

$$s = \frac{L}{D} \ln \frac{m_1}{m_2} \frac{\mathcal{T}}{\dot{m}_f} \frac{u}{g},$$

which shows that for a given flight speed, the range of an aircraft is directly proportional to the ratio of thrust and fuel flow rate. This ratio is so important that its inverse, the *thrust specific fuel consumption*, TSFC, defined by

$$\text{TSFC} = \frac{\dot{m}_f}{\mathcal{T}},$$

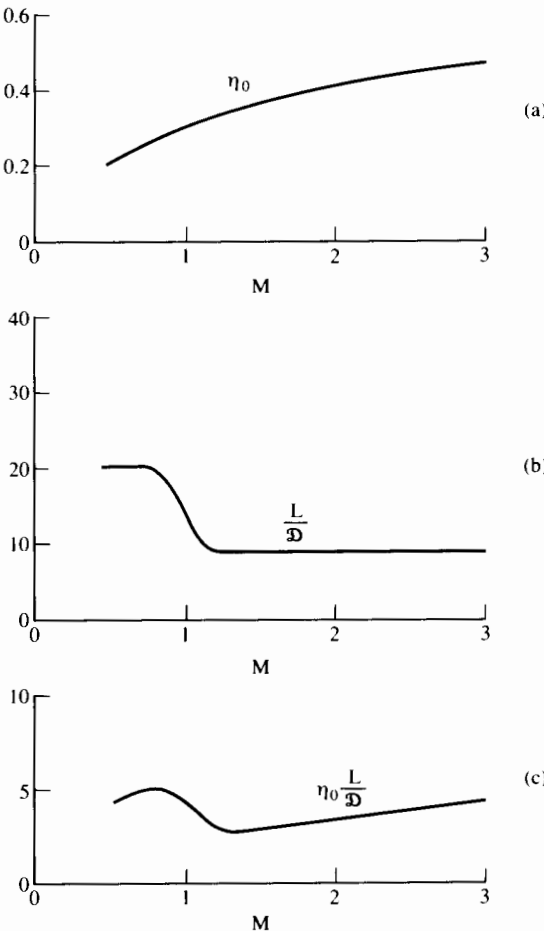


FIGURE 5.5 Typical variations of overall efficiency η_0 and aircraft lift-drag ratio L/D with flight Mach number.

is widely used as an experimental indicator of engine quality. For a turbojet (with $P_a \approx P_e$) Eq. (5.6) shows that

$$\text{TSFC} = \frac{\dot{m}_f}{\dot{m}_a[(1+f)u_e - u]}. \quad (5.22)$$

One can use this expression for turbofan and turboprop engines by replacing the symbol u_e with the \bar{u}_e of Eq. (5.20).

Equation (5.22) indicates that the TSFC of a given engine depends strongly on flight speed. Typical values of TSFC for modern engines are as follows:

	kg/N · hr	lb/lb _f · hr
Ramjets (M = 2)	0.17–0.26	1.7–2.6
Turbojets (static)	0.075–0.11	0.75–1.1
Turbofans (static)	0.03–0.05	0.3–0.5

For turbine engines that produce shaft power, a *brake specific fuel consumption*, BSFC, is defined by

$$\text{BSFC} = \frac{\dot{m}_f}{\mathcal{P}_s}$$

To account for the thrust of the hot gases, we may define an *equivalent brake specific fuel consumption*, EBSFC, as

$$\text{EBSFC} = \frac{\dot{m}_f}{\mathcal{P}_{es}} = \frac{\dot{m}_f}{\mathcal{P}_s + \mathcal{T}_e u},$$

in which \mathcal{P}_s is the shaft power supplied to the propeller, \mathcal{T}_e is the thrust produced by the turbine engine exhaust, and u is an arbitrarily selected flight speed. Typical values of equivalent brake specific fuel consumptions are

$$\text{EBSFC} = 0.45 - 0.60 \frac{\text{lb}/\text{hr}}{\text{hp}} \quad \text{or} \quad 0.27 - 0.36 \frac{\text{kg}}{\text{kWh}}$$

In this respect the best turboprop engines are as efficient as the best piston engines. In addition, the turboprop engine is considerably lighter and smaller (in frontal area) than a piston engine of equal power, at least in the high-power sizes.

5.3 THE RAMJET

The simplest of all air-breathing engines is the ramjet. As Fig. 5.6 shows schematically, it consists of a diffuser, a combustion chamber, and an exhaust nozzle. Air enters the diffuser, where it is compressed before it is mixed with the fuel and burned in the combustion chamber. The hot gases are then expelled through the nozzle by virtue of the pressure rise in the diffuser as the incoming air is decelerated from flight speed to a relatively low velocity within the combustion chamber. Consequently, although ramjets *can* operate at subsonic flight speeds, the increasing pressure rise accompanying higher flight speeds renders

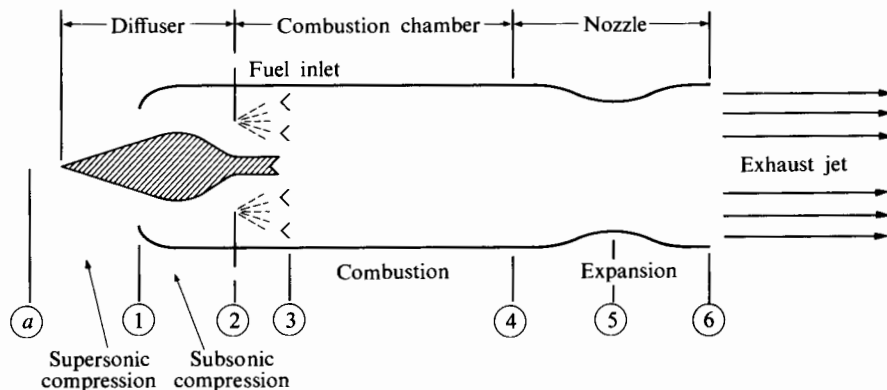


FIGURE 5.6 Schematic diagram of a ramjet engine.

the ramjet most suitable for supersonic flight. Figure 5.6 is typical of supersonic ramjets that employ partially supersonic diffusion through a system of shocks. Since the combustion chamber requires an inlet Mach number of about 0.2 to 0.3, the pressure rise at supersonic flight speeds can be substantial. For example, for isentropic deceleration from $M = 3$ to $M = 0.3$, the static pressure ratio between ambient and combustion chamber pressures would be about 34! Only a fraction of the isentropic pressure ratio is actually achieved since, especially at high Mach numbers, the stagnation pressure losses associated with shocks are substantial. After compression the air flows past the fuel injectors, which spray a stream of fine fuel droplets so that the air and fuel mix as rapidly as possible. The mixture then flows through the combustion chamber, which usually contains a "flameholder" to stabilize the flame, much as is indicated in Fig. 5.6. Combustion raises the temperature of the mixture to perhaps 3000 K before the products of combustion expand to high velocity in the nozzle. The reaction to the creation of the propellant momentum is a thrust on the engine in accordance with Eq. (5.6). This thrust is applied by pressure and shear forces distributed over the internal surfaces of the engine.

The materials used at present for the walls of combustion chambers and nozzles cannot tolerate temperatures much above 1200 K, but they can be kept much cooler than the main fluid stream by a fuel-injection pattern that leaves a shielding layer of relatively cool air next to the walls. In contrast, the turbine engine cannot be operated at nearly so high a temperature as 3000 K. The turbine blades are subjected to high centrifugal stresses and cannot be cooled so readily. The lower maximum temperature limit of the turbojet greatly affects the relative performance and operating ranges of the two engines, as we will see.

This relatively high peak-temperature limit of the ramjet allows operation at high flight Mach numbers. As the Mach number is increased, however, the combustion chamber inlet temperature also increases, and at some limiting Mach

number it will approach the temperature limit set by the wall materials and cooling methods. For example, at a flight Mach number of 8 in an atmosphere at 225 K, the stagnation temperature is about 2500 K.

At temperatures above 2500 K, dissociation of the combustion products may be significant. At high temperatures the major effect of further fuel addition is further dissociation rather than actual temperature rise. If the dissociated combustion products recombine as they expand in the nozzle, the combustion energy can still be partly transformed to kinetic energy of the propellant. If not, the occurrence of dissociation could severely penalize performance. This question is considered in the discussion of nozzles in Chapter 12.

A disadvantage of the ramjet is that the pressure ratio is strictly limited by flight speed and diffuser performance. The most serious consequence of this is the fact that the ramjet cannot develop static thrust and therefore cannot accelerate a vehicle from a standing start. Furthermore, the diffuser, whose behavior is so important to the engine as a whole, is difficult to design for high efficiency. This is due to detrimental boundary layer behavior in rising pressure gradients, especially in the presence of shocks, which are practically unavoidable during supersonic operation. Supersonic diffusers designed for best efficiency at a given Mach number usually have poor performance at other Mach numbers unless their geometry is variable. The development of a large supersonic diffuser of reasonable performance and operating range requires extensive experimental work and substantial test facilities.

Figure 5.7 is a view of a ramjet showing the geometry of the supersonic and subsonic diffusers, the fuel injector, the flameholder, the combustion chamber, and the nozzle. We discuss these components in Chapter 6.

The Ideal Ramjet

To understand the performance of the ramjet, it is helpful to perform a thermodynamic analysis of a simplified model. Let us assume that the compression and expansion processes in the engine are reversible and adiabatic, and that the combustion process takes place at constant pressure. These assumptions are not, of course, realistic. In the actual diffuser, there are always irreversibilities due to shocks, mixing, and wall friction. Further, referring back to Chapter 3, we may note that, unless the combustion occurs at very low fluid velocity, both static and total pressures will drop, owing to heat addition. Departures from isentropic flow in a real nozzle occur because of friction and heat transfer. The ideal ramjet is a most useful concept, however, since its performance is the highest that the laws of thermodynamics will permit, and is the limit that real engines will approach if their irreversibilities can be reduced.

Using the station numbers of Fig. 5.6, Fig. 5.8 shows, on a temperature-entropy diagram, the processes the air goes through in an ideal ramjet. The compression process takes the air from its condition at station (a) isentropically to its

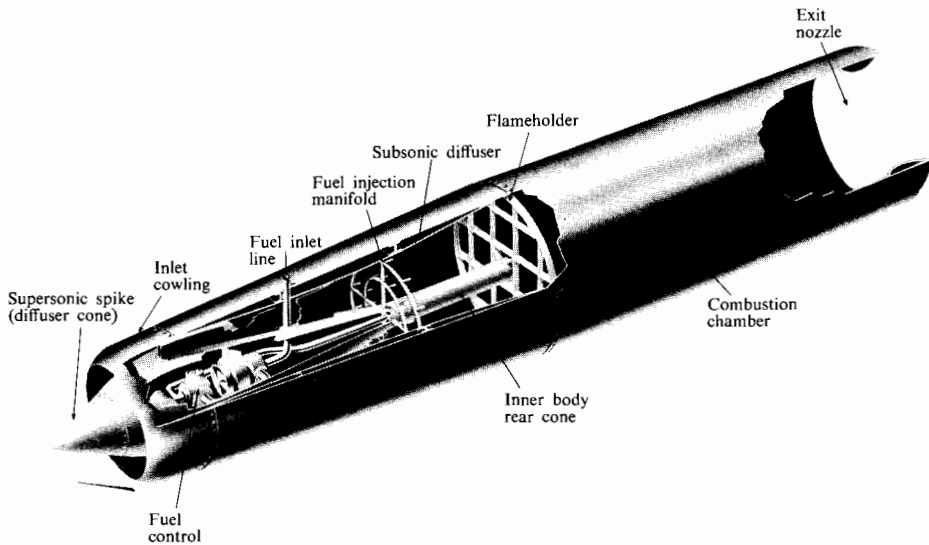


FIGURE 5.7 Cutaway view of a ramjet engine. (Courtesy Marquardt Aircraft Co.)

stagnation state (02) at station (2) . The combustion process is represented by a constant-pressure heat and mass addition process (02) to (04) up to the maximum temperature T_{04} . The exit nozzle expands the combustion products isentropically to the ambient pressure.

The ideal engine thrust may be obtained from Eq. (5.6):

$$\mathcal{T} = \dot{m}_a[(1 + f)u_e - u]. \quad (5.23)$$

With isentropic compression and expansion processes, and low-speed constant-pressure heat and mass addition, it follows that the stagnation pressure must be constant throughout the engine. Therefore $p_{0a} = p_{06}$.

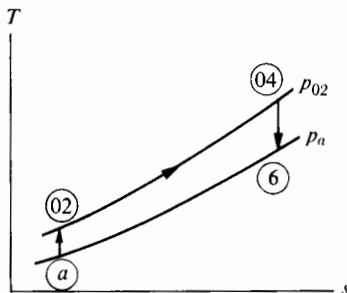


FIGURE 5.8 Thermodynamic path of the fluid in an ideal ramjet.

If we ignore variations in fluid properties (R, γ) through the engine for this ideal case, then

$$\frac{p_{0a}}{p_a} = \left(1 + \frac{\gamma - 1}{2} M^2\right)^{\gamma/(\gamma-1)} \quad \text{and} \quad \frac{p_{0e}}{p_e} = \left(1 + \frac{\gamma - 1}{2} M_e^2\right)^{\gamma/(\gamma-1)},$$

in which M is the flight Mach number and M_e is the Mach number in the plane of the exhaust. Therefore, with the condition $p_e = p_a$, it is clear that

$$\frac{p_{0a}}{p_a} = \frac{p_{0e}}{p_e} \quad \text{and} \quad M_e = M_a.$$

Thus we can determine the exhaust velocity from

$$u_e = \frac{a_e}{a_a} u,$$

where a is the speed of sound. Since $a = \sqrt{\gamma RT}$, then $a_e/a_a = \sqrt{T_e/T_a}$. However, for the case $M_e = M_a$, $T_e/T_a = T_{0e}/T_{0a}$ and, since $T_{04} = T_{0e}$, then

$$u_e = \sqrt{T_{04}/T_{0a}} u. \quad (5.24)$$

The energy equation applied to the idealized combustion process, if we neglect the enthalpy of the incoming fuel, is

$$(1 + f)h_{04} = h_{02} + fQ_R, \quad (5.25)$$

where f is the fuel-air ratio and Q_R is the heating value of the fuel. If the specific heat is assumed constant, then Eq. (5.25) may be solved for f in the form

$$f = \frac{(T_{04}/T_{0a}) - 1}{(Q_R/c_p T_{0a}) - T_{04}/T_{0a}}. \quad (5.26)$$

Equations (5.23) and (5.24) may be combined to give the thrust per unit mass flow of air,

$$\frac{\mathcal{T}}{\dot{m}_a} = M \sqrt{\gamma RT_a} \left[(1 + f) \sqrt{T_{04}/T_a} \left(1 + \frac{\gamma - 1}{2} M^2\right)^{-1/2} - 1 \right], \quad (5.27)$$

where f is given by Eq. (5.26). The thrust specific fuel consumption is given by

$$\text{TSFC} = \frac{\dot{m}_f}{\mathcal{T}} = \frac{f}{\mathcal{T}/\dot{m}_a}. \quad (5.28)$$

Figure 5.9 shows, for the ideal ramjet, the dependence of specific thrust and fuel-air ratio on flight Mach number and maximum temperature. The calculations are quite approximate, since:

1. The variations with temperature of specific heat ratio have been neglected;
2. No frictional or shock losses have been allowed for;
3. No allowance has been made for dissociation of the combustion products.

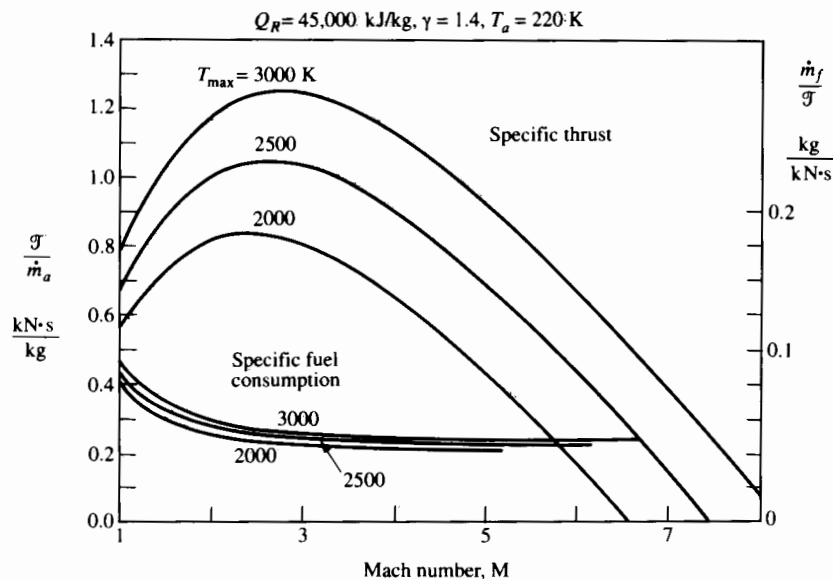


FIGURE 5.9 Ideal ramjet thrust and fuel consumption.

Despite these approximations, however, Fig. 5.9 shows qualitatively the same behavior as that of real ramjets, which require supersonic flight speed for acceptable specific thrust and reasonably low specific fuel consumption. Figure 5.10, which also applies to the ideal ramjet, shows that, though highest specific thrust is associated with a flight Mach number of about 2.6, Mach numbers well above 3 could provide much better range. Figure 5.10 shows the overall efficiency increasing sharply, while the specific thrust declines sharply, with increasing M . This is an example of a common result that the conditions for minimum fuel consumption (or maximum range) are quite different from those for which engine size per unit thrust is minimum. As the trends in Fig. 5.9 indicate, the thrust specific fuel consumption remains finite as the specific thrust approaches zero.

The Effect of Aerodynamic Losses

The propellant in a real ramjet engine, of course, suffers stagnation pressure losses as it flows through the engine. Figure 5.11 shows, on a $T-s$ diagram, the effect of these irreversibilities on the processes of compression, burning, and expansion. The compression process, (a) to (02) , is no longer isentropic, though the isentropic process is shown for comparison. The stagnation pressure at the end of the process is lower than it would be if the compression were isentropic. The performance of diffusers may be characterized by a stagnation pressure ratio r_d defined by

$$r_d = \frac{p_{02}}{p_{0a}}. \quad (5.29)$$

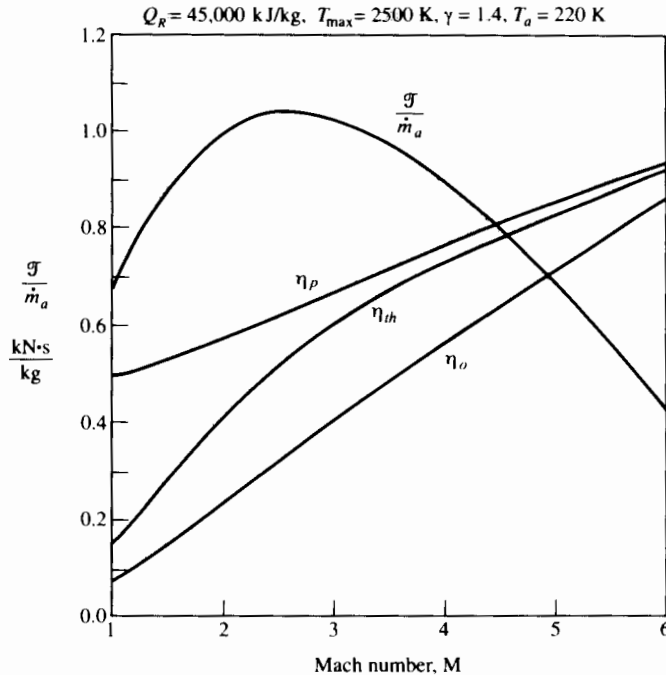


FIGURE 5.10 Ideal ramjet thrust and efficiencies.

Similarly, stagnation pressure ratios can be defined for combustors r_c and nozzles r_n as follows:

$$r_c = \frac{p_{04}}{p_{02}}, \quad (5.30)$$

$$r_n = \frac{p_{06}}{p_{04}}. \quad (5.31)$$

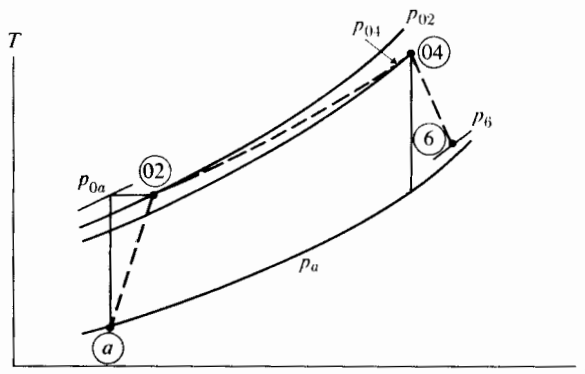


FIGURE 5.11 A T - s diagram showing aerodynamic losses incurred during ramjet processes.

The overall stagnation pressure ratio is therefore

$$\frac{p_{06}}{p_{0a}} = r_d r_c r_n.$$

Further, the actual exhaust pressure p_e or p_6 may not equal the ambient pressure p_a . However, using Eq. (3.11) for constant γ , we may write the exhaust Mach number as

$$M_e^2 = \frac{2}{\gamma - 1} \left[\left(1 + \frac{\gamma - 1}{2} M^2 \right) \left(\frac{p_{06}}{p_{0a}} \frac{p_a}{p_e} \right)^{(\gamma-1)/\gamma} - 1 \right].$$

Thus, in terms of the component stagnation pressure ratios,

$$M_e^2 = \frac{2}{\gamma - 1} \left[\left(1 + \frac{\gamma - 1}{2} M^2 \right) \left(r_d r_c r_n \frac{p_a}{p_e} \right)^{(\gamma-1)/\gamma} - 1 \right]. \quad (5.32)$$

If heat transfer from the engine is assumed negligible (per unit mass of fluid), then the exhaust velocity is given by $u_e = M_e \sqrt{\gamma R T_e}$ or, in terms of the exhaust stagnation temperature,

$$u_e = M_e \sqrt{\gamma R T_{04}} / \left(1 + \frac{\gamma - 1}{2} M_e^2 \right). \quad (5.33)$$

Since irreversibilities have no effect on stagnation temperatures throughout the engine, the fuel-air ratio necessary to produce the desired T_{04} is given by a modified form of Eq. (5.26):

$$f = \frac{(T_{04}/T_{0a}) - 1}{(\eta_b Q_R/c_p T_{0a}) - (T_{04}/T_{0a})},$$

where η_b is the combustion efficiency and $\eta_b Q_R$ is the actual heat release per unit mass of fuel. The thrust per unit airflow rate then becomes

$$\frac{T}{\dot{m}_a} = [(1 + f)u_e - u] + \frac{1}{\dot{m}_a}(p_e - p_a)A_e$$

or, if we use Eqs. (5.32) and (5.33),

$$\frac{T}{\dot{m}_a} = (1 + f) \sqrt{\frac{2\gamma R T_{04}(m - 1)}{(\gamma - 1)m}} - M \sqrt{\gamma R T_a} + \frac{p_e A_e}{\dot{m}_a} \left(1 - \frac{p_a}{p_e} \right), \quad (5.34)$$

in which

$$m = \left(1 + \frac{\gamma - 1}{2} M^2 \right) \left(r_d r_c r_n \frac{p_a}{p_e} \right)^{(\gamma-1)/\gamma}.$$

Again, the thrust specific fuel consumption is given by the equivalent of Eq. (5.22):

$$\text{TSFC} = \frac{f}{T/\dot{m}_a}.$$

We will discuss the performance of inlets, combustors, and nozzles in considerably more detail in Chapter 6. At this point, however, we can test the effects

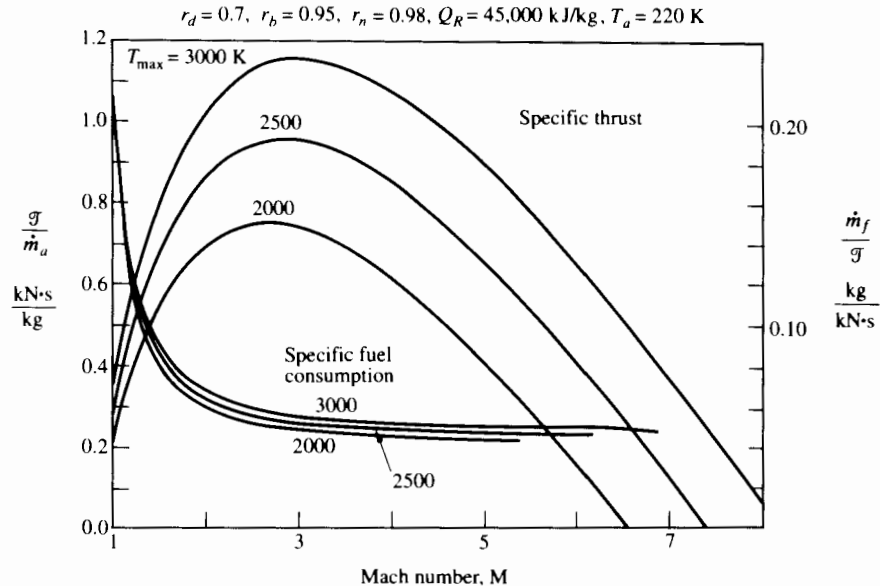


FIGURE 5.12 Ramjet thrust and fuel consumption.

of aerodynamic losses by assuming loss coefficients $r_d = 0.7$, $r_b = 0.95$, and $r_n = 0.98$. Their effects are expressed through a change in m , and Figs. 5.12 and 5.13 provide the results. Comparison of these with Figs. 5.9 and 5.10 shows less than 10% reduction in maximum specific thrust and also in specific fuel consumption.

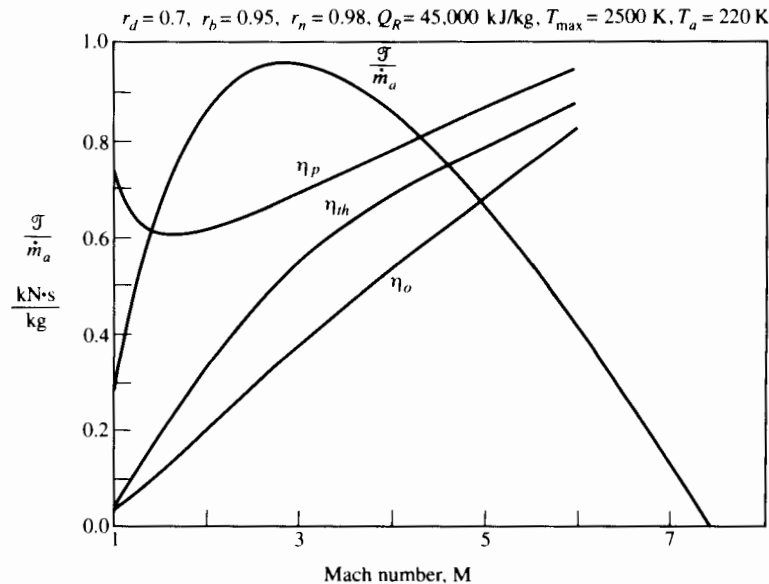


FIGURE 5.13 Ramjet thrust and efficiencies.

It is no doubt unrealistic to assume that these loss coefficients, especially r_d , are independent of flight Mach number. Diffuser losses can be expected to be strongly dependent on diffuser geometry; for efficient flight over a large Mach number range, the supersonic air intake would need to have variable (and possibly complex) geometry to avoid excessive shock losses. Part of the reason why variability is needed is that to keep shock losses low, a combination of oblique shocks would be needed, and the angle of an oblique shock is dependent on the upstream Mach number, as we saw in Chapter 3.

5.4 TURBOJET ENGINES

We mentioned that one of the disadvantages of the ramjet is that its pressure ratio depends on the flight Mach number. It cannot develop takeoff thrust and, in fact, it does not perform well unless the flight speed is considerably above the speed of sound. One way to overcome this disadvantage would be to install a mechanical compressor in the inlet duct, so that even at zero flight speed air could be drawn into the engine, burned, and then expanded through a nozzle. However, this introduces the need for power to drive the compressor. If a turbine is coupled to the compressor and driven by the hot gas passing from the burner on its way to the exhaust nozzle, the ramjet has become a turbojet. The addition of the turbomachinery, however, entirely changes the characteristic performance of the engine.

The internal arrangement of the turbojet is shown schematically in Fig. 5.14. In flowing through the machine, the air undergoes the following processes:

- (a)–(1) From far upstream, where the velocity of the air relative to the engine is the flight velocity, the air is brought to the intake, usually with some acceleration or deceleration.
- (1)–(2) The air velocity is decreased as the air is carried to the compressor inlet through the inlet diffuser and ducting system.
- (2)–(3) The air is compressed in a dynamic compressor.

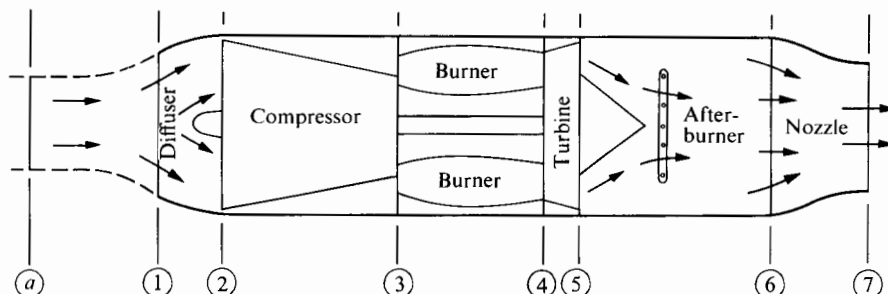


FIGURE 5.14 Schematic diagram of a turbojet engine.

- ③–④ The air is “heated” by the mixing and burning of fuel in the air.
- ④–⑤ The air is expanded through a turbine to obtain power to drive the compressor.
- ⑤–⑥ The air may or may not be further “heated” by the addition and burning of more fuel in an afterburner.
- ⑥–⑦ The air is accelerated and exhausted through the exhaust nozzle.

Before proceeding with thermodynamic analyses, we look at examples of turbojet engines, each with distinctive features.

Figure 5.15 shows the General Electric F404 afterburning jet engine. All of the airflow enters the three-stage low-pressure compressor, but there is a bypass flow around the high-pressure compressor and the burner that provides a cooling flow to the outer region of the afterburner downstream of the turbine. The bypass flow is typically about 34% of the flow in the high-pressure compressor; the engine could be called a low-bypass-ratio turbofan engine. The high- and low-pressure compressors of the F404 are each driven by single-stage turbines—through concentric and independent shafts.

The afterburner nozzle area is variable to accommodate the different volume flow rates with and without the afterburner in operation. Because the temperature of the hot gas entering the turbine must be maintained far below the adiabatic combustion temperature (and because the combustion process is very nearly adiabatic), plenty of oxygen is left for a second combustion to take place in the afterburner chamber. Shown in the cross-sectional drawing are two concentric rings of V-shaped cross section, which are used for stabilizing the flame in the afterburner.

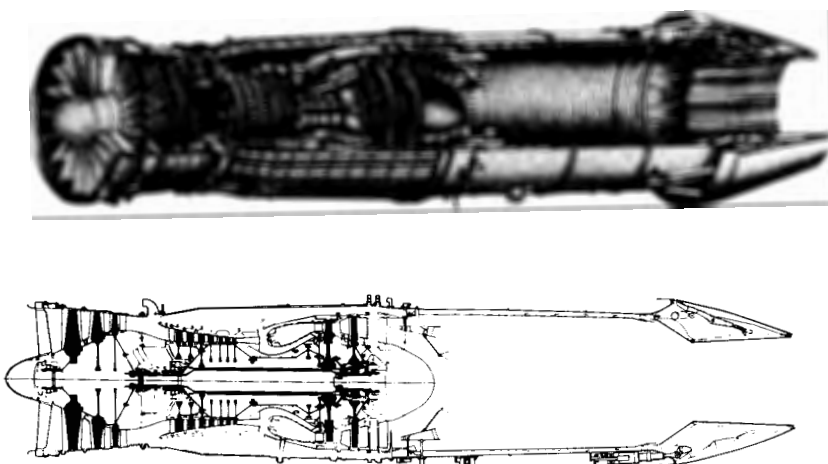


FIGURE 5.15 General Electric F404 afterburning or low-bypass turbofan engine. (Courtesy GE Aircraft Engines.)

The F404 is the successor to the General Electric J79, which has been in service many years and has about the same thrust (approximately 16,000 lb_f, or 71 kN). Compared with the J79, the F404 has half the weight and double the pressure ratio (25:1); this is one indication of the progress that has been made in turbojet engine development since the 1960s. The overall weight of the F404 is about 1000 kg (2200 lb_m). The inlet diameter is 0.79 m (31 in.), and the airflow rate in static sea-level operation is 64.4 kg/s (142 lb/sec).

Figure 5.16 shows the two Rolls-Royce Olympus 593 engines used in the Concorde, which cruises at twice the speed of sound, at altitudes up to 60,000 ft (18,300 m), and with a range of 4000 miles (6440 km). Each engine produces 38,000 lb_f (169 kN) at takeoff; with flight Mach number of 2 and an altitude of 53,000 ft (16,100 m), the thrust per engine is about 10,000 lb_f (44.6 kN). The engine weight is 7465 lb (3386 kg).

While the Concorde is cruising at Mach 2, the engine specific fuel consumption is about 1.19 lb/hr/lb_f (33.7 g/kNs). Approximate cycle calculations indicate that in this condition the exhaust jet velocity ratio u/u_e is about 0.55, so that the propulsion efficiency is about 0.70. The estimated thermal efficiency of the engine during cruise is 0.60, so that the overall efficiency η_0 is approximately 0.42.

The compressor of the Olympus engine has a pressure ratio of 11.3:1. Both low-pressure and high-pressure compressor sections (driven by concentric and independent shafts) are powered by single-stage turbines. Each compressor section has seven stages. The air intake (not shown in Fig. 5.16) to the low-pressure compressor has the variable geometry shown in Fig. 6.18 to provide for the very different inlet conditions corresponding to takeoff, subsonic cruise, and supersonic cruise. The particular problems of designing an intake for supersonic flight are discussed in Chapter 6.

The maximum turbine inlet temperature for the Olympus engine is about 1350 K. The afterburner or "reheat" chambers of the Concorde Olympus engines are used for boosting thrust during takeoff and in acceleration through near-sonic flight speeds.

The Concorde is the world's first commercially operated supersonic passenger aircraft; it is not likely to be the last. Designers are studying a number of con-

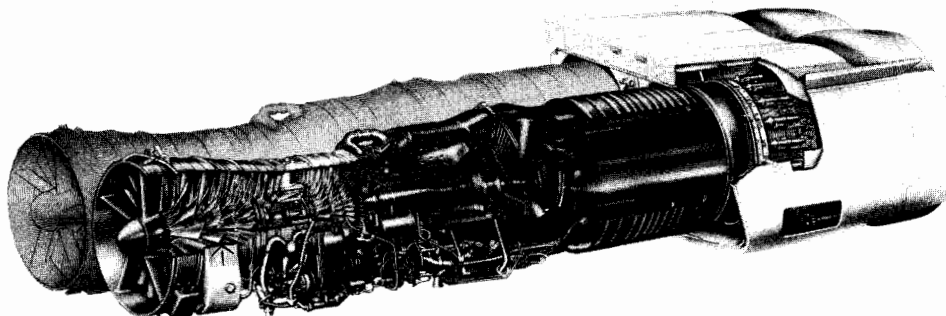


FIGURE 5.16 Rolls-Royce Olympus 593 engines used in the Concorde. (Courtesy Rolls-Royce, plc.)

cepts that could reduce the costs of supersonic flight. Currently the Concorde produces only about 13 seat-miles per gallon of fuel, whereas large subsonic passenger aircraft are able to provide about 75 seat-miles per gallon. Part of the reason for the difference lies in size (the Concorde having only 100 seats versus 400–500 for a Boeing 747); part is due to the compromises necessary in designing for both subsonic and supersonic cruise. The afterburner is, for thermodynamic reasons, fuel inefficient (though it can supply a large thrust increment without requiring a large addition to engine weight). One concept being explored for supersonic passenger aircraft involves a variable engine configuration: The engine would act as a turbofan during takeoff and subsonic cruise but revert to turbojet operation for flight Mach number of 2 or 3. For still higher Mach number, the turbomachinery could be bypassed altogether to provide ramjet propulsion. In this way the propulsion efficiency could be raised to a high level over a wide range of Mach number. Selection of the cruise flight Mach number that will provide maximum seat-miles per gallon will no doubt be strongly affected by new developments in aircraft structures and materials. At very high flight Mach number, cooling will be needed because of high “skin” temperatures.

The thermodynamic path of the fluid within a turbojet may be conveniently shown on an enthalpy–entropy or temperature–entropy diagram. To gain an understanding of the overall process, it is useful at first to study a highly simplified model. For this reason let us assume that all components except the burners are reversible and adiabatic, that the burners may be replaced by simple frictionless heaters, and that velocities at sections (2) through (6) are negligible. The T – s diagram for such an engine is shown in Fig. 5.17 for nonafterburning and afterburning engines, assuming the working fluid to be a perfect gas.

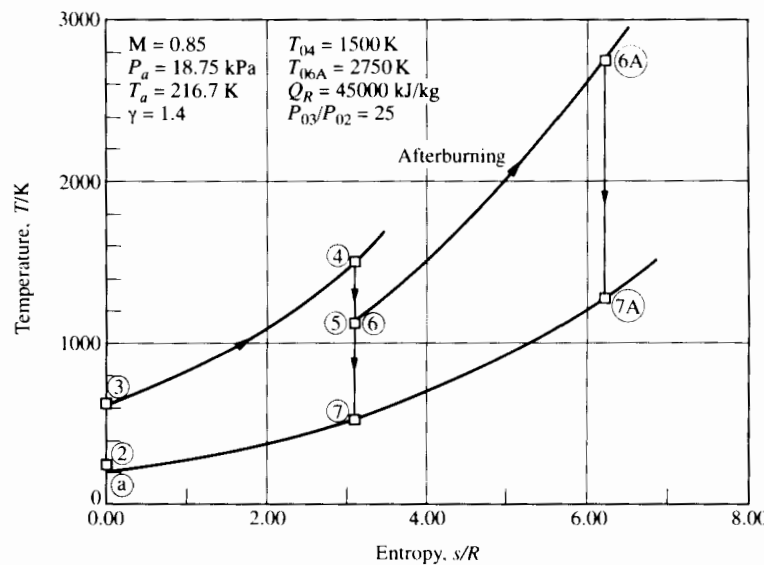


FIGURE 5.17 Ideal turbojet T – s diagram.

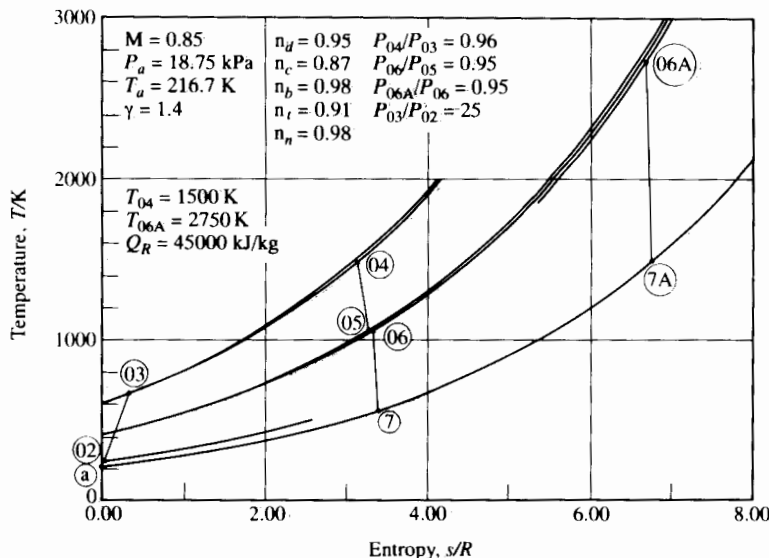
In the ideal case the pressure rises from (a) to (1), and still more from (1) to (2) as the air is decelerated relative to the engine. Since the velocity at (2) is assumed zero and the deceleration is isentropic, p_2 is the stagnation pressure for states (a), (1), and (2). Also, T_2 is the stagnation temperature for these states. The power consumed in compression from (2) to (3) must be supplied through the turbine in expansion from (4) to (5). Hence, if the compressor and turbine mass-flow rates are equal, $h_3 - h_2 = h_4 - h_{5s}$, and if the specific heat is constant, the corresponding temperature differences are also equal. In the nonafterburning case, states (5) and (6) are identical and the enthalpy drop from (5) to (7) or (6A) to (7A) is proportional to the square of the exhaust velocity. In the afterburning case, the air is reheated between (6) and (6A). From the shape of the constant-pressure curves we can see that $(T_{6A} - T_{7A})$, and hence the exhaust velocity, will be greater in the afterburning case. In fact, as we will see later, the absence of highly stressed material in the afterburner allows T_6 to be much higher even than T_4 , so that the increase in exhaust velocity can be on the order of 50%.

Although greatly simplified, this model illustrates the functions of the various components and the relationships between them. It shows clearly that the output of kinetic energy of the exhaust fluid is, in a sense, a remainder after power has been extracted from the fluid to drive the compressor.

An actual engine differs from this ideal model in several respects. First, and most important, no components are actually reversible, though it is usually reasonable to assume them adiabatic. Second, the burners are not simple heaters, and the composition of the working fluid will change during the combustion processes. Third, the fluid velocities within the engine are not negligible. If the fluid velocity in the combustor were actually zero (as constant-pressure combustion requires), it would be impossible to have a stable flame, since the flame propagates relative to the fluid at fairly large velocities. There is a fourth difference, in that the turbine and compressor flow rates may not be equal since, on the one hand, fuel is added between the two and, on the other, air may be extracted at various positions for cooling purposes.

Figure 5.18 shows a temperature-entropy diagram for a real engine with reasonable irreversible effects, and typical temperatures, for a compressor pressure ratio of 10. Afterburning and nonafterburning processes are shown, with the exhaust pressure equal to ambient pressure in both cases.

The process begins with atmospheric air at h_a, p_a . By virtue of the relative (flight) velocity between the air and the engine, this air has a stagnation enthalpy h_{0a} , higher than h_a . Further, since no work or heat transfer occurs between (a) and (2), the stagnation enthalpy is constant through station (2). The air is externally decelerated from (a) to (1). For all practical purposes this external deceleration is an isentropic process (unless an external shock occurs); hence state (1) is on an isentrope with state (a) and $p_{01} = p_{0a}$. From (1) to (2) the air is further decelerated, with an increase in entropy through frictional effects and a decrease in stagnation pressure. From (2) to (3) the air is compressed, again with an increase of entropy due to irreversibilities in the compression process. State (3s) is

FIGURE 5.18 Turbojet T - s diagram.

defined as the state that would exist if the air could be compressed isentropically to the actual outlet stagnation pressure. State (03) is the actual outlet stagnation state. We will discuss these states later when we define compressor efficiency.

From station (03) to station (04) (see Fig. 5.14), some fuel is mixed with the air, and combustion occurs. Strictly speaking, the fluid composition changes between these stations, and a continuous path between them should not be shown. However, since the fluid characteristics do not change markedly, there is no difficulty in showing the two substances on different portions of the same diagram. The stagnation pressure at (04) must be less than at (03) because of fluid friction, and also because of the drop in stagnation pressure due to heat addition at finite velocity. As we will see later, it is advantageous to make T_{04} as high as material limitations will allow. Hence states (04) and (04) are fairly well fixed.

From (04) to (05) the fluid expands through the turbine, providing shaft power equal to the shaft power input to the compressor (plus any mechanical losses or accessory power). Since no work or heat transfer occurs downstream of station (05), the stagnation enthalpy remains constant throughout the rest of the machine. State (06) depends on the geometry involved, but p_{06} must be less than p_{05} . The exhaust pressure p_7 generally equals the atmospheric pressure p_a , but it may be different if the exhaust flow is supersonic. If state (07) is known, the velocity u_7 can be calculated from the known h_{07} (or h_{05}) regardless of the properties at (06). If the afterburner is operative, the fluid is raised in temperature to state (06A), after which it expands in the nozzle to state (07A).

Again we can see that the exhaust kinetic energy is the relatively small difference between the total available enthalpy drop from state (04) and the compressor

work input. For a given compressor pressure ratio, irreversibilities increase the compressor power requirement while at the same time increasing the necessary turbine pressure drop. Both effects decrease the exhaust kinetic energy, so that overall performance may be expected to be very sensitive to compressor and turbine performance.

Utilizing the fact that compression and expansion processes in turbojet engines are very nearly adiabatic, we can make realistic estimates of engine performance by defining the adiabatic component efficiencies as follows:

For the inlet diffuser, an adiabatic efficiency η_d may be defined as the ratio of the ideal to the actual enthalpy change during the diffusion process (for the same pressure ratio p_{02}/p_1), or

$$\eta_d = \frac{h_{02s} - h_a}{h_{02} - h_a}.$$

Alternatively, the stagnation pressure ratio as defined for the ramjet (Eq. 5.30) may be used.

Correspondingly, for a compressor, a useful definition of an adiabatic efficiency η_c is the ratio of the work required in an *isentropic* process to that required in the *actual* process, for the same stagnation pressure ratio and inlet state:

$$\eta_c = \frac{h_{03s} - h_{02}}{h_{03} - h_{02}}.$$

For the turbine, the adiabatic efficiency may be defined as

$$\eta_t = \frac{h_{04} - h_{05}}{h_{04} - h_{05s}},$$

which is the ratio of actual turbine work to that which would be obtained during an isentropic expansion to the same exhaust stagnation pressure.

A nozzle adiabatic efficiency may be defined as

$$\eta_n = \frac{h_{06} - h_7}{h_{06} - h_{7s}}.$$

In addition to these four adiabatic efficiencies, a fifth kind of efficiency is often employed: the burner efficiency η_b , which is simply the fraction of the chemical energy of the fuel that is released in the combustor.

For well-designed engines the foregoing efficiencies will generally be in the following range:

$$0.7 < \eta_d < 0.9 \text{ (depending strongly on flight Mach number)},$$

$$0.85 < \eta_c < 0.90, \quad 0.90 < \eta_t < 0.95,$$

$$0.95 < \eta_n < 0.98, \quad 0.97 < \eta_b < 0.99.$$

Note that these definitions have utilized stagnation values of enthalpy. It is usually much more convenient experimentally to measure stagnation, rather than

static, values of pressure and temperature in a fluid stream. Stagnation values are convenient analytically, since they contain the kinetic-energy terms.

Later studies of components will focus on the questions of component performance in more detail. The immediate objective of this discussion is to show how overall engine performance depends on component performance and, in particular, on maximum pressure ratio and temperature.

Two questions of considerable importance are: How large is the thrust per unit mass flow through the engine, and what is the fuel consumption per unit thrust? Since an engine of given diameter is limited in mass flow rate for given inlet conditions, the answer to the first question largely governs the thrust-size relationship.

If we use the thrust equation (5.6) for the case in which the exhaust plane pressure is atmospheric, the thrust per unit airflow is

$$\frac{\mathcal{T}}{\dot{m}_a} = [(1 + f)u_e - u], \quad (5.35)$$

and the thrust specific fuel consumption is given by

$$\text{TSFC} = \frac{\dot{m}_f}{\mathcal{T}} = \frac{f}{(1 + f)u_e - u}. \quad (5.36)$$

Given flight speed u , ambient conditions p_a , T_a , compressor pressure ratio p_{03}/p_{02} , and turbine inlet temperature T_{04} , our task is to determine the fuel-air ratio f and the exhaust velocity u_e . Then we can evaluate the engine thrust and specific fuel consumption from Eqs. (5.35) and (5.36). We proceed through the engine as follows:

1. Compressor inlet conditions. With flight Mach number $M = u/\sqrt{\gamma RT_a}$, in which γ is the specific heat ratio (assumed constant for the diffuser process), we evaluate the stagnation temperature T_{02} with

$$T_{02} = T_a \left(1 + \frac{\gamma - 1}{2} M^2 \right). \quad (5.37)$$

Give the definition of the diffuser adiabatic efficiency η_d , we can evaluate the corresponding stagnation pressure with

$$p_{02} = p_a \left[1 + \eta_d \left(\frac{T_{02}}{T_a} - 1 \right) \right]^{\gamma_d/(\gamma_d - 1)}. \quad (5.38)$$

2. Compressor outlet conditions. Since the compressor pressure ratio $p_{rc} = p_{03}/p_{02}$ is specified, we can determine the outlet stagnation pressure from

$$p_{03} = p_{02} p_{rc} \quad (5.39)$$

and the outlet stagnation temperature from

$$T_{03} = T_{02} \left[1 + \frac{1}{\eta_c} \{ P_{rc}^{(\gamma_c - 1)/\gamma_c} - 1 \} \right], \quad (5.40)$$

in which γ_c is the specific heat ratio (assumed constant) for the compression process and η_c is the compressor adiabatic efficiency.

3. Burner fuel-air ratio. With specified burner outlet temperature T_{04} , we can determine the fuel-air ratio from

$$f = \frac{T_{04}/T_{03} - 1}{Q_R/c_p T_{03} - T_{04}/T_{03}}, \quad (5.41)$$

whose derivation is similar to that of Eq. (5.26).

4. Turbine inlet pressure. Given the pressure ratio p_{04}/p_{03} across the burner, we find the turbine outlet stagnation pressure from

$$p_{04} = p_{03}(p_{04}/p_{03}). \quad (5.42)$$

5. Turbine outlet conditions. Since the turbine must supply the power required by the compressor, we write (for steady adiabatic flow in both components):

$$\dot{m}_t(h_{04} - h_{05}) = \dot{m}_c(h_{03} - h_{02})$$

or

$$\dot{m}_t c_{pt}(T_{04} - T_{05}) = \dot{m}_c c_{pc}(T_{03} - T_{02}). \quad (5.43)$$

The mass flow ratios \dot{m}_t and \dot{m}_c are not quite the same, since fuel is added in the burner and air is extracted from the compressor for turbine cooling. Nor are the average specific heat ratios c_{pt} and c_{pc} the same. For modest rates of cooling air extraction from the compressor, we may say, as a first approximation,

$$\dot{m}_t c_{pt} \approx \dot{m}_c c_{pc},$$

so that

$$T_{05} \approx T_{04} - (T_{03} - T_{02}). \quad (5.44)$$

Then, from the definition of the adiabatic efficiency for the turbine, we may evaluate the stagnation pressure p_{05} from

$$p_{05} = p_{04} \left[1 - \frac{1}{\eta_t} (1 - T_{05}/T_{04}) \right]^{\gamma_t/(\gamma_t - 1)},$$

in which γ_t is the specific heat ratio (assumed constant) for the turbine.

6. Nozzle inlet conditions. With no afterburner installed, the nozzle inlet conditions are

$$T_{06} = T_{05} \quad \text{and} \quad p_{06} = p_{05}.$$

7. Nozzle exit velocity. The nozzle exit kinetic energy is, by definition,

$$\frac{u_e^2}{2} = h_{07} - h_7 = \eta_n(h_{07} - h_{7s}),$$

in which η_n is the nozzle adiabatic efficiency. With steady adiabatic flow in the nozzle $h_{07} = h_{06}$, so

$$u_e = \sqrt{2\eta_n \frac{\gamma_n}{\gamma_n - 1} RT_{06} [1 - (p_a/p_{06})^{(\gamma_n - 1)/\gamma_n}]} \quad (5.45)$$

as long as the nozzle exit flow is unchoked.

With the fuel-ratio f now determined from (Eq. 5.41) and also with the exhaust velocity u_e (from Eq. 5.45) we can determine the engine thrust and specific fuel consumption from Eqs. (5.35) and (5.36), respectively.

We now consider examples of turbojet thrust and fuel consumption variation with compressor pressure ratio, turbine inlet temperature, and flight Mach number. For sample calculations we make the assumptions about component efficiency, fluid properties, and engine conditions shown in Table 5.1. Each flight Mach number is assumed to correspond to a different altitude and thus a different pair of ambient pressure and temperature values p_a and T_a . In these calculations we assume, as before, that the product $\dot{m}c_p$ is the same in the turbine as in the compressor.

Figures 5.19 to 5.22, inclusive, show the thrust and specific fuel consumption calculated under these conditions for three values of turbine inlet temperature

TABLE 5.1 Turbojet calculation parameters

Component	Adiabatic efficiency	Average specific heat ratio
Diffuser	$\eta_d = 0.97$	1.40
Compressor	$\eta_c = 0.85$	1.37
Burner	$\eta_b = 1.00$	1.35
Turbine	$\eta_t = 0.90$	1.33
Nozzle	$\eta_n = 0.98$	1.36
Fuel heating value, 45,000 kJ/kg		
Flight altitude (cruise Mach no.)	Ambient pressure (kPa)	Ambient temperature (K)
Sea level (0)	101.30	288.2
40,000 ft (12,200 m) (0.85)	18.75	216.7
60,000 ft (18,300 m) (2.0)	7.170	216.7
80,000 ft (24,400 m) (3.0)	2.097	216.7

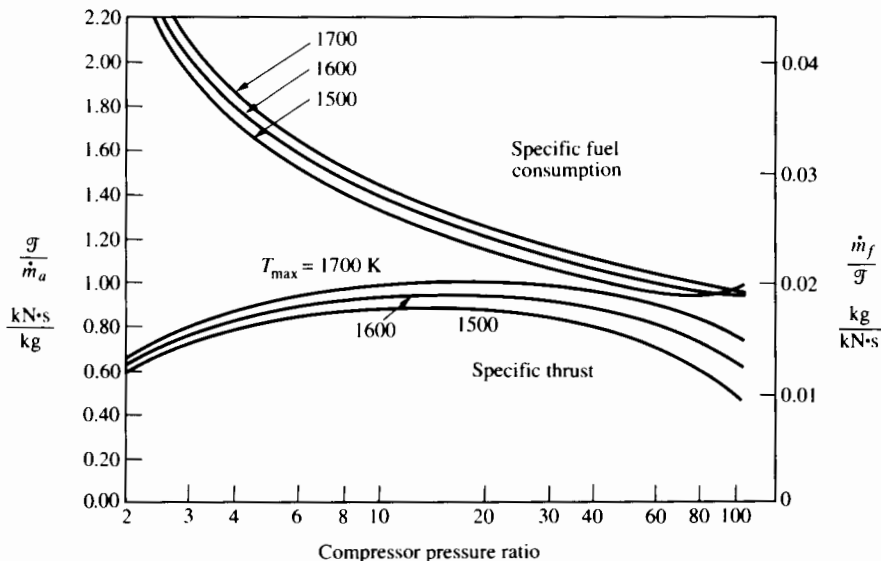


FIGURE 5.19 Turbojet static thrust and fuel consumption ($M = 0$).

and four values of flight Mach number. Both of these parameters, as well as the compressor ratio, strongly influence the engine performance.

We see in particular from these graphs:

1. At a given flight Mach number and a given turbine inlet temperature, the pressure ratio that maximizes specific thrust does not provide minimum

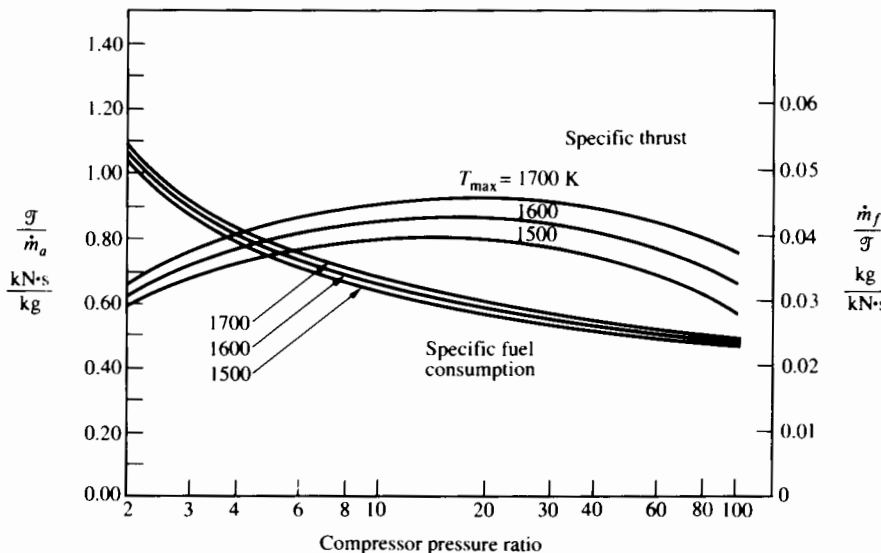


FIGURE 5.20 Turbojet cruise thrust and fuel consumption ($M = 0.85$).

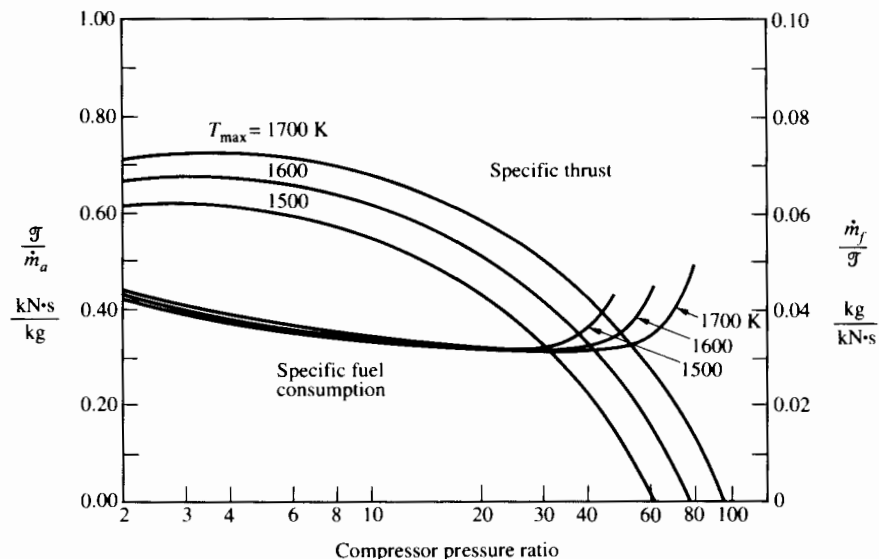


FIGURE 5.21 Turbojet cruise thrust and fuel consumption ($M = 2$).

fuel consumption. Since the mass of the engine depends strongly on airflow rate and substantially affects aircraft carrying capacity, both specific thrust and specific fuel consumption have to be considered in selecting the best compressor pressure ratio. The choice of pressure ratio for best cruis-

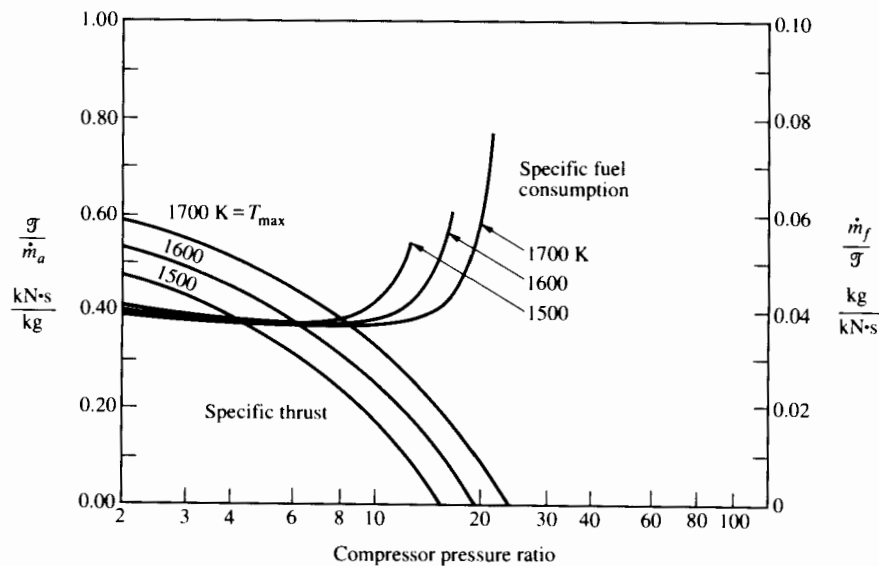


FIGURE 5.22 Turbojet cruise thrust and fuel consumption ($M = 3$).

ing range will require a compromise that takes into account both engine and aircraft characteristics.

2. Raising turbine inlet temperature can substantially improve specific thrust. The maximum temperature shown, 1700 K, is far below the maximum stoichiometric combustion of hydrocarbon fuels but requires not only high-temperature alloys for the turbine blades but also quite intensive blade cooling as well.
3. With a given compressor pressure ratio, raising turbine inlet temperature may or may not raise fuel consumption per unit thrust. For pressure ratios associated with minimum fuel consumption, increasing turbine inlet temperature can reduce specific fuel consumption somewhat. (It may, though, require an increase in the rate of cooling air extracted from the compressor, and the present calculations have not taken this into account.)
4. The compressor pressure ratio required to minimize specific fuel consumption is much less for supersonic than for subsonic flight. At Mach 3, peak specific thrust occurs with a compressor pressure ratio of 1; in this case no compressor or turbine is required, and the turbojet becomes a ramjet. The ramjet could, of course, tolerate much higher maximum temperature, not having exposure of the hot gas to highly stressed turbine blades.

Figures 5.19 to 5.22 do not display the sensitivity of engine performance to engine component efficiencies. The designer has great incentive to make the compression, combustion, and expansion processes as efficient as possible.

In Chapters 6-9 we discuss the physical factors that explain engine performance limitations. Since these factors strongly influence the configuration of actual machines, it is appropriate to point them out here before making component analyses. Basically they are of two kinds: material limits, as expressed by allowable stress and temperature levels, and aerodynamic limits, imposed mainly by the behavior of boundary layers in the presence of rising pressure.

As it does in all flight applications, the desire for minimum engine mass leads to highly stressed engine components as well as high peak temperatures. The largest stresses on turbine blades are due to centrifugal force, and the allowable stress in these blades is directly related to the temperature at which they must operate. Thus compromise is needed between the turbine blade stress and combustion temperature. With currently available material, the maximum stagnation temperature of the turbine inlet gas is limited to about 1200 K for uncooled blades. If the blades are cooled internally by passing air through small interior passages, it is possible to use stagnation temperatures of 1700 K or more. Operation at such high temperatures, however, may require a substantial fraction of the compressor air flow (as much as 10% or more) to be diverted to turbine cooling rather than to entering the combustor.

Owing primarily to the necessity of avoiding boundary layer separation, and (to a lesser degree) to the high losses associated with compressibility, the pressure ratio that can be accommodated in a single stage of a turbomachine is limited. (A *stage* may be defined as a single circumferential row of rotating blades and an as-

sociated set of stationary guide vanes, stators, or nozzles.) This limitation is most severe in compressors where the fluid necessarily flows against a rising pressure gradient (see Chapter 4). Primarily for this reason, axial-compressor-stage pressure ratios are much lower than turbine-stage pressure ratios. Hence axial compressors of 10 to 20 stages can be driven by turbines of 2 or 3 stages.

5.5 TURBOFAN ENGINES

As Section 5.2 showed, the range of an aircraft is directly proportional to the overall efficiency $\eta_0 = \eta_p \eta_{th}$. For $f \ll 1$ the propulsion efficiency and thrust are given approximately by

$$\eta_p = \frac{2u}{u_e + u}$$

and

$$\mathcal{T} = \dot{m}_a(u_e - u).$$

Using the second of these relations to eliminate u_e , we obtain

$$\eta_p = \frac{1}{1 + \frac{\mathcal{T}}{2\dot{m}_a u}}. \quad (5.46)$$

Thus for a given flight speed the propulsion efficiency can be raised by reducing the specific thrust \mathcal{T}/\dot{m}_a .

One way to do this, for a turbojet, is to reduce turbine inlet temperature (see, e.g., Fig. 5.20). However, this idea is not a good one since η_p could only be raised in this way at the cost of an unacceptable increase in engine mass for the same thrust. A better procedure is to investigate changes in engine design.

Figure 5.23 shows that the propulsion efficiency will depend strongly on the type of engine chosen as well as on the flight speed. For a turbojet cruising at $M = 0.85$, the flight speed is around 250 m/s (560 mph), while exhaust jet velocity may be about 600 m/s, so that the propulsive efficiency $\eta_p = 2u/(u_e + u)$, is about $2(250)/(600 + 250) = 0.6$.

At the same flight speed, Fig. 5.23 shows that a high-bypass turbojet—that is, a turbofan—could have substantially higher propulsion efficiency than a true turbojet. At flight speeds below 400 mph, the turboprop engine would have the highest propulsion efficiency. Having higher effective “bypass ratio,” the turboprop would have lower mass-averaged u_e and thus, according to the above formula, higher η_p than the turbofan engine. Figure 5.23 reflects the failure of conventional propellers to act efficiently at high speeds. For propeller aircraft with the traditional design of propeller blades, the flight Mach number is typically limited to less than about 0.5. At higher flight speeds propeller operation becomes excessively noisy and propeller efficiency η_p falls unacceptably because the flow over the outer part of the blade (being supersonic relative to the blade) tends to suffer

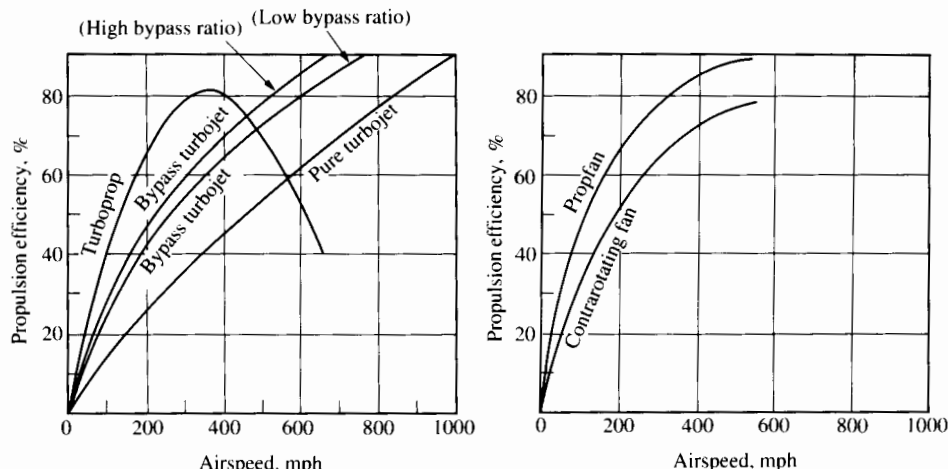


FIGURE 5.23 Typical propulsion efficiencies. (After Rolls-Royce, plc [4].)

from shock waves and flow separation. There is strong incentive for the development of new kinds of propellers that can operate at high subsonic flight Mach number (say, 550 mph) with higher propulsion efficiency (say, 80%) and acceptably low noise. Such high-speed propellers could significantly reduce fuel consumption costs. Currently, new types of propellers with thin "highly swept" blades (see Fig. 5.2d) are being developed with the hope that high efficiency and acceptably low noise can be demonstrated in flight Mach numbers as high as 0.8. With swept-back blades the component of the relative Mach number perpendicular to the leading edge of the blades can be substantially reduced, and this reduces the danger of shock waves and shock-induced flow separation (and noise). Minimizing blade thickness also helps. Making the blades thin reduces the allowable thrust per blade so that more blades are needed. Designs of 8 to 12 blades or more, and with two counterrotating sets of blades, are being developed.

Development of fan and propeller engines has become so important to the development of aircraft propulsion that, after reviewing some current designs, we extend our thermodynamic analysis to examine these developments in some detail.

Figure 5.24 shows the General Electric CF6-80C2 engine, whose sea-level takeoff thrust is about 53,000 lb_f (233 kN); the corresponding airflow rate is about 1770 lb/sec (800 kg/s). The bypass ratio for this engine is 5, and the fan tip diameter is 93 in. (2.36 m). The total compression pressure ratio is 31:1. The weight of the engine is 8946 lb (4058 kg), and its overall length is 160.9 in. (4.087 m). The 2-stage high-pressure turbine drives the 14-stage high-pressure compressor. The 5-stage low-pressure turbine drives the 3-stage low-pressure compressor and the fan through a shaft internally concentric with the rotating structure that connects the high-pressure compressor and turbine.

This high-bypass engine, certified in 1985 and used in the European Airbus and the Boeing 767 aircraft, incorporates the benefits of research conducted

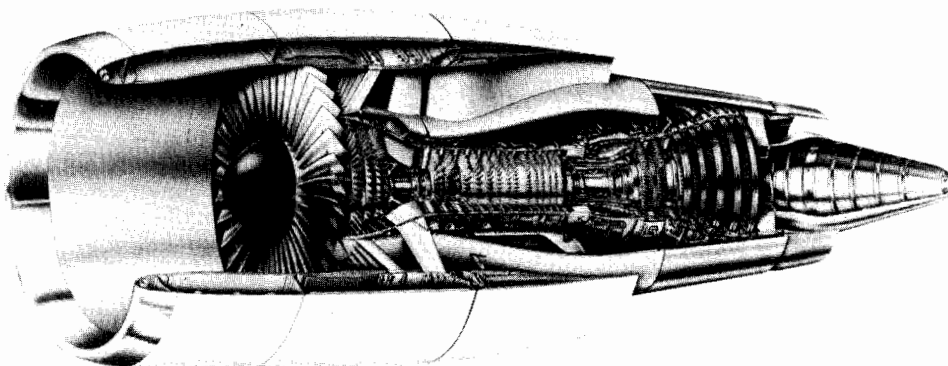


FIGURE 5.24 General Electric CF6-80C2 high-bypass turbofan engine. (Courtesy GE Aircraft Engines.)

(with the collaboration of General Electric) in the NASA Energy Efficient Engine Program [5]. The turbine inlet temperature for this engine is about 1600 K (higher than 2400°F).

Figure 5.25 shows the Pratt & Whitney PW4000 engine, which incorporates the results of the Pratt & Whitney collaboration in the Energy Efficient Engine Program [5]. The engine thrust is in the range of 222 to 289 kN (50,000 to 65,000 lb_f). At 252 kN (56,750 lb_f) thrust, the bypass ratio is 4.8 and the overall pressure ratio is 30.2. The high-pressure turbine inlet temperature is about 1628 K (2450°F) and the total airflow rate is 773 kg/s (1750 lb/sec). The cruise thrust specific fuel consumption is 0.59 lb/hr/lb_f of thrust (17 g/kN · s).

The PW4000 fan inlet tip diameter is 2.38 m (93.4 in.), and its pressure ratio is about 1.72. The 38 fan rotor blades are made of titanium; the fan stators are fabricated from carbon-fiber composite. The rotor and stator blades in the low-pressure compressor are made of titanium, as are the high-pressure compressor rotor blades (the corresponding stators are of nickel steel).

At the entrance of the high-pressure turbine, the vanes are air cooled and are of nickel steel. The first-stage turbine blades are each cast as single crystals to improve their strength (resistance to creep) at high temperatures. The last-stage turbine rotor tip diameter is 1.36 m (53.4 in.).

Figure 5.26 shows the Rolls-Royce RB211 turbofan engine (in the 535E4 version). In the Boeing 757 this engine-aircraft combination has achieved record-breaking fuel economy. The overall thrust of the engine is approximately 41,000 lb_f (92 kN), and the bypass ratio is 4. (This is not the largest of the RB211 family of engines; the 523L version develops 65,000 to 70,000 lb_f of thrust.) The overall compressor pressure ratio is 28.5:1. The tip diameter of the fan is approximately 74 in. (1.88 m), and the engine length is 117.9 in. (3 m). The mass of the engine is 7264 lb (3300 kg), and the airflow rate is 1150 lb/sec (523 kg/s).

The engine has three concentric shafts; the outer “shaft” connects the single-stage high-pressure turbine to the six-stage high-pressure compressor. The intermediate shaft connects the single-stage intermediate turbine to the six-stage

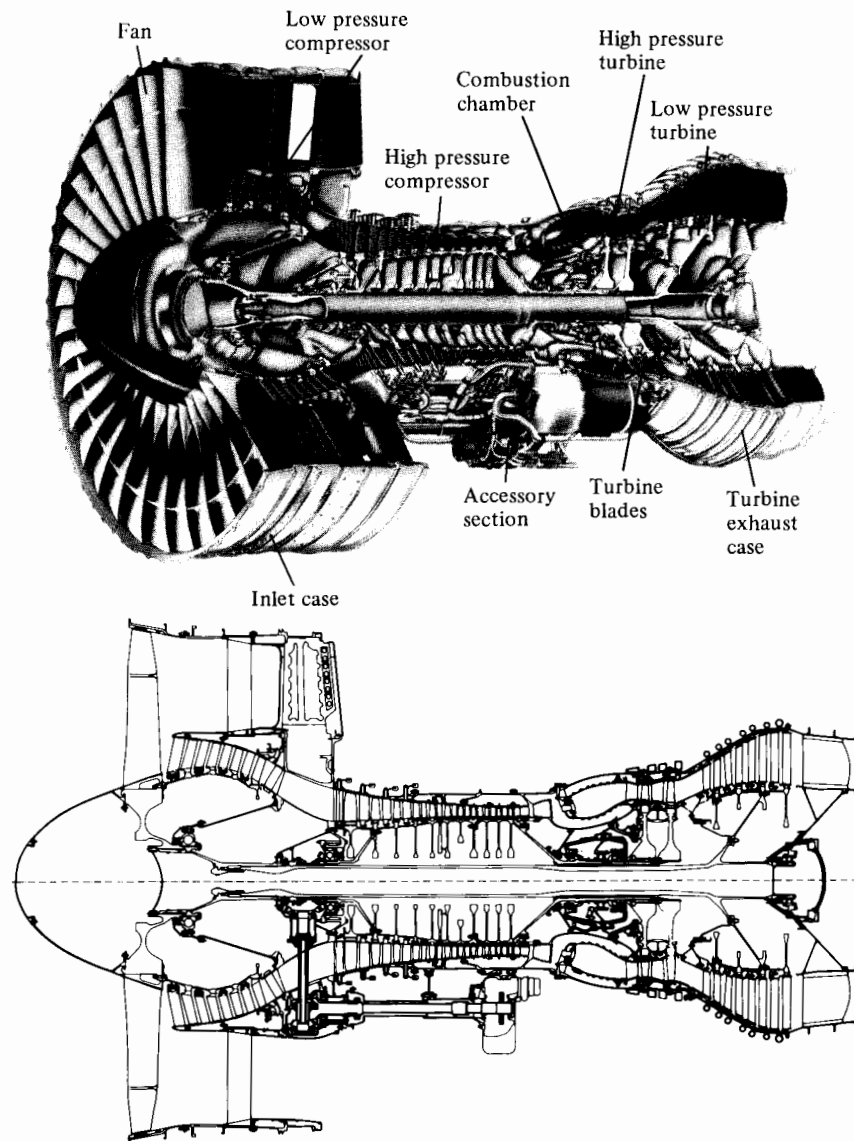


FIGURE 5.25 Pratt & Whitney PW4000 turbofan engine. (Courtesy Pratt & Whitney, a division of United Technologies Corp.)

intermediate compressor. The three-stage low-pressure turbine drives the single-stage fan, which requires about 36,000 hp (27,000 kW). With directionally solidified nickel alloy blades, the maximum turbine inlet temperature is about 1530 K.

An important feature of this engine is the use of wide-chord fan blades [6], which we discuss further in Chapter 7. These blades have no need for the part-span shrouds or “snubbers” commonly used on turbofan blades to prevent undue

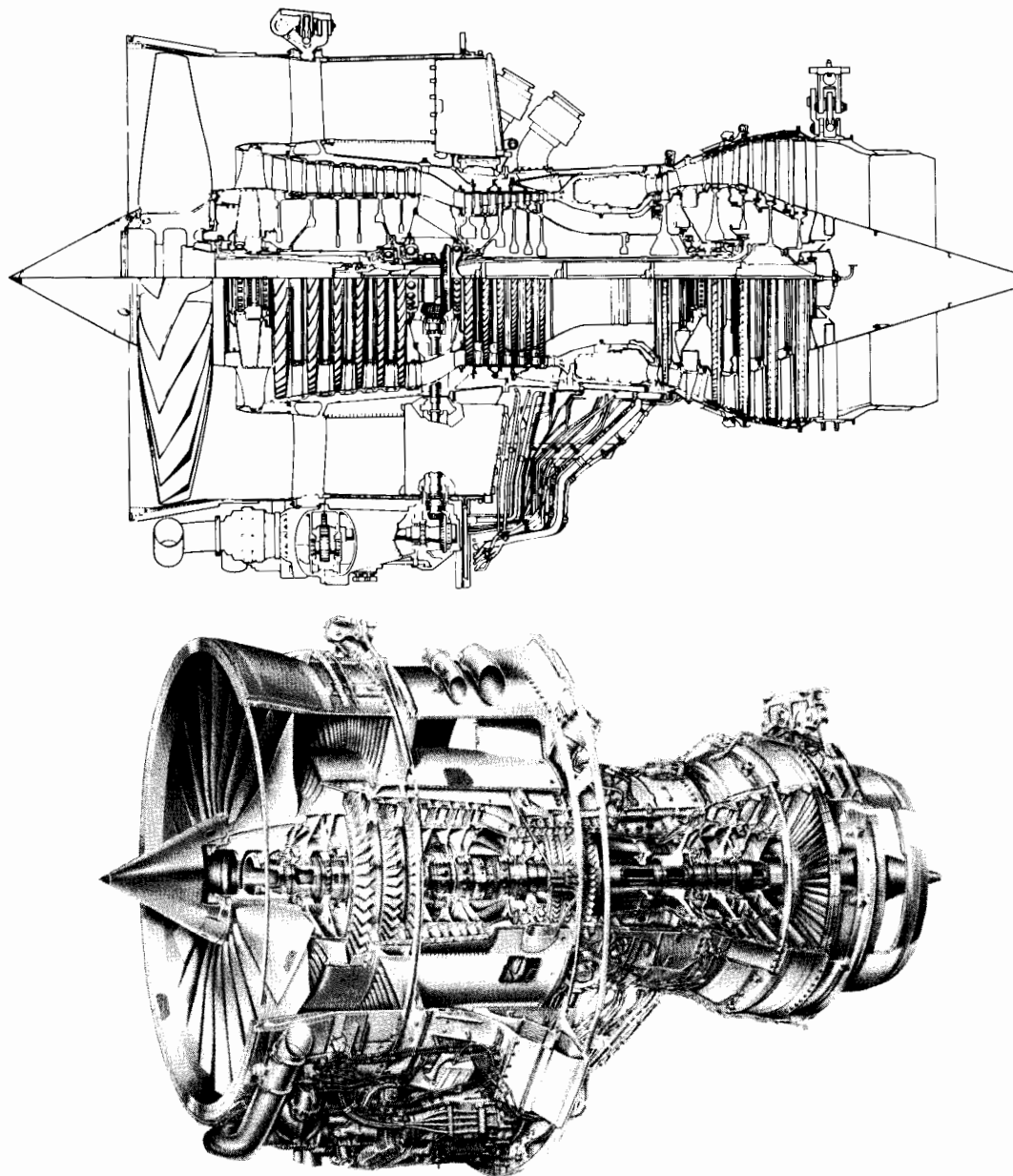


FIGURE 5.26 Rolls-Royce RB211-535E4 turbofan engine. (Courtesy Rolls-Royce, plc.)

vibration of the blades, which are characteristically quite flat toward the tip diameter. Elimination of these flow-obstructive features appears to have provided a 1% to 2% improvement in fan efficiency and up to a 4% reduction in thrust specific fuel consumption. The fan tip speed is about 450 m/s (1500 ft/sec), so the

fan blades are highly stressed; a 15-lb blade is subject to a centrifugal force of about 60 tons. The fan must be designed to survive bird strikes (one test requiring 30 minutes of continued engine operation after the fan is hit with eight 1.5-lb birds during a 1-second period). The RB211 fan blades are fabricated from titanium alloy surface panels that enclose a volume filled with a titanium honeycomb. The honeycomb is precision formed from titanium foil 0.075 mm (0.003 in.) thick and is bonded to the surface panels. The structure has high strength-to-weight ratio, good impact resistance, and long fatigue life under vibratory strains.

Another interesting feature of this engine is that the fan exhaust stream and the core engine exhaust stream are mixed before expansion in a common nozzle. Figure 5.27 shows the mixing section of the Rolls-Royce RB211-524L engine. Mixing of core and bypass streams can be shown, for thermodynamic reasons, to yield a small but important efficiency advantage. Also, it may provide a reduction in jet noise emission. The intensity of jet noise has been shown to be proportional to the eighth power of the velocity of the jet relative to the ambient air; thus small reductions in velocity may mean significant reductions in noise. On the other hand, a good deal of the noise of a jet engine, especially those noise emissions with frequencies uncomfortable to people, may come from the compressor.

Figure 5.28 shows a quite different bypass engine—the Rolls-Royce Pegasus used to power the V/STOL (vertical or short takeoff and landing) Harrier aircraft [7]. This engine develops a vertical takeoff thrust of 98 kN (22,000 lb_f), which is 5.5 times its own weight. The horizontal thrust under static sea-level conditions is about 77 kN (17,000 lb_f). Figure 5.28(b) shows the exhaust nozzles, which may be rotated to provide any combination of horizontal or vertical thrust.

The Pegasus engine has three low-pressure compressor stages and a bypass ratio (for flow around the eight-stage high-pressure compressor) of 1.4. The high- and low-pressure compressors are on separate concentric shafts, each driven by two-stage turbines. The low-pressure compressor flow rate is 198 kg/s (435 lb/sec), and the overall pressure ratio is 14:1. The low-pressure compressor casing diameter is 1.219 m (48 in.). The first stage of the high-pressure turbine has single crystal blades.

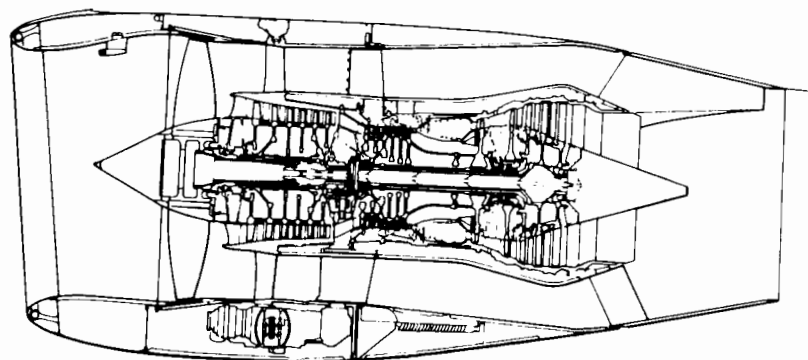


FIGURE 5.27 Rolls-Royce RB211-535E4 installation cross section. (Courtesy Rolls-Royce, plc.)

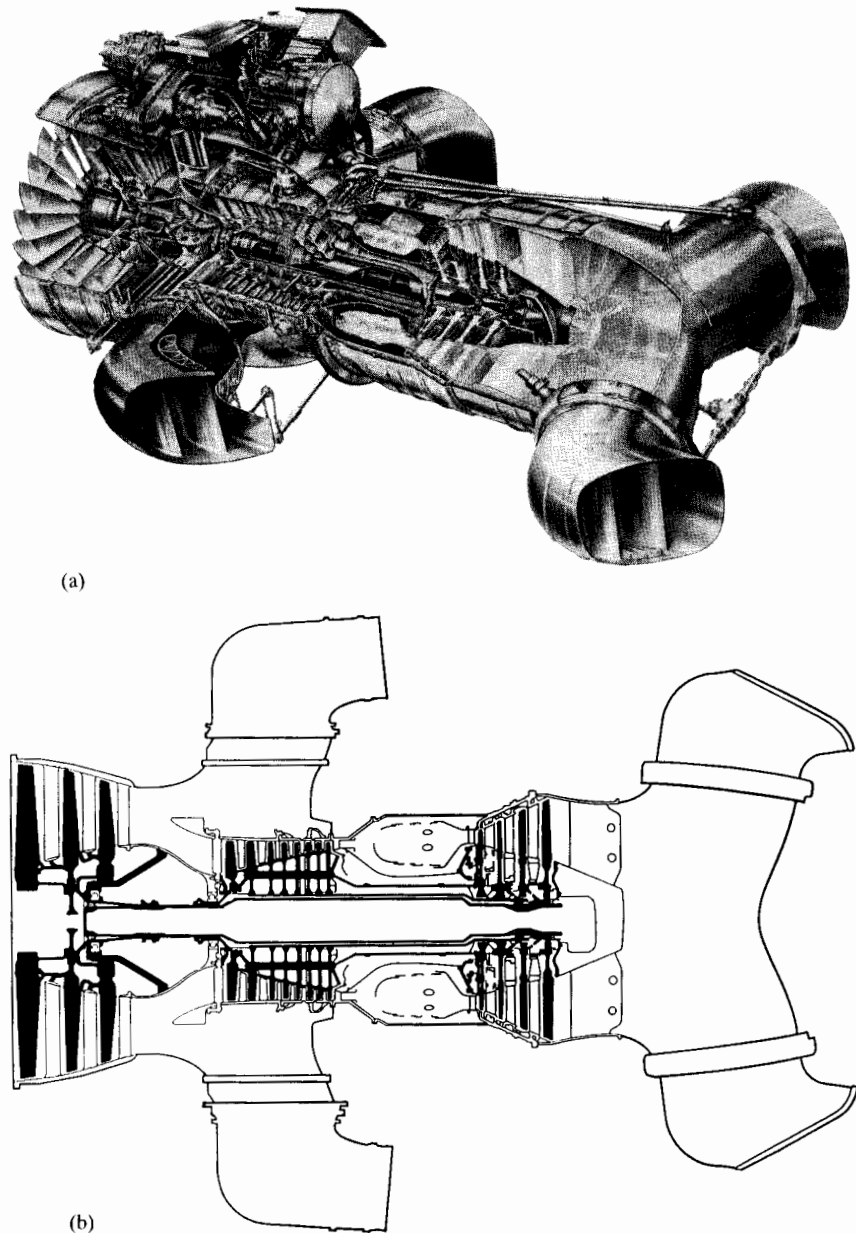


FIGURE 5.28 Rolls-Royce Pegasus V/STOL engine. (Courtesy Rolls-Royce, plc.)

Having briefly reviewed some of the main features of examples of modern bypass engines, we resort to fundamental thermodynamic analysis to examine the rationale for the development of turbofan engines and to assess in a preliminary way their benefits relative to turbojet engines.

For analysis of fan engine performance, we modify the turbojet performance analysis by allowing for the bypass ratio \mathcal{B} (ratio of the bypass airflow rate to the core engine airflow rate). In what follows we assume that the core engine flow and the bypass flow expand separately to ambient pressure. If the two streams are mixed before expansion, the analysis must be modified somewhat.

First we recognize that the specific thrust and fuel consumption equations must be modified such that

$$\frac{\mathcal{T}}{\dot{m}_a} = (1 + f)u_e + \mathcal{B}u_{ef} - (1 + \mathcal{B})u,$$

in which u_e is the core exhaust velocity and u_{ef} is the bypass stream exhaust velocity. The thrust specific fuel consumption equation may be written

$$\text{TSFC} = \frac{\dot{m}_f}{\mathcal{T}} = \frac{f}{(1 + f)u_e + \mathcal{B}u_{ef} - (1 + \mathcal{B})u}. \quad (5.47)$$

The turbofan engine internal analysis is the same as that of the turbojet for steps 1 through 4 of the procedure outlined in Section 5.4. Modification of the rest of the procedure is as follows:

5. Fan inlet conditions. Since the fan and core engine compressor receive air from the same diffuser, the fan inlet stagnation conditions are T_{02} and p_{02} , previously determined from the flight Mach number M , ambient pressure temperature p_a and T_a , and diffuser efficiency η_d .

6. Fan outlet conditions. We suppose the fan has a design pressure ratio $p_{rf} = p_{08}/p_{02}$ and an adiabatic efficiency η_f , in which case the fan outlet stagnation pressure is

$$p_{08} = p_{02}p_{rf} \quad (5.48)$$

and the outlet stagnation temperature is

$$T_{08} = T_{02} \left[1 + \frac{1}{\eta_f} (p_{rf}^{(\gamma_f - 1)/\gamma_f} - 1) \right], \quad (5.49)$$

in which γ_f is the (assumed constant) ratio of specific heats for the fan stream.

7. Fan nozzle exit velocity. By a derivation similar to that of Eq. (5.45) we can show that the fan nozzle exit velocity u_{ef} is given by

$$u_{ef} = \sqrt{2\eta_{fn} \frac{\gamma_f}{\gamma_f - 1} RT_{08} [1 - (p_a/p_{08})^{(\gamma_f - 1)/\gamma_f}]}, \quad (5.50)$$

in which η_{fn} is the adiabatic efficiency for the fan nozzle.

8. Turbine outlet conditions. Here, allowing for the work done by the core engine on the fan stream, we write the turbine power balance in the form

$$\dot{m}_t C_{pt}(T_{04} - T_{05}) = \dot{m}_a C_{pc}(T_{03} - T_{02}) + \mathcal{B}\dot{m}_a C_{pc}(T_{08} - T_{0a}),$$

in which the second term on the right-hand side is the power absorbed by the fan stream. As before, we make the approximation $\dot{m}_t C_{pt} \approx \dot{m}_a C_{pc}$, so that

$$T_{05} = T_{04} - (T_{03} - T_{02}) - \mathcal{B}(T_{08} - T_{0a}), \quad (5.51)$$

in which T_{08} is the fan outlet stagnation temperature. As before

$$p_{05} = p_{04} \left[1 - \frac{1}{\eta_t} \left(1 - \frac{T_{05}}{T_{04}} \right) \right]^{\gamma_t / (\gamma_t - 1)}.$$

9. Nozzle inlet conditions. As before, with no afterburner, $T_{06} = T_{05}$ and $p_{06} = p_{05}$.

10. Nozzle exit conditions. Again we find that the core engine exit velocity may be written

$$u_e = \sqrt{2\eta_n \frac{\gamma_n}{\gamma_n - 1} RT_{06} \left[1 - \left(\frac{p_7}{p_{06}} \right)^{\gamma_n - 1/\gamma_n} \right]},$$

with $p_7 = p_a$ unless the exit nozzle is choked.

To illustrate the performance improvement possible with bypass engines, we use the same calculation assumptions as shown in Table 5.1 and the bypass fan assumptions shown in Table 5.2 to obtain the results shown in Figs. 5.29 to 5.34.

We can see the effect of bypass ratio on takeoff thrust by comparing Figs. 5.19 and 5.29. Other conditions remaining the same, the takeoff thrust per unit core engine flow rate \dot{m}_a has nearly doubled, as the bypass ratio has changed from 0 to 5. At the same time the thrust specific fuel consumption has decreased substantially.

Comparison of Figs. 5.20 and 5.30 shows the same kinds of benefits for high subsonic ($M = 0.85$) cruise thrust, though the relative gains are considerably less. For supersonic flows the bypass idea would have little potential benefit, and the problem of shock losses associated with a large nacelle would be formidable, if not prohibitive.

Figure 5.31 shows the efficiencies of the turbojet engine for $M = 0.85$ cruise conditions. In contrast, Fig. 5.32 shows the corresponding efficiencies for the turbofan engine with $\mathcal{B} = 5$. The overall efficiency is significantly greater than for the turbojet ($\mathcal{B} = 0$).

TABLE 5.2 Bypass fan characteristics

Component	Efficiency	Specific heat ratio
Diffuser	$\eta_d = 0.97$	$\gamma_d = 1.4$
Fan	$\eta_f = 0.85$	$\gamma_f = 1.4$
Fan nozzle	$\eta_{fn} = 0.97$	$\gamma_n = 1.4$
Fan pressure ratio	$p_{rf} = 1.50$	

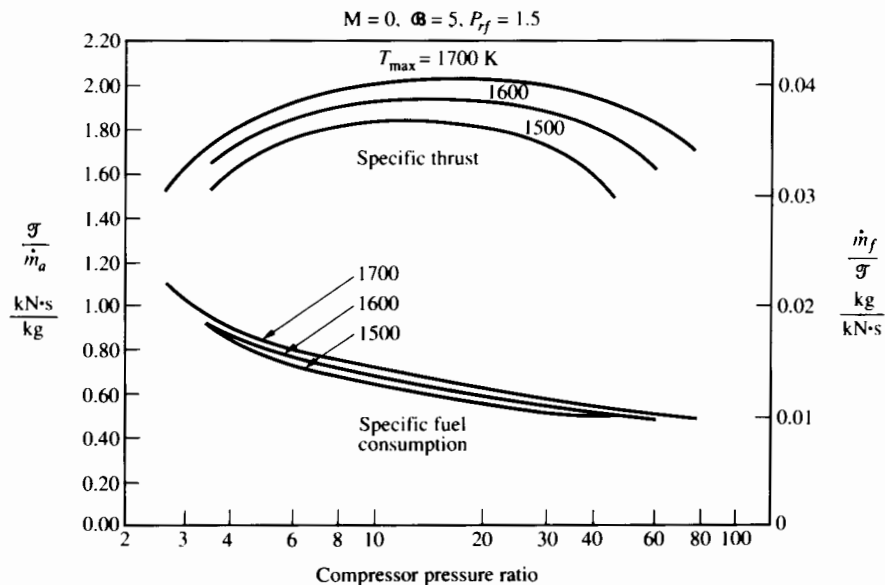


FIGURE 5.29 Turbofan static thrust and fuel consumption.

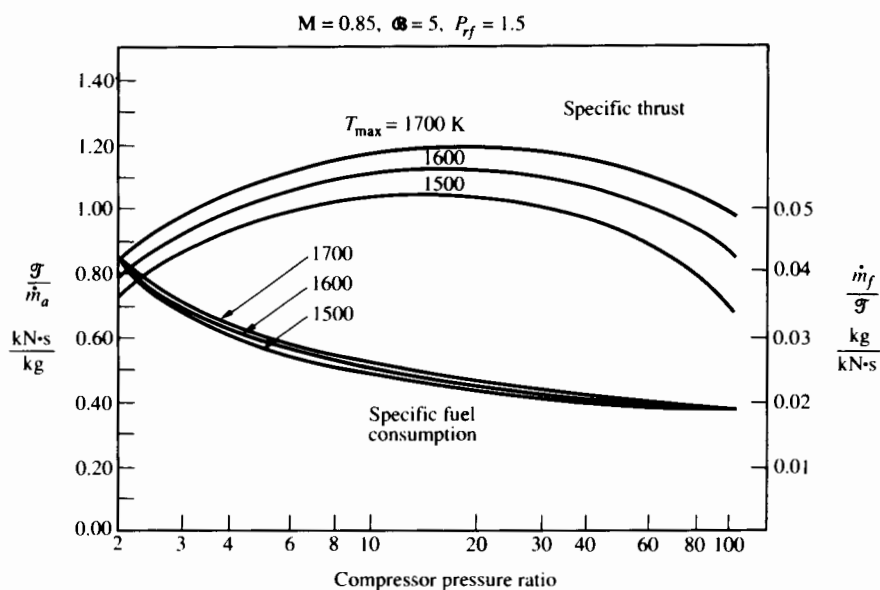


FIGURE 5.30 Turbofan cruise thrust and fuel consumption.

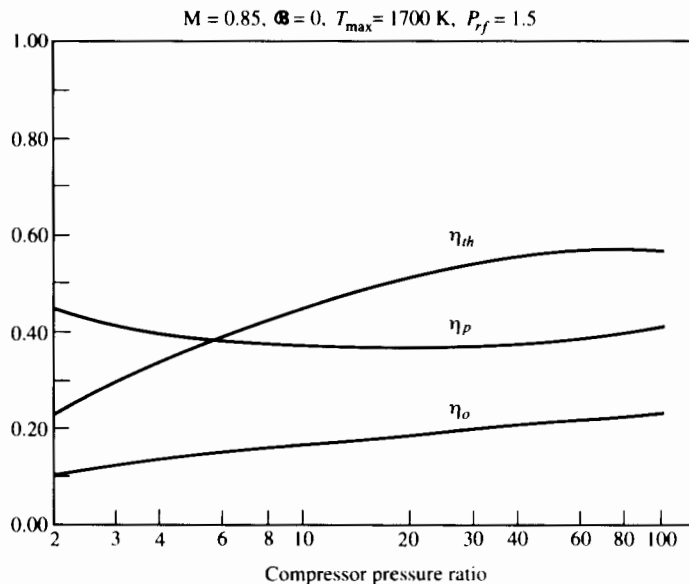


FIGURE 5.31 Turbojet thermal and propulsion efficiencies.

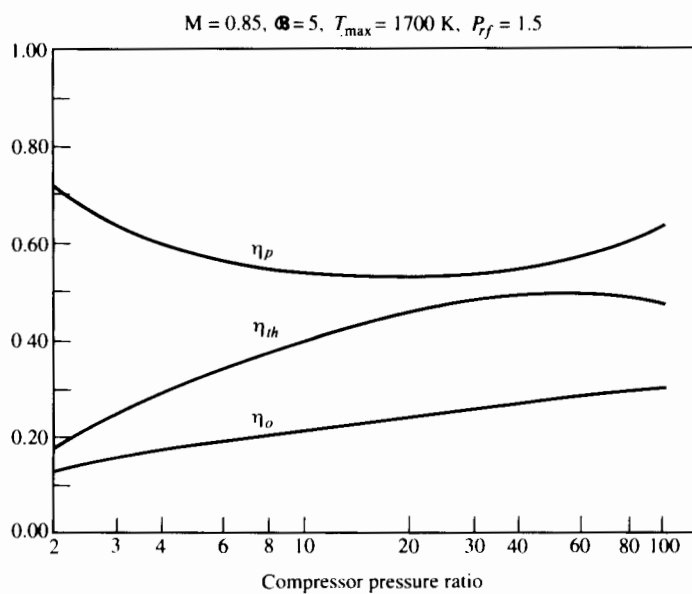


FIGURE 5.32 Turbofan thermal and propulsion efficiencies.

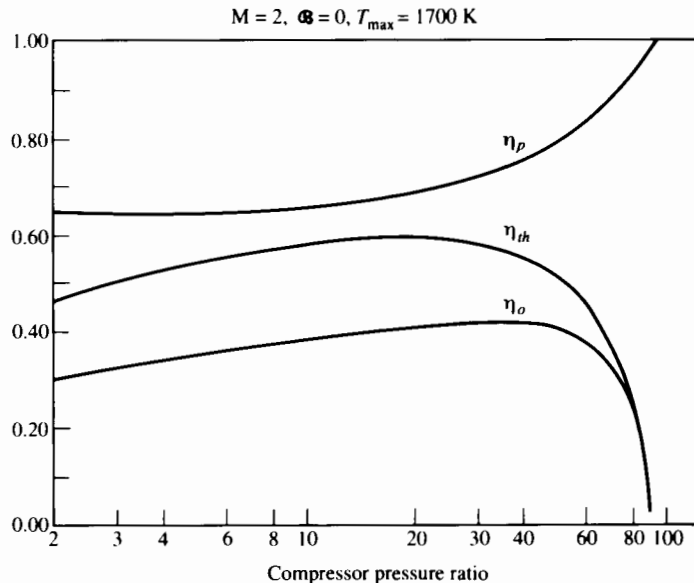


FIGURE 5.33 Thermal and turbojet propulsion efficiencies.

Figures 5.33 and 5.34 show the large values of the overall efficiency potentially attainable with supersonic flight. The compressor pressure ratio that maximizes η_o drops rapidly as the design flight Mach number increases above, say, 2.

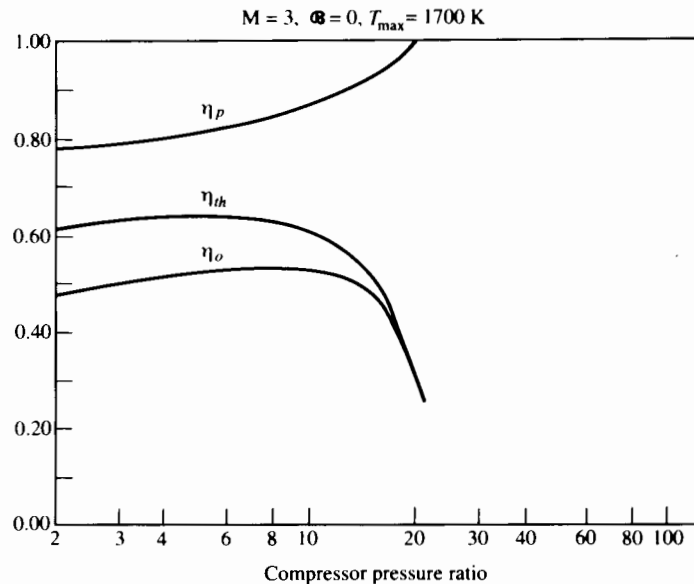


FIGURE 5.34 Thermal and turbojet propulsion efficiencies.

For an aircraft that is required to cruise at both subsonic and supersonic speeds, the choice of engine compression ratio implies an important compromise.

For subsonic flight there is a strong propulsion efficiency advantage in using a bypass rather than a turbojet engine. The higher the turbine inlet temperature (and thus the higher the exhaust velocity of the corresponding turbojet), the greater the benefit. The questions of optimum bypass ratio and optimum fan pressure ratio deserve serious exploration and may lead to further refinements of turbofan designs. In the absence of geared power transmission to the fan, the problem of speed mismatch between the fan and its driving turbine tends to limit the bypass ratio of turbofan engines. Other considerations affecting the choice of bypass ratio include the structural weight and the aerodynamic drag of the engine nacelle. Designing a gearbox to transmit 30,000 kW would mean confronting serious questions concerning gearbox weight and reliability. Nevertheless, the geared fan is a future possibility.

5.6 TURBOPROP AND TURBOSHAFT ENGINES

Figure 5.35 is a schematic diagram of a typical turboprop engine. The propeller receives its power from a "power turbine" that is mechanically independent of the gas generator rotor elements. This so-called free-turbine configuration, though not the only possibility, has the advantage of flexibility in meeting a range of performance demands.

Stress limitations require that the large-diameter propeller rotate at a much lower rate than the relatively small power turbine. Hence a rather large speed-reduction unit, having a speed ratio of perhaps 15:1, is required. (A fan of the same diameter would also require a speed reducer.) The propeller, its pitch control mechanism, and the power turbine contribute additional weight, so that a turboprop engine may be about 1.5 times as heavy as a conventional turbojet of the same gas-generator size. However, the performance benefits that the turboprop provides on takeoff and at low flight speeds can compensate for this added weight.

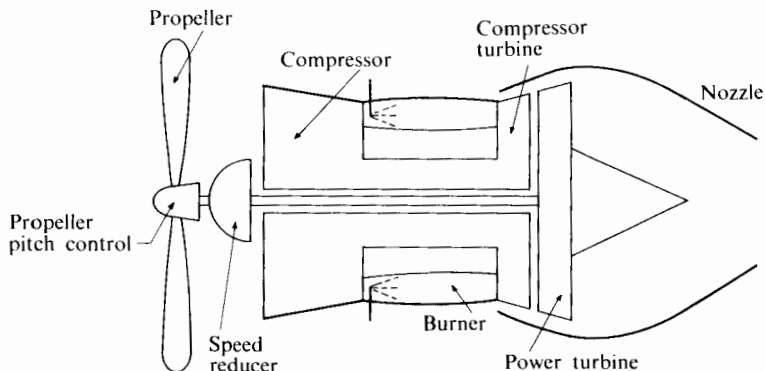


FIGURE 5.35 Schematic diagram of a typical free-turbine turboprop engine.

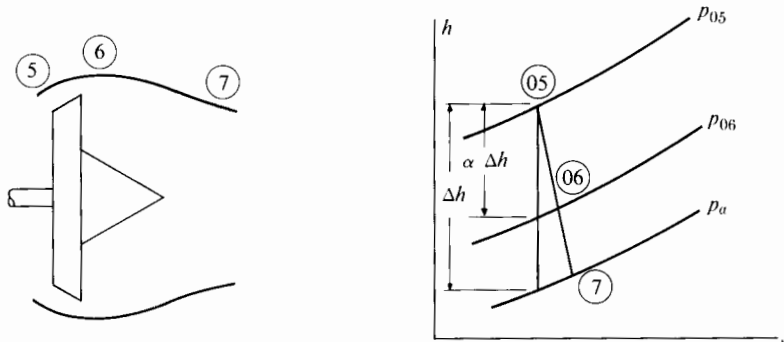


FIGURE 5.36 Enthalpy–entropy diagram for power turbine–exhaust nozzle analysis.

Turboprop engines may exert a significant part of their thrust by means of the hot-exhaust jet. Figure 5.36 indicates on an enthalpy–entropy diagram the thermodynamic path of the hot gases expanding through the power turbine and exhaust nozzle. It has been shown [8] that there is an optimum hot-gas exhaust velocity that yields maximum thrust for a given gas generator and flight speed. Referring to Fig. 5.36, let

Δh = enthalpy drop available in an ideal (isentropic) power turbine and exhaust nozzle,

α = fraction of Δh that would be used by an isentropic turbine having the actual stagnation pressure ratio,

η_{pt}, η_n = adiabatic efficiencies of the power turbine and exhaust nozzle, respectively,

η_g, η_{pr} = gear and propeller efficiencies, respectively.

The propeller thrust \mathcal{T}_{pr} may be determined by considering the energy flux through the free-turbine and propeller shafts:

$$\mathcal{T}_{pr}u = \eta_{pr}\eta_g\eta_{pt}\alpha\Delta h\dot{m} \quad \text{or} \quad \mathcal{T}_{pr} = \frac{\eta_{pr}\eta_g\eta_{pt}\alpha\Delta h\dot{m}}{u}, \quad (5.52)$$

where u is the flight velocity and \dot{m} is the hot-gas flow rate. The exhaust nozzle thrust \mathcal{T}_n may be written as $\mathcal{T}_n = \dot{m}(u_e - u)$, where the exhaust velocity is given by $u_e = \sqrt{2(1 - \alpha)\Delta h\eta_n}$. Thus the total thrust is

$$\mathcal{T} = \frac{\eta_{pr}\eta_g\eta_{pt}\alpha\Delta h\dot{m}}{u} + \dot{m}(\sqrt{2(1 - \alpha)\Delta h\eta_n} - u). \quad (5.53)$$

Maximizing the thrust \mathcal{T} for fixed component efficiencies, flight speed, and Δh yields an optimum value of

$$\alpha = 1 - \frac{u^2}{2\Delta h} \left(\frac{\eta_n}{\eta_{pr}^2 \eta_g^2 \eta_{pt}^2} \right). \quad (5.54)$$

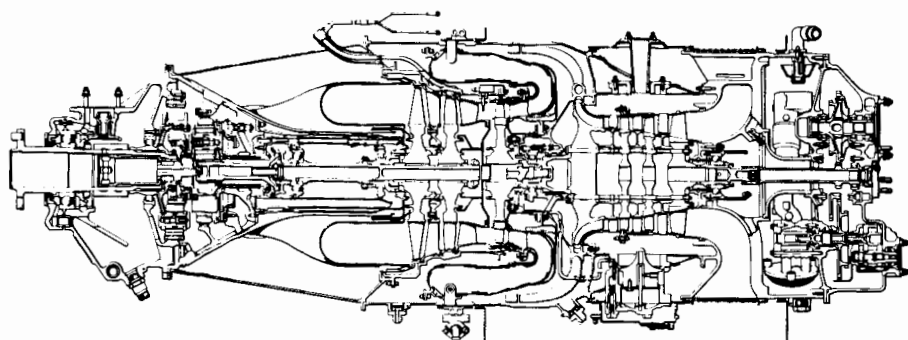


FIGURE 5.37 Pratt & Whitney Canada PT6A-65 turboprop engine. (Courtesy Pratt & Whitney Canada, Inc.)

A turboshaft engine might be defined as a gas turbine engine designed to produce only shaft power. Such engines find application in helicopters, where their light weight and small size compared with piston engines render them attractive. Turboshaft engines are similar to turboprop engines, except that the hot gases are expanded to a lower pressure in the turbine, thus providing greater shaft power and little exhaust velocity. (For a review of turboprop engine development over the past few decades, see Saravanamuttoo [9].)

Figure 5.37 shows a cross-sectional view of the Pratt & Whitney PT6 turboprop engine, of which well over 25,000 have entered service in the 600-to-1200-hp range. The compressor of this engine has three axial stages, followed by one centrifugal stage. The compressor inlet tip diameter is 0.22 m (8.7 in.). Air leaves the centrifugal stage through diffuser pipes (which are discussed in Chapter 9) to enter a reversing-flow-direction combustor. The combustion products flow through a single-stage high-pressure turbine that drives the compressor. The turbine blades are not cooled but are able to withstand a turbine inlet temperature of approximately 1400 K. After leaving the gas generator (high-pressure) turbine, the combustion products pass through the free-power turbine that drives the propeller. With the rated propeller speed being 1700 rpm, a large speed reducer is required between the free turbine and the propeller.

Under standard sea-level atmospheric conditions the power output of the engine is limited by the gearbox design to 1200 hp (900 kW). Under these conditions the compressor pressure ratio is 9.2, the turbine inlet temperature is 1300 K (1875°F), and the gas generator rpm is 36,300. The airflow rate is about 4.5 kg/s (10 lb/sec). The exhaust thrust developed by the engine under these conditions is approximately 800 N (180 lb_f), and this is taken into account in calculating the equivalent shaft horsepower (eshp) of 1270. The equivalent specific fuel consumption is about 0.55 lb/hr per equivalent shaft horsepower. If we take only the actual shaft horsepower into account, the specific fuel consumption is 0.575 lb/hr/hp.

As we will see in the next section, the power generated by any turboprop engine falls off substantially during operation with high ambient temperature. With

high ambient temperature the PT6 power output is no longer limited by what the gearbox can transmit. In this case the standard sea-level performance used (as described in the next section) as a base for determining the hot-day performance is as follows:

Shaft horsepower	1600 (900 kW)
Gas generator speed	38,200 rpm
Airflow rate	11 lb/sec (5 kg/s)
Compressor pressure ratio	11
Turbine inlet temperature	2050°F (1400 K)
Exhaust thrust	235 lb _f (1050 N)
Equivalent shaft power	1700 hp (1370 kW)
Specific fuel consumption	0.53 lb/hr/shp
Equivalent specific fuel consumption	0.505 lb/hr/eshp

This performance is the sea-level standard-day performance that the engine could demonstrate if the gearbox power were not limiting.

Figure 5.38 shows a cutaway view of the Pratt & Whitney PW100 engine [10,11]. The engine has been designed for 2000 eshp. The propeller speed for normal takeoff is 1200 rpm; the propeller drive speed is about 20,000 rpm. The compressor mass flow rate under static sea-level operation is 14.8 lb/sec (6.7 kg/s), and the compressor pressure ratio is 14.8. The PW100 is a three-shaft engine. Both the centrifugal compressor stages are driven by single-stage axial turbines. The propeller is driven, through a gearbox, by a two-stage axial turbine. Morris [10] gives an account of the design rationale for the choice of cycle pres-

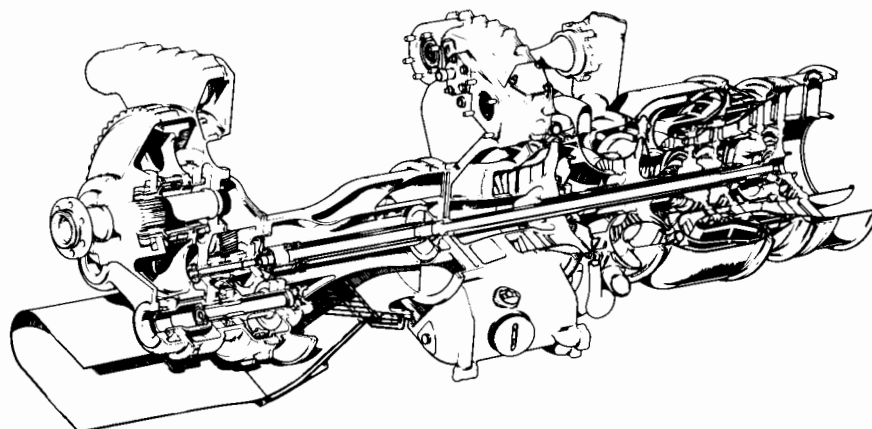


FIGURE 5.38 Pratt & Whitney PW100 turboprop engine. (Courtesy Pratt & Whitney Canada, Inc.)

sure and temperature, for the selection of centrifugal rather than axial compressor stages, and for the selection of a reversing-direction flow path through the combustor. The first stage turbine has cooled blades. Shown in Fig. 9.1 is the low-pressure centrifugal compressor impeller whose shaft speed is determined by the volumetric flow rate and the allowable (supersonic) Mach number of the flow relative to the blades at the entrance to the impeller.

The design of small gas turbines, as Morris shows in the results of cycle calculations presented in Figs. 5.39 and 5.40, differs significantly from that of large gas turbines. Figure 5.39 gives the results of cycle calculations made with component efficiencies appropriate to large flow passages through the compressor and turbine; these indicate that, in the range of parameters considered, a pressure ratio of 30:1 and a turbine inlet temperature of 1700 K (2600°F) give lowest specific fuel consumption. As we have seen from examples discussed earlier, these numbers are typical of large modern gas turbine engines. Small gas turbines suffer significantly from efficiency penalties as the pressure ratio gets high and the blade heights at the compressor exit become unduly low. This is because there are minimum reasonable clearances between the blade and the adjacent casing. As the blade height becomes small, the aerodynamic losses associated with flow over the blade tips become proportionally greater. (We discuss such effects in greater detail in Chapter 7.) Cycle analysis that estimates the effects of small blade size on efficiency produces the results shown in Fig. 5.40. Here the optimum pressure ratio is indicated to be only 20:1—and the specific fuel consumption at 15:1 is not very much larger than for 20:1. At the design point for the

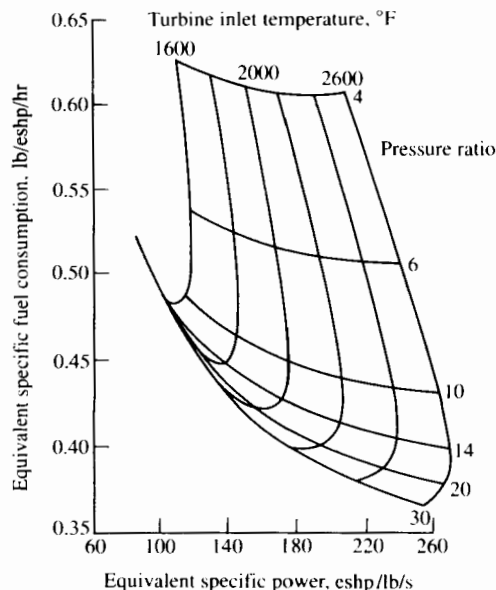


FIGURE 5.39 Turboprop thermodynamic optimization: 25,000 ft, 350 mph cruise, no size effect. (From Morris [10].)

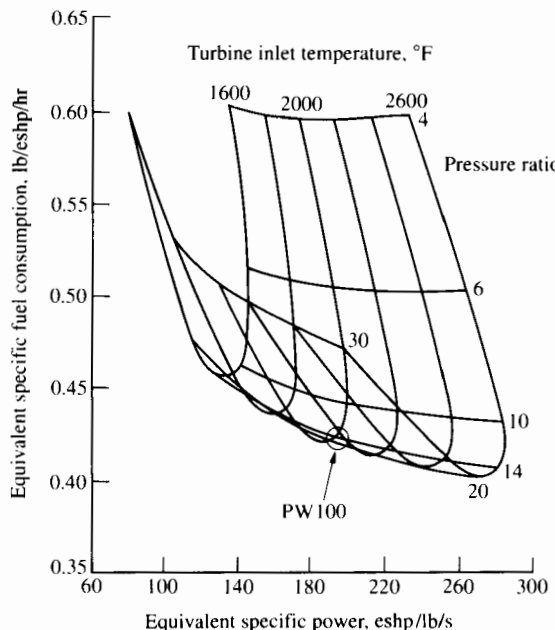


FIGURE 5.40 Size effects reduce optimum pressure ratio and turbine temperature: 25,000 ft, 350 mph cruise, constant power 1300 eshp. (From Morris [10].)

PW100, the turbine inlet temperature is 1367 K (2000°F), which does not require a large flow of cooling air to the blades; this is fortunate, since it is more difficult to arrange the cooling passages in a small blade than in a large one. The size effect (which the calculations of Morris demonstrate) affects not only the choice of cycle pressure ratio and maximum temperature but also the choice of compressor configuration. In small sizes the centrifugal compressor stage can be more efficient than the axial one.

Figure 5.41 shows the General Electric T700 helicopter turboshaft engine, which develops about 1700 hp under sea-level standard-day conditions. The same power producer is also used in the CT7 turboprop engine. The specific fuel consumption is about 0.46 lb/hr/shp, and the basic engine weight is about 427 lb. The engine has a pressure ratio of over 15:1, with five axial stages followed by a single centrifugal compressor stage (whose rotor is shown separately in Fig. 9.2). The airflow rate is about 10 lb/sec (4.6 kg/s).

The General Electric propfan shown in Fig. 5.42 could be considered an evolutionary development of the turboprop engine, having a "propeller" designed for exceptionally high flight Mach number. Alternatively, as its name implies, it could be considered a turbofan of exceptionally high bypass ratio; the concept is also called the unducted fan. The effective bypass ratio of the propfan can be as high as 25:1. This, as Fig. 5.23 suggests, means that the propulsion efficiency of the propfan can be significantly higher than that of the turbofan with a bypass ratio of 5:1 or 6:1. The General Electric unducted fan has two counterrotating

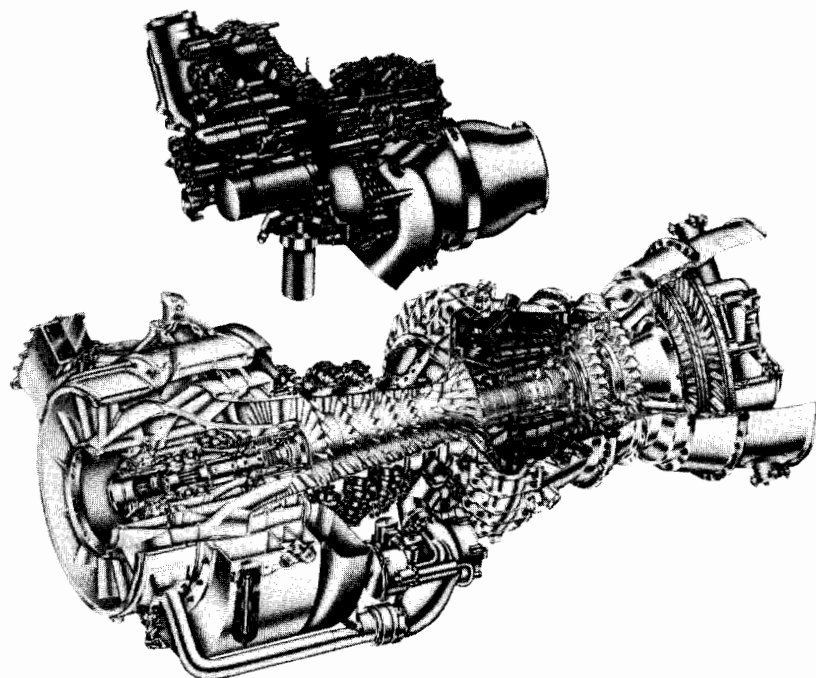


FIGURE 5.41 General Electric T700 turboshaft engine. (Courtesy GE Aircraft Engines.)

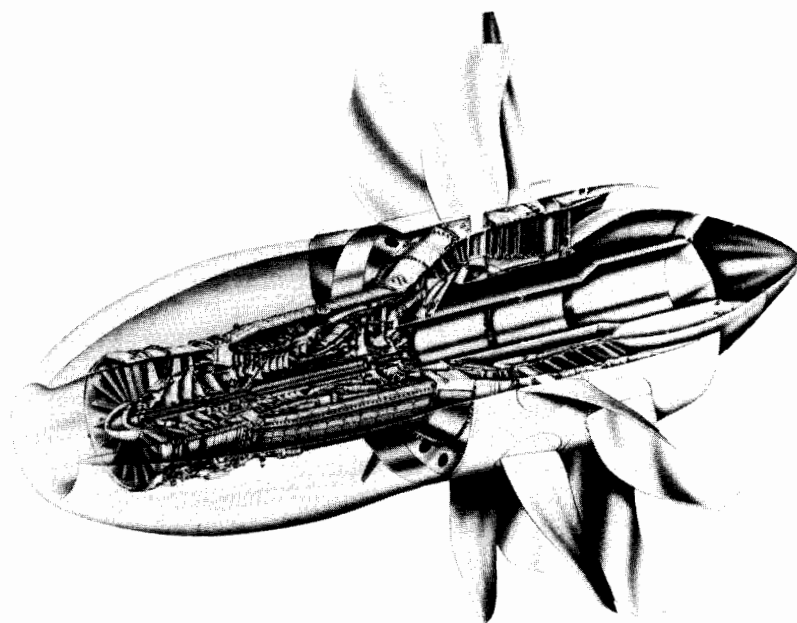


FIGURE 5.42 General Electric propfan engine. (Courtesy GE Aircraft Engines.)

fan rotors (see Fig. 5.42). To alleviate the effects of high relative Mach number, the blades are thin and "swept back" at large radii. Noise control is an important challenge for the propfan; it is being addressed by continuing research.

5.7 TYPICAL ENGINE PERFORMANCE

In previous sections we have presented methods for calculating the overall performance of an aircraft engine in terms of the performances of its components. Calculated performances are accurate, of course, only to the extent that realistic component efficiencies are assumed, and we will have more to say about actual components in the following four chapters. In this section we present typical examples of actual (or estimated) overall engine performance, and in addition we show how dimensional analysis permits a correlation of engine performance variables in a form that has minimum complexity and maximum generality. There are many ways to present performance data for an engine, of course, and we will show different forms.

Considering the complexity of some of the engines, it is appropriate first to determine how many of the engine variables can actually be considered independent. We can perhaps most easily determine this by considering the actual variables by which an engine is controlled. If the engine has fixed geometry, there are only two ways to change the thrust or power output: (1) alter the fuel flow or (2) change the condition of the incoming airstream.

If the engine geometry can be altered (e.g., by varying the nozzle exit area or the angle of pitch of the propeller blades or the angular setting of the compressor blades), then this constitutes a third kind of independent control of engine output. In practice such variations in geometry are usually automatically controlled by a given device as a fixed function of speed, fuel flow, or other variables, and may not therefore be considered capable of independent control by the pilot or test engineer.

The condition of the incoming airstream can be described by three variables, such as pressure, temperature, and velocity; or pressure, density, and Mach number. Standard tables (Appendix III) are available that give the mean dependence of the pressure and temperature (or density) of the ambient atmosphere as a function of altitude only. Using such a "standard-day" relationship, we can describe the state of the airstream entering an engine simply as a function of two variables, such as altitude and flight speed, or altitude and flight Mach number. To be precise, of course, the angle at which the air enters the engine should also be specified, because this may (at very high angles of attack) have a definite effect on engine performance. For the sake of simplicity, however, we will ignore this factor in the immediate discussion: We will assume that the air enters the inlet in the direction for which the inlet was designed.

Thus the performance of a given engine can be considered to depend wholly on the fuel flow, flight velocity, and altitude (i.e., ambient pressure and temperature). This set of independent variables is complete but not unique. Another set of three variables could equally well be considered a complete set of independent

variables. For example, fuel flow rate could be replaced by shaft speed or engine pressure ratio.

With three independent variables, the operating characteristics of an engine can be presented in a series of charts, on each of which one independent variable is held constant.

Figure 5.43 shows the specific fuel consumption of a Rolls-Royce RB211 plotted against thrust as a function of high-pressure turbine shaft speed, and true airspeed (1 knot = 0.5144 m/s). At 30,000 ft altitude the standard-day temperature is 228.7 K, for which the speed of sound is 303.1 m/s. Thus a true airspeed of 500 knots means a flight Mach number of $500 \times 0.5144/303.1 = 0.848$. Comparing parts (a) and (b) of Fig. 5.43, we can see that the thrust is strongly dependent on altitude and appreciably affected by airspeed. The minimum specific fuel consumption is somewhat lower at altitude than at sea

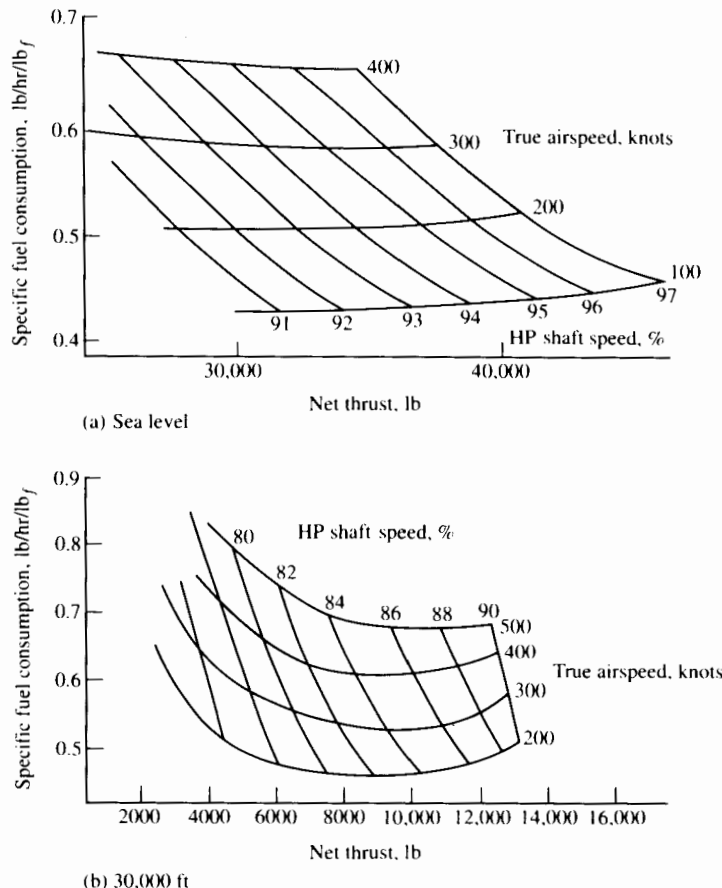


FIGURE 5.43 Typical RB211 turbofan performance (ISA, 100% intake). (Courtesy Rolls-Royce, plc.)

level and is quite strongly affected by airspeed. The information presented in Fig. 5.43(a) and (b) could be described as a function of the form

$$\mathcal{T}, \frac{\dot{m}_f}{\mathcal{T}} = f(u, N_g, \text{altitude}), \quad (5.55)$$

in which u is the airspeed and N_g is the speed of the high-pressure shaft. Other variables, such as the low-pressure shaft speed, the turbine inlet temperature, and the engine pressure ratio, may also be said to be dependent on $(u, N_g, \text{altitude})$.

The turboprop engine, as normally equipped with a variable-pitch propeller, possesses four independent variables; hence a complete presentation of performance would require a much larger set of charts. With the flexibility of a variable-pitch propeller, this engine could, at the same rpm, provide less power at any given altitude and speed by simply reducing the fuel flow rate while adjusting the propeller (decreasing the blade pitch) to absorb less power. Since such an engine usually operates with an automatic pitch-control mechanism, however, there are effectively only three independent variables, and Eq. (5.55) still applies. Figure 5.44 shows the power, thrust, airflow, and specific fuel consumption of the Rolls-Royce Tyne R. Ty. 11 engine as functions of flight speed and altitude for a given engine speed. The propeller pitch is controlled so as to maintain constant turbine inlet temperature (1173 K) or maximum fuel flow rate.

The performance of an engine can be presented in a compact form by using appropriate dimensionless groups of variables. To derive a general set of such groups, it is necessary to consider, in addition to the independent variables already mentioned, all the fluid properties that could be considered important in the operation of the engine. Thus we must consider the air viscosity μ and the gas constants R and γ . The fuel heating value is another physical property of importance that affects engine performance. Other fuel properties might come to mind that could theoretically affect engine performance; in theory, we could state quite a long list—for example, density, specific heat, viscosity, surface tension, vapor pressure. It is therefore important to pause for a moment and the restrict our attention to the fuel properties that can be expected to have a measurable effect on engine performance. If we consider only the fuels that burn with very high efficiency (and only these would be of interest to engine designers) and the liquid fuels (i.e., fuels whose volumetric flow rates are so small that they will have no effect on engine flow patterns), then we might conclude that the only fuel variable of primary physical significance for engine performance would be the product $\dot{m}_f Q_R$, since this is the rate at which fuel energy is added to the engine. Thus we might revise our specific fuel consumption parameter to read $\dot{m}_f Q_R / \mathcal{T}$, in which Q_R is the fuel-heating value.

Instead of “altitude,” it is better to identify the ambient pressure and temperature, p_a and T_a , which vary with altitude. For completeness we need also to specify the geometry of the engine. With these points in mind we could write a complete form of Eq. (5.55) as

$$\mathcal{T}, \frac{\dot{m}_f Q_R}{\mathcal{T}} = f(u, N_g, p_a, T_a, \mu, R, \gamma, D, \text{design}), \quad (5.56)$$

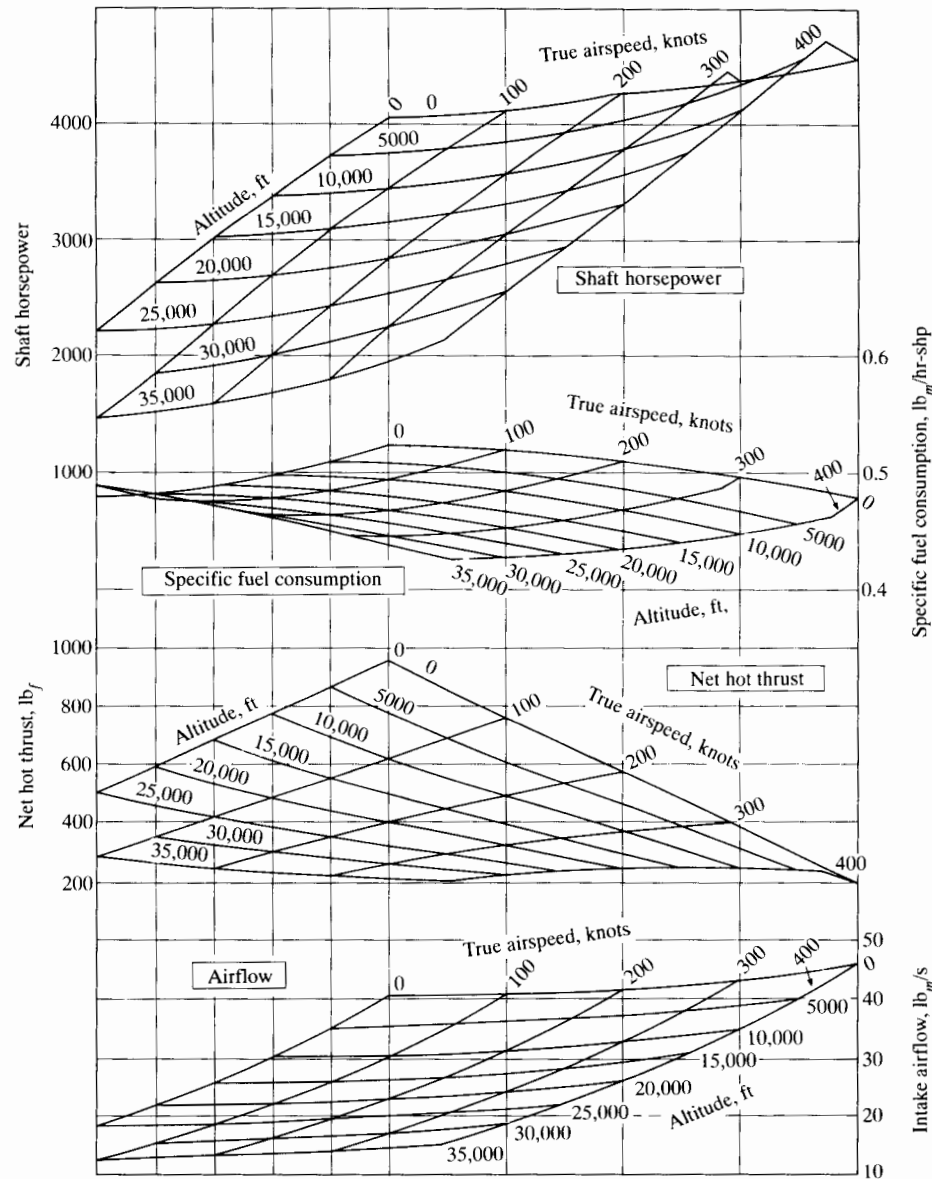


FIGURE 5.44 Performance of Rolls-Royce R. Ty. 11 at cruising rpm of 13,500, as limited by turbine inlet temperature or fuel flow rate; ICAO standard atmosphere. (Courtesy Rolls-Royce, plc.)

where D , engine diameter, and “design,” engine shape (expressed in terms of a very large number of dimension ratios), entirely determine the engine geometry.

By doing a thought experiment (or by experimental tests), we could assure ourselves that the terms in parentheses constitute a complete set of independent

variables. The adjectives *complete* and *independent* imply that each variable can be changed (one at a time) without necessarily altering any of the others, and that it is not possible to add another such variable to the set.

The basic theorem of dimensional analysis may be stated in the following form. Any function of n variables involving q fundamental quantities (such as mass, length, time, or temperature) can be reduced to a function of $(n - q)$ dimensionless groups. The form of the $(n - q)$ groups is arbitrary, but as in most compressible flow problems, we can conveniently express these variables in terms of a Mach number, a Reynolds number, a temperature ratio, and the design ratios. Thus we can show that the functional relationship (5.56) may be simplified to the equally general form

$$\frac{\mathcal{T}}{p_a D^2}, \frac{\dot{m}_f Q_R}{\mathcal{T} \sqrt{RT_a}} = f\left(\frac{u}{\sqrt{\gamma RT_a}}, \frac{N_g D}{\sqrt{\gamma RT_a}}, \frac{\rho_a u D}{\mu}, \gamma, \text{design}\right). \quad (5.57)$$

Instead of nine independent variables, we have here only five.

At this point we restrict our attention to a given geometrically similar series of engines and so regard "design" as a constant. Further, defining the Reynolds number as

$$Re = \frac{\rho_a u D}{\mu}$$

and the flight Mach number as

$$M = \frac{u}{\sqrt{\gamma RT_a}},$$

we can simplify Eq. (5.57) to

$$\frac{\mathcal{T}}{p_a D^2}, \frac{\dot{m}_f Q_R}{\mathcal{T} \sqrt{RT_a}} = f\left(M, \frac{N_g D}{\sqrt{RT_a}}, Re, \gamma\right), \quad (5.58)$$

which still involves only dimensionless variables. The validity of a functional relationship such as Eq. (5.58) will not be affected by multiplying any of its variables by a constant. This permits further simplification because we can regard γ and R as approximately constant. Further, for a given engine and fuel we could take D and Q_R as constants. Thus for this special case it would be legitimate to write

$$\frac{\mathcal{T}}{p_a}, \frac{\dot{m}_f}{\mathcal{T} \sqrt{T_a}} = f\left(M, \frac{N_g}{\sqrt{T_a}}, Re\right). \quad (5.59)$$

One further step is commonly taken to put this relationship in a form convenient for representing test data. We define the ratios

$$\delta = \frac{p_a}{p_{a\text{std}}}, \quad \theta = \frac{T_a}{T_{a\text{std}}},$$

in which $p_{a\text{std}}$ (0.101325 MPa) and $T_{a\text{std}}$ (288.15 K) are the constant or standard values of sea-level ambient pressure and temperature given in the standard atmo-

sphere tables in Appendix III. With these definitions we can write Eq. (5.59) in the form

$$\frac{\mathcal{T}}{\delta}, \frac{\dot{m}_f}{\mathcal{T}\sqrt{\theta}} = f\left(M, \frac{N_g}{\sqrt{\theta}}, Re\right). \quad (5.60)$$

This allows easy correction of test data for any departure from sea-level standard ambient conditions. We now look to see whether Eq. (5.60) is consistent with the information presented, for example, in Fig. 5.43(a) and (b). We take $\delta = \theta = 1$ for the sea-level standard condition and $\delta = 0.297$ and $\theta = 0.793$ for the standard-day values for 30,000 ft altitude. If Reynolds number changes between the two altitudes were unimportant, then, according to Eq. (5.60), the data of Fig. 5.43(a) and (b) should produce single curves of \mathcal{T}/δ and $\dot{m}_f/\mathcal{T}\sqrt{\theta}$ versus $N_g/\sqrt{\theta}$ at a given flight Mach number.

As an example, we choose at sea level a flight speed of 400 knots = 205.8 m/s. The speed of sound at standard-day sea-level conditions is 340.3 m/s, so the standard-day flight Mach number would be $205.8/340.3 = 0.605$. At 400 knots we take from Fig. 5.43(a) the thrust and specific fuel consumption numbers for 93%, 95%, and 97% hp shaft speed and plot the numbers (without change since $\theta = \delta = 1$) as the \mathcal{T}/δ and $\dot{m}_f/\mathcal{T}\sqrt{\theta}$ values shown in Fig. 5.45 for sea level.

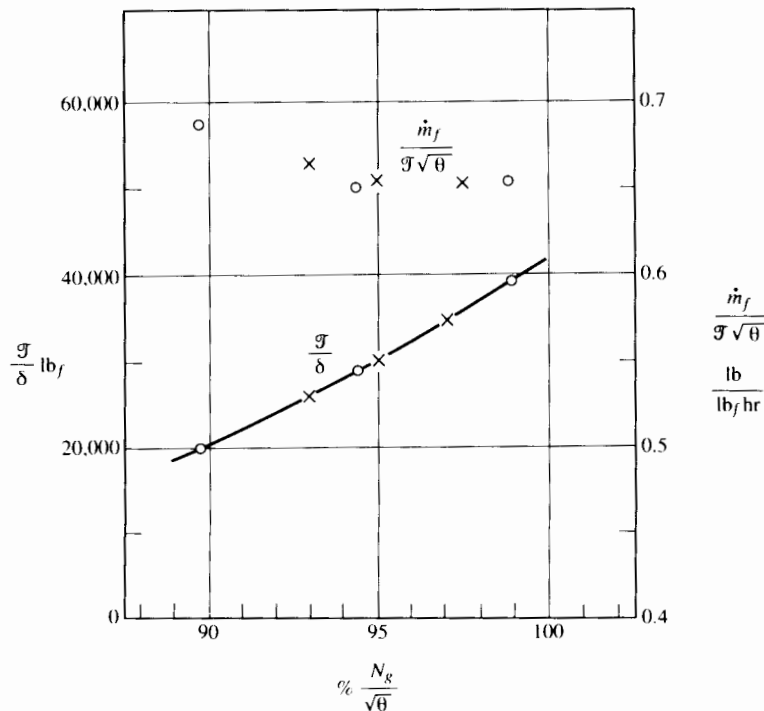


FIGURE 5.45 Rolls-Royce RB211 thrust and fuel consumption. $M = 0.605$, \times = sea level, \circ = 30,000 ft.

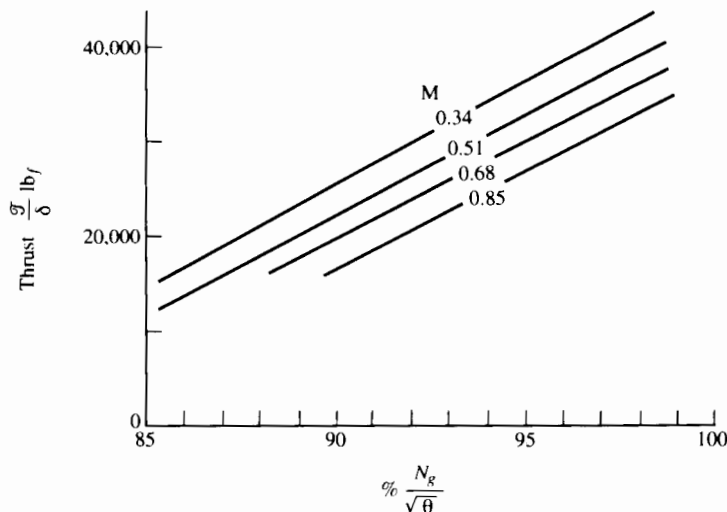


FIGURE 5.46 Rolls-Royce RB211 thrust; thrust = 30,000 ft.

At 30,000 ft altitude where $\theta = 0.793$, the standard-day temperature is 288.15 (0.793) = 228.7 K and the local speed of sound drops by the factor $\sqrt{\theta}$ from 340.3 to 303.2 m/s. Thus for a flight Mach number of 0.605, the flight speed must be $0.605 \cdot (303.0)/0.5144 = 356.7$ knots. At this flight speed we can read from Fig. 5.43(b) the values of thrust and specific fuel consumption at 80%, 84%, and 88% shaft speed. Using $\delta = 0.297$ and $\theta = 0.793$, we can transform these numbers to T/δ and $\dot{m}_f/T\sqrt{\theta}$ and plot them as shown in Fig. 5.45 for 30,000 ft altitude.

Bearing in mind uncertainties arising from reading numbers from Fig. 5.43(a) and (b), we can say that these numbers appear quite compatible with the idea that the change in Reynolds number (by nearly a factor of 3) in going from sea level to 30,000 ft altitude appears to have had negligible effect in performance, because apparently T/δ and $\dot{m}_f/T\sqrt{\theta}$ depend only on M and $N_g/\sqrt{\theta}$.

If changes in combustion efficiency η_b were important, the significant fuel energy variable would have been $\eta_b \dot{m}_f Q_R$. One can conclude from Fig. 5.45 that, between the two altitudes considered, changes in combustion efficiency are apparently insignificant. We will see in Chapter 7 that there is an important physical reason why combustion efficiency must deteriorate at extremely high altitude. One can say that, from Fig. 5.45, this effect is not apparent at 30,000 ft.

Figure 5.46 shows the variation of the “corrected” RB211 thrust with engine speed at several flight Mach numbers. These results will be valid at any altitude for which changes in Reynolds number or combustion efficiency (from sea-level values) will have insignificant effect.

5.8 ENGINE-AIRCRAFT MATCHING

Our first task here is to consider general representations of engine thrust and aircraft drag.

Engine Thrust

In the following we disregard the possible problem of combustor efficiency decrease and Reynolds number effect at high altitude and write the results of Section 5.7 for dimensional analysis of engine performance in the form

$$\frac{\mathcal{T}}{m_a a}, \frac{\dot{m}_f Q_R}{\mathcal{T}_a} = f\left(M, \frac{ND}{a}\right),$$

in which $a = \sqrt{\gamma R T_a}$ and N is the engine shaft speed.

So that we may see more clearly the interaction between the engine and the aircraft characteristics, we transform this statement (using the procedure of Taylor [12]) in the following way. First we recognize that a similar kind of dimensional analysis could have produced the following result for the engine airflow:

$$\frac{\dot{m}_a a}{p_a s_e} = f\left(M, \frac{ND}{a}\right),$$

in which s_e is a characteristic engine flow area—for example, the cross-sectional area at the entrance to the engine.

Multiplying the dimensionless thrust variable by this dimensionless airflow variable, we obtain

$$\frac{\mathcal{T}}{p_a s_e}, \frac{\dot{m}_f Q_R}{\mathcal{T}_a} = f\left(M, \frac{ND}{a}\right).$$

Then multiplying the second term of the left-hand side by the first, we obtain

$$\frac{\mathcal{T}}{p_a s_e}, \frac{\dot{m}_f Q_R}{p_a s_e a} = f\left(M, \frac{ND}{a}\right);$$

but since $M = u/a$, we can equally well write this as

$$\frac{\mathcal{T}}{p_a s_e}, \frac{\dot{m}_f Q_R}{p_a s_e u} = f\left(M, \frac{ND}{a}\right),$$

and now the dimensionless fuel flow rate term is proportional (since Q_R , p_a , and T_a are constants) to the fuel consumption per unit distance traveled by the aircraft at a given altitude, which is \dot{m}_f/u .

Finally we redefine the engine rotational speed variable as a tip speed Mach number

$$M_t = \frac{U_t}{a} \propto \frac{ND}{a},$$

so that the engine characteristics can be written without loss of generality (as long as changes in γ , Reynolds number, and combustion efficiency are unimportant):

$$\frac{\mathcal{T}}{p_a s_e}, \frac{\dot{m}_f Q_R}{p_a s_e u} = f(M, M_t). \quad (5.61)$$

Figure 5.47 is a typical display of engine characteristics in this form for M_t values of 1.4, 1.5, and 1.6. To see the significance of these values, we suppose a

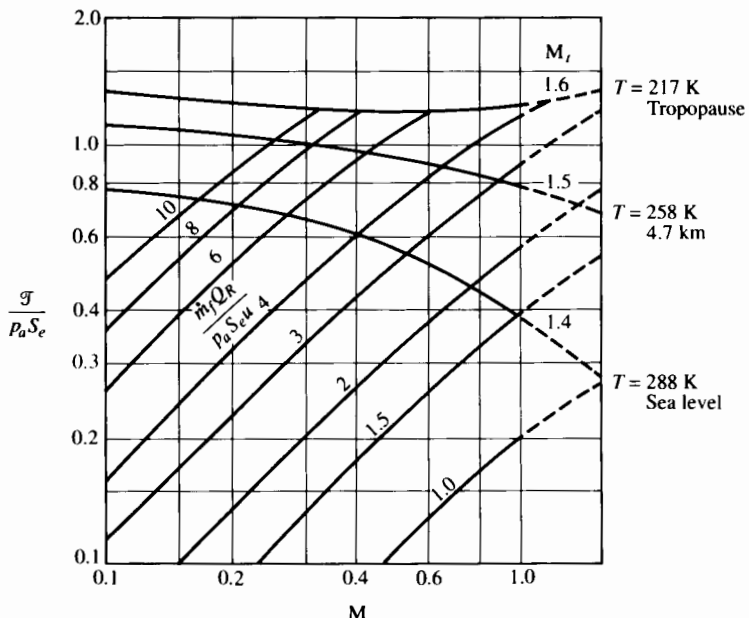


FIGURE 5.47 Typical turbofan characteristics. Adapted with permission from E.S. Taylor, *Dimensional Analysis for Engineers*, Clarendon Press, Oxford, 1974.

maximum turbine tip speed of 475 m/s. (In Chapter 8 we discuss how turbine tip speed is fixed by stress and turbine inlet temperature.) Then from Table 1 of Appendix III we obtain the following values of ambient temperature (and corresponding speed of sound) at various altitudes.

h (km)	T_a (k)	a_a (m/s)	M_l (with $U_t = 475$ m/s)	p_a (kPa)
0	288.15	340.3	1.4	101.3
6	249.19	316.5	1.5	47.2
12 [†]	216.65	295.1	1.6	19.4

[†]Approximately 40,000 ft (in the large layer of nearly uniform temperature known as the tropopause).

Figure 5.47 shows that for a given flight Mach number M , a substantial increase in the limiting engine Mach number M_l (associated with fixed engine rpm and stress level) means a substantial rise in the dimensionless thrust variable. More important, it means a significant decrease in the fuel consumed per unit distance traveled by the aircraft. At, for example, $M = 0.8$, in going from sea level to 12 km (about 40,000 ft), $\dot{m}_f Q_R / p_a S_e u$ increases from about 1.8 to 4.9. At the same time, however, the ambient pressure (see the above table) decreases

from 101.3 to 19.4 kPa. This means that the fuel consumption per unit distance traveled, \dot{m}_f/u , decreases by nearly 50% as the altitude is increased from sea level to 12 km. One sees from Fig. 5.47 the tendency for the effect to be increasingly important with increasing flight Mach number.

Aircraft Drag

Usually aircraft lift and drag are presented in the forms of coefficients defined as follows:

$$\text{Lift coefficient: } C_L = \frac{L}{\frac{1}{2} \rho_a u^2 s},$$

$$\text{Drag coefficient: } C_D = \frac{\mathcal{D}}{\frac{1}{2} \rho_a u^2 s},$$

in which s is the aircraft wing area. Since $M = u/\sqrt{\gamma RT_a}$, we can write these relationships as

$$C_L = \frac{2}{\gamma M^2} \frac{L}{p_a s}, \quad (5.62)$$

$$C_D = \frac{2}{\gamma M^2} \frac{\mathcal{D}}{p_a s}. \quad (5.63)$$

For a given aircraft C_L and C_D are related: The higher the former, at a given flight speed (i.e., the more heavily the aircraft is loaded), the higher the latter. Figure 5.48 shows a representation of measured lift and drag data for a given aircraft shape. The wing Reynolds number can be considered high enough that changes in it do not affect C_L and C_D , so that Fig. 5.48 is an explicit example of the relationship

$$C_D = f(M, C_L). \quad (5.64)$$

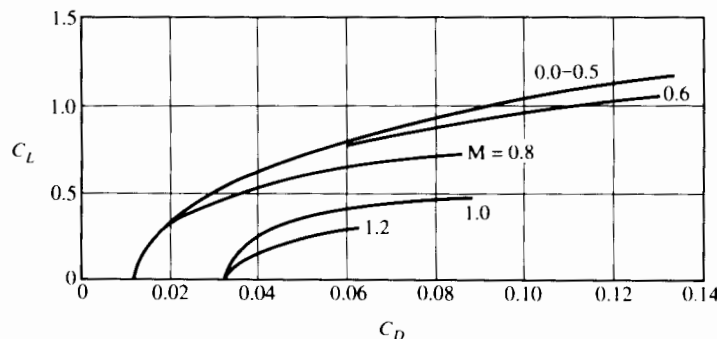


FIGURE 5.48 Aircraft drag characteristics. Adapted with permission from E. S. Taylor, *Dimensional Analysis for Engineers*, Clarendon Press, Oxford, 1974.

Combining Eqs. (5.62), (5.63), and (5.64) means that we can write

$$\frac{2}{\gamma M^2} \frac{\mathcal{D}}{p_a s} = f\left(M, \frac{2}{\gamma M^2} \frac{L}{p_a s}\right)$$

or, for given γ ,

$$\frac{\mathcal{D}}{p_a s} = f\left(M, \frac{L}{p_a s}\right). \quad (5.65)$$

Therefore we can transform the aircraft lift–drag characteristics from the curves given in Fig. 5.48 to the curves given in Fig. 5.49. (As an example, the $L/p_a s = 0.1$ curve could be calculated by choosing a series of M values. For each of these, the lift coefficient would be calculated from Eq. [5.62]. With C_L and M specified, C_D could be obtained from Fig. 5.48 and then $\mathcal{D}/p_a s$ calculated from Eq.[5.63].)

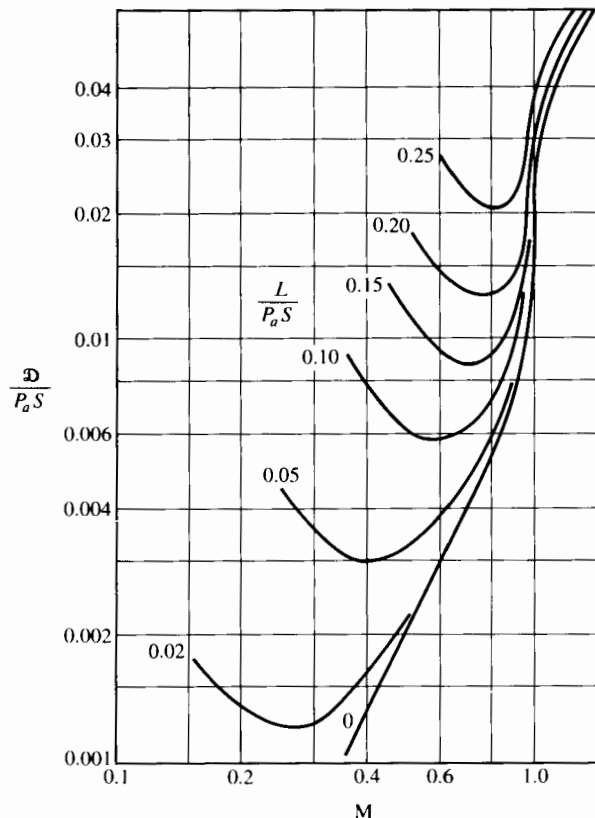


FIGURE 5.49 Transformed airframe characteristics. Adapted with permission from E. S. Taylor, *Dimensional Analysis for Engineers*, Clarendon Press, Oxford, 1974.

An interesting feature of Fig. 5.49 is the existence of a minimum point on each curve of constant lift. For a given aircraft weight (balanced by the lift L) and altitude (i.e., given p_a, T_a), there is a flight Mach number that is associated with minimum drag. Figures 5.47 (the engine characteristics) and 5.49 (the aircraft characteristics) can now be related easily under the following conditions:

1. $\mathcal{T} = \mathcal{D}$; that is, we are considering level flight at constant speed.
2. We choose the ratio of the characteristic engine flow area s_e to the wing area s . This is a measure of the size (and number) of engines powering a given aircraft.

To take an example, suppose that $s/s_e = 60$. Then it is possible to overlay the engine and aircraft characteristics on a single graph as in Fig. 5.50, which permits us to explore the effect of altitude, weight, and flight Mach number on fuel consumption per unit distance.

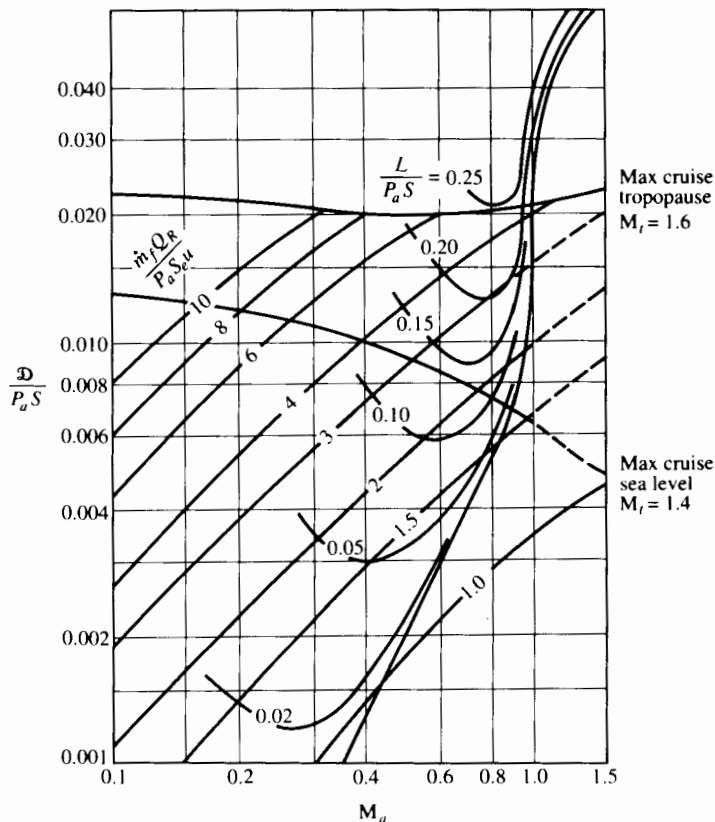


FIGURE 5.50 Aeroplane and engine characteristics for $s/s_e = 60$. Adapted with permission from E. S. Taylor, *Dimensional Analysis for Engineers*, Clarendon Press, Oxford, 1974.

In the tropopause we would clearly like to operate at $M_t = 1.6$. Figure 5.50 indicates that with this aircraft the flight Mach number associated with minimum fuel consumption per unit distance would be about 0.85. At that flight Mach number we can obtain from Fig. 5.50

$$\frac{\dot{m}_f Q_R}{p_a s_e u} \approx 4.5$$

and

$$\frac{L}{p_a s_e} \approx 0.24.$$

At 12 km altitude we have

$$p_a / p_{a \text{ sea level}} = 0.194.$$

Thus for the same lift the value of $L/p_a s_e$ at sea level would be

$$\frac{L}{p_a s} \approx 0.24(0.194) = 0.048.$$

Reading from Fig. 5.50 with

$$\frac{L}{p_a s} = 0.048,$$

we see that the minimum fuel consumption rate is associated with

$$M \approx 0.6 \quad \text{and} \quad \frac{\dot{m}_f Q_R}{p_a s_e u} \approx 1.4.$$

From these numbers we can deduce that

$$\left(\frac{\dot{m}_f}{u} \right)_{\text{altitude}} \approx 0.63 \left(\frac{\dot{m}_f}{u} \right)_{\text{sea level}}.$$

Thus we can conclude that at altitude the most economical flight consumes 37% less fuel than the most economical flight near sea level and the most economical flight speed is 23% faster.

At this most efficient sea-level operating condition, the required engine speed Mach number M_t would be substantially below the maximum allowable value shown in Fig. 5.50 ($M_t = 1.4$). This means that the engine would have plenty of reserve thrust for acceleration and climbing.

Graphs such as Figs. 5.47 and 5.49 show in principle how the engine size can be matched to the aircraft requirements for takeoff, climb, and cruise at high altitude.

PROBLEMS

1. Consider the acceleration of a streamtube through a conventional unshrouded aircraft propeller from flight velocity u to exhaust velocity $u_e = u + \Delta u$.

Neglect the cross-sectional area of the propeller hub and engine compared with the total area $A = \pi D^2/4$. Consider the propeller as an "actuator" disc with discontinuous pressure change but continuous variation in velocity through the propeller.

Show from the thrust equation and the Bernoulli equation applied upstream and downstream of the propeller that the velocity through the actuator disc is

$$u_m = u + \Delta u/2$$

Show that the propulsion efficiency η_p and the thrust per unit area depend on the ratio u/u_e according to

$$\eta_p = \frac{2 \frac{u}{u_e}}{1 + \frac{u}{u_e}}, \quad \frac{\mathcal{T}}{A \rho u_e^2} = \frac{1}{2} \left[1 - \left(\frac{u}{u_e} \right)^2 \right].$$

Since $\Delta u/u_e \ll 1$ (typically), and since the flight M number will be subsonic, the density of the air can be considered to be uniform upstream and downstream of the propeller.

2. Given that a commercial airliner has a range of 6000 miles using 200 tonnes of JP4 fuel, estimate the range of the aircraft burning either gaseous or liquid hydrogen and
 - a. The same mass of hydrogen as JP4,
 - b. The same volume of hydrogen as JP4.

The dry mass of the aircraft is 800 tonnes. The fuel properties are as follows:

Fuel	Density (kg/m ³)	Heating value (kJ/kg)
JP4	800.0	45000
H ₂ (gaseous, S.T.P.)	0.0824	120900
H ₂ (liquid, 1 atm)	70.8	120900

3. The idling engines of a landing turbojet produce forward thrust when operating in a normal manner, but they can produce reverse thrust if the jet is properly deflected. Suppose that while the aircraft rolls down the runway at 150 km/h the idling engine consumes air at 50 kg/s and produces an exhaust velocity of 150 m/s.
 - a. What is the forward thrust of this engine?
 - b. What are the magnitude and direction (i.e., forward or reverse) if the exhaust is deflected 90° without affecting the mass flow?
 - c. What are the magnitude and direction of the thrust (forward or reverse) after the plane has come to a stop, with 90° exhaust deflection and an airflow of 40 kg/s?

4. After verifying the derivation of Eq. (5.27) for the ideal ramjet, find the Mach number M that maximizes \mathcal{T}/\dot{m}_a for $T_{04} = 2500$ K, $T_a = 220$ K. Evaluate the specific thrust at that Mach number and compare your results with Fig. 5.9.

Both Fig. 5.9 (for the ideal ramjet) and Fig. 5.12 (which makes allowance for losses) indicate that at a given flight Mach number the specific fuel consumption rises with T_{\max} . Looking for an explanation of this effect, determine the variation of propulsion, thermal, and overall efficiencies with T_{\max} for the ideal ramjet for $M = 3$ and $2000 < T_{\max} < 3000$ K.

Show for the limiting case $\mathcal{T}/\dot{m}_a \rightarrow 0$ that

$$f \rightarrow 0, M \rightarrow \sqrt{\frac{2}{\gamma - 1} \left(\frac{T_{04}}{T_a} - 1 \right)},$$

and

$$\text{TSFC} \rightarrow \frac{2}{M \sqrt{\gamma R T_a} \left[1 + \frac{Q_R}{c_p T_a} / \left(1 + \frac{\gamma - 1}{2} M^2 \right) \right]}$$

5. Show that for the ideal turbojet (all efficiencies equal unity), the exhaust Mach number M_e is given by

$$M_e^2 = \frac{2}{\gamma - 1} \left[\left(\frac{P_{03}}{P_{02}} \right)^{(\gamma-1)/\gamma} \left(1 + \frac{\gamma - 1}{2} M^2 \right) \times \left\{ 1 - \frac{1 + \frac{\gamma - 1}{2} M^2}{T_{04}/T_a} \left[\left(\frac{P_{03}}{P_{02}} \right)^{(\gamma-1)/\gamma} - 1 \right] \right\} - 1 \right],$$

in which

M is the flight Mach number,

$\frac{P_{03}}{P_{02}}$ is the compressor pressure ratio,

$\frac{T_{04}}{T_a}$ is the ratio of turbine inlet and ambient temperatures,

γ is the ratio of specific heats (assumed constant).

The mass flow rates through the compressor and turbine may be assumed equal.

6. For a given work input per unit mass of fluid and given adiabatic efficiency η_c , how does the actual pressure ratio for a compressor differ from the ideal (isentropic) pressure ratio? Derive an expression that relates the actual pressure ratio to the ideal one and η_c . As mentioned in Chapter 5, the adiabatic efficiency η_c is usually defined by

$$\eta_c = \frac{h_{03s} - h_{02}}{h_{03} - h_2}.$$

Show the dependence for $\eta_c = 0.8, 0.9$, and ideal pressure ratio $10 < p_{03}/p_{02} < 30$ and $\gamma = 1.4$.

For a diffuser, the adiabatic efficiency cannot be written as a work ratio since the adiabatic work is zero. Using the appropriate definition of adiabatic diffuser efficiency

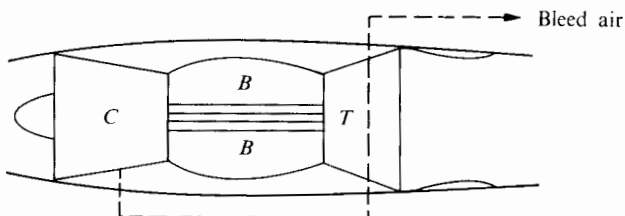
$$\eta_d = \frac{h_{02s} - h_a}{h_{02} - h_a},$$

show how the actual ratio of exit stagnation pressure to inlet static pressure depends on the diffuser efficiency and the ideal ratio. Show the dependence for $\eta_d = 0.9, 0.95$, and flight Mach number $0.5 < M < 0.9$.

7. Estimate the propulsion and thermal efficiencies of a turbojet engine during subsonic cruise. The flight Mach number is 0.8, and the ambient temperature is 225 K. The compressor pressure ratio is 12, and the turbine inlet temperature is 1300 K. The respective adiabatic efficiencies of the diffuser, compressor, turbine, and nozzle are 0.92, 0.85, 0.85, and 0.95. The burner stagnation pressure ratio is 0.97, and the average specific heat during and after combustion is 1.1 kJ/kg · K, and the average molecular weight is 29.
8. Compare the specific fuel consumption of a turbojet and a ramjet that are being considered for flight at $M = 1.5$ and 50,000 ft altitude (ambient pressure and temperature: 11.6 kPa and 205 K, respectively).

The turbojet pressure ratio is 12 and the maximum allowable temperature is 1400 K. For the ramjet the maximum temperature is 2500 K. For simplicity ignore aerodynamic losses in both engines. Conventional hydrocarbon fuels are to be used (heating value 45,000 kJ/kg). Assume $\gamma = 1.4$ and $c_p = 1.0 \text{ kJ/(kg} \cdot \text{K)}$.

9. Consider two versions of a jet engine. The first is a standard engine run with a turbine inlet temperature of 1200 K. The second is identical, except that its turbine is cooled by bleeding air from the compressor; in this way the allowable turbine inlet temperature may be raised to 1600 K. The basic engine and the bleed air line are indicated in the figure. To make an estimate of the effect of this modification on the thrust, suppose that the engine is flying at Mach 2 at an altitude where the ambient temperature is 200 K and that compressor pressure ratio is 9:1. Suppose also that for the second engine 10% of



PROBLEM 9

the airflow is bled from the compressor at a point where the pressure ratio is 9:1. After cooling the turbine, the bleed air is exhausted from the engine with no appreciable velocity. For simplicity assume all components of both engines to be reversible. Let $\gamma = 1.4$ and $c_p = 1.0 \text{ kJ/(kg} \cdot \text{K)}$.

- a. Determine the thrust of the two engines per unit mass flow of air entering the compressor.
- b. What is the ratio of the thrust specific fuel consumption of the second engine to that of the first?
10. For a bypass engine it may be shown that if the specific heat c_p is constant, the fuel-air ratio $f \ll 1$, and all losses are negligible, the static engine thrust can be determined from

$$\frac{\mathcal{T}}{\dot{m}\sqrt{2c_p T_1}} = \sqrt{\frac{T_3}{T_1} - \left(\frac{T_2}{T_1} - 1\right) - \mathcal{B}\left(\frac{T_f}{T_1} - 1\right) - \left(\frac{T_3}{T_1}\right)\left(\frac{T_2}{T_1}\right)} + \mathcal{B}\sqrt{\frac{T_f}{T_1} - 1},$$

in which T denotes stagnation temperature and subscript

- 1 denotes the compressor and fan inlet,
- 2 denotes compressor outlet,
- f denotes fan outlet,
- 3 denotes turbine inlet,

and \mathcal{B} is the bypass ratio.

- a. Prove or disprove that this expression is valid.
 - b. For a given ratio T_3/T_1 , what compressor pressure ratio will maximize the static thrust?
 - c. For a given bypass ratio \mathcal{B} , what fan pressure ratio will maximize the static thrust?
 - d. With optimum compressor and fan pressure ratios, how will the thrust vary with T_3/T_1 and \mathcal{B} ?
 11. Compare the takeoff thrusts of two engines operating with the same core engine airflow rate, compressor exit pressure (12 atm), and turbine inlet temperature (1500 K), and at the same ambient pressure and temperature. One of them is a turbojet (bypass ratio equals zero) and one has bypass ratio equal to 10 and fan pressure ratio 1.6.
- For convenience we here neglect the effect of losses in the compressor, burner, and turbine and make approximations associated with fuel-air ratio $f \ll 1$ and constant specific heat of the working fluid (with $\gamma = 1.4$).
- Find the ratio of thrusts at takeoff, with flight velocity $u \ll u_e$, the exhaust velocity.
12. A ramjet is to propel an aircraft at Mach 3 at high altitude where the ambient pressure is 8.5 kPa and the ambient temperature T_a is 220 K. The turbine inlet temperature T is 2540 K.

If all components of the engine are ideal—that is, frictionless—determine

- a. The thermal efficiency,
- b. The propulsion efficiency,
- c. The overall efficiency.

Let the specific heat ratio be $\gamma = 1.4$ and make the approximations appropriate to $f \ll 1$.

13. Preliminary design calculations are being made for a turbofan engine with a bypass ratio of 8:1.

Concept A has core engine exhaust and bypass streams separately expanding to different final velocities. The bypass stream (after the fan) has stagnation pressure $p_0 = 0.16 \text{ MPa}$ and stagnation temperature $T_0 = 350 \text{ K}$. The core engine exhaust has stagnation temperature $T_{0c} = 700 \text{ K}$ and the same stagnation pressure as the bypass stream and $f = 0.025$.

Concept B would have the two streams mixing at constant pressure before expansion through the same pressure ratio p_0/p_e as in concept A.

Determine the ratio of takeoff thrusts (flight speed $\equiv 0$) of concepts B and A. Assume ambient pressure of 0.1 MPa in the nozzle exhaust plane. The ratio of specific heats may be taken to be 1.4 for both streams, as a first approximation.

14. An ideal bypass turbojet (no losses in compressor, burner, turbine, nozzle, fan, and fan nozzle) has a bypass ratio B of 8:1 and a maximum turbine inlet temperature of 1200 K. At takeoff the ambient conditions are 298 K and 101 kPa. The bypass nozzle exhaust and core engine nozzle exhaust velocities are identical.

What compressor pressure ratio will maximize takeoff thrust? For ease of calculation the approximation $f \ll 1$ may be used (f being the fuel-air ratio for the core engine) and the specific heat ratio γ may be taken to be 1.4 throughout.

15. A turbofan engine is being designed for a bypass ratio of 6:1. During cruise ($M = 0.85$) at 12,000 km, the ratio of the exit stagnation pressure to ambient pressure p_0/p_a is 1.6:1 (the same for the fan as for the core engine). The stagnation temperature at exit from the core engine is 600 K; at exit from the fan it is only 340 K.

The question is whether:

- a. The fan and core streams should expand in separate nozzles to ambient pressure, or
- b. They should first be mixed to uniform stagnation temperature, then expanded in a single nozzle.

Determine the ratio of thrusts (case a to case b) on the understanding that mixing of the two streams can be done with no loss in stagnation pressure.

For simplicity assume that the specific heat ratio and the gas constant are the same for both streams and that $\gamma = 1.4$ and $R = 0.287 \text{ kJ/kg} \cdot \text{K}$.

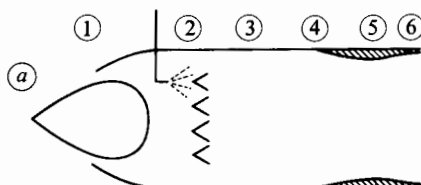
The fuel-air ratio for the core engine is approximately 0.018, and nozzle losses are negligible.

16. The performance results in Figs. 5.19 and 5.20 indicate that as the turbine inlet temperature of a turbojet is raised (while its flight speed remains constant), the thrust specific fuel consumption increases. Why should this be so? Consider the $M = 0$ case and assume that as the turbine inlet temperature is raised from 1500 to 1700 K, the compressor pressure ratio remains at 20:1. Table 5.1 provides the component efficiencies. Estimate the change in TSFC for this change in T_{04} .
17. An existing aircraft with payload has total mass of 300,000 kg (dry) and 420,000 kg (full of fuel). These totals exclude the mass of the four engines, which are in the preliminary design stage and are expected to be about 4000 kg each. It appears that a 100 K increase in turbine engine temperature could increase the engine specific thrust at takeoff by 4%, while specific fuel consumption during cruise would increase by 5%. For a given takeoff thrust, one might assume that the mass of the required engine would be proportional to the $3/2$ power of the inlet airflow rate during takeoff. If this is the case, how would the 100 K increase in turbine inlet temperature indirectly affect the cruise range of the aircraft? Assume that a change in the estimated engine mass does not affect the fuel load or the required takeoff or cruise thrust.
18. The performance of a series of ramjet engines, each operating under design conditions, is to be calculated as a function of flight Mach number. The engines are to fly at an altitude of 50,000 ft, where $T_a = 205$ K, $p_a = 11.6$ kPa. The fuel-heating value is 45000 kJ/kg, and the peak temperature is limited to 3000 K. According to the Aircraft Industries Association, a reasonable estimate of ramjet diffuser losses is given by

$$\frac{p_{02}}{p_{0a}} = 1 - 0.1(M - 1)^{1.5}, \quad M > 1,$$

in which M is the flight Mach number.

The stagnation pressure ratio across the flameholders, (2) to (3), is 0.97, and the stagnation pressure loss in the combustor, (3) to (4), may be estimated to be 5%. The nozzle and combustion efficiencies are 0.95 and 0.98, respectively, and the combustion chamber exit Mach number is 0.5. For the nozzle $A_6 \leq A_4$. Assume the propellant is a perfect gas having $R = 0.287$ kJ/(kg · K) throughout, but having $\gamma = 1.4$ from (a) to (3) and $\gamma = 1.3$ from



PROBLEM 18

- (3) to (6). Check to see that the fuel-air mass ratio does not exceed stoichiometric (about 0.0667). Calculate TSFC and specific thrust for flight Mach numbers of 1.0, 2.0, 3.0, and 4.0.
19. A turbojet engine (with $\mathcal{B} = 0$) has a pressure ratio of 30 and a maximum temperature of 1700 K. The component efficiencies and ambient conditions are the same as those given in Table 5.1. For a flight Mach number of 0.85 determine
- The specific thrust,
 - The thrust specific fuel consumption,
 - The engine thermal efficiency,
 - The propulsion efficiency,
 - The overall efficiency.
20. A turbofan engine with bypass ratio $\mathcal{B} = 5$ is to operate at the same core engine pressure ratio and maximum temperature as prescribed in the previous problem. Determine the specific thrust, the thrust specific fuel consumption, and the efficiencies for a fan pressure ratio $p_{rf} = 1.5$. The component efficiencies and ambient conditions are as given in Tables 5.1 and 5.2.
- If you are using a spreadsheet for your calculations, explore the possibility of finding a combination of bypass ratio and fan pressure ratio that maximizes the overall efficiency.
21. Thought is being given to developing a new turboprop engine with an eight-bladed propeller specially designed for flight at $M = 0.7$ at an altitude of 40,000 ft. (12 km). An existing turbojet engine has a gas generator design that (with the addition of a free turbine, gear reducer, propeller, and new propulsion nozzle) would be used for the engine. At the above altitude and flight Mach number the gas generator exit conditions are

$$\dot{m} = 100 \text{ kg/s}$$

$$p_0 = 0.04 \text{ MPa}$$

$$T_0 = 1200 \text{ K}$$

If these same conditions were to apply at entrance to the free-power turbine of the turboprop, determine the best combination of propeller thrust and nozzle thrust for the turboprop engine given the following expected adiabatic efficiencies:

propeller	$\eta_{pr} = 0.79$
nozzle	$\eta_n = 0.98$
power turbine	$\eta_{pt} = 0.89$

The mechanical efficiency of the gearbox is $\eta_g = 0.97$. Assume the turbine working fluid has $\gamma = 1.33$ and molecular weight of 30.

REFERENCES

1. Ferguson, C. *Internal Combustion Engines*. New York: Wiley, 1968.
2. Heywood, J. B. *Internal Combustion Engine Fundamentals*. New York: McGraw-Hill, 1988.
3. Taylor, C. F. *The Internal Combustion Engine in Theory and Practice*, 2nd. ed. Cambridge, Mass.: M.I.T. Press, 1985.
4. "The Jet Engine," Technical Publications Department, Rolls-Royce, Derby, U.K., 1986.
5. Ciepluch, C. C., D.Y. Davis, and D.E. Gray. "Results of NASA's Energy Efficient Engine Program," *AIAA J. Propulsion and Power* 3 (1987):560–568.
6. Cundy, J. "Saving Fuel with the Wide-Chord Fan," *Rolls-Royce Magazine*, June 1983, pp. 13–18.
7. Lewis, G. M. "V/STOL from the Propulsion Viewpoint," *Aerospace*, June/July 1983.
8. Lancaster, O. E., ed. *Jet Propulsion Engines*, vol. 12 of *High-Speed Aerodynamics and Jet Propulsion*. Princeton, N.J.: Princeton University Press, 1959.
9. Saravanamuttoo, H. I. H. "Development of Modern Turboprop Engines," *CASI J.* 31 (1985):131–139.
10. Morris, R. E. "The Pratt and Whitney PW100: Evolution of the Design Concept," *CASI J.* 28 (1982):211–221.
11. Cook, D. L. "Development of the PW100 Turboprop Engine," *CASI J.* 30 (1984): 230–239.
12. Taylor, E. S. "Dimensional Analysis for Engineers," Clarendon Press, Oxford, 1974.



C H A P T E R

6

AEROTHERMODYNAMICS OF INLETS, COMBUSTORS, AND NOZZLES

6.1 INTRODUCTION

In Chapter 5 we used the laws of thermodynamics and fluid mechanics to explain the behavior of aircraft jet engines. We treated the several engine components as "black boxes," in the sense that we confined discussion to the inlet and outlet conditions of the propellant, without regard to the internal mechanisms that produce its change of state. Where necessary, we related the actual performance to some easily calculated or "ideal" performance by the definition of an appropriate component efficiency or stagnation pressure ratio. The purpose of this and the following chapter is to examine the internal mechanisms of the various components in order to describe the factors that impose practical limits on performance. We consider conditions required for high performance of components and, in some cases, present methods for quantitative prediction of their behavior.

For the ramjet, Eq. (5.34) indicated that a given percentage loss in stagnation pressure has the same effect on engine performance wherever it occurs through the engine. For turbine engines the same conclusion holds, though it is not so easily seen, since component performances are usually stated in terms of adiabatic efficiencies rather than stagnation pressure ratios. Hence high performance is of equal importance for all engine components. The *attainment* of high performance is generally more difficult in those regions requiring a rise in static pressure than in those where the pressure falls. This, as we pointed out in Chapter 4, may be attributed to boundary layer behavior and the tendency for separation in the presence of a rising static pressure. Thus inlets (which generally have rising

pressure gradients even for turbojets) may be more difficult to design for efficient operation than nozzles. Similarly, as we will see in Chapter 7, compressors are more difficult to design (and have lower ultimate efficiency) than turbines.

In this chapter we are concerned with the major components of turbine engines other than the turbomachinery (which is the subject of Chapters 7, 8, and 9). The common theme is steady flow in stationary ducts, and the chief interest lies in the arrangements that are necessary for high efficiency in inlets, burners, and nozzles.

6.2 SUBSONIC INLETS

An engine installed in an aircraft must be provided with an air intake and a ducting system. Figure 5.27 shows the inlet duct for the Rolls-Royce RB211-535E4 engine mounted in an underwing installation. We will see in Chapter 8 that for turbojet engines the airflow entering the compressor or fan must have low Mach number, in the range 0.4 to 0.7, with the upper part of the range suitable only for transonic compressors or fans. If the engine is designed for subsonic cruise at, for example, $M = 0.85$, the inlet must be designed to act as a diffuser with reasonably gentle diffusion from $M = 0.85$ to perhaps $M = 0.6$. Part of this deceleration occurs upstream of the inlet entrance plane. One can see in Fig. 5.27 the relatively small increase in area associated with the internal deceleration.

The inlet must be designed to prevent boundary layer separation, even when the axis of the intake is not perfectly aligned with the streamline direction far upstream of the inlet. In other words, the performance of the inlet must not be unduly sensitive to pitch (up-and-down) and yaw (side-to-side) motions of the aircraft. It is important that the stagnation pressure loss in the inlet be small. It is even more important that the flow velocity and direction leaving the inlet be uniform, since distortions in the velocity profile at the compressor inlet can severely upset the compressor aerodynamics and may lead to failure of the blades due to vibrations. Design of inlets that must operate efficiently in both supersonic and subsonic flight poses special problems; we consider these in Section 6.3.

Flow Patterns

Depending on the flight speed and the mass flow demanded by the engine, the inlet may have to operate with a wide range of incident stream conditions. Figure 6.1 shows the streamline patterns for two typical subsonic conditions and the corresponding thermodynamic path of an “average” fluid particle. During level cruise the streamline pattern may include some deceleration of the entering fluid external to the inlet plane [Fig. 6.1(a)]. During low-speed high-thrust operation (e.g., during takeoff and climb), the same engine will demand more mass flow and the streamline pattern may resemble Fig. 6.1(b), which illustrates external acceleration of the stream near the inlet. In both cases there is an external change of state that is essentially isentropic, since there are no walls on which friction may act. For given air velocities at stations (a) and (2), external accelera-

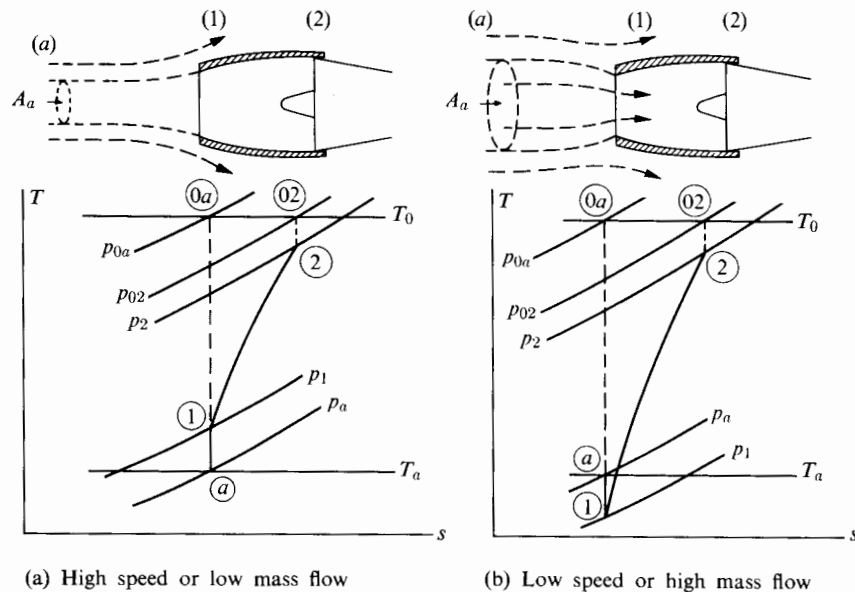


FIGURE 6.1 Typical streamline patterns for subsonic inlets.

tion raises the inlet velocity and lowers the inlet pressure, thereby increasing the internal pressure rise across the diffuser. If this pressure increase is too large, the diffuser may stall because of boundary layer separation; stalling usually reduces the stagnation pressure of the stream as a whole. Conversely, external deceleration requires less internal pressure rise and hence a less severe loading of the boundary layer. Therefore the inlet area is often chosen so as to minimize external acceleration during takeoff, with the result that external deceleration occurs during level-cruise operation. Under these conditions the “upstream capture area” A_a is less than the inlet area A_1 , and some flow is “spilled over” the inlet, accelerating as it passes over the outer surface. For high-Mach-number subsonic flight this acceleration (and subsequent deceleration) must not be too large or there would be danger of shock-induced boundary layer separation on the outer surface and excessive nacelle drag. For supersonic flight such “spilling” action would necessarily be accompanied by a shock system that reduces the relative velocity at inlet to subsonic values—so that the air may sense the presence of the inlet and flow around it.

Internal Flow

Qualitatively the flow in the inlet behaves as though it were in a “diffuser,” which is a common element in fluid machinery. A better term might be *decelerator*, since the device is not primarily concerned with molecular or turbulent diffusion, but we will retain here the traditional term *diffuser* and define it to mean any section of a duct in which fluid momentum decreases and pressure rises, no

work being done. Considerable experimental and analytical work has been done on cylindrical (especially conical [1] and annular [2]) diffusers, but little of this is directly applicable to subsonic aircraft inlets. The reason is that most work on diffusers focuses on the conditions that are related to maximum pressure recovery—which is usually associated with a highly nonuniform exit velocity profile and perhaps even with some flow unsteadiness. In typical subsonic aircraft inlets there is a stringent requirement that the flow velocity entering the compressor be steady and uniform. Consequently inlet design does not depend so much on the results of diffuser research as on potential flow calculations, coupled with boundary layer calculations and followed by wind tunnel testing to assess inlet performance under a wide range of test conditions.

In the actual engine inlet, separation can take place in any of the three zones shown in Fig. 6.2. Separation of the external flow in zone ① may result from local high velocities and subsequent deceleration over the outer surface. We will discuss this possibility, which leads to high nacelle drag, subsequently.

Separation on the internal surfaces may take place in either zone ② or zone ③, depending on the geometry of the duct and the operating conditions. Zone ③ may be the scene of quite large adverse pressure gradients, since the flow accelerates around the nose of the center body, then decelerates as the curvature decreases. In some installations it has not been possible to make the exit area of the intake more than about 30% greater than the inlet area without the incidence of stall and large losses. Reynolds number effects may also be important for large inlets and high-speed flow. At high angles of attack, all three zones could be subjected to unusual pressure gradients.

External Flow

As we already indicated, inlet design requires a compromise between external and internal deceleration. Both can lead to difficulties, and a balance is needed. To examine the effect of external deceleration on inlet design, methods are needed for calculating both potential flow (internal and external) and boundary layer growth on intake surfaces. References [3], [4], and [5] provide details on how such methods have been applied to subsonic engine intakes. These methods are not valid for separated flow, but they are able to warn the designer of the danger of separation, and so provide guidance on design modifications that may be needed to avoid separation. Expressed in computer codes, these methods can

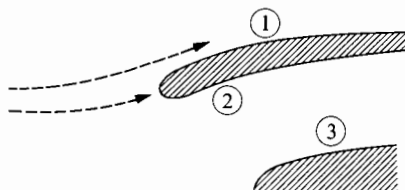


FIGURE 6.2 Possible locations of boundary layer separation.

determine the pressure and velocity field at all points in the flow. They are able to predict the momentum thickness (and the associated nacelle drag) due to the boundary layer on the external surface of the nacelle. They are also able to define the velocity distribution of the flow approaching the compressor.

We will not go into the details of these methods here but instead will focus on a qualitatively valid and much simpler explanation of the fact that external deceleration must be limited to prevent excessive nacelle drag. Following the method of Küchemann and Weber [6], we here ignore compressibility and suppose that the only effect of the boundary layer is flow separation (if the deceleration pressure coefficient becomes too large).

Figure 6.3 shows a typical streamline pattern for large external deceleration. In flowing over the lip of the inlet, the external flow is accelerated to high velocity, much as the flow is accelerated over the suction surface of an airfoil. This high velocity and the accompanying low pressure can adversely affect the boundary layer flow in two ways: For entirely subsonic flow, the low-pressure region must be followed by a region of rising pressure in which the boundary layer may separate. Hence one might expect a limiting low pressure p_{\min} or, equivalently, a maximum local velocity u_{\max} , beyond which boundary layer separation can be expected downstream. For higher flight velocities (or higher local accelerations), partially supersonic flow can occur. Local supersonic regions usually end abruptly in a shock, and the shock-wall intersection may cause boundary layer separation. One might expect a limiting local Mach number that should not be exceeded. Whatever the cause, boundary layer separation is to be avoided, since it results in poor pressure recovery in the flow over the after portions of the aircraft or engine housing. This, of course, results in a net rearward force or drag on the body.

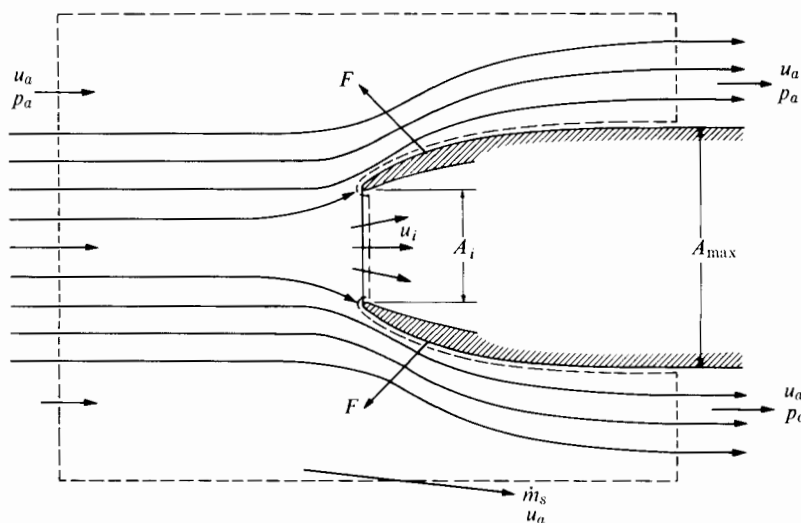


FIGURE 6.3 Control volume for the calculation of thrust on inlet surface.

To illustrate the major features of the external flow near the inlet, consider the simplified problem of an inlet on a semi-infinite body.[†] Küchemann and Weber have shown how to relate the external flow over such a body to the extent of external deceleration of the flow entering the inlet. Suppose (see Fig. 6.3) that the external cross section of the inlet grows to a maximum area A_{\max} and that the body remains cylindrical from this point downstream. A control surface is indicated that extends far from the inlet on the sides and upstream end, crosses the inlet at its minimum area A_i , passes over the inlet surface, and extends downstream far enough for the external fluid velocity to return essentially to the upstream or flight velocity u_a (neglecting boundary layer effects). Thus all the external flow enters and leaves the control volume with an axial velocity component u_a , if one assumes that the sides of the control volume are sufficiently removed from the inlet. The internal flow enters the control volume with velocity u_a and leaves with velocity u_i (assuming, for simplicity, one-dimensional flow in the inlet). The net momentum flux out of the control volume is then, ignoring changes in the air density,

$$\dot{m}_s u_a + \rho u_i^2 A_i - \rho u_a^2 A_{\max}.$$

From continuity, the side flow rate is $\dot{m}_s = \rho u_a A_{\max} - \rho u_i A_i$, so that the net momentum flux can be expressed as $\rho A_i(u_i^2 - u_i u_a)$. The net force in the axial direction on the control volume is

$$p_a A_{\max} - p_i A_i - F_x,$$

where F_x is the axial component of the force on the control volume due to the forces on the external surface of the inlet. If we neglect friction,

$$F_x = - \int_{\text{inlet}} p \mathbf{x} \cdot \mathbf{n} dA = \int_{A_i}^{A_{\max}} p dA_x,$$

where p = pressure on surface,

\mathbf{x} = unit vector along axis in the flow direction,

\mathbf{n} = outward (from the inlet surface) pointing unit vector,

dA = increment of external surface area,

dA_x = increment of external surface area normal to \mathbf{x} ($2\pi r dr$ for an axisymmetric inlet).

Combining these expressions, the momentum equation requires

$$p_a A_{\max} - p_i A_i - \int_{A_i}^{A_{\max}} p dA_x = \rho A_i(u_i^2 - u_i u_a)$$

or

$$\int_{A_i}^{A_{\max}} (p_a - p) dA_x = \rho A_i(u_i^2 - u_i u_a) + (p_i - p_a) A_i. \quad (6.1)$$

[†] An inlet followed by a cylindrical portion several diameters in length would behave similarly, but few practical engine housings are actually cylindrical over any appreciable length.

The equation is arranged in this form because we can consider the integral a component of thrust $\Delta\mathcal{T}_i$, which acts on the front external surface of the inlet due to reduction of local surface pressure. Applying Bernoulli's equation to the external deceleration of internal flow, we obtain

$$p_i - p_a = \rho \left(\frac{u_a^2 - u_i^2}{2} \right).$$

Thus

$$\int_{A_i}^{A_{\max}} (p_a - p) dA_x = \rho A_i (u_i^2 - u_a u_i) + \rho A_i \left(\frac{u_a^2}{2} - \frac{u_i^2}{2} \right)$$

or

$$\frac{\Delta\mathcal{T}_i}{\frac{1}{2}\rho u_a^2 A_i} = \left(1 - \frac{u_i}{u_a} \right)^2. \quad (6.2)$$

This shows that the greater external deceleration (i.e., the smaller the ratio u_i/u_a), the larger must be the “thrust” increment:

$$\Delta\mathcal{T}_i = \int_{A_i}^{A_{\max}} (p_a - p) dA_x.$$

On the outer surface of the nacelle, the pressure must rise from some minimum value p_{\min} (at the point where the local free-stream velocity is u_{\max}) to the ambient value p_a associated in this simplified case with straight parallel flow downstream. Here we neglect the boundary layer except to say that the pressure coefficient

$$C_p = \frac{p_a - p_{\min}}{\frac{1}{2}\rho_a u_{\max}^2}$$

must not be too large or the boundary layer will separate. If, still for the outer surface of the nacelle, we define an average pressure difference

$$\overline{p_a - p} = \frac{\int_{A_i}^{A_{\max}} (p_a - p) dA_x}{A_{\max} - A_i} = s(p_a - p_{\min}),$$

where s is a factor between 0 and 1, we can write

$$\Delta\mathcal{T}_i = s(p_a - p_{\min})(A_{\max} - A_i),$$

so that Eq. (6.2) becomes

$$\frac{s(p_a - p_{\min})(A_{\max} - A_i)}{\frac{1}{2}\rho u_a^2 A_i} = \left(1 - \frac{u_i}{u_a} \right)^2.$$

We can rewrite this as

$$\frac{A_{\max}}{A_i} = 1 + \frac{\left(1 - \frac{u_i}{u_a} \right)^2}{s C_{p\max} \left(\frac{u_{\max}}{u_a} \right)^2}$$

or

$$\frac{A_{\max}}{A_i} = 1 + \frac{\left(1 - \frac{u_i}{u_a}\right)^2 (1 - C_{p\max})}{sC_{p\max}}. \quad (6.3)$$

The value of s will depend on the shape of the nacelle. Taking $s = 0.5$ for purposes of illustration, we can show, as in Fig. 6.4, the dependence of the size of the external surface necessary to prevent external boundary layer separation, for any given value of u_i/u_a .

The main point here is that the larger the external deceleration (i.e., the smaller the value of u_i/u_a), the larger must be the size of the nacelle if one is to prevent excessive drag. Even in the absence of separation, the larger the nacelle, the larger the aerodynamic drag on it. But if the external deceleration is modest (e.g., $u_i/u_a > 0.8$), its effect on minimum nacelle size is quite small. The use of partial internal deceleration is, of course, doubly effective in reducing maximum diameter because it permits a reduction in both A_i and A_{\max}/A_i .

With an aircraft flight Mach number of 0.85, an engine with a transonic fan will require little deceleration of the incoming air, since the allowable absolute Mach number at entry to the fan may be as high as 0.6 or even higher. Still the inlet must be carefully designed for this case. With a flight Mach number of 0.85, the maximum velocity near the external surface could easily be supersonic, so that there is the possibility of shock-induced boundary layer separation. Full allowance for compressibility effects is therefore necessary for inlet design.

To summarize: This analysis pertains to a simplified picture of the real flow around inlets. Nevertheless, it shows that the performance of an inlet depends on the pressure gradient on both internal and external surfaces. The external pressure rise is fixed by the external compression and the ratio, A_{\max}/A_i , of maximum

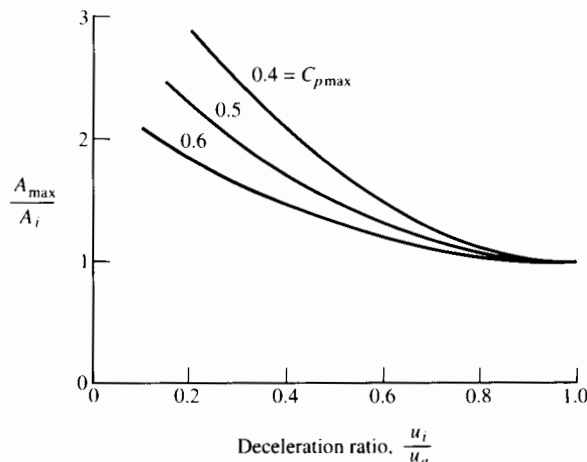


FIGURE 6.4 Minimum frontal area ratio. Various pressure coefficients, $C_{p\max}$ (Eq. 6.3, with $s = 0.5$).

area to inlet area. The internal pressure rise depends on the reduction of velocity between entry to the inlet diffuser and entry to the compressor (or burner, for a ramjet). Nacelle size required for low drag can be quite strongly dependent on the degree of external deceleration. In realistic analyses one must consider compressibility effects.

Inlet Performance Criterion

As Chapter 5 showed, one may characterize the differences between actual and ideal performance of aircraft engine inlets by a “diffuser efficiency” or by a stagnation pressure ratio. We define these as follows:

a. Isentropic efficiency. Referring to Fig. 6.5, we can define the isentropic efficiency of a diffuser in this form:

$$\eta_d = \frac{h_{02s} - h_a}{h_{0a} - h_a} \approx \frac{T_{02s} - T_a}{T_{0a} - T_a}.$$

State $(02s)$ is defined as the state that would be reached by isentropic compression to the *actual* outlet stagnation pressure. Since

$$\frac{T_{02s}}{T_a} = \left(\frac{p_{02}}{p_a} \right)^{(\gamma-1)/\gamma} \quad \text{and} \quad \frac{T_{02}}{T_a} = 1 + \frac{\gamma-1}{2} M^2,$$

the diffuser efficiency η_d is also given by

$$\eta_d = \frac{(p_{02}/p_a)^{(\gamma-1)/\gamma} - 1}{[(\gamma-1)/2]M^2}. \quad (6.4)$$

b. Stagnation pressure ratio, r_d . The stagnation pressure ratio,

$$r_d = p_{02}/p_{0a}, \quad (6.5)$$

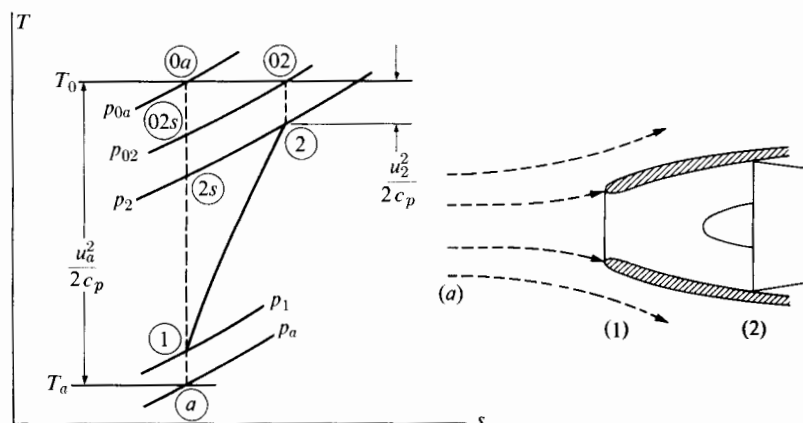


FIGURE 6.5 Definition of inlet states.

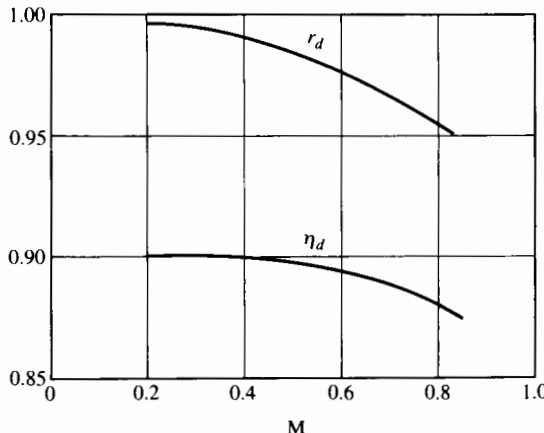


FIGURE 6.6 Typical subsonic diffuser performance; $\gamma = 1.4$.

is widely used as a measure of diffuser performance. Diffuser efficiency and stagnation pressure ratio are, of course, related. In general,

$$\frac{p_{02}}{p_a} = \frac{p_{02}}{p_{0a}} \cdot \frac{p_{0a}}{p_a} = \frac{p_{02}}{p_{0a}} \left(1 + \frac{\gamma - 1}{2} M_2\right)^{\gamma(\gamma-1)},$$

and, with Eqs. (6.4) and (6.5),

$$\eta_d = \frac{\left(1 + \frac{\gamma - 1}{2} M^2\right) (r_d)^{(\gamma-1)/\gamma} - 1}{[(\gamma - 1)/2] M^2}. \quad (6.6)$$

Because η_d will be primarily affected by the internal deceleration ("diffusion"), it is unfortunate that these criteria are based on overall deceleration rather than on internal deceleration. The relationship between internal and external deceleration depends on engine mass flow rate as well as flight Mach number M . But for illustrative purposes Fig. 6.6 gives typical values of stagnation pressure ratio r_d . The diffuser efficiency η_d was calculated from r_d , with the use of Eq. (6.6).

6.3 SUPERSONIC INLETS

Even for supersonic flight it remains necessary, at least for present designs, that the flow leaving the inlet system be subsonic. Compressors capable of ingest-ing a supersonic airstream could provide very high mass flow per unit area and, theoretically at least, very high pressure ratio per stage. However, the difficulty of passing a fully supersonic stream through the compressor without excessive shock losses (especially at off-design conditions) has so far made the development of fully supersonic compressors a possibility that is somewhat remote. As we will see in Chapter 8, the Mach number of the axial flow approaching a subsonic

compressor should not be much higher than 0.4; for a transonic stage it can be about 0.6. The term *transonic* refers here to the flow velocity relative to the blade tip, not to the absolute entrance velocity.

For a ramjet there is no such limitation based on compressor aerodynamics. Also it is possible to have combustion in a supersonic stream without prohibitive aerodynamic losses [7]. The acronym SCRAMJET denotes the supersonic-combustion ramjet, a concept that has long been under study for flight Mach numbers so high that the ramjet should be superior to the turbojet in propulsion efficiency. The SCRAMJET concept has not yet found application in a flight vehicle; ramjets developed to date require subsonic airstreams to provide stable combustion without excessive aerodynamic losses. We do, however, briefly discuss supersonic combustion in Section 6.5. Section 6.6 will give some insight into why a typical Mach number at inlet to a subsonic combustor is 0.4.

Here we focus attention on means of decelerating a supersonic flow to subsonic speeds tolerable by existing compressors or fans (or ramjet combustors).

Reverse Nozzle Diffuser

Figure 3.8 shows that deceleration from supersonic to subsonic flow speeds can be done by a simple normal shock with small stagnation pressure loss if the upstream Mach number is quite close to 1. For high Mach number the loss across a single normal shock would be excessive; in this case it would be better to use a combination of oblique shocks. Isentropic deceleration would be still better. From a simple one-dimensional analysis, it might appear that a supersonic (converging-diverging) nozzle operated in reverse, would be the ideal device to produce nearly isentropic deceleration. There are formidable difficulties, however, in implementing such a concept. These have chiefly to do with the problem of successful operation of a reversed-nozzle inlet over a range of flight Mach numbers and with the serious problem of the interactions of internal shocks with boundary layers. There is also the problem of flow instability; under certain conditions the flow can become quite violently oscillatory.

The Starting Problem

Internal supersonic deceleration in a converging passage (of nonporous walls) is not easy to establish. In fact, as we will now show, design conditions cannot be achieved without momentarily overspeeding the inlet air or varying the diffuser geometry. This difficulty is due to shocks that arise during the deceleration process, and it need not be related to boundary layer behavior. Therefore let us neglect boundary layer effects for the moment, while we examine the starting behavior of a converging-diverging diffuser that is one-dimensional and isentropic except for losses that occur in whatever (normal) shocks may be present. This simplified analysis contains the essential features of the phenomena, and it could be a valid representation of a real flow from which the wall boundary layer fluid was carefully removed by suction through porous walls.

Figure 6.7 illustrates successive steps in the acceleration of a fixed-geometry converging-diverging inlet. To isolate the inlet behavior from that of the rest of the propulsion device, we assume that whatever is attached to the diffuser exit is always capable of ingesting the entire diffuser mass flow. Thus mass flow rate is limited only by choking at the minimum diffuser area A_t .

Condition (a) illustrates low subsonic speed operation, for which the inlet is not choked. In this case the airflow through the inlet, and hence the upstream capture area A_a , is determined by conditions downstream of the inlet. In condition (b), though the flight velocity is still subsonic, the flow is assumed to be accelerated to sonic velocity at the minimum area A_t , and the inlet mass flow rate is limited by the choking condition at A_t . Since the flow is assumed isentropic, then $A_t = A^*$ and the upstream capture area A_a is given by

$$\frac{A_a}{A^*} = \frac{A_a}{A_t} = \frac{1}{M} \left[\frac{2}{\gamma + 1} \left(1 + \frac{\gamma - 1}{2} M^2 \right) \right]^{(\gamma+1)/2(\gamma-1)}. \quad (3.15)$$

For sufficiently high subsonic values of M [see point (b) in Fig. 6.8], we have

$$\frac{A_a}{A^*} = \frac{A_a}{A_t} < \frac{A_i}{A_t}.$$

Thus for these conditions the capture area A_a must be less than the inlet area A_i , and therefore spillage will occur around the inlet.

For sonic or supersonic flight speeds the spillage mechanism is necessarily nonisentropic. That is, in order to "sense" the presence of the inlet and flow around it, the spilled air must be reduced to subsonic velocity upstream of the

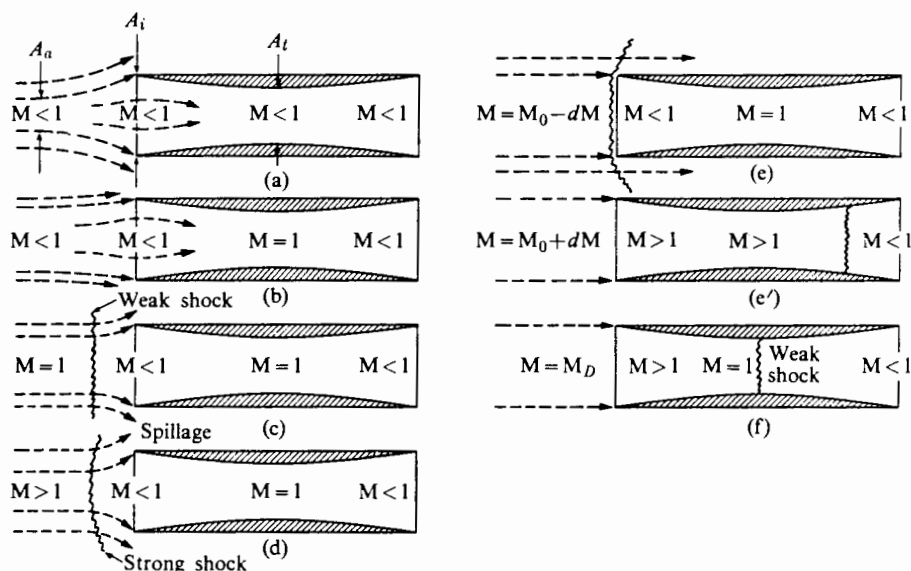


FIGURE 6.7 Successive steps in the acceleration and overspeeding of a one-dimensional supersonic inlet.

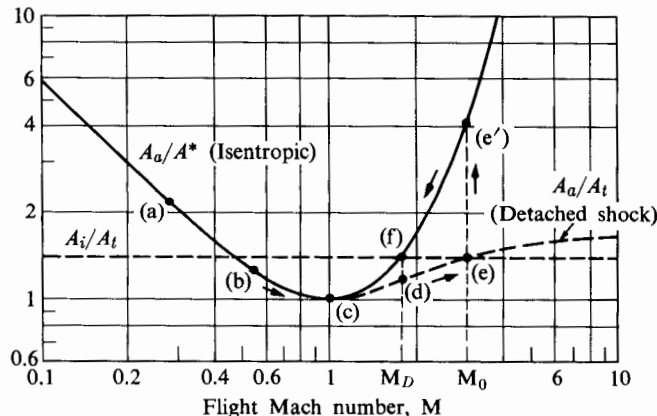


FIGURE 6.8 Acceleration and overspeeding of a one-dimensional supersonic inlet; $A_i/A_t = 1.5$.

inlet plane. The mechanism for this deceleration is a detached “bow wave” that stands sufficiently far upstream to allow the required spillage. One can imagine the process of establishing the detached shock wave as follows: Suppose that when the air first reached supersonic velocity there were no shock. Then flow would have to enter, without deviation, the entire inlet area, in effect making A_i act as the capture area A_a . But for low supersonic Mach numbers (see Fig. 6.8, where $A_i/A_t > A_a/A^*$), the *allowable* capture area as limited by choking at A_t is less than A_i . Hence there would be an accumulation of mass and a rise in pressure in the inlet. This pressure rise would build up rapidly until a shock of sufficient strength moved upstream against the supersonic flow and became established at a position that would allow the required spillage.

Once the shock is established, the flow entering the inlet is no longer isentropic. Hence when the design Mach number of the aircraft is first reached, as at (d) in Fig. 6.7, the “reversed isentropic nozzle” mass flow cannot pass through the throat area A_t . This follows from Eq. (3.14), which indicates that the choked mass flow through a given area (A_t) is proportional to p_0 , and from the fact that the fluid suffers a stagnation pressure loss in traversing the shock. For the flow that *does* enter the inlet (assuming isentropic flow from a point just downstream of the shock to the throat), Eq. (3.15) gives

$$\frac{A_2}{A_t} = \left(\frac{A}{A^*} \right)_2 = \frac{1}{M_2} \left[\frac{2}{\gamma + 1} \left(1 + \frac{\gamma - 1}{2} M_2^2 \right) \right]^{(\gamma+1)/2(\gamma-1)}, \quad (6.7)$$

where the subscript 2 refers to conditions just downstream of a normal shock. We may assume that the slightly curved shock may be approximated over the capture area by a normal shock, so that M_2 may be expressed as a function of the upstream Mach number M by the normal shock relation

$$M_2 = \sqrt{\frac{[2/(\gamma - 1)] + M^2}{[2\gamma/(\gamma - 1)]M^2 - 1}}. \quad (6.8)$$

These two expressions may be combined to give the ratio of capture area to throat area, A_a/A_t , as a function of flight Mach number for the flow that includes a detached normal shock. The result, plotted in Fig. 6.8, indicates that the inlet area A_i will remain too large and spillage will continue even beyond the design Mach number M_D , unless the inlet can be *overspeeded* to a Mach number M_0 . At this Mach number [or just below it, as at (e)], the inlet is capable of ingesting the entire incident mass flow without spillage. The shock position will be just on the lip of the inlet, as in Fig. 6.7(e), and a slight increment in speed, as to (e'), will cause the shock to enter the convergence. Since a shock cannot attain a stable position within the convergence,[†] it will move quickly downstream to come to rest within the divergence, at a position determined by downstream conditions. The flow to the throat is now isentropic, and the area ratio A_a/A^* (now greater than A_a/A_t , since $A_t > A^*$) would be given by (e') of Fig. 6.8. The incoming flow is decelerated from A_i to A_t , whereupon it is reaccelerated supersonically in the divergence. Having thus attained isentropic flow in the inlet, the Mach number may be reduced from M_0 to M_D , as at (f). At exactly the design speed, the throat Mach

[†] Suppose that conditions are such that a stationary shock exists someplace within the convergence. Two conditions are possible for the flow downstream of the shock: Either it is choked at A_t , or it is not choked. If it is choked, the mass flow through the throat is given by Eq. (3.14),

$$\dot{m}_t = p_0 \left[\frac{A_t}{\sqrt{RT_0}} \sqrt{\gamma} \left(\frac{2}{\gamma + 1} \right)^{(\gamma+1)/2(\gamma-1)} \right] = \mathcal{C} p_{02},$$

where, for constant inlet velocity (flight speed), \mathcal{C} is a constant and p_{02} is the stagnation pressure downstream of the shock. Now suppose that a small disturbance moves the shock slightly upstream where the shock Mach number is slightly higher. A greater stagnation pressure loss will occur across the shock, lowering the downstream stagnation pressure and the throat mass flow. Since conditions upstream of the shock are not affected, the mass flow through the shock remains constant and there results an accumulation of mass and a rise in pressure behind the shock. As the static pressure ratio across the shock increases, its propagation speed relative to the fluid increases and the shock moves farther upstream. This further increases the stagnation pressure loss, of course, so that the mass flow imbalance increases and the shock continues to move upstream and out of the inlet. The final position of the shock is far enough outside the inlet area to allow the correct "spilling" of air. By similar arguments one can see that slight motion downstream by the shock is continued until the shock is carried through the throat.

If the flow downstream of A_t is not choked, an appropriate downstream boundary condition might be that at some exit area A_e a constant static pressure p_e is maintained. In this case, for steady flow,

$$\dot{m}_t = \dot{m}_e = \rho_e u_e A_e = \frac{A_e p_e}{R T_e} \sqrt{2 C_p (T_0 - T_e)}.$$

Assuming isentropic flow downstream of the shock, we can express this as

$$\dot{m}_t = \frac{A_e p_e}{\sqrt{RT_0}} \sqrt{\frac{2\gamma}{\gamma-1} \left(\frac{p_{02}}{p_e} \right)^{(\gamma-1)/\gamma} \left[\left(\frac{p_{02}}{p_e} \right)^{(\gamma-1)/\gamma} - 1 \right]}.$$

Thus it can be seen that, since \dot{m}_t is dependent only on p_{02} , changes in shock position result in a mass flow imbalance similar to that for the choked case, and the same conclusions hold: Since any shock would exist in the convergence by moving into it, it follows that no shock can reach a stable position within the convergence.

number would be just unity and isentropic deceleration from supersonic to subsonic flow would exist. Even for this simplified model, however, this condition would be unstable. A slight decrease of flight speed or increase of back pressure would require spillage, and a shock would move rapidly out through the inlet to reestablish condition (d). Thus it might be better to maintain the throat Mach number slightly greater than unity while reaching subsonic velocities through a very weak shock just downstream of the throat.

This simplified description contains the essential feature of the starting problem associated with an internally contracting passage. That is, an inlet having A_i/A_t greater than 1 will *always* require spillage upon reaching supersonic flight velocities, since A_a/A_t will always pass through a minimum of 1 just as sonic flight velocity is attained. It is necessary to perform some operation other than simply accelerating to the design speed in order to "swallow" the starting shock and establish isentropic flow. Overspeeding is one such operation, but there are others.

If overspeeding is not feasible (note that, except for very modest design Mach numbers, substantial overspeed would be required), it might be possible to swallow the shock by a variation of geometry at constant flight speed. The principle is easily seen in terms of simple one-dimensional analysis. Suppose the inlet is accelerated to the design Mach number M_D with the starting shock present, as at point (d) in Figs. 6.8 and 6.9. Now, if the actual area ratio can be *decreased* from A_i/A_t to the value that can ingest the entire inlet flow behind the shock, the shock will be swallowed to take up a position downstream of the throat. This variation would normally involve a momentary *increase* of throat area from A_t to a new value that we will call A'_t (see Fig. 6.9). Having thus achieved isentropic flow within the convergence, the throat Mach number $M_{t'}$ is greater than 1, and a relatively strong shock occurs farther downstream. Completely isentropic flow

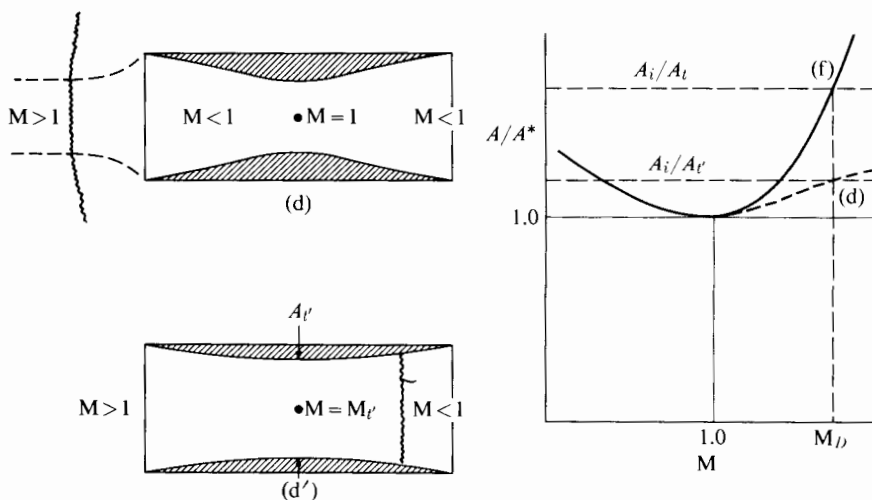


FIGURE 6.9 Shock swallowing by area variation.

can then be achieved by returning the area ratio to its original value, while the operating conditions move from (d) to (f).

A geometric variation such as that shown schematically in Fig. 6.9 would be difficult, mechanically, for axisymmetric flow. However, geometries that permit the axial motion of a center plug between nonparallel walls can be used. A somewhat similar effect can be had through the use of porous convergent walls. With the shock external, the high static pressure within the convergence causes considerable "leakage" through the walls, thus effectively increasing the throat area to permit shock swallowing. Once this occurs, the lower static pressure within the convergence somewhat decreases the flow loss. But since the total porosity required is even greater than the throat area [8], there remains a high mass flow loss under operating conditions. This is desirable to the extent that it removes boundary layer fluid, but the lost flow is more than is needed for this purpose. Flow that is decelerated but not used internally contributes substantially to the drag of the propulsion device.

From this discussion it would seem that one could avoid the starting problem altogether by using a simple divergent inlet, that is, one for which $A_i/A_t = 1$, as shown in Fig. 6.10. For supersonic flight speeds and sufficiently low back pressure, it is possible to accelerate the internal flow within the divergence before decelerating it in a shock. To reduce stagnation pressure losses, it is desirable to have the shock occur at the minimum possible Mach number, which, for this geometry, is the flight Mach number. One can achieve this condition by adjusting the back pressure (by varying the engine exhaust area, for example) so that the shock is positioned just on the inlet lip.

A slight improvement, called the Kantrowitz-Donaldson inlet by Foa [9], is also illustrated in Fig. 6.10. This configuration uses the maximum internal convergence that will just permit shock swallowing at the design flight Mach number. Referring to Fig. 6.9, we can see that this is just $A_i/A_{t'}$ for a design Mach number

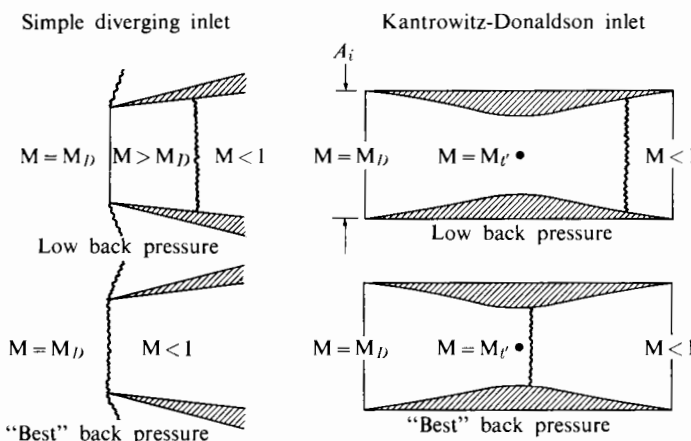


FIGURE 6.10 Fixed-geometry diffuser with intentional normal shocks at the design Mach number M_D . (Refer to Fig. 6.9.)

of M_D . As in the simple divergent inlet, it is necessary to adjust the back pressure to assure that the shock occurs at the minimum possible Mach number. The advantage of the internal convergence is, of course, that this minimum Mach number is less than the free-stream value. A disadvantage is that there is an abrupt change in performance just at the design Mach number, since the shock will not be swallowed below this value and it will be immediately disgorged if the speed falls off slightly from the design value. Further, since shocks of any origin are unstable within the convergence, such an inlet would be quite sensitive to changes in angle of attack.

The condition in which a shock just hangs on the inlet lip is called the *critical condition*. Operation with the shock swallowed is called *supercritical*, whereas that with a detached shock and spillage is called *subcritical*. Note that subcritical operation may occur as the result of choking in the inlet, as discussed here for inlets alone; or, for a complete engine, as the result of any downstream flow restriction that cannot accept the entire mass flow $\rho_a u_a A_i$.

The Shock-Boundary Layer Problem

As we noted earlier, sketches such as Figs. 6.9(d') and 6.10 are realistic only if the boundary layer fluid is removed from the walls between which the shock is located. Across a shock wave of appreciable strength, the boundary layer separates, and this separation may have a large effect on the structure of the shock. We might suppose, in accord with the boundary layer concepts discussed in Chapter 4, that a turbulent boundary layer will separate when the shock-induced velocity reduction is between 20% and 30% ($0.36 < C_p < 0.51$). Using the normal shock relationships of Chapter 3, we can see that this would correspond to upstream Mach numbers of 1.15 (20% reduction in velocity) or 1.25 (30% reduction).

To begin, we consider the interaction of a weak shock with a boundary layer. Figure 6.11 is a series of schlieren photographs of the interaction of a shock wave and a boundary layer for upstream free-stream Mach numbers ranging from 1.30 to 1.55. Schlieren photographs show regions of high-density gradient [7], so they reveal sharply the presence of stationary shock waves as well as the presence of boundary layers in a compressible flow. In Fig. 6.11(a) we can see what is nearly a plane normal shock wave (with an upstream Mach number M of 1.3) and a wall boundary layer whose thickness is growing perceptably in the flow direction. In Fig. 6.11(d), for $M = 1.4$, the shock wave near the boundary layer has taken up a "lambda" shape, with an oblique shock reaching ahead of the main shock location. Because a large fraction of the boundary layer is subsonic, the pressure rise due to the shock is sensed (near the wall) some distance ahead of the main shock wave. This upstream pressure gradient causes the boundary layer to grow rapidly, as one can see from close inspection of Fig. 6.11(d). The increase in displacement thickness affects the flow in the same way as would a wedge in inviscid flow; hence an oblique shock is formed ahead of the main wave.

As the free-stream Mach number increases above perhaps 1.25, the boundary layer thickens very rapidly under this lambda shock system (see, e.g., Fig. 6.11(i)) and causes the boundary layer to separate. The pressure gradient near the wall

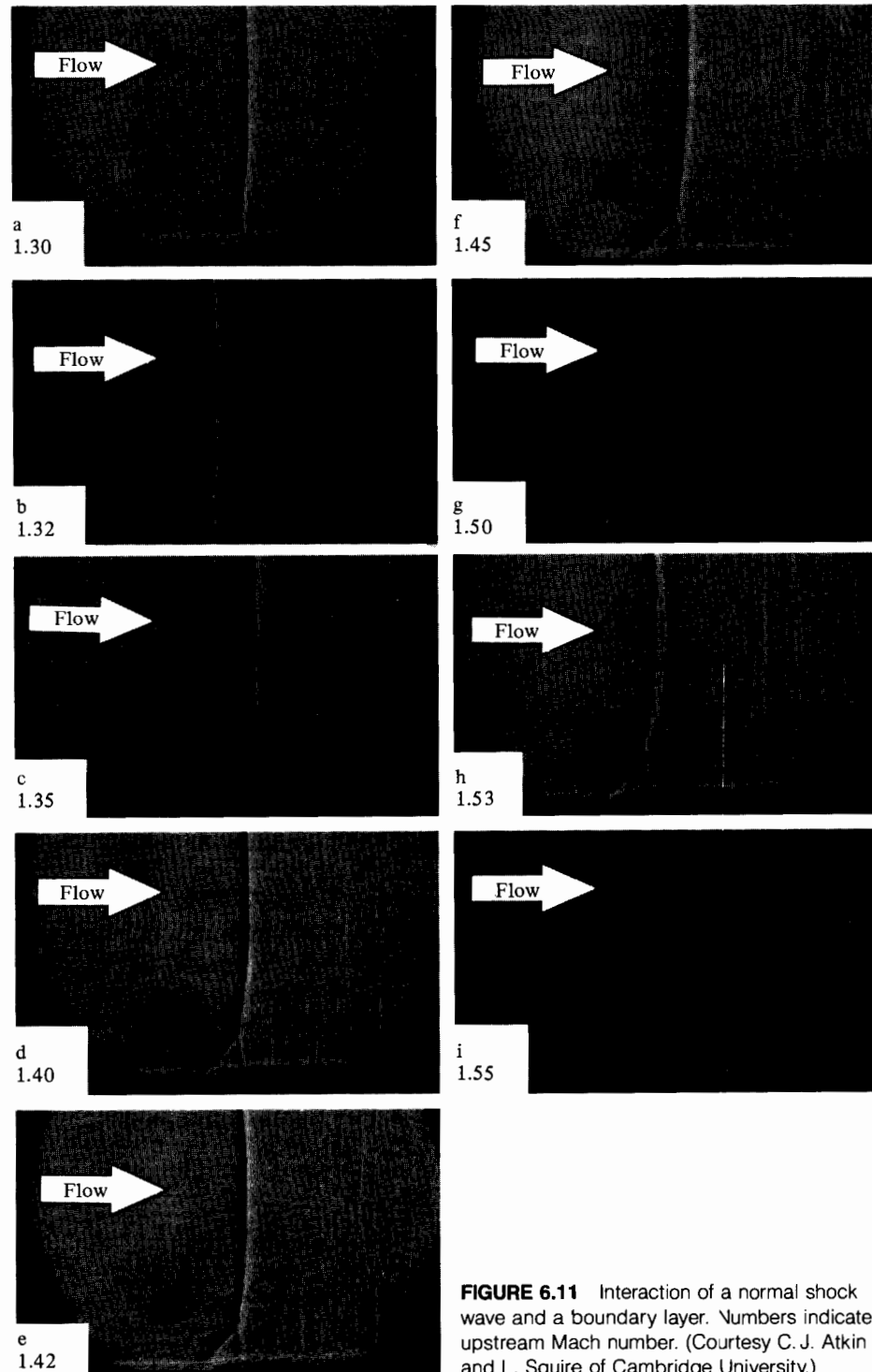


FIGURE 6.11 Interaction of a normal shock wave and a boundary layer. Numbers indicate upstream Mach number. (Courtesy C. J. Atkin and L. Squire of Cambridge University.)

has become too large for the slow-moving fluid near the wall to continue moving in the main flow direction.

Figure 6.12 shows the effect of a strong shock in a diverging duct. Here the main stream-flow adjustment is very far from the simple normal shock picture in Fig. 6.11. Instead the interaction between the "shock" and the boundary layer results in at least five major pressure adjustments (shown by the X-like dark regions in Fig. 6.12). Large separation zones cause a highly distorted, and probably unsteady, flow field that may require an axial distance of 10 duct widths or more to return to reasonable uniformity of flow. The flow field disturbances and distortions shown in Fig. 6.12 would have seriously harmful effects on the behavior of a compressor or combustor placed immediately downstream.

The chief lesson here is that unless one makes a strenuous effort to remove the wall boundary layer, strong shocks may have disastrous effects on duct flow. If a shock wave must be placed in a supersonic stream of given Mach number, then:

- a. An oblique shock is much better than a normal one because the pressure rise is less;
- b. The shock should interact with the wall at the point where the boundary layer is thinnest—preferably at the leading edge for the simple diverging inlet of Fig. 6.10.

External Deceleration

The absence of a starting problem for the normal shock inlet is offset by the accompanying stagnation pressure loss at all but low flight Mach numbers (less than about 1.5). For example, Fig. 3.8 indicates a 28% stagnation pressure loss at $M = 2$ ($\gamma = 1.4$). If we wish to obtain reasonable performance while maintaining the starting characteristics of a simple divergent inlet, then it is clear that some *external* deceleration must occur upstream of the inlet plane in order to reduce the Mach number of the normal shock to a suitable value.

The simplest and most practical external deceleration mechanism is an oblique shock or, in some cases, a series of oblique shocks. Though such shocks are

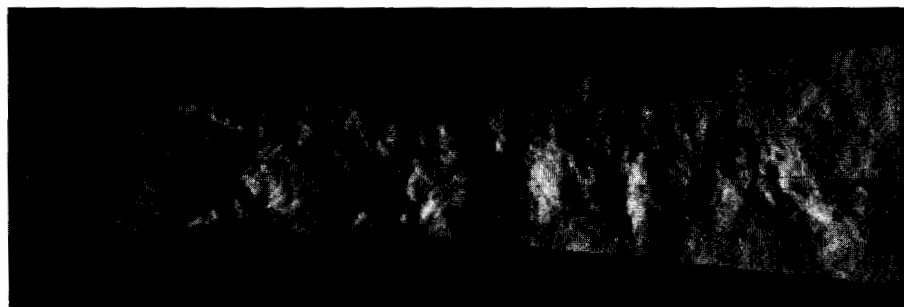


FIGURE 6.12 Shock–boundary layer interactions in a duct. Flow from left to right. (Courtesy M.I.T. Gas Turbine Laboratory.)

not isentropic, the stagnation pressure loss in reaching subsonic velocity through a series of oblique shocks followed by a normal shock is less than that accompanying a single normal shock at the flight velocity. The losses decrease as the number of oblique shocks increases, especially at high flight Mach numbers.

In the external compression process, shocks and boundary layers may interact strongly, so that it is highly desirable to locate the oblique shocks at points where boundary layers are absent. This can be arranged easily if one uses a center body (primarily for axisymmetric flow), as in Fig. 6.13. These schematics, taken from Oswatitsch [10], illustrate the typical single oblique shock system and two double oblique shock systems. Although the double shock systems theoretically give better performance, one can see that several problems may arise in their use. In the configuration of Fig. 6.13(b), the second shock, generated by a turn of the wall, occurs at a point where the boundary layer has had time to develop, and separation may result. The configuration of 6.13(c) avoids this at the point of shock generation, but the second shock still intersects the boundary layer on the center body.

With (if need be) boundary layer removal, we can appreciate the performance gain to be expected through the use of multiple oblique-shock deceleration by looking at a two-dimensional example. Consider the diffuser in Fig. 6.14, in which the flow is deflected through two 15° angles before entering a normal shock. Using Fig. 3.12, we can show that the Mach numbers in regions (2), (3), and (4) are 2.26, 1.65, and 0.67, respectively. Then, using Fig. 3.11, we can obtain the stagnation pressure ratios as follows:

$$\frac{p_{02}}{p_{01}} = 0.895, \quad \frac{p_{03}}{p_{02}} = 0.945, \quad \frac{p_{04}}{p_{03}} = 0.870.$$

Thus the overall stagnation pressure ratio is approximately $p_{04}/p_{01} = 0.735$. If the deceleration had been achieved by a single normal shock, the overall stagnation pressure ratio would have been only 0.33. Remember that these estimates do not include losses due to boundary layer effects, which may be especially important in the subsonic diffuser.

This example does not necessarily employ the best arrangement of three shocks, of course, since a variation of their relative strengths might provide a higher overall stagnation pressure ratio. For the simple two-dimensional case, in

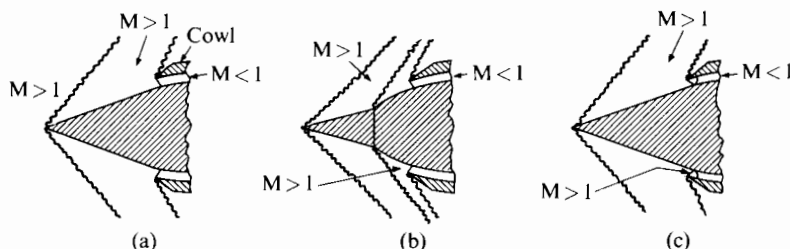


FIGURE 6.13 Typical configurations for oblique shock diffusers. (Adapted from Oswatitsch [10].)

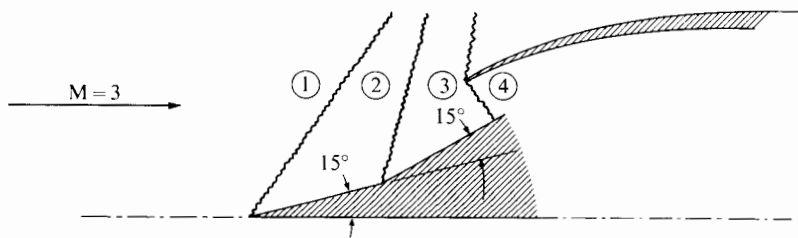
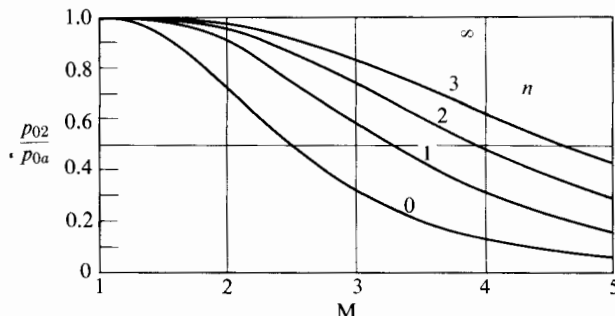


FIGURE 6.14 Two-dimensional diffuser.

which conditions downstream of each shock are uniform, Oswatitsch [10] has shown by theoretical analysis that, for a given flight Mach number and a given number of oblique shocks followed by one normal shock, the overall stagnation pressure ratio will be maximized if all the oblique shocks have equal strength, that is, if the Mach numbers of the velocity components normal to each shock, and incident to it, are equal. It follows, of course, that the stagnation pressure ratios will also be equal. This result will not seem unreasonable if we recall that for a normal shock the stagnation pressure loss rises very quickly with incident Mach number. Oswatitsch found that the Mach number of the final normal shock should be *less* than the normal component of the oblique shocks (about 0.94 times as great). Figure 6.15 shows the best performance using n oblique shocks of equal strength followed by one normal shock.

For axisymmetric inlets and conical shocks, the best arrangement is not so easily determined, since the downstream flow of a conical shock is not uniform. In fact, fluid properties are constant along conical surfaces emanating from the shock vertex, and the streamlines downstream of the shock are curved [11]. The effect of the streamline curvature is further diffusion, which can be very nearly isentropic, so that subsequent shocks occur at reduced (but nonuniform) Mach numbers. It is even possible to achieve deceleration to subsonic velocities behind a conical shock without subsequent shocks, as shown for a rather low Mach number in Fig. 6.16.

The performance advantage of multiple conical shocks is qualitatively similar to that of the multiple-plane shocks shown in Fig. 6.15. Going to the limit (for

FIGURE 6.15 Best stagnation pressure ratio for diffuser consisting of n oblique shocks of uniform strength and one normal shock; $\gamma = 1.4$. (After Oswatitsch [10].)

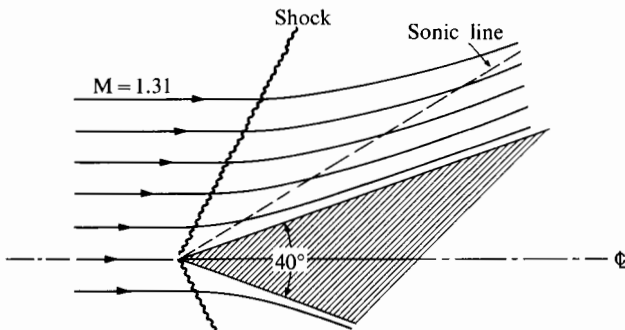


FIGURE 6.16 Typical conical-flow streamlines. (After Shapiro [12].)

either axisymmetric or two-dimensional geometries) of an infinite number of infinitesimal shocks, generated by continuous wall curvature, one could, theoretically at least, achieve isentropic external deceleration to sonic velocity. Such an inlet, indicated qualitatively in Fig. 6.17, would seem to provide the ideal geometry to achieve low losses, while at the same time avoiding the starting problems of an internal convergence. However, several practical difficulties would be encountered in the operation of such an inlet. This geometry, like that of the isentropic internal flow diffuser, would function properly at only one Mach number, and performance would be very sensitive to angle of attack. Furthermore, the boundary layer along the curved surface, unlike that along plane or conical surfaces, would be subject to a high adverse pressure gradient, which might cause separation. Finally, for high flight Mach numbers it would be necessary that the flow turn through large angles before reaching sonic velocity. The resultant large cowl angle would at least exhibit high drag and perhaps even interfere with the inlet flow.

It will be clear from the foregoing that variable geometry is an almost inescapable requirement for an engine inlet that must operate at both subsonic and supersonic speeds. Fig. 6.18 shows the design of the two-dimensional intake adopted for the Concorde aircraft, whose design flight Mach number is 2; the Concorde is also required to cruise over certain land areas at subsonic speeds.

Figure 6.18 shows the intake geometry during takeoff; here the ramp assembly is raised to allow as much air as possible to the engine. Shock waves are of

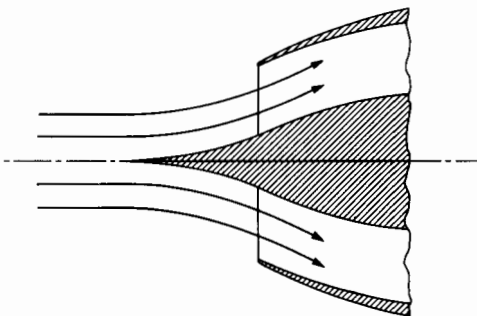


FIGURE 6.17 Isentropic external diffuser.

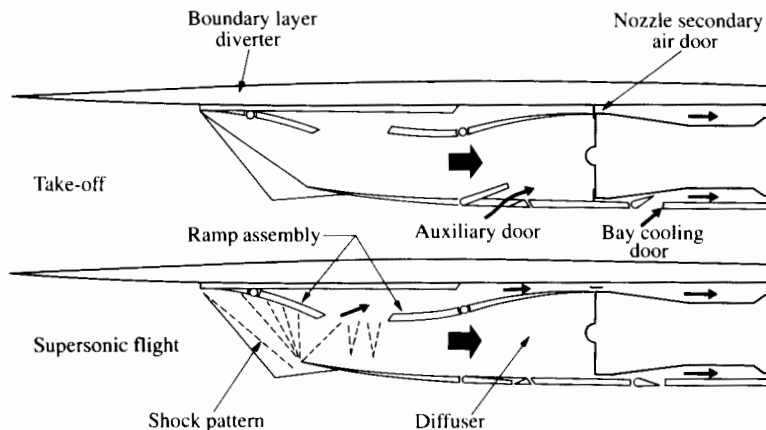


FIGURE 6.18 Cross sections of variable-geometry intake for Concorde supersonic aircraft.
(Courtesy Rolls-Royce, plc.)

course absent as the air enters the engine with a Mach number of about 0.5. As the Concorde reaches a flight Mach number of about 0.7, the auxiliary door closes. Above a flight Mach number of 1.3, the ramps are progressively lowered; the forward ramp controls the position of the oblique shock waves that decelerate the airstream from supersonic to subsonic speeds at the engine intake.

The Flow Stability Problem

The operation of external shock diffusers is divided into subcritical, critical, and supercritical modes, which depend on the external and internal shock configuration. The three modes are shown schematically for a typical case in Fig. 6.19. With entirely diverging internal flow such as this, the normal shock position is determined by a downstream flow restriction rather than by the inlet geometry. Hence the operating mode is sensitive to variations in exhaust-nozzle area and fuel flow rate. Subcritical operation entails “spilling” of flow and a normal shock upstream of the inlet. “Low” and “high” subcritical operations differ only in the extent of spilling. Supercritical operation occurs at the same mass flow as critical operation, but with increased losses, since the normal shock occurs at a higher Mach number.

Numerous investigators have tested the performance of experimental supersonic diffusers, owing to the substantial importance of inlet performance, especially at high Mach numbers. A wide variety of geometries have been considered, each depending on a particular application. Special attention is paid to the off-design performance of an inlet; this is of great importance in an actual flight application but is not so amenable to analysis as the design performance. Various adjustable intakes have been considered to extend the favorable operating range of an inlet.

The data of Dailey [13] are typical of many investigations of an important instability that occurs during the subcritical operation of most supersonic intakes. This phenomenon, known as “buzz,” consists of a rapid oscillation of the inlet

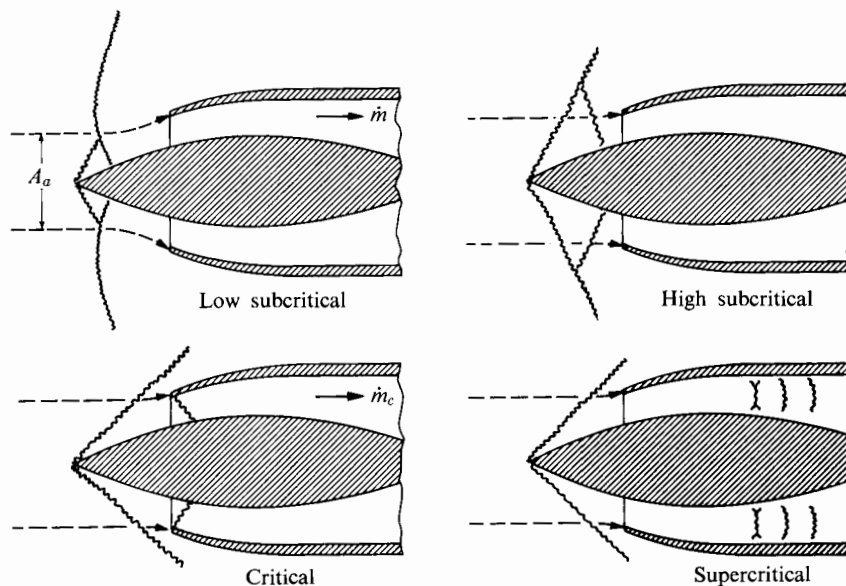


FIGURE 6.19 Typical modes of inlet operation.

shock and flow pattern; the resultant internal disturbance is very detrimental to engine performance. In a ramjet, for instance, the onset of buzz usually extinguishes combustion. Although the pulses of the shock system are similar, the interval between pulses is not constant [13]; hence buzz cannot be considered a periodic phenomenon. Although it is not thoroughly understood at present, buzz has been shown to be a function of conditions only at, and immediately downstream of, the inlet. In some cases boundary layer bleed from the center body can delay the onset of buzz. In other cases the use of a length of nondivergent subsonic passage just downstream of the inlet can have a beneficial effect. This latter case could be attributed either to the establishment of a healthy boundary layer (as compared with a separated one just downstream of the normal shock) or to the establishment of more uniform free-stream conditions (see below) before subsonic diffusion is attempted.

Figure 6.20 is a plot of typical diffuser performance as a function of mass flow, expressed as the ratio of actual to critical (or supercritical) mass flow rate \dot{m}_c , or the equivalent ratio of actual to critical capture area. Ratios of \dot{m}/\dot{m}_c less than 1 signify subcritical operation. One can see that for mass flows slightly less than critical (the so-called high-subcritical flow) the stagnation pressure ratio increases slightly with decrease in mass flow rate. This is explained by the presence of lower aerodynamic losses in the internal passages due to reduced mass flow and velocity. *Overall* performance, of course, does not increase with subcritical operation, since spilling is accompanied by both increased drag and decreased thrust. As the flow is further reduced, the normal shock is pushed farther stream and the stagnation pressure ratio decreases. A portion of the air entering the cowl may travel through a single strong shock (see "low subcritical," Fig. 6.19)

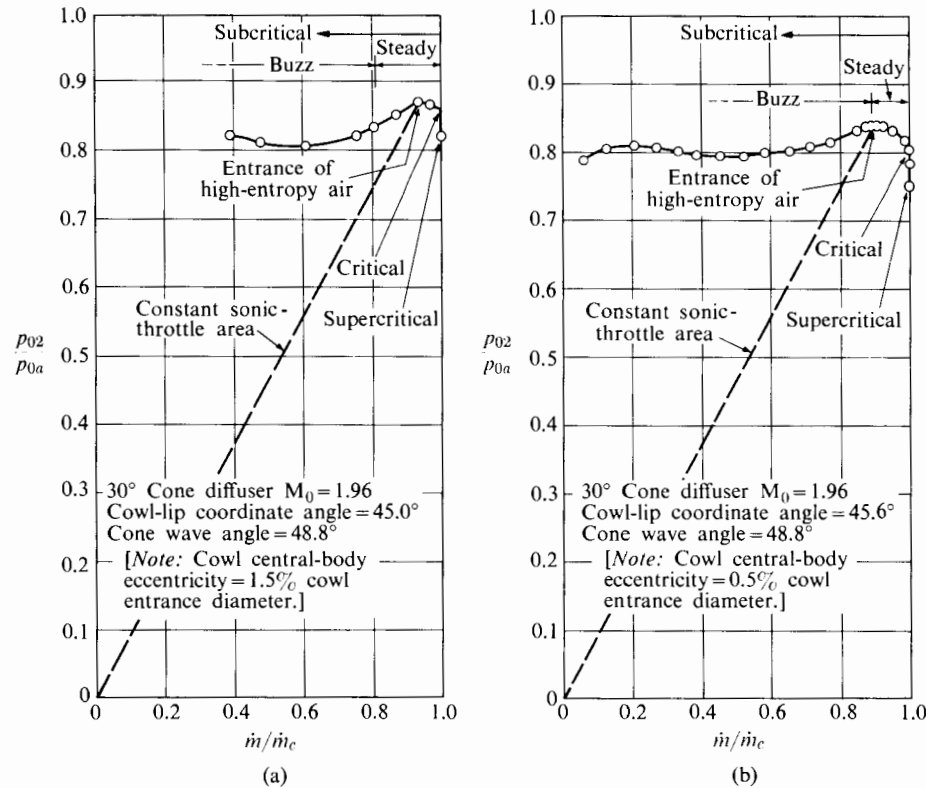


FIGURE 6.20 Typical supersonic inlet performances. (Courtesy Dailey [13].)

rather than the two weaker shocks it would pass through during critical operation. The entrance of this low-stagnation pressure (or high-entropy) air causes a reduction in performance. In supercritical operation the stagnation pressure ratio drops rather rapidly at constant mass flow rate.

We can see by comparing Figs. 6.20(a) and (b) that the ingestion of low-stagnation pressure air may or may not correspond to the onset of buzz (although it usually does).

For both subsonic and supersonic intakes, the best balance of external and internal deceleration is a matter of concern because of the need to keep nacelle drag as low as possible and to supply uniform flow to the engine. For the subsonic intake, fixed geometry can generally provide acceptable boundary layer behavior over all flight speeds from takeoff to cruise. For supersonic flight, shock waves are a practical necessity for deceleration of the inlet air to subsonic speeds; the inlet geometry required to minimize shock and boundary layer losses depends strongly on Mach number. This means that to cope with a wide range of flight Mach numbers, variable geometry is needed. The control of the intake geometry must be done carefully to avoid flow instability. Large perturbations in the geometry of the inlet shock pattern could disturb the engine intake flow sufficiently to cause serious problems for the compressor or burner.

6.4 GAS TURBINE COMBUSTORS

The working fluid in the engine is “heated” by an internal combustion process. Before this chemical reaction can occur, the liquid fuel must be injected into the airstream, atomized, and vaporized, and the vapor must be mixed with the air. All this takes time and space. Space is of course at a premium in aircraft applications, so that great effort is made to reduce the size of the combustion chamber by hastening completion of the above processes. To keep engine size small, the intensity of combustion (measured in, e.g., $\text{kJ}/\text{m}^3\text{s}$) must be as high as possible. The combustion rate in gas turbines at sea level is of the order of 500,000 $\text{kJ}/\text{m}^3\text{s}$, which is more than 100 times as intense as the combustion in a large stationary power plant furnace. Part of the reason for the difference is that in the gas turbine the density of the reactants is perhaps 10 times as high as in an atmospheric-pressure furnace. Part of the reason is the fineness of atomization of the injected fuel and another part is the intensity of the turbulence in a typical gas turbine combustor. The more intense the turbulence, the more rapid the mixing of the vaporized fuel and air, and the faster the propagation of flame through the unburned mixture. Before considering typical designs of combustors for air-breathing jet propulsion engines, we consider the combustion temperatures available with typical fuels.

Combustion Temperature and Fuel–Air Ratio

Table 6.1 shows the properties of fuels commonly used in gas turbine combustors. Each fuel is a mixture of hydrocarbon compounds, and the mixture composition is variable to some extent. Table 6.1 therefore provides representative (rather than exact) properties typical of the mixtures that fall within the specification limits for each fuel. JP-4 is relatively volatile and so has high vapor pressure.

TABLE 6.1 Typical property values for aviation fuels

Property	Aviation kerosine	JP-4	JP-5	Jet A
H–C ratio	1.93	2.02	1.92	1.94
Vapor press at 38°C, kPa		18	0.3	0.7
Initial boiling point, °C	50	60	180	170
End point, °C	260	246	260	265
Flash point, °C		–25	65	52
LHV, kJ/kg	43,200	43,400	43,000	43,400
Density, kg/m ³	800	760	820	810
Stoich. fuel-air mass ratio	0.0679	0.0673	0.0680	0.0678
Stoich. air-fuel mass ratio	14.72	14.85	14.71	14.74

JP-4 and Jet A are widely used fuels for gas turbines. Aviation kerosine is not in plentiful supply.

For approximate calculation of fuel-air ratio and combustion temperature we can describe these fuels as having hydrogen-carbon ratios of 2 and lower heating values (LHV) of 43,400 kJ/kg. Then, treating the turbojet combustion process as though it were a heating process, we can write

$$\dot{m}_f Q_R = \dot{m}_a c_p (T_{04} - T_{03}),$$

where \dot{m}_f is the fuel flow rate, \dot{m}_a is the airflow rate, and c_p is the specific heat at constant pressure. In terms of the fuel-air ratio $f = \dot{m}_f / \dot{m}_a$,

$$f = \frac{c_p}{Q_R} (T_{04} - T_{03}).$$

As an example, an engine flying in a 222-K (-60° F) atmosphere at Mach 0.8 with a compressor pressure ratio of 30:1 and a compressor adiabatic efficiency of 85% will have a burner inlet temperature of about 600 K. If the turbine inlet temperature is 1600 K, Q_R is 43,400 kJ/kg, and the average c_p is 1.08 kJ/kg · K, the fuel-air ratio would be

$$f = \frac{1.08(1600 - 600)}{43,400} = 0.025.$$

From Table 6.1 the stoichiometric fuel-air ratio is about 0.067. The so-called equivalence ratio is

$$\phi = \frac{f}{f_{\text{stoich}}} = \frac{0.025}{0.067} = 0.37.$$

Thus, to prevent excessive temperature at the exit of the combustion chamber, the fuel-air ratio must be much less than stoichiometric. Figure 6.21 illustrates the difficulty of lean-mixture combustion of hydrocarbon fuels for a gasoline-air mixture. If f were required to be 0.025 and if all the air were to be initially mixed with all the fuel, the resulting mixture would be much too lean for ignition and combustion. For this reason the fuel in gas turbine combustors is initially mixed and burned with a small amount of "primary" air. After combustion the products are diluted and cooled by the remaining air.

In the preceding discussion we used an approximate method of finding the fuel-air ratio for a given turbine inlet temperature. Figures 6.22 and 6.23 show the results of more exact calculations that allow for variability of specific heats and also for the possibility of dissociation.

Figure 6.22 pertains to the product mixture leaving the combustor and entering the turbine. At mixture temperatures of less than 1800 K ($\phi < 0.5$), there is no observable effect of dissociation, that is, no apparent effect of pressure on product temperature. With respect to the previous example of 600 K reactant temperature and 1600 K product temperature, the equivalence ratio shown in Fig. 6.22 is 0.41. (This differs somewhat from the above approximate value but does not lead to a different conclusion.) With Figs. 6.22 and 6.23 in mind, one

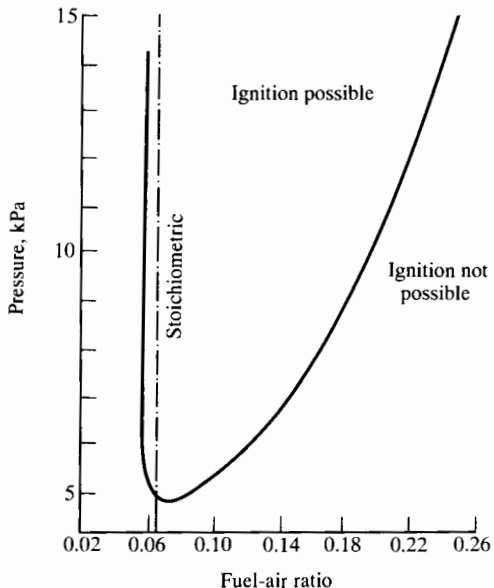


FIGURE 6.21 Inflammability limits of gasoline-air mixtures. (Adapted from Olson, Childs, and Jonash [14].)

can appreciate why, to promote stable and rapid burning, it is necessary to supply less than half the compressor delivery air directly to the primary combustion zone; most is used for diluting the combustion products to reduce the temperature following combustion.

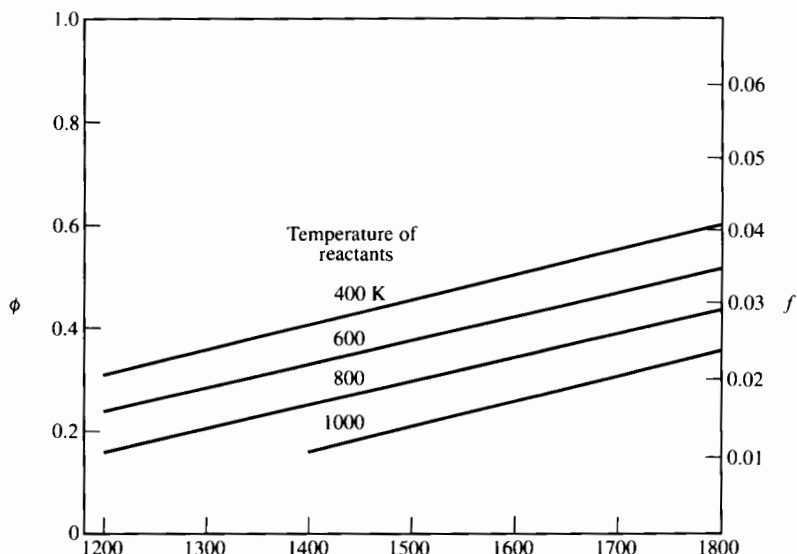


FIGURE 6.22 Turbine inlet temperature K; fuel H-C ratio = 2, $Q_R = 43,400 \text{ kJ/kg}$.

Figure 6.23 allows us to consider the combustion zone where ϕ will be close to unity. It shows the effect of equivalence ratio on the adiabatic flame temperature. The pressure dependence is solely a result of dissociation (greater at lower pressure). In these calculations we assume that each constituent of the combustion product mixture behaves like an ideal gas. The dissociated products include CO, NO, H, OH, O, and N. With no dissociation and a combustor inlet temperature of 1000 K, the maximum temperature would be about 3000 K. Dissociation at 30 atm pressure reduces this temperature to about 2750 K. Lowering the pressure by an order of magnitude (corresponding to the difference between high-altitude and sea-level flight) reduces the maximum temperature to about 2650 K. The significance of this is not that it has much effect on the combustor efficiency or stability, but that the oxides of nitrogen, formed during the high-temperature combustion, do not entirely disappear as the temperature is lowered. The combustion gases can be close to equilibrium in the high-temperature zone of the combustor, but the rapid subsequent “quenching” of the product mixture leaves a portion of the nitrogen oxides locked in, and they emerge from the turbine as potential contributors, along with unburned hydrocarbons, to photochemical smog.

A major challenge in gas turbine or ramjet combustor design is in protecting the metal chamber liner from direct contact with hot combustion gas. As we

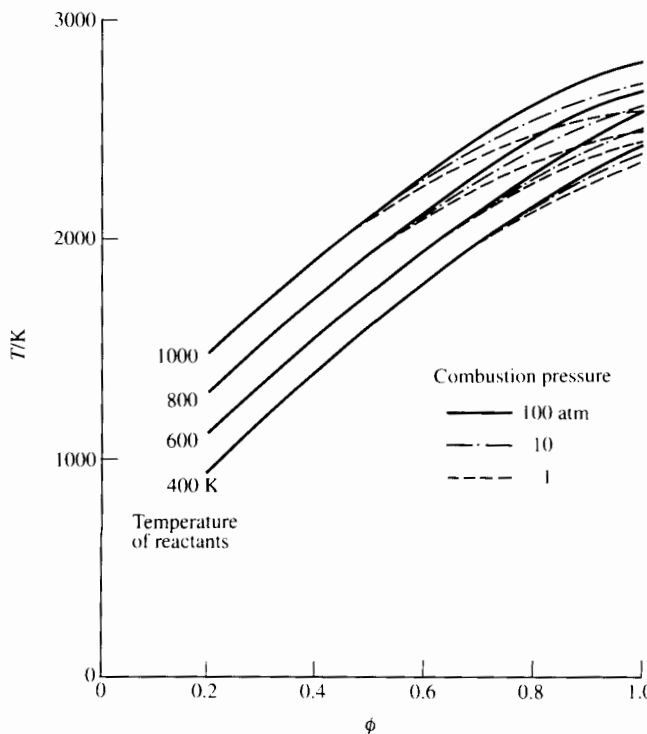


FIGURE 6.23 Adiabatic flame temperature; fuel H–C ratio = 2, $Q_R = 44,300 \text{ kJ/kg}$.

noted in Chapter 5, typical turbine inlet temperatures can be as high as 1600–1700 K, whereas the limiting metal temperature would be of the order of 1200 K. So far, high-temperature ceramic surfaces have not proved sufficiently durable for practical use. Substantial quantities of cooling air are needed to prevent warping, buckling, or even melting of the chamber liner. This is in principle no problem since, as noted earlier, allowable turbine inlet temperatures are much less than stoichiometric, and much of the air supplied must therefore bypass the combustion zone. In practice though, it is not easy to distribute the airflow within the combustor to meet all combustion and cooling requirements at all operating conditions.

Flame Propagation

In general the performance of air-breathing jet engines is strongly dependent on the mass flow rate per unit cross-sectional area of the engine. A large area for a given flow rate implies not only large engine mass per unit thrust but also large nacelle drag for an externally mounted engine or large volume for an engine placed inside the fuselage. For this reason it is desirable for the velocity of the working fluid to be as high as possible without incurring excessive losses due to shocks, wall friction, and viscous mixing. A limitation is imposed by the combustor since it is necessary to maintain a stationary flame within a moving airstream.

For the moment we neglect the complications of injection, and so on, and imagine the flame as propagating through a combustible mixture at the “flame speed,” while the mixture is carried downstream. To avoid flame travel out of the combustion chamber, it is necessary to maintain the mixture velocity within certain limits: If the velocity is too high, the flame will be “blown out” the exit; if too low, the flame will travel upstream and be extinguished. It is not necessary, however, that the mixture velocity be exactly equal to the flame speed since, as we will see, the flame front need not be normal to the flow. (If it were, an enormous cross-sectional area would be required.)

A flame will travel into a mixture of reactants at a rate that is dependent on the state of the reactants and is limited either by mixture turbulence or by chemical kinetics. (We first consider flames whose rate of burning is limited primarily by turbulence level.) A flame remains stationary in a traveling mixture of reactants if the speed of the flame relative to the reactants is just equal to the reactant-mixture velocity. Figure 6.24 shows typical mixture velocities associated with stable flames. The lower curve represents undisturbed (laminar) flow, and the upper curve represents combustion in the highly turbulent flow downstream of a perforated plate. These curves were obtained for one particular inlet temperature and pressure. Figure 6.24 points out two important things. First, it reemphasizes the necessity of initial burning in primary air—for lean final mixtures. Second, it shows the tremendous influence of turbulence on flame velocity. The perforated plate creates local low-velocity regions that “hold” the flame and generate enough turbulence to make flame speed an order of magnitude greater than for laminar flow. The turbulence level varies considerably in various combustion chambers and may differ considerably from that behind a perforated

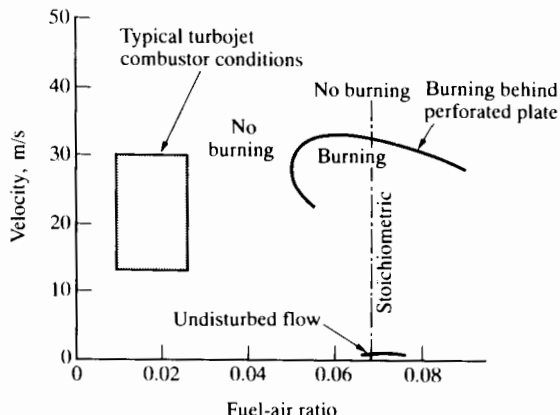


FIGURE 6.24 Dependence of flame speed on fuel-air ratio. (Adapted from Olson, Childs, and Jonash [14].)

plate, so the upper curve of Fig. 6.24 only qualitatively describes flame speed in actual combustors.

To keep the engine cross section small, the average axial velocity of the reactants passing through the combustor is of the order of 30 m/s. For hydrocarbon fuels the velocity of a laminar flame (relative to the unburned mixture) ahead of the flame would be about 1 m/s at combustor inlet conditions. Turbulence can raise the burning velocity to perhaps 5–8 m/s, but even so the flame could not possibly have a stable position in a stream of velocity 30 m/s. Part of the art of combustor design is provision of zones of low velocity in which flames can propagate into an unburned mixture. In ramjet combustors this is done by placing obstructions (V-shaped “gutters”) in the flow, in whose wake regions a stable combustion may be maintained. In gas turbine combustors recirculations can be established that provide regions of slow velocity. These are mainly due to swirling motion around the chamber axis set up by jets of cooling air entering the chamber. Associated with the swirl is backflow along the axis of the combustion zone.

As we mentioned earlier, the rates of reaction in a gas turbine combustion chamber are affected by both mixture turbulence (which controls the rate of mixing of fuel and air and the instantaneous geometry of the flame surface) and chemical kinetics. The latter are strongly dependent on mixture pressure. During sea-level operation the pressure is high enough that chemical reaction rates are typically much faster than turbulent mixing rates. This means that combustion intensity depends mainly on turbulence intensity (and the provision of a recirculation flow pattern to keep the combustion zone stable). At high altitude, where the pressure is greatly reduced, chemical reaction rates may be much slower than turbulent mixing rates. Thus even though a high degree of mixing occurs, combustion may be incomplete.

One demonstration of the importance of this effect is the typical decline in combustion efficiency with altitude. Figure 6.25 shows the experimental effect of altitude on three combustion chambers. Combustion efficiency is a measure of combustion completeness and may be defined as the actual temperature rise

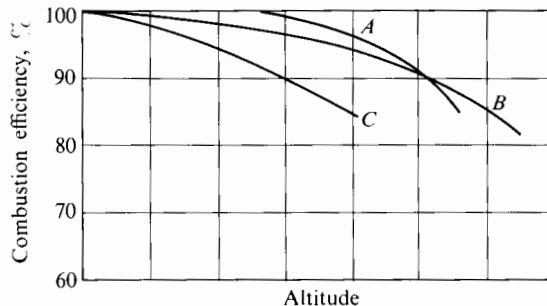


FIGURE 6.25 Variation of combustion chamber efficiency with altitude, for three combustors.
(Courtesy Olson, Childs, and Jonash [14].)

divided by the theoretical (complete-combustion) temperature rise. Although efficiencies of 99% are possible at sea level, at some altitude a given combustor will cease operating altogether.

One can appreciate the effects of pressure and temperature on combustion by considering the nature of the chemical process. The probability of chemical combination of atoms or molecules depends on the frequency of molecular collisions and on the energy of the colliding molecules. Below the ignition temperature, practically no reaction occurs. A certain "threshold" energy level is necessary to initiate significant reaction. Combustion proceeds as a chain reaction in which energy released from one combination is sufficient to raise neighboring atoms above the threshold energy, thereby inciting further chemical combinations so that the process continues. Raising the temperature decreases the energy that, on average, must be added to a particle before the reaction threshold is reached. For a given temperature, high pressure corresponds to high density, and this means greater frequency of collision of fuel and oxidant atoms.

In part we can understand the consequence of operating gas turbine combustors at high altitude by considering the relative effects of pressure level on reaction rates and on the rate of supply of the reactants to the combustion chamber. Generally the turbine flow is choked over most of the operating range of the engine. This means that the mass flow rate through the combustor will be proportional to $p/\sqrt{T_{04}}$, in which p is the pressure level in the combustor and T_{04} is the turbine inlet temperature. In going from sea level to cruise altitude, the relative change in $\sqrt{T_{04}}$ is quite small, whereas p changes by an order of magnitude. This means that the mass flow rate through the burner is approximately proportional to the pressure. The rate of chemical reaction in the burner is a considerably stronger function of pressure; typically it is proportional, at low pressure, to p^n , in which n is about 1.9. In going from sea level to 50,000-feet altitude, the standard-day ambient pressure reduces by a multiplying factor of 0.1145. This means that the flow of reactants into the combustion chamber at altitude is about 11% of the sea-level value (for the same engine speed). The overall chemical reaction rate, however, will only be $(0.1145)^{1.9}$, or 1.6% of its sea-level value. The ratio of the chemical reaction rate to the rate of supply of reactants to the chamber has

dropped to 14% of the sea-level value. Typically, at sea level the rate of chemical reaction is considerably faster than the rate of fuel evaporation or of mixing of fuel vapor and air; in this case the chemical reaction rate would not be the factor-limiting the performance of the burner. At altitude, however, the chemical reaction rates may have fallen off sufficiently that they become the limiting factor. The lower the pressure, the greater the reaction time and the greater the danger of the flame being blown out of the chamber. At some altitude combustion efficiency will inevitably be much lower than at sea level.

Much experimental effort has been devoted to this problem. Figure 6.26 is a characteristic representation of experimental data on gas turbine combustors, showing what is commonly called a stability loop; only between the upper and lower branches of the curve is stable combustion possible. The equivalence ratio on the y -axis pertains to the fuel-air ratio in the primary zone; it is important that ϕ be close to 1 in this zone. The x -axis parameter is the combustion flow rate \dot{m} divided by the combustor volume V and the pressure term $p^{1.9}$. Clearly the lower the pressure, the greater the danger of being to the right of the stability loop, that is, in a region where stable combustion is not possible.

In this way the pressure level determines whether chemical reaction rates or the rates of fuel evaporation or of fuel-air mixing limit the ability of the com-

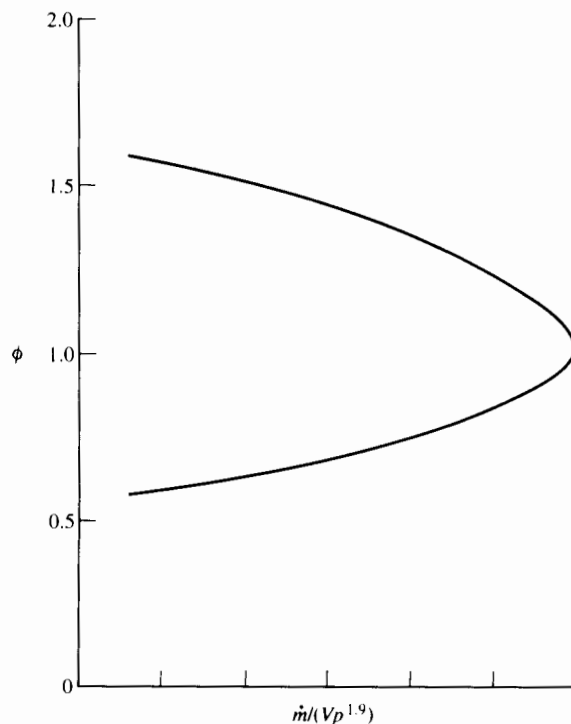


FIGURE 6.26 Typical blow-off limits for a gas turbine combustor; ϕ = equivalence ratio in primary zone.

bustor to achieve high efficiency. For both possibilities LeFebvre [15] describes the characteristic dependency of combustor efficiency on pressure, liner pressure drop, mass flow rate, entrance temperature, and combustor cross-sectional area and length.

Chamber Geometry

Over the years combustion chamber geometry has evolved considerably with respect to the objectives of:

- a. Improving flame stability (both at sea-level and altitude conditions);
- b. Reducing chamber size (while still burning all the fuel and maintaining reasonable pressure drop);
- c. Reducing emissions of the oxides of nitrogen, carbon monoxide, and unburned hydrocarbons;
- d. Increasing chamber life;
- e. Controlling the temperature distribution at inlet to the turbine.

Combustion stability, intensity, and efficiency all depend heavily on the fluid flow and turbulence distribution within the combustor. So does the heat transfer to the chamber walls. For these reasons much combustor development has focused on internal flow patterns. Much of the historical development was preceded by experimental trials of prototype combustors or studies of flow patterns in geometries similar to those in combustors. Only in recent years have analytical tools been developed for detailed mathematical simulation of combustion flow fields. These, in conjunction with experiments, can assist designers in optimizing combustor geometry. In principle these analytical methods should be able to predict turbulence intensity, reaction rates (including rates of formation of pollutants), and both convective and radiative heat transfer rates. Much, however, remains to be done to develop their full potential. Combustor development still relies heavily on laboratory testing.

Early models of gas turbine combustors (e.g., the pioneering Whittle engines developed in the late 1930s in the United Kingdom) had reverse-flow combustors (shown schematically in Fig. 6.27) mainly to keep turbine and compressor close together. At the time, this appeared to be necessary to prevent whirling vibrations of the shaft. Subsequent improvements in shaft design made it possible to eliminate whirling vibrations in long shafts so that straight-through flow combustion chambers could be used. These chambers were easier to develop for acceptable flow distribution and combustion efficiency, though reverse-flow combustors are still used in small turboshaft engines where overall cross-sectional area is not a serious concern.

In each type of combustor the chemical reaction is confined to the interior of a perforated metal liner mounted within the outer casing. Airflow between the liner and the casing keeps the metal cool enough to retain its strength despite the very much higher temperatures of the central combustion zone.

Figure 6.28 shows a typical configuration for a can-annular combustor in which 10 cylindrical combustion zone liners are enclosed within an annular space between the inner and outer combustion casings. At the entrance to each is

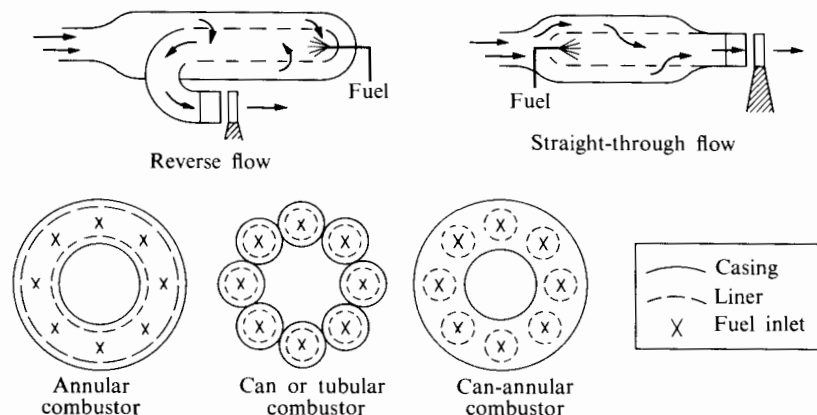


FIGURE 6.27 Combustion chamber, longitudinal and cross sections.

a passage of diverging area to reduce the velocity from a typical compressor outlet value (100–150 m/s) to the bulk flow average velocity in the combustion zone (20–30 m/s). Shown also are the swirl vanes used to set up high swirl within the combustor. The chief value of the swirl is in establishing a region of backflow or recirculation within the central and forward part of the combustion chamber; the flame is stabilized within this region of low and reversing velocity. Swirl also helps to distribute the fuel droplets leaving the atomizer and to intensify the turbulence needed for rapid combustion. The combustion liners, or flame tubes, as they are denoted in Fig. 6.28, have many small holes for transpiration cooling of

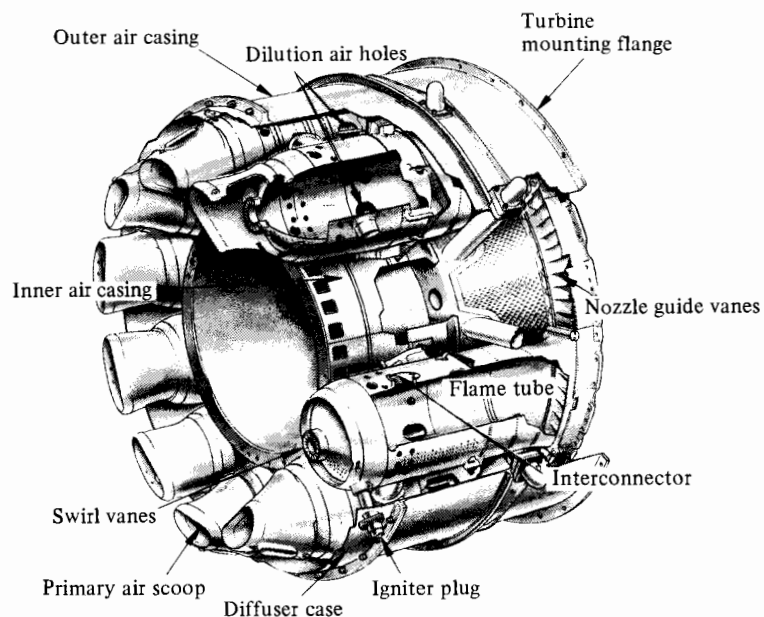


FIGURE 6.28 Can-annular combustion chamber. (Courtesy Rolls-Royce, plc.)

the liner, larger holes for dilution of the combustion products, and interconnector passages through which the pressure is communicated from one combustion zone to another. The interconnectors help to maintain circumferentially uniform outlet conditions.

Figures 6.29 and 6.30 show examples of fully annular combustion chambers in which the combustion zone itself occupies an annular space. Figure 6.29 shows also the annular diffuser at the entrance to the combustor. Air dilution holes on the inner surface of the combustion chamber liner are indicated, as well as annular slots on the outer surface, which provide both cooling and dilution air. The liner geometry shown in Fig. 6.30 is quite different. It has a large number of small holes through which air enters in small jets to provide a stable combustion zone and cooling air for the walls. Shown are 18 fuel and air inlets to the individual combustion initiation zones within the annular chamber.

LeFebvre [15] and Odgers and Kretschmer [16] discuss the relative advantages of can, can-annular, and fully annular combustion chambers. The tubular or can-type chamber has the advantages of ease of control of the fuel-air ratio and simplicity and low cost of replacement of a damaged liner, as well as the important advantage of requiring a relatively small air supply for combustion chamber testing during the development period. Though interconnectors have been commonly used for tubular designs, each chamber can be designed and tested as though it behaved independently of the other chambers. The disadvantages of this configuration for large engines include the relatively large size and weight of the chamber components, the relatively large pressure drop, and the need to provide numerous igniters. It is not easy with the tubular configuration to provide nearly simulta-

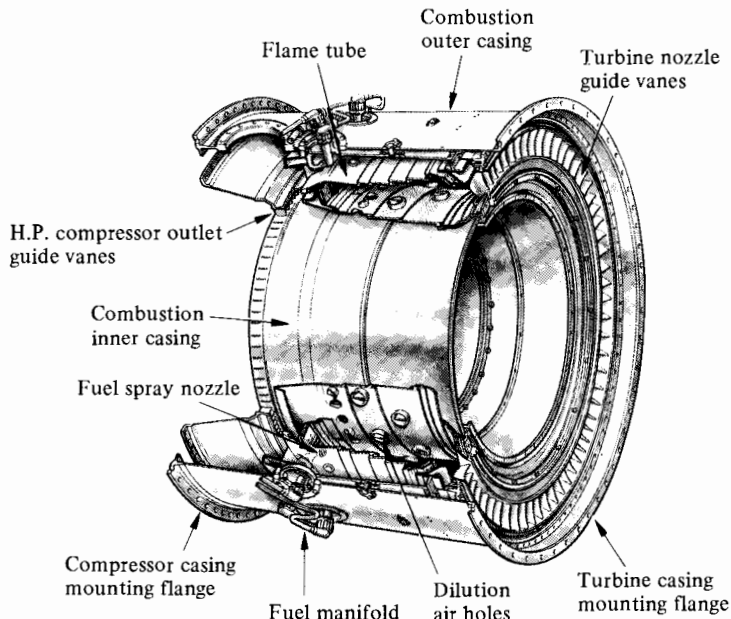


FIGURE 6.29 Annular combustion chamber. (Courtesy Rolls-Royce, plc.)



FIGURE 6.30 General Electric F404 annular combustor liner. (Courtesy GE Aircraft Engines.)

neous ignition of all chambers. The disadvantages have outweighed the advantages, and tubular chambers are now seldom used for large gas turbines for aircraft applications.

The can-annular chamber has the advantages of providing ease of ignition, minimum total cross-sectional area, minimum pressure drop, and minimum length and weight. The disadvantages include difficulties in development to obtain circumferentially uniform fuel-air ratio and outlet temperature. A failure of the liner in one spot means replacement of a relatively expensive component. There tends to be a heavy buckling load, due to thermal expansion on the outer surface of the chamber liner.

Both the annular and the can-annular chambers require large airflow rates during testing. The latter requires somewhat more volume and poses more difficult ignition problems than the former. Also it will typically have higher pressure drop. It can be mechanically more robust, however, because of the geometry of the combustion liner. Also it allows better control of the circumferential distribution of the fuel-air ratio and the outlet temperature.

To create the high turbulence necessary for intense combustion, there must be considerable pressure drop across the small holes in the chamber liner through which most of the air enters the combustion zone. Other causes of pressure drop in combustors include the bulk acceleration of the hot gas as its density decreases because of combustion (in a roughly constant area channel), and friction on the channel walls. For best engine performance the sum of these pressure losses should not be greater than a few percentage points of the combustor inlet pressure. LeFebvre [15] quotes typical overall combustor pressure drops as follows:

Tubular	7%
Can-annular	6
Annular	5

Satisfactory burning rates require fine atomization of the fuel. If fuel flow rates were constant, adequate atomization—to produce a spray of droplets whose surface-area averaged diameter is between 10 and 30 microns—could be obtained by flow through a nozzle whose outlet jet velocity was of the order of 100 m/s. The difficulty, however, is that over the whole range of turbojet operation, from sea-level takeoff to high-altitude cruise, the fuel flow rate can vary through a ratio of 40:1. To avoid problems in combustor reliability and durability, variable-area nozzles have not been used. Early engines had dual fuel flow systems; for small flow rates only one system was active, providing a high-velocity fuel jet through a small nozzle. With increase in engine thrust and airflow rate, a second system with larger nozzles was activated to provide most of the fuel required at high thrust. Subsequently the “air blast” nozzle has been developed and widely applied. It provides, almost independently of fuel flow rate, high relative velocity between fuel and air by blasting an airflow over a small cone on which the fuel flows before being entrained into the airstream in the form of fine droplets. The airstream, rather than a liquid jet, supplies the relative velocity needed for adequate atomization. The pressure drop required for the air blast is the same as the pressure drop across the chamber liner, that is, on the order of 0.25 atm or about 2% to 3% of the combustor inlet pressure. This will provide an air velocity of the order of 100 m/s. The air-blast nozzle may not perform adequately when the engine is starting and the air velocity is low; for starting, a small supplementary spray may be needed.

Figure 6.31 shows typical distributions of airflow into a can-contained combustion zone. About 12% of the intake air passes through the swirling vanes that surround the central fuel spray nozzle. The primary zone, in which the fuel-air ratio is nearly stoichiometric, is fed by other airflows (8% and 12% in Fig. 6.31). These flows are designed to interact in such a way that a large and steady swirl is established in the primary combustion zone. Because of the swirl, there is a large radial pressure gradient, that is, relatively low pressure on the chamber axis. Because the swirl decays owing to friction, the magnitude of the radial pressure gradient decreases in the main flow direction through the combustor. This means that on the chamber axis in the primary combustion zone the static pressure rises sharply from left to right. This strong axial pressure gradient impels the mixture to flow from right to left along the chamber axis and creates the “recirculation” of hot exhaust products necessary to provide zones of low velocity in which the

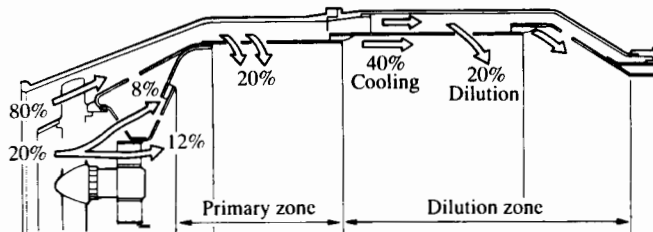


FIGURE 6.31 Airflow distribution in a gas turbine combustor. (Courtesy Rolls-Royce, plc.)

flame position can be stabilized. Increasingly, methods of theoretical analysis [17, 18] are being used to predict the flow field for gas turbine combustors. However, development of combustion chambers typically requires much testing. One can obtain useful information from flow visualization even in the absence of combustion, for example, by injecting bubbles into a transparent chamber through which water, instead of air, flows at an appropriately high Reynolds number.

Figure 6.31 indicates the dilution zone (downstream of the primary zone) in which the temperature of the combustion products is reduced to a level acceptable to the turbine. Great care is necessary in arranging the distribution of the dilution holes so that the gas leaving the combustor will be acceptably uniform in temperature. The length of this part of the chamber needs to be between 0.5 and 0.7 times the chamber diameter [15] both for completion of combustion and for satisfactory mixing. At high altitude the pressure reduction slows the reaction rates, so that part of the combustion may be taking place in the dilution zone. For this reason also, combustion efficiency may be appreciably less at altitude than at sea level. A chamber designed for high efficiency at altitude may require a dilution zone one diameter in length.

It is possible to estimate approximately the effect of variations in the size of liner and casing and in the distribution of liner holes. Grobman, Diltrich, and Graves [19] have performed such an analysis for a tubular combustion chamber with constant casing and liner diameters, as shown in Fig. 6.32(a).

Figure 6.32(b) is an idealized picture of the flow through a typical hole in the combustor liner. With the aid of empirical data it is possible to estimate this flow by idealizing it as a jet whose discharge coefficient and direction depend not only on the hole geometry but also on the velocities u_A and u_L . The subscripts A and L refer to the annular and liner flow, respectively.

Considering the holes to be small, and uniformly and closely spaced, one can predict the flow in both annulus and liner by approximate application of momentum and continuity equations. Figure 6.33 is a typical result of Grobman's, for the case in which combustion is absent. One may see that, owing to wall friction, the stagnation pressure in the annulus p_{0A} drops below the inlet stagnation pressure value p_{01} . The static pressure p_A in the annulus rises as fluid is transferred to the interior of the liner and the fluid remaining in the annulus decelerates. Because of the irreversibility of the jet discharge, the value of the stagnation pressure in-

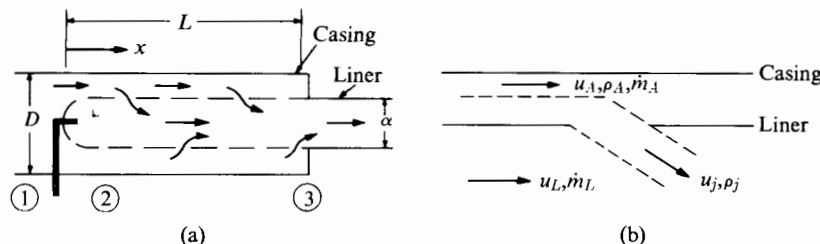


FIGURE 6.32 Idealized combustor.

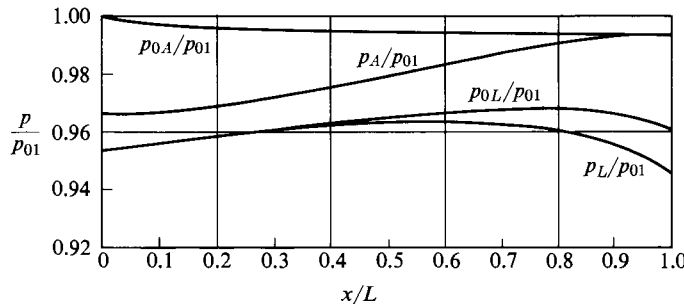


FIGURE 6.33 Typical distributions of annulus and liner pressure, for cold flow. (Courtesy Grobman, Diltrich, and Graves [19].)

side the liner is significantly below p_{0A} at $x = 0$. However, p_{0L} varies somewhat with x , as the result of assumptions about the speed and magnitude of discharge from the liner holes. Initially the velocity inside the liner is low enough that the stagnation and static pressures p_{0L} and p_L are nearly identical. Toward the exit of the liner, however, the velocity is significant.

The presence of combustion would of course have a considerable effect on these results. One could estimate the effect by assuming an axial temperature distribution or by more detailed assumptions concerning the rate of chemical reaction within the chamber.

Confining our attention to the aerodynamics of the cold flow only, we turn next to Fig. 6.34, which gives typical losses in stagnation pressure for the combustion chamber of Fig. 6.32. Figure 6.34 can be derived directly from the result of calculations (typically shown in Fig. 6.33) of pressure distributions for a variety of combustor area ratios. Two area ratios are significant: the ratio of the cross-

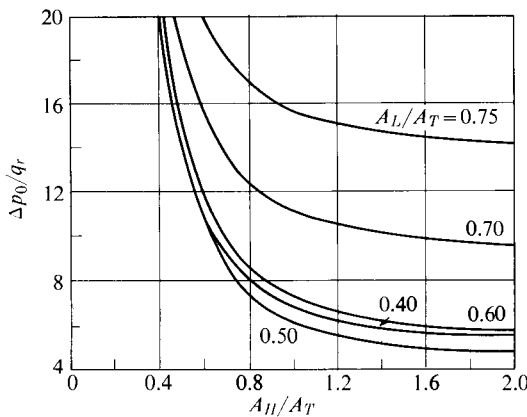


FIGURE 6.34 Typical stagnation pressure loss for cold flow. (Courtesy Grobman, Diltrich, and Graves [19].)

sectional area A_L of the liner to the total cross section A_T , and the ratio of the total hole area A_H to the total cross section A_T . The stagnation pressure loss Δp_0 is normalized in Fig. 6.34 by the upstream dynamic pressure p_{dyn} , which may be expressed as

$$p_{dyn} = \frac{\dot{m}^2}{2\rho_1(A_T)^2},$$

in which \dot{m} is the mass flow through the combustor and ρ_1 is the inlet density.

This figure indicates that Δp_0 can be greatly reduced if A_H/A_T is made as large as 1.5, but that relatively little is gained by further increase. It also appears that there is a value of A_L/A_T (lying between 0.6 and 0.4) that will produce minimum stagnation pressure loss.

Analytical results of this kind may be useful in providing a general picture of pressure and mass flow distributions. In addition they may help the designer to decide the relative liner, casing, and hole areas. A much more complete discussion is given in Reference [19].

6.5 AFTERBURNERS AND RAMJET COMBUSTORS

Figure 6.35 shows in schematic form the general configuration of turbojet afterburners and ramjet combustors. Usually these burners consist of a straight-through flow region containing bluff bodies that act as "flameholders." In principle a perforated liner, as shown in Fig. 6.34(b), might be used to stabilize the flow, but this arrangement is not the configuration that is widely used.

Figure 6.36 shows the internal arrangement of a turbojet afterburner. Shown are the fuel injection points, the V-shaped gutters used to stabilize the flame, and the igniter. Figure 5.7 showed the structure of a ramjet burner that also uses a V-shaped gutter for flame stabilization. These configurations apply to subsonic burner flows. An alternative concept, the supersonic combustion ramjet, is described in a subsequent section.

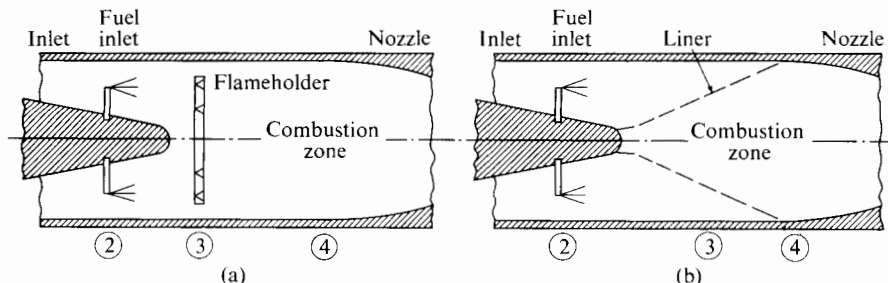


FIGURE 6.35 Schematic ramjet (or afterburner) combustion chambers.

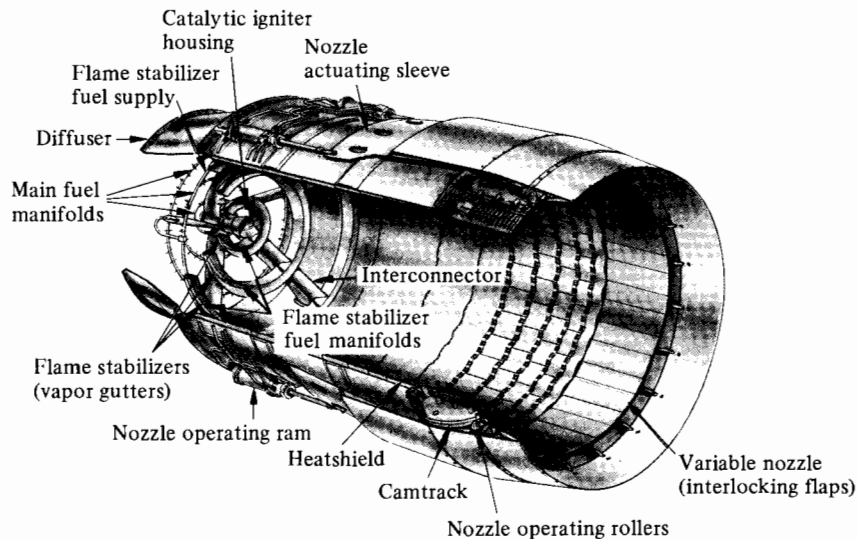


FIGURE 6.36 Typical afterburning jet pipe equipment. (Courtesy Rolls-Royce, plc.)

Flameholders

The simplified model in Fig. 6.37 illustrates the performance of a bluff body as a flameholder. Suppose that a combustible mixture travels with uniform and parallel velocity u_m , and that the flame speed within the mixture is u_f , where $u_f < u_m$. Combustion initiated by an intermittent spark in such a flow would proceed into the unburned mixture, producing a series of spherical regions of burned material, as in Fig. 6.37(a). Each sphere's radius would increase at the rate u_f

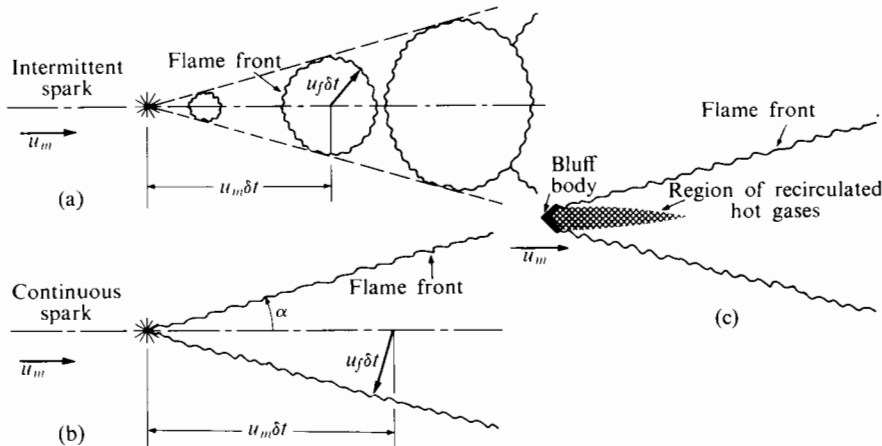


FIGURE 6.37 Simplified picture of the operation of a flameholder.

(with the simplifying assumption that reactants and products are of the same density), while its center travels downstream at the rate u_m . If the intermittent spark is replaced by a continuous one, a conical region of combusted material will result, as in 6.37(b), the cone angle being $\sin^{-1}(u_f/u_m)$. The flameholding effect of a bluff body results from the recirculation of hot and combusting gases in its wake, as in Fig. 6.37(c). This region acts as a continuous ignition source just as a spark does; and a diverging region of burned material will result, much as in the case of the spark. By this means one can maintain a stationary flame within a stream whose average velocity is greater than the flame speed, and the combustion chamber velocity need not be as low as the flame speed. For given flame and mixture speeds, the length of a combustion chamber can be reduced if a larger number of flameholders can be installed. However, a compromise must be reached in the flameholder arrangement. If the total cross-sectional area of the obstructions is too large, an excessive stagnation pressure loss will occur across the flameholders.

Stagnation Pressure Loss

Flameholding is essential, but it does apply drag to the flow, thereby causing stagnation pressure loss. Even without frictional drag the combustion “heating” process in a constant area duct will decrease the stagnation pressure. We wish to inquire how these contributions to stagnation pressure loss are related to the upstream flow Mach number and the stagnation temperature increase.

One can make an informative yet simple analysis of combustion in a conventional afterburner or ramjet burner by approximating the flow as one-dimensional, as Fig. 6.38 suggests. Here the flow entering and leaving the combustion chamber is assumed to have uniform velocity and temperature. No allowance is made here for any flow through porous side walls. The flameholders exert a total leftward drag D on the flow that will be approximately proportional to the inlet dynamic pressure $1/2 \rho_2 u_2^2$.

Hence we can write the momentum equation for the burner as

$$(p_2 - p_4)A - D = \dot{m}_4 u_4 - \dot{m}_2 u_2$$

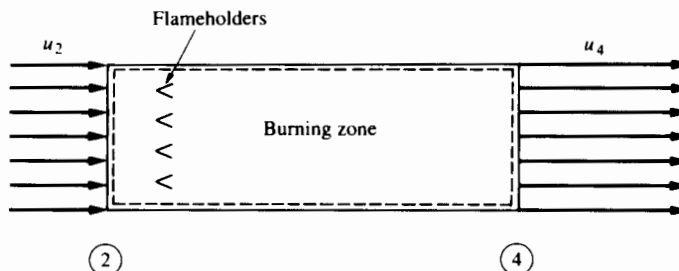


FIGURE 6.38 Simplified combustion chamber flow.

or

$$p_2 - p_4 = \rho_4 u_4^2 - \rho_2 u_2^2 + K\left(\frac{1}{2}\rho_2 u_2^2\right), \quad (6.9)$$

in which K can be considered the ratio of the pressure drop (due to the effect of friction) to the upstream dynamic pressure. We might expect the effective value of K for an actual burner to be something like 1 or 2 allowing also for wall friction. Since

$$M^2 = u^2 / \left(\frac{\gamma p}{\rho} \right),$$

We can write Eq. (6.9) (with the approximation $\gamma_2 = \gamma_4 = \gamma$) as

$$\frac{p_2}{p_4} = 1 + \gamma M_4^2 - \gamma M_2^2 \frac{p_2}{p_4} + K \frac{\gamma M_2^2}{2} \frac{p_2}{p_4}$$

or

$$\frac{p_2}{p_4} = \frac{1 + \gamma M_4^2}{1 + \gamma M_2^2 \left(1 - \frac{K}{2} \right)}. \quad (6.10)$$

Using the relationship between static and stagnation pressures (Eq. 3.15), we can write this (again for constant γ) as

$$\frac{p_{04}}{p_{02}} = \frac{1 + \gamma M_2^2 \left(1 - \frac{K}{2} \right)}{1 + \gamma M_4^2} \left[\frac{1 + \frac{\gamma - 1}{2} M_4^2}{1 + \frac{\gamma - 1}{2} M_2^2} \right]^{\gamma/(\gamma-1)}. \quad (6.11)$$

Since the ratio of the fuel flow rate to the burner inlet gas flow rate is small, that is, $\dot{m}_f \ll \dot{m}_2$, we can make the approximation $\dot{m}_4 = \dot{m}_2$, so that

$$\rho_4 u_4 = \rho_2 u_2. \quad (6.12)$$

With $p = \rho RT$ we can write Eq. (6.12) as

$$\frac{p_2}{p_4} = \frac{u_4}{u_2} \frac{T_2}{T_4} = \frac{M_4}{M_2} \sqrt{\frac{T_2}{T_4}}. \quad (6.13)$$

But since the stagnation temperatures at stations ③ and ④ are considered to be known, we write

$$\frac{T_2}{T_4} = \frac{T_{02}}{T_{04}} \frac{\left(1 + \frac{\gamma - 1}{2} M_4^2 \right)}{\left(1 + \frac{\gamma - 1}{2} M_2^2 \right)},$$

so that Eq. (6.12) becomes

$$\frac{p_2}{p_4} = \frac{M_4}{M_2} \sqrt{\frac{T_{02}}{T_{04}} \frac{\left(1 + \frac{\gamma - 1}{2} M_4^2\right)}{\left(1 + \frac{\gamma - 1}{2} M_2^2\right)}}. \quad (6.14)$$

Now Eq. (6.10), which is a momentum equation, and Eq. (6.14), which is essentially a mass conservation equation, provide two different conditions that the static pressure p_2/p_4 must satisfy. Equating the right-hand sides of both these equations, we can show that

$$\frac{T_{04}}{T_{02}} = \frac{M_4^2}{M_2^2} \frac{\left(1 + \frac{\gamma - 1}{2} M_4^2\right)}{\left(1 + \frac{\gamma - 1}{2} M_2^2\right)} \frac{\left[1 + \gamma M_2^2 \left(1 - \frac{K}{2}\right)\right]^2}{[1 + \gamma M_4^2]^2}. \quad (6.15)$$

As Chapter 3 shows, both friction ($K > 0$) and combustion ($T_{04}/T_{02} > 1$) increase the Mach number toward the limiting value $M_4 = 1$. We now look at the question of how large M_2 must be if a given burner with known K is to have a given stagnation temperature ratio T_{04}/T_{02} . To do this we substitute $M_4 = 1$ in Eq. (6.15) and try various values of M_2 . The results are shown in Fig. 6.39, which displays the overall pressure ratio p_{02}/p_{04} as well as the temperature ratio T_{04}/T_{02} .

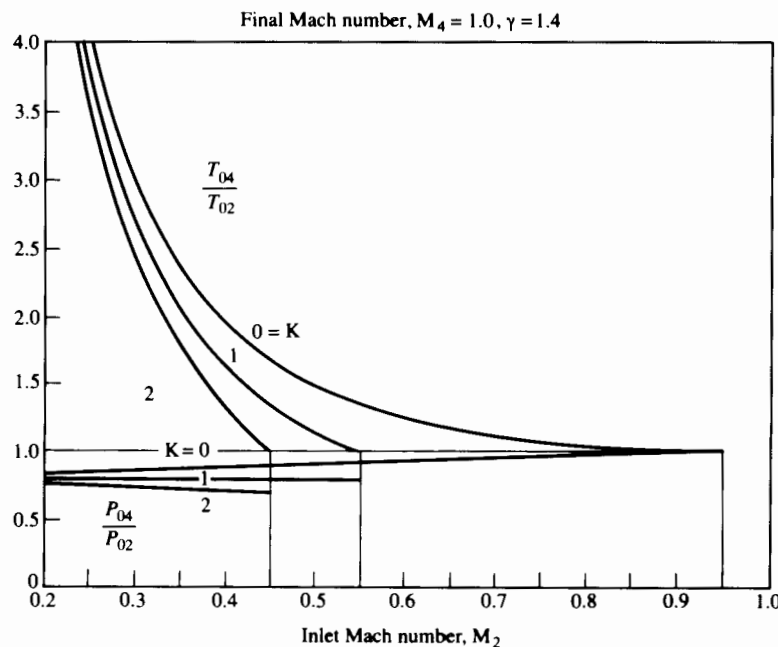


FIGURE 6.39 Constant-area burner.

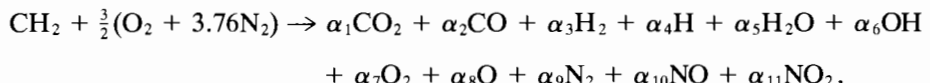
In a turbojet afterburner the temperature ratio could be around 2. For this case and $K = 1$, the maximum allowable burner inlet Mach number would be around 0.35 and the overall stagnation pressure loss would be about 22%. One can see from Fig. 6.39 that most of the pressure drop is due to the "heating" rather than the frictional effect (with K of order 1). This stagnation pressure loss penalty is so severe that one would like to know how it could be reduced and how the required burner cross-sectional area would be affected if M_4 were reduced from 1 to, say, 0.8. Figure 6.39 applies only to constant-area combustion chambers. If the cross-sectional area were to increase in the flow direction, the inlet Mach number restriction could be eased considerably. However, this would increase the overall cross-sectional area of the engine.

For a subsonic ramjet combustor and flight Mach number of 3, with near-stoichiometric combustion of hydrocarbon fuel, the required stagnation temperature ratio could be as high as 4. For this case one can see from Fig. 6.39 that (with $K = 1$) the burner inlet Mach number would need to be very low indeed, and there may be a substantial pressure loss penalty.

6.6 SUPERSONIC COMBUSTION

As we have seen, the losses associated with subsonic ramjet combustion can be substantial. If ramjets are to be applied to hypersonic flight, additional problems arise because of extremely high temperature at the entrance to the combustion chamber. This not only makes vehicle cooling very difficult, but it leads to severe combustion loss due to dissociation.

Figure 6.40 shows the air temperature reached after adiabatic deceleration from a high-altitude ambient temperature of 220 K and from flight Mach number M to a chamber pressure of either 1 or 10 atm. For hypersonic flight (e.g., for $M > 8$) the temperature of the air in the chamber is quite dependent on the pressure: The higher the pressure, the less dissociation and the higher the temperature of the mixture. The temperature of the combustion products is likewise pressure dependent. The temperatures shown in Fig. 6.40 were calculated with the use of the STANJAN computer program [20], which computes the equilibrium composition. For air (considered to consist of O_2 and N_2 in the mole ratio 1:3.76), the high-temperature composition allows for the presence of O_2 , O , N_2 , NO , N , and NO_2 . Combustion is considered to take place according to



and the α_i are calculated by using the STANJAN program for a given mixture pressure and temperature. At a temperature of 4000 K and a pressure of 1 atm, all of these constituents have mole fractions greater than 0.001.

As Fig. 6.40 indicates, for a combustion pressure of 10 atm and a flight Mach number of 10, there is no temperature rise due to combustion; all of the combus-

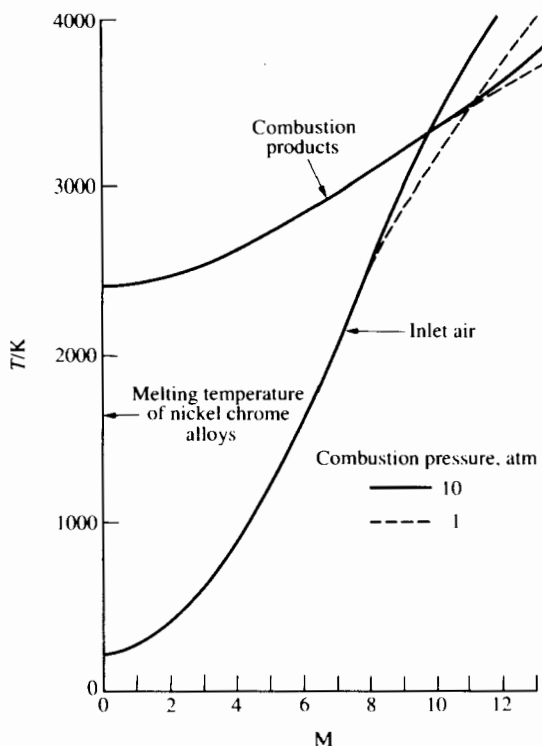


FIGURE 6.40 Hypersonic ramjet with kerosine fuel; adiabatic compression and combustion. equivalence ratio, $\phi = 1$.

tion energy, so to speak, is absorbed by dissociation. One sees from Fig. 6.40 the strange result that, at sufficiently high Mach number, the temperature of the combustion products can be lower than that of the incoming air. Consideration of the speed with which the fuel and air can be converted into dissociation products may show that there is sufficient residence time in the combustion chamber to approach equilibrium composition. But during the subsequent expansion in the nozzle, one cannot take equilibrium composition for granted. It is quite possible that the expansion will be too rapid for the composition to readjust, after each step of temperature and pressure reduction, to a new equilibrium composition. If the expansion is extremely rapid, the mixture may be effectively “frozen” with the initial (high-temperature) composition. This would mean that little of the combustion energy of the fuel (for the $M = 10$ case) would be available for acceleration of the combustion products to provide thrust. The chemical kinetics of the recombination processes in the nozzle would, in general, have a strong effect on the thrust and the propulsion efficiency of the engine. We will deal with this matter in more detail in the discussion of rocket nozzles in Chapter 12.

Some researchers have proposed the concept of the supersonic combustion ramjet as a way to avoid this dissociation loss as well as the stagnation pressure

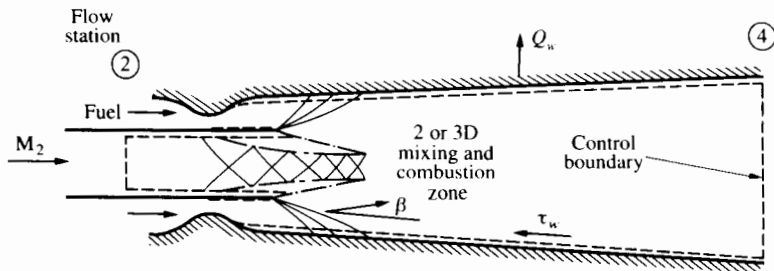
losses associated with deceleration in supersonic-to-subsonic inlets. With supersonic combustion, fluid temperatures are relatively low, and this decreases the dissociation loss because dissociation depends on static rather than stagnation temperature. Wall heat transfer, in contrast, depends essentially on stagnation temperature, so the wall-cooling problem is not removed by employing supersonic combustion. (Cooling supplied by liquid hydrogen on its way from fuel tank to engine has been considered as one possible method of keeping the engine and vehicle cool enough to survive the period of hypersonic flight.) The stagnation pressure loss due to supersonic heating depends on the extent to which the fluid is being accelerated while combustion is taking place.

The use of supersonic combustion requires fuel to be injected into, and mixed with, a supersonic stream without excessive shock losses. Billig [7] has demonstrated supersonic combustion of hydrogen in the apparatus shown schematically in Fig. 6.41. As indicated, the airstream enters the combustor at a supersonic Mach number M_2 . Hydrogen fuel in gaseous form is injected at an angle to the airflow direction. The combined disturbances of the fuel injection and the combustion set up a complex shock pattern that is associated with the rather gradual rise in pressure shown in Fig. 6.41(b). Here p_{04} and T_{04} are the stagnation pressure and temperature of the gas stream leaving the combustor, and p_w is the wall static pressure. The stagnation temperature and the fuel gas temperature are T_{0f} and p_{0f} . The fuel-air equivalence ratio is denoted by ϕ , and η_b is the combustion efficiency. Following the initial pressure rise, the mixture accelerates supersonically in the diverging passage—even though combustion may still be in the process of being completed. Billig reports that at moderate inlet air Mach numbers (e.g., 1.5–4) and with fuel-air equivalence ratios in the range 0.5 to 1, the pressure rise associated with the shock train may be high enough to separate the incoming boundary layers. This may call for the design of an “isolator” to prevent the combustion-induced disturbances from seriously distorting the flow in the inlet. Billig [7] provides other experimental examples; he also describes methods of theoretical analysis of the supersonic combustion flow field. A number of researchers are investigating methods of supersonic combustion.

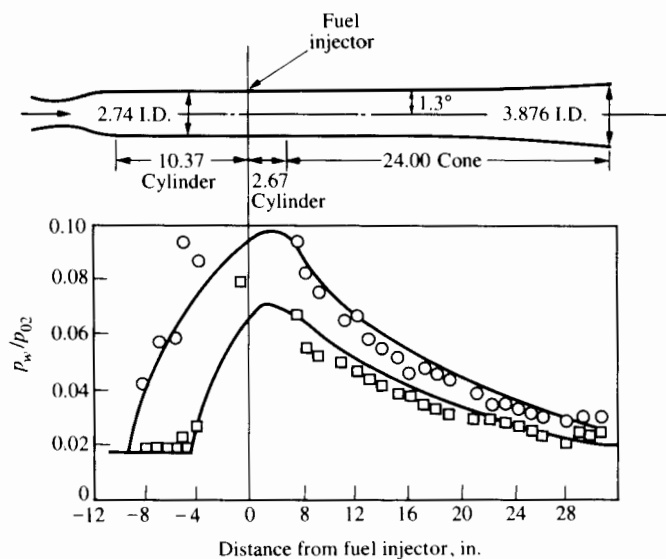
6.7 EXHAUST NOZZLES

From the standpoint of fluid dynamics, at least, the ramjet or turbojet exhaust nozzle is an engine component that is relatively easy to design, since the pressure gradient can be favorable all along the wall. If one considers mechanical design, however, the exhaust nozzle can be rather complex if the area of the nozzle needs to be adjustable, especially if a converging-diverging (i.e., supersonic) configuration is desired. Adjustable nozzles are often constructed of a series of pie-shaped segments that can be moved to form a conical fairing of variable outlet area.

Figure 6.42 shows the variable exhaust nozzle of the F404 afterburning turbojet engine with the nozzle area low for cruise operation (part a) and wide open (part b) for afterburner operation. Figure 6.43 shows the integrated nozzle



(a) Flow processes in combustor with supersonic diffusive flames



Distance from fuel injector, in.

T_{02}	P_{02}	T_2	P_2	T_{of}	ϕ	η_b
$^{\circ}\text{R}$	psia	$^{\circ}\text{R}$	psia	$^{\circ}\text{R}$		
○ 4135	456	1581	7.52	1158	0.78	0.81
□ 4150	456	1590	7.52	1160	0.49	0.92

(b) Comparison of theoretical and experimental wall pressure distributions in a conical combustor at $M_2 = 3.23$ **FIGURE 6.41** Supersonic combustion results. (Courtesy AIAA; © AIAA. Reprinted with permission [7].)

of the Rolls-Royce RB211-524 engine. The bypass streams mix before expansion in a common nozzle. The figure also shows the deep corrugations of the core flow exhaust duct, which greatly increase the mixing area between the core and bypass streams and substantially lessen the required length of the mixing chamber.

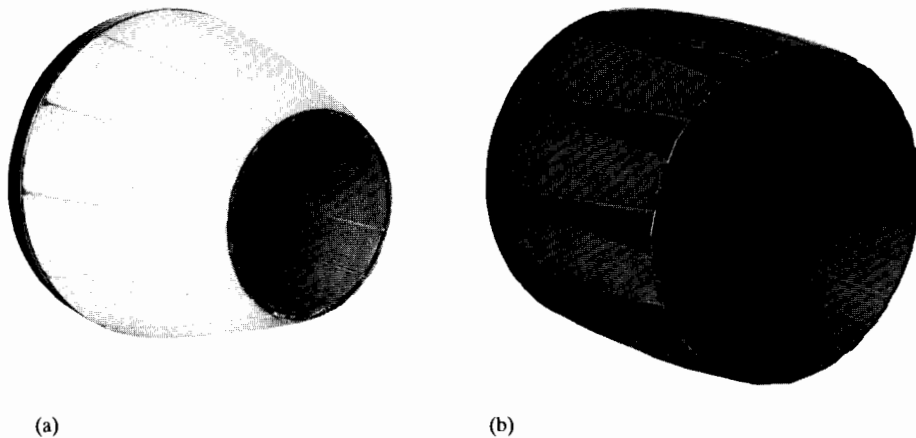


FIGURE 6.42 General Electric F404 variable exhaust nozzle. (Courtesy GE Aircraft Engines.)

Figure 6.44 shows the operation of the Rolls-Royce RB211-535E4 turbofan engine with and without the thrust reverser activated. Here again the primary and secondary streams are well mixed before expansion in a common nozzle. The thrust reverser deflects only the bypass stream. The main thrust reversal is due not so much to imparting a forward component of velocity to the bypass stream as to making use of the $-\dot{m}_a u$ term in the thrust equation (Eq. 5.6) as the engine is speeded up to swallow as much air as possible during deceleration of the aircraft on the runway.

The process in the nozzle, like that in the diffuser, can be very close to adiabatic, since the heat transfer per unit mass of fluid is much smaller than the difference of enthalpy between inlet and exit. Unlike the diffuser process, however, the equations of one-dimensional isentropic flow can describe the nozzle

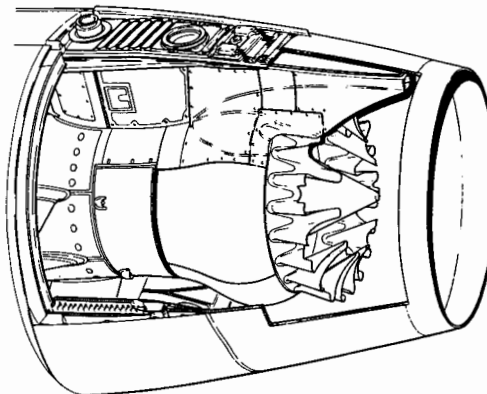


FIGURE 6.43 Rolls-Royce RB211-524D4D mixer and nozzle. (Courtesy Rolls-Royce, plc.)

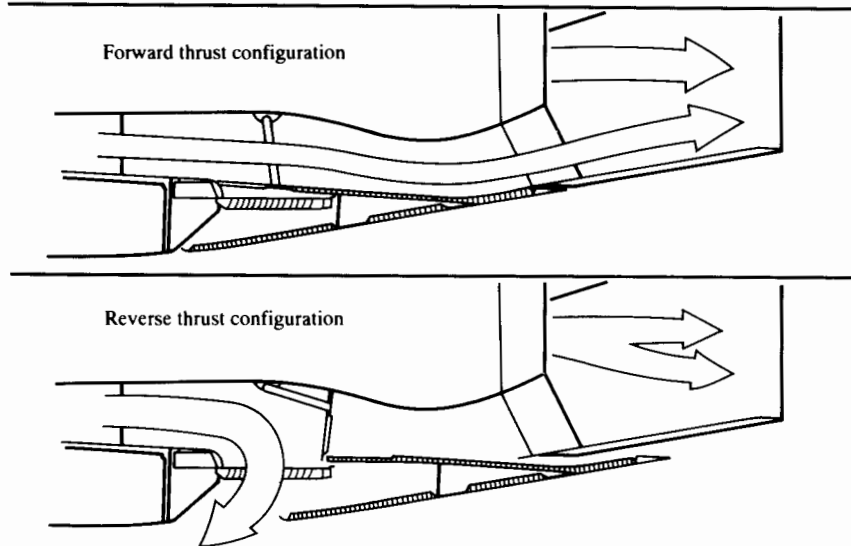


FIGURE 6.44 Rolls-Royce RB211-535E4 mixer, nozzle, and thrust reverser. (Courtesy Rolls Royce, plc.)

process quite well. Friction may reduce the nozzle adiabatic efficiency (Fig. 6.45), defined by

$$\eta_n = \frac{h_{06} - h_7}{h_{06} - h_{7s}},$$

to values in the range $0.95 < \eta_n < 0.98$, provided the nozzle is well designed. If the expansion (of a divergent section) is too rapid, it is possible for boundary layer separation to occur, which considerably lowers the efficiency.

Since the flow is approximately adiabatic, $h_{06} = h_{07}$. Also $h_{07} = h_7 + (u_7^2/2)$. Thus the exhaust velocity may be calculated from

$$u_7 = \sqrt{2(h_{06} - h_7)} \quad \text{or} \quad u_7 = \sqrt{2(h_{06} - h_{7s})\eta_n}.$$

If the specific heat ratio γ is taken to be constant, then

$$u_7 = \sqrt{2[\gamma/(\gamma - 1)]\eta_n RT_{06}[1 - (p_7/p_{06})^{(\gamma-1)/\gamma}]} \quad (6.16)$$

By introducing the Mach number M_7 , we have $M_7 = u_7/\sqrt{\gamma RT_7}$. Equation (6.16) may be transformed to

$$M_7^2 = \frac{2}{\gamma - 1} \left\{ \frac{\eta_n[1 - (p_7/p_{06})^{(\gamma-1)/\gamma}]}{1 - \eta_n[1 - (p_7/p_{06})^{(\gamma-1)/\gamma}]} \right\}.$$

If the flow, up to the throat, is assumed isentropic with nozzle entrance conditions M_6, A_6, p_{06}, T_{06} , the throat area A_t will be given by

$$\frac{A_t}{A_6} = \frac{M_6}{M_t} \frac{[1 + (\gamma - 1)/2M_t^2]^{(\gamma+1)/2(\gamma-1)}}{[1 + (\gamma - 1)/2M_6^2]^{(\gamma+1)/2(\gamma-1)}}.$$

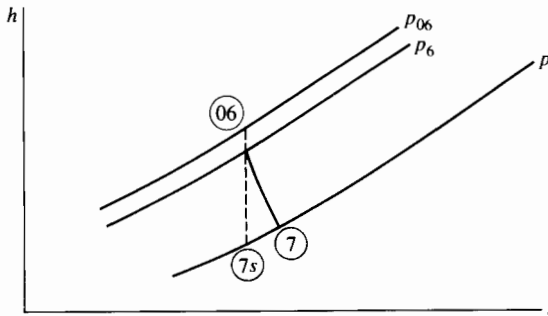


FIGURE 6.45 Definition of fluid states in a nozzle. The numbers correspond to the turbojet nomenclature of Chapter 5.

For most cases of interest to ramjets, the throat will be choked, so that $M_t = 1$ and

$$\frac{A_t}{A_6} = \frac{M_6[(\gamma + 1)/2]^{(\gamma+1)/2(\gamma-1)}}{[1 + (\gamma - 1)/2M_6^2]^{(\gamma+1)/2(\gamma-1)}}.$$

The mass flow that will pass through the choked throat is given by

$$\dot{m} = \frac{A_t p_{06}}{\sqrt{RT_{06}}} \sqrt{\gamma} \left(\frac{2}{\gamma + 1} \right)^{(\gamma+1)/2(\gamma-1)}. \quad (6.17)$$

If the flow is to be expanded ideally so that the pressure in the exhaust plane equals the ambient pressure, the required exhaust area may be obtained from

$$\frac{A_7}{A_6} = \frac{p_{06}}{p_{07}} \frac{M_6}{M_7} \left\{ \frac{1 + [(\gamma - 1)/2]M_7^2}{1 + [(\gamma - 1)/2]M_6^2} \right\}^{(\gamma+1)/2(\gamma-1)}. \quad (6.18)$$

The ratio p_{06}/p_{07} may be obtained from the pressure ratio and the adiabatic nozzle efficiency. Writing

$$\eta_n = \frac{1 - (T_7/T_{06})}{1 - (T_{7s}/T_{06})} = \frac{1 - (T_7/T_{07})}{1 - (T_{7s}/T_{07})}$$

and recognizing that

$$\frac{T_7}{T_{07}} = \left(\frac{p_7}{p_{07}} \right)^{(\gamma-1)/\gamma}, \quad \frac{T_{7s}}{T_{06}} = \left(\frac{p_7}{p_{06}} \right)^{(\gamma-1)/\gamma},$$

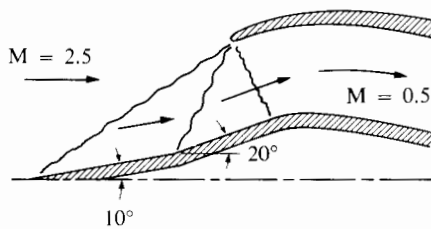
we may show that

$$\frac{p_{06}}{p_{07}} = \frac{p_{06}}{p_7} \left\{ 1 - \eta_n \left[1 - \left(\frac{p_7}{p_{06}} \right)^{(\gamma-1)/\gamma} \right] \right\} ^{\gamma(\gamma-1)}. \quad (6.19)$$

In a practical case it may easily happen that the ratio A_7/A_6 calculated from Eq. (6.18) will exceed unity by a considerable margin. Considerations of external drag on the nacelle or of structural limitations may then suggest the desirability of reducing A_7/A_6 to near 1, even though this will mean incomplete expansion.

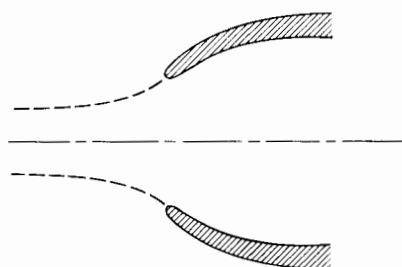
PROBLEMS

1. A two-dimensional or wedge-type diffuser consists of two external oblique shocks, a normal shock, and a subsonic internal section, as shown in the figure. Assuming no external losses other than shock losses, and assuming the subsonic section stagnation pressure loss is 3%, find the overall total pressure ratio at a flight Mach number of 2.5. Sketch the inlet shock system roughly to scale and label all angles.



PROBLEM 1

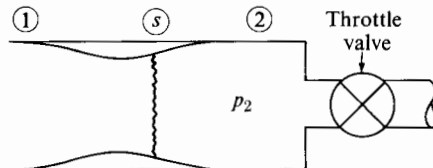
2. A jet engine in an aircraft flying at $M = 0.9$ ingests an airflow of 100 kg/s through an inlet area of 3.07 m^2 . The adiabatic efficiency of the (internal) diffuser is 0.9, and the Mach number of the flow entering the compressor is 0.4. The ambient temperature and pressure are 222 K and 9.57 kPa , respectively.
- What is the ratio of the inlet static pressure (at entrance to the engine intake) to the ambient pressure?
 - What is the static pressure ratio across the internal diffuser?
 - What fraction of the inlet dynamic pressure is converted to static pressure in the intake?



PROBLEM 2

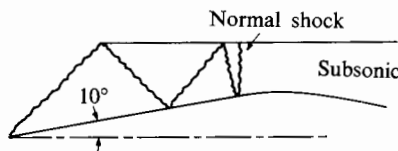
3. The figure indicates a hypothetical one-dimensional supersonic inlet installed in a wind tunnel and equipped with a throttle valve by which the downstream static pressure p_2 might be varied. Suppose that the inlet is designed for a Mach number $M = 3.0$ and that with this flight Mach number the shock has been swallowed and an internal shock exists, as at (s). Neglecting all losses except those occurring in the shock, calculate and plot the shock Mach number M_s and the stagnation pressure ratio p_{02}/p_{0a} as a function of the static

pressure ratio p_2/p_a (for $\gamma = 1.4$). Let p_2/p_a range from unity to well beyond that value which disengages the shock.



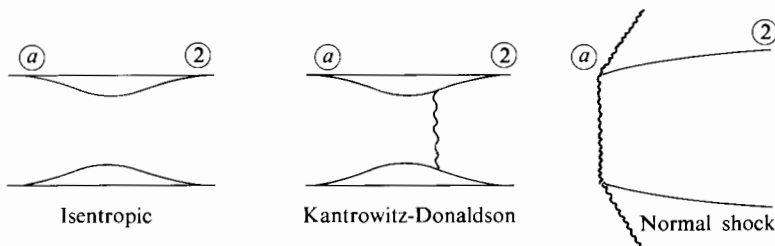
PROBLEM 3

4. The figure indicates a two-dimensional diffuser that produces no net turning of the flow. For the geometry shown, calculate the overall stagnation pressure ratio for a flight Mach number of 3.0. Neglect all losses except those occurring in the shocks. Would this diffuser be easy to start?



PROBLEM 4

5. Sketched are three supersonic inlets: an isentropic inlet, the Kantrowitz-Donaldson inlet of Fig. 6.10, and a simple normal shock inlet. For flight Mach numbers M from 1 to 4, calculate the plot p_{02}/p_{0a} as a function of M , with each inlet operating with best back pressure.

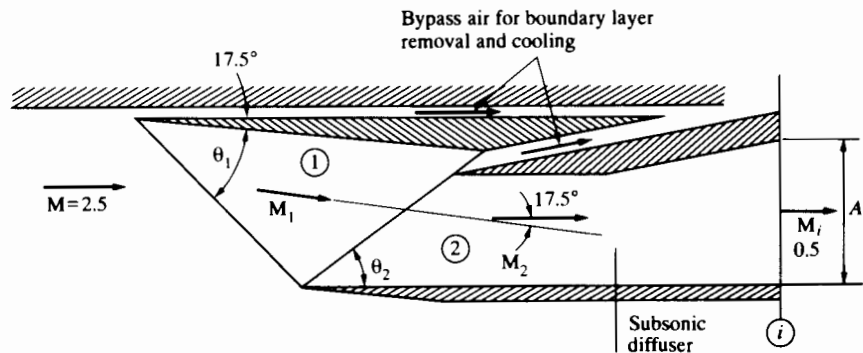


PROBLEM 5

6. It was shown that, during starting, an isentropic diffuser would experience a detached shock and consequent losses. In order to swallow the shock, a fixed-geometry diffuser must be overspeeded. However, as shown in Fig. 6.9, as the design Mach number increases, the required overspeeding increases very

rapidly, so that even if the aircraft could be infinitely overspeeded, the design Mach number would be limited to a finite value. Assuming one-dimensional flow and constant γ (1.4), determine the absolute maximum *design* Mach number for which an otherwise isentropic diffuser of fixed geometry may be expected to start, any amount of overspeed being possible.

7. A new supersonic passenger aircraft is being designed for flight Mach number 2.5 at an altitude where the ambient pressure and temperature are 9 kPa and 220 K, respectively. The engine inlet configuration shown below allows for double oblique shock deceleration followed by a zone of subsonic deceleration. The Mach number is 0.5 at the engine inlet plane (i). Losses in the subsonic diffuser are neglected. Determine:
- The Mach numbers M_1 and M_2 in the zones (1) and (2) shown on the drawing,
 - the wave angles θ_1 and θ_2 , also shown on the drawing,
 - the overall stagnation pressure ratio p_{oi}/p_{oa} ,
 - the overall static pressure ratio p_i/p_a ,
 - the velocity ratio c_i/c_2 for the subsonic diffuser, and
 - the cross-sectional area $A_i(m^2)$ at the engine inlet plane if the engine mass flow rate is 500 kg/s.



PROBLEM 7

8. A ramjet engine is to fly at a Mach number of 4 in an atmosphere whose temperature is 223 K. At entrance to the burner, the Mach number of the flow is 0.3. Combustion in the burner (whose cross-sectional area is constant) may be represented approximately as heating of a perfect gas with constant specific heat ratio. At the exit from the burner the temperature of the gas is 2462 K. Neglecting frictional effects in the burner and considering the flow to be one-dimensional throughout, estimate the Mach number of the gas leaving the burner. Determine also the stagnation pressure loss due to heating (i.e., calculate the ratio of outlet and inlet stagnation pressures).

9. In an afterburning jet engine during a static test, the fluid entering the afterburner has a temperature of 900 K, a pressure of 0.235 MPa and a mass flow rate of 75 kg/s. These conditions are maintained with and without operation of the afterburner. Without afterburning, the stagnation pressure loss between afterburner entrance and exit is 3 percent and the specific heat ratio of the fluid in the nozzle is 1.33. When the afterburner is operating, the exit stagnation temperature rises to 1800 K, the stagnation pressure loss changes to 8 percent and the specific heat ratio in the nozzle drops to 1.29. In both cases the nozzle flow is simply converging and choked. Determine the required nozzle exit area in both cases.
10. A ramjet has a constant-diameter combustion chamber followed by a nozzle whose throat diameter is 0.94 times the chamber diameter. Air enters the combustion chamber with $T_0 = 1450$ K and $M = 0.3$. How high may the temperature rise in the combustion chamber without necessarily changing the chamber inlet conditions? For simplicity, neglect frictional losses in the chamber and nozzles and assume that the working fluid has specific heat ratio $\gamma = 1.333$.
11. Consider the use of hydrogen fuel for gas turbines (in the way that Fig. 6.22 does for kerosine-type fuels). For the special case in which at entrance to the burner the hydrogen is at 77 K and in vapor form, and the air is at 600 K, determine the dependence of fuel-air ratio f and equivalence ratio ϕ on the turbine inlet temperature in the range 1200–1800 K. Dissociation may be considered negligible. Average specific heats may be assumed as follows:

Constituent	c_p kJ/kmol · K
H ₂	30.2
O ₂	33.8
N ₂	32.0
H ₂ O	40.0

The heat of formation of H₂O is -241,827 kJ/kmol.

12. A ramjet burner is being designed for an overall stagnation temperature ratio of 4 and outlet Mach number of 0.85. Two possibilities are being considered:
- The burner cross-sectional area is to be constant.
 - The burner cross-sectional area is to be varied in the stream direction in such a way as to maintain the Mach number uniform within the burner. As a first approximation, assume the static pressure varies linearly with duct cross-sectional area.

For both cases determine the ratio of outlet and inlet stagnation pressures. For the second case determine the ratio of outlet and inlet areas. Here ignore the effect of frictional losses and take $\gamma = 1.3$.

13. How might the effect of frictional drag, caused by the flameholder, modify the estimates of stagnation pressure loss ratio and required area ratio for the constant-Mach number combustion case considered in Problem 12?

Assume total frictional drag is twice the inlet dynamic pressure times the inlet area.

14. In a supersonic combustion concept air enters the combustor with Mach number 6, static pressure of 1 atm, and temperature 1500 K. Hydrogen (in the stoichiometrically correct proportion) enters the combustor with the same velocity, pressure and temperature as the air and mixes with the air without frictional loss. Combustion proceeds to completion over a distance of 1 m with the fuel-burned fraction proportional to distance x from the inlet. During combustion the mixture accelerates in such a way as to keep the static temperature constant
- Determine the variation of mixture velocity and molecular weight with distance x .
 - Determine the exit Mach number.
 - Show how to determine the exit static pressure and the ratio of outlet to inlet area.

Use the same specific heat and heat of formation values as in Problem 11 and take $\gamma = 1.35$ for air.

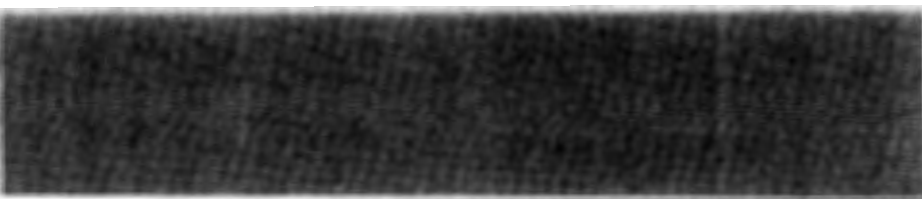
15. The hot gas supply to a propulsion nozzle is at a pressure of 55 kPa and a temperature of 800 K. The ambient pressure is 15 kPa. If the ratio of specific heats is 1.33, approximately constant, and the molecular weight of the mixture is 30, determine the ratio of gross thrusts for two cases:
- The nozzle is converging-diverging with the area ratio for correct expansion to ambient pressure.
 - The nozzle is converging only.

What is the nozzle-exit-to-throat area ratio for case (a)? The gross thrust is the contribution to engine thrust made by the exhaust nozzle only.

REFERENCES

- Kenny, D. P. "A Turbulent Boundary Analysis for Conical Diffusers," *CASI Transactions* 7 (1974).
- Sovran, G., and E. D. Klomp. "Experimentally Determined Optimum Geometries for Diffusers with Rectangular, Conical, or Annular Cross-Section," in G. Sovran, ed., *Fluid Mechanics of Internal Flow*. New York: Elsevier, 1967.
- Caughey, D. A., and A. Jameson. "Accelerated Iterative Calculation of Transonic Nacelle Flow Fields," *AIAA J.* 15 (1977): 1474-80.
- McNally, W. D. "Fortran Program for Calculating Compressible Laminar and Turbulent Boundary Layers in Arbitrary Pressure Gradients," NASA TN D-5681, May 1970.

5. Sinha, R. "Transient Inlet Nacelle Code," *AIAA J. Propulsion and Power* 4 (1988): 252–255.
6. Küchemann, D., and J. Weber. *Aerodynamics of Propulsion*. New York: McGraw-Hill, 1953.
7. Billig, F.S. "Combustion Processes in Supersonic Flow," *AIAA J. Propulsion and Power* 4 (1988).
8. Wu, J. H.T. "On a Two-Dimensional Perforated Intake Diffuser," *Aerospace Engineering* 21 (1962): 58.
9. Foa, J.V. *Elements of Flight Propulsion*. New York: Wiley, 1960.
10. Oswatitsch, K. "Pressure Recovery for Missiles with Reaction Propulsion at High Supersonic Speeds" (transl.), NACA TM-1140, 1947.
11. Shapiro, A. H. *The Dynamics and Thermodynamics of Compressible Fluid Flow*, vol. 1. New York: Ronald Press, 1953. Reprint ed., Wiley.
12. Shapiro, A. H. *The Dynamics and Thermodynamics of Compressible Fluid Flow*, vol. 2. New York: Ronald Press, 1954. Reprint ed., Krieger. Reprinted with permission.
13. Dailey, C. H. "Supersonic Diffuser Instability," *J. Aero Sciences* 22 (1955): 733–749. Reprinted with permission.
14. Olson, W. K., J. H. Childs, and E. R. Jonash. "The Combustion Problem of the Turbojet at High Altitude," *Trans. ASME* 77 (1955): 605–615. Reprinted with permission.
15. LeFebvre, A.W. *Gas Turbine Propulsion*. New York: McGraw-Hill, 1983.
16. Odgers, J., and D. Kretschmer. *Gas Turbine Fuels and Their Influence on Combustion*. Energy and Engineering Series, Tunbridge Wells, Kent: Abacus Press, 1986.
17. Peters, J. E. "Current Gas Turbine and Fuels Research and Development," *AIAA J. Propulsion and Power* 4 (1988).
18. Sturgess, G.T., R. H. James, and S. A. Syed. "Computing Gase Turbine Combustors," *Proc. ASME Symposium on Computers in Engineering*. (1988): 261–275.
19. Grobman, J.S., C. C. Diltrich, and C. C. Graves. "Pressure Drop and Air Flow Distribution in Gas Turbine Combustors," *Trans. ASME* 79 (1957) 1601–9. Reprinted with permission.
20. Reynolds, W. C. "STANJAN," Thermosciences Division, Department of Mechanical Engineering, Stanford University, Palo Alto, Calif., Jan. 1981.



C H A P T E R

7

AXIAL COMPRESSORS

7.1 INTRODUCTION

The axial compressor (like the axial turbine and the centrifugal compressor) is often referred to as a “dynamic” machine. Fluid dynamics is indispensable to its mode of operation because finite change in fluid momentum within the compressor is required for finite pressure change. In contrast, a “positive-displacement” compressor (such as a reciprocating piston compressor) can impart pressure without the need for any finite change in the momentum of its working fluid. For large aircraft engines, dynamic machines—that is, turbomachines—are preferred to positive-displacement ones because they are generally much less massive. It is because their internal velocities are so high, and because the fraction of internal volume allocated to flow can be so high, that they can be made much smaller for a given flow rate. For this reason we devote the next three chapters entirely to turbomachines.

Using the methods of analysis of turbine engines described in Chapter 5, one can show that engine performance, and thus aircraft range, is strongly dependent on compressor pressure ratio and efficiency. For subsonic flight the optimum compressor pressure ratio can be as high as 30:1 or more. The compressor tends therefore to have many stages and to be a fairly massive part of the engine. Since the engine mass must be made as low as possible without sacrificing efficiency, the design of axial compressors for aircraft engines is a great challenge—both aerodynamically and mechanically.

In this chapter we examine the way in which an axial compressor works and the way in which fluid dynamics limits compressor performance and provides a solid foundation for design. In all its detail a complete description of the internal fluid flow would be extremely complex and difficult to calculate. We do not therefore aim for exactness or completeness in our analyses. Fairly simple approximations, however, can provide great insight and (combined discretely with experimental information) can be useful for preliminary design. The closing sections of the chapter provide illustrations of how one can use fundamental principles in devising preliminary design strategies for both subsonic and transonic compressor stages.

We will see that, whereas the behavior of a single-stage machine is relatively easy to understand, the combination of many similar stages to make a multistage compressor or turbine raises a number of problems. Still more problems are introduced when one multistaged machine is driven by another, for example, the turbine-compressor combination in a jet engine. Others occur when the combination is called on to operate under conditions different from those for which it was designed. We will discuss a number of these effects in the following pages.

Fundamentally the axial compressor is limited by boundary layer behavior in pressure gradients that are positive in the flow direction. We may think of each blade passage of a compressor as a diffuser, so that boundary layers on internal walls are generally subject to pressure increase. Unless this pressure increase is kept under control, boundary layer separation, or "stall," will occur. Internal flow separation can lead not only to severe loss in efficiency but also to flow unsteadiness with oscillatory blade stresses of such amplitude that blades may readily fail in fatigue.

Chapter 4 shows that one may predict theoretically the growth of a two-dimensional turbulent boundary layer in an adverse pressure gradient for those cases in which the boundary layer remains reasonably well behaved (i.e., not separated). But in turbomachine blade passages the boundary layers are generally three-dimensional, and possibly unsteady as well, so that elementary boundary layer methods cannot provide a full description of flow development. Much progress has been made in recent years with fully viscous channel flow solutions in turbomachine passages. These solutions generally require much computer time and still suffer to some extent from incomplete knowledge of turbulent boundary layer behavior. One cannot absolutely trust them as methods of prediction, though they can greatly aid a designer in visualizing the kind of fluid behavior that might be expected. Combined wisely with test data, these methods of numerical analysis can substantially reduce the effort needed to modify a compressor design for best performance. They are, however, too complex to serve in an introduction to compressor operation and design. To make the fundamental principles as clear as possible, we begin with simple analytical procedures and supplement these with pertinent test data that illustrate design limitations quantitatively. We bring these together at the end of the chapter in what might be called preliminary design procedures for axial compressor stages.

We now examine the basic physical principle of operation of the dynamic axial compressor.

7.2 ANGULAR MOMENTUM

The concept of angular momentum is very useful for describing the dynamics of turbomachinery. Consider the motion of a single particle of fluid of mass δm , shown in Fig. 7.1. For convenience a cylindrical coordinate system (r, θ, z) is specified in which radial, tangential, and axial particle velocity components are c_r , c_θ , and c_z , respectively. The angular momentum of the particle about the z -axis is simply $\delta m r c_\theta$. Newton's law for the particle may be written

$$\mathbf{F} = \delta m \frac{d\mathbf{c}}{dt}, \quad (7.1)$$

in which

$$\mathbf{F} = \mathbf{r}F_r + \boldsymbol{\theta}F_\theta + \mathbf{z}F_z, \quad \mathbf{c} = \mathbf{r}c_r + \boldsymbol{\theta}c_\theta + \mathbf{z}c_z,$$

and $(\mathbf{r}, \boldsymbol{\theta}, \mathbf{z})$ are unit vectors in the radial, tangential, and axial directions. (We will clarify later the use of \mathbf{c} for velocity.) The unit vectors \mathbf{r} and $\boldsymbol{\theta}$ may change direction so that their time derivatives are not zero, even though their magnitudes are constant. In fact,

$$\frac{d\mathbf{r}}{dt} = \boldsymbol{\theta} \frac{d\theta}{dt} \quad \text{and} \quad \frac{d\boldsymbol{\theta}}{dt} = -\mathbf{r} \frac{d\theta}{dt}.$$

Thus we can resolve Eq. (7.1) into three component equations:

$$\mathbf{r}: \quad F_r = \delta m \left(\frac{dc_r}{dt} - c_\theta \frac{d\theta}{dt} \right), \quad (7.2)$$

$$\boldsymbol{\theta}: \quad F_\theta = \delta m \left(\frac{dc_\theta}{dt} + c_r \frac{d\theta}{dt} \right), \quad (7.3)$$

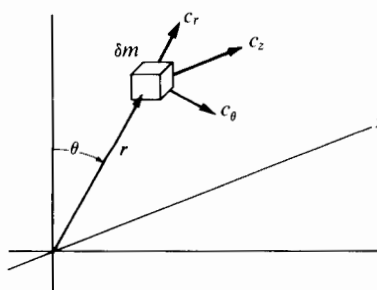


FIGURE 7.1 Motion of a single particle in a cylindrical coordinate system.

$$\text{z: } F_z = \delta m \left(\frac{dc_z}{dt} \right), \quad (7.4)$$

Multiplying by r , we can write Eq. (7.3) as

$$rF_\theta = \delta m \left(r \frac{dc_\theta}{dt} + c_r r \frac{d\theta}{dt} \right).$$

Since $c_r = dr/dt$ and $c_\theta = r(d\theta/dt)$, we can write this expression as

$$rF_\theta = \delta m \frac{d}{dt} (rc_\theta). \quad (7.5)$$

The product rF_θ is called the *torque* acting on the particle with respect to the z -axis. The right-hand side of Eq. (7.5) is the time rate of change of the angular momentum of the particle. If no torque acts on the particle, then the product rc_θ must obviously be constant. The angular momentum rc_θ per unit mass of fluid about any given axis may be considered a property of the fluid, just as are velocity and kinetic energy.

As we mentioned in Chapter 2, when one is dealing with fluid flows it is usually much more convenient to write Newton's laws as they apply to control volumes than as they apply to particular portions of matter. The next step, then, is to transform Eq. (7.5) into a form that is applicable to a control volume. Consider the general control volume shown in Fig. 7.2 with a fixed z -axis that may, or may not, intersect the control surface. By using reasoning exactly analogous to that which led to the derivation of Eq. (2.4), we can show that the total torque $\Sigma \tau$ acting on the control volume is given by

$$\Sigma \tau = \frac{d}{dt} \int_{cv} \rho rc_\theta dV + \int_{cs} \rho rc_\theta (\mathbf{c} \cdot \mathbf{n}) dA,$$

where \mathbf{n} , as before, is a unit vector pointing outward from the control surface. The first integral, extending throughout the control volume, represents the rate of change of angular momentum stored within the control volume. The second integral, extending over the entire control surface, is the net outward flux of angular momentum for the control volume.

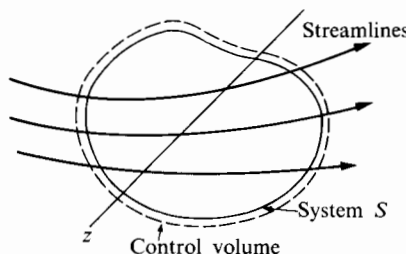


FIGURE 7.2 General control volume.

We now consider a cylindrical coordinate system set up along the axis of a rotating machine, as shown in Fig. 7.3. The control surface illustrated completely encloses a single row of rotating blades mounted on a disc and shaft. Figure 7.3 does not show these elements except for the cross section of the shaft where it is intersected by the control surface. The blades can be of any shape. The control surface includes inlet and outlet flow areas and a cylindrical surface located at the tip diameter of the rotor housing.

The cylindrical coordinates are axial position z , radius r , and angle θ (which is here defined as positive in the direction of rotation of the machine Ω).

Because of the blading arrangements, the flow inside a turbomachine rotor is both unsteady and asymmetric relative to a control surface fixed in space. However, the unsteadiness is periodic (and of high frequency) so that, on average, we may omit the time-dependent term in the torque equation and write

$$\sum \tau = \int_{cs} \rho r c_\theta (\mathbf{c} \cdot \mathbf{n}) dA. \quad (7.6)$$

The flow in a turbomachine passage is also necessarily asymmetric. The blades exert force on the flow, so between the blades there must be tangential variation of fluid pressure and velocity. Upstream and downstream of the rotor, these tangential gradients can be negligible; hence for the control surface of Fig. 7.3, which completely encloses the rotor, we make the assumption that the flow crossing the inlet and outlet surfaces is axisymmetric as well as steady.

The fluid velocity components can vary considerably in the radial direction, so we first consider only the increment of flow rate that enters the control volume

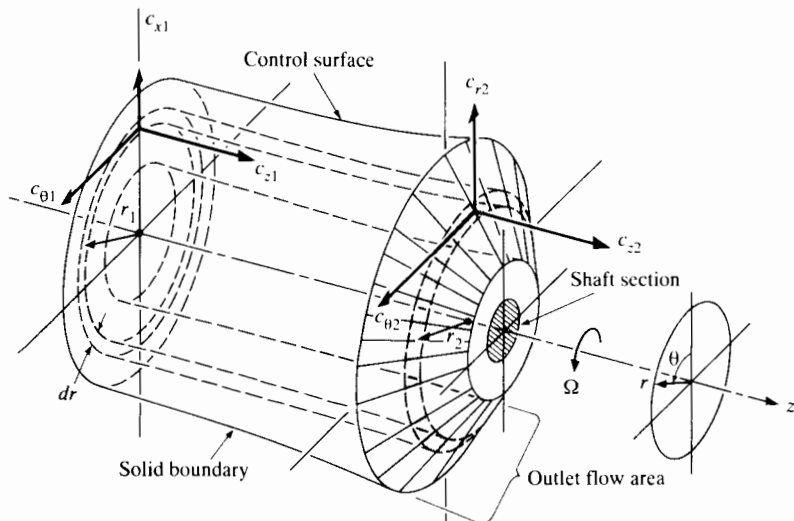


FIGURE 7.3 Special control volume for application to steady axisymmetric flow entering and leaving a rotor.

through an incremental area of mean radius r_1 and radial width dr . This flow occupies a cylindrical annular stream tube that leaves the control volume at radius r_2 . The assumptions of steadiness and axisymmetry mean that both at inlet and outlet the velocity components c_z , c_r , and c_θ will be taken to be independent of r and θ .

The equation of angular momentum (Eq. 7.6) for steady flow through this incremental control volume requires that the incremental torque acting on it be proportional to the incremental mass flow rate times the change in fluid angular momentum per unit mass:

$$d\tau = d\dot{m}(r_2 c_{\theta 2} - r_1 c_{\theta 1}),$$

where $d\tau$ is the sum of the torques acting on the inner and outer surfaces of the angular stream tube.

The sum of these incremental torques may be expressed in terms of integrals over the inlet and exit flow areas, in the form

$$\sum \tau = \int_{A_2} (rc_\theta) \rho c_n dA - \int_{A_1} (rc_\theta) \rho c_n dA, \quad (7.7)$$

where c_n is the component of velocity normal to the area dA . Alternatively, we may obtain Eq. (7.7) directly from Eq. (7.6) without this intermediate step.

If the flow is such that rc_θ is a constant (so-called free-vortex flow) at each area, or if a "suitable average" is taken, we may integrate the equation to

$$\sum \tau = \dot{m}[(rc_\theta)_2 - (rc_\theta)_1]. \quad (7.8)$$

For preliminary work the conditions at the mean inlet and outlet radii often represent suitable averages. Actual design procedure very often begins with a mean radius analysis, after which the designer considers radial variations, from which one can make refined estimates of torque and power requirements.

If the right-hand sides of Eqs. (7.7) and (7.8) adequately represent the net rate of outflow of angular momentum from the control volume, then the term $\sum \tau$ must stand for the sum of all torques applied to the control surface. For a well-designed axial compressor rotor, almost all of $\sum \tau$ is due to the torque applied by the shaft. In addition, there will be small negative-torque contributions due to tangential components of fluid friction forces applied to the lateral surface of the control volume. It is in neglecting these small frictional torques that we identify $\sum \tau$ with the shaft torque.

The axial compressor derives its name from the fact that the air being compressed has very little motion in the radial direction. In contrast, the motion of the air in a centrifugal compressor is characterized by large radial velocity components. This means that for the same outside diameter, the axial machine has much greater mass flow rate than the centrifugal one. For this reason, and because of a small but significant efficiency advantage, the axial configuration is preferred for large turbojet engines.

Figure 7.4 shows a simplified view of an axial compressor in which rows of closely spaced rotor blades (*R*), which rotate with the shaft, are each followed by rows of closely spaced stator blades (*S*). One rotor blade row plus a succeeding stator blade row makes up a single stage of the compressor. For a reason we will discuss later, some compressors have a stationary set of blades, known as inlet guide vanes, just ahead of the first rotor blade row.

As Fig. 7.4 indicates the blade height is much less at the back end of the compressor than at the front end. This is because most axial compressors are designed so that the axial component of the average velocity is approximately the same for all stages. With little change in average blade diameter, this means that, on average, the ratio of axial velocity component to blade speed varies little from stage to stage; this explains why in many compressors the blade angles are similar for all stages. Constancy of axial velocity component (under design conditions) requires that the annular flow area at the entrance to each stage vary inversely with density. Thus at the back end of the compressor, where pressure and density are highest, blade height is least.

The simplified sketch of Fig. 7.4 shows the outer blade diameter to be the same from end to end of the machine. In some axial compressors the mean blade diameter (or the inner one) may be more nearly constant than the outer one. The sketch also shows all rotor blades attached to the same rotor. One example of such a rotor is the compressor from the General Electric J85 turbojet engine. The compressor shown in Fig. 7.5 has seven stages; each rotor blade row is mounted on a separate disc, but all discs are bolt connected and driven by a single shaft.

Many axial compressors in turbine engines have two or three separate compressor sections; these are able to rotate at different speeds but are mounted on concentric shafts. Figure 7.6(a) shows the low-pressure compressor and turbine combination of the General Electric F404 engine. A single-stage low-pressure

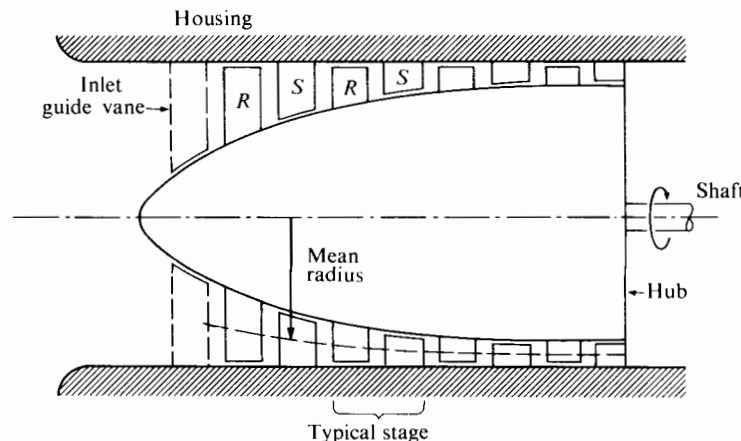


FIGURE 7.4 Schematic of a section of an axial compressor.

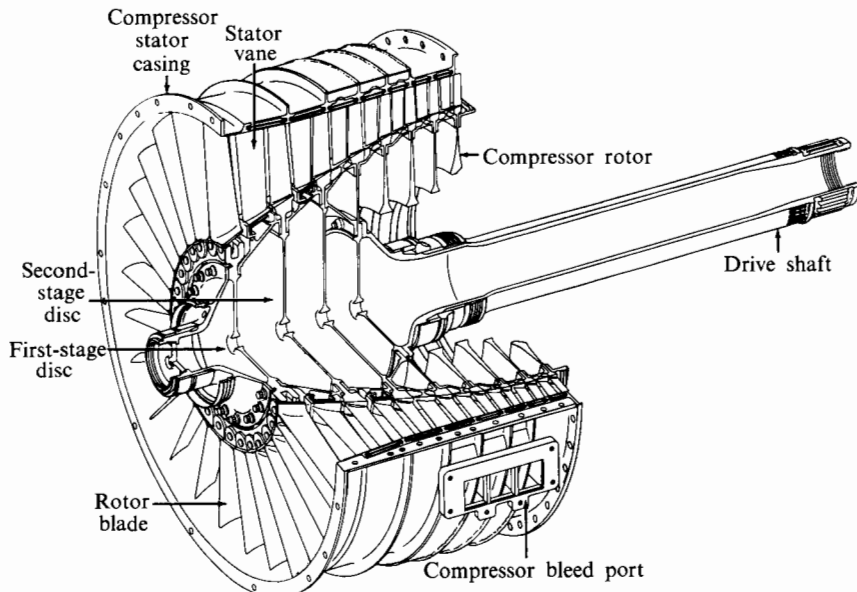


FIGURE 7.5 Cutaway sketch of a typical axial compressor assembly: the General Electric J85 compressor. (Courtesy GE Aircraft Engines.) This particular compressor has an overall pressure ratio of about 6.5. A later version has an extra stage and an overall pressure ratio of 9.3. It ingests 69.6 lb/sec under static sea-level conditions; the inlet blade tip diameter is 0.51 m (20 in.).

turbine drives a 3-stage axial compressor. Figure 7.6(b) shows the close spacing, flatness, and thinness of the first-stage rotor blades. At the outer radius the velocity of the flow relative to these blades is supersonic. Figure 7.6(c) shows the 7-stage high-pressure compressor, which is driven by a separate high-pressure turbine through a shaft concentric with the one shown in Fig. 7.6(a). The overall compressor ratio is about 26:1, so the average pressure ratio per stage ($26^{1/10}$) is about 1.39. The flow rate through the low-pressure compressor is approximately 64.5 kg/s (142 lb/sec). Later in the chapter we discuss the rationale for designing high-pressure-ratio axial compressors with separate and independently driven sections, as well as the problems of designing for supersonic velocity relative to the blade.

7.3 WORK AND COMPRESSION

We consider here the way in which fluid motion through a stage is related to the stage work and pressure ratio.

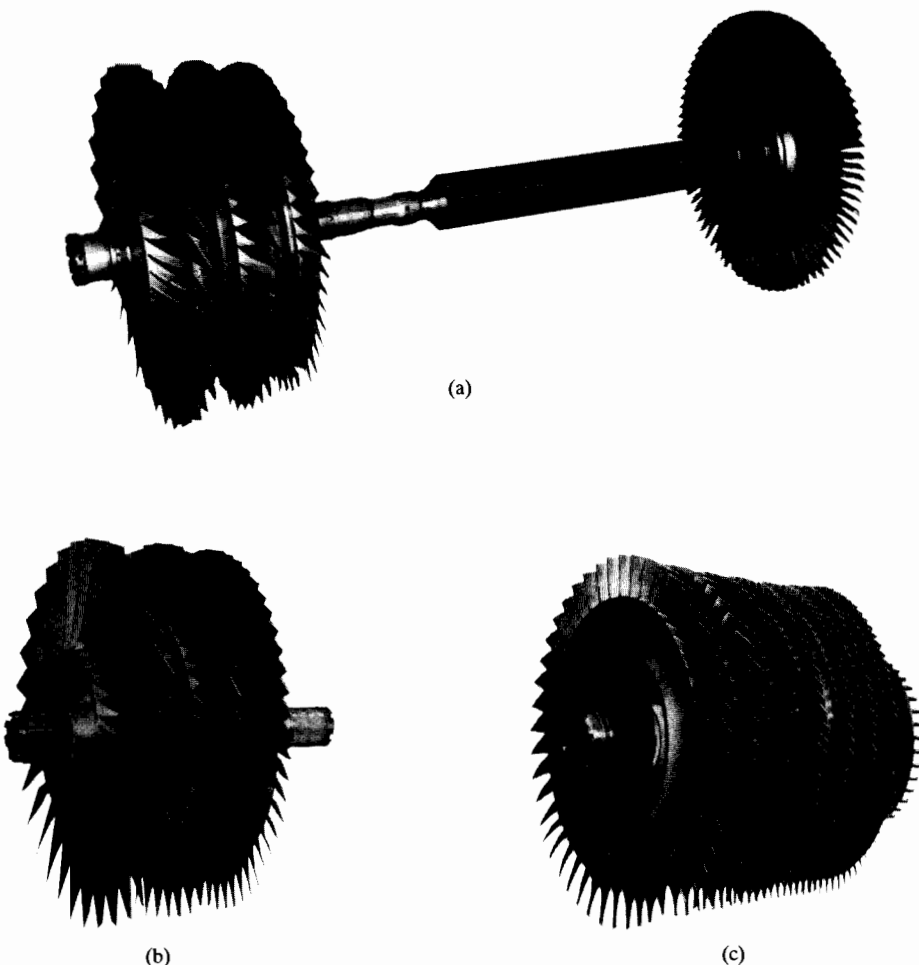


FIGURE 7.6 (a) Low-pressure rotor. (b) Low-pressure compressor. (c) High-pressure compressor of the General Electric F404 engine. (Courtesy GE Aircraft Engines.)

The velocity of an object, such as a fluid “particle,” is dependent on the motion of the observer as well as on that of the object. Within a turbomachine, observations may be considered from two reference frames of importance: the *absolute* reference frame, which is fixed to the frame of the machine (test bed or aircraft frame, for instance), and the *relative* reference frame, which rotates with the rotor of the machine. Fluid velocities observed from the absolute reference frame are denoted by c and are called *absolute velocities*, whereas those viewed from the relative reference frame are denoted by w and are called *relative velocities*. The vector difference between c and w at any point is simply the local blade

velocity, which we will denote here as U , and the three quantities are, by definition, related by the vector addition:

$$\mathbf{c} = \mathbf{U} + \mathbf{w}.$$

The graphical solution of this equation results in a triangular figure called the *velocity triangle*.

We begin our study of the dynamics of a single axial compressor stage with an analysis of the velocity triangles at the mean radius. If an approximately cylindrical surface at the mean radius of the typical stage of Fig. 7.4 is “unwrapped,” part of it would appear as in Fig. 7.7, which indicates both absolute and relative fluid velocity vectors at the entrance and exit of each blade row of the stage. Absolute flow angles are denoted by α , while β denotes the direction of the flow relative to the rotor. Velocity triangles are constructed at ① and ② to show the relation of absolute and relative velocities.

The angular momentum of the fluid is changed as it travels through a compressor blade row, as the result of pressure forces on the blade surface. The pressure on the convex surface is generally relatively low, and the pressure on the concave side is generally relatively high. For this reason the convex and concave surfaces are customarily called the *suction* and *pressure* sides, respectively, of the blade.

The absolute velocity of the flow entering the rotor is \mathbf{c}_1 . The velocity relative to the rotor \mathbf{w}_1 is then derived by vector subtraction of the rotor velocity, as indicated by the velocity triangle. The flow turns in the blade passage to the new relative velocity vector \mathbf{w}_2 . The absolute velocity \mathbf{c}_2 at the rotor exit or stator entrance is obtained by adding this relative velocity to the rotor speed, as shown by the second vector triangle. One may see that in this case the rotor imparts angular momentum to the air, since the component of the absolute velocity in the tan-

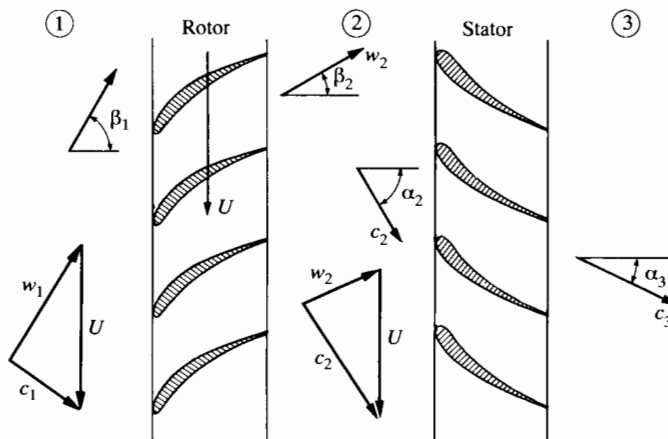


FIGURE 7.7 Mean radius section of a compressor stage. The absolute exit angle from the previous stage is α_1 , which may be equal to α_3 .

gential direction increases. In both rotor and stator, the velocity inside the blade passage (relative to the blades) usually decreases; hence the pressure rises in each blade row.

As Fig. 7.4 suggests there will generally be a little radial displacement of a fluid particle as it moves through a rotor blade row, so that, strictly speaking, $r_2 \neq r_1$ and $U_2 \neq U_1$. Usually, however, $r_2 - r_1 \ll r_1$, so for simplicity in the following discussion we make the approximation $U_2 = U_1 = U$. With this approximation the velocity triangles can be superimposed as in Fig. 7.8 in such a way as to make the change in tangential velocity immediately obvious.

Figure 7.8 indicates that the axial velocity components c_{z1} and c_{z2} are approximately equal. This may be so as a design condition at mid-radius, but the two components will not be generally equal. Typically they will vary with radius in different ways upstream and downstream of the rotor. Even at mid-radius they may differ appreciably when the compressor runs at off-design flow or speed. Since, however, we are interested initially in examining in a simple way how the stage pressure ratio depends on fluid velocities under design conditions, we confine our attention here to the mid-radius design flow condition and make the approximation

$$c_{z1} = c_{z2} = c_z.$$

(Later we will discuss radial variations of c_z , c_θ , and blade angles, as well as off-design conditions.)

If for the moment we assume that each fluid particle passing through the stage had the velocity vectors shown in Fig. 7.8, then we could easily determine the torque and power required to drive the rotor. Referring to the velocity changes indicated in Fig. 7.8, the torque acting on the fluid within the rotor may be determined from Eq. (7.8), applied to a control volume that contains only the rotor. That is,

$$\tau = \dot{m}[(rc_\theta)_2 - (rc_\theta)_1].$$

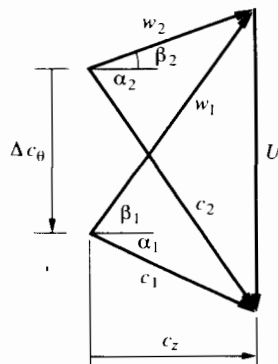


FIGURE 7.8 Velocity triangles for a compressor stage.

The power required to drive the stage is $\tau\Omega$, and according to our thermodynamic convention (Chapter 2), the power output from the machine is negative:

$$\mathcal{P}_s = \tau\Omega = -\dot{m}\Omega[(rc_\theta)_2 - (rc_\theta)_1].$$

Since Ωr equals the blade speed U , and since U is constant, we have

$$\mathcal{P}_s = -\dot{m}U(c_{\theta 2} - c_{\theta 1}). \quad (7.9)$$

The work per unit mass w_c done on the fluid by the rotor is

$$w_c = -\frac{\mathcal{P}_s}{\dot{m}} = U(c_{\theta 2} - c_{\theta 1}) \quad (7.10)$$

or

$$w_c = U\Delta c_\theta.$$

The work done by the stator on the fluid is zero, of course (even though $\Delta c_\theta \neq 0$), because $U = 0$. There is, however, a torque on the stator (opposite to that on the fluid) of magnitude

$$\tau = \dot{m}[(rc_\theta)_3 - (rc_\theta)_2].$$

The flow between stations (1), (2), and (3) is close to adiabatic, since even at the high-temperature end of the compressor, the heat transfer from the air (per unit mass of air) is negligible relative to the work transfer. Assuming uniform stagnation enthalpy in the radial direction, we apply Eq. (2.8) over the rotor and find that

$$0 = \dot{m}(h_{02} - h_{01}) + \mathcal{P}_s,$$

where \mathcal{P}_s is shaft power. With Eq. (7.9), then, we obtain

$$h_{02} - h_{01} = U(c_{\theta 2} - c_{\theta 1}). \quad (7.11)$$

If we assume the specific heat is constant, we can derive a nondimensional stagnation temperature rise across the rotor from Eq. (7.11):

$$\frac{\Delta T_0}{T_{01}} = \frac{U\Delta c_\theta}{c_p T_{01}}. \quad (7.12)$$

Since the flow is adiabatic and no work is done on the fluid as it passes through the stator row, $T_{03} = T_{02}$, so that Eq. (7.12) represents the entire stagnation temperature rise across the stage.

The isentropic efficiency of the stage does not enter into Eq. (7.12), since the work done on the fluid depends only on the kinematic changes in the flow. The stagnation pressure rise across the blade stage does depend strongly on the efficiency, however. Figure 7.9 shows on the temperature–entropy plane the path of the compression process through the stage. If the whole process were isentropic, the final stagnation pressure for the same work input would be $p_{0 \max}$ as shown. However, because of losses in the rotor and stator, $p_{03} < p_{02} < p_{0 \max}$.

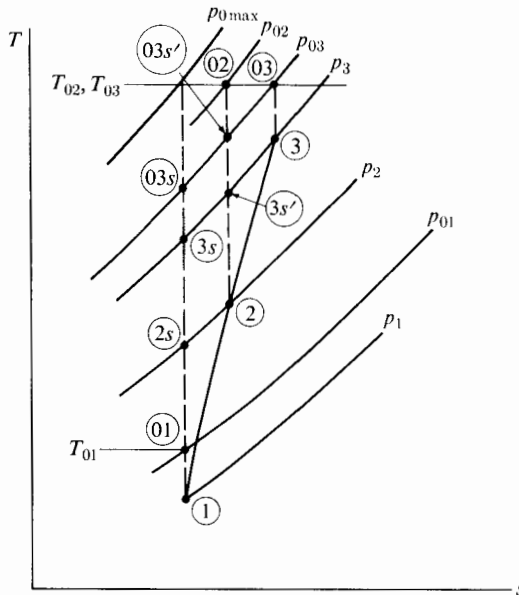


FIGURE 7.9 Single-stage compression process.

If we knew the stage efficiency η_{st} , defined by

$$\eta_{st} = \frac{h_{03s} - h_{01}}{h_{03} - h_{01}}, \quad (7.13)$$

we could determine the stagnation pressure ratio across the stage as follows: With the constant specific heat approximation, we could write Eq. (7.13) as

$$\frac{T_{03s}}{T_{01}} = 1 + \eta_{st} \frac{\Delta T_0}{T_{01}},$$

in which $\Delta T_0 = T_{03} - T_{01}$. From this, using the isentropic pressure–temperature relationship, we could write

$$\frac{p_{03}}{p_{01}} = \left[1 + \eta_{st} \frac{\Delta T_0}{T_{01}} \right]^{\gamma(\gamma-1)}. \quad (7.14)$$

Combining Eqs. (7.12) and (7.14), we find that the stage pressure ratio may be written

$$\frac{p_{03}}{p_{01}} = \left[1 + \eta_{st} \frac{U \Delta c_\theta}{c_p T_{01}} \right]^{\gamma(\gamma-1)}, \quad (7.15)$$

which shows, not unexpectedly, that the higher the blade speed U and the higher the change Δc_θ in tangential velocity component, the higher the stage pressure ratio. This will be true only up to the point at which a given stage can still provide a given Δc_θ with reasonably high stage efficiency. Past that point, misbehav-

ior of the boundary layers on the blade surfaces or on the end walls of the blade passages may prevent any further increase in stage pressure ratio. It can quite easily lead to large-scale flow unsteadiness and large viscous losses. Section 7.6 provides a summary of knowledge available to the designer who wishes to maximize the pressure ratio of an axial compressor stage while maintaining high mass flow rate per unit cross-sectional area. Sections 7.10 and 7.11 demonstrate how this knowledge may be used in preliminary design procedures. Before going into the factors on which to base best design, we review in Sections 7.4 and 7.5 the typical behavior of axial stages and multistage compressors over a wide range of operating conditions.

We may note here that though it is usually true for axial compressor stages that

$$\frac{\Delta T_0}{T_{01}} = \frac{U \Delta c_\theta}{c_p T_{01}} \ll 1,$$

it is usually unsatisfactory to approximate Eq. (7.15) as

$$\frac{p_{03}}{p_{01}} \approx 1 + \frac{\gamma}{\gamma - 1} \eta_{st} \frac{U \Delta c_\theta}{c_p T_{01}} = 1 + \eta_{st} \frac{U \Delta c_\theta}{R T_{01}}.$$

7.4 CHARACTERISTIC PERFORMANCE OF A SINGLE COMPRESSOR STAGE

We suppose at this point that we have an axial compressor stage whose blading is portrayed in Fig. 7.7 and that Fig. 7.8 represents the flow velocities and angles when the stage is operating at design values of shaft speed and mass flow rate. The question before us is how we may expect the performance of the stage to change as a result of departure from these design conditions. To consider this question, we modify the work Eq. (7.11) by writing (with reference to Fig. 7.8)

$$c_{\theta 2} = U - c_z \tan \beta_2$$

and

$$c_{\theta 1} = c_z \tan \alpha_1,$$

so that Eq. (7.11) becomes

$$U \Delta c_\theta = \Delta h_0 = h_{02} - h_{01} = U[U - c_z(\tan \alpha_1 + \tan \beta_2)]$$

or, in dimensionless form,

$$\frac{\Delta c_\theta}{U} = \frac{\Delta h_0}{U^2} = 1 - \frac{c_z}{U} (\tan \alpha_1 + \tan \beta_2). \quad (7.16)$$

A departure from design flow rate will change the axial velocity component c_z ; departure from design shaft speed will necessarily change the blade speed U . Changing either c_z or U will alter the angle β_2 at which the flow approaches the rotor (or α_2 , at which it approaches the stator).

In seeking to understand the effects of small changes from design conditions, we make the assumption that small changes in β_1 , for example, do not affect β_2 . The blades are considered to provide sufficiently strong flow guidance that the outlet angle β_2 is essentially independent of the inlet angle (for small changes). With this assumption we can see that it is significant that the only blade angles appearing in Eq. (7.16) are outlet angles (β_2 from the rotor and α_1 from the preceding stator). Thus in this equation we can take $(\tan \alpha_1 + \tan \beta_2)$ to be a constant while the entire results of departure from design conditions are concentrated in a single variable c_z/U .

Equation (7.16) then gives us an ideal stage characteristic that we may plot as in Fig. 7.10 and compare there with a representation of a measured stage characteristic. Figure 7.10 shows that for small departures from $(c_z/U)_{\text{design}}$, the actual and ideal work curves ($\Delta h_0/U^2$) agree quite closely, and there is little effect on measured stage efficiency. For large departures from $(c_z/U)_{\text{design}}$ there are large differences between ideal and actual work. We can understand these differences by realizing that, as Fig. 7.11 illustrates, the rotor inlet angle β_1 is uniquely determined by the value of c_z/U . Figure 7.11 shows the velocity changes associated with changes in c_z (with constant U) and constant stator outlet angle α_1 . Qualitatively the results would have been the same if U had been varied while c_z was held constant. The main point of Figure 7.11 is that for sufficiently large departures from $(c_z/U)_{\text{design}}$, one can expect boundary layer separation. When that happens,

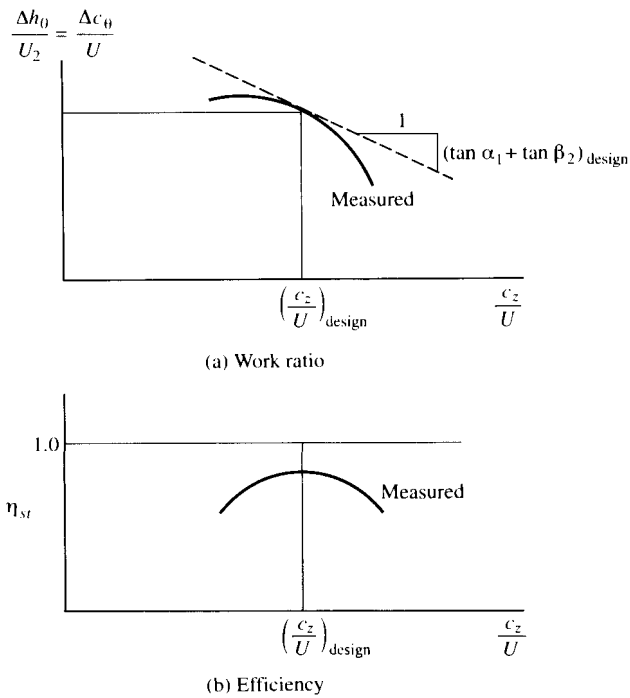


FIGURE 7.10 Ideal and actual stage characteristics.

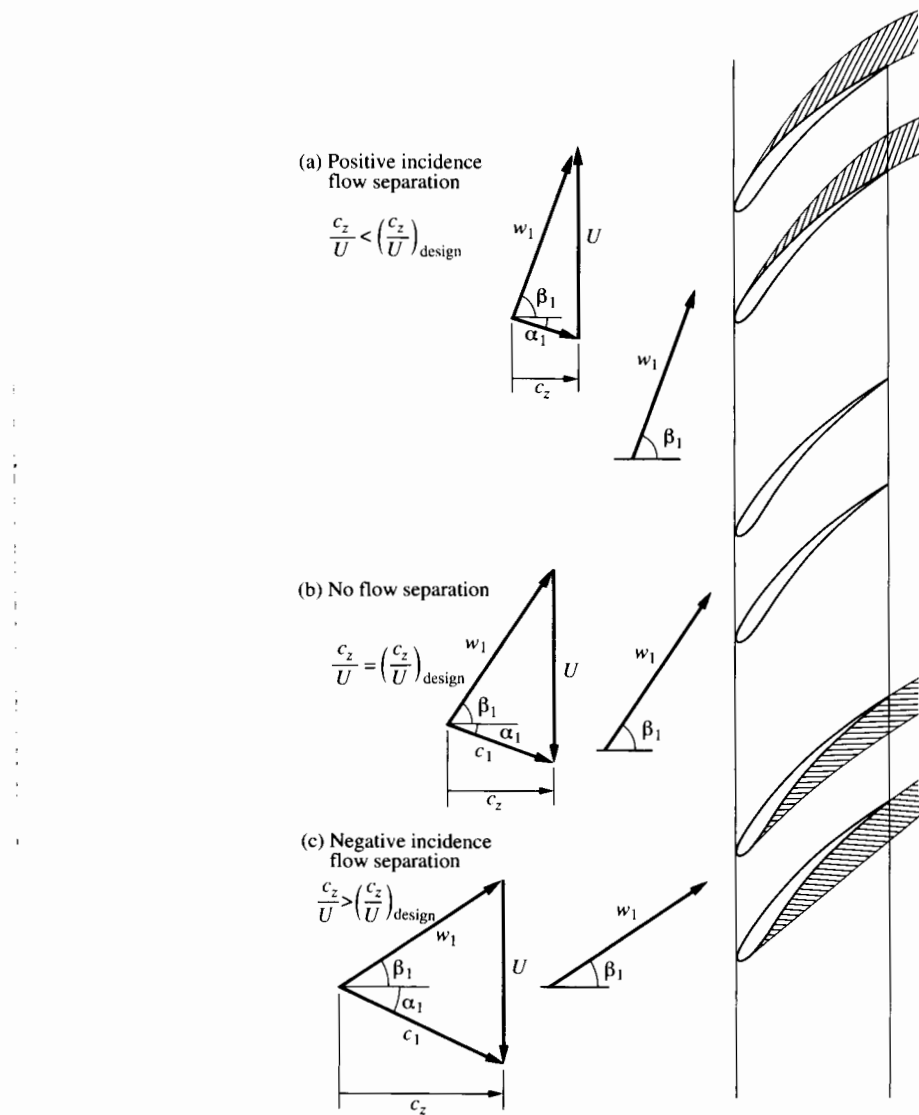


FIGURE 7.11 Design and stalling conditions for an axial compressor stage.

the blades are no longer effective in controlling the flow, and $\Delta c_\theta/U$ drops considerably below the ideal characteristic, as Fig. 7.10(a) shows. Flow separation also results in increased viscous mixing loss. Hence the stage efficiency drops considerably below the design value, as Fig. 7.10(b) shows. One should not take Fig. 7.11 to imply that the flow is necessarily steady when flow separation has taken place. Often the reverse is the case, and possibly dangerously so, as Section 7.5 explains.

So far we have considered an isolated single-stage compressor over a range of off-design conditions. In a multistage axial compressor, a small departure from

design point operation at the first stage causes progressively increasing departure from design conditions from the first stage onward. To understand this, we can consider a multistage compressor consisting of stages having identical characteristics as shown in Fig. 7.10. For simplicity we might assume that at the design point all stages operate with the same value of c_z/U . If, at constant speed, the flow rate into the compressor is slightly reduced, this will slightly lower c_z/U and slightly increase the work done by the first stage. At entrance to the second stage, the value of c_z/U will fall for two reasons: the decrease in mass flow rate and the extra increase in density of the air leaving the first stage (because of higher-than-design work being done in the first stage). This enhanced departure from $(c_z/U)_{\text{design}}$ causes even greater work and density increase in the second stage, with the result that c_z/U at entrance to the third stage is still lower than it was at entrance to the second. Thus a small reduction from $(c_z/U)_{\text{design}}$ at entrance to the first stage could lead to positive-incidence flow separation in the last stage of the compressor.

In a similar way a moderate increase in c_z/U at the first stage could lead to large negative-incidence flow separation in the last stage. It is possible, with the front stages operating normally, that the end stages of the compressor could be faced with such high values of c_z/U as to produce negative pressure rise, that is, to act as throttles rather than as compressor stages.

The most extreme mismatching of front and back stages of a multistage axial compressor may take place during starting, which for a high-pressure-ratio compressor could be a major problem. Under design conditions such a machine operates with a large change in density from entrance to exit. There is a corresponding change in blade length to accommodate this density variation, as Fig. 7.4 shows. When the compressor is started, the density ratio is unity, and it remains low until the compressor is actually working properly. This means that while the axial velocity is still very low in the first stage, it may be large enough in the last stage to choke the flow. The differences in velocity triangles between starting and design are shown in Fig. 7.12.

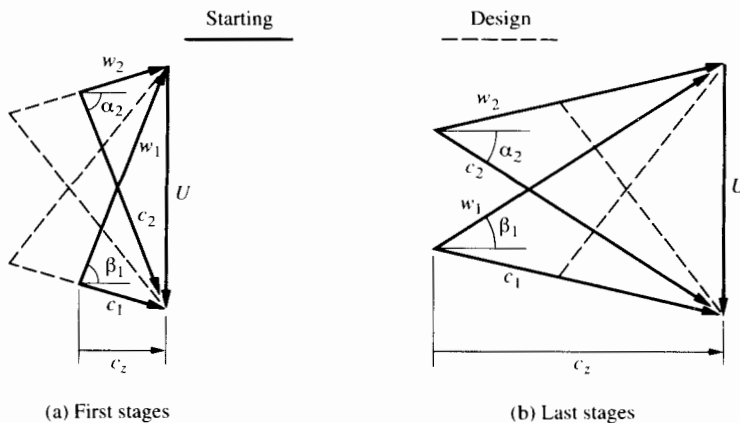


FIGURE 7.12 Effect of axial velocity change.

Considering the first stages, we can see that decreased c_z with α_1 and β_2 constant results in increased α_2 and β_1 or *increased loading on both rotor and stator blades*. Considering the last stages, we can see that the opposite is true, that increased c_z results in *decreased loading of both rotor and stator blades*. The starting difficulty can now be restated in more specific terms: Operation at below-design-density ratio causes variations in c_z that tend to overload the leading stages, thus causing stall and preventing proper compression, which would correct the poor density ratio.

Designers use several solutions to allow compressors with high pressure ratios to be self-starting. Variation of blade speed is of little help, since the two ends of the compressor require opposite variations. External assistance such as an air blast to increase c_z in the leading stages is inconvenient for aircraft use,[†] although it is used in some stationary power plants.

The simplest device to aid starting is a blow-off valve located at about the middle of the compressor, which allows some of the incoming air to bypass the second half of the compressor. Such a valve is shown in Fig. 7.5 as a compressor bleed port. In this way the axial velocity is reduced in the last stages, allowing these stages to do more work, while at the same time the apparent downstream restriction encountered by the first stages is reduced, allowing an increase in c_z . In effect this solution temporarily creates two low-pressure compressors in series with a variable mass flow relationship between them. The variation is accomplished by a rather rapid or on-off type control, which is acceptable for starting purposes but undesirable for in-flight application. Since in-flight conditions might involve off-design operation similar to that encountered in starting, the blow-off valve is employed only as an auxiliary device to be used with other continuously variable devices.

Another solution is suggested by the above statement that the two ends of the compressor demand opposite variations of blade speed. If the compressor can be broken into two mechanically independent units, the first or low-pressure stages being driven by one turbine and the last or high-pressure stages being driven by another, these demands can be met. With this arrangement the lightly loaded high-pressure stages will automatically run faster, improving their velocity triangles and picking up a greater share of the starting load. This has the effect of reducing the downstream restriction encountered by the low-pressure stages, while at the same time the overloaded low-pressure stages will automatically run more slowly, also improving their velocity triangles and avoiding stall. This is the two- or three-shaft compressor configuration of which several examples were given in Chapter 5.

Noting that the overloading of the first stages is the result of an increased angle of attack on the blades, one can suggest the solution of variable blade angles. Though it would be desirable to vary all blade angles, it is mechanically feasible to vary only stator blade angles, by rotating the stator blades about their radial axis. Figure 7.13 shows how much change in stator angle $\Delta\alpha_1$ is necessary to re-

[†] Aircraft have occasionally used the exhaust blast from another aircraft to assist in starting.

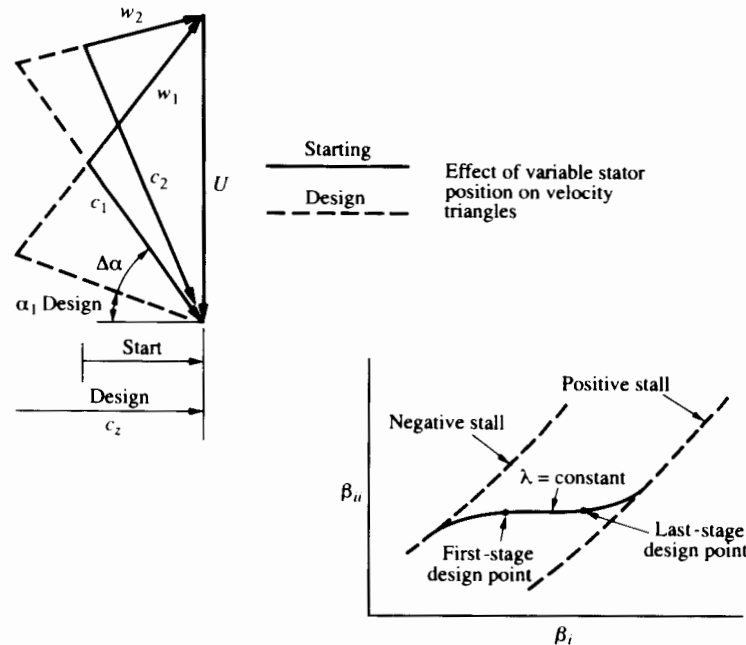


FIGURE 7.13 Variation of stage design points.

store β_1 to approximately the design value for a given c_z/U . This does not change α_2 , but if the following stator is rotated in the same manner as the preceding one, the angle of attack on the following stator will be reduced by the same quantity. This is the variable-stator configuration.

There is some benefit to be had from varying the design point loading throughout the stages. Realizing that the first stages will be overloaded during starting, one may be wise to design them for light loading. Conversely, the last stages should be heavily loaded. The first- and last-stage design points should appear as shown in Fig. 7.13. Note that this choice leaves a relatively large range of increased β_1 before stall occurs in the first stages. The light loading of the first stages is somewhat compensated for by the heavy loading of the last stages. This technique alone may be sufficient to provide starting ability in moderate-pressure-ratio machines, but it is not adequate for high-pressure ratio machines. Hence one or more of the mechanical methods just described finds application on all modern high-pressure-ratio engines.

In this section we have discussed mainly the work ratio $\Delta h_0/U^2$ and the stage efficiency η_{st} (as functions of the axial velocity ratio c_z/U for a given stage). We can obtain the stage pressure ratio by using a modification of Eq. (7.15) in the form

$$\frac{p_{03}}{p_{01}} = \left[1 + \eta_{st} \frac{U^2}{c_p T_{01}} \frac{\Delta c_\theta}{U} \right]^{\gamma/(\gamma-1)}$$

or

$$\frac{p_{03}}{p_{01}} = \left[1 + \eta_{st}(\gamma - 1) \left(\frac{U}{\sqrt{\gamma RT_{01}}} \right)^2 \frac{\Delta c_\theta}{U} \right]^{\gamma(\gamma-1)}. \quad (7.17)$$

Here we see that to estimate the stage pressure ratio it is necessary to specify not only the values of $\Delta c_\theta/U$ and η_{st} but also the value of the ratio $U/\sqrt{\gamma RT_{01}}$. The latter variable can be called a blade speed Mach number since it is the ratio of the blade speed to the speed of sound (at the inlet stagnation temperature).

The preceding analysis with its use of variables such as c_z/U and $\Delta c_\theta/U$, was intended primarily to explain how an axial compressor stage behaves over a range of operating conditions. These variables may not be particularly easy to measure during a compressor test, so in the following section we use a different kind of analysis in deriving the variables commonly employed in presenting measured compressor behavior.

7.5 CHARACTERISTIC PERFORMANCE OF A MULTISTAGE AXIAL COMPRESSOR

We now consider the characteristic behavior of a multistage axial compressor operating between inlet station ① and outlet station ②. Changing nomenclature a little, we designate the overall stagnation pressure ratio for the multistage axial compressor as p_{02}/p_{01} , and the overall adiabatic efficiency as η_c .

The first matter we must address is the choice of independent variables to use in expressing the results of experimental tests of multistage compressor performance. It is helpful to develop a very general result, so we now step back from examining the internal details of particular compressors and consider the variables that are used to describe the performance of any compressor on the test stand. The derivation that follows is not restricted to axial compressors. It is useful for any kind of gas compressor because it is not limited to any particular blading geometry and because it identifies in a general way the properties of the gas being compressed. The analysis is useful not only because it shows how to organize test data in the simplest general form, but also because it helps to introduce the design procedure that Sections 7.10 and 7.11 present.

For any gas compressor we could express the dependence of the stagnation pressure at the compressor outlet p_{02} and the adiabatic efficiency η_c on the other important physical variables in the following form:

$$p_{02}, \eta_c = f(\dot{m}, p_{01}, T_{01}, \Omega, \gamma, R, v, \text{design}, D),$$

in which the subscripts 01 and 02 denote the compressor inlet and outlet stagnation states, respectively. The mass flow rate is denoted by \dot{m} , and p_{01} and T_{01} denote the inlet stagnation pressure and temperature, respectively. The symbol Ω denotes the rotational speed of the shaft. The gas properties significant to the compression process are specified by stating the kinematic viscosity v , the specific heat ratio γ , and the gas constant R that appears in the perfect-gas law. (Instead

of stating R , we could have given the molecular weight.) Included, in a completely general way, in this statement of physical dependence are the design of the machine and its characteristic size D . By *design* we mean a complete specification of the geometric shape of the machine, for example, in the form of a set of ratios of every important dimension to the characteristic size D . For an axial compressor we might take D to be the tip diameter of the first-stage rotor.

The physical relationship we have just stated needs to be tested (either literally on the test stand or by means of a thought experiment) to see if the variables mentioned on the right-hand side consist of a complete set of independent variables. The adjective *independent* indicates that each variable in the set can be varied without necessarily altering the value of any other member of the set. The important question is whether one can experimentally, or at least conceptually, change all of these variables one at a time. The set is complete only when it contains the maximum number of variables for which this is possible. The requirement that must be satisfied before dimensional analysis can properly begin is that a complete set of independent and physically significant variables be present on the right-hand side of any statement such as given above for compressors.

Here we have named nine independent variables. The task of measuring their separate effects on machine performance and reporting the results in the form of graphs or tables would be gigantic. Dimensional analysis helps considerably to reduce the complexity. Since there are four significant primary variables (mass, length, time, and temperature) in this thermodynamic problem, we can reduce the statement of physical dependence to one in which each (dimensionless) dependent variable is seen to be a function of only $9 - 4 = 5$ dimensionless independent variables. There are many ways in which these dimensionless variables; could be composed; the only absolute requirement is that each significant variable identified in the original statement appear at least once in the final result.

The variables γ and "design" are already dimensionless. We can make the mass flow rate dimensionless by multiplying it by a quantity that has the dimensions of velocity ($\sqrt{\gamma RT_0}$), so that it acquires the dimensions of momentum flow rate, and then dividing it by a quantity that has the dimensions of force ($p_{01}D^2$). We can make the rotational speed dimensionless by multiplying it by the length term D and dividing it by $\sqrt{\gamma RT_0}$ so that it becomes the ratio of two velocities. The viscosity term ν is conveniently expressed in the form of a Reynolds number.

In this way the dimensionless analysis of compressor variables can lead to the following general statement of the relationship between performance variables:

$$\frac{p_{02}}{p_{01}}, \eta_c = f\left(\frac{\dot{m}\sqrt{\gamma RT_0}}{p_{01}D^2}, \frac{\Omega D}{\sqrt{\gamma RT_0}}, \frac{\Omega D^2}{\nu}, \gamma, \text{design}\right). \quad (7.18)$$

Checking, we see that each of the physical variables identified is present in at least one of these parameters. For a given design of machine, compressing air whose inlet state is in such a range that γ does not vary appreciably, we may reduce the statement to

$$\frac{p_{02}}{p_{01}}, \eta_c = f\left(\frac{\dot{m}\sqrt{RT_0}}{p_{01}D^2}, \frac{\Omega D}{\sqrt{RT_0}}, \frac{\Omega D^2}{\nu}\right). \quad (7.19)$$

The question of whether viscosity has an important effect on changes in the operation of the compressor may be answered by considering the question of whether changes in the Reynolds number (holding the dimensionless mass flow and shaft speed variables constant) would significantly affect the pressure ratio or the efficiency. In general one may say that compressors for propulsion engines are designed to operate at Reynolds numbers high enough that changes in the number (as the engine changes speed or altitude) have little effect on performance. It is not that viscous effects are unimportant at high Reynolds number, but that they have become insensitive to change in Reynolds number. So we can expect that if the Reynolds number range is sufficiently high, the compressor performance can be adequately described by

$$\frac{p_{02}}{p_{01}}, \eta_c = f\left(\frac{\dot{m}\sqrt{RT_{01}}}{p_{01}D^2}, \frac{\Omega D}{\sqrt{RT_{01}}}\right). \quad (7.20)$$

Since for a given air compressor D and R are fixed, we can correlate the experimental performance in the form

$$\frac{p_{02}}{p_{01}}, \eta_c = f\left(\frac{\dot{m}\sqrt{T_{01}}}{p_{01}}, \frac{N}{\sqrt{T_{01}}}\right), \quad (7.21)$$

in which N is the shaft rpm. No difference in functional relationship is implied when each of the variables on the right-hand side is multiplied by a constant, so we can equally well express Eq. (7.21) as

$$\frac{p_{02}}{p_{01}}, \eta_c = f\left(\frac{\dot{m}\sqrt{\theta}}{\delta}, \frac{N}{\sqrt{\theta}}\right), \quad (7.22)$$

in which

$$\theta = \frac{T_{01}}{(T_{01})_{\text{std day}}}$$

and

$$\delta = \frac{P_{01}}{(p_{01})_{\text{std day}}},$$

in which

$$(T_{01})_{\text{std day}} = 288.15 \text{ K}$$

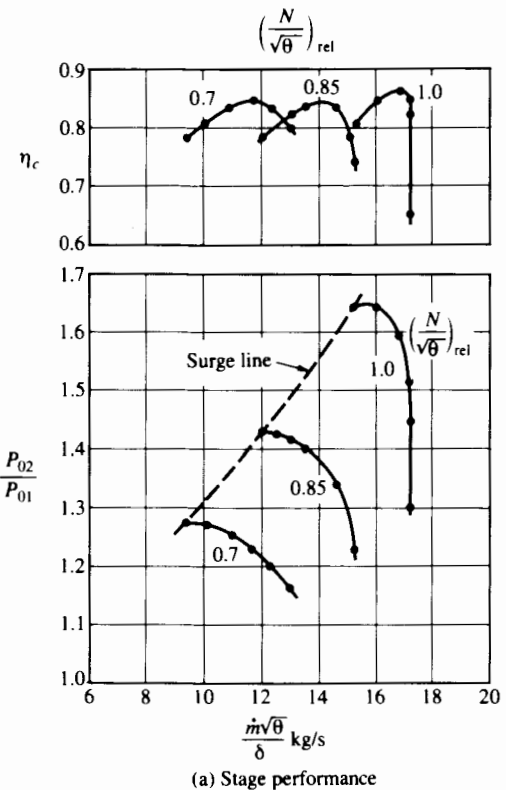
and

$$(p_{01})_{\text{std day}} = 101.325 \text{ kPa}.$$

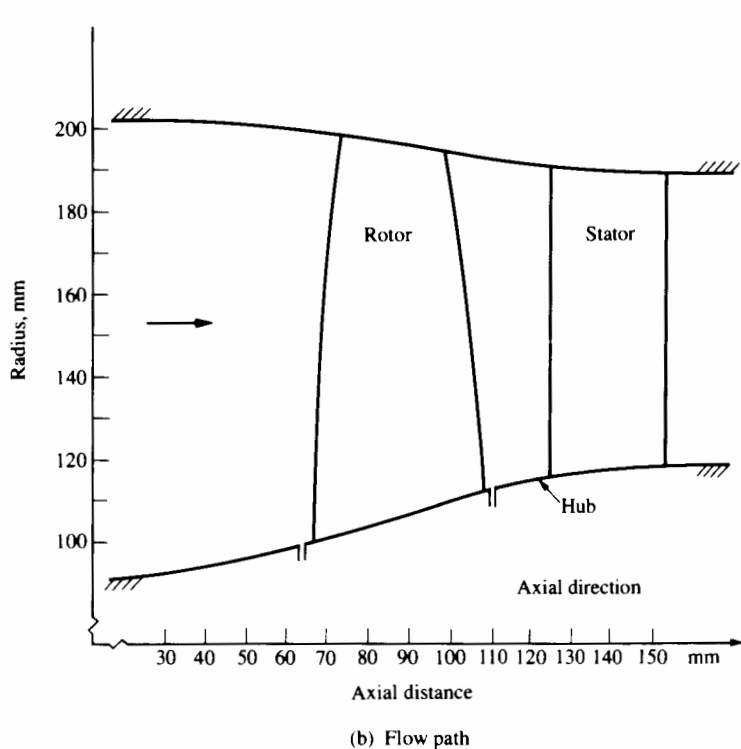
Graphs plotted with these variables display the performance of the compressor and also provide a method of determining the changes in performance when the inlet stagnation pressure and temperature differ from those of the standard day.

Examples of Compressor Performance

Figure 7.14(a) demonstrates this form of correlation (Eq. 7.22) in presenting the performance of a single-stage transonic rotor designed for a tip speed of



(a) Stage performance



(b) Flow path

FIGURE 7.14 Transonic compressor stage. (Adapted from Weyer [2].)

425 m/s. As the flow-path sketch of Fig. 7.14(b) shows, there were no inlet guide vanes, and the inlet diameter was approximately 200 mm. From the dimensions given, one can estimate that the inlet axial Mach number at the blade tip at 100% design speed (20,260 rpm) as 0.5 and the Mach number of the flow relative to the blade tip as 1.37. Figure 7.14(a) shows the pressure ratio and efficiency at three rotor speeds (100%, 85%, and 70% of design speed) and the corresponding efficiencies. The peak efficiency at design speed is around 86%.

The dashed line terminating the solid constant-speed lines is usually denoted as the "surge line," surge meaning a condition of violently unsteady flow in the compressor that is an end result of boundary layer separation. We discuss the reason for this flow instability in subsequent paragraphs.

Another interesting feature of Fig. 7.14(a) is the tendency of the constant-speed lines to have slopes approaching minus infinity at maximum flow rate. This indicates a kind of choking, since the flow rate leaving the compressor is essentially independent of the exit pressure. The same effect is often observed with multistage compressors, for which Cumpsty [1] points out that the appearance of choking need not mean that flow velocities at the back end of the compressor are actually sonic. It could simply mean that while the front stages of the compressor continue to act normally, the flow separation produced by negative flow incidence at the back end had become so severe that the last stage or two act like throttles rather than compressor stages.

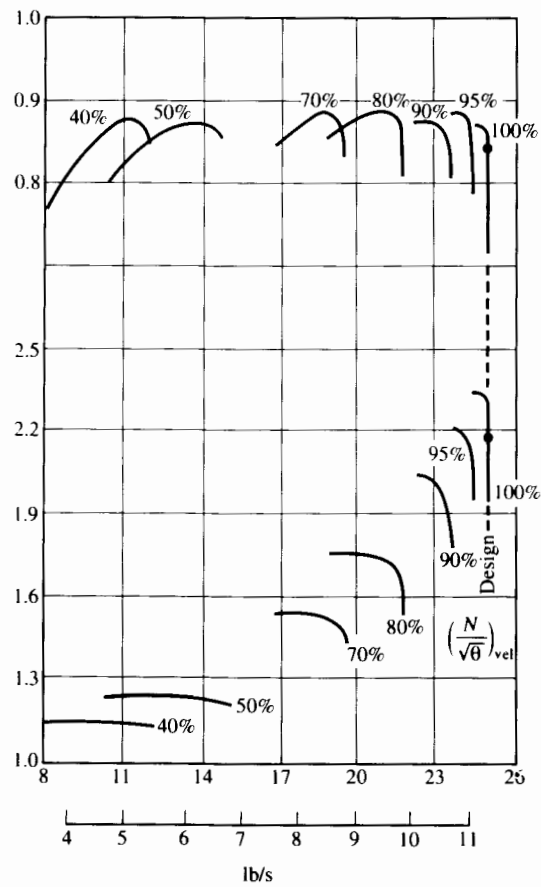
Figure 7.15(a) shows the performance characteristics of another transonic compressor. This is one with considerably higher pressure ratio (and nearly the same maximum efficiency) and with inlet guide vanes shown in the flow path of Fig. 7.15(b). The rotor design rpm is 20,462 and its tip diameter is 0.3556 m. Note the large contraction in the annulus area through the rotor. The average aspect (height–chord) ratios of rotor and stator blades are 0.720 and 0.836, respectively.

For peak efficiency operation at 100% of design speed, the mass flow rate of air was 11.38 kg/s and the total pressure ratios were 2.41 (rotor) and 2.29 (stage). The corresponding adiabatic efficiencies were 0.909 (rotor) and 0.851 (stage). Much experience in the past had indicated the difficulty of using inlet guide vanes with a transonic rotor. This achievement was the result of a design based on three-dimensional flow analysis coupled with experimental modification to a first design that led to a second, improved design.

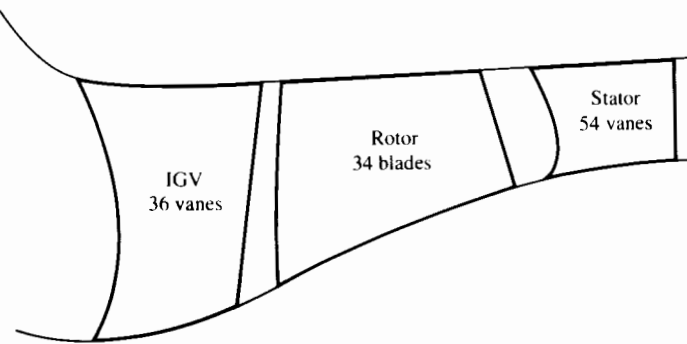
We now turn to the question of the abrupt termination of the constant-speed lines in Figs. 7.14 and 7.15 at what is usually called the surge (or rotating stall) line.

Surge

The "surge line" in Fig. 7.14 denotes the locus of unstable operation of the compressor. The possibility of this instability, which may easily lead to pressure oscillation violent enough to destroy the compressor blades, can be explained as follows: Consider a single stage whose constant-speed (U) pressure-rise characteristic might be as shown in Fig. 7.16 if surge were not to occur. Suppose that



(a) Compressor performance



(b) Blade geometry
 Rotor tip diameter, 35.6 cm
 Design RPM, 20,463
 Rotor blade average aspect ratio, 0.720
 Stator vane average aspect ratio, 0.836

FIGURE 7.15 Transonic stage with inlet guide vanes. (After Law and Wennerstrom [3].)

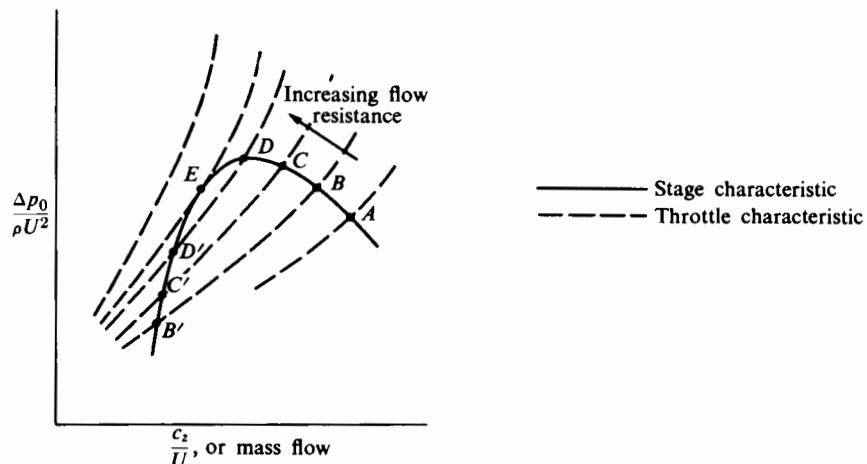


FIGURE 7.16 Pressure-rise characteristic compared with throttle characteristic of downstream resistance.

the stage exhausts into a duct in which flow is controlled by a throttle whose pressure-drop mass flow characteristics for a series of throttle settings are also shown in Fig. 7.16. An operating point for a particular throttle setting is determined by the intersection of that throttle characteristic with the stage characteristic. If the slope of the throttle characteristic is greater than that of the stage, the operating point will be stable. For example, at A , B , C , or D a momentary increase of mass flow will be met by a throttle demand for pressure rise greater than that provided by the compressor so that mass flow will return to the original value. The converse is true for a momentary mass flow decrease. By a similar argument the intersections B' , C' , and D' are unstable, and any shift from the operating point would be followed by a transition either toward B , C , or D (for increased flow) or to zero flow (for decreased flow). The point of neutral stability is E , where the throttle characteristic is just tangent to the stage characteristic, and small departures from the operating point are neither opposed nor reinforced.

These considerations all have to do with the static stability of the system. Suppose now that the system is operating at B and the throttle is gradually closed. Stable operation should persist through C and D until point E is reached. A further closing of the throttle causes a very rapid reduction in flow, since a reduction in mass flow causes the stage operation to travel along its characteristic (assuming this line describes its transient behavior), while the throttle characteristic moves away from the compressor characteristic altogether. Once air delivery is stopped, or perhaps even reversed, the pressure in the discharge region drops until the compressor can start again, rapidly refill the exhaust chamber, and repeat the cycle. The possibility of cyclic behavior depends on the filling and emptying characteristics of the discharge system as well as on its throttling characteristics.

This simple model would predict that stable operation is possible for any mass flow and throttle setting greater than that for which the characteristics are

just tangent, as at *E*. In fact, however, the region between *E* and *D* of positive compressor characteristic slope is not always stable, and this requires us to recognize that consideration of static instability may be insufficient. Depending on the flow system in which it is placed, the compressor could be dynamically unstable. Point *D* in Fig. 7.16, which looks statically stable, could well be associated with dynamic instability. Before mentioning an explanatory model we look at some test data.

That surge can lead to a large (violent), periodically steady oscillation in pressure rise and flow is demonstrated in Fig. 7.17 by the data of Greitzer [4, 5] for a single-stage compressor. The lines in Fig. 7.17 indicate the possible steady-state performance characteristic, *U* being the rotor tip speed and c_z/U the axial velocity ratio. The symbols in the figure show points recorded during several seconds of oscillatory behavior extending over a period of about a half-minute of repeated cycles of deliberately induced surge.

The possibility of dynamic instability requires an interaction between the compressor and the system in which it is placed. A simplified model that provides a physical understanding of this instability has been developed by Greitzer [4], who considered the effect of an air storage volume placed between the compressor and the throttle previously examined. His model shows that the larger the storage volume, the larger the slope of the throttle curve (Fig. 7.14), and the smaller the fluid inertia in the lines connecting compressor reservoir and throttle, the greater the likelihood of surge. In effect, point *D* in Fig. 7.16 becomes the limit of unconditional stability. Most compressor-performance graphs indicate the danger of surge at points on the constant-speed lines where the slope is still positive.

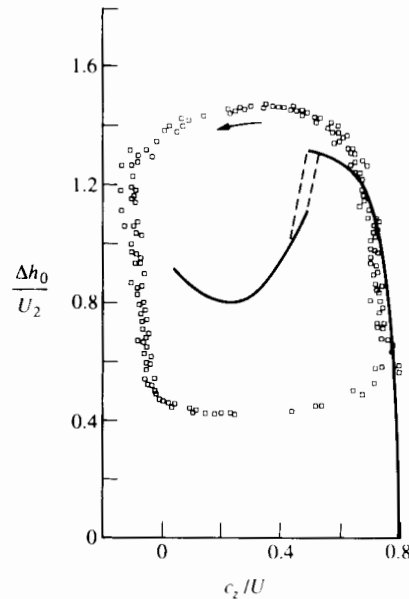


FIGURE 7.17 Surge cycle showing reverse flow periods. (Courtesy Greitzer [5].)

Because surge can destroy compressors, engine designers are not only concerned to provide controls that will prevent the compressor from entering the surge region; they are also very much interested in measures that will extend the so-called surge margin, the fraction of flow (or c_z/U) reduction from the best operating point, at a given speed, to the surge line. Designers can take certain steps to influence the location of the surge line. One of them is to make sure the flow at inlet to the stage is as uniform as possible. Other and more subtle measures have to do with blading configurations at the back end of the compressor and even with the texture of the casing surface adjacent to the tips of the blades.

Rotating Stall

As Figs. 7.10 and 7.11 show qualitatively, the tendency toward boundary layer separation—with $c_z/U > (c_z/U)_{\text{design}}$, that is, $\beta_1 > \beta_{1\text{design}}$ —causes the stage characteristic curve to reach a maximum as flow is reduced. Not all stages in an axial compressor are likely to exhibit flow separation at the same time. Even in a single stage, not all blade passages will “stall” (i.e., suffer from boundary layer separation) at the same time. This can give rise to a destructive phenomenon known as rotating stall.

The term *rotating stall* refers to a progression around the blade annulus of a stall pattern in which one or several adjacent blade passages are instantaneously stalled, then are cleared for unstalled flow as the stall pattern progresses. We can appreciate why a stall zone can move from blade passage to blade passage by considering Fig. 7.18, which shows two locations of a single stall cell.

As we can see in Fig. 7.18(a), a single stalled blade results in a flow diversion that tends to overload one adjacent blade and unload the other adjacent blade. The overloaded blade will then stall, and the resulting flow diversion will unload the originally stalled blade, as in Fig. 7.18(b). This process is repeated, and the stall cell propagates forward in the direction indicated. Usually there is more than one stall cell rotating on a single-blade row. The zones of stall, which may cover several blade spacings, rotate at about half the engine speed. The phenomenon is also observed on rectilinear cascades, where the motion is linear rather

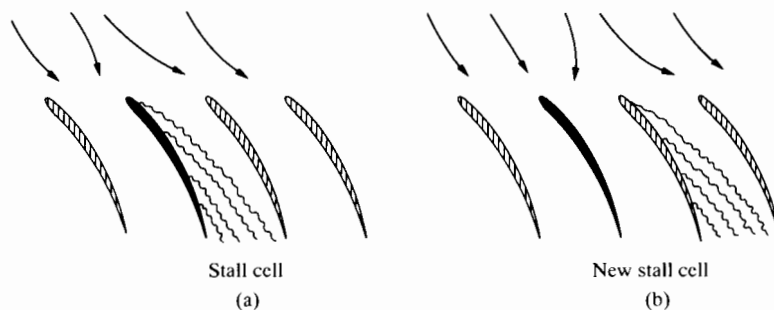


FIGURE 7.18 The propagation of rotating stall.

than circular. The alternate loading and unloading of the blades sets up an alternating stress on each blade. This stress in itself is not large unless the forcing frequency happens to match a blade vibrational frequency. In this case large stresses are incited and fatigue failure can occur, resulting in complete destruction of an entire blade row. Rotating stall may be experienced in a given machine before the onset of surge; hence the surge line may be replaced by a rotating stall boundary.

7.6 BOUNDARY LAYER LIMITATIONS

So far this chapter has described qualitatively the effect of boundary layer separation on the characteristic behavior of compressor stages. We have seen that separation not only has serious possible consequences for efficiency and pressure rise, but it is also the cause of flow instability (rotating stall or surge), which in turn can cause physical damage to the compressor.

With the general significance of the turbulent boundary layer in mind, we now proceed to consider approximate quantitative limitations that the boundary layer imposes on compressor design. Questions of importance in achieving best-design-point performance are:

- a. What is required to prevent boundary layer separation on blade passage end walls and on compressor blades?
- b. What are the effects of Reynolds number and Mach number?
- c. What limits does boundary layer behavior place on the pressure ratios that may be developed in subsonic or transonic stages?
- d. What is the connection between boundary layer behavior and stage efficiency?

In these few pages we can present only the main features of answers to these questions, but this is enough to show the kind of knowledge essential for stage design.

End-Wall Boundary Layers

We begin by thinking of each blade row as a diffuser whose pressure rise is limited by boundary layer separation. As Fig. 7.7 shows, $|w_2| < |w_1|$, so the flow relative to the blades is decelerating and therefore in danger of boundary layer separation. The same is true for the stator blade passage because $|c_3| < |c_2|$. Thus we are led to recall the typical behavior (discussed in Chapter 4) of boundary layers in adverse pressure gradients. For the moment we focus attention on the end walls, at the outer or casing radius or at the inner or hub radius, of the blade passage. Later we will consider the possibility of boundary layer separation on the blade surface. The boundary layers on the end walls are not simple, steady, two-dimensional incompressible boundary layers; but they are boundary layers, so for the moment we ignore the complexities while looking at what boundary layer knowledge would lead us to expect about limiting pressure rise on end walls.

A two-dimensional turbulent boundary layer on a flat surface will separate if the pressure increase in the flow direction exceeds a certain value of the pressure coefficient C_p defined by

$$C_p = \frac{\Delta p}{\frac{1}{2} \rho w_i^2},$$

where w_i is the free-stream velocity (relative to the surface in question) at the point where the boundary layer begins to grow, and Δp is the static pressure rise from point (i) to the point where C_p is evaluated. The value of the pressure coefficient corresponding to separation lies in the range $0.4 < C_p < 0.8$, depending largely on whether the pressure rise is sudden (as in a shock) or gradual, and on the initial condition of the boundary layer.

To make a rough estimate of the allowable stage pressure ratio, we might assume that each blade row behaves as a diffuser with a limited pressure coefficient. The validity of this idea has been explored by Koch [6], whose results are displayed in Fig. 7.19. This graph shows the experimental pressure coefficients associated with a large number of low-speed diffusing blade passages of various length-to-exit-width ratios and various aspect ratios. (For rectangular cross sections the aspect ratio is defined as the ratio of the largest dimension to the smallest at the inlet cross section.) As Fig. 7.19 shows, the maximum pressure coefficient is apparently strongly dependent on diffusion-length-to-exit-width ratio. The trend is roughly in agreement with the two-dimensional diffuser correlation of Sovran and Klomp [7] for a 9% blockage ratio. The blockage ratio is the ratio of

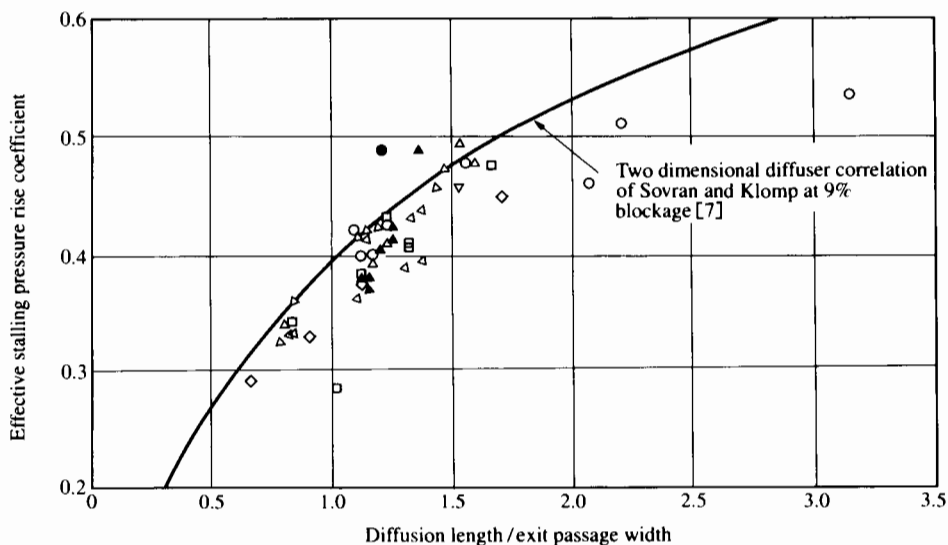


FIGURE 7.19 Stalling pressure coefficient in compressor flow passages. Symbols denote various test geometries. Exit-passage width measured perpendicular to flow direction. Reynolds number = 130,000. (After Koch [6].)

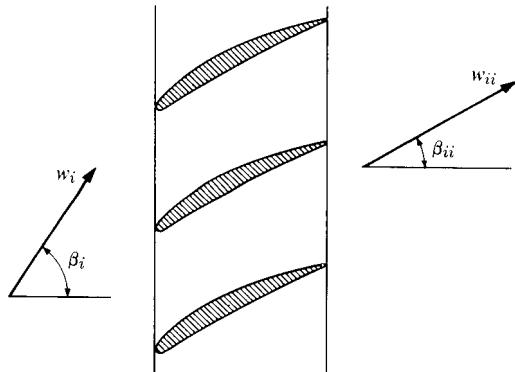


FIGURE 7.20 Two-dimensional blade row.

the area occupied by the displacement thickness divided by the total area at the inlet plane. These results pertain to blade-chord Reynolds number of at least 1.3×10^5 . A tenfold reduction in Reynolds number below this value leads to about 10% reduction in the stalling pressure coefficient. These features of the behavior of diffusers can be understood in the light of turbulent boundary layer calculations discussed in Chapter 4 (even though a given calculation method may not precisely predict the point of separation).

With this brief summary of diffuser experience, we turn now to consider rotor and stator blade passages as diffusers.

For the rotor we write

$$C_p = \frac{p_2 - p_1}{\frac{1}{2} \rho_1 w_1^2}. \quad (7.23)$$

Since for small density variation in the rotor, Bernoulli's equation will hold for fluid on a streamline in the blade passage, we write $C_p = 1 - (w_2/w_1)^2$. Similarly, for the stator we have $C_p = 1 - (c_3/c_2)^2$. Thus a limitation on C_p directly implies a limitation on the relative velocity reduction within a blade row.

The limiting pressure coefficient can be rather easily expressed for a simple case in terms of blade angles. Consider a two-dimensional incompressible flow, as in Fig. 7.20, in which the blades may be either rotor or stator blades.[†] For this flow, continuity requires that the velocity component c_z normal to the blade row be the same at inlet and outlet. The assumptions are not as restrictive as they may sound, since the axial velocity varies little in an actual machine, and the pressure ratio per blade row may be quite low so that density change in a single

[†] The inlet and outlet of a general blade row will be denoted as i and ii , respectively, to distinguish them from the inlet and outlet of a compressor stage. To emphasize the fact that it is the flow *relative to the blades* that is of importance, w and β will be used for velocity and flow angle, with the understanding that they are automatically c and α if the expressions are applied to a stator.

blade row may be small. Because the axial velocity is assumed constant,

$$w_i \cos \beta_i = w_{ii} \cos \beta_{ii},$$

and therefore

$$C_p = 1 - \frac{\cos^2 \beta_i}{\cos^2 \beta_{ii}}.$$

Curves of constant C_p may be plotted as a function of β_i and β_{ii} , as in Fig. 7.21. This analysis is good for either stator or rotor if w and β are taken to be the flow velocity and angle relative to the blade. In Fig. 7.21 the region of interest for axial compressors is limited, for positive values of β_i , to positive values of β_{ii} to avoid excessive absolute velocities at station (ii).

Relative Mach Number

The line of reasoning so far has led us to the conclusion that end-wall separation in axial compressor blade rows can be prevented by limiting the blade row pressure coefficient (or equivalently by limiting the relative velocity reduction ratio, or equivalently by applying a constraint to the relative flow angles β_i and β_{ii}). Imposing such a condition can prevent separation, but it does not in itself fix the

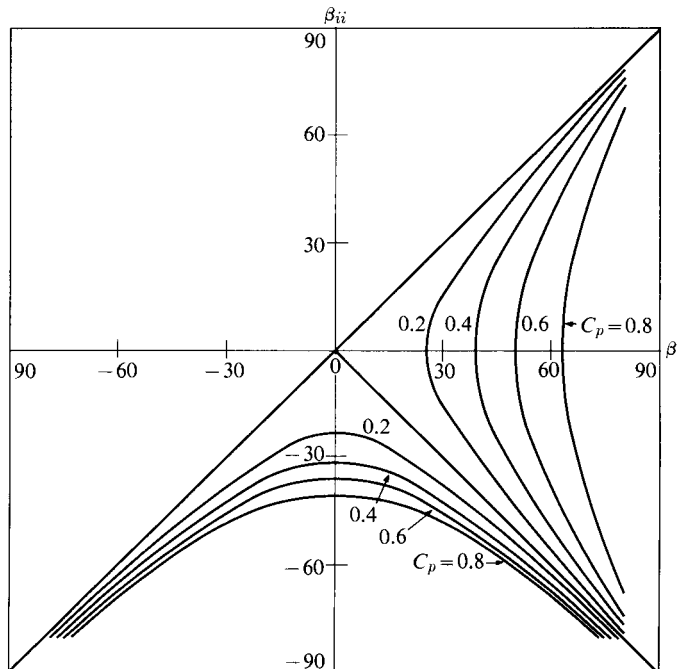


FIGURE 7.21 Pressure coefficient as a function of blade angles. Uniform axial velocity.
(Courtesy M.I.T. Gas Turbine Laboratory.)

maximum stage pressure ratio. To see how this is so, we can rewrite Eq. (7.16) by introducing the relative Mach number

$$M_{1\text{rel}} = \frac{w_1}{\sqrt{\gamma RT_1}} = \frac{w_1}{\sqrt{\gamma p_1/\rho_1}}.$$

With this definition we can write Eq. (7.16) as

$$\frac{p_2}{p_1} = 1 + C_p \frac{\gamma M_{1\text{rel}}^2}{2}$$

for the rotor. If the stator should have the same values of pressure coefficient and entrance relative Mach number, the overall static pressure ratio would be

$$\frac{p_3}{p_1} = \left[1 + C_p \frac{\gamma M_{1\text{rel}}^2}{2} \right]^2.$$

If, in addition, the absolute Mach numbers at entrance to and exit from the stage were the same, then one could estimate the maximum overall stagnation pressure ratio as

$$\frac{p_{03}}{p_{01}} = \left[1 + C_p \frac{\gamma M_{1\text{rel}}^2}{2} \right]^2. \quad (7.24)$$

The advantage of high Mach number operation (provided reasonable efficiency can be maintained) is that stage pressure ratio and mass flow per unit area will both be high. We will discuss limitations on $M_{1\text{rel}}$ subsequently, but here we may say that for subsonic compressors, values of $M_{1\text{rel}}$ of about 0.75 or 0.8, depending on the blade shape, are feasible. Figure 7.22 shows the stage pressure ratios that one may estimate in this way for subsonic compressor stages ($M_{1\text{rel}} < 1$). With $M_{1\text{rel}}$ limited to 0.75 and C_p limited to 0.4 for both rotor and stator stages, the maximum stage pressure ratio would be about 1.35.

Many subsonic compressor stages have pressure ratios appreciably less than this limit. (Turbine stages, on the other hand, operate with pressure ratios as high as 3 without encountering excessive boundary layer losses.) In practice the pressure ratio across rotor and stator may be even less than 1.35 because of the problems of operating the compressor at flows and speeds for which it was not designed. This lower pressure-rise limitation is a function of interactions between stages and the possibility of cumulative loss effects. A single stage may have reasonable efficiency but rather nonuniform outlet flow. The effect of such a velocity distortion on subsequent stages in a multistage compressor could produce poor overall efficiency.

For subsonic compressors, inlet guide vanes have been used to reduce the relative Mach number of the flow relative to the first rotor blade. These vanes give the incoming air a tangential velocity component in the direction of the blade velocity, as Fig. 7.23 shows. For the same rotor exit velocity, the use of guide vanes will reduce the stage work. However, it can allow the compressor to operate with a higher mass flow rate than would otherwise be possible with a given $M_{1\text{rel}}$.

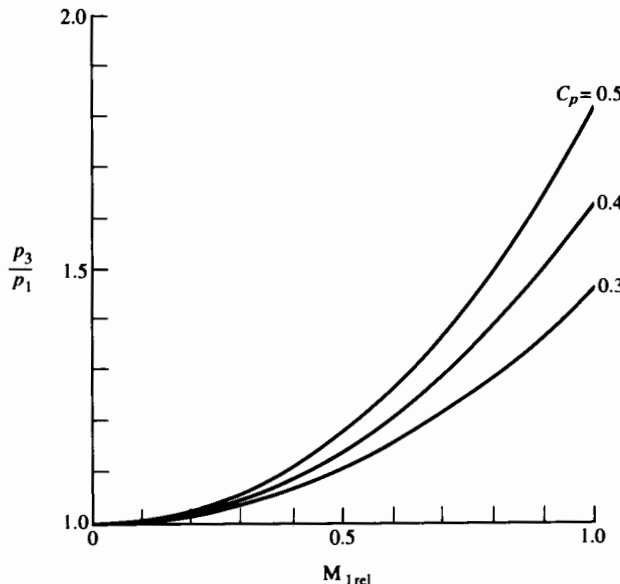


FIGURE 7.22 Single-stage pressure ratios from Eq. (7.24); $\gamma = 1.4$ subsonic flows.

limitation. Figure 7.23 shows that the inlet guide vanes act as nozzles rather than as diffusers since the flow in their passages accelerates. Hence there should be no boundary layer difficulty in these blade passages.

For transonic compressor stages the allowable value of $M_{1\text{rel}}$ is as high as 1.65. But for this case the stator and rotor typically have quite different values of $M_{1\text{rel}}$ and also of C_p , so that Eq. (7.24) does not apply. Also the “nearly incompressible” assumption we have been using in our approximate estimates is quite inexact for this case.

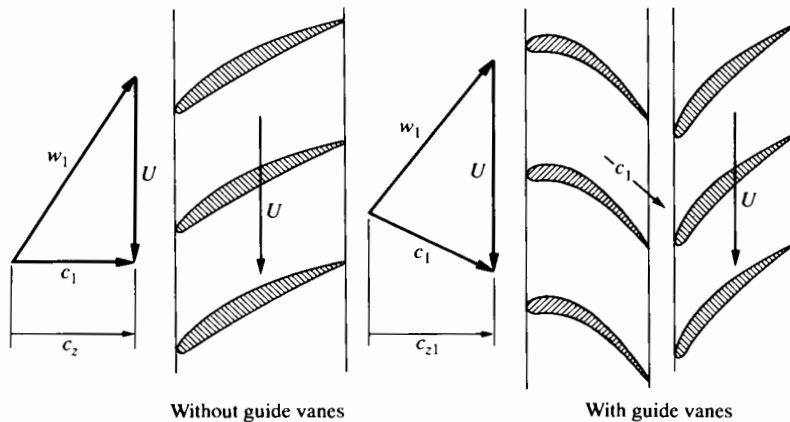


FIGURE 7.23 Effect of inlet guide vanes with constant mass flow and blade speed.

Blade Surface Boundary Layers

So far we have spoken only about the possibility of boundary layer separation on the end walls of the rotor or stator passages. We also have to think about the question of separation on the blade surfaces. This question is particularly important on the low-pressure (suction) side of the blade. On this surface the fluid accelerates from the leading-edge stagnation line and the pressure falls rapidly to a point of minimum pressure. Between that point and the trailing edge of the blade, the pressure rise may be sufficiently large to cause flow separation. If the blade is sufficiently curved, separation may happen even if the angle of the oncoming flow is the same as the inlet blade angle. If the flow angle and the blade angle are mismatched, the possibility is that much greater. The danger and the adverse consequences of boundary layer separation from the blade surface are sufficiently important that this has been the subject of much experimental and analytical work; the chief lessons arising from this work are reviewed in the next section of this chapter, where the effects of blade geometry, Reynolds number, and Mach number on blade separation are demonstrated. A summary of the principal points follows:

1. Compressor blades must not be operated with the “blade-chord” Reynolds number so low that the boundary layer between the minimum pressure point and the trailing edge reverts from turbulent to laminar; laminar layers separate much more easily than turbulent ones.
2. Separation on the suction surface of the compressor blade will occur if the attempted turning angle is too large; this would imply excessive pressure coefficient between the minimum pressure point and the trailing edge.
3. For a given turning angle one can reduce the likelihood of flow separation by decreasing the blade spacing; this reduces the difference between the minimum pressure and the trailing edge pressure on the suction surface. An empirically derived method is available for estimating the required spacing for any stage for which the velocity triangles have been determined.
4. With conventional airfoil shapes it is necessary to limit the relative Mach number to subsonic values (in the range 0.65–0.85, depending on the blade geometry) to prevent shock-induced boundary layer separation.
5. With specially designed and closely spaced airfoils and with uniform flow at inlet to a transonic stage, the presence of shocks need not lead to a shock-induced boundary layer separation with disastrous consequences. With appropriate blading it is possible to have stage efficiencies as high as 85% with a relative Mach number as high as 1.5 or 1.6.

Cascade Aerodynamics

A cascade is a stationary array of blades, as shown in Fig. 7.24. The cascade is constructed for measurement of performance of blading similar to that used in axial compressors. The cascade has end walls, but these are usually porous and suction is applied to remove the boundary layer so that the flow between the blades is as nearly two-dimensional as possible. Thus the end-wall boundary layer

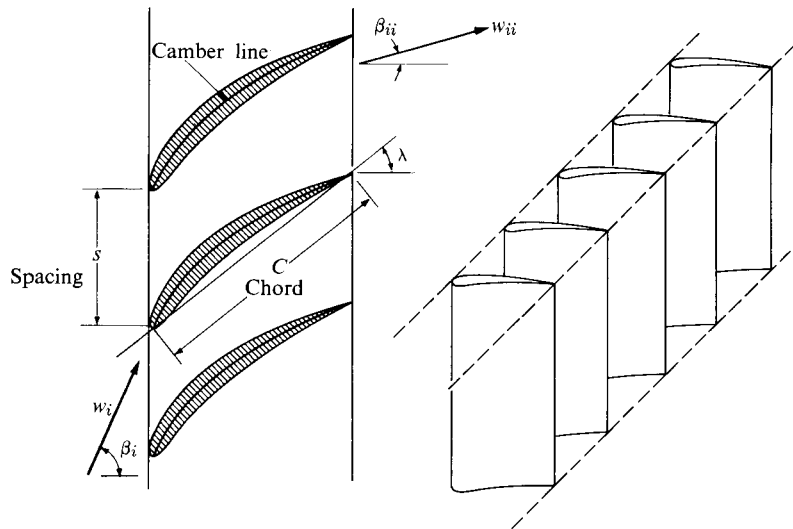


FIGURE 7.24 Geometry of a rectilinear cascade.

effects and the radial variations in the velocity field in compressor blade rows are deliberately excluded so that one can study the flow over the blades in detail under carefully controlled conditions. The objective of the measurements is to relate the fluid turning angles to the blading geometry and to measure losses in stagnation pressure due to friction. The effects of boundary layer separation become evident when the fluid exit angle deviates markedly from the blade exit angle and when the stagnation pressure losses are substantially greater than minimum. Researchers have acquired much experimental information on this subject from cascade wind tunnels and have learned much about the sensitivity of blade performance to Reynolds number and to Mach number.

Figure 7.25 shows a typical cascade wind tunnel for low-speed flow. Measurements are made (downstream of the cascade) of velocities, flow angles, and stagnation pressures. Behind each blade a wake will be detected in which the stagnation pressure is lower than in the adjacent stream. The size of the wake will

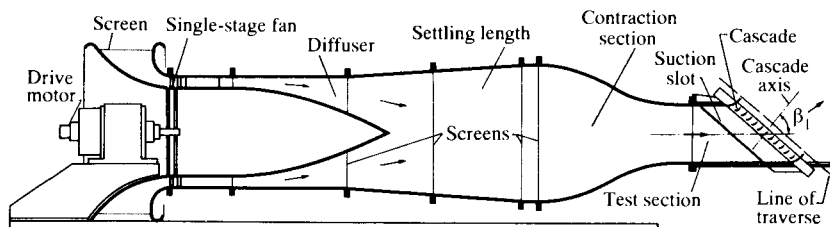


FIGURE 7.25 Layout of a conventional low-speed cascade tunnel.

depend on the angle of incidence of the flow as it approaches the blade, and on friction and compressibility as well.

Though there is no transverse or spanwise gradient of pressure and velocity (as in an axial compressor), we can learn much from cascade data about the effects of blade shape, orientation, and spacing on the degree to which the flow can be turned without flow separation from the blade surfaces.

To consider how to organize conveniently the information from cascade testing, we first write a statement of physical dependence for the outlet angle β_{ii} and the mass averaged stagnation loss Δp_0 in the following form:

$$\beta_{ii}, \Delta p_0 = f(w_i, \beta_i, s, C, \lambda, v, T_1, p_1, \gamma, R, \text{blade shape}),$$

in which w_i is the inlet velocity; β_i is the inlet angle; and s (spacing), C (chord), and λ (stagger) are geometrical variables defined in Fig. 7.24. The fluid properties are specified by the kinematic viscosity v , the inlet temperature T_1 and inlet pressure p_1 , the ratio of specific heats γ , and the gas constant R . The “blade shape” can be considered to be specified by a large number of dimensionless ratios (of coordinate positions to the chord C).

Specification of the blade shape requires that the camber (or midthickness) line be specified, as well as the distribution of blade thickness along the camber line. Often the camber line is a circular arc or part of a parabola. In the following discussion we will refer to results of two-dimensional cascade tests on a series of blades developed by the National Advisory Committee for Aeronautics (NACA, now NASA) and known as the 65 Series Cascade Data. Each blade in the series is specified by a design lift coefficient and a maximum thickness–chord ratio. A convention for identification of the blades is as follows:

$$65(x)y \quad \text{or} \quad 65 - x - y,$$

where x is 10 times the design lift coefficient and y is the maximum thickness–chord ratio.

Recognizing on the right-hand side a complete set of 11 independent variables, and having 4 pertinent primary variables (mass, length, time, and temperature), we can expect (with no loss in generality) to reduce the right-hand side to a set of 7 independent dimensionless variables that may be expressed as follows:

$$\beta_{ii}, \frac{\Delta p_0}{\frac{1}{2} \rho_1 w_i^2} = f\left(\beta_i, \frac{w_i C}{v} \frac{w_i}{\sqrt{\gamma R T_1}}, \frac{C}{s}, \lambda, \gamma, \text{blade shape}\right),$$

in which $\rho_1 = p_1/RT_1$ and in which the dependent variable Δp_0 has also been rendered dimensionless. Seven independent variables is too many to consider simultaneously, so we begin by taking γ and blade shape to be constants and assume (for the moment) that the Reynolds number ($w_i C/v$) and the Mach number do not strongly affect the outlet angle. (We will examine the effects of Mach number and Reynolds number subsequently.) With these restrictions and assumptions,

$$\beta_{ii}, \frac{\Delta p_0}{\frac{1}{2} \rho_1 w_i^2} = f\left(\beta_i, \frac{C}{s}, \lambda\right).$$

It is common to call the ratio C/s the “solidity” of the cascade because the higher it is, the more closely packed are the blades. The stagnation loss ratio is usually given the symbol

$$\xi = \frac{\Delta p_0}{\frac{1}{2} \rho_1 w_i^2}. \quad (7.25)$$

The number of variables present in a series of tests for even one type of airfoil means that the results must be presented in a series of curves. Mellor [9, 10] has correlated data for the NACA 65 Series of airfoils in the following way. For a given blade and a particular solidity (C/s), curves of β_{ii} versus β_i are plotted for a series of values of stagger angle λ . Then, for other values of solidity, the plot is repeated, giving a series of plots covering all possible variables for that particular blade shape. Similar series are found for other blade shapes. Further family relations may be presented if the blade shape is considered to be made up of separately specified camber line, thickness distribution, and maximum thickness, but this is just an organizational refinement. Figure 7.26 shows typical results, where blade shape is specified by the array of numbers appearing on each graph, and approximate appearance is indicated in the inset. With the proper curve of this type, β_{ii} can be found as a function of β_i . One may see that, within a certain range of β_i , β_{ii} is nearly constant for fixed C/s and λ . However, the range of possible angles β_i is restricted by “stall” limits. Stall, as mentioned earlier, is the result of boundary layer separation on the blade surface.

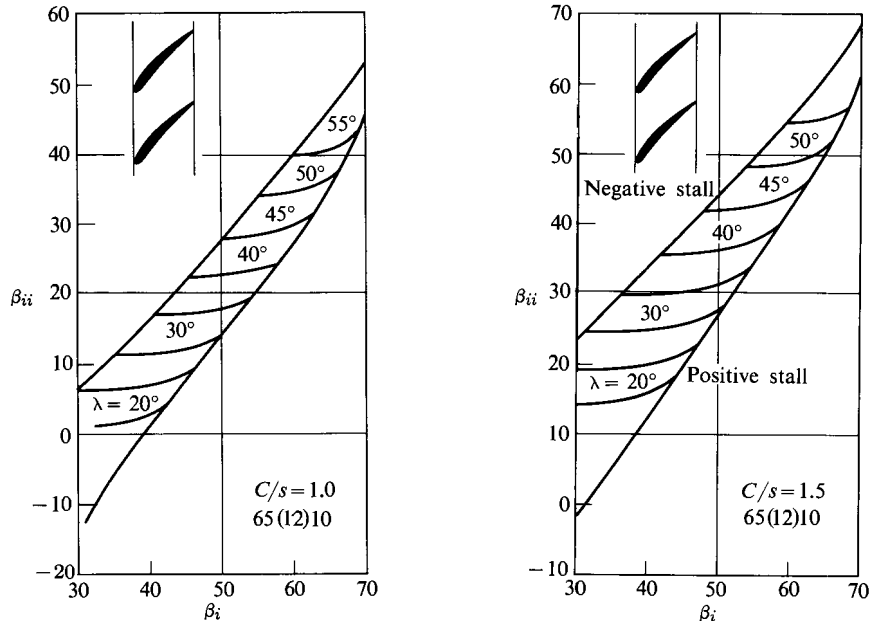


FIGURE 7.26 Typical results of cascade tests on the NACA 65 Series of airfoils.

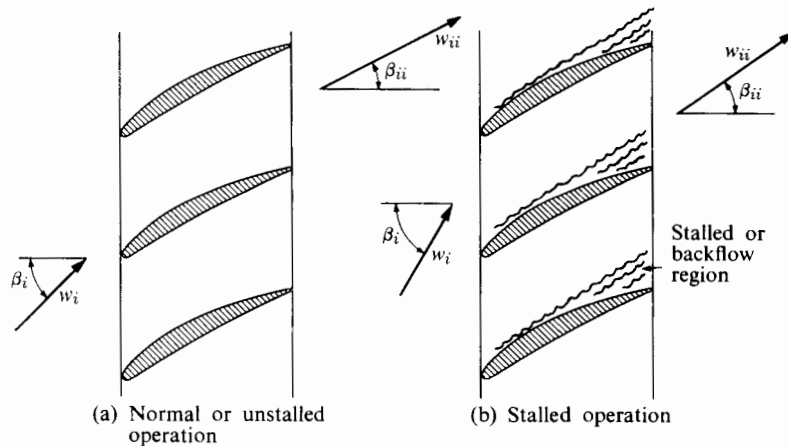


FIGURE 7.27 Cascade stall.

Consider, for example, a cascade operating under normal conditions, as in Fig. 7.27(a). For normal operation, increasing β_i does not change β_{ii} substantially, but it does increase the adverse pressure gradient on the suction surface of the blades. When this is raised to an intolerable value, boundary layer separation takes place. The separated region is the scene of a large amount of turbulent mixing action that leads to marked stagnation pressure loss and an increase in β_{ii} as the streamlines cease to follow the convex surface of the blades. For operation in and beyond this range, β_{ii} varies considerably with β_i and the flow losses are prohibitively high. The same can be said for decreases of β_i beyond reasonable values, decreases for which separation occurs on the pressure side of the blade. Separation resulting from an increase of β_i is termed "positive stall." "Negative stall" is separation due to drastically reduced β_i . The losses usually become prohibitively high before the flow is fully stalled, and the stall limit is commonly defined as that condition for which losses are some arbitrary multiple of their minimum value. For the NACA 65 Series blades, Mellor has arbitrarily defined stall as a 50% increase in the blade profile loss coefficient. It is important to recognize that in a compressor blade row the profile drag is only one of the sources of stagnation pressure loss. Other losses that we will discuss subsequently include losses due to the end-wall boundary layer and also those which have been commonly ascribed to secondary flows.

Figure 7.28 shows a typical measurement of the stagnation pressure loss coefficient: $\xi = \Delta p_0 / \frac{1}{2} \rho w_i^2$ for one of the 65 Series of blades. It is this definition of negative and positive stall that is used in defining the boundaries shown in Fig. 7.26.

The effect of Reynolds number on cascade loss coefficient ξ is shown in Fig. 7.29 for two types of compressor blade with specified inlet angles and solidities. For high Reynolds number (10^6 or greater) the loss coefficient changes very little with change in Reynolds number. However, at some critical value (depend-

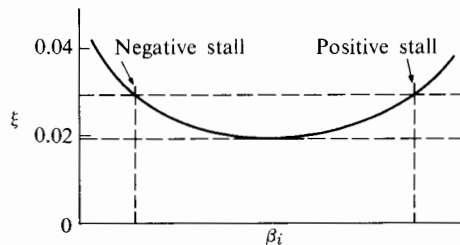


FIGURE 7.28 Typical stagnation pressure loss measurement for a cascade of NACA series airfoils.

ing more or less on the free-stream turbulence as shown in Fig. 7.29), the loss coefficient will begin to rise, perhaps sharply, as the Reynolds number decreases. This is due to the greater susceptibility of the blade flow to separation (stall) at low Reynolds number; the boundary layer is then more likely to be laminar than

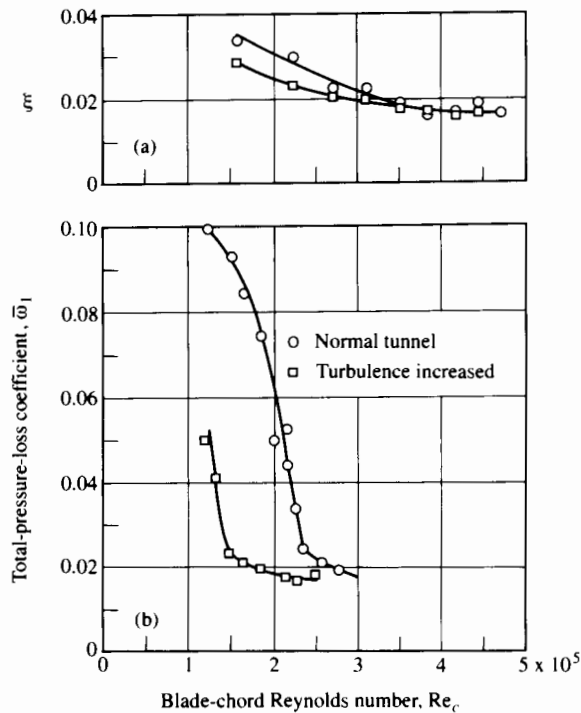


FIGURE 7.29 Effect of blade-chord Reynolds number and free-stream turbulence on minimum-loss coefficient of cascade blade section in two-dimensional tunnel. (a) NACA 65-(12) 10 blade. Inlet-air angle, 45°; solidity, 1.5 (b) Lighthill blade, 50 percent laminar flow. Inlet-air angle, 45.5°; solidity, 1.0 (From NASA SP-36 [8].)

turbulent on that portion of the blade surface where the pressure should be rapidly rising (but will not if the boundary layer separates).

The conclusion is that axial compressors should be designed for operation at blade-chord Reynolds numbers well above, say, 5×10^5 . Writing the Reynolds number as

$$\text{Re} = \frac{\rho_1 w_i C}{\mu},$$

we can see that special measures might have to be taken to design a compressor that will work well at extremely high altitudes. At sea level where the kinematic viscosity is approximately $1.4 \times 10^{-5} \text{ m}^2/\text{s}$, a compressor blade of chord 10 cm (approximately 4 in.) with relative velocity $w_i = 300 \text{ m/s}$ would have a blade-chord Reynolds number of about 2.1×10^6 . At an elevation of 30 km (approximately 100,000 ft), the ambient density is two orders of magnitude lower than at sea level, and so the Reynolds number would be about 2×10^4 . For satisfactory operation at such a height, the compressor blade chord might need to be much larger, and other measures (such as change in surface roughness) might be needed to keep the boundary layer turbulent and attached to the blade so that the loss coefficient ξ would not rise unduly.

We can see the effect of increasing Mach number on a cascade of airfoils designed for subsonic flow in the schlieren photographs of Fig. 7.30, which shows operation with fixed cascade geometry and flow inlet angle (and high Reynolds number) but variable Mach number. As the flow moves around the convex surface of the blade, it accelerates and becomes supersonic, at which point a shock wave (shown by the dark line perpendicular to the surface) may appear. As Fig. 7.30 illustrates, the first appearance of a shock wave is associated with an upstream Mach number of only 0.75. If the incidence angle β_i were extra large, the shock wave could appear even earlier. Shock waves, being such sudden jumps in pressure, can readily induce flow separation and are normally associated with substantial increase in loss coefficient ξ .

This behavior is demonstrated in Fig. 7.31, which shows the effect of relative Mach number $M_{1,\text{rel}}$ and incidence angle on the loss coefficient for four blade geometries. In each case, increasing the relative Mach number substantially reduces the range (i.e., the possible variation of upstream flow angle that does not lead to excessive loss coefficient). In some cases the minimum loss coefficient is also raised substantially as the relative Mach number approaches, say, 0.8.

From the mass of data that have been accumulated in the testing of airfoil cascades (at "high" Reynolds numbers and in the absence of shock-induced boundary layer separation), one may ask whether general conclusions have emerged on how to prevent flow separation on blade surfaces. The answer is encouraging. In 1953 Lieblein [11] proposed an empirical dimensionless number, called the diffusion factor D , to serve as an indicator of the possibility of boundary layer separation on blades of various shapes. This factor has been widely used over the years for subsonic compressors, and there are strong indications, as Serovy [12] shows, that it is useful for transonic compressors as well.

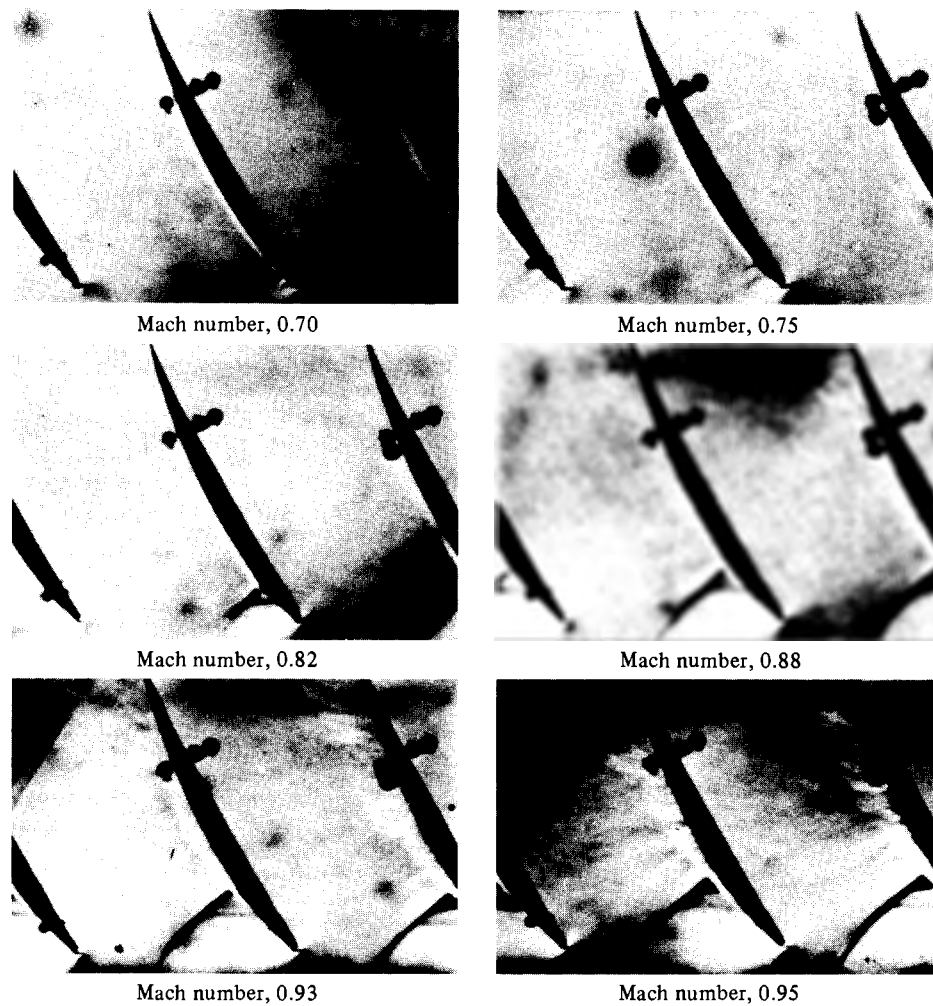


FIGURE 7.30 Schlieren photographs for a range of Mach number. (From NASA SP-36 [8].)

The Lieblein diffusion factor D is defined as

$$D = 1 - \frac{w_{ii}}{w_i} + \frac{w_{\theta ii} - w_{\theta ii}}{2\left(\frac{C}{s}\right)w_i}. \quad (7.26)$$

In this expression w refers to the velocity relative to the blades, whether it is a rotor or a stator blade row.

The idea behind the Lieblein parameter is that separation can be associated with deceleration on the suction surface of the airfoil. Figure 7.32 shows the potential-flow surface velocity distribution on an airfoil, with w_{\max} indicating the ideal surface velocity at the minimum pressure point and w_{ii} being the ideal

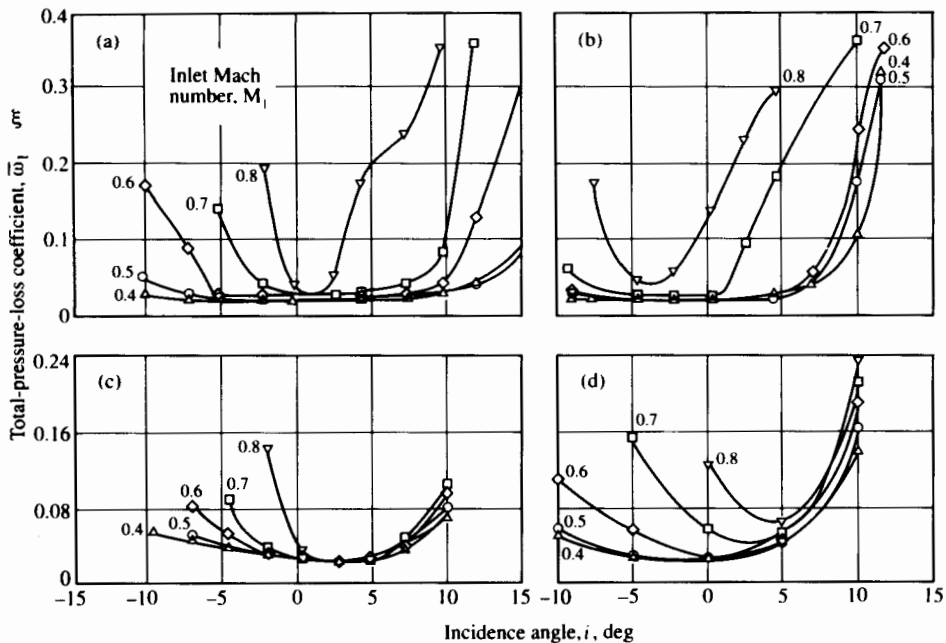


FIGURE 7.31 Effect of inlet Mach number on loss characteristics of cascade blade sections.
 (a) C.4 Circular-arc blade. Camber angle, 25°; maximum-thickness ratio, 0.10; solidity, 1.333; blade-chord angle, 42.5° (ref. 40). (b) C.4 Parabolic-arc blade. Camber angle, 25°; maximum-thickness ratio, 0.10; solidity, 1.333; blade-chord angle, 37.6° (ref. 40).
 (c) Double-circular-arc blade. Camber angle, 25°; maximum-thickness ratio, 0.105; solidity, 1.333; blade-chord angle, 42.5° (ref. 40). (d) Sharp-nose blade. Camber angle, 27.5°; maximum-thickness ratio, 0.08; solidity, 1.15; blade-chord angle, 30° (ref. 205).
 (From NASA SP-36 [8].)

velocity at the trailing edge. Recognizing that the greater the relative deceleration $(w_{\max} - w_{ii})/w_{\max}$, the greater the danger of separation, one would have naturally defined a characteristic dimensionless parameter as

$$D = \frac{w_{\max} - w_{ii}}{w_{\max}} = 1 - \frac{w_{ii}}{w_{\max}}$$

or (with a limiting pressure coefficient in mind)

$$D = 1 - \left(\frac{w_{ii}}{w_{\max}} \right)^2$$

to be a measure of this tendency toward separation.

For Leiblein the difficulty with these expressions was that computers were not available in 1953 for convenient evaluation of w_{ii}/w_{\max} as a function of blade shape and cascade configuration. As a result he proposed the purely empirical parameter of Eq. (7.26), which has several important features:

1. It is expressed entirely in terms of quantities known or measured during cascade testing.

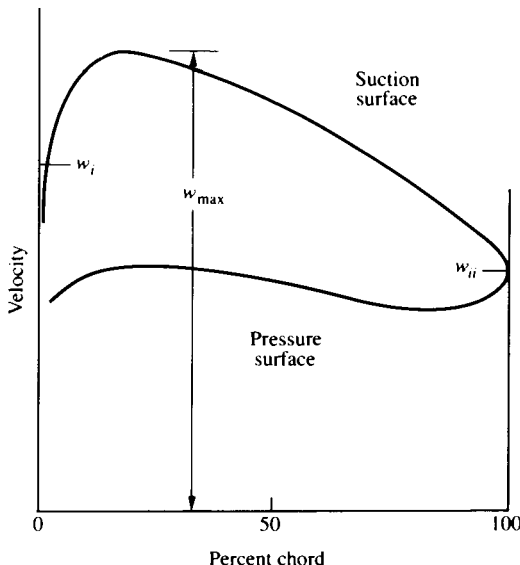


FIGURE 7.32 Blade surface velocity distributions.

2. It has proved to be a dependable indicator of the approach to separation for a variety of blade shapes and with a variety of solidities (as long as the upstream flow angle is the one associated with minimum loss).
3. It depends quite strongly on the blade solidity. This feature is reasonable because, for given flow angles β_i and β_{ii} , it may be shown by considering a control volume around a single blade that the blade force is inversely proportional to solidity. This, in turn, means that the magnitude of the adverse pressure gradient on the suction surface will also be strongly dependent on solidity.

The importance of Leiblein's D parameter suggests that we should look at an example of its correlation with measured cascade loss coefficients (defined by Eq. 7.25). Here we take ξ to be the loss coefficient corresponding to the upstream flow angle β_i that produces minimum loss. Figure 7.33 shows that data from various cascade configurations can be approximately represented by a single curve of

$$\xi \frac{\cos \beta_{ii}}{2 \left(\frac{C}{s} \right)} \left(\frac{\cos \beta_{ii}}{\cos \beta_i} \right)^2 \quad \text{vs. } D .$$

The important point to notice is that this loss parameter begins to grow rapidly for D values greater than 0.4 or 0.5. This indicates an approach toward boundary layer separation. It is with such data in mind that designers have limited compressor stage designs to values of D not greater than about 0.5.

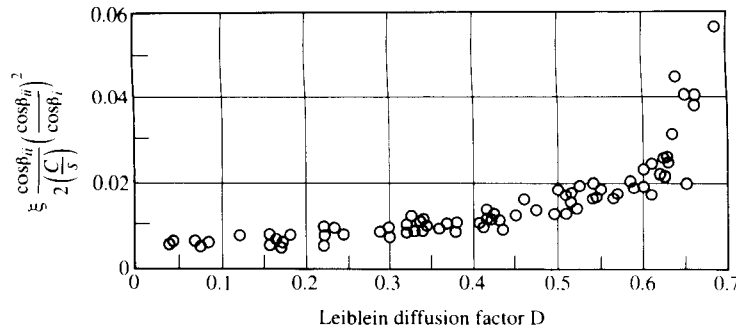


FIGURE 7.33 Variation of loss parameter with diffusion factor at reference minimum-loss incidence angle computed from low-speed-cascade data of NACA 65-(A₁₀)10 cascade blades. (From NASA SP-36 [8].)

Taking Eq. (7.26) seriously (while not ignoring the end-wall limitation on C_p), we can see that one way to reduce the danger of suction surface separation is to increase the blade solidity, that is, to place the blades more closely together.

7.7 COMPRESSOR EFFICIENCY

Efficiency Definitions and Interrelationships

Three kinds of efficiency are used in relating actual and ideal adiabatic work for compressors:

1. The stage efficiency η_{st} is the ratio of ideal to adiabatic work for a single stage, as discussed in Section 7.3.
2. The adiabatic efficiency η_c is the ratio of ideal to adiabatic work for the whole compressor. It may differ significantly from η_{st} .
3. The polytropic compressor efficiency η_{pc} is defined as the ratio of ideal to adiabatic work for an infinitesimal step in the compression process. In an axial compressor of many stages, the stage efficiency η_{st} may be approximately equal to η_{pc} . If η_{pc} can be taken to be constant for all steps of the compression process, there is, as we will see, a simple algebraic relationship between η_{pc} and the overall adiabatic efficiency η_c . This relationship may be used in estimating η_c for an assembly of stages whose stage efficiency η_{st} is approximately the same.

We first review the relationship between η_{pc} and η_c , before considering the factors that govern the stage efficiency η_{st} . Referring to Fig. 7.34, we consider an incremental pressure rise from p_0 to $p_0 + dp_0$. The temperature rise accompanying this pressure rise is dT_0 , whereas the temperature rise for an isentropic process would have been dT_{0s} . The polytropic compression efficiency, η_{pc} , is defined

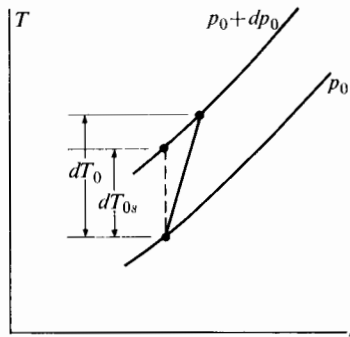


FIGURE 7.34 Definition of terms for an incremental compression of a perfect gas.

for this incremental process just as the overall efficiency is defined for a finite compression:

$$\eta_{pc} = \frac{dT_{0s}}{dT_0}. \quad (7.27)$$

For the isentropic process,

$$dT_{0s} = T_0 \left[\left(\frac{p_0 + dp_0}{p_0} \right)^{(\gamma-1)/\gamma} - 1 \right].$$

Using the binomial expansion for $dp_0/p_0 \ll 1$ results in

$$\left(1 + \frac{dp_0}{p_0} \right)^{(\gamma-1)/\gamma} = 1 + \frac{\gamma-1}{\gamma} \frac{dp_0}{p_0}.$$

Thus we can write Eq. (7.27) as

$$\eta_{pc} \frac{dT_0}{T_0} = \frac{\gamma-1}{\gamma} \frac{dp_0}{p_0}. \quad (7.28)$$

For a compressor process between any pair of stagnation states ① and ② (and if η_{pc} and γ are constant), we can integrate Eq. (7.28) to obtain

$$\frac{T_{02}}{T_{01}} = \left(\frac{p_{02}}{p_{01}} \right)^{(\gamma-1)/\gamma \eta_{pc}}. \quad (7.29)$$

For constant specific heats the adiabatic compression efficiency is given by

$$\eta_c = \frac{h_{02s} - h_{01}}{h_{02} - h_{01}} = \frac{\frac{T_{02s}}{T_{01}} - 1}{\frac{T_{02}}{T_{01}} - 1} = \frac{\left(\frac{p_{02}}{p_{01}} \right)^{(\gamma-1)/\gamma} - 1}{\frac{T_{02}}{T_{01}} - 1}. \quad (7.30)$$

Combination of Eqs. (7.29) and (7.30) shows that the relationship between overall adiabatic and polytropic compression efficiency depends on overall pressure ratio:

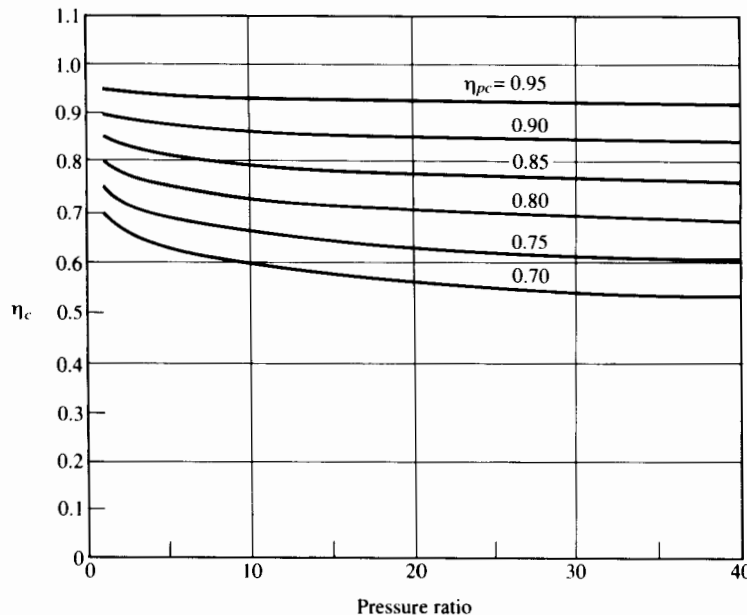


FIGURE 7.35 Adiabatic and polytropic compression efficiencies.

$$\eta_c = \frac{\left(\frac{p_{02}}{p_{01}}\right)^{(\gamma-1)/\gamma} - 1}{\left(\frac{p_{02}}{p_{01}}\right)^{(\gamma-1)/\gamma\eta_{pc}} - 1}. \quad (7.31)$$

Figure 7.35, a plot of η_c versus pressure ratio for various values of η_{pc} , shows that η_c is less than η_{pc} and that the difference increases as the pressure ratio increases. For pressure ratios as low as those encountered in a single stage, we can see that $\eta_c = \eta_{st} \approx \eta_{pc}$; hence the polytropic and stage efficiencies are about the same. In contrast, at a pressure ratio of 30, a polytropic efficiency of 0.9 would correspond to an adiabatic efficiency of 0.845, a serious reduction.

Because the entropy generated in turbomachines can, in principle, be estimated directly from various viscous effects (in, e.g., boundary layers or zones of flow separation), it is of interest to relate the overall adiabatic efficiency of a stage to its total internal entropy generation. Referring to the stagnation states (03_s) and (03) in Fig. 7.9, we may use the Gibbs equation to calculate the entropy difference between these states. As Chapter 3 showed, the Gibbs equation may be written

$$ds = c_p \frac{dT_0}{T_0} - R \frac{dp_0}{p_0}.$$

Since the end states are at the same stagnation pressure, we may calculate the difference in entropy as

$$\Delta s = c_p \ln \frac{T_{03}}{T_{03s}}.$$

Thus

$$\frac{T_{03}}{T_{03s}} = e^{\Delta s/c_p}$$

and

$$\frac{T_{03}}{T_{01}} = \frac{T_{03s}}{T_{01}} e^{\Delta s/c_p}. \quad (7.32)$$

For the end states given in Fig. 7.9, the stage efficiency may be written

$$\eta_{st} = \frac{h_{03s} - h_{01}}{h_{03} - h_{01}}.$$

With the use of Eq. (7.32), we may write this as

$$\eta_{st} = \frac{\left(\frac{T_{03}}{T_{01}}\right) e^{-\Delta s/c_p} - 1}{\frac{T_{03}}{T_{01}} - 1} \quad (7.33)$$

or alternatively

$$\eta_{st} = \frac{\left(\frac{p_{03}}{p_{01}}\right)^{(\gamma-1)/\gamma} - 1}{\left(\frac{p_{03}}{p_{01}} e^{\Delta s/R}\right)^{(\gamma-1)/\gamma} - 1}. \quad (7.34)$$

Thus if we know the total internal entropy generation rate and either the overall temperature ratio or the overall pressure ratio, we can readily determine the stage efficiency. Similar expressions can be stated for the compressor efficiency η_c .

Losses in stagnation pressure in compressor blade rows may be readily related to entropy generation by the adiabatic form of Eq. (7.31):

$$ds = -R \frac{dp_0}{p_0}. \quad (7.35)$$

It has been traditional to discuss viscous losses in turbomachines in terms of stagnation pressure losses rather than entropy generation; Eq. (7.35) shows the sense in which the two terminologies are equivalent. Either may be used in estimating stage efficiency from knowledge of particular viscous effects.

Stage Efficiency

The efficiency of a single stage is less than 1 because of frictional effects on the flow channel surfaces (blades, hub, and housing) and because of viscous mixing downstream of each blade row. If we think of separately identifying the generation of entropy in the rotor and stator of the stage, we could (again referring to Fig. 7.9) write

$$\Delta s_{\text{rotor}} = s_2 - s_{2s} = s_{02} - s_{02s} \approx R \frac{\Delta p_{0r}}{p_{02}}$$

and

$$\Delta s_{\text{stator}} = s_3 - s_{3s'} = s_{03} - s_{03s'} \approx R \frac{\Delta p_{0s}}{p_{03}},$$

in which Δp_{0r} and Δp_{0s} are the total stagnation pressure losses in rotor and stator, respectively.

The formulation of efficiency in terms of stagnation pressure losses relative to each blade row would appear to be convenient because it is well matched to the experimental information (shown typically in Fig. 7.28) available from cascade performance tests. Stagnation pressure losses in compressor stages, however, are generally much larger than one would estimate from cascade data alone.

Figure 7.36 shows, for a low-speed axial stage, the typical dependence of efficiency on flow coefficient. Only part of the efficiency loss is accounted for by the blading. This part can be obtained empirically from cascade data and, to some extent, analytically by use of two-dimensional boundary layer theory, as Koch

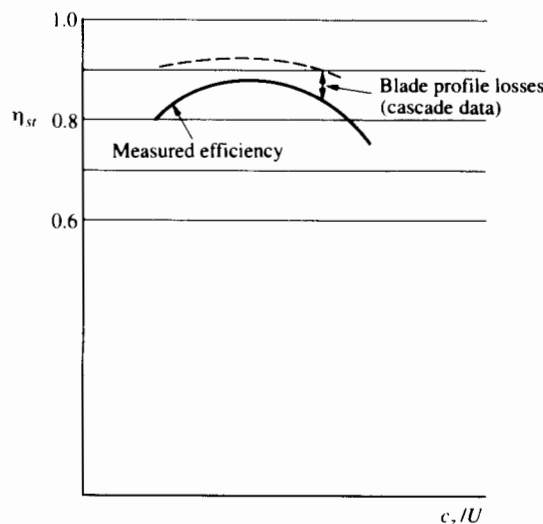


FIGURE 7.36 Stage efficiency.

and Smith [13] have shown in their development of a semiempirical method of estimating axial compressor efficiency.

Another important contribution to the loss in a compressor stage is associated with the end-wall boundary layers on the hub and outer casing. These boundary layers are generally three-dimensional and, on the casing wall, essentially unsteady as well as turbulent and therefore rather difficult to calculate.

Still another contribution to loss is associated with flow through the clearance spaces between the tips of the blades and the casing. One more important source of loss for high-speed compressors is the presence of shock waves.

Of these sources of stagnation pressure loss, the second is probably the most difficult to quantify. The measurements reported by Cumpsty [14] give profiles of axial velocity in the annulus of a four-stage axial compressor at various flow rates. Figure 7.37 shows the measured compressor characteristic; the pressure rise coefficient $(p_{0\text{exit}} - p_1)/\rho_1 U_m^2$ is plotted against the flow coefficient $\phi = \bar{c}_z/U_m$, in which U_m is the mean blade speed, $p_{0\text{exit}}$ is the compressor exit stagnation pressure, and \bar{c}_z is the mean axial velocity at entrance to the stage. The figure shows the effect of removing half of the blades from the compressor as leading to reduced work at a given flow coefficient; wider blade spacing means that there will be less turning of the fluid and therefore less torque at a given speed. The flow

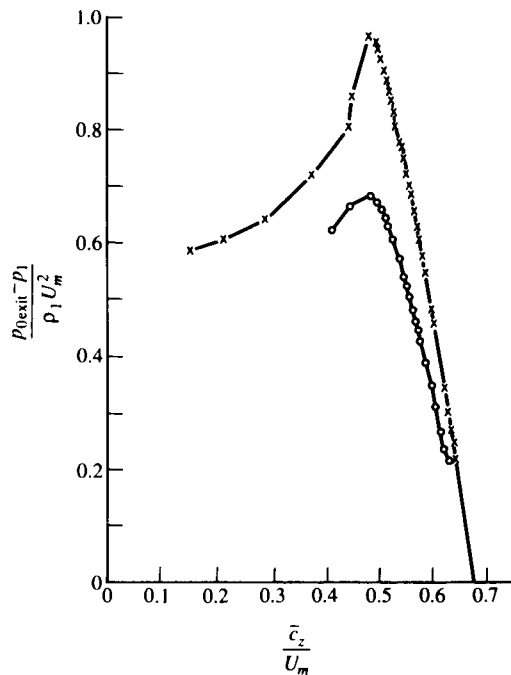


FIGURE 7.37 Pressure-rise measurements for a four-stage axial compressor. Stagger angle, 35°; blade camber angle, 20°; x-x, 72 blades per row; o-o, 36 blades per row. (After Cumpsty [14].)

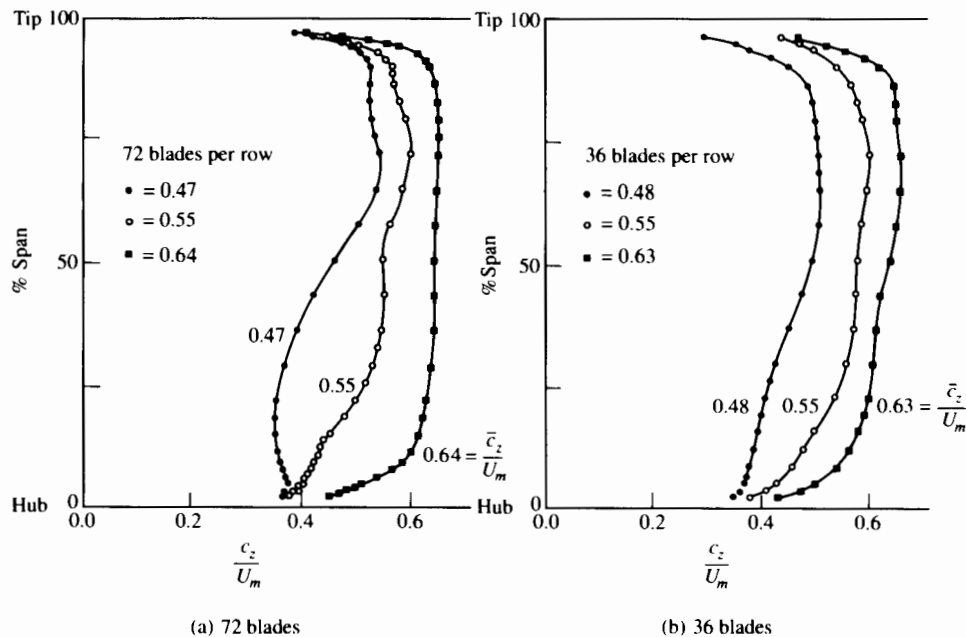
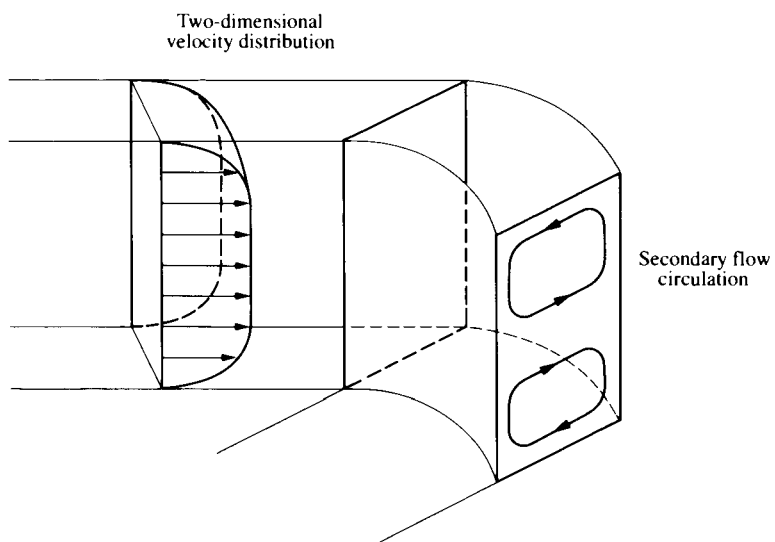


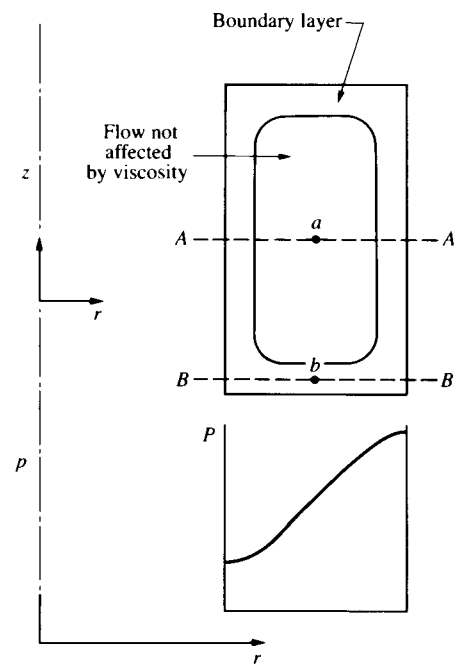
FIGURE 7.38 Axial velocity profiles downstream of rotor 4. (After Cumpsty [14].)

coefficient corresponding to peak pressure coefficient is not, however, much affected by blade spacing. Apparently in the two cases the blade flow begins to stall at much the same incidence angle, which (for a given machine) is controlled by the flow coefficient \bar{c}_z/U_m . Figures 7.38(a) and 7.38(b) show profiles of axial velocity measured downstream of the last rotor at three flow coefficients for both the cases identified in Fig. 7.37. With a flow coefficient of 0.64 (which could be considered close to the design value for this machine), Fig. 7.38(a) shows quite uniform axial velocity in the bulk of the flow and boundary layers whose thickness is evidently about 10% of the annulus width. Reducing flow coefficient renders the axial velocity profile much less uniform and makes it more difficult to decide what the boundary layer “thickness” is. However, we will mainly consider operation near the design point. (It is difficult enough to estimate stage efficiency under design conditions; off-design is almost out of reach.)

An important characteristic of these end-wall boundary layers is that they are three-dimensional, so that the axial velocity profiles of Fig. 7.38(a) and (b) tell only part of the story. To see how the three-dimensionality arises, we can refer to Fig. 7.39(a), which displays the strong tendency in a curved channel for cross-flow to arise near the end walls and for circulation patterns to arise in the planes that are perpendicular to the main flow directions. These circulations are generally called secondary flow, and there are many references in the literature to “secondary flow loss,” but usually this term is not very well defined. One can appreciate the reason for the existence of these secondary flows by referring to Fig. 7.39(b),



(a) Generation of secondary flow due to boundary layer entering a curved passage



(b) Channel cross section and pressure distribution at plane A-A

FIGURE 7.39 Secondary flow in a curved channel.

which shows the radial pressure distribution at plane $A-A$ associated with the turning. At point a on plane $A-A$ the tangential velocity (in the θ -direction, not shown) is W_θ and the velocity components in the r - and z -directions are essentially zero. Viscosity does not affect this portion of the flow, and the pressure gradient necessary to keep a particle of fluid at that location turning on a segment of a circle with radius r is

$$\frac{1}{\rho} \frac{dp}{dr} = \frac{W_\theta^2}{r}.$$

Since, for most of the flow, velocities in the z -direction are very small, we can write

$$\frac{1}{\rho} \frac{dp}{dz} \ll \frac{1}{\rho} \frac{dp}{dr}.$$

This means that the pressure distribution shown in Fig. 7.39(b) for plane $A-A$ is essentially the same at all other planes—in particular, the plane $B-B$, which is deep in the end-wall boundary layer. At point b on that plane the tangential velocity is $w_\theta < W_\theta$. But here the imposed radial pressure gradient is larger than needed to keep a particle at b moving in a circle of radius r , that is,

$$\frac{1}{\rho} \frac{dp}{dr} = \frac{W_\theta^2}{r} > \frac{w_\theta^2}{r},$$

so there is a tendency to drive a particle at that location radially inward. Thus we could write

$$\frac{1}{\rho} \frac{dp}{dr} = \frac{W_\theta^2}{r} = \frac{w_\theta^2}{r} - w_r \frac{\partial w_r}{\partial r} + \text{small viscous terms},$$

so that in the boundary layer there is a strong tendency for cross-flow velocity components (negative w_r) to develop, and it is the local pressure gradient that is the driving force for the circulation patterns shown in Fig. 7.39(a).

In transporting slow-moving fluid from the high-pressure side of the channel to the low-pressure side, this secondary or three-dimensional boundary layer flow can substantially increase the tendency toward boundary layer separation on the inner corner of the channel (or on the low-pressure surface of the blade in a blade row).

Taking into account the complexities of secondary flow, tip leakage flow, and shock-boundary layer interaction, one is not surprised that a fully reliable method of predicting axial compressor losses has not yet been developed. Much work has been devoted to empirical correlations, but these tend to be incomplete and uncertain. Rather than review existing empirical correlations, we focus here on the thermodynamics of aerodynamic compressor losses, and in particular on entropy generation. Improvement of viscous flow calculation methods for axial compressor stages will, we trust, eventually provide a secure foundation for determining in detail the entropy generation within the stage and thus provide in principle a fully rational method for optimizing stage design.

The connection between the entropy and the flow field has been derived in a pleasingly simple way by Denton and Cumpsty [15], who point out that the rate of

entropy generation in a turbulent boundary layer can be rationally estimated by the following formula:

$$\dot{S} = 0.002 \frac{\rho w^3}{T}, \quad (7.36)$$

in which \dot{S} is the entropy generation rate per unit time per unit area of surface adjacent to the boundary layer, w is the local velocity just outside the boundary layer, ρ is the local density, and T the local temperature. If w is in m/s, ρ in kg/m³, and T in K, then \dot{S} has the units of J/K · m² · s. Evidently it matters little whether the boundary layer is thick or thin, or even whether it is separated. As noted below, however, separation zones could lead to substantial entropy generation downstream of the blade row.

Because of the w^3 term, Eq. (7.36) indicates that entropy generation is much higher on the suction side of a blade than on the pressure side, where w^3 may be much lower. Because of the ρ term in Eq. (7.36), the entropy generation per unit area may be four to six times as high at the high-pressure end of the compressor as at the low-pressure end. Thus the small high-pressure blades may contribute appreciably to the total entropy generation.

One can express Eq. (7.36) in terms of local Mach number M just outside the boundary layer:

$$\dot{S} = 0.002 \frac{p_0}{\sqrt{RT_0}} \frac{\gamma^{3/2} M^3}{\left(1 + \frac{\gamma - 1}{2} M^2\right)^{(\gamma+1)/2(\gamma-1)}},$$

in which p_0 and T_0 are the (approximately constant) stagnation pressure and temperature relative to a coordinate system in which the blades appear to be stationary.

Denton and Cumpsty do not separately estimate entropy generation because of secondary-flow. They recognize that the end-wall boundary layer is subject to a number of complexities, including skewing, possible vortex formation at the inner corners of the blade passage, and downstream mixing of the vortex, boundary layer, and free stream. In addition there is complexity due to the relative motion of the blades and the end-wall casing. In the absence of detailed information on all of these effects, these authors suggest that the best available approximation for the end walls is Eq. (7.36), provided one uses for w the velocity outside the boundary layer relative to the end wall in question.

Using Eq. (7.36), one could integrate over the entire surface area to estimate the total entropy generation rate within the blade passages. There is also significant entropy generation downstream of the blade due to mixing behind the blade of the wake and the free stream. The wake mixing loss can be shown [15] to be strongly dependent on whether the mixing takes place in an accelerating or a decelerating flow and on the size of the "wake" zone, that is, on whether or not there is a large separation zone at the trailing edge of the blade. Depending on the thickness of the trailing edge, the downstream mixing losses might be 10% to 30% of the total for the stage (in the absence of separated flow).

The development of transonic compressors has underscored the importance of losses due to shocks and shock-wave interactions in compressors. Semiempirical methods for estimating these losses are described by Koch and Smith [13] and

Wennerstrom and Puterbaugh [16]. Here too is a problem area of considerable complexity.

Senoo and Ishida [17] have determined the stage efficiency loss that one may expect because of leakage through the clearance space at the blade tip. Tests, as well as analysis, show that for a variety of axial compressor stages the relative efficiency loss can be expressed in the form

$$\frac{\Delta\eta_c}{\eta_c} = -\mathcal{C} \frac{\Delta}{h},$$

in which Δ is the clearance between blade tip and casing, h is the blade height, and \mathcal{C} is a constant having the magnitude 2 ± 0.5 . Reduction of tip clearance loss is of such importance that in certain engines tip clearance is actively controlled by adjustment of the airflow that cools the turbine casing adjacent to the blade tip. The thermal expansion or contraction of the casing is used to adjust the casing diameter as the blade tip diameter increases with speed and temperature.

In summary, one cannot yet say that estimation of losses or of entropy generation in turbomachines is a routine matter. Much remains to be learned. Cumpsty and Denton conclude that after years of intensive study, "prospects of an a priori quantitative prediction of efficiency are very distant," and that "for a long time efficiency prediction will continue to be based on correlation of experimental data from similar machines and improvements will be made by modifications based on a qualitative understanding of the flow rather than on quantitative prediction." Nevertheless, we can see the way in which development might proceed to improve predictive capability.

Even in the absence of a fully reliable predictive theory, designers may attempt improvements in blading configurations with boundary layer behavior in mind. One example of experimental innovation to accommodate boundary layer realities is the "end-bend" compressor airfoils that are shown in Fig. 7.40. These

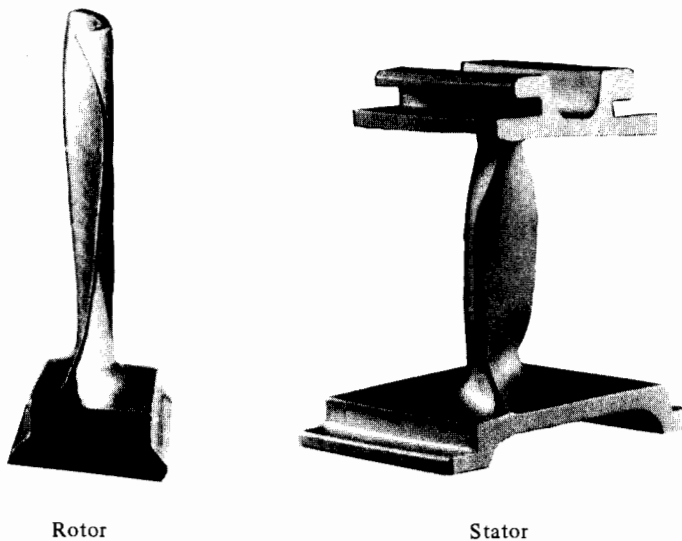


FIGURE 7.40 End-bend compressor airfoils of the Rolls-Royce RB211-535E4 engine. (Courtesy Rolls-Royce, plc.)

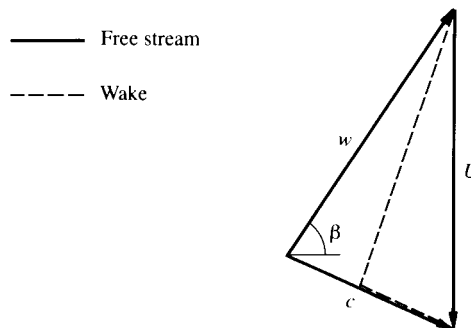


FIGURE 7.41 Velocity triangles for wake and free-stream fluid. In rotor coordinates the wake from the preceding stator appears predominantly as a change in incidence angle rather than as a change in velocity magnitude.

are designed to permit boundary layer fluid leaving a stator, for example, to flow more smoothly onto the following stator. Figure 7.41 shows velocity triangles for both wake and free-stream fluid leaving a stator and entering a rotor. The free-stream fluid has absolute velocity c as well as velocity w and flow angle β relative to the rotor. The relative wake velocity magnitude is not much different from that of w ; the rotor “sees” the effect of the oncoming wake not so much as a velocity defect than as an incidence angle change. Thus a qualitative consideration can motivate the development of the geometry shown in Fig. 7.32.

7.8 DEGREE OF REACTION

Having reviewed what cascade testing can tell us about the aerodynamics of single-blade rows in which the flow is nearly two-dimensional, we will now consider how rotor and stator blades interact to form a stage. The subject of this section is the sharing of the pressure rise between rotor and stator. It is followed in Section 7.9 by analysis of important variations in flow velocities and angles from blade root to blade tip diameter.

In general one may define the degree of reaction R of a turbomachine rotor as the change in enthalpy in the rotor divided by the change in stagnation enthalpy in the stage.

For an axial compressor stage in which the change in density is small, the degree of reaction is approximately equal to the static pressure rise in the rotor divided by the stagnation pressure rise in the whole stage. If the flow is taken to be (approximately) isentropic in the rotor,

$$Tds = 0 = dh - \frac{dp}{\rho}.$$

For nearly incompressible flow this integrates to

$$h_2 - h_1 \approx \frac{1}{\rho}(p_2 - p_1)$$

for the rotor. Similarly, for the stage,

$$h_{03} - h_{01} \approx \frac{1}{\rho} (p_{03} - p_{01}).$$

Thus

$$R = \frac{h_2 - h_1}{h_{03} - h_{01}} \approx \frac{p_2 - p_1}{p_{03} - p_{01}}.$$

Writing the energy equation of the entire stage with the use of Eq. (7.11), we have

$$h_{03} - h_{01} = h_3 - h_1 + \frac{c_3^2}{2} - \frac{c_1^2}{2} = U(c_{\theta 2} - c_{\theta 1}),$$

in which, as before, c_{θ} signifies the absolute velocity in the tangential direction. If, as is often the case for a single stage within a multistage machine, the initial and final absolute velocities are nearly identical, this reduces to

$$h_3 - h_1 = U(c_{\theta 2} - c_{\theta 1}).$$

For the rotor we can take a coordinate system fixed to the rotor blade and there observe adiabatic deceleration from w_1 to w_2 . In this system there is no work observed since (relative to the observer) the blade is stationary. Hence the steady-flow energy equation becomes

$$h_2 - h_1 = \frac{w_1^2}{2} - \frac{w_2^2}{2}.$$

Thus the degree of reaction R is

$$R = \frac{h_2 - h_1}{h_{03} - h_{01}} = \frac{w_1^2 - w_2^2}{2U(c_{\theta 2} - c_{\theta 1})}. \quad (7.37)$$

If the axial velocity is constant,

$$w_1^2 - w_2^2 = w_{\theta 1}^2 - w_{\theta 2}^2.$$

Also

$$w_{\theta 1} - w_{\theta 2} = c_{\theta 1} - c_{\theta 2}.$$

Thus

$$R = -\frac{w_{\theta 1} + w_{\theta 2}}{2U} = -\frac{c_z}{U} \left(\frac{\tan \beta_1 + \tan \beta_2}{2} \right) \quad (7.38)$$

or

$$R = \frac{1}{2} - \frac{c_z}{U} \left(\frac{\tan \alpha_1 + \tan \beta_2}{2} \right). \quad (7.39)$$

If the exit flow angles α_1 and β_1 (see Figs. 7.7 and 7.8) are equal and of opposite sign and if the axial velocity is constant, the velocity triangles are symmetrical and the degree of reaction is 0.5. This is the 50% reaction stage, in which half

the enthalpy rise takes place in the stator and half in the rotor. One might expect that best efficiency would be attained with R about 0.5; if the degree of reaction were much different from 50%, one of the blade rows would have greater pressure rise than the other; its boundary layer would be more highly loaded and more likely to stall or at least create higher losses. In practice it appears that stage efficiency is not much reduced for considerable departure from $R = 0.5$. However, greater stage pressure rise can be obtained if both blade rows are loaded to about the same limiting pressure rise.

The foregoing indicates that setting the degree of reaction near 0.5 at the mean diameter of the axial compressor stage is a reasonable possibility. There may, however, be substantial departure from $R = 0.5$ at root and tip diameter, depending on the radial variations of flow angles and velocities.

7.9 RADIAL EQUILIBRIUM

In the derivation of Eq. (7.11) we ignored radial variations in the flow through the compressor annulus and restricted attention to average or “mean-radius” conditions. To establish a satisfactory compressor design, it is necessary to take into account radial variations in

- Blade speed $U = \Omega r$,
- Axial velocity c_z ,
- Tangential velocity c_θ ,
- Static pressure

The axial velocity at the inlet to a multistage machine may be quite uniform radially, but large variations can develop after the fluid has passed through two or three stages. The radial variation in tangential velocity depends on the way in which the blade angles vary with radius. The radial pressure gradient depends directly on the absolute tangential velocity component as follows:

Consider a small element of fluid δm with tangential velocity component c_θ , as in Fig. 7.42. It has a centripetal acceleration toward the axis of $-c_\theta^2/r$. If the radial velocity does not change ($\partial c_r/\partial r \approx 0$), this is the total radial acceleration of the fluid, and the radial pressure force must be equal to

$$F_r = -\delta m(c_\theta^2/r),$$

where

$$\begin{aligned} F_r &= p(r d\theta dz) - \left(p + \frac{\partial p}{\partial r} dr \right) (r + dr) d\theta dz + 2(p dr dz) \frac{d\theta}{2} \\ &\simeq -\frac{\partial p}{\partial r} dr r d\theta dz. \end{aligned}$$

Also, $\delta m = \rho r dr d\theta dz$. Combining these expressions, we have

$$\frac{\partial p}{\partial r} = \rho \frac{c_\theta^2}{r}, \quad (7.40)$$

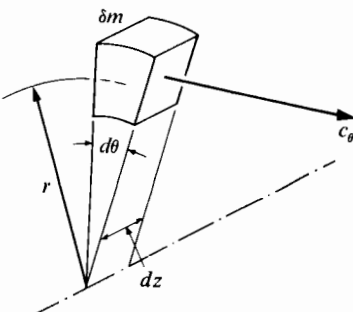


FIGURE 7.42 Tangential motion of a small fluid element.

which is the equation of simple radial equilibrium. Actual velocity distributions must satisfy this relationship at the entrance and exit of each blade row:

In order to provide a reasonably uniform flow at the exit of a compressor, it is desirable to maintain a uniform work input along the radial length of a rotor. As we have shown, the change in stagnation enthalpy along a streamline through any stage in an axial compressor is $\Delta h_0 = U \Delta c_\theta$. The radial gradient is

$$\frac{\partial}{\partial r}(\Delta h_0) = \Omega \frac{\partial}{\partial r}(r \Delta c_\theta). \quad (7.41)$$

Thus to keep the fluid at constant stagnation enthalpy, the product $r \Delta c_\theta$ must be constant with radius.

One configuration that satisfies this requirement as well as the requirements of radial equilibrium is the “free-vortex” design, in which the product rc_θ is held constant across the exit of each blade row. Unfortunately the blading of a free-vortex compressor will require excessive blade twist, unless the blade height is quite small compared with the blade tip diameter.

Consider a rotor with hub, mean, and tip radii related by

$$r_t = 1.25r_m, \quad r_h = 0.75r_m,$$

and suppose that the mean radius velocity triangles have been specified, as in Fig. 7.43. For free vortex upstream and downstream of the rotor, we can determine the hub and tip velocities from

$$c_{\theta h} = c_{\theta m} \frac{r_m}{r_h} \quad \text{and} \quad c_{\theta t} = c_{\theta m} \frac{r_m}{r_t}.$$

With constant c_z and with blade speed, of course, proportional to radius, we can determine the complete velocity triangles as shown. Also shown are blade cross sections as they might appear at the various radii. Here we can see that rather large blade twist is required, as mentioned above.

Aside from the undesirable blade twist, note the very high absolute velocity at the exit of the rotor hub. This follows from the high turning and the relatively

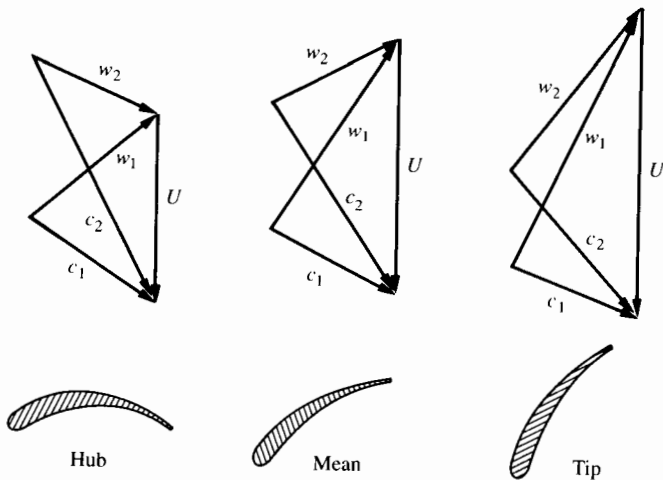


FIGURE 7.43 Free-vortex velocity diagrams and blade rotor profiles for $r_h/r_m = 0.75$, $r_t/r_m = 1.25$; c_z independent of radius.

small amount of diffusion within the rotor, and may result in intolerably large pressure rise in the stator at this radius.

Both the blade twist and the unequal rotor-to-stator diffusion distribution can be improved while constant work is maintained if one specifies that only $r\Delta c_\theta$ instead of rc_θ be constant with radius. Starting with the same mean radius diagram and assuming symmetric diagrams at hub and tip to equalize diffusion, we arrive at the set of diagrams of Fig. 7.44.

Such a blade system is desirable in that it avoids the drawbacks encountered by the free-vortex blading. However, it can be shown that these velocity triangles are incompatible because they violate the conditions of radial equilibrium. Radial equilibrium is simply the satisfaction of the *three-dimensional* equations of fluid motion rather than the two-dimensional equations that we have considered. Except for a few fortunate cases that are automatically satisfied, the velocity varia-

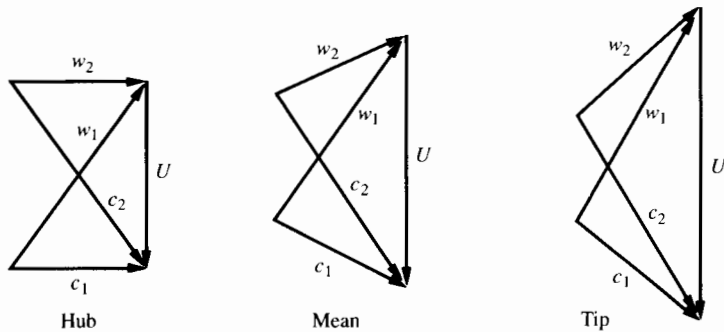


FIGURE 7.44 Symmetric diagrams for $r\Delta c_\theta = \text{constant}$; $r_h/r_m = 0.75$, $r_t/r_m = 1.25$.

tions in the radial direction cannot be arbitrarily specified. An attempt to produce incompatible velocity diagrams such as these would be met by radial adjustments in the flow pattern to something that would satisfy all equilibrium conditions.

We therefore look for a way to satisfy the requirements of radial equilibrium, with no radial variation in the work done, while avoiding the shortcomings of the free-vortex distribution. In an approximate design procedure, we could take steps to satisfy the radial equilibrium condition only upstream and downstream of the blade row, assuming that if we do this, the flow will be reasonably well behaved within the blade row.

The distribution of angular momentum with radius can be regarded as a design choice that will affect the velocity triangles directly. A number of possible distributions have been suggested [18], including

Free vortex	$rc_\theta = a,$
Forced vortex	$rc_\theta = ar^2,$
Exponential	$rc_\theta = ar + b,$
Constant reaction	$rc_\theta = ar^2 + b,$

in which a and b are constants, a being positive and b positive or negative. In Sections 7.10 and 7.11 we will consider two of these as examples. We need first to express the radial equilibrium requirement in terms of the velocity field and return to the state equation

$$Tds = dh - \frac{dp}{\rho}$$

or

$$T \frac{ds}{dr} = \frac{dh}{dr} - \frac{1}{\rho} \frac{dp}{dr}. \quad (7.42)$$

Since we can write the stagnation enthalpy (with $c_r^2 \ll c_z^2$) as

$$h_0 = h + \frac{c_\theta^2 + c_z^2}{2},$$

We can express Eq. (7.42) as

$$T \frac{ds}{dr} = \frac{dh_0}{dr} - \frac{d}{dr} \left(\frac{c_\theta^2 + c_z^2}{2} \right) - \frac{1}{\rho} \frac{dp}{dr}.$$

With Eq. (7.40) we transform it further to

$$T \frac{ds}{dr} = \frac{dh_0}{dr} - \frac{d}{dr} \left(\frac{c_\theta^2 + c_z^2}{2} \right) - \frac{c_\theta^2}{r}. \quad (7.43)$$

With the assumptions that the radial gradients of the entropy and the stagnation enthalpy are zero, we obtain from Eq. (7.43) the following widely useful relationship between the radial gradients of the angular momentum and the axial velocity component:

$$\frac{d}{dr}(c_z^2) = -\frac{1}{r^2} \frac{d}{dr}(rc_\theta)^2. \quad (7.44)$$

For the case in which the angular momentum is independent of radius (the free-vortex case discussed earlier), there is no radial gradient of the axial component of velocity. In general both rc_θ and c_z will vary with radius.

We will demonstrate the use of Eq. (7.44) in Sections 7.10 and 7.11 in preliminary design exercises for both subsonic and transonic rotors.

7.10 DESIGN OF A SUBSONIC AXIAL COMPRESSOR

The underlying purpose of this section is to show how a few basic principles determine the conditions under which one may obtain best performance of an axial compressor stage. The goal is essentially to determine a flow field that will be compatible with high compressor efficiency and minimum compressor size for a given pressure ratio. If the flow field is properly designed, one can specify blading that will guide the flow accordingly.

The need for simulation of the whole flow field within the compressor raises the question as to what level of complexity is needed in describing the fluid behavior. Turbomachinery designers have available a variety of computerized methods of calculating two- and three-dimensional flow fields. For calculations of blade passage flow fields with the two-dimensional approximation, Denton [19] distinguishes four kinds of methods:

1. Streamline curvature method,
2. Stream function method,
3. Potential function method,
4. Euler equation solvers.

The first three of these are limited to calculations of adiabatic flows that are frictionless and, in general, free of shock waves. The last is able to allow for the effects of friction and shock waves by solving the conservation equation written for a large number of small volumes mounted in a grid in the flow field. For the Euler equation solution method, Denton presents the equations, boundary conditions, numerical approximations, and solution techniques for two-dimensional flows in turbomachine passages. He also presents the extension of the Euler method to three dimensions, including flows with boundary layers. With some difficulty the other methods may also be extended to three-dimensional calculations, but it is the fourth method that appears to have widest application to turbomachinery design.

Before using these complex and expensive flow calculation techniques, however, the designer will likely go through a series of preliminary design exercises. These may involve working first with simple radial equilibrium, as outlined in Section 7.9, and with the equations of continuity and angular momentum, to establish approximate velocity triangles, the number of stages required, and the machine size resulting from various design assumptions. At this point the designer may also be able to predict the consequences of small departures from design

point operation for a multistage machine. All of this could be called the preliminary design procedure, which is the subject of the following pages.

After the preliminary design procedure, however, a large effort in flow field calculation will usually be made to improve the design as much as possible before building the first prototype. The results of prototype testing will then call for further calculation and design modifications so that experiments and advanced flow field calculations work together toward achieving best possible performance.

In this section our purpose in discussing preliminary-design considerations is to bring together in a reasonably simple, though approximate, way the ideas of continuity, angular momentum, radial equilibrium, and the essential fluid dynamic limitations, and to explore design possibilities for a single-stage subsonic axial compressor. Section 7.11 contains a similar exploration for a transonic stage. It is interesting to see how much depends on a very few foundational principles.

Design Strategy

As Section 7.5 shows, one can represent in a general way the performance of an axial air compressor in the form

$$\frac{p_{03}}{p_{01}}, \eta_c = f\left(\frac{\dot{m} \sqrt{RT_{01}}}{p_{01} D^2}, \frac{U_t}{a_{01}}, \text{design}\right), \quad (7.45)$$

in which $a_{01} = \sqrt{\gamma RT_{01}}$, U_t is the first-stage rotor tip speed and p_{03}/p_{01} is the overall pressure ratio.

It is of course desirable that the compressor have high efficiency, high stage pressure ratio (because fewer stages would be required for a given overall pressure ratio), and high value of the dimensionless mass flow parameter $\dot{m} \sqrt{RT_{01}}/(p_{01} D^2)$ (because this will mean minimum cross-sectional area for given engine mass flow rate and given inlet stagnation conditions). The smaller the compressor cross-sectional area and the smaller the number of stages, the smaller its mass. The aircraft engine designer must place strong emphasis on reducing compressor mass as well as on improving efficiency.

High efficiency means that one must make every effort to avoid flow separation on the internal surfaces of the compressor. It is important to remember that flow separation may take place on the end walls of the compressor as well as on the blade surfaces.

Three factors are particularly important:

1. As we pointed out before, operation at high Reynolds number tends to keep boundary layers turbulent and thus resistant to flow separation.
2. Another requirement is the avoidance of strong shock waves that can easily separate even highly turbulent boundary layers. The flow approaching a given blade may be subsonic but can accelerate, on passing over the convex portion of the blade surface, to supersonic speeds so that local shock waves could develop on the blade surface.

3. A third requirement for avoidance of flow separation is that the pressure coefficient for the blade row (defined in Section 7.3) not be excessive. Even with high Reynolds number and in the absence of shock waves, boundary layers will separate if the pressure coefficient exceeds a value of, say, 0.5. One must also consider the Leiblein diffusion parameter, but this comes up when making the choice of blading to satisfy the design flow field.

It follows that with the high-efficiency objective a design procedure should provide for high Reynolds number operation, control of flow Mach number relative to the blade, and avoidance of excessive local pressure coefficient. It would be nice if reliable equations were available with which to calculate the effect on efficiency of all changes in compressor geometry. Unfortunately these do not exist, and the estimation of aerodynamic losses in compressors is still, as Section 7.7 suggests, a matter of rough approximation. However, we may note that compressors of various designs that do comply with the three guidelines given above do not differ radically in maximum efficiency. We can expect good efficiency to be the result of a design in which flow separation is avoided by adherence to these guidelines and by matching the blade geometry to a design flow field that satisfies the pertinent continuity, momentum, and energy equations.

The objectives of high pressure ratio per stage and high mass flow rate per unit cross-sectional area may seem to be somewhat in conflict. One way to formulate a design procedure would be to try to maximize flow rate per unit area (within the appropriate constraints) for a given stage pressure ratio. We could write our relationship between dimensionless variables in the form

$$\frac{\dot{m} \sqrt{RT_{01}}}{p_{01} D^2} = f\left(\frac{p_{03}}{p_{01}}, \frac{U_t}{a_{01}}, \text{design}\right).$$

For a given pressure ratio we could search for the combination of blade tip speed and geometric design ratios that will maximize the flow per unit area. The choice of blade speed may not be entirely free since blade stresses have to be kept in mind; however the most serious design limitations for axial air compressors are typically aerodynamic (flow separation) rather than mechanical (blade stress). The opposite is the case for high-temperature axial turbines, which are typically stress limited.

Exploring design choices with a given pressure ratio is not necessarily restrictive, since one can use the same design procedure with a series of choices for compressor pressure ratio.

By stating the design problem in terms of dimensionless variables, we can see that it is not necessary, in principle, to do a different design optimization for every combination of inlet stagnation pressure and temperature. The problem has been reduced to one having the smallest number of independent design variables.

Our design process here is essentially limited to determining a suitable flow field within the axial compressor. With this in mind we can say that the design is specified in a preliminary way by determining the flow angles at inlet and outlet of each blade row as a function of radial position, and by specifying the ratio of inner and outer diameters for the blade row in question. We imply that if

the fluid-flow angles are properly determined, blades of suitable shape and twist can be manufactured to match the specified fluid-flow angles.

One point we must keep in mind of course is that if a rotor blade is excessively twisted, the centrifugal force on the "overhanging" mass may give rise to excessive bending stresses. Defining the twist as the difference between the root and tip average flow angles, we should limit the allowable twist to, say, 30° or 35°.

Our consideration here is with the compressor operating under design conditions, that is, with flow angle and blade angles essentially the same at each location. (In Section 7.3 we considered the effects of small departures from design condition for a given machine.)

In the design procedure outlined in this section we endeavor to make appropriate allowance for fluid dynamics and thermodynamics, though under somewhat idealized conditions. The first approximation is the one we have constantly used to this point—that radial velocity components are negligible in the sense that

$$c_r^2 \ll c_\theta^2 \quad \text{or} \quad c_z^2.$$

The second approximation is that frictional effects are neglected (though allowance is made for the stage efficiency being less than 1). In a well-designed machine operating at design conditions, frictional effects will be concentrated in thin boundary regions near the annular walls of the compressor or on the blade surfaces; most of the fluid will behave as though it were frictionless. Modern design methods for axial compressors do make allowance for radial velocity components and for frictional effects (at least to account for the effects of boundary layer displacement thickness), but for the sake of clarity in capturing the main ideas, we dispense with these complexities here.

With these approximations we now proceed to take account of the dynamics and thermodynamics of the flow in a simplified way.

Stagnation Temperature

Though there are, in the radial direction, large variations of blade speed, flow speed and angle, and pressure, we assume that there is no radial variation in the stagnation temperature. This follows from the ideas that the fluid enters the compressor with uniform stagnation temperature, that the compression is essentially adiabatic, and that the work done should be the same for all streamlines. If the stagnation temperature were not radially uniform at a given axial location, one might expect irreversible mixing to occur.

Entropy

If, as a first approximation, we assume that the compression process is both frictionless (for the bulk of the fluid) and adiabatic, then it follows that the entropy will be everywhere the same within the stage, given that the fluid enters the compressor with uniform stagnation pressure and temperature, that is, with uni-

form thermodynamic state. Chapter 3 showed that for a given particle of fluid, one can write the entropy change as

$$\frac{ds}{R} = \frac{\gamma}{\gamma - 1} \frac{dT_0}{T_0} - \frac{dp_0}{p_0}.$$

It follows that if the compression is isentropic from the same initial state for all streamlines, and if the stagnation temperature is independent of radius at a given axial location, the stagnation pressure will also be independent of radius at a given axial location.

Mass Flow Rate

For any plane perpendicular to the axis of the compressor, one may express the mass flow rate as an integral, extending from inner radius r_h to outer radius r_t in the form

$$\dot{m} = \int_{r_h}^{r_t} \rho c_z 2\pi r dr, \quad (7.46)$$

in which ρ is the density and c_z , the axial component of the fluid velocity.

We have in mind the application of Eq. (7.46) immediately upstream of the rotor, and view the velocity field within a fixed (nonrotating) coordinate system. The relationship between the local density and the velocity is given by the isentropic relationship

$$\frac{\rho}{\rho_{01}} = \left(\frac{T}{T_{01}} \right)^{1/(\gamma-1)}$$

and the definition of stagnation temperature

$$T_{01} = T + \frac{c^2}{2c_p} = T + \frac{c_\theta^2 + c_z^2}{2c_p},$$

so that

$$\frac{\rho}{\rho_{01}} = \left(1 - \frac{c_\theta^2 + c_z^2}{2c_p T_{01}} \right)^{1/(\gamma-1)}. \quad (7.47)$$

Work and Pressure Ratio

As Section 7.3 showed, we can write the stage pressure ratio as

$$\frac{p_{03}}{p_{01}} = \left[1 + \eta_{st} \frac{U \Delta c_\theta}{c_p T_{01}} \right]^{1/(\gamma-1)}, \quad (7.48)$$

in which we assume, in the light of abundant experience, that a stage efficiency of, perhaps, $\eta_{st} = 0.88$ is a reasonable target.

Rotor Inlet Relative Mach Number

Here we make the starting assumption that the highest relative Mach number in the stage is at the inlet to the rotor and at the maximum radius. To avoid the adverse effects of shock-wave boundary layer interactions, we limit this relative Mach number

$$M_{1\text{rel}} = \frac{w_{1t}}{\sqrt{\gamma RT_{1t}}} \quad (7.49)$$

to a value of 0.75 or 0.8. Here the value of the relative velocity at the tip radius w_{1t} is given by

$$w_{1t}^2 = c_{z1t}^2 + (U_t - c_{\theta1t})^2,$$

in which the subscript $_{1t}$ denotes entrance to the rotor and tip radius.

Radial Equilibrium

We impose two conditions here. First is the general requirement for simple radial equilibrium derived in Section 7.9:

$$\frac{d}{dr}(c_z^2) = -\frac{1}{r^2} \frac{d}{dr}(rc_\theta)^2. \quad (7.50)$$

The second is the designer's choice of the distribution of angular momentum with radius. Here we choose, as an example,

$$rc_\theta = ar + b. \quad (7.51)$$

The angular momentum distribution will be different upstream and downstream of the rotor, so that it might seem (at first sight) that we are here introducing four arbitrary constants (a_1, b_1, a_2, b_2). However, to keep the work the same at all radii, $\Delta(rc_\theta) = (rc_\theta)_2 - (rc_\theta)_1$ must be independent of radius; this requires that $a_1 = a_2 = a$. This being the case, we determine b_2 from b_1 by

$$b_2 = b_1 + \frac{U \Delta c_\theta}{\Omega}.$$

Also a must satisfy the requirement that at the inlet tip radius

$$rc_{\theta1t} = ar_t + b_1.$$

Thus, of the four parameters specifying the angular momentum distribution, only one (we here take b_1) can be considered open to the choice of the designer. Part of the design process involves a search for the most appropriate value of b_1 . The designer is of course free to choose an angular momentum distribution of a type quite different from Eq. (7.50). We have chosen this example only so that we could explore one case quantitatively; the case selected is not necessarily the best case.

Mid-Radius Constraints

We have applied two further conditions for the series of design calculations whose results are summarized in Figs. 7.45 to 7.48. The first of these is that, in the light of the discussion of Section 7.8, the degree of reaction at the mid-radius has been fixed at a value of

$$R_{r=r_m} = 0.5. \quad (7.52)$$

The second is that, again at mid-radius, the design has been constrained to constant axial velocity component, namely,

$$(c_{z1})_{r=r_m} = (c_{z2})_{r=r_m}. \quad (7.53)$$

Neither of these conditions is absolutely required; a designer might wish to examine the results of small departures from these conditions.

In summary, Eqs. (7.46) to (7.53) can be considered a framework for preliminary design of a subsonic axial stage. Appendix IV shows how one can express these equations in terms of dimensionless parameters to simplify the work of calculation while searching for conditions that will maximize the dimensionless flow rate identified in Eq. (7.45).

The process begins with starting values of:

Overall pressure ratio	p_{03}/p_{01} ,
Stage efficiency	η_{st} ,
Maximum relative Mach number	$M_{1\text{rel}}$,
Mid-radius degree of reaction	R ,

and searches for the best values of:

Dimensionless tip speed	U/a_{01} ,
Dimensionless swirl number	$B = b_1/\Omega r_t^2$,
Hub-tip radius ratio	$\zeta = r_h/r_t$,

while avoiding excessive blade twist. Typical values of these parameters are presented in Figs. 7.45 to 7.48.

Figure 7.45 shows the dependence of the dimensionless flow rate on stage pressure ratio with differing swirl parameter B (for fixed values of the tip speed, relative Mach number, and hub-tip ratio). For the range of cases considered, the highest end-wall pressure coefficient is at the stator hub. We define C_{psh} as the pressure coefficient at that location. Lines of $C_{psh} = 0.5$ and 0.6 are shown in Figs. 7.45 to 7.48 to indicate when these values are becoming excessive. Likewise, values of rotor twist $\Delta\beta_m$ of 30° and 35° are shown ($\Delta\beta_m$ being the absolute difference between the average of the inlet and outlet blade angles at hub and tip radii). Figure 7.45 indicates that with $C_{psh} \leq 0.5$ and $\Delta\beta_m \leq 35^\circ$, the maximum stage pressure ratio would be about 1.3. This conclusion is of course linked to the assumed values of $M_{1\text{rel}}$, U_t/a_{01} , and ζ . Figure 7.46 shows that reducing the tip speed ratio below 1 (still with $\Delta\beta_m \leq 35^\circ$ and $C_{psh} \leq 0.5$) can increase the stage mass flow rate per unit area, at the expense of a small decrease in stage pressure ratio.

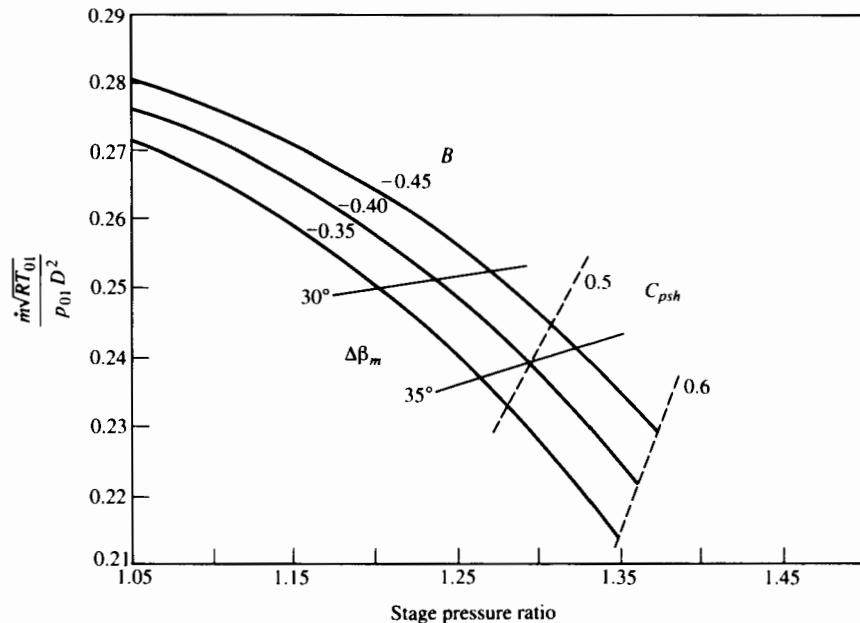


FIGURE 7.45 Subsonic axial compressor stage; $U_t/a_{01} = 1$, $M_{rel} = 0.75$, $\zeta = 0.6$.

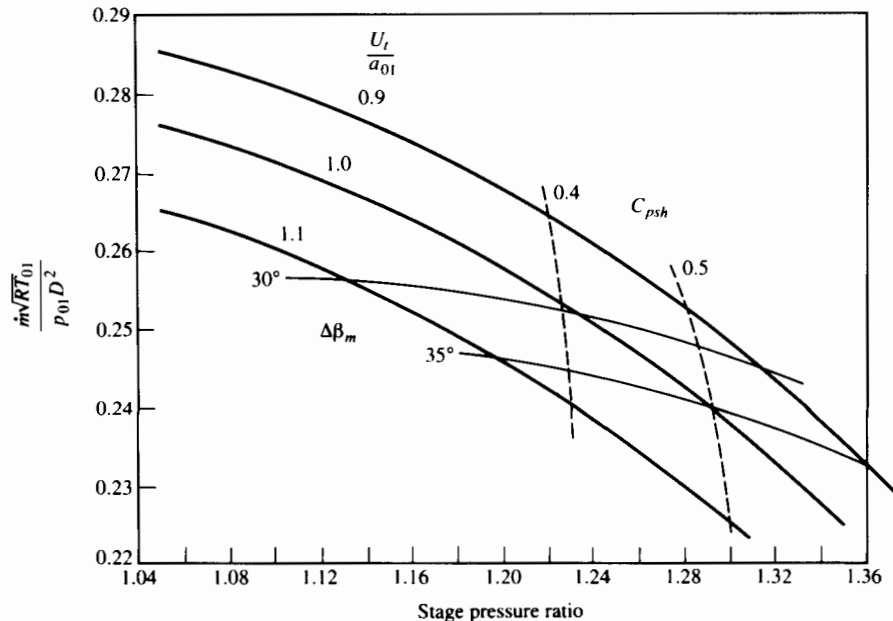


FIGURE 7.46 Subsonic axial compressor stage; $M_{rel} = 0.75$, $\zeta = 0.6$, $B = -0.4$.

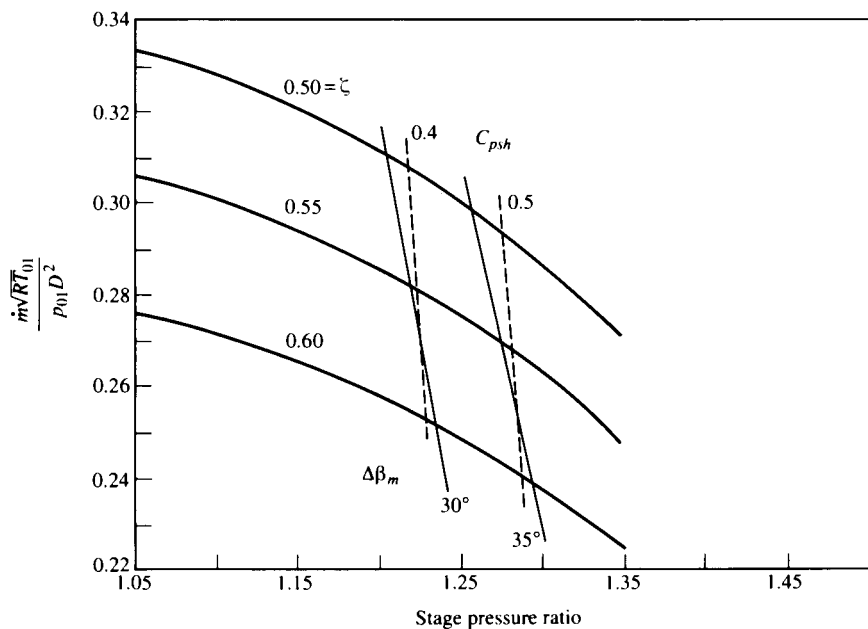


FIGURE 7.47 Subsonic axial compressor stage; $U_t/a_{01} = 1$, $M_{i,\text{rel}} = 0.75$, $B = -0.4$.

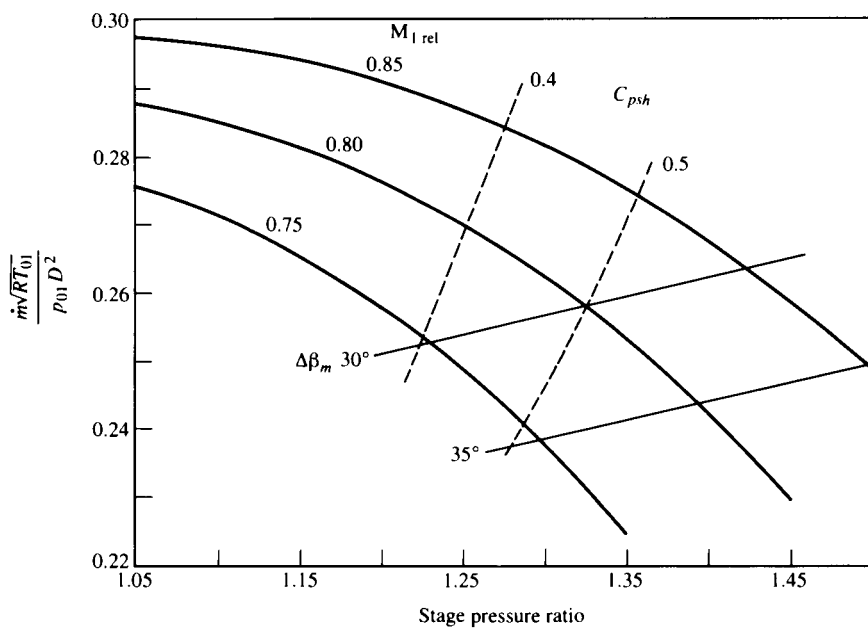


FIGURE 7.48 Subsonic axial compressor stage; $U_t/a_{01} = 1$, $\zeta = 0.6$, $B = -0.4$.

Figure 7.47 shows the effect of reducing the hub-tip ratio ζ . The stage mass flow rate per unit area can be significantly increased, but the stage pressure ratio drops back to around 1.25.

If the allowable Mach number can be increased, both the stage pressure ratio and the mass flow rate per unit area can be increased, as Fig. 7.48 shows.

Figures 7.45 to 7.48 demonstrate in an approximate way the factors that limit subsonic axial compressor stage performance under design conditions. Bear in mind, of course, that all of these results pertain to one set of angular momentum distribution profiles and that radial velocity components have been ignored in the solution of the radial equilibrium equation.

We now turn to the second application of a preliminary design procedure.

7.11 TRANSONIC FAN STAGE

In the past three decades one of the greatest achievements of axial compressor research has been the development of the transonic compressor. The term *transonic* is used because, while part of the internal flow field may be subsonic relative to the blades, part is definitely supersonic. The damage that shock waves can do to a flow, particularly when intersecting a wall boundary layer, is the chief reason that supersonic flow fields are difficult to design successfully in turbomachines. For a time it looked as though the only way to avoid trouble was to limit the Mach number of the flow approaching each blade row to a value sufficiently below 1 so that, with the usual acceleration over the blade surface, the maximum velocity would become only modestly supersonic. However, such a limitation on the relative Mach number of the approach flow has serious consequences for the size of machine needed to accommodate a certain mass flow rate. The argument is as follows:

It is at the inlet plane of the compressor that the air density is lowest and the required flow area the greatest. It is also at the inlet plane that the speed of sound is the least, because here the air temperature is lowest. Because the rotor speed increases with radius, the relative velocity (and thus the relative Mach number) tends to be the greatest at the blade-tip diameter at the inlet plane. If the relative Mach number in the flow approaching the blade has to be constrained to a modest subsonic value at that point, this means that the blade speed and the absolute approach velocity must also be limited. The first of these directly limits the minimum diameter of the rotor needed to handle a given flow rate. The second directly affects the pressure rise per stage, and thus the number of stages needed for a given overall pressure ratio. Thus for two reasons a fully subsonic compressor will be much larger than a transonic one having a tip relative Mach number of 1.7 or more.

With a subsonic compressor the consequences of the relative Mach number limitation can be partially alleviated by the use of inlet guide vanes placed before the first rotor in such a way as to impart swirl to the air in the direction the rotor is moving. This means that with the same relative Mach number limitation, the

designer can make the inlet diameter somewhat smaller than without the use of inlet guide vanes. But the improvement is small compared with what a good transonic stage can offer.

The problem of the inlet relative Mach number restriction is especially acute for the design of a high-bypass-ratio fan. As Chapter 5 shows, one can greatly improve the propulsion efficiency by converting a turbojet into a turbofan with a bypass ratio of 6 or even more. The great achievement for fan design has been the successful development of a transonic stage that, without needing inlet guide vanes, can be very much lighter and smaller than its subsonic counterpart.

The design principle of the transonic stage is not the avoidance of shocks but the control of their locations and strengths so as to minimize aerodynamic losses. This is easiest to do for a fan stage (or for the first stage of a multistage compressor), since it is at the inlet that the approach flow is most uniform and therefore most likely to be predictable for design purposes. In the interior of the compressor, the flow is not likely to have a uniform axial velocity component; the need for transonic stages, however, is not so great at the high-pressure end of the compressor. There the problem is not that the stage diameter is too big, but rather that the blade height tends to become too small for efficient operation. Thus in this chapter it is appropriate to consider the design of both transonic and subsonic stages.

Figure 7.49 shows experimental data compiled by Sandercock and presented by Serovy [12] on transonic fan pressure ratios and efficiencies, indicating successful operation at tip speeds as high as 550 m/s (1800 ft/sec) and with Lieblein diffusion factors for the rotor as high as 0.5.

Figure 7.50 shows the arrangement of the fan, the low-pressure compressor, and the high-pressure compressor of the Pratt & Whitney 2037 engine, for which the bypass ratio is 6:1. The fan consists of 36 wide-chord blades. The overall pressure ratio of the fan, the four low-pressure stages, and the five high-pressure ones is 31.8. The static sea-level mass flow rate is 550 kg/s (1210 lb_m/sec) under standard-day conditions. The tip diameter of the fan blades shown in Fig. 7.50 is 1.994 m (78.5 in.). This means that the axial Mach number at entrance to the fan is approximately 0.5. At the tip diameter, however, the Mach number for the approach velocity relative to the blade is of the order of 1.6. The fan pressure ratio is 1.7. The blade geometry typical of transonic compressor blades (see Fig. 7.51) differs considerably from the geometry characteristic of subsonic compressor blades.

Figure 7.51 shows the blade shape near the tip of the fan used by Giffen [20], which was designed for a tip relative Mach number of 1.52. In the hub region, where the relative flow is subsonic, the blade camber line is similar to that of a double circular arc. (We may note here that the design value of the relative Mach number at inlet to the following stator is only 0.67.) Shown on Fig. 7.51 are the contours of static pressure measured on the outer casing wall during fan operation under design conditions. These pressures were obtained from the signals from 10 high-frequency-response crystals; the signals were collected from each transducer at the blade passing frequency, and with variable phase shift so that the whole blade-passage pressure field could be mapped out. Indicated in

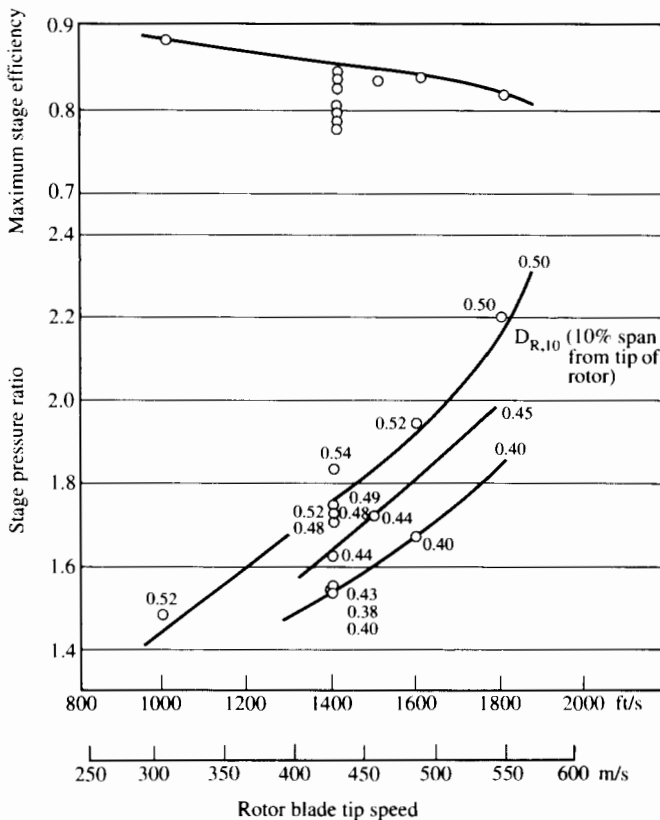


FIGURE 7.49 Measured trends in axial-flow compressor stage performance. (D.M. Sandercock of NASA.) Numbers on symbols are the tip-region Lieblein diffusion factors of Eq. (7.26). (Courtesy AIAA. © AIAA. Reprinted with permission.)

Fig. 7.51 is the result of two oblique shock waves—one at the leading edge and one on the pressure surface at about the midchord position. The pressure transducers have finite size and spacing, and the pressure distribution patterns may fluctuate somewhat from one cycle to the next. Also the intersection of the shock wave and the outer boundary layer may be complex. For these reasons the experimental measurements do not reveal the thin discontinuities one would normally associate with shock waves; nevertheless, one can see quite clearly from Fig. 7.51 where the oblique shocks are located. On the forward part of the suction surface (upper surface of the lower airfoil), the pressure is about 1.17 times the upstream value, owing to the wedge-type deceleration. As Chapter 3 indicates, this would correspond to a wedge deflection of about 3° . The included angle between the suction and pressure surfaces is about 4° . On the pressure surface the static pressure ratio of the leading-edge oblique shock is about 1.7; this corresponds to a deflection of about 10° and a shock angle of about 61° , which one may approxi-

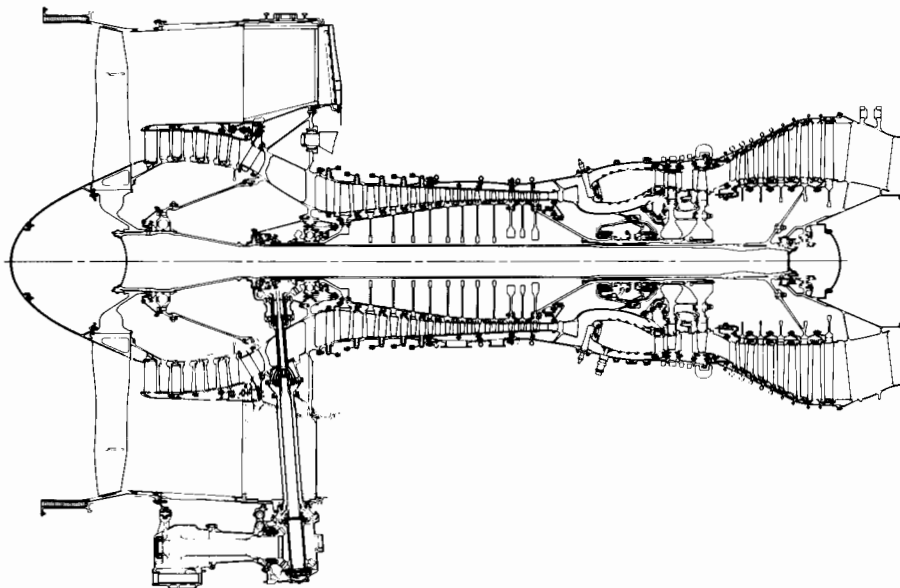


FIGURE 7.50 The fan and compressor section of the Pratt & Whitney 2037 engine. (Courtesy Pratt & Whitney, a division of United Technologies Corp.)

mately verify from Fig. 7.51. The leading-edge shock appears to be of approximately constant strength for about two-thirds of the passage. Then it seems abruptly to lose strength as it interacts with the expansion wave generated by the fairly sudden change of angle on the suction and pressure surfaces and the influence of the passage-exit shock, which has a static pressure ratio of about 2. This shock strength implies an incident Mach number of about 1.37. The overall adiabatic efficiency of the stage of which Fig. 7.51 shows the rotor-tip pressure field is

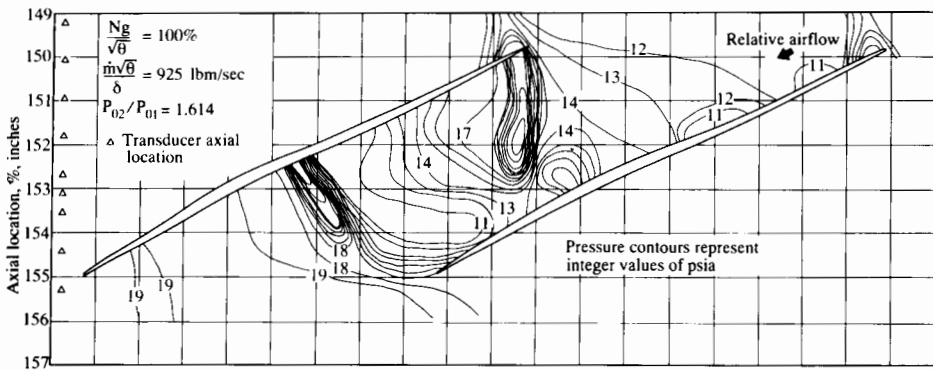


FIGURE 7.51 Rotor static pressure contours in a transonic fan rotor passage. (Adapted from Griffen [20].)

about 85%. Hence one can say that this blade geometry successfully accommodates transonic flow despite the presence of internal shock waves. The shock waves may have caused a small closed separation zone in the neighborhood of the expansion corner, but not a separation that seriously disturbs the flow.

From Eq. (7.26) we can see that one way to control the diffusion factor D (and thus reduce the danger of suction surface separation) is to increase the blade solidity, that is, to place the blades relatively close together. The transonic stage of Fig. 7.51 has a solidity of about 1.4 and a design diffusion factor D of 0.324 at the rotor tip, and a solidity of 2.45 and a diffusion factor of 0.454 at the rotor root diameter. Since aerodynamic and structural problems at the hub radius limit the number of blades one can use in a fan, one way to provide high solidity at the tip radius is to use a blade of wide chord. However, blades that are thin and have very little camber angle may be insufficiently rigid and may fail in vibration. The conventional practice, as shown in Fig. 7.52, has been to use interlocking platforms (called snubbers or midspan shrouds) by which the blades provide mutual lateral support to reduce the magnitude of lateral vibration. These snubbers are undesirable aerodynamically, as a source of drag, and structurally, because of their mass and induced centrifugal and bending stresses. Rolls-Royce developed the snubberless fan shown in Fig. 7.52 for the RB211 engine. The blade chord has

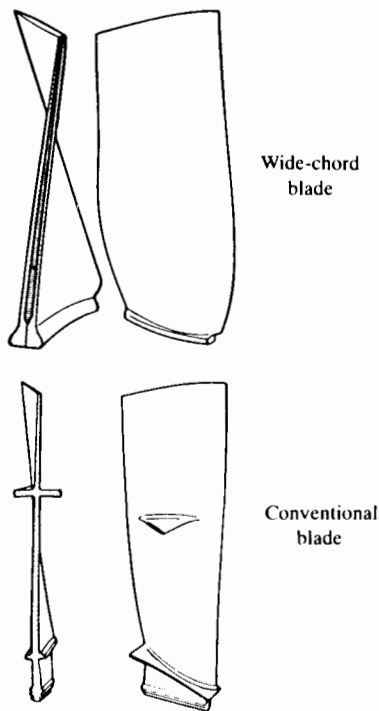


FIGURE 7.52 Wide-chord fan blade. (Courtesy Rolls-Royce, plc.)

been increased about 40%, and the blade has been fabricated from titanium surface panels enclosing a titanium honeycomb core.

For preliminary design of the transonic fan, we assume no inlet guide vanes; the flow enters the rotor with uniform and purely axial velocity. This leads to a set of preliminary design equations that are considerably simpler than the set required for the subsonic stage with swirling flow approaching the rotor.

One reason for this simplification is that the only way for the stage work to be uniform with radius (rc_θ being zero upstream of the rotor) is for the swirl between rotor and stator to be free vortex, that is, $(rc_\theta)_2 = b$, where b is a constant. This in turn leads (as shown in Section 7.9) to the simplification that, both upstream and downstream of the rotor, the axial velocity c_z must be independent of radius.

A further simplification is that numerical integration of the mass flow rate equation is no longer required. As Appendix V shows, one can write the dimensionless flow rate as

$$\frac{\dot{m} \sqrt{RT_{01}}}{p_{01} D^2} = \sqrt{\gamma} \frac{\pi}{4} \frac{M_1(1 - \zeta^2)}{\left[1 + \frac{\gamma - 1}{2} M_1^2\right]^{(\gamma+1)/2(\gamma-1)}}, \quad (7.54)$$

in which $M_1 = c_1 / \sqrt{\gamma RT_1}$ is the axial (absolute) Mach number at inlet to the rotor, and $\zeta = r_h/r_t$ is the hub-tip ratio. For a given value of M_1 the dimensionless mass flow ratio is clearly independent of stage work and pressure ratio. We could write the pressure ratio equation (7.48) in this case as

$$\frac{p_{03}}{p_{01}} = \left[1 + \eta_{st} \frac{U_t}{c_p} \frac{c_{\theta2t}}{T_{01}} \right]^{\gamma(\gamma-1)}. \quad (7.55)$$

Here we can state the maximum allowable relative number at the rotor tip as

$$M_{1\text{rel}} = \frac{w_{1t}}{\sqrt{\gamma RT_{1t}}}, \quad (7.56)$$

in which w_{1t} can be obtained from

$$w_{1t}^2 = c_1^2 + U_t^2.$$

Downstream of the rotor we can adopt the condition $c_z = c_1$ at all radii.

With constant axial velocity and $c_\theta \propto r^{-1}$ upstream and downstream of the rotor, flow angles are easy to determine.

Imposing the condition that the flow leaving the stator must be in the axial direction can cause difficulty in the stator at hub radius due to excessive pressure rise. Recognizing this, we impose a design condition that the stator hub pressure-

rise coefficient not exceed a prescribed value. Though the hub flow is compressible, we could define the pressure coefficient as

$$C_{psh} = 1 - \left(\frac{c_3}{c_2} \right)^2.$$

If we also impose the condition

$$c_3 = c_1, \quad (7.57)$$

the stator hub “pressure” coefficient becomes

$$C_{psh} = 1 - \left(\frac{c_1}{c_2} \right)^2. \quad (7.58)$$

Avoidance of the end-wall separation at the hub might require C_{psh} to be limited to a value of, say, $C_{psh} = 0.5$.

It is, of course, not absolutely necessary that the flow be purely axial at the stage exit (though the kinetic energy of swirl contributes to overall loss), and it is not essential that the axial velocity be absolutely uniform through the stage. The designer may well wish to examine the effects of deviations from these nominal conditions. However, these conditions were adopted for the calculations whose results are shown in the next three figures.

Through the transonic stage there will generally be considerable density increase and hence considerable reduction of the annular area of the flow. For this reason the radial slope dr/dx —for example, at the hub radius—may be quite considerable, so that our assumption $c_r^2 \ll c_z^2$ or c_θ^2 may be in doubt. Thus the preliminary analysis may not produce a very accurate description of the flow field in the hub region.

Accepting this limitation on the accuracy of the results, we can regard Eqs. (7.54) through (7.58) as providing the framework for preliminary design of the transonic stage. Appendix V shows that one may transform these equations into dimensionless form in such a way that, given the basic design assumptions (swirl-free rotor inlet and stator exit flow, and uniform axial velocity), one may readily determine the dimensionless mass flow ratio $\dot{m} \sqrt{RT_{01}/p_{01} D^2}$ and the inlet tip relative Mach number $M_{1\text{rel}}$ for prescribed values of:

Stage pressure ratio	p_{03}/p_{01} ,
Stage efficiency	η_{st} ,
Hub-tip ratio	ζ ,
Stator hub pressure coefficient	C_{psh} .

Figures 7.53, 7.54, and 7.55 show the results of using these relationships to explore the possibilities of transonic stage design.

Figure 7.53 shows, as one would expect from Eq. (7.54), that changing the pressure ratio and C_{psh} has no effect on the stage mass flow rate, which depends only on M_1 and ζ . Both p_{03}/p_{01} and C_{psh} do, however, have a significant effect on

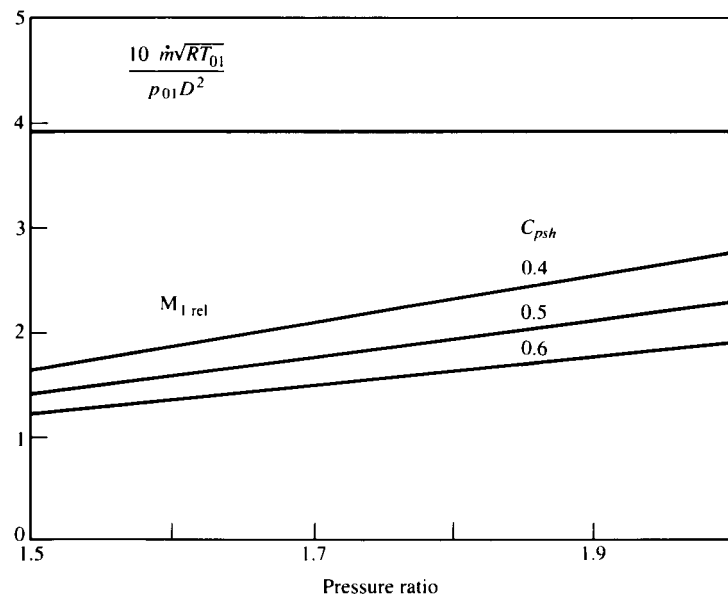


FIGURE 7.53 Transonic axial fan stage; $M_1 = 0.7$, $\zeta = 0.45$.

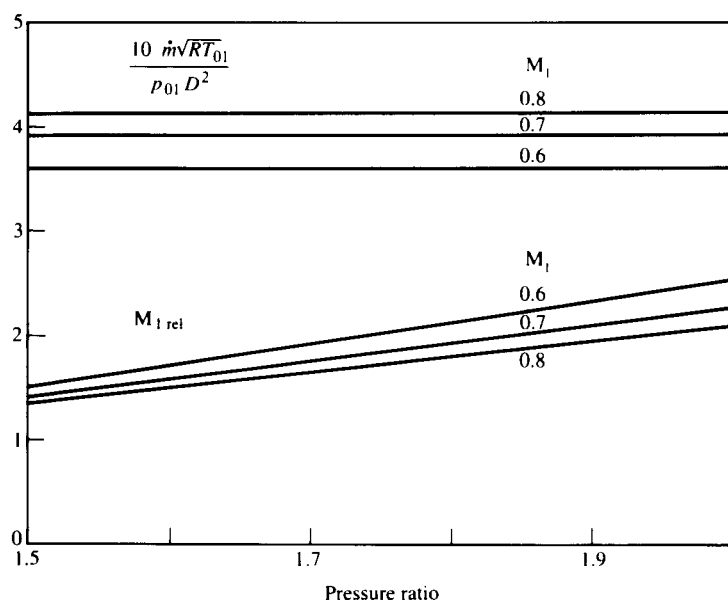


FIGURE 7.54 Transonic axial fan stage; $C_{psh} = 0.5$, $\zeta = 0.45$.

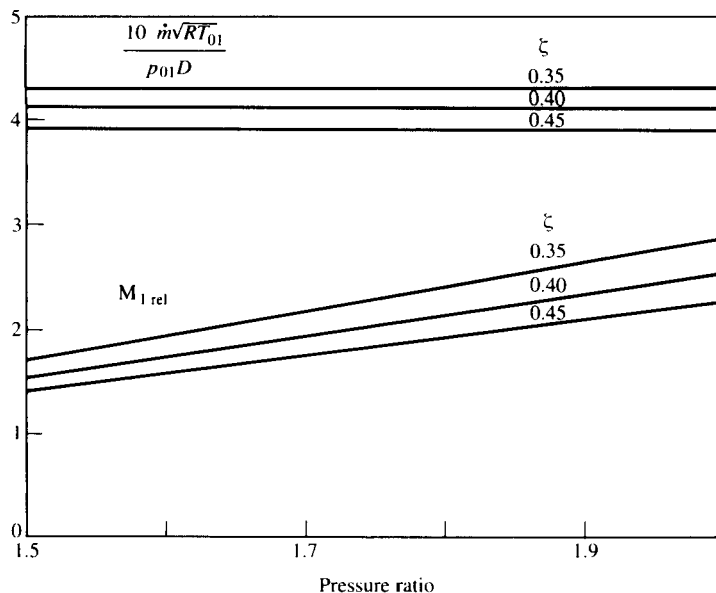


FIGURE 7.55 Transonic axial fan stage; $C_{psh} = 0.5$, $M_1 = 0.7$.

the relative Mach number required at the blade tip. We see here the reason for loading the end-wall boundary layers as heavily as possible. It may be shown, however, that increasing C_{psh} tends to increase the rotor twist angle. To keep the twist angle in the range of 30° to 40° , we choose $C_{psh} = 0.5$. With $M_1 = 0.7$ and $\zeta = 0.45$, this keeps the rotor hub pressure coefficient less than 0.6.

Figure 7.54 shows the effect of M_1 on the mass flow rate that we would expect from Eq. (7.54). Since $M_{1\text{rel}}$ is much larger than M_1 , it is not strongly affected by changes in M_1 at a given pressure ratio. Increasing M_1 tends to lower the value of $M_{1\text{rel}}$ for a given pressure ratio. However, increasing M_1 also increases the rotor twist at a given pressure ratio. For $\zeta = 0.45$ and $C_{psh} = 0.5$, $M_1 = 0.7$ seems to be a reasonable value.

Figure 7.55 shows the influence of the hub-tip ratio. Decreasing it means smaller tip diameter for a given mass flow rate. For a given $M_{1\text{rel}}$ limit, however, this may lead to a large reduction in allowable pressure ratio.

Like those for the subsonic design, we must regard these results as approximate, since they do not account for streamline curvature in the meridional plane. Nevertheless, they illustrate the kind of adjustment of parameters that is necessary in designing a transonic stage.

After carrying out this kind of preliminary exercise, the designer is ready to make use of three-dimensional mathematical simulations of the transonic flow field such as those demonstrated in Figs. 7.56 and 7.57, the work of Miller and

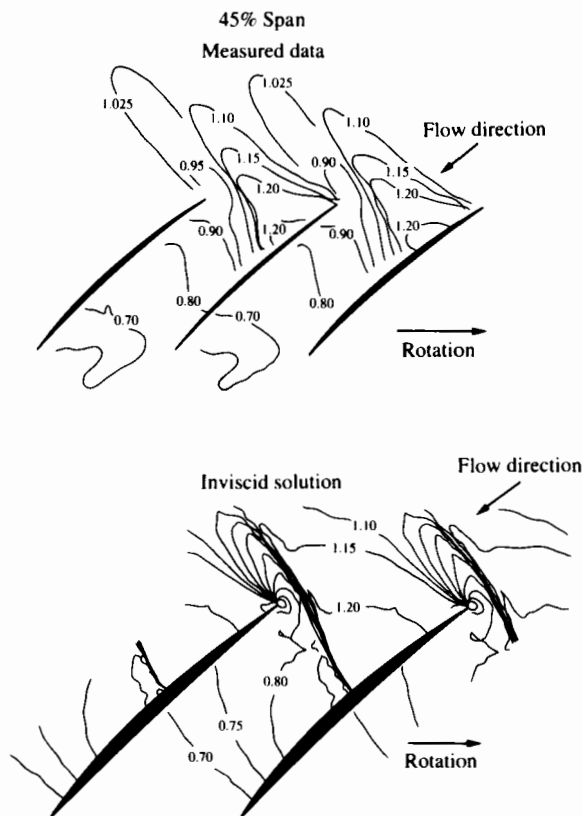


FIGURE 7.56 Blade-to-blade contours at peak efficiency. (From Miller and Bryans [20].)

Bryans [21]. These authors have used two methods of calculating the flow in a transonic stage with a stagnation pressure ratio of 1.626. Figure 7.56 shows a comparison of the measured and calculated lines of constant Mach number at a blade cross section separated from the blade tip by 45% of the span. Figure 7.57 compares the measured and experimental values of the blade surface pressures at the same distance from the blade tip. Their calculation method does not take viscosity into account; nevertheless it represents the main features of the flow field quite well. Fully three-dimensional methods of calculating the flow field (in which the mass, energy, and momentum equations are satisfied iteratively for a very large number of elements of the flow passage volume) are complicated and expensive to use. However, they can supply invaluable guidance to the designer as the design is being refined. Such guidance can be especially helpful in planning development tests that, for a large transonic stage, can be extremely expensive. Best use of theory and experiment in combination can greatly shorten the necessary development period.

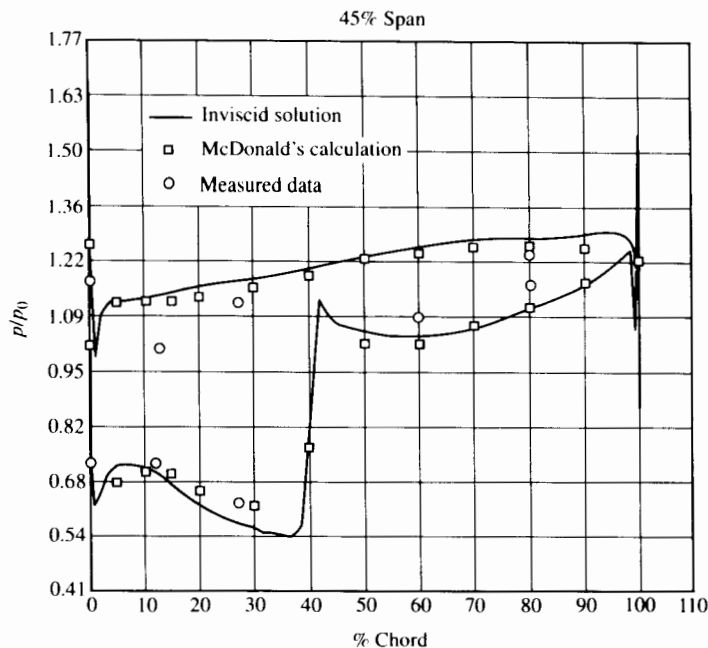
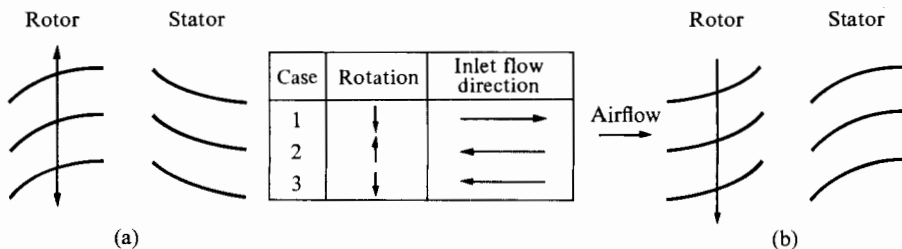


FIGURE 7.57 Surface pressures at peak efficiency. (From Miller and Bryans [20].)

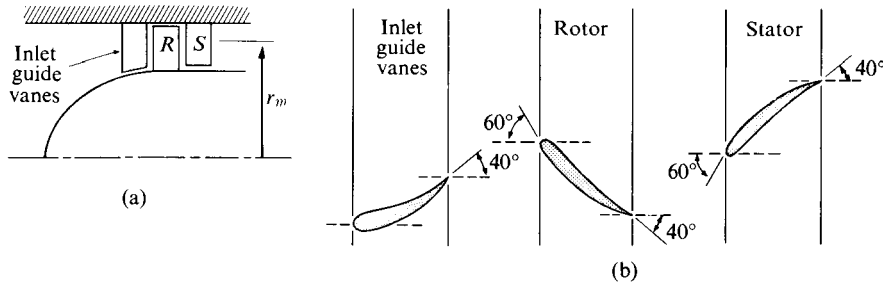
PROBLEMS

1. Shown schematically in part (a) of the figure is the blading of a single-stage axial turbomachine. What kind of machine is represented by cases 1 and 2? What would happen in case 3? Would it be desirable to build a compressor stage as in part (b) of the figure?



PROBLEM 1

2. Estimate the power required to drive a single-stage compressor shown schematically in parts (a) and (b) of the figure.

**PROBLEM 2**

At the mean radius ($r_m = 30$ cm), the blade configuration is as shown in part (b). For simplicity, assume that the air angles and blade angles are identical.

The overall adiabatic efficiency of the stage is 90%. The hub-tip radius ratio is 0.8, high enough so that conditions at the mean radius are a good average of conditions from root to tip.

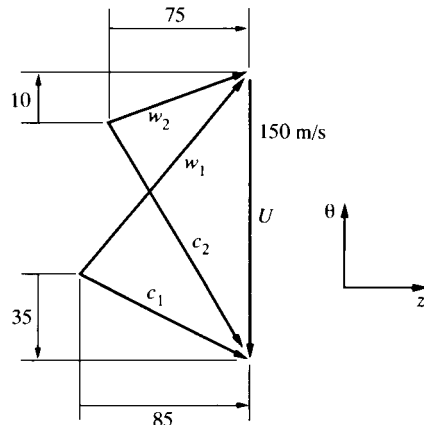
The axial velocity component at design flow rate is uniformly 125 m/s, and the inlet air is at 1 atm and 20° C. What should the shaft speed be under these conditions?

3. At a certain operating condition the mid-radius velocity triangles for an axial compressor stage are as shown in the figure. Here subscripts 1 and 2 denote entrance to rotor and stator, respectively. The stagnation temperature and pressure at entrance to the rotor are 340 K and 185 kPa.

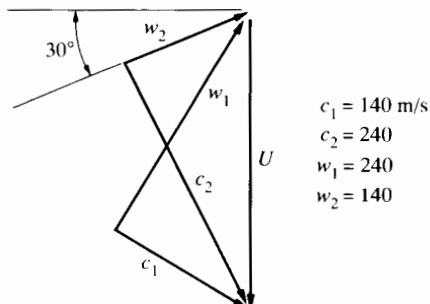
Neglecting frictional effects, determine:

- a. The specific work kJ/kg;
- b. The stagnation and static temperatures between rotor and stator;
- c. The stagnation and static pressures between rotor and stator;
- d. The mid-radius pressure coefficient

$$C_p = (p_2 - p_1)/\frac{1}{2}\rho_1 w_1^2.$$

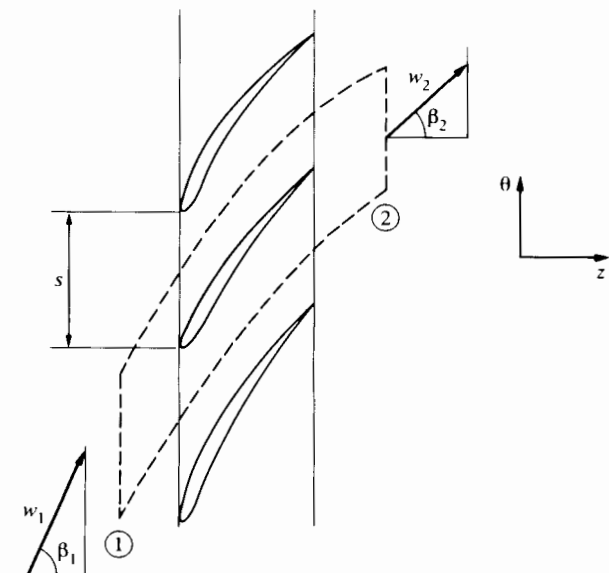
**PROBLEM 3**

4. At design flow and speed the mean velocity triangles for the second stage of a high-pressure-ratio axial compressor are as shown in the figure. (a) What is the total pressure ratio of this stage if the stage efficiency is 0.85 and the inlet temperature is 300 K? (b) During starting, the axial velocity rises to 60 m/s and no more after the rotor has reached design speed. To prevent stalling in the first stages, variable stator angles are to be employed. How far and in what direction must the stator upstream of this stage be rotated to bring β_1 to the design value when c_z is only 60 m/s?



PROBLEM 4

5. The figure shows a control volume surrounding one blade in a two-dimensional cascade of airfoils that turn the flow from inlet angle β_1 to outlet angle β_2 . The inlet velocity relative to the blades is w_1 , and the density of the fluid is ρ and may be assumed constant for this particular flow. If there are no losses in stagnation pressure, show that the axial velocity component stays constant



PROBLEM 5

and that the sums of the forces exerted by the fluid on the blade in the z - and θ -directions are (per unit blade height)

$$F_z = s(p_1 - p_2)$$

$$F_\theta = \rho w_1^2 \cos \beta_1 s(\sin \beta_1 - \cos \beta_1 \tan \beta_2).$$

6. An incompressible fluid flows axially down a straight pipe with uniform stagnation pressure then passes through vanes producing a free-vortex ($rc_\theta = k$) tangential velocity distribution on the downstream side. Neglecting friction, show that it is proper to assume a uniform axial velocity on the downstream side of the vanes. If there are 20 equally spaced blades and

$$k = 200 \text{ m}^2/\text{s},$$

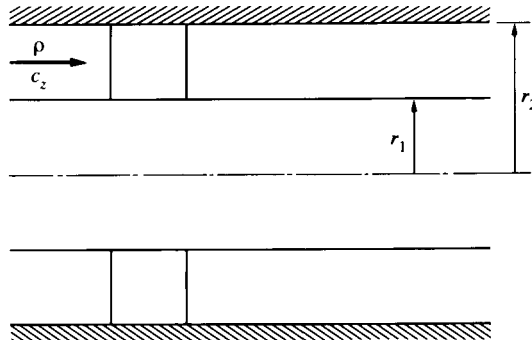
$$c_z = 100 \text{ m/s},$$

$$\rho = 1.22 \text{ kg/m}^3,$$

$$r_1 = 0.25 \text{ m},$$

$$r_2 = 0.5 \text{ m},$$

determine the total axial and tangential forces on each blade.



PROBLEM 6

7. Using the typical cascade performance data of Fig. 7.26 show how, for a stagger angle of 40° , the turning angle and pressure rise depend on the inlet flow angle. Plot $\beta_1 - \beta_2$ and $(p_2 - p_1)/\frac{1}{2}\rho w_1^2$ as functions of β_1 for solidities of 1.0 and 1.5, assuming no stagnation pressure loss. Qualitatively, how would you expect these results to change with Reynolds number and Mach number?
8. Accepting a limiting rotor or stator pressure rise coefficient of 0.5 (defined as though the flow were incompressible and isentropic) and assuming uniform axial velocity, plot the dependence of stage work ratio $\psi = \Delta h_0/U^2$ and inlet velocity ratio w_1/U on flow coefficient $\phi = c_z/U$ for degree of reaction $R = 0.5$ and

$$0.3 < \phi < 1.$$

What are the implications of these results for designing for high-pressure ratio per stage? How must ϕ and ψ be limited if w_1/U is not to exceed 1?

9. A three-stage air compressor has the following stage pressure ratios and adiabatic efficiencies:

Stage	Stagnation Pressure Ratio	Adiabatic Efficiency
1	1.6	0.87
2	1.4	0.89
3	1.3	0.90

What are the compressor pressure ratio and the overall adiabatic efficiency? What is the average polytropic efficiency? If the stage temperature ratios and adiabatic efficiencies had been uniform through the stages and the overall temperature ratio the same as above, by how much would the stage efficiency have differed from the polytropic efficiency?

10. A single-stage axial compressor uses 65(12)10 blading with a solidity at the mean diameter of 1.0. It is designed for 50% reaction and an axial velocity ratio of 0.5. Determine the rotor and stator flow angles. Using the cascade data of Fig. 7.26, choose a suitable stagger angle for the blades and determine the ideal stage work characteristic (ψ vs. ϕ) between stalling limits. For fixed blading assume that the absolute flow angle α_1 at entrance to the rotor is independent of axial velocity ratio.
11. An axial compressor was tested in Albuquerque, New Mexico, on a day when the barometric pressure was 25.5" Hg (86.4 kPa) and the ambient temperature was 27° C. When it was running at 15,200 rpm, the measured compressor flow rate was 27.2 kg/s and the delivery pressure was 526.5 kPa.
- Determine from these test conditions the shaft speed, mass flow rate, and pressure ratio that could be considered equivalent performance if the machine were operated at standard atmospheric conditions (101 kPa and 15° C).
 - Following a modification, the machine was retested in Los Angeles at the same rpm on a day when the ambient air was at 20° C and 30.2" Hg (102 kPa). This time the measured flow rate was 30.1 kg/s and the delivery pressure was 605 kPa. Could one consider the modification a success?
12. In a preliminary design study of an axial compressor stage, the assumption of axial velocity ratio proportional to radius, that is,

$$\frac{c_z}{U} = \left(\frac{c_z}{U} \right)_t,$$

is being explored. The subscript t denotes the tip radius.

At the tip radius the tangential velocity ratio $c_{\theta 1}/U$ and the work ratio ($\Delta c_{\theta}/U$), are specified. The rotor tip speed ratio U/a_0 (in which a_0 is the speed of sound) is also specified, and the inlet stagnation pressure and temperature, p_0 and T_0 , are known. The compressor work per unit mass is to be independent of radius.

In terms of the parameters specified above, determine:

- The distribution with radius of the tangential velocity ratio $c_{\theta 1}/U$ at inlet to the rotor;
 - The corresponding distribution of $c_{\theta 2}/U$ at exit from the rotor;
 - The rotor inlet relative Mach number at the tip diameter;
 - The variation with radius of the outlet angle α_1 of the inlet guide vanes.
13. An axial compressor stage has a hub-tip ratio $\zeta = 0.6$ and the following conditions at mean radius:

$$\text{Axial velocity ratio} \quad \frac{c_z}{U} = 0.4,$$

$$\text{Degree of reaction} \quad R = 0.5,$$

Absolute flow angle at rotor inlet = 30°

(providing tangential velocity component in the U -direction).

If free-vortex rotation ($c_\theta \propto r^{-1}$) is chosen, determine:

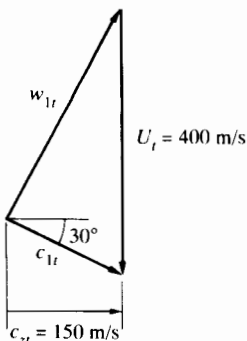
- The rotor inlet relative flow angle at tip radius;
 - The degree of reaction at the tip radius.
14. We wish to explore the idea of designing an axial compressor with degree of reaction constant from root to tip. To that end we consider the angular momentum distribution

$$rc_\theta = ar^2 + b$$

to apply both upstream of the rotor (where the constants are $a = a_1, b = b_1$) and downstream (where $a = a_2, b = b_2$).

- How must the upstream and downstream constants be related if the stage work is to be independent of radius?
 - How must the constants be related if the degree of reaction is to be independent of radius?
 - How must the constants be related if, in addition to the above, the degree of reaction must be $1/2$ at all radii?
 - How would the axial velocity distribution upstream of the rotor depend in general on a_1, b_1 ?
 - In terms of the upstream constant b_1 , the mid-radius upstream velocity terms c_{zm} and U_m , and the ratio r/r_m , what is the particular axial velocity distribution corresponding to case (c) above?
15. At the entrance to one stage of a multistage compressor, the hub-tip ratio is $\zeta = 0.7 = r_h/r_t$, and the inlet velocity triangle at the tip radius is as shown. If the axial velocity is to be proportional to radius, determine:

- The value of the absolute flow angle α_{1h} at the hub;
- The corresponding value of the relative flow angle β_{1h} at the hub.



PROBLEM 15

- 16.** In a preliminary design study of the first stage of an axial compressor, the consequences of assuming

$$\frac{c_z}{c_{zm}} = \left(\frac{r}{r_m} \right)^k$$

are being investigated. The subscript m denotes mean radius, and k is a constant.

As a first approximation (in the initial exploration of this idea), radial gradients of density as well as of entropy and stagnation enthalpy are taken to be negligible. The mean radius conditions at exit from the inlet guide vanes are

$$\frac{c_{zm}}{U_m} = 0.5 ,$$

$$\frac{c_{\theta m}}{U_m} = 0.3 ,$$

in which U is the rotor speed and c_θ the tangential velocity component. At the tip radius w_1/U is not to exceed 0.9.

- Show how c_θ/U depends on r/r_m and k (as well as on c_{zm}/U_m and $c_{\theta m}/U_m$).
- Show how to obtain the dimensionless mass flow rate $\dot{m}/(\rho \pi r_t^2 U_t)$.

- 17.** A subsonic axial compressor stage has been designed for $rc_\theta = ar + b$ with degree of reaction $R = 0.5$ at the mean diameter and Δh_0 independent of radius. The expected adiabatic efficiency of the stage is $\eta_c = 0.88$. In the preliminary design procedure outlined in Section 7.10, the following parameters have been chosen:

Pressure ratio	1.3
$M_{1\text{rel}}$	0.75
U_t/a_{01}	1.0
ζ	0.6
B	-0.4

The following results have been obtained.

r/r_t	1	0.8	0.6
$c_{\theta 1}/U$	0.3618	0.3272	0.1585
c_{z1}/U	0.3553	0.6032	0.9322
$c_{\theta 2}/U$	0.5829	0.6727	0.7728
c_{z2}/U	0.2049	0.6033	1.1220
β_1	60.89	48.11	42.07
β_2	63.83	28.48	11.45
α_2	70.62	48.12	34.56
α_3	45.52	28.47	9.65
w_1/U	0.7305	0.9036	1.2558
w_2/U	0.4647	0.6862	1.1448
R	0.7181	0.5000	0.2169
$M_{1\text{rel}}$	0.7500	0.7457	0.7790

Assess whether these results are consistent with the design assumptions and procedure of Section 7.10. The dimensionless flow rate is

$$\frac{\dot{m} \sqrt{RT_{01}}}{p_{01} D^2} = 0.2378.$$

18. A transonic axial compressor stage is being designed with no inlet guide vanes, free-vortex velocity distribution downstream of the rotor, and no exit swirl. The design pressure ratio is $p_r = 1.7$, the hub-tip ratio is 0.45, and the stator hub pressure coefficient is set at 0.4. The axial inlet Mach number M_1 is 0.7. The following results have been obtained.

r/r_t	1	0.725	0.45
$c_{\theta 1}/U$	0	0	0
c_{z1}/U	0.3525	0.4863	0.7835
$c_{\theta 2}/U$	0.1295	0.2464	0.6397
c_{z2}/U	0.3525	0.4863	0.7835
β_1	70.58	64.06	51.92
β_2	67.95	57.16	24.70
α_2	20.17	26.88	39.23
α_3	0	0	0
w_1/U	1.0603	1.1120	1.2704
w_2/U	0.9391	0.8968	0.8624
R	0.9352	0.8767	0.6801
$M_{1\text{rel}}$	2.1052	1.6006	1.1350

The dimensionless mass flow rate is

$$\frac{\dot{m} \sqrt{RT_{01}}}{p_{01} D^2} = 0.3919$$

and the value of B is 0.1295. The stage efficiency is 0.88.

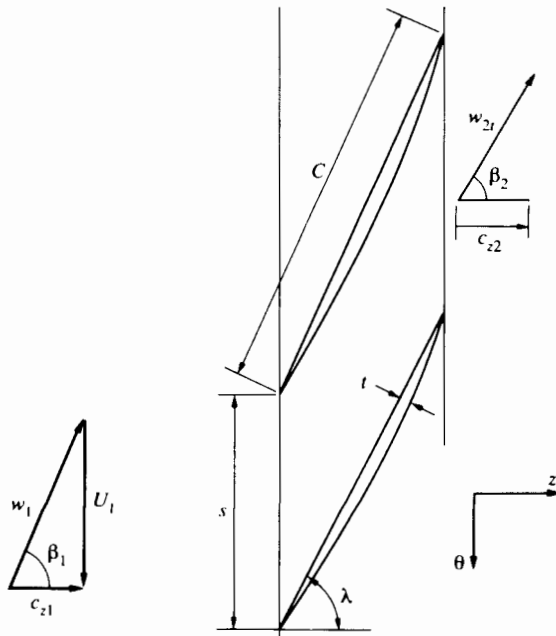
Check whether these results are consistent with the design procedure of Section 7.11.

19. Shown in the figure is the flow and blading at the tip radius of a transonic fan rotor. The inlet and outlet angles of the flow relative to the blade are β_1 and β_2 , respectively. The flow approaching the rotor is in the axial direction (absolute velocity), and its Mach number is 0.6.

The blade speed at the tip radius is 500 m/s, and the inlet stagnation pressure and temperature are 0.1 MPa and 300 K. The axial velocity component downstream of the rotor is radially uniform but is 10% lower than the axial velocity approaching the rotor.

The stagger angle λ is 60° , and the solidity C/s is 0.7; the blade chord is 20 cm. The relative leaving angle of the flow β_2 is 62° . Relative to a coordinate system fixed to the rotor, the stagnation pressure is 8% less leaving the rotor than entering it. Estimate:

- The static pressure ratio across the rotor;
- The stagnation pressure ratio (relative to a nonrotating coordinate system) across the rotor;
- The tangential force per blade per unit blade height at the rotor tip;
- The axial force per blade per unit blade height at the rotor tip.



PROBLEM 19

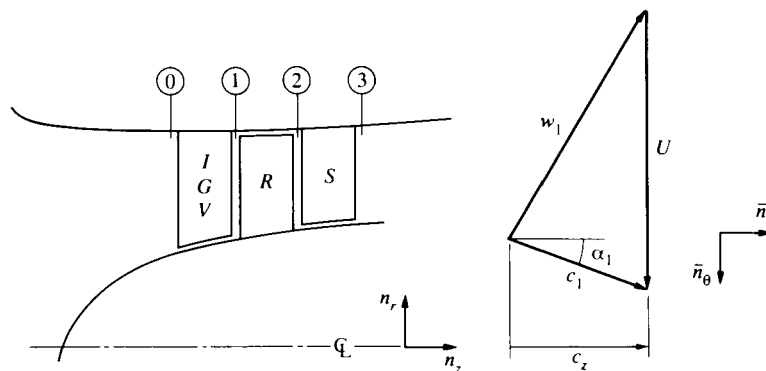
20. An axial compressor stage (see the accompanying drawing) has a row of inlet guide vanes (IGV) placed before the first set of rotor blades. Air enters the IGV with no swirl and with no radial variation in velocity, temperature, or

pressure. The work Δh_0 done by the rotor is independent of radius. The air leaves the IGV at an angle α_1 , which is the same at all radial locations. The shaft speed is $\Omega \text{ s}^{-1}$.

- a. Satisfying radial equilibrium, show that at station ① the axial velocity component will vary with radius according to

$$c_z = c_{zI} \left(\frac{r}{r_t} \right)^{-\sin^2 \alpha}$$

- b. Specify the variation with radius of the angular momentum upstream and downstream of the rotor.

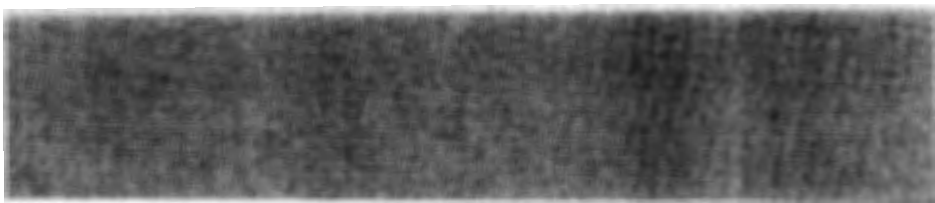


PROBLEM 20

REFERENCES

1. Cumpsty, N. A. *Compressor Aerodynamics*. London: Longman Scientific and Technical, 1989.
2. Weyer, H. B. "Compressible Design and Experimental Results," *Proc. of 47th Meeting of AGARD Propulsion and Energetics Panel*, May 20, 21, 1976, AGARD Conf. Proceedings no. 195.
3. Law, C. H., and A. J. Wennerstrom. "Performance of Two Transonic Axial Compressor Rotors Incorporating Inlet Counterswirl," *Trans. ASME* 109 (1987): 142–148.
4. Greitzer, E. M. "The Stability of Pumping Systems," 1980 Freeman Scholar Lecture, *ASME J. Fluids Eng.* 103 (1981): 193–242.
5. _____ . "Flow Instabilities in Turbomachines," in A. S. Ucer, P. Stow, and C. Hirsch, eds., *Thermodynamics and Fluid Mechanics of Turbomachinery*. vol. 2. Dordrecht: Martinus Nijhoff, 1985. Reprinted with permission.
6. Koch, C. C. "Stalling Pressure Rise Capability of Axial Flow Compressor Stages," *Trans. ASME J. Eng. for Power* 103 (1981): 645–646.
7. Sovran, G., and E. D. Klomp. "Experimentally Determined Optimum Geometries for Rectilinear Diffusers with Rectangular, Conical, or Annular Cross-Section," in *Fluid Mechanics of Internal Flow*. Amsterdam: Elsevier, 1967.

8. Johnsen, I. A., and R. O. Bullock (Eds.). "Aerodynamic Design of Axial Flow Compressors," Report SP-36, NASA, Washington, D.C., 1965.
9. Mellor, G. L. "The 65 Series Cascade Data" (unpublished) Gas Turbine Laboratory, M.I.T., Cambridge, Mass., 1958.
10. _____. "The Aerodynamic Performance of Axial Compressor Cascades with Application to Machine Design," Report no. 38, Gas Turbine Laboratory, M.I.T., Cambridge, Mass., 1957.
11. Lieblein, S., F. C. Schwenck, and R. L. Broderick. "Diffusion Losses and Limiting Blade Loadings in Axial Flow Compressor Blade Elements," NACA RM E53 D01, 1953.
12. Serovy, G. P. "Axial Flow Compressor Aerodynamics," in G. C. Oates, ed., in *Aerothermodynamics of Aircraft Engine Components*, AIAA Education Series. New York: AIAA, 1985.
13. Koch, C. C., and L. H. Smith, Jr. "Loss Sources and Magnitudes in Axial-Flow Compressors," *ASME J. Eng. for Power* 98 (1976): 411-424.
14. Cumpsty, N. A. "Annulus Wall Boundary Layer Measurement in a Four-Stage Compressor," *Trans. ASME J. Eng. for Gas Turbines and Power* 188 (1986): 3-6.
15. Denton, J. D., and N. A. Cumpsty. "Losses in Turbomachines," *Proc. I. Mech. E. Int. Conf. on Turbomachinery-Efficiency Prediction and Improvement*, Robinson College, Cambridge, Sept. 1-3, 1987, pp. 1-14.
16. Wennerstrom, A. J., and S. L. Puterbaugh. "A Three-Dimensional Model for the Prediction of Shock Losses in Compressor Blade Rows," *Trans. ASME J. Eng. for Gas Turbines and Power* 106 (1984): 295-299.
17. Senoo, Y., and M. Ishida. "Pressure Loss Due to the Tip Clearance of Impeller Blades in Centrifugal and Axial Blowers," *Trans. ASME J. Eng. for Gas Turbines and Power* 108 (1986): 32-37.
18. Horlock, J. H. *Axial Flow Compressors*. Reprint ed. with suppl. Huntingdon, N.Y.: Krieger, 1973.
19. Denton, J. D. "Solution of the Euler Equations for Turbomachinery Flows," pts. 1 and 2, in A. S. Ucer, P. Stow, and C. Hirsch, eds. *Thermodynamics and Fluid Mechanics of Turbomachinery*. Dordrecht: Martinus Nijhoff, 1985.
20. Giffen, R. G. "General Electric Co. Experimental Quiet Engine Program: Performance of Fan C," NASA CR 120981 (NTIS N73-11799), Aug. 1972.
21. Miller, D. P., and A. C. Bryans. "The Relative Merits of Inviscid Euler 3D and Quasi-3D Analysis for Design of Transonic Rotors," ASME Paper no. 88-GT-69, presented at Gas Turbine and Aero Engine Congress, Amsterdam, June 6-9, 1988.



C H A P T E R

8

AXIAL TURBINES

8.1 INTRODUCTION

Turbines, like compressors, can be classified into radial, axial, and mixed-flow machines. In the axial machine the fluid moves essentially in the axial direction through the rotor. In the radial type the fluid motion is mostly radial. The mixed-flow machine is characterized by a combination of axial and radial motion of the fluid relative to the rotor. The choice of turbine type depends on the application, though it is not always clear that any one type is superior.

Comparing axial and radial turbines of the same overall diameter, we may say that the axial machine, just as in the case of compressors, is capable of handling considerably greater mass flow. On the other hand, for small mass flows the radial machine can be made more efficient than the axial one. The radial turbine is capable of a higher pressure ratio per stage than the axial one. However, multi-staging is very much easier to arrange with the axial turbine, so that large overall pressure ratios are not difficult to obtain with axial turbines.

In order to minimize the turbojet engine nacelle drag and the engine weight per unit thrust, the mass flow per unit cross-sectional area must be as large as possible. The limiting mass flow of turbojet engines depends mainly on the maximum permissible Mach number of the flow entering the compressor. It is generally large enough to require the mass flow capability of an axial turbine, even with engines that have centrifugal (radial flow) compressors. Thus the following study concerns axial turbines only.

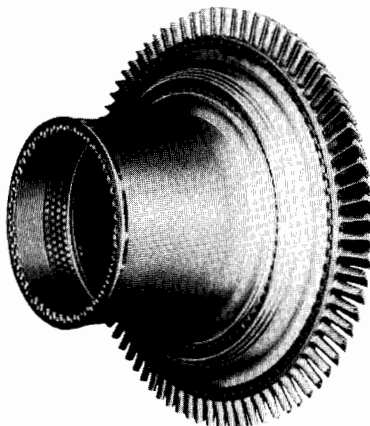


FIGURE 8.1 High-pressure turbine rotor for the CFM56 engine. (Courtesy GE Aircraft Engines.)

Generally the efficiency of a well-designed turbine is higher than the efficiency of a compressor. Moreover, the design process is somewhat simpler. The principal reason for this fact is that the fluid undergoes a pressure *drop* in the turbine and a pressure *rise* in the compressor. The pressure drop in the turbine is sufficient to keep the boundary layer fluid generally well behaved, and separation problems that are often serious in compressors can be relatively easily avoided. Offsetting this advantage is the much more critical stress problem, since turbine rotors must operate in very high temperature gas. Actual blade shape is often more dependent on stress and cooling considerations than on aerodynamic considerations, beyond the satisfaction of the velocity-triangle requirements.

Because of the generally falling pressure in turbine flow passages, much more turning in a given blade row is possible without danger of flow separation than in an axial compressor blade row. This means much more work, and considerably higher pressure ratio, per stage.

In recent years advances have been made in turbine blade cooling and in the metallurgy of turbine blade materials. This means that turbines are able to operate successfully at increasingly high inlet gas temperatures and that substantial improvements are being made in turbine engine thrust, weight, and fuel consumption.

By way of illustration, Fig. 8.1 presents the high-pressure turbine rotor for the CFM56 engine[†] (shown in Fig. 5.24). Figure 8.2 is a photograph of the blades showing the "fir tree" root geometry and the holes in the blade surface from which cooling air emerges to shield the blade from the high-temperature gas. Small tip clearances are needed for high turbine efficiency. Note that there is a recessed region at the tip of the blade; an accidental "rub" of the blade tip on the turbine casing is not nearly as serious with a recessed tip as with a blade that has a full cross section at the tip diameter. Figure 8.1 shows that the hub-tip ratio for

[†] Produced by CFM International, a joint company of GE Aircraft Engines and Société Nationale d'Etude et de construction de Moteurs d'Aviation.

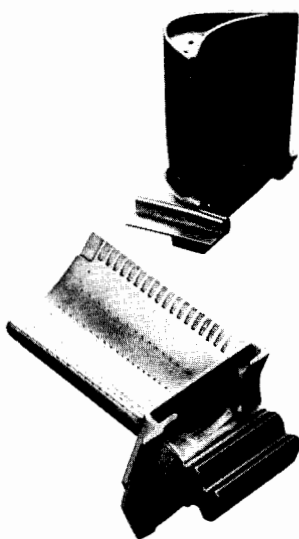


FIGURE 8.2 High-pressure turbine rotor blades for the CFM56 engine. (Courtesy GE Aircraft Engines.)

this turbine is quite high. Thus very little blade twist is required for the blade to match the radial variations in gas velocity and wheel speed. Low-pressure turbines (handling low-density gas) will typically have a much lower hub-tip ratio and a larger blade twist.

Figure 8.3 shows the stator or “nozzle” blades that feed swirling high-velocity gas to the turbine rotor. These too are cooled by a flow of high-pressure air from the compressor that passes through each stator blade, exhausting through a pat-

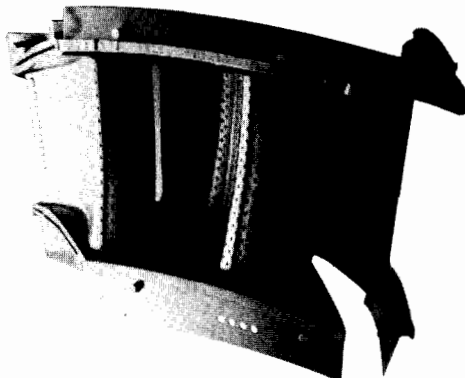


FIGURE 8.3 High-pressure turbine stator blades for the CFM56 engine. (Courtesy GE Aircraft Engines.)

tern of small holes in the blade surface. We will address the subject of film cooling of the blades later in this chapter.

8.2 THE AXIAL TURBINE STAGE

An axial turbine stage consists of a row of stationary blades, called nozzles or stators, followed by the rotor, as Fig. 8.4 illustrates. Because of the large pressure drop per stage, the nozzle and rotor blades may be of increasing length, as shown, to accommodate the rapidly expanding gases, while holding the axial velocity to something like a uniform value through the stage.

A section through the mean radius would appear as in Fig. 8.5. One can see that the nozzles accelerate the flow, imparting an increased tangential velocity component. The velocity diagram of the turbine differs from that of the compressor in that the change in tangential velocity in the rotor, Δc_θ , is in the direction opposite to the blade speed U . The reaction to this change in the tangential momentum of the fluid is a torque on the rotor in the direction of motion. Hence the fluid does work on the rotor. Again applying the angular momentum relationship as in Eq. (7.8), we may show that the power output is

$$\mathcal{P} = \dot{m}(U_2 c_{\theta 2} - U_3 c_{\theta 3}). \quad (8.1)$$

In an axial turbine, $U_2 \approx U_3 = U$. The turbine work per unit mass is

$$W_T = U(c_{\theta 2} - c_{\theta 3}) \quad \text{or} \quad W_T = c_p(T_{01} - T_{03}).$$

Defining

$$\Delta T_0 = T_{01} - T_{03} = T_{02} - T_{03},$$

we find that the stage work ratio is

$$\frac{\Delta T_0}{T_{01}} = \frac{U(c_{\theta 2} - c_{\theta 3})}{c_p T_{01}}. \quad (8.2)$$

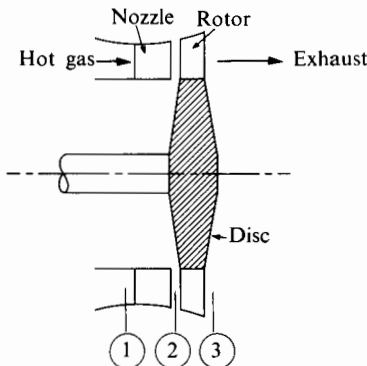


FIGURE 8.4 An axial turbine stage.

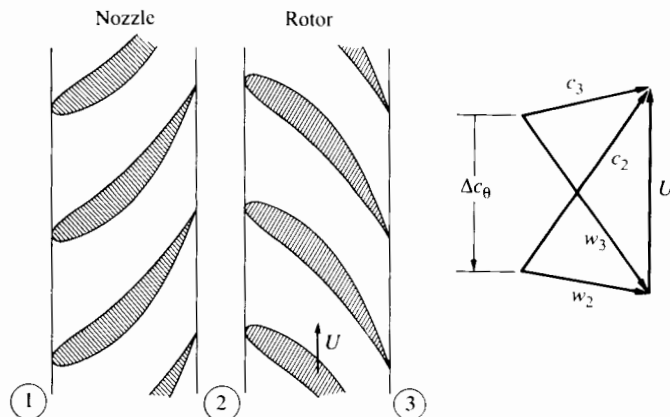


FIGURE 8.5 Turbine blading and velocity triangles.

In considering the possibility of maximizing the turbine work per stage, we can see that the work may be limited in one of two ways: (1) The available pressure ratio (and thus $\Delta T_0/T_{01}$) may be limited. In this case the maximum work will be directly proportional to T_{01} . (2) The available pressure ratio may be sufficiently high that the work will be limited by the allowable blade speed U and the allowable turning Δc_θ of the fluid. Blade speed is limited by the allowable rotational stresses at the operating temperature, while Δc_θ must be limited to maintain high efficiency. The allowable turning in a turbine stage is much higher than in a compressor stage, but the turning must not be too large if the turbine is to be highly efficient.

Boundary layers in turbines tend to be well behaved because of the generally falling pressure gradient. Figure 8.6 indicates that the greater the acceleration—that is, the larger the pressure drop—in a given blade row, the smaller the losses. If, perhaps during off-design operation, a part of the flow passage were loaded with decelerating flow, losses could rise considerably.

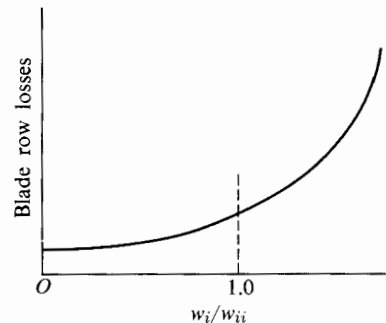


FIGURE 8.6 Turbine blade row losses.

Even though the pressure may be generally falling within a blade passage, locally (on the suction surface of the blade) there could be a zone of adverse gradient, depending on the turning and on the spacing of the blades. Thus boundary layers could grow rapidly or even separate in such a region, with adverse effect on turbine efficiency.

Instead of using the temperature-drop ratio given by Eq. (8.2), turbine designers generally refer to the turbine work ratio that is defined by

$$\frac{W_T}{U^2} = \frac{\Delta h_0}{U^2} = \frac{c_{\theta 2} - c_{\theta 3}}{U}. \quad (8.3)$$

The boundary layer limitation on compressor blading points to the desirability of approximately equal pressure change per blade row. Turbine blade row performance is not nearly so sensitive to the condition of the boundary layer (as long as the pressure is not rising through the passage). Thus the turbine designer has considerably more freedom to distribute the total stage pressure drop between rotor and stator.

Stage Dynamics and Degree of Reaction

Turbine stages in which the entire pressure drop occurs in the nozzle are called *impulse stages*. Stages in which a portion of the pressure drop occurs in the nozzle and the rest in the rotor are called *reaction stages*.

The degree of reaction may be defined for a turbine as the fraction of overall enthalpy drop occurring in the rotor. If in the rotor the enthalpy is constant, the pressure would ideally be constant also. An impulse turbine would therefore be a zero reaction machine. In a 50% reaction machine, the enthalpy drop in the rotor would be half of the total for the stage.

An impulse turbine stage is shown in Fig. 8.7, along with a typical diagram for the common case of constant axial velocity. Since no enthalpy change occurs within the rotor, the energy equation within the rotor requires that $|w_2| = |w_3|$. If the axial velocity component is held constant, then this requirement is satisfied by

$$\beta_3 = -\beta_2.$$

The effect of nozzle outlet angle on impulse turbine work can be seen by transforming Eq. (8.3) as follows: From the velocity diagram we can see that

$$w_{\theta 3} = -w_{\theta 2}$$

and that

$$c_{\theta 2} - c_{\theta 3} = 2w_{\theta 2} = 2(c_{\theta 2} - U),$$

so that

$$c_{\theta 2} - c_{\theta 3} = 2U \left(\frac{c_z}{U} \tan \alpha_2 - 1 \right).$$

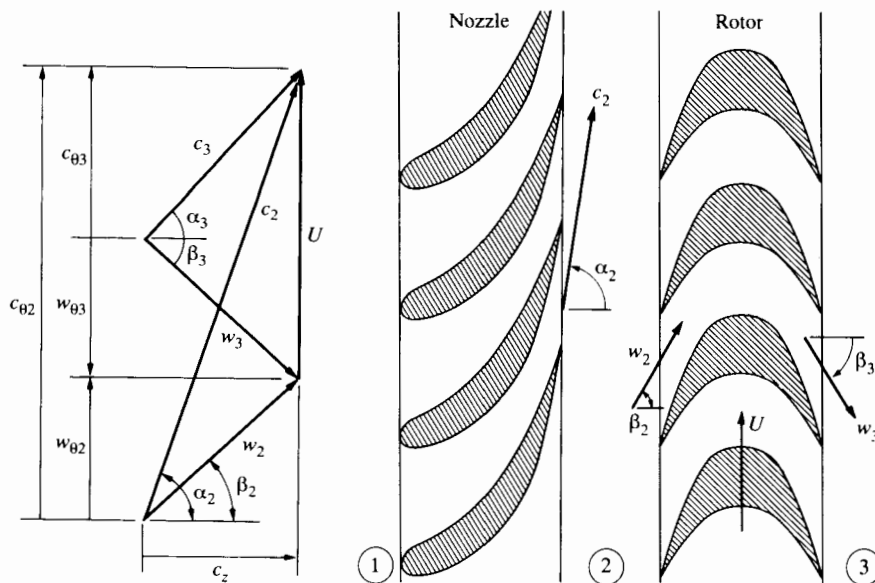


FIGURE 8.7 Impulse turbine stage and constant axial velocity.

Thus we can write Eq. (8.3) as

$$\frac{\Delta h_0}{U^2} = 2 \left(\frac{c_z}{U} \tan \alpha_2 - 1 \right). \quad (8.4)$$

It is evident, then, that for large power output the nozzle angle should be as large as possible. Two difficulties are associated with very large α_2 . For reasonable axial velocities (i.e., reasonable flow per unit frontal area), it is evident that large α_2 creates very large absolute and relative velocities throughout the stage. High losses are associated with such velocities, especially if the relative velocity w_2 is supersonic. In practice, losses seem to be minimized for values of α_2 around 70°. In addition, one can see that for large α_2 [$\tan \alpha_2 > (2U/c_z)$], the absolute exhaust velocity will have a swirl in the direction opposite to U . While we have not introduced the definition of turbine efficiency as yet, it is clear that, in a turbojet engine where large *axial* exhaust velocity is desired, the kinetic energy associated with the tangential motion of the exhaust gases is essentially a loss. Furthermore, application of the angular momentum equation over the entire engine indicates that exhaust swirl is associated with an (undesirable) net torque acting on the aircraft. Thus the desire is for axial or near-axial absolute exhaust velocity (at least for the last stage if a multistage turbine is used). For the special case of constant c_z and axial exhaust velocity, $c_{03} = 0$ and $c_{02} = 2U$. So Eq. (8.2) becomes

$$\frac{\Delta h_0}{U^2} = 2. \quad (8.5)$$

For a given power and rotor speed, and for a given peak temperature, Eq. (8.4) is sufficient to determine approximately the mean blade speed (and hence radius) of a single-stage impulse turbine having axial outlet velocity. If, as is usually the case, the blade speed is too high (for stress limitations), or if the mean diameter is too large relative to the other engine components, it is necessary to employ a multistage turbine in which each stage does part of the work.

If the ratio of blade length to mean radius is small, this mean-radius analysis is sufficient for the entire blade length. If the blade is relatively long, however, one should consider radial variations; and we will see that impulse design at the mean radius may lead to difficulty at the hub. We saw previously that the 50% reaction compressor stage (with constant c_z) has symmetrical velocity triangles. The same is true for the 50% reaction turbine stage. Since the changes in static enthalpy are the same in both blade rows, the change in kinetic energy relative to each blade row must be the same. Thus for constant axial velocity, the velocity triangles are as shown in Fig. 8.8. Since the diagram is symmetrical,

$$c_{\theta 3} = -(c_z \tan \alpha_2 - U)$$

for constant axial velocity. Therefore Eq. (8.2) for this case becomes

$$\frac{\Delta h_0}{U^2} = \left(2 \frac{c_z}{U} \tan \alpha_2 - 1 \right). \quad (8.6)$$

Again the desirability of large α_2 is indicated and the same limitations are encountered, so that typical values of α_2 are near 70°. For the special case of axial

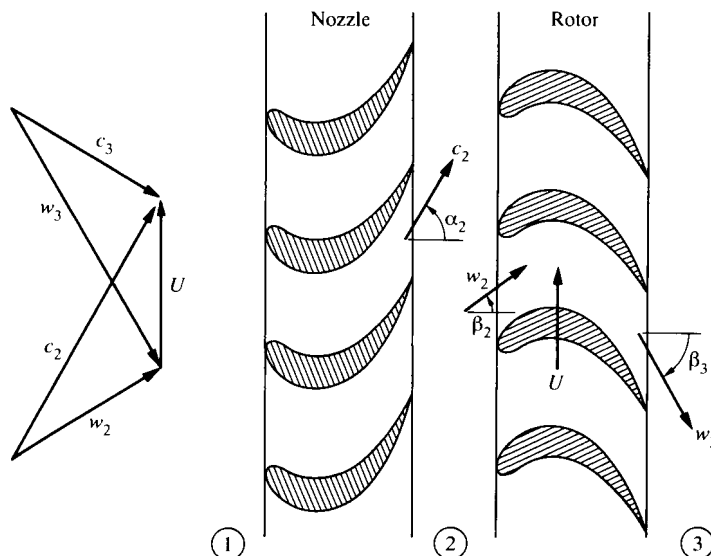


FIGURE 8.8 Fifty-percent reaction blading and constant axial velocity.

outlet velocity and constant c_z , α_3 and β_2 are zero and the velocity diagram becomes a rectangle. The stage work output is then

$$\frac{\Delta h_0}{U^2} = 1. \quad (8.7)$$

Thus, for the same blade speed and for axial outlet velocities, the impulse stage work is twice that of the 50% reaction stage. We can expect the impulse stage to have somewhat greater loss, however, since the average fluid velocity in the stage is higher and since the boundary layer on the suction side of the rotor blades may be significantly thicker and closer to separation, depending on the turning angle and blade spacing.

The 50% reaction stage is not uniquely desirable, of course. One can use any degree of reaction (greater than zero) to design a turbine of acceptable performance. As we will see, the mean-radius velocity triangles may be largely dependent on radial variations and problems encountered near the hub.

For the special case of axial turbines designed for a given stator exit flow angle, and for zero exit swirl, the stage work ratio, defined as $W_T/U^2 = \Delta h_0/U^2$, and the degree of reaction R , depend on flow coefficient, as shown in Fig. 8.9. Here, for zero exit swirl,

$$W_T = \Delta h_0 = U c_{\theta 2} = U c_z \tan \alpha_2,$$

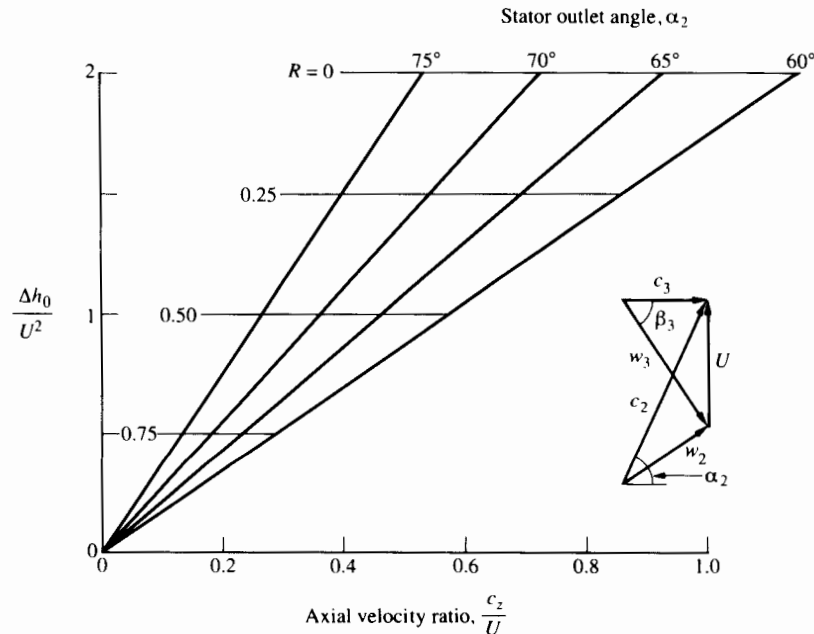


FIGURE 8.9 Work ratio $\Delta h_0/U^2$ and degree of reaction R of axial turbine stages designed for zero exit swirl.

so

$$\frac{\Delta h_0}{U^2} = \frac{c_z}{U} \tan \alpha_2. \quad (8.8)$$

We can define the degree of reaction for axial turbines (with reference to Fig. 8.5) as

$$R = \frac{h_2 - h_3}{h_{01} - h_{03}}. \quad (8.9)$$

Since, in a coordinate system fixed to the rotor, the apparent stagnation enthalpy is constant,

$$h_2 - h_3 = \frac{w_3^2}{2} - \frac{w_2^2}{2}.$$

If the axial velocity is the same upstream and downstream of the rotor, this becomes

$$h_2 - h_3 = \frac{1}{2}(w_{\theta 3}^2 - w_{\theta 2}^2) = \frac{1}{2}(w_{\theta 3} - w_{\theta 2})(w_{\theta 3} + w_{\theta 2}).$$

Also, since $h_{01} - h_{03} = U(c_{\theta 2} - c_{\theta 3})$, we can write the degree of reaction as

$$R = \frac{(w_{\theta 3} - w_{\theta 2})(w_{\theta 3} + w_{\theta 2})}{2U(c_{\theta 2} - c_{\theta 3})}.$$

But since $w_{\theta 3} - w_{\theta 2} = c_{\theta 3} - c_{\theta 2}$, we find

$$R = -\frac{w_{\theta 3} + w_{\theta 2}}{2U}.$$

For constant axial velocity we can write

$$w_{\theta 3} = c_z \tan \beta_3$$

and

$$w_{\theta 2} = c_z \tan \alpha_2 - U,$$

so that

$$R = \frac{1}{2} \left[1 - \frac{c_z}{U} (\tan \alpha_2 + \tan \beta_3) \right]. \quad (8.10)$$

Equation (8.10) is a general result. For the special case of symmetrical triangles ($\alpha_2 = -\beta_3$), we have $R = 1/2$. For the case $w_{\theta 3} = -w_{\theta 2}$ we have $R = 0$. For the special case $c_{\theta 3} = 0$ it follows that $w_{\theta 3} = c_z \tan \beta_3 = -U$, so that the degree of reaction becomes

$$R = 1 - \frac{1}{2} \left(\frac{c_z}{U} \right) \tan \alpha_2. \quad (8.11)$$

Equations (8.8) and (8.11) have been used in plotting Fig. 8.9, which pertains to design conditions only. Here we see that for a given stator outlet angle, the im-

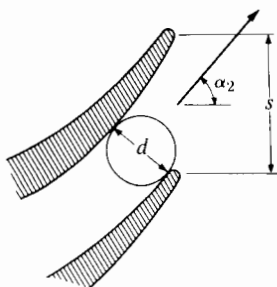


FIGURE 8.10 Flow at nozzle exit.

pulse stage requires a much higher axial velocity ratio than does the 50% reaction stage. In the impulse stage all flow velocities are higher, and that is one reason why its efficiency is lower than that of the 50% reaction stage.

Deviation

The flow at the exit of a turbine rotor or nozzle blade, just as is the case in compressors, does not leave at exactly the blade exit angle. However, the generally well-behaved flow in a turbine blade row, unlike compressor behavior, is more amenable to simple correlations.

Figure 8.10 shows the conditions between two turbine blades. It has been found by experience that the actual exit flow angle at the design pressure ratio of the machine is fairly well approximated by $\alpha_2 = \cos^{-1}(d/s)$, so long as the nozzle is not choked. If the nozzle is choked, then a supersonic expansion may take place at the blade exit and alter the flow direction, providing the exit pressure is sufficiently low.

Figure 8.11 shows a schlieren photograph of such an expansion for a two-dimensional flow through a cascade of blades representing a rotor with 130° of turning and an isentropic outlet Mach number of 1.15. The blade-chord Reynolds number is 7×10^5 . For cooling and structural integrity the blade thickness at each “trailing edge” has finite thickness. An oblique shock leaving the trailing edge on the pressure side of the blade intersects with the boundary layer on the suction surface of the opposite blade. The shock-boundary layer interaction and reflected shock are both visible in Fig. 8.11; so is the thickness of the blade wake region.

8.3 STAGE EFFICIENCY

As the preceding implies, aerodynamic losses in the turbine differ with the stage configuration, that is, the degree of reaction. Improved efficiency is associated with higher reaction, which tends to mean less work per stage and thus a larger number of stages for a given overall pressure ratio.

The understanding of aerodynamic losses is important to design, not only in the choice of blading type (impulse or reaction) but also in devising ways to



FIGURE 8.11 Schlieren visualization of flow through a linear cascade of high-pressure transonic turbine rotor blades (130° turning). A three-color filter was aligned with the suction surface to show details of the shock-laminar boundary layer interaction. The characteristic "tramline" shocks separated by an expansion are clearly visible. Transition occurs on reattachment of the separation bubble. The isentropic outlet Mach number is 1.15, and the Reynolds number is 7×10^5 (based on chord). (Photo by J. J. Camus, Whittle Laboratory, Cambridge, from a research program sponsored by Rolls-Royce.)

control these losses, for example, methods to control the clearance between the tip of the turbine blade and the outer casing wall. The choices of blade shape, aspect ratio, spacing, Reynolds number, Mach number, and flow incidence angle can all affect the losses and hence the efficiency of turbine stages. To describe the actual process of expansion in a turbine, and thus be able to relate work output to fluid pressure, it is convenient to define an ideal expansion that is reversible and to relate the actual expansion to the ideal through an empirical efficiency. The actual turbine work is expressed in Eq. (8.2) as the drop in stagnation enthalpy $\Delta h_0 = c_p \Delta T_0$. Since even high-temperature turbines are essentially adiabatic devices, the ideal turbine would be an isentropic one. The relationships we will define between actual and ideal processes are shown in the $T-s$ diagram of Fig. 8.12.

Efficiency Definitions

Two turbine efficiencies are in common usage; the choice between them depends on the application for which the turbine is used. For many conventional turbine applications, useful turbine output is in the form of shaft power and ex-

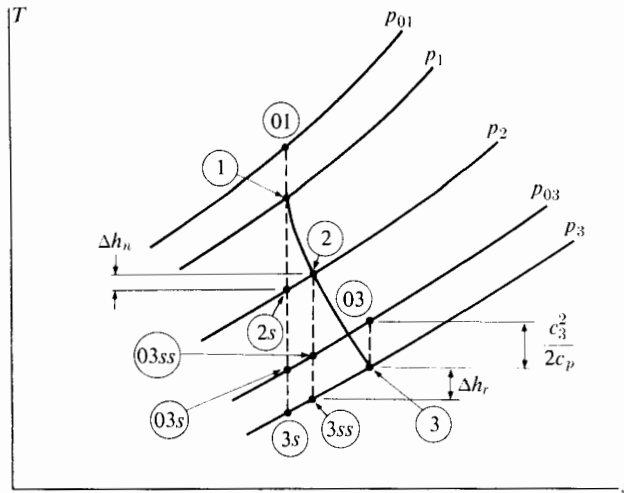


FIGURE 8.12 Expansion in a turbine.

haust kinetic energy, $c_3^2/2$, is considered a loss. In this case the ideal turbine would be an isentropic machine with no exhaust kinetic energy, and

$$W_{T,\text{ideal}} = c_p(T_{01} - T_{3s}).$$

If the actual turbine work is compared with this ideal work, the efficiency is called *total-to-static turbine efficiency*, since the ideal work is based on total (or stagnation) inlet conditions and static exit pressure.

The total-to-static turbine efficiency η_{ts} is defined by

$$\eta_{ts} = \frac{T_{01} - T_{03}}{T_{01} - T_{3s}},$$

or

$$\eta_{ts} = \frac{T_{01} - T_{03}}{T_{01}[1 - (p_3/p_{01})^{(\gamma-1)/\gamma}]} = \frac{1 - (T_{03}/T_{01})}{1 - (p_3/p_{01})^{(\gamma-1)/\gamma}}. \quad (8.12)$$

In some applications, particularly turbojets, the exhaust kinetic energy is not considered a loss since the exhaust gases are intended to emerge at high velocity. The ideal work in this case is then $c_p(T_{01} - T_{03s})$ rather than $c_p(T_{01} - T_{3s})$. This requires a different definition of efficiency, the *total-to-total turbine efficiency* η_{tt} , defined by

$$\eta_{tt} = \frac{T_{01} - T_{03}}{T_{01} - T_{03s}} = \frac{1 - (T_{03}/T_{01})}{1 - (p_{03}/p_{01})^{(\gamma-1)/\gamma}}. \quad (8.13)$$

It is this latter efficiency that is of most interest for turbojet turbines. We may compare the two by making the approximation (see Fig. 8.12) that

$$T_{03s} - T_{3s} \approx T_{03} - T_3 = c_3^2/2c_p,$$

and using Eqs. (8.12) and (8.13) to show that

$$\eta_{tt} = \frac{\eta_{ts}}{1 - c_3^2[2c_p(T_{01} - T_{3s})]}.$$

Thus

$$\eta_{tt} > \eta_{ts}.$$

Regardless of these definitions, the energy associated with the *tangential component* of the turbine exhaust velocity must be considered a loss, since it will not be transformed to axially directed momentum at the exit of the turbojet exhaust nozzle. These definitions also serve for multistage turbines. If the states ① and ③ correspond to inlet and outlet, respectively, we may write the actual turbine work as

$$w_t = \eta_{tt} c_p T_{01} \left[1 - \left(\frac{p_{03}}{p_{01}} \right)^{(\gamma-1)/\gamma} \right].$$

or

$$w_t = \eta_{ts} c_p T_{01} \left[1 - \left(\frac{p_3}{p_{01}} \right)^{(\gamma-1)/\gamma} \right].$$

The difficulties in predicting the efficiency of a turbine stage are comparable to those discussed for compressor stages in Chapter 7. However, it appears that experimental results for the efficiency of well-designed turbines can be correlated quite well with stage work ratio and axial velocity ratio.

In designing a turbine for high efficiency, one of the important questions is how widely spaced the turbine blades should be. Close spacing of blades means large total surface area, numerous blade surface boundary layers, and plentiful opportunity for viscous dissipation both in the boundary layers and in the "wake" mixing regions downstream of the blades. If the blades are widely spaced, the number of boundary layers and wakes is less, but the total force exerted by each blade on the flow must be large (for a given total torque). Larger blade force necessarily means larger pressure difference between suction and pressure surfaces and, in particular, more danger of adverse pressure gradient (on the suction surface between the minimum pressure point and the trailing edge). As we mentioned earlier, such an adverse gradient could lead to large boundary layer growth (even to flow separation) and larger viscous losses. These considerations indicate that there will be an optimum spacing. In the light of lengthy historical experience, turbine designers are widely agreed that this optimum can be determined by using the criterion first devised by Zweifel in the form of a blade force coefficient Z , which is defined as

$$Z = \frac{F_\theta}{(p_{0i} - p_{ii})b_z}.$$

Here F_θ is the tangential component of blade force (per unit blade height) and b_z is the width of the blade row in the axial direction; p_{0i} is the stagnation pressure

at entrance to the blade row, and p_{ii} is the static pressure at exit. If the flow were incompressible, with the same axial velocity component upstream and downstream of the blade row, we could write the force coefficient (see Problem 8.16) as:

$$Z = 2 \frac{s}{b_z} \cos^2 \beta_{ii} (\tan \beta_i - \tan \beta_{ii}). \quad (8.14)$$

Though this expression was originally derived for incompressible flow, it has been found that even with compressible flow the optimum blade spacing can be obtained from Eq. (8.14) by setting $Z = 0.8$. In these pages we are discussing the efficiency of axial turbines whose blade spacing is governed by approximately this value of Z .

The efficiency that a well-designed turbine stage may achieve depends quite strongly on the stage work and flow coefficients $\Delta h_0/U^2$ and c_z/U . Figure 8.13 shows the correlation of Kacker and Okapuu [1], a modification of the earlier work of Smith [2], who plotted the total-to-total efficiencies of some 69 turbines against design axial velocity ratio, showing a point for each design value of the work ratio. The experimental numbers were “corrected” to correspond to zero tip leakage, then the contours shown in Fig. 8.13 were drawn with the guidance of the adjusted experimental data. These provide a good general indication of what to expect for the efficiency of typical gas turbines (except for allowing for tip clearance loss).

Figure 8.13 indicates that if the stage work is kept low enough (and if tip clearance losses are kept to 1% or 2%), the axial turbine stage efficiency can be

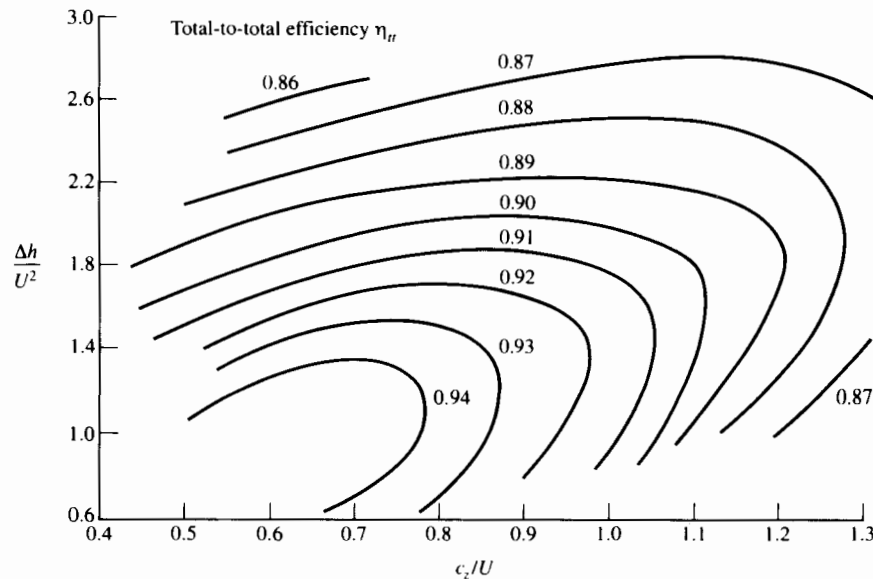


FIGURE 8.13 Turbine stage efficiency at zero tip leakage calculated by the method of Kacker and Okapuu [1].

as high as 92% or 93%. The graph shows that for maximum efficiency $\Delta h_0/U^2$ should not be much greater than 1 and that the axial velocity ratio should be around 0.6 or 0.7. If the turbine were designed for zero exit swirl, Fig. 8.9 suggests that under these conditions the degree of reaction would be of the order of 0.5 and the stator outlet angle would be considerably less than maximum (possibly less than 60°). In aircraft turbine engines the typical efficiency is appreciably less than maximum because of the need to increase stage work ratios to reduce the number of stages and the weight of the turbine. A severe test of the effect of high stage loading has been reported by Moustapha, Okapuu, and Williamson [3]. They built three turbine stages with pressure ratio 3.76, stage work parameter $\Delta h_0/U^2 = 2.47$, and axial velocity ratio at the mean radius of 0.64. The stage efficiency exceeded 80%.

Much work has been done in the past fifty years to correlate the various sources of loss on gas and steam turbines. Intensive reviews of this subject have been prepared by Horlock [4], Denton [5], Gregory-Smith [6], and Sieverding [7]. One of the most widely used methods of performance prediction is that of Ainley and Mathieson, as modified by Dunham and Came [8]. Unfortunately there are considerable disagreements among various empirical loss-correlation methods, and Sieverding concludes his survey by remarking: "The clearance flow mechanism and its effect on the total flow field are still far from being understood. Aerodynamic parameters such as blade load distribution, Mach number and coolant ejection from the blade tip, and geometric configurations such as partial shrouds and recessed casings for unshrouded blades will need attention in the future."

With this in mind we return to the Denton-Cumpsty framework [9] for discussion of entropy generation in turbomachines. For a turbine with stagnation pressure ratio p_{04}/p_{05} , we may write the total-to-total efficiency as

$$\eta_{tt} = \frac{h_{04} - h_{05}}{h_{04} - h_{05s}}$$

or, with constant specific-heat ratio,

$$\eta_{tt} = \frac{1 - \left(\frac{p_{05}}{p_{04}}\right)^{(\gamma-1)/\gamma} e^{\Delta s/c_p}}{1 - \left(\frac{p_{05}}{p_{04}}\right)^{(\gamma-1)/\gamma}}, \quad (8.15)$$

so that if we know the total entropy generation Δs per unit mass of working fluid, we can determine the adiabatic efficiency. The assumptions made for entropy generation in boundary layers are appropriate for turbines as well as for compressors, so that for turbine blades also we may estimate the entropy generation rate per unit area of turbine blade surface by using Eq. (7.36).

In general the same considerations apply (for turbines and compressors) to entropy generation in blade wakes and at end walls. But, there are at least four

qualitative differences: First, for unshrouded blades[†] the stationary casing acts more strongly to promote cross-flow in the outer end-wall boundary layer of a turbine than it does in a compressor. In the compressor the effect of the transverse (tangential) pressure gradient due to blade curvature is opposed by the tangentially directed shearing motion of the outer wall relative to the blade passage. In the turbine the passage curvature tends to be much larger than in a compressor, and its effect is reinforced by the tangential shearing motion of the casing relative to the blade passage. The combined effect will typically result in the formation of a vortex near the inner corner of the bend at the outer radius of the blade passage. Thus the use of Eq. (7.36) to estimate entropy generation in turbine end-wall boundary layers is likely to be more inaccurate for turbines than for compressors. Only a detailed knowledge of the link between shear stress and total velocity in the complex flow field comprised of three-dimensional boundary layers and vortex motion would allow us to evaluate \dot{S} with confidence.

A second qualitative distinction is in the relative importance of entropy generation associated with trailing-edge thickness. To keep the trailing edge of a gas turbine blade sufficiently cool to support high centrifugal stress, its thickness is typically much larger than for compressor blades. This thickness has considerable effect on the flow pattern, as Fig. 8.11 would suggest, and the wake region behind the trailing edge is an important source of loss, especially when the Mach number of the flow is high. Denton and Cumpsty [9] conclude that accurate prediction of entropy generation due to trailing-edge thickness of turbine blades will have to await further development of methods for calculating compressible viscous flows.

A third qualitative difference between compressor and turbine blades is that high-performance turbine blades are typically film cooled. There is additional entropy generation due to mixing of cooling air with the high-temperature stream of combustion products.

A fourth difference between turbine and compressor flows is that while in the former the boundary layer must be kept turbulent to prevent flow separation, there is a tendency in turbine flow passages for boundary layers—for example, on the end walls—to revert from turbulent to laminar. The Moses method (Chapter 4) of estimating turbulent boundary development shows that if the free-stream pressure falls rapidly, the boundary layer momentum thickness Reynolds number R_θ can decrease in the flow direction. In a turbine passage this decrease in Reynolds number may not be large enough for the boundary layer to revert fully to a laminar state; yet it is typically less than fully turbulent. This tends to cast further doubt on the use of Eq. (7.36) for entropy generation in turbine boundary layers. A corresponding expression [9] exists for entropy generation in laminar boundary layers, but the typical turbine boundary layer may be in between “fully turbulent” and “fully laminar.”

In contrast to these extra complications for estimating entropy generation in turbine stages, there is the somewhat simplifying factor that in aircraft gas tur-

[†] Blades whose tip-radius cross sections are not connected by a circular band or “shroud.”

bines (as we will see in Section 8.6) the turbine tends to operate near its design point most of the time. Also the effect of a small departure from design point operation may have less effect on entropy generation than in a compressor.

8.4 ROTOR BLADE AND DISC STRESSES

Typically the turbine blades for high-performance gas turbines are designed to avoid creep of the material during extended high-temperature operation. The allowable stress level will depend strongly on the operating temperature and may be specified as that stress which will not exceed a creep extension of, for example, 1% for 100,000 hours of operation at the temperature in question. Since 100,000 hours (11.4 years) is a long period for testing a material, it is common to see materials compared on the results of measurements of stress to cause rupture after 100 hours. Figure 8.14 from Immarigeon [10] is one such comparison. Other data have been provided by Glenny, Northwood, and Burwood-Smith [11]. We will see that for turbine blade or disc stress calculations, it is always the ratio of stress to density (the so-called strength-to-weight ratio) that is important. Hence the y-axis of Fig. 8.14 is the blade strength σ (in kPa) divided by the material density ρ (in kg/m³). Taking the density of nickel alloys to be around 8000 kg/m³ and the working temperature to be 1000°C, one sees that the σ/ρ ratio is about 20 at

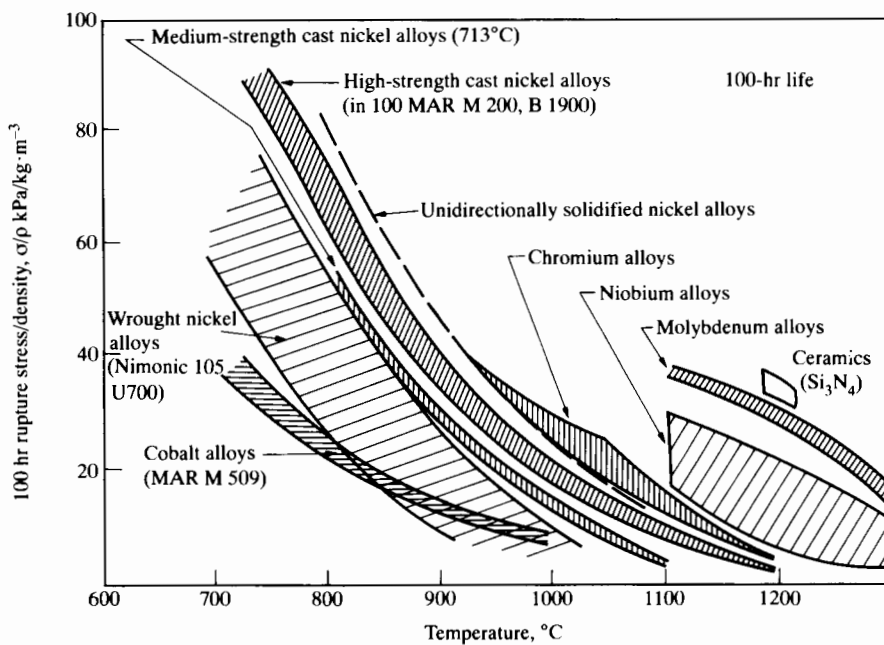


FIGURE 8.14 Variations in specific rupture strength (100 hr) with service temperature for various classes of heat-resistant materials. (Courtesy Immarigeon [10].)

most. This would imply a rupture stress of $20 \times 8000 = 160,000$ kPa, or about $23,000 \text{ lb}_f/\text{in}^2$. With a safety factor of 2, the allowable working stress would only be 80 MPa, or less than $12,000 \text{ lb}_f/\text{in}^2$. The rapid decline in strength with temperature shows the importance of the measures that have been taken in recent years to use compressor exit air to cool high-temperature blading and thus to allow gas inlet temperatures as high as 1300° to 1400°C .

Figure 8.14 shows the superior strength-temperature characteristics of ceramics. Work has been done to cast single-piece bladed turbine discs; they are cast in one piece because there is as yet no general solution to the problem of joining ceramics. Though these materials are very strong, they tend to be brittle and unreliable owing to the effect of small inclusions that severely reduce strength. There is the prospect that ceramic composites, possibly including very high strength tin whiskers, may provide a solution to the problem of how to obtain high strength along with high reliability. However, this has yet to be proved in engine practice. Alloys of chromium have limited ductility and are said to be prone to nitrogen embrittlement. Alloys of niobium and molybdenum have insufficient oxidation resistance, and they too are not used commercially in gas turbines. Cobalt-based alloys can be stronger than nickel alloys above 1050°C . They are typically more oxidation and sulfidation resistant than nickel alloys and are commonly used for turbine stator blades (nozzle vanes). The nickel-based alloys are used for highly stressed components, such as turbine blades and discs.

Grain boundaries in turbine blades tend to be the sources of weakness in materials operated at sufficiently high stress and temperature that creep is the design limitation. One way to raise turbine blade strength is to use the technique of "directional solidification," in which the blades are cast in such a way that the solid-liquid interface advances in the stress direction of the blade, allowing columnar crystals to form, aligned in that direction. Directionally solidified blades may be capable of operating at, say, 100°C , a higher temperature than with conventionally cast materials. The next step that has been taken is to cast turbine blades as single crystals, and this confers the possibility of even higher temperature operation.

Three types of stress may be of importance in various turbomachine elements: centrifugal, bending, and thermal. Centrifugal stresses are important both in blades and in the discs that support them. Bending stresses arise in the blades from the aerodynamic forces acting on them, both steady and unsteady. Thermal stresses can arise because of substantial temperature gradients within the blade that may be caused by high-intensity internal cooling.

For a given hub-tip ratio, centrifugal stress at the blade root depends primarily on blade alloy density, hub-tip radius ratio, and blade-tip speed. It is increased by blade twist, which sets up bending stress due to centrifugal loading; it can be reduced somewhat by tapering the blade cross section. Centrifugal stress is always of great concern to the designer of high-performance gas turbines. The centripetal acceleration of the center of mass of a typical turbine blade is in the range of 10,000 g to 100,000 g, so that it is not difficult to appreciate the importance of centrifugal stress in a blade whose creep strength may be greatly reduced by operation at high temperature.

Blade-root stress can also be significantly affected by the force on the blade due to the change in tangential momentum of the gas passing through the turbine rotor. As one can show by control volume analysis of the forces applied by the fluid to a turbine blade, the axial component of force is essentially equal to the difference in pressure (upstream vs. downstream of the blade row) multiplied by the annulus area and divided by the number of blades. The tangential aerodynamic force on the blade is well estimated by multiplying the total mass flow rate by the change in tangential velocity component across the blade row and, again, dividing by the number of blades. The result of such analysis shows that the gas deflection force is typically two orders of magnitude smaller than the total centrifugal force on the blade. Nevertheless, because it is applied perpendicularly to the blade rather than along its axis, it could (if the blade were sufficiently slender) set up bending stresses at the root that would be of the same order of magnitude as the centrifugal stress. The maximum bending stress will be proportional to the applied moment around the principal bending axis at the root cross section, divided by the section modulus. With this in mind one can show that for a blade of given shape (i.e., given turning angle and given thickness-to-chord ratio), the bending stress will be inversely proportional to the cube of the blade chord. Since by doubling the chord the designer can reduce bending stress by one order of magnitude, it is usually possible to maintain bending stresses at levels much smaller than centrifugal ones.

(Allowing the center of mass axis of the blade to lean slightly away from the radial direction could cause a cancellation of the root-bending stress at a given flow rate and shaft speed; the problem with this measure for an aircraft gas turbine is that at altitude the engine mass flow rate would be very much reduced, while the engine speed and turbine inlet temperature would still be high.)

The assumption implied in the foregoing is that the flow past each turbine blade is steady. As each blade passes through the wake shed by the blades of the preceding blade row, it experiences a small aerodynamic force fluctuation that could be serious if one of the critical vibration frequencies of the blade were to coincide with this wake-passing frequency. At such a resonance, destructive strain amplitudes can develop (depending on the damping available), even if the force amplitude is small. This is more likely to be a danger for slender compressor blades than for turbine blades of much sturdier cross section. It is especially serious during rotating stall (Chapter 7). Here, typically oscillating aerodynamic forces, distributed over a band of frequencies, can quickly lead to compressor blades passing through large stall zones such as may occur in surge or fatigue failure, and probably to destruction of the compressor. For turbine blades, however, stresses due to aerodynamic forces are typically much less important than stresses due to centrifugal loads.

The same is not necessarily true of thermal stresses. If blade temperature is nonuniform (as it may well be, if exposed to a gas 400° to 500°C hotter than the blade and subject to intense inner cooling through a distribution of air passages), it can suffer fairly large thermal stresses. It can be shown that at a point on the blade cross section where there is a temperature difference ΔT above or below the

mean temperature for the cross section, the local thermal stress will be about $E\alpha\Delta T$, where E is the bulk modulus for the blade material (about 2×10^5 MPa), and α is the thermal expansion coefficient (about $7 \times 10^{-6}/^\circ\text{C}$). This means that if ΔT were 50°C , the local thermal stress could be 70 MPa, or about 10,500 lb./in.², a substantial addition to the total stress. From this, one sees the importance of maintaining blade temperature uniformity. Allen [12] shows how serious thermal stresses can be in turbine blades with small internal cooling passages.

To estimate the centrifugal stresses on blades and discs, one might use Fig. 8.15 to represent one of the turbine rotors shown in, for example, the engine of Figs. 5.25 and 5.26. Taking first a cylinder of radius r that slices through the blades where their local cross sections are A_b , and defining the cross-sectional average radial stress as σ_r , we can write (for a thin section of blade dr thick in the radial direction):

$$d(\sigma_r A_b) = -(\rho_b A_b dr)\Omega^2 r, \quad (8.16)$$

in which Ω is the speed of rotation and ρ_b is the blade density. If A_b is independent of r , the equation becomes

$$\frac{d\sigma_r}{dr} = -\rho_b \Omega^2 r,$$

which may be integrated to

$$\sigma_r = -\rho_b \frac{\Omega^2 r^2}{2} + \text{const.}$$

Since $\sigma_r = 0$ at $r = r_i$, we can evaluate the constant and find that

$$\sigma_r = \rho_b \frac{\Omega^2}{2} [r_i^2 - r^2]$$

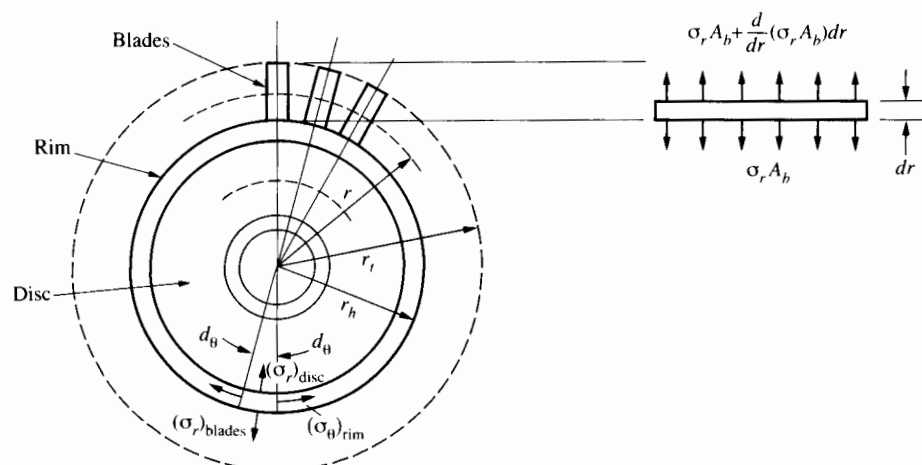


FIGURE 8.15 Turbine disc and blades.

or

$$\sigma_r = \rho_b \frac{U_t^2}{2} \left[1 - \left(\frac{r}{r_t} \right)^2 \right],$$

so that centrifugal stress at any point is proportional to U_t^2 . This can be regarded as a special case of a more general statement applicable to a rotor of any geometry that centrifugal stress will be proportional to $\rho_b U_t^2$, in which ρ_b is the material density and U_t is a characteristic (tip) speed.

The maximum centrifugal stress is located at the turbine blade hub radius ($r = r_h$) and is

$$\sigma_b = \rho_b \frac{U_t^2}{2} (1 - \zeta^2), \quad (8.17)$$

in which $\zeta = r_h/r_t$ is the hub-tip ratio. Figure 8.16 shows the maximum blade stress factor $\sigma_b/(\rho_b U_t^2)$ as a function of hub-tip ratio. In one of the problems at the end of the chapter, the effect of tapering the blade cross section so that A_b varies linearly with radius is suggested as a means of reducing σ .

We now proceed to consider the stresses in the disc that supports the blades. Bearing in mind the turbine (and compressor) disc configurations displayed in Figs. 5.25 and 5.26, we analyze, for simplicity, the disc design shown in Fig. 8.17,

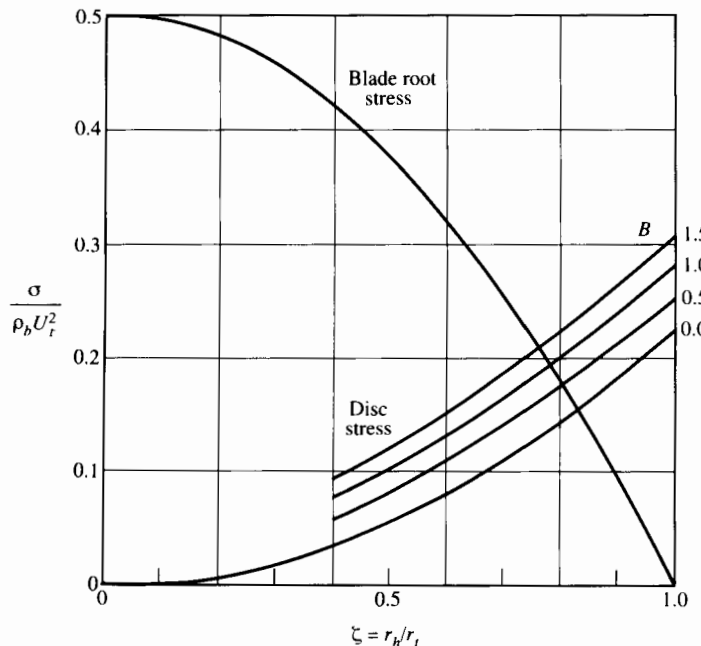


FIGURE 8.16 Centrifugal stresses with untapered blades and discs of uniform stress; $A_i/A_0 = 10$, $r_i/r_h = 0.25$.

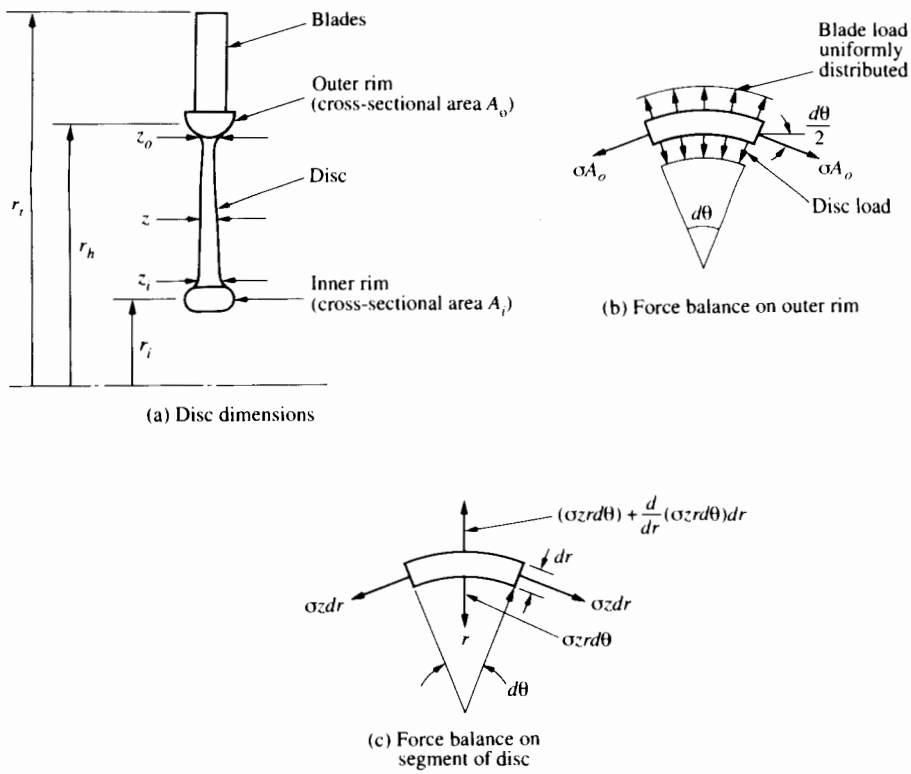


FIGURE 8.17 Disc of uniform stress with thin outer and inner rims.

which shows the upper half of a cross section of a disc consisting of two thin rims connected by a tapered disc. To make our analysis as simple as possible, we assume the following:

1. The centrifugal load applied by the blades to the rims can be considered equivalent to a radial load distributed uniformly in the circumferential direction and of the same total magnitude. (This eliminates the need to calculate circumferential variations in disc stress.)
2. The disc is tapered in such a way that its circumferential and radial stresses are everywhere equal to the same value σ .
3. The rims are thin enough that they have uniform tangential stress that, in both cases, is equal to σ . Thus the disc and both rims are “working to full capacity” with maximum allowable stress level σ throughout.
4. The discs are thin enough that we can adopt the simplified dimension scheme shown in Fig. 8.17(a). (This simplifies the algebra considerably so that we can more easily see the final results. Designers, of course, will use fairly elaborate finite-element analyses to take full account of stress concentrations, three-dimensional effects, thermal stresses, and the like. Here we

are seeking only the principal features of the effects of centrifugal loads in blades and discs.)

We begin with the force balance on the segment of the outer rim shown in Fig. 8.17(b). The radial components of forces for infinitesimal $d\theta$ are

$$2\sigma A_0 \frac{d\theta}{2} - N_b \sigma_b A_b \frac{d\theta}{2\pi} + \sigma r_h d\theta z_0 = \rho_b (A_0 r_h d\theta) r_h \Omega^2.$$

The first term is the radially inward component of the circumferential force in the rim. The second is the equivalent outward, uniformly distributed load corresponding to N_b blades for the entire circumference but here acting on only a fraction $d\theta/2\pi$ of the circumference.

The third term is the radially inward load due to the stress in the disc. The right-hand side is the mass of the rim segment multiplied by its radially inward acceleration. We assume here that the disc material density is the same as for the blades. Dividing by $A_0 d\theta \rho_b U_t^2$ and rearranging terms, we can write this equation as

$$\frac{\sigma}{\rho_b U_t^2} = \frac{\frac{N_b}{2\pi} \frac{A_b}{A_0} \frac{\sigma_b}{\rho_b U_t^2} + \zeta^2}{1 + \frac{r_h z_0}{A_0}}, \quad (8.18)$$

in which again $\zeta = r_h/r_t$, and A_b is the cross-sectional area at hub diameter of each of the N_b blades.

Figure 8.17(c) shows the forces applied to a segment of disc of dimensions dr , $r d\theta$, and z . Here we can apply $F = ma$ again and write

$$2(\sigma z dr) \frac{d\theta}{2} - \frac{d}{dr} (\sigma z r d\theta) dr = \rho_b (dr r d\theta z) \Omega^2 r.$$

Since σ is required to be constant, we can simplify this equation (by dividing by $\sigma dr d\theta$) to

$$z - \frac{d}{dr}(zr) = -\frac{rdz}{dr} = \frac{\rho_b \Omega^2 r^2 z}{\sigma}$$

or

$$\frac{dz}{z} = -\frac{\rho \Omega^2}{\sigma} r dr,$$

which (between approximate limits $z = z_i$ at $r = r_i$ and $z = z_0$ at $r = r_h$) integrates to

$$\ln \frac{z_0}{z_i} = -\frac{\rho \Omega^2}{2\sigma} (r_h^2 - r_i^2).$$

Another way of expressing this is to write

$$\frac{\sigma}{\rho_b U_i^2} = \frac{\zeta^2 \left[1 - \left(\frac{r_i}{r_h} \right)^2 \right]}{2 \ln \left(\frac{z_i}{z_0} \right)}. \quad (8.19)$$

For the inner rim a force analysis very similar to the one for the outer rim leads to

$$\frac{\sigma}{\rho_b U_i^2} = \frac{\zeta^2 \left(\frac{r_i}{r_h} \right)^2}{1 - \frac{z_i r_i}{A_i}}. \quad (8.20)$$

Combination of Eqs. (8.18), (8.19), and (8.20) shows that we have, effectively, a disc stress function of this form:

$$\frac{\sigma}{\rho_b U_i^2} = f \left(\zeta, B, \frac{r_i}{r_h}, \frac{A_0}{A_i} \right),$$

in which the blade-loading term

$$B = \frac{N_b}{2\pi} \frac{A_b}{A_0} \frac{\sigma_b}{\rho_b U_i^2}$$

expresses the loading of the disc by the blades. Equation (8.17) (or a modification of it for tapered blades) shows how to evaluate $\sigma_b/(\rho_b U_i^2)$. The magnitude of B will typically be of order 1. With some effort the combination of Eqs. (8.18) to (8.20) can be expressed as the somewhat inconvenient function

$$\frac{A_i}{A_0} = \left(\frac{r_i}{r_h} \right) \left[\frac{B + \zeta^2 - S}{S - \zeta^2 \left(\frac{r_i}{r_h} \right)^2} \right] \exp \left\{ \frac{\zeta^2 \left[1 - \left(\frac{r_i}{r_h} \right)^2 \right]}{2S} \right\}, \quad (8.21)$$

in which $S = \sigma/(\rho_b U_i^2)$. Figure 8.16 displays typical numerical results obtained, iteratively, by using this equation to calculate S as a dependent quantity. The figure shows that whether highest stress is to be found at the blade root or in the disc depends on ζ and the other parameters. For the example given, Fig. 8.16 shows that, depending on the blade-loading parameter

$$B = \frac{N_b}{2\pi} \left(\frac{A_b}{A_0} \right) \frac{\sigma_b}{\rho_b U_i^2},$$

the disc stress can considerably exceed the blade-root stress for $\zeta > 0.7$. Aerodynamic design will tend to fix N_b , ζ , and A_b , while blade shape, as we have seen, fixes the value of $\sigma_b/\rho_b U_i^2$. Thus the only free variable affecting B is the outer rim cross-sectional area A_0 . Increasing A_0 reduces B but leads to a heavier disc. Figure 8.16 provides only an example of the use of Eq. (8.21), but we will not take further space here to discuss the determination of optimum values of A_0/A_i and r_i/r_h .

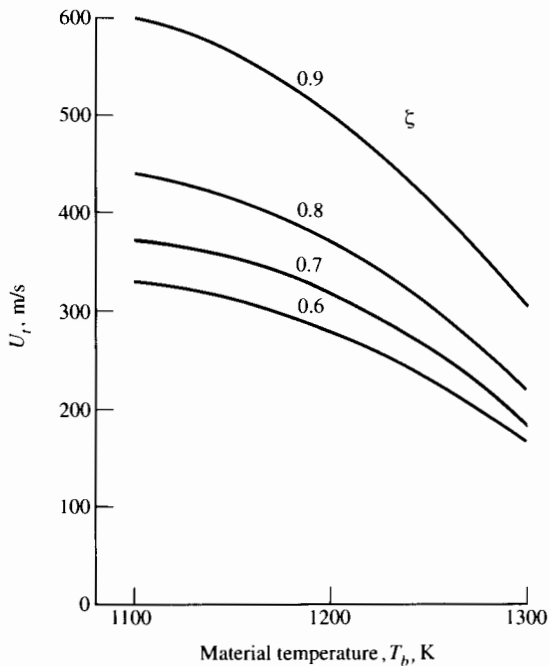


FIGURE 8.18 Allowable tip speed for various hub-tip ratios; $\zeta = r_h/r_t$.

Because the temperature of the disc can be considerably lower than the working temperature of the blades, the allowable stress on the disc can be considerably higher than on the blade; for this reason we will assume in subsequent discussion that it is blade-root stress that limits turbine design.

To see the implications of Fig. 8.14 on the allowable tip speed of turbines, we use our simplified estimate of root stress and take various values of allowable stress from Fig. 8.14 (and take the material density as 8000 kg/m^3) as a function of temperature as follows:

T/K	σ_b/MPa
1100	280
1200	200
1300	70

From these stress and density numbers one can estimate from Eq. (8.17) the allowable tip speeds shown in Fig. 8.18. We keep in mind of course that the analysis leading to these results is quite approximate and that there can be a large

difference between the temperature of the bulk of the hot gas and the blade temperature.

For typical turbojet and turbofan engines at inlet to the high-temperature section of the turbine, the gas density is sufficiently high that the hub-tip ratios are likely to be in the range 0.85 to 0.95. From the results of calculations such as the above, one might conclude that for nickel alloy turbine blades the allowable first-stage tip speed and blade temperature would be around 500 m/s and 1200 K, respectively.

8.5 BLADE COOLING

Since the maximum rotor blade stress is to be expected at the root radius of the blade, we look first at the worst case: no blade cooling and no conduction of heat away from the blade root into the turbine disc. We assume that in this case the blade temperature is nearly equal to the stagnation temperature of the hot gas (as defined for a coordinate system fixed to the blade). Given the absolute stagnation temperature T_0 (defined for a stationary coordinate system), the temperature T that would be measured upstream of the rotor at the hub radius by an observer traveling with the stream would be

$$T = T_{04} - \frac{c^2}{2c_p} = T_{04} - \frac{\gamma - 1}{2\gamma R} (c_{\theta h}^2 + c_{zh}^2)$$

or

$$\frac{T}{T_{04}} = 1 - \frac{\gamma - 1}{2} \left(\frac{U_t}{a_0} \right)^2 \zeta^2 \left[\left(\frac{c_\theta}{U} \right)_h^2 + \left(\frac{c_z}{U} \right)_h^2 \right], \quad (8.22)$$

in which the subscripts h and t denote hub and tip, respectively, and a_0 is the speed of sound at the absolute stagnation temperature T_{04} . As before, the symbol ζ indicates the hub-tip radius ratio.

The stagnation temperature relative to the coordinate system moving with the blade would be

$$T_{0\text{rel}} = T + \frac{w_{2h}^2}{2c_p}.$$

With no blade cooling or conduction into the disc, the blade would take up a temperature somewhat less than this as defined by

$$T_s = T + r_f \frac{w_{2h}^2}{2c_p}, \quad (8.23)$$

in which r_f is the “recovery” factor that accounts for the fact that the deceleration of the flow (as it enters the boundary layer next to the blade surface) is not precisely adiabatic. Some heat transfer takes place between the slowest—and therefore the hottest—streamlines and their more rapidly moving neighbors. For this reason the recovery factor is not 1 but typically in the range 0.9 to 0.95.

Combining Eqs. (8.22) and (8.23), we obtain

$$\frac{T_s}{T_{04}} = 1 - \left(\frac{\gamma - 1}{2} \right) \left(\frac{U_t}{a_0} \right)^2 \zeta^2 \left[\left(\frac{c_{\theta h}}{U} \right)^2 + \left(\frac{c_{zh}}{U} \right)^2 - r_f \left\{ \left(\frac{c_{zh}}{U} \right)^2 + \left[1 - \frac{c_{\theta h}}{U} \right]^2 \right\} \right]. \quad (8.24)$$

As an example we consider a 50% reaction blade with $c_{zh}/U = 0.5$ and $c_{\theta h}/U = 1$ (at entrance to the rotor at the hub radius) and with tip speed 500 m/s and hub-tip ratio 0.9. In this case

$$w^2 = c^2 - U^2 = c_\theta^2 + c_z^2 - c_\theta^2 = c_z^2,$$

and we find that, with $r_f = 0.9$, $\gamma = 1.33$, and $R = 0.287 \text{ kJ/kg} \cdot \text{K}$, the surface temperature T_s is 81 K below the temperature T_{04} .

Thus, even with the uncooled turbine, the rotor blade temperature at the hub, where the stress is highest, can be significantly below the "absolute" stagnation temperature of the gas at inlet to the turbine.

With blade cooling, by means of air taken from the compressor exit, it is possible to keep the blade-root temperature 300 to 400 K below the absolute stagnation temperature of the gas entering the turbine. This can be done by extraction of less than 10% of the compressor exit airflow to cool the stator and rotor blades and the turbine disc. The temperature of this cooling air depends, of course, on the compressor pressure ratio and on the flight Mach number and temperature.

More than one stage may require cooling. Even without blade cooling, gas turbines use compressor bleed air to cool the turbine disc.

The penalties of blade cooling include loss of work (and some loss of efficiency) because of that portion of the air taken from the compressor exit and ejected from the stator or rotor. In general, however, these losses are much smaller than the gains associated with operating the engine at much higher turbine inlet temperature than would be possible without cooling.

General practice in cooled turbines has been to introduce cooling air so that it exhausts through small holes on the blade surface. Figure 8.19 shows typical cooling-passage configurations in stator and rotor blading of Rolls-Royce turbines. Unlike the turbine rotor blades shown in Fig. 8.1, each of these has a platform on the outer end; the platforms of neighboring blades fit together in such a way as to create an outer ring or "shroud" at the rotor tip diameter. Shown are the separate supplies of high-pressure air—for the stator blades (nozzle guide vanes) and turbine blades—and low-pressure air for disc cooling. Figure 8.20, a turbine blade cross section, shows a five-pass internal recirculation inside the rotor blade.

Even small gas turbines are amenable to internal blade cooling using many small cooling passages. Figure 8.21 shows the blading for the General Electric T700 high-pressure rotor blades.

The question of how much airflow is required to maintain a blade at a temperature well below the gas temperature requires an estimate of heat transfer to film-cooled blades. Only an approximate estimate is possible here, but even an approximate estimate takes some care. We resort to the method outlined by

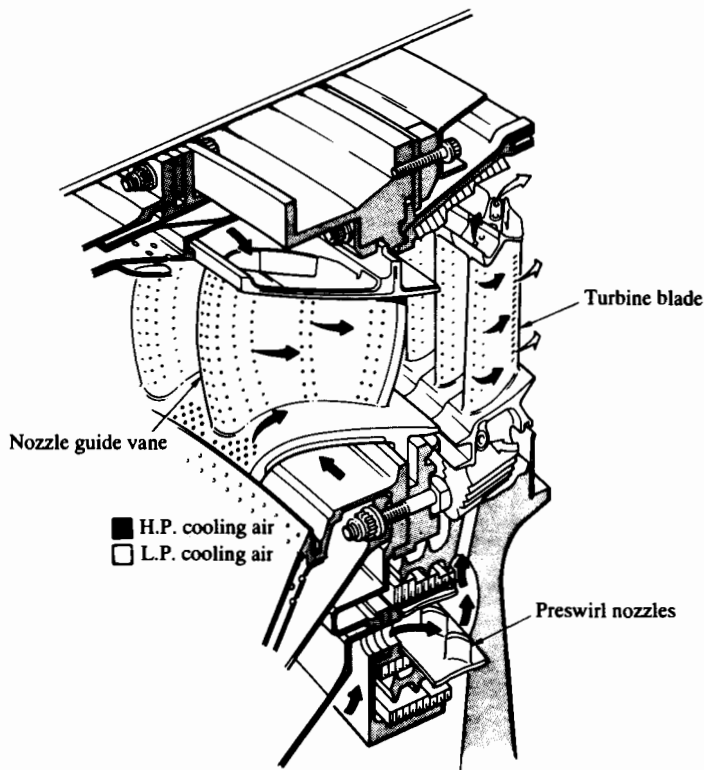


FIGURE 8.19 Cooled high-pressure turbine stage. (Courtesy Rolls-Royce, plc.)

Eckert [13], who focuses attention on a wall that is exposed on its outer surface to a hot-gas stream of temperature T_g , while the inner surface is subject to a cooling heat flux q (per unit area). At the same time, coolant air at temperature T_i is forced through holes in the walls so as to form a cooled layer of gas next to the wall, downstream of the hole. As Fig. 8.20 indicates, such cooling holes can be drilled (in production a laser drilling process may be used) at various angles relative to the cooled surface.

By reasoning with the boundary layer energy equation, Eckert shows that the heat flux from the hot gas to the wall can be written

$$q = h_0(T_{aw} - T_w), \quad (8.25)$$

in which h_0 is the film coefficient for convective heat transfer to the wall, T_w is the wall temperature, and T_{aw} is the adiabatic wall temperature. With no "film cooling"—that is, no injection of cooling air—the adiabatic wall temperature would be close, as mentioned earlier, to the stagnation temperature $T_{0\text{rel}}$ of the gas relative to the blade surface. With coolant injection T_{aw} can be quite different

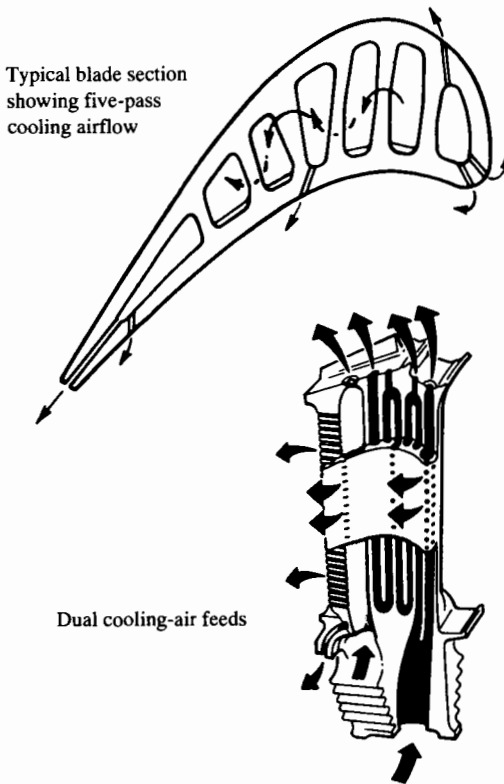


FIGURE 8.20 Five-pass cooling of turbine rotor blade. (Courtesy Rolls-Royce, plc.)

from $T_{0\text{rel}}$; we need a means of estimating T_{aw} as well as h_0 . The parameters widely used for analysis of heat transfer to film-cooled surfaces are:

1. The effectiveness η_f defined by

$$\eta_f = \frac{T_g - T_{aw}}{T_g - T_c}; \quad (8.26)$$

in which the subscript g denotes the hot-gas conditions, and T_c is the temperature of the coolant at the point of injection.

2. The Stanton number St_0 defined here as

$$St_0 = \frac{h_0}{\rho_g c_{pg} w_g}, \quad (8.27)$$

With no coolant injection the Stanton number for heat transfer to a flat plate is well known; Eckert reports that an empirically validated equation is

$$St = 0.0295 \text{Pr}^{-0.4} \text{Rex}^{-0.2}, \quad (8.28)$$

in which Pr is the Prandtl number and Rex is the Reynolds number whose length dimension is x , the distance from the leading edge of the flat plate.



FIGURE 8.21 General Electric T700 high-pressure turbine rotor blades. (Courtesy GE Aircraft Engines.)

With coolant injection the Stanton number depends on parameters additional to Pr and Re_x . The injection rate and the hole spacing are two important variables. In addition, both Stanton number and film effectiveness may be dependent on Mach number [14] (as well as on Reynolds number and Prandtl number). This dependence, however, is not very strong for typical turbine flow passages.

With film cooling, the coolant ejection hole area per unit area of surface is important; this may be written $n \pi/4 d^2$, in which d is the hole diameter and n the number of holes per unit area of cooled surface. However, n will be inversely proportional to P^2 in which P is the “pitch” or spacing between holes. Thus the coolant flow area per unit area of “porous” surface is inversely proportional to $(P/d)^2$. We can sense the importance of P/d by visualizing the spreading of the jet emitted at each coolant hole; the lateral influence of each hole will depend on the pitch-diameter ratio.

One can also expect the mass of coolant injected per unit mass of surface to be important. We can express this as

$$n \frac{\pi}{4} d^2 \rho_c u_c \propto \rho_c u_c \left(\frac{P}{d} \right)^2,$$

in which ρ_c and u_c are the density and velocity of the injected coolant. Recognizing that P/d has separate importance (affecting the flow field in the vicinity of the holes), we can define a dimensionless “blowing parameter” as

$$M_b = (\rho_c u_c) / (\rho_g u_g)$$

and write that for film cooling on a plate

$$\eta_f, \text{St}_0 = f(\text{Pr}, \text{Re}_x, P/D, M_b).$$

Typical data for effectiveness and Stanton number are shown in Fig. 8.22 for the special case $P/d = 10$ and for 11 rows of coolant in a flat plate. These data pertain to two values of the blowing parameter $M_b = 0.2$ and $M_b = 0.5$. The full line in the Stanton-Reynolds number graph represents Eq. (8.23) and shows that

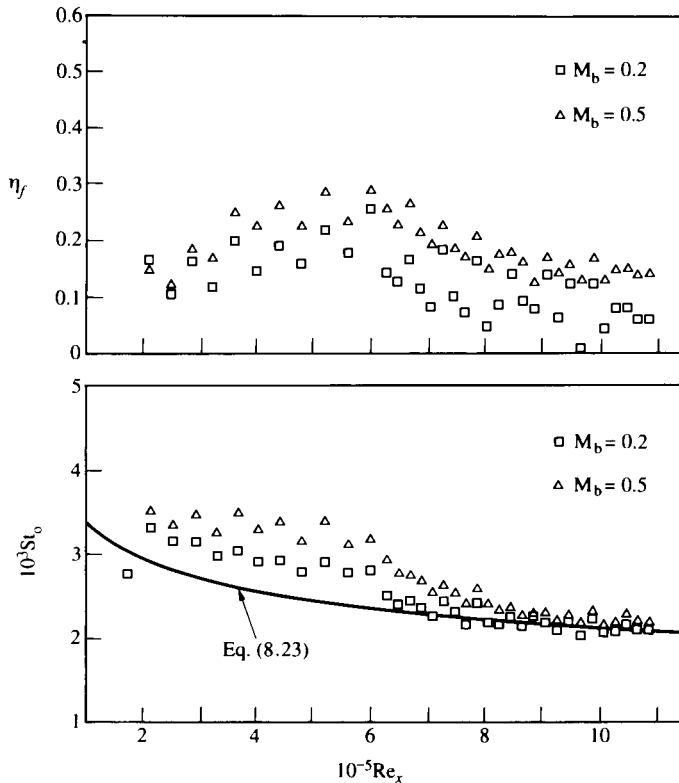


FIGURE 8.22 Effectiveness and Stanton number for a film-cooled flat-plate normal injection; $P/D = 10$. (Adapted from Eckert [13].)

coolant injection actually raises the Stanton number and thus the film coefficient of heat transfer. Nonetheless, the presence of the cool injection fluid can reduce the wall temperature.

To see the implications of these numbers for turbine blades, we assume that the blade-chord Reynolds number is 5×10^5 and that the blowing parameter is 0.5. Then from Fig. 8.22 we can take typical values for the average film-cooling effectiveness and Stanton number for the blade as

$$\eta_f = 0.2 \quad \text{and} \quad St_0 = 0.003.$$

We then suppose that these flat-plate data can be applied to the curved surfaces of an airfoil to estimate roughly the coolant flow needed to maintain a certain temperature. As the air flows up through the blade passages, we can estimate the heat transfer to it from

$$\dot{Q}_a = \dot{m}_a c_{pa} (T_c - T_i), \quad (8.29)$$

in which T_i is the temperature of the air as it is drawn off the compressor. If the heat-flow rate from blades to disc is small enough, \dot{Q}_a will be balanced by \dot{Q}_b , the

rate of heat transfer from the hot gas to the blade surface. Using Eckert's terminology for h_0 and T_{aw} , we may estimate this as

$$\dot{Q}_b = h_0(T_{aw} - T_b)A_s, \quad (8.30)$$

in which A_s is the surface area of the blade. To a first approximation, the required cooling-airflow rate can be obtained by equating \dot{Q}_a and \dot{Q}_b with the result

$$\dot{m}_a = \frac{h_0(T_{aw} - T_b)}{(T_c - T_i)} \frac{A_s}{c_{pa}}$$

or, dividing by \dot{m}_g ,

$$\frac{\dot{m}_a}{\dot{m}_g} = St_0 \frac{A_s}{A_g} \frac{c_{pg}}{c_{pa}} \left(\frac{T_{aw} - T_b}{T_c - T_i} \right),$$

in which A_g is the hot-gas flow area (plane perpendicular to w_g).

From the definition of effectiveness

$$T_{aw} - T_b = T_g - T_b + \eta_f(T_g - T_c),$$

so that

$$\frac{\dot{m}_a}{\dot{m}_g} = St_0 \frac{A_s}{A_g} \frac{c_{pg}}{c_{pa}} \left[\frac{T_g - T_b}{T_c - T_i} - \eta_f \left(\frac{T_g - T_c}{T_c - T_i} \right) \right]. \quad (8.31)$$

We can take here a few typical numbers to estimate the magnitude of \dot{m}_a/\dot{m}_g . Suppose:

Gas temperature	$T_g = 1600$ K,
Blade temperature	$T_b = 1200$ K,
Compressor exit temperature	$T_i = 850$ K,
Coolant ejection temperature	$T_c = 1100$ K,

and the product

$$\frac{A_s c_{pg}}{A_g c_{ps}} \approx 10.$$

Then with the value of $St_0 = 0.003$ and $\eta_f = 0.2$ we find

$$\frac{\dot{m}_a}{\dot{m}_g} \approx 0.036.$$

This estimate pertains to one rotor row. One might double this for the first stage. Cooling the second stage would not require so much air since T_g would be lower. However, from this we can see that bleeding 10% or more of compressor airflow may well be needed if high gas-inlet temperatures are used.

The use of a substantial fraction of compressor mass flow rate raises the question as to how this affects the turbine efficiency. Before we can answer this question, we must define what we mean by the efficiency of a turbine that has a number of entry points for its working fluid, each with its own stagnation pressure and temperature. It would seem reasonable in such a case to define the effi-

ciency as the ratio of the actual work to the maximum possible work of adiabatic expansion. In this case we could define, for example, the total-to-total efficiency as

$$\eta_{tt} = \frac{w_{actual}}{\sum \alpha_i \Delta h_i},$$

in which w_{actual} is the total actual work done in the turbine and Δh_i is the isentropic stagnation enthalpy drop of the i th input stream (of mass fraction α_i) expanding adiabatically by itself to the same final stagnation pressure. With the assumption of uniform and constant γ , we could write

$$\eta_{tt} = \frac{w_{actual}}{\sum \alpha_i c_{pi} T_{01i} \left[1 - \left(\frac{p_{02}}{p_{01i}} \right)^{(\gamma-1)/\gamma} \right]},$$

in which 02 denotes the final stagnation state and 01 the initial state. Estimation of the actual stage work requires several assumptions. One might, for example, assume that the coolant stream entering the first stage does no work in that stage and mixes with the hot gas at the exit of that stage without loss of stagnation pressure. The working fluid then enters the second stage with a uniform stagnation temperature to expand adiabatically in that stage before mixing with second-stage coolant at the end of that stage. These matters are too complex to discuss in detail here, but References 13, 14, and 15 present various assumptions and procedures with which to quantify the irreversibilities associated with turbine blade cooling.

8.6 TURBINE PERFORMANCE

In Chapter 7 we saw that for any compressor the overall pressure ratio, for example, may (by dimensional analysis) be written

$$\frac{p_{02}}{p_{01}} = f\left(\frac{\dot{m} \sqrt{RT_{01}}}{p_{01} D^2}, \frac{\Omega D}{\sqrt{\gamma RT_{01}}}, \gamma, \frac{\Omega D^2}{\nu}\right),$$

in which the subscripts 01 and 02 denote inlet and outlet conditions and D is the scale or size of a series of geometrically similar machines. The Reynolds number $\Omega D^2/\nu$ is not an important variable so long as it is large enough, as we discussed earlier. The same logic as used for a compressor can be used for a turbine with the same kind of result. Thus for a given design of turbine operating with a given fluid at sufficiently high Reynolds number,

$$\frac{p_{04}}{p_{05}} = f\left(\frac{\dot{m} \sqrt{RT_{04}}}{p_{04} D^2}, \frac{\Omega D}{\sqrt{\gamma RT_{04}}}\right), \quad (8.32)$$

where stagnation states 04 and 05 are at the turbine inlet and outlet, respectively, in keeping with the scheme of Chapter 5 for numbering turbojet engines. Figure 8.23 shows the overall performance of a particular single-stage turbine. One

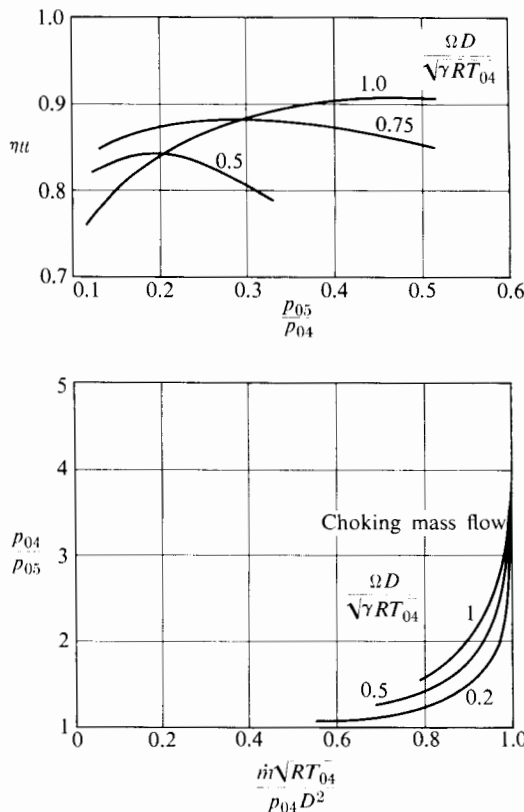


FIGURE 8.23 Typical characteristics of a single-stage free-vortex turbine. (Courtesy M.I.T. Gas Turbine Laboratory.)

can see that pressure ratios much greater than those for compressor stages can be obtained with satisfactory efficiency.

The performance of turbines is limited principally by two factors: compressibility and stress. Compressibility limits the mass flow that can pass through a given turbine and, as we will see, stress limits the wheel speed U . The work per stage, for example, depends on the square of the wheel speed. However, as Chapter 5 showed, the performance of the engine depends very strongly on the maximum temperature. Of course, as the maximum temperature increases, the allowable stress level diminishes; hence in the design of the engine there must be a compromise between maximum temperature and maximum rotor tip speed U .

For given pressure ratio and adiabatic efficiency, the turbine work per unit mass is proportional to the inlet stagnation temperature. Since, in addition, the turbine work in a jet or turboshaft engine is commonly two or three times the useful energy output of the engine, a 1% increase in turbine inlet temperature can produce a 2% or 3% increase in engine output. This considerable advantage has supplied the incentive for the adoption of fairly elaborate methods for cooling the turbine nozzle and rotor blades.

8.7 TURBINE AND COMPRESSOR MATCHING

The problem of matching turbine and compressor performance has great importance for jet engines, which must operate under conditions involving large variations in thrust, inlet pressure and temperature, and flight Mach number. Matching the components of turbofan and turboprop engines involves similar considerations and procedures, but for simplicity we focus our discussion here on turbojet engines.

Essentially the matching problem is simple, though the computations can be lengthy. The steady-state engine performance at each speed is determined by two conditions: continuity of flow and a power balance. The turbine mass flow must be the sum of the compressor mass flow and the fuel flow, minus compressor bleed flow. Also the power output of the turbine must be equal to that demanded by the compressor.

For given flight Mach number, ambient conditions, diffuser and nozzle efficiencies, and flow areas, one can determine the performance of a jet engine from the "maps" of compressor and turbine performance indicated in Fig. 8.24. These diagrams are similar to those of Figs. 7.14 and 8.23, except that, for a given machine, the constants D , R , and γ have been omitted and the speed U is replaced by the rotor rpm, N . In principle, the matching computations could proceed as follows:

1. Select operating speed.
2. Assume turbine inlet temperature T_{04} .
3. Assume compressor pressure ratio.

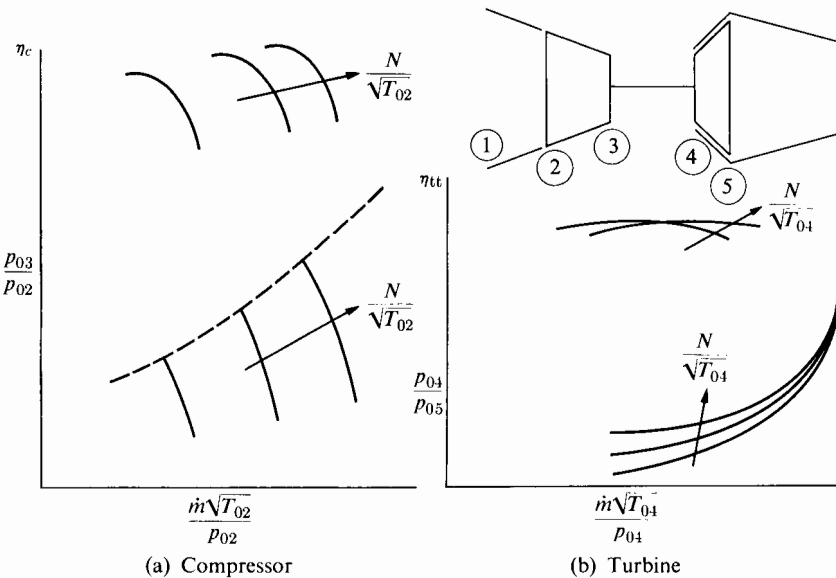


FIGURE 8.24 Typical compressor and turbine performance maps.

4. Calculate compressor work per unit mass.
5. Calculate turbine pressure ratio required to produce this work.
6. Check to see (Fig. 8.24) if compressor mass flow plus fuel flow equals turbine mass flow; if it does not, assume a new value of compressor pressure ratio and repeat steps 4, 5, and 6 until continuity is satisfied.
7. Now calculate the pressure ratio across the jet nozzle from the pressure ratios across the diffuser, compressor, combustor, and turbine.
8. Calculate the area of jet nozzle outlet necessary to pass the turbine mass flow calculated in step 6 with the pressure ratio calculated in step 7 and the stagnation temperature calculated. If the calculated area does not equal the actual exit area, assume a new value of T_{04} (step 2) and repeat the entire procedure.

The designer will try to match turbine and compressor so that the compressor is operating near its peak efficiency through the entire range of operation, as indicated in Fig. 8.25, where the operating line (i.e., the locus of steady-state matching conditions) runs through the centers of the islands defined by the constant-efficiency lines. It may happen that an operating line located in this manner will be dangerously close to the surge line. If this is the case, it might be possible to adjust the stage velocity triangles so that the maximum efficiency of the compressor occurs farther from the surge line.

Figure 8.25 is useful in a discussion of the important problem of acceleration of gas turbine engines. If an attempt is made to accelerate the engine quickly by increasing the fuel flow very rapidly, there is danger of the compressor surging, which usually causes flameout of the combustor. Also it is possible that the violent changes in aerodynamic load on the compressor blades during the surge period may cause them to fail.

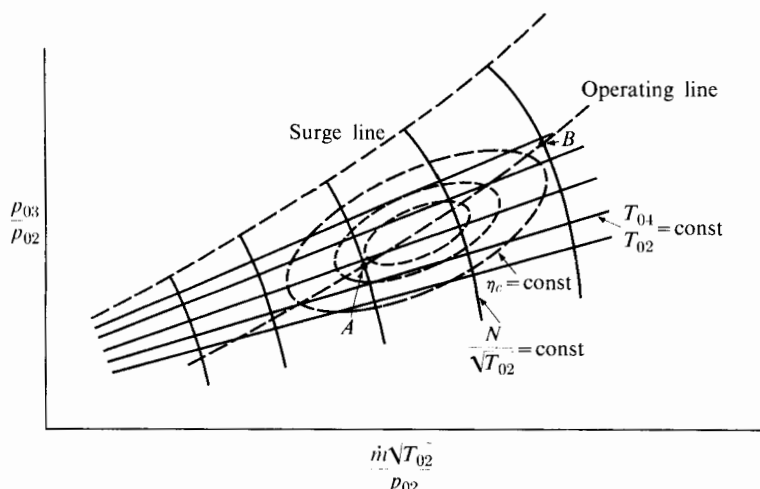


FIGURE 8.25 Operating line on a compressor map.

It is convenient to note the form of constant T_{04} lines on the compressor map. In general (referring to Fig. 8.25),

$$\frac{\dot{m} \sqrt{T_{02}}}{p_{02}} = \frac{\dot{m} \sqrt{T_{04}}}{p_{04}} \cdot \frac{p_{04}}{p_{03}} \cdot \frac{p_{03}}{p_{02}} \cdot \sqrt{\frac{T_{02}}{T_{04}}}.$$

The value of p_{04}/p_{03} is practically constant (with a value close to unity). If the turbine nozzles are choked, as they are over a good part of the operating range of turbine engines, then

$$\frac{\dot{m} \sqrt{T_{04}}}{p_{04}} = \text{const.}$$

Thus

$$\frac{p_{03}}{p_{02}} \propto \sqrt{\frac{T_{04}}{T_{02}}} \cdot \frac{\dot{m} \sqrt{T_{02}}}{p_{02}},$$

and lines of constant T_{04}/T_{02} may be plotted as shown in Fig. 8.25, straight lines radiating from the origin. Of course, at lower speeds when the turbine nozzle ceases to be choked, the lines are no longer straight.

Suppose we wish to accelerate the engine between equilibrium operating points *A* and *B*. If the fuel flow is suddenly increased, the first effect will be a sudden rise in T_{04}/T_{02} . Thus, before the rotor has time to accelerate, the compressor operation will move along a line of constant $N/\sqrt{T_{02}}$ toward the new T_{04}/T_{02} condition; that is, *toward* the surge line. Thus the fuel control system must limit the rate of additional fuel flow during the acceleration period. As a result, the acceleration process may be quite slow, though some engines (with variable stator blades in the compressor) can accelerate from idle to takeoff power in about six seconds, or from landing approach to full power in about three seconds.

The procedure for matching the compressor and the turbine in a turbojet engine can be much simpler, for most of the operating range, than the iterative procedure just outlined. This is because both the main propulsion nozzle and the turbine will be choked over most of the operating range. The nozzle will be choked as long as the pressure ratio across it exceeds about 2. As Fig. 8.23 shows, the turbine will also be choked when there is sufficiently high pressure across it.

Again using ④ and ⑤ to denote stagnation states at entrance to the turbine and main propulsion nozzle, respectively, we may write for the turbine choke condition

$$\frac{\dot{m} \sqrt{RT_{04}}}{p_{04} D^2} = \text{const}$$

and for nozzle choke

$$\frac{\dot{m} \sqrt{RT_{05}}}{p_{05} D^2} = \text{const.}$$

Dividing the first by the second, we have

$$\frac{p_{05}}{p_{04}} = \text{const} \left(\frac{T_{05}}{T_{04}} \right)^{1/2}. \quad (8.33)$$

But at the same time we can write

$$\frac{p_{05}}{p_{04}} = \left(\frac{T_{05}}{T_{04}} \right)^{\gamma(\gamma-1)\eta_{pt}} \quad \text{or} \quad \frac{p_{05}}{p_{04}} = \left[1 - \frac{1}{\eta_{tt}} \left(1 - \frac{T_{05}}{T_{04}} \right) \right]^{\gamma(\gamma-1)},$$

in which η_{pt} is the polytropic efficiency of the turbine expansion and η_{tt} is the total-to-total adiabatic efficiency. The only way in which these equations can all be satisfied as the engine speed and the thrust change is for both P_{04}/P_{05} and T_{04}/T_{05} to remain constant.

This has further implications. One can express the work done by a single stage in the turbine as

$$c_p \Delta T_0 = U \Delta c_\theta = U [c_z (\tan \alpha_e + \tan \beta_e) - U], \quad (8.34)$$

in which α_e and β_e signify the exit flow angles from the rotor and the stator, respectively. Even if c_z/U were to change, α_e and β_e would stay very nearly constant; as long as the blades are spaced closely enough, they can guide the flow to the same outlet flow angle regardless of small changes in the inlet flow angle, that is, in c_z/U .

If, for the moment, we consider that the turbine has only one stage, Eq. (8.34) could be written (after dividing by $c_p T_{04}$)

$$1 - \frac{T_{05}}{T_{04}} = (\gamma - 1) \frac{U}{\sqrt{\gamma R T_{04}}} \left[\frac{c_z}{\sqrt{\gamma R T_{04}}} (\tan \alpha_e + \tan \beta_e) - \frac{U}{\sqrt{\gamma R T_{04}}} \right].$$

But if that turbine stage were choked—for example, at the stator exit—it would follow that $c_z/\sqrt{\gamma R T_{04}}$ would be constant, that is, the velocity in the stage would be independent of downstream pressure and temperature. Then if γ , α_e , and β_e were also constant, it would follow that the only way T_{04}/T_{05} could be maintained constant would be for $U/\sqrt{\gamma R T_{04}}$ to remain constant. This then says that, over most of the operating range of the jet engine (as long as both the turbine and the propulsion nozzle stay choked) $U \propto \sqrt{T_{04}}$ or $T_{04} \propto N^2$, in which N is the shaft rpm. With both U and $c_z \propto \sqrt{T_{04}}$, it follows that c_z/U is constant.

If c_z/U stays constant, then (even though the turbine inlet temperature and the shaft speed vary through a wide range) all internal flow angles remain fixed. The geometry of the streamlines within the turbine does not change; the turbine may be said to be fixed at the same operating point—as defined in dimensionless terms—even though the pressure, velocity, and temperature within the turbine may vary considerably.

For a multistage turbine the argument is a little more complicated, requiring the addition of a series of equations such as (8.34) to obtain the overall tempera-

ture ratio, but the result is the same, namely, double-choking requires (as T_{04} and N change)

$$\begin{aligned}\frac{P_{05}}{P_{04}} &= \text{const}, \\ \frac{T_{05}}{T_{04}} &= \text{const}, \\ U \propto N \propto \sqrt{T_{04}},\end{aligned}\tag{8.35}$$

and the entire turbine remains at the same (dimensionless) operating point and has the same fluid-flow angles throughout.

We now consider the consequences of the turbine remaining at the same operating point (during steady operation of the compressor-burner-turbine combination) and ask how these results control the location of the operating line shown in Fig. 8.25.

The compressor flow rate may be written

$$\frac{\dot{m} \sqrt{RT_{01}}}{p_{01} D^2} = \frac{\dot{m} \sqrt{RT_{04}}}{p_{04} D^2} \frac{p_{04}}{p_{03}} \frac{p_{03}}{p_{02}} \frac{p_{02}}{p_{01}} \sqrt{\frac{T_{01}}{T_{04}}}.$$

Since $T_{04} \propto N^2$, $\dot{m} \sqrt{RT_{04}}/p_{04} D^2$ is constant, and P_{04}/P_{03} is always close to 1; it follows that the compressor pressure ratio

$$\frac{p_{03}}{p_{02}} \propto \frac{N}{\sqrt{T_{01}}} \frac{\dot{m} \sqrt{RT_{01}}}{p_{01} D^2}.\tag{8.36}$$

Thus the operating line will have a steeper slope on the compressor map than the lines of constant T_{04}/T_{02} .

It is interesting to note that all of these results are independent of the flight Mach number of the aircraft; in terms of the compressor map there is a single operating line. If, however, the turbine or nozzle becomes unchoked—at low shaft speed—then the operating line will become dependent on flight Mach number, as shown in Fig. 8.26.

The foregoing discussion focused on the turbojet that, for a high-pressure ratio engine, is likely to have both its propulsion nozzle and its turbine choked over most of its operating range. The turbofan engine, with high bypass ratio, will typically have a much lower pressure ratio across the core engine propulsion nozzle, which may operate unchoked over part of the operating range. The bypass stream will generally be unchoked. For these conditions the simplifying considerations affecting the matching of the compressor and turbine will not apply, and one must carry out an iterative procedure for matching the compressor, fan, and turbine.

8.8 TURBINE STAGE DESIGN

In Section 7.10 we mentioned the use of two- and three-dimensional viscous compressible flow calculation procedures for compressor design. The same pro-

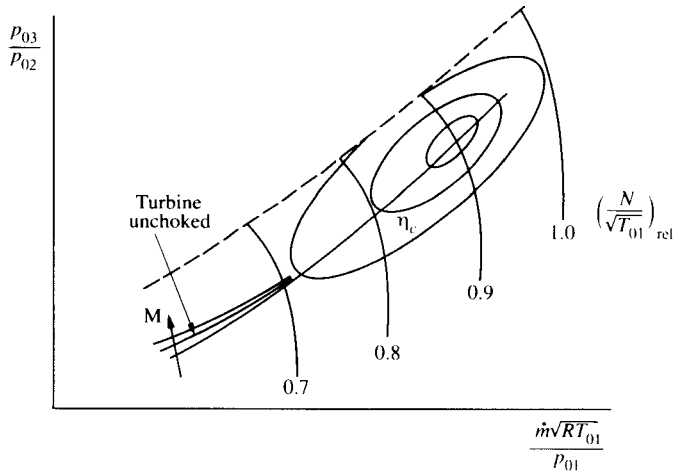


FIGURE 8.26 Operating line on compressor map.

cedures are available for turbine flows and are widely used in design and development work (see, e.g., Refs. 16 and 17). Here, as in Sections 7.9 and 7.10, we focus on more elementary methods appropriate to the preliminary design of turbine stages.

As we pointed out in Section 8.6, the dimensional analysis leading to Eq. (7.71) for axial compressors is equally applicable to compressors and turbines. Therefore we can adapt this statement of physical dependence to turbines simply by changing subscripts so that

$$\frac{p_{04}}{p_{05}}, \eta_t = f\left(\frac{\dot{m} \sqrt{RT_{04}}}{p_{04} D^2}, \frac{U_t}{a_0}, \text{design}\right). \quad (8.37)$$

The design of a turbine for a turbojet engine will be strongly affected by the compressor design as well as by the results of cycle analysis. Since the compressor is more difficult to design to high efficiency, and is generally more massive, it is the compressor that largely determines the shaft speed Ω and the maximum allowable diameter of the turbine. (Each compressor-turbine combination could theoretically have a gear transmission so that the turbine could operate on a different speed from that of the compressor, but this option appears impractical because of the mass penalty and possible unreliability of the gearbox.)

The results of cycle analysis will determine (at least approximately) the mass flow rate \dot{m} and the turbine inlet stagnation pressure p_{04} and temperature T_{04} . In addition, the design of the turbine will typically be constrained so that its maximum diameter does not much exceed that of the core compressor. However, as Figs. 5.24, 5.25, and 5.26 have indicated, the maximum diameter of the turbine is unlikely to be associated with its first stage. Thus the parameters $\dot{m} \sqrt{RT_{04}}/p_{04} D^2$

and $U_t/a_0 = \Omega D/2\sqrt{\gamma RT_{04}}$ for the first turbine stage are not rigidly determined by the results of compressor design and cycle analysis. This discussion will concern the first stage only.

In the same way as for the axial compressor, we define the preliminary design of the stage to be the determination of the overall diameter, the hub-tip ratio, the fluid-flow angles at all radii, and the blade speed ratio.

In considering the design of the first turbine stage, we could say (with reference to Eq. 8.37) that our objective is maximum pressure ratio p_{04}/p_{05} while maintaining high efficiency. Optimizing the design will mean finding values of U_t/a_0 and $\dot{m}\sqrt{RT_{04}}/p_{04}D^2$ that best satisfy the need for:

- a. A high (but not necessarily maximum) efficiency,
- b. Maximum blade-root stress consistent with the strength of available materials (e.g., Fig. 8.14) and with blade-cooling possibilities.

Stage Efficiency

Guidance on the conditions under which high turbine efficiency can be obtained is given by Fig. 8.13, which shows the wisdom of making sure that the mean-radius parameters $\Delta h_0/U^2$ and c_z/U are kept within reasonable limits. In the design process we specify the values of these parameters at the mid-radius of the stage. In addition, with high efficiency in mind, we set the mid-radius degree of reaction at 50%.

In a multistage turbine, rotor exit swirl does not necessarily imply an efficiency penalty, so zero exhaust swirl is not a requirement in the following procedure.

Blade-Root Stress

Transforming Eq. (8.17), we can write

$$\frac{2\sigma_b}{\rho_b a_0^2} = \left(\frac{U_t}{a_0}\right)^2 (1 - \zeta^2). \quad (8.38)$$

The ratio σ_b/ρ_b at which a given material may safely operate will depend strongly on the blade-root temperature, which in turn will depend on $T_{04} = a_0^2/\gamma R$ and the blade-cooling effectiveness. With turbine blade-cooling technology allowing blade temperatures to be maintained a few hundred Kelvin below T_{04} , we can deduce from Fig. 8.14 that reasonable design limits for stress can be expressed by

$$0.02 < \frac{\sigma_b}{\rho_b a_0^2} < 0.04.$$

Stagnation Temperature

As in the axial compressor, we assume that the stagnation temperature is uniform in the radial direction at each axial location in the turbine. This is consistent with radially uniform temperature at inlet to the turbine and with the work done

on each streamline being independent of radial position. In practice the flow entering the turbine will have a somewhat rounded stagnation temperature profile (lower temperature at hub and tip diameter), but we do not allow for that here.

Entropy

Again, as in the axial compressor analysis, we assume that the entropy is everywhere uniform within the stage. In this preliminary procedure we assume that the losses are accounted for by adjustments made in the stagnation pressure at exit from each blade row as the boundary layers mix with the main stream.

Radial Equilibrium

Because of high fluid density the through-flow area will be much less for the first turbine stage than for the first compressor stage. For roughly the same overall diameter we would expect the hub-tip ratio to be high. It will not be so high as to yield high efficiency without blade twist, but it will be high enough to assume that the free-vortex swirl pattern will yield a satisfactory solution to the turbine flow field.

Mass Flow Rate

As for an axial compressor stage, the mass flow rate is given approximately by

$$\dot{m} = \int_{r_h}^{r_t} \rho c_z 2\pi r dr. \quad (8.39)$$

As Section 7.8 showed, radially uniform angular momentum is compatible with a radially uniform axial velocity component. Thus the only difficulty in evaluating the integral in Eq. (8.39) is in accommodating the radial variation in density. In evaluating the integral, we have assumed that $\gamma = 4/3$. This assumption is a reasonable approximation for the specific heat ratio of the working fluid of a gas turbine; it has the additional merit of allowing Eq. (8.39) to be integrated to a closed form (as shown in Appendix VI) under the assumption of radially uniform angular momentum (i.e., a free-vortex distribution) and radially uniform entropy and stagnation temperature.

The result of the integration is a specific function in which

$$\frac{\dot{m} \sqrt{RT_{04}}}{p_{04} D^2} = f \left[\frac{U_t}{a_0}, \left(\frac{c_z}{U} \right)_t, \left(\frac{c_{\theta 2}}{U} \right)_t, \zeta \right]. \quad (8.40)$$

Here, as before, the subscript t denotes the tip diameter.

The requirement of 50% reaction at mid-radius leads (as Appendix VI shows) to

$$\left(\frac{c_{\theta 2}}{U} \right)_t = \frac{(1 + \zeta)^2}{8} \left[1 + \left(\frac{\Delta h_0}{U} \right)_m \right].$$

Also, the uniformity of c_z means that

$$\left(\frac{c_z}{U}\right)_t = \left(\frac{1 + \zeta}{2}\right) \left(\frac{c_z}{U}\right)_m.$$

Thus we can effectively consider the function represented by Eq. (8.40) to be

$$\frac{\dot{m} \sqrt{RT_{04}}}{P_{04} D^2} = f\left[\frac{U_t}{a_0}, \left(\frac{c_z}{U}\right)_m, \left(\frac{\Delta h_0}{U^2}\right)_m, \zeta\right]. \quad (8.41)$$

Work and Pressure Ratio

With constant specific heat the definition of the total-to-total efficiency of the turbine stage can be written

$$\eta_{tt} = \frac{h_{04} - h_{05}}{h_{04} - h_{05s}} = \frac{T_{04} - T_{05}}{T_{04} - T_{05s}},$$

in which 04 denotes the inlet stagnation state and 05 and 05s denote the outlet stagnation state (actual and ideal, respectively). Rearranging, we obtain

$$\frac{T_{05s}}{T_{04}} = 1 - \frac{T_{04} - T_{05}}{\eta_{tt} T_{04}}.$$

Now

$$\frac{T_{05s}}{T_{04}} = \left(\frac{P_{05}}{P_{04}}\right)^{(\gamma-1)/\gamma},$$

and at the mid-radius we may write

$$T_{04} - T_{05} = \frac{U_m (\Delta c_\theta)_m}{c_p} = \frac{U_t^2}{c_p} \left(\frac{1 + \zeta}{2}\right)^2 \left(\frac{\Delta c_\theta}{U}\right)_m.$$

Combining these expressions, we obtain

$$\left(\frac{P_{04}}{P_{05}}\right)^{(\gamma-1)/\gamma} = 1 - \frac{U_t^2}{\eta_{tt} c_p T_{04}} \left(\frac{1 + \zeta}{2}\right)^2 \left(\frac{\Delta c_\theta}{U}\right)_m$$

or

$$\frac{P_{05}}{P_{04}} = \left[1 - \frac{(\gamma - 1)}{\eta_{tt}} \left(\frac{U_t}{a_0}\right)^2 \left(\frac{1 + \zeta}{2}\right)^2 \left(\frac{\Delta h_0}{U^2}\right)_m\right]^{\gamma/(\gamma-1)}. \quad (8.42)$$

Thus, except for $(c_z/U)_m$, which does not appear in Eq. (8.42), P_{04}/P_{05} has the same independent variables as $\dot{m} \sqrt{RT_{04}}/P_{04} D^2$, and the preliminary design process can be reduced to a search for the best combination of these variables:

$$\frac{U_t}{a_0}, \left(\frac{c_z}{U}\right)_m, \left(\frac{\Delta h_0}{U^2}\right)_m, \zeta.$$

Appendix VI shows one way in which to conduct this search.

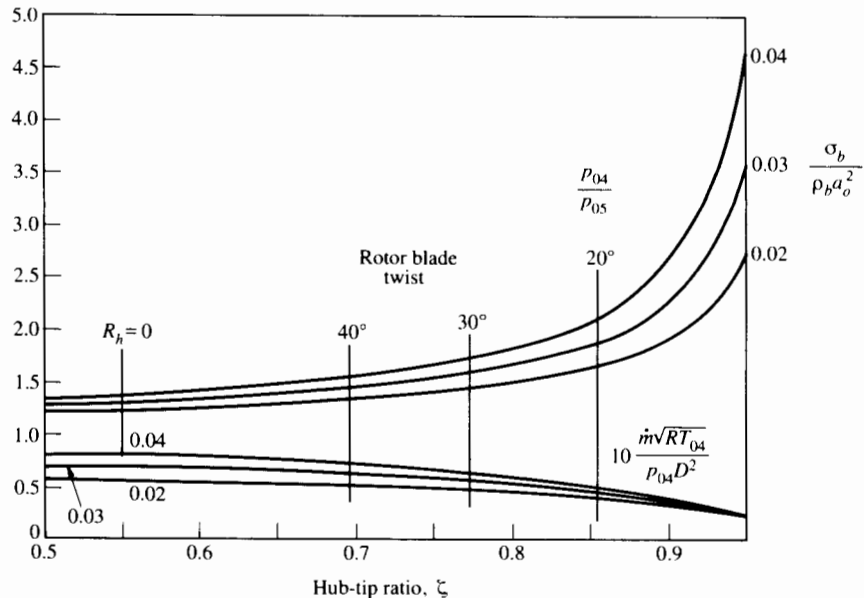


FIGURE 8.27 Axial turbine stage; $(\Delta h_0/U^2)_m = 1$ ($c_z/U_m = 0.5$).

Figures 8.27, 8.28, and 8.29 show typical results of the procedure for designs for which the mid-radius degree of reaction is 50%. Figure 8.27 shows the dependence of the stage pressure ratio and mass flow rate per unit area on the hub-tip ratio for a given stress factor $\sigma_b/\rho_b a_0^2$. Taking an inlet stagnation temperature of 1600 K would give $a_0 = 801$ m/s. Referring to Fig. 8.14 and taking $\sigma_b/\rho_b = 20$ kPa/kg · m⁻³ would provide a value of $\sigma_b/\rho_b a_0^2 = 0.03$, which is in the middle of the range of values suggested earlier. If one were designing the first stage of a turbine for a turbojet, the values of P_{04}, T_{04} and the mass flow rate would be known from the results of cycle calculations. Further, design of the axial compressor would have provided a size D within which the turbine rotor should fit. Using the allowable stress parameter $\sigma_b/\rho_b a_0^2$, Fig. 8.27 would indicate the approximate hub-tip ratio of the turbine and the stage pressure ratio (for $[\Delta h_0/U^2]_m = 1$ and $c_z/U_m = 0.5$). If ζ were very close to 1, the danger would be that, with small blade height, the tip clearance losses would be excessive. On the other hand, as Fig. 8.27 shows, if the hub-tip ratio ζ were as low as 0.7 to 0.75, the rotor blade twist would become excessive. This could call for using a different swirl distribution from the free vortex on which Fig. 8.27 is based. Remember, however, that if the turbine stage were required to have zero exit swirl, the free-vortex distribution in front of the rotor is the only one that has radially uniform stage work.

As an alternative to setting the stage reaction at 50% at the mean radius, one could use the design condition that the degree of reaction be always zero at the hub radius. This would appreciably affect the calculated results. For the special case chosen (free-vortex swirl and 50% reaction at mid-radius), it is possible to

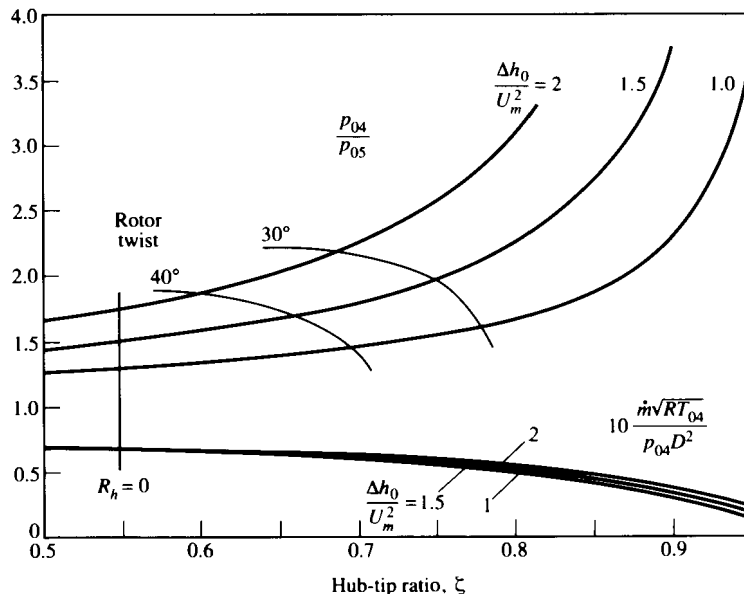


FIGURE 8.28 Axial turbine stage; $\sigma_b/\rho_b a_0^2 = 0.03, (c_z/U)_m = 0.5$.

show that the hub-tip ratio is always zero for a hub-tip radius ratio of 0.547. (This of course refers to the design condition; for off-design conditions the zero-degree-of-reaction point can move to a higher radius.)

Figure 8.28 shows the large effect of the work ratio $(\Delta h_0/U^2)_m$ on the stage pressure ratio (and the small effect on the mass flow rate per unit area). Here we see that, for given mass flow rate parameter $\dot{m} \sqrt{RT_{04}}/P_{04} D^2$, the hub-tip ratio is not strongly affected by the work ratio.

Figure 8.29, for a given work ratio and stress parameter value, shows the effect of hub-tip ratio and flow coefficient on the overall pressure ratio and on blade twist. Raising the flow coefficient can significantly reduce blade twist; it does not under the assumed conditions affect stage pressure ratio. The higher the hub-tip ratio, the higher the allowable tip speed for a given blade-root stress; this also means higher stage work and hence a higher overall pressure ratio. Since, as mentioned earlier, the first turbine stage is likely to have a relatively high hub-tip ratio, Fig. 8.29 indicates that there will be relatively little blade twist. Thus the assumption of free-vortex swirl will be acceptable. In contrast, for the last stage of a multistage turbine, where the hub-tip ratio may be as low as 0.5, free-vortex blading could give quite unsatisfactory conditions at the blade root. Figure 8.29 indicates that the degree of reaction at the hub radius is negative for hub-tip ratios less than about 0.55 (for the chosen stage design conditions).

We have carried out this preliminary design exercise on the assumption that the radial velocity components are unimportant. Looking at the flow path of an axial turbine, however, one may see that the assumption $c_r^2 \ll c_z^2, c_\theta^2$, is not necessarily accurate. Figure 8.30, showing a low-pressure turbine, indicates that one

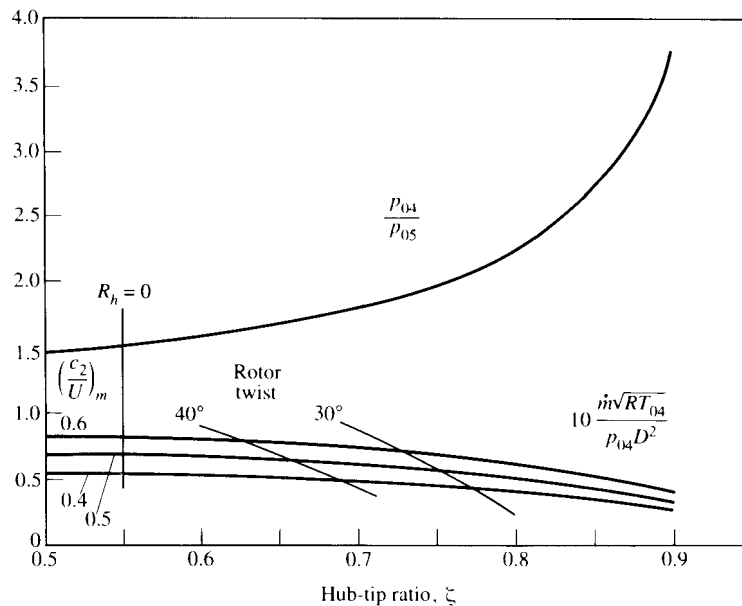


FIGURE 8.29 Axial turbine stage; $\sigma_b/\rho_b a_0^2 = 0.03$, $W/U_m^2 = 1.5$.

should take into account the radial velocity components in satisfying radial equilibrium and that a fully three-dimensional solution is needed. Procedures like those of References 16 and 17 are available to provide a good simulation of the three-dimensional flow field (except for the boundary layers) in the whole turbine.

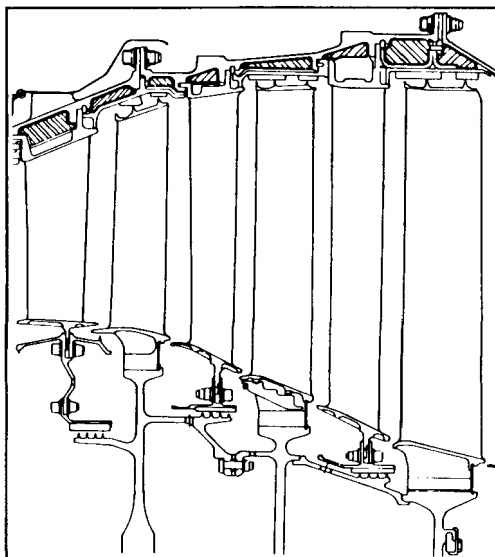
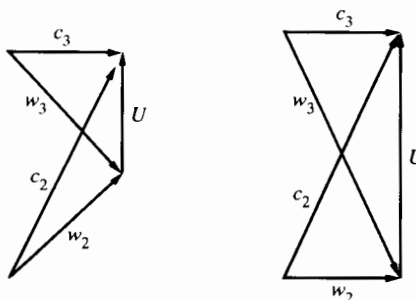


FIGURE 8.30 Low-pressure turbine flow path. (Courtesy Rolls-Royce, plc.)

PROBLEMS

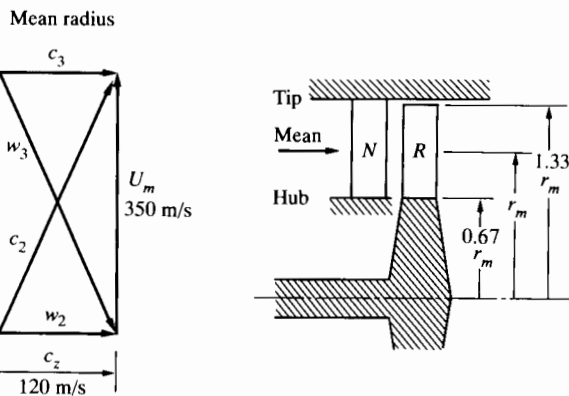
1. The figure shows velocity diagrams for impulse and 50% reaction turbines at different rotor speeds. The subscripts 2 and 3 denote conditions before and after the rotor, respectively. In both cases the absolute velocity c_2 is 400 m/s at an angle $\alpha_2 = 70^\circ$, and the absolute exhaust velocity c_3 is axial. If the blades are uncooled and well insulated from the turbine disc, approximately what would the equilibrium temperature of the blades be in each case, for an inlet gas temperature $T_{02} = 1100$ K?



PROBLEM 1

2. A single-stage axial turbine is to be designed for 50% reaction and a work ratio $(\Delta c_\theta/U)_m$ of 1.0 at the mean radius. The mid-radius axial velocity ratio $(c_z/U)_m$ is 0.4. If the swirl distribution upstream and downstream of the rotor is to be free vortex, what is the minimum hub-tip ratio for which the degree of reaction R is positive at all radii?
3. A turbine is to be designed with a “free-vortex” velocity distribution. This means that the absolute tangential velocity varies with radius according to

$$(rc_\theta)_2 = K_2, \quad (rc_\theta)_3 = K_3,$$



PROBLEM 3

where K_2 and K_3 are constants and the subscripts 2 and 3 signify the rotor entrance and exit, respectively.

(a) Show that, with this velocity distribution, the work extracted from any unit mass of fluid flowing through the turbine is independent of radial position. (b) Construct velocity triangles (drawn roughly to scale) for the hub (r_h) and tip (r_t) velocities if the mean-radius diagram and variation of radius are as shown in the figure.

First complete the following table. Draw approximate *rotor* blade shapes at hub, mean, and tip radii.

Variable	Hub	Mean	Tip
r	$0.667r_m$	r_m	$1.33r_m$
c_z			
$c_{\theta 2}$			
$c_{\theta 3}$			

(c) Calculate the percentage reaction [$\Delta h_{\text{rotor}}/\Delta h_{\text{total}}$] at hub, mean, and tip radii. Note that the nozzle inlet velocity is axial, so $c_1 = c_{z1} = 120$ m/sec.

(d) What features of this design would be undesirable from boundary layer considerations?

4. An axial turbine of high hub-tip ratio runs with zero degree of reaction and peak efficiency at design flow and speed. The nozzle exit angle is 70° (from the axial direction). Estimate:

- a. The percentage change in torque accompanying a 20% drop in speed (from the design value) while operating with design mass flow;
- b. The corresponding degree of reaction.

Changes in density in the rotor may be considered negligible under design and off-design conditions. The rotor exit relative flow angle may be assumed not to vary with shaft speed.

5. An axial turbine whose hub-tip ratio is 0.57 has a flow coefficient of 0.5, a work ratio $\Delta h_0/U^2 = 1.0$, and a degree of reaction of 0.5, all at mean radius.

- a. If a free-vortex angular momentum distribution is used, determine the degree of reaction at the hub. Is there danger of pressure rise in the rotor?
- b. If a forced-vortex distribution ($c_\theta = Kr^n$) were to be adopted and the degree of reaction at the root set equal to zero, how would you determine the hub velocity triangles?

6. An axial turbine stage has an inlet temperature of 1400 K. At mid-radius, while operating at design speed and flow rate, the axial velocity ratio c_z/U is 0.5, the degree of reaction is 50% and there is no swirl in the absolute velocity leaving the rotor. The tip blade speed is 400 m/s, and the hub-tip ratio $\zeta = 0.8$.

- a. Estimate the stagnation pressure ratio for the stage.

- b. If, during off-design operation, the inlet flow conditions are unchanged but the speed increases 20%, show how the change in stagnation pressure ratio may be estimated. Assume that the rotor and stator exit flow angles are unchanged with departure from design conditions, and that the downstream axial velocity component does not change.

The turbine polytropic efficiency is 0.9, and the ratio of specific heat is 1.33.

7. An axial turbine (for one stage of a multistage turbine) is to be designed for a work ratio at the mid-radius of

$$\left(\frac{\Delta c_\theta}{U} \right)_m = 2$$

and a free-vortex swirl distribution upstream and downstream of the rotor. At the mid-radius the degree of reaction is to be 50%. The hub-tip ratio is to be 0.8, and the question is whether free-vortex blading would be satisfactory.

At the hub radius the stator exit angle α_{1h} is 70° to the axial direction.

- a. Draw the mean and hub velocity triangles (roughly to scale).
 - b. Determine the axial velocity ratio c_z/U_m .
 - c. Determine the rotor blade angles β_{2h} and β_{3h} at the hub radius.
 - d. Determine the degree of reaction at the hub radius.
8. An uncooled axial turbine stage is to be designed for a maximum stress at the blade root of 150 MPa (approximately 22,000 lb/in²), and the blade material density is 8200 kg/m³ (approximately 500 lb_m/ft³).

The rotor tip diameter is 0.75 m. Since the hub-tip ratio $\zeta = r_h/r_t$ is 0.9, conditions at mid-radius, where the degree of reaction is 50%, can be taken as a good average for the stage.

The turbine inlet pressure and temperature are 3.0 MPa and 1300 K (stagnation values), and the specific-heat ratio is 1.3.

If the outlet angle of the stator, at the mean radius, is 68° from the axial direction and the swirl component of the absolute velocity is zero at the stage exit, estimate:

- a. The blade-tip speed and shaft rpm;
 - b. The stage work (kJ/kg);
 - c. The pressure ratio;
 - d. The mass flow rate (kg/s).
9. At mid-radius an axial turbine stage is designed for 50% reaction, zero outlet swirl, and an axial velocity component of 200 m/s (uniform through the stage). The absolute flow angle at outlet from the stator is 65° from the axial direction.
- a. At the design point, what is the work done by the fluid at mid-radius on the rotor (kJ/kg)?
 - b. For no change from turbine design flow conditions, but with a 20% drop from design rotor rpm, estimate the work (kJ/kg) done by the rotor at mid-radius.

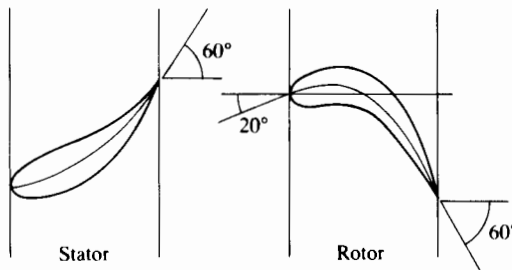
- 10.** The stator and rotor geometry of an axial turbine is shown in the accompanying sketch for a mean-radius cross section.

a. Establish the best operating values of:

- Flow coefficient $\phi = c_z/U$;
- Head or work coefficient $\psi = \Delta h_0/U^2$;
- Degree of reaction R .

b. Given that the working fluid is air entering the stator at 1200 K, estimate:

- The stage stagnation temperature drop, for a mean blade speed of 360 m/s;
- The stagnation pressure ratio of the stage.



PROBLEM 10

- 11.** The free-power turbine of an axial gas turbine is required to produce 1000 kW, operating under the following conditions:

- Tip speed limited to 400 m/s;
- Hub-tip radius ratio 0.6;
- Inlet stagnation pressure 300 kPa;
- Inlet stagnation temperature 850 K;
- Outlet static pressure 101 kPa;
- Axial exhaust direction;
- 50% reaction at mean diameter;
- Axial velocity ratio 0.5 at mean diameter;
- Same velocity triangles for all stages.

Determine:

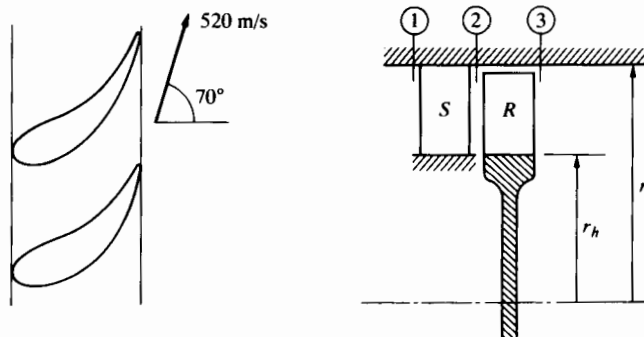
- The number of stages required;
- The rotor inlet and exit angles at the mean diameter;
- The stagnation temperature drops in rotor and stator.

The specific heat for the flow is 1187 J/kg · K and $\gamma = 1.333$.

- 12.** Air leaves the nozzle of an axial turbine with a velocity of 520 m/sec at an angle of 70° with respect to the axial direction. Find the rotor blade angles

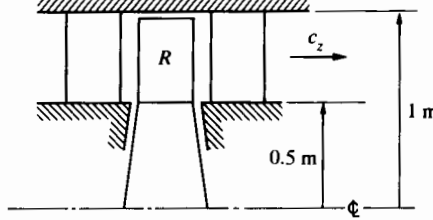
and design blade speed U such that the degree of reaction is 50% and the rotor exit swirl is zero. Assume that the blade and fluid angles are identical at inlet and outlet, respectively.

With the blade angles determined above, and the assumption that at rotor exit the relative flow angle remains equal to blade angle, show how the turbine work per unit mass varies with blade speed (i.e., at 50%, 100%, and 150% of design speed as determined above) and the same axial velocity.



PROBLEM 12

13. The flow at the exit of a turbine rotor R is swirling at "off-design" conditions. The rotor exit swirl velocity c_θ is roughly independent of radius and has a value of about 100 m/sec. The stagnation enthalpy and the entropy are also independent of radius. The gas density is approximately 1.5 kg/m^3 . Estimate:
- The static pressure difference between root and tip;
 - The axial velocity at the tip, given that it is 150 m/sec at the blade root.



PROBLEM 13

- 14.** Show that for blades whose cross-sectional area varies linearly with radius from r_h to r_t , the average centrifugal stress at the blade-hub cross section can be expressed in the form

$$\sigma = \frac{\rho_b U_t^2}{2} \left[1 - \zeta^2 + c \left(1 - \frac{\zeta^2}{3} - \frac{2}{3\zeta} \right) \right],$$

in which

$$c = \frac{\zeta \left(1 - \frac{A_h}{A_t} \right)}{1 - \zeta}.$$

Show how with taper ratios $A_h/A_t = 0.9$ or 0.8 , the dependence of the maximum blade stress on the hub-tip ratio $\zeta = r_h/r_t$ shown in Fig. 8.16 must be modified.

- 15.** As indicated in Section 8.4, the disc stress analysis calculation shown in Fig. 8.16(b) does not provide the results of an attempt to find optimum values for the geometric parameters of the disc. Using a spreadsheet (or another technique to facilitate iterative calculations), apply Eqs. (8.20) and (8.21) to see if the choices of r_i/r_h and A_i/A_0 , other than those used in the calculations for Fig. 8.16, will provide lower disc stress. Consider $B = 1$ and $0.4 < \zeta < 1.0$.
- 16.** For the control volume surrounding a single turbine rotor blade and shown in the figure, show that the tangential and axial components of blade force (per unit blade height) are given by

$$F_\theta = \rho_1 w_{z1} s (w_{\theta2} - w_{\theta1})$$

and

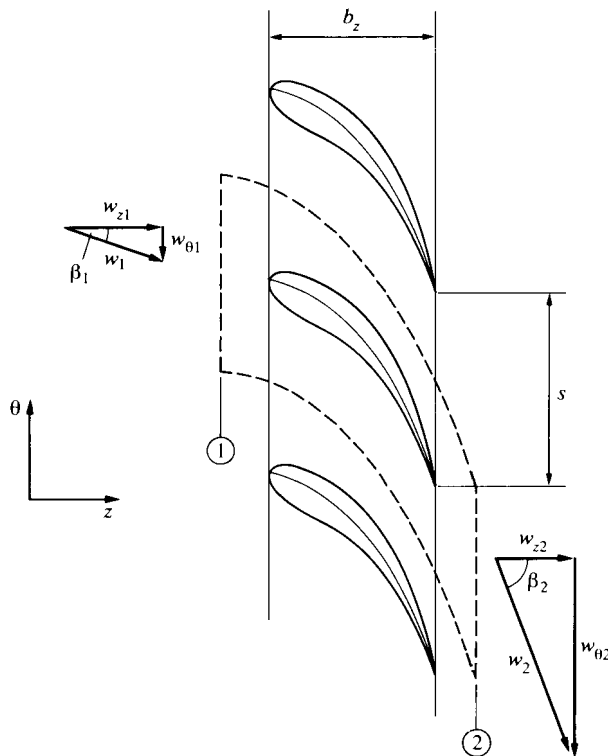
$$F_z = \rho_1 w_{z2} s (w_{z1} - w_{z2}) - s(p_1 - p_2),$$

in which s is the blade spacing and ρ_1 is the upstream density.

Defining the Zweifel coefficient as

$$Z = \frac{F_\theta}{(p_{01} - p_2)b_z},$$

show that if the flow is incompressible and $w_{z1} = w_{z2}$, the F_θ equation reduces to Eq. (8.14). If flow compressibility were allowed for, how should Eq. (8.14) be modified? Would you expect this change to be of great importance?



PROBLEM 16

17. An axial turbine stage has the hub-tip ratio of $\zeta = 0.6$. At the mean radius it has:

$$\text{Work ratio} \quad \frac{\Delta h_0}{U^2} = 1.2,$$

$$\text{Axial velocity ratio} \quad \frac{c_z}{U} = 0.6,$$

$$\text{Degree of reaction} \quad R = 0.5.$$

Two swirl distributions are being considered for the flow: One is free vortex and the other is defined by

$$rc_\theta = a(r + r_m)$$

in which r_m is the midradius.

If the stage work and stagnation conditions are radially uniform in the turbine rotor, determine the hub and tip velocity triangles for these two cases and identify the significant differences.

18. A single-stage axial turbine is designed for zero exit swirl but is called on to work at a range of flow coefficients. The mid-radius flow angle α_2 at the sta-

tor exit is specified and can be assumed to be independent of flow coefficient, as is the rotor exit relative flow angle β_3 . Show that the difference between off-design and design values of the work coefficient can be related to the flow coefficient and the nozzle (stator) flow angle by

$$\frac{\Delta h_0}{U^2} = \frac{c_z}{U} \left[\frac{\left(\frac{\Delta h_0}{U^2} \right)_{\text{design}}}{\left(\frac{c_z}{U} \right)_{\text{design}}} + \tan \beta_3 \right] - 1.$$

Regarding exit swirl kinetic energy as a loss, show how the loss ratio defined by

$$\zeta = \frac{c_{\theta 3}^2}{2 \Delta h_0}$$

varies with flow coefficient and β_3 for given values of $(\Delta h_0/U^2)_{\text{design}}$ and $(c_z/U)_{\text{design}}$.

19. A free-vortex axial turbine stage is being designed for zero exit swirl. Preliminary design calculations carried out as outlined in Section 8.8 have produced the following results in which R_h is the degree of reaction at the hub radius and twist is the absolute difference between hub and tip values of $(\beta_1 - \beta_2)$. Check whether these results are correct. The stage efficiency is $\eta_u = 0.9$ and $\gamma = 1.33$.

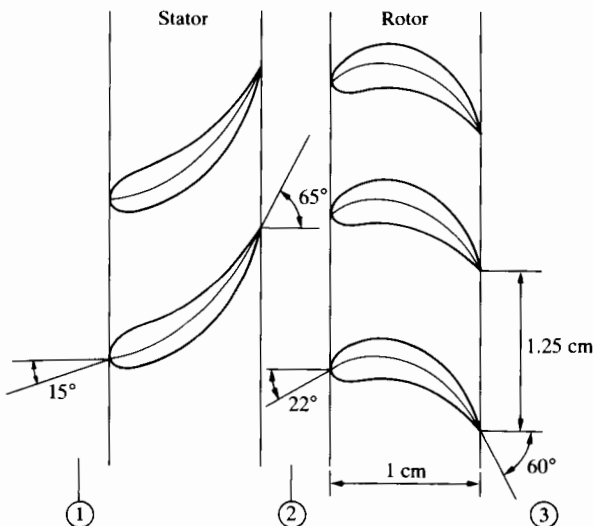
$\frac{\sigma}{\rho_b a_{01}^2}$	ζ	$\frac{\Delta h_0}{U_m^2}$	$\frac{c_z}{U_m}$	$\frac{p_{01}}{p_{02}}$	$\frac{\dot{m} \sqrt{RT_{01}}}{p_{01} D^2}$	$\frac{U_t}{a_{01}}$	R_h	Twist
0.04	0.8	1	0.5	1.316	0.0617	0.471	0.367	26.65
0.04	0.9	1	0.5	1.834	0.0415	0.649	0.443	13.11
0.03	0.8	1	0.5	1.228	0.0550	0.408	0.367	26.65
0.03	0.9	1	0.5	1.562	0.0383	0.562	0.443	13.11
0.02	0.8	1	0.5	1.145	0.0443	0.333	0.367	26.65
0.02	0.9	1	0.5	1.338	0.0333	0.459	0.443	13.11

20. In one stage of a multistage gas turbine, the blades have the mean-radius cross sections shown in the sketch.

The mean radius is 30 cm and the rotor blade height is 6 cm. At inlet to the stage the stagnation pressure and temperature are 1900 kPa and 1200 K, respectively. The absolute velocity leaving the stator is 600 m/s.

- Estimate the rotor rpm corresponding to best efficiency.
For that rotor speed determine:
- The stage pressure ratio;
- The tangential component of the aerodynamic force (per unit blade height) applied to one rotor blade at the mean radius.

The specific heat ratio of the gas is 1.33, and the gas constant is $R = 0.29 \text{ kJ/kg} \cdot \text{K}$. The axial velocity ratio c_z/U may be taken to be constant through the stage. Losses may be neglected.



PROBLEM 20

21. An aft-fan turbofan has the overall dimensions and main gas generator flow at sea-level static operation indicated in the figure. Stress limitations set the revolutions per minute of this assembly at 10,300 rpm. Since the original was designed, improvements in compressor blading allow fan operation at a maximum inlet absolute Mach number of 0.6 and a pressure ratio of 1.5.

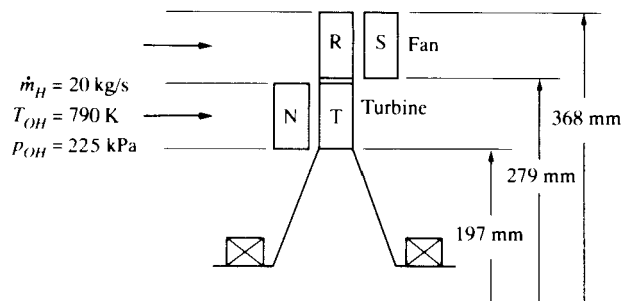
For economic reasons it is not feasible to change the radial dimensions of this element, but we wish to see what performance advantages can be gained by modifying blade shapes.

Make a preliminary design for this machine, to the extent of specifying hub, tip, and mean velocity triangles for the fan, and the mean-radius velocity triangle for the turbine. Sketch rough blade shapes (including stator and nozzle) for each velocity triangle. You may use some or all of the following design assumptions.

- (a) Constant work from hub to tip of fan.
- (b) No inlet guide vanes on fan.
- (c) Axial outlet for fan and turbine.
- (d) Constant axial velocity in fan and in turbine.
- (e) Isentropic diffuser at fan inlet (*Note:* Compressor inlet velocity, density, and area determine fan flow rate and hence power and turbine power.)
- (f) Ambient conditions: $p_{\text{atm}} = 100 \text{ kPa}$, $T_{\text{atm}} = 15^\circ\text{C}$, engine not moving.
- (g) You may use $R = 0.290 \text{ kJ/kg} \cdot \text{K}$ and $c_p = 1.1 \text{ kJ/kg} \cdot \text{K}$ for both hot- and cold-gas streams.

Check the pressure coefficient at the hub and tip of both rotor and stator.

If the turbine efficiency is assumed 0.90, what is the hot-gas exhaust velocity for an isentropic hot-exhaust nozzle? If the fan efficiency is 0.85, what is the cold-gas exhaust velocity for an isentropic cold-gas nozzle?

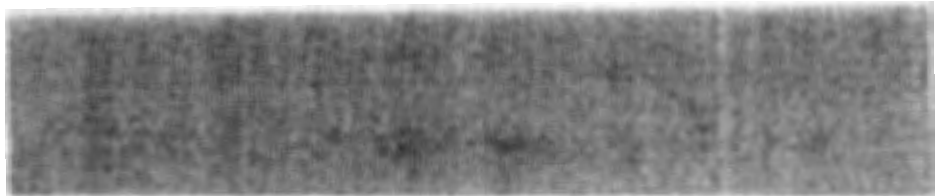


PROBLEM 21

REFERENCES

1. Kacker, S. C., and U. Okapuu. "A Mean Line Prediction Method for Axial Flow Turbine Efficiency," *Trans. ASME J. Eng. for Power* 104 (1982): 111–119.
2. Smith, S. F. "A Simple Correlation of Turbine Efficiency," *J. of Royal Aeronautical Soc.* 69 (1965): 467–470.
3. Moustapha, S. H., U. Okapuu, and R. G. Williamson. "Influence of Rotor Blade Loading on Aerodynamic Performance of a Highly Loaded Turbine Stage," *ASME J. Turbomachinery* 109 (1987): 155–162.
4. Horlock, J. H. *Axial Flow Turbines: Fluid Mechanics and Thermodynamics*. London: Butterworths, 1966.
5. Denton, J. D. "A Survey of Comparison of Methods for Predicting the Profile Loss of Turbine Blades," in *Heat and Fluid Flow in Steam and Gas Turbine Power Plant*. Inst. Mech. Engrs., (1973).
6. Gregory-Smith, D. G. "Secondary Flows and Losses in Axial Flow Turbines," *Trans. ASME Series A, J. Eng. for Power* 104 (1982): 819–823.
7. Sieverding, C. H. "Axial Performance Prediction Methods," in *Thermodynamics and Fluid Mechanics of Turbomachinery*, A. S. Ucer, P. Stow, and C. Hirsch, eds. Dordrecht: Martinus Nijhoff, 1985.
8. Dunham, J., and P. M. Came. "Improvements to the Ainley-Mathieson Method of Turbine Performance Prediction," *Trans. ASME J. Eng. for Power* (1970): 252–256.
9. Denton, J. D. and N. A. Cumpsty. "Loss Mechanisms in Turbomachines," *Proc. I. Mech. E. Int. Conf. on Turbomachinery*, Cambridge, Sept. 1–3, 1987.
10. Immarigeon, J.-P. "The Super Alloys: Materials for Gas Turbine Hot Section Components," *Canadian Aeronautics and Space Institute Journal* 27 (1981): 336–354. Reprinted with permission.

11. Glenny, R. J. E., J. E. Northwood, and A. Burwood-Smith. "Materials for Gas Turbines," *Int. Met. Rev.* 20, (1975): 1-28.
12. Allen, J. M. "Effect of Temperature Dependent Mechanical Properties on Thermal Stress in Cooled Turbine Blades," *Trans. ASME J. Eng. for Gas Turbines and Power* 104 (1982): 345-353.
13. Eckert, E. R. G. "Analysis of Film Cooling and Full Coverage Film Cooling of Turbine Blades," *Trans. ASME J. Eng. for Gas Turbines and Power* 106 (1984): 206-213.
14. Kerrbrock, J. C. *Aircraft Engines and Gas Turbines*. Cambridge, Mass.: M.I.T. Press, 1977.
15. El-Masri, M. A. "On Thermodynamics of Gas Turbine Cycles," pt. 2, *ASME J. Eng. for Gas Turbines and Power*, 108 (1986): 151-159.
16. Denton, J. D. "An Improved Time Marching Method for Turbomachinery Calculations," *J. Eng. for Power* 105 (1983): 514-525.
17. _____. "Solution of the Euler Equation for Turbomachinery Flows," pts. 1 and 2, in *Thermodynamics and Fluid Mechanics of Turbomachinery*, vol. 1, A. S. Ucer, P. Stow, and C. Hirsch, eds. Dordrecht: Martinus Nijhoff, 1985.



C H A P T E R

9

THE CENTRIFUGAL COMPRESSOR

9.1 INTRODUCTION

The first two independently developed jet engines each employed a centrifugal compressor. At the time they were developed (1935–1940), the centrifugal machine was the only type of compressor sufficiently ready for application. Since that time the axial compressor has completely replaced the centrifugal one in large gas turbines, though the latter is widely used in small gas turbines.

For large turbojet or turbofan engines, the axial compressor has the great advantage of smaller cross-sectional area per unit airflow rate. The overall cross-sectional area of the axial machine may be only half or one-third that of the centrifugal machine. This means that the aerodynamic drag on the nacelle housing the engine would be much affected by whether the compressor was axial or centrifugal. The axial compressor may be said to be more amenable to multistaging and thus to the large overall pressure ratios typically needed for large engines. In addition to the foregoing advantages, the large multistage axial compressor is typically more efficient (perhaps 4% to 5%) than its centrifugal counterpart. Thus there are important reasons why the axial compressor is used, exclusively, in large engines.

For “small” gas turbines used to drive propellers or helicopter rotors and for small turbojet engines, overall diameter may not be such an important consideration as for large engines (though engine weight is still a factor of great importance). Also there are aerodynamic reasons why in small sizes the centrifugal compressor may be at least as efficient as its axial counterpart. Turboprop or

turboshaft engines are usually in the less-than-10,000-horsepower range and have optimum engine compressor ratios in the range 15:1 to 25:1. Under these conditions, if an axial compressor were used, the blade height at the back end of the compressor might be so small that tip leakage and other effects would seriously reduce efficiency. At the same mass flow rate and exit air density, the centrifugal compressor does not suffer so badly from reduced passage size. The reason for this is partly that fewer stages are necessary and partly that the mechanism of pressure rise is different. In the centrifugal rotor the pressure rises not because of deceleration within the flow passage but because of displacement in the centrifugal force field.

Figure 9.1 shows the compressor of the PW100 engine developed by Pratt & Whitney in recent years following the success of the PT6 engine. The PW100 has a power level of around 2000 hp (in early versions) and has a compressor pressure ratio of 15:1, produced by two centrifugal stages in series (see Fig. 5.38). Relative to a multistage axial compressor of the same flow rate, it has higher efficiency, shorter axial length, and about the same weight, with separate low- and high-speed compressor shafts it does not need variable geometry or to allow the engine to be started.

In small gas turbines, one may find axial and centrifugal stages together, as shown in Fig. 9.2. The axial stages handle the low-density air; the centrifugal stage at the end generates a relatively large pressure ratio. Another example of an axial-centrifugal compressor is the Pratt & Whitney PT6 engine shown in Fig. 5.37.

In recent years designers have made great progress in raising the stage pressure ratio and in improving the efficiency of centrifugal compressors. Single-stage centrifugal compressors have been built [2] with pressure ratios of 5:1 (and adiabatic efficiencies of 85%) and even 10:1 (with adiabatic efficiencies exceeding 80%).

These achievements have required major advances in both aerodynamic and mechanical design. Rotor tip speeds are now as high as 650 m/s, so that the ve-

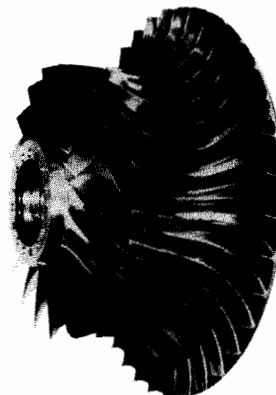


FIGURE 9.1 Low-pressure compressor of the Pratt & Whitney Canada PW100 engine.
(Courtesy Pratt & Whitney Canada, Inc.)

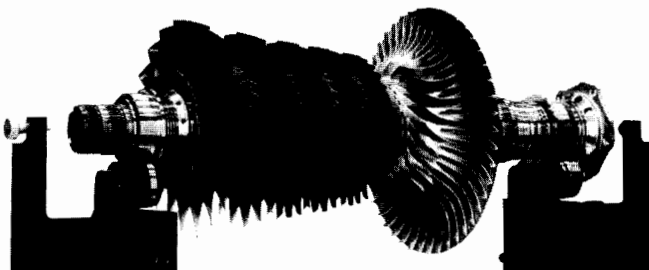


FIGURE 9.2 Axial-centrifugal compressor of the General Electric T700 engine. (Courtesy GE Aircraft Engines.)

locity at the rotor exit is definitely supersonic; means have had to be found for decelerating this supersonic flow without excessive shock-induced or other losses.

9.2 CENTRIFUGAL COMPRESSOR STAGE DYNAMICS

Figure 9.3 shows a common type of centrifugal compressor. The velocity of the air leaving this impeller, in contrast to that of the air leaving the axial impeller or rotor, has no axial component. Fluid enters the impeller through the inducer, whose function is to turn the relative flow as it enters the impeller passages. At the impeller exit, the blades shown in Fig. 9.3 are straight and in the radial direction. After leaving the impeller, the air passes through a radial diffuser, consisting of vaned flow passages in which momentum is exchanged for pressure. Radial diffusers may consist of a vaneless portion, as shown, followed by a series of stator vanes. The air leaving the diffuser is collected and delivered to the outlet. Figure 9.3 is not characteristic of all centrifugal compressors, and subsequently we will discuss different design features. This compressor is adequate, however, for an introduction to the working principle of the centrifugal machine.

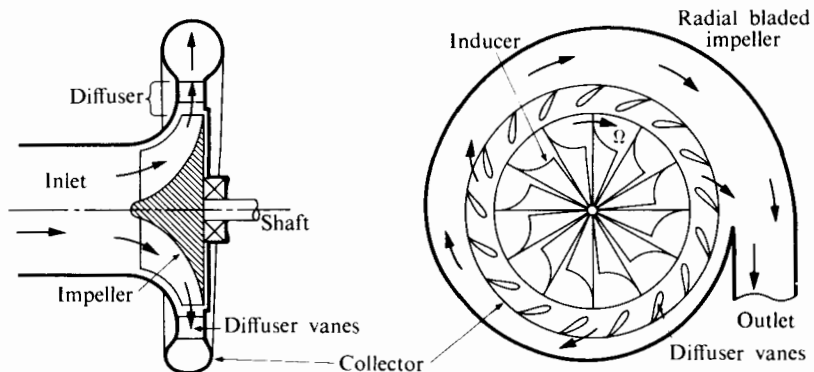


FIGURE 9.3 Typical centrifugal compressor.

To understand the comparative features of centrifugal and axial compressor stages, it is helpful to consider the energy equation for a streamline passing through the rotor.

As shown in Eq. (7.8), the sum of the torques applied to a control volume surrounding a single compressor rotor is

$$\sum \tau = \dot{m}[(rc_\theta)_2 - (rc_\theta)_1],$$

where subscripts 1 and 2 denote the compressor inlet and outlet, respectively. The $\sum \tau$ term will be nearly equal to the torque τ_s applied by the shaft to the rotor, so that we can express the total work per unit mass done by the rotor on the air as

$$w = \Omega\tau_s/\dot{m} = \Omega(rc_\theta)_2 - \Omega(rc_\theta)_1$$

or

$$w = (Uc_\theta)_2 - (Uc_\theta)_1, \quad (9.1)$$

in which $U = \Omega r$ and Ω is the rotational speed of the shaft. While it is true that not all streamlines passing through a given rotor may undergo the same change of angular momentum, we can think of Eq. (9.1) as applying to a given streamline.

For steady-flow adiabatic compression, the control-volume energy equation (Eq. 2.8) shows us that if gravitational and other body forces are unimportant, the work done on the fluid equals the stagnation enthalpy increase. Thus

$$w = h_{02} - h_{01} = h_2 - h_1 + \frac{c_2^2}{2} - \frac{c_1^2}{2},$$

and therefore we may write Eq. (9.1) as

$$h_2 - h_1 = (Uc_\theta)_2 - (Uc_\theta)_1 - \frac{c_2^2}{2} + \frac{c_1^2}{2}. \quad (9.2)$$

But now we move to a reference frame fixed to the rotor and, using the notation of Chapters 7 and 8 for absolute and relative velocities, we write:

$$c_\theta = U + w_\theta,$$

$$c_r = w_r,$$

$$c_z = w_z,$$

$$c^2 = c_r^2 + c_\theta^2 + c_z^2,$$

$$w^2 = w_r^2 + w_\theta^2 + w_z^2.$$

Here, with centrifugal compressors in mind, we definitely do not neglect c_r^2 relative to c_θ^2 or c_z^2 . By using these relationships (and adding and subtracting terms), we can transform Eq. (9.2) to read

$$h_2 - h_1 = \frac{U_2^2}{2} - \frac{U_1^2}{2} - \left(\frac{w_2^2}{2} - \frac{w_1^2}{2} \right),$$

which we could call the energy equation for a reference frame fixed to the rotor (and applying to a streamline observed in that coordinate system). For an incremental change along a streamline, we can write

$$dh = d\left(\frac{\Omega^2 r^2}{2}\right) - \frac{dw^2}{2}. \quad (9.3)$$

Bringing in the state equation again ($Tds = dh - dp/\rho$) allows us to write

$$\frac{dp}{\rho} = d\left(\frac{\Omega^2 r^2}{2}\right) - \frac{dw^2}{2} - Tds$$

or, for isentropic flow,

$$\frac{dp}{\rho} = d\left(\frac{\Omega^2 r^2}{2}\right) - d\left(\frac{w^2}{2}\right). \quad (9.4)$$

For axial compressors, $dr \approx 0$ along a streamline, and Eq. (9.4) reverts to $dp/\rho = -d(w^2/2)$. Thus in an axial compressor rotor, one can obtain pressure rise only by decelerating the flow; the rotor (and the stator) flow passages act like diffusers. In the centrifugal compressor the term $d(\Omega^2 r^2/2)$ being greater than zero means that pressure rise could develop in the rotor even if there were no change in the relative velocity w . With no change in w , the rising pressure field would not be liable to cause boundary layer separation, because it would not affect the relative velocities of boundary layer and free-stream fluid. Of course, one could design the centrifugal rotor with decelerating w , and there is, as we will see, another reason also why boundary layer separation can occur in such rotors. Nevertheless, the centrifugal rotor is not essentially limited by separation the way the axial one is. Consequently much higher stage pressure ratios are possible than with axial compressor stages.

To examine the mechanism of pressure development in a centrifugal compressor, we first consider the work done in the rotor of Fig. 9.4. For simplicity we assume that the angular momentum of the incoming fluid, (rc_θ), is the same for all streamlines. Many centrifugal compressors have swirl-free inlet flow, but others have swirl at entrance that is due to a compressor stage upstream or to inlet

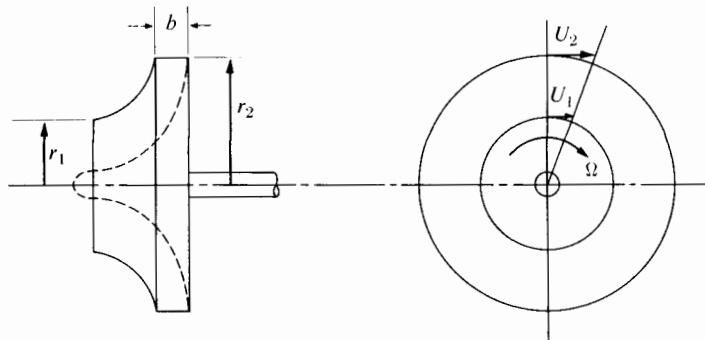


FIGURE 9.4 Centrifugal compressor rotor.

guide vanes placed just before the rotor entrance. With swirl uniform upstream and downstream, we can write Eq. (9.1) as $w = c_p(T_{02} - T_{01}) = U_2 c_{\theta 2} - U_1 c_{\theta 1}$, in which T_{01} and T_{02} are the stagnation temperatures at entrance to and exit from the rotor. If we divide by $c_p T_{01}$, this equation becomes

$$\frac{T_{02} - T_{01}}{T_{01}} = (\gamma - 1) \left(\frac{U_2}{a_{01}} \right)^2 \left[\frac{c_{\theta 2}}{U_2} - \frac{(U c_{\theta})_1}{U_2^2} \right], \quad (9.5)$$

in which $a_{01} = \sqrt{\gamma R T_{01}}$, the speed of sound at the inlet stagnation temperature. In principle, the blading of a centrifugal compressor rotor may be any one of the three types shown in Fig. 9.5: straight radial, as in Fig. 9.3; backward leaning; or forward leaning. Figure 9.5 shows the three types schematically, together with typical velocity triangles in the radial plane for the outlet of each type. The three rotors are shown with the same tip speed U_2 and the same radial velocity component $w_r = c_r$. As a first approximation, the *relative* fluid velocity leaving the impeller, w_2 , is assumed parallel to the blade. The angle of the blade at exit with respect to the radial direction is given the symbol β_2 and is positive for a backward leaning blade. Because the rotor speed U is entirely tangential, the radial components of relative and absolute velocity, w_r and c_r , respectively, are equal.

For the typical machine with purely axial inlet velocity—that is, $c_{\theta 1} = 0$ —Eq. (9.5) becomes

$$\frac{T_{02} - T_{01}}{T_{01}} = (\gamma - 1) \left(\frac{U_2}{a_{01}} \right)^2 \frac{c_{\theta 2}}{U_2}.$$

Since, for all three impellers, $c_{\theta 2} = U_2 - w_{r2} \tan \beta_2$, then

$$\frac{T_{02} - T_{01}}{T_{01}} = (\gamma - 1) \left(\frac{U_2}{a_{01}} \right)^2 \left(1 - \frac{w_{r2}}{U_2} \tan \beta_2 \right). \quad (9.6)$$

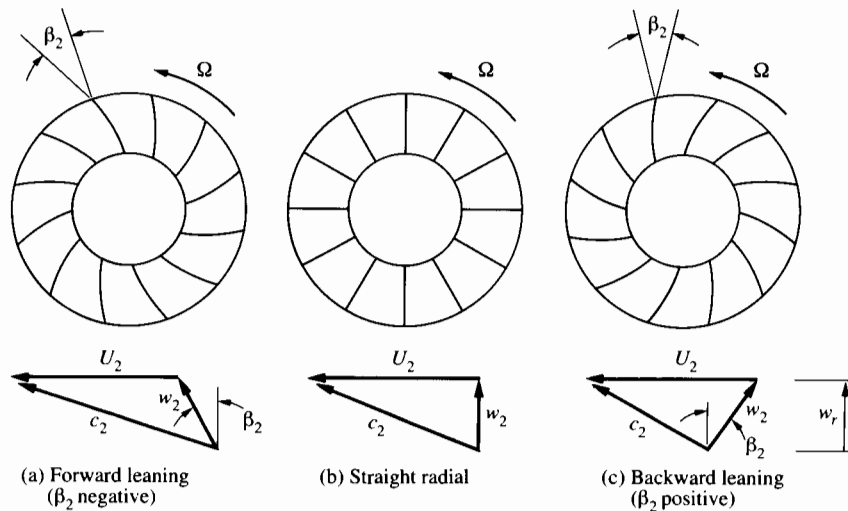


FIGURE 9.5 Shapes of centrifugal impeller blades and outlet velocity triangles.

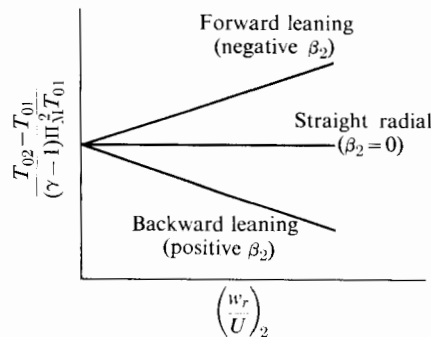


FIGURE 9.6 Relative temperature rise characteristics of centrifugal compressors.

From continuity we see that

$$w_{r2} = \frac{\dot{m}}{2\pi r_2 b \rho_2}, \quad (9.7)$$

where b is the blade height at exit and ρ_2 is the exit density.

For any fixed inlet condition and tip speed, these expressions state that the three machines would produce the same stagnation temperature rise at zero mass flow rate.[†] For an increase in mass flow the stagnation temperature rise will decrease for backward-leaning blades, remain constant for straight radial blades, and increase for forward-leaning blades. Figure 9.6 shows these characteristics graphically.

For the centrifugal compressor with no swirl in the entering fluid, the ratio $(w_r/U)_2$ has the same significance as the ratio (c_z/U) for the axial compressor. In both cases the relative stage temperature rise is a linear function of this variable, which we could refer to as a flow coefficient because it is directly proportional to the mass flow rate and inversely proportional to shaft speed.

At the same mass flow rate and tip speed U_2 , the rotor with forward-leaning blades will do more work on the fluid and might at first sight be expected to produce higher pressure rise than one could obtain with, for example, the straight radial compressor. The problem is that its output pressure tends to rise with mass flow rate. As the analysis of Section 7.5 shows (valid for both centrifugal and axial compressors), a positive slope on such a curve is generally associated with dynamic instability. For this reason forward-leaning blades are never used in centrifugal compressors for aircraft engines.

Comparing radial-blade and backward-leaning-blade rotors, we note that the former is capable of greater pressure rise at a given tip speed but has higher Mach number in the air entering the diffuser. Because of the centrifugal bending-stress problem associated with backward-leaning blades, high-speed centrifugal

[†] Actually, small flow rates are characterized by surging instability; the simple assumptions of this analysis hold only at flow rates reasonably near the design flow rate.

compressors were designed for many years with straight radial blades at exit. If the stage pressure exceeds about 4:1, however, the absolute velocity of the air leaving the impeller becomes supersonic, and the higher the pressure ratio, the more difficult it is to design an efficient diffuser. For this reason, and to improve the flow in the outer part of the rotor, modern centrifugal compressor designs have blades leaning back from the radial direction as much as 30° or so. In spite of the extra bending stresses this may entail, materials and designs have evolved that have permitted greatly increased tip speeds as well. Cumpsty [3] shows that the effect of backsweep can actually be obtained in an impeller in which the outlet blade geometry consists of radial line elements and thus entails no additional bending stress. The characteristic feature of this impeller is that if one draws a cross section of the blade in the tangent ($z-\theta$) plane at the blade exit, one sees that the blade has a definite angle (the "lean" angle) away from the axial direction and against the direction of rotation. This imparts an extra three-dimensional effect to the flow field that on average across the impeller outlet plane creates the effect of backsweep. This development therefore means that backsweep does not necessarily imply a stress penalty.

It is interesting at this point to estimate the effect of exit blade angle and flow coefficient (w_r/U)₂ on centrifugal compressor performance. With the same definition of stage adiabatic efficiency as we used for axial machines, we can write that the overall stagnation pressure ratio for the stage is

$$\frac{P_{03}}{P_{01}} = \left[1 + \eta_c \left(\frac{T_{03} - T_{01}}{T_{01}} \right) \right]^{\gamma/(\gamma-1)},$$

in which the subscript 03 denotes the diffuser exit stagnation state. But with adiabatic flow in the diffuser, we can therefore use $T_{03} = T_{02}$ and Eq. (9.6) with the above equation to produce this result:

$$\frac{P_{03}}{P_{02}} = \left[1 + \eta_c (\gamma - 1) \left(\frac{U_2}{a_{01}} \right)^2 \left(1 - \frac{w_{r2}}{U_2} \tan \beta_2 \right) \right]^{\gamma/(\gamma-1)}. \quad (9.8)$$

We can write the absolute Mach number M_2 at the exit of the impeller (with reference to Fig. 9.5) as

$$M_2 = \frac{c_2}{a_2}. \quad (9.9)$$

We can obtain the absolute exit velocity c_2 (see Fig. 9.5) from

$$c_2^2 = (U_2 - w_{r2} \tan \beta_2)^2 + w_{r2}^2. \quad (9.10)$$

The speed of sound at the rotor exit is given by

$$a_2^2 = \gamma R T_2 = a_{01}^2 \frac{T_{02}}{T_{01}} \left/ \left(1 + \frac{\gamma - 1}{2} M_2^2 \right) \right., \quad (9.11)$$

in which $a_{01}^2 = \gamma R T_{01}$ and, from Eq. (9.6),

$$\frac{T_{02}}{T_{01}} = 1 + (\gamma - 1) \frac{U_2^2}{a_{01}^2} \left(1 - \frac{w_{r2}}{U_2} \tan \beta_2 \right). \quad (9.12)$$

Combination of Eqs. (9.8) to (9.12) yields the useful result

$$M_2 = \sqrt{\frac{A}{1 - \frac{\gamma - 1}{2} A}}, \quad (9.13)$$

in which

$$A = \left(\frac{U_2}{a_{01}}\right)^2 \frac{\left[\left(1 - \frac{w_{r2}}{U_2} \tan \beta_2\right)^2 + \left(\frac{w_{r2}}{U_2}\right)^2\right]}{\left[1 + (\gamma - 1) \left(\frac{U_2}{a_0}\right)^2 \left(1 - \frac{w_{r2}}{U_2} \tan \beta_2\right)\right]}.$$

Based on Eqs. (9.8) and (9.13), Figs. 9.7 and 9.8 display the dependence of stage pressure ratio and exit Mach number M_2 on the rotor exit blade angle β_2 and on the flow coefficient w_{r2}/U_2 for a stage whose overall adiabatic efficiency is 85%.

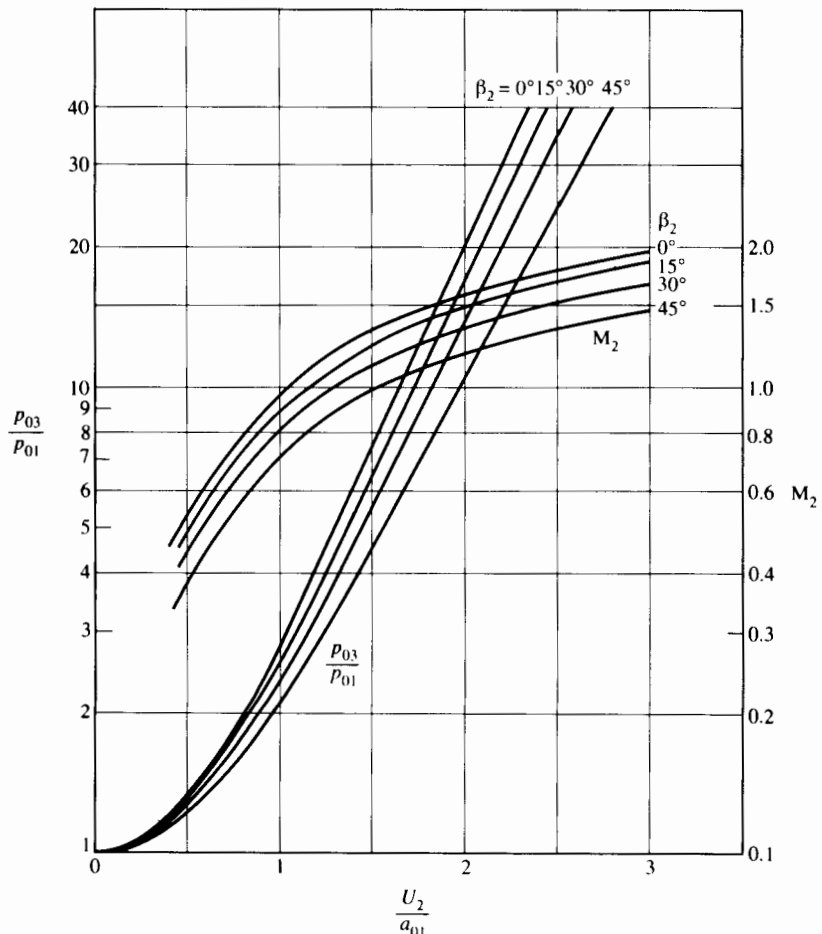


FIGURE 9.7 Centrifugal compressor stage; $\eta_c = 0.85$, $w_{r2}/U_2 = 0.30$.

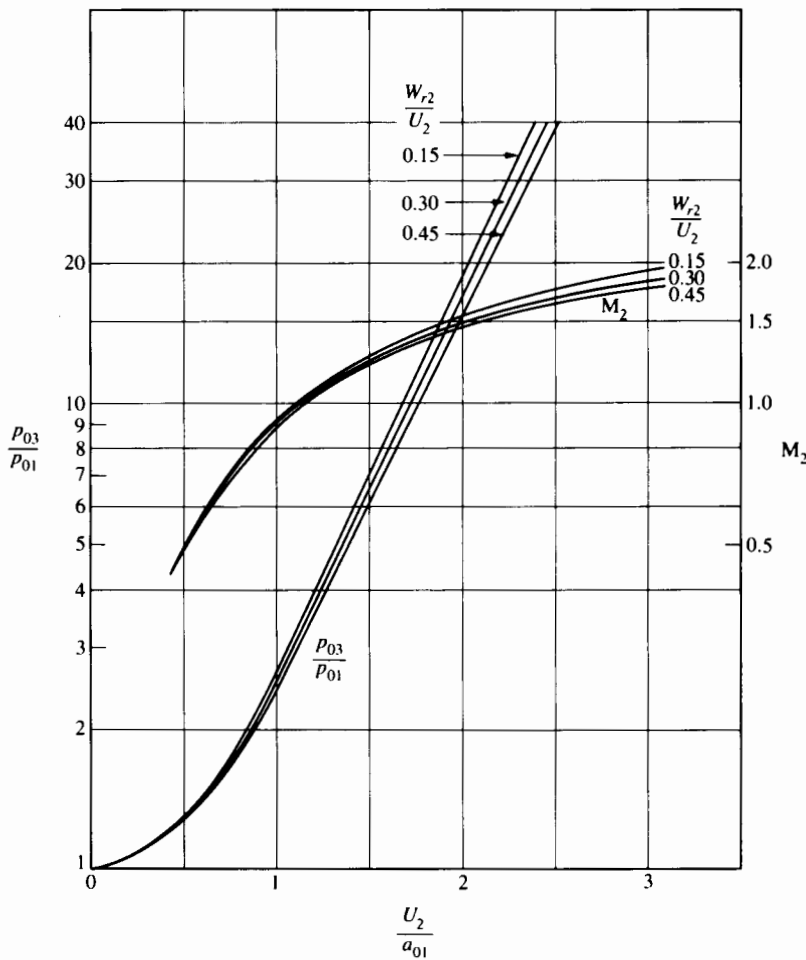


FIGURE 9.8 Centrifugal compressor stage; $\eta_c = 0.85$, $\beta_2 = 15^\circ$.

The discussion of centrifugal stresses in Chapter 8 led to the conclusion that peak stress in a rotor of any geometry will be proportional to the square of tip speed. Taking 650 m/s as a stress-limited tip speed (achievable only with a material that, like titanium, has an exceptionally high strength-to-density ratio) and taking inlet air at 300 K, we find that the maximum currently allowable value of U_t/a_{01} would be under 2.

Figure 9.7 shows that, for all cases calculated, the flow at entrance to the diffuser is supersonic for overall stagnation pressure ratios greater than 4.6. For the stress-limited case mentioned above, the pressure ratio could be as high as 20, with $\beta_2 = 0$, but this would mean a diffuser entrance Mach number of 1.6. Because of the possibility of shock-induced irreversibilities, it would be difficult (to put it mildly) to develop an efficient diffuser for this case. Increasing the

blade exit angle β_2 to, say, 45° helps (but for stress reasons one may have to purchase the benefit with a reduction in U_2); reducing the exit flow coefficient w_{r2}/U_2 helps very little, as Fig. 9.8 shows.

The main point shown by Figs. 9.7 and 9.8 is that the centrifugal compressor stage is only able to achieve a high overall pressure ratio by placing a very heavy demand on the diffuser for efficient, partly supersonic operation. For the cases in which M_2 is strongly supersonic, it may be very difficult to achieve an overall adiabatic efficiency of 85%. We will have more to say later about diffuser design innovations to meet such a demand. We turn now to the design of the rotor.

9.3 THE INDUCER AND IMPELLER

The inducer is the impeller entrance section, in which the tangential motion of the fluid is changed with little or no acceleration in the radial direction. This part of the impeller acts essentially as though it were part of an axial compressor rotor, and one may understand its design with the aid of ideas similar to those we discussed in Chapter 7. It is in the remainder of the impeller that the radial component of the velocity is much stronger than the axial one.

So that the flow may enter the impeller smoothly, it is essential to install an inducer. Centrifugal fans that do not have inducers are usually very noisy because of flow separation and fairly violent mixing near the leading edge of the impeller vane. Figure 9.9 shows velocity triangles for an axial flow entering a centrifugal impeller, showing the flow angles for root, mean, and tip radii. Here we may note that at the impeller tip the angle between the relative velocity vector and the flow may be very large. Thus, near the tip, the vane needs to be set at an angle large

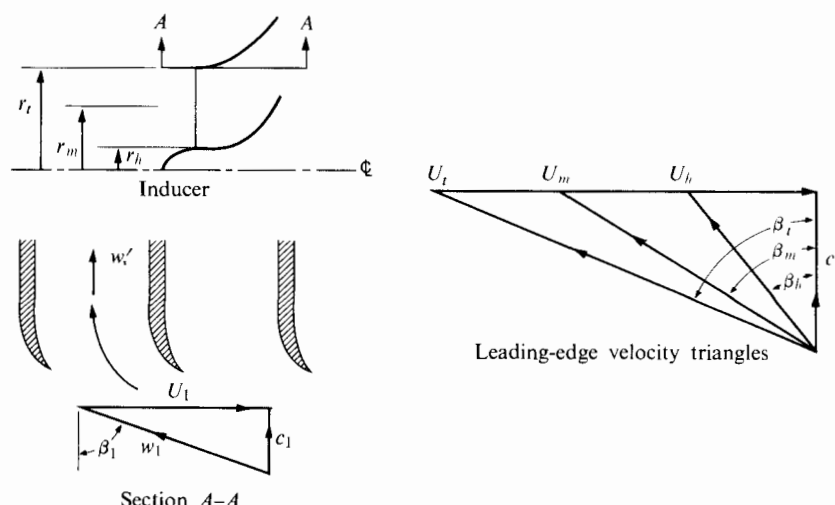


FIGURE 9.9 Diagram of inducer inlet velocity.

with respect to the axial direction if the flow is to enter the inducer without leading-edge separation. There is, however, a limit to the amount of turning that can occur within the inducer, if one is to avoid separation on the curved inducer surface.

If we assume that the inducer accomplishes the turning of the relative velocity vector without a change in radius, then we can show these velocities in a cylindrical section of radius r_1 , presented "unwrapped" in Fig. 9.9. If there is no radial velocity component in the inducer, continuity for incompressible flow requires that the axial component of velocity remains constant. Thus, at the tip radius,

$$w'_t = w_{1t} \cos \beta_{1t},$$

where w' denotes the relative velocity at the inducer outlet. The fact that $w' < w_1$ indicates diffusion in the inducer. In order to estimate the maximum permissible turning angle that would not produce separation on the inducer surface, it is necessary to know the pressure coefficient $C_{p\max}$ corresponding to separation. As defined previously, the pressure coefficient is

$$C_p = \frac{p' - p_1}{\frac{1}{2} \rho w_1^2} = 1 - \left(\frac{w'}{w_1} \right)^2.$$

Then the maximum turning angle is given by

$$\cos \beta_1 = \sqrt{1 - C_{p\max}}. \quad (9.14)$$

If $C_{p\max}$ is again taken to be 0.6, as seems reasonable for turbulent boundary layers, then the maximum turning angle is around 50° . Unfortunately, however, the behavior of the turbulent boundary layer can be markedly affected by the curvature of the surface over which it is traveling, and it may separate earlier on a curved surface than on a flat one for the same variation of pressure with distance in the flow direction.

The inducer is also subject to the effects of compressibility. At high Mach numbers a shock may appear near the tip and cause the performance to deteriorate, as is the case for the axial compressor stage. The question of how high the inlet Mach number may be without excessive flow deterioration in the rotor has been the subject of much work in recent years. The question is of great practical importance since, as we will see, the size of machine necessary to handle a given flow rate (and develop a certain pressure ratio) depends strongly on the allowable Mach number relative to the tip of the inducer blade at inlet.

For a long time the assumption was that one should avoid supersonic flow in the rotor. However, improved methods of flow analysis have assisted in the development of transonic flow designs. Kenny [2] describes a rotor with an inducer inlet tip relative Mach number of 1.48 that operated with a stage pressure ratio of 12:1 (and an overall efficiency of 75%). For that rotor Fig. 9.10 shows the calculated lines of constant relative Mach number inside the inducer flow passages with the tip relative Mach number being about 1.3. The tip-radius blade angle is 60° .

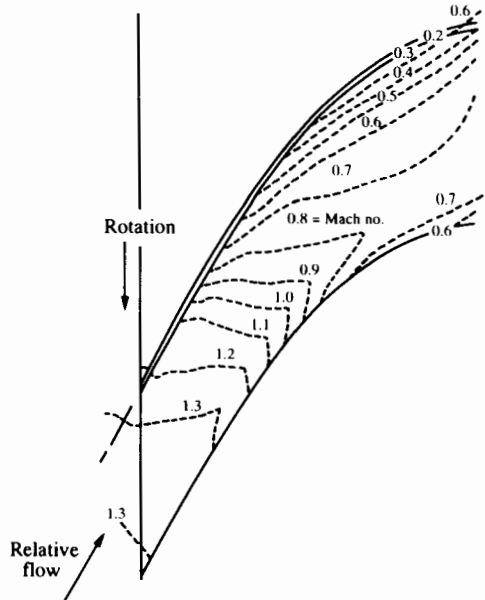


FIGURE 9.10 Lines of constant relative Mach number in a transonic inducer. (From Kenny [2].)

To show the effect of variations of inlet tip-radius blade angle and relative Mach number on impeller design, we perform sample calculations for the inlet of a centrifugal compressor that ingests 5 kg/s of air with inlet stagnation conditions of 100 kPa and 300 K. Bearing in mind manufacturing considerations and the room required to accommodate the compressor driving shaft, we assume a hub diameter of 0.1 m. We have in mind a transonic inducer inlet and decide to do without inlet guide vanes (more on this subject in Section 9.6). The incoming flow will then have zero swirl; with adequate intake design the axial velocity approaching the rotor will be uniform.

It is possible to operate inducers at such high inlet (axial) Mach numbers that the density of the air in the inlet plane is substantially lower than the stagnation density. To make matters easy in exploring the design possibilities for our inducer, we could begin by choosing a series of inlet Mach numbers M_1 and a series of inlet tip-radius blade angles β_{1t} .

Given the absolute Mach number M_1 of the entering flow, we can calculate the relative Mach number from

$$M_{1\text{rel}} = M_1 / \cos \beta_{1t}. \quad (9.15)$$

We obtain the inlet temperature T_1 , density ρ_1 , and velocity c_1 from

$$T_1 = T_{01} \left/ \left(1 + \frac{\gamma - 1}{2} M_1^2 \right) \right., \quad (9.16)$$

$$\rho_1 = \rho_{01} \left(1 + \frac{\gamma - 1}{2} M_1^2 \right)^{1/(\gamma-1)}, \quad (9.17)$$

$$c_1 = M_1 \sqrt{\gamma R T_1}. \quad (9.18)$$

Then we can find the blade-tip velocity at the inducer inlet plane from

$$U_{1t} = c_1 \tan \beta_{1t} \quad (9.19)$$

and the inlet-tip diameter from

$$D_{1t} = \sqrt{D_n^2 + \frac{4}{\pi} \frac{\dot{m}}{\rho_1 c_1}}. \quad (9.20)$$

Finally we obtain the shaft rpm from

$$N = \frac{60}{\pi} \frac{U_{1t}}{D_{1t}}. \quad (9.21)$$

For the conditions of our example with $D_h = 0.1$ m, $T_{01} = 300$ K, $p_{01} = 100$ kPa, and an airflow rate of 5 kg/s, the calculated variation of shaft speed N with inlet axial Mach number M_1 and inlet tip blade angle β_{1t} is as shown in Fig. 9.11. Here we see that if, for example, β_{1t} must not exceed 50° and M_{1rel} must not exceed 1.4, the shaft speed must not exceed 35,000 rpm. Increasing β_{1t} to 60° would allow the shaft speed to increase to about 38,000 rpm. Given that

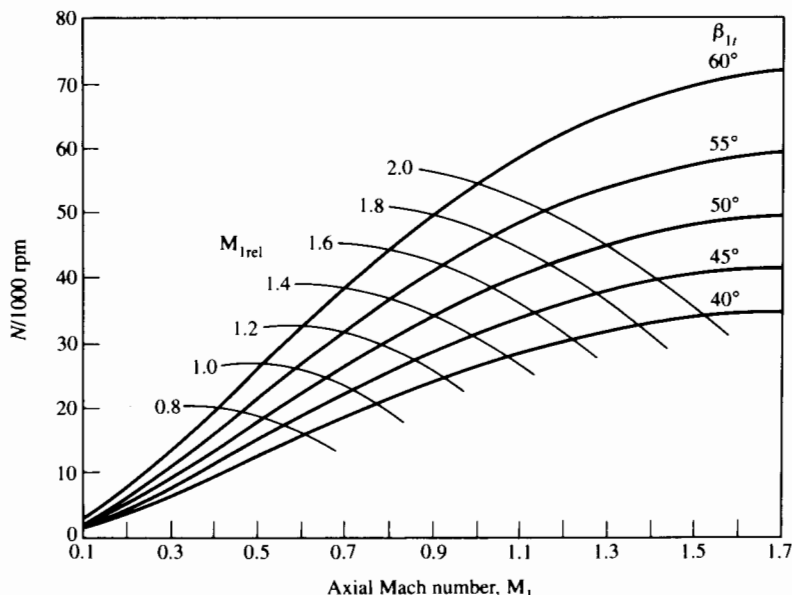


FIGURE 9.11 Centrifugal compressor inducer; $\dot{m} = 5$ kg/s, $D_h = 0.1$ m, $p_{01} = 100$ kPa, $T_{01} = 300$ K.

the exit tip speed is essentially set by the pressure ratio required of the stage, the maximum shaft speed of the rotor fixes the minimum size of the rotor. Thus the inducer aerodynamics play a critically important role in establishing the minimum size of the compressor.

The foregoing illustrates the point that the inlet to the impeller (specifically the allowable relative Mach number and pressure coefficient) determines the allowable compressor rotational speed for a given mass flow rate and inlet pressure and temperature. The choice of inlet hub-tip ratio ζ has a relatively small influence if $\zeta^2 \ll 1$. Once the rotational speed is fixed, then (since the compressor pressure ratio and efficiency determine the required impeller tip speed) the impeller diameter and thus the size of the compressor are fixed. Thus the essential design limitations are:

1. aerodynamic—*inlet relative Mach number at the tip diameter limits the rotational speed N* ;
2. stress related—*impeller stresses limit the tip speed at the exit of the impeller. The tip speed in turn affects the pressure ratio.*

The combination of these constraints limits the minimum size of the machine.

The inlet relative Mach number limitation being so important, we return to it in the discussion of stage design in Section 9.6, in which we explore the use of inlet guide vanes to attempt to alleviate the problem.

The shape of the impeller passages in a modern high-speed centrifugal compressor is illustrated in Figs. 9.1 and 9.12. To lessen the possibility of boundary layer separation, the average flow velocity should be kept roughly constant in the radial flow part of the impeller. One can do this by decreasing, with increasing radius, the axial width of the impeller passage. The pressure is rising rapidly in the flow direction, but this is not a cause of boundary layer separation since it is due to the centrifugal forces rather than to the slowing down of the fluid as in a stationary diffuser.

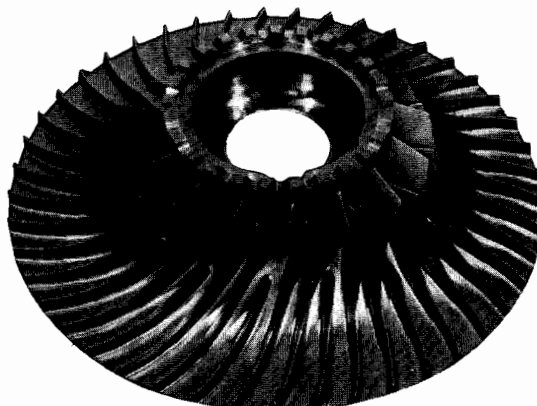


FIGURE 9.12 General Electric T700 centrifugal impeller rotor. (Courtesy GE Aircraft Engines.)

Schumann, Clark, and Wood [4] have reported the results of a systematic study of the effect of rotor passage velocity ratio w_2/w_1 (in which w_2 and w_1 represent the passage average relative velocities at outlet and inlet of the rotor). They measured the pressure and velocity distributions in a rotor whose exit blade height was reduced, in a series of steps, by machining the blade tips by a constant axial displacement that left the inlet area unchanged and allowed the same outer casing and the same tip clearance to be used in each test. The tests gave evidence of flow passage separation for w_2/w_1 less than 0.65 or 0.7. This shows that the flow passages in centrifugal rotors, like those in axial compressor rotors, behave like nonrotating diffusers insofar as they tend toward flow separation at a given overall velocity ratio. It is fully consistent with the idea we expressed earlier that since deceleration of the relative velocity in the inducer is inevitable and should be limited to a minimum value of perhaps 0.7, the mean relative velocity in the remainder of the flow passage should be held nearly constant. Controlling the streamwise variation of mean velocity w within the impeller constrains the variation in blade width from inlet to outlet.

We must qualify the argument presented earlier—that pressure change due to the centrifugal force field is not a cause of boundary layer separation—by referring to the Coriolis forces that are also at work in the impeller. Figure 9.13 shows a particle of fluid traveling radially outward (at velocity w relative to the impeller) when the rotational velocity is Ω . In full lines it shows the absolute and relative velocities of the particle, c and w , respectively, at time t ; in broken lines it shows the absolute and relative velocities c' and w' shortly thereafter, at time $t + dt$. The magnitude of the relative velocity is unchanged, but the particle has suffered

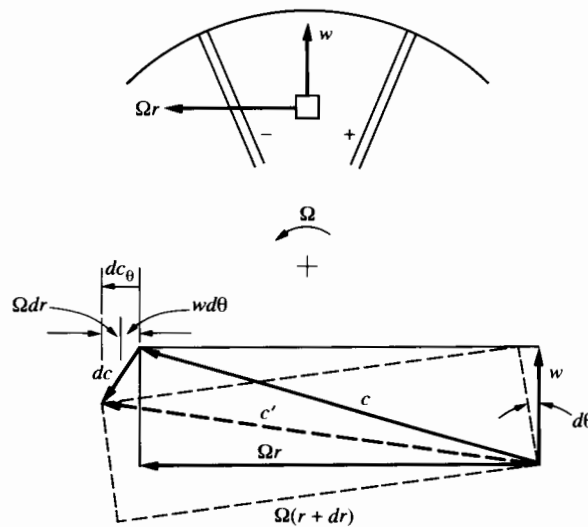


FIGURE 9.13 Coriolis acceleration in a centrifugal impeller with relative velocity w constant in the radial direction.

an absolute change of velocity that (for infinitesimal dt and $d\theta = \Omega dt$) can be seen to be equivalent to a change in the θ -direction of $dc_\theta = \Omega dr + w d\theta$. We may write this as

$$dc_\theta = \Omega w dt + w \Omega dt.$$

Thus the Coriolis acceleration $a_\theta = dc_\theta/dt$ is

$$a_\theta = 2\Omega w,$$

and it requires a pressure gradient in the tangential direction of magnitude

$$\frac{1}{r} \frac{\partial p}{\partial \theta} = -2\rho\Omega w. \quad (9.22)$$

We can verify this result by writing $F = ma$ in the tangential direction for a cubical particle of volume $r d\theta dr dz$ and setting $a = a_\theta$.

The existence of the tangential pressure gradient means there will be a positive gradient of w in the tangential direction; we can determine its magnitude by using Eq. (9.4) in the tangential direction to write

$$\frac{1}{\rho r d\theta} \frac{dp}{dr} = - \frac{d\left(\frac{w^2}{2}\right)}{rd\theta} = - \frac{w dw}{rd\theta}$$

(on the assumption that all streamlines have the same stagnation pressure in the rotating frame of reference).

Coupling these statements with Eq. (9.22), we see that

$$\frac{1}{r} \frac{dw}{d\theta} = 2\Omega, \quad (9.23)$$

so that there will be a tangential variation in relative velocity, as shown in Fig. 9.14. Now it is interesting that this tangential gradient of w is independent

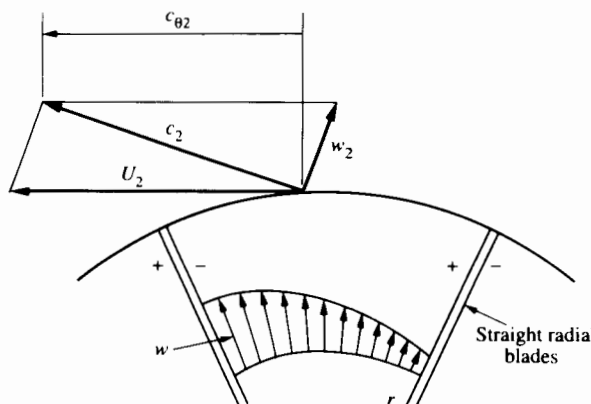


FIGURE 9.14 Relative velocity slip at the exit of an impeller with straight radial blades.

of flow rate. For finite spacing of blades, reducing the flow rate will necessarily produce backflow on the pressure face, whether or not there is a boundary layer on that wall.

The existence of the Coriolis pressure gradient will also mean pressure differences across the blades shown in Fig. 9.14 by the + and - signs. At the exit of the impeller, however, the static pressure will be essentially constant in the tangential direction. This means that near the tip of the impeller, the flow will undergo an adjustment with three consequences:

1. As the Coriolis pressure gradient disappears (toward the outlet of the impeller), a fluid particle in the middle of the channel will be unable to continue in a purely radial direction; it will "slip" back against the direction of rotation. The consequence (with straight radial blades) is that the velocity triangle at the impeller exit will have the appearance of Fig. 9.14. The absolute tangential velocity component $c_{\theta 2}$ at exit will be significantly less than U_2 unless the blades are extremely close together.

With an impeller of 20 blades, this means that the calculated work at a given U_2 is reduced almost 10% by taking this phenomenon into account. One sees from this why, despite some stress disadvantage, extra blades reaching only part way to the hub may be inserted into the impeller as in Fig. 9.12.

2. As the boundary layer on the pressure side (+) approaches the impeller tip diameter, the fluid will accelerate as the tangential pressure gradient in the channel is relieved. This local and favorable pressure gradient contribution (negative in the flow direction) tends to keep the boundary layer on the outer part of the pressure surface well behaved.

3. The opposite is the case on the suction (-) surface, where the addition to the streamwise gradient of pressure (due to removal of the Coriolis deceleration) tends to cause the boundary layer to separate. This possibility may be enhanced by the secondary flow driven by the Coriolis pressure gradient, which tends to transport slow-moving fluid to the suction surface. The effects of flow across the tip clearance and of the transverse shearing due to one of the passage walls being stationary are also complex, and it is doubtful whether any analytical method is at present capable of accurately predicting all these effects.

However, the tendency of the suction surface to display a zone of flow separation (particularly if the impeller flow rate is less than the design value) has been well established experimentally. It is therefore not surprising that, taking this effect into account (as well as benefitting from reduction of diffuser inlet Mach number; see Fig. 9.7), some of the latest designs show backward-tipped blades at the impeller exit (again see Fig. 9.12), despite the addition of the bending stress that this might imply. The effect of the exit angle and blade spacing on the ratio of the tangential component of the absolute leaving velocity to the tip velocity has been studied in great detail in potential flow calculations that show the effect of blade number on the velocity variation from blade to blade at the impeller outlet. For blades whose direction at the impeller outlet is radial, we can summa-

rize concisely the results of these calculations of the average velocity by defining a slip factor

$$\sigma_s = \frac{c_{\theta 2}}{U_2},$$

in which $c_{\theta 2}$ is the momentum-averaged tangential velocity component. The Stanitz potential flow calculations [5] show that the slip factor is approximately related to the number of blades in the impeller by (for more than 10 blades)

$$\sigma_s \approx 1 - \frac{2}{N_b}, \quad (9.24)$$

in which N_b is the number of blades. This expression applies only to straight radial blades. The effect of back sweep on β_2 is taken into account in empirical correlations discussed by Wiesner [6], which we modify to write

$$\sigma_s = \left(1 - \frac{\text{const}}{N_b} \sqrt{\cos B_2}\right) \left(1 - \frac{w_{r2}}{U_2} \tan B_2\right),$$

in which B_2 is the exit blade angle with respect to the radial direction. To make this expression agree with the well-tested result of Stanitz for $B_2 = 0$, we set const = 2 and obtain

$$\sigma_s = \left(1 - \frac{2}{N_b} \sqrt{\cos B_2}\right) \left(1 - \frac{w_{r2}}{U_2} \tan B_2\right). \quad (9.25)$$

With this result we may show that

$$\tan \beta_2 = \tan B_2 + \frac{2}{N_b} \sqrt{\cos B_2} \left[1 / \left(\frac{w_{r2}}{U_2} \right) - \tan B_2 \right] \quad (9.26)$$

and notice that $\beta_2 \rightarrow 90^\circ$ for $w_{r2} \rightarrow 0$, for all values of B_2 .

A characteristic feature of the centrifugal compressor is small blade height (as measured in the axial direction) at the outside diameter of the wheel. This small blade height is the consequence of large density increase across the wheel, expansion of diameter from inlet to outlet, and the limitation discussed earlier on relative velocity reduction within the rotor flow passage. It leads naturally to the question of how the stage efficiency depends on the clearance between the rotor and casing adjacent to the edges of the blades. The analyses and measurements of Senoo and Ishida [7] indicate that the stage efficiency η_c depends on tip clearance as follows:

$$\frac{\Delta \eta_c}{\eta_c} = -\mathcal{C} \frac{\Delta_2}{b_2},$$

in which Δ_2 and b_2 are the tip clearance and blade height (both measured in the axial direction) at the exit of the rotor. In the range of clearances $0 < \Delta_2/b_2 < 1$, \mathcal{C} appears to have magnitude 0.3 ± 0.05 .

Design of centrifugal impellers for high efficiency and low weight is so important for small gas turbines that one must use the very best methods available

to simulate the internal fluid dynamics. Prince and Bryans [8] describe the results of a fully three-dimensional finite-volume potential flow method in which the impeller flow passage is considered to consist of approximately 100 volume elements defined by the grid lines shown in Fig. 9.15(a). Here the “upstream boundary” is

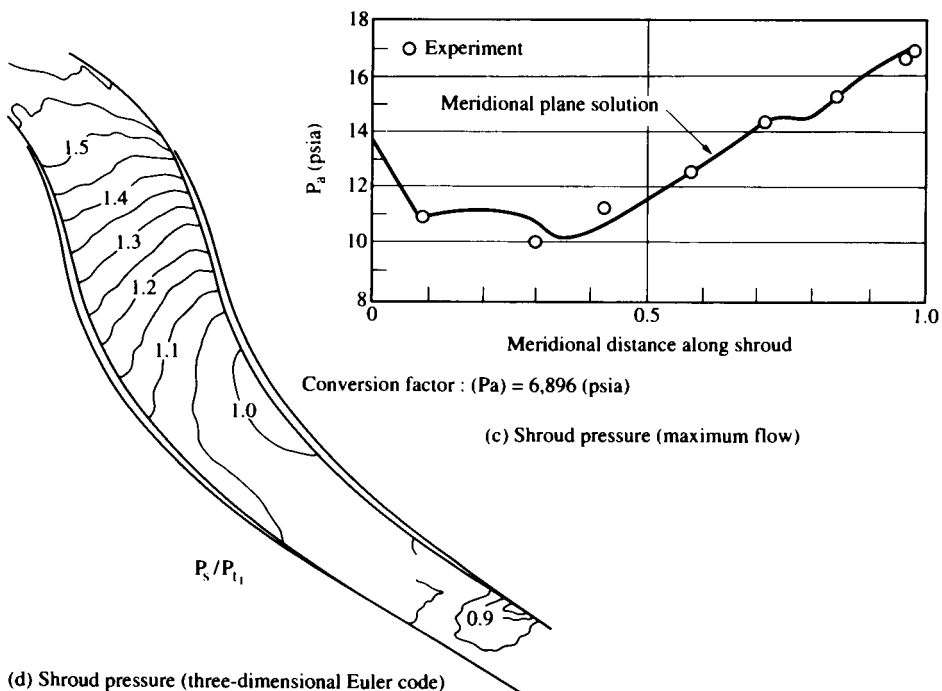
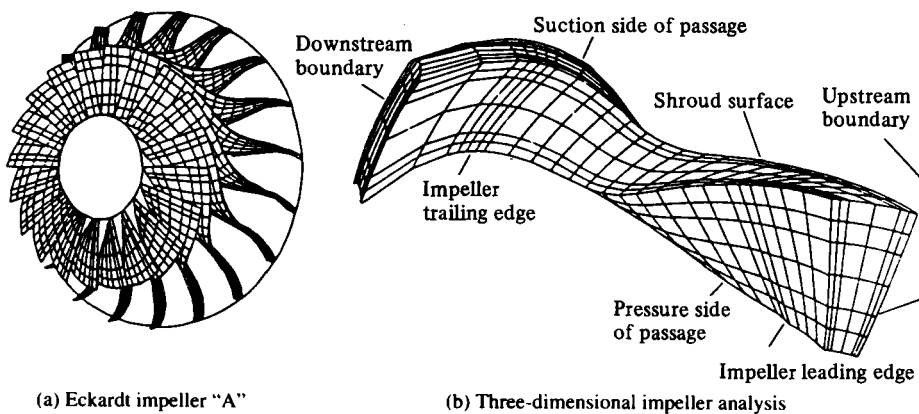


FIGURE 9.15 Centrifugal compressor flow. (From Prince and Bryans [8].)

at the impeller entrance and the “downstream boundary” is at the impeller passage exit. The “shroud” surface refers to the open side of the flow passage next to the compressor casing. For each volume element the continuity, momentum, and energy equations are satisfied by an iterative numerical procedure that allows for the distribution of swirl at the rotor inlet and determines the flow field in the absence of flow separation. Boundary layer growth is not calculated, but the pressure gradients on the wall (calculated on the assumption that the boundary layers are negligibly thin) provide an indication of whether in the real flow there is danger of flow separation. If there is, one can, in principle, modify the passage geometry to remove the danger.

Figure 9.15(b) shows typical results of the calculation of static pressure within the blade passage at the shroud surface. Figure 9.15(c) compares measured shroud surface pressures on a meridional plane (the plane that contains the axis of rotation) with calculated pressures.

The use of such complex mathematical models of the flow field, while not eliminating the need for experimental testing, can guide the designer searching for the optimum geometry of the impeller.

9.4 THE DIFFUSER

Although the relative velocity within the impeller is low, Fig. 9.8 shows that high impeller tip speed results in a high absolute velocity leaving the impeller. Absolute exit Mach numbers of the order of 1.3 are not uncommon. This high velocity is reduced (while the pressure rises) in a diffuser in which the fluid flows radially outward from the impeller, first through a vaneless region and then through vanes, as Fig. 9.16 shows, or through a pipe diffuser (to be discussed shortly).

Before examining the typical behavior of vane or pipe diffusers, we investigate the deceleration of the flow that takes place in the vaneless space shown in Fig. 9.16 ($r_1 < r < r_2$).

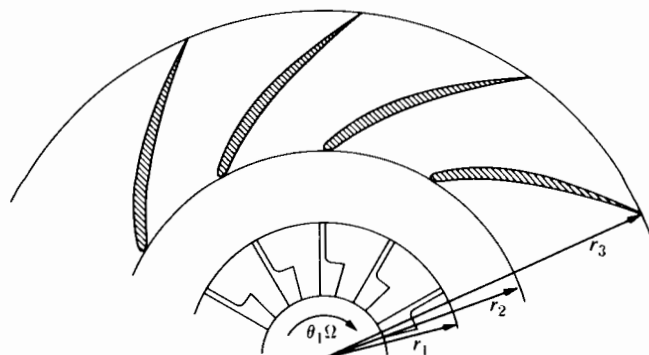


FIGURE 9.16 Radial diffuser.

For incompressible flow in a vaneless region of constant axial width h , continuity requires that

$$\dot{m} = \rho(2\pi rh)c_r = \text{constant} \quad \text{or} \quad rc_r = \text{constant}.$$

At the same time, the absence of any torque-transmitting mechanism (except wall friction, which is neglected) requires that angular momentum be conserved throughout the vaneless region. Thus $rc_\theta = \text{constant}$. Combining these two equations, we have $c_\theta/c_r = \text{constant} = \tan \alpha$, where α is the angle between the velocity and the radial direction, as indicated in Fig. 9.17.

Thus the streamline makes a constant angle with the radial direction, and its shape is sometimes called a logarithmic spiral. Since α is constant, it follows that velocity is inversely proportional to radius, or $c_2/c_1 = r_1/r_2$.

Compressible flow in a vaneless diffuser is also easily analyzed if we assume that the flow is reversible. As in most compressible-flow problems, it is convenient to relate fluid properties at any point to their values at a point where the Mach number is 1. Thus, from continuity, $\rho rc_r = \rho^*r^*c_r^*$, where the * denotes the value attained in reversible adiabatic flow from the local condition to sonic velocity.

The conservation of angular momentum requires that $rc_\theta = r^*c_\theta^*$. These two equations can also be written

$$\rho rc \cos \alpha = \rho^*r^*c^* \cos \alpha^*, \quad (9.27)$$

$$rc \sin \alpha = r^*c^* \sin \alpha^*, \quad (9.28)$$

and combined to yield

$$\frac{\tan \alpha^*}{\tan \alpha} = \frac{\rho^*}{\rho}.$$

Applying the equations of one-dimensional reversible adiabatic flow along any streamline, we have

$$\frac{\tan \alpha^*}{\tan \alpha} = \left[\frac{2}{\gamma + 1} \left(1 + \frac{\gamma - 1}{2} M^2 \right) \right]^{1/(\gamma-1)}. \quad (9.29)$$

With this relation for α as a function of M , Eq. (9.28) can be used to find r as a function of M . Thus

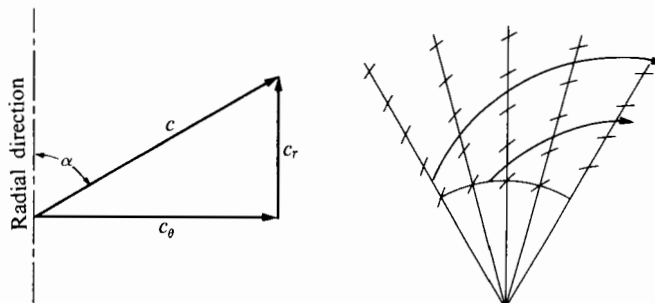


FIGURE 9.17 Streamlines in a parallel-walled radial diffuser.

$$\frac{r^* \sin \alpha^*}{r \sin \alpha} = \frac{c}{c^*} = M \sqrt{T/T^*},$$

and, using the isentropic equations for T/T^* , we obtain

$$\frac{r^* \sin \alpha^*}{r \sin \alpha} = M \left\{ \frac{(\gamma + 1)/2}{1 + [(\gamma - 1)/2]M^2} \right\}^{1/2}. \quad (9.30)$$

The known inlet conditions serve to determine the * quantities, after which we can find α from Eq. (9.29) and r from Eq. (9.30), as a function of M . Rather than using these consecutive equations, it is convenient to plot their results for any fixed γ , as in Fig. 9.18. In this diagram we determine the inlet state from the known angle and Mach number, α_1 and M_1 . From this we can determine $(r/r^*)_1$ along with α_1^* . Since the value of α^* is constant, the state of the fluid follows a line of constant α^* until the desired outlet Mach number, M_2 , is reached. Thus we find $(r/r^*)_2$, and the actual radius ratio of the diffuser is

$$\frac{r_2}{r_1} = \frac{(r/r^*)_2}{(r/r^*)_1}. \quad (9.31)$$

Along a line of constant α^* , two directions are possible: one corresponding to diffusion and the other to supersonic acceleration. Only the diffusion is of interest for compressors. For example, if $M_1 = 1.3$ and $\alpha_1 = 70^\circ$, then $\alpha^* = 75^\circ$ and

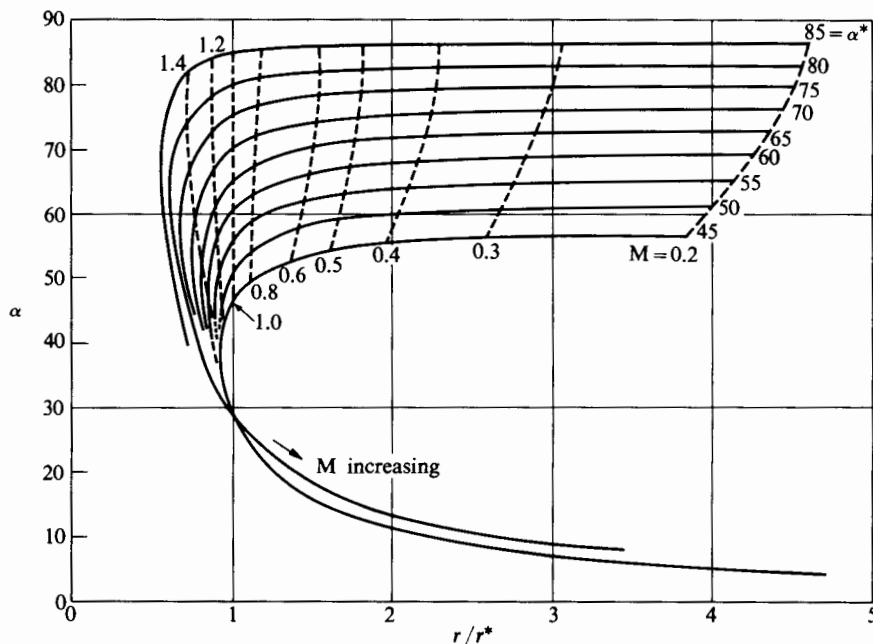


FIGURE 9.18 Compressible flow in a vaneless diffuser; $\gamma = 1.4$. (Courtesy M.I.T. Gas Turbine Laboratory.)

$(r/r^*)_1 = 0.8$. If one wishes to diffuse to $M_2 = 0.4$ before entering a combustion chamber, then $(r/r^*)_2 = 2.3$ and

$$\frac{r_2}{r_1} = \frac{2.3}{0.8} = 2.9.$$

The advantage of the vaneless diffuser is that it can provide deceleration from supersonic to subsonic flow without a shock. A disadvantage, as we see from this example, is that the desired deceleration may require an excessively large radius ratio across the vaneless diffuser. This feature is especially undesirable in aircraft applications, where one must avoid large engine diameters. To save space, vanes (as shown in Fig. 9.16) may be employed to reduce angular momentum and thereby increase pressure more rapidly in the radial direction. Figure 9.16 shows a diffuser consisting of curved vanes with a vaneless space separating the impeller and the vanes. It is possible in the vaneless space to decelerate the flow from

$$M = 1.3 \text{ to } M = 0.8 \text{ or } 0.9.$$

In this way shock-wave effects can be minimized. Thus, although the vaneless diffuser does not provide a complete answer to the problem of making use of the huge kinetic energy discharge from the rotor, it does play a very helpful role.

Both vaned and vaneless diffusers are controlled by boundary layer behavior. The frictionless theory outlined above would lead us to expect that the vaneless diffuser would operate successfully at all inlet angles α_2 . This is not true in practice because of the boundary layers on the diffuser walls. At large angles α_2 , the boundary layer fluid may begin to flow inward, forming a zone of separated flow.

Rodgers [9] has tested the effect of inlet flow angle α_2 on the pressure recovery of a vaneless diffuser of diameter ratio $D_3/D_2 = 1.7$ (D_2 being the rotor outlet diameter and D_3 the outlet diameter of the vaneless space). He defined the diffuser pressure coefficient by

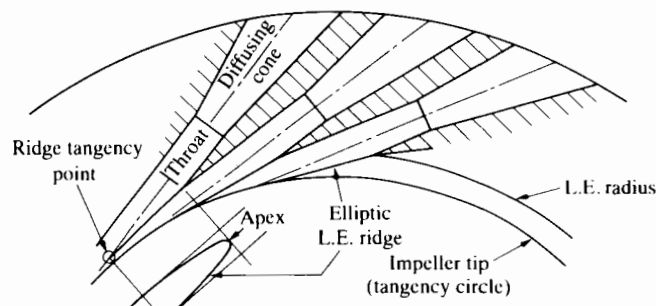
$$C_{pd} = \frac{p_3 - p_2}{p_{02} - p_2}$$

(in which p and p_0 denote static and stagnation pressures). Rodgers found that C_{pd} varied from about 0.6 (at $\alpha_2 = 50^\circ$) to only 0.3 to 0.4 (at $\alpha_2 = 80^\circ$). The larger the value of α_2 (the angle between the streamline and the radial direction at entrance to the vaneless diffuser), the greater the detrimental effects of the wall boundary layer. At large values of α_2 , zones of reverse flow can occur in the vaneless diffuser [10, 11]; these are usually associated with unsteady flow and high losses in stagnation pressure. For a given angular momentum at the impeller exit, the flow angle α_2 will be directly dependent on the axial width of the vaneless diffuser; with too large a width, α_2 will be too large, and poor efficiency will be the consequence.

Cumpsty [3] points out the great importance of correctly matching the diffuser to the impeller if the compressor is to operate efficiently. He cites the data of Steifel showing a strongly detrimental effect on compressor pressure ratio and mass flow rate when the axial width of the diffuser was increased from 8 mm to 10.5 mm.

With thin vanes of small curvature, the vaned diffuser can operate successfully with transonic or even supersonic inlet flow. The performance of vaned diffusers, however, tends to suffer seriously when the flow incidence angle deviates appreciably from the design incidence angle. With transonic inlet flow, departure from design flow rate or rotor speed can lead to shock-induced separation on the vane surfaces.

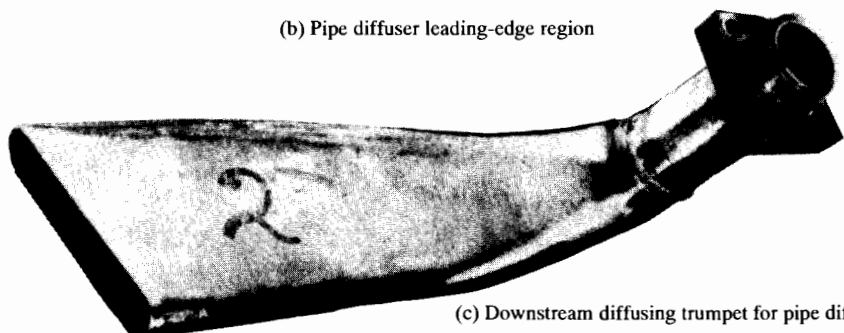
A quite different design strategy has been used by Pratt & Whitney, who have developed the "pipe diffuser" shown in Fig. 9.19. Here the flow is decelerated in



(a) Pipe diffuser geometry



(b) Pipe diffuser leading-edge region



(c) Downstream diffusing trumpet for pipe diffuser

FIGURE 9.19 Pipe diffuser of Kenny [2].

a series of converging-diverging passages whose axes are placed at small angles relative to the tangential direction. This geometry has proved capable of decelerating supersonic flow with low aerodynamic loss and with high tolerance to differences in direction between the approaching flow and the diffuser axis. This means that the compressor efficiency may be less sensitive to departure from design speed or flow rate than a compressor with a vane type of diffuser.

Kenny [12] shows that the pressure recovery, defined as the static pressure increase divided by the difference between the inlet stagnation and static pressures, can be in the range of 0.6 to 0.65 for a straight conical diffuser with a total included angle of 4° to 5° and an area ratio of 5:1. The recovery factor is affected by the Reynolds number and the entrance boundary layer thickness, as well as by the inlet Mach number, so we can regard these only as typical numbers.

Figure 9.20 shows Kenny's [13] correlation of the dependence of the diffuser static pressure recovery on the boundary layer blockage at the throat of the diffuser. The blockage is defined as the effective fractional reduction in flow area due to boundary layer displacement thickness. Viewed in a coordinate system fixed to the rotor, the velocity distribution of the air leaving the rotor is typically quite nonuniform, owing to boundary layer growth within the rotor. But the ve-

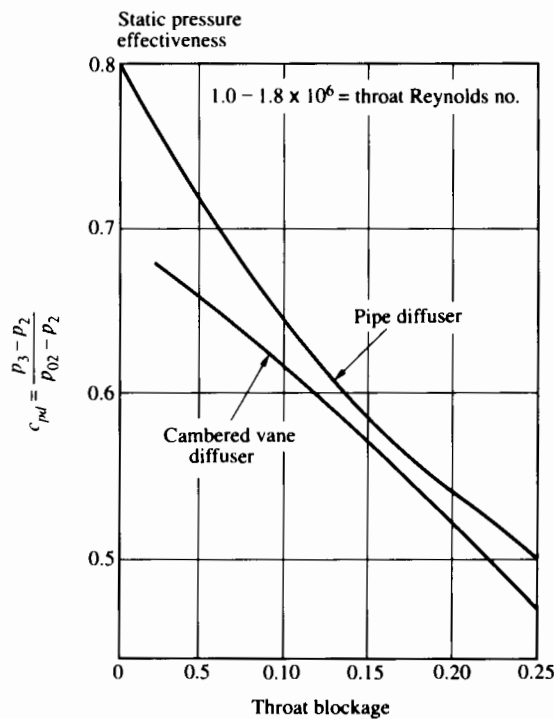


FIGURE 9.20 Diffuser effectiveness. (From Kenny [2].)

locity relative to the rotor is typically much smaller than the tip speed, so that (after vectorial addition of the relative velocity and the tip velocity) the absolute velocity field at the impeller outlet can appear quite uniform. This means that conventional methods of estimating boundary layer growth within a pipe diffuser can provide a good estimate of the throat blockage. Kenny showed that the experimentally determined throat blockages in pipe diffusers are well predicted by the boundary layer calculation method of Moses presented in Chapter 4. He also derived a method [14] for estimating the effect on throat blockage of variation from the design value of the angle between the absolute velocity vector at the diffuser entrance and the tangential direction. This has been used successfully to predict the off-design behavior of centrifugal compressors.

9.5 PERFORMANCE CHARACTERISTICS

The dimensional analysis described for axial compressor stages is directly applicable to centrifugal stages because the derivation was not restricted to one kind of impeller. Thus for a given air-handling centrifugal compressor operating at high Reynolds number, we expect its performance on the test stand to be consistent with the following relationship:

$$\frac{p_{03}}{p_{01}}, \eta_c = f\left(\frac{\dot{m}\sqrt{\theta}}{\delta}, \frac{N}{\sqrt{\theta}}\right), \quad (7.22)$$

in which, as before,

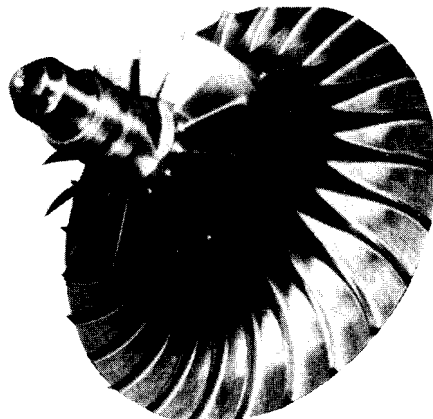
$$\theta = \frac{T_{\text{ambient}}}{(T_{\text{ambient}})_{\text{standard day}}},$$

$$\delta = \frac{P_{\text{ambient}}}{(P_{\text{ambient}})_{\text{standard day}}},$$

and N is the shaft speed, rpm.

Figure 9.21 shows a high-tip-speed impeller designed by Noel Penney Turbines and tested by Chevis [15]. The internal stress distribution of the rotor is shown in Fig. 9.21(c); the contours of constant stress were calculated from a three-dimensional stress analysis of the final rotor design. The material chosen for the rotor was a martensitic stainless steel (0.12% C, 12% Cr, and 3% Ni). The figure also shows the compressor design data. The diffuser for the impeller of Fig. 9.21 incorporates a transonic vaneless space ($1.0 < D/D_2 < 1.05$) followed by 13 constant-thickness vanes ($t/c = 0.025$) on circular arc camber lines.

Figure 9.22 shows the performance of the compressor, indicating the final static pressure divided by the inlet stagnation pressure as a function of the mass flow ratio. The reference flow rate is the design flow rate shown in Fig. 9.21,



(a) Impeller

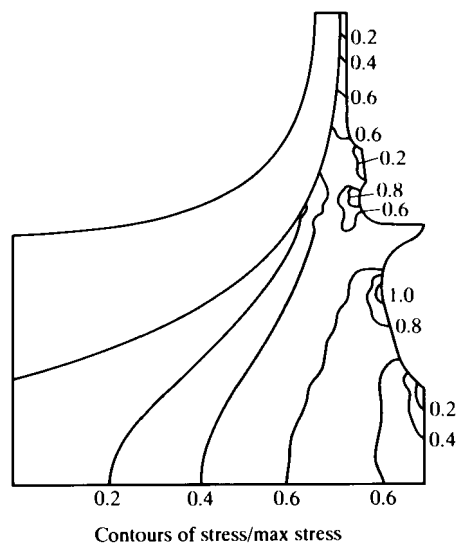
Inducer hub diameter, mm (in.)	65.3 (2.57)
Inducer shroud diameter, mm (in.)	160.0 (6.30)
Impeller tip diameter, mm (in.)	301.8 (11.88)
Number of vanes/splitters	13/13
Axial length (flow path), mm (in.)	98.4 (3.87)

Impeller vane backsweep angle, degrees	36.0
Rotational speed $N/\sqrt{\theta}$, rpm	38,950
Mass flow $m \sqrt{\theta}/\delta$, kg/s (lb/s)	3.22 (7.1)
Pressure ratio $T-S$ (overall)*	8.13
Isentropic efficiency $T-S$	0.78

Impeller pressure ratio ($T-T$)	9.4
Impeller isentropic efficiency $T-T$	0.86
Inducer shroud relative Mach number	1.19
Impeller tip absolute Mach number	1.14

Impeller tip speed, m/s (ft/s)	615 (2018)
Specific speed (Balje)	0.62
Loading $\Delta h/U^2$	0.795

Reference conditions: ISA SLS



(b) Impeller design data

(c) Impeller radial stress distribution

FIGURE 9.21 Centrifugal compressor of Chevis [15].

namely, 3.22 kg/s. We can see that, as we would expect, the pressure ratio is very sensitive to impeller speed. What we might not have expected is that the range of flows between surge (see Chapter 7) and choke is very narrow—only about 13% or 14% in flow rate. This narrowness of range, associated with the behavior of the diffuser mentioned earlier, is quite characteristic of high-performance centrifugal compressors. However, it does not preclude satisfactory matching of turbine and compressor over a wide range of speed.

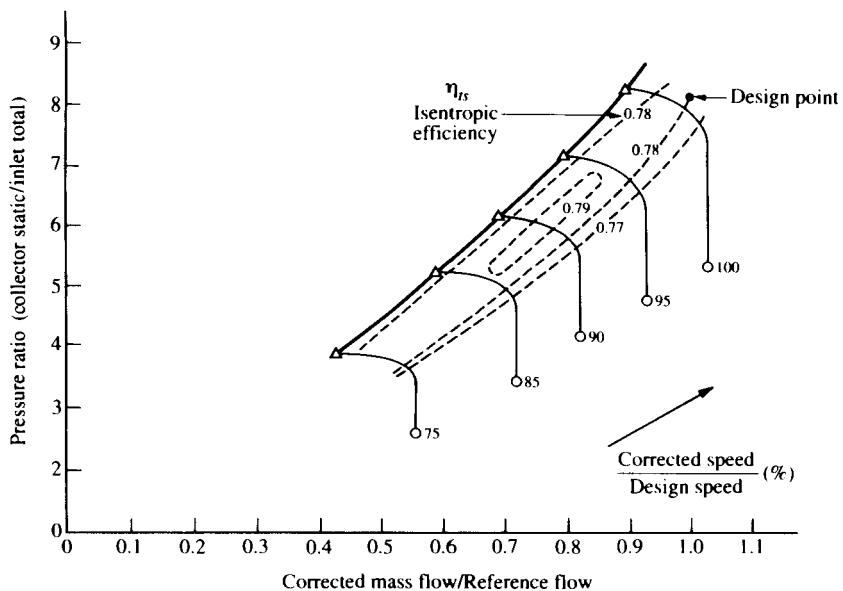


FIGURE 9.22 Performance of centrifugal compressor whose rotor is shown in Fig. 9.21.

Figure 9.23 shows the performance reported by Kenny [14] for a centrifugal compressor at somewhat smaller pressure ratio but higher stage adiabatic efficiency. Here the normalized mass flow rate is expressed as before by $\dot{m} \sqrt{\theta}/\delta$ and is in lb/sec. The normalized shaft speed is the same as $N/\sqrt{\theta}$, in which N is expressed in thousands of rpm. For this rotor the exit blade angle was 30° . The diffuser was of the type shown in Fig. 9.19. The surge margin lines shown in Fig. 9.23 indicate that at standard-day rpm of 28,250, the surge line is removed from the best-efficiency operating point by a 20% reduction in mass flow rate. The best operating point occurs at a mass flow rate only about 4% less than the choking value at that rpm.

9.6 CENTRIFUGAL COMPRESSOR STAGE DESIGN

We now consider the preliminary design of a centrifugal compressor stage for a given air mass flow rate \dot{m} and with given inlet stagnation pressure and temperature p_{01} and T_{01} . We would like to have a high stage pressure ratio with minimum size as well as with high efficiency. Our purpose, with certain simplifying assumptions, is to explore the way in which the basic conservation principles, coupled with Mach number, diffusion, and stress limits, effectively determine the design. We do not mention boundary layer growth explicitly, but this does not mean that we are overlooking its importance. By restricting Mach numbers and diffusion limits, we are concentrating on the conditions for which boundary layers should be thin and free of separation.

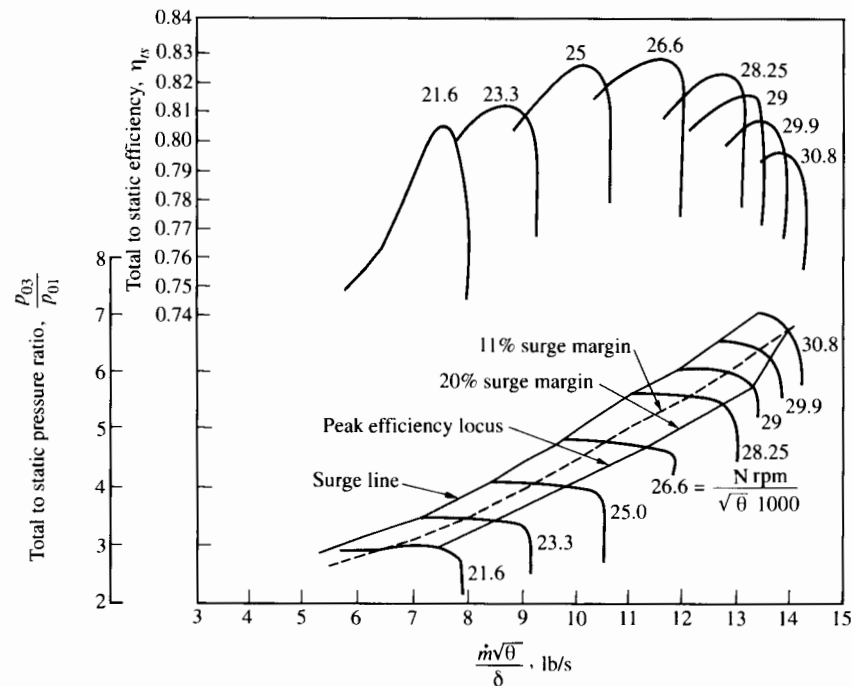


FIGURE 9.23 Performance of a centrifugal compressor. (Adapted from Kenny [14].)

The treatment we adopt here uses the same kinds of assumptions as used for axial compressors (Section 7.10) and axial turbines (Section 8.8), except that here c_r^2 is not considered to be negligible compared with c_θ^2 or c_z^2 .

The principal questions before us are:

1. For given inlet air conditions and a given mass flow rate, how do conditions at the inducer inlet determine the allowable shaft rotational speed?
2. For a given stage pressure ratio (in addition to the conditions specified in question 1), how is the impeller diameter determined?
3. What factors determine the general shape of the impeller, for example, the ratio of outlet diameter to inlet tip diameter and the ratio of outlet blade height to rotor diameter?

It is clear from Fig. 9.7 that for high stage pressure ratio the centrifugal compressor impeller should be operated with the highest tip speed U_2 consistent with allowable impeller material stress. Since the overall size of the compressor will be proportional to the outlet diameter of the impeller, it follows that for a given impeller tip speed, the overall size will be inversely proportional to the rotational speed.

Impeller Shaft Speed

The example of Section 9.3 (for an impeller with no prewhirl) demonstrates that we can determine the shaft speed Ω by considering only the impeller inlet conditions

$$\dot{m}, T_{01}, p_{01}, M_{1\text{rel}}, \beta_{1t}, \text{ and } D_h.$$

The example leaves us dissatisfied, however, because it implies that every time we change one of these variables, we need to do a new calculation. Sensing that dimensional analysis has something to contribute here, we conclude that this dependence of Ω on the six independent variables given above is unnecessarily complex. So we go back and think about Eqs. (9.15) to (9.21) for a while and find, to our satisfaction, that we can reduce this whole set of equations to a single statement:

$$\frac{\Omega \dot{m}^{1/2}}{p_{01}^{1/2}(RT_{01})^{1/4}} = \frac{\gamma^{3/4}\sqrt{\pi(1-\zeta^2)}(\cos \beta_{1t})^{3/2} \tan \beta_{1t} M_{1\text{rel}}^{3/2}}{\left[1 + \frac{\gamma-1}{2} M_{1\text{rel}}^2 \cos^2 \beta_{1t}\right]^{(3\gamma-1)/(4\gamma-1)}} \quad (9.32)$$

in which ζ is the hub–tip radius ratio at the inlet to the impeller, and in which the shaft speed Ω in radians per second has replaced N rpm. Thus we see that for a given γ this equation has the functional dependence of

$$\frac{\Omega \dot{m}^{1/2}}{p_{01}^{1/2}(RT_{01})^{1/4}} = f(M_{1\text{rel}}, \beta_{1t}, \zeta), \quad (9.33)$$

and that it is surely not necessary to do a new calculation for every new combination of \dot{m} , p_{01} , and T_{01} .

We could consider Eq. (9.32) a general result, except that it does not allow for prewhirl. In Fig. 9.2 we see an example of a centrifugal stage mounted behind several axial stages. There could be swirling flow leaving the stator of the last axial stage and entering the centrifugal rotor. Even without axial stages upstream, a set of inlet guide vanes might be installed. As shown in Fig. 9.24, this could provide swirl in the rotor direction to reduce $M_{1\text{rel}}$ in the flow approaching the centrifugal rotor. To allow for the prewhirl possibility, we now extend our analysis of inducer inlet conditions to accommodate a designer's choice of inlet swirl profile. To obtain specific results, we make a particular choice here, namely, $c_{\theta 1} \propto r$, and show (in Appendix VII) how this in effect alters Eq. (9.33) to read

$$\frac{\Omega \dot{m}^{1/2}}{p_{01}^{1/2}(RT_{01})^{1/4}} = f\left(M_{1\text{rel}}, \beta_{1t}, \zeta, \frac{c_{\theta 1}}{\sqrt{RT_{01}}}\right), \quad (9.34)$$

in which the swirl parameter (plus the assumption $c_{\theta 1} \propto r$) completely specifies the rotor inlet profile. To show the way in which the dependent variable in Eq. (9.34) could be calculated, we write

$$\frac{\Omega \dot{m}^{1/2}}{p_{01}^{1/2}(RT_{01})^{1/4}} = \sqrt{\left(\frac{\dot{m} \sqrt{RT_{01}}}{p_{01} D^2}\right) 4\gamma \left(\frac{U_t}{a_{01}}\right)^2},$$

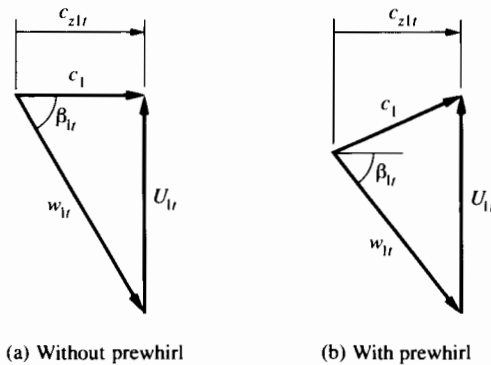


FIGURE 9.24 Velocity diagrams showing possible effect of inlet guide vanes on relative velocity w_{1t} at inlet tip radius.

for which we can evaluate $\dot{m} \sqrt{RT_{01}} / p_{01} D^2$ at the rotor inlet plane in much the same way as we did for an axial compressor rotor (using the radial equilibrium equation [7.44] to determine the axial velocity distribution corresponding to the prescribed swirl distribution). We can obtain the term U_t/a_{01} from $c_{\theta1t}/\sqrt{RT_{01}}$, $M_{1\text{rel}}$, and β_{1t} by considering the inlet-tip radius velocity triangle.

Appendix VII provides the formulas for calculating the relationship of Eq. (9.34), and Fig. 9.25 provides a sample result for the case $\zeta = 0.3$. The figure

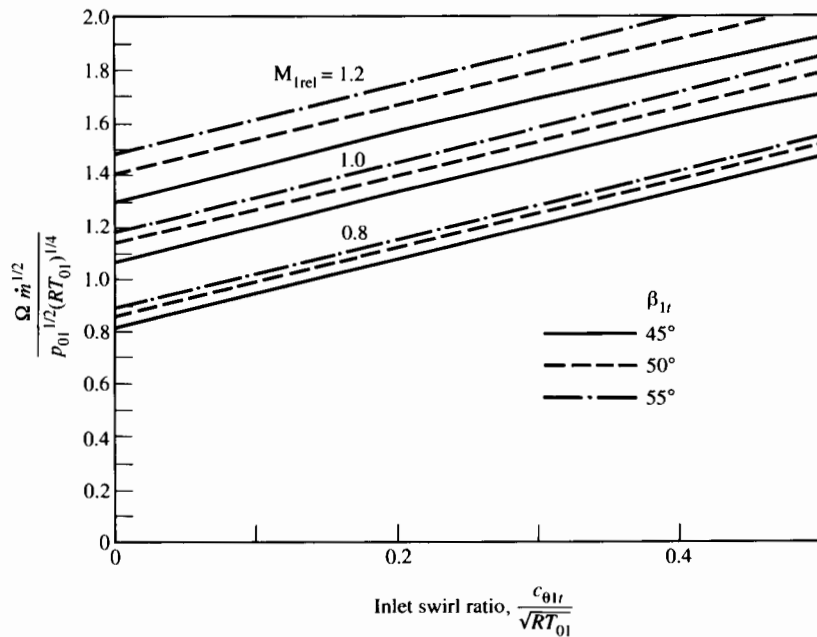


FIGURE 9.25 Centrifugal compressor; $\zeta = 0.3$.

indicates the sensitivity of the shaft speed to variations in $M_{1\text{rel}}$ and β_{1t} . We might, in accord with the limiting pressure coefficient idea, take β_{1t} as 50° . The question of whether to use prewhirl is linked to the allowable value of $M_{1\text{rel}}$. With no prewhirl, the flow approaching the rotor can become transonic at the rotor tip without excessive shock loss. With upstream guide vanes producing blade wakes and other flow nonuniformities, the maximum allowable value of $M_{1\text{rel}}$ could be appreciably lower than 1.2. As Fig. 9.25 shows, prewhirl would be of no advantage if this meant reducing the value of $M_{1\text{rel}}$ from 1.2 to, say, 0.8. To accommodate transonic flow at the tip, the blade angle β_{1t} might have to be even less than 50° . Reducing the hub-tip ratio below 0.3 (say to 0.2) would not greatly increase the inlet flow area or the dimensionless shaft speed parameter. (However, with ζ much closer to 1, the results could be quite different from those shown in Fig. 9.25.)

Taking these factors into account, one might question whether the centrifugal compressor is appreciably helped by prewhirl. With no prewhirl and with $M_{1\text{rel}}$ as high as 1.2 and β_{1t} equal to 50° , the dimensionless shaft speed would have a value as high as

$$\frac{\Omega \dot{m}^{1/2}}{p_{01}^{1/2} (RT_{01})^{1/4}} = 1.4.$$

Impeller Size

With the rotational speed and inlet geometry determined (for any given air mass flow rate and inlet stagnation temperature and pressure), we can proceed to determine the impeller outlet diameter and width.

Given, from stress considerations, the outlet tip speed U_2 , we can determine the impeller diameter from

$$D_2 = \frac{2U_2}{\Omega}$$

or, in dimensionless form,

$$\frac{D_2}{\sqrt{\frac{\dot{m}}{p_{01}} (RT_{01})^{1/4}}} = \frac{2}{\sqrt{\frac{\dot{m}}{p_{01}} \frac{\Omega}{(RT_{01})^{1/4}}}} \frac{U_2}{\sqrt{RT_{01}}}. \quad (9.35)$$

Stage Pressure Ratio

Allowing for prewhirl, we can express the work done by the rotor as

$$\Delta h_0 = h_{02} - h_{01} = h_{03} - h_{01} = U_2 c_{\theta 2} - \overline{U_1 c_{\theta 1}}, \quad (9.36)$$

in which, as an average over the inlet plane,

$$\overline{U_1 c_{\theta 1}} = \frac{1}{\dot{m}} \int_{\zeta}^1 U c_{\theta} d\dot{m}.$$

Defining the adiabatic efficiency as

$$\eta_c = \frac{h_{03s} - h_{01}}{h_{03} - h_{01}} = \frac{T_{03s} - T_{01}}{T_{03} - T_{01}},$$

we have

$$\frac{T_{03s}}{T_{01}} = \left(\frac{P_{03}}{P_{01}} \right)^{(\gamma-1)/\gamma} = 1 + \eta_c \left(\frac{T_{03} - T_{01}}{T_{01}} \right)$$

or

$$\frac{P_{03}}{P_{01}} = \left[1 + \eta_c \frac{(U_2 c_{\theta 2} - U_1 c_{\theta 1})}{c_p T_{01}} \right]^{\gamma/(\gamma-1)}. \quad (9.37)$$

The ratio $\sigma_s = c_{\theta 2}/U_2$ is affected by the number of blades and the outlet blade angle; under best conditions one could expect this ratio to approach 0.9.

We may use Eq. (9.37) to determine the pressure ratio of a function of the allowable tip speed ratio $U_2/\sqrt{RT_{01}}$ and the inlet swirl parameter $c_{\theta 1}/\sqrt{RT_{01}}$ for a given exit swirl ratio $\sigma_s = c_{\theta 2}/U_2$, and a given adiabatic efficiency η_c . The inlet tip parameters $M_{1,rel}$ and β_{1t} can indirectly affect the compressor efficiency, but they do not explicitly appear in Eq. (9.37). Figure 9.26 shows an example of this relationship and indicates how very strongly compressor pressure ratio depends on the tip speed ratio $U_2/\sqrt{RT_{01}}$. The larger the inlet swirl for a given $U_2/\sqrt{RT_{01}}$, the smaller the pressure ratio, but this dependence is quite weak. At

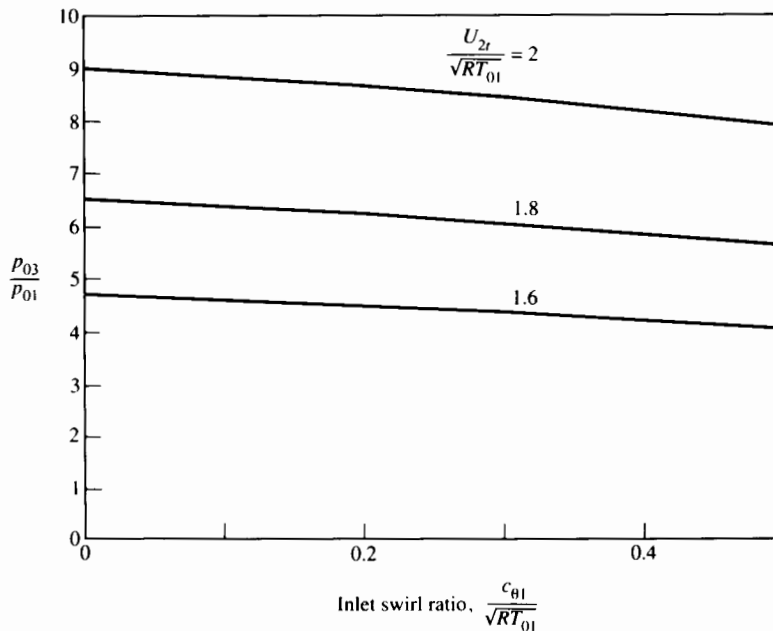


FIGURE 9.26 Centrifugal compressor; $\beta_{1t} = 45^\circ$, $M_{1,rel} = 1$, $\zeta = 0.3$, $\eta_c = 0.85$.

TABLE 9.1 Rotor diameter ratios

$M_{1\text{rel}}$	$\frac{c_{\theta 1t}}{\sqrt{RT_{01}}}$	$\frac{D_2}{D_{1t}}$
0.8	0	2.47
	0.5	2.51
1.0	0	2.00
	0.5	2.03
1.2	0	1.70
	0.5	1.73

an inlet stagnation temperature of 300 K, a value of $U_{2t}/\sqrt{RT_{01}} = 2$ would imply a tip speed of about 600 m/s, which is just within reach of current compressor design technology.

Impeller Shape

To get an idea of the general shape of the rotor, we consider here two ratios:

- The ratio of the impeller outlet diameter to the inducer inlet tip diameter;
- The ratio of the axial width of the impeller blades at exit to the impeller diameter.

Appendix VII shows how to estimate values of D_2/D_{1t} from given values of β_{1t} , $M_{1\text{rel}}$, $c_{\theta 1t}/\sqrt{RT_{01}}$, and $U_2/\sqrt{RT_{01}}$. Table 9.1 provides sample values.

Appendix VII provides the derivation of the following approximate relationship for estimating the axial-blade-width ratio:

$$\frac{b_2}{D_2} = \frac{\left(\frac{\gamma + 1}{2}\right)^{1/(\gamma-1)} (1 - \zeta^2) \left(\frac{D_{1t}}{D_2}\right)^2}{4 \left[1 + \left(\frac{1 + \eta_c}{2}\right) \left(\frac{\gamma - 1}{2}\right) \left(\frac{U_2}{\sqrt{RT_{01}}}\right)^2 \sigma_s\right]^{1/(\gamma-1)}}. \quad (9.38)$$

Using $\gamma = 1.4$, $\zeta = 0.3$, $\eta_c = 0.85$, $U_2/\sqrt{RT_{01}} = 2.0$, $\sigma_s = 0.9$, and the diameter ratios from Table 9.1, Table 9.2 gives typical results for $c_{\theta 1} = 0$. This table illus-

TABLE 9.2 Centrifugal impeller blade-length ratios

$M_{1\text{rel}}$	$\frac{D_2}{D_{1t}}$	$\frac{b_2}{D_2}$
0.8	2.47	0.024
1.0	2.00	0.037
1.2	1.70	0.051

trates an advantage of operation at higher $M_{1\text{rel}}$ with a given tip speed parameter $U_2/\sqrt{RT_{01}}$. The larger the value of b_2 , the smaller the clearance ratio Δ_2/b_2 that can be maintained.

PROBLEMS

1. A centrifugal compressor with 30 straight radial blades and no inlet guide vanes operates at a tip speed of 500 m/s. Estimate the pressure ratio for air if the inlet conditions are 1 atm and 25°C, and if the overall adiabatic efficiency is (a) 0.70, and (b) 0.85.
2. A centrifugal air-compressor rotor has been designed to operate with the inlet and outlet velocity triangles shown in the figure.

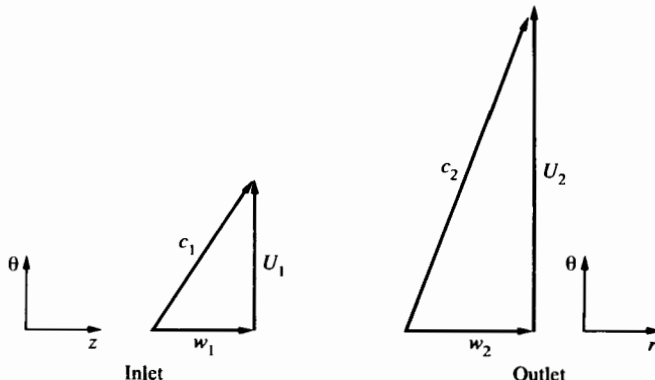
Each velocity triangle represents midpassage conditions, so that we may expect it to indicate approximately the average behavior of the fluid. Because of prewhirl the fluid enters the rotor in the axial direction (relative to the rotor), so a curved-vane inducer is not needed. At the exit of the rotor the relative velocity is in the radial direction. The rotor outlet radius is 0.157 m, and the midpassage inlet radius is 0.052 m. The rpm is 36,500. The inlet stagnation conditions are

$$p_{01} = 101 \text{ kPa}, \quad T_{01} = 288 \text{ K}.$$

For the special case $|w_1| = |w_2| = |U_1|$ and assuming isentropic flow in the rotor, determine:

- The velocities U_1, U_2, w_1, c_1, c_2 (m/s);
- The stagnation temperature T_{02} (K);
- The static pressures p_1 and p_2 (kPa);
- The stagnation pressure p_{02} (kPa).
- The Mach number $M_2 = c_2/a_2$

Noticing the large difference between p_{02} and p_2 , one can see the need for an efficient diffuser following the rotor.

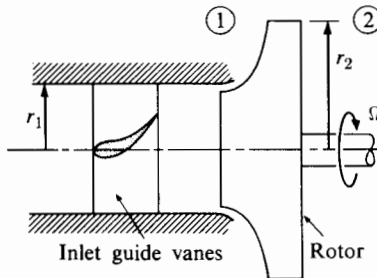


PROBLEM 2

3. Air enters a radial vaneless diffuser at Mach number 1.4 and at an angle 75° from the radial direction. Estimate the pressure ratio across the diffuser if its radius ratio is 1.5.
4. In an attempt to reduce aerodynamic losses associated with the turning of the relative velocity vector in the inducer, it is proposed that stationary inlet guide vanes be installed upstream of the rotor, as shown in the figure. The purpose of these vanes is to give the incoming fluid swirl in the direction of the rotor motion. If the swirl is solid body rotation, $c_\theta = r\Omega$, where Ω is the rotor speed, the inlet turning can be completely eliminated.
- (a) Show that if $c_{\theta 1} = r\Omega$, $c_{\theta 2} = U_2$, the axial velocity c_z and the density ρ are constant over the inlet plane (1), and if the inlet hub-tip ratio $\zeta \ll 1$, the average work done per unit mass of fluid is

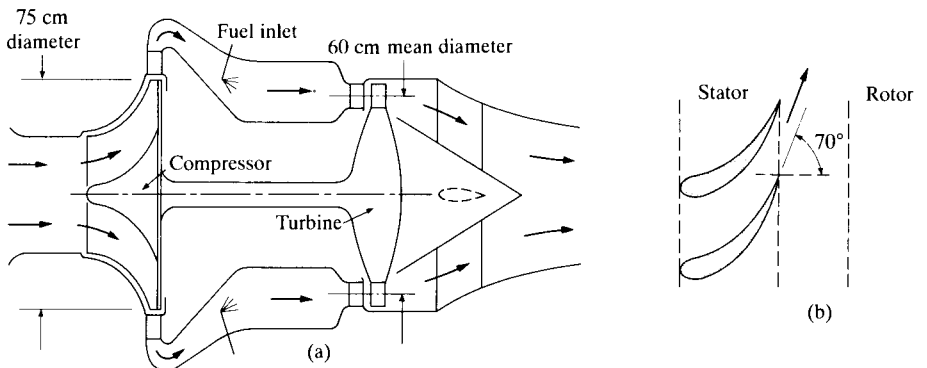
$$\Omega^2 r_2^2 \left[1 - \frac{1}{2} \left(\frac{r_1}{r_2} \right)^2 \right].$$

- (b) Is the assumption of constant axial velocity at plane (1) reasonable?
 (c) Would the inlet guide vanes present boundary layer problems? (d) Per unit mass flow rate, what is the torque on the inlet guide vanes?



PROBLEM 4

5. Shown in part (a) of the figure is a cross-sectional sketch of a turbojet engine, using a single-stage centrifugal compressor. The compressor tip diameter is 75 cm, and the turbine mean diameter is 60 cm as shown. There is no swirl in the compressor inlet, and the fuel-air ratio, f , is 0.015 kg fuel/kg air. The axial velocity throughout the turbine (nozzle and rotor) is to be held constant at 125 m/s. This axial velocity and the stator outlet velocity have set the nozzle design as in part (b) of the figure. The turbine is to be designed to give *minimum exhaust kinetic energy*, and a slip factor of 0.9 may be assumed for the compressor.
- (a) At how many rev/min will the turbine and compressor run? (b) Determine the inlet and outlet relative flow angles for the rotor, and sketch a row of turbine blades to show these angles at the mean diameter.

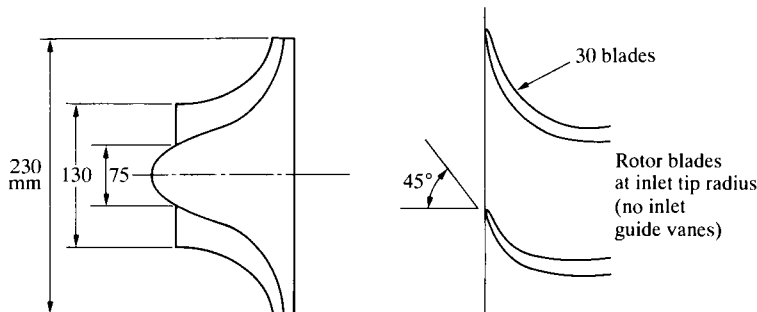


PROBLEM 5

6. A centrifugal air compressor has the dimensions shown in the figure. It operates with a tip speed of 400 m/s. The air inlet conditions are $p_a = 0.1 \text{ MPa}$ and $T_a = 298 \text{ K}$. The adiabatic compression efficiency is approximately 85%. Estimate:

- The design flow rate kg/s;
- The overall stagnation pressure ratio;
- The Mach number of the flow leaving the rotor.

You may assume that the outlet relative velocity is much smaller than the tip speed and that the slip factor is 0.9.



PROBLEM 6

7. The design mass flow rate of a certain centrifugal compressor is 7.5 kg/s with inlet stagnation temperature and pressure of 100 kPa and 300 K, respectively.

The compressor has straight radial blades at outlet, no inlet guide vanes, and a blade angle β_{1t} of 50° at the axial inducer inlet tip diameter. The inlet hub-tip ratio is 0.5.

The impeller is designed to have a relative Mach number of 0.9 at the inducer inlet tip diameter. The tip speed is 450 m/s.

- Show that the axial velocity at the inducer inlet may be determined from

$$c_1 = \frac{a_{01} M_{1\text{rel}} \cos \beta_{1t}}{\sqrt{1 + \frac{\gamma - 1}{2} (M_{1\text{rel}} \cos \beta_{1t})^2}},$$

in which a_{01} is the speed of sound at the inlet stagnation temperature.

- b. Determine:**
- The air density at the inducer inlet plane;
 - The inducer inlet diameter;
 - The rotor rpm;
 - The impeller outlet diameter.
- 8.** The centrifugal compressor impeller of Problem 7 is designed so that the relative velocity at the outlet of the rotor has the same magnitude as the axial velocity at the inlet to the inducer. The impeller has 30 blades and, as before, an outlet tip speed of 450 m/s. For the impeller outlet, determine:
- The ratio of stagnation temperature to the inlet stagnation temperature;
 - The ratio of temperature T to the inlet stagnation temperature;
 - The ratio of stagnation pressure p_0 to the inlet stagnation pressure;
 - The ratio of pressure p to the inlet stagnation pressure;
 - The axial width of the impeller flow passage at the outlet diameter.
- For this analysis assume that aerodynamic losses within the rotor are negligible and that the specific-heat ratio is 1.4.
- 9.** Review the logic by which the inducer characteristics determine the maximum allowable shaft speed of the centrifugal compressor. For the no-prewhirl case make an independent check of whether Eq. (9.32) correctly results from Eqs. (9.15) to (9.21).
- 10.** The following table represents the results of the preliminary design procedure whose results are shown in Figs. 9.25 and 9.26. Perform a check of these calculations and establish the consequences of changing the hub-tip ratio from 0.3 to 0.8. Present the results of your calculations in the same form as the following table, which is based on the assumptions of adiabatic stage efficiency of 0.85 and rotor exit slip factor of 0.9 (with straight radial blades at rotor exit).

$\frac{c_{\theta 1t}}{\sqrt{RT_{01}}}$	$M_{1\text{rel}}$	ζ	β_{1t}°	$\frac{\Omega \dot{m}^{1/2}}{p_{01}^{1/2} (RT_{01})^{1/4}}$	$\frac{U_{1t}}{\sqrt{RT_{01}}}$	$\frac{U_2}{\sqrt{RT_{01}}}$	$\frac{p_{03}}{p_{01}}$	$\frac{D_2}{D_{1t}}$
0	0.8	0.3	45	0.817	0.648	2	9.01	3.08
0.3	0.8	0.3	45	1.211	0.944	2	8.41	3.10
0	1.0	0.3	45	1.069	0.797	1.6	4.74	2.01
0.3	1.0	0.3	45	1.468	1.092	1.6	4.30	2.02
0	1.0	0.3	50	1.140	0.871	2	9.01	2.74
0.3	1.0	0.3	50	1.538	1.165	2	8.27	2.75
0	1.2	0.3	50	1.403	1.028	2	9.01	2.32
0.3	1.2	0.3	50	1.800	1.321	2	8.17	2.33

11. A centrifugal compressor is being designed for a mass flow rate of 10 kg/s of air at inlet stagnation conditions of 100 kPa and 300 K. A limiting inlet relative Mach number of 1.2 and tip blade angle of 50° have been chosen, but the combination of 1.0 and 55° is also being considered. The hub-tip radius ratio is to be 0.35, and there will be no prewhirl. Determine the maximum allowable shaft rotational speed and the entrance diameter for both these cases.
12. At the outlet of the impeller of a single-stage centrifugal compressor and with respect to a stationary reference frame, the stagnation pressure and temperature are 723 kPa and 510 K, and the Mach number is 1.2. The angle between the absolute velocity vector and the radial direction is to be not greater than 70°. The compressor flow rate is 1.5 kg/s and the impeller diameter is 15 cm.
 - a. What should be the axial width of the vaneless space just outside the impeller?
 - b. If the diffuser effectiveness (for definition see Fig. 9.20) is 0.7, what will the static pressure ratio across the diffuser be?
13. At the entrance to a vaned diffuser the radius is 0.42 m and the absolute flow Mach number is 0.9 at an angle of 68° with respect to the radial direction. The outlet radius of the vanes is 0.515 m and their axial width is constant. If the flow were isentropic in the vaned passages and the diffuser effectiveness (defined in Fig. 9.20) were 0.65, what would the outlet blade angle be? Given a drop in stagnation pressure in the vaned passages of 5% and the same static recovery ratio in this case, determine the required exit blade angle. As a first approximation assume that the vane and flow angles are the same.
14. A “pipe” diffuser has a throat diameter of 1.0 cm and a boundary layer displacement thickness at the throat of 0.05 mm. The diffuser is to operate with sonic flow at the throat. Downstream of the throat the conical section has a divergence angle of 11° (total angle). Negligible stagnation pressure loss is expected upstream of the throat. For a diffuser effectiveness of 0.7, what will be the exit diameter of the diffuser and what will be the length of the conical divergence? Calculations indicate that the boundary layer displacement thickness will be about 0.78 mm at the outlet diameter. The flow in the diffuser core may be considered isentropic.
15. A radial compressor impeller operating at 21,500 rpm has a diameter of 0.40 m and 40 straight radial vanes at exit. At a diameter of 0.37 m, the flow in the impeller is in the radial direction and the local fluid density is 2.9 kg/m^3 . The axial width of the impeller blades at that diameter is 21 mm, and the blade thickness is 1.5 mm. Plot the blade-to-blade velocity profile at that diameter if the total mass flow rate is 9.5 kg/s. Also plot the velocity profile if the mass flow rate drops by 50% while the local density remains unchanged. Ignore viscous effects. Show the direction of blade rotation and estimate the local pressure difference across the blades.
16. Consider the impeller of Fig. 9.21 (whose performance under design conditions is stated in Fig. 9.22(b)). From the data in Fig. 9.22(b) and (c), deduce

the impeller slip factor at best efficiency and from 75% to 100% of design speed. Compare your result at design speed with the slip factor estimated with Eq. (9.25).

17. The compressor whose performance is shown in Fig. 9.23 is to be operated at an altitude condition where the inlet stagnation pressure is 17.5 kPa and the inlet stagnation temperature is 243 K. The required pressure ratio is 5.5. At what speed and mass flow rate must it be operated if the efficiency is to be maximum? At the same shaft speed, how low can the mass flow rate drop before surge sets in?

REFERENCES

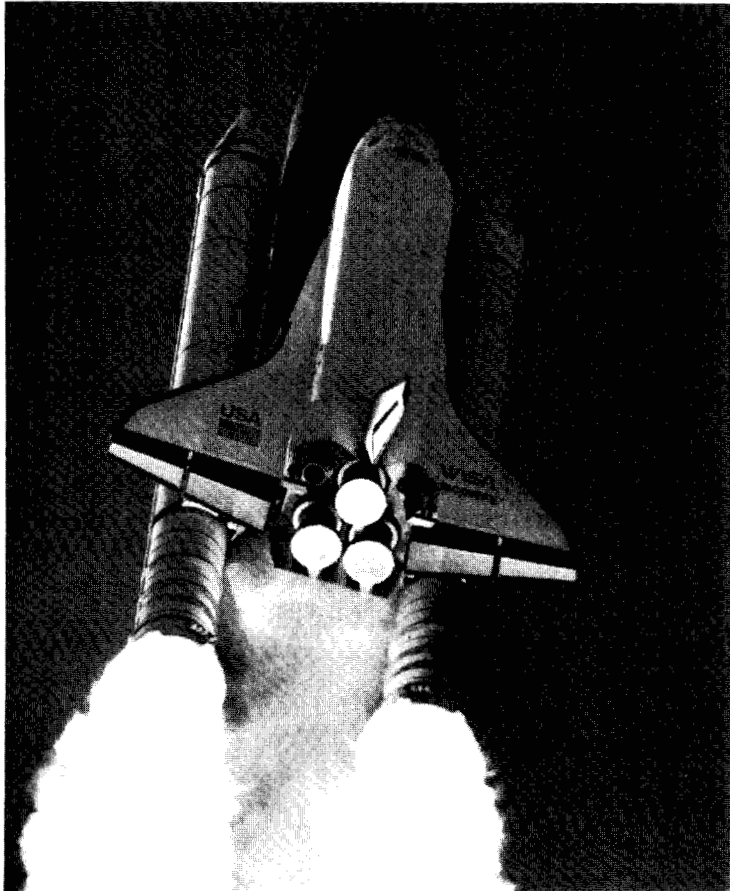
1. Morris, R. E. "The Pratt & Whitney PW100—Evolution of the Design Concept," *CASI J.* 28 (1982): 211–221.
2. Kenny, D. P. "The History and Future of the Centrifugal Compressor in Aviation Gas Turbines," First Cliff Garrett Turbomachinery Award Lecture, Society of Automotive Engineers Publication SP-602, Oct. 16, 1984. ©1990 Society of Automotive Engineers, Inc. Reprinted with permission.
3. Cumpsty, N. A. *Compressor Aerodynamics*. New York: Wiley, 1989.
4. Schumann, L. F., D. A. Clark, and J. R. Wood. "Effect of Area Ratio on the Performance of a 5.5:1 Pressure Ratio Centrifugal Impeller," *Trans. ASME J. Turbomachinery* 105 (1987): 10–19.
5. Taylor, E. S. "The Centrifugal Compressor," in *Aerodynamics of Turbines and Compressors*, vol. 10 of *High-Speed Aerodynamics and Jet Propulsion*, W. R. Hawthorne, ed. Princeton, N.J.: Princeton University Press, 1964.
6. Wiesner, F. J. "A Review of Slip Factors for Centrifugal Impellers," *Trans. ASME Series A, J. Eng. For Power* 89 (1967): 588–592.
7. Senoo, Y., and M. Ishida. "Deterioration of Compressor Performance Due to Tip Clearance of Centrifugal Compressors," *Trans. ASME J. Turbomachinery* 103 (1987): 55–61.
8. Prince, T. C., and A. C. Bryans. "Three-Dimensional Inviscid Computation of an Impeller Flow," *J. Eng. for Gas Turbines and Power* 106 (1984): 523–528. Reprinted with permission.
9. Rodgers, C. "Static Pressure Recovery Characteristics of Some Radial Vaneless Diffusers," *CASI J.* 30 (1984): 42–54.
10. Jansen, W. "Rotating Stall in Radial Vaneless Diffuser," *Trans. ASME J. Basic Engineering* 86 (1964): 750–758.
11. Senoo, Y., and Y. Kinoshita. "Influence of Inlet Flow Conditions and Geometries of Centrifugal Vaneless Diffusers on Critical Flow Angles for Reverse Flow," *Trans. ASME J. Fluids Eng.* 99 (1977): 98–103.
12. Kenny, D. P. "A Comparison of the Measured and Predicted Performance of High Pressure Ratio Centrifugal Compressor Diffusers," ASME Paper no. 72-GT-54, 1972.

13. _____. "A Turbulent Boundary Layer Analysis of Conical Diffusers," *CASI Trans.* (1974): 49-59.
14. _____. "A Novel Correlation of Centrifugal Compressor Performance for Off-Design Prediction," AIAA/SAE/ASME First Joint Propulsion Conference, June 18-20, 1979, Las Vegas, Nev. Reprinted with permission.
15. Chevis, R.W. "Design and Test of Two 8:1 Pressure Ratio Single-Stage Centrifugal Compressors of Different Flow Size," *Canadian Aeronautics and Space Institute Journal* 30 (1984): 16-32. Reprinted with permission.

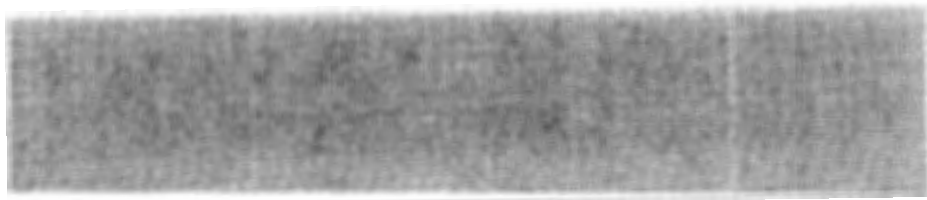
P A R T

3

ROCKET ENGINES



Space shuttle. (Courtesy Rockwell International, Rocketdyne Division.)



C H A P T E R

10

PERFORMANCE OF ROCKET VEHICLES

10.1 INTRODUCTION

Rockets are distinguished from air-breathing propulsion engines by the fact that they carry all of their propellant with them. They develop thrust by imparting energy and momentum to the propellant as it is expelled from the engine. The necessary energy source in a rocket may be chemical, nuclear, or solar. Momentum may be given to the fluid by pressure or by electrostatic or electromagnetic forces. There is thus a variety of possible rocket engines, each with its own characteristic performance. The purpose of this chapter is to discuss in general the performance of rocket vehicles in order to show which characteristics of a rocket engine are most desirable for a given mission. The rocket most suitable for a long space journey, for example, is quite different from the one most suitable for launching from the earth's surface.

In this chapter we discuss the thrust and acceleration of rocket engines and vehicles. We consider the effects of exhaust velocity and the proportionate distribution of vehicle mass between propellant, payload, engine, and structure, for both single and multistage vehicles. A brief discussion of space-flight mechanics and missions is included at the end of the chapter in order to show how requirements are established for propulsion systems to be used in space missions.

10.2 STATIC PERFORMANCE

Thrust

It is useful to begin by examining the performance of a rocket under static tests. An application of the momentum equation developed in Chapter 2 will show how the thrust developed depends on the propellant flow rate, the exhaust velocity and pressure, and the ambient conditions.

Consider the thrust of a stationary rocket indicated schematically in Fig. 10.1. For simplicity assume that the flow is one-dimensional, with a steady exit velocity u_e and propellant flow rate \dot{m} . Consider a stationary control surface S that intersects the jet perpendicularly through the exit plane of the nozzle. Positive thrust T acts in the direction opposite to u_e . The *reaction* to the thrust is shown in Fig. 10.1 as it acts on the control volume. If the expelled fluid can be considered a continuum, it is necessary to consider the pressures just inside the exit plane of the nozzle, p_e , and in the environment, p_a . The cross-sectional area of the jet is A_e , the exit area of the nozzle. The momentum equation for any such control volume is

$$\sum F_x = \frac{d}{dt} \int_{cv} \rho u_x dV + \int_{cs} u_x d\dot{m}, \quad (10.1)$$

where F_x = force component in the x -direction,

ρ = density of fluid,

u_x = velocity component of fluid in the x -direction,

V = volume, and

\dot{m} = mass rate of flow (positive for outflow),

and where the subscripts cv and cs denote the control volume and control surface, respectively.

Since u_x is zero within the propellant tank or tanks (the control volume includes the tanks), and the flow is steady within the thrust chamber, the time-derivative term is zero. We can also write the momentum-flux term as

$$\int_{cs} u_x d\dot{m} = \dot{m} u_e. \quad (10.2)$$

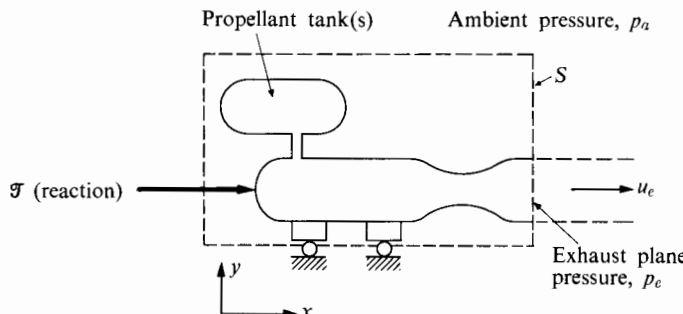


FIGURE 10.1 Rocket in static firing.

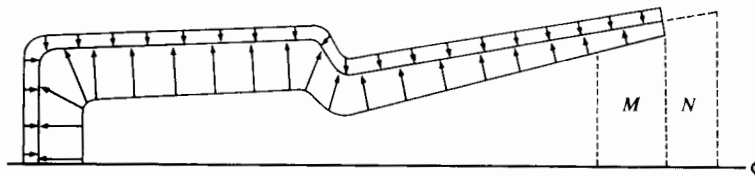


FIGURE 10.2 Pressure distribution on rocket casing.

Considering the pressure on the control surface to be uniformly p_a , except in the plane of the jet, we may write the force summation as

$$\sum F_x = \mathcal{T} + A_e p_a - A_e p_e. \quad (10.3)$$

Thrust is actually a result of pressure or stress distribution over interior and exterior surfaces, as shown typically for a chemical rocket in Fig. 10.2. However, we defer the questions of how these forces depend on geometry and propellant behavior to later discussions of individual rocket types. For the present, the momentum equation permits calculation of the overall thrust in terms of conditions in the exhaust plane. Combining Eqs. (10.1), (10.2), and (10.3), we obtain

$$\mathcal{T} = \dot{m} u_e + (p_e - p_a) A_e. \quad (10.4)$$

If the pressure in the exhaust plane is the same as the ambient pressure, the thrust is given by $\mathcal{T} = \dot{m} u_e$.

The condition $p_a = p_e$ is called correct or optimum expansion because it corresponds to maximum thrust for given chamber conditions. We can show this quite simply. Suppose that a length of diverging nozzle passage (N in Fig. 10.2) is added to a nozzle undergoing correct expansion. Owing to further expansion, the pressure inside N will be less than the ambient pressure, so that the total pressure force on it will oppose the thrust. Thus the fluid should not be expanded below ambient pressure. On the other hand, expanding the fluid to a pressure above ambient is equivalent to removing length M from the correct nozzle, and we can see that this also reduces the thrust. Consequently the thrust of the rocket is maximized, for given chamber conditions and throat area, when the fluid expands to ambient pressure. As we will see in Section 10.3, it is convenient to define an equivalent exhaust velocity, u_{eq} , such that

$$u_{eq} = u_e + \left(\frac{p_e - p_a}{\dot{m}} \right) A_e. \quad (10.5)$$

With this definition we can write the thrust equation as

$$\mathcal{T} = \dot{m} u_{eq}. \quad (10.6)$$

Specific Impulse

The impulse per unit mass of propellant is an important performance variable. If the velocity u_{eq} is constant, Eq. (10.6) shows that the total impulse I imparted to the vehicle during acceleration is

$$I = \int \mathcal{T} dt = M_p u_{eq},$$

where M_p is the total mass of expelled propellant. The impulse per unit mass of propellant is therefore

$$\frac{I}{M_p} = \frac{\mathcal{T}}{\dot{m}} = u_{eq}.$$

The term *specific impulse*, I_{sp} , is usually defined by

$$I_{sp} = \frac{I}{M_p g_e} = \frac{u_{eq}}{g_e}, \quad (10.7)$$

where g_e is the acceleration due to gravity at the earth's surface. The presence of g_e in the definition is arbitrary, but it does have the advantage that in all common systems of units the specific impulse is expressed in seconds.

Since the mass of the propellant is often a large part of the total mass, it would seem desirable to have as large a specific impulse as possible. This conclusion holds directly for chemical rockets. For electrical rockets, high specific impulse implies massive power-generating equipment; hence maximum specific impulse does not generally mean best vehicle performance. We will discuss these factors in more detail subsequently.

10.3 VEHICLE ACCELERATION

Since a large fraction of the total mass of a rocket before firing may be propellant, the mass of the vehicle varies a great deal during flight. One must take this into account in order to determine the velocity the vehicle attains during the consumption of its propellant. Consider an accelerating rocket as indicated in Fig. 10.3. At some time t its mass is instantaneously M and its velocity u . During a short time interval dt , it exhausts a mass increment dm with an exhaust velocity u_e relative to the vehicle as the vehicle velocity changes to $u + du$.

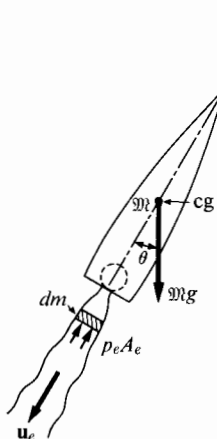


FIGURE 10.3 Acceleration of rocket vehicle in a gravity field.

The change of momentum (in the u -direction) of the vehicle during the interval dt is

$$\mathcal{M}(u + du) - \mathcal{M}u = \mathcal{M}du.$$

The change of momentum of the mass dm is

$$dm(u - u_e) - dm u = -dm u_e.$$

Consider the forces acting on a system composed of the masses \mathcal{M} and dm . Unless the exhaust pressure is equal to the atmospheric pressure, there will be a net pressure force $(p_e - p_a)A_e$ acting on the system in the positive \mathbf{u} -direction. In general, a drag force \mathcal{D} will act in the negative \mathbf{u} -direction, along with a gravitational force $(\mathcal{M} + dm)g \cos \theta$, where g is the local gravitational acceleration and θ is the angle between \mathbf{u} and \mathbf{g} as in Fig. 10.3. The net force on the system in the \mathbf{u} -direction, neglecting dm relative to \mathcal{M} , is

$$\sum F = (p_e - p_a)A_e - \mathcal{D} - \mathcal{M}g \cos \theta.$$

The resultant impulse $(\sum F)dt$ must equal the momentum change of the system during this interval. Therefore

$$\mathcal{M}du - dm u_e = [(p_e - p_a)A_e - \mathcal{D} - \mathcal{M}g \cos \theta]dt. \quad (10.8)$$

Since

$$dm = +\dot{m} dt = -\frac{d\mathcal{M}}{dt} dt,$$

where \dot{m} is the propellant flow rate, Eq. (10.8) becomes

$$\mathcal{M}du = [(p_e - p_a)A_e + \dot{m}u_e - \mathcal{D} - \mathcal{M}g \cos \theta]dt$$

or, using the definition of u_{eq} in Eq. (10.5), we obtain

$$du = -u_{eq} \frac{d\mathcal{M}}{\mathcal{M}} - \frac{\mathcal{D}}{\mathcal{M}} dt - g \cos \theta dt. \quad (10.9)$$

In the absence of drag and gravity, integration of Eq. (10.9), with the assumption of constant equivalent velocity u_{eq} , leads to

$$\Delta u = -u_{eq} \ln \frac{\mathcal{M}}{\mathcal{M}_0} = +u_{eq} \ln \frac{\mathcal{M}_0}{\mathcal{M}}, \quad (10.10)$$

where Δu is the change in vehicle velocity and \mathcal{M}_0 is its initial mass. Thus the total change Δu in velocity during the burning period is

$$\Delta u = u_{eq} \ln \mathcal{R}, \quad (10.11)$$

where the mass ratio $\mathcal{R} = \mathcal{M}_0/\mathcal{M}_b$, and \mathcal{M}_b = burnout mass, or mass at the end of the thrust period. We will show that this term can characterize the propulsion requirements for any mission, including those with gravity and drag effects.

Gravity

One can deduce the variation in gravitational attraction with distance from the earth's surface from Newton's law of gravitation:

$$g = g_e \left(\frac{R_e}{R_e + h} \right)^2, \quad (10.12)$$

where g = local acceleration due to gravity,

g_e = acceleration due to gravity at the surface of the earth,

R_e = radius of the earth,

h = distance from the surface of the earth.

The thrust period of chemical rockets usually ends when the distance that the vehicle travels is a small fraction of the earth's radius and the gravitational acceleration has not altered very much. At an altitude of 100 miles, for example, $g = 0.95g_e$. Assuming constant equivalent exhaust velocity, zero drag, and constant gravitational acceleration, we may integrate Eq. (10.9) with the result that

$$\Delta u = u_{eq} \ln \mathcal{R} - g \overline{\cos \theta t_b}, \quad (10.13)$$

where t_b is the burning period and $\overline{\cos \theta}$ is the integrated average value of $\cos \theta$. This approach is convenient only for relatively short thrust periods. When one considers gravity, it is clear that the absolute thrust level is important as well as the exhaust velocity and mass ratio. When a vehicle is launched from the earth's surface, the thrust of the vehicle should be from one and one-half to two times the initial weight in order that the vehicle may leave the ground with reasonable acceleration.

Drag

One can estimate the resistance of the atmosphere to the passage of a rocket through it from empirical drag-coefficient information. It is conventional to express the drag on any body passing through a real fluid in the form

$$\mathcal{D} = C_D \frac{1}{2} \rho u^2 A_f, \quad (10.14)$$

where \mathcal{D} = retarding force due to viscous and pressure forces,

ρ = local air density,

u = vehicle velocity,

A_f = frontal cross-sectional area of the vehicle,

C_D = drag coefficient.

The coefficient C_D depends on the vehicle shape, speed, and inclination, ϕ , to the flight direction. A typical variation is suggested by Fig. 10.4.

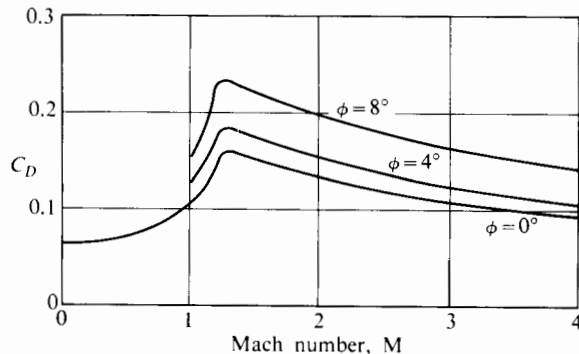


FIGURE 10.4 Typical drag coefficient.

Atmospheric density may vary considerably during the thrust period of a rocket. Density varies with altitude approximately as

$$\rho(h) = a \exp(-bh^{1.15}),$$

in which ρ is the atmospheric density and h the height above the surface of the earth. For ρ in kg/m^3 and h in m ,

$$\begin{aligned} a &= 1.2, \\ b &= 2.9 \times 10^{-5}. \end{aligned}$$

For ρ in lb_m/ft^3 and h in ft,

$$\begin{aligned} a &= 0.075, \\ b &= 7.4 \times 10^{-6}. \end{aligned}$$

Appendix III shows the variation of density with height in the ICAO standard atmosphere.

The atmospheric density is reduced to 1% of its sea-level value at an altitude of just 30 km, that is, 100,000 ft. With adequate data on drag coefficient and density variations it is possible to calculate accurately the actual performance of a given rocket vehicle rising against gravitational forces through the atmosphere.

For guidance purposes, of course, accurate trajectory calculations are required. Equation (10.13) is then inadequate, since it requires foreknowledge of the trajectory. Figure 10.5 indicates an approximate calculation procedure that accounts for the effects of gravitational and drag forces on the path of a typical maneuver, a gravity turn. In a gravity turn the vehicle is assumed to begin at some angle θ_1 to the local gravity vector, with all subsequent turning being due only to gravity. The thrust and drag are always parallel to the vehicle velocity (with no aerodynamic lift). Figure 10.5(a) illustrates the changing vehicle velocity components parallel and normal to the earth's surface (u_x and u_y , respectively). The calculation proceeds stepwise through small time and velocity increments from the initial condition. During each time interval δt , D/M , g , and θ are assumed constant. The vehicle velocity change δu in any time increment is the vector sum of three terms: δu_T due to thrust, parallel to u at the start of δt ;

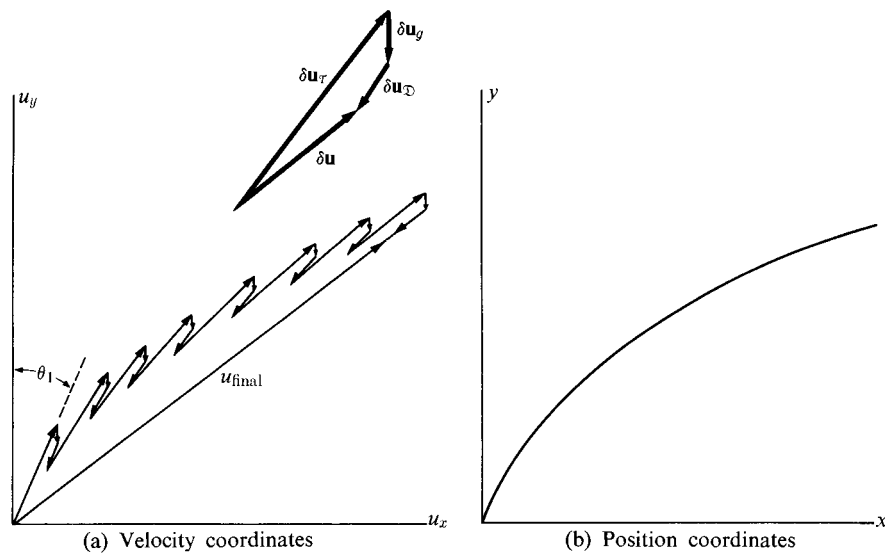


FIGURE 10.5 Approximate calculation of the trajectory of a vehicle undergoing a gravity turn from launch at angle θ_1 .

$\delta\mathbf{u}_D$ due to drag, parallel and opposite to $\delta\mathbf{u}_T$; and $\delta\mathbf{u}_g$ due to gravity, parallel to \mathbf{g} . Each of these terms can be calculated from the velocity at the beginning of δt . Of course, the accuracy of this procedure depends on the size of the time intervals δt compared with t_b .

Having obtained the solution of \mathbf{u} as a function of time, one can easily plot the trajectory, Fig. 10.5(b) from the velocity diagram. That is, $\delta\mathbf{y} = \mathbf{u}_y \delta t$, $\delta\mathbf{x} = \mathbf{u}_x \delta t$, for each δt . This figure is intended only to indicate the nature of the complete problem and to point out that for our purposes we are interested simply in the summation of the magnitudes of the $\delta\mathbf{u}_T$ terms. Clearly, this is

$$\sum |\delta\mathbf{u}_T| = |\mathbf{u}_{eq}| \ln \mathcal{R}.$$

Thus, having properly calculated the actual trajectory, the simple integration of Eq. (10.9), as given by Eq. (10.11), adequately describes the propulsion requirements for a given mission even in the presence of gravity and drag.

Single-Stage Sounding Rocket

As a simple example, consider the height to which a single-stage rocket will rise if we neglect drag and assume that the effective exhaust velocity is constant.

For vertical flight the altitude attained at burnout, h_b , is

$$h_b = \int_b^{t_b} u dt,$$

where u is given by

$$u = -u_e \ln \frac{M}{M_0} - g_e t.$$

If the rate of fuel consumption is constant, the mass varies with time as

$$M(t) = M_0 - (M_0 - M_b)t/t_b.$$

Then

$$u = -u_e \ln \left[1 - \left(1 - \frac{1}{\mathcal{R}} \right) \frac{t}{t_b} \right] - g_e t, \quad (10.15)$$

and

$$h_b = -u_e t_b \frac{\ln \mathcal{R}}{\mathcal{R} - 1} + u_e t_b - \frac{1}{2} g_e t_b^2. \quad (10.16)$$

Equating the kinetic energy of the mass at burnout, M_b , with its change of potential energy between that point and the maximum height, h_{\max} , we obtain

$$M_b \frac{u_b^2}{2} = M_b g_e (h_{\max} - h_b),$$

and thus

$$h_{\max} = h_b + \frac{u_b^2}{2g_e}. \quad (10.17)$$

Finally,

$$h_{\max} = \frac{u_e^2 (\ln \mathcal{R})^2}{2g_e} - u_e t_b \left(\frac{\mathcal{R}}{\mathcal{R} - 1} \ln \mathcal{R} - 1 \right). \quad (10.18)$$

Burning Time

The result we have just obtained points out the desirability of reducing the burning time as much as possible while accelerating against a gravity field. Physically, short burning times reduce the energy consumed in simply lifting the propellant. Very short burning times, however, imply not only very high accelerations, which may impose severe stresses on the structure and instruments, but also exceedingly high propellant flow rates. The size of the machinery necessary to handle large flows is a limiting factor. In addition, atmospheric drag imposes a penalty if the vehicle is accelerated too quickly within the earth's atmosphere. Burning times for existing high-thrust rockets are usually in the range of 30 to 200 seconds.

In the absence of gravitation or drag, burning time has no influence on stage velocity increment, as we may see from Eq. (10.11). In this case the velocity of the vehicle is a function only of the fraction of propellant expended and not of the time consumed in acceleration.

10.4 CHEMICAL ROCKETS

Chemical rockets are essentially energy-limited devices, whereas electrical rockets are mainly power limited. Their performance characteristics are quite different, and we will deal with them separately. We begin in this section with the single-stage chemical rocket and then discuss multistaging.

Single-Stage Rockets

We can more readily describe the performance of both single- and multistage rockets by first considering certain definitions. The total mass of a rocket stage may be considered the sum of several parts. Most important among these, though often the smallest, is the mass of the *payload*, M_L . The mass necessary to give the payload the desired motion is usually divided into the *propellant mass*, M_p , and the *structural mass*, M_s . Unless otherwise stated, the structural mass includes all mass other than payload and propellant. In particular this includes the engine and the guidance and control equipment, as well as tankage and supporting structures. The *initial mass* M_0 is the sum of all of these quantities:

$$M_0 = M_L + M_p + M_s. \quad (10.19)$$

If the rocket consumes all its propellant during firing, the burnout mass consists simply of structure and payload:

$$M_b = M_L + M_s. \quad (10.20)$$

It is useful to arrange these variables in certain ratios. The first of these is the previously introduced mass ratio \mathcal{R} , given by

$$\mathcal{R} = \frac{M_0}{M_b} \approx \frac{M_0}{M_L + M_s}, \quad (10.21)$$

the last expression applying when Eq. (10.20) is valid. Another is the payload ratio, λ , defined by

$$\lambda = \frac{M_L}{M_0 - M_L} = \frac{M_L}{M_p + M_s}. \quad (10.22)$$

Large payload ratios are, of course, desirable. To the scientist interested in performing certain observations requiring rocket transportation of instrument payloads, the payload ratio invariably seems too small. Obviously, the larger the payload a given rocket carries, the lower its maximum attainable velocity:

$$\epsilon = \frac{M_s}{M_p + M_s} \approx \frac{M_b - M_L}{M_0 - M_L}. \quad (10.23)$$

The last expression applies exactly when the burnout mass includes no propellant. For a chemical rocket the structural coefficient ϵ is a measure of the vehicle designer's skill in designing a very light tank and support structure.

Combining these definitions, we may express the mass ratio \mathcal{R} as

$$\mathcal{R} = \frac{1 + \lambda}{\epsilon + \lambda}. \quad (10.24)$$

If the rocket vehicle is so large that the total structure and engine mass is essentially proportional to the initial propellant mass, then ϵ would be a constant, independent of vehicle size or mission velocity.

For vehicles or missions in which engine mass is not negligible, this will not be so. To see how the structural coefficient ϵ and the payload ratio M_p/M_0 may depend on the fuel and mission, we can use the data on the *Apollo* J-2 (hydrogen) and H-1 (hydrocarbon fuel) engines provided by Martin [1] and cited in Table 10.1. The two engines have the same thrust. The engine and tank are substantially larger for fueling with hydrogen fuel. The specific impulse of hydrogen, however, is substantially higher than for hydrocarbon fuel. In Table 10.1 the term M_{tank} includes the mass of the support structure.

We consider the size of either of these engines in a rocket vehicle that is to achieve a velocity increment Δu . (The term Δu is adjusted to compensate for the effects of velocity reductions due to gravity and drag.)

Balancing masses, we obtain that the payload M_p is

$$M_p = M_0 - (M_{\text{engine}} + M_{\text{tank}}) - M_p.$$

We may then write the payload ratio as

$$\frac{M_p}{M_0} = 1 - \frac{M_{\text{engine}}}{M_0} - \frac{M_{\text{tank}}}{M_p} \frac{M_p}{M_0} - \frac{M_p}{M_0}.$$

But since, from Eq. (10.11), we can show that

$$\mathcal{R} = \frac{M_0}{M_0 - M_p} = e^{\Delta u/u_e},$$

it follows that

$$\frac{M_p}{M_0} = 1 - e^{-\Delta u/u_e},$$

TABLE 10.1 Apollo rocket engines

	J-2	H-1
Fuel	H ₂	hydrocarbon
Thrust, kN	1023	1023
$M_{\text{engine}}, \text{Mg}$	1.622	0.921
M_{engine}/M_0	0.024	0.014
M_{tank}/M_p	0.046	0.016
$u_e \text{ m/s}$	4175	2891
I_{sp}, s	426	295

so that

$$\frac{M_L}{M_0} = 1 - \frac{M_{\text{engine}}}{M_0} - \left(1 + \frac{M_{\text{tank}}}{M_p}\right) \left(1 - e^{-\Delta u/u_e}\right). \quad (10.25)$$

We can then express the structural coefficient as

$$\epsilon = \frac{M_{\text{tank}} + M_{\text{engine}}}{M_p + M_{\text{tank}} + M_{\text{engine}}},$$

which is equivalent to

$$\epsilon = \frac{\frac{M_{\text{tank}}}{M_p} \left(1 - e^{-\Delta u/u_e}\right) + \frac{M_{\text{engine}}}{M_0}}{\left(1 - e^{-\Delta u/u_e}\right) \left(1 + \frac{M_{\text{tank}}}{M_p}\right) + \frac{M_{\text{engine}}}{M_0}}. \quad (10.26)$$

With these two relationships we can see how ϵ and M_L/M_0 depend on the mission for the two fuels. Figure 10.6 shows how the payload ratio M_L/M_0 and the structural coefficient ϵ depend on the mission and the fuel, using the tank and engine mass data that Martin provides. At low values of Δu the structural coefficient declines sharply with Δu ; only for large Δu does ϵ become independent of Δu .

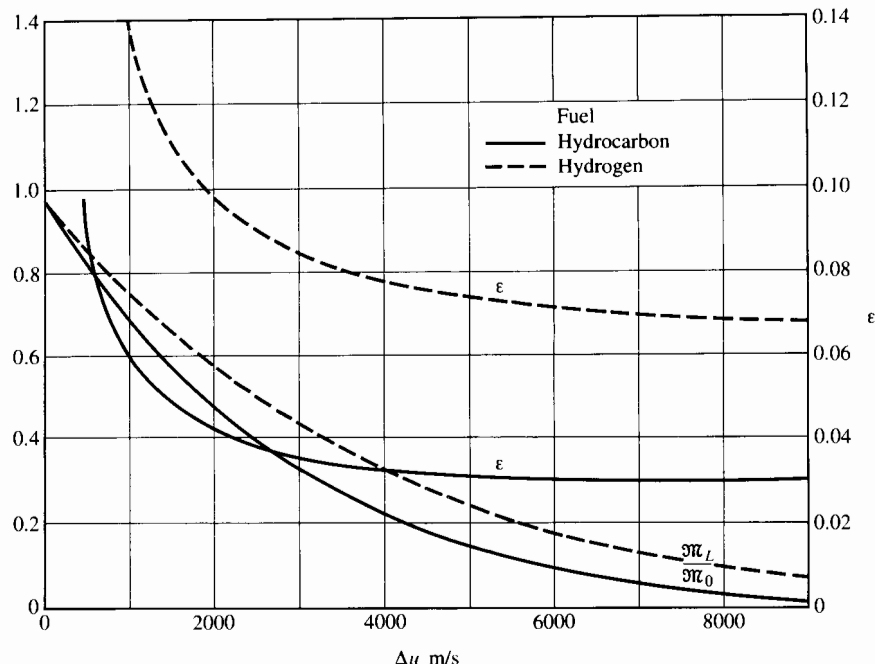


FIGURE 10.6 Structural coefficient ϵ and payload ratio M_L/M_0 .

Multistage Rockets

For many important missions with chemical rockets, the propellant mass is much larger than the payload. The mass of the propellant tanks and support structure may, in itself, be larger than the payload. Unless portions of this structure and tankage are discarded as they become empty, much energy is consumed in their acceleration, and therefore less is available for acceleration of the payload. This is one of the reasons for designing rocket vehicles that can discard tank sections as they become empty. In addition, an engine large enough to accelerate the initial mass of the vehicle may produce excessive acceleration stresses when the propellant is nearly consumed. Since it is difficult to operate a given engine at reduced thrust, multistage rocket vehicles are often employed. A multistage rocket is a series of individual vehicles or stages each with its own structure, tanks, and engines. The stages are so connected that each operates in turn, accelerating the remaining stages and the payload before being detached from them. In this way excess structure and tankage are discarded, and the engines of each stage can be properly matched to the remaining vehicle mass. Stages are numbered in the order of firing, as illustrated in Fig. 10.7 for a three-stage chemical rocket carrying payload M_p .

The analysis of multistage rockets is similar to that for single-stage rockets, since the payload for any particular stage is simply the mass of all subsequent stages. The payload for the first stage of Fig. 10.7 is simply the sum of the masses of stages 2 and 3 (including M_p).

The definitions given above may be extended to apply to the generalized i th stage of a rocket consisting of a total of n stages. The nomenclature used is as follows:

$$i = \text{any of the stages } 1 \leq i \leq n;$$

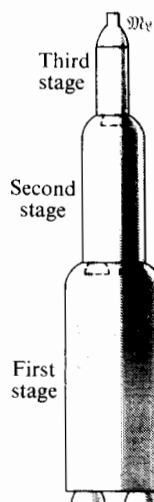


FIGURE 10.7 Typical multistage rocket.

M_{0i} = total initial mass of the i th stage prior to firing, including its effective payload;

M_{bi} = total mass of the i th stage after burnout, including its effective payload;

$M_{\mathcal{L}}$ = payload of the last stage to fire;

M_{si} = structural mass of the i th stage alone, including the mass of its engine, controls, and instruments.

Since, as we mentioned, the payload of any stage is simply the mass of all subsequent stages, the payload ratio λ_i of the i th stage is

$$\lambda_i = \frac{M_{0(i+1)}}{M_{0i} - M_{0(i+1)}}. \quad (10.27)$$

The structural coefficient of the i th stage becomes

$$\epsilon_i = \frac{M_{si}}{M_{0i} - M_{0(i+1)}}, \quad (10.28)$$

or, if the i th stage contains no propellant at burnout,

$$\epsilon_i = \frac{M_{bi} - M_{0(i+1)}}{M_{0i} - M_{0(i+1)}}. \quad (10.29)$$

The mass ratio \mathcal{R}_i of the i th stage may be written

$$\mathcal{R}_i = M_{0i}/M_{bi}, \quad (10.30)$$

which, with the aid of the definitions, becomes

$$\mathcal{R}_i = \frac{1 + \lambda_i}{\epsilon_i + \lambda_i}. \quad (10.31)$$

Example

To illustrate the gains to be made by multistaging, consider first a single-stage rocket whose exhaust velocity is 3048 m/s. Suppose we must accelerate a 1000-kg payload with a total initial mass of 15,000 kg and a total structural mass of 2000 kg (including engine, controls, and instruments). Using the foregoing definition with this data, we find that the structural coefficient of the rocket is $\epsilon = 0.143$ and the payload factor is $\lambda = 0.0714$. We can obtain the velocity to which the payload could be accelerated in a zero gravity field from

$$u = u_e \ln \mathcal{R} = u_e \ln \frac{1 + \lambda}{\epsilon + \lambda},$$

which yields a value of u of 4904 m/s.

Consider next a two-stage rocket of the same initial mass, total structural mass, payload, and exhaust velocity as the first rocket. If we assume that the payload ratios of the two stages are equal, then

$$\lambda_1 = \lambda_2 = \lambda = \frac{M_{02}}{M_{01} - M_{02}} = \frac{M_{\mathcal{L}}}{M_{02} - M_{\mathcal{L}}}.$$

With $M_{\infty} = 1000 \text{ lb}_m$ and $M_{01} = 15,000 \text{ kg}_m$, this requirement is satisfied by $M_{02} = 3873 \text{ kg}$ and $\lambda_1 = \lambda_2 = 0.348$. Assuming the structural coefficients of the two stages to be the same, we obtain

$$\epsilon_1 = \epsilon_2 = \epsilon = \frac{M_{s1}}{M_{01} - M_{02}} = \frac{M_{s2}}{M_{02} - M_{\infty}}.$$

Also

$$M_{s1} + M_{s2} = 2000 \text{ kg}.$$

Solving these two equations, we find that

$$M_{s1} = 1589 \text{ kg}, \quad M_{s2} = 411 \text{ kg}, \quad \epsilon_1 = \epsilon_2 = 0.143.$$

Since the mass ratio $\mathcal{R} = (1 + \lambda)/(\epsilon + \lambda)$, and since the exhaust velocity of each stage is the same, the final velocity attained by the vehicle is

$$u = 2u_{eq} \ln\left(\frac{1 + \lambda}{\epsilon + \lambda}\right) \quad \text{or} \quad u = 6160 \text{ m/s}.$$

The performance of the two rockets is summarized in Table 10.2, which shows that the two-stage rocket is clearly superior to the single-stage rocket in terminal velocity of the payload.

Returning to the general n -stage rocket, the stage velocity increment in the absence of gravity and drag is $\Delta u_i = u_{ei} \ln \mathcal{R}_i$, and the payload terminal velocity is simply the sum of the n velocity increments:

$$u_n = \sum_{i=1}^n u_{ei} \ln \mathcal{R}_i. \quad (10.32)$$

TABLE 10.2 Performance of single-stage and two-stage rockets^a

	Two stage		
	Single stage	Stage 1	Stage 2
Total initial mass M_0 , kg (including payload)	15,000	15,000	3,873
Payload, kg	1,000	3,873	1,000
Structural mass, kg	2,000	1,589	411
Structural coefficient, ϵ	0.143	0.143	0.143
Payload ratio, λ	0.0714	0.348	0.348
Mass ratio, \mathcal{R}	5	2.75	2.75
Velocity increment, u , m/s	4,970	3,080	3,080
Terminal payload velocity, m/s	4,970		6160

^aSame payload, exhaust velocity and total structural mass. Exhaust velocity 3048 m/s. Zero gravity and drag.

If the exhaust velocities are all the same, this reduces to

$$u_n = u_e \ln \left(\prod_1^n \mathcal{R}_i \right), \quad (10.33)$$

where $\prod_1^n \mathcal{R}_i$ is the product of the n mass ratios. If the exhaust velocities, structural coefficients, and payload ratios are all identical, this reduces further to

$$u_n = n u_e \ln \mathcal{R},$$

or

$$u_n = n u_e \ln \frac{1 + \lambda}{\epsilon + \lambda}. \quad (10.34)$$

The stages are said to be similar if they have the same values of λ and ϵ . This special case is quite useful for approximate calculations, especially if the exhaust velocities we are considering are reasonably uniform and the structural coefficient does not vary markedly from stage to stage. We can see (consult Appendix VIII) that under these conditions it is desirable to have identical stage payload ratios.

The overall mass ratio is related to the stage payload ratios as follows: From Eq. (10.27) we have

$$\begin{aligned} \frac{\mathcal{M}_{01}}{\mathcal{M}_{02}} &= \frac{1 + \lambda_1}{\lambda_1}, \\ \frac{\mathcal{M}_{02}}{\mathcal{M}_{03}} &= \frac{1 + \lambda_2}{\lambda_2}, \\ &\vdots &&\vdots \\ \frac{\mathcal{M}_{0(n-1)}}{\mathcal{M}_{0n}} &= \frac{1 + \lambda_{n-1}}{\lambda_{n-1}}, \\ \frac{\mathcal{M}_{0n}}{\mathcal{M}_{\mathcal{L}}} &= \frac{1 + \lambda_n}{\lambda_n}. \end{aligned}$$

Multiplying these ratios together, we obtain as a result:

$$\frac{\mathcal{M}_{01}}{\mathcal{M}_{\mathcal{L}}} = \prod_{i=1}^n \left(\frac{1 + \lambda_i}{\lambda_i} \right). \quad (10.35)$$

If the payload ratios are identical, the overall mass ratio is given by

$$\frac{\mathcal{M}_{01}}{\mathcal{M}_{\mathcal{L}}} = \left(\frac{1 + \lambda}{\lambda} \right)^n. \quad (10.36)$$

We can determine the variation of payload terminal velocity with overall mass ratio from Eqs. (10.34) and (10.36) for the special case of the rocket with similar stages. The result is

$$\frac{u_n}{u_e} = n \ln \left\{ \frac{(\mathcal{M}_{01}/\mathcal{M}_{\mathcal{L}})^{1/n}}{\epsilon[(\mathcal{M}_{01}/\mathcal{M}_{\mathcal{L}})^{1/n} - 1] + 1} \right\}. \quad (10.37)$$

We can take gravitational forces into account approximately by replacing the term on the left side by

$$\frac{u_n + g_e t_b \cos \theta}{u_e}.$$

Figure 10.8 illustrates Eq. (10.37) for a value of the structural coefficient $\epsilon = 0.10$. For a ratio of terminal and exhaust velocities of 3 (which corresponds approximately to earth escape using high-energy propellants), two or three stages could be used; but a single-stage rocket would not be able to do the job even if the payload mass were negligible.

The ratio of payload terminal velocities with several similar stages to that for one stage, and with the same overall mass ratio, is shown in Fig. 10.9, again for the assumption that $\epsilon = 0.10$. Here it is evident that increasing the number of stages yields diminishing returns for a given u_n/u_e . It is of interest to determine the terminal velocity obtained with an infinite number of similar stages for a given overall mass ratio M_{∞}/M_{01} . Using Eq. (10.37), we find that this limit is given by

$$\lim_{n \rightarrow \infty} u_n = u_e \lim_{n \rightarrow \infty} \left\{ -n \ln \left[\epsilon + \frac{1 - \epsilon}{(M_{01}/M_{\infty})^{1/n}} \right] \right\}$$

or

$$\lim_{n \rightarrow \infty} u_n = u_e (1 - \epsilon) \ln \left(\frac{M_{01}}{M_{\infty}} \right). \quad (10.38)$$

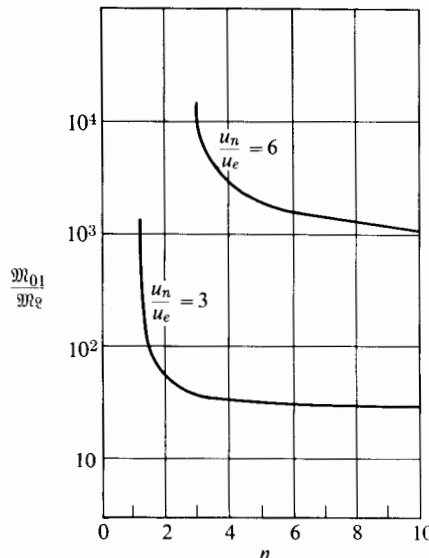


FIGURE 10.8 Variation of overall mass ratio with number of stages for fixed terminal velocity ratios; similar stages and structural coefficient $\epsilon = 0.10$.

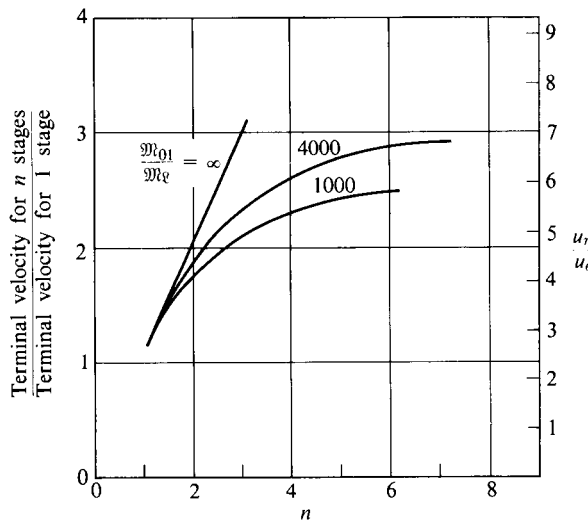


FIGURE 10.9 Variation of terminal velocity with payload ratio and number of similar stages; $\epsilon = 0.10$.

For the example summarized in Table 10.2, we obtain

$$\frac{M_{01}}{M_e} = 15, \quad \epsilon = 0.143, \quad u_e = 3048 \text{ m/s},$$

and Eq. (10.38) yields

$$\lim_{n \rightarrow \infty} u_n = 7074 \text{ m/s},$$

which compares with 4904 m/s for one stage and 6160 for two.

It is also interesting to determine the limiting value of the terminal velocity for a massless structure. From Eq. (10.35),

$$\lim u_n = u_e \ln \frac{M_{01}}{M_e}, \quad \epsilon \rightarrow 0.$$

As one might expect, with the limiting case of a massless structure there is no advantage in multistaging.

As in most engineering problems, economy is important in the design of rocket vehicles. Optimization analyses of the various vehicles have as their goal the design of the most economical system for the proposed mission. However, the approximations that one must make in order to do optimization mathematically are usually severe, and thus one should view the results of such analyses as general guides rather than as specific answers.

The analyses we discuss here concern minimizing the initial mass of the vehicle for a given mission. The implication is that the significant cost considerations are closely related to the mass of equipment and propellant that constitute the vehicle. This assumption ignores many important factors that help to deter-

mine the best design. The choice of propellant, for example, may be a major consideration. It often depends on factors such as availability, storability, and ease of handling. Another factor is the time necessary to design and develop a new rocket vehicle. Often it is not feasible to design and build a completely new vehicle for a particular application, and the best vehicle under some circumstances may consist of a combination of existing components or stages—a vehicle that is not necessarily optimum in the narrow sense already defined.

An important question arises in the design of multistage chemical rocket vehicles: For a given number of stages, what should their relative sizes be? The answer employs the techniques of the calculus of variations. Appendix VIII shows that if the structural coefficients ϵ and the exhaust velocities u_e are uniform through the stages, the stage payload ratios λ should also be uniform in order to minimize the overall mass ratio for a given terminal velocity. If the structural coefficient or the exhaust velocity, or both, are variable, methods are available (Appendix VIII) for determining the best variation in payload ratio through the stages.

Table 10.3 shows approximate mass and thrust data for the *Saturn II* launch vehicle that was used to send astronauts Neil Armstrong and Buzz Aldrin to the

TABLE 10.3 *Saturn V Apollo* flight configuration

Mass and thrust features	Stage		
	1	2	3
Engine	F-1	J-2	J-2
Fuel	RP1 (hydrocarbon)	LH ₂	LH ₂
Oxidant	LO ₂	LO ₂	LO ₂
Number of engines	5	5	1
Total thrust			
lb _f	7,500,000	1,000,000	200,000
kN	33,400	4,450	890
Total initial mass			
lb	6,115,000	1,488,000	473,000
kg	2,780,000	677,000	215,000
Mass of propellant			
lb	4,393,000	943,000	239,000
kg	1,997,000	429,000	109,000
Mass of structure and engines			
lb	234,000	71,600	56,500
kg	106,000	32,600	25,700
ϵ_i	0.050	0.071	0.191
Payload			
lb		178,000	
kg		81,100	
λ_i	0.321	0.466	0.603

moon on July 20, 1969. The payload for stage 3 included the command module containing the three astronauts (including Mike Collins) and the lunar module and landing gear with separate stages for descent to and ascent from the moon, plus fuel and oxidizer for these stages. *Apollo II* lifted off the launch pad at 9:32 A.M. EDT on July 16. In about 1 minute 9 seconds the vehicle had reached Mach 1. The first-stage engines had completed their burning, the first stage had separated from the vehicle, and the second-stage engines were already at full power in under 3 minutes. In just over 9 minutes the second-stage engines had shut down, the second stage had separated, and the single third-stage engine began its burn till shutdown at 11 minutes 42 seconds after liftoff. Now the astronauts were in orbit, in which they continued until, over Australia, the J-2 engine was restarted for a 6-minute burn to take *Apollo II* to the moon. It was on July 20, as they passed by the far side of the moon, that Armstrong and Aldrin entered the lunar module (leaving Collins in the command module) and prepared to descend to the surface of the moon, touching down at 4:18 A.M. EDT. They took off early in the afternoon of July 21 and linked up with the command module. Then the lunar module ascent stage was abandoned, and one more firing put them on a trajectory for the earth. *Apollo II* landed in the Pacific Ocean on July 24 at 12:51 A.M. EDT, only 24 km from the recovery ship. Thus the end of a pioneering journey, of which Table 10.3 hardly indicates the excitement.

The payload and structural coefficients in Table 10.3 show a considerable departure from the textbook ideal of the same λ_i and ϵ_i for each stage. With the same total initial mass and payload, one can determine the uniform value of λ for each of the three stages from

$$\frac{M_{01}}{M_0} = \left(\frac{1 + \lambda}{\lambda} \right)^n \quad \text{or} \quad \lambda = 0.44.$$

The uniform value of ϵ could have been determined from

$$\epsilon = \frac{\sum m_{si}}{\sum m_{si} + \sum m_{pi}} = 0.060.$$

The ideal case $\lambda_i = \lambda$ and $\epsilon_i = \epsilon$ is associated with the same exhaust velocity $u_{ei} = u_e$ for each stage. In this case the first-stage hydrocarbon-fueled engines would have had a u_e value of about 2900 m/s, whereas for the hydrogen-fueled second- and third-stage engines u_e would have been about 4200 m/s. The higher density of the hydrocarbon fuel is consistent with the structural coefficient being lower for the first stage than for the second.

The space shuttle vehicle shown in Fig. 10.10 is another example of staging with rocket engines of different types. The three space shuttle main engines (SSME), fueled by hydrogen, burn for eight minutes after liftoff, but during the first two minutes of this burning period 80% of the thrust is supplied by two solid-propellant rocket motors (SRM) that are disconnected from the vehicle at the end of the two-minute period.

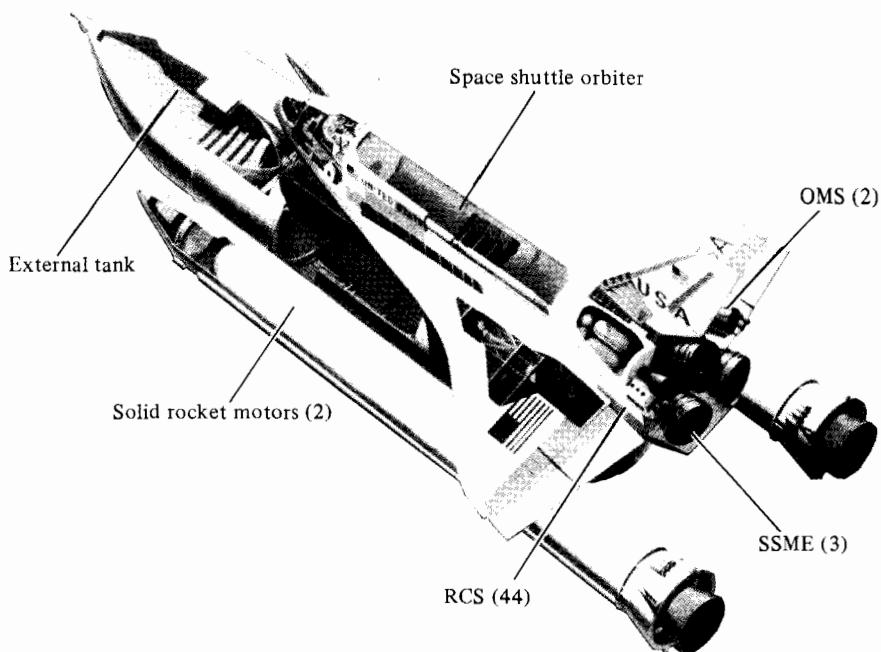


FIGURE 10.10 Space shuttle. (Courtesy Rockwell International, Rocketdyne Division.)

Table 10.4 shows approximate data for the vehicle masses and engine thrusts. The specific-impulse figures are calculated for each kind of engine from the total thrusts and total flow rates; estimates of the latter assume constant propellant flow rate over the burning period of each engine.

During the first two minutes with the SRMs and SSMEs simultaneously burning, the equivalent specific impulse for the total engine combination will be the sum of all engine thrusts divided by the sum of all propellant flow rates. This gives a total specific impulse for this period of 312 seconds, which, as one would expect, is between the SRM and SSME values, and much closer to the former than to the latter.

Neglecting gravity and drag decrements and using the mass data of Table 10.4, we find that the velocity increment for this two-minute burning period would be

$$\Delta u |_0^2 = g_e I_{sp} \ln \frac{M_{01}}{M_{b1}} = 9.81(312) \ln \frac{2,010,000}{820,000} = 2740 \text{ m/s.}$$

For the burning period from two to eight minutes, we would have

$$\Delta u |_2^8 = g_e I_{sp} \ln \frac{M_{02}}{M_{b2}} = 9.81(428) \ln \left(\frac{660,000}{118,000} \right) = 7230 \text{ m/s,}$$

TABLE 10.4 Space shuttle data

Engine features	Solid rocket booster	Space shuttle main engine		
		Time, min		
Vehicle masses		0	2 ⁻	2 ⁺
2 solid rocket motors				
lb	2,580,000	360,000	0	0
kg	1,170,000	164,000	0	0
External fuel tank ^a				
lb	1,650,000	1,255,000	1,255,000	70,000
kg	750,000	571,000	571,000	32,000
Orbiter plus payload				
lb	190,000	190,000	190,000	190,000
kg	86,400	86,400	86,400	86,400
Total				
lb	4,420,000	1,810,000	1,445,000	260,000
kg	2,010,000	820,000	660,000	118,000

Source: Courtesy William C. Horne.

^a Includes the mass of the SSMEs and the supporting structure.

and the total velocity increment would then be

$$\Delta u = \Delta u|_0^2 + \Delta u|_2^8 = 9970 \text{ m/s} (32,700 \text{ ft/s}).$$

This is well above the velocity required (7600 m/s; see Table 10.8) for a circular earth orbit at 200-to-300-km altitude, but, as we noted earlier, this estimate makes no allowance for drag and gravity effects, which could well be equivalent to a decrement of the order of 2000 m/s.

10.5 ELECTRICAL ROCKET VEHICLES

Electrical and electromagnetic rockets differ fundamentally from chemical rockets with respect to their performance limitations. Chemical rockets are essentially *energy limited*, since the quantity of energy (per unit mass of propellant)

that can be released during combustion is limited by the fundamental chemical behavior of propellant materials. If, on the other hand, a separate energy source (e.g., nuclear or solar) is used, much higher propellant energy is possible. Further, if the temperature limitations of solid walls could be made unimportant by direct electrostatic or electromagnetic propellant acceleration without necessarily raising the fluid and solid temperatures, there would be no necessary upper limit to the energy that could be added to the propellant. However, the rate of conversion of nuclear or solar energy to electrical energy and thence to propellant kinetic energy is limited by the mass of conversion equipment required. Since this mass is likely to be a large portion of the total mass of the vehicle, the electrical rocket is essentially *power limited*.

Electrostatic and electromagnetic rockets convert electrical energy directly to propellant kinetic energy without necessarily raising the temperature of the working fluid. For this reason the specific impulse is not limited by the temperature limitations of wall materials, and it is possible to achieve very high exhaust velocities, though at the cost of high power consumption.

Suppose a fraction η of the generated electrical power is transformed to propellant kinetic energy. For a given machine with constant η , or for different machines with similar η , the exhaust power per unit thrust is

$$\frac{\mathcal{P}_e}{\mathcal{T}} \propto \frac{\dot{m}u_e^2/2}{\dot{m}u_e} = \frac{u_e}{2},$$

whereas the mass flow rate per unit thrust is $\dot{m}/\mathcal{T} = 1/u_e$. From this we can see that high exhaust velocity (high specific impulse) requires high power and hence large capacity for power conversion per unit thrust. On the other hand, low exhaust velocity requires high mass flow rate per unit thrust and hence large propellant storage capacity for a given thrust duration. Between these extremes lies an optimum exhaust velocity. The optimum exhaust velocity is that which gives a maximum payload ratio for the mission under consideration. We give an approximate method for establishing this optimum in the following paragraphs. We assume that the vehicle must accelerate through a velocity increment Δu during a period t_b of constant thrust. We will discuss subsequently the way in which the variables Δu and t_b depend on the mission. Variables of importance for the rocket itself are the *specific mass* α of the power plant and the efficiency of the thrust chamber η . We define the specific mass here as the mass of power plant and structure per unit of electrical power output. The structural mass is included in the definition for convenience. It is likely to be a small fraction of the power-plant mass:

$$\alpha = \frac{\mathcal{M}_p + \mathcal{M}_s}{\mathcal{P}}, \quad (10.39)$$

where \mathcal{P} = electrical power output,

\mathcal{M}_p = mass of the power plant,

\mathcal{M}_s = mass of the structure.

The thrust chamber efficiency is the fraction of electrical power that is converted to exhaust kinetic energy,

$$\eta = \frac{\dot{m}u_e^2}{2\mathcal{P}}. \quad (10.40)$$

The velocity increment is given by Eq. (10.10),

$$\Delta u = u_e \ln \frac{M_0}{M_b},$$

or

$$\frac{M_b}{M_0} = e^{-\Delta u/u_e}. \quad (10.41)$$

If all the propellant is consumed, the mass of the vehicle at the end of the thrust period is $M_b = M_p + M_s + M_x$. The burnout mass ratio, when we use Eq. (10.39), is

$$\frac{M_b}{M_0} = \frac{\alpha\mathcal{P}}{M_0} + \frac{M_x}{M_0}. \quad (10.42)$$

Using Eq. (10.40), we obtain

$$\frac{\alpha\mathcal{P}}{M_0} = \frac{\alpha\dot{m}u_e^2}{2\eta M_0},$$

and if the propellant flow rate is constant,

$$\frac{\alpha\mathcal{P}}{M_0} = \frac{\alpha u_e^2 M_p/t_b}{2\eta M_0} \quad \text{or} \quad \frac{\alpha\mathcal{P}}{M_0} = \frac{\alpha u_e^2}{2\eta t_b} \left(1 - \frac{M_b}{M_0}\right).$$

Combining this expression with Eq. (10.42) yields

$$\frac{M_b}{M_0} = \frac{(\alpha u_e^2/2\eta t_b) + (M_x/M_0)}{1 + (\alpha u_e^2/2\eta t_b)}.$$

Substituting this expression in Eq. (10.41), we find that the payload-to-initial-mass ratio is given by

$$\frac{M_x}{M_0} = e^{-\Delta u/u_e} \left(1 + \frac{\alpha u_e^2}{2\eta t_b}\right) - \frac{\alpha u_e^2}{2\eta t_b}. \quad (10.43)$$

Figure 10.11 illustrates the variation of this ratio with specific impulse for a one-month transfer between earth and moon orbits. During this period the thrust is assumed constant through a velocity increment $\Delta u \approx 7350$ m/s (24,000 ft/sec).

Figure 10.11 shows that, as one would expect, the optimum specific impulse depends quite strongly on the efficiency and specific mass of the power plant. The latter, in turn, may be expected to be quite dependent on the absolute size of the power plant. Estimates used by Buden and Sullivan [2] for space vehicle nuclear power plants would place the power-plant specific mass as shown in Table 10.5.

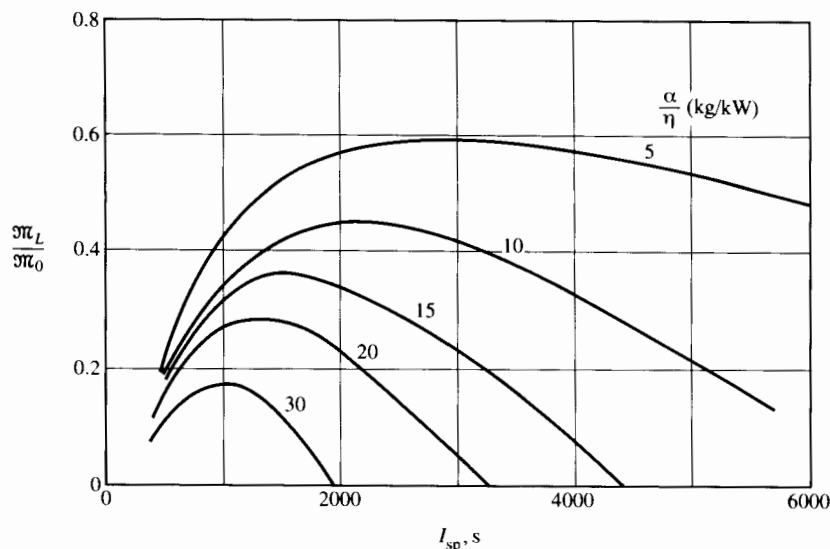


FIGURE 10.11 Variation of payload ratio with specific impulse according to Eq. (10.43) for a one-month earth-moon transfer.

The efficiency of conversion of electrical power into exhaust kinetic energy depends on the type of electrical thruster used and on the specific impulse required. Auweter-Kurtz, Kurtz, and Schrade [3] have reviewed experimental data on a number of electrical thrusters and find that over a considerable range of specific impulse the thruster efficiency can be written

$$\eta = \eta_{\max} \frac{u_e^2}{u_e^2 + K^2}. \quad (10.44)$$

(We will discuss the reason for the form of this correlation in Chapter 14.) Data on two of the most efficient electrical thrusters (the xenon and argon ion electrostatic thrusters described in Chapter 14) lead to the results shown in Table 10.6.

TABLE 10.5 Specific mass of nuclear power plants for space vehicles [2]

Electrical power level (kW)	Specific mass (kg/kW)
100	30.0
500	7.0
1,000	3.9
5,000	1.9
10,000	1.6

TABLE 10.6 Measured efficiencies of ion thrusters

Ion thruster	I_{sp} range	η_{max}	K m/s
Xe ion	3000–4000	0.93	19,670
Ar ion	4000–6000	0.84	36,690

Over a range of specific impulse from 2000 to 6000, Eq. (10.44) for the xenon ion thruster would indicate a variation in η from 45% to 85%. With this approximation one could change Eq. (10.43) to read

$$\frac{M_L}{M_0} = e^{-\Delta u/u_e} \left[1 + \frac{\alpha(u_e^2 + K^2)}{2\eta_{max}t_b} \right] - \alpha \frac{(u_e^2 + K^2)}{2\eta_{max}t_b}. \quad (10.45)$$

Taking, as an example, a 500-kW power plant with (from Table 10.5) $\alpha = 30$ kg/kW and the data of Table 10.6 for η_{max} and k for the two ion thrusters, Fig. 10.12 shows the payload fraction as a function of specific impulse. In both cases the broken portions of the payload fraction lines indicate extrapolation outside the range of measurements.

The following section discusses briefly the way in which to find equivalent values of Δu and t_b for space missions.

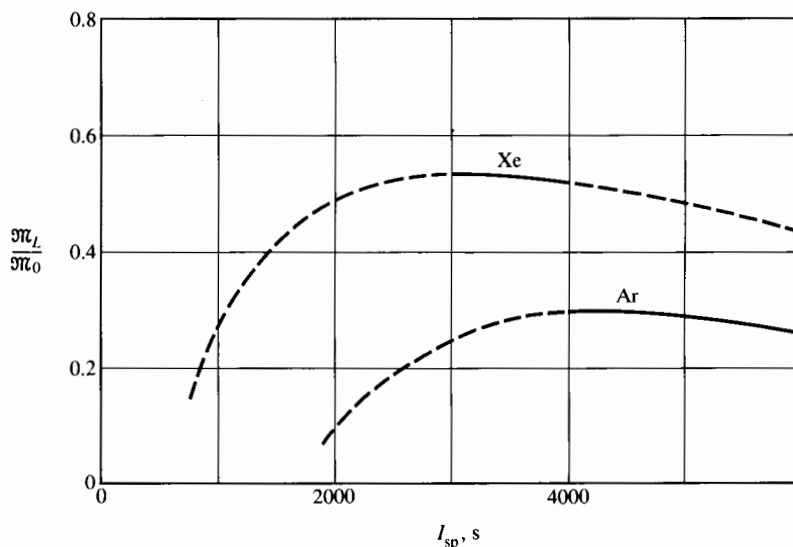


FIGURE 10.12 Payload ratios with xenon and argon ion thrusters; $\Delta u = 6000$ m/s, $t_b = 150$ days, $\alpha = 30$ kg/kW.

10.6 SPACE MISSIONS

In order to demonstrate the relationship of engine performance to vehicle trajectory for a space mission, it is necessary to introduce the subject of orbital and ballistic mechanics. To start the discussion, we assume that the vehicle is accelerated impulsively at certain points and that it travels between these points without thrust under the influence of gravitational force alone.

High Thrust

For our purposes it is satisfactory to simplify the general trajectory problem by considering the gravity force between the vehicle and only one other body. Even for the case of interplanetary transfer, this simplification will suffice for most calculations. That is, one may consider escape from or capture by a planet to be an interaction between the vehicle and that particular planet alone, whereas the transfer process is considered an interaction between the vehicle and the sun alone. The transition from one operation to another has only minor influence on propulsion requirements.

Since the vehicle will always be much smaller than the other body under consideration, the latter is uninfluenced by the vehicle motion, and its center can serve as a stationary coordinate origin. Under these conditions it is easy to see that an unpowered vehicle must travel in a stationary plane that passes through the center of the influencing planet. At any time the instantaneous velocity of the vehicle and the center of mass of the planet together determine a plane that the vehicle cannot leave, because the only force (gravitational) acting on the vehicle is in the plane.

Consider the motion of a vehicle of mass M moving past a large body of mass M' as shown in Fig. 10.13. The minimum separation between the two is r_{\min} . The

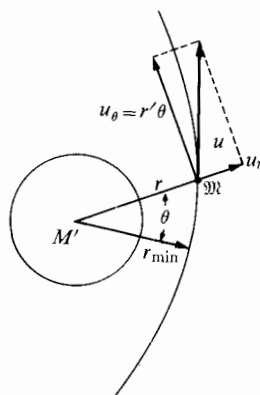


FIGURE 10.13 Vehicle coordinates and velocity components.

gravitational force acts in the negative r -direction and is given by Newton's law of gravitation:

$$F_r = -\frac{GM'M}{r^2}, \quad (10.46)$$

where G = universal gravitational constant = $6.670 \times 10^{-11} \text{ N} \cdot \text{m}^2/\text{kg}^2$. Equating the gravitational force to the radial inertial forces, we have

$$-\frac{GM'M}{r^2} = M(\ddot{r} - r\dot{\theta}^2), \quad (10.47)$$

where $\ddot{r} = d^2r/dt^2$ and $\dot{\theta} = d\theta/dt$. Since the only force acting on M is radial, its angular momentum h must remain constant:

$$h = Mr^2\dot{\theta} = \text{constant}. \quad (10.48)$$

Eliminating $\dot{\theta}$ from Eq. (10.47) by using Eq. (10.48), we obtain

$$M\ddot{r} - \frac{h^2}{Mr^3} = -\frac{GM'M}{r^2}. \quad (10.49)$$

We may express the velocity and acceleration as follows:

$$\dot{r} = \frac{dr}{d\theta} \frac{d\theta}{dt} = \dot{\theta} \frac{dr}{d\theta} = \frac{h}{Mr^2} \frac{dr}{d\theta}, \quad \ddot{r} = \frac{d\dot{r}}{dt} = \frac{d\dot{r}}{d\theta} \frac{d\theta}{dt} = \frac{h}{Mr^2} \frac{d\dot{r}}{d\theta}.$$

Using also the substitution [2] $Z = 1/r - GM'M^2/h^2$, we can show that Eq. (10.49) can be transformed to $d^2Z/d\theta^2 = -Z$, which has the solution

$$Z = A \cos \theta + B \sin \theta \quad \text{or} \quad \frac{1}{r} = \frac{GM'M^2}{h^2} + A \cos \theta + B \sin \theta.$$

Using the boundary conditions at $r = r_{\min}$,

$$\frac{d}{d\theta} \left(\frac{1}{r} \right) = 0, \quad \theta = 0,$$

we find that

$$\frac{1}{r} = \frac{GM'M^2}{h^2} + \left(\frac{1}{r_{\min}} - \frac{GM'M^2}{h^2} \right) \cos \theta. \quad (10.50)$$

We may compare this with the equation of a conic (ellipse, parabola, or hyperbola) in polar coordinates:

$$\frac{1}{r} = \frac{1}{a(1 - \epsilon^2)} + \frac{\epsilon \cos \theta}{a(1 - \epsilon^2)}, \quad (10.51)$$

where, referring to Fig. 10.14, we have a = semimajor axis, b = semiminor axis, ϵ = eccentricity = c/a , and $b^2/a^2 = 1 - \epsilon^2$.

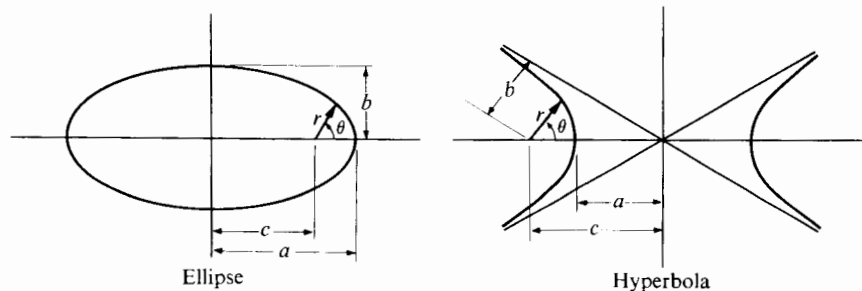


FIGURE 10.14 Conic sections.

Hence the vehicle travels in a hyperbola, a parabola, or an ellipse, with the planet as focus. By comparing terms in Eqs. (10.50) and (10.51), we can show that

$$\epsilon = \frac{h^2}{GM'M^2r_{\min}} - 1 \quad (10.52)$$

and, referring to Fig. 10.14 for the ellipse, we have

$$\frac{a}{r_{\min}} = \frac{1}{1 - \epsilon}. \quad (10.53)$$

If $\epsilon > 1$, the trajectory is hyperbolic; if $\epsilon = 1$, it is parabolic; and if $\epsilon < 1$, it is elliptic.

The conic is completely specified by its shape and size. The size, expressed by a , will now be shown to be a function of *orbital energy*. This orbital energy, defined as the sum of the kinetic and potential energies of the vehicle with respect to the influencing planet, must remain constant. The potential energy is defined as

$$PE = \int_{\infty}^r \frac{GM'M}{r^2} dr = -\frac{GM'M}{r}. \quad (10.54)$$

At infinity the potential energy is zero, and for all finite r it is negative. The orbital energy E is then

$$E = KE + PE = \frac{Mu^2}{2} - \frac{GM'M}{r} = \frac{M}{2}[\dot{r}^2 + (r\dot{\theta})^2] - \frac{GM'M}{r}. \quad (10.55)$$

When we evaluate at $r = r_{\min}$, $\dot{r} = 0$, and use Eq. (10.48), this becomes

$$E = \frac{1}{2} \frac{h^2}{Mr_{\min}^2} - \frac{GM'M}{r_{\min}}, \quad (10.56)$$

which is constant for an unpowered vehicle.

After we combine Eqs. (10.56), (10.53), and (10.52), we obtain

$$E = -\frac{GM'M}{2a}. \quad (10.57)$$

Equations (10.52), (10.53), and (10.56) can be used to show that

$$a = -\frac{GM'}{2(E/M)} \quad (10.58)$$

and

$$\epsilon^2 = 1 + \frac{2(h/M)^2(E/M)}{(GM')^2} \quad (10.59)$$

Thus the orbit or trajectory of a given mass M about a given mass M' is completely determined by the orbital energy E and the angular momentum h . Conversely, these quantities are *properties* of fixed orbits, as are, for example, the orbits of the various planets about the sun. Table 10.7 contains data on the planets and their orbits.

Since kinetic energy is positive whereas potential energy is negative, the total orbital energy E may be either positive or negative, and three distinctly different behaviors are observed corresponding to positive, zero, or negative orbital energy.

$E > 0$

In this case the kinetic energy is greater than the rise in potential energy between the initial radius and infinity. Thus the vehicle possesses sufficient energy to coast away from the influencing planet, arriving at infinity with some excess kinetic energy. With $E > 0$, Eq. (10.56) shows that $h^2/GM'M^2r_{\min}^2 > 2$, so that, from Eq. (10.52), $\epsilon > 1$. Thus the vehicle trajectory will be hyperbolic.

TABLE 10.7 Some properties of planets and their orbits around the sun

Body	Relative mass ^a	Relative mean diameter ^a	Orbit radius, km $\times 10^{-6}$	Eccentricity	Period, years
Sun	332,488.	109.15	—	—	—
Mercury	0.0543	0.38	57.9	0.2056	0.241
Venus	0.8136	0.967	108.1	0.0068	0.615
Earth	1.0000	1.000	149.5	0.0167	1.000
Mars	0.1069	0.523	227.8	0.0934	1.881
Jupiter	318.35	10.97	777.8	0.0484	11.862
Saturn	95.3	9.03	1426.1	0.0557	29.458
Uranus	14.58	3.72	2869.1	0.0472	84.015
Neptune	17.26	3.38	4495.6	0.0086	164.788
Pluto	<0.1?	0.45	5898.9	0.2485	247.697
Moon	0.0123	0.273	0.3844	0.0549	27.322 (days)

Source: From Smithsonian Physical Tables [4].

^aRelative to earth: Earth mass = 5.975×10^{24} kg; earth mean diameter = 12,742.46 km.

$E = 0$

In this case the vehicle possesses kinetic energy just sufficient to coast to infinite radius with zero velocity. This special case is important in that it determines the minimum kinetic energy necessary to escape the planet's influence. The *escape velocity*, u_{esc} , is then, if we set $E = 0$ in Eq. (10.55):

$$\frac{\mathcal{M}u_{\text{esc}}^2}{2} - \frac{GM'\mathcal{M}}{r} = 0,$$

or

$$u_{\text{esc}} = \sqrt{2GM'/r}. \quad (10.60)$$

We may also find escape velocity directly by equating kinetic energy with work done against gravity from r to infinity,

$$\frac{\mathcal{M}u_{\text{esc}}^2}{2} = \int_r^\infty F_r dr = \int_r^\infty \left(+ \frac{GM'\mathcal{M}}{r^2} \right) dr,$$

with the same result. Again using Eq. (10.58), we find that $\epsilon = 1$ for $E = 0$, and the escape trajectory is parabolic.

 $E < 0$

In this case the vehicle possesses kinetic energy that is insufficient to allow it to escape the planet. With Eq. (10.58), we can see that $\epsilon < 1$; thus the orbit is elliptic. For the special case of a circular orbit, $\epsilon = 0$, $u_{\text{circ}} = r\dot{\theta}$, $r = \text{constant}$, and, using Eqs. (10.48) and (10.52), we have

$$\epsilon = 0 = \frac{(\mathcal{M}ru_{\text{circ}})^2}{GM'\mathcal{M}^2r} - 1,$$

or

$$u_{\text{circ}} = \sqrt{GM'/r}. \quad (10.61)$$

We may also find this result by equating centrifugal and gravitational forces for the circular case. Note, by comparing Eqs. (10.60) and (10.61), that the velocity for escape from circular orbit is simply a constant times the orbital velocity at that radius:

$$u_{\text{esc}} = \sqrt{2}u_{\text{circ}}.$$

The period of an elliptical orbit is given by Kepler's law, which expresses the conservation of angular momentum. From Eq. (10.48), the conservation of angular momentum requires

$$r^2\dot{\theta} = \frac{h}{\mathcal{M}} = \text{constant}.$$

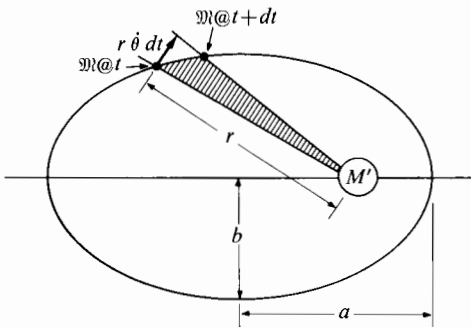


FIGURE 10.15 Interpretation of Kepler's law.

Referring to Fig. 10.15, we can see that the area swept out by the radius vector during time dt is $dA = \frac{1}{2}r^2\dot{\theta}dt$. Thus

$$\frac{dA}{dt} = \frac{1}{2}r^2\dot{\theta} = \frac{1}{2}\frac{h}{M}.$$

For a complete period τ , the vehicle sweeps out the entire ellipse area πab . Since dA/dt is constant, $(dA/dt)\tau = \pi ab$, and the period is $\tau = 2\pi ab/(h/M)$ or, if we use Eqs. (10.52) and (10.53),

$$\tau = \frac{2\pi a^{3/2}}{\sqrt{GM'}}. \quad (10.62)$$

Interplanetary trajectories have been studied by Hohmann [5] and Oberth [6]. Hohmann treated earth escape and interorbital transfer as two separate problems (see Fig. 10.16). The first step in an earth-to-Mars trip, for example, would be an escape from the earth's influence achieved by attaining escape velocity in any direction from the surface of the earth. After escape, the vehicle finds itself free of the earth, but in an orbit about the sun, an orbit that is essentially identical to that of the earth about the sun. (The vehicle has zero velocity relative to the earth.) A second velocity increment Δu_T is then added, which places the vehicle in an elliptic "transfer" orbit about the sun. This orbit at its perigee (nearest approach to sun) is tangent to the earth's orbit, and at its apogee (greatest distance from sun) is tangent to the orbit of Mars. A third velocity increment, Δu_{Mars} , is necessary at this point to bring the vehicle to that velocity corresponding to the Mars orbit. The total velocity increment that the vehicle needs to arrive in the Mars orbit is then

$$\Delta u_{\text{Hohmann}} = u_{\text{esc}} + \Delta u_T + \Delta u_{\text{Mars}}, \quad (10.63)$$

and the change in orbital energy per unit mass (with respect to the earth) needed in order to put the vehicle into the transfer orbit is

$$E_{\text{Hohmann}} = E_{\text{esc}} + \frac{(\Delta u_T)^2}{2} = \frac{(\Delta u_T)^2}{2},$$

since the escape energy is zero.

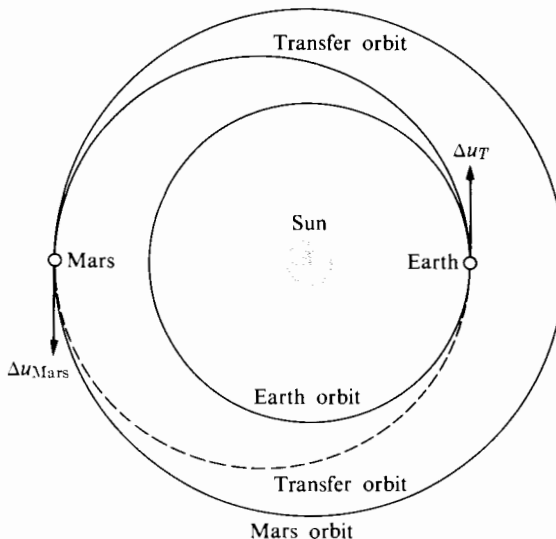


FIGURE 10.16 Earth–Mars transfer orbit.

Escape from earth while carrying enough propellant to produce Δu_T involves unnecessary work done against gravity, work that can be avoided if the initial velocity is properly directed and of sufficient magnitude. Oberth [6] treated this problem and arrived at a smaller total velocity increment. His maneuver requires a larger launch velocity u_{Oberth} at the earth's surface, which places the vehicle in the same transfer orbit as Hohmann's; that is, the Hohmann ellipse. The orbital energy is therefore the same. With respect to the earth, this energy is given by

$$E_{\text{Oberth}} = \frac{u_{\text{Oberth}}^2}{2} - \frac{GM'_e}{R_e},$$

where R_e is the earth's radius and M'_e is its mass.

Equating these two energies and using Eq. (10.58) for GM'_e/R_e , we obtain

$$\frac{u_{\text{Oberth}}^2}{2} - \frac{u_{\text{esc}}^2}{2} = \frac{(\Delta u_T)^2}{2}$$

or

$$u_{\text{Oberth}} = \sqrt{u_{\text{esc}}^2 + (\Delta u_T)^2}. \quad (10.64)$$

Thus the Oberth velocity is less than the direct sum of escape and transfer velocities necessary for the Hohmann transfer. The total Oberth velocity increment is then

$$\Delta u_{\text{Oberth}} = u_{\text{Oberth}} + \Delta u_{\text{Mars}}. \quad (10.65)$$

This establishes the minimum propulsive requirement to arrive in the orbit of Mars. The transit time does not appear in this calculation since, for this case, it is a dependent variable determined by the characteristics of the orbits of the

earth and Mars. The effects of atmospheric drag during the escape maneuver have been neglected.

Actually, one might be interested in more than simply reaching the orbit of a given target planet. One might want to achieve an orbit around the target planet itself, or at least pass within a certain observational distance of it. These goals require correct coordination of time as well as space and, generally, additional powered flight within the influence of the target planet.

In addition, the transfer time on a minimum-energy transfer might be excessive for some missions, especially those involving manned vehicles. Faster trajectories requiring greater Δu_{total} but fewer supplies might be advantageous. These faster trajectories, which involve nontangential transfer and initial orbit intersections, are wasteful of propellant, since the resultant velocity is not the summation of collinear orbital and incremental velocities.

Irving and Blum [7] have presented a study of the propulsive requirements of a round-trip mission to Mars as a function of total travel time. The results are shown in Fig. 10.17.

At least four separate velocity increments are necessary to perform the following tasks:

Δu_1 : escape from the earth toward Mars with excess (over the Hohmann transfer ellipse) velocity that determines one-way transit time. If the trajectory were a Hohmann ellipse, this combined escape and transfer maneuver would correspond to the Oberth velocity.

Δu_2 : increment applied in the gravitational field of Mars to effect "capture" in an orbit about Mars.

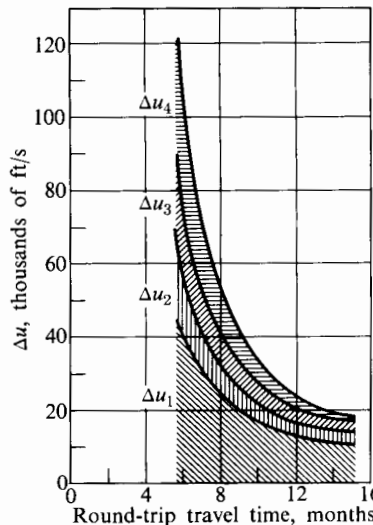


FIGURE 10.17 Total velocity impulse required for round-trip travel to Mars. (After Irving and Blum [6].)

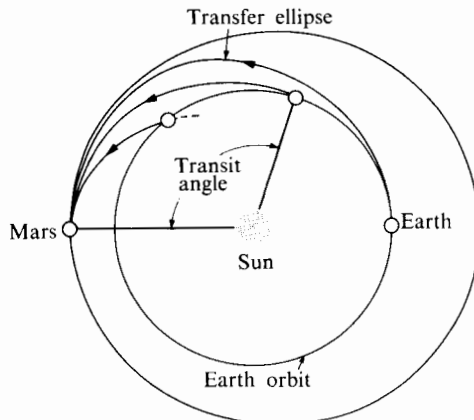


FIGURE 10.18 Ballistic rocket paths to Mars at perihelion. (After Irving and Blum [6].)

Δu_3 : the opposite of Δu_2 , to effect escape from Mars and return to a transfer ellipse back toward the earth.

Δu_4 : increment applied to decelerate the vehicle to a safe reentry velocity after it has been captured by the earth's gravitational field.

Typical transfer orbits are illustrated in Fig. 10.18.

For this study the orbit of the earth was assumed a circle of 92,833,000-km radius, while the orbit of Mars was assumed a coplanar ellipse of eccentricity $\epsilon = 0.093366$ and 128,250,000 miles distant from the sun at perihelion (closest approach to sun). All transfer paths were assumed tangent to the Mars orbit at perihelion, although this is not necessarily desirable, since the appropriate relative positions of the earth and Mars for these missions do not occur frequently. Figure 10.19 presents the one-way transit time as a function of transit angle (Fig. 10.18), with the minimum-energy or Hohmann-ellipse trajectory occupying approximately 7.8 months.

All trajectories arrive in the Mars orbit with less velocity than Mars has at that point. Thus the vehicle approaches Mars in a rearward direction, having energy greater than zero with respect to Mars. The shorter-transit trajectories have lower velocities relative to the sun at this point, and thus higher energy rela-

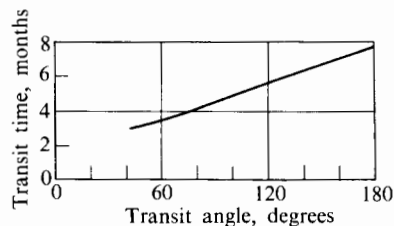


FIGURE 10.19 One-way earth-to-Mars transit time. (After Irving and Blum [7].)

tive to Mars, requiring greater Δu_2 to effect capture by Mars. The assumption that Δu_3 is the mirror image of Δu_2 is artificial in that it may require inordinate waiting until the vehicle, Mars, and the earth are all in a favorable position for this maneuver, but the resultant figures are valid for comparisons.

Low Thrust

Electrical rockets of very low thrust-to-mass ratio are capable of only very low accelerations, perhaps 10^{-5} to 10^{-3} times the acceleration of gravity at the earth's surface. Thus they are incapable of performing the initial launch function. However, once launched into orbit by conventional chemical rockets, these devices are intended to accelerate continuously over long periods of time until the required velocity increment is achieved. Since the electrical rocket is a power-limited device, it is advantageous to operate it at constant power, using variation of thrust direction, and perhaps magnitude, to achieve the desired motion. The escape trajectory then becomes a gradual outward spiral until escape velocity is reached. The transfer trajectory also becomes a spiral about the sun, and the capture maneuver a spiral around the target planet. In the absence of high-thrust chemical rockets, the approach to the target planet is quite critical in that it must not necessitate maneuvering beyond the very limited capability of the low-thrust device.

Tsien [8] considered the case of takeoff from a satellite orbit using a constant radial or tangential acceleration low-thrust vehicle. Since torque is applied to the vehicle by the circumferential thrust component, its angular momentum is no longer constant. If the thrust \mathcal{T}_θ is applied in the circumferential direction, the tangential equation of motion may be written

$$\mathcal{T}_\theta = M(r\ddot{\theta} + 2r\dot{\theta})$$

or

$$\frac{\mathcal{T}_\theta r}{M} = \frac{d}{dt}(r^2\dot{\theta}). \quad (10.66)$$

In the absence of a radial thrust component, Eq. (10.47) still applies:

$$-\frac{GM'M}{r^2} = M(\ddot{r} - r\dot{\theta}^2). \quad (10.47)$$

When we introduce the dimensionless variables,

$$\rho = \frac{r}{r_0}, \quad \tau = \sqrt{\frac{GM'}{r_0^3}}t, \quad \text{and} \quad \nu = \frac{\mathcal{T}_\theta r_0^2}{GM'M} = \frac{\mathcal{T}_\theta}{Mg},$$

where r_0 = initial orbit radius and g = acceleration of gravity in initial orbit, we can write these two equations of motion as

$$\frac{d^2\rho}{d\tau^2} = \rho \left(\frac{d\theta}{d\tau} \right)^2 - \frac{1}{\rho^2}, \quad (10.67)$$

$$\frac{d}{d\tau} \left(\rho^2 \frac{d\theta}{d\tau} \right) = \nu \rho . \quad (10.68)$$

At $t = 0$, when thrust is initiated with the vehicle already in circular orbit, $\dot{r} = \ddot{r} = 0$ and $r = r_0$. Using Eq. (10.47), we can write these conditions (when $t = 0$) as

$$\dot{\theta}^2 = \frac{GM'}{r_0^3}, \quad \dot{r} = 0, \quad r = r_0 \quad (10.69)$$

or, in terms of the dimensionless variables (when $\tau = 0$), as

$$\frac{d\theta}{d\tau} = 1, \quad \frac{d\rho}{d\tau} = 0, \quad \rho = 1 . \quad (10.70)$$

For $d\theta/d\tau = 1$ and $\rho = 1$, Eq. (10.67) requires that

$$\frac{d^2\rho}{d\tau^2} = 0 . \quad (10.71)$$

Combining Eqs. (10.67) and (10.68) yields a third-order differential equation for ρ ,

$$\frac{d}{d\tau} \left(\rho^3 \frac{d^2\rho}{d\tau^2} + \rho \right)^{1/2} = \nu \rho , \quad (10.72)$$

with initial conditions given by (10.70) and (10.71). This equation cannot be solved directly, but Tsien [8] has given an approximate solution, while Irving [9] has given a more accurate one.

Figure 10.20 illustrates the solution of Eq. (10.72) for a constant \mathcal{T}_e/M escape maneuver from an initial 200-mile circular orbit about the earth. Time is mea-

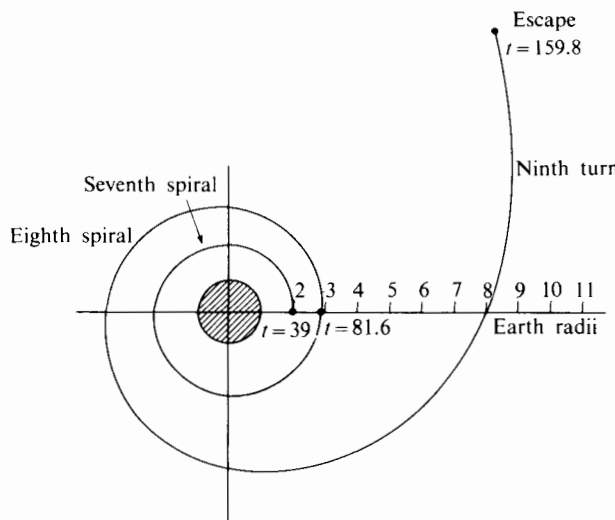


FIGURE 10.20 Escape maneuver for $\mathcal{T}_e/M = 0.005g$ from earth. (After Irving [9].)

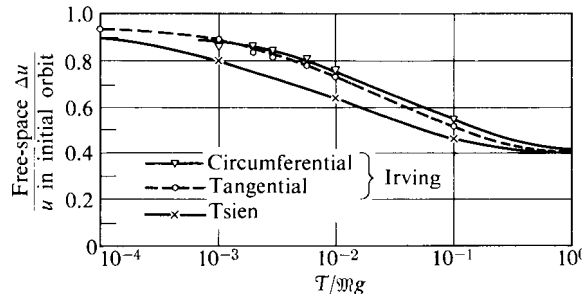


FIGURE 10.21 Velocity increment for vehicle escape as a function of vehicle thrust-to-mass ratio. (After Irving [9].)

sured in multiples of the time required to travel one radian in the initial orbit, about 14.5 minutes in this case. For any solution of this type, the propulsion requirement for escape, expressed as the equivalent free space Δu (that is, $u_e \ln \mathcal{R}$), can be calculated, since in this case Δu is simply \mathcal{T}/\mathcal{M} times the propulsion time.

The relationship between Δu and \mathcal{T}/\mathcal{M} is shown in Fig. 10.21 for several solutions of different \mathcal{T}/\mathcal{M} . Both circumferential and tangential (parallel to vehicle velocity) thrust solutions are shown; Δu and \mathcal{T}/\mathcal{M} have been nondimensionalized with respect to the vehicle velocity and gravitational acceleration, respectively, in the initial orbit. It is apparent that for lower \mathcal{T}/\mathcal{M} , higher velocity increments are required.

Sandorff [10] presents data for the tangential thrust case, as in Fig. 10.22, that indicate the “penalty” associated with escape using less than impulsive thrust. Low-thrust vehicles are advantageous in spite of this penalty because the extremely low propellant consumption more than compensates for the higher velocity increment required.

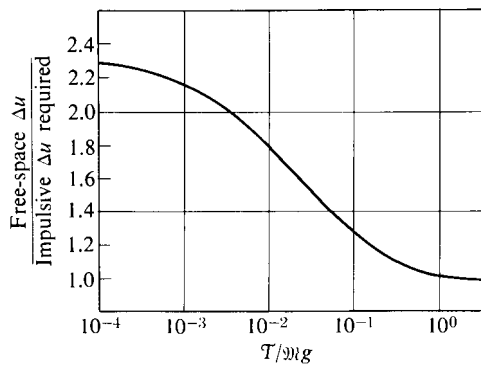


FIGURE 10.22 Increase of Δu for escape associated with low-thrust engine. (After Sandorff [10].)

As an example of an interplanetary mission, Stuhlinger [11] has presented an account of a round trip to Mars by a low-thrust space ship of the following type:

Total initial mass	730 tons	Exhaust velocity	84 km/sec
Total propellant mass	365 tons	Initial acceleration	$0.67 \times 10^{-4}g$
Propellant consumption rate	5.8 gm/sec	Payload	150 tons

From this, one can calculate the total velocity increment required for this mission, assuming the difference between initial and burnout mass to be the total propellant mass. Actually, additional mass might be discarded or added in the course of the mission, but the propulsion requirements are known in any case in terms of the total propellant, the rate of consumption of propellant, and the exhaust velocity.

If we assume coplanar circular orbits for the earth and Mars, the outward trajectory would appear as in Fig. 10.23. The earth-escape spiral consumes 124 days. The deceleration and acceleration periods are found necessary to reach Mars at the correct time and with the correct velocity for capture. The energy relative to Mars should be nearly zero. After an exploration period of 472 days, the earth and Mars are favorably positioned for a return trip of 311 days.

Garrison and Stocky [12] have tabulated the velocity increment requirements for a number of space missions in comparison with the velocity increments for launch from the earth's surface and placement in a circular orbit about the earth. Their results are shown in Table 10.8 for differing burning times. In each case the propulsion unit burns "impulsively," but the travel time depends strongly on the thrust-mass ratio of the propulsion unit.

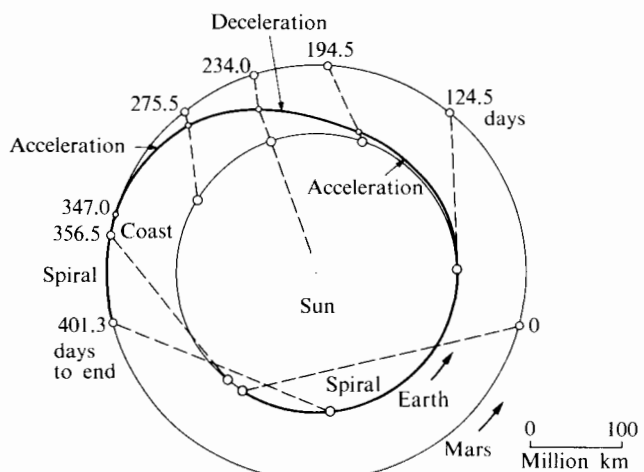


FIGURE 10.23 Low-thrust earth escape and transfer to Mars orbit. (After Stuhlinger [11].)

TABLE 10.8 Typical mission velocity requirements [12]

Mission	m/s
Earth to LEO ^a	7,600
LEO to GEO ^b	4,200
LEO to earth escape	3,200
LEO to lunar orbit (7 days)	3,900
LEO to Mars orbit (0.7 yr)	5,700
LEO to Mars orbit (40 days)	85,000
LEO to Neptune orbit (29.9 yr)	13,400
LEO to Neptune orbit (50 yr)	70,000
LEO to solar escape	8,700
LEO to 1000 AU ^c (50 yr)	142,000
LEO to Alpha-Centauri (50 yr)	30×10^6

^a Low earth orbit (270 km)^b Geosynchronous earth orbit (42,227 km radius)^c Astronomical units (1 AU = 149,558,000 km)

PROBLEMS

- Find the ratio of the velocities of two vehicles, one powered by a liquid-chemical rocket and the other by a solid-chemical one, when they are used for acceleration of a 10,000-kg payload in a zero-gravity field. Both vehicles have a total initial mass of 510,000 kg. The liquid-propellant rocket has 60% greater specific impulse and 30% greater mass of empty vehicle (without propellant and payload), and the solid-propellant rocket has a structural coefficient of $\epsilon = 0.080$.
- A sounding rocket is to be launched vertically from the earth's surface. It is to be designed for a 350-kg payload that must not suffer an acceleration greater than 5 g during the burning period. The maximum propellant mass is 1000 kg, and the structural efficiency factor ϵ is 0.1. The solid propellant rocket motor that will be designed for this vehicle is expected to have a specific impulse of 250 s.
Taking $g = g_e$ and neglecting aerodynamic drag, determine:
 - The minimum allowable burning period,
 - The maximum height attainable,
 - The height allowable if the maximum payload acceleration were limited to 4 g.
- A sounding rocket vehicle whose instantaneous total mass is 200 kg is at an elevation of 10,000 m above the surface of the earth and moving vertically upward at a velocity of 1000 m/s when firing ceases. The cross-sectional area of the rocket is 0.065 m^2 . What is the instantaneous rate of deceleration?
- Show that if engine mass were a negligible part of the entire total mass of a rocket vehicle, and if the total structural and engine mass were simply pro-

portional to the initial propellant mass, the structural efficiency factor ϵ would be independent of the mission Δu . A single-stage solid-propellant booster has the following characteristics:

$$\frac{M_{\text{engine}}}{M_0} = 0.005,$$

$$\frac{M_{\text{tank}}}{M_p} = 0.03,$$

$$I_{\text{sp}} = 200.$$

Show how the payload ratio λ and the structural efficiency ϵ depend on the mission velocity Δu and compare your results for ϵ with Fig. 10.6. The definition of the structural factor in this case may be written

$$\epsilon = \frac{M_{\text{tank}} + M_{\text{engine}}}{M_{\text{propellant}} + M_{\text{tank}} + M_{\text{engine}}}.$$

Here neglect gravity and drag effects.

5. A vehicle that utilizes a liquid-chemical rocket is to be used for escape of a payload of 100,000 kg from the earth. The vehicle is to have two stages, each with $\epsilon = 0.06$ and $I_{\text{sp}} = 400$ s, and both having the same structural coefficient λ . Estimate the total mass of the vehicle. Assume as a first approximation that $g \cos \theta t_b = 2000$ m/s and that drag effects are negligible. To ensure acceptable launch acceleration (say $0.2 g_e$), what restriction must be placed on the burning period for the first stage?
6. As shown in Appendix VIII, the optimum arrangement for multistaging is that the payload and structural ratio λ_i and ϵ_i be the same for all stages. Consider the effect of a departure from this optimum arrangement for a three-stage rocket with the same engine specific impulse ($I_{\text{sp}} = 400$) for all three stages. The mass distribution for the stages is as follows:

	Stage		
	1	2	3
Total initial mass, kg	100,000	18,000	4,000
Propellant, kg	75,000	12,000	2,000
Payload, kg			1,025

- a. For each stage determine λ_i and estimate the total velocity increment for the three stages with drag and gravity effects neglected.
- b. Now consider an optimized stage with the same payload, total propellant mass, and total structural mass (tankage plus engine plus all other structural mass). What velocity increment Δu could be obtained in this case?

7. Figure 10.11 shows that for electrical propulsion with

$$\alpha = 10 \text{ kg/kW} \quad \text{and} \quad \Delta u = 7300 \text{ m/s},$$

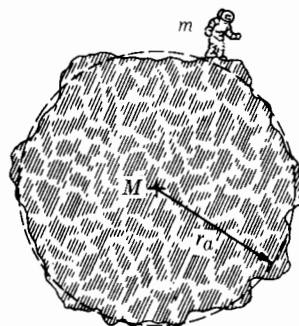
the optimum specific impulse would be about 2000 s, which is too high for chemical rockets and too low for ion thrusters. The Δu was calculated for a one-month earth-moon transfer. Using the data of Table 10.8 and assuming $\alpha/\eta = 10 \text{ kg/kW}$, determine the optimum specific impulse for a 0.7-year transfer from low earth orbit (LEO) to Mars orbit.

8. Show how to find the optimum specific impulse for an electrical propulsion system to be used for missions with large payload. Assume that the thrust is constant. Consider the mass of the electrical power generation equipment M_p to be proportional to the power produced, and all other structural mass to be proportional to the sum of the payload, power plant, and propellant masses. That is,

$$M_p = \alpha P_s, \quad M_s = \beta(M_p + M_p + M_p)$$

Show how the results of using these assumptions with $\beta = 0.05$ and $\alpha = 10 \text{ kg/kW}$ compare with the results shown in Fig. 10.11.

9. One can expect the performance of electrically propelled vehicles to depend strongly on power-plant size, mission velocity increment, and mission duration. Figure 10.12 shows the payload ratios that one could expect for a 100-kW power plant ($\alpha = 30 \text{ kg/kW}$) and for a particular mission ($\Delta u = 6000 \text{ m/s}$). Show, for the xenon ion thruster (whose performance is given in Table 10.6), how payload ratio depends on mission Δu (2000, 6000, 10,000 m/s) and on mission time (75, 150, 300 days). The thruster is to be supplied with a 100-kW power plant and is to operate with a specific impulse of 3500 s.
10. An astronaut is about to explore an asteroid of average density $\rho = 5000 \text{ kg/m}^3$. He is worried that he may accidentally jump from its surface and float off into space. How big (i.e., what diameter) must it be before he can neglect this possibility? The astronaut knows that his mass m , including space suit, is 91 kg (200 lb). He also knows that on the earth he can raise



PROBLEM 10

his center of gravity 0.6 m by jumping with his space suit on. (This is only about two feet, but try it yourself sometime, even without a space suit.) It seems reasonable to assume that the maximum energy output of his legs will be the same on the asteroid as on the earth. For simplicity assume $M \gg m$, such that M does not move significantly during the action, and then check this assumption.

11. a. Calculate the minimum total velocity increment and transit time that would be required for a two-impulse transfer from the orbit of the earth into the orbit of Mars about the sun.
b. Calculate the same quantities for a two-impulse transfer from the surface of the earth into the orbit of Mars.
12. The Mars trip described in Fig. 10.23 required the expulsion of 365 tons of propellant at a velocity of 84 km/s for an initial vehicle mass of 730 tons. From these data calculate the equivalent free space Δu of this mission, assuming that no other mass is expelled. For the stated propulsion time, compare the actual specific impulse with the optimum specific impulse obtained from Eq. (10.43), assuming $\alpha/\eta = 5 \text{ kg/kW}$.
13. In the year 2028 weekly bus service is to be established between Boston and the moon. To avoid the need for large, expensive boosters for moon escape, the following plan has been suggested.

Since there is no moon atmosphere, there is no drag loss associated with high velocity at low altitude. Therefore, it is proposed that a long, smooth track be built on the surface of the moon. On this track a rocket-powered sled is to accelerate the bus to escape velocity, after which the bus leaves, carrying with it a few passengers, a member of the carmen's union, and a rocket engine powerful enough to effect guidance and landing in Boston.

(a) What does a scheme of this type gain over conventional escape trajectories (neglecting friction of sled)? (b) Would there be any incentive for designing a very light sled for this purpose? (c) Is there any reason to multistage the sled? (d) What should the track configuration be at the point where escape velocity is reached? (e) If there is absolutely no limit on track length, even to the extent of circling the moon, is there any advantage in making the track very long? or very short?

14. Numerical integration of Eq. (10.72) is needed to determine the equivalent free-space velocity increment required for constant-thrust interorbital transfers of long duration. Show that the equation may be written as three simultaneous first-order equations:

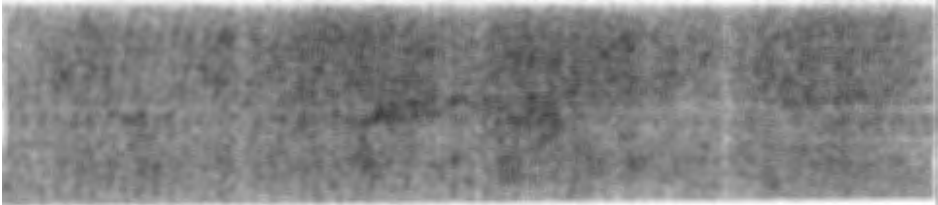
$$\begin{aligned}\frac{d\rho}{d\tau} &= A, \\ \frac{dA}{d\tau} &= \frac{B^2 - \rho}{\rho^3}, \\ \frac{dB}{d\tau} &= \nu\rho.\end{aligned}$$

with initial conditions $\rho = 1$, $A = 0$, and $B = 1$.

Beginning with low-altitude earth orbit (LEO) and $\nu = 10^{-4}$, 10^{-3} , 10^{-2} , and 10^{-1} , determine the time required and the equivalent free-space velocity increment ratio for escape. It may be helpful to use a standard Runge-Kutta routine, for example, Runge-Kutta-Merson, which integrates the simultaneous first-order differential equations with a step size varied according to an error estimate. Compare your results with the circumferential solution shown in Fig. 10.21.

REFERENCES

1. Martin, J. A. "Comparing Hydrocarbon and Hydrogen Booster Fuels," *AIAA J. Spacecraft and Rockets* 25 (1988): 58–94.
2. Buden, D., and J. A. Sullivan. "Nuclear Power Systems for Orbit Raising and Maneuvering," in *Orbit Raising and Maneuvering Propulsion Research Status and Needs*, L. H. Coveney, ed., vol. 89 of *Progress in Aeronautics and Astronautics*. New York: AIAA, 1984.
3. Auweifer-Kurtz, M., H. L. Kurtz, and H. O. Schrade. "Optimization of Elective Propulsion Systems Considering Specific Power as a Function of Specific Impulse," *AIAA J. Propulsion and Power* 4 (1988): 512–519.
4. Forsythe, W. E. *Smithsonian Physical Tables*, 9th rev. ed. Washington, D.C.: Smithsonian Institution, 1954. (See also R. A. Meyers, ed., *Encyclopedia of Astronomy and Astrophysics*, San Diego: Academic Press, 1988.) Reprinted with permission.
5. Hohmann, W. *Die Erreichbarkeit der Himmelskörper*. Munich and Berlin: R. Oldenbourg, 1925.
6. Oberth, H. *Wege zur Raumschiffahrt*. Munich and Berlin: R. Oldenbourg, 1929.
7. Irving, J. H., and E. K. Blum. *Comparative Performance of Ballistic and Low-Thrust Vehicles for Flight to Mars*, vol. 2 of *Vistas in Aeronautics*. New York: Pergamon Press, 1959.
8. Tsien, H. S. "Takeoff from Satellite Orbits," *J. Amer. Rocket Soc.* 23 (1953): 233–236.
9. Irving, J. H. "Low-Thrust Flight: Variable Exhaust Velocity in Gravitational Fields," Chapter 10 in *Space Technology*, Howard Siefert, ed. New York: Wiley, 1959.
10. Sandorff, P. E. "Orbital and Ballistic Flight" M.I.T. Department of Aeronautics and Astronautics (unpublished paper), Cambridge, Mass., 1960.
11. Stuhlinger, E. "Flight Path of an Ion-Propelled Spaceship," *Jet Propulsion*, 27 (1957): 410.
12. Garrison, P. W., and J. F. Stocky. "Future Spacecraft Propulsion," *AIAA J. Propulsion and Power* 4 (1988): 520–525.



C H A P T E R

11

CHEMICAL ROCKET THRUST CHAMBERS

11.1 INTRODUCTION

Chemical rockets are distinguished from other kinds of rockets in that all of the energy required to accelerate the propellant comes from the propellant itself, and specifically from combustion of a fuel-oxidizer combination. Figure 11.1 shows schematically both liquid- and solid-propellant rockets. For the liquid rocket the fuel and oxidizer are stored in separate thin-walled tanks at low pressure. Before combustion they pass through turbine-driven pumps and are injected into the combustion chamber, where they burn at high pressure. In contrast, solid propellants consist of a premixed combination of fuel and oxidant that burns when it is sufficiently heated. The entire block of propellant, called a grain, is stored within the combustion chamber itself. Combustion proceeds from the surface of the propellant at a rate that depends on the temperature and pressure in the combustion chamber and on the geometry of the burning surface.

One of the principal performance characteristics of a rocket propellant, as shown in Chapter 10, is its specific impulse, that is, the ratio of thrust to the propellant flow rate. This, as one would expect, is limited by the chemical energy (“heating value”) of the fuel. But, as we will see in this chapter, it varies inversely with the square root of the molecular weight of the products of combustion. The molecular weight factor is the main reason why hydrogen-rich mixtures of H_2 and O_2 have exceptionally high values of specific impulse (around 450 s or 4400 m/s). Other chemical rockets have appreciably lower specific impulse values (many in

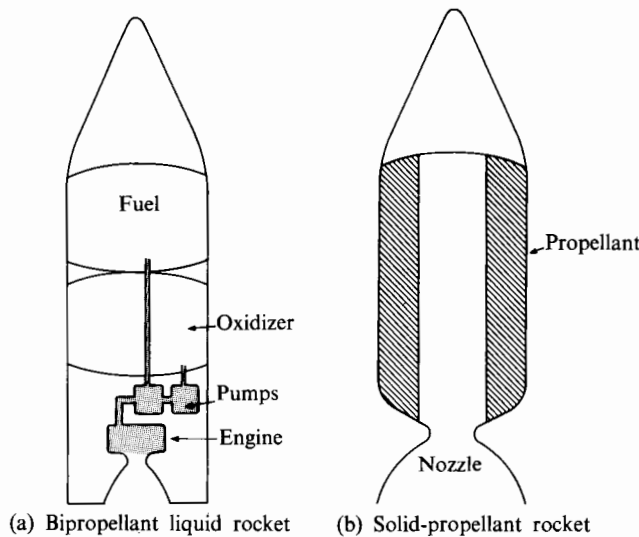


FIGURE 11.1 Schematic diagrams of liquid- and solid-propellant rockets.

the range of 250 to 450 s); this indicates that specific impulse is not the only factor that influences the choice of propellant.

Besides specific impulse, the masses of the fuel and oxidant tanks, turbomachinery, and engines must be considered. The relatively low density of liquid hydrogen gives it a strong disadvantage in tank size; Table 10.1 indicates that tanks for liquid hydrogen must be 2-3 times as massive as those for liquid hydrocarbon fuel. Hydrogen stays in liquid form at low pressure only if its temperature is less than 77 K. Thermal insulation required to keep it liquid for long periods would be prohibitively massive. Thus liquid hydrogen is not considered a storable propellant for space missions. Elimination of turbomachinery, and of liquid transfer and injection, means a substantial mass advantage in favor of solid-propellant rockets. Thus, depending on the mission, there are a variety of fuel-oxidant combinations with lower specific impulse than that of the H₂-O₂ combination that are widely used. (There are fuel-oxidant combinations that can have even higher specific impulse than H₂ and O₂, but they are not widely used because of factors such as toxicity, instability, or unavailability at reasonable cost.)

Because the variety of chemical propellants is so large, we defer a review of their individual properties, and of the principal differences between liquid- and solid-propellant combustion chambers, to Chapter 12. We also leave to that chapter the complexities of nonequilibrium-product composition and two-phase flow in nozzles. Our concern here is in how thrust is developed by hot high-pressure products of combustion and in the factors that govern the design of thrust chambers. We begin with a simplified analytical model and consider the lessons one may learn from that. Then we proceed to consider selected experimental data and heat transfer effects not accounted for in elementary methods of analysis.

11.2 PERFORMANCE CHARACTERISTICS

Chemical rockets, whether powered by liquid or solid propellants, consist in varying complexity of a propellant supply and feed system, a combustion chamber, and an exhaust nozzle. To simplify our analysis of the thrust chamber (that is, the combustion chamber and nozzle), we here assume the following:

1. The working fluid is a perfect gas of constant composition.
2. The chemical reaction is equivalent to a constant-pressure heating process.
3. The expansion process is steady, one-dimensional, and isentropic.

With these assumptions we may describe the thrust chamber schematically and on a $T-s$ diagram as in Fig. 11.2. Propellant enters at state (1). A quantity of heat Q_R (the “heating value” of the propellant combination per unit mass) is added at constant pressure, and the propellant reaches the nozzle inlet at state (2). The propellant expands isentropically from state (2) through the throat, where the Mach number is unity, to the exhaust, where the velocity is u_e . Application of the energy equation, Eq. (2.8), to the heating process gives

$$\dot{\mathcal{Q}} = \dot{m}(h_{02} - h_{01}) = \dot{m}c_p(T_{02} - T_{01})$$

or

$$T_{02} = T_{01} + \frac{Q_R}{c_p}, \quad (11.1)$$

where $\dot{\mathcal{Q}}$ = equivalent heating rate, and \dot{m} = propellant mass flow rate.

Assuming adiabatic nozzle expansion, the energy equation requires constant stagnation enthalpy in the nozzle:

$$h_{02} = h_{0e} \quad \text{or} \quad \frac{u_e^2}{2} = h_{02} - h_e = c_p(T_{02} - T_e),$$

and if the expansion is isentropic, we use Eq. (3.6) to obtain

$$u_e = \sqrt{2c_p T_{02} \left[1 - \left(\frac{P_e}{P_{02}} \right)^{(\gamma-1)/\gamma} \right]}. \quad (11.2)$$

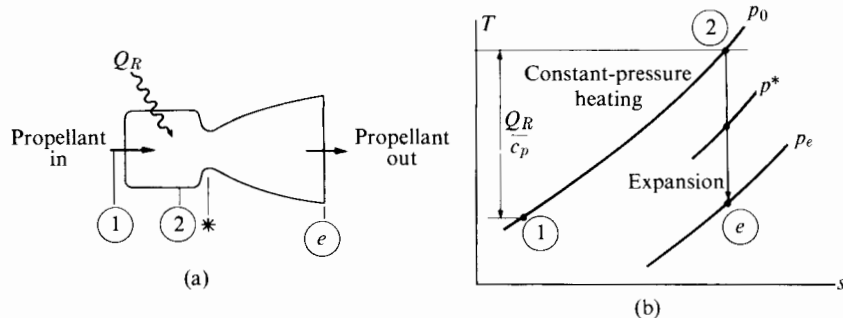


FIGURE 11.2 Simple rocket thrust chamber.

Expressing c_p in terms of γ the universal gas constant \bar{R} , and the propellant molecular weight \bar{M} , we have

$$u_e = \sqrt{\frac{2\gamma\bar{R}}{(\gamma-1)\bar{M}}} T_{02} \left[1 - \left(\frac{p_e}{p_{02}} \right)^{(\gamma-1)/\gamma} \right]. \quad (11.3)$$

Thus, at least for a given T_{02} , it is advantageous to employ propellants with a low molecular weight in order to achieve high u_e . In terms of the “heating value” Q_R per unit mass of propellant, substitution of Eq. (11.1) in (11.2) yields

$$u_e = \sqrt{2c_p \left(T_{01} + \frac{Q_R}{c_p} \right) \left[1 - \left(\frac{p_e}{p_{02}} \right)^{(\gamma-1)/\gamma} \right]} \approx \sqrt{2Q_R \left[1 - \left(\frac{p_e}{p_{02}} \right)^{(\gamma-1)/\gamma} \right]}. \quad (11.4)$$

The last expression assumes $T_{01} \ll Q_R/c_p$, as is generally the case. Expressing Q_R in terms of the heating value per mole of propellant, \bar{Q}_R , we obtain

$$u_e \approx \sqrt{2\frac{\bar{Q}_R}{\bar{M}} \left[1 - \left(\frac{p_e}{p_{02}} \right)^{(\gamma-1)/\gamma} \right]}. \quad (11.5)$$

Calculation of \bar{Q}_R according to the methods of Section 2.4 will be considered in Section 12.1. For this simple model we assume that \bar{Q}_R is known, perhaps in terms of the “complete” chemical reaction assumption. The desirability of propellant mixtures with large \bar{Q}_R/\bar{M} may be seen from Eq. (11.5). Both \bar{Q}_R and \bar{M} will depend on the fuel–oxidant ratio. In many cases fuel-rich mixtures are burned, as it is found that the resultant reduction in \bar{M} more than offsets the accompanying reduction of \bar{Q}_R .

The propellant mass flow rate \dot{m} is given in terms of the properties of the combustion chamber fluid and the nozzle throat area by Eq. (3.14):

$$\dot{m} = \frac{A^* p_{02}}{\sqrt{RT_{02}}} \sqrt{\gamma \left(\frac{2}{\gamma+1} \right)^{(\gamma+1)/(\gamma-1)}}, \quad (11.6)$$

where A^* = nozzle throat area and $R = \bar{R}/\bar{M}$.

For isentropic flow we may use the results of Section 3.3 to calculate propellant properties throughout the exhaust nozzle. In particular, we can find the exhaust pressure p_e in terms of the exhaust area ratio A_e/A^* . The thrust of the simple chemical rocket engine may, as shown in Chapter 10, be written

$$\mathcal{T} = \dot{m} u_e + (p_e - p_a) A_e,$$

where p_a = ambient pressure.

Substituting Eqs. (11.3) and (11.6) for u_e and \dot{m} , we obtain the result

$$\frac{\mathcal{T}}{A^* p_0} = \sqrt{\frac{2\gamma^2}{\gamma-1} \left(\frac{2}{\gamma+1} \right)^{(\gamma+1)/(\gamma-1)} \left[1 - \left(\frac{p_e}{p_0} \right)^{(\gamma-1)/\gamma} \right]} + \left(\frac{p_e}{p_0} - \frac{p_a}{p_0} \right) \frac{A_e}{A^*}, \quad (11.7)$$

in which p_0 is the stagnation pressure in the combustion chamber. It is remarkable that there is no mention here of stagnation temperature and molecular weight

(both of which strongly affect exhaust velocity). Since ideal thrust depends only on pressure forces, it is reasonable that this equation contains only the variables that control geometry and pressure distribution.

Characteristic Velocity

The ideal rocket, aside from serving as a simple analytical model, provides a basis for the comparison and evaluation of real rockets. In order to describe separately the performance of each component of the thrust chamber, two coefficients are defined.

For the combustion chamber the *characteristic velocity*, c^* , is defined as

$$c^* \equiv \frac{p_0 A^*}{\dot{m}}. \quad (11.8)$$

Utilizing Eq. (11.6), we obtain

$$c^* = \sqrt{\frac{1}{\gamma} \left(\frac{\gamma + 1}{2} \right)^{(\gamma+1)/(\gamma-1)} \frac{\bar{R} T_0}{M}} \quad (11.9)$$

for the ideal rocket. Thus c^* is primarily a function of combustion chamber properties.

To illustrate the magnitude of c^* and its dependence on the fuel-oxidizer composition, Table 11.1 presents values for three fuels (liquid hydrogen, a liquid hydrocarbon fuel known as RP1, and liquid methane) used with liquid oxygen. In each case the fuel-oxidizer ratio was chosen to maximize specific impulse (by a method described in Chapter 12). The combustion temperature stated is the steady-flow adiabatic combustion temperature, pertaining to typical fuel and oxidizer inlet conditions and to a chamber pressure of 6.89 MPa (1000 psia). As we

TABLE 11.1 Vacuum expansion $p_{01} = 1000$ psia (6.89 MPa); $\frac{A_e}{A^*} = 40$

Oxidizer	LO ₂	LO ₂	LO ₂
Fuel	LH ₂	RP1	CH ₄
Oxidizer-fuel mass ratio	4.83	2.77	3.45
T_{01}/K	3250	3700	3560
Average bulk density of propellant, kg/m ³	320	1030	830
I_{sp}	455	358	369
u_e m/s	4464	3512	3620
c^* m/s	2386	1838	1783

Source: Data from Rocketdyne Chemical and Material Technology, Rocketdyne Division, Rockwell International.

can see, the molecular weights of the propellants and the values of c^* (defined by Eq. 11.9) depend significantly on the fuel-oxidant combustion.

Table 11.1 also shows that, for a given nozzle ($A_e/A^* = 40$), the exhaust velocity is substantially higher than c^* . This is a measure of the importance of providing a well-shaped nozzle to expand the hot high-pressure gas to low pressure.

Thrust Coefficient

For the nozzle, the *thrust coefficient*, $C_{\mathcal{T}}$, is defined as[†]

$$C_{\mathcal{T}} \equiv \frac{\mathcal{T}}{p_0 A^*}. \quad (11.10)$$

Using Eq. (11.7), we have

$$C_{\mathcal{T}} = \sqrt{\frac{2\gamma^2}{\gamma - 1} \left(\frac{2}{\gamma + 1}\right)^{(\gamma+1)/(\gamma-1)} \left[1 - \left(\frac{p_e}{p_0}\right)^{(\gamma-1)/\gamma}\right]} + \frac{p_e - p_a}{p_0} \frac{A_e}{A^*} \quad (11.11)$$

for the ideal rocket. We can see that $C_{\mathcal{T}}$ is a function of nozzle geometry only, since the variable $(p_e - p_a)/p_0$ can be regarded as a measure of how well the nozzle geometry is suited to the actual pressure ratio. Combining Eqs. (11.8) and (11.10), we find that the thrust of a rocket is given by

$$\mathcal{T} = \dot{m} c^* C_{\mathcal{T}},$$

in which c^* and $C_{\mathcal{T}}$ characterize the performances of combustion chamber and nozzle, respectively. For a real rocket, comparison of c^* and $C_{\mathcal{T}}$, calculated from Eqs. (11.8) and (11.10) with ideal values from (11.9) and (11.11), indicates how well each component of the real thrust chamber is performing.

If the nozzle does not have a diverging portion, then the pressure ratio p_e/p_0 is given by Eq. (3.11) with $M = 1$:

$$p_e/p_0 = \left(\frac{2}{\gamma + 1}\right)^{\gamma/(\gamma-1)},$$

and the thrust coefficient reduces to

$$C_{\mathcal{T}_{\text{conv}}} = (\gamma + 1) \left(\frac{2}{\gamma + 1}\right)^{\gamma/(\gamma-1)} - \frac{p_a}{p_0}, \quad (11.12)$$

in which $C_{\mathcal{T}_{\text{conv}}}$ is the thrust coefficient for a converging nozzle. The ratio of thrusts, with and without a diverging section, is given by

$$\frac{\mathcal{T}}{\mathcal{T}_{\text{conv}}} = \frac{C_{\mathcal{T}}}{C_{\mathcal{T}_{\text{conv}}}}$$

[†] The vacuum thrust \mathcal{T}_v of a nozzle is the thrust corresponding to zero ambient pressure. In accordance with Eq. (11.10), the vacuum thrust coefficient $C_{\mathcal{T}_v}$ is defined by $C_{\mathcal{T}_v} = \mathcal{T}_v/p_0 A^*$. For finite back pressure p_a , the thrust coefficient $C_{\mathcal{T}}$ is related to $C_{\mathcal{T}_v}$ by

$$C_{\mathcal{T}} = C_{\mathcal{T}_v} - A_e p_a / A^* p_0.$$

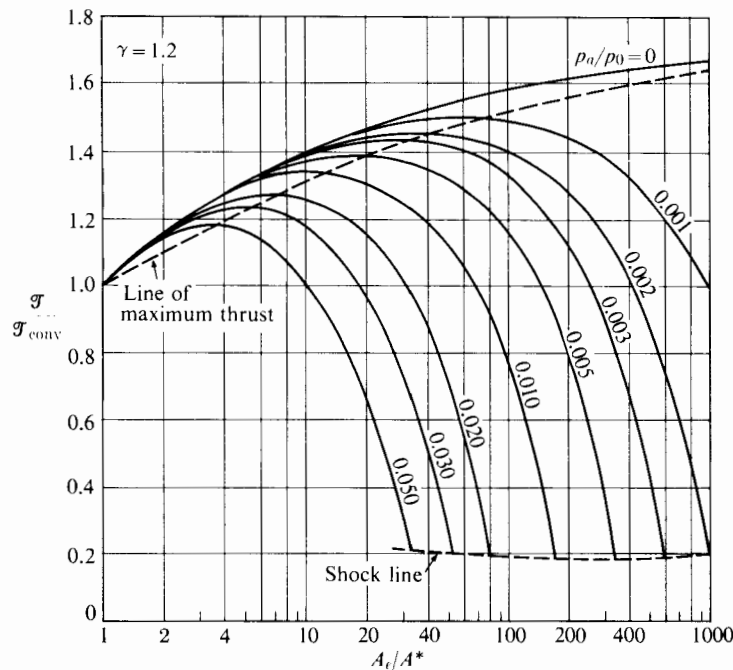


FIGURE 11.3 Performance characteristics of a one-dimensional isentropic rocket nozzle; $\gamma = 1.2$. (After Malina [1].)

and may be evaluated by means of Eqs. (11.11) and (11.12) above as a function of γ , p_e/p_0 , and p_a/p_0 . For the special case $\gamma = 1.2$, Fig. 11.3 shows how the diverging portion of the nozzle contributes to the rocket thrust at various area and pressure ratios. We can see that for each value of the ambient pressure ratio p_a/p_0 there is an optimum area ratio for the nozzle; it is the one for which $p_e = p_a$ (see discussion of Fig. 10.2).

We can see from Fig. 11.3 that the thrust of a rocket will actually be reduced by adding a diverging section of too large an area ratio. However for reasonable pressure ratios ($p_a/p_0 < 0.02$) this would not happen unless A_e/A^* were greater than about 30. For very small pressure ratios (such as $p_a/p_0 = 0.001$), we will see that very large area ratios are associated with maximum thrust.

Figure 11.3 displays a shock line that shows the pressure ratios and area ratios for which a shock enters the nozzle. One may derive it as follows: Suppose that a normal shock sits in the exit plane of the nozzle and that the conditions just ahead of it are p_e , M_e , and so on; the pressure just behind it is p_a . Then, according to Eq. (3.36) for normal shocks,

$$\frac{p_a}{p_e} = \frac{2\gamma}{\gamma + 1} M_e^2 - \frac{\gamma - 1}{\gamma + 1}.$$

For the isentropic nozzle the pressure ratio p_0/p_e is related to M_e by

$$\frac{p_0}{p_e} = \left(1 + \frac{\gamma - 1}{2} M_e^2\right)^{\gamma/(\gamma-1)},$$

so that

$$\frac{p_a}{p_0} = \left(\frac{2\gamma}{\gamma+1} M_e^2 - \frac{\gamma-1}{\gamma+1}\right) / \left(1 + \frac{\gamma-1}{2} M_e^2\right)^{\gamma/(\gamma-1)}.$$

Further, the area ratio is related to M_e by (applying Eq. 3.15)

$$\frac{A_e}{A^*} = \frac{1}{M_e} \left[\frac{2}{\gamma+1} \left(1 + \frac{\gamma-1}{2} M_e^2\right) \right]^{(\gamma+1)/2(\gamma-1)}.$$

These last two relations, then, show that for a given γ there is only one pressure ratio p_a/p_0 for which a normal shock will locate in the plane of a nozzle of a given area ratio A/A^* . Further discussion of back pressure effects follows in Section 11.3.

It is appropriate, after this description of a simplified rocket, to ask certain questions about the operation and analysis of real rockets. Foremost among the questions on operation is: How is the combustion pressure chosen? Equation (11.7) indicates that high p_0 is desirable, in that for a given thrust, rocket size (characterized by A^*) may be decreased as the combustion chamber pressure p_0 is increased. Offsetting this advantage are certain difficulties associated with high p_0 . Thrust chamber stresses increase with p_0 , and so do heat transfer rates. In addition, for pump-fed liquid rockets, pump power and size increase with p_0 . In some cases combustion behavior and products may be significantly influenced by combustion pressure. Thus many considerations enter into the choice of combustion pressure, most of which are sufficiently complex to prohibit simple analytical treatment. After considering the various rocket components separately we will again approach the choice of chamber pressure, but no simple analytical answer will emerge.

The analytical simplifications of the ideal rocket should be compared with more realistic models. For example, is the actual combustion process accompanied by significant pressure losses? How nearly does the actual nozzle flow approach one-dimensional isentropic flow? We know, of course, that real nozzles are neither entirely frictionless nor entirely adiabatic. Under certain conditions, nozzle flow patterns may even include shocks. Does the propellant composition remain constant throughout the nozzle, or does it shift in accordance with the rapidly changing propellant temperature? And finally, for a given area ratio, how does the shape of the nozzle affect performance? We will take up questions such as these in the following sections and in Chapter 12.

11.3 NOZZLES

If one assumes that the flow in a rocket nozzle is one-dimensional and isentropic, then the only important geometric variable is the area ratio. However, real nozzle flows are never truly one-dimensional, and the shape of the nozzle walls

can be quite important. The design of an actual nozzle requires the specification of the entire nozzle shape and generally takes into account variations in velocity and pressure on surfaces normal to the streamlines. In addition, the influence of friction, heat transfer, composition change, or shocks must be considered. However, let us first consider the determination of suitable nozzle shapes without these latter complications.

The exact shape of the subsonic or converging portion of the nozzle is not, within limits, a matter of great importance. In a region of favorable pressure gradient such as this, almost any reasonably smooth contour provides good subsonic flow. On the other hand, the shape of the supersonic or diverging portion of the nozzle is important since, even in the absence of boundary layer effects, improper shaping can result in shock formation and substantial performance loss.

Nozzle performance, assuming constant (and known) composition flow, is more easily related to the simple model. The ideal nozzle flow can be refined slightly to account, in the case of conical nozzles, for the effect of nonaxial exhaust velocities.

Conical Nozzles

Consider the flow out of the conical nozzle of Fig. 11.4, and assume that the streamlines in the expanding part of the nozzle are straight lines that all intersect at the point O . A control surface is indicated, passing through the spherical segment (of radius R) over which exhaust properties are constant. The reaction to the thrust is again shown as the vector \mathcal{T} . Applying the momentum equation (2.4), in the axial x -direction gives, for steady flow,

$$\sum F_x = \mathcal{T} + (p_a - p_e)A_e = \int_{cs} \rho(\mathbf{u} \cdot \mathbf{n})u_x dA,$$

where A_e is the plane exhaust area πr^2 . No mass crosses the control surface except over the spherical exhaust segment, and there it is convenient to let

$$dA = 2\pi R \sin \phi R d\phi.$$

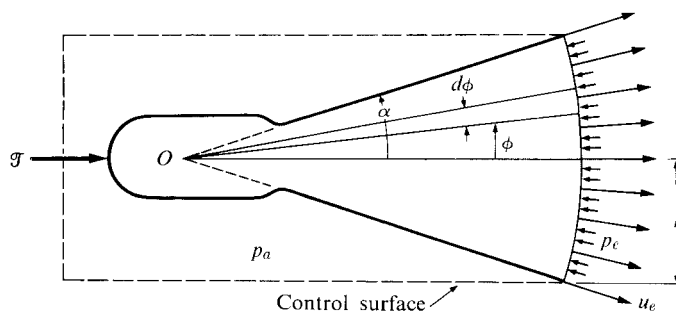


FIGURE 11.4 Spherically symmetric nozzle flow.

Further, in this case,

$$\mathbf{u} \cdot \mathbf{n} = u_e \quad \text{and} \quad u_x = u_e \cos \phi.$$

Thus

$$\mathcal{T} = \int_0^\alpha \rho(u_e) u_e \cos \phi 2\pi R^2 \sin \phi d\phi + (p_e - p_a) A_e.$$

Integrating, we obtain

$$\mathcal{T} = 2\pi R^2 \rho u_e^2 \frac{1 - \cos^2 \alpha}{2} + (p_e - p_a) A_e.$$

Since the area of the spherical exhaust segment A'_e is $2\pi R^2(1 - \cos \alpha)$, the propellant flow rate is

$$\dot{m} = \rho u_e \times 2\pi R^2(1 - \cos \alpha),$$

and the thrust equation becomes

$$\mathcal{T} = \dot{m} u_e \frac{1 + \cos \alpha}{2} + (p_e - p_a) A_e$$

or, since the spherical area segment A'_e is $[2/(1 + \cos \alpha)]A_e$,

$$\mathcal{T} = \frac{1 + \cos \alpha}{2} [\dot{m} u_e + (p_e - p_a) A'_e]. \quad (11.13)$$

Since, for reasonable nozzles, both the difference between A_e and A'_e and the contribution of the pressure term to the thrust are small, it is adequate to replace A'_e in Eq. (11.13) by the plane area A_e . Thus the thrust of an ideal conical rocket of half-angle α is reduced by a factor λ ,

$$\lambda = \frac{1 + \cos \alpha}{2}, \quad (11.14)$$

over that of an axial-outlet rocket with the same exhaust conditions.

Approximate experimental verification of the thrust correction due to radial flow of Eq. (11.14) is shown in Fig. 11.5, which compares actual to ideal (axial exhaust velocity) thrusts for a series of conical nozzles. In this figure the ex-

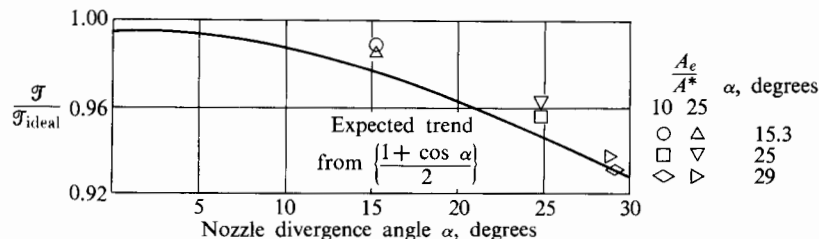


FIGURE 11.5 Radial-flow thrust loss of conical nozzles [2].

pected performance has been reduced arbitrarily about 0.5% to account for boundary layer losses.

The problem with small cone angles is excessive nozzle length. For a conical nozzle with half-angle α , length L , and diameter D , we can express the ratio of exit to throat areas as

$$\frac{A_e}{A^*} = \left(\frac{D^* + 2L \tan \alpha}{D^*} \right)^2,$$

so that

$$L = D^* \left(\sqrt{\frac{A_e}{A^*}} - 1 \right) / 2 \tan \alpha.$$

For an area ratio of 100, we would have $L/D^* = 7.8$ for 30° and 16.8 for 15° . The throat diameter D^* will be fixed by the combustion chamber condition and the specific thrust so that nozzle length and mass are strongly dependent on α . Reducing α from 30° to 15° would more than double the mass of the diverging part of the nozzle.

A better way to minimize divergence loss is to use a shaped nozzle. In the following paragraphs we review the ideas and methods important for determining nozzles of optimum shape.

The Shaped Nozzle

With a nozzle shaped so as to provide uniform parallel flow at exit, one could completely eliminate flow divergence loss. We will see shortly that this ideal case is not a practical option. However, the analytical method used for determining this shape, the method of characteristics [3], is widely used for nozzles of more practical shape. So we take time here to review the method and apply it to the particular case of isentropic expansion of a perfect gas with constant specific heat ratio γ . The method can also be used with variable γ , chemical reaction during expansion [4], and wall friction [5].

Designing a shaped nozzle requires consideration of two-dimensional flow. The curvature of the streamlines is significant, so that gradients (of velocity and pressure) perpendicular to streamlines become important.

Given a specified nozzle geometry, one way to treat this problem is to set up a numerical solution of the equations of motion for the whole nozzle using an iterative finite-difference technique [6] to solve for the velocity and pressure at a large number of grid points in the flow field. This method can provide a very accurate solution to the inviscid flow problem, but it is time consuming. The method of characteristics, which is applicable only to supersonic flow, has been much more widely used because of its simplicity and also because it is the supersonic portion of the nozzle that is responsible for most of its size and mass. Through extensive tests and analyses Back, Cuffel, and Massier [7] showed that large variations in the geometry of the converging portion of the nozzle had little effect on specific impulse. For these reasons we turn now to the method that has been most widely used in calculating supersonic flow in nozzles.

The method of characteristics depends on the fact that, in supersonic flow, the influence of a small pressure disturbance is limited to a specific region. In subsonic flow the region of influence is unlimited and there is no comparable calculation procedure. The region of influence is illustrated in Fig. 11.6, which shows a small disturbance originating at a point A in a field of uniform parallel supersonic flow. If the pressure disturbance is small, it will propagate *relative to the fluid* as a spherical pressure wave at the local velocity of sound a . The center of the spherical sound wave is moving downstream with velocity u . Thus the zone of influence is limited to a cone of half-angle α , which is given by

$$\alpha = \sin^{-1} \left(\frac{at}{ut} \right) = \sin^{-1} \left(\frac{1}{M} \right)$$

or

$$\alpha = \tan^{-1} \frac{at}{\sqrt{(ut)^2 - (at)^2}} = \tan^{-1} \frac{1}{\sqrt{M^2 - 1}}, \quad (11.15)$$

where M is the Mach number. The angle α is called the *Mach angle*, and the limit of influence is called the *Mach line*. If the flow upstream of a given Mach line is uniform, it will be straight, and all properties of the flow immediately downstream of it will be uniform. In a sense, changes in fluid properties may be thought of as propagating along Mach lines.

Suppose that uniform parallel supersonic flow enters the divergent portion of a duct, as in Fig. 11.7. Due to the wall curvature, there are established pressure gradients that turn the streamlines so that the fluid follows the wall. Since we are ignoring friction in this discussion, the fluid may be assumed to slide freely over the wall surface. At A an incremental turning $d\theta$ causes a small pressure disturbance dp that propagates into the fluid along the Mach line $A-C$ at an angle determined by the local Mach number. Similarly, at A' the wall's initial influence propagates along $A'-C$. Continuous wall curvature beyond A or A' may be considered to generate an infinite number of successive Mach lines, a few of which are

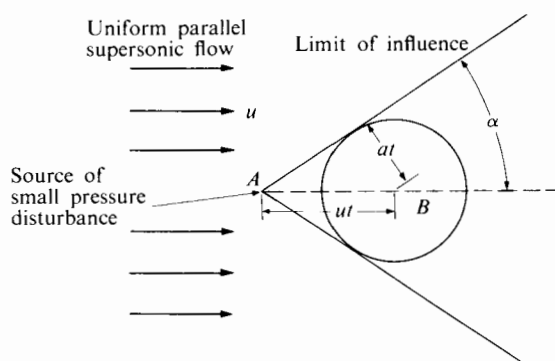


FIGURE 11.6 Propagation of a small pressure disturbance in supersonic flow.

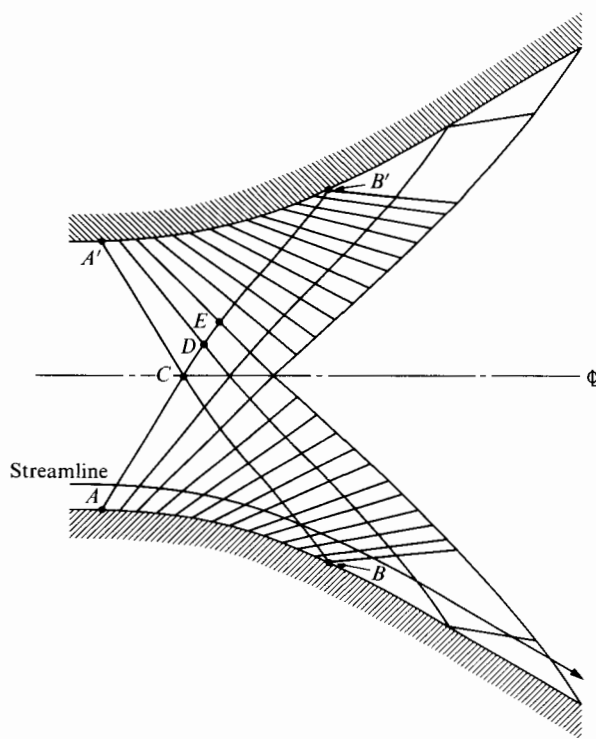


FIGURE 11.7 Supersonic flow entering duct divergence. The flow is two-dimensional, but it may be either plane or axisymmetric.

illustrated. Those Mach lines emanating from the lower duct wall are called left-running Mach lines, and those from the upper wall right-running Mach lines. The designations refer to the direction in which the Mach lines appear to propagate downstream to an observer looking downstream.

In a region such as ABC or $A'B'C$ where Mach lines of only one type are present, the fluid properties are constant just upstream or downstream of each Mach line. Thus specification of fluid properties along any streamline (such as the wall streamline) is sufficient to describe the entire region. Suppose, as in Fig. 11.8, the wall undergoes an infinitesimal turning $d\theta$. The flow upstream has a Mach number M ; thus the disturbance emanating from the infinitesimal corner propagates into the flow field on line OA at an angle

$$\alpha = \tan^{-1} \frac{1}{\sqrt{M^2 - 1}}$$

to the upstream flow direction. The fluid on any streamline crossing the Mach line must have its direction changed so that it will continue to travel parallel to the wall. Thus it must turn through angle $d\theta$. Further, the vectorial change $d\mathbf{U}$ in

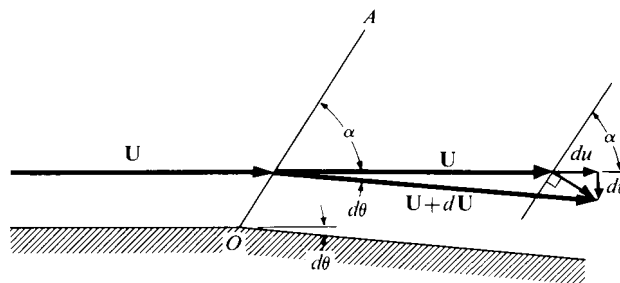


FIGURE 11.8 Expansion at an infinitesimal corner.

its velocity must be normal to the Mach line, since there can be no change in the momentum component parallel to the Mach line (the fluid is not acted on by any forces in that direction). These considerations fix the magnitude of $d\mathbf{U}$ and its components du and dv . We may easily verify that

$$dv = U d\theta, \quad (11.16)$$

$$du = dU, \quad (11.17)$$

$$\tan \alpha = \frac{du}{dv}. \quad (11.18)$$

Combining Eqs. (11.15), (11.16), (11.17), and (11.18), we obtain

$$\frac{dU}{U} = \frac{d\theta}{\sqrt{M^2 - 1}}. \quad (11.19)$$

Combining the definitions of Mach number and stagnation temperature,

$$U^2 = M^2 \gamma RT \quad \text{and} \quad \frac{T_0}{T} = 1 + \frac{\gamma - 1}{2} M^2,$$

yields

$$U^2 = \frac{\gamma R T_0 M^2}{1 + [(\gamma - 1)/2] M^2}. \quad (11.20)$$

From this we may show that since the stagnation temperature is constant along a streamline,

$$\frac{dU}{U} = \frac{dM^2}{2M^2 \{1 + [(\gamma - 1)/2] M^2\}}, \quad (11.21)$$

and therefore we may transform Eq. (11.19) to

$$dM^2 = \frac{2M^2 \{1 + [(\gamma - 1)/2] M^2\} d\theta}{\sqrt{M^2 - 1}}. \quad (11.22)$$

Thus the change in Mach number is easily related to the change in direction of the streamline, so long as the flow may be considered isentropic. Changes in all

fluid properties may be determined from the change in Mach number evaluated from Eq. (11.22). In particular Eq. (11.21) gives the change in fluid velocity. Changes in temperature, density, and pressure may be obtained from

$$\frac{dT}{T} = -\frac{\gamma - 1}{2} \frac{dM^2}{1 + [(\gamma - 1)/2]M^2}, \quad (11.23)$$

$$\frac{dp}{\rho} = -\frac{dM^2}{2\{1 + [(\gamma - 1)/2]M^2\}}, \quad (11.24)$$

$$\frac{dp}{p} = -\frac{\gamma}{2} \frac{dM^2}{1 + [(\gamma - 1)/2]M^2}. \quad (11.25)$$

Equations (11.21) through (11.25) may be used to evaluate, by a numerical process, the conditions in the flow field ABC or $A'CB'$ in Fig. 11.7 by replacing the wall curvature by a finite number of straight line segments.

In the region downstream of BCB' in Fig. 11.7 the Mach lines cross each other, and conditions downstream of a given Mach line are no longer uniform.

Consider the flow in the neighborhood of a general Mach line intersection as indicated in Fig. 11.9. The Mach number and flow direction immediately upstream of OA_2 are not the same as they are upstream of OA_1 . Therefore the Mach lines change direction upon intersecting. If we know the flow in regions B_1OA_2 and A_1OB_2 , we may determine the flow in region A_2OB_2 as follows:

The deflection of the streamlines crossing OA_2 and OB_2 is fixed by Eq. (11.22) and by the requirement that all the streamlines in region A_2OB_2 be parallel; they must therefore have a uniform Mach number.

Referring to Fig. 11.9, we can see that the streamlines in A_2OB_2 will be parallel if

$$\delta\theta_1 - \delta\theta_2 = \delta\theta_3 - \delta\theta_4, \quad (i)$$

and the Mach number will be uniform if

$$\delta M_1 + \delta M_2 = \delta M_3 + \delta M_4. \quad (ii)$$

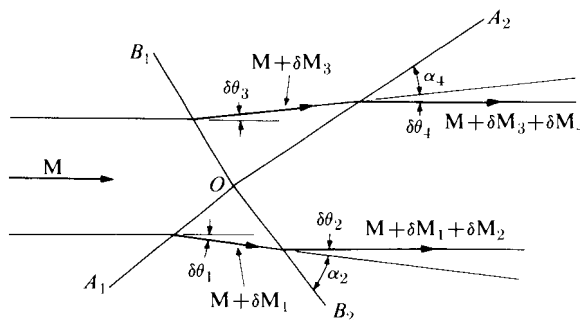


FIGURE 11.9 Intersection of Mach lines.

A finite-difference approximation of Eq. (11.22) yields

$$\delta\theta_2 = m_1 \delta M_2 \quad (\text{iii})$$

and

$$\delta\theta_4 = m_3 \delta M_4, \quad (\text{iv})$$

in which

$$m_1 = \frac{\sqrt{(M + \delta M_1)^2 - 1}}{(M + \delta M_1) \{1 + [(\gamma - 1)/2](M + \delta M_1)^2\}}$$

and

$$m_3 = \frac{\sqrt{(M + \delta M_3)^2 - 1}}{(M + \delta M_3) \{1 + [(\gamma - 1)/2](M + \delta M_3)^2\}}.$$

Equations (i) through (iv) can easily be solved for $\delta\theta_2$, $\delta\theta_4$, δM_2 , and δM_4 . For example,

$$\delta M_4 = \frac{(\delta\theta_3 - \delta\theta_1) - m_1(\delta M_1 - \delta M_3)}{m_3 - m_1}.$$

Thus so long as M , $\delta\theta_1$, $\delta\theta_3$, δM_1 , δM_3 in Fig. 11.9 are known, the flow immediately downstream of O may be solved directly. If $\delta\theta_3 = \delta\theta_1$, we can see that $\delta M_1 = \delta M_3$ and $m_1 = m_3$ so that the formula for δM_4 becomes indeterminate. However, in this case the flow in A_2OB_2 is parallel to M so that $\delta\theta_4$ will be known and δM_4 may be calculated from Eq. (iv).

Now, referring to Fig. 11.7, we see how we can determine the flow downstream of $B'CB$. First we can calculate the flow just downstream of C by the above method, since the flow in regions $A'CB'$ and ACB has already been determined. Next we may obtain the flow just downstream of D in a similar way, and so on to E and all the other points of Mach-line intersection.

For a subsonic-supersonic nozzle, the starting boundary for the calculation merits some consideration. In the vicinity of the throat, we may obtain contours of constant Mach number either by experiment or by calculation of the subsonic flow. Figure 11.10 shows contours for $M = 0.9$ and $M = 1.0$, and we may note that the flow is not exactly one-dimensional. It is not possible to start the finite-difference calculation process right on the $M = 1$ line because here the Mach angles are 90° . However, it will make negligible difference to the calculation of the flow field as a whole if the location of the $M = 1.1$ line is assumed and the calculation is started from there. First a number of starting points (for example, 1–5) are selected and the characteristic lines are drawn from them, giving points of intersection (6–11). The flow immediately downstream of points 2–5 may be obtained by the method just outlined. Along the nozzle center line and immediately adjacent to the wall the flow direction is known; hence the flow downstream of points 6–11 may be determined in the same way. In this manner the whole flow field can be determined.

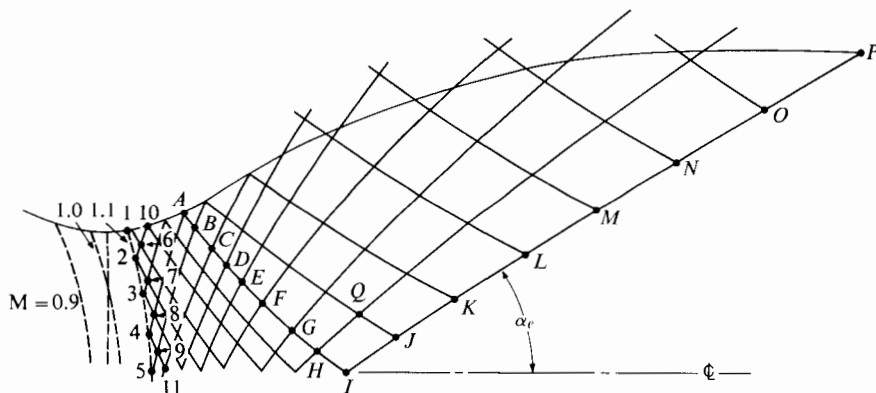


FIGURE 11.10 Supersonic flow in a converging-diverging nozzle.

The purpose of the preceding discussion is to illustrate simply the way in which an isentropic, two-dimensional supersonic flow can be calculated, by using a finite-difference method. As mentioned earlier, the method in general use for solving problems of this type is called the method of characteristics [3]. It is adaptable to axisymmetric flows and is readily useful with computer programming of the calculation procedure.

It is of interest to consider the design of a so-called perfect nozzle, that is, one giving uniform axial exhaust velocity and uniform exhaust pressure. We can use Fig. 11.10 to illustrate the design of this nozzle by the method of characteristics. Suppose again that the location of the $M = 1.1$ contour is assumed and, in addition, a small portion of the shape of the supersonic part of the nozzle; that is, 1–10–A in Fig. 11.10. Then we can use the method of characteristics to solve the flow field. At some point along the axis the design exhaust Mach number will be reached. For illustration, suppose this occurs at I (although it is unlikely that it would occur exactly on a mesh point). Downstream of this point, and hence downstream of a Mach cone extending from the point, fluid properties remain constant and the velocity is parallel to the axis. Hence we may draw the characteristic or Mach line $I-P$, a straight line, at the exit Mach angle α_e , and at points along this line, such as J, K , and O , we know the fluid properties. The solution from line 1–5 has extended downstream to line $A-I$, utilizing the arbitrary wall contour 1–10–A. Downstream of A the wall contour is no longer arbitrary since streamlines in this region are determined by the known properties at A, B, \dots, I and I, J, \dots, P . That is, from these known points we may fill in the solution between $A-I$ and $I-P$. For example, we find Q from the points H and J , and so on. Once the mesh is obtained, streamlines may be drawn throughout the region. In particular, that streamline $A-P$ passing through A is the required portion of the wall contour 1–A–P.

With a sufficiently fine mesh, the method of characteristics can provide good accuracy. For example, Fig. 11.11 shows predicted and measured pressures along

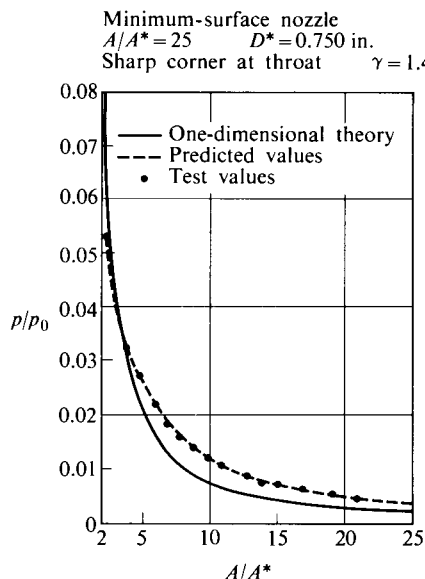


FIGURE 11.11 Comparison of actual and predicted pressure distributions. (Courtesy Ahlberg et al. [8].)

a particular nozzle. For comparison, the simple one-dimensional prediction of pressure is also shown.

Nozzle Length

The length of a perfect nozzle is usually large for a given area ratio. The length is somewhat dependent on the assumed wall contour 1–10–A, and the minimum length for a given area ratio corresponds to a sharp corner at which the points 1 and A converge. Although this configuration is perfectly suitable aerodynamically (some wind tunnels requiring uniform test section properties employ a sharp corner at the throat), it is not desirable in rocket applications where sharp corners can create heat-transfer difficulties. Figure 11.12 compares the lengths of perfect (or “ideal”) nozzles and three other types. The perfect-nozzle throat contour was assumed to be a circular arc of radius 0.4 times the throat radius. We will discuss the so-called optimum-contour, plug, and expansion-deflection (E-D) nozzles in the following paragraphs.

Examination of Figure 11.10 indicates that near the exhaust end of the nozzle a large portion of the nozzle wall is nearly parallel to the axis. A consideration of the pressure forces on this portion suggests that it might be removed with a saving in weight that would more than compensate for the loss of thrust. In fact, when wall friction is considered, removal of part of the nozzle can result in an *increased* thrust. With this in mind it is not surprising that the shape of actual rocket nozzles does not closely resemble that of the “perfect” nozzle of

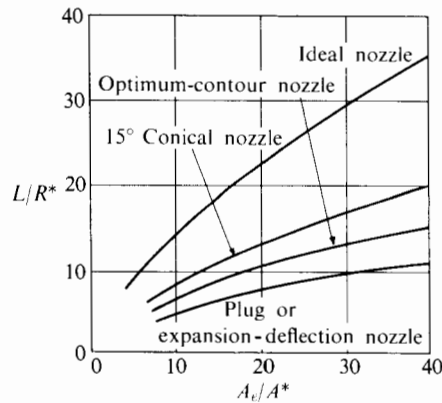


FIGURE 11.12 Comparison of lengths of various types of nozzles for $\gamma = 1.23$. (Courtesy Rao [9].)

Fig. 11.10. Figure 11.13 shows the shape of a hydrogen-oxygen rocket designed for a thrust of 4200 N and having an exceptionally large area ratio of 300:1. The combustion chamber, throat, and early-expansion part of the nozzle (up to 80:1) are cooled with 40 slotted channels (see section B-B) containing a flow of hydrogen that enters the nozzle at $A_e/A^* = 80$. The rocket develops a vacuum specific impulse of 458 s with chamber pressure of 3.5 MPa (507 psia) with an O:H mass ratio of 5:1. It is notable that the slope of the nozzle wall dr/dx is not zero at the nozzle exit; we may infer from this that the fluid properties are not uniform in the exit plane.

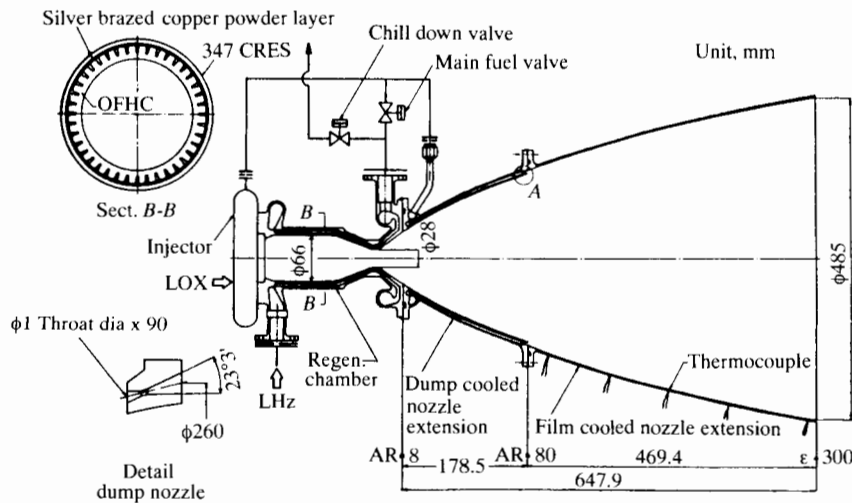


FIGURE 11.13 H_2-O_2 rocket nozzle; $A_e/A^* = 300$. (Courtesy AIAA [10]. © AIAA. Reprinted with permission.)

The “optimum-contour” nozzle whose length is shown in Fig. 11.12 is not the result of a search for a perfect nozzle. Rather it is the result of an attempt to define the wall geometry that will maximize thrust for a nozzle of given length. Allman and Hoffman [11] show how it is done by finding the optimum shape of the “polynomial nozzle” shown in Fig. 11.14. Downstream of the throat, which is defined by two circular arcs, the nozzle shape is defined by $y(x) = a + bx + cx^2$. Making the slope continuous at the throat attachment point means there are only two free parameters, θ_a and y_e as defined by Fig. 11.14. For any chosen pair of these values, the nozzle geometry is fixed and we may use the method of characteristics, provided that we assume the location of a Mach contour line—for example, $M = 1.1$. After we have solved for the flow field, we calculate the nozzle thrust from

$$\mathcal{T} = \int_{A_e} (p - p_a + \rho u^2 \cos \theta) dA,$$

in which the integral extends over the entire exhaust plane and θ is the local angle between the velocity vector and the axial direction. We repeat the method of characteristics solution and the thrust calculation for a series of pairs of θ_a and y_e until we find the best combination. Figure 11.15 shows the contours of constant thrust on a θ_a - y_e plane for a nozzle of given chamber conditions, throat geometry, and nozzle length and for zero ambient pressure. Also shown are the results of three optimizing strategies used to arrive at optimum shape. The best thrusts obtained by Allman and Hoffman are within a small fraction of 1% of the values obtained in the procedure that Rao [9] used.

As mentioned earlier, it is necessary to begin the characteristics solution with an assumed location for a slightly supersonic Mach contour, for example, $M = 1.1$. This can introduce some uncertainty since the location of such a contour depends significantly on throat geometry. Dutton and Addy [12] have used perturbation methods to solve for the Mach contours in throats bounded by circular-arc-shaped walls. Figure 11.16 shows an example of measured and calcu-

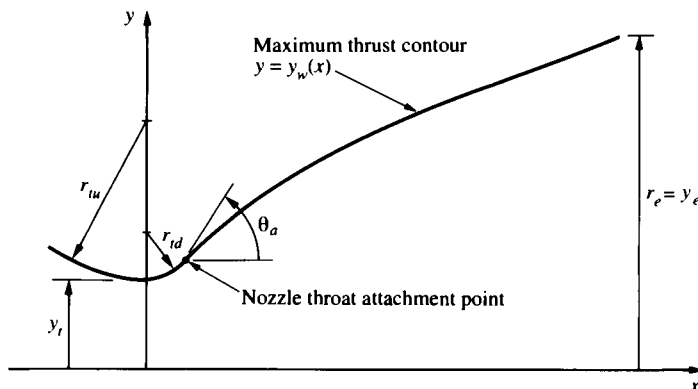


FIGURE 11.14 Two-parameter supersonic wall contour. (After Allman and Hoffman [11].)

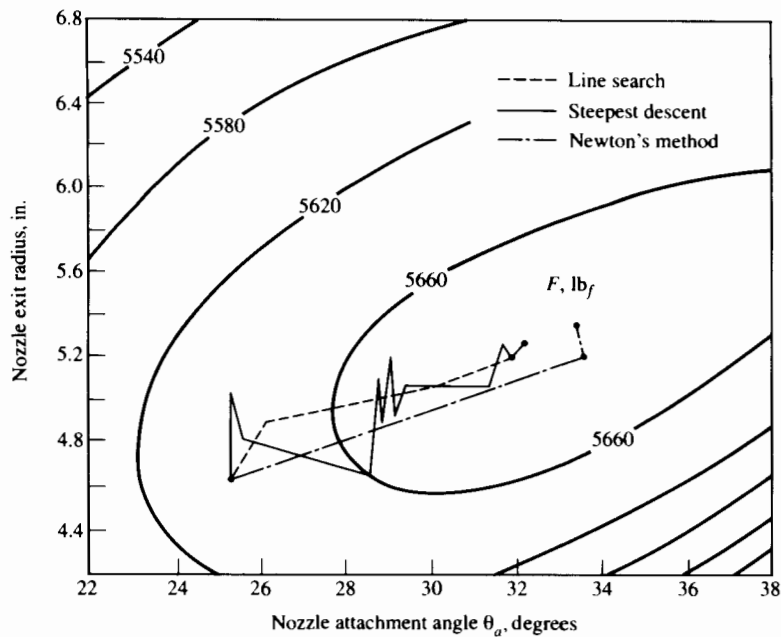


FIGURE 11.15 Example of optimization calculations for the nozzle of Fig. 11.14; thrust contours in lb_f . (Courtesy AIAA [11]. ©AIAA. Reprinted with permission.)

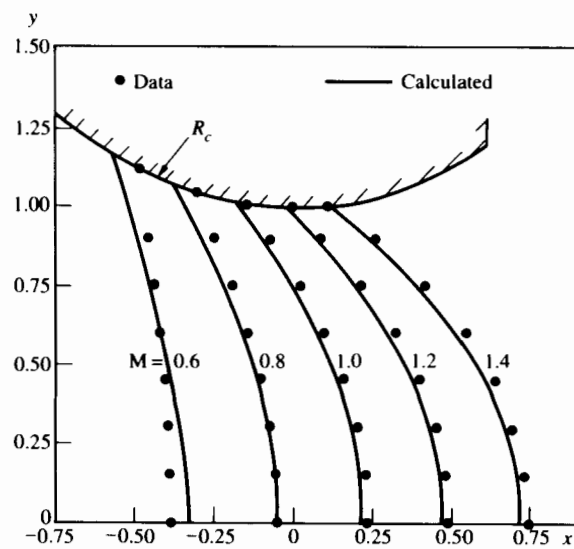


FIGURE 11.16 Experimental data compared with calculated Mach contours in the throat of a subsonic-supersonic nozzle; $R_c/R^* = 1$. (Courtesy AIAA [12]. © AIAA. Reprinted with permission.)

lated Mach contours for the case in which the radius of curvature of the wall equals the throat radius. Finite difference methods such as that of Reference 6 could also be used to generate such Mach contours as well as to solve for the entire subsonic-supersonic flow field. Characteristics methods are, however, much faster because, built on the principle that in supersonic flow small disturbances can only travel downstream, they require only one pass in the downstream direction to find the flow field solution. For subsonic flows, in which the flow is in principle everywhere affected by a disturbance (e.g., due to a change in wall slope), the entire flow field must be solved iteratively. With many grid points, several variables, and many iterations, this can be quite time-consuming.

By repeating calculations such as those whose results are shown in Fig. 11.3 for various values of γ , we can show that nozzle geometry for maximum thrust is quite strongly dependent on γ . In general, γ depends on temperature and thus may vary considerably during the nozzle expansion. This variation is, however, possible to incorporate within the method of characteristics solution. It is also possible to include chemical reaction associated with the recombination of dissociated combustion products. We return to this subject in Chapter 12.

The Effects of Friction

Propellant flow in rocket nozzles, like other fluid flows, is altered by viscous effects near the fluid boundaries. However, since the pressure gradient within a nozzle is generally favorable, the boundary layer is usually quite thin. Apart from its important effects on heat transfer (to be discussed shortly), the boundary layer may be considered to affect nozzle performance in three ways.

First, the presence of the boundary layer slightly alters the free-stream characteristics. By definition, the boundary layer *displacement thickness* is that thickness of free-stream flow which is apparently lost owing to the velocity defect within the boundary layer. Hence the free stream is in effect displaced from the wall by this thickness. At the throat the result is a slight reduction of A^* and hence of mass flow rate. The displacement thickness will also affect the distribution of A/A^* through the nozzle, and this in turn will affect the pressure distribution and nozzle thrust. For large-diameter nozzles, this effect is typically small.

Second, the boundary layer affects the rocket thrust directly through the shear stress or skin friction on the nozzle wall, since thrust is simply the integrated stress over the thrust chamber surface. For typical rocket propellants, viscous stresses are very small relative to pressure stresses, so that viscous contributions to thrust are usually negligible. An exception occurs near the exhaust of a perfect nozzle. Examination of the pressure forces in this region reveals that although they may be large, they are almost radially directed, with very little axial component. In contrast, the skin friction is very nearly axially directed and, since it detracts from thrust, a net negative thrust may exist on this portion of the nozzle.

The third influence of the boundary layer on nozzle performance has to do with shock-boundary layer interactions. Under certain ambient pressure conditions, shocks can occur even within well-designed nozzles. The position and

strength of the shock or shock system depend on boundary layer behavior as well as on free-stream and ambient conditions. We will discuss this phenomenon when we consider the effects of back pressure on nozzle performance.

The discharge coefficient of choked nozzles has been measured quite accurately [13, 14], and from these measurements we can infer the magnitude of the typical displacement thickness of the nozzle throat. Tang and Fenn [13] have shown that for adiabatic flow the experimental discharge coefficients are quite well correlated by

$$C_D = 1 - \left(\frac{\gamma + 1}{2} \right)^{3/4} \left\{ \frac{-2.128}{\gamma + 1} + 3.266 \right\} R^{-1/2} + 0.9428 \frac{(\gamma - 1)(\gamma + 2)}{(\gamma + 1)^{1/2}} R^{-1}, \quad (11.26)$$

in which

$$R = R_e^* \left(\frac{R^*}{R_c} \right)^{1/2}$$

and R_e^* is the nozzle throat Reynolds number, R^* the throat radius, and R_c the radius of curvature of the throat section. Taking $R^* = R_c$ and $\gamma = 1.2$, we find that this formula provides the discharge coefficients shown in Table 11.2. If we write the discharge coefficient as

$$C_D = \frac{\pi(R^* - \delta^*)^2}{(R^*)^2}$$

and look at cases where $\delta^*/R^* \ll 1$, it follows that

$$\frac{\delta^*}{R^*} = \frac{1 - C_D}{2}.$$

For a rocket nozzle with $D^* = 0.2\text{m}$, $u^* = 500\text{ m/s}$, and $\nu = 10^{-5}\text{ m}^2/\text{s}$, the throat Reynolds number would be of order 10^7 , so that from Table 11.2 one would expect δ^*/R^* of order 0.0004, and the effective flow area reduction due to friction

TABLE 11.2 Nozzle discharge coefficients; Tang and Fenn [13] formula, eq. (11.26), with $\gamma = 1.2$, $R_c = R^*$, and $C_D = 1 - 2.4691/R_e^{1/2} + 0.4068/R_e$

R_e^*	C_D	$\frac{\delta^*}{R^*}$
10^8	0.9998	0.0001
10^7	0.9992	0.0004
10^6	0.9975	0.0012
10^5	0.9922	0.0039
10^4	0.9753	0.0124
10^3	0.9223	0.0389

would be only 0.08%. Table 11.2 helps to explain the agreement between measurement and inviscid flow theory shown in Fig. 11.11. In that case the nozzle was only 0.019 m (0.75 in.) in diameter, yet frictional effects apparently had little effect on the nozzle pressure field. In contrast, the effect of the boundary layer on rocket nozzle heat transfer is large (and is discussed in Section 11.4).

The Effect of Back Pressure

Thrust chambers that are called on to operate within the atmosphere may be subject to wide variations in ambient or “back” pressure. Launch vehicles, especially, which operate from sea level to high altitudes, experience large variations in back pressure. Under certain conditions the performance of a thrust chamber designed for one back pressure can be significantly reduced at other back pressures.

So long as the ambient pressure is *less* than the nozzle exhaust pressure, the flow within the nozzle remains undisturbed. That is, the influence of a pressure *decrease* downstream of a supersonic nozzle cannot propagate upstream into the nozzle, since an expansion wave travels only at the local speed of sound. Thus the pressure adjustment occurs beyond the exit plane as a series of expansion waves whose initial influence propagates at the exit Mach angle α_e . Such an *underexpanded nozzle* (so called because the flow has not expanded to ambient pressure within the nozzle) is illustrated in Fig. 11.17(a). The expansion waves reflect from the jet boundary as compression waves that may actually converge to form a shock. The pattern of alternate expansion and compression is repeated downstream, and the associated temperature pattern may, because of varying gas incandescence, render the pressure pattern visible.

A slightly overexpanded ($P_e < P_a$) nozzle might appear as in Fig. 11.17(b), where the required pressure adjustment occurs outside the nozzle through an

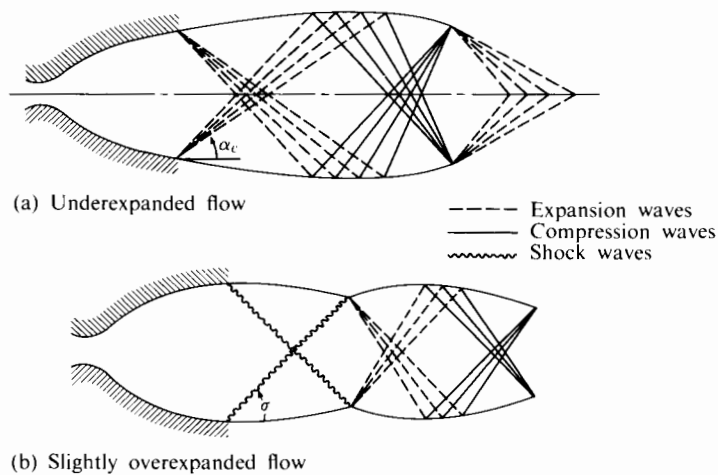


FIGURE 11.17 Exhaust jet behavior at various back pressures.

oblique shock. The shock angle σ is determined by the required pressure ratio, P_a/P_e , and the exhaust Mach number. As P_a increases, the shock angle also increases, since stronger shocks propagate at higher speeds. For sufficiently high P_a/P_e the shock angle σ will approach 90° . For still higher P_a/P_e the shock will enter the nozzle and interact with the wall boundary layer. All of this is possible because a strong shock propagates at supersonic velocity relative to the fluid. Typically the shock is strongly affected by interacting with the nozzle boundary layer. Since a portion of the boundary layer is subsonic, the influence of the shock-induced pressure rise can influence boundary layer behavior upstream of the wall-shock intersection point. The shock can separate the boundary layer and set up a complex flow disturbance within the nozzle, which in turn will greatly affect the shock configuration.

Figure 11.18 provides experimental data on the wall pressure distribution inside a nozzle with high exit plane pressure. This pressure distribution shows that the shock is definitely not plane normal. The shock and boundary layer configuration are indicated in the simplified diagram of Fig. 11.18.

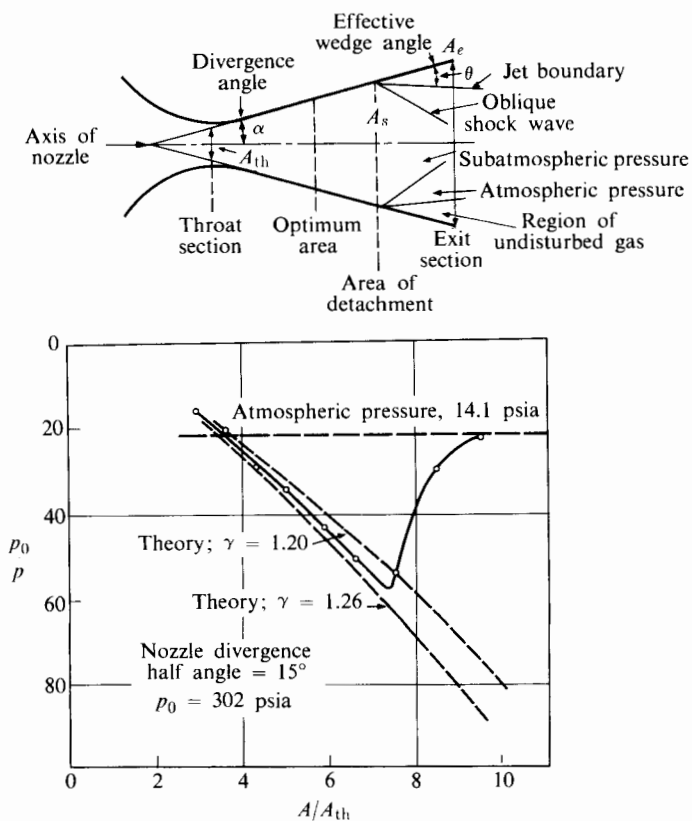


FIGURE 11.18 Effect of shock-boundary layer interaction on the pressure distribution within a nozzle. (Courtesy Altman et al. [15].)

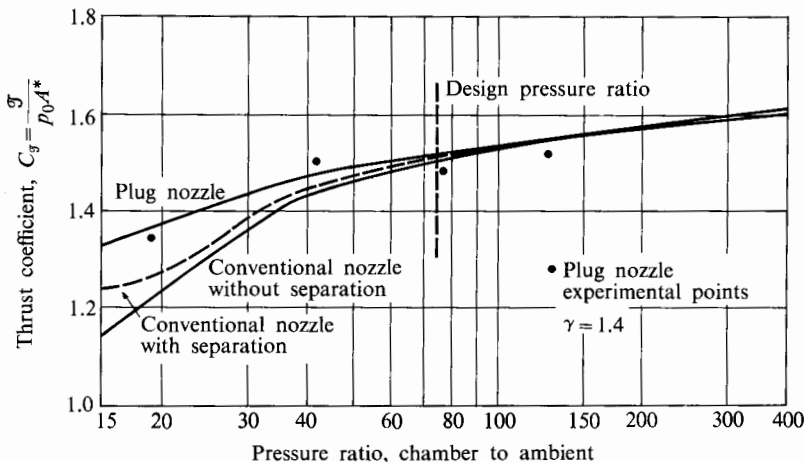


FIGURE 11.19 Off-design thrust coefficients of conventional and plug nozzles. (Courtesy Berman [16].)

A nozzle designed for low-altitude (high p_a) operation will not produce as much thrust at high altitude (low p_a) as a nozzle specifically designed for the higher altitude. As a result, rocket engines for launch vehicles are often designed for an intermediate pressure, with overexpanded sea-level operation and under-expanded high-altitude operation. Figure 11.19 indicates the performance loss of conventional (i.e., internal flow) nozzles associated with off-design back pressures, both with and without separation.

Plug and Expansion-Deflection Nozzles

In an attempt to offset the thrust loss associated with overexpansion, and for several other reasons, designers have developed nozzle shapes other than conventional internal-flow configurations. Plug and expansion-deflection nozzles are shown schematically in Fig. 11.20. Flow from the combustion chamber passes through an annular throat in both configurations. For the plug nozzle the flow expands around a corner at the throat to ambient pressure on one side and along a central body or plug on the other. Expansion-deflection nozzles achieve the same end in an inverse geometry; that is, with the solid boundary surrounding the free-jet boundary.

In both configurations the presence of a free-jet boundary to the expansion process lends a kind of self-adjustment to back-pressure variations. Figure 11.21 indicates the variation of exhaust pattern for a plug nozzle flow with increasing back pressure. The flow expands around the corner to the actual ambient pressure, and thus overexpansion is essentially avoided. Figure 11.19 illustrates how the performance of a plug nozzle exceeds that of a conventional nozzle at high back pressures. The design-point performance of plug nozzles can be as good as that of conventional nozzles. For plug shapes designed by the method of characteristics to give axial exhaust velocity (as in Fig. 11.21), the thrust was measured

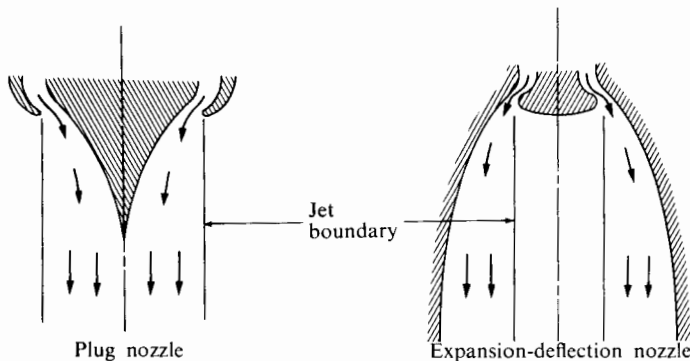
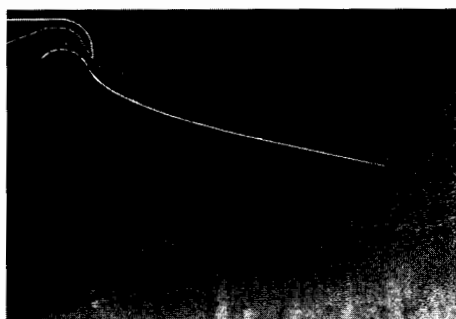


FIGURE 11.20 Schematic cross sections of plug and expansion-deflection nozzles.

to be 98% of the ideal thrust (isentropic flow, axial exhaust velocity, $p_e = p_a$) at a design pressure ratio of 16. However, when the back pressure was increased to obtain a pressure ratio of only 1.5, the thrust was observed to decrease only to 96% of the ideal. The complicated contoured shape may be replaced by a mechanically



(a) At design p_0/p_e



(b) Below design p_0/p_e

FIGURE 11.21 Shadowgraphs of flow around plug nozzle at design back pressure and above design back pressure. (a) $p_0/p_a = 75$; no external flow. (b) $p_0/p_a = 20$; no external flow. (Courtesy Berman [16].)

simpler conical shape without serious performance penalty. With cones of half-angles 30° to 40°, the performance is reduced by about 1% over that of the contoured plug, while the insensitivity to variations in back pressure is retained.

Further advantages of these configurations are as follows: Both types are substantially shorter than comparable internal-flow nozzles. We can see this in Fig. 11.12, where the length required of a plug nozzle in order to produce 99.5% of the vacuum thrust coefficient of an ideal nozzle of the same area ratio is shown. The annular combustion chamber of the plug-nozzle design might be built up of relatively small and easily developed segments. The propellant flow from these segments might be separately controlled in such a way as to produce nonaxial thrust, thus avoiding the necessity of gimbaling the entire engine to achieve thrust vector variations. The combustion chamber of an expansion-deflection nozzle design would be very similar to that for a conventional engine. The main difficulties associated with these configurations arise in the process of adequately cooling the central plug.

The aerospike nozzle shown in Fig. 11.22 is an advanced form of the plug nozzle that has proved very successful under test. Here the central plug is cooled by the discharge of a cooling gas. The flow pattern resulting from this central discharge is shown in schlieren photographs for three levels of back pressure. The sketch in Fig. 11.22 describes features of the flow for discharge into near vacuum. One version of this thruster is called the linear aerospike. It consists of modules that can be assembled in an annular ring for a large rocket booster or used in a linear array, possibly for turborocket propulsion of an aircraft.

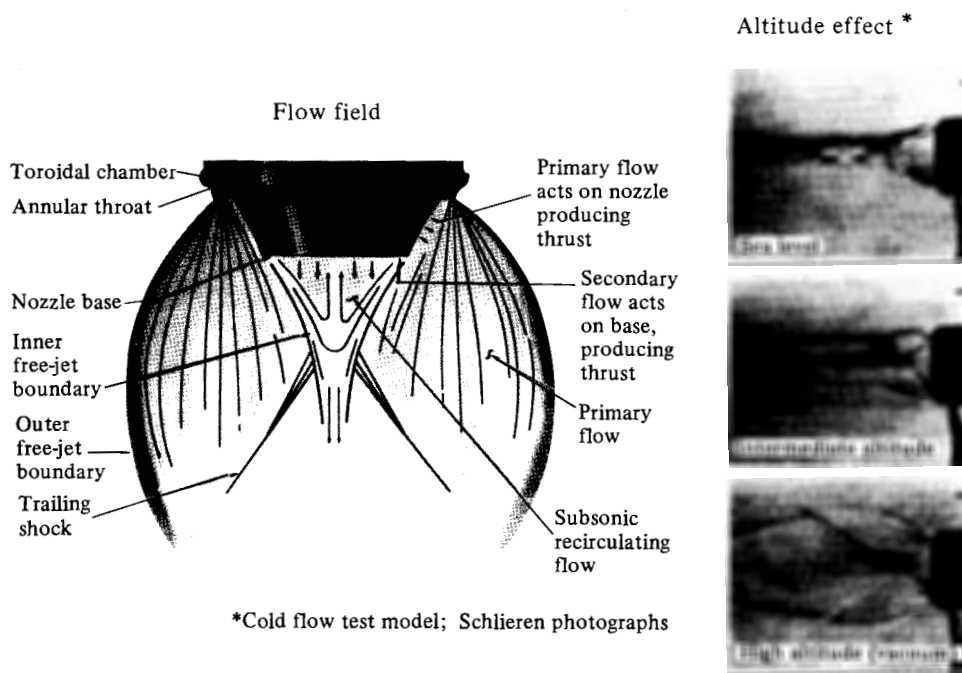


FIGURE 11.22 The aerospike nozzle. (Courtesy Rockwell International, Rocketdyne Division.)

11.4 ROCKET HEAT TRANSFER

Combustion temperatures of rocket propellants typically are higher than the melting points of common metals and alloys and even of many refractory materials. Short of the actual melting point, of course, the strength of most materials declines rapidly at high temperature, as may be seen in Fig. 8.14. Since the thickness (and therefore the mass) of the thrust chamber wall depends strongly on the stresses it can support, it is desirable to use highly stressed materials, and the wall should be cooled to a temperature considerably below its melting point and therefore much below the propellant stagnation temperature. In order to design a suitable cooling system, it is of course necessary to understand nozzle heat transfer phenomena.

We can gain a rough idea of the magnitude of the cooling problem by considering typical heat transfer rates, which are of the order of 10 kW/cm^2 near the throat of a liquid-propellant rocket and even greater in a high-pressure solid-propellant rocket. This is an order of magnitude greater than typical rates in the combustion chamber of a high-performance aircraft engine. Three basic cooling methods are commonly used:

1. For liquid-propellant rockets it is common to use the fuel or oxidizer as a coolant, flowing in tubes or passages in or directly outside the chamber wall. Such a system is called *regenerative cooling*, since heat lost from the hot propellant is added to the incoming propellant. In addition, it is possible to protect the chamber walls to some extent from the high-temperature gases by use of an injection pattern that provides a layer of relatively cool gas near the walls. This *film cooling* can substantially reduce heat transfer to the walls. It is illustrated by the hydrogen-cooled nozzle of Fig. 11.13, in which the film is caused by injection parallel to the walls.
2. For solid-propellant rockets it is common to surround the nozzle walls with a mass of metal or other material that absorbs heat from the hot surface. The time during which such a heat sink can be effective is limited by its heat capacity, the allowable material temperature, and the heat transfer rate.
3. Additional cooling may be attained by the vaporization or sublimation of material from the inner surface of the chamber wall or from the wall itself. The injection of liquids or gases through porous walls is called *sweat cooling*, and the intentional loss of wall material is called *ablation cooling*.

Regenerative Cooling of Liquid-Propellant Rockets

The walls of large regeneratively cooled liquid-propellant rockets usually consist of an array of suitably shaped tubes brazed together to form the thrust chamber. Figure 11.23 shows the nozzle of the Pratt & Whitney RL-10 hydrogen rocket engine used in the *Saturn* vehicle of the *Apollo* mission: One can see the brazed-tube array being supported circumferentially by steel bands. Figure 11.24 shows the cooling system in schematic form. In this engine the initially liquid hydrogen (state ① on the $T-s$ diagram) is heated to a temperature (state ③)



FIGURE 11.23 The Pratt & Whitney Aircraft RL-10 hydrogen-oxygen rocket engine. (Courtesy Pratt & Whitney Aircraft, Division of United Aircraft Corp.)

sufficiently high above the critical temperature that it can be used to expand as a gas through the turbine that drives the liquid hydrogen and oxygen pumps. The pressure of the hydrogen is well above the critical pressure, so no boiling takes place as the fluid is continuously transformed from "liquid" to "gaseous" states. Gaseous hydrogen is a very good coolant, having high specific heat ($C_p = 14.3 \text{ kJ/kg} \cdot \text{K}$ at room temperature versus 1.0 for air) and high thermal conductivity ($k = 0.182 \text{ W/m} \cdot \text{k}$ at 300 K versus 0.026 for air). Thus the cooling system can be designed to absorb high heat flux without danger of hot spots or burnout occurring (even at the nozzle throat, where the heat flux is highest). In such regeneratively cooled nozzles it is common to flatten partially the tubes in the vicinity of the throat to perhaps double the coolant velocity and thus enhance the liquid-side heat transfer coefficient in the throat region.

As Fig. 11.24 shows, the fairly large area ratio (40:1) of the RL-10 nozzle requires a "pass-and-a-half" tube design, in which hydrogen enters alternate tubes partway down the nozzle and flows toward the exit, through a return manifold, and back up to the combustion chamber in alternate tubes. Thus a portion of the nozzle contains twice as many tubes as does the combustion chamber.

Since the RL-10 uses gaseous hydrogen heated in passing through the nozzle and combustion chamber walls, no separate gas generator is needed and all propellants are burned in the main combustion chamber with no loss of specific im-

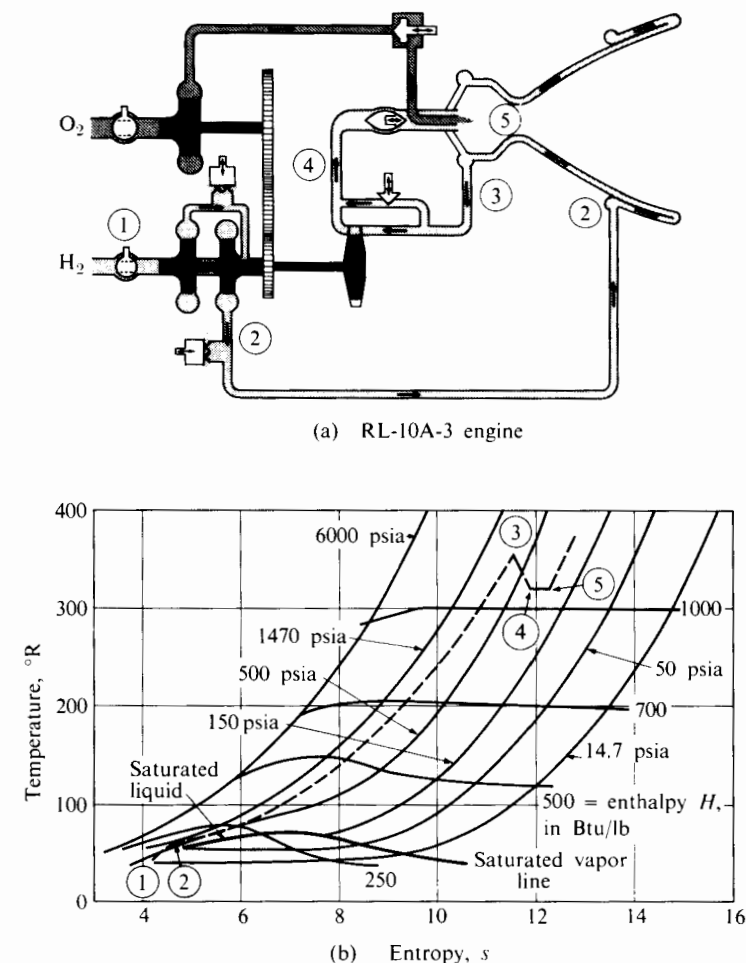


FIGURE 11.24 Schematic of the RL-10A-3 hydrogen-oxygen rocket engine, and typical T - s diagram of the hydrogen flow. (Courtesy Pratt & Whitney Aircraft, Division of United Aircraft Corp.)

pulse. The system is capable of self-starting in space from the pressure available in the hydrogen tank and the residual thermal energy in the thrust chamber. The gear train that drives the liquid-oxygen pump is cooled with gaseous hydrogen and run dry to avoid low-temperature problems that would accompany more conventional lubrication systems. The very low turbine-inlet temperature minimizes turbine stress problems and at the same time greatly reduces the problem of heat transfer between turbine and pump. Hence a relatively compact turbopump results; we refer to this system again in Chapter 13.

We now turn to the question of how one can estimate heat fluxes and wall temperatures with regenerative cooling of liquid-propellant rockets.

Convective Heat Transfer

The first task in providing thermal protection is to estimate the convective and radiative heat transfer rates from hot gases to chamber and nozzle walls. We take these up in turn and begin with the remark that convective heat transfer is a boundary layer problem and that, for a mixture of combustion gases flowing over a hot wall, the thickness of the velocity and temperature boundary layers are (as mentioned in Chapter 4) of the same order of magnitude. Thus before reviewing heat transfer rates, it is in order to think about the character of boundary layer growth on rocket nozzle walls.

In rapidly accelerating flows the Moses integral method (Chapter 4) or integral methods [17] that take compressibility into account can be used to show that the boundary layer thickness may decrease in the flow direction, reaching a minimum at the throat of the nozzle. This effect is demonstrated in Fig. 11.25 by the approximate calculation of Bartz [18], who used an integral method. He estimated the shear stress on the wall with a flat plate skin friction formula similar to Eq. (4.19) and used a one-seventh-power low-boundary-layer profile (i.e., $u/U = [y/\delta]^{1/7}$).

One would not expect Fig. 11.25 to represent an accurate portrayal of boundary layer growth, but various approximate calculation procedures agree on these features:

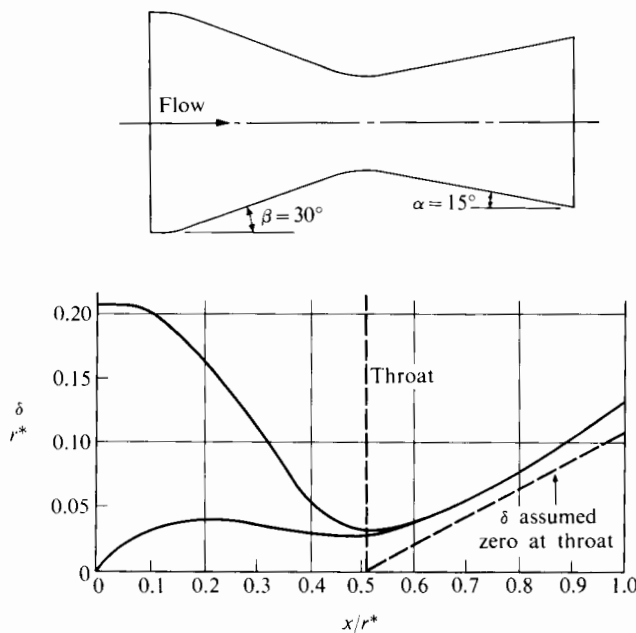


FIGURE 11.25 Typical calculated boundary layer development in a rocket nozzle; r^* = nozzle throat radius. (Courtesy Bartz [18].)

1. The boundary layer thickness δ at the throat is not strongly dependent on the boundary layer thickness at entrance to the nozzle, nor is it strongly dependent on the rate of nozzle convergence.
2. The value of δ tends to be a minimum near the throat; this warns us to expect a maximum convective heat transfer rate at the throat.
3. The rate of boundary layer growth downstream of the throat tends to be independent of the value of δ at the throat.

The rate of convective heat transfer from combustion gases to thrust chamber walls is difficult to calculate accurately, because the boundary layer is strongly affected by wall curvature, axial pressure gradient, and the normal temperature gradients associated with high-intensity heat flux. However, we will see that semiempirical methods can provide useful estimations of heat transfer rates, even under these conditions—for which not many experimental data are available.

In its simplest form regenerative cooling consists of the steady flow of heat from a hot gas through a solid wall to a cool liquid. Although the actual configuration may be a series of tubes or coolant channels, as in Fig. 11.26(a), one can study the essential features of regenerative cooling within a rocket without geometric complications by considering a one-dimensional model, as in Fig. 11.26(b). For the moment we ignore the heat transfer through the walls that separate the coolant passages (Fig. 11.26a). The convective heat transfer at the solid–fluid interfaces may be described by a *film coefficient*, as discussed in Chapter 4. For the hot-gas side, this is often written

$$\dot{Q}_c = h_g(T_{wa} - T_{wh}), \quad (11.27)$$

where \dot{Q}_c = convective heat transfer rate per unit area,

h_g = hot-gas film coefficient (defined by Eq. 11.27),

T_{wa} = adiabatic wall temperature,

T_{wh} = hot side-wall temperature.

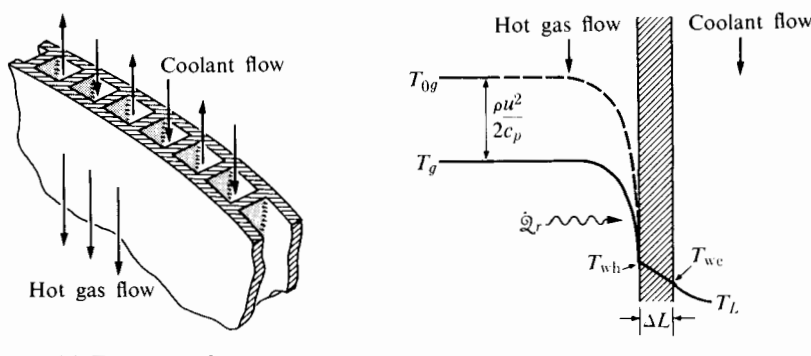


FIGURE 11.26 Regenerative cooling definitions.

The *adiabatic wall temperature* (or recovery temperature) T_{wa} is, as Eq. (11.27) shows, the temperature that would be attained by the surface of an adiabatic or insulating wall ($\dot{Q}_c = 0$). One might expect that T_{wa} would be the stagnation temperature of the fluid, since the fluid adjacent to the wall has been brought to rest. However, especially for high-speed flow as encountered in rocket nozzles, the temperature rise accompanying stagnation is large enough that the viscous slowing-down process is not exactly adiabatic. That is, there is significant heat transfer from the low-speed (high static temperature T_g) fluid near the wall to the higher-speed (lower T_g) fluid farther from the wall. Hence the stagnation temperature of the fluid at the wall is *less* than that of the free stream, as shown schematically in Fig. 11.27. On the other hand, to satisfy the steady-flow energy equation, there must be a region in which the stagnation temperature is slightly greater than that in the free stream. The magnitude of T_{wa} may be related to T_{0g} and T_g by the *recovery factor*, r , which is defined by

$$r = \frac{T_{wa} - T_g}{T_{0g} - T_g}. \quad (11.28)$$

For compressible turbulent boundary layers up to Mach numbers of 4, the recovery factor is about 0.91 for typical rocket propellants [1].

Near the nozzle throat, where the maximum heat transfer rate occurs (as we will show), the difference between T_{wa} and T_{0g} is rather small. For instance, if γ is 1.2,

$$\frac{T^*}{T_0} = \frac{2}{\gamma + 1} = 0.91,$$

and if $T_{0g} = 3330$ K, $T_g^* = 3030$, and for $r = 0.91$, $T_{wa} = 3305$. This difference of only about 1% is well within the uncertainty of heat transfer calculations and, since the throat region presents the most severe cooling requirements, T_{wa} is often replaced by T_{0g} for rocket heat transfer calculations. That is, Eq. (11.27) is often written simply as

$$\dot{Q}_c = h_g(T_{0g} - T_{wh})$$

with little loss of accuracy.

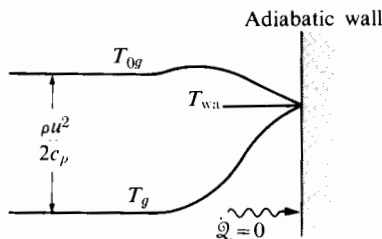


FIGURE 11.27 The adiabatic wall or recovery temperature.

One-dimensional heat transfer through the solid wall is described by

$$\dot{\mathcal{Q}}_w = -k_w \frac{dT_w}{dx} = \frac{k_w}{\Delta L} (T_{wh} - T_{wc}), \quad (11.29)$$

where k_w = thermal conductivity of the wall material, ΔL = wall thickness, and T_{wc} = cold-surface wall temperature.

The conductivity of the liquid-side film is described by an additional film coefficient h_L defined by

$$\dot{\mathcal{Q}}_L = h_L (T_{wc} - T_L), \quad (11.30)$$

where T_L = liquid free-stream temperature ($T_L \cong T_{0L}$ for an incompressible fluid), and $\dot{\mathcal{Q}}_L$ is the heat transfer from the wall to the liquid film.

For steady conditions the heat flow from the hot gas (including radiation heat transfer $\dot{\mathcal{Q}}_r$) may be written

$$\dot{\mathcal{Q}} = \dot{\mathcal{Q}}_c + \dot{\mathcal{Q}}_r = \dot{\mathcal{Q}}_w = \dot{\mathcal{Q}}_L. \quad (11.31)$$

The (usually small) radiant heat transfer rate $\dot{\mathcal{Q}}_r$ to the hot wall surface will be discussed subsequently. We can combine Eqs. (11.27), (11.29), and (11.30) with Eq. (11.31) to give

$$\dot{\mathcal{Q}} = \frac{T_{wa} - T_L + (\dot{\mathcal{Q}}_r/h_g)}{(1/h_g) + (\Delta L/k_w) + (1/h_L)} \approx \frac{T_{0g} - T_L + (\dot{\mathcal{Q}}_r/h_g)}{(1/h_g) + (\Delta L/k_w) + (1/h_L)}. \quad (11.32)$$

Equation (11.28) may be used to express T_{wa} more accurately in terms of T_{0g} , T_g , and r , but the assumption $T_{0g} \cong T_{wa}$ is adequate near the throat. Having determined $\dot{\mathcal{Q}}$, we may use the previous equations to calculate the local temperatures. The hot-wall temperature is, of course, of great interest:

$$T_{wh} = T_{wa} - \frac{\dot{\mathcal{Q}}_c}{h_g} = T_{wa} - \frac{\dot{\mathcal{Q}} - \dot{\mathcal{Q}}_r}{h_g} \approx T_{0g} - \frac{\dot{\mathcal{Q}} - \dot{\mathcal{Q}}_r}{h_g}.$$

One may modify this one-dimensional model to account for the actual geometry of the coolant system. The most common configuration consists of an array of rectangular (or truncated pie-shaped) thin-walled tubes welded or brazed together as in Fig. 11.26. The thin walls extend into the coolant passages much as cooling fins and, as such, they significantly decrease the coolant side heat-flow resistance. A simple modification to account for this would be to define "effective" wall and liquid-side areas that are larger than the actual areas. Equation (11.31) would then be written

$$\dot{\mathcal{Q}} A_g = (\dot{\mathcal{Q}}_c + \dot{\mathcal{Q}}_r) A_g = \dot{\mathcal{Q}}_w A_w = \dot{\mathcal{Q}}_L A_L,$$

where A_g = gas-side area, A_w = effective wall area, and A_L = effective liquid-side area. Equation (11.32) would become

$$\dot{\mathcal{Q}} = \frac{T_{wa} - T_L + (\dot{\mathcal{Q}}_r/h_g)}{(1/h_g) + (A_g \Delta L / A_w k_w) + (A_g / A_L h_L)}. \quad (11.33)$$

A more detailed analysis would include the essentially two-dimensional heat transfer pattern. That is, the gas-side wall temperature would not be uniform, being lower near the "cooling fins" or tube corners and reaching a maximum at the tube center plane. Sellers [19] presents an analysis for this situation and defines a fin factor f as

$$f = \frac{T_{w\text{hm}} - T_L}{(T_{w\text{h}} - T_L)_{\text{one-dimensional}}} \quad \text{at constant } \dot{Q}, \quad (11.34)$$

where

$T_{w\text{hm}}$ = maximum (center plane) hot-wall temperature,

and

$(T_{w\text{h}} - T_L)_{\text{one-dimensional}}$ = one-dimensional wall temperature drop

as in Eq. (11.33).

Figure 11.28 shows typical results for rectangular tubes of constant wall thickness, assuming \dot{Q} distributed evenly over the hot wall surface. This assumption and the comparison, in Eq. (11.34) of one- and two-dimensional temperatures for the same \dot{Q} is reasonable for $T_{0g} >> T_{w\text{h}}$. Note that $T_{w\text{hm}}$ can be substantially less than the one-dimensional result, $T_{w\text{h}}$.

As suggested in Chapter 4, our most important source of experimental knowledge on turbulent shear stress and heat transfer comes from fully developed flow in long tubes. This information is directly useful for estimating the convective heat transfer coefficient h_L for long liquid-filled channels used in cooling thrust chamber walls. The liquid-side film coefficient in the cooling tubes of a

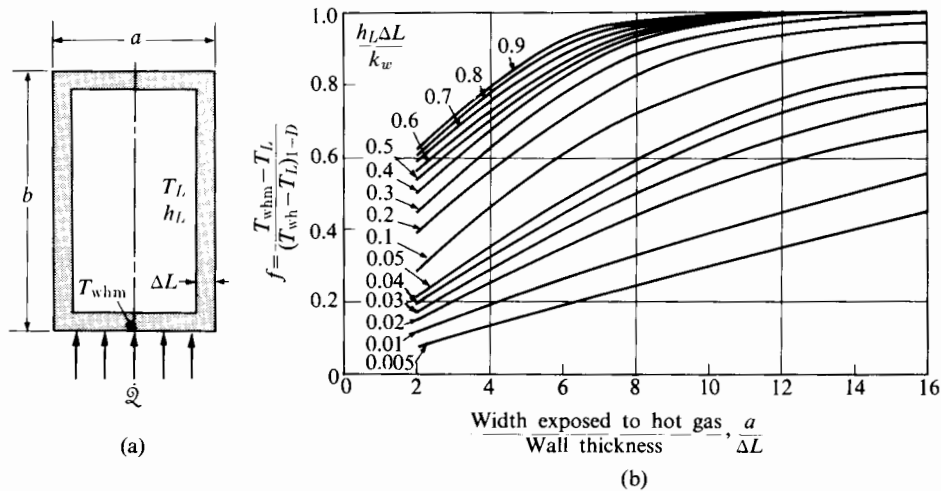


FIGURE 11.28 Comparison of one- and two-dimensional heat transfer. The influence of b is small so long as $b/a > 1$. (Courtesy Sellers [19].)

regeneratively cooled rocket can be reasonably predicted by an equation of form equivalent to Eq. (4.41):

$$\frac{h_L}{Gc_p} = 0.023 \left(\frac{GD}{\mu_b} \right)^{-0.2} \left(\frac{\mu c_p}{k} \right)_b^{-0.67}, \quad (11.35)$$

where D is the tube diameter, G is the average mass flow per unit area ($4\dot{m}/\pi D^2$ or $\bar{\rho}\bar{u}$). The subscript b denotes fluid properties evaluated at the bulk mean temperature. For non-circular tubes D is the hydraulic diameter (4 times the tube flow area divided by its internal circumference).

Bartz [20] has shown that this kind of correlation can also be used for an approximate estimate of the gas-side heat transfer coefficient h_g . Although nozzles are not of constant diameter and the propellant flow is not fully developed, this relation appears to be a reasonably good approximation of the actual nozzle heat transfer, if D is the local nozzle diameter, so that we may write

$$\frac{h_g}{Gc_p} = 0.023 \left(\frac{GD}{\mu_b} \right)^{-0.2} \left(\frac{\mu c_p}{k} \right)_b^{-0.67}. \quad (11.36)$$

Although this equation may not always provide suitable accuracy as to magnitude, it does correctly predict the trends of the variation of h_g with nozzle diameter and pressure. Since G is $4\dot{m}/\pi D^2$, and \dot{m} is constant for a given nozzle, we can see from the above that

$$h_g \propto \frac{1}{D^{1.8}},$$

so that the most severe cooling requirements for a given rocket and propellant occur at the throat, where D is a minimum. Experimentally, the maximum heat transfer rate is observed slightly upstream of the throat.

Second, if G is written as ρu , we can see that since the gas temperature is rather insensitive to pressure for most propellants, and μ , c_p , and k vary primarily with temperature, not pressure, then

$$h_g \propto \rho^{0.8} \propto p_0^{0.8}.$$

Thus cooling problems increase rather rapidly with increasing chamber pressure (although researchers experimentally observe that the exponent is not precisely 0.8).

Empirically determined refinements of this equation are suggested in Reference 15. In the combustion chamber (especially near the nozzle end) and at the throat the equation is inadequate as it stands except, perhaps, for a refinement in the determination of fluid properties at the throat. In the supersonic portion of the nozzle an alternative form has been suggested:

$$\frac{h_g L}{k} = a \left(\frac{GL}{\mu} \right)^{0.8} \left(\frac{\mu c_p}{k} \right)^{0.33}, \quad (11.37)$$

where L is the distance downstream of the throat and a varies from 0.025 to 0.028.

Since the gas properties ρ , c_p , μ , and k vary with temperature, and since large temperature variations occur across high-velocity, high-heat-flux boundary layers, it is necessary to specify a temperature at which one should evaluate these properties. In these correlations a so-called film temperature T_f is used. In the combustion chamber or at the throat, the film temperature may be defined as the arithmetic mean temperature

$$T_f = \frac{T_g + T_{wh}}{2}.$$

Reference 15 suggests, for the supersonic portions of the flow and perhaps at the throat, an empirical formula,

$$T_f = T_{wh} + 0.23(T_g - T_{wh}) + 0.19(T_{wa} - T_{wh}).$$

Near the throat the difference between these two methods of specifying T_f is slight, and the fluid properties are usually not precisely known anyway. Furthermore, the wall temperature, T_{wh} , may not be known with precision.

Bartz [18] has developed an equation that can be shown to be almost equivalent in form to Eq. (11.28). According to Bartz,

$$h_g = \left[\frac{0.026}{(D^*)^{0.2}} \left(\frac{\mu^{0.2} c_p}{Pr^{0.6}} \right)_0 \left(\frac{p_0}{c^*} \right)^{0.8} \left(\frac{D^*}{r_c} \right)^{0.1} \right] \left(\frac{A^*}{A} \right)^{0.9} \sigma, \quad (11.38)$$

in which the subscript 0 signifies stagnation conditions and

$$Pr = \frac{\mu c_p}{k}, \text{ the Prandtl number,}$$

$$c^* = \frac{p_0 A^*}{\dot{m}}, \text{ the characteristic velocity,}$$

D^* = throat diameter,

r_c = throat radius of curvature in a plane that contains the nozzle axis,

$$\sigma = \frac{1}{\left[\frac{1}{2} \frac{T_{wh}}{T_{0g}} \left(1 + \frac{\gamma - 1}{2} M^2 \right) + \frac{1}{2} \right]^{0.8-0.2\omega} \left(1 + \frac{\gamma - 1}{2} M^2 \right)^{0.2\omega}},$$

in which M = local Mach number, and ω = exponent of the viscosity-temperature relation $\mu \propto T^\omega$ ($\omega = 0.6$ for diatomic gases).

An advantage of this unusual grouping of terms is the fact that the term in square brackets in Eq. (11.38) is a constant, since all fluid properties are evaluated at the stagnation temperature. There is reasonably good agreement between Eq. (11.38) and experiment, as indicated in Fig. 11.29.

We can see that the peak heat flux occurs near the throat. The deviation between predicted and measured heat flux in this region appears to be dependent on combustion pressure. It was observed that for variations of Reynolds number at a given nozzle position, due to variations of combustion pressure, the Nusselt

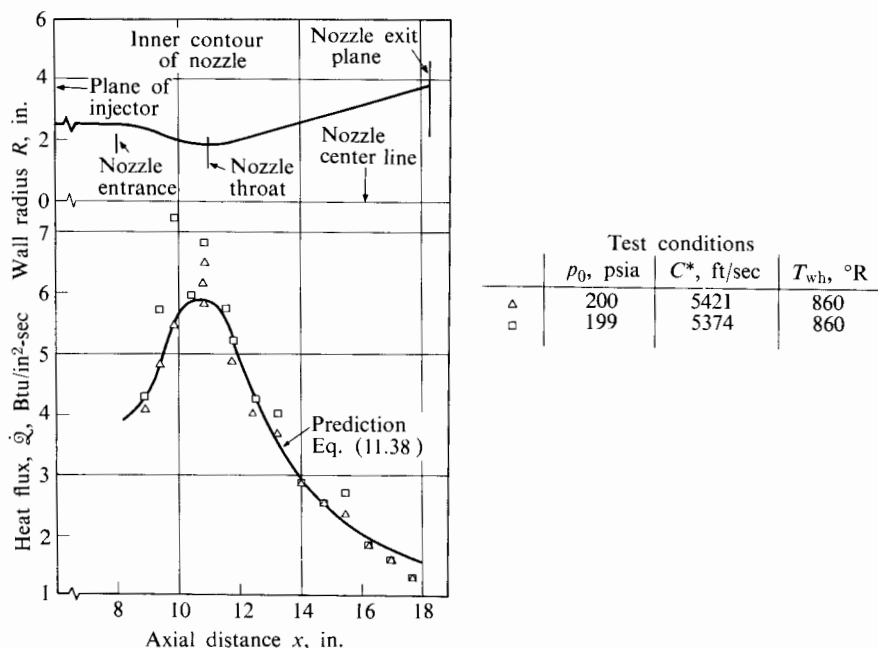


FIGURE 11.29 Experimental heat flux compared with Eq. (14.17) for a nitrogen tetroxide (N_2O_4) and hydrazine (N_2H_4) rocket. (Courtesy California Institute of Technology Jet Propulsion Laboratory [21].)

number did not vary with $Re^{0.8}$ as predicted. Hence the complete validity of equations of this type is not certain, and one should not rely on them for the design of radically different nozzle types.

Bartz [20] has also developed a turbulent boundary layer method of calculating rocket nozzle heat transfer that is in fair agreement with data [21] at Reynolds numbers typical of large high-pressure thrust chambers. At low Reynolds number, and especially in the presence of a strongly negative streamwise pressure gradient, there is a tendency for turbulent kinetic energy to decay and for the boundary layer to revert to laminar flow. This tendency is somewhat enhanced by flow over the high-curvature surface around the throat.

Radiative Heat Transfer

A combination of complex geometric considerations and radiation, absorption, and reflection mechanisms makes the calculation of radiative heat transfer from the hot propellant to the thrust chamber walls a complicated task. Radiation from a comparatively transparent hot gas may reach a particular point on the chamber wall from any point in the gas volume. In the typically nonuniform conditions within a combustion chamber, energy radiated from one location within the gas may be effectively absorbed by another portion of the gas before reaching

the walls. Also gases, unlike solid radiators, do not radiate over a continuous spectrum of wavelengths but rather over discrete intervals or "bands." Furthermore, if some of the bands of the different gases possess common wavelengths, the total energy radiated from a mixture of radiating gases is not the simple sum of radiations from the gases considered separately. The important radiating gases from common propellants, in approximate descending order of emissive powers, are CO₂, H₂O, CO, NO, OH, and HF. These gases display considerable overlapping of bands.

Consider the radiation to an element of area dA in the wall of a thrust chamber, as shown in Fig. 11.30. The energy reaching dA from within the solid angle $d\phi$ would be the integral over the "beam length" l of the energy emitted toward dA from the volume elements $x dx d\phi$ (assuming it is not absorbed in the intervening gas). The energy radiated per unit volume is proportional to the concentration (or partial pressure) of the radiating material and represents a summation over the important radiating materials and the appropriate wavelengths (with corrections for overlapping band effects). The total energy reaching dA is the integral over the entire solid angle "visible" from dA but evaluation of the integral, making full allowance for the nonuniform gas properties and the actual geometry, would be difficult. For simplicity, one usually assumes that the gas is uniform throughout the volume. The actual geometry may be replaced by an "equivalent" hemisphere, with dA as the center, if one chooses an appropriate radius. The appropriate radius for an element on the wall of an infinite cylinder of diameter D is $0.9D$ (Ref. 15 of Chapter 4), and this value is often used for calculations within combustion chambers [15]. Defining the emissivity ϵ_g of the volume of gas visible from dA to include all the geometric and radiative complexities, we may write the total radiant energy per unit area reaching dA as

$$\dot{Q}_r = \epsilon_g \sigma T_g^4, \quad (11.39)$$

where $\sigma = \text{the Stefan-Boltzmann constant} = 5.6697 \times 10^{-8} \text{ W/m}^2 \cdot \text{K}^4$. The energy radiated from dA is also a complex function of the gas properties, since the gases absorb radiation as they radiate it, over discrete wavelength bands rather than over a complete spectrum. However, since $T_{wh} \ll T_g$, the wall is usually assumed to absorb all incident radiation (i.e., it absorbs as a blackbody) while reradiating negligible energy. Hence Eq. (11.39) approximately represents the net radiant heat flux to the wall.

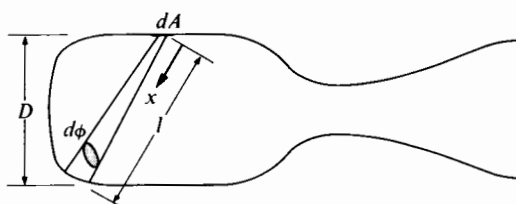


FIGURE 11.30 Radiative heat transfer to thrust chamber wall.

If the gases contain solid or liquid particles (as, for example, soot from excess fuel), an appreciable portion of the radiant energy may originate from the particles. The particles radiate over a continuous spectrum of wavelengths just as solids do. For a high concentration of particles or for large beam lengths, the radiating volume may behave much as a blackbody; that is, ϵ_g may approach unity.

In the absence of complete calculations (for which data are often lacking), Sutton [22] suggests that for temperatures ranging from 2200 to 4100 K (3500° to 7000°F), radiation accounts for 5% to 35% of the total heat transfer.

Solid-Propellant Rockets

A solid-propellant rocket casing is primarily a pressure vessel that must be provided with suitable ports for nozzles, igniters, and so on. Its walls must withstand high pressure and be protected briefly from the hot combustion products (or use materials that retain reasonable strength at very high temperatures). Figure 11.31 shows the location of the solid propellant within the chamber. Burning takes place in the cylindrical inner hole of the propellant as well as at the flat end face. The solid propellant is bonded to the outer chamber; with this arrangement much of the combustion chamber wall is shielded from the hot gas for much of the burning period. As Fig. 11.31 shows, insulating material is provided between the solid propellant and the nozzle throat.

The absence of a liquid cooling medium makes the design of a solid-propellant rocket nozzle difficult. Since the wall heating rate varies considerably throughout a given nozzle (reaching a maximum near the throat), many nozzles are composite structures, as Fig. 11.31 indicates. In this way the best material is used only in the throat region, whereas other materials—which may be lighter, cheaper, or easier to form—are sufficient in other regions. Figure 11.31 is typical of concepts for high-performance solid-propellant rockets, while simpler structures would be adequate for operation at lower temperatures and pressures. This composite construction has been called a “modified” hot structure, because the lining material tolerates a temperature near that of the propellant but is cooled somewhat by a backup or heat-sink material. Figure 11.31 shows a high-strength outer shell

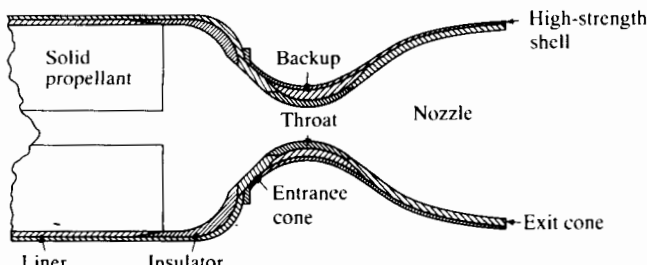


FIGURE 11.31 Schematic diagram of an advanced solid-propellant nozzle. (Courtesy Kelble and Bernados [23].)

that remains at relatively low temperature and carries most of the stress in the nozzle wall.

With careful design and manufacturing, solid rocket casings of high-strength steel or titanium can withstand stresses well above 1350 MPa (200,000 psia). Since the important quantity is the strength-to-mass ratio, titanium has an advantage over steel in that its density is 35% less. Casings wound with glass filaments have been stressed to values for which the strength-to-density ratio is several times that of steel.

Heat Sinks

We can appreciate the need for a heat sink for a solid-propellant rocket nozzle by doing a simple calculation for a nozzle wall suddenly exposed to a heat flux \dot{Q} of 10 kW/cm² (at the throat of the nozzle). We consider this heat flux to be plane normal to a wall that is of thickness L and is not appreciably cooled on its outer surface. The rate at which the mean temperature T_m of the wall increases is given by

$$dT_m/dt = \dot{Q}/(\rho c L),$$

in which ρ is the density of the wall material and c is the specific heat. From this equation we could estimate the time for the mean wall temperature to increase 1000 K under such a heat flux. This time would be

$$t = \Delta T(\rho c L)/\dot{Q} = \Delta T k L / (\dot{Q} \alpha),$$

in which k is the thermal conductivity of the wall material and $\alpha = k/(\rho c)$ is the so-called thermal diffusivity. Handbooks provide us with the typical values of k and α shown in Table 11.3.

From Table 11.3 we could take, for high-temperature steels, representative values of k equal to 25 W/m · K and of α equal to 10⁻⁵ m²/s. Taking the wall thickness as 6 mm and the temperature rise as 2000 K, we calculate from the above formula a heating time of only 0.15 s. The formula is highly approximate because it neglects the fact that the heat flux will decrease as the temperature of the nozzle wall increases; but even taking this into account, we find that the calculated heating time would still be much less than 1 s. It is important to note that the temperature of the inner surface of the nozzle wall may increase much more rapidly than the mean temperature. This rough calculation then warns us that the time for an unprotected solid wall to reach a dangerously high temperature may be as low as 0.1 s; the burning period may be 2000 times as long as this—hence the need to provide a heat sink that can shield the wall for some minutes.

In deciding how this could be done, we think about how long it would take a thermal wave to penetrate a solid protective wall of suitable material located inside the stress-bearing walls of the nozzle. As a heat sink material, graphite has the great advantage of high sublimation temperature (and high strength at high temperature). Although not particularly strong at low temperature, it increases in strength as its temperature rises—to a maximum at about 2250 K (4500°F). It is

TABLE 11.3 Thermal conductivity and diffusivity of solid materials

Material	α (m ² /s)	k (W/m · K)
1% C steel		
20°C	1.17×10^{-5}	43
600°C		35
1000°C		29
20% Ni steel		
20°C	0.53×10^{-5}	19
5% Cr steel		
20°C	0.64×10^{-5}	22
600°C		24
1000°C		29
Cu		
20°C	11.23×10^{-5}	386
600°C		353
C (amorphous graphite ^a)		
0°C		0.015
100°C		0.018
C (pyrolytic graphite, ^a parallel to layer planes)		
0°C		21.3
100°C		15.1
C (pyrolytic graphite, ^a perpendicular to layer planes)		
0°C		0.064
100°C		0.044

^a The specific heat of graphite is about 0.715 J/g · K, and its density is reported in the range 2.30 to 2.72 g/cm³.

available in various forms, two of which are mentioned in Table 11.3. Pyrolytic graphite, formed by a vapor deposition process, consists largely of well-aligned crystals. As Table 11.3 shows, it is highly nonisotropic. It could be applied to a nozzle wall in such a way that it acts as an insulator in the radial direction, though its high coefficient of thermal expansion makes it susceptible to failure in the presence of large temperature gradients. Amorphous graphite has exceptionally low thermal conductivity. Tungsten, with a melting temperature of 3680 K, and various tungsten alloys and sintered tungsten have also been used as throat inserts in solid-propellant rocket nozzles.

With such materials in mind, we focus here on an approximate estimate of the time required for a thermal wave to propagate across a solid wall. For simplicity we consider a wall that is thin relative to its radius of curvature and that might be represented as the flat wall shown in Fig. 11.32.

If the wall material is isotropic and the heat flux one-dimensional in the x -direction, we can readily show that the transient conduction process is governed by

$$\frac{\partial^2 T}{\partial x^2} = \frac{1}{\alpha} \frac{\partial T}{\partial t}, \quad (11.40)$$

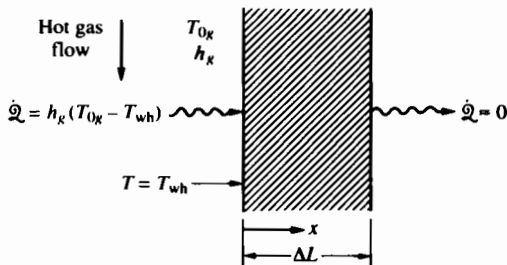


FIGURE 11.32 One-dimensional heat sink cooling model.

where $T(x, t)$ is the wall temperature; $\alpha = k/\rho c_p$ is the thermal diffusivity of the solid; and k, ρ, c_p are the thermal conductivity, density, and specific heat, respectively of the solid.

At the hot face of the wall, we could express the boundary condition as

$$\dot{Q} = h_g(T_{0g} - T) = k(dT/dx), \quad (11.41)$$

in which T_{0g} is the hot-gas stagnation temperature, h_g is the convective heat transfer coefficient, and dT/dk is the temperature gradient just inside the wall. For this approximate calculation we ignore the radiative heat flux and estimate h_g from experimental knowledge that \dot{Q} can be as high as 10 kW/cm^2 with a temperature difference of the order of 2000 K. Thus we could give h_g a value of $\dot{Q}/(T_g - T)$ of $50,000 \text{ W/m}^2 \cdot \text{K}$.

We could also establish a boundary condition at the cold surface of the wall and proceed to discuss the solution of Eq. (11.40) that satisfies the two boundary conditions. Because this particular solution is rather complicated mathematically, and because we are primarily interested in cases in which the thermal wave has hardly reached the cool wall, it is appropriate here to think about the propagation of a thermal wave into a semi-infinite wall. For this, and for the boundary condition that Eq. (11.41) specifies, the solution of Eq. (11.40) is given in various heat transfer textbooks as

$$\frac{T - T_i}{T_{0g} - T_i} = 1 - \operatorname{erf}\left(\frac{x}{2\sqrt{\alpha t}}\right) - \left[\exp\left(\frac{h_g x}{k} + \frac{h_g^2 \alpha t}{k^2}\right) \right] \left[1 - \operatorname{erf}\left(\frac{x}{2\sqrt{\alpha t}} + h_g \frac{\sqrt{\alpha t}}{k}\right) \right], \quad (11.42)$$

in which T_i is the initial wall temperature. The error function that appears in this equation is defined by

$$\operatorname{erf}(y) = 2/\sqrt{\pi} \int_0^y e^{-z^2} dz,$$

whose numerical values are given in standard mathematical tables. In particular, $\operatorname{erf}(0) = 0$, $\operatorname{erf}(1) = 0.84278$, and $\operatorname{erf}(\infty) = 1$.

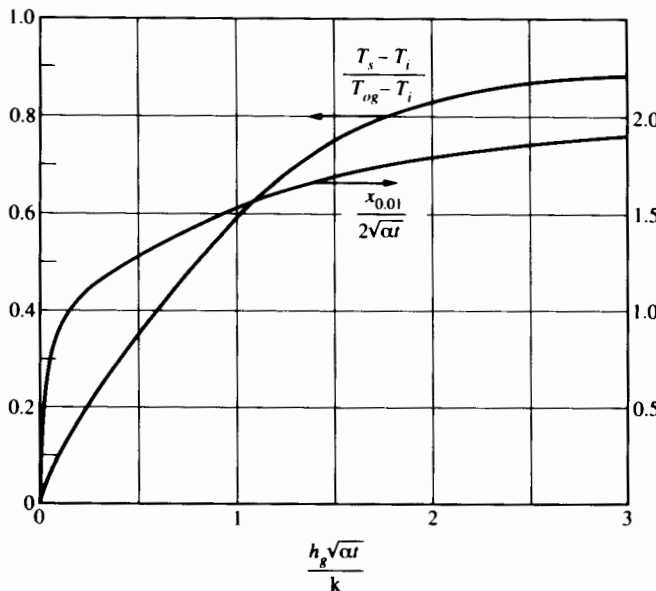


FIGURE 11.33 Transient conduction through a semi-infinite wall; $x_{0.01}$ is the thermal wave penetration distance for $(T_s - T_i)/(T_{0g} - T_i) = 0.01$.

Figure 11.33 shows two of the implications of Eq. (11.42). One curve shows how the surface temperature T_s varies with time t for given values of h , k , and α . We see that for the increase in the hot-surface temperature to be about 60% of the difference between the gas stagnation temperature and the solid initial temperature,

$$\frac{h_g \sqrt{\alpha t}}{k} = 1 \quad \text{or} \quad t = k^2 / (h_g^2 \alpha). \quad (11.43)$$

Figure 11.33 also shows the thermal wave penetration distance $x_{0.01}$ as a function of time; we define this as the distance from the hot surface for which

$$\frac{T - T_i}{T_{0g} - T_i} = 0.01.$$

Keeping in mind graphite and the properties mentioned in Table 11.3, as well as the large h_g value estimated above, we consider the example conditions

$$h_g = 50,000 \text{ W/m}^2 \cdot \text{K},$$

$$k = 0.02 \text{ W/m} \cdot \text{K}.$$

With this value of k , with $\rho = 2,500,000 \text{ g/m}^3$, and with the specific heat as $0.715 \text{ J/g} \cdot \text{K}$, we obtain

$$\alpha = k / (\rho c_p) = 1.1 \times 10^{-8} \text{ m}^2/\text{s}$$

and observe that this diffusivity is three orders of magnitude lower than for the steels mentioned in Table 11.3. Using these values in Eq. (11.43) gives a time of only $15 \mu\text{s}$, so we see that the surface temperature of a heat sink material with very low diffusivity very quickly rises toward the combustion gas stagnation temperature. Thus one should ideally select the material with a melting temperature above the combustion temperature.

As a measure of how thick the heat sink material must be to give adequate protection to the stress-bearing wall of the nozzle, we could use the “1% temperature-rise” penetration distance given in Fig. 11.33 for the semi-infinite wall. We see from the figure that, for times that are long compared with the time for the hot-surface temperature to rise, the dimensionless penetration distance approaches 2, so that

$$x_{0.01} \rightarrow 4\sqrt{\alpha t}.$$

For a burning time of 5 min and with heat sink diffusivity of 10^{-8} , this thickness is only 7 mm; with the diffusivity 10 times as large, it would be 20 mm—not excessively large for a nozzle of diameter 300 mm.

Thus with suitable materials heat-sink shielding can protect nozzle walls from intense heat flux for quite a few minutes.

11.5 LIQUID-PROPELLANT ROCKET PERFORMANCE DATA

Table 11.4 provides engine characteristics and test performance data for three hydrogen-oxygen rockets. The RL-10 (used in *Apollo*) has been described in Figs. 11.26 and 11.27. The space shuttle main engine (SSME) was designed for shuttle operation over a life span of 55 missions and a total burning time of $7\frac{1}{2}$ hours. The engine can be throttled from 109% to 65% of rated thrust. The combustion chamber and turbomachinery for the space shuttle main engine are briefly described in Chapter 13. The engine denoted HM60 in Table 11.4 has been built as the main engine for European space transportation systems (launch to low earth orbit, LEO, or geosynchronous earth orbit, GEO) and is described by Pouliquen [24].

Note from Table 11.4 that though the engines range in thrust over a factor of 30:1 and in chamber pressure over a factor of 8:1, the specific impulse values of all three are very close. They are also very close in their ratios of actual to ideal specific impulse, as one can see in Fig. 11.33, which shows that doubling the area ratio (from 50 to 100) raises the specific impulse by only about 2%. The “characteristic length” in Table 11.4 is defined as

$$L^* = V_c/A^*,$$

in which V_c is the total combustion chamber volume up to the nozzle throat plane, and A^* is the throat area. Comparing the SSME and the HM60, one can see that the product $L^*A^* = V_c$ is about the same for both; since the flow rate is

TABLE 11.4 Hydrogen-oxygen rocket characteristics and performance

Rocket Characteristic	RL-10	SSME	HM60
Total injector mass flow rate, kg/s	18.5	469	195.8
Combustion chamber inner diameter, mm	262	450	415
Characteristic length L^* , mm	980	800	850
Chamber contraction ratio	2.95	2.96	2.99
H_2 injection temp., K	180	850	95
Coolant temp. rise, K	150	254	61
Max. wall temp., K	—	~740	600
Max. heat flux, kW/cm ²	—	12.8	6.4
Chamber pressure, MPa	2.7	20.5	10
Mixture ratio, kgO ₂ /kgH ₂	5.0	6.0	5.1
Area ratio	57	77.5	110.5
Length, m	1.78	4.24	4.0
Exit diameter, m	1.00	2.39	2.52
Combustion time, s	450	480	291
Weight (dry), kg	132	3000	1300
Vacuum thrust, kN	67	2090	900
Vacuum specific impulse, s	444	455.2	445
Use	Centaur, Saturn	Space shuttle	European space transportation

Source: Data from Pouliquen [24].

proportional to pressure, this implies that the intensity of chemical reaction (kW/m³) is roughly proportional to pressure. It is also notable that the maximum heat flux is apparently proportional to chamber pressure.

PROBLEMS

1. A rocket is to be designed to produce 5 MN of thrust at sea level. The pressure in the combustion chamber is 7 MPa and the temperature is 2800 K. If the working fluid is assumed to be a perfect gas with the properties of air at room temperature, determine the following: (a) specific impulse, (b) mass flow rate, (c) throat diameter, (d) exit diameter.

For the same nozzle find (e) thrust at 30-kM altitude; (f) thrust at sea level if chamber pressure were increased to 21 MPa; (g) thrust with hydrogen at the same inlet stagnation conditions; and (h) thrust with stagnation temperature increased to 3600 K.

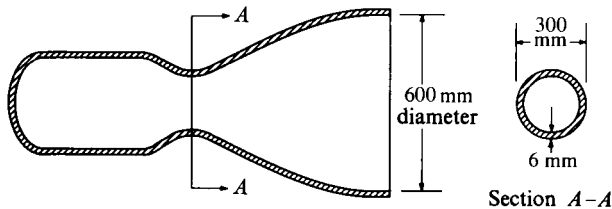
2. A rocket thrust chamber contains a propellant of molecular weight 25 and specific-heat ratio 1.2. The chamber pressure is 10 MPa, and the combustion temperature is 3000 K. The throat area is 0.1 m^2 .

Determine the thrust for the following conditions:

Ambient pressure			
MPa	psia	Exhaust area, m^2	
1	0	0	0.1
2	0	0	4.06
3	0.101	14.7	0.1
4	0.101	14.7	4.06

Compute the axial force exerted by the products of combustion on the expanding part of the nozzle for case 4, and compare with the corresponding value of the thrust.

3. The rocket nozzle shown in the figure operates in steady flow with standard atmospheric back pressure. Estimate the axial stresses at the throat if the stagnation conditions are 12 MPa and 3000 K. The molecular weight is 29, and the specific-heat ratio $\gamma = 1.4$



PROBLEM 3

4. Using a propellant of molecular weight 15 and flame temperature 3300 K, determine the rocket throat and exhaust areas required for a thrust of 500 kN and an ideal specific impulse of 300 sec. The ambient pressure is 0.1 MPa, and the specific-heat ratio of the propellant is 1.4.

How much thrust would this rocket develop if the ambient pressure were changed to 0.03 MPa? How much thrust would be developed by a rocket designed to expand to 0.03 MPa if it had the same stagnation conditions, throat area, and propellant?

5. A toy rocket (see figure) containing water and compressed air weighs 0.21 kg when empty and can carry 1 kg of water. The initial air pressure is 0.35 MPa.

(a) What is the minimum nozzle diameter (assuming reversible flow in nozzle) that will permit vertical takeoff? Sketch a suitable nozzle shape.

(b) What is the specific impulse under these conditions? (c) Why is the water

added? (d) Show how exhaust velocity depends on time during a static "firing" for given values of

\mathcal{V} internal volume of rocket,

p_0 initial pressure,

T_0 initial temperature,

m_w initial mass of water,

A_e exhaust area,

p_e exhaust pressure.



PROBLEM 5

6. Consider the performance of a solid-propellant rocket under conditions that change with time. The stagnation temperature is constant at 3000 K. The stagnation pressure changes slowly with time, according to

$$p_0 = 20 - 0.04t, \quad 0 < t < 100,$$

for p_0 in MPa and t in seconds. The nozzle has an area ratio of 5 and a throat area of 0.3 m^2 . It exhausts into a vacuum. The fluid may be considered to have $\gamma = 1.4$ and molecular weight $\bar{M} = 20$. How do the following vary with time? (1) Exhaust velocity. (2) Mass flow rate. (3) Thrust.

7. A new high-energy liquid propellant whose chemical reactions are not entirely known is to be fired in a static-test thrust chamber. From the following measurements, show how to estimate the thrust and specific impulse that this propellant would develop in any other rocket nozzle.

Thrust

\mathcal{T}

Pressure in chamber near injection nozzles

p_1

Pressure in nozzle near exit plane

p_2

Ambient pressure

p_a

Rate of mass flow of liquid propellant into the chamber \dot{m}

Exit area	A_e
Throat area	A_t

What factors might contribute error in such an estimate?

8. How long would it take for a thrust of a rocket to diminish to 10% of its steady value if the fuel and oxidant flows into the chamber were suddenly stopped? Consider, for example, the following conditions:

Initial combustion chamber pressure	$p_0 = 10 \text{ MPa}$
Initial combustion chamber temperature	$T_0 = 3000 \text{ K}$
Combustion chamber volume	$V = 0.15 \text{ m}^3$
Throat area	$A^* = 0.1 \text{ m}^2$
Molecular weight of propellant	$\bar{M} = 10$
Ratio of specific heats	$\gamma = 1.2$
Ambient pressure	$p_a = 0$

9. A rocket thrust chamber has been designed for a chamber pressure P_0 of 2.0 MPa and "correct" expansion at 10-km altitude where the ambient pressure is 26.5 kPa. The chamber has to be tested at sea level with the design value of the chamber pressure but with back pressure nearly four times the design value.

Is it likely that a shock wave will enter the nozzle under test conditions? At what back pressure could a plane normal shock stand in the end plane of the nozzle? Let $\gamma = 1.4$.

10. The following table provides the diameters and boundary layer thicknesses at the throat and exit of a rocket thrust chamber. The chamber pressure and temperature area $p_0 = 12 \text{ MPa}$ and $T_0 = 2950 \text{ K}$. The molecular weight of the hot gas in the nozzle is 13.4, and the average specific-heat ratio is 1.2. The ambient pressure is 97.5 kPa.

	Throat	Exit
Diameter, mm	150	675
Displacement thickness, mm	4.0	12.9
Momentum thickness, mm	3.0	10.5

Determine:

- The mass flow rate,
- The exhaust velocity,
- The rocket thrust,

and find the percentage change in each of these estimates that results from taking the boundary layer into account.

- 11.** In a nozzle of very small diameter and thrust, heat loss from the hot gas to the nozzle wall may become significant. In a particular nozzle expansion the rate of heat transfer per unit mass of fluid per unit temperature drop is approximately constant; that is,

$$\frac{dq}{dT} = c_q = \text{constant}.$$

Show that with given rocket chamber pressure p_0 and temperature T_0 and with exhaust plane pressure p_e , one may determine the exhaust velocity in this case from

$$u_e = \sqrt{\frac{2\gamma'}{\gamma' - 1} RT_0 \left[1 - \left(\frac{p_e}{p_0} \right)^{\gamma'-1/\gamma'} \right]},$$

in which

$$\frac{\gamma'}{\gamma' - 1} = \frac{\gamma}{\gamma - 1} - \frac{c_q}{R}.$$

For the case in which $\gamma = 1.4$, the molecular weight is 28.9 and $c_q = 0.5 \text{ kJ/kg} \cdot \text{K}$, determine the percentage change in the exhaust velocity due to heat transfer in choked nozzle flow rate. The nozzle pressure ratio p_0/p_e is 30.

- 12.** A chemical rocket is used for launch into earth orbit. At the end of the combustion chamber the stagnation temperature is 3000 K. The molecular weight of the combustion products is 26. The gases expand isentropically as an ideal gas mixture with specific-heat ratio 1.2. The area ratio A_e/A^* of the nozzle is 20, and the throat diameter is 0.1 m. Determine:
- The stagnation pressure if the expansion is correct at sea level;
 - The rocket thrust at sea level, 15-km, 30-km, and 60-km altitude.
- 13.** A liquid-propellant combustion chamber is 1 m long and 0.3 m in diameter. The temperature and pressure in the chamber are uniform at approximately 3200 K and 15 MPa, and the diameter Reynolds number of the flow through the chamber is of the order of 10^7 . The chamber wall is type 301 stainless steel 2.5 mm thick and is maintained at 110 K on the outside surface. Radiation is one-third the total heat flux. What would be the steady-state inner surface temperature? Use the following data:

Conductivity of stainless steel 26 W/m · K,

Conductivity of chamber gases 0.17 W/m · K.

Prandtl number for chamber gases 0.7

14. An experimental rocket thrust chamber has an outside wall temperature of 400 K at the throat, with a 3200-K chamber temperature. The local heat transfer rate is measured to be 15 MW/m^2 , of which 25% may be assumed due to radiation. If the wall is of stainless steel 2.5 mm thick with $k = 26 \text{ W/m} \cdot \text{K}$, and if the coolant surface area is the same as the hot-gas surface area, (a) what is the inner wall temperature? (b) It is expected that this temperature will cause failure in the actual application. The throat is to be lined with a ceramic of conductivity $k = 8 \text{ W/m} \cdot \text{K}$ to protect the metal. Assuming that the fraction of heat transfer by radiation is unchanged and that all gas properties are unchanged, what ceramic thickness is necessary to reduce the peak metal temperature to 1370 K while the coolant side remains at 400 K?

The heat flux is steady and the effects of the wall curvature and axial heat conduction can be considered negligible.

15. An early rocket design using a propellant at 3000 K is limited by wall-cooling problems to a chamber pressure of 2 MPa. Under these conditions a hot-side wall temperature, T_{wh} , of 1100 K is observed at the throat. A new material will allow an increase of T_{wh} to 1300 K. What new combustion chamber pressure p_0 will be allowed by this new material if you assume that its resistance to heat transfer ($\Delta L/k_w$) is about the same as the old, and that the coolant side temperature T_L and film coefficient h_L do not change? The fraction of total heat transfer due to radiation may also be assumed to be unchanged.

Data from the original rocket (at the throat):

$$T_L = 300 \text{ K} \text{ (coolant temperature)},$$

$$T_{0g} = 3300 \text{ K} \text{ (propellant temperature)},$$

$$\Delta L = 3.8 \text{ mm} \text{ (wall thickness)},$$

$$k_w = 22 \text{ W/m} \cdot \text{K} \text{ (wall conductivity)},$$

$$h_L = 0.7 \text{ MW/m}^2 \cdot \text{K} \text{ (coolant film coefficient)}.$$

The wall is sufficiently thin that heat transfer through it may be approximated as plane one-dimensional.

16. Show that for a thick-walled rocket nozzle the overall resistance to heat transfer ($\text{m}^2 \cdot \text{K/W}$) can be written as

$$R = \frac{1}{h_g} + \frac{A_g t}{A_w k_w} + \frac{A_g}{A_L h_L},$$

where

t = wall thickness,

k_w = wall conductivity,

h_L = liquid or coolant side heat transfer coefficient,

h_g = hot-gas-side heat transfer coefficient,

A_g, A_w, A_L = area normal to heat transfer on gas side, in the wall
(on average) and on the coolant side.

An experimental rocket shown in the figure has a combustion chamber temperature of 3600 K, and the nozzle throat diameter is 0.3 m. On the basis of reasonably accurate data on heat transfer in tubes, conductivity of the tube material, and the geometry of the coolant tube system, we can calculate that, at the throat,

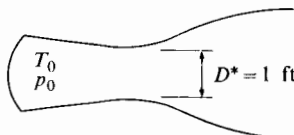
$$\frac{A_g t}{A_w k_w} + \frac{A_g}{A_L h_L} = 8.8 \times 10^{-6} \frac{\text{m}^2 \cdot \text{K}}{\text{W}}.$$

In one experimental test, with water-cooled walls and water temperature $T_L = 310$ K, the total heat transfer rate, based on the gas-side area, was measured as

$$\frac{\dot{Q}}{A_g} = 19.2 \text{ MW/m}^2.$$

If radiant heat transfer is neglected, what will the heat transfer rate per unit area be if p_0 is doubled?

(Note: In both cases assume the recovery factor, r , to be 1. That is, $T_{wa} = T_{0g}$. The viscosity and thermal conductivity of the gas may be assumed functions of temperature only.)



PROBLEM 16

17. The specific heat of a certain mixture of gases expanding in a rocket nozzle varies with temperature according to

$$c_p = a + bT,$$

in which $a = 2.5 \text{ kJ/kg} \cdot \text{K}$ and $b = 0.0005 \text{ kJ/kg} \cdot \text{K}^2$. The molecular weight of the gases is 12. The mixture behaves as perfect gas and expands isentropically from chamber pressure $p_0 = 10 \text{ MPa}$, and temperature $T_0 = 3000 \text{ K}$ to a given final velocity. Determine:

- The maximum possible expansion velocity, $u_{e\max}$;
- The pressure ratio required for exhaust velocity, $u_e/u_{e\max} = 0.9$;
- The pressure ratio required for $u_e/u_{e\max} = 0.9$ with $b = 0$.

- 18.** Using the data on the SSME engine presented in Table 11.4 deduce the specific heat ratio γ that would be needed to account for the measured thrust if the expansion had been isentropic and one-dimensional with constant γ . Are the thrust, mass flow rate, and specific impulse figures fully consistent?

Table 11.4 shows the peak heat flux for two H₂-O₂ rockets that differ in throat diameter, combustion pressure, and fuel-oxidant ratio. Is the pipe flow correlation Eq. (11.36) roughly consistent with the relative magnitudes of these maximum heat flux numbers? As a first approximation assume that the viscosity, thermal conductivity, and specific heat of the hot gas, and the inner wall temperature of the nozzle are the same in both cases.

- 19.** Considering a two-dimensional version of the expansion-deflection nozzle, such as that demonstrated in Fig. 11.21, estimate the total turning angle required for a supersonic expansion from $M = 1$ through pressure ratios $p_0/p_a = 75$ and 20 and with a γ value of 1.4. Compare the deflection angles that one can measure approximately with a protractor on Figs. 11.21(a) and (b) for the outer flow streamline from the throat ($M = 1$).

A first step in the solution of this problem is to verify that the integration of Eq. (11.22) can be expressed as

$$\theta + \sqrt{\frac{\gamma + 1}{\gamma - 1}} \tan^{-1} \sqrt{\frac{\gamma - 1}{\gamma + 1} (M^2 - 1)} - \tan^{-1} \sqrt{M^2 - 1} = \text{const.}$$

This is the solution to the Prandtl-Meyer expansion problem.

- 20.** Near the exit end of a shaped cylindrical nozzle the radius of the cross section varies as

$$r = r_e \left[1 - a \left(\frac{z}{r_e} \right)^2 \right],$$

whereas the boundary layer thickness varies with

$$\delta^* = \delta_e^* \left[1 - b \left(\frac{z}{r_e} \right) \right],$$

where z is the distance from the nozzle exit plane. The question has been raised as to whether the expansion ratio p_0/p_e in this nozzle is actually smaller than if it were shortened. Given

$$\frac{\delta_e^*}{r_e} = 0.01, \quad a = 0.1, \quad b = 1.00, \quad \frac{A_e}{A^*} = 100, \quad \gamma = 1.2,$$

determine:

- the shortening $\Delta L/r_e$ that would maximize the expansion ratio;
- by how much the pressure ratio would change.

21. For the SSME engine whose characteristics are given in Table 11.4, estimate the growth of boundary layer displacement thickness $\delta^*(x)$ in the expanding portion of the nozzle. You may use the following approximations and assumptions.
- Throat boundary layer thickness $\delta = 0.3$ mm
 - Throat wall friction factor $C_f = 0.003$
 - Distance from throat to exit plane $L = 3.8$ m
 - Linear variation of free-stream velocity with distance between throat and exit plane; throat velocity 1300 m/s
 - Estimated average kinematic viscosity $\nu \approx 3 \times 10^{-6}$ m²/s.

Though it was not developed for compressible flow, the Moses method (Chapter 4) may be used for approximate estimation of the boundary layer growth. For sufficiently low values of R_θ the Thwaites method (Chapter 4) could be used.

REFERENCES

1. Malina, F. J. "Characteristics of the Rocket Motor Based on the Theory of Perfect Gases," *J. Franklin Inst.* 203, (1940): 4.
2. Campbell, C. E., and J. M. Farley. "Performance of Several Conical Convergent-Divergent Rocket-Type Exhaust Nozzles," NASA TN D47, Sept. 1960.
3. Shapiro, A. H. *The Dynamics and Thermodynamics of Fluid Flow*. New York: Ronald Press, 1953. vol. 1 reprint. ed., Wiley; vol. 2, reprint. ed., Krieger, 1973.
4. Taylor, A. A., and J. N. Hoffman. "Design of Maximum Thrust Nozzles for Nonequilibrium Chemically Reacting Flow," *AIAA J.* 12 (1974): 1299–1300.
5. Scofield, M. P., and J. D. Hoffman, "Maximum Thrust Nozzles for Nonequilibrium Simple Dissociating Flows," *AIAA J.* 9 (1971): 1824–32.
6. Riedelbauch, S., and C. Welland. "Inviscid Laval Nozzle Flowfield Calculation," *J. Rocket and Spacecraft* 25, (1988): 88–90.
7. Back, L. H., R. F. Cuffel, and P. F. Massier. "Influence of Contraction Section Shape and Inlet Flow Direction on Supersonic Flow and Performance," *J. Spacecraft and Rockets* 9 (1972): 420–427.
8. Ahlberg, J. H., et al. "Truncated Perfect Nozzles in Optimum Nozzle Design," *J. Amer. Rocket Soc.* 31 (1961): 614–619.
9. Rao, G.V.R. "Recent Developments in Rocket Nozzle Configurations," *J. Amer. Rocket Soc.* (1961): 1488–94.
10. Miyajima, H., and K. Nakahashi. "Low-Thrust LO/LH Engine Performance with a 300:1 Nozzle," *J. Spacecraft and Rockets* 22 (1985): 188–194.
11. Allman, J. G., and J. A. Hoffman. "Design of Maximum Thrust Nozzle Contours by Direct Optimization Methods," *AIAA J.* 19 (1981): 750–751.
12. Dutton, J. C., and A. L. Addy. "Transonic Flow in the Throat Region of Axisymmetric Nozzles," *AIAA J.* 19 (1981): 801–804.

13. Tang, S. P., and J. P. Fenn. "Experimental Determination of the Discharge Coefficient for Critical Flow through an Axisymmetric Nozzle," *AIAA J.* 16 (1978): 41–47.
14. Massier, P. F., et al. "Viscous Effects on the Flow Coefficient for a Supersonic Nozzle," *AIAA J.* 8 (1970): 605–607.
15. Altman, D., et al. *Liquid-Propellant Rockets*. Princeton, N. J.: Princeton Aeronautical Paperbacks, Princeton University Press, 1960.
16. Berman, K. "The Plug Nozzle: A New Approach to Engine Design," *Astronautics* 5 (1960): 4.
17. Sasman, P. K., and R. J. Cresci. "Compressible Turbulent Boundary Layers with Pressure Gradient and Heat Transfer," *AIAA J.* 4 (1966): 19–25.
18. Bartz, D. R. "An Approximate Form of Compressible Turbulent Boundary Layer Development in Convergent-Divergent Nozzles," *Trans. ASME* 77 (1955): 1235–45.
19. Sellers, J. P., Jr. "Effect of Two-Dimensional Heat Transfer and Wall Temperatures in a Tubular Thrust Chamber," *J. Amer. Rocket Soc.* 31 (1961): 445–446, and "Two-dimensional Heat Conduction in a Tubular Thrust Chamber," *J. Amer. Rocket Soc.* 32 (1962): 1111–12.
20. Bartz, D. R. "Heat Transfer from Rapidly Accelerating Flow of Rocket Combustion Cases and from Heated Air," in *Advances in Heat Transfer*, vol. 2, J. P. Hartnett and T. F. Irvine, Jr., eds. New York: Academic Press, 1965.
21. Witte, A. B., and E. Y. Harper. "Experimental Investigation and Empirical Correlation of Local Heat Transfer Rates in Rocket-Engine Thrust Chambers," Technical Report no. 32-244, Jet Propulsion Lab., California Institute of Technology, Pasadena, Calif., March 19, 1962.
22. Sutton, G. P. *Rocket Propulsion Elements*. New York: Wiley, 1986.
23. Kelble, J. M., and J. E. Bernados. "High-Temperature Nonmetallic Materials," *Aerospace Engineering* 22 (1968): 56–75.
24. Pouliquen, M. F. "HM60 Cryogenic Rocket Engine for Future European Launchers," *J. Spacecraft and Rockets* 21 (1984): 346–353.

CHAPTER

12

CHEMICAL ROCKET PROPELLANTS: COMBUSTION AND EXPANSION

12.1 INTRODUCTION

In Chapter 11 we showed that the specific impulse of a rocket propellant depends quite significantly on the composition and temperature of the combustion products. Another important incentive for studying combustion in rockets is that the intensity of combustion (energy transformed per unit time per unit volume) directly determines the size, and therefore the mass, of the combustion chamber. The performance of the rocket vehicle depends to some extent on the mass of the engine as well as on its specific impulse.

The products of combustion in a well-designed rocket combustion chamber are very nearly in thermodynamic equilibrium. That is, at typical combustion chamber temperatures and pressures, the time required for mixing of fuel and oxidant and for chemical reactions is small compared with the average residence time (several milliseconds) of the propellant within the combustion chamber. Therefore one may employ the equilibrium thermodynamic methods of Chapter 2 to calculate the state of the propellant as it enters the exhaust nozzle; typically one finds that the combustion temperatures are so high that a substantial portion of the products of combustion are dissociated. During expansion in the nozzle, the temperature falls so rapidly that there may be insufficient time for the dissociation products to recombine. The gas composition at each stage of the expansion may not be the equilibrium composition for the instantaneous temperature. Under certain conditions the rates of recombination are so slow that the gas composition effectively “freezes” (surely an odd word for gases as hot as 3000 K), and

the gas expands at constant composition. For both extremes, equilibrium and frozen-composition expansion, convenient analytical methods are available for calculating isentropic expansions. For the intermediate cases (which we might call the “finite-rate” problems) analytical methods exist, but they are typically quite complex and can be only briefly introduced here.

A special case arises with those solid rocket propellants that use powdered metals—for example, aluminum—as a fuel additive. The aluminum particles burn with oxygen to form Al_2O_3 particles that are initially liquid and solidify during expansion. They tend also to agglomerate to become large particles that do not accelerate as quickly as the gas surrounding them. Since in some propellants aluminum particles constitute as much as 15% to 20% of the total mass, nozzle design for such cases must deal with the rapid acceleration of a two-phase flow.

Hence we discuss both combustion and expansion in this chapter. For solid and liquid propellants we outline separately the factors that govern combustion rate and minimum combustion chamber size. In addition we note the important problem of combustion stability.

12.2 LIQUID PROPELLANTS

Liquid propellants for chemical rockets can be classified as either monopropellants (single substances that are capable, upon igniting, of exothermic breakdown) or bipropellants (fuel and oxidizer—substances that are separately stored, pressurized, and then injected into the combustion chamber).

Hydrazine (N_2H_4) is an example of a monopropellant; it has had considerable application in small rockets for altitude control of spacecraft [1]. It is storable for long periods and can be used to provide short-duration thrust (pulsed operation). Liquid hydrazine has a heat of formation of 50.2 kJ/gmol. With exposure to an iridium catalyst it decomposes to ammonia (NH_3) and other compounds [2] that dissociate at high temperature. At a combustion chamber pressure of 6.94 MPa (1000 psia) it can theoretically generate a specific impulse of 245 s. For pulsed operation the actual specific impulse could be substantially less owing to transient thermal and dynamic effects.

Most chemical rockets are bipropellants. Table 12.1 gives representative fuel and oxidizer combinations and optimum performance for isentropic expansion. One can see that the optimum mixture ratio and specific impulse depend substantially on whether the back pressure is 1 atm or zero. In each case one calculates the specific impulse assuming that the product mixture is in chemical equilibrium at each stage of the expansion (shifting equilibrium). We discuss this matter in Section 12.3.

The oxygen-hydrogen combination has now been the subject of much experience in the *Saturn* and shuttle vehicles. Liquid oxygen has a vapor pressure of 1 atm at 90 K, at which its density is 1.14 g/cm³. The density of liquid hydrogen (which boils at 20 K) is only 0.071 g/cm³. This leads to the low-bulk average density shown in Table 12.1 for the two $\text{O}_2\text{-H}_2$ fuel combinations and indicates that,

TABLE 12.1 Optimum performance of liquid bipropellants for chemical rockets; shifting equilibrium; isentropic one-dimensional expansion

I. Expansion from 6.94 MPa (1000 psia) to 1 atm (14.7 psia)

Oxidizer	Fuel	Oxidizer-fuel mass ratio (r)	Adiabatic combustion temperature (T/K)	Average bulk density (g/cm ³)	C^* (m/s)	I_{sp} (s)
O ₂	H ₂	4.13	3013	0.29	2416	389
O ₂	RP1	2.58	3676	1.03	1799	300
F ₂	H ₂	7.94	3962	0.46	2556	411
N ₂ O ₄	MMH	2.17	3396	1.19	1745	288
N ₂ O ₄	N ₂ H ₄ (50%)					
	UDMH(50%)	1.98	3368	1.12	1747	288

II. Expansion from 6.94 MPa (1000 psia) to area ratio 40 and vacuum

Oxidizer	Fuel	Oxidizer-fuel mass ratio (r)	Adiabatic combustion temperature (T/K)	Average bulk density (g/cm ³)	C^* (m/s)	I_{sp} (s)
O ₂	H ₂	4.83	3251	0.32	2386	455
O ₂	RP1	2.77	3701	1.03	1783	358
F ₂	H ₂	9.74	4258	0.52	2530	479
N ₂ O ₄	MMH	2.37	3398	1.20	1724	342
N ₂ O ₄	N ₂ H ₄ (50%)					
	UDMH(50%)	2.15	3369	1.20	1731	342

Source: Data from Rocketdyne Chemical and Material Technology, Rocketdyne Division, Rockwell International.

for a given propellant mass, the tank volume will be as much as four times as large as for some of the other fuel-oxidant combinations shown in the table.

The fuel designated RP1 is a liquid hydrocarbon (kerosene-like) fuel whose average hydrogen–carbon atom ratio is 1.95 to 1.97. Its density is in the range of 0.8 to 0.815, so that the bulk average propellant density for the oxygen-RP1 propellant is relatively high.

Florine (F₂) is an oxidant that, with hydrogen, could produce extremely high specific impulse. It is, however, toxic and corrosive and reacts spontaneously with many metals. It has not been used in production rocket engines.

The oxidizer nitrogen tetroxide (N₂O₄) has a density of 1.45 g/cm³ and relatively high vapor pressure (1 atm at 294 K), so that it requires relatively thick-walled tanks for use in a near-vacuum environment. It is considered a storable oxidizer, though its freezing point is 261 K. As Table 12.1 indicates, N₂O₄ is used with MMH (monomethyl hydrazine CH₃NHNH₂). MMH has a density of

0.88 g/cm³ at 293 K and a vapor pressure of only 0.0069 MPa at that temperature. Its freezing point is 220.7 K. It has several properties that make it safer and easier to handle than hydrazine [2]. Unsymmetrical dimethyl hydrazine (CH₃)₂NNH₂ is also preferable in some ways to hydrazine; its boiling point is 336 K (versus 386 K for hydrazine); its freezing point is 216 K (versus 274.5 K for hydrazine). Its density is 0.85 at 244 K. N₂O₄ has been used with MMH in relatively small rockets in the space shuttle orbiter and was used in the *Apollo* command and service modules.

12.3 EQUILIBRIUM COMPOSITION

At the rocket combustion temperatures shown in Table 12.1, the propellant composition at equilibrium could differ considerably from the composition resulting from complete combustion. For example, consider a stoichiometric mixture of hydrogen and oxygen, initially at a temperature of 300 K and maintained at a pressure of 100 atm. If one assumes that combustion proceeds to completion according to H₂ + $\frac{1}{2}$ O₂ → H₂O, then the resultant chamber temperature can be easily calculated. According to Eq. (2.33), the net heat of reaction Q_{net} is

$$Q_{\text{net}} = (H_{P2} - H_{Pf}) - (H_{R1} - H_{Rf}) + H_{RPf} = 0, \quad (2.33)$$

in which H_P and H_R are the enthalpies of given masses of products and reactants, respectively. The symbol H_{RPf} is the change of enthalpy during a transformation from reactants to products at a reference temperature T_f . From Eq. (2.32) and Table 2.1,

$$\begin{aligned} H_{RPf} &= n_{H_2O} Q_{fH_2O} - n_{O_2} Q_{fO_2} - n_{H_2} Q_{fH_2} = 1 \times (-241.8) \\ &= -241.8 \text{ MJ/kmol H}_2\text{O at } T_f = 300 \text{ K}. \end{aligned}$$

Since the reactants enter the combustion chamber at the reference temperature T_f , $H_{R1} - H_{Rf} = 0$, and for adiabatic combustion we find, from Eq. (2.33), that

$$H_{P2} - H_{Pf} = 241.8 \text{ MJ/kmol of H}_2\text{O}.$$

Using Fig. 2.5, we see that H_{Pf} at 300 K is zero, so $H_{P2} = 241.8$, and (again from Fig. 2.5) $T_{P2} \approx 5000$ K. This very high temperature would actually be accompanied by considerable product dissociation. As Fig. 2.14 indicates, the equilibrium mole fractions (extrapolated to 5000 K) would be approximately

H ₂ O	0.15
H ₂	0.21
O ₂	0.05
H	0.25
O	0.13
OH	0.21
	1.00

Thus the mole fractions of O and H would be of the same order of magnitude as that of H₂O at this temperature. As Fig. 2.15 shows, the actual adiabatic combus-

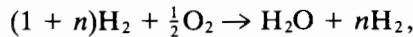
tion temperature would be approximately 3800 K and the product composition quite different from the product resulting from complete combustion.

To demonstrate the striking effect of dissociation on rocket performance, Fig. 12.1 shows the results of calculations of specific impulse as a function of fuel-oxidant ratio for the two extremes:

1. Complete combustion; that is, either all the fuel or all the oxidant consumed.
2. Equilibrium; that is, combustion product composition determined by thermodynamic equilibrium in the combustion chamber.

For both these cases we have assumed that there is no chemical reaction in the nozzle.

For complete combustion we can easily estimate the variation of specific impulse with fuel-oxidant ratio. With excess hydrogen the reaction is



where n can have any positive value. From this and Eq. (11.4) we can see that

$$I_{sp} = \frac{u_e}{g_e} = \frac{1}{g_e} \sqrt{2 \left(c_p T_{01} + \frac{\bar{Q}_R}{18 + 2n} \right) \left[1 - \left(\frac{p_e}{p_0} \right)^{(y-1)/y} \right]}, \quad (12.1a)$$

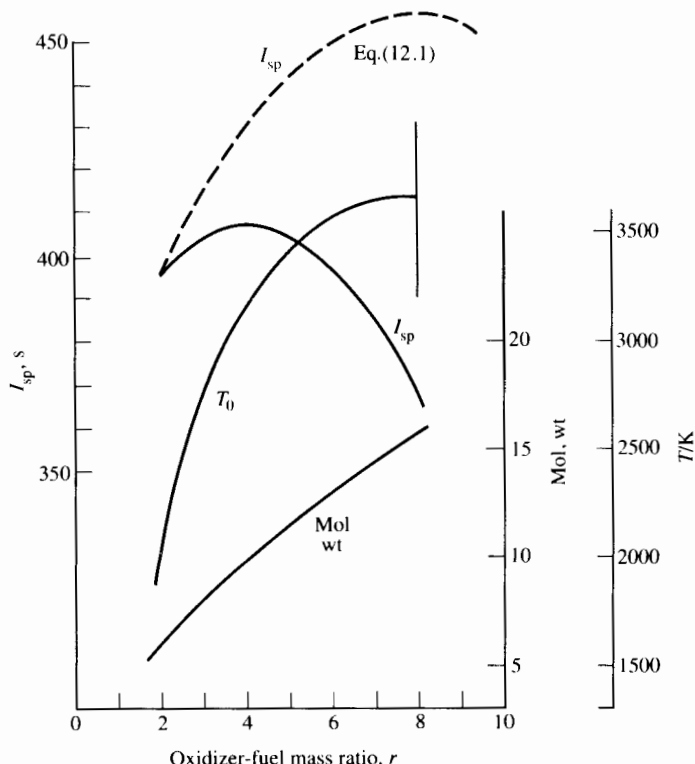


FIGURE 12.1 $\text{H}_2\text{-O}_2$: shifting equilibrium expansion from 6.89 MPa (1000 psia) to 0.1 MPa (14.7 psia); reactants at 298 K.

in which \bar{Q}_R is the heat of reaction per mole of H_2O . For excess oxygen reacting according to $\text{H}_2 + (\frac{1}{2} + m)\text{O}_2 \rightarrow \text{H}_2\text{O} + m\text{O}_2$, where m can have any positive value, the specific impulse is given by

$$I_{sp} = \frac{1}{g_e} \sqrt{2 \left(c_p T_{01} + \frac{\bar{Q}_R}{18 + 32m} \right) \left[1 - \left(\frac{p_e}{p_0} \right)^{(y-1)/y} \right]}. \quad (12.1b)$$

The specific impulse determined by Eqs. (12.1) is shown in Fig. 12.1 as a function of the ratio r of the oxidizer-fuel mass. The stoichiometric value of r is 8, so that Eq. (12.1a) applies when $r < 8$ and Eq. (12.1b) when $r > 8$; the two equations are identical when $r = 8$. Figure 12.1 shows that if the combustion reaction goes to completion, the best value of the fuel-air ratio would be stoichiometric.

A very different result is obtained if we employ the more realistic equilibrium assumption. The solid lines of Fig. 12.1 show the results of specific-impulse calculations that follow from this assumption. The product composition, specific-heat ratio, and molecular weight have been determined by methods discussed in Chapter 2. The specific impulse has been calculated from Eq. (11.3), by using a nominal value of the nozzle pressure ratio.

We can see from Fig. 12.1 that, owing to dissociation, the oxidizer-fuel ratio must be much less than stoichiometric for maximum specific impulse. The difference between the results of the “complete combustion” calculation (Eqs. 12.1) and the more realistic equilibrium calculation is largely due to the reduced release of energy if the reactants remain partially dissociated. This effect becomes greater as the mixture approaches the stoichiometric ratio and the combustion temperature increases. In general, though dissociation usually results in slightly lower molecular weight \bar{M} , the most important effect is that of reduced energy release and hence reduction in T_0 and I_{sp} .

Using the STANJAN code [3], we can investigate the dependence of composition and specific impulse on mixture ratio for the fuel-oxidant combinations shown in Table 12.1. Taking H_2 and O_2 , for example, and restricting our attention to the fuel-rich case only ($n > 0, r < 8$), we can see that since the heats of formation of H_2 and O_2 are zero, the calculation is particularly simple if the H_2 and O_2 enter the chamber at 298 K. In this case the enthalpy h_0 of the mixture is zero and remains so for adiabatic combustion. Then specifying (for any oxidant-fuel mass ratio r) the $\text{H}_2\text{-O}_2$ mole ratios as $16/r:1$, we can use the STANJAN code to determine the steady-flow adiabatic combustion temperature and the mixture composition and molecular weight. The temperatures so obtained are consistent with the numbers shown in Table 12.1.

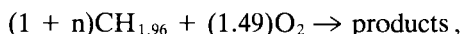
To determine the shifting-equilibrium specific impulse—for example, for expansion to 1 atm—we can ask the STANJAN code to find the mixture state at that pressure and the same entropy as in the 68.0-atm $h = 0$ state. With the initial and final enthalpies determined, we can find the specific impulse from $\sqrt{2(h_0 - h_e)/g_e}$.

With RP1 as fuel, the enthalpy of the mixture at combustion temperature is not zero (even if the fuel and oxidant enter the chamber at 298 K). However, we can infer the heat of formation of RP1 by using the STANJAN code to determine

TABLE 12.2 Equilibrium gas composition; reactants at 298.15 K

Fuel	H ₂	H ₂	N ₂ H ₄	N ₂ H ₄	CH _{1.96} (RP1)
Oxidizer	O ₂	O ₂	O ₂	O ₂	O ₂
Oxidizer-fuel mass ratio	5	5	0.92	0.92	2.58
Pressure					
MPa	6.89	10.34	6.89	10.34	6.89
psia	1000	1500	1000	1500	1000
Temperature					
K	3429	3466	3410	3453	3676
Mole fractions					
H ₂	0.3607	0.3622	0.0215	0.0197	0.086
O ₂	0.977 × 10 ⁻³	0.795 × 10 ⁻³	0.1518	0.1518	0.019
H ₂ O	0.5744	0.5795	0.4473	0.4521	0.326
OH	0.0260	0.0238	0.0786	0.0766	0.060
O	0.0015	0.0013	0.01832	0.01675	0.012
H	0.0363	0.0324	0.00847	0.00735	0.030
N ₂			0.2382	0.2383	
NO			0.03578	0.03722	
NO ₂			0.977 × 10 ⁻⁴	0.121 × 10 ⁻³	
N			0.835 × 10 ⁻⁵	0.844 × 10 ⁻⁵	
CO					0.319
CO ₂					0.148

the mixture enthalpy. The stoichiometric oxidant–fuel mass ratio for CH_{1.96}–O₂ is 3.41, so the mixture to which Table 12.2 refers is fuel rich, and we may write



using the value of n to calculate the mixture ratio

$$r = \frac{(1.49)31.999}{(1 + n)13.997}.$$

Since the heat of formation of O₂ is zero, the enthalpy of the products will be the same for all mixture ratios r if the RP1 and O₂ enter the combustion chamber at 298 K. Taking this simplified case and noting that, from the STANJAN code, the mixture enthalpy inferred as above from $T = 3676$ K and $r = 2.58$ is -7.5×10^5 J/kg, we can then generate the results with STANJAN shown in Fig. 12.2. For both the H₂ and RP1 fuels one can see that the optimum mixture ratio is fuel-rich in both cases (the stoichiometric r being 8 for H and 3.41 for RP1). These results, like those of Fig. 12.1, pertain to an arbitrary chamber pressure of 68.0 atm (1000 psia).

Fig. 12.2 shows how specific impulse, equilibrium temperature, and molecular weight (in the combustion chamber) vary with oxidant–fuel mass ratio. The spe-

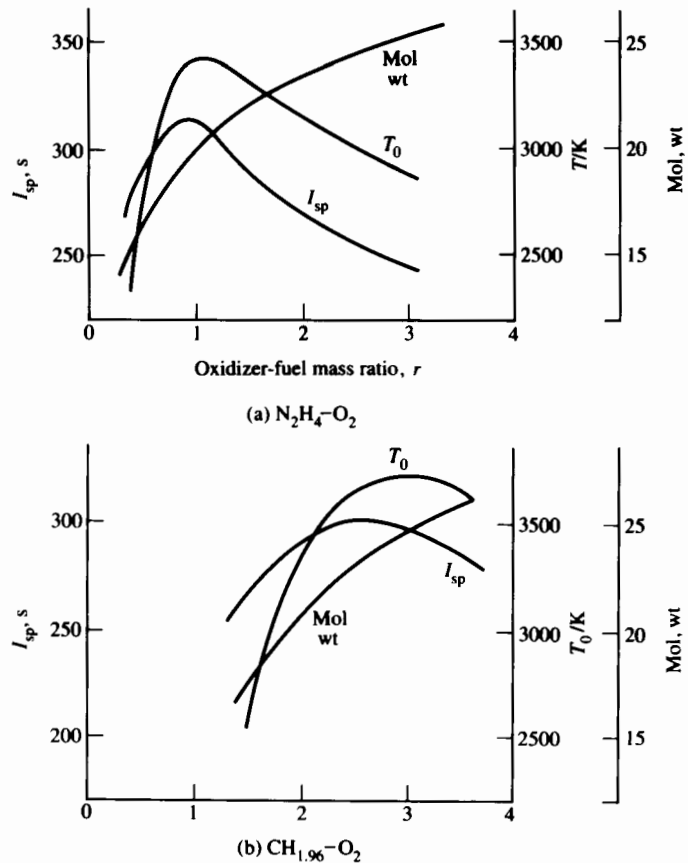
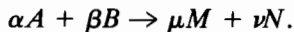


FIGURE 12.2 Ideal rocket performance; ideal equilibrium expansion; reactants at 298 K.

cific impulse for the RP1 ($\text{CH}_{1.96}$) and hydrazine fuels was calculated by assuming isentropic expansion and shifting equilibrium between initial and final pressures. The results obtained for these two fuel-oxidizer combinations are qualitatively similar to those obtained for H_2-O_2 (Fig. 12.1). In each case maximum I_{sp} is associated with less than maximum combustion temperature because of the importance of molecular weight.

The effect of increasing chamber pressure is generally to reduce dissociation. Consider the following dissociation reaction:



The equilibrium concentration in terms of mole fractions must satisfy (see Chapter 2)

$$K_n = \frac{\chi_M^\mu \chi_N^\nu}{\chi_A^\alpha \chi_B^\beta} = p_{\text{mix}}^{(\alpha+\beta)-(\mu+\nu)} K_p, \quad (12.2)$$

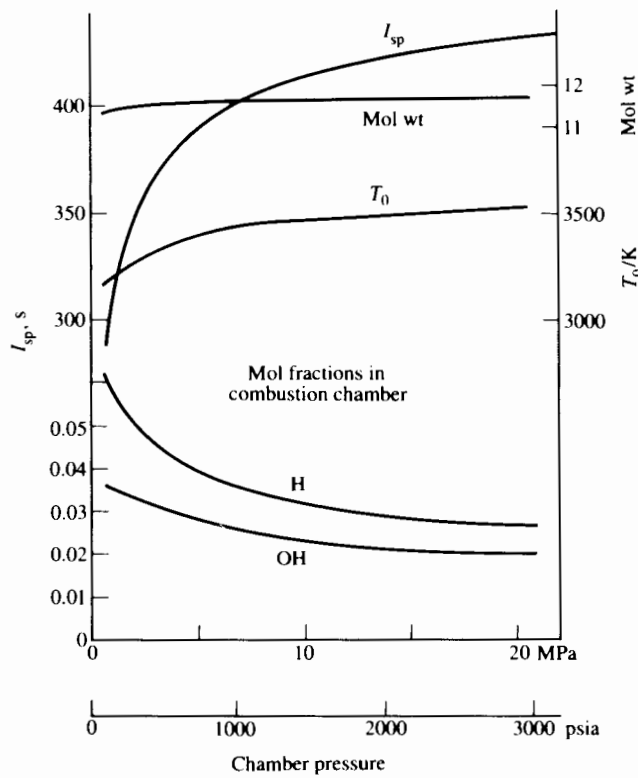
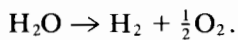


FIGURE 12.3 H_2 - O_2 shifting equilibrium expansion to 1 atm; O_2 : H_2 mass ratio, 5:1, reactants at 298 K.

in which p_{mix} is the pressure of the mixture. For a given temperature (and thus a given K_p), one can see that high pressure reduces the relative concentration of M and N if $(\mu + \nu)$ is greater than $(\alpha + \beta)$, as is the case with the dissociation of H_2O , for example:



Increasing the mixture pressure at constant temperature reduces the dissociation of the H_2O .

Figure 12.3 illustrates this effect for an oxygen-hydrogen propellant of mixture ratio (5:1). As Eq. (11.3) shows, the specific impulse may be written

$$I_{sp} \propto \sqrt{c_p T_{O_2} \left[1 - \left(\frac{p_e}{p_0} \right)^{(\gamma-1)/\gamma} \right]}.$$

The tendency toward recombination of H_2 and O_2 raises the mixture temperature so that both T_{O_2} and the term $[1 - (p_e/p_0)^{(\gamma-1)/\gamma}]$ increase with pressure. The effect of pressure on mixture specific heat is not so obvious, but Fig. 12.3 shows that the specific impulse increases appreciably with pressure.

12.4 NONEQUILIBRIUM EXPANSION

We have seen that the *equilibrium* composition of the combustion products is dependent on pressure and temperature and that, at common combustion chamber conditions, these products may include large quantities of dissociated material. In the exhaust nozzle the disassociated compounds will tend to recombine because of the large drop in temperature. This (exothermic) chemical reaction during expansion acts as an apparent heat source in the flow, in addition to causing changes in c_p and γ .

Figure 12.4 illustrates the relative importance of dissociation energies before and after an equilibrium expansion of a stoichiometric mixture of hydrogen and oxygen. The “dissociation” energy in each case refers to the extra thermal energy that the mixture would have had if the product composition had been entirely undissociated. The term *kinetic energy* refers to the directed bulk motion of the products following the expansion.

For the propellant to maintain equilibrium composition as it expands, it is necessary that the recombination processes occur in a time that is short relative to the expansion time. Since the expansion process is very rapid, this condition is not always met. In the limit, if reaction rates are very slow, no recombination occurs at all, and the propellant is said to be “frozen,” at constant composition. The difference between “equilibrium” and “frozen flow” performance can be appreciable for some propellants. For a given equilibrium composition before expansion, and a given expansion pressure ratio, the final kinetic energy (or specific impulse) is higher with equilibrium than with frozen expansion. This is because, as mentioned earlier, progressive recombination of the dissociation products is

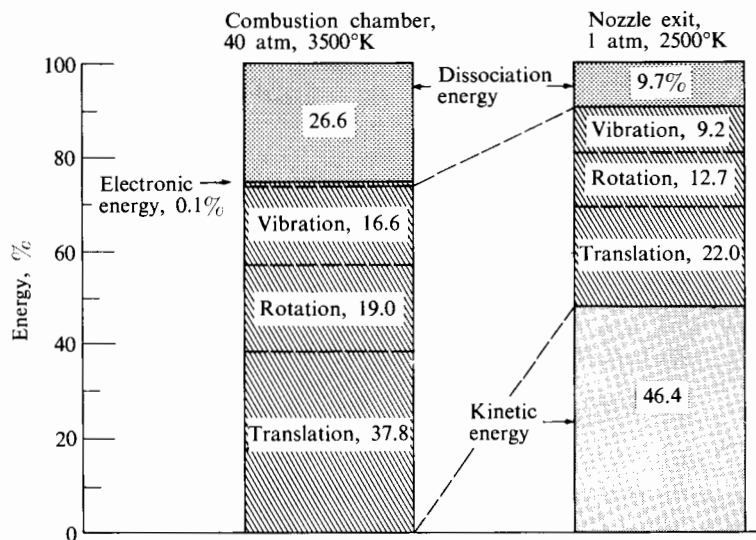
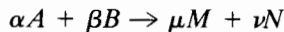


FIGURE 12.4 Typical equilibrium energy distribution in rocket gases. (Courtesy Olson [4].)

equivalent to a process of heating the mixture during expansion. However, as Fig. 12.1 indicates, the specific impulse will always be lower with dissociation than with no dissociation at all.

The maintenance of equilibrium or near-equilibrium composition as the propellant expands requires that the speed of the important reactions be high relative to the speed at which changes take place in the state of the propellant. Suppose that the general reaction



describes an important recombination occurring during expansion. In general one may observe that the rate of change of the concentration, C , of any species is described by an equation of the form

$$-\frac{dC_A}{dt} = -\frac{\beta}{\alpha} \frac{dC_B}{dt} = \frac{\mu}{\alpha} \frac{dC_M}{dt} = \frac{\nu}{\alpha} \frac{dC_N}{dt} = k C_A^\alpha C_B^\beta, \quad (12.3)$$

where k is the temperature-dependent reaction rate constant, *provided* that the reaction occurs directly as written; that is, without the formation of intermediate species. At the same time as this recombination is proceeding, the temperature is dropping so that k will drop rapidly. The temperature change of a small "particle" of fluid is given by

$$\frac{dT}{dt} = \frac{dT}{dx} \frac{dx}{dt} = u \frac{dT}{dx}. \quad (12.4)$$

One may calculate u and dT/dx throughout the nozzle, assuming either frozen or equilibrium flow. In principle, the temperature changes due to reduction of pressure of the expanding fluid and also to changes in its composition may be found by simultaneously satisfying the continuity, momentum, and energy equations if the appropriate rate constants are known.

Because the degree of departure from equilibrium during expansion depends on how the reaction time scale compares with the characteristic expansion time, nonequilibrium effects may be much more serious for short nozzles than for long ones. Timnat [5] suggests that dissociation times may be important for expansion times of the order of 10^{-4} s or less, depending on the complexity of the recombination reactions.

Since concentration is proportional to pressure, one can see from Eq. (12.3) that, because $\alpha + \beta > 1$, raising the pressure will hasten reaction rates and keep the composition closer to shifting equilibrium. This is one of the potential advantages of high combustion pressure in chemical rockets.

Though it is possible to have isentropic flow with constant composition or with shifting equilibrium, Timnat [5] has provided proof that an expanding flow in which the rates of recombination are finite cannot be characterized as isentropic. Nonetheless, the temperature changes due to reduction of pressure of the expanding fluid and also to changes in its composition may be found by simultaneously satisfying the continuity, momentum, and energy equations if the appropriate rate constants are known. General methods [6, 7] have been worked out for

calculating the expansion of chemically reacting mixtures when the reaction rate "constants" are specified as a function of temperature. For each reaction of interest it is typical to find empirical equations such as

$$k = AT^n \exp\left(-\frac{B}{RT}\right), \quad (12.5)$$

where A , n , and B are empirical constants peculiar to that reaction.

In considering the dissociation and recombination of the products of hydrogen-fluorine (H_2-F_2) combustion, Taylor and Hoffman [6] identified six reactions of importance and established the small dependence on combustion pressure and nozzle scale (doubling it from 63.5 mm [25 in.]) of the calculated nozzle thrust. In this case the thrust calculated for frozen flow (for a given pressure ratio) was 5.4% less than with shifting equilibrium. With finite reaction rates the thrust was about 1.5% less.

Bray [8] pointed out an implication of the exponential term in Eq. (12.5); depending on the value of B , a particular reaction rate may vanish very quickly at some point in the nozzle. At equilibrium the forward and backward reaction rates for a given dissociation are balanced. If during this expansion one rate suddenly dies, the other will quickly drive the reaction to completion in one direction, and the composition in that respect becomes "frozen." It is typical for freezing not to occur upstream of the throat; Timnat suggests that as a rough approximation one might assume shifting equilibrium to the throat, and frozen composition thereafter.

Figures 12.5 and 12.6 show experimental data compared with shifting-equilibrium and frozen-flow calculations for two propellants. JP4 is an aviation fuel of the kerosene type. For these experiments the nozzle length scale was relatively small and the combustion pressures modest. The data were adjusted to correct for nozzle divergence and combustion loss. The results appear to indicate that H_2-O_2 propellant remains close to equilibrium composition during expansion, whereas the $JP4-O_2$ products of combustion are more nearly characterized by frozen flow.

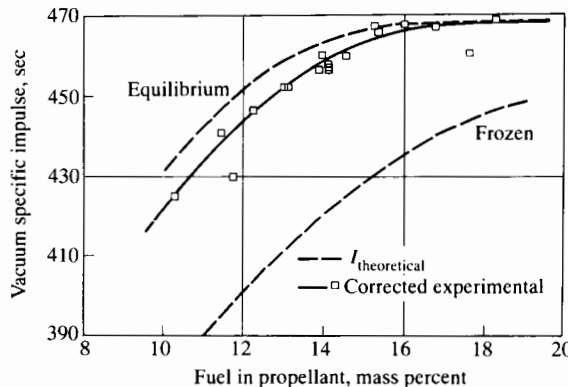


FIGURE 12.5 "Corrected" specific impulse of hydrogen-oxygen rocket. Combustion pressures 0.27, 0.14, 0.5 MPa. (Courtesy Olson [4].)

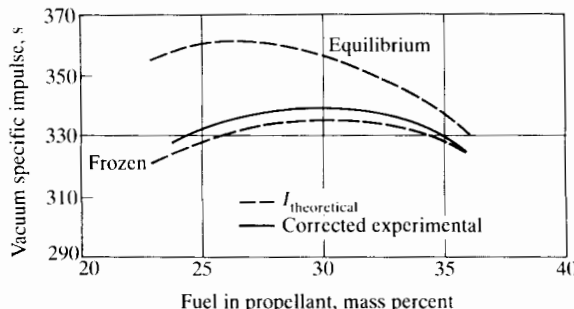


FIGURE 12.6 "Corrected" specific impulse of JP4-oxygen rocket. Combustion pressure 4 MPa. (Courtesy Olson [4].)

12.5 LIQUID-PROPELLANT COMBUSTION CHAMBERS

The function of the combustion chamber is to generate high-temperature and high-pressure combustion products. For a liquid-propellant rocket the combustion chamber must have an appropriate array of propellant injectors and a volume in which the propellant constituents can vaporize, mix, and burn, attaining near-equilibrium composition before entering the nozzle. For a solid-propellant rocket the combustion chamber is a high-pressure tank containing the solid propellant and sufficient void space to permit stable combustion. An ignition system is required unless, as for certain liquid propellants, the chemicals ignite on contact (hypergolic propellant combination). The combustion chamber may be cooled or uncooled.

One may gain an appreciation of the intensity of rocket combustion by comparing it with that of other combustion processes. Typical rates of energy release for steam power plants are 0.3 MW/m^3 , and for jet engines 300 MW/m^3 . In rocket chambers rates of the order of $30,000 \text{ MW/m}^3$ are achieved. Thus it is understandable that serious combustion problems have been encountered in the development of chemical rockets. In the following paragraphs we discuss combustion chambers for liquid and solid propellants separately, after which we consider combustion instabilities qualitatively.

In considering the design of a liquid-propellant combustion chamber, one might pose three questions:

1. What are the most important constraints on propellant injector design?
2. What factors determine the necessary chamber length?
3. What considerations govern the choice of contraction ratio A_c/A^* (A_c being the chamber cross-sectional area)?

We now address these questions in order.

Fuel and Oxidant Injection

Liquid propellants must be injected into the combustion chamber, atomized, and sufficiently mixed (except for monopropellants) before they can react. The *in-*

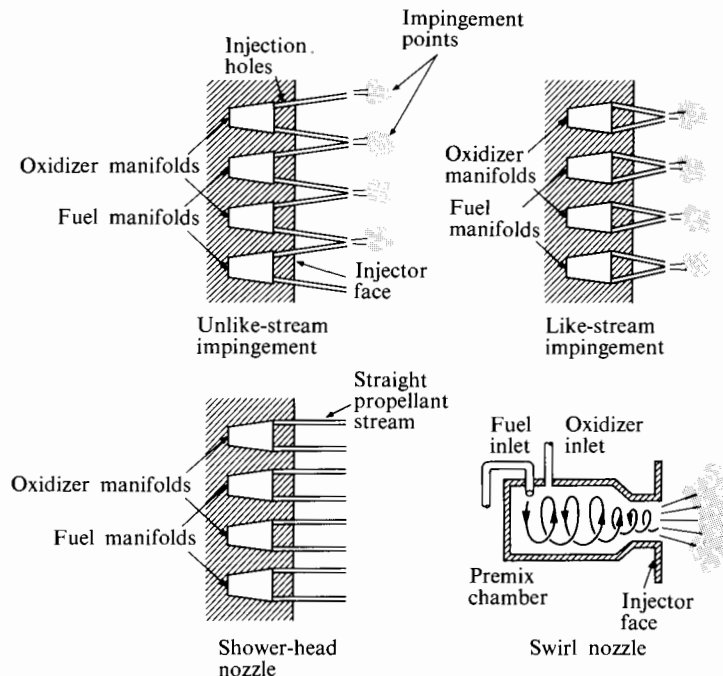


FIGURE 12.7 Schematic diagrams of several injector systems. (Adapted from Sutton [2].)

jector is a series of small nozzles through which the propellant or propellants are introduced as a fine spray into the combustion chamber. These nozzles should be arranged to promote adequate mixing of the propellants and uniform properties across the combustion chamber. For certain hypergolic propellant combinations, such as nitric acid with unsymmetrical dimethyl hydrazine (UDMH), where ignition occurs as a result of liquid mixing, adequate mixing requires an unlike-stream-impinging injector, as illustrated in Fig. 12.7. Nonhypergolic propellant combinations require rapid vaporization to promote adequate mixing of the gaseous phase. Like-stream or unlike-stream impingement, shower-head, and swirl-nozzle injectors have been successful. Monopropellants, though not requiring mixing, do require rapid vaporization and adequate distribution. Swirl injectors have been successful in promoting mixing.

Injector configuration can substantially affect local wall temperatures throughout the rocket. Often it is possible, by controlling the injection pattern, to create a layer of relatively cool gas near the walls. Poor injection can lead to local hot spots and even to actual burnout of the wall material.

Figure 12.8 shows the injector configuration of the Rolls-Royce RZ.2 engine installed in the thrust chamber.

The mass flow rate of propellant and the pressure drop across the injector are related by an equation of the form

$$\dot{m} = C_d \rho A_i \sqrt{2(\Delta p/\rho)}, \quad (12.6)$$

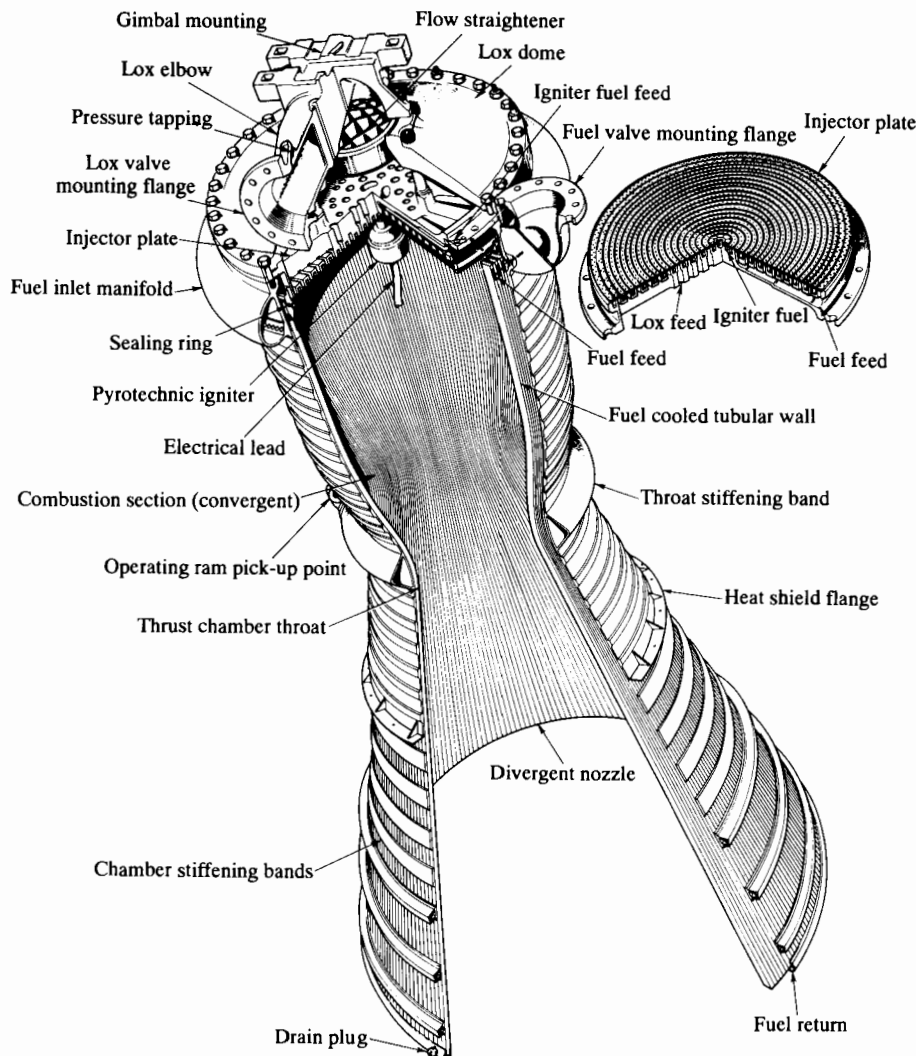


FIGURE 12.8 Rolls-Royce RZ.2 rocket engine thrust chamber. Propellant is liquid oxygen and kerosene. Sea-level thrust, 610 kN (137,000 lb). (Courtesy Rolls-Royce.)

where

$$\rho = \text{propellant density (liquid)},$$

$$C_d = \text{discharge coefficient},$$

$$A_i = \text{injector nozzle area},$$

$$\Delta p = \text{pressure drop across injector nozzle}.$$

For injector nozzles that are essentially short tubes with rounded inlets, discharge coefficients from 0.97 to 0.99 are attainable. For sharp-cornered tubes or

orifices, the discharge coefficient drops to 0.6 to 0.8, primarily because of contraction of the jet cross section. If Δp is measured across the entire inlet manifold system, rather than just across the inlet nozzle itself, C_d will of course be lower than these values. Typical pressure drops for injectors are several MPa (several hundred psi). A large drop in pressure promotes good atomization and tends to suppress those combustion instabilities associated with pressure oscillations in the chamber coupled with pressure oscillations in the propellant supply system. On the other hand, high pressure drop also produces high propellant inlet velocity, which we will show to be undesirable. Further, high pressure drop requires increased power in the propellant pump or, for pressure-fed propellants, high-pressure propellant tanks. Thus the "best" injector pressure drop is not well defined, except by saying that it would probably be desirable to have the minimum Δp consistent with good atomization and combustion stability.

Chamber Length

It is desirable to attain minimum chamber size for a given propellant, since this permits thinner chamber walls and lighter thrust chambers in general. In addition, the total chamber-wall heat transfer rate decreases as size is decreased. The minimum acceptable chamber volume depends directly on the time required for propellant injection, mixing, vaporization, and chemical reaction. Of these processes, the slowest (for typical propellants) is vaporization of the liquid drops, and this fact is the basis of simplified but enlightening one-dimensional analyses [9, 10] of liquid-propellant combustion chamber behavior. In order to illustrate what one may learn from these analyses, let us now consider their approximations and typical results.

Following Spalding [10], we consider the idealized cylindrical combustion chamber of Fig. 12.9, making the following assumptions:

1. Drops of uniform size and velocity are injected into the chamber at plane ①. No distinction is made between drops of fuel and oxidant.
2. The flow in the chamber is one-dimensional; all properties of the gas-liquid mixture are uniform at any plane of constant x .
3. Chemical reactions proceed infinitely fast; thus the composition of the gas is everywhere in local equilibrium.

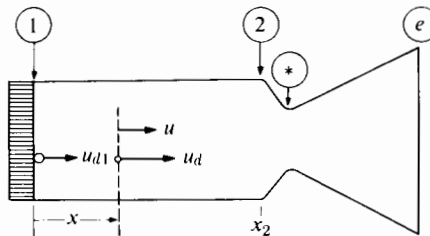


FIGURE 12.9 Idealized liquid-propellant combustor.

4. The time required for combustion is equal to the time required for vaporization of the drops.
5. The pressure and temperature of the chamber are uniform.

In order to determine the behavior of the drops injected into this idealized chamber, we must formulate equations for (1) the rate of drop evaporation, and (2) the frictional interaction (drag) between the drops and the gas flow. In addition, we need equations to express the conservation of mass, momentum, and energy for the gas-liquid mixture as a whole. Spalding has shown how differential equations that express these physical requirements can be formulated and integrated, using the following dimensionless variables:

$$\text{Drop size} \quad R = \frac{r}{r_0}, \quad (12.7)$$

$$\text{Gas velocity} \quad \omega = \frac{\rho u A_c}{\dot{m}}, \quad (12.8)$$

$$\text{Drop velocity} \quad \chi = \frac{\rho u_d A_c}{\dot{m}}, \quad (12.9)$$

$$\text{Axial distance} \quad \xi = \frac{x}{r_0^2} \frac{k}{c_p \rho_l} \frac{\rho A_c}{\dot{m}} \ln(1 + B), \quad (12.10)$$

$$\text{Drag} \quad \mathcal{S} = \frac{9}{2} \frac{c_p \mu}{k B}, \quad (12.11)$$

in which r = local drop radius, r_0 = initial drop radius, u = gas velocity, u_d = drop velocity, ρ = gas density, ρ_l = liquid density, \dot{m} = total mass flow through the chamber, A_c = chamber cross-sectional area, k = thermal conductivity, and μ = viscosity. The variable B is defined by

$$B = \frac{c_p(T_0 - T_f)}{h_{fg}},$$

in which c_p = specific heat of gas, T_0 = gas stagnation temperature, T_f = saturation temperature of liquid, and h_{fg} = heat of vaporization of the liquid.

Representative results of Spalding's calculations are displayed in Fig. 12.10 for the typical value of $\mathcal{S} = 0.5$, showing the effect of variation of initial injection velocity χ_0 . Since gas is formed only by liquid evaporation, the gas velocity u is zero at entrance to the chamber. Hence the drops are initially decelerated by the slower-moving gas and then accelerated as the gas velocity increases. Of particular interest is the value of $\xi = \xi_2$, at which the drop vanishes ($R \rightarrow 0$), since this determines the chamber length theoretically required for complete combustion.

Spalding concluded that the required chamber length could be correlated with droplet injection velocity and the drag parameter by the equation

$$\xi_2 = \frac{\chi_0 + 3\mathcal{S}/10}{2 + \mathcal{S}} \quad (12.12)$$

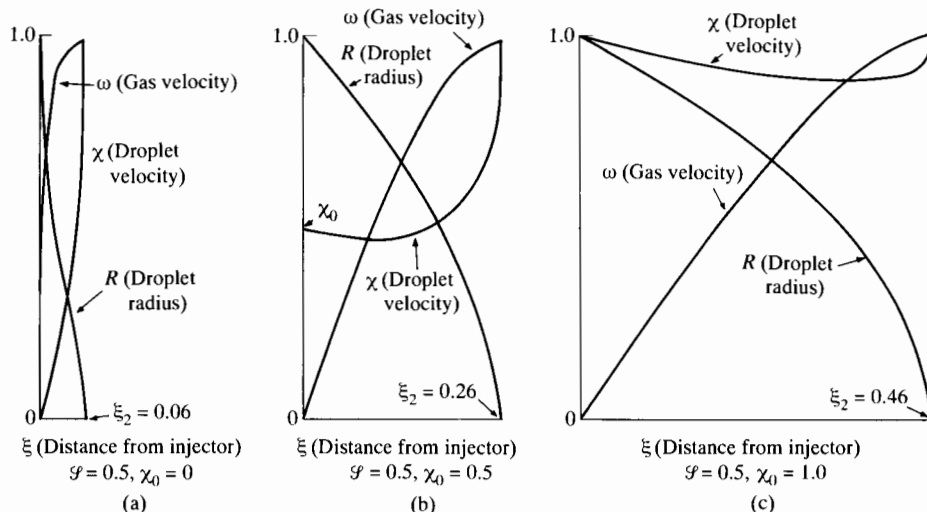


FIGURE 12.10 Effect of initial drop size on dimensionless combustor performance variables. Variation of χ , ρ , and ω (defined by Eq. (12.8) as a function of ξ for $\mathcal{G} = 0.5$. (Courtesy Spalding [10].)

or, taking L as the required chamber length,

$$L = r_0^2 \left(\frac{u_{d0} \frac{\rho A_c}{\dot{m}} + \frac{3g}{10}}{2 + g} \right) \frac{\dot{m}}{A_c} \frac{\rho_l}{\rho} \frac{c_p}{k} \frac{1}{\ln(1 + B)}. \quad (12.13)$$

Here we see the strong dependence of required chamber length on initial droplet radius and on chamber flow rate, as well as on the physical properties of the propellant. The importance of droplet velocity depends on the value of \mathcal{L} . Writing

$$\frac{\rho A_c}{\dot{m}} = \rho_0 \frac{A_c}{A^*} \frac{A^*}{\dot{m}}$$

and using the choked-flow formula, we can estimate this quantity as

$$\frac{\rho A_c}{\dot{m}} = \frac{A_c}{A^*} \frac{1}{\sqrt{\gamma R T_0}} \left(\frac{\gamma + 1}{2} \right)^{(\gamma+1)/2(\gamma-1)}$$

Thus we could write Eq. (12.13) as

$$L = r_0^2 \left[\frac{u_{d0}}{\sqrt{\gamma R T_0}} + \frac{3}{\Gamma} \left(\frac{A^*}{A_c} \right) \frac{\mathcal{G}}{10} \right] \frac{c_p \rho_l}{k} \frac{\sqrt{\gamma R T_0}}{\ln(1+B)} \frac{1}{(2+\mathcal{G})}, \quad (12.14)$$

in which

$$\Gamma = \left(\frac{\gamma + 1}{2} \right)^{(\gamma+1)/2(\gamma-1)}.$$

To estimate the quantity $3/\Gamma(A^*/A_c)\mathcal{S}/10$, we can deduce from the discussion below as well as from Table 11.4 that $A_c/A^* = 3$ is reasonable for a high-performance liquid-propellant rocket chamber. Using $\gamma = 1.2$, we have $\Gamma = 1.7$, so that we could write Eq. (12.14) as

$$L = r_0^2 \frac{\left[\frac{u_{d0}}{\sqrt{\gamma RT_0}} + \frac{\mathcal{S}}{17} \right]}{2 + \mathcal{S}} \frac{c_p \rho_l}{k} \frac{\sqrt{\gamma RT_0}}{\ln(1 + B)}. \quad (12.15)$$

For a hydrogen-oxygen mixture with $T_0 = 3000$ K, molecular weight MW = 8, and $\gamma = 1.2$, we find that $\sqrt{\gamma RT_0} \approx 2000$ m/s. Since a maximum reasonable droplet velocity will be around 100 m/s (with high-pressure injection), the term $\mathcal{S}/17$ is likely to be of the same order of magnitude as $u_{d0}/\sqrt{\gamma RT_0}$.

As an example we take the following numbers:

$$\mathcal{S} = 0.5$$

$$\frac{k}{\rho_l c_p} \ln(1 + B) = 2 \times 10^{-7} \text{ m}^2/\text{s},$$

$$\sqrt{\gamma RT_0} = 2000 \text{ m/s},$$

$$u_{d0} = 100 \text{ m/s},$$

$$r_{d0} = 50 \times 10^{-6} \text{ m},$$

and find from Eq. (12.12) that the required chamber length is $L = 0.8$ m. This is of the same order of magnitude as for the rockets of Table 11.4. This does not, of course, show that we have here a quantitatively exact theory, the input numbers chosen above being rather uncertain. It does suggest, though, the importance of initial drop size (r_{d0}) and injection velocity u_{d0} . It therefore suggests directions in which to move in attempting to minimize combustion chamber length. It also encourages effort to develop a more exact mathematical model applicable to a specific combustion chamber and propellant.

The size of the combustion chamber is usually sufficient to permit the attainment of near-equilibrium product composition. The average residence time Δt of a fluid element in a chamber is given by

$$\Delta t = \frac{\rho_0 \mathcal{V}_0}{\dot{m}} = \frac{\rho_0 A_c L}{\dot{m}},$$

in which \mathcal{V}_0 is the combustion chamber volume and ρ_0 is the average gas density in the chamber. For choked nozzles Eq. (3.14) shows that

$$\frac{\dot{m}}{A^*} = \frac{p_0 \sqrt{\gamma}}{\sqrt{RT_0}} \left(\frac{2}{\gamma + 1} \right)^{(\gamma+1)/2(\gamma-1)}.$$

Thus the transit time Δt can be related to propellant properties and to L by

$$\Delta t = \frac{L}{\sqrt{\gamma RT_0}} \left(\frac{\gamma + 1}{2} \right)^{(\gamma+1)/2(\gamma-1)} \left(\frac{A_c}{A^*} \right).$$

Again, assuming $L = 1$ m, $\sqrt{\gamma RT_0} = 2000$ m/s, and $\gamma = 1.2$, we can estimate $\Delta t = 3$ ms, which is long compared with typical chemical reaction times at combustion temperature.

Chamber Cross-Sectional Area

The elementary rocket analysis given in Chapter 11 assumes constant-pressure combustion. Within actual combustion chambers there may be an appreciable drop in both static and stagnation pressure between the injector end and the nozzle end of the chamber. This pressure drop is due primarily to the equivalent “heat” addition, and it increases with increasing Mach number within the chamber. An accurate calculation of combustion pressure drop would be difficult even for a geometrically simple combustion chamber, because of the complex fluid dynamic and chemical phenomena involved. However, we can easily obtain an approximate estimate of the pressure drop and its dependence on Mach number for a constant-area combustion chamber by using the relationships developed in Chapter 3. Returning to the combustion chamber of Fig. 12.9, we rewrite Eq. (3.18) as

$$\frac{p_{02}}{p_{01}} = \frac{1 + \gamma M_1^2}{1 + \gamma M_2^2} \left\{ 1 + [(\gamma - 1)/2] M_2^2 \right\}^{\gamma(\gamma-1)}. \quad (3.16)$$

Also the static pressure ratio p_2/p_1 is

$$\frac{p_2}{p_1} = \frac{1 + \gamma M_1^2}{1 + \gamma M_2^2}.$$

At the injector the Mach number will be very low. Thus, for $M_1 \ll 1$, we rewrite these equations as

$$\frac{p_{02}}{p_{01}} = \frac{\{1 + [(\gamma - 1)/2] M_2^2\}^{\gamma(\gamma-1)}}{1 + \gamma M_2^2} \quad \text{and} \quad \frac{p_2}{p_1} = \frac{1}{1 + \gamma M_2^2}. \quad (12.16)$$

If we assume that the flow in the exhaust nozzle is isentropic, M_2 is determined by the area contraction ratio A_c/A^* , in accordance with Eq. (3.15):

$$\frac{A_c}{A^*} = \frac{1}{M_2} \left[\frac{2}{\gamma + 1} \left(1 + \frac{\gamma - 1}{2} M_2^2 \right) \right]^{(\gamma+1)/2(\gamma-1)}. \quad (3.15)$$

Figure 12.11 indicates the Mach numbers and pressure ratios derived from this equation and Eq. (12.16) as a function of the contraction ratio A_c/A^* for a propellant of $\gamma = 1.2$. Typical combustion chamber cross sections are also indicated in

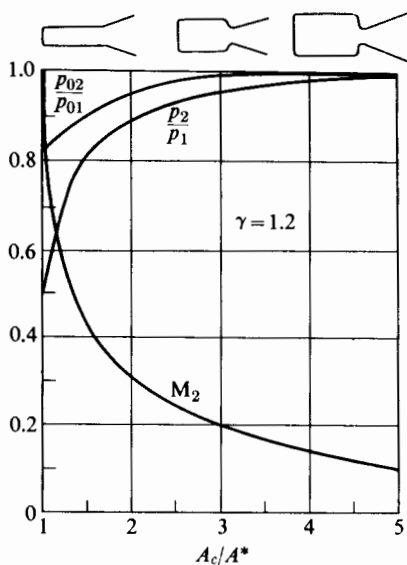


FIGURE 12.11 Variation of static and stagnation pressure ratios and Mach number with contraction ratio for $\gamma = 1.2$. A_c = chamber cross-sectional area.

Fig. 12.11. Although straight combustion chambers ($A_c/A^* = 1$) have been used, the contraction ratio is more typically 3 (see Table 11.1).

12.6 SOLID PROPELLANTS

Solid propellants contain all the elements necessary for their combustion. Two types of solid propellant are distinguished, according to the distribution of fuel and oxidant. If fuel and oxidant are contained within the same molecule, the propellant is called *homogeneous*. Double-base propellants, combinations of nitroglycerin-nitrocellulose [$C_3H_5(NO_2)_3-C_6H_7O_2(NO_2)_3$] with small quantities of additives, are the most common example of homogeneous solid propellants.

Table 12.3 gives the composition of a typical double-base propellant, along with the functions of the various ingredients. The potassium salt promotes smooth burning at low temperatures, and the diethyl phthalate serves as an auxiliary plasticizer to improve mechanical properties. Ethyl centralite is added to counteract the autocatalytic decomposition of the major constituents. Such decomposition, if unchecked, could lead to self-ignition of the propellant. The carbon black is added to the nearly transparent propellant to prevent the transmission of radiant energy, which might cause internal ignition around internal voids or impurities. The candelilla wax is added to propellants formed by an extrusion process. In some cases metallic powders such as aluminum have been added, along with additional oxidizer of the composite type, to achieve higher performance.

TABLE 12.3 Typical Double-Base Propellant (JPN)

Material	Weight %	Purpose
Nitrocellulose (13.25%N)	51.40	Polymer
Nitroglycerin	42.93	Explosive plasticizer
Diethyl phthalate	3.20	Nonexplosive plasticizer
Ethyl centralite	1.00	Stabilizer
Potassium sulfate	1.20	Flash suppressor
Carbon black (added)	0.20	Opacifying agent
Candelilla wax (added)	0.07	Die lubricant

Source: Courtesy Geckler and Klager [11].

Heterogeneous mixtures of oxidizing crystals in an organic plasticlike fuel binder are called *composite* propellants. Oxidizers usually consist of ground crystals of one of the following:

- Ammonium perchlorate (AP)
- Ammonium nitrate (AN)
- Nitronium perchlorate (NP)
- Potassium perchlorate (KP)
- Potassium nitrate (KN)
- Cyclotrimethylene trinitramine (RDX)
- Cyclotetramethylene tetranitramine (HMX)

The binder that contains the oxidizer crystals serves as fuel and must withstand severe thermal and mechanical stress without cracking. Binders are mainly made of synthetic rubbers. A commonly used binder is hydroxyl terminated polybutadiene (HTPB).

Figure 12.12 shows the effect of oxidizer concentration on flame temperature, molecular weight, and specific impulse for the oxidizers named above. RDX and HMX are effectively a stoichiometrically balanced fuel-oxidant combination, so maximum flame temperature is associated with 100% oxidizer.

Figure 12.13 shows the flame temperature and specific impulse that can be obtained with double-base propellant composition

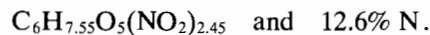


Figure 12.14 shows the flame temperature and specific impulse for a double-base propellant to which various amounts of ammonium perchlorate (AP) have been added. The term AP-CMDB denotes ammonium perchlorate-composite modified double-base propellant.

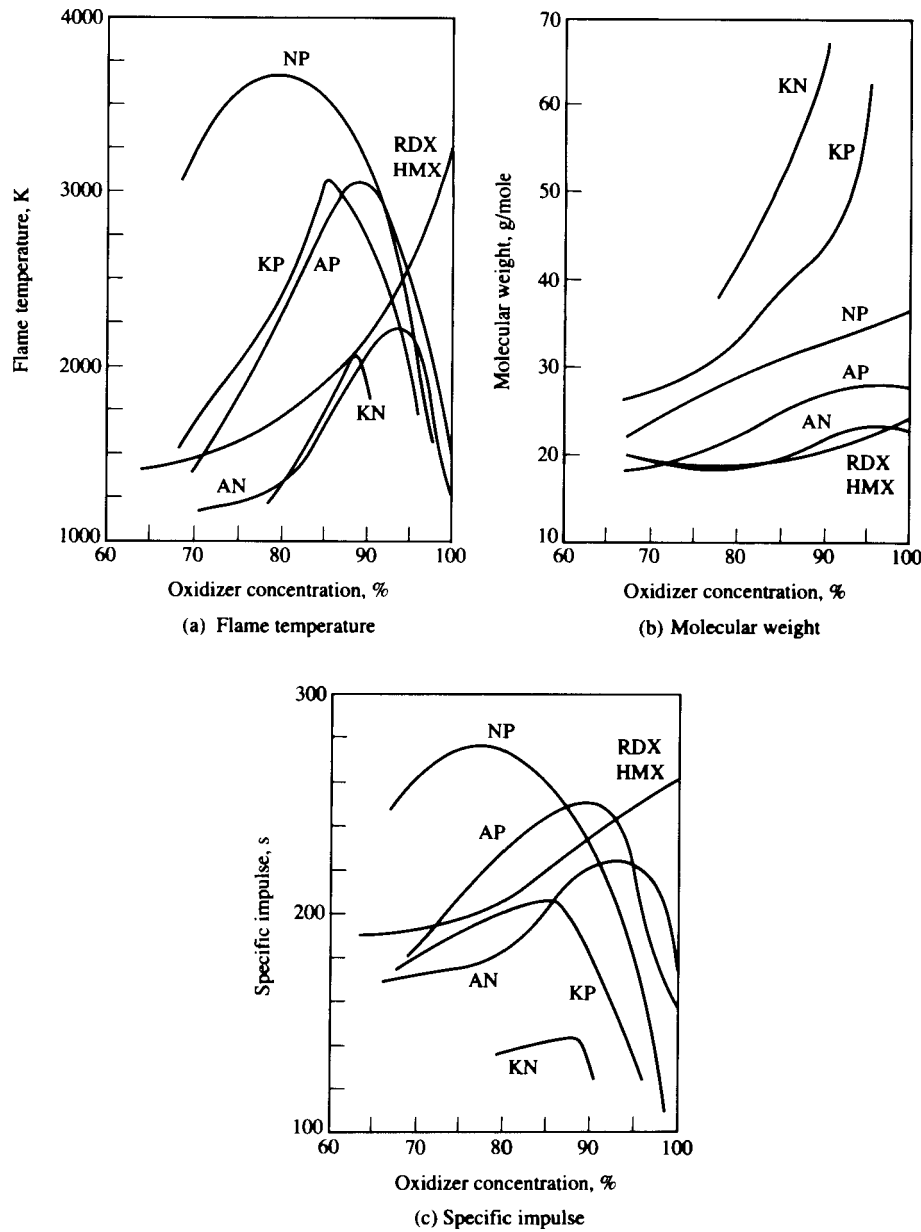


FIGURE 12.12 HTPB-based composite propellants. (Courtesy Kubota [12].)

Burning Rates

Figure 12.15 shows the burning rates of RDX with various amounts of polyurethane binder. Note that none of these solid propellants achieves a specific impulse exceeding 300 s.

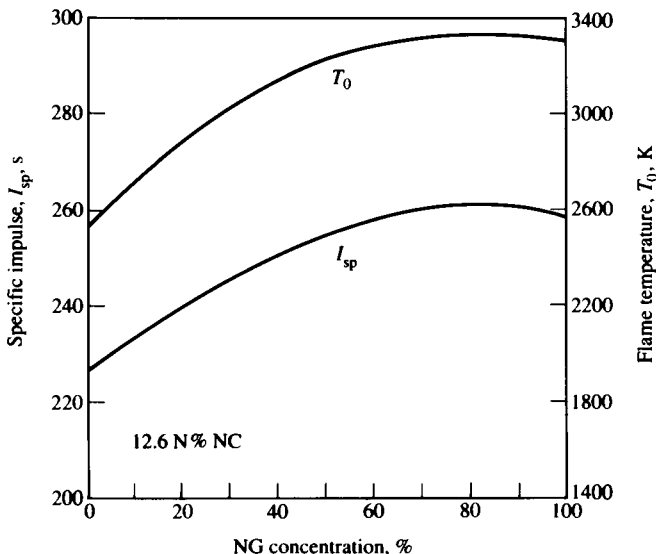


FIGURE 12.13 Specific impulse and flame temperature versus nitroglycerin concentration of double-base propellants. (Courtesy Kubota [12].)

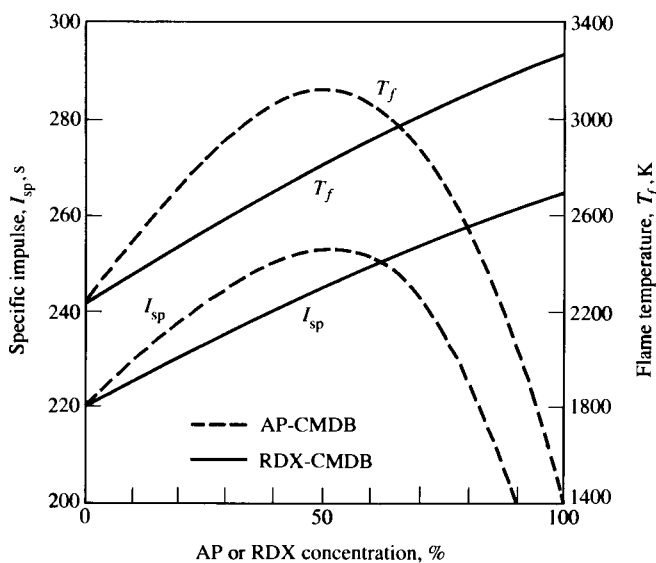
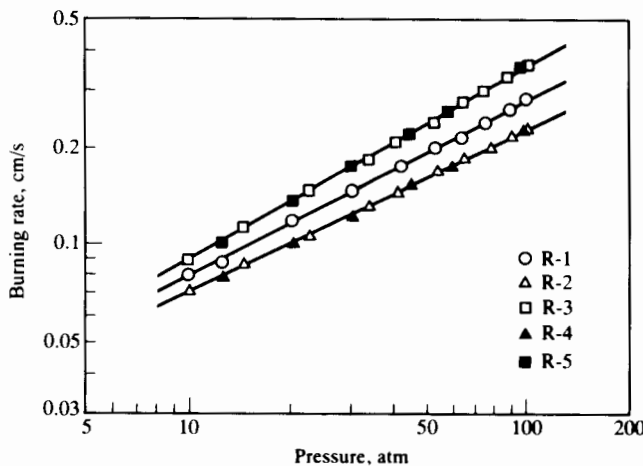


FIGURE 12.14 Specific impulse and flame temperature versus AP or RDX concentration of AP-CMDB and RDX-CMDB propellants. (Courtesy Kubota [12].)



Prop.	RDX	PU [†]	d_L/d_S^{++}
R-1	80.0	20.0	7/3
R-2	75.0	25.0	7/3
R-3	85.0	15.0	7/3
R-4	75.0	25.0	3/7
R-5	85.0	15.0	3/7

[†] Polyurethane binder: HO – (– CH – CH₂ – O –)_n – H, n = 34.
 $\begin{array}{c} | \\ \text{CH}_3 \end{array}$

⁺⁺ d_L/d_S denotes the mixture ratio of large-and small-sized RDX particles: $d_L = 120 \mu\text{m}$ and $d_S = 2 \mu\text{m}$.

FIGURE 12.15 Burning rate characteristics of RDX composite propellants. (Courtesy Kubota [12].)

Metal Powders

Metal powders can be added to solid propellants to increase specific impulse and fuel density. Metals that have been used or considered include aluminum, magnesium, boron, zirconium, and beryllium. Commonly they are randomly mixed with the other ingredients in particle size ranges of 10 to 40 μm . During burning, aluminum particles tend to coalesce at the burning surface into aggregates as large as 50 to 200 μm . Gany, Caveny, and Summerfeld [13] measured a mean Al_2O_3 agglomerate size of 250 μm . The most successful experience has been with aluminum powders that constitute 12% to 22% of the total propellant mass [14]. With the optimum concentration of metal powders, one can expect considerable two-phase pressure loss in the nozzle.

Table 12.4 shows the equilibrium concentrations associated with a solid propellant consisting of 15% aluminum, 73% ammonium perchlorate oxidizer (AP),

TABLE 12.4 Equilibrium composition of reaction products of a typical aluminized solid propellant (15% Al, 12% PBAN binder, 73% AP)

Species	Molecular weight	Mole fraction at 6.9 MPa	Mass fraction at 6.9 MPa	Mole fraction at 0.10 MPa	Mass fraction at 0.10 MPa
Al ₂ O ₃	102	0.0725	0.3110	0.0794	0.3205
CO	28	0.1923	0.2264	0.1889	0.2093
CO ₂	44	0.0270	0.0497	0.0391	0.0681
Cl	17	0.0188	0.0134	0.0026	0.0017
H	1	0.0365	0.0015	0.0042	0.0002
HCl	18	0.1412	0.1069	0.1748	0.1245
H ₂	2	0.1826	0.0154	0.1967	0.0156
H ₂ O	18	0.2078	0.1573	0.2227	0.1586
N ₂	28	0.0870	0.1024	0.0915	0.1014
OH	17	0.0206	0.0147	—	—
Other	—	0.014	0.0009	—	—

Source: Courtesy Price [14].

and 12% PBAN (copolymer of butadiene, acrylic acid, and acrylonitrile) binder. The table shows that after expansion to low pressure, all the aluminum in the equilibrium composition is in the form of Al₂O₃ and constitutes 32% of the total mass flow rate.

Many questions remain to be answered concerning the chemical and physical behavior of powdered-metal fuel additives. There is considerable evidence, however, that they can lead to oxide particles large enough that their velocity and temperature may differ considerably from the velocity and temperature of the gas with which they are transported through the nozzle. It therefore becomes important to think about how the presence of large particles in the nozzle might affect specific impulse and thrust.

Two-Phase Flow

We begin by considering a kind of "frozen-flow" model in which the particles are formed within the combustion chamber, there being no subsequent formation or growth of particles within the nozzle. Under such conditions the mass flow rates of solid (or liquid) and gaseous materials, \dot{m}_s and \dot{m}_g , respectively, are constant throughout the nozzle, as shown in Fig. 12.16. When we apply the general momentum relation, Eq. (2.4), to the incremental control volume of Fig. 12.16, the result is

$$-A dp = \dot{m}_s(u_s + du_s) + \dot{m}_g(u_g + du_g) - \dot{m}_s u_s - \dot{m}_g u_g, \quad (12.17)$$

where u_s = particle velocity and u_g = gas velocity. From continuity we see that

$$\dot{m}_s = \rho_s A u_s, \quad \dot{m}_g = \rho_g A u_g, \quad (12.18)$$

where ρ_s = solid density (mass of solid material per unit volume of mixture) and ρ_g = gas density.

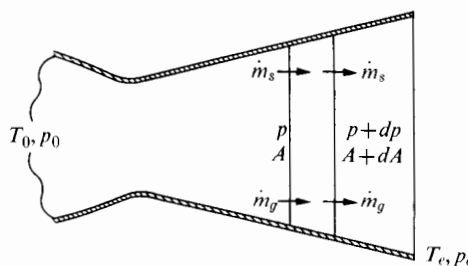


FIGURE 12.16 Incremental control volume for the development of two-phase flow equations.

Combining Eqs. (12.17) and (12.18), we obtain

$$-dp = \rho_s u_s du_s + \rho_g u_g du_g. \quad (12.19)$$

The energy equation for steady adiabatic flow relates the particle and gaseous enthalpies and kinetic energies according to

$$\dot{m}_s(c_s dT_s + u_s du_s) + \dot{m}_g(c_p dT_g + u_g du_g) = 0, \quad (12.20)$$

where T_s = temperature of solid material,

T_g = temperature of gaseous material,

c_s = specific heat of solid,

c_p = specific heat at constant pressure of gas.

If we define X as the fraction of total mass flow in solid (or liquid) form, then $1 - X$ is the gaseous fraction, and we can write Eq. (12.15) as

$$X c_s dT_s + (1 - X) c_p dT_g + X u_s du_s + (1 - X) u_g du_g = 0. \quad (12.21)$$

From Eq. (12.19) we obtain

$$u_g du_g = -\frac{dp}{\rho_g} - \frac{\rho_s}{\rho_g} u_s du_s,$$

and, from the definition of $X = \rho_s u_s / (\rho_g u_g + \rho_s u_s)$,

$$u_g du_g = -\frac{dp}{\rho_g} - \frac{X}{1 - X} u_g du_s.$$

Substituting this expression in Eq. (12.21), we have

$$\frac{X}{1 - X} c_s dT_s + c_p dT_g + \frac{X}{1 - X} (u_s - u_g) du_s = \frac{dp}{\rho_g}. \quad (12.22)$$

In general, the solution of this equation requires knowledge of heat transfer and drag processes in order to express T_s and u_s in terms of overall flow properties. However, one can obtain four limiting solutions quite easily for the following extremes of behavior: (1) The heat transfer may be very fast, $T_s \approx T_g$, or (2) very

slow, $T_s \approx \text{constant}$. (3) The particle drag may be very high, $u_s \approx u_g$, or (4) very low, $u_s \approx \text{constant}$.

For example, consider the case $T_s = T_g = T$, $u_s = u_g = u$. Then Eq. (12.22) reduces to

$$\left(\frac{X}{1-X} c_s + c_p \right) dT = \frac{dp}{\rho_g}.$$

Assuming that the gas behaves as a perfect gas, we have

$$\rho_g = \frac{p}{RT} \quad \text{and} \quad \left\{ \frac{[X/(1-X)]c_s + c_p}{R} \right\} \frac{dT}{T} = \frac{dp}{p}.$$

Integrating from stagnation (combustion chamber) conditions, T_0 and p_0 , to exhaust conditions, T_e and p_e , we obtain

$$\frac{T_e}{T_0} = \left(\frac{p_e}{p_0} \right)^n \quad \text{where } n = \frac{R}{[X/(1-X)]c_s + c_p}.$$

For these conditions Eq. (12.21) becomes

$$[Xc_s + (1-X)c_p]dT + u du = 0,$$

which may be integrated to give the exhaust velocity in terms of T_0 and T_e . There results

$$u_e = \sqrt{2[Xc_s + (1-X)c_p]T_0[1 - (p_e/p_0)^n]}, \quad (12.23)$$

in which, as before,

$$n = \frac{R}{[X/(1-X)]c_s + c_p}.$$

If for simplicity we consider the case $c_p = c_s$, the only difference the particles would make to the expansion would be to change the effective value of n from

$$n = \frac{\gamma - 1}{\gamma} \quad \text{to} \quad n = \frac{\gamma - 1}{\gamma}(1 - X),$$

and Eq. (12.23) would become

$$u_e = \sqrt{2c_p T_0[1 - (p_e/p_0)^n]}.$$

This would mean that for a given pressure ratio p_e/p_0 , the temperature ratio $(p_e/p_0)^n$ would be higher. Thus the specific impulse predicted by Eq. (12.18) would be lowered by the presence of even very fine particles whose velocities and temperatures are essentially identical to those of the adjacent gas.

For a second example, suppose that $T_s = \text{constant}$ and $u_s = \text{constant}$. In this case Eq. (12.22) becomes

$$c_p dT_g = \frac{dp}{\rho_g}.$$

Proceeding as above, we obtain the familiar relationship

$$\frac{T_{eg}}{T_{0g}} = \left(\frac{p_e}{p_0} \right)^{(\gamma-1)/\gamma}$$

and, from Eq. (12.21), the exhaust gas velocity is

$$u_{eg} = \sqrt{2c_p T_0 [1 - (p_e/p_0)^{(\gamma-1)/\gamma}]}.$$

In this case the gas velocity is not affected by the presence of the solid particles. However, the specific impulse is reduced. If several constituents are present, we can write the specific impulse as

$$I_{sp} = \frac{1}{g_e} \frac{\sum \dot{m}_i u_{ei}}{\sum \dot{m}_i},$$

in which i denotes a particular constituent. Considering the case $\dot{m}_s u_{es} \ll \dot{m}_g u_{eg}$, $T_s = T_0$,

$$I_{sp} \cong \frac{1}{g_e} (1 - X) u_{eg},$$

where u_{eg} is independent of the presence of the particles. Thus the effect of the particles is to reduce the specific impulse by the factor $1 - X$.

The other two combinations of T_s and u_s variations may be found by similar developments of Eqs. (12.21) and (12.22). If we know the gas exhaust velocity and the fraction of solid material, we can calculate the effect of particle behavior on specific impulse (for an assumed u_s if $u_s \neq u_g$). For example, consider the following typical conditions:

$$T_0 = 2780 \text{ K}, \quad \text{mol wt} = 25, \quad \gamma = 1.2, \quad c_s = 2.09 \text{ kJ/kg} \cdot \text{K},$$

$$p_0 = 54.4 \text{ atm}, \quad p_e = 1 \text{ atm}, \quad X = 0.1.$$

The following table indicates the effect of the particles on specific impulse under these limiting conditions. In those cases where the particles were not accelerated, their momentum flux was neglected in the calculation of thrust (that is, $\dot{m}_s u_s \ll \dot{m}_g u_g$). We can see that the mere presence of the particles brings about a significant loss (since the condensed material does not expand in the nozzle). The velocity lag of nonaccelerated particles accounts for a substantial additional loss of specific impulse. Beyond this, however, note that the presence or absence of fluid-particle heat transfer is of little importance. In practice we observe that the thermal lag of the particles is greater than the velocity lag, but, as expected, its influence on performance is small. The effect of the velocity lag can be substantial, however.

	Accelerated particles		Nonaccelerated particles		
	No particles present	Complete heat transfer	No heat transfer	Complete heat transfer	No heat transfer
I_{sp}	236	$u_s = u_g,$ $T_s = T_g$	$u_s = u_g,$ $T_s = \text{const}$	$u_s \approx 0,$ $T_s = T_g$	$u_s \approx 0,$ $T_s = \text{const}$
	228	224	216	213	

Thus the benefits of higher propellant energy and higher flame temperature can be offset to some extent by what may be called the two-phase flow loss in the nozzle. These elementary analyses serve only to indicate the character of the two-phase flow loss. References 15 and 16 describe detailed flow calculation methods for transonic and supersonic flows with entrained solid particles. These methods require detailed accounting of the drag and heat transfer interaction between gas and particle flows. Valentine [17] has tabulated a variety of particle Nusselt number and drag coefficient correlations for use in evaluating these effects.

12.7 SOLID-PROPELLANT COMBUSTION CHAMBERS

The combustion chamber of a solid-propellant rocket is essentially a high-pressure tank containing the entire solid mass of propellant, or *grain*, as it is called. Combustion proceeds from the surface of the grain. The rate of generation of gaseous propellant is, of course, equal to the rate of consumption of solid material. Hence it is given by

$$\dot{m}_g = \rho_p A_b r, \quad (12.24)$$

where \dot{m}_g = gas generation rate, mass per unit time,

ρ_p = solid propellant density,

A_b = area of burning surface,

r = surface recession rate, length per unit time.

The surface recession rate r , called the *burning rate*, is an empirically determined function of the propellant composition and certain conditions within the combustion chamber. These conditions include propellant initial temperature, combustion pressure, and the velocity of the gaseous combustion products over the surface of the solid. Figure 12.15 illustrates the burning rates of propellants as a function of pressure and initial temperature in the absence of appreciable gas velocity. These curves can be approximated by

$$r = ap_0^n, \quad (12.25)$$

where a and n are constants for any one curve and p_0 is the pressure within the combustion chamber. The pressure exponent n , associated with the slope of the curves in Fig. 12.15, is almost independent of propellant temperature. The coefficient a is a function of initial propellant temperature T_p , but not a function of pressure. As a rough approximation one can express a as

$$a = \frac{A}{T_1 - T_p}, \quad (12.26)$$

where T_1 and A are empirical constants. Other equations, for example,

$$r = c + bp_0^n,$$

have been used to describe burning rates of certain propellants. Subsequently we will discuss a correction for the so-called erosive burning associated with high gas velocities over the solid surface.

Combustion Pressure

Both the rate of mass flow through the nozzle \dot{m}_n and the gas generation rate \dot{m}_g are strongly dependent on the combustion chamber pressure p_0 , which in turn depends on the mass M_s of gas within the chamber.

The gas generation rate \dot{m}_g is given by Eqs. (12.24) and (12.25). The rate of increase of gas “stored” within the combustion chamber is

$$\frac{dM_s}{dt} = \frac{d}{dt}(\rho_0 V_0),$$

where ρ_0 is the instantaneous gas density in the chamber and V_0 is the instantaneous gas volume. Considering the recession of the burning surface, $dV_0/dt = rA_b$, so that

$$\frac{dM_s}{dt} = \rho_0 r A_b + V_0 \frac{d\rho_0}{dt}.$$

The rate at which gas flows through the nozzle is given by Eq. (3.14):

$$\dot{m}_n = \frac{p_0}{\sqrt{RT_0}} \sqrt{\gamma} \left(\frac{2}{\gamma + 1} \right)^{(y+1)/2(y-1)} A^*. \quad (3.14)$$

Conservation of mass requires the balance

$$\dot{m}_g = \frac{dM_s}{dt} + \dot{m}_n \quad \text{or} \quad \rho_p A_b r = \rho_0 A_b r + V_0 \frac{d\rho_0}{dt} + \dot{m}_n.$$

Using Eqs. (12.25) and (3.14), we obtain

$$\rho_p A_b a p_0'' = \rho_0 A_b a p_0'' + V_0 \frac{d\rho_0}{dt} + \frac{p_0}{\sqrt{RT_0}} \sqrt{\gamma} \left(\frac{2}{\gamma + 1} \right)^{(y+1)/2(y-1)} A^*. \quad (12.27)$$

The density derivative may be expressed as

$$\frac{d\rho_0}{dt} = \frac{1}{RT_0} \frac{dp_0}{dt},$$

since T_0 is practically independent of changes in combustion pressure for typical solid propellants. Equation (12.27) may then be written

$$\frac{V_0}{RT_0} \frac{dp_0}{dt} = A_b a p_0'' (\rho_p - \rho_0) - \sqrt{\frac{\gamma}{RT_0}} \left(\frac{2}{\gamma + 1} \right)^{(y+1)/(y-1)} A^* p_0. \quad (12.28)$$

If the combustion pressure remains constant, the left-hand side of this equation vanishes, and therefore we may determine p_0 from

$$p_0 = \left[\frac{A_b}{A^*} \frac{a(\rho_p - \rho_0)}{\sqrt{\frac{\gamma}{RT_0} \left(\frac{2}{\gamma+1} \right)^{(\gamma+1)/(\gamma-1)}}} \right]^{1/(1-n)}. \quad (12.29)$$

Generally one may neglect ρ_0 in Eq. (12.29), since it is much less than ρ_p .

For constant p_0 (and hence constant thrust), it is clear that the burning area A_b must remain constant. Even if the burning area is not constant, however, the left-hand term of Eq. (12.28) may be negligible compared with the other terms, so that the instantaneous stagnation pressure is given by Eq. (12.29), in which A_b is the instantaneous burning area. The variation of A_b with time depends on the burning rate and the initial geometry of the propellant grain. Geometric variations can provide increasing thrust (*progressive* burning), constant thrust (*neutral* burning), or decreasing thrust (*regressive* burning) with time. Figure 12.17 indicates several internal-burning sections, along with their subsequent partially burned shapes and their resultant thrust histories. High-thrust rockets, requiring large A_b , are usually of the internal-burning type. Lower thrust may be provided by solid cylindrical grains that burn only on the end surface.

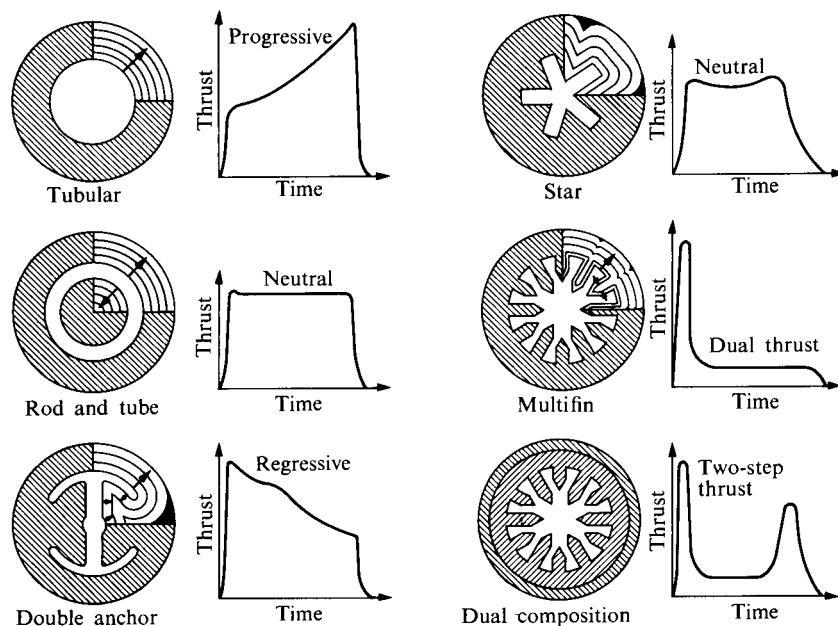


FIGURE 12.17 Internal-burning charge designs with their thrust-time programs. (Courtesy Shafer [18].)

Burning Stability

The burning-rate exponent n must be less than unity for stable combustion, as we can demonstrate by the following simple argument. Neglecting the relatively small gas storage terms, nozzle flow rate and gas generation rate must be equal. Equation (3.14) shows that the nozzle gas flow rate is directly proportional to p_0 . We have also seen that the gas generation rate is proportional to p_0^n . Figure 12.18 indicates typical curves of nozzle flow rate and gas generation rate versus pressure. Two gas generation rate curves, one for $n < 1$ and one for $n > 1$, are shown, both having the same operating point with the given nozzle. Consider a small decrease from the operating-point pressure. We can see that for $n < 1$ the resultant gas generation rate will then exceed the nozzle flow rate, and thus the chamber pressure will return toward the original value. For $n > 1$, any small decrease in chamber pressure means that nozzle flow rate will exceed the gas generation rate, and the pressure will drop even further. Thus for $n > 1$, small disturbances are amplified and the combustion cannot be stable. Hence for stable combustion n must be less than unity. Typical values of burning-rate exponent n for solid propellants are in the range $0.4 < n < 0.7$.

The variation of burning rate r with temperature, indicated in Fig. 12.15 and accounted for by an equation of the form of Eq. (12.24), can seriously alter the performance of a given rocket under different firing-temperature conditions. For example, Fig. 12.19 indicates the time variation of chamber pressure for three different initial temperatures. The thrust histories would be similar to the pressure histories since, from Eq. (11.7), thrust is proportional to p_0 . However, since at constant T_0 the mass flow rate will also be proportional to p_0 , the thrust *duration* will be *inversely* proportional to p_0 . Hence the total impulse, $\int T dt$, will be practically constant, as will the area under the above p_0-t curves, regardless of propellant temperature. However, excessive variation of burning rate can have serious consequences. If it is too high, excessive vehicle acceleration or chamber failure can occur. If it is too low, insufficient thrust may prevent satisfactory performance, especially for operation within a gravity field. Efforts have been made

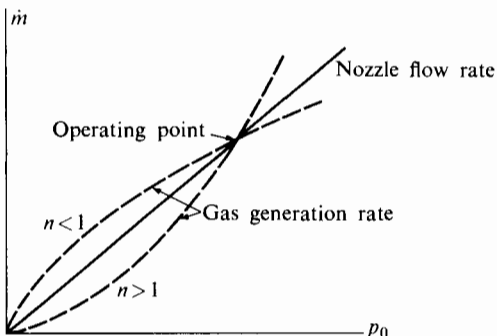


FIGURE 12.18 Stability argument for solid-propellant combustion.

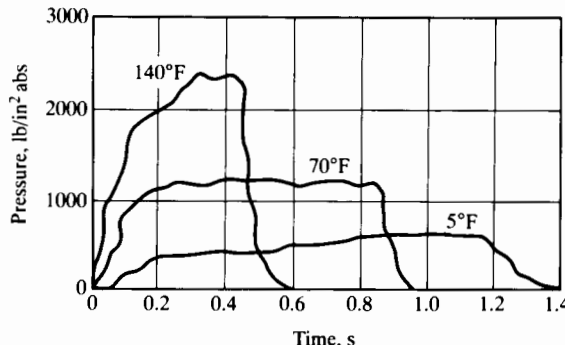


FIGURE 12.19 The variation of chamber pressure with time for a 9-lb cruciform, semirestricted-burning, ballistite-grain, 3.25-in. rocket motor. (Courtesy Huggett, Bartley, and Mills [19].)

to reduce this temperature-sensitive behavior; Cohen and Flanagan [20] have reviewed work on this subject.

The sensitivity of burning rate to propellant temperature at constant pressure, Π_r , is defined as

$$\Pi_r = \frac{1}{r} \left(\frac{\partial r}{\partial T_p} \right)_{p_0}. \quad (12.30)$$

Since the temperature variation of r is contained in a , Eq. (12.26) gives

$$\Pi_r = \frac{1}{r} \left(\frac{\partial r}{\partial T_p} \right)_{p_0} = \frac{1}{a} \frac{da}{dT_p} = -\frac{1}{T_1 - T_p}. \quad (12.31)$$

Thus as T_p approaches the empirical constant T_1 , the burning rate becomes very temperature sensitive. Propellants should have high values of T_1 relative to their expected operational temperatures.

The variation of equilibrium pressure with initial temperature, shown in Fig. 12.19 is also of importance. From Eq. (12.29) we can see that if n approaches unity, the pressure can become an extremely sensitive function of initial temperature, through the factor $a^{1/(1-n)}$. We may express the dependence of the chamber pressure p_0 on the propellant temperature T_p as

$$\Pi_p = \frac{1}{p_0} \left(\frac{\partial p_0}{\partial T_p} \right)_{A_b/A^*, T_0}. \quad (12.32)$$

Differentiation of Eq. (12.29) yields

$$\Pi_p = \frac{1}{1-n} \frac{1}{a} \frac{da}{dT_p} = \frac{1}{1-n} \Pi_r.$$

Thus the sensitivity of chamber pressure to grain temperature is greater than the sensitivity of burning rate to grain temperature by the factor $1/(1-n)$. Hence, in addition to high T_1 , a desirable propellant should have low n . As mentioned before, n must be less than unity for stability.

Erosive Burning

The surface-combustion process is a complex interaction that requires heat transfer from the combustion products to the solid material to bring about vaporization and perhaps decomposition of the solids. As in more conventional heat transfer processes, high fluid velocity over the surface can substantially increase the heat transfer rate. Although the phenomena occurring in solid-propellant combustion are complicated by the outflow of mass from the solid surface, it is observed that burning rate increases with increased combustion-product velocity. This effect is called *erosive burning*, although it seems that the increased heat transfer is much more important than any actual erosion of the solid material. The increased burning rate can be accounted for by a variety of empirical corrections of the form

$$r = r_0(1 + k_1 u), \quad r = r_0(1 + k_2 \rho u),$$

or

$$r = r_0, \quad u < u_0, \quad r = r_0[1 + k_3(u - u_0)], \quad u > u_0,$$

in which r is the burning rate at gas velocity u and r_0 , u_0 , k_1 , k_2 , and k_3 are empirical constants. The velocity u_0 may be thought of as a threshold value below which no appreciable erosive effect occurs.

Within the void space of an internal-burning grain the gas velocity varies appreciably, and it is actually zero only at the head end of the grain. As a result the burning rate can vary significantly along the grain length, thus complicating the grain design problem. It is desirable to have the grain burning completed instantaneously along its entire length, since nonuniform burn-through may reduce the chamber pressure enough to extinguish combustion before all the propellant is consumed. Even if combustion did not cease, the prematurely exposed chamber wall could fail because of overheating.

Nonuniform burning rates may be compensated for by simultaneous axial variations of the flow area and the thickness and shape of the grain. In one design the effect of erosion is made uniform by increasing the port (gas flow) area in the flow direction, thus tending to reduce the variations in gas velocity. The propellant web thickness (burning-path length) may be maintained constant by varying the shape of the void cross section or by varying the outside diameter of the grain. In another design the web thickness is increased near the nozzle end of the chamber to compensate for the greater burning rate there. This may result in decreased port area and further increased erosive burning effects. Rather long and thin grains have been constructed in this manner.

The relatively continuous variation of burning characteristics with variation of combustion chamber conditions is subject to certain limitations. Investigators have observed that for very low chamber pressures combustion becomes very unsteady or ceases altogether. The pressure at which this occurs is called the *combustion limit* of a particular propellant. There is also an upper *pressure limit*, above which combustion again becomes erratic and unpredictable. For most propellants this is above 30 MPa (5000 psi) [19]. Variation of propellant mechanical

properties with temperature places limits on the temperatures at which solid-propellant rockets may be stored and fired. For example, at high temperature the propellants may tend to flow or "slump," especially if stored for a considerable time. At low temperature the propellant may become brittle and crack, exposing a much larger burning surface than intended.

As in the liquid-propellant combustion chamber, there is a pressure drop along the axis of the combustion chamber, a drop that is necessary to accelerate the increasing mass flow of gas out of the void space. The axial variation of pressure may offset to some extent the uneven erosive burning due to axial variations in gas velocity. Figure 12.20 illustrates an incremental control volume within a typical internal-burning propellant grain. In addition to the changes in pressure, velocity, and area, there is an incremental increase in mass flow rate $d\dot{m}$ over the length of the control volume. Neglecting the effect of wall friction on the gas flow, the momentum equation (Eq. 2.4) may be used for this control volume to obtain

$$-A dp = \dot{m} du + u d\dot{m} = d(\dot{m}u). \quad (12.33)$$

Integrating from $x = 0$, $p = p_1$, to any position x where the static pressure is p yields

$$p_1 - p = \int_{x=0}^x \frac{d(\dot{m}u)}{A}, \quad (12.34)$$

and for the special case, $A \approx \text{constant}$,

$$p_1 - p = \frac{(\dot{m}u)_x}{A}. \quad (12.35)$$

Since $u = \dot{m}/\rho A$, where ρ is the gas density, Eq. (12.35) becomes

$$p_1 - p = \frac{1}{\rho} \left(\frac{\dot{m}}{A} \right)^2. \quad (12.36)$$

If the port area and shape do not vary with x , and if the compensating effects of pressure variation and erosive burning have negligible net effect on local gas generation rate, then

$$\dot{m} = cr\rho_p x,$$

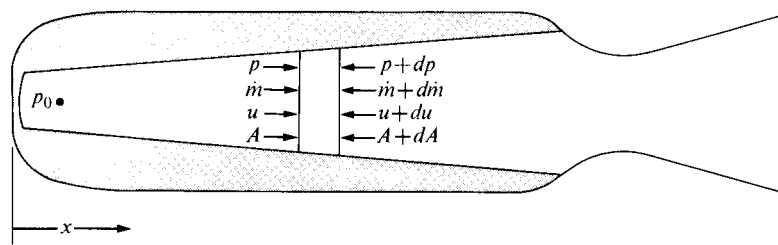


FIGURE 12.20 Incremental control volume for the calculation of pressure drop within a solid-propellant combustion chamber.

where c is the port circumference and ρ_p the propellant (solid) density. Using this approximation and the perfect-gas law in combination with Eq. (12.36) gives us

$$\frac{p}{p_1} = \frac{1}{2} \left[1 + \sqrt{1 - 4RT \left(\frac{cr\rho_p x}{p_1 A} \right)^2} \right]. \quad (12.37)$$

As a further approximation, one may assume that the axial variation in temperature is negligible while using Eq. (12.37) to estimate the axial variation in pressure.

Figure 12.21 illustrates this distribution of pressure and Mach number along a cylindrical port 0.3 m in diameter, for typical propellant properties. As burning proceeds and the port area increases, axial variations of both pressure and gas velocity decrease.

Early solid-propellant grains were often molded or extruded prior to being inserted into the combustion chamber. The grain was then held in place within the combustion chamber by suitable, and sometimes relatively complex, support structures. There were several disadvantages to this practice. The support structure, which had to withstand combustion temperatures, represented undesirable inert mass. In most such configurations a part, if not all, of the chamber walls was directly exposed to combustion temperatures. For a given combustion pressure this necessitated relatively heavy chamber walls. In many cases the reduced grain thickness near the end of combustion resulted in mechanical failure of the grain, with subsequent erratic or destructive burning.

The stress loading of a propellant grain can be quite complex. The axial pressure distribution, viscous shear from the gas flow, and vehicle acceleration all tend to move the propellant toward the nozzle. Opposing these forces is the support system or wall shear force for the case-bonded grain. The resultant bulging of the propellant near the nozzle may reduce the port area, thus accentuating pressure and viscous forces. For a given configuration and propellant there may be a critical Young's modulus for the propellant, below which bulging and pressure rise continue until the chamber bursts. Reference [19] treats this problem in detail.

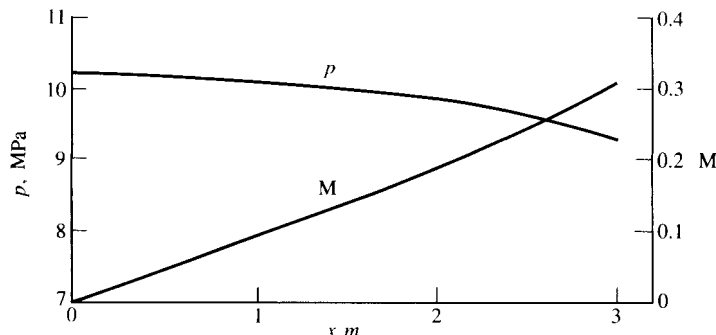


FIGURE 12.21 Variation of pressure according to Eq. (12.35) for a cylindrical port 0.3 m in diameter; typical propellant properties.

The modern tendency has been to use internal-burning case-bonded grains, as illustrated in Fig. 12.17. In this configuration the grain is bonded directly to the chamber wall, or perhaps to a thin layer of inert material (inhibitor) that is itself bonded to the wall. The primary advantage of this design is that the propellant itself serves as an insulator, enabling the chamber walls to remain relatively cool throughout their operation (provided the propellant does not prematurely burn through locally). Much lighter combustion chambers are thus possible, since no internal structures are necessary and thinner walls are permissible. A much higher fraction of the total chamber volume (greater than 80% as opposed to about 65% for separately formed grains) may be filled with propellant, and the grain remains adequately supported right up to burnout. Very large grains may be constructed by casting directly in the combustion chamber, although extremely large grains may require internal support elements.

The solid-propellant rocket motors (SRM) of the space shuttle (shown in Fig. 10.10) have four sections of casing-bonded grain, the sections being connected by flexible joints with seals to contain the high pressure of the combustion gas. It was the failure of one of these seals that led to the tragic destruction, little more than a minute after liftoff, of the vehicle of the space shuttle *Challenger* mission 51-C. The presidential commission of enquiry, whose report [21] points to both technical and managerial deficiencies, concluded that "a combustion gas leak through the right SRM aft field joint initiated at or shortly after ignition eventually weakened or penetrated the External Tank, initiating vehicle structural breakup and loss of the Space Shuttle Challenger during STS Mission 51-C." The leak was due to the failure of an O ring seal, at unusually low ambient temperature and under the influence of dynamic loading associated with liftoff, which allowed combustion gas to escape in a hot high-speed jet pointed at the external tank. This led to the failure of the tank and the destruction of the vehicle, and to the deaths of the astronauts in a fiery explosion.

12.8 COMBUSTION INSTABILITIES

Both liquid- and solid-propellant rocket engines are sometimes subject to combustion instabilities in the form of large pressure oscillations within the chamber. Such instabilities can cause engine failure either through excess pressure, increased wall heat transfer, or a combination of the two. Instabilities are especially a danger to the larger rockets. When instability is encountered, it is usually necessary to take corrective measures on the full-scale engine itself, since one cannot often observe similar behavior on smaller-scale models. Hence experimental study is quite difficult and expensive, and once a "fix" has been found, experimentation often ceases. For these reasons, and also because of the extreme complexity of the problem, rocket combustion instabilities cannot be said to be fully understood.

Instabilities occurring within liquid-propellant combustion chambers may be divided into at least two distinct categories. Low-frequency (less than 100 cycles

per second) oscillations, often called *chugging*, result from a coupling between the combustion process and the feed system. Qualitatively it can be explained as follows: Suppose the chamber pressure were to rise instantaneously above the steady-state value. This would be followed by a decrease in rate of delivery of the propellant. This in turn would bring about a decrease in chamber pressure and an increase in pump delivery pressure, followed by an increase in rate of delivery of the propellant, an increased chamber pressure, and so on. A self-sustaining oscillation is therefore possible, depending on the dynamic behavior of the system components. Chugging is relatively well understood and easily corrected. Usually a greater injector pressure drop, tending to make chamber pressure oscillations small relative to pump-delivery pressure, will eliminate chugging in a given rocket. This, of course, requires higher pump pressure and power, so that an arbitrarily large injector pressure drop is undesirable.

High-frequency oscillations (of the order of thousands of cycles per second), often called *screaming*, are not so well understood. They are usually associated with one or more of the acoustic vibration modes within the chamber: longitudinal, radial, transverse, or tangential. Ordinarily such vibrational motion of the propellant would be damped by viscous effects as well as carried out through the nozzle. However, if the combustion process is pressure sensitive, a mechanism of nonuniform energy release is available that can maintain the oscillations. Such energy release must occur in the proper place and at the proper time relative to the pressure oscillations if it is to feed energy to the oscillating propellants. Hence changes in combustion pattern—as produced, for example, by small modifications of the injector—can mean the difference between stable and unstable operation. With the possibility of so many vibrational modes, it is not at all simple to determine which corrective action is called for. Screaming, unlike chugging, can occur entirely within the combustion chamber and with essentially steady inlet conditions.

A third or intermediate frequency range has been described in which pressure oscillations within the chamber interact with the injector-spray pattern but not with the propellant-delivery rate or system.

Solid-propellant rockets are also subject to a nonuniform pattern of energy release since, as we have seen, the combustion rate is influenced by propellant pressure and velocity. It is possible that the energy release and the propellant velocity and/or pressure pattern that causes nonuniformity can interact to produce sustained oscillations. Such oscillations produce high rates of erosive burning that may change the combustion geometry to a stable one rapidly enough to avoid damage, or they may lead to engine failure. Investigators have found that placing an irregular rod of nonburning material within the burning volume, or drilling radial holes at intervals along the grain, can reduce instabilities. The rod or the combustion gases issuing from the radial holes tend to break up the wave patterns within the burning gases.

Reference 17 summarizes the experience of instability with liquid-propellant rockets, and Reference 22 contains an extensive discussion of the instabilities of solid-propellant combustion.

PROBLEMS

1. The results of calculations with the STANJAN code show that the equilibrium composition resulting from a mixture of 1 kg N₂H₄ and 0.92 kg O₂ at 3410 K and 6.89 MPa has the mole fractions shown in Table 12.2. Given the following values of the equilibrium constant K_p at 3410 K, check whether the stated mole fractions are approximately consistent with these values.

$$K_{p1} = \frac{p_{\text{O}_2}^{1/2} p_{\text{H}_2}}{p_{\text{H}_2\text{O}}} = 0.151 \text{ atm}^{1/2}$$

$$K_{p2} = \frac{p_{\text{H}} p_{\text{O}_2}^{1/2}}{p_{\text{H}_2\text{O}}} = 0.061 \text{ atm}^{1/2}$$

$$K_{p3} = \frac{p_{\text{OH}} p_{\text{H}_2}^{1/2}}{p_{\text{H}_2\text{O}}} = 0.207 \text{ atm}^{1/2}$$

$$K_{p4} = \frac{p_{\text{O}}^2}{p_{\text{O}_2}} = 0.144 \text{ atm}$$

$$K_{p5} = \frac{p_{\text{NO}}^2}{p_{\text{N}_2} p_{\text{O}_2}} = 0.0340 \text{ atm}^0$$

$$K_{p6} = \frac{p_{\text{N}}^2}{p_{\text{N}_2}} = 1.9 \times 10^{-8} \text{ atm}$$

2. The results of calculations with the STANJAN code show that the equilibrium composition resulting from a mixture of 1 kg of RP1 fuel (composition given by CH_{1.96}) and 2.58 kg of O₂ at 3676 K and 6.89 MPa has the mole fractions shown in Table 12.2. Given the following values of the equilibrium constant K_p at 3676 K, check whether the stated mole fractions are approximately consistent with these values.

$$K_{p1} = \frac{p_{\text{O}_2}^{1/2} p_{\text{H}_2}}{p_{\text{H}_2\text{O}}} = 0.295 \text{ atm}^{1/2}$$

$$K_{p2} = \frac{p_{\text{H}}^2}{p_{\text{H}_2}} = 0.740 \text{ atm}$$

$$K_{p3} = \frac{p_{\text{OH}} p_{\text{H}_2}^{1/2}}{p_{\text{H}_2\text{O}}} = 0.44 \text{ atm}^{1/2}$$

$$K_{p4} = \frac{p_{\text{CO}} p_{\text{O}_2}^{1/2}}{p_{\text{CO}_2}} = 2.42 \text{ atm}^{1/2}$$

$$K_{p5} = \frac{p_{\text{O}}^2}{p_{\text{O}_2}} = 0.559 \text{ atm}$$

3. A mixture of 5 kg O₂ and 1 kg H₂ has the composition shown in Table 12.2 at 3429 K and 6.89 MPa. Figure 12.3 shows that with correct expansion to

0.1 MPa the mixture can develop a specific impulse of 402 s with shifting equilibrium. If the mixture composition had been frozen throughout the expansion, determine how much the specific impulse would have been (for the same pressure ratio).

The molecular weight of the mixture may be obtained from the original composition. The average value of the specific-heat ratio for the mixture may be calculated at 2000 K from the formulas for specific heat given in Table 1 of Appendix II for H₂, O₂, and H₂O. For OH take $\gamma = 1.3$; for O and H assume $\gamma = 1.67$.

4. Given the mixture composition for 5 kg O₂ and 1 kg H₂ shown in Table 12.2 at 3429 K and 6.89 MPa, set up a procedure for deducing the mixture composition at the same temperature but at 20 MPa from this information. First derive two equations for the unknown mole fractions of H₂ and H₂O. If time permits, implement your solution procedure with a computer.
5. Consider the possibility of using finely powdered carbon and oxygen as propellant in a rocket motor. Suppose the carbon (solid) and oxygen (gaseous) both enter the combustion chamber at 25°C, and that the chamber pressure is to be 100 atm (10.13 MPa).
 - a. If dissociation were unimportant, what would be the adiabatic flame temperature of a stoichiometric carbon-oxygen mixture?
 - b. If the oxygen and carbon are supplied to the chamber in the molar ratio 2:1 and the mixture contains only CO₂, CO, and O₂, determine the mixture temperature and composition. The specific heats may be approximated as

	\bar{C}_p kJ/kmol
CO ₂	60
CO	62
O ₂	42

The equilibrium constant defined by

$$K_p = \frac{p_{CO}^2 p_{O_2}}{p_{CO_2}}$$

can be approximated by

$$\ln K_p = 19.458 - \frac{65,040}{T},$$

where T is in K.

6. The products of combustion of a stoichiometric combination of carbon and oxygen are at 100 atm (10.13 MPa) and 5000 K. Determine the equilibrium composition of the products under the assumption that the dissociation O₂ ⇌ 2O is of negligible importance.

Taking into account the dissociation of CO_2 into CO and O_2 , use the same thermodynamic property approximations as in Problem 12.5.

Determine also the specific impulse for expansion to 1 atm with no change of mixture composition.

7. Because of its high density relative to hydrogen, liquid methane as a rocket fuel offers the advantage of smaller tank size and mass than would be required for hydrogen. Methane (CH_4) has a heat of formation Q_f of -74.873 kJ/gmol . It is to be used in a rocket thrust chamber at a pressure of 50 atm (5.07 MPa). It enters the chamber at 250 K with an enthalpy ($\bar{h} - \bar{h}_{25^\circ\text{C}}$) of -2.15 kJ/gmol . The oxidant is O_2 , which enters the chamber at 25°C .

For the products of combustion of a stoichiometric combination of CH_4 and O_2 at 50 atm, the compositions at 3800 K are as follows:

Mole fractions								
H_2O	CO_2	O_2	H_2	O	H	OH	CO	
0.3792	0.1021	0.0800	0.0733	0.0393	0.0421	0.1194	0.1646	

Would the adiabatic flame temperature be above or below 3800 K? At 3800 K the enthalpy differences of the products ($\bar{h} - \bar{h}_{25^\circ\text{C}}$ kJ/gmol) are: H_2O : 171.724, CO_2 : 202.999, O_2 : 130.629, H_2 : 119.064, CO: 123.495. For O and H assume $\gamma = 1.67$; for OH $\gamma = 1.33$.

8. Table 12.2 gives the equilibrium composition of the products of combustion of the hydrazine-oxygen reaction (0.92 kg N_2H_4 :1 kg O_2) at 3410 K and 1000 psia (6.8 MPa). Suppose the mixture expands adiabatically to 1000 K, at which temperature the H_2 , OH, O, H, N, NO, and NO_2 have essentially disappeared. Determine the exhaust velocity. To simplify calculations, take $\gamma = 1.3$ for all constituents.
9. Show that one can write Eq. (12.15), for the predicted chamber length for full droplet evaporation, as

$$L = \frac{r_0^2 \left[\frac{u_{d0}}{\sqrt{\gamma R T_0}} + \frac{9}{34} \frac{\text{Pr}}{B} \right]}{\left[2 + \frac{9}{2} \frac{\text{Pr}}{B} \right]} \frac{\sqrt{\gamma R T_0}}{\nu} \left(\frac{\rho_l}{\rho} \right) \frac{\text{Pr}}{\ln(1 + B)},$$

in which $B = c_p(T_0 - T_f)/h_{fg}$ and ν and $\text{Pr} = \mu c_p/k$ are the kinematic viscosity and Prandtl number of the combustion gas, while ρ_l/ρ is the ratio of liquid and gas densities.

Estimate the minimum chamber length required for a hydrazine rocket in which droplets are injected with a velocity of 60 m/s and a mean droplet diameter of 50 μm . The chamber temperature and pressure are 3000 K and 10 MPa, respectively. The physical properties of the products of the gaseous products of combustion are

$$\text{Pr} = 0.7,$$

$$\text{Mol wt} = 30,$$

$$\gamma = 1.2,$$

$$\nu = 2 \times 10^{-6} \text{ m}^2/\text{s}.$$

The density of the liquid droplets is $\rho_l = 700 \text{ kg/m}^3$. The heat of vaporization of the liquid hydrazine h_{fg} and T_f may be taken as 750 kJ/kg and 275 K, respectively.

As a rough approximation, doubling the gas injection velocity will reduce mean droplet size by a factor of 2. What would be the effect on L of doubling u_{d0} under the above conditions?

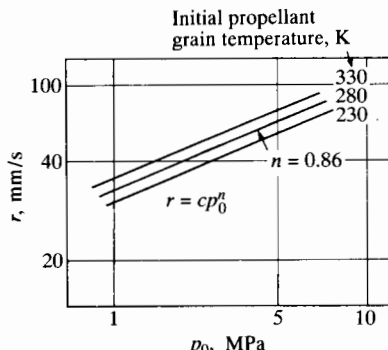
10. The estimates of reduction in static pressure drop and stagnation pressure drop that are shown in Fig. 12.11 are based on the ideas that the effect of combustion on the gas dynamics can be simulated by simple heating and that the cross-sectional area of the combustor is constant.

Suppose that the cross-sectional area of the combustor is 20% larger at the downstream end than at the droplet injector end and that the axial distribution of combustion (“heating”) rate is such that the static pressure varies linearly with chamber flow area. How would these assumptions affect the locations of the curves shown in Fig. 12.11?

11. Using the burning-rate data for propellant R-5 shown in Fig. 12.15, determine the ratio of burning area to throat area required for a steady combustion pressure p_0 of 7 MPa and a combustion temperature T_0 of 2500 K. The propellant density is $\rho_p = 1900 \text{ kg/m}^3$. The combustion gas specific heat ratio γ is 1.25; the molecular weight is 20.5.

If the burning-area ratio A_b/A^* were to increase from the value determined above by 0.7% per second, how long would it take for the chamber pressure to double?

12. A certain solid propellant burns at a rate shown in the figure. It is being used in a rocket combustion chamber in which the stagnation pressure is approximately constant at 3.5 MPa. The initial grain temperature is 280 K. Suddenly a large crack develops in the propellant grain, which increases the burning area by 10%. What will happen to the chamber pressure? If the gas temperature, chamber volume, burning area, and throat area were known, show how the pressure transient could be calculated.

**PROBLEM 12**

13. The grain in a solid propellant rocket is a hollow cylinder bonded to the casing so that it burns only on its inner cylindrical surface and on one end. Its density is 1650 kg/m^3 , and its burning rate is characterized by $r = 13.3 (p_0 \text{ MPa})^{0.63} \text{ mm/s}$. At a point in the burning period when $p_0 = 0.7 \text{ MPa}$, the grain $d/D = 0.4$ and $L/D = 6$, L being the grain length and d and D being its inner and outer diameters. Determine the rate of change of chamber pressure, assuming the gas temperature stays constant at 2750 K and that the gas specific heat ratio is $\gamma = 1.24$. $D = 1 \text{ m}$.
14. The diameter of the hollow core of a solid-propellant grain remains axially uniform during burning. Its length is 5 m , and initially its inner diameter is 0.37 m ; the outer diameter of the grain is 0.82 m . The burning rate r is 1.2 cm/s , which as a first approximation may be assumed uniform over the entire inner surface of the grain. The grain density is 1875 kg/m^3 . The combustion chamber pressure and gas temperature downstream of the grain are 2.17 MPa and 2580 K , respectively. Neglecting the effects of friction, estimate, at the beginning and end of combustion,
- The static pressure ratio p_2/p_1 along the length of the grain;
 - The Mach number M_2 at the downstream end of the grain.
- The gas specific heat ratio and molecular weight are 1.2 and 20 .
15. A mixture of very small solid particles and a perfect gas expands adiabatically through a given pressure ratio. The particles, which are some fraction μ of the total mass flow, are so small that they may be considered to have the same speed as the gas at all points in the flow. It may be assumed further that the relative volume of the solid material is negligible and that the specific heats of gas and solid are identical. (a) Assuming that during the expansion no heat transfer takes place between solid and gaseous phases, show that the presence of the solid particles reduces the exit velocity by the factor $\sqrt{1 - \mu}$. (b) Assuming that the solid particles always have the same temperature as the gas, show that the ideal exhaust velocity is given by

$$\frac{u}{u_{\mu=0}} = \sqrt{\frac{1 - (p_2/p_p)^{(1-\mu)(\gamma-1)/\gamma}}{1 - (p_2/p_1)^{(\gamma-1)/\gamma}}},$$

in which p_2/p_1 is the pressure ratio across this nozzle.

16. A rocket vehicle is to be designed for a single-stage solid-propellant thruster with constant acceleration of 3 g_e during the burning period and a specific impulse of 250 s. How should the propellant grain be designed to provide constant acceleration? Specify the required variation with time of the ratio of burning area to initial burning area. The burning period is 2 minutes.

As a first approximation suppose the exhaust velocity is not dependent on the chamber pressure. The combustion chamber temperature may be taken to be 2950 K, a constant, and the burning rate is the same as that of propellant R-5 shown in Fig. 12.15.

17. The burning rate of a particular propellant is given by $r = c/(T_1 - T)p_0^n$ in which r is in mm/s, p_0 is in MPa, T is in K and

$$c = 176,$$

$$T_1 = 415 \text{ K},$$

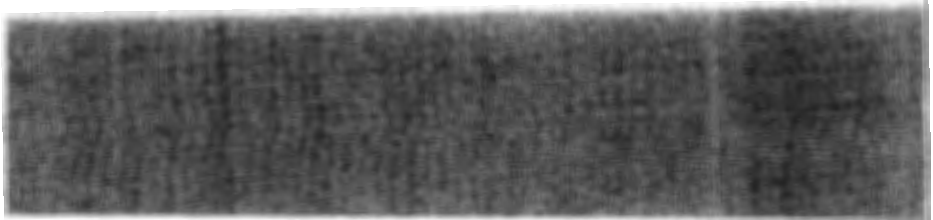
$$n = 0.716.$$

When the propellant initial temperature is 20°C , the chamber pressure is 3 MPa (steady) for 4 min. If the same propellant grain in the same rocket is heated to 45°C , what would be the new steady state pressure level and burning period. Assume the time required to reach steady state is small compared to the burning time.

REFERENCES

1. Sackheim, R. S. "Survey of Space Applications of Monopropellant Hydrazine Propulsion Systems," Tenth Inter. Symposium on Space Tech. and Science, Tokyo, 1973.
2. Sutton, G. P. *Rocket Propulsion Elements*. New York: Wiley, 1986.
3. Reynolds, W. C. "STANJAN: The Element Potential Method for Chemical Equilibrium Analysis," Version 3, Department of Mechanical Engineering, Stanford University, Palo Alto, Calif., Jan. 1986.
4. Olson, W. T. "Recombination and Condensation Processes in High Area Ratio Nozzles," *J. Amer. Rocket Soc.* 32 (1962): 672-680.
5. Timnat, Y. M. *Advanced Chemical Rocket Propulsion*. New York: Academic Press, 1987.
6. Taylor, A. A., and J. D. Hoffman. "Design of Maximum Thrust Nozzles for Nonequilibrium Chemically Reacting Flow," *AIAA J.* 12 (1974): 1299-1300.
7. Hoffman, J. D. "A General Method for Determining Optimum Thrust Nozzle Contours for Chemically Reacting Flows," *AIAA J.* 5 (1967): 670-676.
8. Bray, K. N. C. "Simplified Sudden Freezing Analysis for Non-Equilibrium Nozzle Flows," *J. Amer. Rocket Soc.* 31 (1961): 831-834.

9. Penner, S. S. *Chemical Rocket Propulsion and Combustion Research*. New York: Gordon and Breach, 1962.
10. Spalding, D. B. "Combustion in Liquid-Fuel Rocket Motors," *Aero. Quarterly* 10 (1959): 1-27.
11. Geckler, R. D., and K. Klager. "Solid Propellant Rocket Engines," in *Handbook of Aeronautical Engineering*, H. Koelle, ed. New York: McGraw-Hill, 1961.
12. Kubota, N. "Survey of Rocket Propellants and Their Combustion Characteristics," in *Fundamentals of Solid-Propellant Combustion*, K. Kuo and M. Summerfeld, eds., vol. 90 of *Progress in Astronautics and Aeronautics*. New York: AIAA, 1984.
13. Gany, A., L. H. Caveny, and M. Summerfeld. "Aluminized Solid Propellant Burning in a Rocket Motor Flowfield," *AIAA J.* 16 (1978): 736-739.
14. Price, E.W. "Combustion of Metallized Propellants," in *Fundamentals of Solid-Propellant Combustion*, K. Kuo and M. Summerfeld, eds., vol. 90 of *Progress in Astronautics and Aeronautics*. New York: AIAA, 1984.
15. Chapy, I. "One and Two-Phase Nozzle Flows," *AIAA J.* 18 (1980): 1455-61.
16. Regan, J. F., H. D. Thompson, and R. F. Hoglund. "Two-Dimensional Analysis of Transonic Gas Flows in Two-Dimensional Nozzles," *J. Spacecraft and Rockets* 8 (1971): 346-351.
17. Valentine, R. S. "Liquid Propellant Rocket Performance, Stability, and Compatibility," *J. Spacecraft and Rockets* 9 (1972): 304.
18. Shafer, J.I. "Solid Rocket Propulsion," in *Space Technology*, H.S. Seifert, ed. New York: Wiley, 1969.
19. Huggett, C., C.E. Bartley, and M.M. Mills. *Solid Propellant Rockets*. Princeton, N.J.: Princeton Aeronautical Paperbacks, Princeton University Press, 1960.
20. Cohen, N.S., and D.A. Flanagan. "Mechanisms and Models of Solid Propellant Burn Rate Temperature Sensitivity: A Review," *AIAA J.* 23 (1985): 1538-47.
21. Rogers, W.P. Report to the President on the Space Shuttle Challenger Accident, Washington, D.C., June 6, 1986.
22. Price, E.W. "Experimental Observations of Combustion Instability," in *Fundamentals of Solid-Propellant Combustion*, K. Kuo and M. Summerfeld, eds. vol. 90 of *Progress in Astronautics and Aeronautics*. New York: AIAA, 1984.



CHAPTER

13

TURBOMACHINERY FOR LIQUID-PROPELLANT ROCKETS

13.1 INTRODUCTION

The rates of supply of propellant for three well-known liquid-propellant rocket engines are as follows:

F1	(<i>Apollo Saturn II</i> first stage, LO ₂ -RP1)	2600 kg/s
SSME	(space shuttle main engine, LO ₂ -LH ₂)	468 kg/s
J2	(<i>Apollo Saturn II</i> second and third stages, LO ₂ -LH ₂)	250 kg/s

Not only are the propellant mass flow rates huge, but the delivered pressures are also very great, running as high as 55 MPa (8000 psia) for the SSME liquid-oxygen pump and 45 MPa (6500 psia) for the hydrogen pump. Added to these demands is the requirement that the turbomachinery be designed to have as little mass as possible. Table 13.1 shows the ratio of power to mass of the turbopumps for several liquid-propellant engines. At 100 hp per pound, the high-pressure fuel turbopump for the SSME surely holds the world record for power density. These few statistics are mentioned here to indicate what has happened in a very challenging field of engineering design.

Starting with the basic question of how to pressurize liquid propellants and deliver them to a rocket combustion chamber, we look at the two possibilities shown in Fig. 13.1. In the first of these, a gas such as helium or nitrogen is stored in a high-pressure tank, at pressure as high as 35 MPa (5000 psia). Through regulator valves this gas is transferred directly to the fuel and oxidizer tanks to push the propellants into the combustion chamber. The advantages of this system are

TABLE 13.1 Approximate power-to-weight ratios of turbopumps

Rocket	Liquid	Pressure rise		Power/weight	
		MPa	(psia)	kW/kg	(hp/lb)
H1	O ₂	9	(1300)	20	(12)
	RP1	6	(900)	20	(12)
F1	O ₂	14	(2000)	36	(22)
	RP1	10	(1500)	36	(22)
J2	H ₂	8	(1200)	41	(25)
	O ₂	6	(800)	15	(9)
J2S	H ₂	14	(2000)	50	(30)
	O ₂	10	(1400)	25	(15)
ASE	H ₂			80	(50)
	O ₂			50	(30)
SSME	H ₂	48	(7000)	160	(100)
	O ₂	60	(8500)	90	(53)

Source: Data from Stangeland [1].

its avoidance altogether of the need for turbomachinery and the simplicity of its piping and control. The great disadvantage is the need to design fuel and oxidant tanks (as well as the high-pressure gas supply) to withstand much-greater-than-combustion pressure. For large fuel consumption—that is, missions with large

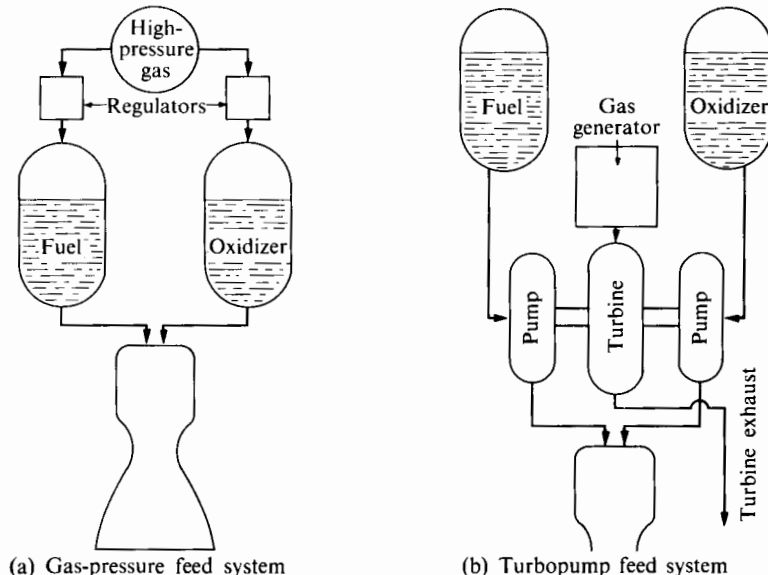


FIGURE 13.1 Propellant feed-system schematics. Control valves, check valves, safety devices, fill and drain systems, and so on, are not shown.

vehicle-velocity change Δu —the mass of the required tanks would be prohibitive. This would be especially so for a rocket used for launch from the surface of the earth, and for which combustion pressures are necessarily high to provide reasonable size for a large thrust requirement.

For space missions, thrust demands may be much lower, and considerably lower combustion pressures can be satisfactory. Hearn [2, 3] has explored the possibilities of gas-pressurized propellant supply for orbit adjustment and the like. It is possible that in such uses a “blowdown” system could be used in which the regulator valves shown in Fig. 13.1(a) would be replaced by solenoid valves that would be either closed or opened to allow a burst of thrust at a chamber pressure depending on the remaining quantities of propellant and pressurization gas. This idea would require the combustion chamber to operate satisfactorily through a range of combustion pressures, declining from perhaps 5 MPa (300 psia). Satisfactory ignition and combustion stability would have to be assured at all pressures.

For a given mission the vehicle payload ratio may be shown (by the methods outlined in Chapter 10) to depend significantly on the masses of engines, tanks, and turbomachinery. Figure 13.2 gives a typical representation of the way in which payload can depend on mission velocity increment for both gas-pressurization and turbopump systems. For mission velocity increments greater than, say, 3000 m/s, the relative payload advantage associated with turbopump systems is substantial.

Figure 13.3 shows three kinds of turbopump systems used for liquid-propellant rockets. The gas generator system shown in Fig. 13.3(a) takes fuel and oxidant (after being pressurized by the pumps) into a “gas generator” combustion chamber separate from the main chamber. The products of combustion in this small chamber are then used to drive the turbines before being exhausted to ambient pressure. In this case the pressure ratio across the turbine is very large, so that, with a small number of turbine stages (to minimize mass), one cannot expect very high turbine efficiency. For this kind of system one might expect to find op-

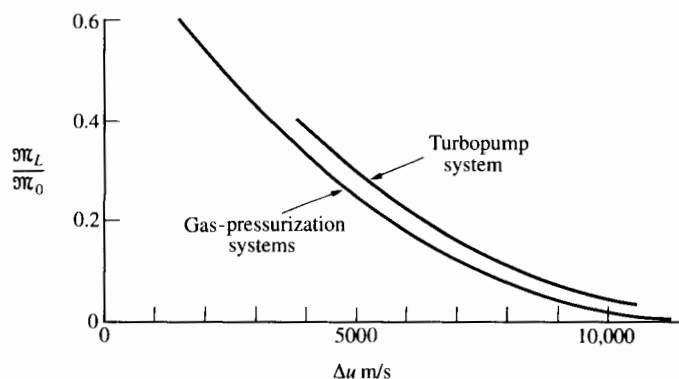


FIGURE 13.2 Payload ratio for typical pressurization and pump pressurization. (After Stangeland [1].)

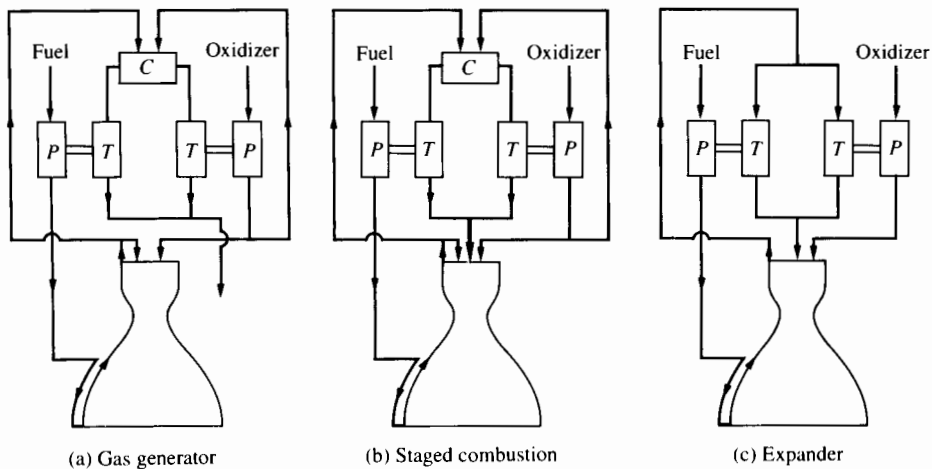


FIGURE 13.3 Turbopump systems for rockets; P = pump, T = turbine, and C = combustor.

timum combustion pressure to be at a moderate level. The J2 O₂-H₂ engine, which uses this system, has a combustion pressure of about 5.4 MPa (350 psia). The F1 rocket mentioned earlier also uses this type of propellant pressurization.

Figure 13.3(b) shows the staged-combustion system, which differs from the gas generator configuration only in that the turbine exhaust gases are fed into the main combustion chamber. The fuel-oxidizer ratio in the gas generator chamber need not be the same as in the main combustion chamber, and the turbine pressure ratio will typically be much less than for the gas generator case. The space shuttle main engine (SSME) uses this staged combustion arrangement, except that separate gas generators are used for the hydrogen and oxygen turbopumps. With gas generator pressures around 80 MPa (5000 psia) and an injector inlet pressure of 50.9 MPa (3286 psia), the turbine pressure ratio is modest, so that relatively high efficiency can be achieved in a two-stage turbine. The chamber pressure (46.6 MPa or 3006 psia) is much higher than appropriate for the concept of Fig. 13.3(a).

Figure 13.3(c) illustrates the “expander” configuration used in the RL10 O₂-H₂ rocket shown in Figs. 11.23 and 11.24. It has the great advantage of not requiring a separate gas generator combustion chamber, and uses all the propellants in the main combustion chamber. The work available from the hydrogen (heated while cooling the thrust chamber) is limited, so that in its optimum configuration this kind of system will have relatively low combustion pressure. The chamber pressure in the RL10 is only 2.7 MPa (174 psia). Using the figures shown in Table 11.1, one can show that the vacuum thrust per unit throat area for this engine is only about one-tenth the corresponding value for the SSME. From indicators such as these, we can see that choice of turbomachinery system configuration is strongly related to choice of combustion pressure and to the size of engine needed to produce a given thrust.

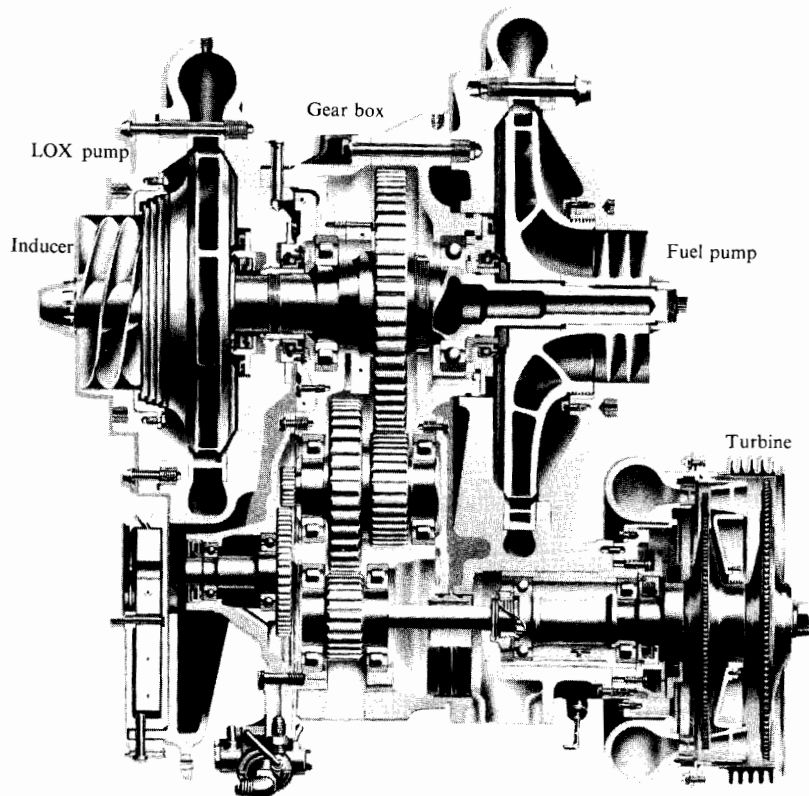


FIGURE 13.4 Rocketdyne Mark 3 turbopump. (Courtesy Rockwell International, Rocketdyne Division.)

Before considering turbomachine components in some detail, we look first at two specific turbopump systems.

Figure 13.4 shows the Rocketdyne Mark 3 turbopump, which has been used for over 30 years in several rocket vehicles and is still being produced; over 2500 of these units have been made so far. Table 13.2 gives its vital statistics. We take special note here of the following features:

1. Each pump consists of a single centrifugal stage preceded by an axial inducer running on the same shaft. Both pumps and inducers are thereby forced to operate at the same rpm.
2. The two-stage axial flow turbine runs at about 4.9 times the pump speed, and a substantial gear-reduction unit is needed.

Figure 13.5 shows, by way of contrast, a very different system. The oxygen and hydrogen inducers (not shown) are separated from their respective pumps and driven by different turbines at very different speeds. One may also see from Fig. 13.5 that, whereas only one centrifugal stage is used for the O₂ pump (and it

TABLE 13.2 Rocketdyne Mark 3 turbopump

Feature	Fuel	Oxidizer	Turbine
Propellant	RP1	O ₂	
Flow			
m ³ /s	0.138	0.198	
gpm	2188	3148	
Discharge pressure			
MPa	15.9	15.9	
psia	1025	1025	
rpm	6792	6792	33,178
Power			
hp		4432	
kW		3306	

delivers the highest pressure), the hydrogen pump has three centrifugal stages. Notably absent from Fig. 13.5 is any sign of a gear-reduction unit.

Table 13.3 shows the performance data for this turbopump system. The hydrogen turbopump absorbs 63,200 horsepower; avoiding the mass and durability problem of a gear transmission unit is a major advantage. The disadvantage is the provision of separate turbine drives for each of the inducers, which (as we will see) need to operate at much lower rpm than the turbines.

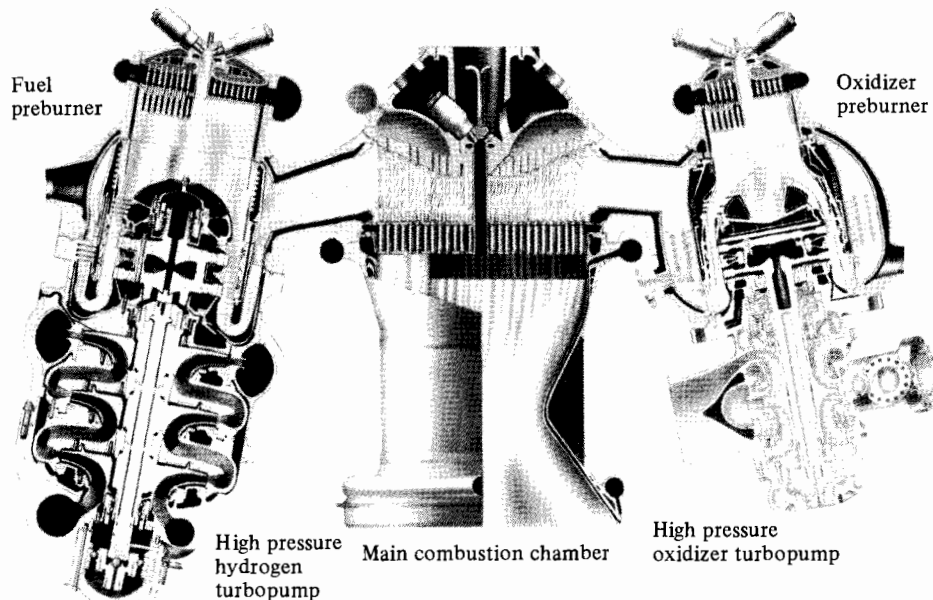
**FIGURE 13.5** SSME turbopumps. (Courtesy Rockwell International, Rocketdyne Division.)

TABLE 13.3 Rocketdyne SSME turbopumps

Feature	Hydrogen	Oxygen
Pump		
Number of stages	3	1
Flow rate		
kg/s	67.7	407
lb/s	149	896
gpm	15340	5660
Outlet pressure		
MPa	42.1	49.7
psia	6110	7211
rpm	34,386	27,263
Power, kW	49,200	19,600
Turbine		
Number of stages	2	2
Flow rate, kg/s	74.1	27.3
Pressure ratio	1.48	1.53
Inlet pressure, MPa	33.6	34.7
Inlet temperature, K	997	804

Preliminary consideration of Figs. 13.4 and 13.5 suggests the need to think about how to choose the best configuration (axial versus radial), the number of stages, and the best shaft speed for each inducer, pump, or turbine. These choices are so vital to the performance of a liquid-propellant engine that we look in this chapter at the characteristics of individual turbomachines. We begin with simplified analyses to point out the important phenomena, using experimental data to illustrate design limitations. Then we consider certain generalized performance correlations that can guide the designer in selecting turbomachine configurations, stage numbers, and speeds.

13.2 CENTRIFUGAL PUMPS

The power input \mathcal{P} to a centrifugal pump, if there is no swirl in the incoming flow, is given by an expression identical to that for a centrifugal compressor (see Chapter 9):

$$\mathcal{P} = \dot{m}U_2c_{\theta_2}, \quad (13.1)$$

where \dot{m} = fluid mass flow rate,

U_2 = impeller tip speed,

c_{θ_2} = tangential component of absolute fluid velocity leaving impeller tip.

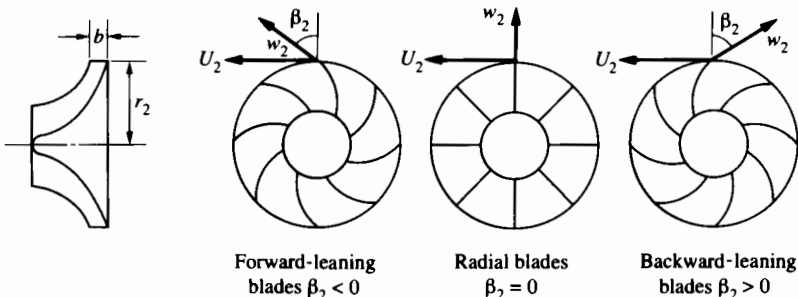


FIGURE 13.6 Centrifugal impellers.

For incompressible flow the tangential component of the fluid leaving velocity, c_{θ_2} , is rather easily related to the exit fluid angle and the impeller geometry. Thus, referring to Fig. 13.6, we see that

$$c_{\theta_2} = U_2 + w_{\theta_2} = U_2 - w_{r_2} \tan \beta_2 \quad \text{or} \quad c_{\theta_2} = U_2 - \frac{\dot{m}}{2\pi r_2 b \rho} \tan \beta_2,$$

where w = relative velocity,

β = angle of relative velocity from radial,

ρ = fluid density.

As in Chapter 9, the fluid angle β may be related to the blade angle in terms of an empirical slip factor. As a further refinement the radial flow area, $2\pi r_2 b$, might be reduced to account for the blockage of finite-thickness blades. However, neglecting these rather minor effects, we can write Eq. (13.1) as

$$\mathcal{P} = \dot{m} U_2^2 \left(1 - \frac{\dot{m}}{2\pi r_2 b \rho U_2} \tan \beta_2 \right)$$

or, using the steady-flow energy equation (2.8), we can show that, since the flow is adiabatic,

$$\frac{\mathcal{P}}{\dot{m}} = \Delta h_0 = U_2^2 \left(1 - \frac{\dot{m}}{2\pi r_2 b \rho U_2} \tan \beta_2 \right), \quad (13.2)$$

in which Δh_0 is the increase in stagnation enthalpy of the fluid. Using the definition of enthalpy, $h = e + pv$, we can write

$$Tds = dh - \frac{dp}{\rho},$$

in which $\rho = 1/v$, the density. Applied to the stagnation states of an incompressible fluid, this relationship becomes

$$T_0 ds_0 = dh_0 - \frac{dp_0}{\rho}.$$

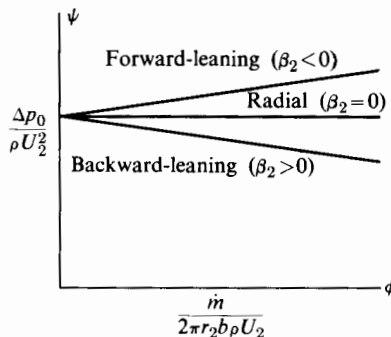


FIGURE 13.7 Ideal performance of centrifugal pump impeller.

Thus if the process under consideration is isentropic, $dh_0 = dp_0/\rho$, and Eq. (13.2) may be used to determine the ideal pressure rise through the impellers of Fig. 13.6:

$$\frac{\Delta p_0}{\rho} = U_2^2 \left(1 - \frac{\dot{m}}{2\pi r_2 b \rho U_2} \tan \beta_2 \right). \quad (13.3)$$

The pump efficiency η_p is conventionally defined as the ratio of ideal (isentropic) work to actual work for the same pressure rise. Thus

$$\eta_p = \frac{\Delta h_{0s}}{\Delta h_0} = \frac{\Delta p_0}{\rho \Delta h_0} = \frac{\Delta p_0}{(\Delta p_0)_{\text{ideal}}},$$

and the actual pressure rise resulting from the work input is given by

$$\frac{\Delta p_0}{\rho} = \eta_p U_2^2 \left(1 - \frac{\dot{m}}{2\pi r_2 b \rho U_2} \tan \beta_2 \right).$$

The term $\Delta p_0/\rho g_e$ is called the pump head.

Prediction of η_p is often difficult; in practice η_p is either determined experimentally or is estimated from past experience rather than from purely theoretical procedures.

Defining the dimensionless pressure and flow variables[†]

$$\psi = \frac{\Delta p_0}{\rho U_2^2} \quad \text{and} \quad \phi = \frac{\dot{m}}{2\pi r_2 b \rho U_2},$$

we can write Eq. (13.3) (for an ideal pump) as

$$\psi = 1 - \phi \tan \beta_2. \quad (13.4)$$

Thus the ideal performance of the centrifugal impeller is as shown in Fig. 13.7. For a given impeller a single curve determines the pressure rise as a function of speed, flow rate, and fluid density.

[†] These variables take on slightly different definitions in different applications in this chapter.

In practice the angle of the flow leaving the impeller will not be exactly equal to the exit blade angle and will depend somewhat on the flow rate for a given blade angle. If, however, we were to regard β_2 as ideally constant, we could plot the ideal impeller pressure rise characteristics as shown in Fig. 13.7. Of the three possibilities illustrated, the forward-leaning case ($\beta_2 < 0$) is rejected because, as shown in Section 7.5, this will be associated with pump instability. At a given flow rate the pressure rise for $\beta_2 > 0$ will be less than for $\beta_2 = 0$; however, the efficiency will usually be greater, and $\beta_2 > 0$ is not generally ruled out for stress reasons. Thus with pumps the backward-leaning case ($\beta_2 > 0$) is of common practical interest.

Before showing from experimental data how actual pump performance differs from the ideal, we resort to the technique of dimensional analysis. For the moment we ignore cavitation (which we will discuss subsequently) and assert that the pump pressure rise Δp_0 and efficiency η_p depend essentially on the following variables:

$$\Delta p_0 = f(\Omega, \dot{m}, \rho, \mu, \text{design}, D)$$

$$\eta_p = g(\Omega, \dot{m}, \rho, \mu, \text{design}, D)$$

in which

η_p = pump efficiency

= $\dot{m} \Delta p_0 / \rho \mathcal{P}$,

Ω = rotational speed of the pump,

\dot{m} = mass flow rate,

ρ = density,

μ = viscosity,

and "design" signifies a sufficient number of dimensionless geometrical ratios to specify the shape completely, with D indicating the size or scale of the pump; D can refer to any typical dimension of the pump, for example, rotor tip diameter. By dimensional analysis we can show that the performance of the pump may be represented by

$$\frac{\Delta p_0}{\rho \Omega^2 D^2} = f\left(\frac{\dot{m}}{\rho \Omega D^3}, \frac{\rho \Omega D^2}{\mu}, \text{design}\right), \quad (13.5)$$

$$\eta_p = g\left(\frac{\dot{m}}{\rho \Omega D^3}, \frac{\rho \Omega D^2}{\mu}, \text{design}\right). \quad (13.6)$$

For a given pump design this represents a valuable improvement of the initial statement of physical dependence, since the number of independent variables has been reduced from five to two. For a given design we can easily show that

$$\psi \propto \frac{\Delta p_0}{\rho \Omega^2 D^2} \quad \text{and} \quad \phi \propto \frac{\dot{m}}{\rho \Omega D^3},$$

in which ψ and ϕ are the variables previously defined in the analysis of the idealized pump. Further, the viscosity variable may be identified as a Reynolds number, Re . With these variables we can write relationships (13.5) and (13.6) as

$$\psi = f(\phi, Re, \text{design}), \quad (13.7)$$

$$\eta_p = g(\phi, Re, \text{design}). \quad (13.8)$$

Note that we could equally well write the actual pressure or head rise coefficient ψ as

$$\psi = \frac{g_e H}{\Omega^2 D^2},$$

in which H is the hydraulic head of the pump.

In the absence of cavitation, performance tests of a geometrically similar series of pumps (i.e., of a given design) will yield results shown typically in Fig. 13.8. We note first of all that variations in Reynolds number appear to have little effect. This is not to say that friction is unimportant; it *is* important, and η_p is appreciably less than unity. Nevertheless, beyond a certain value for which the flow in the pump is turbulent, further increases in Re have little effect on the flow pattern or the efficiency. Rocket turbopumps will generally operate at high values of the Reynolds number. An approximate indication of the Reynolds number above which variations cease to have significant influence on performance is perhaps $Re = \rho w L / \mu = 10^6$, in which w and L are a typical relative velocity and passage width. For a given design, a precise limit can really only be established by tests. Figure 13.8, of course, refers to a series of pumps that are geometrically similar. If test data on a series of pumps that are not exactly geometrically similar are plotted, one could not expect their performance to be so nearly described by a single curve as in Fig. 13.8.

The actual pressure coefficient ψ is always less than ideal for two reasons:

1. The fluid does not leave the impeller at the blade angle β and is said to “slip” past the impeller. Consequently the impeller does not do so much work on the fluid as the idealized analysis implies.

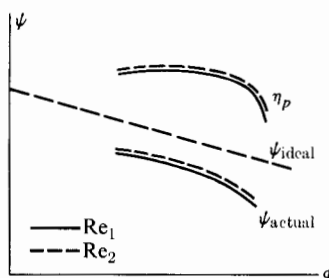


FIGURE 13.8 Typical performance of a backward-leaning pump; cavitation absent.

2. There are frictional losses in the rotor and stator, and these are especially magnified if the flow is partially stalled. The presence of separations leads to energy losses due to the mixing of slow- and fast-moving fluid.

The dimensionless flow variable ϕ has an important physical interpretation. For a given design it can be shown to be uniquely related to the flow angles at entrance to the rotor and stator. For example, at the rotor inlet the axial velocity component c_i may be written $c_i = \dot{m}/\rho A_i$. The rotor speed at some radius r_i is $U_i = \Omega r_i$; thus, referring to Fig. 13.9, we observe that the angle of the flow relative to the rotor at its radius r_i is

$$\tan \beta_i = \frac{c_i}{U_i} = \frac{\dot{m}}{\rho A_i \Omega r_i}.$$

For a given pump design we can see that $\tan \beta_i \propto \phi$. A similar argument shows that the flow incident to the stator is also uniquely dependent on ϕ , and therefore the incidence angle of the flow entering both rotor and stator blades depends only on ϕ . At large positive or negative incidence, pressure gradients near certain parts of the blade surface may be large enough to stall the boundary layer. Thus at sufficiently high or low values of ϕ (relative to the design value), the performance of the pump may drop off as indicated in Fig. 13.8.

Figure 13.10 shows the performance of the three-stage hydrogen centrifugal pump used in the space shuttle main engine. Here the head in feet is plotted against the flow rate in gallons per minute. The impeller of this pump operates with a tip speed of 610 m/s (2000 ft/s) at an rpm of 35,015, so its tip diameter is $2U_i/\Omega = 0.333$ m (1.091 ft). Assuming that all three stages contribute equally to the total head and that their efficiencies are identical, one can calculate from these data the dimensionless stage performance shown later in Fig. 13.11.

So far we have considered how one can present the performance of a pump in its simplest general form, that is, $\psi, \eta_p = f(\phi, \text{design})$.

If the best operating point is taken to be the maximum-efficiency point, one could take the values of ϕ and ψ at that point and call them ϕ^* and ψ^* , using the

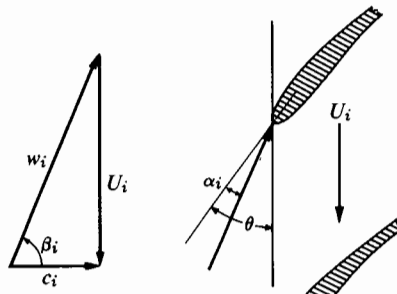


FIGURE 13.9 Typical pump inlet geometry.

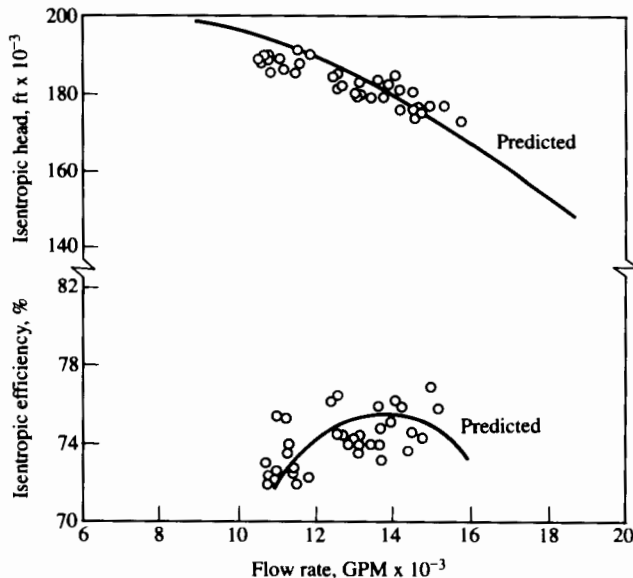


FIGURE 13.10 Space shuttle main engine, high-pressure fuel turbopump performance (measured and predicted at 35,015 rpm). (Courtesy Rockwell International, Rocketdyne Division.)

asterisk to denote maximum-efficiency operation. Each design would have its own characteristic values of ϕ^* and ψ^* , so we could write

$$\left. \begin{aligned} \phi^* &= f_1(\text{design}) = \left(\frac{Q}{\Omega D^3} \right)_{\eta_p \max}, \\ \psi^* &= f_2(\text{design}) = \left(\frac{\Delta p_0}{\rho \Omega^2 D^2} \right)_{\eta_p \max}, \\ \eta_p^* &= f_3(\text{design}) = \eta_p \max. \end{aligned} \right\} \quad (13.9)$$

Let us suppose that a pump is required to provide a certain stagnation pressure rise Δp_0 with a fluid of density ρ and with volumetric flow rate Q . We wish to have high efficiency and a pump size as small as possible consistent with good efficiency. The question is: How do we use our extensive knowledge of the best values of ϕ^* and ψ^* (for a whole series of designs) to help us select the best design for this problem? We cannot use Eqs. (13.9) directly because, to start with, we do not know the speed Ω and the size D of the required pump. To use this previous knowledge, we need to organize it. We can do this by first defining two new variables. The first is called the specific speed,

$$n_s = (\phi^*)^{1/2} (\psi^*)^{-3/4} = \frac{\Omega Q^{1/2}}{\left(\frac{\Delta p_0}{\rho} \right)^{3/4}}.$$

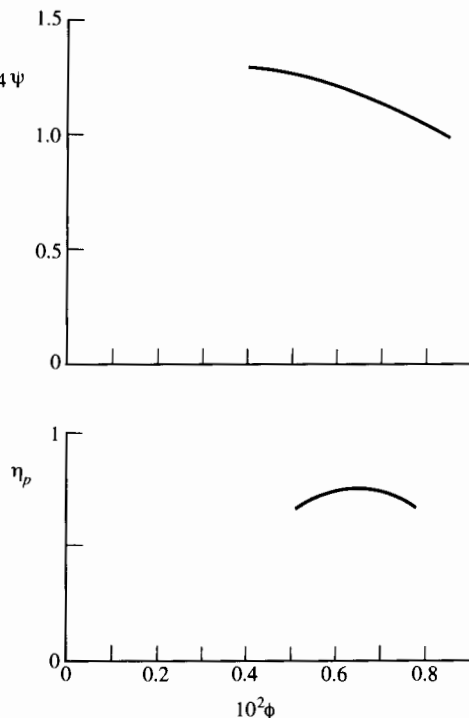


FIGURE 13.11 Single-stage performance; high-pressure hydrogen fuel pump, space shuttle main engine. (Data from Fig. 3.10.)

The second is called the specific diameter,

$$d_s = (\psi^*)^{1/4}(\phi^*)^{-1/2} = \frac{D \left(\frac{\Delta p_0}{\rho} \right)^{1/4}}{\sqrt{Q}}.$$

Though it may not immediately seem so, this simplifies matters because, unlike ϕ^* and ψ^* , which both contain Ω and D , n_s and d_s each contain only one of these variables. Again thinking of best-operating-point experience with many designs, we can transform Eqs. (13.9) to

$$\left. \begin{aligned} n_s &= f_1(\text{design}), \\ d_s &= f_2(\text{design}), \\ \eta_p^* &= f_3(\text{design}). \end{aligned} \right\} \quad (13.10)$$

Now it becomes highly interesting to realize that for a given class of designs (such as various versions of centrifugal pumps), it is possible to take all the experimental or analytical information represented by Eqs. (13.9) or (13.10) and plot it on one piece of paper. Balje [4] has done this, and Fig. 13.12 shows his results for the centrifugal pumps.

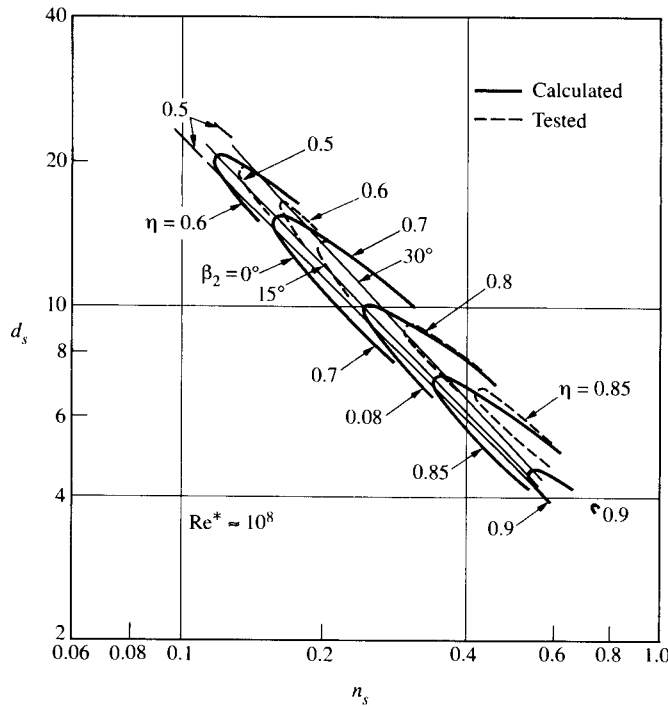


FIGURE 13.12 Comparison of calculated efficiency contours with test data on centrifugal pumps. (Courtesy Balje [4].)

Each point in Fig. 13.12 represents a different design, and the efficiency contours indicate the characteristic efficiency to be associated with each point. An idea of how the designs differ from one another is indicated by the lines of constant impeller exit blade angle β_2 . We may draw several conclusions from Fig. 13.12:

1. Best-efficiency operation occupies a rather narrow zone on the n_s-d_s plane. This says, for example, that if a pump for given $\Delta p_0, \rho, Q$ is to have a given impeller diameter (i.e., a given value of d_s), it can be operated at maximum efficiency only if its speed Ω falls in a fairly narrow range.
2. Best efficiency is associated with highest-specific-speed impellers (within the range indicated). With given ρ, Q , and overall Δp_0 , the specific speed may be increased by increasing the number of stages.
3. The efficiency curves that Balje calculated (by individually estimating the losses that contribute to the inefficiency of the pump) differ from the curves he deduced from experimental pump data, but they have the same general character, and the differences are not large.

As a point of reference, the high-pressure hydrogen turbopump whose performance is shown in Fig. 13.11 has the following characteristic values:

$$\phi^* = 0.00653 ,$$

$$\psi^* = 0.0121 .$$

From these we may calculate

$$n_s = (\phi^*)^{1/2}(\psi^*)^{-3/4} = 0.39 ,$$

$$d_s = (\psi^*)^{1/4}(\phi^*)^{-1/2} = 7.3 ,$$

and see that this pump too falls approximately within the "high-efficiency" operating band in Fig. 13.12. Thus one can use Fig. 13.12 as a guide to the conditions under which a centrifugal pump may be suitable as a rocket engine turbopump.

13.3 INDUCERS AND AXIAL PUMPS

The inducer is a pump whose task is to pressurize fluid whose static pressure is not much higher than its vapor pressure. Because the fuel and oxidant tanks are so large, the tank pressure must be kept as low as possible to minimize tank mass. After the fluid leaves the tank, its pressure drops because of pipe friction and also because of acceleration as it enters the pump. If the fluid were introduced to a conventional centrifugal pump right from the tank, it would suffer such a large static pressure drop in moving over the suction surfaces of the pump blades that it would begin to "boil," or "cavitate." This could cause the flow passages to fill up with vapor and drastically reduce both flow rate and pressure rise. Pumps that are faced with large amounts of vapor in the incoming flow usually fail to produce any significant pressure rise. The inducer requires special geometry to accept low-pressure fluid without causing it to vaporize.

Inducers

Figure 13.13 shows the typical inlet blade shape of a rocket turbopump inducer. One can see that the inducer blades are like thin, sharp-edged, flat plates formed in spirals around the hub. Quite commonly the leading "edge" is swept back toward the tip of the impeller at the inlet. Figure 13.14 shows a cross-sectional view of the inlet blading; the cavity shown on the suction surface of the blade (for operation with low flow coefficient) is due to vapor.

Cavitation

The term *cavitation* may be defined as the spontaneous formation of bubbles of vapor in the liquid as the static pressure falls below the vapor pressure. It can be seriously detrimental to pump performance in two ways:

1. The vapor bubbles may grow into a sufficiently large region in the impeller passages that the pressure rise across the pump falls toward zero. One can



FIGURE 13.13 Turbopump inducer. (Courtesy Rockwell International, Rocketdyne Division.)

see from Eq. (13.5) and the definition of ψ that the pressure rise Δp_0 is directly proportional to the density of the fluid within the impeller.

- Even when cavitation is confined to so small a region of the impeller passage that the pressure rise is virtually unaffected, the blading of the impeller can be seriously eroded if the period of operation is sufficiently lengthy. Generally the point of minimum pressure in an impeller passage (as in the flow about an airfoil) is located on a solid surface. Thus cavitation begins near the surface, and the rapid growth and collapse of a vast number of minute bubbles immediately adjacent to the surface can lead to serious erosion, depending on the kind of material and the time duration. The mechanism of cavitation damage cannot be said to be fully understood.

Damage caused to the surface by cavitation is generally insignificant in rocket pumps whose operating life is of the order of minutes. However, the effect of cavitation on pressure rise is most important and exercises a controlling influence on pump design. We must therefore take account of it in providing a general account of rocket pump behavior.

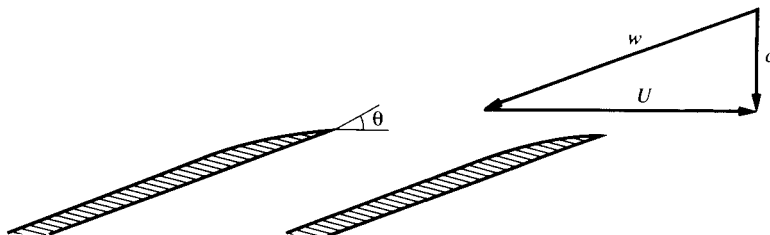


FIGURE 13.14 Typical leading-edge blade geometry and velocity triangle.

With highly purified liquids it has been shown possible under laboratory conditions to reduce the pressure of the liquid far below the vapor pressure without vapor formation. It is even possible for the liquid to exist under tension without any vapor formation. In general the presence of dust particles or other impurities to be expected in untreated fluids is sufficient to promote nearly immediate production of vapor bubbles when the static pressure falls below the vapor pressure. Minute cracks in the surface of the impeller blade are also thought to play a role in nucleating vapor bubbles. General experience with pumps suggests that the assumption that cavitation begins when the local pressure reaches the vapor pressure is approximately valid. Thus the difference ($p_{01} - p_v$) between the vapor pressure and the inlet stagnation pressure can be regarded as a significant performance variable.

To get an idea of how cavitation affects turbopump inducers, it is useful to review some experimental data.

As we will see, there is a difference between the cavitating behavior of a fluid such as hydrogen and that of water. However, we begin with a consideration of test results on water (which has been the subject of much more experimental work than has hydrogen). Figure 13.15 shows the progressive development of cavitation in an inducer such as the one shown in Fig. 13.1(a). The term *net positive suction head* (NPSH) is defined as

$$\text{NPSH} = \frac{p_{01} - p_v}{\rho g_e}$$

in which ρ is the density of the liquid. The term *suction specific speed* is defined as

$$S_s = \left(\frac{Q}{\Omega D^3} \right)^{1/2} \left(\frac{g_e \text{NPSH}}{\Omega^2 D^2} \right)^{-3/4} = \frac{\Omega \sqrt{Q}}{(g_e \text{NPSH})^{3/4}},$$

Although S_s is dimensionless in principle, the units commonly used in its evaluation are not always compatible in that sense. The units for the S_s numbers quoted in Fig. 13.15 are

$$\frac{\text{rpm} \sqrt{\text{gpm}}}{(\text{ft})^{3/4}},$$

the term g_e being deleted; to convert the value of S_s in these units to a dimensionless value (based on shaft speed in radians per second), one divides by 2730.

Referring to the sequence of photographs in Fig. 13.15, we note that the highest value of NPSH (NPSH = 137 ft or 39 m) corresponds to the lowest value of S_s ; for this case, cavitation can be seen in the bubbles associated with the tip vortex that forms at the leading edge of the impeller. The tip vortex is a region of low static pressure and has often been observed as the place where cavitation begins on a ship propellor. Reducing the NPSH to 72.4 ft (22 m), one sees the first signs (inception) of bubble formation on the blade surface, but the pump head is apparently unaffected. Even at 38.2 ft (12 m), where one can see a substantial pocket of bubbles in the blade passage, the head is hardly changed. How-

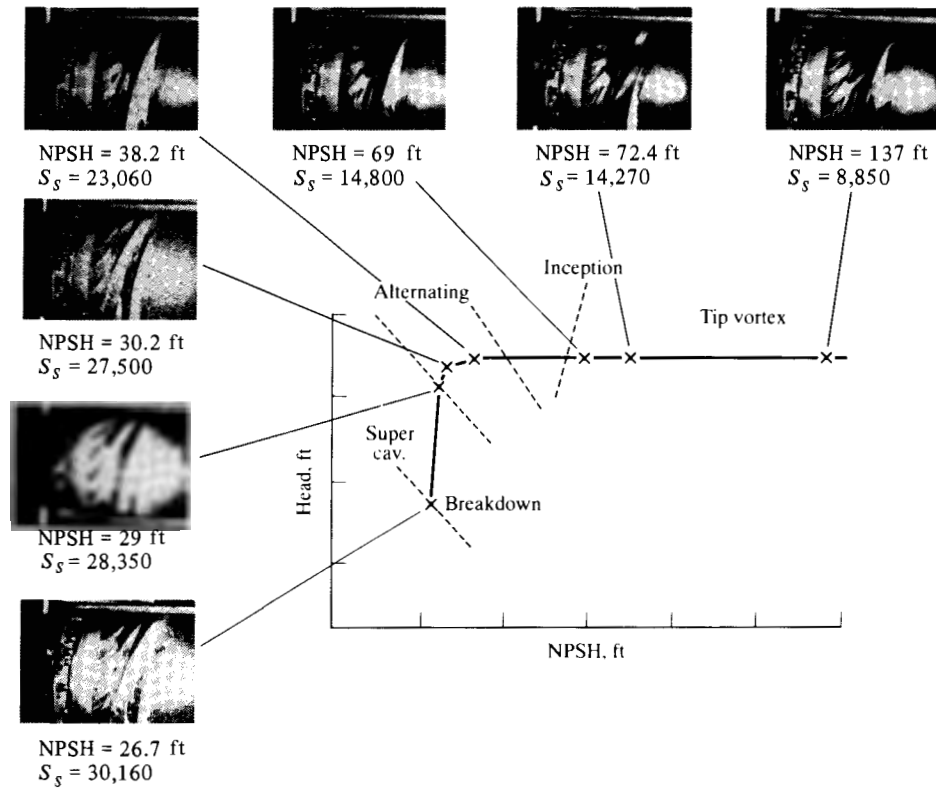


FIGURE 13.15 Experimental inducer cavitation characteristics. (Courtesy Rockwell International, Rocketdyne Division.)

ever, with small further reduction in NPSH, the head drops drastically. One can use the value of S_s at which the head begins to deteriorate as an indicator of the quality of the inducer.

Operating with hydrogen, the inducer can tolerate significantly lower NPSH than it can with water. As bubbles begin to form in a cavitating liquid, the local temperature of the fluid drops, and this reduces the local vapor pressure below its value at inlet to the pump. One could write, for the reduction in vapor pressure,

$$\Delta p_v \approx \Delta T \frac{dp_v}{dT} = \frac{\chi_v h_{fg}}{c_{pl}} \frac{dp_v}{dT}$$

where χ_v is the local mass fraction of vapor formed, h_{fg} is the heat of vaporization, c_{pl} is the liquid specific heat, and p_v is the saturation vapor pressure.

The Clapeyron equation [5] shows that

$$\frac{dp_v}{dT} = \frac{h_{fg}}{v_g T} \approx \frac{p_v h_{fg}}{R_v T^2}.$$

Thus the fractional reduction in local vapor pressure due to local "boiling" is

$$\frac{\Delta p_v}{p_v} \approx \left[\left(\frac{h_{fg}}{c_{pl} T} \right)^2 \left(\frac{R_v}{c_{pl}} \right) \right] \chi_v.$$

For hydrogen the value of the term in square brackets is much higher than it is for water. (For liquid oxygen the value is intermediate.) As a result, designers treat these fluids differently. Stangeland [1] recommends that the allowable values of $2gNPSH/c_m^2$ be greater than 3 for water, 2 for liquid oxygen, and 1 for hydrogen (c_m being the absolute inlet velocity in the meridional plane—the plane containing the pump axis). He also recommends that for impeller durability the operating NPSH be at least 50% greater than the one associated with head breakdown, and that the inducer-tip speed be limited to 170 m/s (550 ft/s) to control the losses due to the tip vortex.

We now consider the way in which the inducer inlet geometry and tip speed affect its cavitation performance, following the approach of Stripling and Acosta [6]. To put our results in as general a form as possible, we return to the dimensional analysis of pump/inducer behavior.

Consistent with the experimental data of Fig. 13.15, we can show the effect of cavitation on performance in a general way, as in Fig. 13.16. The pump geometry will strongly affect the value of τ at which ψ begins to drop rapidly with decreasing τ .

If the dimensional analysis of pump performance is repeated, this time recognizing $(p_{01} - p_v)$ as a significant variable, the following more general result may be obtained:

$$\psi = f(\phi, Re, \tau, \text{design}), \quad \eta = g(\phi, Re, \tau, \text{design}),$$

in which

$$\tau = \frac{p_{01} - p_v}{\rho U_z^2 / 2}.$$

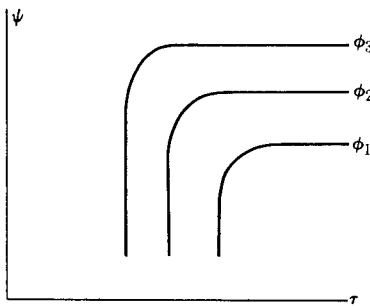


FIGURE 13.16 Typical effect of cavitation on turbopump performance; given design of pump.

For a given design, τ is proportional to $(p_{01} - p_v)/\rho\Omega^2D^2$. It is only one of the possible variables that could be used to express the influence of cavitation on performance. Instead of τ , the previously defined suction specific speed could be used.

Considering Fig. 13.9, we see that the difference between the static pressure p_1 just outside the blade row and the minimum pressure p_{\min} on the blade may be written (for high Reynolds numbers)

$$\frac{p_1 - p_{\min}}{\rho w_i^2/2} = f(\alpha_i, \text{blade geometry}),$$

in which α_i is the incidence angle of the fluid approaching the blade and w_i is the relative velocity of the fluid at inlet. The blade geometry is specified by the blade shape and orientation. For given blade geometry, α_i depends uniquely on ϕ . In addition, since c_i/U and w_i/U depend only on ϕ , and also since

$$\frac{p_{01}}{\rho} = \frac{p_1}{\rho} + \frac{c_i^2}{2},$$

we may write the above relationship as

$$\frac{p_{01} - p_{\min}}{\rho U^2/2} = f(\phi, \text{blade geometry}).$$

If we assume that head breakdown begins to occur when the minimum static pressure equals the vapor pressure, the minimum tolerable value of τ is given by

$$\tau_{\min} = \frac{p_{01} - p_v}{\rho U^2/2} = f(\phi, \text{blade geometry}). \quad (13.11)$$

Since inducers must operate with high values of U_2 to keep the inducer size and mass small, special blade geometry is needed to keep τ_{\min} as small as possible. Usually the inducer consists of helical passages bounded by thin blades whose inlet direction is only a few degrees from the tangential. The tip blade angle θ in Fig. 13.14 may be as low as 5° or 6° , and only two or three blades may be used. The fluid enters the inducer, which gently raises its static pressure until

the flow can enter the main pump without cavitating. For inducers of this type, Stripling and Acosta [6] have shown, on the basis of a theoretical analysis, that the relationship (13.11) may be represented quite acceptably by a correlation of this form:

$$\frac{p_{01} - p_v}{\rho U_i^2 / 2} = f \left(\frac{\sin \theta}{1 + \cos \theta} \phi \right), \quad (13.12)$$

in which U_i is the blade speed at the outer radius of the inlet and θ is the tip blade angle relative to the tangential direction.

Data on the cavitation breakdown of performance of several turbopumps with helical inducers varying widely in design correlate fairly well in this way, as shown by Fig. 13.17. The scatter in the data is not unreasonable, since, in the derivation of the below correlation parameters, no account is taken of leading-edge blade shapes and of flow conditions other than at the tip of the inducer inlet. To be able to pump a fluid of low NPSH, it is desirable to have a very small value of θ .

Axial Pumps

Figure 13.18 shows the typical geometry of an axial turbopump. This one consists of six stages; a similar pump with seven stages (the Mark 15 version) was used in the J2 rockets of the *Apollo Saturn V* (Table 10.3). As one may see from Fig. 13.18, the blades are of constant height. With constant fluid density it follows that the mean axial velocity component is constant through the stages.

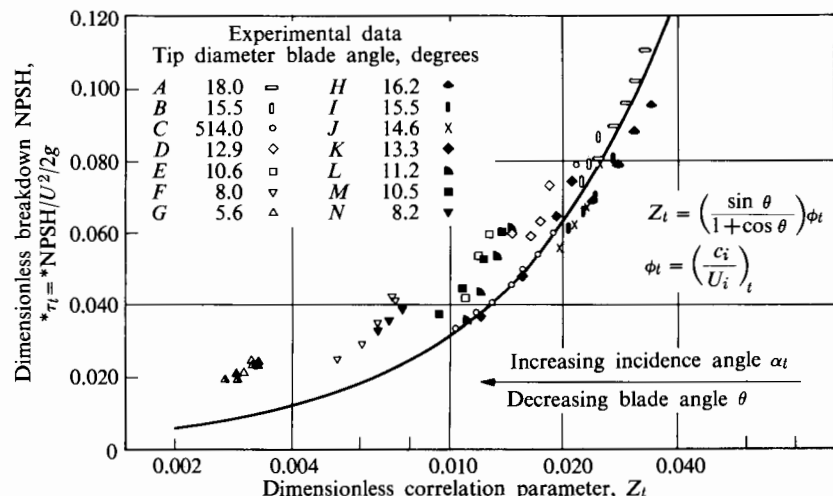


FIGURE 13.17 Correlation of the breakdown of cavitation performance for several helical inducers; mean data curve. (Courtesy Stripling [6].)

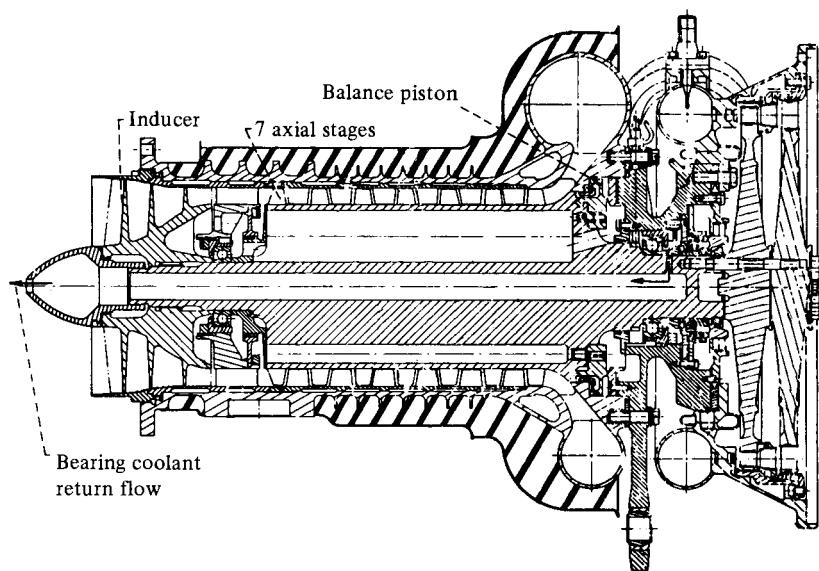


FIGURE 13.18 J2 (Mark 15) axial turbopump. (From Huppert and Rothe [7].)

Since the mean blade speed is also constant, it is not surprising that blade angles appear to be the same for all stages. Figure 13.19 shows the axial pump of Fig. 13.18 with the inducer mounted directly on the front end. Limiting the tip speed of the inducer to control tip vortex effects means that the stage head rise is thereby limited.

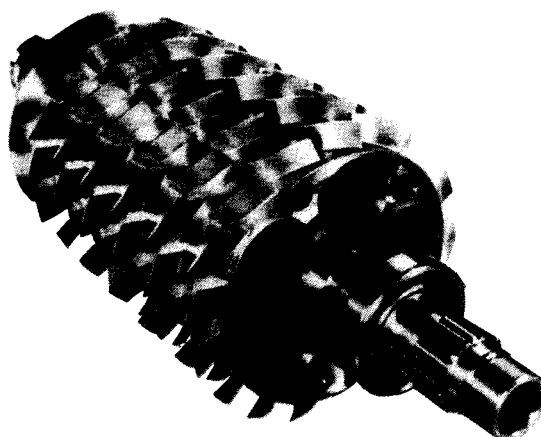


FIGURE 13.19 J2 (Mark 9) axial turbopump. (Courtesy Rockwell International, Rocketdyne Division.)

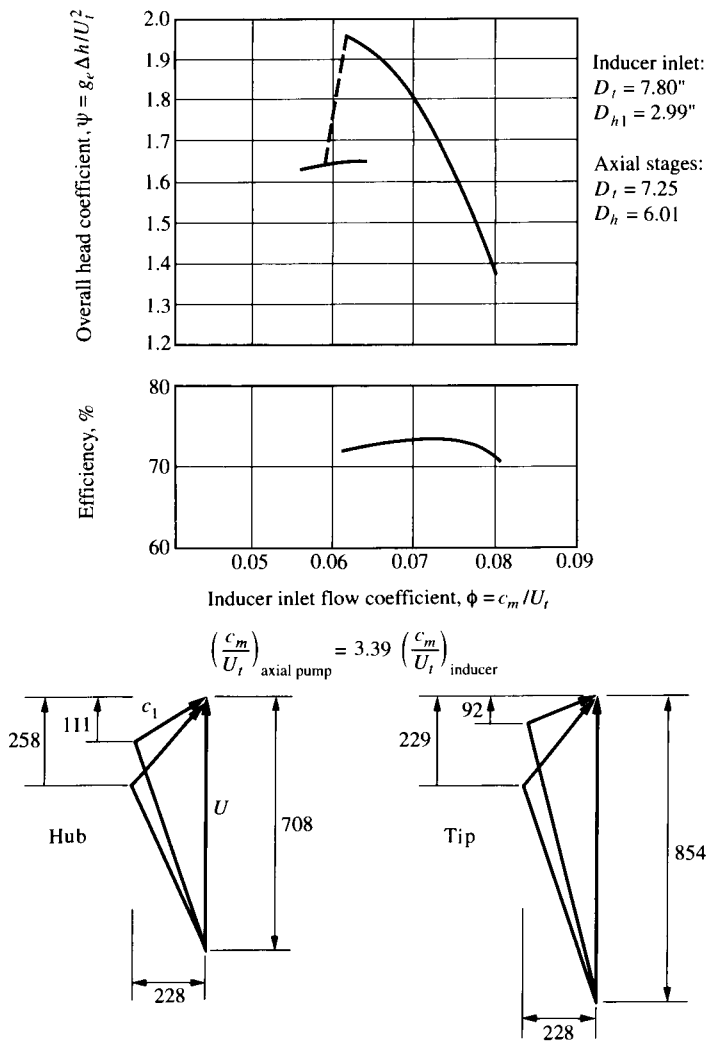


FIGURE 13.20 J2 (Mark 15) axial pump performance and velocity diagrams; velocities in ft/s. (From Huppert and Rothe [7].)

Figure 13.20 shows the design-point-stage velocity diagrams and the measured performance of the seven-stage Mark 15 hydrogen turbopump. Here the head coefficient is defined as

$$\psi = \frac{g_e H}{U_t^2},$$

in which U_t is the blade-tip speed and the flow coefficient is defined as

$$\phi = \frac{c_m}{U_t},$$

in which c_m is the mean meridional velocity (Q/A). The tip diameter is 18.41 cm (7.25 in.), and the hub diameter is 91.5 cm (6.01 in.).

In passing from the inducer to the axial pump, the cross-sectional area reduces by a factor of 3.16 and the tip diameter reduces from 7.80 in. to 7.25 in., so the flow coefficient (c_m/U_t) defined for the axial pump is $3.16 \times 7.8/7.25 = 3.39$ times as large as it is for the inducer.

Figure 13.21 shows Balje's correlation of best performance of axial pump stages on an n_s-d_s plane. For the axial pump whose performance is shown in Fig. 13.20, we can deduce characteristic best-efficiency points as

$$\phi^* = \frac{Q}{\Omega D^3} = \frac{c_m \pi (D_t^2 - D_n^2)}{2U_t 4D_t^2} = \frac{\pi}{8} \frac{c_m}{U_t} \left[1 - \left(\frac{D_n}{D_t} \right)^2 \right] = 0.032$$

and (per stage)

$$\psi^* = \frac{gH}{\Omega^2 D^2} = \frac{1}{4} \frac{gH}{U_t^2} = 0.055.$$

One may use these to calculate

$$n_s = (\phi^*)^{1/2} (\psi^*)^{-3/4} = 1.6$$

and

$$d_s = (\phi^*)^{-1/2} (\psi^*)^{1/4} = 2.7.$$

This point of reference in Fig. 13.21 indicates efficiency around 70%—approximately the experimental value. The ranges of n_s and d_s values for best axial stages in Fig. 13.21 are quite different from the corresponding ranges for centrifugal pumps shown in Fig. 13.12. One can use Fig. 13.21 to assess the conditions under

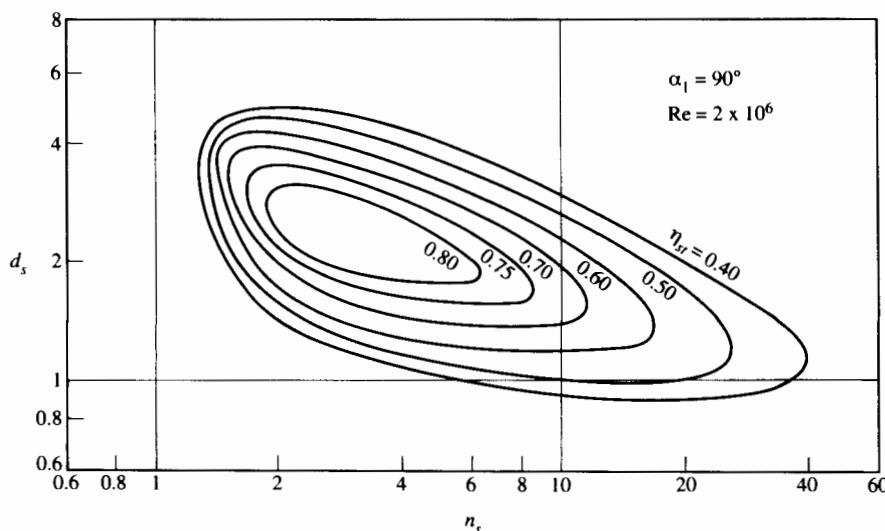


FIGURE 13.21 n_s-d_s diagram calculated for single-stage axial pumps. (Courtesy Balje [4].)

which a single axial stage will operate with high efficiency. Of course, by using several stages one can substantially alter the values of n_s and d_s for the same overall pressure rise.

13.4 AXIAL TURBINES

The driving turbines used in turbopumps are usually of the impulse type. In order to minimize the required number of stages, it is desirable to produce high power per stage. As discussed in Chapter 8, the power output per stage of an impulse turbine is greater than that of a reaction turbine for the same blade speed (given axial exhaust velocities). Figure 13.22 indicates three turbine types. For each, the work output per unit mass flow is stated for cases in which the axial velocity is held constant through the stage and the outlet velocity has no swirl component. Thus, at a given rpm, the single-stage impulse turbine can deliver twice the power of a 50% reaction turbine of the same size.

The velocity-compound impulse turbine is, in a sense, a single impulse stage since all the pressure drop occurs in the first nozzle. The fluid leaves the first rotor with swirl in the direction opposite to the rotation. This is redirected in the second "nozzle" (without pressure drop) to enter the last rotor. If the fluid leaves the last rotor without swirl, it is easily shown that the power output of the two rotors is four times that of a single-impulse rotor, and thus about twice that of an ordinary two-stage impulse turbine. For this reason the velocity-compound impulse turbine is commonly used in turbopumps for those cases in which a single-impulse stage is inadequate. For lightness, two rows of rotor blades are often mounted on a single disc that branches near the blade roots since, at typical speeds, stresses need not be intolerable. The velocity-compound turbine is, however, significantly less efficient than a single-impulse stage (which in turn is less efficient than the 50% reaction stage) owing largely to the very high fluid veloc-

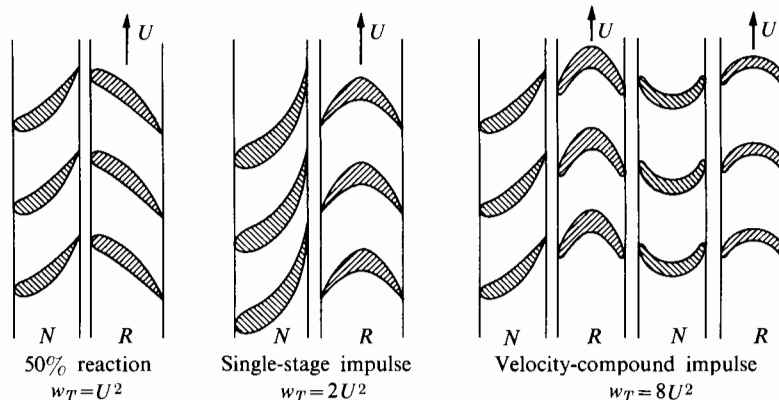


FIGURE 13.22 Blade cross sections and work outputs of three typical turbines, for constant axial velocity and axial outlet velocity.

ties encountered in the first nozzle and rotor blades, and to the requirement that the fluid travel through three successive blade rows without the beneficial effect of pressure drop on the boundary layer.

Designating the turbine inlet as state (1) and the outlet as (2), the turbine power is given by

$$\mathcal{P}_T = \dot{m}_T(h_{01} - h_{02}),$$

where \dot{m}_T is the turbine mass flow rate. Since the useful turbine output is entirely shaft power, it is appropriate to describe its performance in terms of total-to-static turbine efficiency, η_{ts} , as defined in Eq. (8.12):

$$\eta_{ts} = \frac{h_{01} - h_{02}}{h_{01} - h_{2s}},$$

where h_{2s} is that enthalpy attained by *isentropic* expansion to the outlet *static* pressure, p_2 . Assuming the working fluid a perfect gas with constant c_p , we may write this as

$$\eta_{ts} = \frac{1 - (T_{02}/T_{01})}{1 - (p_2/p_{01})^{(\gamma-1)/\gamma}},$$

and the turbine power as

$$\mathcal{P}_T = \dot{m}_T \eta_{ts} c_p T_{01} \left[1 - \left(\frac{p_2}{p_{01}} \right)^{(\gamma-1)/\gamma} \right]. \quad (13.13)$$

Because designers aim at light-weight turbines, they may tolerate turbine efficiencies that are quite low; even less than 60% in some cases.

Turbines must supply enough power for the pumps, plus power to make up for losses incurred in the power transmission system. If the system includes a gear train, the losses can be appreciable. Thus, defining η_m , the mechanical efficiency of the power transmission system, as the ratio of power transmitted to power received, we have

$$\mathcal{P}_T = \frac{1}{\eta_m} \left\{ \left[\frac{\dot{m}(\Delta p_0/\rho)}{\eta_p} \right]_{\text{oxidant}} + \left[\frac{\dot{m}(\Delta p_0/\rho)}{\eta_p} \right]_{\text{fuel}} \right\}. \quad (13.14)$$

From this, and using Eq. (13.13), we can determine the turbine mass flow for given inlet conditions, exhaust pressure, and turbine efficiency.

Typical efficiencies of turbines designed for low specific mass are shown in Fig. 13.23. Here the total-to-static adiabatic efficiency is shown as a function of U_t/c_0 , in which U_t is the blade tip speed and c_0 is the velocity calculated for isentropic expansion through the turbine pressure ratio. The term *reaction stage* refers to the relatively high-efficiency stages discussed in Chapter 8. For the reaction stage the maximum work (with zero exhaust swirl) is only U^2 . The impulse stages (with one, two, or three rotor blade rows) have much lower peak efficiency.

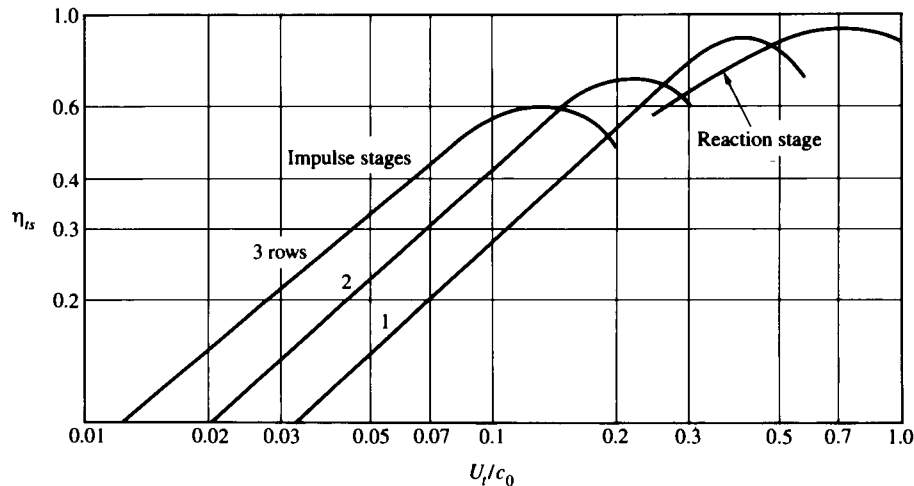


FIGURE 13.23 Typical efficiencies of high-work turbines. (After Stangeland [1].)

In considering the shaft speed best suited for an axial turbine, we need to consider blade-root stresses. Chapter 8 shows that blade-root stresses are approximately given by

$$\sigma_b = \frac{\rho_b U_t^2}{2} \left[1 - \left(\frac{D_h}{D_t} \right)^2 \right],$$

in which ρ_b is the blade density and U_t is the tip speed. We may rewrite this as

$$\sigma_b = \rho_b \frac{\Omega^2 [D_t^2 - D_h^2]}{8}. \quad (13.15)$$

Considering a velocity-compound impulse stage as illustrated in Fig. 13.24, we write the continuity equation at station ② as

$$\dot{m} = \rho_2 c_z \frac{\pi}{4} (D_t^2 - D_h^2),$$

in which ρ_2 is the gas velocity at station ② and c_z is the axial velocity component.

With $c_z \approx c_0 \cos \alpha_2$ (in which c_0 is the isentropic velocity and α_2 the stator exit flow angle), we have

$$\dot{m} = \rho_2 c_0 \cos \alpha_2 \frac{\pi}{4} (D_t^2 - D_h^2). \quad (13.16)$$

Combining Eqs. (13.15) and (13.16) results in

$$\Omega = \sqrt{\frac{2\pi\sigma_b \rho_2}{\rho_b \dot{m}}} c_0 \cos \alpha_2. \quad (13.17)$$

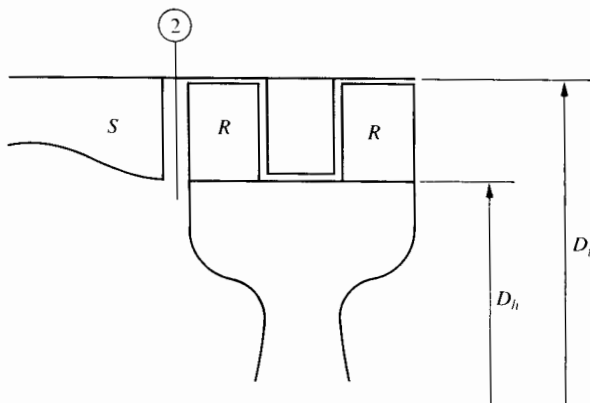


FIGURE 13.24 Two-row impulse turbine; S = stator blade, R = rotor blade.

If the turbine inlet conditions are fixed, then ρ_1 and c_0 are determined by the turbine pressure ratio. The angle α_2 will be as large as feasible for structural and mechanical reasons. Figure 13.25 shows profiles of typical velocity-compound blading. The maximum flow angle will be not much more than 70° .

Thus the shaft speed needed by the turbine depends basically only on the allowable strength-to-mass ratio of the blades, the flow rate, and the isentropic velocity. Given the required Ω and the desired ratio U_t/c_0 (Fig. 13.22), the turbine tip diameter follows from

$$D_t = 2U_t/\Omega = 2\frac{c_0}{\Omega} \left(\frac{U_t}{c_0} \right).$$

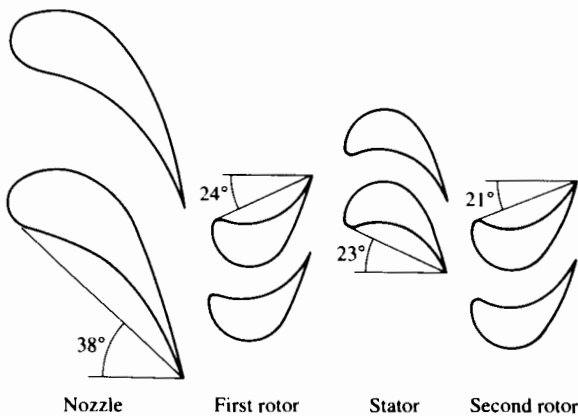


FIGURE 13.25 Velocity-compound turbine blading. (Kamijo, Sogame, and Okayasu [8]. © AIAA. Reproduced with permission.)

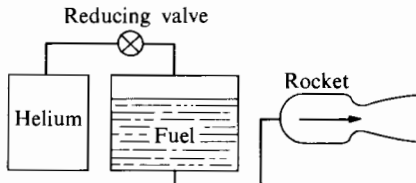
The design of a turbopump system obviously entails many compromises between conflicting requirements. For example, the detrimental effect of low turbine blade speed on turbine efficiency can be overcome by using higher turbine speeds along with suitable gear drives. This reduces the fuel consumed by the turbopump unit, but increases the mass of the unit itself. Whether the benefits of reduced fuel consumption outweigh the disadvantage of increased turbopump mass is dependent on the time duration of the thrust and on other design conditions.

The pump cavitation problem can be alleviated by increasing the pressurization of the propellant storage tanks. However, this increases the tank weight. Again a compromise is required between the fixed turbopump weight and a duration-dependent tank weight. Since so many complicated interactions are involved, the final choice of a design is usually made only after comparing a number of designs for the specific application.

The mechanical design of a 63,000-horsepower unit such as the high-pressure hydrogen turbopump shown in Fig. 13.5 presents extraordinary challenges. As an example, Ek [9] describes how a vibration problem known as subsynchronous shaft swirl was solved after intensive detective work leading to the adjustment of stiffness and damping and the dynamic response of certain interstage seals.

PROBLEMS

1. Consider the pumps necessary to supply a booster engine of 6.7 MN pounds of thrust. The engine consumes liquid oxygen and RP1 in the ratio 2.5:1. The flame temperature is 3300 K, the chamber pressure 10 MPa, and the specific impulse 242 sec. Densities of liquid oxygen and RP1 are 1140 and 750 kg/m³, respectively. What total shaft power is necessary, assuming a pump efficiency of 0.65 and propellant tank pressure of 0.35 MPa? Make allowance for the injector pressure drop with injection velocity of 50 m/s.
2. The 2.8-m³ fuel tank shown in the figure is pressurized by helium at 10 MPa and 300 K. The helium enters the fuel tank from a storage tank through a pressure reducer that keeps the pressure in the fuel tank constant. In the fuel tank the helium temperature is the same as that of the fuel—300 K. If the pressure in the helium tank is 40 MPa when the fuel tank is full, determine the volume of the helium tank necessary to pump all the fuel into the rocket. Is the initial helium temperature of any consequence? Would the use of air instead of helium alter the performance?



PROBLEM 2

3. Sketched in the figure is a turbopump feed system pumping a total propellant mass flow of 92 kg/s. If the component efficiencies are as listed below, what fraction of the total propellant flow is diverted through the gas generator and turbine?

Fuel pump efficiency	$\eta_{Pf} = 0.70$
LOX pump efficiency	$\eta_{PL} = 0.65$
Turbine efficiency	$\eta_{ts} = 0.70$
Turbine discharge pressure	$p_2 = 0.14 \text{ MPa}$
Mechanical efficiency	$\eta_m = 0.90$

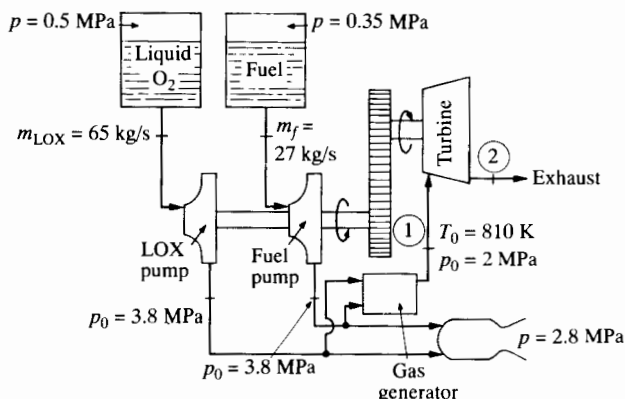
Fluid properties are:

$$c_p = 1.07 \text{ kJ/kg} \cdot \text{K} = \text{const. for turbine fluid},$$

$$\gamma = 1.3 = \text{const. for turbine fluid},$$

$$\rho_{\text{LOX}} = 1140 \text{ kg/m}^3,$$

$$\rho_{\text{fuel}} = 800 \text{ kg/m}^3.$$



PROBLEM 3

4. A design is required for a liquid-oxygen pump to pressurize $0.455 \text{ m}^3/\text{s}$ (7223 gpm) of liquid oxygen to 21.45 MPa (3112 psia). Could a single-stage centrifugal pump be expected to meet these requirements at high efficiency? If so, what would be the appropriate shaft speed and impeller diameter? What efficiency could one reasonably expect? If a single-stage centrifugal pump would not be satisfactory, select the number, shaft speed, and diameter of the stages. The density of the liquid oxygen is 1116 kg/m^3 . An inducer with a separate shaft drive is provided upstream of the pump, so that cavitation is not a limiting factor in this design. However tip speed must be limited to control centrifugal stress.

5. A design is required for a liquid-hydrogen pump to pressurize $1.24 \text{ m}^3/\text{s}$ ($19,750 \text{ gpm}$) to 25.8 MPa (3743 psia). If a centrifugal pump is used, what should be the number of stages, the shaft speed, and the impeller diameter? What maximum efficiency could be expected? The density of the liquid hydrogen is 68.73 kg/m^3 , and it enters the pump at sufficiently high pressure that cavitation is not a limiting factor in the design. The impeller tip speed should not exceed 450 m/s .
6. Hot pressurized gas at 21.0 MPa (3045 psia) and 964 K (1735 R) is available for an axial turbine that might drive the liquid-oxygen pump whose flow and pressure rise are specified in Problem 4. The available pressure ratio for the stage is 1.5. The molecular weight of the combustion gas is 26.5, and its specific-heat ratio is 1:3. If the pump and turbine both rotate at 15,000 rpm, select the pump size and efficiency from Fig. 13.12. If the tip diameter D is to be the same for pump and turbine, what turbine stage configuration and hub-tip ratio would be appropriate?
7. Hot pressurized combustion gas at 7.7 MPa (1120 psia) and 850 K with an available pressure ratio of 3.65 is available to drive the liquid-hydrogen turbopump of Problem 5. The molecular weight of the combustion gas is 12.1, and the specific-heat ratio γ is 1.3. In one concept the hydrogen pump is to have 3 centrifugal stages and be driven directly by a single-stage axial turbine at 30,000 rpm. If the turbine and pump are to have the same impeller diameter, what would the hub-tip ratio of the turbine be?
8. Show that for a single-stage centrifugal pump the flow and ideal head coefficients may be defined as

$$\phi = \frac{Q}{\Omega D^3} = \frac{\pi}{2} \frac{b}{D} \frac{w_r}{U}$$

(in which D is the impeller diameter, b the axial blade width at exit, U the tip speed, and w_r the radial velocity component at the impeller exit), and

$$\psi = \frac{1}{4} \left(1 - \frac{2\phi \tan \beta_2}{\pi(b/D)} \right),$$

in which β_2 is the impeller outlet flow angle relative to the impeller. For high efficiency the ratio b/D should not be too low. Determine from the Balje plot (Fig. 13.12) and the above relationships the values of w_r/U and b/D that are associated with best experimental efficiency for impellers with $\beta_2 = 30^\circ$.

9. Show that the ideal head and flow coefficients for an axial pump stage may be written

$$\psi = \frac{\Delta h_0}{\Omega^2 D^2} = \frac{1}{4} \left[1 - \frac{8\phi}{\pi(1 - \zeta^2)} (\tan \alpha_1 + \tan \beta_2) \right]$$

and

$$\phi = \frac{Q}{\Omega D^3} = \frac{\pi}{8}(1 - \zeta^2) \frac{c_z}{U},$$

in which α_1 is the stator outlet angle, β_2 is the rotor outlet angle, and ζ is the hub-tip ratio.

For axial stages one might expect high efficiency to be associated with

$$0.1 < \frac{\Delta h_0}{U^2} < 0.3$$

and

$$0.2 < \frac{c_z}{U} < 0.4.$$

From the Balje plot (Fig. 13.21) for axial pump stages and the above relationships, determine values of $\Delta h_0/U^2$ and c_z/U for the high-efficiency point $n_s = 2$, $d_s = 2.5$, and hub-tip ratios $\zeta = 0.7, 0.8, 0.9$. Compare your results with those of the velocity diagrams of Fig. 13.20 (for which $\zeta = 0.828$).

10. For each of a series of identical axial pump stages with stator outlet angle 38° and rotor outlet angle 68° , hub-tip ratio 0.8, and design-point axial-velocity ratio of 0.25 at mid-radius, use Fig. 13.21 to estimate the stage efficiency.
11. The LH₂ pump, whose performance is shown on Figs. 13.10 and 13.11, is to be used to pump 2500 gpm of liquid oxygen (density 1140 kg/m³) through a pressure rise of 2000 psi. At what speed should the pump be run for best efficiency? Determine the tip speed and power consumption at this speed. Should the pump be run at a different speed?
12. A liquid-oxygen ($\rho = 1140$ kg/m³) pump is to run at 10,000 rpm and pump 80 kg/s against a pressure rise $\Delta p_0 = 5.5$ MPa. From tests on geometrically similar pumps, its dimensionless suction specific speed is known:

$$S = \frac{\Omega Q^{1/2}}{[(p_{01} - p_{v1})/\rho]^{3/4}} = 10.9.$$

If the LOX is just saturated at atmospheric pressure (i.e., if its vapor pressure is 0.101 MPa), what is the minimum allowable pressure in the LOX tank? Neglect pressure losses in lines from tank to pump and gravitational (hydrostatic) head of tank.

13. An axial inducer (similar to the one shown in Fig. 13.13) can be manufactured with an inlet blade angle at the tip diameter of 10° with respect to the tangential direction. It is to be used to pump liquid oxygen at a flow rate of 0.455 m³/s (7223 gpm) and with an NPSH of 12 m. Using the test data shown in Fig. 13.17, select the speed and diameter of the inducer. The hub-tip ratio may be assumed to be 0.3.

14. Examine the extent to which the Stangeland design rules for cavitation prevention: $(2g \text{ NPSH}/c_m^2 > 3$ for water, 2 for liquid oxygen, and 1 for liquid hydrogen) are consistent with the experimental test data shown in Fig. 13.15. Again assume a low hub-tip ratio (0.3) for the inducer and an inlet tip blade angle of 10° .
15. Show that for a single-stage impulse axial turbine whose velocity triangles are shown in the figure, the exit swirl ratio is

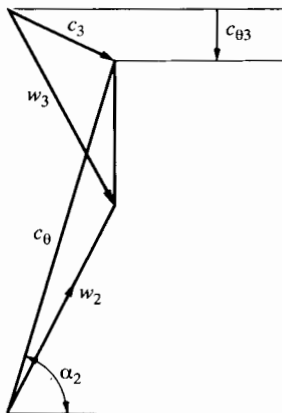
$$\frac{c_{\theta 3}}{c_0} = 2 \frac{U_t}{c_0} - \sin \alpha_2.$$

For a high-work turbine, the maximum value of α_2 would be (for manufacturing reasons) around 70° . With this value of α_2 , compare the value of U_t/c_0 from this formula for zero swirl with the value of U_t/c_0 for maximum efficiency in Fig. 13.23.

Attributing the loss of efficiency to swirl, show that

$$\eta_{\max} - \eta = \left(\frac{c_{\theta 3}}{c_0} \right)^2$$

and compare this with the efficiency curve shown in Fig. 13.23.



PROBLEM 15

16. By drawing velocity triangles beginning with a purely axial absolute exit velocity from the last blade row, show that for an axial velocity-compound turbine with two rows, the maximum work is $8U^2$.
17. For the one-row axial impulse turbine stage with a nozzle exit velocity of 72° and zero exit swirl (corresponding to maximum efficiency) deduce the range of n_s and d_s values corresponding to mean radius axial velocity ratios of

$$0.4 < \left(\frac{c_z}{U} \right)_m < 0.8$$

and hub-tip ratios of

$$0.8 < \zeta < 0.95.$$

Show the lines of constant ζ and $(c_z/U)_m$ on a n_s-d_s chart and thus delineate the region in which exit swirl loss will be negligible.

18. Taking the data of Table 13.3 for the SSME H₂ and O₂ turbopumps, calculate the specific speeds for each stage of the centrifugal pumps. Deduce the pump efficiencies η_p from the experimental data and compare them with the pump efficiency that one might expect for stages operating at these specific speeds.
19. Methane (CH₄) is being considered as a fuel for a liquid-oxygen (LO₂)–liquid-methane (LCH₄) booster for launch from the earth's surface. The density of the liquid methane is 410 kg/m³ at 120 K, and the density of the liquid oxygen is 1116 kg/m³ at 95 K. Both fuel and oxidant are to be raised to 34.5 MPa (5000 psia) in separate turbopumps, each driving at a speed corresponding to highest efficiency. The flow rates for the LO₂ and LCH₄ are 580 kg/s and 290 kg/s, respectively. Estimate the pumping power for the LO₂ and the LCH₄.

If centrifugal pumps are to be used, indicate the number of stages required and impeller diameters and speeds. The impeller tip speed should not exceed 400 m/s.

20. For the liquid-oxygen pumping task specified in Problem 4, consider the possibility of using axial stages instead of centrifugal ones. Determine the required number of stages, the required rpm and overall diameter, and the expected efficiency if the inducer and axial pump are driven by the same shaft and have the same tip diameter. The inlet stagnation pressure is 0.35 MPa above vapor pressure and the suction specific speed is not to exceed 10.

REFERENCES

1. Stangeland, M. C. "Turbopumps for Liquid Rocket Engines," *Threshold* 3 (1988): 34–43. Reprinted with permission.
2. Hearn, H. C. "Evaluation of Bipropellant Pressurization Concepts for Spacecraft," *J. Spacecraft and Rockets* 19 (1982): 320–325.
3. _____. "Thruster Requirements and Concerns for Bipropellant Blowdown Systems," *AIAA J. Propulsion and Power* 4 (1988): 47–52.
4. Balje, O. E. *Turbomachines: A Guide to Design, Selection, and Theory*. New York: Wiley, 1981. Reprinted with permission.
5. Sonntag, G. J., and R. E. Sonntag. *Fundamentals of Classical Thermodynamics*, 3rd ed. New York: Wiley, 1986.
6. Stripling, L. B. "Cavitation in Turbopumps," pt. 2, *Trans. ASME Series D, J. Basic Engineering* (1962): 339; see also Stripling, L. B., and A. Acosta, Jr., "Cavitation in Turbopumps," pt. 1, *Trans ASME Series D, J. Basic Engineering* 84 (1962): 326. Reprinted with permission.

7. Huppert, M.C., and K. Rothe. "Axial Pumps for Propulsion Systems," *Fluid Mechanics, Acoustics, and Design of Fluid Machinery*, vol. 2, NASA SP-304, 1974, pp. 623–654.
8. Kamijo, K., E. Sogame, and A. Okayasu. "Development of Liquid Oxygen and Hydrogen Turbopumps for the LE5 Rocket Engine," *J. Spacecraft and Rockets* 19 (1982): 226–231.
9. Ek, Matthew, C. "Solving Subsynchronous Whirl in the High Pressure Hydrogen Turbomachinery of the SSME," *J. Spacecraft and Rockets* 17 (1980): 208–218.



C H A P T E R

14

ELECTRICAL ROCKET PROPULSION

14.1 INTRODUCTION

By the methods outlined in Section 10.6, one can show that the minimum energy expenditure in taking 1 kg of mass from the surface of the earth and placing it in orbit about the earth is 9 kWh. (Twice this expenditure is required for earth escape.) The maximum chemical energy (lower heating value) that we can obtain per kg of O₂-H₂ propellant is only 3.7 kWh, so we can see that in placing chemical fuel in orbit for orbital transfer propulsion or for space missions, there is a huge energy expense. Chemical energy is inextricably linked to mass, so there is a hard upper limit, around 500 s, to the specific impulse that can be obtained from chemical rockets.

The attractiveness of electrical propulsion is that propellant mass consumption can be greatly reduced because, in principle, any amount of electrical energy can be added to a given quantity of mass. To put it another way, the specific impulse has no hard upper limit, and the energy source for electrical propulsion can be either accessible in space (solar energy) or brought from earth in the form of nuclear fuel whose energy density (kWh/kg) is orders of magnitude greater than that of chemical fuel.

Nuclear energy could serve directly as a heat source for rocket propellant, but the difficulty with this concept is that the heat would have to pass through solid walls; thus the maximum propellant temperature (with purely nuclear heating) would be limited by the allowable wall temperature. Using Eq. (11.3), one could show that the specific impulse would not greatly exceed that of an H₂O₂ chemical

rocket although this would allow use of pure H₂ as propellant. Thus it appears that the most promising way to add energy to propellant in space is to do it electrically, by using either solar or nuclear fuel to generate the electrical power. Much engineering thought has been devoted to these possibilities.

We can classify the most promising concepts for electrical propulsion under three headings:

1. *Electrostatic*. In this case the propellant consists of discrete charged particles accelerated by electrostatic forces. The particles (usually atoms) are charged by electron bombardment.
2. *Electrothermal*. Here the propellant is a fluid heated either by an electrical arc discharge through the fluid (arcjet) or by electrical heating through a wall (resistojet).
3. *Electromagnetic*. For this application of electrical energy, a stream of electrically conducting fluid is accelerated by electromagnetic and pressure forces. For reasons we will note later, electromagnetic forces are most easily used in a pulsed operation producing short bursts of thrust.

All these modes of electrical propulsion have been demonstrated in space, some for long periods but all at low thrust levels (ranging from 10 mN to 220 mN). Electrostatic (ion) propulsion has been demonstrated by the mercury ion accelerator that successfully operated for 10,000 hours (until it ran out of propellant) in the spacecraft called *SERT II* (Space Electrical Rocket Test II). The thrust level was 28 mN, and the electrical power level was 1000 W, the energy source being a solar photovoltaic array. In other space experiments cesium ions have been used with thrusts as high as 90 mN and also with solar energy sources. Figure 14.1 shows the ATS-6 spacecraft mounted with two 4.5 mN cesium ion thrusters

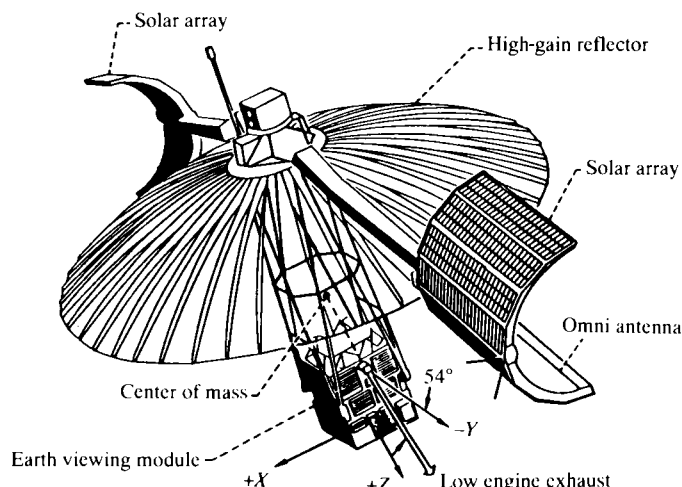


FIGURE 14.1 ATS-6 spacecraft and ion engine configuration. (Courtesy Sovey, Carney, and Knowles [1]. © AIAA. Reprinted with permission.)

whose specific impulse was 2500 s. The purpose of the experiment with this spacecraft was to show how small thrusters such as these could keep a spacecraft properly oriented in a geosynchronous orbit. The cesium ion thrusters have also operated in space from a nuclear source, the SNAP 10A (System for Nuclear Auxiliary Power), which provided heating from the process of isotope decay.

The resistojet is an electrothermal rocket that, using nitrogen, ammonia, or hydrazine, has also been demonstrated in space for satellite attitude control. With hydrazine (which is a chemical monopropellant) we have a combination of electrical and chemical propulsion. Producing very small thrusts (less than 200 mN), the resistojet may have a throat diameter as small as 1 mm. Resistojets will be able to utilize liquid wastes from the space station by using them to produce thrust for orbital maintenance. Figure 14.2 is a cross section of a resistojet showing its long heating passage, small throat, and large expansion area ratio. Power levels in space experiments have ranged up to 500 W.

Electromagnetic propulsive forces have been used in space in the Teflon pulsed-plasma thruster and the magnetoplasmadynamic (MPD) thruster. The term *plasma* denotes an electrically neutral mixture of ions, electrons, and neutral particles flowing at high temperature in a fluid stream. With Teflon propellant, the plasma is created by electric arc discharge that produces a fluoropolymer gas. The hot gas is accelerated both by pressure forces and by the interaction of the discharge current and its self-generated magnetic field. The Teflon pulsed-plasma thruster has been used in satellites to compensate for the effects of small drag forces. Pulsed-MPD thrusters using ammonia and argon propellant have also been demonstrated in space. The argon propellant for one experiment was energized by a 25 kJ discharge during a 1 ms pulse, thus attaining a peak power

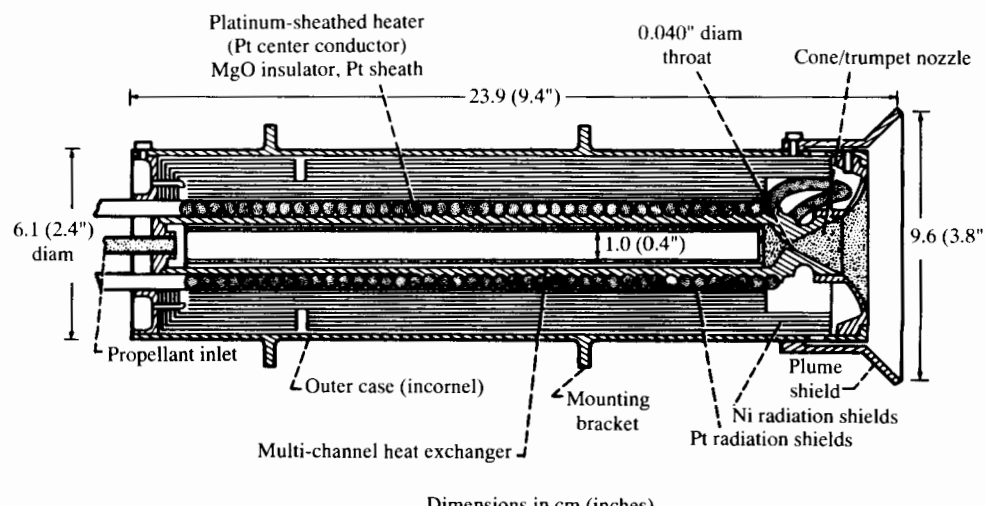


FIGURE 14.2 Advanced development engineering model resistojet. (Courtesy Tacina [2]. © AIAA. Reprinted with permission.)

of 25 MW! A number of electrical propulsion experiments have been successfully done in space by the Soviet Union. One of these was on an electromagnetic thruster using xenon propellant.

Hence there is a large body of knowledge of design and operation of small-scale electrical thrusters. It is interesting to consider whether electrical propulsion will have a much bigger role to play in the future in orbital transfer operations (e.g., from LEO to GEO—low earth orbit to geosynchronous earth orbit) as well as in deep-space missions. Studies [3, 4] indicate substantial potential advantages in using electrical propulsion for the LEO–GEO transfer despite the mass penalty of the power plant that may be needed. The main candidates for these (and much longer) space missions are the electrostatic, the electrothermal (arcjet), and the pulsed-magnetoplasmodynamic thrusters; they are the ones we have chosen for consideration in the following pages.

Scaling up the size of electrical thrusters necessarily brings up the question of the power generation unit, and specifically the role of nuclear power generation in the kW-to-MW range. At large power levels, arrays of solar cells would likely demand too much area and structural support mass to be feasible. Nevertheless, as Fig. 14.3 suggests, even a nuclear-electric generator in the 100-kW range (here shown as the source for arcjet propulsors) can constitute a formidable design problem. As Chapter 11 indicates, the specific mass (kg/kW) of a nuclear plant such as this will be strongly dependent on power-plant size. It is only at power levels of the order of 100 kW or larger that such a generator would be feasible. Figure 14.3 shows that the reactor is located far from the command module and must be supplied with a large radiator area for heat rejection. Heat pipes are to be used to conduct the waste heat to the radiator surfaces. The closed-cycle thermoelectric converter feeds power to the power-processing unit (PPU), which (requiring its own waste-heat radiator) supplies the d.c. voltage needed by the arcjet. In this design the arcjet is to develop a specific impulse of 1050 s at a thruster efficiency of 45% while producing 2.35 N thrust from each of three engines.

The power-plant design problem is beyond the scope of this book, but we keep it in the back of our minds while considering the feasibility of various kinds of electrical thrusters for space propulsion (as opposed to satellite-station-keeping).

14.2 ELECTROSTATIC PROPELLANT ACCELERATION

Figure 14.4 shows, schematically, a typical ion rocket. Neutral propellant is pumped to an ion production chamber, from which ions and electrons are withdrawn in separate streams. The ions pass through the strong electrostatic field established by the acceleration electrodes shown in Fig. 14.2. The ions accelerate to high speeds, and the thrust of the rocket is the total reaction to their accelerating forces. The ionization chamber is maintained at the positive acceleration potential, while the last electrode is “grounded” at the vehicle potential. Intermediate electrodes may be held at other potentials to aid in the extraction of ions and in the formation of a suitable exhaust beam.

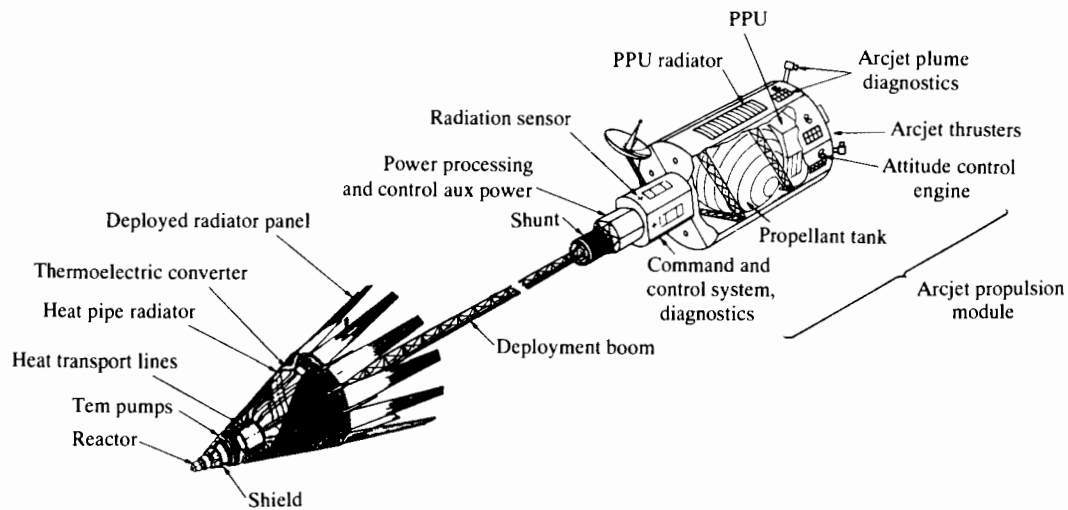


FIGURE 14.3 Proposed spacecraft configuration for the space-reactor-power-system flight experiment. (Courtesy Deininger and Vondra [12]. © AIAA. Reprinted with permission.)

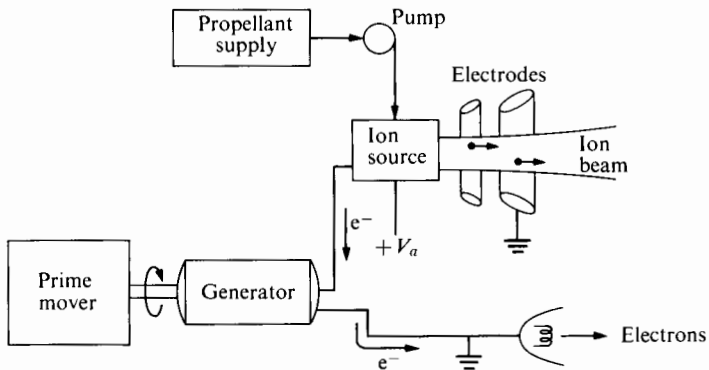


FIGURE 14.4 Ion rocket.

It is also necessary to expel the electrons in order to prevent the vehicle from acquiring a net negative charge. Otherwise ions would be attracted back to the vehicle and the thrust would vanish. To remove the electrons from the vehicle, it is necessary that they first be “pumped” to ground potential by the generator. They may then be removed from the vehicle at a hot filament. Thus the “thrust chamber” of an electrostatic rocket consists of a source of charged propellant and an electrode structure of extract, accelerate, and expel the propellant in a well-defined beam. In addition the system requires a propellant storage and supply system and an electrical power source.

The overall performance of the electrostatic rocket can be derived from basic principles. If a particle of mass m , charge q , and negligible initial velocity passes through a potential difference V_a , it will acquire an exhaust kinetic energy of

$$\frac{mu_e^2}{2} = qV_a,$$

where u_e is the exhaust velocity. Therefore the specific impulse of a beam of such particles is

$$I_{sp} = \frac{1}{g_e} \sqrt{2 \frac{q}{m} V_a}, \quad (14.1)$$

where g_e is the acceleration due to gravity near the surface of the earth. This relationship is shown graphically in Fig. 14.5.

Since the thrust due to the beam acceleration is $\mathcal{T} = \dot{m}u_e$, the mass flow per unit thrust is

$$\frac{\dot{m}}{\mathcal{T}} = \frac{1}{g_e I_{sp}}. \quad (14.2)$$

The total beam current I is given by $I = (q/m)\dot{m}$, or, from Eq. (14.2),

$$\frac{I}{\mathcal{T}} = \frac{q}{m} \frac{1}{g_e I_{sp}}. \quad (14.3)$$

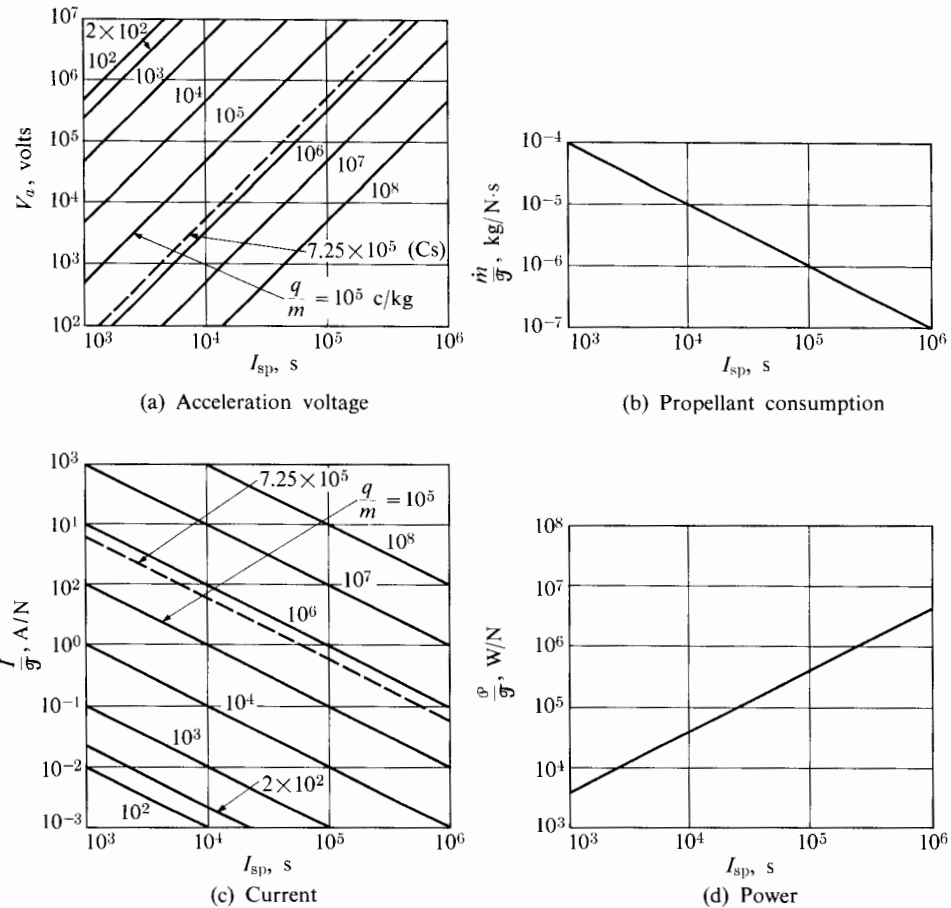


FIGURE 14.5 Performance of an ion rocket.

The beam power \mathcal{P}_b is given by

$$\mathcal{P}_b = IV_a = \frac{\dot{m}u_e^2}{2}$$

or

$$\frac{\mathcal{P}_b}{\mathcal{T}} = \frac{g_e I_{sp}}{2}. \quad (14.4)$$

Equations (14.2), (14.3), and (14.4) are illustrated graphically in Fig. 14.5 for various values of the charge-to-mass ratio q/m , in which q is the charge in coulombs (C) and m is the mass in kilograms (kg). For reference, the characteristics for cesium ($7.25 \times 10^5 \text{ C/kg}$) are shown in Fig. 14.5(a) and (c).

The power consumed by an electrostatic rocket is greater than the beam power defined above, largely because power must be supplied to form the ions. The energy that must be supplied to each atom in order to ionize it is called the *ionization potential*. It is of the order of several electron volts per ion (see Section 14.3). Experimentally, investigators have found that much more than this energy must be supplied to the ionization chamber because of losses to the chamber wall. Smaller quantities of power are lost in interception by the grid system and in power consumed by the electron ejection system. Part of the wall loss is due to radiation from atoms excited by the electron bombardment (by which they are ionized). The density of the ion gas is so low that little of this radiation is absorbed before it reaches the wall. Part of the loss is due to ions impacting the wall and recombining with electrons. After such events atoms may return to the interior of the chamber and be re-ionized. Numerous innovations in chamber design have been motivated by the desire to reduce wall losses in ionization chambers. It appears that total loss levels of the order of 100 eV per ion are possible [6,7,8].

The ratio of beam power to total electrical power consumption is defined as the *power efficiency*, η , of the ion engine:

$$\eta = \frac{\text{beam power}}{\text{total electrical power}}. \quad (14.5)$$

In terms of energy per ion rather than power, and neglecting beam interception and neutralization power requirements,

$$\eta \approx \frac{\text{exhaust kinetic energy}}{\text{exhaust kinetic energy} + \text{charging energy}}$$

or

$$\eta \approx \frac{\frac{1}{2}mu_e^2}{\frac{1}{2}mu_e^2 + e_i + e_l},$$

in which m is the ion mass, e_i is the ionization energy, and e_l is the energy loss per ion. Since in general $e_i \ll e_l$,

$$\eta \approx \frac{\frac{1}{2}mu_e^2}{\frac{1}{2}mu_e^2 + e_l} = \frac{\frac{1}{2}mg_e^2 I_{sp}^2}{\frac{1}{2}mg_e^2 I_{sp}^2 + e_l}.$$

We can see from this equation that if the energy loss from the ionization chamber, per ion, is independent of the propellant, the power efficiency at a given specific impulse is greater for more massive ions. Table 14.1 shows the atomic masses of several elements that could be charged in an electron bombardment chamber.

Estimating the chamber loss per ion as 100 eV, we can compute the efficiency with different propellants and find the result shown in Fig. 14.6. Clearly the heav-

TABLE 14.1 Atomic masses and ionization potentials

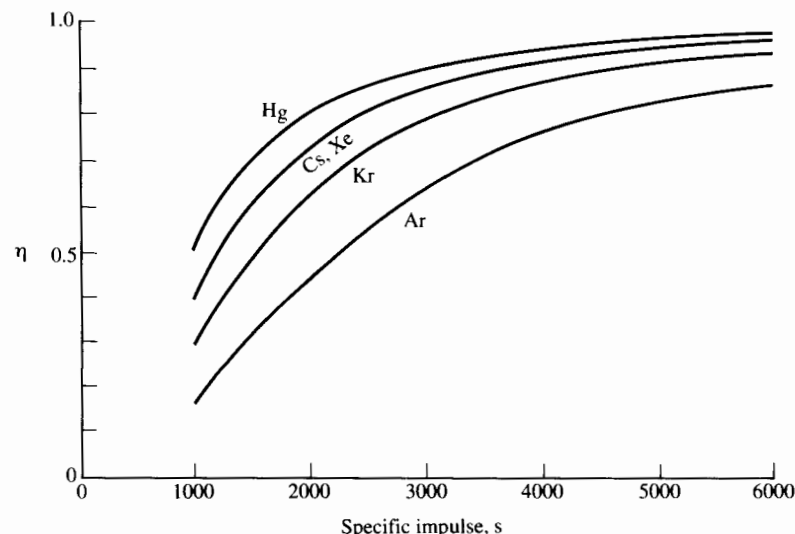
Element	Atomic weight	m (10^{-25} kg)	q/m (singly charged) (10^5 C/kg)	Atomic number	1st ionization potential (eV) ^a	2nd ionization potential (eV) ^a
Cs	132.9	2.21	7.25	55	3.89	25.1
Hg	200.6	3.33	4.80	80	10.44	18.75
Xe	131.30	2.18	7.34	54	12.13	21.21
Kr	83.80	1.39	11.50	36	13.999	24.359
Ar ^b	39.948	0.66	24.13	18	15.799	22.629

^a1 eV = 1.60×10^{-19} J^bA = 6.0225×10^{26} molecules/kmol

ier ions show a substantial efficiency advantage for I_{sp} around 2000. Modifying Eq. (14.4) to allow for the beam power efficiency, we can write

$$\frac{\mathcal{P}}{\mathcal{P}} = \frac{\eta}{g_e I_{sp}}, \quad (14.6)$$

in which \mathcal{P} is the power supplied to the thruster and η is the efficiency just discussed. The results of using Eq. (14.6) for the substances shown in Table 14.1 are shown in Fig. 14.7.

**FIGURE 14.6** Efficiency of ion thrusters with 100 eV loss per ion.

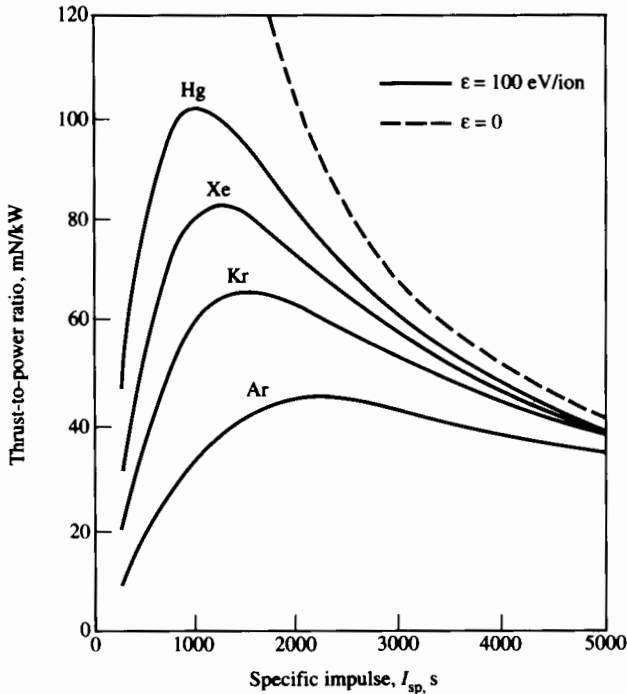


FIGURE 14.7 Thrust-to-power ratios for high-performance ion propulsion subsystem operated on various propellants. (Courtesy Beattie, Matossian, and Poeschl [6]. © AIAA. Reprinted with permission.)

14.3 BOMBARDMENT IONIZATION

In the most successful electrostatic thrusters that have been produced, propellant atoms are ionized by electron bombardment. The electrons are emitted from a cathode surface and gain energy from the potential difference between cathode and anode surfaces in a bombardment ionization chamber.

In 1961 Kaufman [9] presented the design of an ion thruster that has been under active development ever since and can be considered the dominant concept in electrostatic propulsion. Kaufman's thruster was designed for mercury propellant but has also been adapted for use with xenon and argon. Though mercury has the highest potential thruster efficiency (as shown in Fig. 14.6) and needs minimum tankage mass, it is not likely, for environmental reasons, to be used heavily in near-earth-orbit transfers. Both xenon and argon are more likely to be environmentally acceptable, and xenon has nearly as high a thruster efficiency as mercury (see Fig. 14.6). Xenon tends to be relatively expensive, but it can be stored noncryogenically, whereas argon requires cryogenic storage; however, argon is less expensive and is more plentifully available than xenon. For an LEO-GEO transfer the ratio of empty tank mass to full tank mass would be of order 0.01 for mercury and 0.1 for xenon and argon [10].

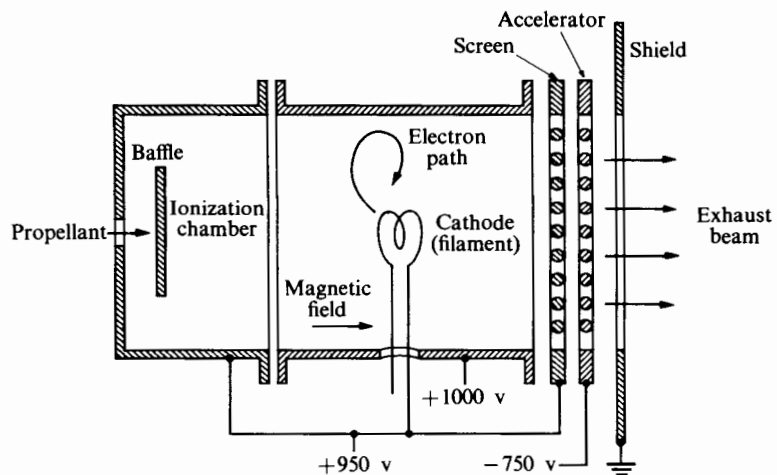


FIGURE 14.8 Schematic of low-density ion engine of Kaufman, showing typical operating voltages.

Figure 14.8 shows a schematic diagram of a Kaufman thruster with its electron-emitting cathode. On their way toward the anode (which is the chamber wall), the electrons accelerate and bombard neutral propellant atoms introduced from the left side of the chamber. If the electron–atom collision is successful, it will produce a positive ion by removing an electron from the atom. The positive ions so produced then pass through the screen and are accelerated by the screen-accelerator potential difference to become a high-velocity exhaust beam. Not shown in Fig. 14.8 is the so-called neutralizer beam of electrons that must be separately emitted from the chamber to maintain zero net charge for the vehicle. Indicated inconspicuously in Fig. 14.8 is the axial magnetic field that Kaufman used to control the motion of the electrons so as to greatly increase the probability of ionizing collisions. The magnetic field does this by forcing the electrode to follow a very long spiral path (instead of a short, straight line) from cathode to anode. Since the mean free path of the atoms in the chamber may be of the order of a centimeter, one can see why special measures are needed to promote contact between electrons and incoming propellant atoms.

Figure 14.9 is a cutaway view of an early ion engine of this type, showing the windings that produce the magnetic field. The acceleration grid in this case consists of perforated plates. The cathode consists of an internally heated composite structure. The mercury feed system is a simple boiler arrangement. Engines of this type have produced ions with an energy consumption of the order of 450 eV per ion (based only on arc power consumption). Propellant efficiencies (ratio of ion mass flow to total propellant flow) greater than 90% have been achieved with less than 0.5% beam interception on the accelerating electrode. Current densities of the order of 1.5 to 2.0 mA/cm² (averaged over the total accelerator area) have been realized.

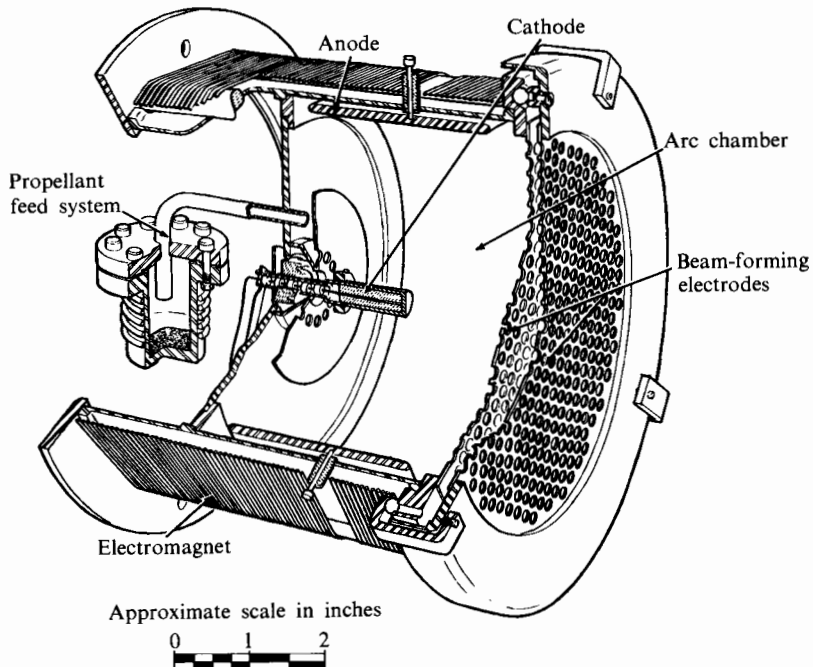


FIGURE 14.9 Low-current-density ion engine. (Courtesy Ion Physics Corporation. Reprinted with permission.)

Modern electrostatic thrust chambers use high-strength permanent magnets, and highly nonuniform field strength in the chamber has been found advantageous. But to throw light on how a magnetic field can promote ionization, we consider here the simple case in which the magnetic-field strength B and the electrostatic potential gradient dV/dr are uniform throughout the chamber. We are looking at the idealized case in which the cathode consists of a long cylinder of radius r_c located coaxially within a cylinder of inner radius r_a that constitutes the anode.

In this case (using the basic equations of electrostatics and magnetostatics given in Appendix IX) we may show that the forces on an electron in such a region are given by:

$$\text{Radial direction} \quad F_r = m_e(\ddot{r} - r\dot{\theta}^2) = e \frac{dV}{dr} \pm er\dot{\theta}B, \quad (14.7)$$

$$\text{Tangential direction} \quad F_\theta = m_e(2\dot{r}\dot{\theta} + r\ddot{\theta}) = \pm e\dot{r}B$$

or

$$rF_\theta = m_e \frac{d}{dt}(r^2\dot{\theta}) = \pm r(e\dot{r}B), \quad (14.8)$$

in which m and e are the mass and charge, respectively, of an electron and B is the magnetic flux intensity defined in Appendix IX. The plus-or-minus sign de-

pends on the direction of the axial magnetic field. While the determination of the radial variation of potential within the ionization chamber (dV/dr in Eq. 14.7) is not a simple matter, Eq. (14.7) may be integrated to obtain the required field strength in terms of the total potential drop regardless of the intervening shape of the potential distribution. We may write Eq. (14.8) as

$$m_e \frac{d}{dt} (r^2 \dot{\theta}) = \pm eB \frac{d}{dt} \left(\frac{1}{2} r^2 \right),$$

which, after we multiply both sides by dt , integrates directly to

$$m_e r^2 \dot{\theta} = \pm \frac{eB}{2} r^2 + \text{const.}$$

At the cathode, $r = r_c$ and $\dot{\theta} \approx 0$; hence the constant of integration is $\pm(eB/2)r_c^2$, and the solution may be written

$$\dot{\theta} = \pm \frac{eB}{2m_e} \left(1 - \frac{r_c^2}{r^2} \right). \quad (14.9)$$

At the anode, if the electron velocity is nearly tangential, then since the sum of the kinetic and electrostatic potential kinetic energies of the electron remain constant,

$$m_e \frac{u_e^2}{2} = e \Delta V_a.$$

Thus

$$\dot{\theta} = \frac{u_a}{r_a} = \frac{\sqrt{2e/m_e \Delta V_a}}{r_a},$$

where r_a = anode radius and ΔV_a = anode potential relative to cathode.

Substituting this expression in Eq. (14.9), we obtain

$$B = \frac{\sqrt{8(m_e/e) \Delta V_a}}{r_a [1 - (r_c^2/r_a^2)]}. \quad (14.10)$$

This derivation, limited to the case of radially uniform magnetic-field strength, serves as an example only of how one may determine the field strength needed to produce nearly tangential motion at the anode for a given ΔV_a . More is said in Section 14.5 about best distribution of B through the chamber.

We now consider the required electrostatic field strength in the chamber. The question is how large the term ΔV_a in Eq. (14.10) should be. This has to do with the energy the electrons need to conduct ionizing collisions successfully. Note that while the magnetic field B strongly affects the path of the electron, it is only the position of the electron in the electrostatic field that affects its energy prior to collision.

The electron structure of an atom consists of a number of shells, each containing a specified number of electrons. The removal of one of these electrons to create a positive ion requires a quantity of energy called the *ionization potential*.

(Negative ions produced by electron attachment have not yet been successfully produced for ion rockets.) As one might expect, those atoms containing single electrons in unfilled outer shells are especially easily ionized; that is, they have relatively low ionization potentials. The alkali metal elements—for example, cesium—have particularly low ionization potentials. Table 14.1 lists first and second ionization potentials (pertaining to the removal of the first and second electrons, respectively) for that element and others that may be used in electrostatic thrusters. The table shows the relatively high ionization potentials of the inert elements, reflecting the fact that electrons must be extracted from a stable outer shell that is completely filled. The second electron extracted from an alkali metal must also come from a full shell, which accounts for the high ratio of second to first ionization potentials of these materials. Mercury, often considered a propellant because of its high atomic mass and relatively easy handling characteristics, normally contains two electrons in its outermost shell. Hence its first two ionization potentials are relatively close together.

If an electron current is conducted through a gas, electron-atom collisions will occur and, if the electrons are of the proper energy, some of these collisions will result in ionization. Although a single atom might conceivably be ionized as the result of several electron collisions, it is reasonable to expect that no appreciable ionization will occur until the bombarding electrons each possess kinetic energies equal to or greater than the ionization potential. As the electron energy is increased above this value, it is experimentally observed that the rate of formation of ions increases sharply to a maximum at an electron energy from three to five times the ionization energy, and then falls off slowly with further increases of electron energy.

If a flux of \dot{N}_e electrons per second per unit area enters a region of length dx (Fig. 14.10), where the atom density is n_a (the atoms being assumed stationary), the rate of formation of ions dn_i/dt will be proportional to \dot{N}_e and n_a . The proportionality constant is called the cross section for ionization Q_i :

$$\frac{dn_i}{dt} = Q_i \dot{N}_e n_a \text{ ions per second per unit volume.} \quad (14.11)$$

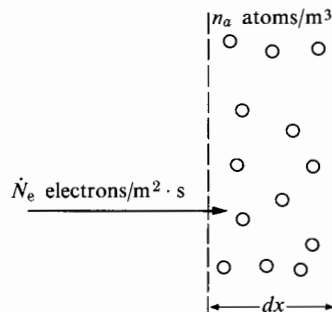


FIGURE 14.10 Definition of cross section for ionization Q_i .

(The reason Q_i is called a cross section is that it can be interpreted as being the effective target area each neutral atom presents to the oncoming electron flux. The picture is that if an electron hits any part of the target area, an ionization occurs.) The cross section, however, is not actually a geometric property. The probability of an electron successfully ionizing a target atom depends very much on the energy of the electron. In addition to the probability that an energetic electron will knock one electron off its target, there are separate probabilities that it will knock two, three, or more away. Thus we can speak of separate energy-dependent cross sections for single, double, and triple ionization, and so on.

Figure 14.11 indicates the energy dependence of the cross section for various degrees of ionization of mercury. Each curve begins approximately at the ionization potential. From Fig. 14.11 one may see that at the electron energy yielding the peak cross section for single ionization, some double- and even triple-charged ions would also be formed. In a given accelerator their charge-to-mass ratios would be much too high, so that they would develop excessive exhaust velocities and perhaps seriously alter the focusing characteristics of the exhaust beam. It is for this reason that propellants with a large difference between first and second ionization potentials are especially desirable.

The choice of ΔV_a depends on the ionization potentials of the propellant being used. Thus, for mercury, ΔV_a should be greater than 10.39 v. Since no Hg^{2+} ions will be formed below 18.65 v, ΔV_a can be raised to at least this value. In practice it is even higher, for two reasons. First, the cross section for single ionization continues to rise rapidly (up to energies of approximately 100 eV for mercury), whereas that for double ionization does not rise so fast. Second, the electron energy is everywhere less than ΔV_a , since the potential increases in the radial direction. Actually, the presence of the conducting plasma within the chamber permits only slight potential variation throughout most of the volume; thus a large fraction of the potential rise (90% or so) occurs in a relatively thin cathode sheath. A value of ΔV_a between 20 and 100 V would appear reasonable for mer-

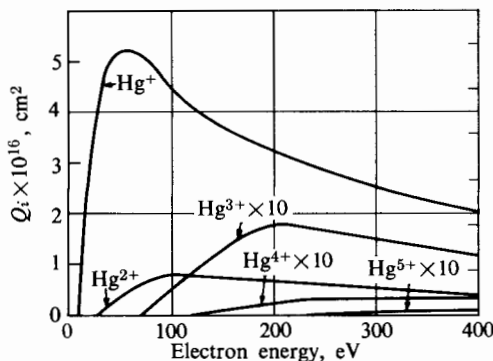


FIGURE 14.11 Cross section for different degrees of ionization of mercury by electron impact.
(Courtesy Bleakney [11].)

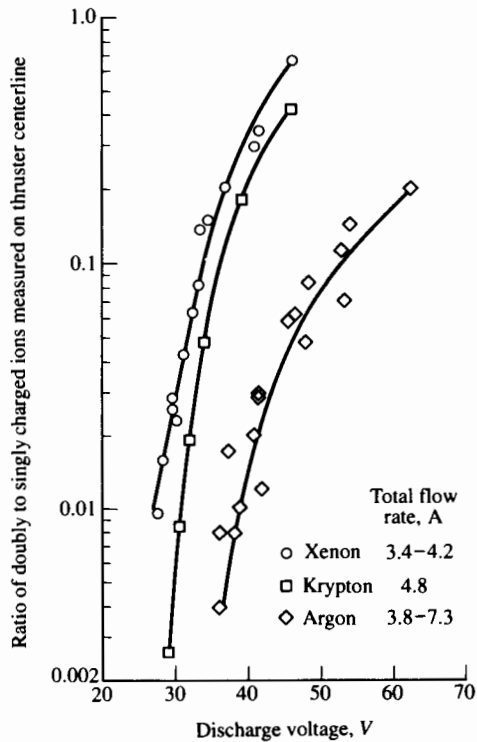


FIGURE 14.12 Ratio of doubly to singly charged ions on thruster centerline versus discharge voltage. (Courtesy Sovey [7]. © AIAA. Reprinted with permission.)

cury propellant. For mercury ion propellant, a value of 40 V is typically used in the bombardment chamber [12].

For xenon, krypton, and argon, Fig. 14.12 shows the ratio of singly to doubly charged ions as function of anode-cathode potential differences. These values were obtained not from ionization potential data but from measurements in a specific experimental chamber, with the use of a spectrometer probe.

Ions that reach the downstream end of the ionization chamber are accelerated through a grid system. For the potentials indicated in Fig. 14.8, the ions are first accelerated through 1750 V and then decelerated through 750 V.

14.4 THE PLANE DIODE

Between the screen and accelerator grids shown schematically in Fig. 14.8 is an intense electrostatic field that is not one-dimensional. Nevertheless, gradients in voltage in the axial (flow) direction are likely to be very much larger than they are in the transverse direction. With this in mind, we look in a simplified way at the ion acceleration process by conceptually replacing these grids with a plane

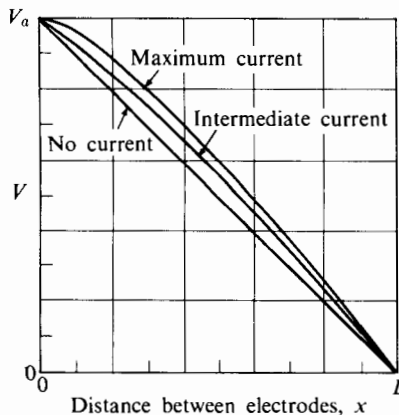


FIGURE 14.13 Potential distribution between infinite parallel-plane electrodes with a current of positive particles.

diode. Here we are thinking of a pair of planes that offer no resistance to the flow of ions, but each of them has fixed uniform voltage on its surface. The electrostatic field between them will be affected both by the voltage difference across the diode and by the distribution of charged ions instantaneously located between them. We can speak of the “current” associated with the ion flow as $j \text{ A/m}^2$ and the charge density as $\rho_i \text{ C/m}^3$. We assume that all ions are singly charged.

Figure 14.13 shows typical potential distributions between two electrodes whose potential difference is V_a . If no current exists between them, the interelectrode potential distribution will be linear. If positive particles are made available at the high-potential electrode, the potential gradient at the surface will “extract” the particles and accelerate them to the opposite electrode. These charges in transit constitute a current between the electrodes, and, at the same time, the cloud of charges within the gap raises the potential in that region. As the charge density increases, the extraction gradient at the charge-emitting surface decreases. If an unlimited supply of charged particles is available, the current will increase until the extraction gradient is reduced to zero, as in Fig. 14.13. This current is called the space-charge-limited current for the potential difference V_a and electrode spacing L .

The effect of the charge distribution on the potential distribution is given by Eq. (IX.9) in Appendix IX, which for this problem becomes

$$\frac{d^2V}{dx^2} = -\frac{\rho_i}{\epsilon_0}, \quad (14.12)$$

where ρ_i = local charge density, corresponding to one absent electron per ion, and $\epsilon_0 = 8.85 \times 10^{-12} \text{ C}^2/\text{N} \cdot \text{m}^2$ is the permittivity of free space.

The current and the charge density are related by the one-dimensional form of Eq. (IX.11), which is

$$j = \rho_i u, \quad (14.13)$$

where j is the current density and u is the charge velocity. The charge velocity in turn is related to the voltage by the energy equation

$$qV + \frac{mu^2}{2} = qV_a, \quad (14.14)$$

assuming that the charges have negligible velocity as they leave the positive electrode.

Equations (14.12), (14.13), and (14.14) may be used with appropriate boundary conditions to determine the distribution of potential and charge velocity, as well as the current density between the electrodes. The solution for maximum current density is of particular interest. Using Eqs. (14.13) and (14.14) to eliminate the variables u and ρ_i , we obtain from Eq. (14.12)

$$\frac{d^2V}{dx^2} = -\frac{j}{\epsilon_0 \sqrt{2q/m}} (V_a - V)^{-1/2}. \quad (14.15)$$

Making the substitutions

$$V_a - V = V^*$$

and

$$\frac{j}{\epsilon_0 \sqrt{2q/m}} = \alpha,$$

we may write Eq. (14.15) as

$$\frac{d^2V^*}{dx^2} = \alpha(V^*)^{-1/2}.$$

Multiplying both sides by $2 dV^*/dx$, we have

$$2\left(\frac{dV^*}{dx}\right)\frac{d^2V^*}{dx^2} = 2\alpha\left(\frac{dV^*}{dx}\right)(V^*)^{-1/2}.$$

After rearrangement this becomes

$$d\left[\left(\frac{dV^*}{dx}\right)^2\right] = 2\alpha(V^*)^{-1/2} dV^*,$$

which may be integrated to

$$\left(\frac{dV^*}{dx}\right)^2 = 4\alpha(V^*)^{1/2} + C_1,$$

in which C_1 is a constant of integration. For maximum current,

$$\frac{dV^*}{dx} = V^* = 0, \quad \text{at } x = 0.$$

Therefore $C_1 = 0$, and hence

$$\frac{dV^*}{dx} = 2\sqrt{\alpha}(V^*)^{1/4}.$$

Integrating again and using the boundary condition $V^* = 0$ at $x = 0$, we have

$$\frac{4}{3}(V^*)^{3/4} = 2\sqrt{\alpha}x.$$

From this equation we may obtain the potential distribution for space-charge-limited current:

$$V = V_a - \left(\frac{9}{4} \frac{j}{\epsilon_0 \sqrt{2q/m}} \right)^{2/3} x^{4/3}. \quad (14.16)$$

For electrodes of spacing L and potential difference V_a , the maximum current is

$$j = \frac{4}{9} \epsilon_0 \sqrt{2q/m} \frac{V_a^{3/2}}{L^2}. \quad (14.17)$$

If the beam could pass through the negative electrode without impingement, the maximum thrust per unit area of beam would be given by

$$\frac{\mathcal{T}}{A} = \frac{\dot{m} u_e}{A},$$

where u_e is the particle velocity at $x = L$. The mass flow per unit area is

$$\frac{\dot{m}}{A} = \frac{\rho_e u_e}{q/m} = \frac{j}{q/m},$$

the exit velocity is

$$u_e = \sqrt{2(q/m)V_a},$$

and the maximum thrust per unit area is

$$\frac{\mathcal{T}}{A} = \sqrt{\frac{2}{q/m}} j V_a^{1/2}$$

or, using Eq. (14.17),

$$\frac{\mathcal{T}}{A} = \frac{8}{9} \epsilon_0 \left(\frac{V_a}{L} \right)^2. \quad (14.18)$$

Thus the maximum thrust per unit area depends only on the average electrostatic field intensity. Field intensity, in turn, is limited by the voltage-breakdown characteristics of the acceleration gap.

Using Eq. (14.1) we obtain

$$\frac{\mathcal{T}}{A} = \frac{2}{9} \frac{\epsilon_0}{L^2} \frac{(g_e I_{sp})^4}{(q/m)^2}, \quad (14.19)$$

where I_{sp} is the specific impulse and g_e is the acceleration due to gravity at the earth's surface. For a finite beam of diameter D that is essentially one-dimensional, the thrust may be written

$$\mathcal{T} = \frac{2\pi}{9} \epsilon_0 V_a^2 R^2 \quad (14.20)$$

in which $R = D/L$ is called the *beam aspect ratio*.

Equation (14.19) demonstrates the strong dependence of thrust per unit area on specific impulse for the space-charge-limited plane diode. For a given propellant the specific impulse determines the acceleration potential that as Eq. (14.16) shows, limits the current density for any given spacing of the electrodes, provided the source is capable of providing this current density. It is advantageous, therefore, to reduce the electrode spacing as much as possible.

Sovey [7] reports successful experience with screen and accelerator grids separated by only 0.7 mm. The screen and accelerator voltages were +1400 and -500 V, respectively. The open-area fraction was 0.75 for the screen grid and 0.29 for the accelerator grid.

The current density can be greatly increased for a given specific impulse (again provided the source is capable of supplying it) by using a so-called accel-decel system employing three electrodes that allow operation at maximum potential gradient, as illustrated in Fig. 14.14. In this way the current density is not limited by the specific impulse. The maximum current density, instead of being given by Eq. (14.17), is given by

$$j = \frac{4}{9} \epsilon_0 \sqrt{2q/m} \frac{(\Delta V)^{3/2}}{L^2}, \quad (14.21)$$

and the thrust per unit area by

$$\frac{\mathcal{T}}{A} = \frac{8}{9} \epsilon_0 \left(\frac{\Delta V}{L} \right)^2 \left(\frac{V_a}{\Delta V} \right)^{1/2}$$

or

$$\frac{\mathcal{T}}{A} = \frac{8}{9} \epsilon_0 \left(\frac{\Delta V}{L} \right)^2 \frac{g_e I_{sp}}{[2(q/m) \Delta V]^{1/2}}. \quad (14.22)$$

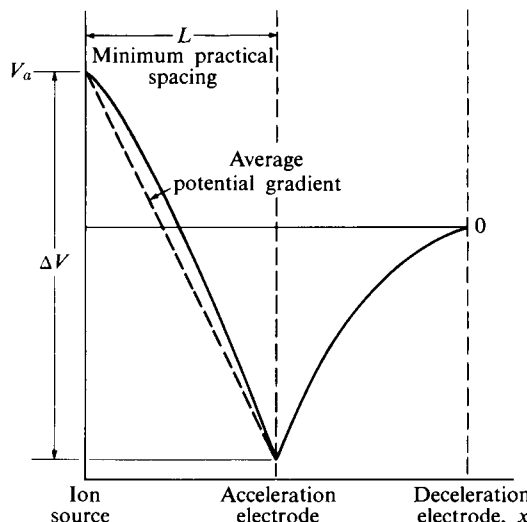


FIGURE 14.14 Plane triode accelerator potential distribution.

Exhaust Neutralization

To avoid a charge buildup in the vehicle that would attract exhausted propellant and reduce thrust, it is necessary to expel charge of both signs at an equal rate. Neutralizing the exhaust-space charge very near the exhaust plane might be thought necessary, since a large, positive potential "hill" arising from inadequately neutralized space charge would seriously perturb the beam. However, the high charge-to-mass ratio of the electrons causes them to be very quickly attracted toward the positive charge if they are emitted in the vicinity of the ion beam, thus eliminating any potential hill that might tend to build up. Experimentally, adequate space-charge neutralization has been easily achieved by a hot-filament electron emitter placed beside the ion exhaust beam. An electron possessing merely thermal energy (2 or 3 eV) travels much faster than the ions in the exhaust beam.

14.5 ELECTROSTATIC THRUSTER PERFORMANCE

Sovey [7] has used high-strength permanent magnets to produce within the ionization chamber a magnetic-field-strength distribution that will both reduce wall losses due to ion recombination and promote forward flux of the ions. Figure 14.15 shows the magnetic-field contours associated with the samarium-cobalt and aluminum-nickel-cobalt permanent magnets, the former mounted on the chamber wall (the anode surface) and the latter on the cathode surface. From the shape of these field lines (as detected by iron filings), the chamber is called a ring-cusp thruster. It is essential to keep the permanent magnets at temperatures of less than 300°C to avoid irreversible loss of magnetism.

Figure 14.16 shows the low levels of loss that have been attained with argon, krypton, and xenon propellants. This kind of data underlies the efficiency and thrust calculations of Figs. 14.6 and 14.7, which assume a loss of 100 eV. The data are the results of effort to find the field-strength distribution that minimizes ion contact with the wall.

Beattie, Matossian, and Poeschl [6] report the following measurements for their xenon ion thruster:

Specific impulse	2900
Power input, W	1316
Thrust produced, mN	63.3
Total propellant efficiency, %	88.4
Total thruster efficiency, %	69
Thrust/power, mN/kW	48.1

The propellant efficiency is the rate of ion production divided by the rate of atom supply.

Steiner [8] has modified the chamber geometry of a ring-cusp thruster to minimize anode surface area. Reducing the residence time of the ions with the chamber reduces wall loss but tends to decrease the fraction of the propellant that is ionized. Using the chamber geometry shown in Fig. 14.17, he reports ion losses

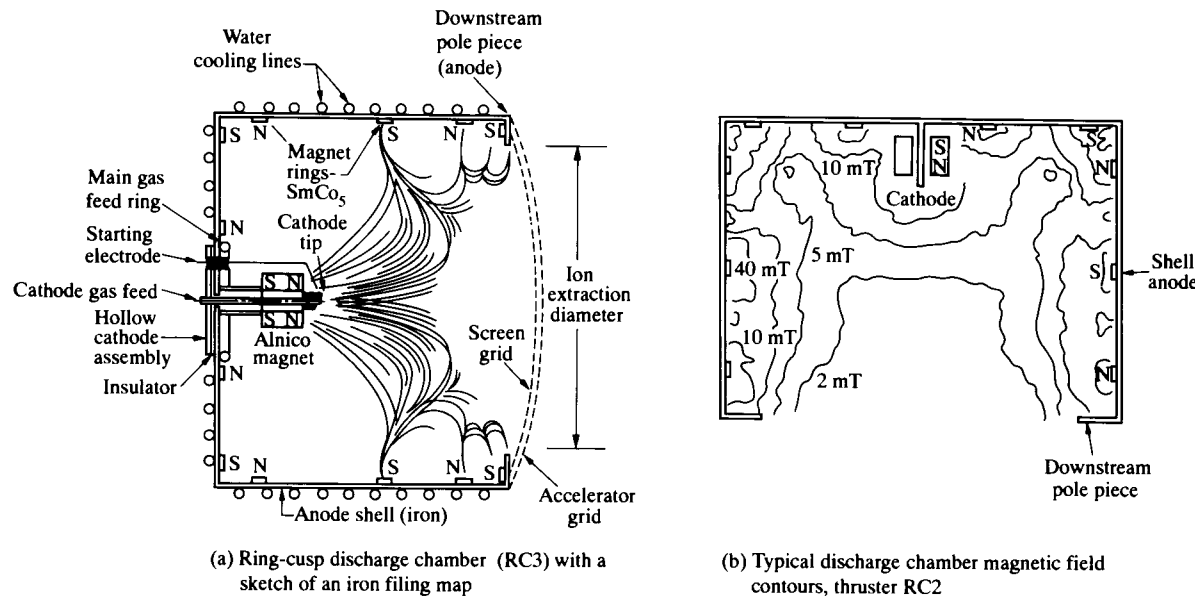


FIGURE 14.15 Magnetic-field distribution in a two-ring-cusp ion bombardment chamber.
(Courtesy Sovey [7]. © AIAA. Reprinted with permission.)

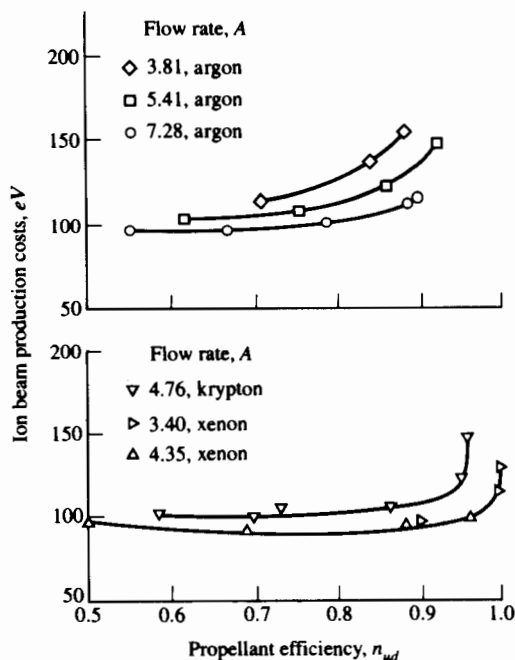


FIGURE 14.16 Discharge chamber performance for thruster RC3 using propellants argon, krypton, and xenon. (Courtesy Sovey [7]. © AIAA. Reprinted with permission.)

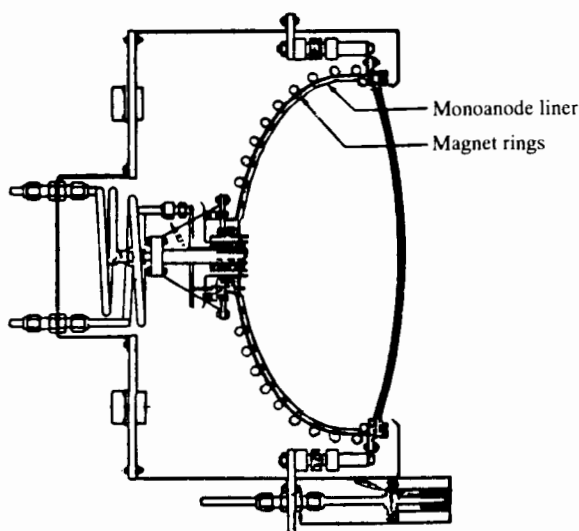


FIGURE 14.17 Thirty-cm monoanode inert gas ion thruster. (Courtesy Steiner [8]. © AIAA. Reprinted with permission.)

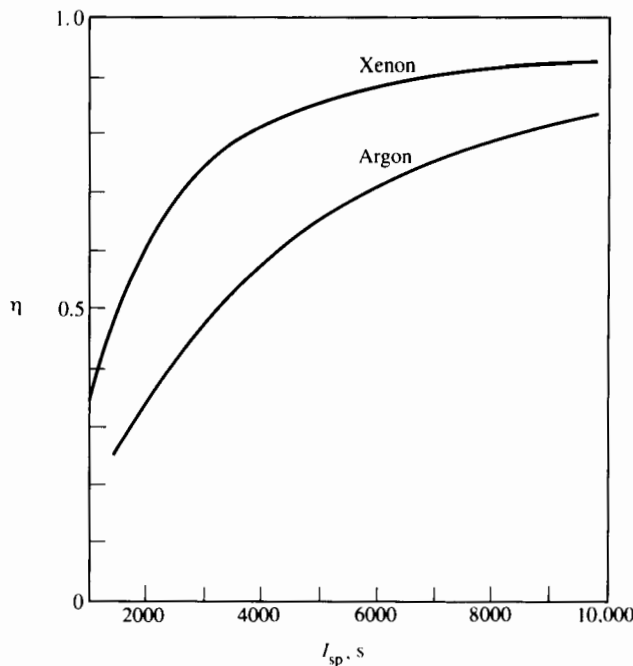


FIGURE 14.18 Efficiency of optimized ion thrusters; results of Kaufman and Robinson [13].

as low as 80 W per beam amp for xenon (rising to 111 W/A at 80% utilization and 126 W/A at 92%). For argon the minimum loss was 91 W/A.

Kaufman and Robinson [13] have conducted an optimizing study using all available experimental data and allowing for the thrust correction needed for beam divergence from a nonplanar accelerator grid such as that shown in Fig. 14.15. Their results for best beam-power efficiency of electrostatic ion thrusters is shown in Fig. 14.18. They expect that if the mercury ion thruster is fully optimized, it could show even greater efficiency than the xenon thruster.

Given the best that chemical rockets can do (with $I_{sp} < 500$) and the low efficiency of ion thrusters for I_{sp} less than 2000 to 3000, there is a gap that motivates work on other kinds of thrusters. It is for this reason that work continues on arcjets and magnetoplasmadynamic thrusters. We turn now to the arcjet.

14.6 THE ARCJET

To have a specific impulse considerably higher than can be obtained with a chemical rocket requires much greater energy content per unit mass of propellant than is supplied by the process of combustion. For some propulsion missions there is need for relatively efficient operation at specific-impulse values in the range of 1000 to 2000 s (in which ion thrusters are quite inefficient).

It has been suggested that one way to obtain the necessary energy content is to use an electric-arc discharge to heat the fluid in a device called an arcjet or plasmajet. Much attention has been given to arcjets for a variety of applications, and their general characteristics and limitations have been identified. The future role of the arcjet in space propulsion is not yet clear, but we discuss it briefly here as the simplest possible use of a conducting fluid in a rocket.

Figure 14.19 shows an arcjet schematically. Propellant is heated to a high temperature in an electric arc and then expanded in a conventional nozzle. If the propellant were to behave as a perfect gas and if the expansion were isentropic, the exhaust velocity would be given by

$$u_e = \sqrt{2 \frac{\gamma}{\gamma - 1} \frac{\bar{R}}{M} T_0 \left[1 - \left(\frac{p_e}{p_0} \right)^{(\gamma-1)/\gamma} \right]}.$$

This represents a considerable oversimplification of actual performance, but it does indicate the desirability of propellants that have high stagnation temperature and low molecular weight. Though hydrogen has the lowest molecular weight, we will see that helium is actually a more attractive propellant largely because it is monatomic and therefore cannot dissociate.

The high-current-density arc discharge is maintained by a voltage difference between cathode and anode. The behavior of high-current discharges in relatively high-pressure gases is not well understood. In general, the arc consists of three zones: a central “arc column” and zones of high potential gradient immediately near the anode and cathode surfaces. The arc column occupies most of the discharge space. Though the potential gradients within it are relatively low, the arc column should have most of the total potential drop in order that a large fraction of the arc power be liberated within the main flow. The potential drops across the anode and cathode zones may be several volts, whereas the total potential across the arc may be of the order of hundreds of volts. The anode and cathode zones are, however, very thin, so that heat transfer into the electrodes can be severe. Near the cathode the discharge is nonuniform, tending to concentrate in “spots,” especially at high current density. If the local current density increases slightly, so do the joule heating and the local conductivity. This leads to further increase in current density and to concentrated heat transfer. Current densities within such spots may be as high as 10^6 A/cm^2 .

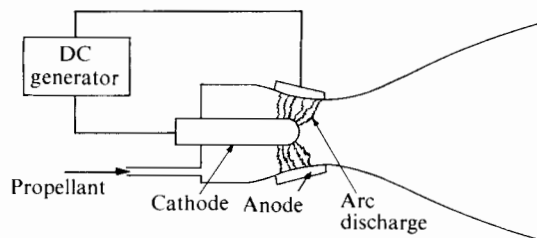


FIGURE 14.19 Schematic diagram of an arcjet.

Near the anode the electrons acquire considerable energy as they fall through the potential drop. If the density is sufficiently high, this energy may be largely consumed through collisions within the gas. Otherwise it is transferred to the anode by direct collision with the surface. Likewise, ion acceleration in the cathode sheath can lead to ion energies sufficient to cause "sputtering" of the cathode, that is, removal of surface material as a result of ion impact. Thus a number of important phenomena govern the behavior of the arc in the vicinity of the electrode surfaces. These may have very strong effects on electrode life. It cannot be said that these effects are well understood, but considerable experience with carbon, copper, and tungsten electrodes has been obtained. It has been found that arc spots that would otherwise cause burnout can be tolerated if kept in motion on the electrode surface. Spot motion may be produced by imparting vortex motion to the propellant gas before it enters the arc, or by the presence of a suitable magnetic field that interacts with the arc current and induces motion of the arc transverse to the current direction.

Most of the transmission of energy of the propellant occurs in the arc column. Electrons and ions, accelerated in the electrostatic field, transfer their energy by collision to neutral gas particles. Since gas conductivity increases rapidly with temperature, attempts to produce high exhaust velocity (high T_0) are hampered by the associated decrease of arc-column resistance relative to the rest of the arc circuit. This results in a decreasing fraction of total electrical power liberated in the arc column.

The efficiency of an arcjet may be defined as the ratio of kinetic energy flux in the exhaust to electric power supplied. As an example of experimental arcjet performance, Figure 14.20 shows the data of Brogan [14] for arc-heated helium, indicating the expected falloff of efficiency at high specific impulse. It may be seen that efficiencies above 50% were obtained with specific-impulse values up to about 1200 s.

The choice of helium as propellant stems from several considerations. Though hydrogen has a lower molecular weight, it tends to dissociate at the high temperature involved in arcjet operation. Energy consumed by dissociation and

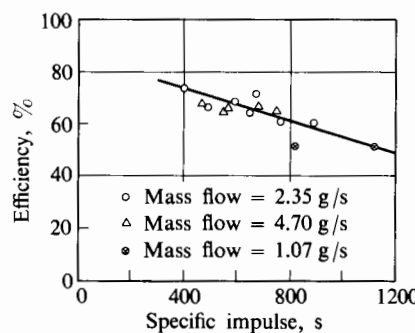


FIGURE 14.20 Efficiency of experimental arcjet. (Courtesy Brogan [14].)

ionization processes is, of course, not available for propellant acceleration unless recombination occurs during expansion. In general, little information is available for recombination rates of typical gases, but it appears that the fluid will expand with much the same composition it had in the chamber (or arc). The fraction f of the total energy supplied to the propellant that appears as thermal energy may be defined, following Camac [10] as

$$f = \frac{e_k}{e_k + \alpha_d e_d + \alpha_I e_I + \alpha_{II} e_{II}},$$

in which e_k is the internal energy added to the propellant per unit mass, and e_d , e_I , and e_{II} are the energies of dissociation, first ionization, and second ionization, respectively. The fractions α_d , α_I , and α_{II} are the respective dissociation and ionization fractions. Figure 14.21 illustrates the results of calculations of the equilibrium dissociation and ionization of hydrogen. One can see that pressure has an important effect.

Using these results and similar ones for the ionization of helium, Fig. 14.22 shows how the efficiency of an otherwise perfect thrust chamber is influenced by dissociation. This efficiency, which considers only losses due to dissociation and ionization, is called the frozen-flow efficiency. It seems clear that helium is superior to hydrogen for specific-impulse values up to at least about 2000 s.

In addition to the lack of dissociation losses, helium exhibits several other favorable characteristics. It is chemically inert, of course. It has a very high ionization potential (see Table 14.1). This contributes to low ionization loss in the event of frozen flow in the nozzle. In addition, high arc-column resistance can be maintained at relatively high gas temperatures, thus promoting good efficiency at high specific impulse. It also seems that potential drops at electrodes are low when helium is used.

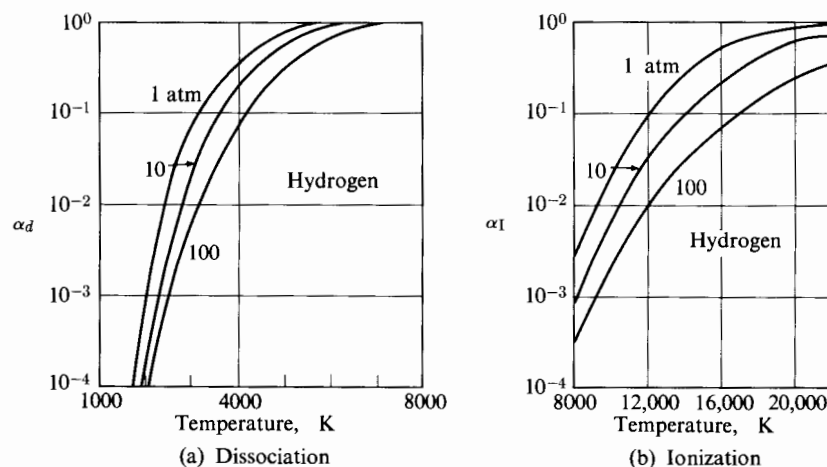


FIGURE 14.21 Equilibrium dissociation and ionization of hydrogen. (Courtesy Camac [10].)

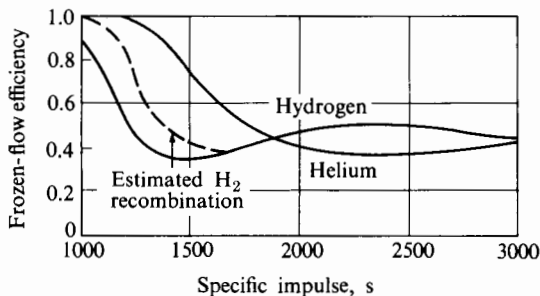


FIGURE 14.22 Frozen-flow efficiency as a function of specific impulse, applicable to arcjet propulsion devices. (Courtesy Camac [10].)

Heat transfer to the walls is, of course, one of the major limitations on arcjet performance. As pointed out already, the electrode surfaces are subject to heat transfer from the zones of high joule heating immediately adjacent to them. Convective and radiative heat transfer to the rest of the nozzle may have total rates of 1 to 10 kW/cm^2 . It has proved possible to water-cool copper electrode surfaces with heat transfer rates as high as 2 kW/cm^2 . At very high temperatures the energy loss by the propellant on account of radiation may be quite significant. Figure 14.23 indicates a characteristic radiation time (the time it would take to radiate all the energy of the gas at the rate corresponding to the initial temperature). It may, at high pressures and temperatures, reduce to the same order of magnitude as the time the propellant takes to pass through the nozzle, perhaps 10^{-3} or 10^{-4} s.

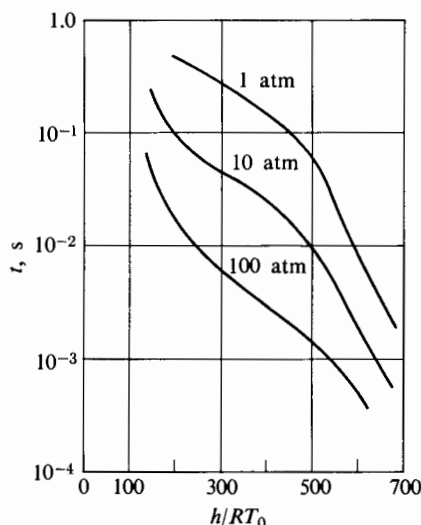


FIGURE 14.23 Characteristic radiation time for heated air; $T_0 = 500^\circ\text{R}$. (Courtesy John and Bode [15].)

Partly owing to the difficulty of transporting supplies of hydrogen and helium on space missions, considerable thought is being given to ammonia as an arcjet propellant [5]. Early experimental work on NH_3 in arcjets indicated efficiencies of around 40% at specific-impulse levels of 1000 s and at power levels of 30 kW.

In summary, the principal limitations on the performance of the arcjet are heat transfer, energy losses through dissociation and ionization, and loss of material from the electrode surfaces. The last point is particularly serious for a space-vehicle propulsion unit that should be capable of long periods of operation. More effort will be required to make the arcjet an operational rocket.

We now move on to a consideration of *electromagnetic propulsion*.

14.7 THE PULSED-MAGNETOPLASMA ACCELERATORS

Whenever an electric current flows perpendicular to a component of magnetic-field-strength vector, a body force $\mathbf{j} \times \mathbf{B}$ is applied to the current conductor (see Appendix IX). The magnetic field may be applied by an electric coil or induced by the current itself. Tahara, Kagaya, and Yoshikawa [16] report work on a thruster with an applied magnetic field. Their purpose was not directly to develop a space propulsion unit (since the electric coils for the applied field would be too massive for a large thruster); it was to study the arc discharge and to learn more about wall losses and surface erosion with magnetoplasma devices.

One can understand the principle of the pulsed-magnetoplasmadynamic device (which generates its own field) by referring to Fig. 14.24. A thin wire is placed across two rails (relatively long, straight electrodes). A high-voltage discharge between the rails vaporizes and ionizes the wire material. The high current, perhaps 10^4 or 10^5 amp, in the loop induces a magnetic field as shown, which interacts with the current to set up a body force, $\mathbf{j} \times \mathbf{B}$ per unit volume, acting on the plasma in a direction parallel to the rails. Velocities of thousands of m/s have been measured experimentally by magnetic pickups. Assuming that all the mass is accelerated to this speed, one may calculate the efficiency from the mass of the wire and the discharge energy. By various experiments, efficiencies of up to 40% have been estimated in this way. However, it seems unlikely that the plasma is accelerated uniformly in these experiments.

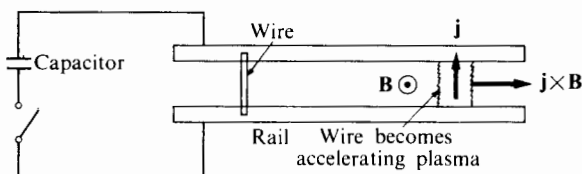


FIGURE 14.24 Schematic of rail-type plasma accelerator.

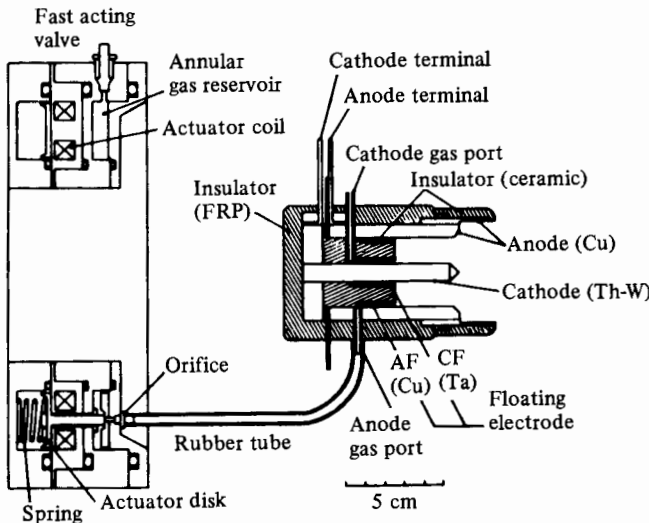


FIGURE 14.25 Schematic diagram of new K-III MPD arcjet and fast-acting valve. (Courtesy Yoshikawa and Kagaya [17]. © AIAA. Reprinted with permission.)

Yoshikawa and Kagaya [17] have designed and tested the magnetoplasma-dynamic (MPD) thruster shown in Fig. 14.25. Propellant gas enters through ports near the anode and cathode. The thruster is driven by a 62-kJ pulse (at 8 kV) that lasts 0.6 ms. Measurements have been made of thrust discharge voltage and current and propellant flow rate. Experiments have been conducted with argon, ammonia, helium, and hydrogen propellants. As for ion thrusters, maximum efficiencies increase with specific impulse. The peak efficiency measured so far with hydrogen in this experiment is 32% (at 4500 s) and for ammonia 21% (at 2500 s). Quite severe cathode erosion problems were encountered.

In summary, then, it appears that whereas electrostatic ion technology is now well established and designs have proved durable and capable of high efficiency (for $I_{sp} > 3000$), the arcjet and magnetoplasmadynamic thruster still have serious problems to be solved concerning losses and material erosion due to arc impingement.

PROBLEMS

1. An electrostatic rocket is to use heavy particles with charge-to-mass ratio of 500 C/kg to produce a specific impulse of 3000 s. What acceleration voltage would be necessary?

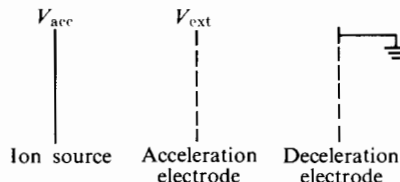
With one-dimensional space-charge-limited current and a maximum allowable gradient of 10^5 V/cm, what is the diameter of a round beam producing 0.5 N thrust?

2. A cesium ion rocket is to be used at a specific impulse of 5000 s. Assuming the cesium to be 100% singly ionized ($q/m = 7.25 \times 10^5 \text{ C/kg}$), what is the required acceleration voltage and the beam power ($\dot{m}u_e^2/2$) per unit thrust?

If the cesium is 90% singly ionized and 10% doubly ionized, what is the specific impulse and beam power per unit thrust, assuming that the acceleration voltage is unchanged?

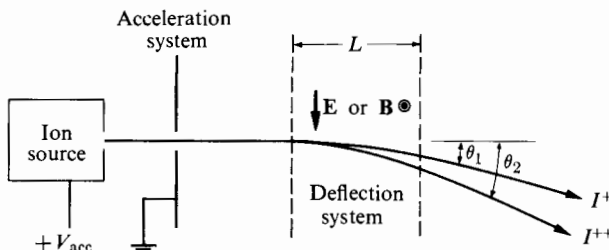
3. A xenon ion rocket of 5 N thrust at a specific impulse of 5000 s is to be built within the following two limitations: (a) minimum electrode space = 5 mm, (b) maximum average gradient between electrodes = 10^5 V/cm . Assuming the acceleration region to behave as a simple space-charge-limited plane diode, what beam area is required?

To reduce the beam area, it is proposed to increase the current density by first accelerating through a larger potential difference. The ions are subsequently decelerated to the proper exhaust speed (see diagram). What is the minimum beam area and the corresponding acceleration potential?



PROBLEM 3

4. Two positive ions of the same mass, one singly charged and the other doubly charged, are accelerated from zero velocity through the same potential, V_{acc} , after which they travel through a deflection region of length L . Calculate the ratio θ_2/θ_1 , where θ_2 refers to the doubly and θ_1 to the singly charged ion for the following cases: (a) deflection due to a uniform \mathbf{E} field as shown; (b) deflection due to a uniform \mathbf{B} field as shown; (c) deflection due to both \mathbf{E} and \mathbf{B} fields as shown. The deflection angles may be assumed small.



PROBLEM 4

5. Using an accel-decel system with 0.2-mm spacing between electrode plates, +1400 V on the screen electrode, and -500 V on the accelerator electrode, determine the space-charge-limited values of the following for Cs, Hg, and Xe ions:

- Current density, mA/cm²;
- thrust density, N/cm².

6. If the loss in an ion thruster may be written as

$$e_l = (100 + 0.1 \Delta V_a) \text{ eV},$$

determine:

- The efficiency;
- The thrust-to-power ratio for the xenon ion thruster operating at I_{sp} values of 1000, 2000, 3000, 4000, and 5000. Compare your results with Figs. 14.6 and 14.7.

7. Determine the space-charge-limited current and thrust-power ratio for xenon and krypton ion thrusters with an accel-decel system with the voltages shown in Fig. 14.8 and electrode spacings of 0.10 mm. Determine the same for 0.05 mm spacings. The loss per ion may be assumed to be 150 eV.

8. Assume that the magnetic-field intensity in the Kaufman thruster shown in Fig. 14.8 varies as

$$B = B_a \left(\frac{r}{r_a} \right)^2.$$

For cathode radius $r_c \rightarrow 0$, show how the field strength near the anode should depend on the bombardment voltage and the anode radius.

- Given the xenon ion thruster data of Beattie and colleagues quoted in Section 14.5, estimate the loss per ion and the effect to be expected on efficiency and power if the specific impulse is doubled with the thrust unchanged.
- A resistojet is to be designed to supply a specific impulse of 310 s and a total thrust of 10 N. It is to be operated with ammonia in a nozzle with an area ratio of 100:1. The specific-heat ratio during the expansion is 1.3, and the expansion may be assumed (first approximation only) to be adiabatic. Determine the maximum temperature for two cases:
 - No dissociation of the NH₃,
 - 50% dissociation of the NH₃ (into N₂ and H₂) in the heating chamber, followed by frozen expansion.
- A resistojet has a throat diameter of 0.3 mm and is to be operated with helium at a pressure of 6.89 MPa (1000 psi). The exhaust nozzle exit diameter is 3.0 mm. The specific heat may be taken as $\gamma = 1.67$. The maximum temperature is 1000 K.

- a. Determine the mass flow rate, specific impulse, and thrust for isentropic expansion with no back pressure.
- b. On the assumption that the cumulative heat loss q is given by $dq/dT = 1.5 \text{ kJ/kg} \cdot \text{K}$, estimate the specific impulse for the same nozzle pressure ratio as in case (a). Neglect frictional effects.
12. Water vapor with specific heat ratio 1.3 expands in a small resistojet nozzle from initial conditions 1000 K and 10 MPa. The overall pressure ratio is 300. Frictional and heat transfer effects are negligible in the converging part of the nozzle, but in the remainder the polytropic index is 1.2, and the exit stagnation temperature is 728 K. Estimate the specific impulse, the required area ratio, and the mass flow rate for a thrust of 1 N with operation in a vacuum.
13. An arcjet heats hydrogen at 50 atm pressure from 300 K to 6000 K. At the latter temperature the reaction $\text{H}_2 \rightarrow 2\text{H}$ is described by the equilibrium constant K_p , defined by

$$K_p = \frac{p_{\text{H}}^2}{p_{\text{H}_2}} \text{ atm}$$

and approximately evaluated by

$$\ln K_p = 14.901 - \frac{55,870}{T}.$$

Over the temperature interval the average specific heats are

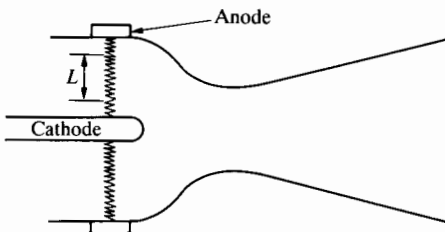
$$\bar{c}_{p\text{H}} = 25 \text{ kJ/kmol} \cdot \text{K}, \quad \bar{c}_{p\text{H}_2} = 38 \text{ kJ/kmol} \cdot \text{K}.$$

The heat of formation of H is +217 kJ/gmol at 300 K. If no recombination takes place in the nozzle, what fraction of the total energy addition to the fluid is "lost" because of dissociation?

14. Nitrogen is heated in an arcjet from 300 to 7350 K at 1 atm and dissociates almost entirely to atomic nitrogen. One-third of the electrical power supplied is lost to the arc chamber walls. The heated N then expands in a nozzle of area ratio $A/A^* = 100$ to vacuum. Assuming frozen flow and negligible effects of friction and heat transfer, estimate the specific impulse and the thrust-to-power ratio. Take $\gamma = 5/3$.
15. In the arcjet illustrated in the diagram, arc length L is 1 cm and the voltage across it is 100 V. The voltage drop across the anode layer, which is $\Delta_a = 1 \text{ mm}$ thick, is 22 V. The voltage difference across the cathode layer, which is $\Delta_c = 3 \text{ mm}$, is 37 V.
- Assuming half the electrical heating energy of the cathode layer goes into the cathode and that all of the heating energy of the anode layer goes into the anode, estimate the fractional loss to the walls of the energy added to the flow and the total power input. The arc current is 25,000 A.

The working fluid is helium, which enters the arcjet at 2.1 MPa and 300 K. Its flow rate is 44.64 g/s, and the polytropic expansion coefficient is estimated to be 1.37. The nozzle area ratio is 20:1.

Determine the specific impulse of the arcjet, assuming as a first approximation that nozzle heat transfer is negligible and that friction is important only downstream of the nozzle throat.



PROBLEM 15

REFERENCES

1. Sovey, J. S., L. M. Carney, and S. C. Knowles. "Electromagnetic Emission Experiences Using Electric Propulsion Systems," *AIAA J. Propulsion and Power* 5 (1989): 534–547.
2. Tacina, R. R. "Space Station Resistojet System Study," *AIAA J. Propulsion and Power* 5 (1989):684–702.
3. Kaufman, J. R. "Electrical Thruster Performance for Orbit Raising and Manoeuvre," *AIAA J. Spacecraft and Rockets* 21 (1984):180–186.
4. Jones, R. M. "Comparison of Potential Electric Propulsion Systems for Orbit Transfer," *AIAA J. Spacecraft and Rockets* 21 (1982):88–95.
5. Deininger, W. D., and R. J. Vondra. "Arcjet Propulsion Systems for an SP-100 Flight Experiment," *AIAA J. Spacecraft and Propulsion* 25 (1988):427–432.
6. Beattie, J. R., J. N. Matossian, and R. L. Poeschl. "Xenon Propulsion Subsystem," *AIAA J. Propulsion* 5 (1989): 438–444.
7. Sovey, J. S. "Improved Ion Containment Using a Ring-Cusp Containment," *AIAA J. Spacecraft and Rockets* 21 (1984): 488–495.
8. Steiner, G. "Development of a Large Inert Gas Ion Thruster," *AIAA J. Spacecraft and Rockets* 22 (1985): 465–468.
9. Kaufman, H. R. "An Ion Rocket with an Electron-Bombardment Ion Source," NASA TN D-585, Jan. 1961.
10. Camac, M. *Plasma Propulsion Devices*, vol. 2, of *Advances in Space Sciences*. New York: Academic Press, 1960. Reprinted with permission.
11. Bleakney, W. "Probability and Critical Potentials for the Formation of Multiply Charged Ions in Hg Vapor by Electron Impact," *Physical Review* 35 (1930):139–148. Reprinted with permission.

12. Hyman, Jr., J. and C. R. Dulgeroff. "Modularized Ion Thrusters for Auxilliary Propulsion," *AIAA J. Spacecraft and Rockets* 15 (1978):184–187.
13. Kaufman, J. R., and R. S. Robinson. "Electric Thruster Performance for Orbit Raising and Manoeuvering," *AIAA J. Spacecraft and Propulsion* 21 (1984):180–186.
14. Brogan, T. R. "Preliminary Evaluation of Helium as an Electric Arc-Heated Propellant," *J. Amer. Rocket Soc.* 29 (1961):662–663. Reprinted with permission.
15. John, R. R., and W. L. Bode. "Recent Advances in Arc Plasma Technology," *J. Amer. Rocket Soc.* 31 (1961):4–17. Reprinted with permission.
16. Tahara, H., Y. Kagaya, and T. Yoshikawa. "Quasisteady Magnetoplasmadynamic Thrusters with Applied Magnetic Fields for Near-Earth Missions," *AIAA J. Propulsion and Power* 5 (1989):713–717.
17. Yoshikawa, T., and Y. Kagaya. "Thrust and Efficiency of the K-II MPD Thruster," *AIAA J. Spacecraft and Rockets* 21 (1984):481–487.



APPENDIXES





A P P E N D I X

CONVERSION FACTORS AND PHYSICAL CONSTANTS

TABLE 1 Conversion factors

1 meter (m) = 100 cm = 39.37 in. = 3.281 ft
1 centimeter (cm) = 10 millimeters (mm) = 0.3937 in.
1 kilometer (km) = 1000 m = 0.6213 mi
1 foot (ft) = 12 in. = 0.3048 m
1 inch (in.) = 0.08333 ft = 2.54 cm
1 mile (mi) = 5280 ft = 1.6094 km
1 liter = 0.001 m ³
1 USGPM = 0.6309×10^{-4} m ³ /s
1 m/sec = 3.281 ft/sec = 2.237 mi/hr = 3.60 km/hr
1 ft/sec = 0.3048 m/sec = 0.6818 mi/hr = 1.097 km/hr
1 mi/hr = 1.467 ft/sec = 0.4470 m/sec = 1.609 km/hr
1 radian (rad) = 57.30° = 57°18'
1° = 0.01745 rad
1 revolution/minute (rev/min) = 0.1047 rad/sec
1 kilogram (kg) = 1000 grams (g) = 0.06852 slug = 2.2046 lb
1 slug = 14.594 kg = 32.174 lb
1 atomic mass unit (amu) = 1.66×10^{-27} kg = 1.49×10^{-10} J = 931 Mev
1 newton (N) = 0.2248 lb _f
1 pound force (lb _f) = 4.4482 N
1 joule (J) = 0.7376 ft · lb _f = 2.389×10^{-4} kcal = 6.24×10^{18} ev
1 kilocalorie (kcal) = 4,186 J
1 foot · pound (ft · lb _f) = 1.3558 J
1 BTU = 1055.1 J
1°F = 0.5555°C = 0.5555 K
1 K = 1.8°F
1 electron volt (eV) = 10^{-6} MeV = 1.60×10^{-19} J = 1.18×10^{-19} ft · lb _f = 3.83×10^{-23} kcal
1 watt (W) = 1 J/s = 0.7376 ft · lb _f /sec
1 faraday = 96,485 coulomb (C)
1 tesla (T) = 1 weber/m ² (Wb/m ²)

TABLE 2 Physical constants

Constant	Units		
	S.I.	cgs	Engineering
Normal specific volume ^a of ideal gas	$22.414 \text{ m}^3/\text{kmol}$	$22.414 \text{ liters/gmol}$	$359 \text{ ft}^3/\text{lb-mole}$
Gas constant, R	$8.3143 \times 10^3 \text{ J/kmol} \cdot \text{K}$	$1.9864 \text{ cal/mole} \cdot \text{K}$ $8.3143 \times 10^7 \text{ erg/gmol} \cdot \text{K}$	$1545.35 \text{ ft} \cdot \text{lb}_f/\text{lb-mole} \cdot {}^\circ\text{R}$
Avogadro's number, N_0	$6.0225 \times 10^{26} \text{ molecules/kmol}$	$6.0225 \times 10^{23} \text{ molecules/gmol}$	$2.732 \times 10^{26} \text{ molecules/lb-mole}$
Normal atmospheric pressure	$1.01325 \times 10^5 \text{ N/m}^2$	$1.01325 \times 10^6 \text{ dyne/cm}^2$	$14.697 \text{ lb}/\text{in}^2$
Velocity of light, c	$2.9979 \times 10^8 \text{ m/s}$	$2.9979 \times 10^{10} \text{ cm/sec}$	$9.836 \times 10^8 \text{ ft/sec}$
Boltzmann's constant, k	$1.3805 \times 10^{-23} \text{ J/K}$	$1.3805 \times 10^{-16} \text{ erg/K}$	$7.269 \times 10^{-27} \text{ Btu/}{}^\circ\text{R}$
Planck's constant, h	$6.6237 \times 10^{-34} \text{ J} \cdot \text{s}$	$6.626 \times 10^{-27} \text{ erg} \cdot \text{sec}$	$6.2779 \times 10^{-37} \text{ Btu} \cdot \text{sec}$
Electronic charge, e	$1.6018 \times 10^{-19} \text{ C}$	$4.8029 \times 10^{-10} \text{ abs} \cdot \text{esu}$	$1.6018 \times 10^{-19} \text{ C}$
Electron mass, m	$9.107 \times 10^{-31} \text{ kg}$	$9.107 \times 10^{-28} \text{ g}$	$2.008 \times 10^{-30} \text{ lb}$

^aFor the S.I. and cgs systems, "normal temperature and pressure" are 0°C and 1 atm. For the engineering system, "normal temperature and pressure" are 32°F and 1 atm.

A P P E N D I X



GASES AT LOW PRESSURES

TABLE 1 Constant-pressure specific heats of various ideal gases

Gas	$\bar{c}_{po} = \text{kJ/kmol K}$ $\theta = T(\text{Kelvin})/100$	Range K	Max. error %
N ₂	$\bar{c}_{po} = 39.060 - 512.79\theta^{-1.5} + 1072.7\theta^{-2} - 820.40\theta^{-3}$	300–3500	0.43
O ₂	$\bar{c}_{po} = 37.432 + 0.020102\theta^{1.5} - 178.57\theta^{-1.5} + 236.88\theta^{-2}$	300–3500	0.30
H ₂	$\bar{c}_{po} = 56.505 - 702.74\theta^{-0.75} + 1165.0\theta^{-1} - 560.70\theta^{-1.5}$	300–3500	0.60
CO	$\bar{c}_{po} = 69.145 - 0.70463\theta^{0.75} - 200.77\theta^{-0.5} + 176.76\theta^{-0.75}$	300–3500	0.42
OH	$\bar{c}_{po} = 81.546 - 59.350\theta^{0.25} + 17.329\theta^{0.75} - 4.2660\theta$	300–3500	0.43
NO	$\bar{c}_{po} = 59.283 - 1.7096\theta^{0.5} - 70.613\theta^{-0.5} + 74.889\theta^{-1.5}$	300–3500	0.34
H ₂ O	$\bar{c}_{po} = 143.05 - 183.54\theta^{0.25} + 82.751\theta^{0.5} - 3.6989\theta$	300–3500	0.43
CO ₂	$\bar{c}_{po} = -3.7357 + 30.529\theta^{0.5} - 4.1034\theta + 0.024198\theta^2$	300–3500	0.19
NO ₂	$\bar{c}_{po} = 46.045 + 216.10\theta^{-0.5} - 363.66\theta^{-0.75} + 232.55\theta^{-2}$	300–3500	0.26
CH ₄	$\bar{c}_{po} = -672.87 + 439.74\theta^{0.25} - 24.875\theta^{0.75} + 323.88\theta^{-0.5}$	300–2000	0.15
C ₂ H ₄	$\bar{c}_{po} = -95.395 + 123.15\theta^{0.5} - 35.641\theta^{0.75} + 182.77\theta^{-3}$	300–2000	0.07
C ₂ H ₆	$\bar{c}_{po} = 6.895 + 17.26\theta - 0.6402\theta^2 + 0.00728\theta^3$	300–1500	0.83
C ₃ H ₈	$\bar{c}_{po} = -4.042 + 30.46\theta - 1.571\theta^2 + 0.03171\theta^3$	300–1500	0.40
C ₄ H ₁₀	$\bar{c}_{po} = 3.954 + 37.12\theta - 1.833\theta^2 + 0.03498\theta^3$	300–1500	0.54

Source: Reprinted by permission of John Wiley and Sons from G. J. Van Wylen and R. E. Sonntag, Fundamentals of Classical Thermodynamics, New York: Wiley, 1985. p. 652.

TABLE 2 Air at low pressures (S.I. units)

T K	t C	c_p $\frac{\text{J}}{\text{kg K}}$	c_v $\frac{\text{J}}{\text{kg K}}$	$k = \frac{c_p}{c_v}$	a $\frac{\text{m}}{\text{s}}$	$\frac{G_{\max}}{p_i}$ $\frac{\text{kg}}{\text{s m}^2} / \text{kPa}$	$\mu \times 10^7$ $\frac{\text{N s}}{\text{m}^2}$	λ $\frac{\text{W}}{\text{m K}}$	Pr = $\frac{c_p \mu}{\lambda}$
50	-223.15	1001.9	714.8	1.402	141.8	5.7179			
75	-198.15	1001.9	714.9	1.402	173.7	4.6686			
100	-173.15	1001.9	714.9	1.401	200.6	4.0431	70.6	.0092	.767
125	-148.15	1002.0	714.9	1.401	224.2	3.6163	87.6	.0115	.763
150	-123.15	1002.0	715.0	1.401	245.6	3.3012	103.8	.0137	.756
175	-98.15	1002.1	715.0	1.401	265.3	3.0563	119.1	.0159	.749
200	-73.15	1002.2	715.1	1.401	283.6	2.8589	133.6	.0181	.740
225	-48.15	1002.4	715.4	1.401	300.8	2.6953	147.4	.0202	.731
250	-23.15	1002.8	715.8	1.401	317.1	2.5569	160.6	.0223	.724
275	1.85	1003.5	716.5	1.401	332.5	2.4378	173.2	.0242	.717
300	26.85	1004.5	717.5	1.400	347.2	2.3338	185.3	.0261	.712
325	51.85	1006.0	718.9	1.399	361.3	2.2420	196.9	.0279	.709
350	76.85	1007.9	720.8	1.398	374.8	2.1601	208.1	.0297	.706
375	101.85	1010.2	723.2	1.397	387.8	2.0864	219.0	.0314	.705
400	126.85	1013.1	726.1	1.395	400.3	2.0196	229.4	.0330	.703
450	176.85	1020.3	733.2	1.391	423.9	1.9027	249.3	.0363	.700
500	226.85	1029.2	742.1	1.387	446.1	1.8035	268.2	.0395	.699
550	276.85	1039.4	752.4	1.381	467.0	1.7177	286.0	.0426	.698
600	326.85	1050.7	763.6	1.376	486.8	1.6426	303.0	.0456	.698
650	376.85	1062.5	775.4	1.370	505.6	1.5761	319.3	.0484	.701
700	426.85	1074.5	787.4	1.365	523.6	1.5168	334.9	.0513	.701
750	476.85	1086.5	799.4	1.359	540.9	1.4634	349.8	.0541	.702
800	526.85	1098.2	811.2	1.354	557.6	1.4151	364.3	.0569	.703
850	576.85	1109.5	822.5	1.349	573.7	1.3711	378.3	.0597	.703
900	626.85	1120.4	833.4	1.344	589.3	1.3309	391.8	.0625	.702

(Continued)

TABLE 2 (Continued)

T K	t C	c_p $\frac{\text{J}}{\text{kg K}}$	c_v $\frac{\text{J}}{\text{kg K}}$	$k = \frac{c_p}{c_v}$	a $\frac{\text{m}}{\text{s}}$	$\frac{G_{\max}}{p_i}$ $\frac{\text{kg}}{\text{s m}^2} / \text{kPa}$	$\mu \times 10^7$ $\frac{\text{N} \cdot \text{s}}{\text{m}^2}$	λ	$\text{Pr} =$ $\frac{c_p \mu}{\lambda}$
1000	726.85	1140.4	853.4	1.336	619.3	1.2598	417.7	.0672	.709
1100	826.85	1158.2	871.2	1.329	647.9	1.1988	442.0	.0717	.714
1200	926.85	1173.8	886.8	1.324	675.2	1.1459	465.0	.0759	.719
1300	1026.85	1187.5	900.5	1.319	701.5	1.0994	488.0	.0797	.727
1400	1126.85	1199.6	912.6	1.315	726.8	1.0581	509.0	.0835	.731
1500	1226.85	1210.2	923.2	1.311	751.3	1.0211			
1600	1326.85	1219.7	932.6	1.308	775.0	.9877			
1700	1426.85	1228.1	941.1	1.305	798.0	.9575			
1800	1526.85	1235.7	948.7	1.303	820.4	.9298			
1900	1626.85	1242.6	955.6	1.300	842.1	.9044			
2000	1726.85	1248.9	961.9	1.298	863.3	.8810			
2100	1826.85	1254.7	967.6	1.297	884.1	.8593			
2200	1926.85	1260.0	973.0	1.295	904.3	.8392			
2300	2026.85	1264.9	977.9	1.294	924.1	.8204			
2400	2126.85	1269.5	982.5	1.292	943.5	.8028			
2500	2226.85	1273.8	986.7	1.291	962.5	.7863			
2600	2326.85	1277.8	990.7	1.290	981.1	.7707			
2700	2426.85	1281.5	994.5	1.289	999.3	.7561			
2800	2526.85	1285.0	998.0	1.288	1017.3	.7422			
2900	2626.85	1288.3	1001.3	1.287	1034.9	.7291			
3000	2726.85	1291.5	1004.4	1.286	1052.2	.7167			
3100	2826.85	1294.4	1007.4	1.285	1069.3	.7049			
3200	2926.85	1297.2	1010.2	1.284	1086.0	.6936			
3300	3026.85	1299.8	1012.8	1.283	1102.6	.6828			
3400	3126.85	1302.3	1015.3	1.283	1118.8	.6726			

Source: Reprinted by permission of John Wiley and Sons from J. H. Keenan, J. Chao, and J. Kaye, Gas Tables, New York: Wiley, 1983: 24.

TABLE 3 Air at low pressures (English units)

T, °R	T, °F	c_p , Btu lb · °F	c_v , Btu lb · °F	$\gamma = \frac{c_p}{c_v}$	a, ft/sec	$\mu \times 10^7$, lb sec-ft	k, Btu hr-ft·°F	$\text{Pr} =$ $\frac{c_p\mu}{k}$
100	-359.7	0.2392	0.1707	1.402	490.5			
150	-309.7	0.2392	0.1707	1.402	600.7			
200	-259.7	0.2392	0.1707	1.402	693.6			
250	-209.7	0.2392	0.1707	1.402	775.4			
300	-159.7	0.2392	0.1707	1.402	849.4			
350	-109.7	0.2393	0.1707	1.402	917.5			
400	-59.7	0.2393	0.1707	1.402	980.9	100	0.0118	0.73
450	-9.7	0.2394	0.1708	1.401	1040.3	109	0.0130	0.72
500	40.3	0.2396	0.1710	1.401	1096.4	118	0.0143	0.71
550	90.3	0.2399	0.1713	1.400	1149.6	126	0.0156	0.70
600	140.3	0.2403	0.1718	1.399	1200.3	135	0.0168	0.70
650	190.3	0.2409	0.1723	1.398	1248.7	143	0.0180	0.69
700	240.3	0.2416	0.1730	1.396	1295.1	151	0.0191	0.68
750	290.3	0.2424	0.1739	1.394	1339.6	158	0.0202	0.68
800	340.3	0.2434	0.1748	1.392	1382.5	166	0.0213	0.68
900	440.3	0.2458	0.1772	1.387	1463.6	179	0.0237	0.67
1000	540.3	0.2486	0.1800	1.381	1539.4	192	0.026	0.66
1100	640.3	0.2516	0.1830	1.374	1610.8	205	0.028	0.66
1200	740.3	0.2547	0.1862	1.368	1678.6	218	0.030	0.66
1300	840.3	0.2579	0.1894	1.362	1743.2	230	0.032	0.66
1400	940.3	0.2611	0.1926	1.356	1805.0	242	0.035	0.65
1500	1040.3	0.2642	0.1956	1.350	1864.5	253	0.037	0.65
1600	1140.3	0.2671	0.1985	1.345	1922.0	264	0.039	0.65
1700	1240.3	0.2698	0.2013	1.340	1977.6	274	0.041	0.65
1800	1340.3	0.2725	0.2039	1.336	2032	284	0.043	0.65

(Continued)

TABLE 3 AIR AT LOW PRESSURES

697

TABLE 3 (Continued)

T, °R	T, °F	c_p , Btu lb · °F	c_v , Btu lb · °F	$\gamma = \frac{c_p}{c_v}$	a, ft/sec	$\mu \times 10^7$, lb sec-ft	k, Btu hr-ft·°F	$\Pr = \frac{c_p\mu}{k}$
1900	1440.3	0.2750	0.2064	1.332	2084	293	0.045	0.65
2000	1540.3	0.2773	0.2088	1.328	2135	302	0.046	0.65
2100	1640.3	0.2794	0.2109	1.325	2185	311	0.048	0.65
2200	1740.3	0.2813	0.2128	1.322	2234	320	0.050	0.65
2300	1840.3	0.2831	0.2146	1.319	2282	329	0.052	0.65
2400	1940.3	0.2848	0.2162	1.317	2329	338	0.053	0.65
2600	2140.3	0.2878	0.2192	1.313	2420			
2800	2340.3	0.2905	0.2219	1.309	2508			
3000	2540.3	0.2929	0.2243	1.306	2593			
3200	2740.3	0.2950	0.2264	1.303	2675			
3400	2940.3	0.2969	0.2283	1.300	2755			
3600	3140.3	0.2986	0.2300	1.298	2832			
3800	3340.3	0.3001	0.2316	1.296	2907			
4000	3540.3	0.3015	0.2329	1.294	2981			
4200	3740.3	0.3029	0.2343	1.292	3052			
4400	3940.3	0.3041	0.2355	1.291	3122			
4600	4140.3	0.3052	0.2367	1.290	3191			
4800	4340.3	0.3063	0.2377	1.288	3258			
5000	4540.3	0.3072	0.3287	1.287	3323			
5200	4740.3	0.3081	0.2396	1.286	3388			
5400	4940.3	0.3090	0.2405	1.285	3451			
5600	5140.3	0.3098	0.2413	1.284	3513			
5800	5340.3	0.3106	0.2420	1.283	3574			
6000	5540.3	0.3114	0.2428	1.282	3634			
6200	5740.3	0.3121	0.2435	1.282	3693			
6400	5940.3	0.3128	0.2442	1.281	3751			

Conversion Factor
for μ

$$1 \frac{\text{lb}}{\text{sec}\cdot\text{ft}} = 14.882 \text{ poises}$$

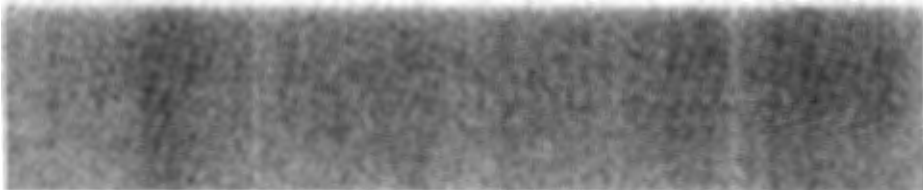
$$= 14.882 \frac{\text{gm}}{\text{sec}\cdot\text{cm}}$$

= 1488.2 centipoises

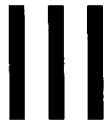
$$= 0.031081 \frac{\text{lb}_f\cdot\text{sec}}{\text{ft}^2}$$

Source: Reprinted by permission of John Wiley and Sons from J. H. Keenan and J. Kaye, Gas Tables, New York: Wiley, 1948. p. 34.





A P P E N D I X



ICAO STANDARD ATMOSPHERE

TABLE 1 Geometric altitude S.I. units

H_G, m	H, m	T, K	$P, \text{N/m}^2$	$\frac{P}{P_0}$	$\rho, \text{kg/m}^{-3}$	$\frac{\rho}{\rho_0}$	$a, \text{m/s}$	$v, \text{m}^2/\text{s}$
0	0	288.150	1.01325 +5	1.00000 +0	1.2250 +0	1.0000 +0	340.294	1.4607 -5
1000	1000	281.651	8.9876 +4	8.87009 -1	1.1117 +0	9.0748 -1	336.435	1.5813 -5
2000	1999	275.154	7.9501 +4	7.84618 -1	1.0066 +0	8.2168 -1	332.532	1.7147 -5
3000	2999	268.659	7.0121 +4	6.92042 -1	9.0925 -1	7.4225 -1	328.583	1.8628 -5
4000	3997	262.166	6.1660 +4	6.08541 -1	8.1935 -1	6.6885 -1	324.589	2.0275 -5
5000	4996	255.676	5.4048 +4	5.33415 -1	7.3643 -1	6.0117 -1	320.545	2.2110 -5
6000	5994	249.187	4.7217 +4	4.66001 -1	6.6011 -1	5.3887 -1	316.452	2.4162 -5
7000	6992	242.700	4.1105 +4	4.05677 -1	5.9002 -1	4.8165 -1	312.306	2.6461 -5
8000	7990	236.215	3.5651 +4	3.51854 -1	5.2579 -1	4.2921 -1	308.105	2.9044 -5
9000	8987	229.733	3.0800 +4	3.03979 -1	4.6706 -1	3.8128 -1	303.848	3.1957 -5
10000	9984	223.252	2.6500 +4	2.61533 -1	4.1351 -1	3.3756 -1	299.532	3.5251 -5
11 000	10 981	216.774	2.2700 +4	2.24031 -1	3.6480 -1	2.9780 -1	295.154	3.8988 -5
12 000	11 977	216.650	1.9399 +4	1.91457 -1	3.1194 -1	2.5464 -1	295.069	4.5574 -5
13 000	12 973	216.650	1.4170 +4	1.63628 -1	2.6660 -1	2.1763 -1	295.069	5.3325 -5
14 000	13 969	216.650	1.4170 +4	1.39851 -1	2.2786 -1	1.8600 -1	295.069	6.2391 -5
15 000	14 965	216.650	1.2112 +4	1.19534 -1	1.9475 -1	1.5898 -1	295.069	7.2995 -5

16 000	15 960	216.650	1.0353 +4	1.02174 -1	1.6647 -1	1.3589 -1	295.069	8.5397 -5
17 000	16 955	216.650	8.8496 +3	8.73399 -2	1.4230 -1	1.1616 -1	295.069	9.9902 -5
18 000	17 949	216.650	7.5652 +3	7.46629 -2	1.2165 -1	9.9304 -2	295.069	1.1686 -4
19 000	18 943	216.650	6.4674 +3	6.38291 -2	1.0400 -1	8.4894 -2	295.069	1.3670 -4
20 000	19 937	216.650	5.5293 +3	5.45700 -2	8.8910 -2	7.2579 -2	295.069	1.5989 -4
21 000	20 931	217.581	4.7274 +3	4.66709 -2	7.5715 -2	6.1808 -2	295.703	1.8843 -4
22 000	21 924	218.574	4.0420 +3	3.99456 -2	6.4510 -2	5.2661 -2	296.377	2.2201 -4
23 000	22 917	219.567	3.4562 +3	3.42153 -2	5.5006 -2	4.4903 -2	297.049	2.6135 -4
24 000	23 910	220.560	2.9554 +3	2.93288 -2	4.6938 -2	3.8317 -2	297.720	3.0743 -4
25 000	24 902	221.552	2.6077 +3	2.51588 -2	4.0084 -2	3.2722 -2	298.389	3.6135 -4
26 000	25 894	222.544	2.1632 +3	2.15976 -2	3.4257 -2	2.7965 -2	299.056	4.2439 -4
27 000	26 886	223.536	1.8555 +3	1.85539 -2	2.9298 -2	2.3917 -2	299.722	4.9805 -4
28 000	27 877	224.527	1.5949 +3	1.59506 -2	2.5076 -2	2.0470 -2	300.386	5.8405 -4
29 000	28 868	225.518	1.3737 +3	1.37224 -2	2.1478 -2	1.7533 -2	301.048	6.8438 -4
30 000	29 859	226.509	1.1855 +3	1.18138 -2	1.8410 -2	1.5029 -2	301.709	8.0134 -4

Source: *International Civil Aviation Organization, Standard Atmosphere Manual, Washington, D.C.: GPO, 1964.*

TABLE 2 Geometric altitude English units

H_G , ft	H , ft	T , °R	P , lb/ft ²	$\frac{P}{P_0}$	ρ , slug/ft ³	$\frac{\rho}{\rho_0}$	a , ft/s	v , ft ² /s
0	0	518.670	2.1162 +3	1.00000 +0	2.3769 -3	1.0000 +0	1116.45	1.5723 -4
2500	2500	509.756	1.9319 +3	9.12910 -1	2.2079 -3	9.2887 -1	1106.81	1.6700 -4
5000	4999	500.843	1.7609 +3	8.32085 -1	2.0482 -3	8.6170 -1	1097.10	1.7755 -4
7500	7497	491.933	1.6023 +3	7.57172 -1	1.8975 -3	7.9832 -1	1087.29	1.8896 -4
10000	9995	483.025	1.4556 +3	6.87832 -1	1.7556 -3	7.3859 -1	1077.40	2.0132 -4
12500	12493	474.120	1.3200 +3	6.23741 -1	1.6219 -3	6.8235 -1	1067.43	2.1472 -4
15000	14989	465.216	1.1948 +3	5.64587 -1	1.4962 -3	6.2946 -1	1057.36	2.2927 -4
17500	17485	456.315	1.0794 +3	5.10072 -1	1.3781 -3	5.7977 -1	1047.19	2.4509 -4
20000	19981	447.415	9.7327 +2	4.59912 -1	1.2673 -3	5.3316 -1	1036.93	2.6233 -4
22500	22476	438.518	8.7576 +2	4.13834 -1	1.1634 -3	4.8947 -1	1026.57	2.8113 -4
25000	24970	429.623	7.8633 +2	3.71577 -1	1.0663 -3	4.4859 -1	1016.10	3.0167 -4
27500	27464	420.730	7.0447 +2	3.32892 -1	9.7544 -4	4.1039 -1	1005.53	3.2416 -4
30000	29957	411.839	6.2962 +2	2.97544 -1	8.9068 -4	3.7473 -1	994.85	3.4882 -4
32500	32449	402.950	5.6144 +2	2.65305 -1	8.1169 -4	3.415 -1	984.05	3.7591 -4
35000	34941	394.064	4.9934 +2	2.35962 -1	7.3820 -4	3.1058 -1	973.14	4.0573 -4
37500	37432.5	389.970	4.4312 +2	2.093965 -1	6.6196 -4	2.78505 -1	968.08	4.48535 -4
40000	39923	389.970	3.9312 +2	1.85769 -1	5.8727 -4	2.4708 -1	968.08	7.70146 -4
42500	42413.5	389.970	3.4878 +2	1.64816 -1	5.2103 -4	2.1921 -1	968.08	5.69855 -4
45000	44903	389.970	3.0945 +2	1.46227 -1	4.6227 -4	1.9449 -1	968.08	6.4228 -4
47500	47392.5	389.970	2.7456 +2	1.29742 -1	4.1015 -4	1.7256 -1	968.08	7.2391 -4
50000	49880	389.970	2.4361 +2	1.15116 -1	3.6391 -4	1.5311 -1	968.08	8.1587 -4

52 500	52 368.5	389.970	2.1615 +2	1.02143 -1	3.2290 -4	1.3585 -1	968.08	9.19505 -3
55 000	54 855	389.970	1.9180 +2	9.06336 -2	2.8652 -4	1.2055 -1	968.08	1.0363 -3
57 500	57 341.5	389.970	1.7019 +2	8.042485 -2	2.5424 -4	1.0697 -1	968.08	1.1678 -3
60 000	59 828	389.970	1.5103 +2	7.13664 -2	2.2561 -4	9.4919 -2	968.08	1.3160 -3
62 500	62 313.5	389.970	1.3402 +2	6.33315 -2	2.0021 -4	8.42325 -2	968.08	1.483 -3
65 000	64 798	389.970	1.1893 +2	5.62015 -2	1.7767 -4	7.4749 -2	968.08	1.6711 -3
67 500	67 282.5	390.8835	1.0555 +2	4.988155 -2	1.5767 -4	6.61885 -2	969.21	1.891 -3
70 000	69 766	392.246	9.3672 +1	4.42898 -2	1.3993 -4	5.8565 -2	970.90	2.1434 -3
72 500	72 249	393.6085	8.3134 +1	3.93432 -2	1.2419 -4	5.18435 -2	972.58	2.4283 -3
75 000	74 731	394.971	7.3784 +1	3.49635 -2	1.1022 -4	4.5914 -2	974.26	2.7498 -3
77 500	77 213	396.3325	6.5487 +1	3.10856 -2	9.7829 -5	4.01681 -2	975.94	3.1125 -3
80 000	79 694	397.693	5.8125 +1	2.76491 -2	8.6831 -5	3.6060 -2	977.62	3.5213 -3
82 500	82 174	399.0545	5.1592 +1	2.460355 -2	7.7022 -5	3.19785 -2	979.285	3.98215 -3
85 000	84 655	400.415	4.5827 +1	2.19023 -2	6.7706 -5	2.8371 -2	980.95	4.5012 -3
87 500	87 134.5	401.7755	4.0757 +1	1.95063 -2	5.9598 -5	2.51815 -2	982.62	5.0857 -3
90 000	89 613	403.135	3.6292 +1	1.73793 -2	5.2531 -5	2.2360 -2	984.28	5.7434 -3
92 500	92 091.5	404.495	3.2354 +1	1.549199 -2	4.6362 -5	1.9864 -2	985.94	6.48345 -3
95 000	94 569	405.854	2.8878 +1	1.38133 -2	4.0970 -5	1.7653 -2	987.59	7.3155 -3
97 500	97 046	407.2135	2.5805 +1	1.23226 -2	3.6251 -5	1.56955 -2	989.245	8.25085 -3
100 000	99 523	408.572	2.3085 +1	1.09971 -2	3.2114 -5	1.3960 -2	990.90	9.3017 -3

Source: *International Civil Aviation Organization, Standard Atmosphere Manual, Washington, D.C.: GPO, 1964.*



APPENDIX

IV

PRELIMINARY DESIGN OF A SUBSONIC AXIAL COMPRESSOR STAGE

The purpose of this appendix is to provide in dimensionless form the equations employed in the preliminary design analysis whose results are shown in Figs. 7.45 to 7.48.

The mass flow rate through the plane just upstream of the rotor may be expressed in the form

$$\dot{m} = \int_{r_h}^{r_t} \rho c_z 2\pi r dr, \quad (\text{IV.1})$$

in which ρ is the density, c_z is the axial velocity component, and r_h and r_t are rotor inlet hub and tip radii, respectively.

By defining $y = r/r_t$, $\zeta = r_h/r_t$, $D = 2r_t$ and using the ideal-gas relationship, we may express this integral in the dimensionless form

$$\frac{\dot{m} \sqrt{RT_{01}}}{p_{01} D^2} = \frac{\pi}{2} \sqrt{\gamma} \frac{U_t}{a_{01}} \int_{\zeta}^1 \frac{\rho}{\rho_{01}} \left(\frac{c_{z1}}{U} \right) y^2 dy. \quad (\text{IV.2})$$

Here U is the local blade speed at any radius r , and the subscript t denotes the outer-radius (blade-tip) location. The subscript 1 denotes the entrance to the first-stage rotor. From the isentropic relationships for a perfect gas,

$$\frac{\rho}{\rho_{01}} = \left(\frac{T}{T_{01}} \right)^{1/(\gamma-1)},$$

in which T_{01} and ρ_{01} are the values of the stagnation temperature and density, respectively, at the rotor inlet.

From the definition of stagnation temperature, it follows that

$$h_0 = h + \frac{c^2}{2}$$

or

$$T_0 = T + \frac{c_\theta^2 + c_z^2}{2c_p},$$

so that

$$\frac{\rho}{\rho_{01}} = \left\{ 1 - \frac{\gamma - 1}{2} \left(\frac{U_t}{a_{01}} \right)^2 y^2 \left[\left(\frac{c_{\theta 1}}{U} \right)^2 + \left(\frac{c_{z1}}{U} \right)^2 \right] \right\}^{1/(\gamma-1)}. \quad (\text{IV.3})$$

Here $c_{\theta 1}$ and c_{z1} are velocity components at any radial position at entrance to the first-stage rotor. This equation shows that the local velocity ratios, which are needed to establish the local velocity triangles and the local blade angles, are also needed to evaluate the mass flow rate integral that is to be minimized. One must take into account the radial variations of the axial and tangential components of velocity in order to develop a satisfactory design.

Both upstream and downstream of the rotor, we need to be able to specify the radial variations of c_θ/U and c_z/U . We begin by examining conditions that will affect these velocity ratios at the tip diameter of the rotor. It is helpful to begin there because it is at the tip radius that the rotor will usually see the maximum relative Mach number.

WORK AND PRESSURE RATIO

As shown in Section 7.2, we can write the pressure ratio for the stage as

$$\frac{p_{03}}{p_{01}} = \left[1 + \eta_c \frac{\Delta T_0}{T_{01}} \right]^{\gamma/(\gamma-1)}, \quad (\text{IV.4})$$

in which η_c is the adiabatic efficiency of compression. For a single axial stage this will be close to the polytropic compression efficiency that was discussed in Section 7.7. The stage temperature rise depends on the work as shown by Eq. (7.12):

$$\Delta T_0 = \frac{U \Delta c_\theta}{c_p}. \quad (\text{IV.5})$$

We may combine Eqs. (IV.4) and (IV.5) to obtain

$$\frac{p_{03}}{p_{01}} = \left[1 + \eta_c(\gamma - 1) \left(\frac{U_t}{a_{01}} \right)^2 \left(\frac{\Delta c_\theta}{U} \right)_t \right]^{\gamma/(\gamma-1)}$$

or

$$\left(\frac{\Delta c_\theta}{U} \right)_t = \frac{\left(\frac{p_{03}}{p_{01}} \right)^{(\gamma-1)/\gamma} - 1}{(\gamma - 1)\eta_c \left(\frac{U_t}{a_{01}} \right)^2}, \quad (\text{IV.6})$$

in which the subscript t denotes the tip or outer-radius location. From this we see that specifying the stage pressure ratio and efficiency and selecting the blade speed helps to determine the velocity triangles at the outer radius.

Rotor Inlet Relative Mach Number

As mentioned in the introduction to Section 7.10, the Mach number of the flow relative to the blades must not be too high if we are to avoid shocks near the blade surface. Because blade speed is highest at the tip radius, the relative Mach number

$$M_{1\text{rel}} = \frac{w_1}{\sqrt{\gamma RT_1}} \quad (\text{IV.7})$$

tends to be the highest at that point also.

Referring to Fig. 7.8, we can see that the relative velocity can be written (for $r = r_t$)

$$w_{1t} = \sqrt{c_{z1t}^2 + (U_t - c_{\theta1t})^2}. \quad (\text{IV.8})$$

The temperature is related to the inlet stagnation temperature T_{01} and the absolute velocity c_1 by

$$T = T_{01} - \frac{c_{\theta1t}^2 + c_{z1t}^2}{2c_p}. \quad (\text{IV.9})$$

Combining Eqs. (IV.7), (IV.8), and (IV.9), we obtain the following relationship between the axial velocity ratio, the tangential ratio, and the limiting relative Mach number:

$$\left(\frac{c_z}{U}\right)_t = \frac{M_{1\text{rel}}^2 \left[\left(\frac{a_{01}}{U_t}\right)^2 - \left(\frac{\gamma - 1}{2}\right) \left(\frac{c_{\theta1}}{U}\right)_t^2 \right] - \left[1 - \left(\frac{c_{\theta1}}{U}\right)_t \right]^2}{1 + \frac{\gamma - 1}{2} M_{1\text{rel}}^2}. \quad (\text{IV.10})$$

Section 7.4 shows that for normal subsonic blading the value of $M_{1\text{rel}}$ should be limited to perhaps 0.75.

At this point we can see (from Eqs. IV.6 and IV.10) that choosing the dimensionless blade speed, the allowable relative Mach number, and the stage pressure ratio (and efficiency) does not completely determine the velocity triangles at the tip diameter. We need therefore to examine the radial variations of the velocity ratios $c_{\theta1}/U$ and c_{z1}/U . The first question to examine is the requirement that the velocity field satisfy the momentum equation in the radial direction. Since there are negligible velocities in the radial direction, this reduces to balancing the radial pressure gradient with the centripetal acceleration. This condition, plus the requirement that the variation of velocity with radius be consistent with con-

stant stagnation temperature, is known as the radial equilibrium condition. The expression of it that we can use for our design study comes from Section 7.9:

$$\frac{d}{dr}(c_z^2) = -\frac{1}{r^2} \frac{d}{dr}(rc_\theta)^2. \quad (7.44)$$

It is helpful to put Eq. (7.44) into dimensionless form with the result

$$\frac{d}{dy} \left[y \frac{c_z}{U} \right]^2 = -\frac{1}{y^2} \frac{d}{dy} \left[y^2 \frac{c_\theta}{U} \right]^2 \quad (\text{IV.11})$$

or

$$\left(\frac{c_z}{U} \right)^2 = \frac{1}{y^2} \left(\frac{c_z}{U} \right)_t^2 - \int_1^y \frac{1}{y^2} \frac{d}{dy} \left[y^2 \frac{c_\theta}{U} \right]^2 dy. \quad (\text{IV.12})$$

As Section 7.6 mentions, the designer is free to choose the radial distribution of angular momentum. Taking the exponential distribution as an example and writing it in dimensionless form results in

$$\frac{c_{\theta 1}}{U} = \frac{A}{y} + \frac{B}{y^2}, \quad A = \frac{a}{\Omega r_t}, \quad B = \frac{b_1}{\Omega r_t^2}, \quad (\text{IV.13})$$

in which the subscript 1 signifies upstream of the rotor and, as before, $y = r/r_t$. If the work done is to be independent of radial position, $(rc_{\theta 2} - rc_{\theta 1})$ must be independent of r . This requires that the value of a must be the same upstream and downstream of the rotor. However, to allow for the work done, the corresponding values of b must differ upstream and downstream of the rotor. The difference of c_θ/U between inlet and outlet of the rotor at the tip radius has already been determined according to Eq. (IV.6). Thus we obtain

$$\frac{c_{\theta 2}}{U} = \frac{A}{y} + \frac{B}{y^2} + \left(\frac{\Delta c_\theta}{U} \right)_t \frac{1}{y^2}. \quad (\text{IV.14})$$

We can show that the combination of Eqs. (IV.13) and (IV.14) satisfies the requirement that the work done be independent of radial position.

Using Eq. (IV.13) in (IV.12), we obtain the relation

$$\frac{c_{z1}}{U} = \frac{1}{y} \sqrt{\left(\frac{c_{z1}}{U} \right)_t^2 - 2A^2 \ln y - 2BA \left(1 - \frac{1}{y} \right)}. \quad (\text{IV.15})$$

To satisfy the condition that the axial velocity component at mid-radius be the same upstream and downstream of the rotor, we can evaluate the integral in Eq. (IV.12) by using Eq. (IV.14) in such a way that $(c_{z2}/U)_m = (c_{z1}/U)_m$. This leads to

$$\frac{c_{z2}}{U} = \frac{1}{y} \sqrt{\left(\frac{c_{z1}}{U} \right)_m^2 y_m^2 - 2A^2 \ln \frac{y}{y_m} - 2A \left[B + \left(\frac{\Delta c_\theta}{U} \right)_t \right] \left(\frac{1}{y_m} - \frac{1}{y} \right)}. \quad (\text{IV.16})$$

Equations (IV.13) and (IV.15) may be used to determine the variations with radius of the flow angles

$$\alpha = \tan^{-1} \left[\left(\frac{c_\theta}{U} \right) / \left(\frac{c_z}{U} \right) \right]$$

and

$$\beta = \tan^{-1} \left[\left(1 - \frac{c_\theta}{U} \right) / \left(\frac{c_z}{U} \right) \right]$$

upstream of the rotor, whereas Eqs. (IV.14) and (IV.16) apply in a corresponding way downstream of the rotor.

Consideration of mass conservation, angular momentum, and the radial equilibrium equation (subject to the aerodynamic limitations on relative Mach number and pressure coefficient) essentially controls the compressor design stage. Stress considerations indicate that the rotor blade twist angle should not be excessive and that the blade-tip speed should not be too high. However, it is principally aerodynamic limitations that control the design of air compressor stages for turbojet and turbofan engines.

To illustrate the application of a general and preliminary design process, we first apply it to a subsonic compressor stage.

Here we suppose that the stage is the first in a series of subsonic compressor stages. The rotor is preceded by inlet guide vanes, and the concept of "repeating" stages is used, that is, the absolute velocity at inlet to the rotor is the same as the absolute velocity leaving the following stator.

Furthermore we assume that the flow annulus through the stage contracts in such a way that the axial velocity at mid-radius is the same at all interblade-row positions. Equations (IV.1) to (IV.16) apply directly to this case. However, we need one more relationship to fix the relationship between the axial and the tangential velocity components. We obtain this by considering the degree of reaction—the parameter that describes the sharing of the enthalpy rise between rotor and stator.

One starting point for preliminary design is to choose at the mid-radius position $R = 0.5$. With equal work at mid- and tip radii,

$$U_m \Delta c_{\theta m} = U_t \Delta c_{\theta t}$$

or

$$\left(\frac{\Delta c_\theta}{U} \right)_m = \frac{1}{y_m^2} \left(\frac{\Delta c_\theta}{U} \right)_t. \quad (\text{IV.17})$$

Because the condition $R = 0.5$ implies symmetrical velocity triangles,

$$\left(\frac{c_{\theta 1}}{U} \right)_m = \frac{1}{2} \left[1 - \left(\frac{\Delta c_\theta}{U} \right)_m \right]$$

or

$$\left(\frac{c_{\theta 1}}{U} \right)_m = \frac{1}{2} \left[1 - \frac{1}{y_m^2} \left(\frac{\Delta c_\theta}{U} \right)_t \right]. \quad (\text{IV.18})$$

This supplies the connection needed for completion of the preliminary design procedure.

SUBSONIC COMPRESSOR STAGE DESIGN PROCEDURE

with "exponential" angular momentum distribution

$$rc_\theta = ar + b$$

Given: The fixed design parameters
 Pressure ratio p_{02}/p_{01} ,
 Stage efficiency η_c ,
 Specific-heat ratio γ ,
 Allowable relative Mach number $M_{1\text{rel}}$,

An initial selection of

Tip speed parameter U_t/a_{01} ,
 Hub-tip ratio $\zeta = r_h/r_t$,
 Swirl parameter B ,

one may follow these steps:

1. Calculate the tip diameter work ratio $(\Delta c_\theta/U)_t$ from Eq. (IV.6).
2. Calculate the mean-radius swirl ratio $(c_{\theta 1}/U)_m$ from Eq. (IV.18).
3. With given swirl parameter B determine A from the relationship

$$\left(\frac{c_{\theta 1}}{U}\right)_m = \frac{A}{y_m} + \frac{B}{y_m^2},$$

in which $y_m = (1 + \zeta)/2$, and thus obtain

$$\left(\frac{c_{\theta 1}}{U}\right)_t = A + B.$$

4. Solve for the tip diameter axial velocity ratio $(c_{z1}/U)_t$ from Eq. (IV.10).
5. Calculate the axial velocity ratios c_{z1}/U and c_{z2}/U by using Eqs. (IV.15) and (IV.16) at each radius and the swirl velocity ratios by using the relationships

$$\frac{c_{\theta 1}}{U} = \frac{A}{y} + \frac{B}{y^2},$$

$$\frac{c_{\theta 2}}{U} = \frac{A}{y} + \frac{1}{y^2} \left[B + \left(\frac{\Delta c_\theta}{U} \right)_t \right].$$

6. Solve at each radius for the density ratio from Eq. (IV.3).
7. Perform a numerical integration of Eq. (IV.2) to obtain the dimensionless mass flow parameter $\dot{m} \sqrt{RT_{01}/p_{01} D^2}$.
8. Systematically vary the input parameter set containing the variables U_t/a_{01} , ζ , and B , which are to be optimized.

9. Determine the variations with radius of the blade angles, the rotor blade twist $\Delta\beta_m = (\beta_{r\text{mean}} - \beta_{h\text{mean}})$, the degree of reaction, and the rotor and stator pressure coefficients.
10. Review the results for indications of optimum design.
11. Repeat this process for other pressure ratios.

Typical results of this design procedure are presented in Figs. 7.45 to 7.48. Sample calculation results are cited in Problem 7.17.

APPENDIX

V

PRELIMINARY DESIGN OF A TRANSONIC AXIAL COMPRESSOR STAGE

Since the flow at entrance to the rotor is taken to be purely axial and one-dimensional, we can adapt Eq. (3.13) directly to produce

$$\frac{\dot{m} \sqrt{RT_{01}}}{p_{01} D^2} = \sqrt{\gamma} \frac{\pi}{4} \frac{(1 - \zeta^2) M_1}{\left[1 + \frac{\gamma - 1}{2} M_1^2 \right]^{(\gamma+1)/2(\gamma-1)}}, \quad (\text{V.1})$$

because the flow area $A = \pi/4D^2(1 - \zeta^2)$, in which $\zeta = r_h/r_t$, and M_1 is the absolute (axial) Mach number just upstream of the rotor.

The only way for the stage work to be uniform with radius, if there is no inlet swirl, is for the rotor exit angular momentum $(rc_\theta)_2$ to be constant, or

$$\left(\frac{c_{\theta 2}}{U} \right) = \left(\frac{c_{\theta 2}}{U} \right)_t / y^2, \quad (\text{V.2})$$

in which $y = r/r_t$. This means uniform axial velocity, so that

$$\left(\frac{c_z}{U} \right) = \left(\frac{c_z}{U} \right)_t / y. \quad (\text{V.3})$$

With free-vortex swirl and low hub-tip ratio, there is danger that the rotor blade twist or the end-wall pressure coefficients may become excessive. It is necessary to limit the swirl (and thus the stage work) to prevent this from happening.

With zero inlet swirl we can write the pressure ratio equation as

$$\frac{p_{03}}{p_{01}} = \left[1 + \eta_c(\gamma - 1) \left(\frac{U_t}{a_{01}} \right)^2 \left(\frac{c_{\theta 2}}{U} \right)_t \right]^{\gamma(\gamma-1)}$$

or

$$\left(\frac{U_t}{a_{01}} \right)^2 \left(\frac{c_{\theta 2}}{U} \right)_t = \frac{\left(\frac{p_{03}}{p_{01}} \right)^{(\gamma-1)/\gamma} - 1}{\eta_c(\gamma - 1)}. \quad (\text{V.4})$$

With zero exit swirl from the stator and $c_3 = c_1$, we can write the stator hub coefficient as

$$C_{psh} = 1 - \left(\frac{c_1}{c_2} \right)^2.$$

For compressible flow this should really be called a kinetic energy reduction coefficient; however, the point remains that excessive local velocity reduction in the blade row is bad for the end-wall boundary layer. Even for a compressible flow we should limit C_{psh} to a value of about 0.5.

Writing

$$c_{2h}^2 = c_{\theta 2h}^2 + c_{z2h}^2 = \frac{c_{\theta 2t}^2}{\zeta^2} + c_1^2,$$

we can express the stator hub pressure coefficient as

$$C_{psh} = 1 - \frac{1}{1 + \left(\frac{c_{\theta 2t}}{c_1 \zeta} \right)^2}$$

or

$$c_{\theta 2t}^2 = \zeta^2 c_1^2 \left(\frac{C_{psh}}{1 - C_{psh}} \right). \quad (\text{V.5})$$

Since

$$c_1 = M_1 \sqrt{\gamma R T_1} = \frac{M_1 a_{01}}{\sqrt{1 + \frac{\gamma - 1}{2} M_1^2}},$$

Eq. (V.5) becomes

$$c_{\theta 2t}^2 = \frac{\zeta^2 M_1^2 a_{01}^2}{1 + \frac{\gamma - 1}{2} M_1^2} \left(\frac{C_{psh}}{1 - C_{psh}} \right)$$

or

$$\left(\frac{U_t}{a_{01}} \right)^2 \left(\frac{c_{\theta 2}}{U} \right)_t^2 = \frac{\zeta^2 M_1^2}{1 + \frac{\gamma - 1}{2} M_1^2} \left(\frac{C_{psh}}{1 - C_{psh}} \right). \quad (\text{V.6})$$

Dividing the left-hand side of Eq. (V.6) by that of Eq. (V.4), we obtain

$$\left(\frac{c_{\theta 2}}{U}\right)_t = \frac{\zeta^2 M_1^2}{1 + \frac{\gamma - 1}{2} M_1^2} \left(\frac{C_{psh}}{1 - C_{psh}}\right) \frac{\eta_c(\gamma - 1)}{\left[\left(\frac{p_{03}}{p_{01}}\right)^{(\gamma-1)/\gamma} - 1\right]}. \quad (\text{V.7})$$

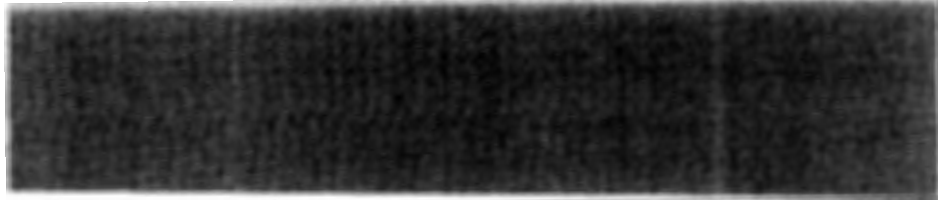
Thus for given values of pressure ratio, hub-tip ratio, and inlet Mach number, we can calculate the rotor tip exit swirl angle that will not lead to excessive stator hub pressure coefficient C_{psh} . With this value of $(c_{\theta 2}/U)_t$, we can determine from Eq. (V.6) that

$$\frac{U_t}{a_{01}} = \sqrt{\frac{\zeta^2 M_1^2}{1 + \frac{\gamma - 1}{2} M_1^2} \left(\frac{C_{psh}}{1 - C_{psh}}\right)} \Bigg/ \left(\frac{c_{\theta 2}}{U}\right)_t. \quad (\text{V.8})$$

Given that $w_{1t}^2 = c_1^2 + U_t^2$, we can show that

$$M_{1\text{rel}} = \sqrt{M_1^2 + \left(\frac{U_t}{a_{01}}\right)^2 \left(1 + \frac{\gamma - 1}{2} M_1^2\right)}. \quad (\text{V.9})$$

The results of using these equations are shown in Figs. 7.53 to 7.55. Sample calculation data are provided in Problem 7.18.



A P P E N D I X

VI

PRELIMINARY DESIGN OF AN AXIAL TURBINE STAGE

Using the assumptions stated in Section 8.8, we proceed to derive equations that enable us to evaluate the general function

$$\frac{\dot{m} \sqrt{RT_{04}}}{p_{04} D^2}, \frac{p_{04}}{p_{05}} = f\left(\frac{U_t}{a_0}, \left(\frac{c_z}{U}\right)_m, \left(\frac{\Delta h_0}{U^2}\right)_m, \zeta\right). \quad (\text{VI.1})$$

The mid-radius values of axial velocity ratio c_z/U and stage work ratio $\Delta h_0/U^2$ are chosen from Fig. 8.3 with the high-efficiency requirement in mind. Separately we consider the dependence of the dimensionless mass flow rate and the pressure ratio on the four independent variables.

MASS FLOW RATE

Equation (IV.2), derived for the axial compressor, applies directly in this case, except for the change in subscripts to denote turbine rather than compressor entrance:

$$\frac{\dot{m} \sqrt{RT_{04}}}{p_{04} D^2} = \frac{\pi}{2} \sqrt{\gamma} \left(\frac{U_t}{a_0}\right) \int_{\zeta}^1 \left(\frac{\rho}{\rho_{04}}\right) \left(\frac{c_z}{U}\right) y^2 dy. \quad (\text{VI.2})$$

With this equation goes the equivalent of Eq. (IV.3) for the relationship between the local gas density and the local gas velocity:

$$\frac{\rho}{\rho_{04}} = \left\{ 1 - \frac{\gamma - 1}{2} \left(\frac{U_t}{a_0}\right)^2 y^2 \left[\left(\frac{c_\theta}{U}\right)^2 + \left(\frac{c_z}{U}\right)^2 \right] \right\}^{1/(\gamma-1)}. \quad (\text{VI.3})$$

Here $a_0 = \sqrt{\gamma RT_{04}}$ is taken to be the speed of sound at the absolute stagnation temperature T_{04} (at entrance to the turbine).

As mentioned earlier, the flow area at entrance to the turbine will be much smaller than at entrance to the compressor. Since D will be nearly the same for both, the hub-tip ratio will be much larger for the first turbine stage than for the first compressor stage. It will not be so high that high efficiency can be obtained without blade twist, but it may well be high enough that the free-vortex solution will yield a satisfactory solution to the turbine flow field.

For the turbine, then, we begin by assuming that a free-vortex solution will do, so that

$$c_\theta = \frac{c_{\theta t}}{y} \quad \text{and} \quad \frac{c_\theta}{U} = \frac{1}{y^2} \left(\frac{c_\theta}{U} \right)_t, \quad (\text{VI.4})$$

in which, as for the compressor design procedure, y is the ratio of the local radius to the tip radius. Since, according to Eq. (7.29), this implies that the axial velocity component c_z is independent of radius,

$$c_z = c_{zt} \quad \text{and} \quad \frac{c_z}{U} = \frac{1}{y} \left(\frac{c_z}{U} \right)_t. \quad (\text{VI.5})$$

For this special case of the free-vortex solution, we may combine Eqs. (VI.2), (VI.3), (VI.4), and (VI.5) in the form

$$\begin{aligned} \frac{\dot{m} \sqrt{RT_{04}}}{p_{04} D^2} &= \frac{\pi}{2} \sqrt{\gamma} \left(\frac{U_t}{a_0} \right) \left(\frac{c_z}{U} \right)_t \int_{\zeta}^1 \left\{ 1 - \frac{\gamma - 1}{2} \left(\frac{U_t}{a_0} \right)^2 y^2 \right. \\ &\quad \times \left. \left[\left(\frac{c_\theta}{U} \right)_t \frac{1}{y^4} + \left(\frac{c_z}{U} \right)_t \frac{1}{y^2} \right] \right\}^{1/(\gamma-1)} y dy. \end{aligned} \quad (\text{VI.6})$$

For γ equal to 1.333 (for the turbine inlet gas), the exponent $1/(\gamma - 1)$ is 3 and the integral may be evaluated in closed form. First we define

$$\begin{aligned} A &= \frac{\gamma - 1}{2} \left(\frac{U_t}{a_0} \right)^2 \left(\frac{c_z}{U} \right)_t^2, \\ B &= \left(\frac{c_\theta}{U} \right)_t^2 / \left(\frac{c_z}{U} \right)_t^2, \\ C &= \frac{\pi}{2} \sqrt{\gamma} \left(\frac{U_t}{a_0} \right) \left(\frac{c_z}{U} \right)_t. \end{aligned}$$

Then we can express the mass flow rate integral equation as

$$\frac{\dot{m} \sqrt{RT_{04}}}{p_{04} D^2} = C \int_{\zeta}^1 \left[1 - A \left(1 + \frac{B}{y^2} \right) \right]^3 y dy,$$

which has the solution

$$\frac{\dot{m} \sqrt{RT_{04}}}{p_{04} D^2} = \frac{C(1 - A)^3}{2} \left[1 - \zeta^2 + 3E \ln \zeta^2 + 3E^2 \left(\frac{1}{\zeta^2} - 1 \right) - \frac{E^3}{2} \left(\frac{1}{\zeta^4} - 1 \right) \right], \quad (\text{VI.7})$$

in which $E = AB/(1 - A)$.

WORK AND PRESSURE RATIO

The overall pressure ratio for the turbine may be expressed in the form

$$\frac{p_{04}}{p_{05}} = 1 \left/ \left[1 - \frac{(\gamma - 1)}{\eta_u} \left(\frac{U_t}{a_0} \right)^2 \left(\frac{\Delta c_\theta}{U} \right)_t \right] \right.^{\gamma/(\gamma-1)}, \quad (\text{VI.8})$$

in which η_u is the total-to-total turbine adiabatic efficiency and a_0 is the speed of sound based on the absolute inlet stagnation temperature.

BLADE-ROOT STRESS

From Eq. (8.17) we can relate the actual blade-root stress to the tip speed parameter in the following way:

$$\frac{2\sigma_b}{\rho_b a_0^2} = \left(\frac{U_t}{a_0} \right)^2 (1 - \zeta^2). \quad (\text{VI.9})$$

DEGREE OF REACTION

With the desire for high stage efficiency in mind, we set the mean-radius degree of reaction at 50%. This implies symmetrical velocity triangles and therefore that the tangential velocities upstream and downstream of the rotor are given by

$$\left(\frac{c_{\theta 2}}{U} \right)_m = \frac{1}{2} \left[1 + \left(\frac{\Delta c_\theta}{U} \right)_m \right] \quad (\text{VI.10})$$

and

$$\left(\frac{c_{\theta 3}}{U} \right)_m = \frac{1}{2} \left[1 - \left(\frac{\Delta c_\theta}{U} \right)_m \right], \quad (\text{VI.11})$$

in which subscripts 2 and 3 denote upstream and downstream, respectively, of the rotor. These follow from the implication that with 50% reaction, the velocity triangles are symmetrical. With free-vortex swirl both upstream and downstream of the rotor, the tip tangential velocity ratio will be given by

$$\left(\frac{c_{\theta 2}}{U} \right)_t = \frac{(1 + \zeta)^2}{8} \left[1 + \left(\frac{\Delta c_\theta}{U} \right)_m \right]. \quad (\text{VI.12})$$

PRELIMINARY DESIGN PROCEDURE

Given: The inlet stagnation temperature T_{04} ,

The inlet stagnation pressure p_{04} ,

The mass flow rate \dot{m} ,

An allowable blade-root stress σ_b (determined from material-strength data, such as those displayed in Fig. 8.13, and an estimate of the blade-root temperature resulting from blade cooling),

The blade material density ρ_b ,

and an initial set of values for:

The mid-radius axial velocity ratio $\left(\frac{c_z}{U}\right)_m$,

The mid-radius work ratio $\left(\frac{\Delta c_\theta}{U}\right)_m$,

The hub-tip radius ratio ζ ,

one may follow these steps:

1. Determine the tip speed ratio from Eq. (VI.9), written in the form

$$\frac{U_t}{a_0} = \sqrt{\frac{2\sigma_b}{\rho_b a_0^2}} / (1 - \zeta^2).$$

2. Obtain the tip axial velocity ratio $(c_z/U)_t$ from

$$\left(\frac{c_z}{U}\right)_t = \left(\frac{c_z}{U}\right)_m \left(\frac{1 + \zeta}{2}\right).$$

3. Determine the tip tangential velocity ratio from Eq. (VI.12):

$$\left(\frac{c_{\theta 2}}{U}\right)_t = \frac{(1 + \zeta)^2}{8} \left[1 + \left(\frac{\Delta c_\theta}{U}\right)_m \right].$$

4. Then calculate the dimensionless mass flow rate from Eq. (VI.7) and deduce the tip diameter D from this result and the given values of \dot{m} , p_{04} , T_{04} . If this value of D is unacceptably large, decrease the hub-tip ratio ζ .

5. Obtain the tip work ratio from

$$\left(\frac{\Delta c_\theta}{U}\right)_t = \left(\frac{\Delta c_\theta}{U}\right)_m \left(\frac{1 + \zeta}{2}\right)^2.$$

6. Estimate the stage efficiency by referring to Fig. 8.13 and allowing 1% to 2% for tip-clearance loss. Alternatively, at this early stage of design, one may estimate the stage efficiency as 0.9.

7. Estimate the stage pressure ratio from Eq. (VI.8).

8. Estimate the stator and rotor flow angles from

$$\tan \alpha = \frac{c_\theta}{U} / \frac{c_z}{U},$$

$$\tan \beta = \left(1 - \frac{c_\theta}{U}\right) / \frac{c_z}{U}.$$

- 9.** Calculate the degree of reaction at, say, root and tip radii from the following relationship:

$$R = \left[\left(\frac{w_2}{U} \right)^2 - \left(\frac{w_1}{U} \right)^2 \right] / \left[2 \frac{\Delta c_\theta}{U} \right].$$

- 10.** Then systematically vary the parameters

$$\left(\frac{c_z}{U} \right)_m \quad \text{and} \quad \left(\frac{\Delta h_0}{U^2} \right)_m$$

to explore the opportunities for optimizing the design while preventing excessive blade twist and excessive variation of degree of reaction from root to tip. Do not allow the degree of reaction to become negative, because this would imply local pressure rise, which, in conjunction with high turning, would probably cause boundary layer separation.

A P P E N D I X

VII

PRELIMINARY DESIGN OF A CENTRIFUGAL COMPRESSOR STAGE WITH PREWHIRL

This appendix provides the equations for:

1. Establishing the upper limit on shaft speed as a function of inducer inlet conditions, including the rotor inlet angular momentum distribution;
2. Estimating the ratio of impeller diameters;
3. Estimating approximately the rotor exit blade width ratio.

IMPELLER SHAFT SPEED

At the entrance to the inducer, the flow is in the axial direction (possibly with superimposed swirl), so the mass flow rate equation developed for axial compressor stages (see Eqs. IV.2 and IV.3) applies directly. We modify it here to read

$$\frac{\dot{m} \sqrt{RT_{01}}}{p_{01} D_{1t}^2} = \frac{\pi}{2} \int_{\zeta}^1 \left\{ 1 - \frac{\gamma - 1}{2\gamma} \left[\left(\frac{c_z}{\sqrt{RT_{01}}} \right)^2 + \left(\frac{c_\theta}{\sqrt{RT_{01}}} \right)^2 \right] \right\}^{1/\gamma-1} \frac{c_z}{\sqrt{RT_{01}}} y dy, \quad (\text{VII.1})$$

in which, in this case, D_{1t} is the tip diameter at inlet to the impeller, $y = 2r/D_{1t}$, and $\zeta = D_{1h}/D_{1t}$. Since, typically, ζ is small for centrifugal compressors, radial variations may be quite important if there is swirling flow at the rotor inlet. One of the questions we would like to consider here is whether a better centrifugal stage could result from using inlet swirl. Thus we need to consider the relation-

ship between c_z and c_θ in Eq. (VII.1). However, since it is the rotational speed Ω that is fixed by the inlet, we need first to transform the left-hand side of Eq. (VII.1) into a dimensionless shaft speed variable. We do this by writing (with reference to Fig. 9.24)

$$D_{1t} = \frac{2U_{1t}}{\Omega} = \frac{2}{\Omega}(c_{\theta1t} + c_{z1t} \tan \beta_{1t}),$$

in which β_{1t} is the inlet tip blade angle. To prevent flow separation at entrance to the inducer, this angle must be limited, as shown in Section 9.3, to not more than about 50° . With this result we can write Eq. (VII.1) as

$$\begin{aligned} \frac{\dot{m}\Omega^2}{p_{01}\sqrt{RT_{01}}} &= 2\pi \left[\frac{c_{\theta1t}}{\sqrt{RT_{01}}} + \frac{c_{z1t}}{\sqrt{RT_{01}}} \tan \beta_{1t} \right]^2 \\ &\times \int_1^1 \left[1 - \frac{\gamma - 1}{2} \left\{ \left(\frac{c_{z1}}{\sqrt{RT_{01}}} \right)^2 + \left(\frac{c_{\theta1}}{\sqrt{RT_{01}}} \right)^2 \right\} \right]^{1/(\gamma-1)} \frac{c_{z1}}{\sqrt{RT_{01}}} y dy. \end{aligned} \quad (\text{VII.2})$$

We wish to find the velocity field between the inlet guide vanes and the inducer that will maximize the left-hand side of the equation for given values of \dot{m} , p_{01} , and T_{01} .

The use of prewhirl brings in the need to consider radial equilibrium. For this purpose we modify the general solution for the radial equilibrium of a swirling axial flow (Eq. 7.44) by using the term $\sqrt{RT_{01}}$ instead of the blade speed to make each velocity component dimensionless, T_{01} being the inlet stagnation temperature. The result is

$$\frac{c_{z1}}{\sqrt{RT_{01}}} = \sqrt{\left(\frac{c_{z1}}{\sqrt{RT_{01}}} \right)_t^2 - \int_1^y \frac{1}{y^2} dy} \left(\frac{yc_{\theta1}}{\sqrt{RT_{01}}} \right)^2 dy. \quad (\text{VII.3})$$

As an example we explore the possibility that the assumption $c_\theta \propto r$ might provide a good solution to the radial equilibrium problem. This would mean

$$\frac{c_{\theta1}}{\sqrt{RT_{01}}} = \left(\frac{c_{\theta1}}{\sqrt{RT_{01}}} \right)_t y, \quad (\text{VII.4})$$

so that

$$\frac{c_{z1}}{\sqrt{RT_{01}}} = \sqrt{\left(\frac{c_{z1}}{\sqrt{RT_{01}}} \right)_t^2 - 2 \left(\frac{c_{\theta1}}{\sqrt{RT_{01}}} \right)_t^2 (y^2 - 1)}. \quad (\text{VII.5})$$

The relative Mach number at the tip diameter of the inlet can be written

$$M_{1\text{rel}} = \frac{w_{1t}}{\sqrt{\gamma RT_{1t}}} = \frac{c_{z1}}{\cos \beta_{1t} \sqrt{\gamma RT_{1t}}},$$

in which, as before, the subscript t denotes the inlet tip radius. We can modify this expression to read

$$M_{1\text{rel}} = \frac{1}{\sqrt{\gamma}} \left(\frac{c_{z1}}{\sqrt{RT_{01}}} \right)_t \left(\frac{T_{01}}{T_{1t}} \right)^{1/2} \frac{1}{\cos \beta_{1t}}. \quad (\text{VII.6})$$

But we may also write

$$T_{01} = T_{1t} + \frac{c_{1t}^2}{2c_p} = T_{1t} + \frac{\gamma - 1}{2\gamma R} (c_{z1t}^2 + c_{\theta1t}^2)$$

or

$$\frac{T_{1t}}{T_{01}} = 1 - \frac{\gamma - 1}{2\gamma} \left[\left(\frac{c_{z1t}}{\sqrt{RT_{01}}} \right)^2 + \left(\frac{c_{\theta1t}}{\sqrt{RT_{01}}} \right)^2 \right]. \quad (\text{VII.7})$$

Combining Eqs. (VII.6) and (VII.7), we obtain a relationship between the tip diameter values of the axial and tangential velocity ratios, the inlet relative Mach number, and the inducer inlet blade angle:

$$\left(\frac{c_{z1t}}{\sqrt{RT_{01}}} \right)^2 = \frac{\gamma \cos^2 \beta_{1t} \left[1 - \frac{\gamma - 1}{2\gamma} \left(\frac{c_{\theta1t}}{\sqrt{RT_{01}}} \right)^2 \right] M_{1\text{rel}}^2}{\left[1 + \frac{\gamma - 1}{2} \cos^2 \beta_{1t} M_{1\text{rel}}^2 \right]}. \quad (\text{VII.8})$$

Combination of Eqs. (VII.4), (VII.5), and (VII.8) with the continuity equation (VII.2) provides a relationship that we may express as

$$\frac{\dot{m} \Omega^2}{p_{01} \sqrt{RT_{01}}} = f \left(\frac{c_{\theta1t}}{\sqrt{RT_{01}}}, \zeta, \beta_{1t}, M_{1\text{rel}} \right). \quad (\text{VII.9})$$

Of the four independent variables, two ($M_{1\text{rel}}$ and β_{1t}) are limited by the need to prevent separation at the inducer tip.

IMPELLER DIAMETER RATIO

We can write the diameter ratio as

$$\frac{D_2}{D_{1t}} = \frac{U_2}{U_{1t}} = \frac{U_2 / \sqrt{RT_{01}}}{U_{1t} / \sqrt{RT_{01}}}$$

or

$$\frac{D_2}{D_{1t}} = \frac{\frac{U_2}{\sqrt{RT_{01}}}}{\frac{c_{\theta1t}}{\sqrt{RT_{01}}} + \frac{c_{z1}}{\sqrt{RT_{01}}} \tan \beta_{1t}}. \quad (\text{VII.10})$$

Equation (VII.8) provides the dependence of $c_{z1}/\sqrt{RT_{01}}$ on $M_{1\text{rel}}$, β_{1t} , and $c_{\theta1t}/\sqrt{RT_{01}}$, thus enabling us to use Eq. (VII.10) for computing the diameter ratio D_2/D_{1t} , for any selected value of $U_2/\sqrt{RT_{01}}$.

IMPELLER EXIT BLADE WIDTH RATIO

In this section we make a number of simplifying approximations, because we are not seeking an exact value of b_2/D_2 but a warning number to indicate conditions under which blade height could become unacceptably small.

We can express the flow rate across the exit plane as

$$\dot{m} = \pi D_2 b_2 \rho_2 w_{r2}$$

if we neglect the thickness of the vanes and the boundary layer displacement thickness.

Across the inlet alone we can write

$$\dot{m} = \frac{\pi}{4} D_{1t}^2 (1 - \zeta^2) \rho_1 c_{z1},$$

in which the product $\rho_1 c_{z1}$ can be taken to be an average value across the rotor inlet plane. From these two relationships we may write

$$\frac{b_2}{D_2} = \left(\frac{D_{1t}}{D_2} \right)^2 \left(\frac{1 - \zeta^2}{4} \right) \left(\frac{\rho_1}{\rho_2} \right) \left(\frac{c_{z1}}{w_{r2}} \right). \quad (\text{VII.11})$$

A reasonable value for c_{z1}/w_{r2} is 1. This is because of the need to minimize the possibility of separation in the rotor flow passages. As discussed in Section 9.3, the mean relative velocity w should remain nearly constant from the end of the inducer to the exit of the impeller. With a nearly axial outlet to the inducer, $w \approx c_{z1}$. At the impeller exit, with the flow nearly radial, $w \approx w_{r2}$. Thus

$$c_{z1}/w_{r2} \approx 1.$$

The density ratio ρ_1/ρ_2 may be written

$$\frac{\rho_1}{\rho_2} = \frac{\rho_{01}}{\rho_{02}} \left[\frac{1 + \frac{\gamma - 1}{2} M_2^2}{1 + \frac{\gamma - 1}{2} M_1^2} \right]^{1/(\gamma-1)},$$

in which M_1 is the average absolute Mach number of the flow entering the inducer and M_2 is the absolute Mach number of the flow leaving the impeller. Making the approximations $M_2 \approx 1$ and $(\gamma - 1)/2M_1^2 \ll 1$, we obtain

$$\frac{\rho_1}{\rho_2} \approx \left(\frac{\rho_{01}}{\rho_{02}} \right)^{1/\gamma} \left(\frac{\gamma + 1}{2} \right)^{1/(\gamma-1)}. \quad (\text{VII.12})$$

We can write the stagnation pressure ratio across the rotor as

$$\frac{p_{02}}{p_{01}} = \left\{ 1 + \eta_{cr} \left[\frac{U c_{\theta 2} - \overline{U_1 c_{\theta 1}}}{c_p T_{01}} \right] \right\}^{\gamma(\gamma-1)}.$$

As an approximation we might write the adiabatic rotor efficiency η_{cr} as $(1 + \eta_c)/2$ in which η_c is the stage adiabatic efficiency. Also we could neglect $\overline{U_1 c_{\theta 1}}$ relative to $U_2 c_{\theta 2}$. This would give us

$$\frac{p_{02}}{p_{01}} = \left[1 + \frac{(1 + \eta_c)}{2} \left(\frac{\gamma - 1}{\gamma} \right) \left(\frac{U_2}{\sqrt{RT_{01}}} \right)^2 c_{\theta 2} \right]^{\gamma(\gamma-1)},$$

so that

$$\frac{\rho_1}{\rho_2} \simeq \left(\frac{\gamma + 1}{2} \right)^{1/(\gamma-1)} \left/ \left[1 + \left(\frac{1 + \eta_c}{2} \right) \left(\frac{\gamma - 1}{\gamma} \right) \left(\frac{U_2}{\sqrt{RT_{01}}} \right)^2 \sigma_s \right]^{1/(\gamma-1)} \right., \quad (\text{VII.13})$$

and hence we can approximately estimate the blade width ratio as

$$\frac{b_2}{D_2} \simeq \frac{\left(\frac{\gamma + 1}{2} \right)^{1/(\gamma-1)} \left(\frac{D_{1t}}{D_2} \right)^2 (1 - \zeta^2)}{4 \left[1 + \left(\frac{1 + \eta_c}{2} \right) \left(\frac{\gamma - 1}{\gamma} \right) \left(\frac{U_2}{\sqrt{RT_{01}}} \right)^2 \sigma_s \right]^{1/(\gamma-1)}}, \quad (\text{VII.14})$$

in which D_{1t}/D_2 is given by Eq. (VII.10).

A P P E N D I X

VIII

OPTIMIZATION OF MULTISTAGE ROCKETS

The optimization of multistage rockets with respect to the distribution of mass has been treated in a number of interesting papers [1, 2, 3, 4]. The problem is reasonably simple if all stages have the same exhaust velocity and the same structural coefficients ϵ . In this case the increment of vehicle velocity due to the i th stage is

$$\Delta u_i = u_e \ln \frac{1 + \lambda_i}{\epsilon + \lambda_i}, \quad (\text{VIII.1})$$

and the final or n th-stage velocity is

$$\frac{u_n}{u_e} = \prod_1^n \ln \frac{1 + \lambda_i}{\epsilon + \lambda_i} = \sum_1^n F(\lambda_i). \quad (\text{VIII.2})$$

The techniques of the calculus of variations may be employed to find the payload ratios of λ_i such that the velocity ratio u_n/u_e is maximized. For a given payload $M_{\mathcal{L}}$ and initial mass M_{01} , the payload ratios λ_i are subject to the constraint of Eq. (10.35):

$$\frac{M_{\mathcal{L}}}{M_{01}} = \prod_1^n \left(\frac{\lambda_i}{1 + \lambda_i} \right).$$

This constraint may be expressed more conveniently in logarithmic form as

$$\ln \frac{M_{\mathcal{L}}}{M_{01}} = \sum_1^n \ln \left(\frac{\lambda_i}{1 + \lambda_i} \right) = \sum_1^n G(\lambda_i). \quad (\text{VIII.3})$$

In order to maximize the quantity $\sum_1^n F(\lambda_i)$ subject to Eq. (VIII.3), it is appropriate to maximize

$$L(\lambda_i) = F(\lambda_i) + \alpha G(\lambda_i), \quad (\text{VIII.4})$$

where α is an undetermined constant, the *Lagrange multiplier*. For a maximum,

$$\frac{\partial L}{\partial \lambda_i} = \frac{\partial F}{\partial \lambda_i} + \alpha \frac{\partial G}{\partial \lambda_i} = 0.$$

Using Eqs. (VIII.2) and (VIII.3), we obtain

$$+ \frac{1}{1 + \lambda_i} - \frac{1}{\epsilon + \lambda_i} + \frac{\alpha}{\lambda_i} - \frac{\alpha}{1 + \lambda_i} = 0, \quad (\text{VIII.5})$$

which we may reduce to

$$\lambda_i = \frac{\alpha \epsilon}{1 - \alpha - \epsilon}. \quad (\text{VIII.6})$$

Since all other terms in the equation are constant, λ_i must be constant. Thus, using Eq. (10.33) again and setting $\lambda_i = \lambda$, we have

$$\frac{\mathcal{M}_{\infty}}{\mathcal{M}_{01}} = \prod_1^n \left(\frac{\lambda}{1 + \lambda} \right) = \left(\frac{\lambda}{1 + \lambda} \right)^n$$

or

$$\lambda = \frac{(\mathcal{M}_{\infty}/\mathcal{M}_{01})^{1/n}}{1 - (\mathcal{M}_{\infty}/\mathcal{M}_{01})^{1/n}}. \quad (\text{VIII.7})$$

If, for a particular case, u_e is constant but some approximate variation of ϵ_i is assumed, perhaps according to Fig. 10.6, then a more refined calculation may be made. In this case, Eq. (VIII.6) becomes

$$(\epsilon_i + \alpha - 1)\lambda_i + \alpha \epsilon_i = 0$$

or

$$\lambda_i = \frac{\alpha \epsilon_i}{1 - \alpha - \epsilon_i}, \quad (\text{VIII.8})$$

and Eq. (10.33) becomes

$$\frac{\mathcal{M}_{\infty}}{\mathcal{M}_{01}} = \prod_1^n \frac{-\alpha \epsilon_i}{\epsilon_i + \alpha - 1 - \alpha \epsilon_i}. \quad (\text{VIII.9})$$

From Eq. (VIII.9), α is found in terms of \mathcal{M}_{∞} , \mathcal{M}_{01} , and the assumed ϵ_i . Then the λ_i are found from Eq. (VIII.8).

For the case where both ϵ_i and u_e are *known* variables, a similar procedure leads to minimum $\mathcal{M}_{01}/\mathcal{M}_{\infty}$ for a given final velocity in the absence of drag and

gravity [2]. Using the definition of \mathcal{R}_i (Eq. (10.31)), we may write the overall mass ratio as

$$\frac{\mathcal{M}_{01}}{\mathcal{M}_{\infty}} = \prod_1^n \left(1 + \frac{\mathcal{R}_i - 1}{1 - \epsilon_i \mathcal{R}_i} \right). \quad (\text{VIII.10})$$

This is to be minimized subject to the constraint

$$u_n = \sum_1^n u_{ei} \ln \mathcal{R}_i = \sum_1^n G(u_{ei}, \mathcal{R}_i). \quad (\text{VIII.11})$$

Again, for convenience, we express the first equation in logarithmic form:

$$\ln \frac{\mathcal{M}_{01}}{\mathcal{M}_{\infty}} = \sum_1^n \ln \left(1 + \frac{\mathcal{R}_i - 1}{1 - \epsilon_i \mathcal{R}_i} \right) = \sum_1^n F(\epsilon_i, \mathcal{R}_i). \quad (\text{VIII.12})$$

If we proceed in the same way as with Eq. (VIII.5), the minimum occurs when \mathcal{R}_i satisfies

$$\frac{\partial}{\partial \mathcal{R}_i} \ln \left(1 + \frac{\mathcal{R}_i - 1}{1 - \epsilon_i \mathcal{R}_i} \right) + \alpha \frac{\partial}{\partial \mathcal{R}_i} (u_{ei} \ln \mathcal{R}_i) = 0, \quad (\text{VIII.13})$$

where α is again the Lagrange multiplier, a constant. After differentiation and rearrangement, we have

$$\mathcal{R}_i = \frac{\alpha u_{ei} + 1}{\alpha \epsilon_i u_{ei}}. \quad (\text{VIII.14})$$

We obtain a solution for α by substituting Eq. (VIII.14) in Eq. (VIII.11) to yield

$$u_n = \sum_1^n u_{ei} \ln \frac{\alpha u_{ei} + 1}{\alpha \epsilon_i u_{ei}}. \quad (\text{VIII.15})$$

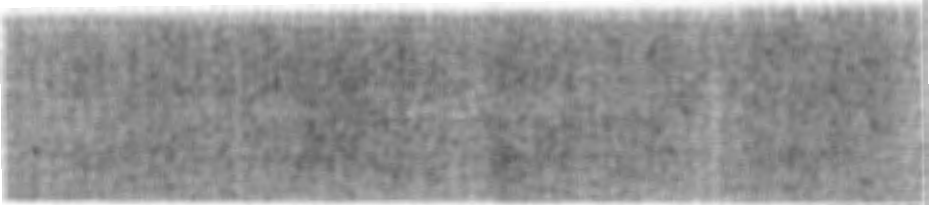
After α is obtained from Eq. (VIII.15), we can determine the mass ratios \mathcal{R}_i from Eq. (VIII.14). The individual payload ratios are given by

$$\lambda_i = \frac{1 - \mathcal{R}_i \epsilon_i}{\mathcal{R}_i - 1}. \quad (\text{VIII.16})$$

Note that this analysis says nothing about selection of the stage exhaust velocities.

REFERENCES

1. Builder, C. H. "General Solution for Optimization of Staging of Multistaged Boost Vehicles," *J. Amer. Rocket Soc.* 29 (1959): 497–499.
2. Hall, H. H., and E. D. Zambelli. "On the Optimization of the *N*-Step Rocket," *Jet Propulsion* 28 (1958): 463–465.
3. Subotowicz, M. "The Optimization of the *N*-Step Rocket with Different Construction Parameters and Propellant Specific Impulse in Each Stage," *Jet Propulsion* 28 (1958): 460–463.
4. Weisbord, L. "Optimum Staging Techniques," *J. Amer. Rocket Soc.* 29 (1959): 445–446.



A P P E N D I X

IX

ELECTROSTATIC AND ELECTROMAGNETIC FORCES

Electrostatic and electromagnetic forces may be used to accelerate a variety of propellants in devices that are described in Chapter 14. The propellant may consist of separate beams of ions and electrons, each capable of acceleration in an electrostatic field; or, alternatively, it may be a mixture of ions, electrons, and neutral particles flowing in a single stream. Such a stream, though electrically neutral, may conduct an electrical current so that the fluid, or plasma, as it is called, is subject to an electromagnetic driving force much the same as a current-carrying conductor in an electric motor.

The force on two charges is given by Coulomb's law, which states that

$$F \propto \frac{q_1 q_2}{r^2},$$

where q_1 and q_2 are the charges and r is the distance between them. We note that forces are vectorially additive, and so the force on a charge q due to n other charges is given by

$$\mathbf{F}_q = \frac{q}{4\pi\epsilon} \sum_{i=1}^n \frac{q_i}{r_i^2} \mathbf{r}_i, \quad (\text{IX.1})$$

where \mathbf{r}_i is a unit vector pointing from q_i to q , and $1/4\pi\epsilon$ is a proportionality constant (depending on the units of F , q , r , and the substance separating the charges). The constant ϵ is called the permittivity of the material. For a vacuum, ϵ has the particular value ϵ_0 , called the permittivity of free space. In the International Sys-

tem of Units (SI), in which F is in newtons (N), r in meters (m), and q in coulombs (C), ϵ_0 has the value $8.85 \times 10^{-12} C^2/N \cdot m^2$. The permittivity of gases is very close to ϵ_0 .

If the number of charges n is large (as is almost always the case), it is convenient to consider the charge as being continuously distributed through space or perhaps over surfaces. Then, defining a volume charge density[†] ρ_q and a surface charge density σ_q , we transform this summation to the integral equation (for gas or vacuum),

$$\mathbf{F}_q = \frac{q}{4\pi\epsilon_0} \left(\int_V \frac{\rho_q \mathbf{r}}{r^2} dV + \int_A \frac{\sigma_q \mathbf{r}}{r^2} dA \right), \quad (\text{IX.2})$$

in which V and A are the entire volume and surface of interest.

It is convenient to define the *electric field strength* \mathbf{E} at a point as the force per unit (positive) charge at that point due to whatever other charges may be present. That is,

$$\mathbf{E} \equiv \frac{\mathbf{F}_q}{q} = \frac{1}{4\pi\epsilon_0} \left(\int_V \frac{\rho_q \mathbf{r}}{r^2} dV + \int_A \frac{\sigma_q \mathbf{r}}{r^2} dA \right). \quad (\text{IX.3})$$

For cartesian coordinates with unit vectors $\mathbf{x}, \mathbf{y}, \mathbf{z}$, we have

$$\mathbf{E} = E_x \mathbf{x} + E_y \mathbf{y} + E_z \mathbf{z}.$$

If Eq. (IX.3) is applied to an infinitesimal volume of size $dx dy dz$ with an internal charge density ρ_q (and no surface charge distribution), we may show that

$$\frac{\partial E_x}{\partial x} + \frac{\partial E_y}{\partial y} + \frac{\partial E_z}{\partial z} = \frac{\rho_q}{\epsilon_0}. \quad (\text{IX.4})$$

By using the vector operator ∇ , Eq. (IX.4) may be written in the more general form

$$\nabla \cdot \mathbf{E} = \frac{\rho_q}{\epsilon_0}. \quad (\text{IX.5})$$

This statement is known as Gauss's law.

The work necessary to move a charge q in any electrostatic field is dependent only on the end points of the displacement. Hence the field may be described by a potential V such that

$$dV = -\mathbf{E} \cdot d\mathbf{s}, \quad (\text{IX.6})$$

where $d\mathbf{s}$ is the (vector) increment of displacement. In the SI system the units of V , work per unit charge, $N \cdot m/C$ or J/C , are commonly called *volts* (V). If an isolated charged particle moves through an electrostatic field, the sum of its electrical

[†] Like any continuum concept, charge density has meaning so long as the spacing between charges is much less than the smallest significant dimension in the problem considered.

potential and kinetic energies remains constant (neglecting changes of gravitational potential energy). Thus for a particle of mass m and charge q ,

$$\frac{mu^2}{2} + qV = \text{const.} \quad (\text{IX.7})$$

Equation (IX.6) may be written, for cartesian coordinates,

$$dV = -(E_x dx + E_y dy + E_z dz),$$

so that

$$E_x = -\frac{\partial V}{\partial x}, \quad E_y = -\frac{\partial V}{\partial y}, \quad E_z = -\frac{\partial V}{\partial z}.$$

Again using the vector operator ∇ , we may relate the field strength and the potential gradient by

$$\mathbf{E} = -\nabla V. \quad (\text{IX.8})$$

Combining Eqs. (IX.5) and (IX.8), we obtain Poisson's equation relating potential and charge density,

$$\nabla^2 V = -\frac{\rho_q}{\epsilon_0}, \quad (\text{IX.9})$$

where $\nabla^2 = \nabla \cdot \nabla$ is the Laplacian operator.

In cartesian coordinates this is

$$\frac{\partial^2 V}{\partial x^2} + \frac{\partial^2 V}{\partial y^2} + \frac{\partial^2 V}{\partial z^2} = -\frac{\rho_q}{\epsilon_0}.$$

The Laplace equation is simply the special case of this expression in which ρ_q is zero.

Moving charges can experience forces other than those they would experience at the same position without motion. These are *magnetic forces*, and the regions in which they occur are called *magnetic fields*. Magnetic forces depend on the magnitude of the charge, the magnitude and direction of the charge velocity, and the strength of the magnetic field. In general the magnetic force on a charge q at velocity \mathbf{u} is given by the vector product

$$\mathbf{F} = q\mathbf{u} \times \mathbf{B}. \quad (\text{IX.10})$$

Equation (IX.10) may be considered a definition of the magnetic field intensity vector \mathbf{B} , which is also called the *magnetic induction* or *magnetic flux density*. Its units, in the SI system, are

$$\frac{\text{newtons/coulomb}}{\text{meters/second}} = \frac{\text{volt-seconds}}{(\text{meter})^2} = \frac{\text{webers}}{(\text{meter})^2} \quad \text{or} \quad \text{Wb/m}^2.$$

The Tesla (T) is another common unit for magnetic flux density and is defined by

$$1 \text{ T} = 1 \text{ Wb/m}^2.$$

The earth's very weak magnetic field is only about 0.5×10^{-4} T, whereas "strong" permanent magnets may produce 0.5 to 1 T at a pole face, and very strong electromagnets may produce 100 T.

Since an electrical current consists of charges in motion, the force on a current-carrying element can be determined from the forces on the individual charges. The current density vector \mathbf{j} is defined as the rate per unit area at which charge travels through the current-carrying element. It is measured in coulombs per second per square meter (C/m^2) or amperes per square meter (A/m^2). The current density is related to the volume charge density ρ_q of the moving charges and their velocity \mathbf{u} by

$$\mathbf{j} = \rho_q \mathbf{u}. \quad (\text{IX.11})$$

The electromagnetic force $d\mathbf{F}$ on the charge $\rho_q dV$ contained within any increment of volume dV is

$$d\mathbf{F} = (\rho_q dV) \mathbf{u} \times \mathbf{B} = (dV) \mathbf{j} \times \mathbf{B}.$$

Therefore the force per unit volume is

$$\mathbf{F} = \mathbf{j} \times \mathbf{B}. \quad (\text{IX.12})$$

Magnetic fields are induced by electrical currents, according to the law of Biot and Savart. The contribution $d\mathbf{B}$ to the magnetic field at a point in space is related to the current I in an increment of conductor $d\mathbf{L}$ at another point by

$$d\mathbf{B} = \frac{\mu I}{4\pi r^2} d\mathbf{L} \times \mathbf{r}. \quad (\text{IX.13})$$

Here r is the distance between field point and conductor, and \mathbf{r} is a unit vector pointing from the current element to the field point. The proportionality constant μ is called the *permeability*. Its magnitude depends on the units employed and the medium separating the two points. In the SI system, the permeability of free space μ_0 has the value

$$\mu_0 = 4\pi \times 10^{-7} \text{ N/A}^2.$$

The permeability of ferromagnetic materials (such as nickel and iron) is much larger than μ_0 , but the permeability of most other materials is extremely close to μ_0 .

The magnetizing field vector \mathbf{H} is often used in place of \mathbf{B} . In vacuum it is defined simply as

$$\mathbf{H} \equiv \frac{\mathbf{B}}{\mu_0} \text{ (vacuum)},$$

with units in amperes per meter (A/m). The vector \mathbf{H} depends only on the distribution of applied currents. If a material medium is present, the magnetic field \mathbf{B} is related to \mathbf{H} by

$$\mathbf{B} = \mu_0 \mathbf{H} + \mathbf{M},$$

where \mathbf{M} is called the magnetization of the material. For many materials \mathbf{M} is proportional to \mathbf{H} (hence the name “magnetizing field”), so that \mathbf{B} may be expressed in the form

$$\mathbf{B} = \mu_0 \mathbf{H}(1 + x_m) = \mu \mathbf{H},$$

in which the constant x_m is called the magnetic susceptibility and μ is the permeability of the material in question. For some materials (permanent magnets, for example), \mathbf{M} is not a function of \mathbf{H} , so that this last expression is not always applicable. In any event, the local \mathbf{B} determines the magnetic force on a moving charge.

MOTION WITHIN ELECTRIC AND MAGNETIC FIELDS

It may be appropriate to treat electric and magnetic effects as observed from a reference frame that is in motion with respect to the devices that create the fields. Hence we should investigate the effect of motion between the “field” and the observer. Consider the motion of a charge q through a uniform electric field \mathbf{E} and magnetic field \mathbf{B} as seen by two observers, one at rest with respect to the magnetic field and the other at rest with respect to the charge. Both see the same charge and both observe the same forces on the charge (so long as the velocity is small compared to the velocity of light). For the observer at rest, Eq. (IX.10) and the definition of the electrostatic field intensity allow the total force on the particle to be written

$$\mathbf{F} = q(\mathbf{E} + \mathbf{u} \times \mathbf{B}).$$

To the moving observer the charge appears to have no velocity. The observer therefore must suppose that all this force is due to an “apparent” electrostatic field \mathbf{E}' .

Equating the two forces, $\mathbf{F} = q(\mathbf{E} + \mathbf{u} \times \mathbf{B}) = q\mathbf{E}'$, or

$$\mathbf{E}' = \mathbf{E} + \mathbf{u} \times \mathbf{B}. \quad (\text{IX.14})$$

The foregoing analysis intentionally avoids the effect of motion on the observation of the magnetic field by specifying that the charge has no motion relative to the moving observer. Consider next the force on a charge q moving with a velocity \mathbf{u}_q relative to the \mathbf{B} -field as seen by an observer moving with a different velocity \mathbf{u}_0 relative to the \mathbf{B} -field. Since the force does not depend on the motion of the observer,

$$\mathbf{F} = q[\mathbf{E}_0 + (\mathbf{u}_q - \mathbf{u}_0) \times \mathbf{B}_0] = q(\mathbf{E} + \mathbf{u}_q \times \mathbf{B}),$$

where \mathbf{E}_0 and \mathbf{B}_0 are the fields seen by the moving observer and $(\mathbf{u}_q - \mathbf{u}_0)$ is the charge velocity relative to the observer. By definition, \mathbf{E}_0 is the force per unit charge on a charge stationary with respect to the observer. Thus from Eq. (IX.14) we have

$$\mathbf{E}_0 = \mathbf{E} + \mathbf{u}_0 \times \mathbf{B}.$$

Therefore

$$q[(\mathbf{E} + \mathbf{u}_0 \times \mathbf{B}) + (\mathbf{u}_q - \mathbf{u}_0) \times \mathbf{B}_0] = q(\mathbf{E} + \mathbf{u}_q \times \mathbf{B})$$

or

$$(\mathbf{u}_q - \mathbf{u}_0) \times \mathbf{B}_0 = (\mathbf{u}_q \times \mathbf{B}) - (\mathbf{u}_0 \times \mathbf{B}) = (\mathbf{u}_q - \mathbf{u}_0) \times \mathbf{B},$$

and it follows that

$$\mathbf{B}_0 = \mathbf{B}.$$

Thus the motion of an observer in a magnetic field can be accounted for entirely by a change in the electrostatic field (so long as the observer's velocity is small compared with the speed of light).

PLASMAS

A *plasma* is an electrically conducting gas. It consists of a collection of neutral atoms, molecules, ions, and electrons. The number of ions and the number of electrons are equal so that, on the whole, electrical neutrality prevails. Because of its ability to conduct electrons, the plasma can be subjected to electromagnetic forces in much the same way as solid conductors of electric motors. Given the practicability of electromagnetic acceleration or deceleration, plasmas may be used as the working fluid in propulsion or electrical power generation. In such cases the plasma can generally be considered a fluid continuum. Nevertheless, in order to understand the conduction of electrons through such a fluid, it is necessary to consider the behavior of both the charged and the neutral constituent particles. This is especially so in the presence of magnetic fields.

Because the masses of electrons and ions differ by orders of magnitude, the acceleration of a singly charged electron by an applied electrostatic and magnetic field may be very different from that of a singly charged ion. Thus the rms velocities of electrons and ions may differ greatly from what one would expect in a mixture near thermal equilibrium. In the same mixture the electrons can be said to have a much higher temperature than the ions. In such a case the electrical conductivity of the plasma could be much higher than one would expect from the bulk temperature of the plasma. The relationship between current density and electric field strength in a plasma therefore requires understanding of the physical behavior of the electrons undergoing acceleration from applied fields and at the same time suffering frequent collisions from neutral particles and ions.

A P P E N D I X



LIST OF SYMBOLS

<i>Symbol</i>	<i>Definition</i>	<i>Symbol</i>	<i>Definition</i>
a	speed of sound	c^*	characteristic velocity
a_a	speed of sound in ambient air	C	chord
A	area	C_f	friction coefficient
A^*	flow area corresponding to $M = 1$	C_L	lift coefficient
A_a	capture area	C_p	pressure coefficient
A_e	exhaust area	c_{PR}	pressure recovery coefficient
A_s	wall surface area	C_d	drag coefficient
B, \mathbf{B}	magnetic field intensity	C_T	thrust coefficient
c	duct circumference	D	duct diameter
c, \mathbf{c}	absolute fluid velocity	D	characteristic size
c	specific heat of liquid	D_H	hydraulic diameter
c	velocity of light	e	electronic charge $(1.602 \times 10^{-19} \text{ C})$
c_p	specific heat at constant pressure per unit mass	e, e_0	internal energy per unit mass
\bar{c}_p	molar specific heat at constant pressure	eV	electron volt
c_v	specific heat at constant volume per unit mass	E	electric field intensity
\bar{c}_v	molar specific heat at constant volume	E'	electric field intensity relative to moving observer
c_r	radial velocity component	E_0	internal energy (including kinetic and potential energy)
c_θ	tangential velocity component	E	internal energy of a system (not including kinetic and potential energy)
c_z	axial velocity component	f	fuel-air ratio

<i>Symbol</i>	<i>Definition</i>	<i>Symbol</i>	<i>Definition</i>
F, \mathbf{F}	force	M	Mach number
F_θ	blade force in the tangential direction	M_{rel}	relative Mach number
F_z	blade force in the axial direction	\overline{M}	molecular weight
g	magnitude of local acceleration due to gravity	\mathbf{n}	a unit vector
g_e	magnitude of local acceleration due to gravity at earth's surface	n	number of moles
G	universal gravitation constant	n	particle density
G	average mass flow per unit area	n_e	number of rocket stages
h	enthalpy per unit mass	N	rotor speed
h_0	stagnation enthalpy per unit mass	N_0	Avogadro's number
\bar{h}	enthalpy per mole	n_s	specific speed
h	blade height	Nu	Nusselt number
h	angular momentum	p	pressure
h_f	heat transfer film coefficient	p_a	ambient pressure
h_g	heat transfer film coefficient on the gas side	p_e	exhaust pressure
h_L	heat transfer film coefficient on the liquid side	p_0	stagnation pressure
H	enthalpy	Pr	Prandtl number
H	shape factor, δ^*/θ	q	heat transfer per unit mass
H_{RPf}	change in enthalpy during transformation from reactants to products at temperature T_f	q	electric charge
I	electrical current	Q	collision cross section
I	total impulse	Q	volume flow rate
I_{sp}	specific impulse	Q	heat interaction
j	current density	Q_R	heat of reaction
k	Boltzmann's constant	Q_f	heat of formation
k	thermal conductivity	\mathbf{r}	unit vector
k_w	thermal conductivity of the wall material	r	radius
K_n	equilibrium constant (based on mole fractions)	r	burning rate
K_p	equilibrium constant (based on partial pressures)	r_c	combustor stagnation pressure ratio
L	length	r_d	diffuser stagnation pressure ratio
L	lift	r_n	nozzle stagnation pressure ratio
L	characteristic dimension	R	radius
L^*	length of duct required for friction to change M to unity	\overline{R}	gas constant
L^*	characteristic rocket chamber length	Re	universal gas constant
m	mass	s	Reynolds number
m_e	electron mass ($9.11 \times 10^{-31} \text{ kg}$)	\overline{s}	blade spacing
\dot{m}_a	airflow rate	S	entropy per unit mass
\dot{m}_f	fuel flow rate	S_s	entropy per mole
		St	entropy
		t	suction specific speed
		t_b	Stanton number
		T	time
		T_f	burning period
		T_L	temperature
		T_0	reference temperature
		T_w	liquid coolant temperature
			stagnation temperature
			wall temperature

<i>Symbol</i>	<i>Definition</i>	<i>Symbol</i>	<i>Definition</i>
T_∞	free-stream temperature	\mathcal{T}	thrust
T_{aw}	adiabatic wall temperature	\mathcal{T}_{pr}	thrust due to propeller
T_{wh}	wall surface temperature, hot side	\mathcal{V}	volume
T_{wc}	wall surface temperature, cold side		
u, \mathbf{u}	velocity, velocity component in the x -direction	α	absolute flow angle
u_e	exhaust velocity	α	Mach angle
u_i	velocity in the inlet plane	α	specific mass of power plant
u_{eq}	equivalent exhaust velocity	β	relative flow angle
u_{esc}	escape velocity	γ	specific-heat ratio
u_{circ}	velocity in a circular orbit	δ	boundary layer thickness
U	blade velocity	δ^*	displacement thickness
U	velocity just outside the boundary layer	ϵ	eddy viscosity
\bar{U}	bulk mean velocity	ϵ_0	permittivity
U_c	center-line velocity in a duct	ϵ	permittivity of free space
U_∞	free-stream velocity	ϵ	structural coefficient
v	velocity component in the y -direction	ϵ_i	eccentricity of conic
V	electrical potential	η	ionization potential
V_a	acceleration potential	η_b	thrust chamber efficiency
w, \mathbf{w}	relative velocity	η_c	burner efficiency
x	streamwise coordinate	η_d	adiabatic compressor efficiency
\mathbf{X}	body force per unit volume	η_g	adiabatic diffuser efficiency
y	coordinate normal to the wall	η_m	gear efficiency
z	coordinate in the axial direction	η_n	mechanical efficiency
z	height above an arbitrary datum	η_o	adiabatic nozzle efficiency
		η_p	overall efficiency
		η_p	propulsion efficiency
		η_t	pump efficiency
		η_{pc}	adiabatic turbine efficiency
		η_{pt}	polytropic compression efficiency
		η_{pr}	propeller efficiency
		η_{pt}	adiabatic power turbine efficiency
		η_{st}	stage efficiency
		η_{th}	thermal efficiency
		η_{ts}	total-to-static turbine efficiency
		η_{tt}	total-to-total turbine efficiency
		χ	mole fraction
		θ	angle
		θ	momentum thickness
		λ	mean free path
		λ	payload ratio
		μ	viscosity
		μ	permeability
		μ_0	permeability of free space
		ν	kinematic viscosity $\nu = \mu/\rho$
		ν	collision frequency

SCRIPT LETTERS

\mathfrak{D}	drag force
\mathfrak{N}_n	equilibrium constant based on number of moles
\mathfrak{R}	typical roughness height
\mathfrak{M}	mass
\mathfrak{M}_x	mass of payload
\mathfrak{M}_p	mass of propellant
\mathfrak{M}_s	structural mass
\mathfrak{M}_0	total initial mass
\mathfrak{M}_b	burnout mass
\mathfrak{P}	power
\mathfrak{P}_s	shear power, shaft power
$\dot{\mathfrak{Q}}$	heat transfer per unit area, per unit time
\mathfrak{R}	mass ratio

<i>Symbol</i>	<i>Definition</i>	<i>Symbol</i>	<i>Definition</i>
ξ	stagnation pressure loss coefficient	τ_t	turbulent shear stress
ρ	density	τ	torque
ρ_q	charge density	v	specific volume
σ	stress	ϕ	specific-heat function
σ	wave angle	ϕ	flow coefficient
σ_q	surface charge density	ϕ	work function
σ	plasma conductivity	ψ	pressure coefficient
τ	shear stress	Ω	rotational speed
τ_0	wall shear stress		

ANSWERS TO SELECTED PROBLEMS

CHAPTER 2

1. 3013 kJ/kg, no, 2725 m/s
4. (900 K) $p_e/p_1 = 0.3127$, $u_e = 820.2$
6. 4540 kW
9. 0.340
12. 2677 K
14. 3500 K
16. 6000 ppm
17. 756.3 kJ/kg

CHAPTER 3

1. $M = 3.057$, $\dot{m}/A = 735.9 \text{ kg/m}^2 \cdot \text{s}$
3. $(p_1 - p_2)/p_1 = 0.202, 0.806, 0.092, 0.202$
6. 0.380 MPa, 1147 K
8. 0.029 s
11. $\delta = 15^\circ$
12. $x = 0.0112D^*$

CHAPTER 4

2. $D = 0.0452 \text{ m}$
3. $Q = 7/8U\delta(2\Delta p/\rho U^2)^4$
6. $x = 0.3 \text{ m}$ ($\theta_1 = 0.23 \text{ mm}$), $\delta^* = 0.374 \times 10^{-4} \text{ m}$, $\theta = 0.158 \times 10^{-4} \text{ m}$
9. 4.8:1
10. 12.4 kPa, 60°
12. (a) 0.5, -0.25

CHAPTER 5

2. (a) 16,120 mi, (b) 1.9, 1582 mi
3. (a) 5417 N, (b) -2083, (c) 0
7. $f = 0.0178$, $u_e = 886 \text{ m/s}$, $\eta_O = 0.199$
8. TSFC = 0.0558 kg/kN · s (ramjet), 0.0252 kg/kN · s (turbojet)
11. Thrust ratio 3.31
15. Thrust ratio 1.033
16. TSFC = 0.0228, 0.0250 kg/kN · s
21. 59 kN (propeller)

CHAPTER 6

1. 0.81
2. 1.376, 1.079, 0.369
4. 0.82
6. 1.985
8. $M_4 = 0.707$, $p_{04}/p_{02} = 0.869$
10. 2262 K
11. $T_{04} = 1500$ K, $f = 0.00982$ kg/kg
14. $M_{exit} = 6.47$

CHAPTER 7

2. 671 kW, 10,200 rpm
4. 1.43, 41°
6. $F_z = 5313$ N, $F_\theta = 1916$ N
9. $\eta_c = 0.873$, $\eta_{pc} = 0.891$, $\eta_e = 0.885$
11. 32.6 kg/s, 6.10, 14,890 rpm, no
13. 69.4°, 0.68

CHAPTER 8

1. 1036 K ($R = 0.5$), 1050 K ($R = 0$)
2. 0.547
4. +10%, -0.125
5. (a) +0.052
7. (b) 0.614, (c) 52.4°, -67.1°, -0.368
9. 184 kJ/kg, 176.6 kJ/kg
11. 2 stages, $\beta_2 = 0$, $\beta_3 = 63.4$, $\Delta T_0 = 86.3^\circ$, 0

CHAPTER 9

1. 4.59, 5.92
3. 2.08:1
5. 7890 rpm
7. 0.988 kg/s, 0.258 m, 17,100 rpm, 0.502 m
8. 1.627, 1.273, 5.494, 2.328, 0.0117 m
11. 22,540, 19,090 rpm

CHAPTER 10

1. 1.451
3. -17.2 m/s^2
5. ≤ 288 s
7. 6000 to 7000 s

- 10.** 4105 m
11. (a) 8616 m/s, (b) 13,960 m/s, 131 days

CHAPTER 11

- 1.** (a) 202.5 s, (b) 2516 kg/s, (c) 0.774 m, (d) 1.952 m, (e) 15.61 kN
3. $38.75 \times 10^6 \text{ N/m}^2$
4. 0.0647, 0.342 m², 529 kN, 533 kN
6. 2415 m/s, $3679(1 - 0.002t)$ kg/s, $9.52(1 - 0.002t)$ MN
8. 0.00310 s
10. 101.7, 91.1 kg/s; 3589, 3598 m/s; 351.5, 294.2 kN
12. 19.9 MPa, 269 kN (sea level)
14. 1840 K, 0.727 mm
16. 32.3 MW/m²

CHAPTER 12

- 3.** 384.6 s
5. 6860 K, 2944 K, CO₂:CO:O₂ = 0.478, 0.018, 0.505 (mole fractions)
7. below 3800 K
9. 0.234 m, 0.098 m
11. 832:1, 39.7 s
13. 0.0862 MPa/s
17. 1.79 min

CHAPTER 13

- 2.** 47,640 kW
3. 0.0198
5. 3 stages, 28,500 rpm, 0.3 m
7. 0.78
10. $n_s \approx 2.5$, $d_s \approx 2.3$, $\eta > 0.8$
12. 0.186 MPa
13. $D \approx 0.32$ m, $N \approx 5200$ rpm

CHAPTER 14

- 1.** 2.84 cm
3. 5.92, 0.0351 m²
4. 1, $\sqrt{2}$, $(E + u_2B)/(E + u_1B)$
6. $I_{sp} = 5000$; 0.861, 35.1 N/MW
9. 248 eV/ion
11. (a) 0.000245 kg/s, 325 s, 0.783 N, (b) 276 s
13. 64%



I N D E X

- adiabatic, 27
adiabatic flame temperature, 44
afterburners, 165, 257
air, properties of ideal gas, 594
aircraft flight performance, 205
aircraft range, 152
aircraft-engine matching, 202
air-breathing engines, 141
Aldrin, Edwin, 9
Angular momentum, 277, 335, 708
 space vehicles, 496
 equation, 278
arcjets,
 configuration, 675
 dissociation, 677
 durability and efficiency, 676
 electrode heating, 678
Armstrong, Neil, 9
atmosphere, ICAO standard, 699
atmospheric density, dependence on altitude, 475
atom balance, 46
axial compressors, 275
 angular momentum, 335, 708
 axial velocity profiles, 324
 boundary layer separation, 289
 cascade losses, 318
 cascade testing, 309
 control volume, 279
 degree of reaction, 330
 dimensional analysis, 294
 entropy generation, 327
 examples, 282, 283
 flow instability, 300
 free vortex, 333
 inlet guide vanes, 308
 Lieblein diffusion effect, 316
 Mach number effect, 315, 317
 mass flow rate, 340
 mid-radius design constraints, 342
 off-design operation, 291
 performance examples, 297, 299
 performance parameters, 296
pressure ratio, 340
pressure rise, 287
radial equilibrium, 332, 343, 708
relative Mach number, 306, 707, 715
relative velocity, 283
Reynolds number effect, 314
rotating stall, 302
schematic, 281
shock losses, 328
stage configuration, 284
stage efficiency, 323
stage loading, 292
stage performance, 288
stage pressure ratio, 307
stage pressure rise, 305
stage temperature rise, 286
stage work, 282, 286
starting problem, 291
subsonic stage design, 343–345, 705, 710
surge, 298
tip clearance loss, 329
torque equation, 285
transonic stage, 348
transonic stage design, 345, 350, 713
work and pressure ratio, 706
axial pumps,
 Balje correlation, 639
 examples, 637
 flow coefficient, 638
 head coefficient, 638
 performance, 638
axial turbines,
 allowable tip speed, 392
 blade alloy strength, 384
 blade cooling, 393, 394, 399
 blade temperature, 394
 blowing parameter, 397
 centrifugal stress, 387, 408, 642
 compressor matching, 402
 cooled blade example, 395, 396
 cooling effectiveness, 396
 degree of reaction, 372, 719
 dimensional analysis of performance, 400

- directionally solidified blades, 385
 disc stress, 388
 efficiency correlation, 381
 efficiency definitions, 378
 entropy generation and efficiency, 382
 examples, 368, 413
 flow patterns, 377
 high work stages, 642
 mass flow rate, 409
 pressure ratio, 410
 rotor and stator blades, 369
 rotor blade stresses, 386
 shaft speed, 642
 single crystal blades, 385
 stage design, 407, 717, 719
 stage design performance, 411, 412
 stage efficiency, 381, 408
 stage work, 370, 373, 375
 turbine blade example, 397
 turbopump configurations, 640
 typical performance, 401
 velocity triangles, 371, 373, 374
 work, 410
 Zweifel criterion, 380
 axial velocity, axial compressor, 325
 Barber, John, 7
 beam power, 658
 Bernoulli equation, 70
 Biot and Savart law, 736
 black powder rockets, 7
 blowing parameter, axial turbine blades, 397
 body force, 28, 66
 bombardment ionization, 660, 664
 boundary layer, 95
 blade surface, 309
 compressor end wall, 303
 concept, 95
 displacement thickness, 535
 equations, 101, 103
 flat plate, 107
 frictional coefficient, 118
 heat transfer, 124
 Howarth solution, 109
 in axial compressors, 276, 303, 325
 in axial turbines, 371, 383
 in chemical rocket nozzles, 534, 544
 laminar, 107, 109, 110
 laminar sub-layer, 116, 119
 mixing length, 114
 momentum integral equation, 104, 105
 momentum thickness, 105, 123
 Moses method, 119
 pressure coefficient, 99, 223, 304
 pressure gradient, 97
 separation, 96, 97, 119, 122, 233, 290
 separation in cascades, 313
 separation in centrifugal rotors, 442
 separation in inducers, 436
 separation in radial diffusers, 448
 shape factor, 106, 123
 shear stress, 127
 shock interaction, 233
 thermal, 125
 three dimensional effect, 106
 Thwaites method, 110
 transition, 99
 turbulent, 111, 118, 119
 turbulent fluctuations, 112
 turbulent shear stress, 99, 113, 114
 velocity fluctuations, 114
 velocity profile, 119
 wall friction coefficient, 123
 Brequet's range formula, 152
 burning rates, solid propellants, 591
 bypass ratio, 20
 cascade aerodynamics, 309
 cascade testing,
 dimensional analysis, 311
 geometry, 310
 loss coefficient, 312, 314
 losses, 318
 Mach number effect, 315, 317
 Reynolds number effect, 314
 stall limits, 312
 typical results, 312
 cavitation, 630
 cavitation breakdown, 633
 centrifugal compressors,
 Coriolis acceleration, 440
 diffusers, 445, 449, 450
 effect of blade angle, 431
 effect of inlet swirl, 455, 724
 effect of tip speed, 433
 examples, 426, 427, 439, 444, 452
 impeller shape ratios, 459
 impeller size, 457
 inducers, 435
 inlet blade angle, 435
 limiting shaft speed example, 438
 losses due to blade clearance, 443
 performance, 453
 performance variables, 451
 pressure ratio, 432
 role in small gas engines, 425
 rotor exit slip velocity, 442
 rotor pressure rise, 429
 rotor velocity profile, 441
 shaft speed limitation, 455, 723

- stage design, 454, 723
stage design characteristics, 456
stage dynamics, 427
stage pressure ratio, 457
stage work, 430
vaneless space, 446
centrifugal pumps,
 Balje correlation, 629
 effect of blade angle, 623
examples, 527
flow coefficient, 624
heat coefficient, 624
incidence angle, 626
stage work, 622
characteristic velocity, 517
chemical equilibrium, 46
chemical reactions, 40
chemical rockets (see also liquid and solid propellant rockets), 572, 580
aerospike nozzle, 540
benefits of staging, 485
burning time, 477
burnout mass ratio, 479
characteristic velocity, 517
chemical reaction rate, 579
combustion instability, 606
convection (two-dimensional), 548
convective heat transfer, 544, 547
cooling methods, 541
examples, 479, 487, 488, 517, 542, 558
expansion-deflection nozzles, 538
frozen expansion, 580
liquid-propellants, 570
multistage performance, 482
non-equilibrium expansion, 578
nozzle area ratio, 520
nozzle back pressure, 536
nozzle length, 530
nozzle performance, 519
nozzles, 521, 523
optimum stage masses, 484, 729
payload ratio, 478
performance characteristics, 515
plug nozzles, 538
radiative heat transfer, 551
regenerative cooling, 541, 545
shaped nozzles, 531
single stage, 476, 478
solid-propellant heat transfer, 553
structural coefficient, 478
thrust coefficient, 518
thrust equation, 516
thrust loss with divergence, 522
typical configuration, 514
choking,
 frictional, 79
 in axial turbines, 404
isentropic flow, 71
 thermal, 77
chugging, 607
collision cross-section, 665
combustion instability, 606
combustion pressure,
 liquid propellant rockets, 520
 solid propellant rockets, 599
combustors,
 afterburner, 257, 258
 dissociation, 262
 gas turbine, 241–255
 ramjets, 257, 259, 262
 rockets, 581–607
 screaming in rockets, 607
 solid propellant burning stability, 601
composition of products, 45
compressor pressure ratio, 21
Congreve, William, 8
conservation equations, 28
continuity equation, 24, 25, 66
control mass (system), 23
control volume, 24
conversion factors, 690
cooling effectiveness, 396
cooling of turbine blades, 393
Coriolis acceleration, centrifugal compressor,
 440
Coriolis pressure gradient, 440
Coulomb's Law, 733
creep-rupture strength, 384
degree of reaction,
 axial compressor, 372
 axial turbine, 376
diffusers (see also inlets), 164, 220, 239
 centrifugal compressor, 445, 449
 oblique shock, 235
 radial vaneless, 447
 stalling pressure coefficient, 304
dimensional analysis,
 aircraft flight performance, 205
 axial compressor, 294
 axial turbines, 400
 cascade testing, 311
 centrifugal pump, 624
 engine, 198, 200, 203
 inducer, 634
 pipe flow, 116
drag coefficient, 205, 474
d'Alembert's paradox, 93
eccentricity, orbital, 496

- efficiency,
 combustion, 247
compressor, 170
compressor adiabatic, 319
compressor polytropic, 319
compressor stage, 319, 322
diffuser, 170, 225
electrostatic rocket, 674
ion beam, 658
ion rocket propellant, 551
nozzle, 170
overall, 151, 152, 187
propeller, 150
propulsion, 149, 178, 187
thermal, 19, 150, 187
total-to-total, 379
turbine, 170
turbine adiabatic, 379
turbine stage, 408
 turbine total-to-static, 379
electric field, strength, 734
electrical rockets,
 ion thruster, 494
low-thrust orbit, 504
optimum specific impulse, 492
payload ratio, 492
power plant specific mass, 491, 493
rationale, 490
types, 652
electromagnetic forces, 733, 735, 737
electromagnetic rockets, 652
electron bombardment, 10
electrostatic forces, 733
electrostatic rockets, 652, 654
 accel-decel electrodes, 670
 acceleration electrodes, 661
beam current, 656
characteristic performance, 657
efficiency, 673
energy loss per ion, 658, 673
example, 662
exhaust neutralization, 671
ion sources, 659
ionization chamber, 661
ionization potential, 659
magnetic field, 661, 663, 672
plane diode, 666, 667
schematic, 656
space-charge limited current, 668
thrust, 669
thruster performance, 671
electrothermal rockets (see also arc jet),
 652, 674
elliptical orbits, 496
endothermic, 40
energy,
 electrical, 28
 internal, 28
 kinetic, 28
 orbital, 497
 potential, 28
energy equation, 27, 28, 67, 126, 428
engines,
 air-breathing, 19, 141
 ramjet, 155
 turbofan, 142
 turbojet, 142
 turboprop, 19, 142
 turboshaft, 143
engine-aircraft matching, 202
enthalpy, 34
enthalpy-temperature diagram, 45
entropy, 31, 32
entropy generation, 327, 382
equilibrium composition, rocket fuels, 572
equilibrium constant, 48
erosive burning, 603
error function, 556
escape velocity, 499
exothermic, 40
Fanno line, 80, 84
film cooling, 397, 398
first law of thermodynamics, 27
flame propagation, 246
flameholders, 257
flow instability, 300
force, control volume, 25
free vortex, velocity, 333
fuel consumption,
 brake specific, 155
 per unit distance, 203
 ramjet, 159
 thrust specific, 153, 159, 166, 174, 197
fuel properties, gas turbine, 242
fuels, flammability limits, 244
gas constant, 33
gas generator, 142
Gauss's law, 734
Gibbs-Dalton law, 38
Gibb's inequality, 32
Goddard, Robert, 8
gunpowder, 8
Hahn, Max, 17
heat, 27
heat of formation, 40, 41, 42
heat of reaction, 44
heat transfer, 28
 film coefficients, 549

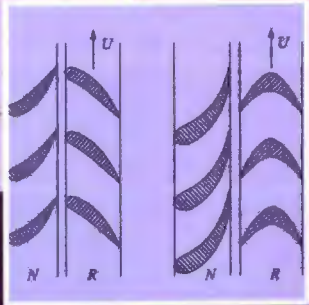
- heat sink cooling, 556
propagation of thermal wave, 555
heat-sink materials, thermal properties, 555
Hero of Alexandria, 6
Hohmann ellipse, 500
hub-tip ratio, 388
hydrogen, 10, 21
ICAO Standard Atmosphere, 699
impulse, 10
impulse turbines, 373, 640
inducers, 435, 630
inlets,
 buzz, 238
 capture area, 229
 choking, 228
 critical and subcritical flow, 240
 critical flow, 233
 external deceleration, 235
 external flow, 220
 flow pattern, 218
 flow separation, 221
 flow stability, 239
 internal flow, 219
Kantrowitz-Donaldson, 232
nacelle boundary layer, 224
Oswatitsch, 237
overspeeding, 228, 230
reverse nozzle diffuser, 227
spillage, 230
stagnation pressure ratio, 226
subsonic, 218
 supersonic, 227, 238
internal energy, 27
ion rocket (see also electrostatic rockets), 651
ionization, bombardment, 660
ionization potential, 659, 664, 665
ions, 10
irreversibility, 32
isentropic flow, 69
JANAF tables, 37
Kaufman ion thruster, 660
Kepler's law, 500
Lieblein diffusion factor, 316, 347
lift coefficient, 205, 311
liquid propellant rockets (see also chemical rockets and turbopumps), 572, 615
 chamber length, 584, 588
 combustion instability, 606
 droplet evaporation length, 585
 effect of pressure, 577
 equilibrium composition, 572
 equilibrium gas composition, 575
 fuel examples, 571
 fuel injection, 581
gas pressurization, 616
heat transfer, 541
non-equilibrium expansion, 578
performance data, 558
turbomachinery, 615
 typical performance, 573
liquid propellants, 570
Mach number, 18, 69, 153, 167, 203, 218, 233, 263, 315, 341
 centrifugal compressor inlet, 437
 centrifugal compressor outlet, 448
 centrifugal rotor outlet, 432
 turbine, 203
magnetic field, bombardment ionization, 661, 663
magnetic flux density, 735
magnetizing field vector, 736
mass conservation, 24
matching turbines and compressors, 402
maximum flow per unit area, 71
metal powders, solid propellants, 593
mixture of gases, 38
mole fraction, 39
momentum equation, 25, 26, 470
momentum flux integral, 30
Moses method, 119
NACA 65 series airfoils, 312
Navier-Stokes equations, 101, 122
net positive suction head, 632
Newton, Isaac, 6
Newton's law of gravitation, 496
Newton's second law, 25
non-equilibrium expansion, 578
nozzles,
 aerospike, 540
 chemical rockets, 519
 conical (chemical rockets), 521
departures from equilibrium composition, 579
discharge coefficient, 535
diverging supersonic, 520
effect of back pressure, 536
equilibrium expansion, 580
expansion at a corner, 526
expansion-deflection, 538
frictional effects, 534
frozen expansion, 580
gas turbine, 265, 266, 267
length, 530
method of characteristics, 524
optimum contour, 531, 533
plug, 538
shaped, 523
two-phase flow, 594

- Nusselt number, 128, 540
 Oberth, Hermann, 9
 one-dimensional flow, 65
 combined effects, 82
 frictional effect, 77, 80
 isentropic, 69, 71
 non-isentropic, 72
 stagnation change, 76
 stagnation temperature change, 74, 76
 step-wise calculation, 82
 orbital energy, 497
 orbital mechanics, 495
 orbital velocity, 499
 orbits, low-thrust rocket, 504
 partial pressure, 38
 payload ratio, chemical rocket, 479, 485
 perfect gas, 33
 perfect-fluid theory, 93, 94
 permeability, 736
 permittivity, 734
 photovoltaic cells, 11
 physical constants, 691
 pipe diffuser, centrifugal compressor, 450
 pipe flow,
 dimensional analysis, 116
 frictional coefficient, 117
 heat transfer, 129
 shear stress, 115
 velocity profile, 116
 planetary masses and orbits, 498
 plasmas, 738
 power generation,
 electrical, 491
 nuclear-space, 13
 nuclear-thermal, 13
 nuclear thermo-electric, 655
 photo-voltaic, 652
 solar-electric, 12
 Prandtl number, 127
 pressure coefficient,
 centrifugal compressor inlet, 436
 stator hub, 351
 propellers, 13, 141
 propfan concept, 143
 propfan engine, 195
 pulsed-magnetoplasma accelerator, 679
 pure substance, 32
 radial equilibrium, 332, 409
 radial equilibrium equation, 335
 radiator, 12
 ramjet engines, 155
 aerodynamic losses, 160
 combustor, 156
 fuel consumption, 162
 ideal, 157
 nozzles, 156
 schematic diagram, 156
 specific thrust, 162
 supersonic diffusers, 156
 ramjets, 16, 21
 Rayleigh line, 80, 84
 reaction turbines, 374
 reactive force, 4
 recovery factor,
 blade cooling, 541
 chemical rocket nozzles, 546
 diffusers, 450
 turbine blades, 393
 resistojet, 653
 reversible, 31
 Reynolds number, 100, 116, 117, 122, 128, 314
 rockets (see also chemical, electrical,
 liquid-propellant, and solid-propellant
 rockets),
 arc heating, 11
 burnout mass, 473
 black powder, 7
 chemical, 9
 drag effects, 474
 effect of back pressure, 471
 electrostatic, 10
 equivalent exhaust velocity, 473
 gravity effects, 474
 liquid propellant rockets, 572
 multistage, 481
 nuclear-heated-hydrogen rocket, 10
 optimum expansion, 471
 resistance heating, 11
 single stage, 478
 solid propellant rockets, 572
 specific impulse, 471
 terminal velocity, 486
 trajectory calculations, 475
 vehicle acceleration, 472
 rotating stall, 302
 rupture strength of alloys, 384
 SCRAMJET, supersonic combustion ramjet,
 21, 177, 263
 screaming, 607
 second law of thermodynamics, 31
 secondary flow, 325, 383
 semipermeable membranes, 46
 sensible enthalpy, 55
 shear power, 28
 shifting equilibrium, 573
 shocks,
 boundary layer interaction, 221, 233
 chemical rocket nozzles, 519

- conical, 88, 237
definition, 83
deflection angle, 87
downstream Mach number, 85, 88
lambda, 233
normal, 83, 85, 230
oblique, 85, 86, 235, 236
pressure ratio, 85
schlieren photographs, 233
supersonic inlet, 229
supersonic nozzle exit, 537
swallowing by area variation, 231
wave angle, 87
slip factor, centrifugal compressors, 443
solidity, 311
solid propellant rockets (see also chemical rockets), 572
burning rates, 591
burning stability, 601
combustion chambers, 598
combustion pressure, 599
effect of grain temperature, 602
erosive burning, 603
fuel oxidant mixtures, 589
grain designs, 600
heat sinks, 554
heat transfer, 553
internal pressure distribution, 604
metal powders, 593
regressive and progressive burning, 600
two-phase flow, 594
typical performance, 591
space power generation, solar, 12
specific diameter, 628
specific heats,
constant, 35
molar, 39
perfect gases, 34
variable, 36
specific heats of gases, formulae, 693
specific impulse, 471
chemical rockets, 573
electrostatic rocket, 656
optimum, 492
specific speed, 628
speed of sound, 69
stagnation enthalpy, 68
stagnation pressure, 68, 73
stagnation state, 67
stagnation temperature, 68
standard atmosphere, 699
standard sea-level pressure, temperature, 200
standard-day conditions, 451
STANJAN, 52
Stanton number, 130
state equation, 33, 37
steady flow, 26
stoichiometric coefficients, 49
stresses in turbine blades, 408
bending, 386
centrifugal, 386
thermal, 386
subsonic axial compressor stage, 336
suction specific speed, 632
supersonic combustion, 252
surface forces, 26
surge, 298
symbols, 739
system (control mass), 23
Système International d'Unités (S.I.), 25
temperature-entropy diagram, 36
thermal diffusivity, 128
thrust, 4, 8, 146
chemical rockets, 516
propeller, 14
rockets, 471
takeoff, 151
thrust coefficient, 518
thrust equation, 147, 532
thrust specific fuel consumption, 153
Thwaites method, 110
tip speed, turbine, 204
torque equation, 279
transonic axial compressor,
design variables, 352
examples, 348
measurements, 348, 354
wide chord blades, 349
transonic axial compressor stage, 345
tropopause, 204
turbine blades, 21
turbine engine performance, 203
turbofan engines, 16, 20, 142
bypass ratio, 177
cruise thrust, 186
cycle calculations, 185
examples, 179, 180, 181
fan and nozzle, 184
fan power, 184
mixing of exhaust streams, 182
performance, 197, 201
propulsion efficiency, 177
static thrust, 186
vertical lift, 183
turbojet engines, 16, 142
afterburner, 165, 167
choice of pressure ratio, 175
combustor, 172

- compressor, 168, 171
cruise thrust, 175
cycle calculations, 173
example, 165, 166
fuel consumption, 171, 174
nozzle, 172
operating line, 403
performance map, 403
schematic diagram, 164
static thrust, 174
thrust specific, 171
turbine, 168, 172
turbine inlet temperature, 166, 176
T-s diagram, 167, 169
turboprop engines, 19, 142, 189
examples, 191, 192
optimum nozzle thrust, 190
optimum pressure ratio, 193
performance, 199
schematic, 189
- turbopumps,
centrifugal pumps, 621
examples, 616, 619, 620, 621
inducers, 630
schematics, 618
specific diameter, 628
specific speed, 628
turboshaft engines, 143, 189, 195
vapor pressure, 632
velocity compound turbines, 640, 643
velocity impulse, interplanetary travel, 502
viscosity,
laminar, 95
turbulent, 128
von Ohain, Hans, 17
vortex street, 94
Whittle, Frank, 16
work, 27
Ziolkovsky, Konstantin, 8
Zweifel criterion, 380

Second Edition



Mechanics and Thermodynamics of Propulsion

Philip Hill | Carl Peterson

In this textbook, the authors show that a few fundamental principles can provide students of mechanical and aeronautical engineering with a deep understanding of all modes of aircraft and spacecraft propulsion. The book also demonstrates how these fundamental principles can lead directly to useful quantitative assessments of performance as well as possibilities for improvement. The second edition provides a wide range of new illustrative material on modern aircraft and rocket engines. The authors have also improved their explanations of pertinent physical phenomena and have introduced preliminary design procedures in this edition.

Sterling Book House, Mumbai
Ph# (91) 22612521
MECHANICS & THERMODYNAMICS OF PROPULSION

P. HILL



MRP Rs. 799

Rs. 401/-

L-0

9788131729519

9 788131 729519

www.pearsoned.co.in

This edition is manufactured in India and is authorized for sale only in India, Bangladesh, Bhutan, Pakistan, Nepal, Sri Lanka and the Maldives.